ACCSCIENCE PUBLISHING

International Journal of BIOPRINTING



ACCSCIENCE PUBLISHING
Volume 10 Issue 3, 2024
ISSN: 2424-8002 (Online) ISSN: 2424-7723 (Print)

ACCSCIENCE PUBLISHING

International Journal of Bioprinting

Print ISSN: 2424-7723

Online ISSN: 2424-8002

International Journal of Bioprinting is an international journal covering the technology, science and clinical application of the broadly defined field of Bioprinting. Bioprinting is defined as the use of 3D printing technology with materials that incorporate viable living cells or biological elements to produce tissue or biotechnological products. We are interested in the scientific topics spanning all stages of bioprinting process from concept creation to fabrication and beyond.



Scan to access website:

Scan to submit papers:

About the Publisher

AccScience Publishing is a publishing company based in Singapore. We publish a range of high-quality, open-access, peer-reviewed journals and books from a broad spectrum of disciplines.

Contact Us

Managing Editor
ijb.office@accscience.sg

AccScience Publishing
8 Burn Road, #15-03 Trivex, Singapore 369977.

Volume 10 Issue 3 • June 2024
ISSN 2424-7723 (print) ISSN 2424-8002 (online)

INTERNATIONAL JOURNAL OF BIOPRINTING

Editor-in-Chief

Chee Kai Chua

Singapore University of Technology and Design, Singapore

ACCSCIENCE PUBLISHING

Access Science Without Barriers

Full issue copyright © 2024 AccScience Publishing
All rights reserved. Without permission in writing from the publisher, this full issue publication in its entirety may not be reproduced or transmitted for commercial purposes in any form or by any means, electronic or mechanical, including photocopying, recording, or any information storage and retrieval system. Permissions may be sought from ijb.office@accscience.sg.

Article copyright © Respective Author(s)
See articles for copyright year. All articles in this full issue publication are open-access. There are no restrictions in the distribution and reproduction of individual articles, provided the original work is properly cited. However, permission to reuse copyrighted materials of an article for commercial purposes is applicable if the article is licensed under Creative Commons Attribution-NonCommercial License. Check the specific license before reusing.

INTERNATIONAL JOURNAL OF BIOPRINTING

ISSN: 2424-7723 (print)
ISSN: 2424-8002 (online)

Editorial and Production Credits

Publisher: AccScience Publishing
Managing Editor: Cathy Huang
Editorial Assistant: Flora Kang
Production Editor: Puvanesswaray Ramakrishnan
Special Issue Commissioning Editors: Shirley Song, Terra Shi
Article Layout and Typeset: Bsmart Publishing (India)

For all advertising queries, contact ijb.office@accscience.sg.

Supplementary file

Supplementary files of articles can be obtained at https://accscience.com/journal/IJB/10/3.



Disclaimer

AccScience Publishing is not liable to the statements, perspectives, and opinions contained in the publications. The appearance of advertisements in the journal shall not be construed as a warranty, endorsement, or approval of the products or services advertised and/or the safety thereof. AccScience Publishing disclaims responsibility for any injury to persons or property resulting from any ideas or products referred to in the publications or advertisements. AccScience Publishing remains neutral with regard to jurisdictional claims in published maps and institutional affiliations.

International Journal of Bioprinting

Editorial Board

Editor-in-Chief

Chee Kai Chua
Singapore University of Technology and Design, Singapore

Associate Editors

Maling Gou
Sichuan University, China

Jiankang He
Xi'an Jiaotong University, China

Liliang Ouyang
Tsinghua University, China

Wai Yee Yeong
Nanyang Technological University, Singapore

Editorial Board Members*

Jason A. Burdick, *USA*

Shweta Agarwala, *Denmark*

Eben Alsberg, *USA*

Anthony Atala, *USA*

Douglas B. Chrisey, *USA*

Amit Bandyopadhyay, *USA*

Andrea Barbetta, *Italy*

Mikhael Bechelany, *France*

Martin Birchall, *UK*

Paulo J.D.S. Bártolo, *Singapore*

Christian Celia, *Italy*

Boris Chichkov, *Germany*

Gianluca Ciardelli, *Italy*

Jeremy Crook, *Australia*

Rui Domingues, *Portugal*

Dennis Douroumis, *UK*

Tal Dvir, *Israel*

Eleonora Ferraris, *Belgium*

Gunter Finkenzeller, *Germany*

Sanjay Garg, *Australia*

Manuela Gomes, *Portugal*

Brunella Grigolo, *Italy*

Yongqiang Hao, *China*

Charlotte Hauser, *Saudi Arabia*

Mei He, *USA*

Dong Nyoung Heo, *Korea*

Geun Hyung Kim, *Korea*

Richard James Bibb, *UK*

Jingchao Jiang, *China*

Qing Jiang, *China*

Hyun-Do Jung, *Korea*

Ali Khademhosseini, *USA*

Dimitrios A. Lamprou, *UK*

Khoon Lim, *Australia*

Fengyuan Liu, *UK*

Veronica MacChi, *Italy*

Elena Martínez Fraiz, *Spain*

Laurence Meagher, *Australia*

Nikolaos Michailidis, *Greece*

Joaquim Miguel Oliveira, *Portugal*

David K. Mills, *USA*

Vladimir Mironov, *Russia*

Mario Moisés Alvarez, *Mexico*

Maurice N Collins, *Ireland*

Makoto Nakamura, *Japan*

Roger Narayan, *USA*

Insup Noh, *Korea*

Ali Nokhodchi, *UK*

Aleksandr Ovsianikov, *Austria*

Sang-Hyug Park, *Korea*

Alokesh Pramanik, *Australia*

Aldo R. Boccaccini, *Germany*

Michael Raghunath, *Switzerland*

Shinji Sakai, *Japan*

Thomas Scheibel, *Germany*

Cijun Shuai, *China*

Swee Leong Sing, *Singapore*

Kedong Song, *China*

Jie Sun, *China*

Ergün Süleyman, *Germany*

Ibrahim Tarik Ozbolat, *USA*

Savas Tasoglu, *Turkey*

S. Vijayavenkataraman, *UAE*

Giovanni Vozzi, *Italy*

Liqiang Wang, *China*

Seung-Schik Yoo, *USA*

Barbara Zavan, *Italy*

Yi Zhang, *China*

Yu Shrike Zhang, *USA*

Assistant Editor

Jia An, *Singapore*

Youth Editorial Board

Yiting Lei, *China*

Lan Li, *China*

Huixin Liang, *China*

Wei Long Ng, *Singapore*

Yogendra Pratap Singh, *USA*

Thiago Domingues Stocco, *Brazil*

Hui Zhu, *China*

*Editorial Board Members as of February 28, 2024

ACCSCIENCE PUBLISHING

Volume 10 | Issue 3 | June 2024 | Page 1 – 617 |

International Journal of Bioprinting

https://accscience.com/journal/IJB

CONTENTS

REVIEW ARTICLES

1 **Exploring the potential of supramolecular hydrogels as advanced bioinks for bioprinting and biomedical applications**
Gopinathan Janarthanan, Shyam Kokkattunivarthil Uthaman, Karthik Murugesh, Sanjairaj Vijayavenkataraman

38 **Techniques, mechanisms, and application of 3D-printed biodegradable metals for bone regeneration**
Lingxiao Wang, Yang Liu, Zhipeng Fan

61 **The promising applications of 3D printing technology in neurotrauma**
Wenbo He, Chongxi Xu, Wenbi Wu, Yuchen Chen, Jingxuan Hou, Zhouhaoran Chen, Jianguo Xu, Maling Gou, Yu Hu

86 **Vascularization strategies for human skin tissue engineering via 3D bioprinting**
Arvind Kumar Shukla, Dongjun Lee, Sik Yoon, Minjun Ahn, Byoung Soo Kim

116 **Challenges and perspectives of liver tissue engineering: From cell therapy to bioprinting**
Julio Rodríguez-Fernández, M. Teresa Donato, Gloria Gallego-Ferrer, Laia Tolosa

141 **3D-bioprinted bone for regenerative medicine: Current concepts and future perspectives**
Borbála Lovászi, Diána Szűcs, Tamás Monostori, Lajos Kemény, Zoltán Veréb

172 **Current advances of 3D-bioprinted microfluidic models with hydrogel bioinks and their applications in drug screening**
Jianing Li, Na Li, Bo Liu, Shen Li, Hangyu Zhang

RESEARCH ARTICLES

197 **Polydopamine chelating strontium on graphene oxide enhances the mechanical and osteogenic induction properties of PLLA/PGA bone scaffold**
Feng Yang, Yun Lin, Saipu Shen, Yulong Gu, Cijun Shuai, Pei Feng

214 **Preparation and characterization of angled dual- and multi-branched nerve guidance conduits**
Yinchu Dong, Wenbi Wu, Haofan Liu, Xuebing Jiang, Li Li, Li Zhang, Yi Zhang, Jing Luo, Maling Gou

228 **Increased stiffness of extracellular matrix enhanced chemoresistance in 3D-bioprinted ovarian cancer model**
Ying Shan, Mingchang Pang, Liqian Wang, Yixin Mao, Ruiyi Yan, Chang Zhou, Jingyuan Ji, Yilei Mao, Ying Jin, Huayu Yang

245 **Distinct toxicity of microplastics/TBBPA co-exposure to bioprinted liver organoids derived from hiPSCs of healthy and patient donors**
Shaojun Liang, Yixue Luo, Yijun Su, Dawei Zhang, Shi-jie Wang, Mingen Xu, Rui Yao

261 **3D-bioprinted bone scaffolds incorporating SR1 nanoparticles enhance blood vessel regeneration in rat calvarial defects**
KyeongWoong Yang, Donghyun Lee, Kyoung Ho Lee, Woong Bi Jang, Hye Ji Lim, Eun Ji Lee, Hojun Jeon, Donggu Kang, Gi Hoon Yang, KyeongHyeon Lee, Yong-Il Shin, Sang-Cheol Han, SangHyun An, Sang-Mo Kwon

277 **Design and optimization of 3D-bioprinted cell-laden scaffolds in dynamic culture**
Jing Li, Feng Chen, Meixia Wang, Xiaolong Zhu, Ning He, Na Li, Haotian Zhu, Xiaoxiao Han

300 **3D-bioprinted hydrogels with instructive niches for dental pulp regeneration**
Nazi Zhou, Shunyao Zhu, Xinlin Wei, Xueyuan Liao, Yu Wang, Yue Xu, Liyun Bai, Haoyuan Wan, Li Liu, Jiumeng Zhang, Ling Zeng, Jie Tao, Rui Liu

322 **Frequency response analysis and *in vitro* verification of 3D-printed ossicular replacement materials**
Jingbin Hao, Yin Zhu, Ding Shen, Md Thowfiqure Rahman, Yinxin Kou, Houguang Liu

340 **A parallel multilayered neurovascular unit-on-a-chip for modeling neurovascular microenvironment and screening chemotherapeutic drugs**
Yuanyuan Xu, Dongsheng Kong, Ting Zhang, Zhuo Xiong, Wei Sun

359 Multi-physical field control piezoelectric inkjet bioprinting for 3D tissue-like structure manufacturing
Huixuan Zhu, Run Li, Song Li, Kai Guo, Chuang Ji, Feiyang Gao, Yuejing Zheng, Runyang Zhu, Heran Wang, Liming Zhang, Lianqing Liu, Xiongfei Zheng

379 Optimizing additively manufactured mouthguards: An evaluation of multi-layer materials for improved shock absorption and durability compared to conventionally fabricated samples
Chenyuan Li, Takahiro Wada, Yumi Tsuchida, Kairi Hayashi, Gen Tanabe, Toshiaki Ueno, Hiroshi Churei

394 A new solution for *in situ* monitoring of shape fidelity in extrusion-based bioprinting via thermal imaging
Simone Giovanni Gugliandolo, Egon Prioglio, Davide Moscatelli, Bianca Maria Colosimo

408 Enhancing cell proliferation in three-dimensional hydrogel scaffolds using digital light processing bioprinting technology
Yejin Choi, Jeong Wook Seo, Goo Jang, Woo Kyung Jung, Yong Ho Park, Hojae Bae

426 Effects of modeling strategies of triply periodic minimal surface on the mechanical properties and permeability of biomedical TC4 porous scaffolds
Binghao Wang, Chengliang Yang, Chuanchuan Zheng, Miao Luo, Zheng Shi, Yuting Lv, Wen Peng, Liqiang Wang

442 Hydrogel bioink formulation for 3D bioprinting: Sustained delivery of PDGF-BB and VEGF in biomimetic scaffolds for tendon partial rupture repair
Sandra Ruiz-Alonso, Jorge Ordoyo-Pascual, Markel Lafuente-Merchan, Fátima García-Villén, Myriam Sainz-Ramos, Idoia Gallego, Laura Saenz-Del-Burgo, Jose L. Pedraz

468 3D bioartificial stretchable scaffolds mimicking the mechanical hallmarks of human cardiac fibrotic tissue
Mattia Spedicati, Francesca Tivano, Alice Zoso, Janira Bei, Mario Lavella, Irene Carmagnola, Valeria Chiono

489 Stereolithography 3D printing of microgroove master moulds for topography-induced nerve guidance conduits
Hexin Yue, Xuzhao Liu, Kejian Hou, Cian Vyas, Paulo Bartolo

508 Drop-on-demand bioprinting: A redesigned laser-induced side transfer approach with continuous capillary perfusion
Mahyar Erfanian, Ahad Mohammadi, Hamid Ebrahimi Orimi, Jennyfer Zapata-Farfan, Joe Saade, Michel Meunier, Bruno Larrivée, Christos Boutopoulos

519 Tuning the mechanical responses of 3D-printed ankle-foot orthoses: A numerical study
Chenxi Peng, Phuong Tran, Simon Lalor, Oren Tirosh, Erich Rutz

532 Engineered 3D-printed poly(vinyl alcohol) vascular grafts: Impact of thermal treatment and functionalization
Ionut-Cristian Radu, Derniza Cozorici, Madalina-Ioana Necolau, Roxana Cristina Popescu, Eugenia Tanasa, Laurentia Alexandrescu, Catalin Zaharia, Rafael Luque

557 Bioprinting native-like 3D micro breast cancer tissues utilizing existing cancer cell lines
Brian E. Grottkau, Zhixin Hui, Yonggang Pang

572 4D printing and simulation of body temperature-responsive shape-memory polymers for advanced biomedical applications
Dahong Kim, Kyung-Hyun Kim, Yong-Suk Yang, Keon-Soo Jang, Sohee Jeon, Jun-Ho Jeong, Su A Park

588 Development of a five-axis printer for the fabrication of hybrid 3D scaffolds: From soft to hard phases and planar to curved surfaces
Michael Kainz, Isabel Caetano da Silva, Paula Schumann, Julia Kastner, Thomas Voglhuber, Lukas Hartung, Sandra Haas, Milan Rathod, Adrián Martínez Cendrero, Tilo Dehne, Daniel Seitz, Gunpreet Oberoi, Erik Kornfellner, Andrés Díaz Lantada, Francesco Moscato, Elena Guillén

604 Early monitoring for 3D-printed patient-specific mandible reconstructive implant biomechanical behavior under different occlusal conditions using a wireless module system
Cheng-Hsien Wu, Hsiao-Kuan Wu, Pei-Jung Tsai, Chun-Li Lin

ACCSCIENCE PUBLISHING

International Journal of Bioprinting

REVIEW ARTICLE

Exploring the potential of supramolecular hydrogels as advanced bioinks for bioprinting and biomedical applications

Gopinathan Janarthanan[1†], Shyam Kokkattunivarthil Uthaman[2†], Karthik Murugesh[2], and Sanjairaj Vijayavenkataraman[1,3*]

[1]The Vijay Lab, Division of Engineering, New York University Abu Dhabi, Abu Dhabi, United Arab Emirates

[2]Research and Development Department, EcoWorld Pharm Co. Ltd, Damyang-gun, Jeollanam-do, South Korea

[3]Department of Mechanical & Aerospace Engineering, Tandon School of Engineering, New York University, Brooklyn, New York, United States of America

Abstract

Supramolecular hydrogels have emerged as versatile bioinks in tissue engineering, providing a promising avenue for constructing intricate and functional biological structures. This paper explores the significance of employing supramolecular hydrogels as advanced bioinks for three-dimensional bioprinting and various biomedical applications. Supramolecular hydrogels possess distinct and tunable characteristics attributed to the dynamic nature of supramolecular host–guest interactions alongside interactions based on DNA and peptides, which increases their significance in tissue engineering. These interactions are essential for enhancing the mechanical properties, injectability, printability, post-printing stability, and biocompatibility of hydrogels. Gelation kinetics and rheological properties can also be manipulated to suit specific printing techniques. Furthermore, these supramolecular interactions facilitate the incorporation of bioactive molecules to regulate cellular behavior and tissue development. These diverse interactions observed in supramolecular hydrogels underscore their ability to emulate the dynamic and responsive nature of the cell's extracellular matrix, which fosters cell growth, adherence, and differentiation. This review specifically highlights the cucurbit[*n*]uril and cyclodextrin-based host–guest supramolecular hydrogels, as well as peptide and DNA-based supramolecular structures as advanced bioinks and brief examples of their applications in various biomedical fields. These advanced bioinks would drive the development of intricate tissue constructs with enhanced biomimicry and therapeutic potential in regenerative medicine.

Keywords: Supramolecular hydrogels; Advanced bioinks; Host–guest; 3D bioprinting; DNA bioinks; peptide bioinks

[†]These authors contributed equally to this work.

***Corresponding author:**
Sanjairaj Vijayavenkataraman (vs89@nyu.edu)

Citation: Janarthanan G, Uthaman SK, Murugesh K, Vijayavenkataraman S. Exploring the potential of supramolecular hydrogels as advanced bioinks for bioprinting and biomedical applications. *Int J Bioprint.* 2024;10(3):3223. doi: 10.36922/ijb.3223

Received: March 20, 2024
Accepted: May 2, 2024
Published Online: June 11, 2024

Copyright: © 2024 Author(s). This is an Open Access article distributed under the terms of the Creative Commons Attribution License, permitting distribution, and reproduction in any medium, provided the original work is properly cited.

Publisher's Note: AccScience Publishing remains neutral with regard to jurisdictional claims in published maps and institutional affiliations.

1. Introduction

Hydrogels are three-dimensional (3D)-crosslinked networks of polymers formed from versatile materials. They are known for their exceptional ability to absorb water

or fluids while retaining their structure, resembling soft biological tissue characteristics. They find applications in fields such as food processing, adhesives, and biomedicine, including drug delivery and tissue engineering.[1] Their high water content and flexibility make them biocompatible and capable of controlled substance release. Hydrogels can also respond to various stimuli like pH, temperature, and electromagnetic fields.[2] Overall, hydrogels can be used in a variety of applications because of their special physical and chemical characteristics.[3,4] Supramolecular hydrogels are pliable substances that consist of self-organized molecules or nanofibers joined by feeble and reversible non-covalent interactions, including van der Waals forces, electrostatic interactions, hydrogen bonding, metal–ligand coordination, π–π stacking, and host–guest recognition.[5,6] They are composed of a new type of non-covalently crosslinked polymer chains in a 3D framework which increases structural adaptability and modifies overall performance.[7,8] Their superior versatility, adaptability, dynamic nature, tunability, and high-end biocompatibility set them apart from conventional hydrogels in biomedical applications.

Supramolecular hydrogels can be divided into three primary types based on the size of their crosslinked networks: macrohydrogels, microhydrogels, and nanohydrogels.[7-9] Supramolecular hydrogels having indefinite crosslinked networks on a macroscale are called macrohydrogels. These hydrogels, formed through multivalent non-covalent interactions, demonstrate significant potential as injectable scaffolds for tissue regeneration and repair, as well as the regulated administration of medications, genes, and proteins. Microhydrogels and nanohydrogels have similar internal structures to macrohydrogels but differ in terms of reactivity and size. Microhydrogels have sizes ranging from 1 to 100 μm, similar to human cells, while nanohydrogels, with sizes below 200 nm, can be effectively endocytosed by cells, providing a platform for targeted delivery of therapeutic agents. Nanohydrogels have potential in bioimaging and drug delivery applications, and controlling their size becomes crucial for optimizing their characteristics, internalization processes, cytotoxicity, and medicinal effectiveness.[9] Modifying the molecular ratio of substances has proven successful in achieving size control of nanohydrogels, enabling the development of size-regulated supramolecular carriers for cancer treatment and diagnosis.[10,11] Further research and advancements in this field are expected to unlock the full potential of nanohydrogels in biomedical applications.[12]

Bioinks were reported with predominantly crosslinking strategies, such as Ca^{2+} for alginate-based gels, ultraviolet (UV) light-crosslinking for methacrylate-based bioinks like methacrylated gelatin (GelMA), enzyme-based, or Schiff's base crosslinking. Instead of these, using supramolecular chemistry like host–guest interactions and others can improve the overall properties and structural performance of the bioinks to a large extent. These supramolecular chemistry-based hydrogels exhibit multifunctionality, boasting a diverse array of attributes that contribute to their versatility and efficacy compared to conventional bioinks. Although several supramolecular hydrogels are reported for tissue engineering applications, this review focuses on specific examples of supramolecular chemistries exclusive to 3D bioprinting. Particularly, we emphasize cucurbit[*n*]uril (CB[*n*]) and cyclodextrin (CD)-based host–guest supramolecular hydrogels, as well as peptide and DNA-based supramolecular structures, for 3D bioprinting and biomedical applications. Additionally, we discuss some of the challenges and prospects associated with developing supramolecular hydrogels and recommend potential research avenues for future studies.

2. Different types of supramolecular hydrogels

The chemistry and synthesis methods involve designing and selecting suitable building blocks, including crosslinking precursors or interacting material components, followed by optimizing the assembly conditions.[7,8] Supramolecular hydrogels can be categorized into three primary types according to the building blocks that were used: (i) molecular hydrogels, (ii) supramolecular polymeric hydrogels, and (iii) supramolecular hybrid hydrogels.[13]

2.1. Molecular hydrogels

Molecular hydrogels encompass the self-assembly of low-molecular-weight building blocks, such as peptide amphiphiles (PAs) or synthetic molecules with supramolecular motifs. These components form structures resembling fibers through non-covalent interactions. The resulting supramolecular nanofibers undergo non-covalent crosslinking or entanglement, which creates a 3D network. These hydrogels are characterized by degradation in physiological conditions and a responsiveness to biological stimuli.[7,8,14,15]

2.2. Supramolecular polymeric hydrogels

Multitopic conventional polymer chains functionalized with complementary supramolecular motifs are crosslinked to generate supramolecular polymeric hydrogels by multivalent non-covalent bonding. The constituents can be organic molecules, peptides, or polymers that exhibit direct or indirect non-covalent bonding, including van der Waals forces, electrostatic interactions, metal–ligand coordination, hydrogen bonding, and π–π stacking.[5,16] Host–guest supramolecular polymeric hydrogels offer

flexibility, biostability, and the capacity to change their structure and characteristics in response to external stimuli.[17,18] Hydrogen bonding offers specificity and directionality, enabling the formulation of smart hydrogels with pH-responsive properties.[19,20] Conversely, in polar liquids, hydrogen bonds can readily dissociate. Metal–ligand coordination allows the formulation of robust hydrogels with superior photoelectric capabilities. Host–guest recognition, particularly using CD and CB[*n*] macrocycles, provides a powerful platform for formulating biocompatible hydrogels with diverse biological applications. Interaction of oppositely charged polyelectrolytes through electrostatic forces can result in strong materials, while incorporating a neutral hydrophilic block prevents phase separation and yields supramolecular hydrogels.[21] Combining multiple non-covalent interactions in one system enhances the biostability, stimuli-responsiveness, and mechanical characteristics of the resultant hydrogels.[5] The growing interest in supramolecular hydrogels can be observed from the recent trend in the publications and their specific application in various fields (Figure 1A and B). Different combinations of various host molecules and their corresponding guest molecules are presented in Figure 1C.

The physiochemical characteristics and macroscopic behaviors of the resulting hydrogel materials are largely dependent on the thermodynamic and molecular dynamic parameters of supramolecular crosslinkages; crosslink density is influenced by the equilibrium constant; and the dynamic character of crosslinkages among the polymer chains is influenced by kinetics. By precisely controlling the synthesis conditions, such as the temperature, pH, concentration, and solvent selection, supramolecular gelation can be achieved to form a stable and functional supramolecular hydrogel. These hydrogels have potential uses in tissue engineering and regulated drug delivery.[5]

2.3. Supramolecular hybrid hydrogels

Supramolecular hybrid hydrogels incorporate metal nanostructures (e.g., gold or silver nanoparticles [NPs]) or inorganic elements (e.g., graphene, clays, carbon nanotubes, quantum dots, etc.) into the crosslinked networks. Furthermore, they introduce additional functionalities, such as fluorescence, antibacterial activity, chiroptical properties, and electrical conductivity.

Overall, supramolecular hydrogels offer versatile platforms for biomedical applications, and their specific types, including molecular, polymeric, and hybrid hydrogels, provide distinct advantages and functionalities that can be customized for different uses in tissue engineering, drug delivery, and other biomedical domains.[5] Apart from the common mixing and self-assembling, additional triggering can also be provided, such as pH or temperature manipulation, enzymatic reactions, electric fields, or other forms of external stimuli. The functional qualities of the specific hydrogel, in terms of its mechanical properties, simplicity of assembly, broad tunability, gelation kinetics, stimuli responsiveness, biocompatibility, and other aspects, will undoubtedly be determined or modified by these additional inducers.[22]

3. Supramolecular hydrogels properties and characteristics

3.1. Mechanical properties

Supramolecular hydrogels exhibit remarkable mechanical properties, like toughness, elasticity, and stiffness, because of their 3D non-covalent crosslinked networks, unlike conventional polymer hydrogels (Figure 2). However, their mechanical weakness and susceptibility to fracture limit their application as structural biomaterials. Strategies, such as increasing crosslink density, combining multiple non-covalent interactions, and incorporating inorganic nanomaterials, have been explored to enhance hydrogel toughness and other mechanical properties. For example, the addition of chemical crosslinkers, utilization of polyampholytes, and hybridization with clay nanosheets have demonstrated improved toughness and transparency in supramolecular hydrogels. With their non-covalent crosslinked networks, they exhibit mechanical characteristics that are highly tunable and react rapidly to different environmental stimuli, enabling controlled swelling or dissociation. These hydrogels have enormous potential for regulated drug delivery and as biosensors, particularly for enzyme-responsive systems with targeted tumor site delivery in cancer therapy.[5] Self-healing is the remarkable ability to repair damage and restore functionality in aquatic environments when subjected to an appropriate external stimulus. In contrast to hydrogels composed of covalently connected polymers, these non-covalent supramolecular interactions are reversible, allowing these materials to repetitively heal at the molecular level and fully restore their original material properties.[6] From a 3D bioprinting perspective, this property is one of the ideal requirements for 3D bioinks.

The degree of swelling and the retention of water in hydrogels are determined by the crosslinking density and hydrophilic properties of the polymer chains.[7,8] Supramolecular hydrogels are formed from the physical entanglement of supramolecular nanofibers or supramolecular crosslinking of hydrophilic polymeric building blocks, both of which have the ability to retain substantial quantities of water in aqueous environment. However, recent advancements have allowed the

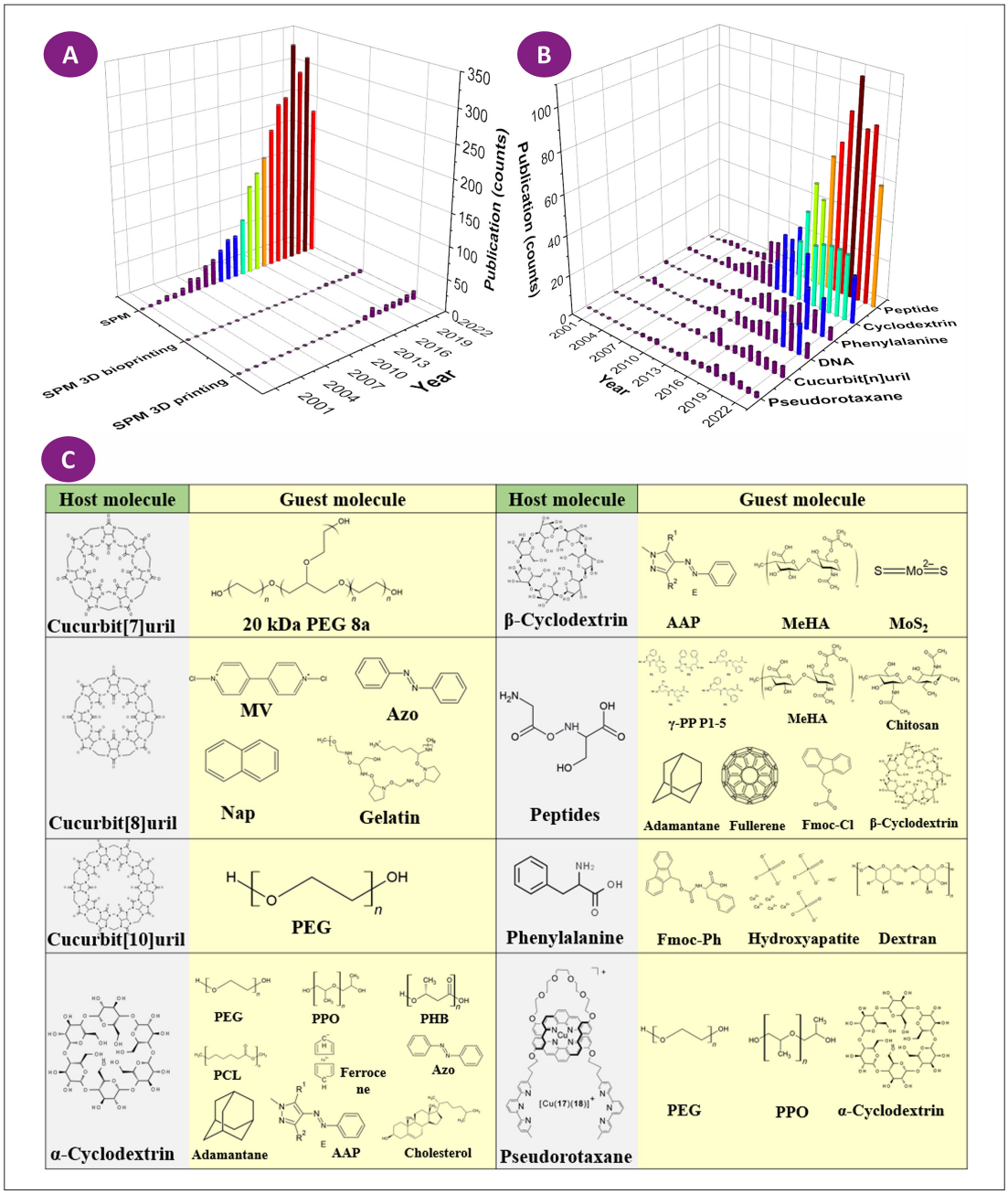


Figure 1. Recent publication trends and examples of host–guest molecules involved in the supramolecular interactions. (A) Recent publication trends of different supramolecular hydrogels, based on a PubMed search of keywords: "supramolecular hydrogels," "supramolecular hydrogel bioinks 3D bioprinting," and "supramolecular hydrogel 3D printing." (B) Publication trend of specific types of supramolecular hydrogels using appropriate keywords. (C) Schematic representation of the dynamic interactions of host–guest chemistry and functional groups involved. Abbreviations: PEG: Poly(ethylene glycol); MV: Methyl viologen; Nap: Naphthalene; Azo: Azobenzene; PPO: Poly(propylene oxide); PHB: Poly-(R)-3-hydroxybutyrate; PCL: Polycaprolactone; AAP: Arylazopyrazole; MeHA: Methacrylated hyaluronic acid; MoS_2: Molybdenite; γ-PP P1-P5: γ-Phenylalanine peptides 1 to 5; Fmoc-Cl: Fluorenylmethoxycarbonyl chloride; Fmoc-Ph: Fluorenylmethoxycarbonyl protected phenylalanine; SPM: Supramolecular hydrogel.

development of ultrahigh concentrations of water (up to 99.7 wt%) in supramolecular hydrogels by incorporating commercially available polymers and conjugation techniques.[7,8,22] The water-retention ability of these hydrogels not only provides aqueous compatibility for biomedical applications but also contributes to lubricity and facilitates the diffusion of solutes. Furthermore, the possibility of loading various pharmaceutical agents and

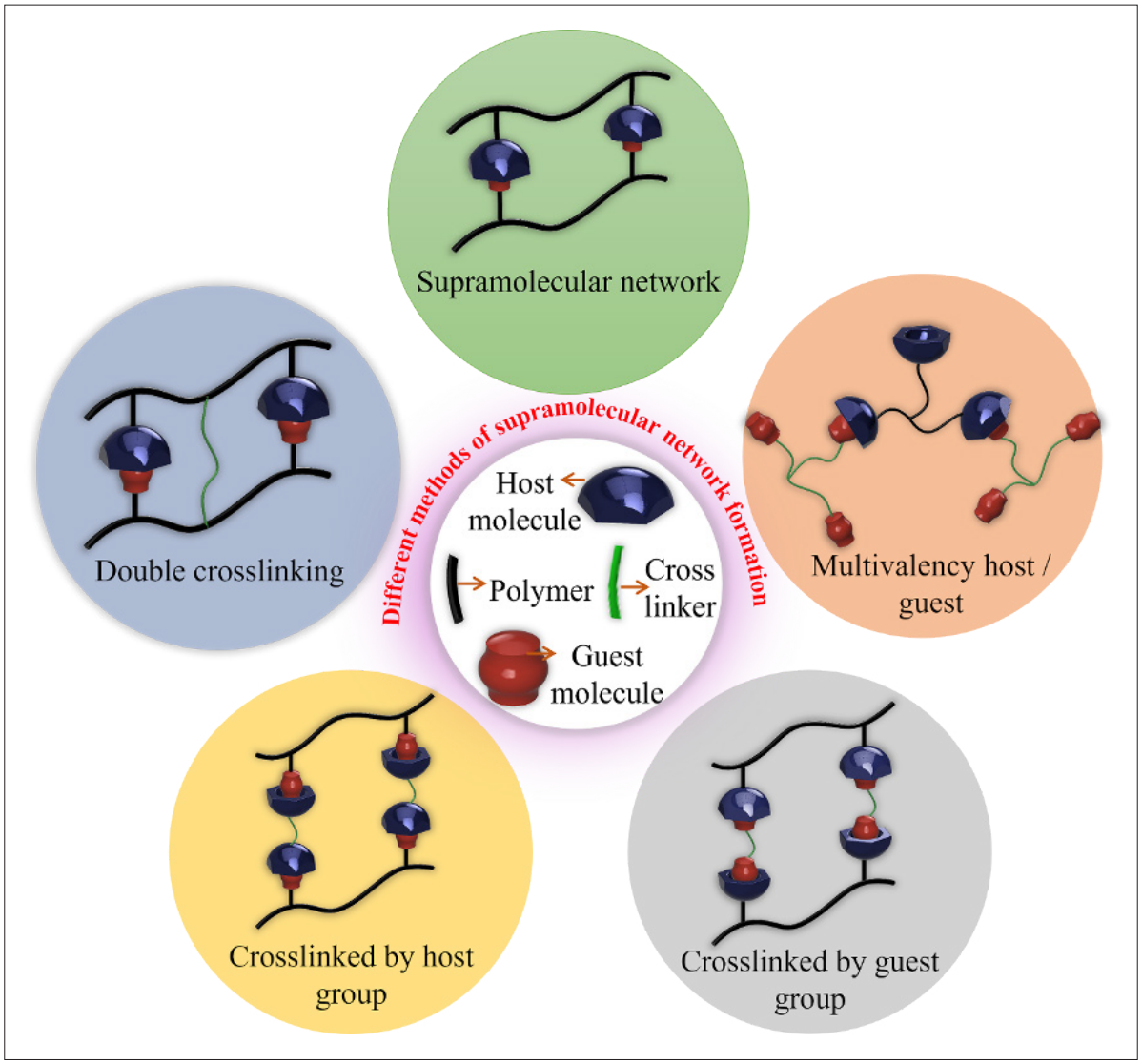


Figure 2. Schematic representation of dynamic interactions of host–guest chemistry and formation of supramolecular host–guest polymer networks.

functional nanostructures expands their potential in drug delivery and biomedical applications.[7,23]

3.2. Rheological properties

The distinct rheological characteristics of supramolecular hydrogels make them highly appealing for minimally invasive tissue engineering procedures, as they facilitate *in situ* gelation. The most desirable characteristic of a hydrogel, particularly in applications like stem cell therapy, bioprinting, and surgery-based regenerative treatments, is its injectability. The supramolecular nature of hydrogels enables injectability; however, it depends on several factors other than the gel monomers, such as the crosslinker. An example is the simple pH-controlled addition of Zn ion to a crosslinked carboxymethyl chitosan (CMCh) supramolecular hydrogel, where the concentration of Zn ion played a vital part in fine-tuning the hydrogel's characteristics and injectability. Increasing the ion concentration effectively strengthened the hydrogel's mechanical properties at the expense of the thixotropic properties.[24,25] Without affecting the injectability of the hydrogel, the crosslinker could impart an antibacterial ability to the prepared gel, highlighting the role of a crosslinker in formulating supramolecular hydrogels.[26] Using a novel non-chemical crosslinking process, Xu et al. reported an injectable supramolecular gelatin cell-laden hydrogel based on the host–guest macromer (HGM) approach that could be efficiently used for therapeutic drug delivery and stem cell therapies.[27] Indeed, the supramolecular mechanism of gel formation

inherently influences the injectability of the hydrogel. In the case of non-covalent interactions, hydrophobic lipid dodecyl chains (C12) were modified with hydroxypropyl methylcellulose (HPMC) via isocyanate coupling chemistry. This modification, along with Arg-Gly-Asp (RGD)-attached 30 nm poly(ethylene glycol) (PEG)-polylactic acid (PLA) NPs, resulted in a synthetic, scalable, and biodegradable hydrogel suitable for cell delivery.[28] Typically, cells are co-injected with hydrogels to prevent cell death and enhance cell availability in the tissue area. In this context, supramolecular hydrogels prove highly beneficial for making self-healing hydrogels.[29,30] The supramolecular assembly also promotes the injectability of the hydrogel and can be used for sustained drug release applications. A notable example is presented by Mol et al., wherein a PEG hydrogel, incorporating ureido-pyrimidinone (UPy) units, demonstrated the controlled release of extracellular vesicles for 4 days post-injection.[31] Recently, the formulation of tunable supramolecular polymer-NP hydrogels has been developed. The network polymer, hydrophobically modified cellulose, dynamically interacts through multivalent connections and self-assembles with non-covalent core–shell NPs as a crosslinker.[32]

3.3. Biological properties

The exceptional biocompatibility, injectability, and adjustable physical and mechanical characteristics of supramolecular hydrogels have led to their increased interest in tissue engineering, especially 3D bioprinting applications.[7,8] One of the most important advantages of supramolecular hydrogels in tissue engineering is their ability to mimic the extracellular matrix (ECM) of native tissues. The ECM provides structural and biochemical support to cells, and its mechanical characteristics and composition greatly affect cell behavior, including migration, differentiation, and proliferation. Supramolecular hydrogels can be tailored to simulate the ECM of diverse tissues by integrating specific amino acid sequences, such as RGD or Tyr-Ile-Gly-Ser-Arg (YIGSR), that encourage cell adhesion and migration.[33,34] Further, some supramolecular hydrogels self-assemble to create a 3D network of nanofibrous structures that mimics the ECM of cells.[35-37]

To prevent harmful accumulation in the human body, biomaterials must exhibit both biodegradability and biocompatibility. Supramolecular hydrogels, unlike covalent hydrogels, possess non-covalent crosslinkages that allow for spontaneous degradation or metabolism in physiological environments. These hydrogels are promising as biomaterials for regenerating cell matrices and drug delivery vehicles as they demonstrate good biodegradability and biocompatibility both *in vitro* and *in vivo*. They can be formed by the self-assembly of naturally occurring amphiphiles that contain biomolecules. Likewise, water-mediated multivalent crosslinking of biodegradable and biocompatible synthetic polymers can be formed with host and guest functionalities.[7,8] Additionally, biostability is essential for supramolecular hydrogels in the detection and management of cancer. Strategies, such as designing hydrogelators based on nucleobase–peptide bioconjugates or utilizing dopamine (Dopa)-Fe^{3+} complexation, have been employed to enhance the biostability of these hydrogels, offering resistance to proteases and oxidative degradation.[7,8,38] Furthermore, bioactive molecules (e.g., growth factors and cytokines) can be incorporated into supramolecular hydrogel bioinks to elevate cellular responses and encourage tissue regeneration. The hydrogel network can immobilize these bioactive molecules, leading to a sustained release over time, augmenting their efficacy, and diminishing the necessary dosage. Moreover, supramolecular hydrogel bioinks can be loaded with cells or other biological agents, such as drugs or NPs, for precise and localized administration.[5,7,8]

4. Supramolecular hydrogels for 3D bioprinting applications

3D bioprinting is a technique where live cells, encapsulated in hydrogel materials, are employed to construct 3D structures that mimic native tissues.[39] The emerging 3D bioprinting technique enables the fabrication of personalized tissue engineering scaffolds for precise therapy. Successful application relies on advanced bioinks meeting criteria, like extrudability, rapid gelation, layer adhesion, self-healing capability, biocompatibility, biodegradability, and stability in physiological conditions. To enhance the properties of current bioinks, the incorporation of diverse chemical strategies is essential.[40]

Most of these supramolecular hydrogels are favorable candidates for tissue engineering and 3D bioprinting applications. The hydrogels were found to be cytocompatible, and the cell viability values range between 74 and 100%.[41-43] 3D-printed PNAGA20%-Clay composite scaffold, reported by Zhai et al., facilitated the differentiation of primary rat osteoblasts (ROBs) into osteogenic cells following *in vivo* implantation with sustained release of intrinsic Mg^{2+} and Si^{4+}. p(*N*-acryloyl glycinamide) (PNAGA) and poly(*N*-acryloyl glycinamide-*co*-carboxybetaine acrylamide) (PNAGA-PCBAA) hydrogels also exhibit antifouling ability with very low (≈ 0.45 μg cm^{-2}) protein adsorption due to the introduction of PCBAA.[42]

Interestingly, supramolecular hydrogels formed based on the sliding filament theory of muscle contraction proved superior to the hydrogen-bond-based physically

crosslinked hydrogels.[44] The concept underlying the dynamically sliding physical crosslinking mechanism involves introducing interstitial stages of small organic molecules into hydrogel networks to enhance hydrogen bonds. This straightforward yet effective approach has proven instrumental in achieving stretchable and self-healing properties in hydrogels. By capitalizing on the high nucleophilicity of amino groups in a water medium, the reaction selectively occurs between carboxyl and amino groups. This method allows for the design and synthesis of hydrogels with exceptional extensibility and self-healing capabilities. Additionally, the gel exhibited remarkable swelling properties, with swelling ratios of nearly 10,000% in distilled water and 2250% in phosphate-buffered saline (PBS). Rat fibroblast cells were used to test the biocompatibility of hydrogels, and the results suggest that hydrogels are promising candidates as bioinks for 3D bioprinting.[44]

A novel thermogelling block copolymer was employed to create a cytocompatible supramolecular hydrogel.[45] This hydrogel undergoes thermogelation within the temperature range from room temperature to body temperature, resulting in the formation of transparent hydrogels. Notably, these hydrogels exhibit an unconventional bicontinuous sponge-like gel network with unexpectedly high strength storage modulus (G') (G′ > 1000 Pa). Derived from a range of block copolymers featuring thermos-responsive poly(2-n-propyl-2-oxazine) (nPrOzi) monomer and hydrophilic poly(2-methyl-2-oxazoline), the synthesized hydrogel demonstrated suitability for tissue engineering applications. Cytocompatibility was confirmed through testing with NIH-3T3 fibroblasts, supported by z-stack analysis, whereby the cells did not sediment in the bioink.[45] In a recent development, Li et al. introduced a bioprintable copolymer that emulates the spatial arrangement found in sea cucumber papillae and skin macroscale structures. By strategically incorporating PEG chains with α-CD onto a polyrotaxane backbone, they achieved adaptable collagen flexibility, highlighting promising future applications in the 3D bioprinting field.[46]

A PEG-grafted chitosan-based supramolecular hydrogel bioink was generated via the relationship between the host and guest molecules, α-CD and PEG side chain, respectively. This hydrogel was printed using an extrusion-based 3D bioprinter (Regenovo, China) equipped with a liquid temperature controller. Post-printing, the hydrogel was subjected to secondary crosslinking with β-galactose-modified chitosan (β-GPS). This bioink exhibited a poly-pseudorotaxane (PpRX) structure with shear-thinning properties, attributed to its dual physical crosslinking mechanism. Consequently, it was demonstrated that supramolecular hydrogels with dual crosslinking capabilities are stable under long-term cell culture conditions, with their mechanical strength being well-suited for bioprinting applications. Notably, this bioink was assessed for its efficacy in inducing stem cell differentiation, utilizing the bone marrow-derived mesenchymal stem cells (MSCs). These findings, as reported by Hu et al., underscore the bioprintability and versatility of this novel bioink formulation.[47]

In another report, a biohybrid gradient supramolecular scaffold was 3D printed to repair osteochondral defects.[48] The bioink consisted of cleavable poly(N-acryloyl 2-glycine) (PACG) and GelMA. To make this biohybrid gradient, the top layer was modified with PACG-GelMA hydrogel-Mn^{2+} combination, whereas the bottom layer was modified with PACG-GelMA hydrogel containing bioactive glass. This could significantly facilitate simultaneous regeneration of the subchondral bone and cartilage in a rat model.[48] Recently, a binary cell-laden hydrogel composed of guanosine and guanosine 5'-monophosphate exhibited sufficient stability to ensure scaffold bio-integration during extrusion-based 3D bioprinting. This development addresses challenges like material spreading and low shape stability over time. It exemplifies the potential use of supramolecular hydrogels for customized scaffold preparation in tissue engineering.[49] The study demonstrated that a porous scaffold was formed from 3D-printed poly(caprolactone) (PCL) scaffold integrated with parathyroid hormone (PTH) peptide-loaded mesoporous silica NPs (PTH@MSNs) and GelMA/methacrylated silk fibroin (SFMA) composite hydrogel, i.e., a hybrid PTH@MSNs/GelMA/SFMA/PCL (PM@GS/PCL) scaffold, which could alleviate critical load-bearing bone defects.[50]

A layer-wise 3D bioprinting approach was employed using a dipeptide self-assembled hydrogel. In this method, the bioink was *in situ* gelled based on the Hofmeister sequence, ensuring high biosafety and biocompatibility.[51] Supramolecular bioinks were also used in 3D-bioprinted scaffolds for drug release applications. An OglcNAc transferase inhibitor (OSMI-4) was incorporated into a fast-gelating supramolecular bioink with GelMA and acrylated β-CD for spinal cord injury therapy based on neural stem cells and neuron differentiation.[52]

Based on the previously discussed chemistry and the biomaterials used, the collective findings suggest that supramolecular hydrogels are highly suitable as bioinks. The hydrogels exhibit cytocompatibility and facilitate effective growth and differentiation of cells. These properties render supramolecular hydrogels highly tunable in terms of core strength, stability, biodegradability, and versatility in composition for 3D bioprinting applications.

5. Supramolecular hydrogels based on different chemistry

5.1. Cucurbit[*n*]uril-based supramolecular hydrogels

Cucurbit[*n*]urils (CB[*n*]s, *n* = 5–8, 10, and 14) are a group of symmetric barrel-like (pumpkin-shaped) macrocyclic host molecules used in supramolecular host–guest chemistry.[57,58] Chemically, they are glycoluril oligomers having two methylene-linked ports with polar ureido-carbonyl groups encircling them. These structures are stable, easily controlled, and versatile in molecular recognition and self-assembly, having a rigid structure with a tunable binding affinity.[58,59] The molecule maintains a constant height of 9.1 angstroms (A), while the size of its inner cavity fluctuates with *n*, i.e., from CB[5] to CB[10]. The inner cavity displays a portal width spanning 2.4–11.0 A and an internal void diameter of 4.4–12.6 A. A guest molecule confined within this molecular host experiences a hydrophobic effect within its internal hydrophobic cavity. Furthermore, the guest molecule engages in interactions including hydrogen bonding and ion-dipole with the carbonyl portals. CB[*n*]s exhibit reversible and notably significant secondary supramolecular interactions, encompassing non-covalent bonds, host-stabilized charge-transfer (HSCT), and host-enhanced π–π linkages. The utilization of CB[*n*]-oriented host–guest chemistry holds promise for the creation of supramolecular systems. These systems integrate diverse elements, such as nucleic acids, proteins, peptides, amino acids, and therapeutic agents.[58]

Following the initial report on CB[8], subsequent investigations revealed CB[5], CB[6], CB[7], and CB[10] as sequential candidates. Among these, CB[8] stands out due to its notable feature of having a substantial internal volume, enabling it to concurrently host two guest molecules. This unique characteristic also renders CB[8] particularly effective as a crosslinker within supramolecular hydrogels.[57,59] Review articles published in 2018 by Zou et al. provide a thorough understanding of the non-covalent combinations found in CB[8]-oriented hydrogels. Many supramolecular polymer hydrogels formed from CB[*n*] host molecules, particularly CB[8], have been extensively studied. These polymers encompass a diverse range, consisting of both small molecule-based and polymer-based systems. Among these, polymer-based hydrogels emerge as the predominant category, showcasing CB[8] as a central component in their design and assembly.[57]

Polymer-based CB[8] hydrogels are synthesized using three distinct strategies: three-component systems involving a 1:1:1 hetero-ternary complex, two-component systems making a 1:1:1 hetero-ternary complex (comprising of CB[8]-incorporated polymer and complementary polymer), or 2:1 homo-ternary complexes. In the context of a 1:1:1 hetero-ternary supramolecular complex, an electron-rich second guest, such as naphthalene or azobenzene (Azo), interacts with an electron-deficient first guest, such as methyl viologen (MV) via CB[8]-mediated host-stabilized charge-transfer (HSCT) mechanisms. Conversely, a 2:1 homo-ternary supramolecular complex is formed through host-stabilized π–π interactions, with two identical guests (e.g., naphthalene or anthracene) strongly dimerizing within the hydrophobic cavity of CB[8]. Micro/nanostructured polymer materials based on CB[8] are available in diverse forms, such as networks, vesicles, hydrogels, micelles, colloidal particles, and microcapsules. CB[8] extensively participates in the formation of ternary complexes with both electron-deficient and electron-rich guests through HSCT interactions, a feature harnessed across these various forms. Consequently, CB[8] finds application in drug delivery platforms, biomedical engineering, and a spectrum of various biomedical applications.

In tissue engineering, CB[8]-based hydrogels exhibit high mechanical strength and advanced self-healing capabilities. A novel microfluidic technique has been introduced to create microfibers of supramolecular hydrogel, effectively mitigating the brittleness inherent in agar hydrogel fibers through the incorporation of CB[8]'s reversible molecular recognition. This study holds potential for generating microscale anisotropic supramolecular functional materials.[60]

Shim et al.[53] described a 3D printing procedure for creating a multilayered 3D construct with human MSCs (hMSCs) and a hydrogel made of supramolecular hyaluronic acid (HA) and atelocollagen (Figure 3A). The utilization of a mechanically stable hydrogel based on host–guest chemistry was found to be crucial as it facilitated the easy printing and stacking of two distinct ECM hydrogel types into a single multilayered construct. This process eliminated the need for hazardous chemical reagents or physical stimuli for post-crosslinking.[53]

Chen et al. explored the use of the CB[7]-adamantane (Ad) complementary pair as non-covalent crosslinks, showcasing a robust binding affinity.[54] They synthesized two N,N-dimethyl acrylamide-based polymers, each featuring CB[7] and Ad pendants, respectively. The gelation kinetics of these polymers underwent significant changes with pre-saturation of the CB[7] pendant polymer with different competing guest molecules and concentrations. The resulting supramolecular hydrogels exhibited unique mechanical properties, including high elasticity, good stability, and shape persistence, due to the strong connection between the CB[7]–AD pairs. Additionally, the hydrogels could be easily adorned with specific groups through host–

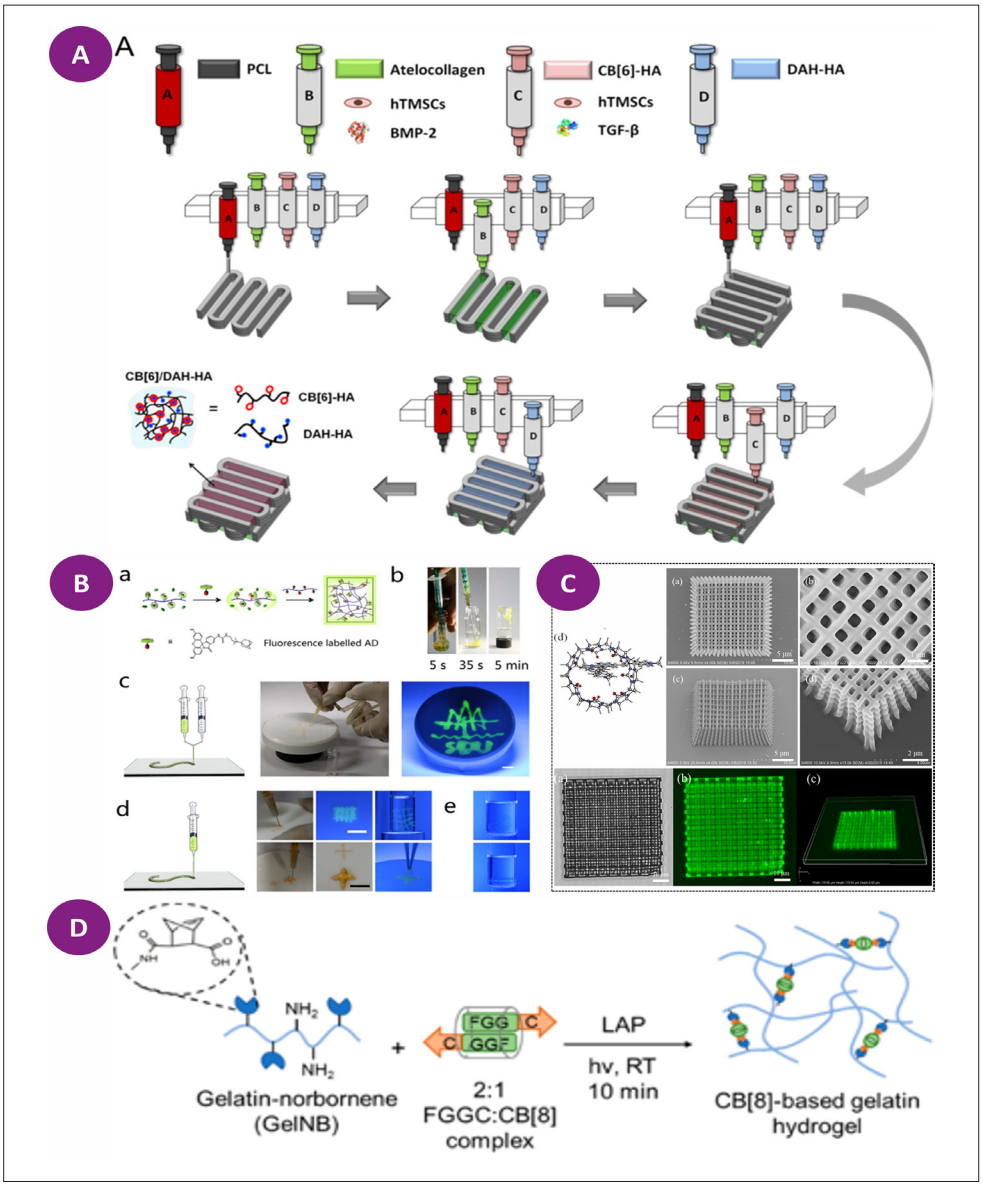


Figure 3. Cucurbit[*n*]uril (CB[*n*])-based supramolecular hydrogels as advanced bioinks. (A) 3D-bioprinted CB[6]-hyaluronic acid (HA) hydrogel containing human turbinate-derived mesenchymal stromal cells (hTMCs) using the multi-head tissue/organ building system (MtoBS). Adapted with permission from.[53] (B) 3D-bioprinted CB[7]-adamantane (AD) crosslinked hydrogel treated with 1,6-diaminohexane dihydrochloride (DAH^{2+}) and (ferrocenylmethyl)trimethyl ammonium iodide ($FTMA^{+}$). Adapted from.[54] (C) Structure of the optimized CB[7]/ 3,6-bis[2-(1-methyl-pyridinium) vinyl]-9-methyl-carbazole diiodide (BMVMC) hydrogel chemistry with confocal fluorescence images of the 3D-printed hydrogel scaffolds. Adapted with permission from.[55] (D) Injectable CB[8]-gelatin-norbornene-based hydrogel. Adapted with permission from.[56] Abbreviations: PCL: Polycaprolactone; BMP-2: Bone morphogenetic protein 2; FGGC: Phenylalanine (F), Glycine (G), Cysteine (C) peptides; LAP: Lithium phenyl (2,4,6-trimethylbenzoyl) phosphinate; RT: Room temperature.

guest interactions, owing to their supramolecular nature. These supramolecular hydrogels are versatile and proved effective for both printing and injection processes, offering not only good strength but also customizable qualities (Figure 3B).

In order to increase the biocompatibility of hydrogel structures for 3D fabrication in an aqueous environment, a novel ionic carbazole water-soluble photo-initiator was reported by Gao et al.[55]. The improved two-photon absorption (TPA) was demonstrated by the synthesized 3,6-bis[2-(1-methyl-pyridinium)vinyl]-9-methyl-carbazole diiodide (BMVMC)–CB[7] complex (Figure 3C). The hydrogel monomer, PEG diacrylate (PEGDA), and BMVMC-CB7 complex were utilized as

an efficient photo-initiator. The resultant photo-initiator demonstrated effective two-photon production capabilities, displaying a low laser threshold and a high accuracy. Confocal imaging using fluorescence was made possible without the need for fluorescent probes by exploiting the photo-initiator's fluorescence characteristics (Figure 3C). The 3D synthetic hydrogel scaffold microstructure, developed using two-photon polymerization techniques, also displayed excellent biocompatibility when cultivated with L929 cells.

Supramolecular gelatin hydrogels containing CB[8]-based crosslinks were synthesized, as reported by Madl et al.[56] Preassembled CB[8]-FGGC peptide ternary structures and grafted norbornenes underwent thiol-ene reactions to produce these linkages on demand (Figure 3D). The gels that were produced were injectable, shear-thinning, and optically clear. These hydrogel-encapsulated human fibroblast cells displayed excellent vitality and a widely distributed shape when cultured. These CB[8]-based gelatin hydrogels have potential uses in drug and cell delivery systems, bioprinting, and other fields.

Cell encapsulation efficiency is an intriguing characteristic, as the responsive dynamic crosslinking of CB[8] supramolecular hydrogels adjusts to cellular forces, thereby enhancing cell viability. Zou et al. developed a thermoresponsive micelle-based percolated CB[8] hydrogel network and reported that the NIH-3T3 fibroblasts were viable even after 30 min post-injection into the patient.[61] In another study, the duration of encapsulation for human fetal lung fibroblasts (MRC-5s) was extended to 7 days in CB[8]–gelatin supramolecular biopolymers.[62] CB[8]-based supramolecular hydrogels are utilized in tissue engineering and various other biomedical contexts. Specifically, they are employed for functions, such as photoluminescence in cellular imaging and biosensors[63] and as tunable polymeric nanostructures.[61,64] Apart from CB[8], studies have also looked at the generation of supramolecular hydrogels based on CB[7] and CB[10] host–guest chemistry.[61,65] A hydrogel has been developed through the combination of nor-seco CB[10] (NS-CB[10]) and two AdA molecules (AdA-four-arm-PEG) to develop a ternary complex. This novel strategy can be used in tissue engineering, cell treatment, and medication administration. Notably, the hydrogel displayed improved rheological characteristics and self-healing capabilities, with a high storage modulus (4.01 ± 0.01 kPa) in contrast to an average loss modulus of 0.49 ± 0.13 kPa.[65] The versatile binding affinity of CB[7] has been extensively investigated to develop hydrogels encompassing a diverse array of documented interactions. Notably, a binding affinity (K_{eq}) of 7.2 x 10^{17} M^{-1} would produce a gel structure that emulates the behavior of covalent gels. This distinctive characteristic governs effective processes, such as encapsulation release, cell filtration, and material clearance *in vivo*.[61] The unique biological properties and tunable functions of host–guest supramolecular hydrogels, enabled by diverse and specific host–guest interactions, make them smart scaffolds in tissue engineering. For instance, CB[6]-conjugated hyaluronic acid and polyamine-conjugated HA self-assembled to generate biocompatible HA hydrogels that provide a controlled 3D atmosphere for the development of cell-entrapped hydrogels and act as synthetic extracellular frameworks.[8,66]

CB[*n*]-based supramolecular assembly is a pivotal intervention in biomedical applications and tissue engineering. The role of CB[*n*] chemistry as a potent crosslinker in supramolecular hydrogels positions it as an excellent candidate for injectable and 3D bioprinting applications. This chemistry accommodates a wide array of biomolecules and therapeutics driven by host–guest interactions. Furthermore, CB[*n*] offers elevated mechanical strength, self-healing capabilities, and efficient cell encapsulation, promoting extended cell viability—a key focus in research and development.

5.2. Cyclodextrin-based supramolecular hydrogels

Cyclodextrins (CDs) are starch-derived cyclic oligosaccharides with a torus-like or truncated cone-like molecular shape having a hydrophobic empty cavity and a hydrophilic external face.[71,72] These hydrophilic groups of the glucopyranose units, projecting toward the outer surface, configure the distinctive features of CDs. Each monomer is linked via an α-1,4-glycosidic bond, and they are classified depending upon the number of linked units, i.e., 6, 7, and 8 for α-CD, β-CD, and γ-CD, respectively.[71,72] The height of these monomers remains constant at approximately 0.78 nm. However, their internal diameter and cavity volume increase with an increasing number of monomer units.[71] The internal cavity volume is directly proportional to the category and K_{eq} of the guest molecule, highlighting its high specificity for molecular recognition.[71] The presence of hydroxyl groups at the 2-, 3-, and 6-positions renders CDs highly adaptable for chemical modifications, establishing them as remarkably versatile compounds. This structural feature also contributes to their distinction as one of the most easily water-soluble hosts. Most importantly, the United States Food and Drug Administration (FDA) has classified all three CD forms as generally recognized as safe (GRAS), and no negative side effects have been reported.[72,73] Xia et al. provided a comprehensive insight into CD-based hydrogels and their chemistry.[74]

A multivalently crosslinked guest polymer, forming a 3D-network hydrogel, is commonly regarded as a CD-crosslinked polymer hydrogel. This hydrogel

possesses significant shear-thinning and self-healing characteristics.[71] Polymers, such as poly(ethylene oxide) (PEO), PEG,[72] poly(propylene oxide) (PPO),[75] or co-polymers with blocks of PEO and/or PPO, alone as PEO-PPO-PEO (Pluronics),[72,76] or in combination with various blocks, such as poly[(R)-3-hydroxybutyrate][77] or PCL,[78] are generally suitable guest molecules.[71,79] The aforementioned characteristics can also be attained using more functional and responsive substances, such as cholesterol, Ad, Azo, ferrocene, and arylazopyrazole (AAP).[71,80]

Further, if the CD-based interactions provide a highly compact polymer network of hydrogels, such forms are referred to as supramolecular nanogels.[71] Nanogels typically contain branched and star-shaped structures or micellar assemblies, constituting miniaturized hydrogels with expected charge distributions.[71] Simple polymer networks are converted to nanogels either by linking or threading CDs to the polymer chains or through inter-hydrogen bonding among CDs. Due to their ease of preparation and biocompatibility, nanogels exhibit improved encapsulation efficiency, thus emerging as promising drug delivery depots.

Cyclodextrins (CDs) can also be employed to develop low molecular weight (LMW) hydrogels. This involves the amalgamation of CDs or CD derivatives as a daisy chain structure (host–guest interaction). CD-modified peptide hydrogels and self-assembled surfactant hydrogels with CD lead to supramolecular configuration. In tissue engineering, these gels supported better spreading of cells. For example, NIH-3T3 fibroblast cells were spread more efficiently in RGD-modified non-covalently linked β-CD hydrogel.[81,82] Recently, an AAP-altered pentapeptide gelator Nap-GFFYS-based magneto-photo-responsive LMW supramolecular hydrogel was developed employing a modular co-assembly technique. β-CDs are multivalently crosslinked with the Nap-GFFYS-AAP gelator, involving the host–guest chemistry of CDs and the self-assembly of peptides. Moreover, β-CD vesicles were embedded with superparamagnetic cobalt ferrite NPs to impart the magnetism. This embedment affects the stiffness of the hydrogel, while the magnetism affects the storage modulus. Additionally, the hydrogel's stiffness may be reversibly altered by employing UV or visible light irradiation to deactivate the AAP moiety and the hydrophobic cavity of the β-CD interface, respectively.[83]

Wang et al. have developed a biocompatible cum injectable polyrotaxane hydrogel mainly for drug delivery applications. A four-arm PEG (4-PEG) was non-covalently crosslinked with α-CD by supramolecular host–guest chemistry. The gel was characterized by potential thixotropic shear-thinning behavior with macro-porous morphology, making it appropriate for the development of injectable drug formulations. NIH-3T3 fibroblasts were used to assess biocompatibility, and when exposed to an elevated dosage of 50 mg/mL for a period of 48 h, the TH50 composition did not exhibit any toxicity.[84] In contrast, Dai and colleagues described a novel injectable and reversible supramolecular gel that exhibited host–guest inclusion complexation between the binary medicine-loaded micelle and the α-CD.[85] The micelle was composed of self-assembled eight-arm PEG-betulinic acid (BA)/hydroxycamptothecin (HCPT) in water. In the hydrogel, the outer-exposed PEG chains in the micelle were threaded into α-CD cavities, positioned along its sides.[85]

The UV-initiated copolymerization of a gel and a supramolecular crosslinker can also be utilized for supramolecular hydrogel production, whereby the CD host can accommodate a guest polymer. In a study by Zhou et al.[67] (Figure 4A), octa-CD polyhedral oligomeric silsesquioxane (OCDPOSS) reacted with acrylamide-modified Ad (Ad-AAm) to form a star-shaped supramolecular crosslinker, which then copolymerized with acrylamide to form the supramolecular hydrogel.[67] The multivalent interlinking demonstrated super-stretchability, rapid self-healing, and injectability of the hydrogels. Moreover, these hydrogels are expected to be biocompatible and can be employed as hydrophobic drug delivery systems. However, these supramolecular hydrogels are not mechanically strong. Miller et al. utilized supramolecular guest–host assembly for making a mechanically robust hydrogel with fibrillar topography.[68] They combined methacrylate-modified HA electro-spun hydrogel nanofiber segments, incorporating β-CD (host) and Ad (guest) supramolecular chemistry (Figure 4B). The gel exhibited a six-fold increase in mechanical strength compared to its parent materials, alongside excellent self-healing and shear-thinning qualities. Moreover, the fibrous gel could support the hMSCs with > 85% cell viability for at least 7 days. Recent studies demonstrated promising potential for utilizing CDs in specific molecular recognition activities with nanomaterials to construct hydrogels with enhanced molecular recognition capabilities. In a recent study,[86] the surface of 2D MoS_2 was conjugated with β-CD via a one-pot nucleophilic exchange between monotosylated β-CD and the sulfur atoms of MoS_2. The resultant material was crosslinked with Ad-modified gelatin, employing supramolecular guest–host assembly. This self-healable and flexible gel displayed a tenfold higher storage modulus than gelatin. In addition to this, the inherent properties of MoS_2, like biodegradability, biocompatibility, antibacterial activity, high loading capacity, and photothermal property, suggest that the new supramolecular polymer gels could serve as a potential solution for tissue engineering.[86]

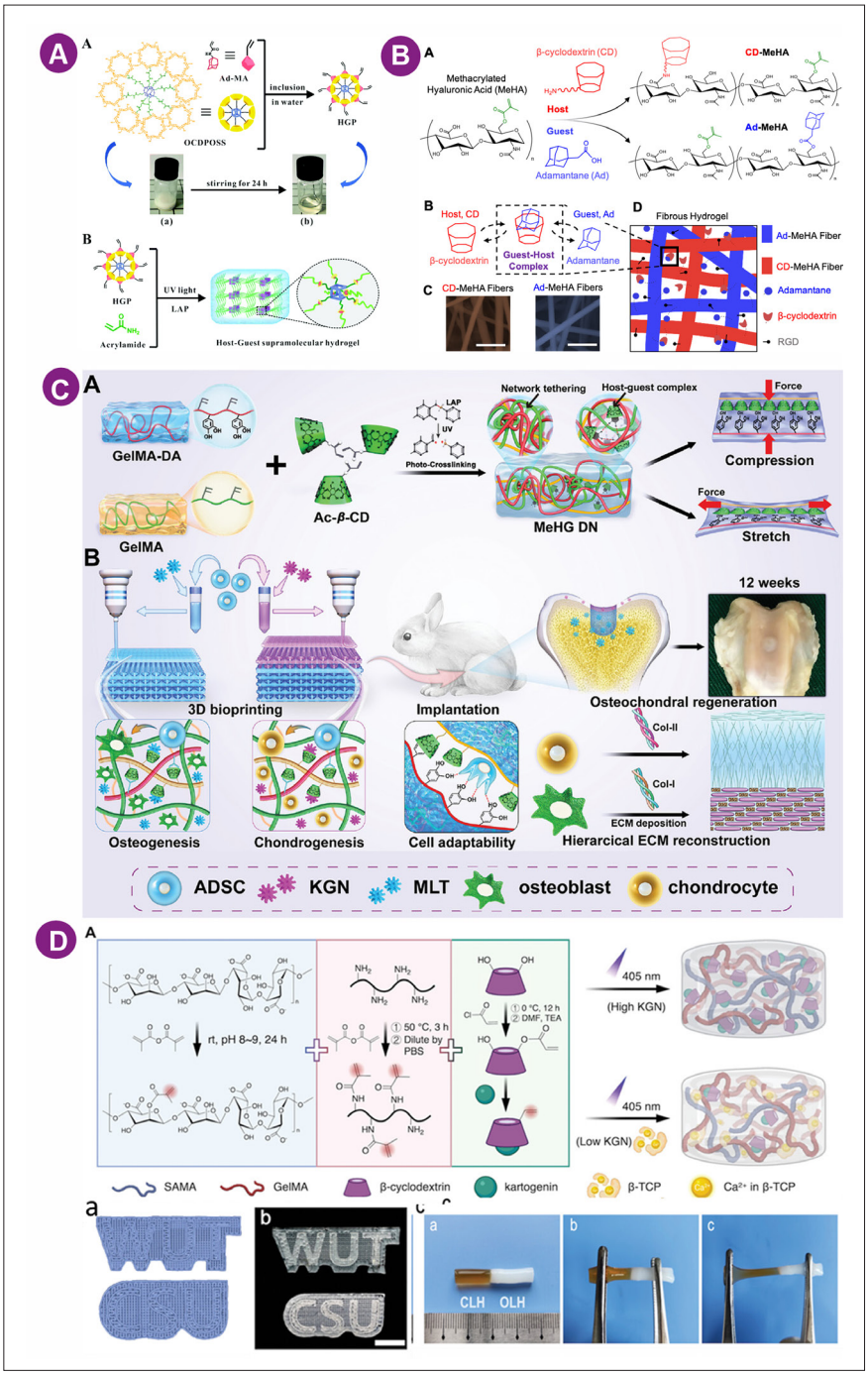


Figure 4. Cyclodextrin-based supramolecular hydrogels as advanced bioinks in 3D printing. (A - *A*) Synthesis of host–guest supramolecular crosslinker based on polyhedral oligomeric silsesquioxane (HGP) induces a visible change in the solution via complexation from (a) suspension to (b) clear solution. (B - *B*) Schematic representation of the HGP gel synthesis process using reversible host–guest interactions. After mixing acrylamide (AAm), photo-initiator (LAP), and supramolecular crosslinker (HGP) in water, ultraviolet (UV)-initiated crosslinking generated the supramolecular hydrogel. Adapted with permission from.[67] (B) Electrospun hyaluronic acid (HA) hydrogel nanofiber segments functionalized with either host *β*-cyclodextrin (*β*-CD) or guest Ad supramolecular moieties to form host–guest complexes. Adapted with permission from.[68] (C) Diagram illustrating the development of bioink and the subsequent 3D bioprinting of heterogeneous constructs for osteochondral defect repair. Adapted with permission from.[69] (D) Synthesis of precursors and UV-crosslinked supramolecular hydrogels (Ac-*β*-CD[KGN], GelMA, SAMA). (D - a and b) 3D-printed supramolecular hydrogel structure. (D, c) Self-healing properties of the supramolecular hydrogel. Adapted with permission from.[70] Abbreviations: SAMA: Methacrylated sodium alginate; Ac-*β*-CD(KGN): Acrylate beta cyclodextrin; KGN: Kartogenin; CLH: Chondral layer hydrogel; OLH: Osseous layer hydrogel; Ad-AAm: Acrylamide-modified adamantane; OCDPOSS: Octavia-cyclodextrin-modified polyhedral oligomeric silsesquioxane; MLT: Meniscus-like tissue; ADSC: Adipose-derived stem cells; β-TCP: Beta tricalcium phosphate; HGP: Star-shaped POSS contains supramolecular crosslinker; LAP: Lithium phenyl-2,4,6-trimethyl-benzoyl phosphinate.

Dai et al.[69] introduced a novel dynamic gel for bioprinting cell-filled structures for osteochondral regeneration (Figure 4C). The bioink, which is made up of acrylate β-CD, Dopa-functionalized GelMA, and GelMA, creates a dynamic network through host–guest interactions. This network amplifies mechanical characteristics, increases cell adhesion, encourages adaptability, and permits variable modulus. To generate a heterogeneous construct that mimics the osteochondral environment, chondrogenic and osteogenic components are incorporated in diverse zones through the sustained drug release from β-CD cavities. The bioink exhibits encouraging *in vivo* and *in vitro* regeneration outcomes, pointing to its potential for broad application in 3D bioprinting for tissue engineering.[69]

Similarly, a different injectable and 3D-printed bi-layered osteochondral hydrogel, consisting of β-tricalcium phosphate (TCP), methacrylated sodium alginate, and methacryloyl gelatin with a compositional gradient, was reported recently. The hydrogel comprised an osseous layer (OLH) with a biochemical gradient of kartogenin (KGN) and a chondral layer (CLH) (Figure 4D). Experiments performed both *in vitro* and *in vivo* revealed that at high KGN concentrations, bone MSCs (BMSCs) promote chondrogenesis, while low KGN concentrations when combined with β-TCP synergistically enhance osteogenic growth via endochondral ossification. Different concentrations of KGN within the hydrogel formulations impacted their mechanical strength and swelling behavior. The sustained release of KGN varied accordingly, with OLH/β-TCP(+)/KGN(+) releasing the highest amount of KGN. The combination of β-TCP and KGN synergistically promoted osteogenic differentiation through endochondral ossification in OLH, while a low concentration of KGN effectively regulated the chondrogenic differentiation of BMSCs. Evaluation in a rat knee joint trochlear defect model reported that the chondrogenic kartogenin (C-K) and osteogenic tissue kartogenin (O-TK) group exhibited the most complete defect filling, highest International Cartilage Repair Society (ICRS) score, and superior osteochondral tissue regeneration, supported by micro-computed tomography (microCT or μCT) and histological analysis. Immunohistochemical staining and Raman spectroscopy indicated an excellent microenvironment for osteochondral repair due to the synergy between KGN and β-TCP in the osseous layer. Further studies are warranted to elucidate the precise molecular mechanism and optimize KGN ratios for clinical translation.[70] In another study, functional α-CD nanobeads threaded onto PEG chains enable the creation of modular PEG hydrogels with controllable properties for stem cell culture and differentiation. CD-based host–guest supramolecular hydrogels have been used as favorable materials for tissue engineering.[87]

In summation, the specialized cone-like molecular shape of CD enables chemical modifications of the molecule to improve inherent features such as cellular adhesion, differentiation, self-healing, and biodegradability. Among the structural variations of CD, polyrotaxane-based supramolecular hydrogels have the highest efficiency, in terms of tissue engineering aspects. Furthermore, the wide range of available guest molecules for CD-crosslinked supramolecular hydrogel formation offers a vast selection of versatile hydrogels suitable for both injectable applications and 3D bioprinting.

5.2.1. Pseudorotaxane-based supramolecular hydrogels

Cyclodextrins (CDs) can create supramolecular assemblies through interlinking within main chain polymer segments or forming side chain complexes via physical interactions or covalent bonds. If these structures are capable of reversible movement along the macromolecular backbone or lateral chains, they are referred to as PpRXs. Conversely, if the mobility of CD is limited because of the presence of bulky molecules (referred to as stopper molecules) entrapped at the ends of PpRXs, these assemblies are termed polyrotaxanes.[72] Polyrotaxanes involve the threading of CDs onto the polymer chain, achieved either through the conventional 1:1 covalent bonding between stopper molecules or by incorporating extra linker molecules or intermolecular hydrophilic interactions. The crosslinking density can be increased by utilizing a dual-threaded redox-responsive inclusion complex in a 1:2 ratio.[88] From a tissue engineering perspective, polyrotaxane-based supramolecular hydrogels possess distinct advantages, notably improved degradability, substantial stretchability, self-repair capabilities, and inherent supramolecular mobility. Furthermore, copolymers incorporating polyrotaxanes have demonstrated enhanced cellular adhesion and augmented differentiation, signifying their potential to promote tissue development and regeneration.[89,90] The hydrogel formed through chemical modifications of CD on the polyrotaxane, such as introducing aldehyde groups, facilitates instant gelation, suggesting efficient self-healing and biodegradability as evidenced by studies involving cell encapsulation.[91]

Cyclodextrins (CDs) are cyclic oligosaccharides capable of forming supramolecular inclusion complexes (SICs) by binding to hydrophobic guest molecules, as noted by Uekama et al.[92] Notably, CDs can also produce PpRXs, an SIC, when interacting with linear synthetic polymers, like PPG or PEG.[92] A PpRX-based supramolecular hydrogel system can function as a depot for sustained drug or

gene delivery. In a study reported in 2012,[93] a hydrogel incorporated with plasmid DNA (pDNA) polyplexes and active cationic copolymers successfully delivered genes. Biodegradable triblock methoxy-PEG (MPEG)-PCL-poly[2-(dimethylamino)ethyl methacrylate] (PDMAEMA) copolymers were developed and effectively condensed pDNA into polyplexes, with hydrophilic MPEG forming the outer corona. These polyplexes were then encapsulated in α-CD-based supramolecular PpRX hydrogels, demonstrating the sustained release of pDNA as polyplex NPs for up to 6 days. The released pDNA polyplexes exhibited high bioactivity comparable to the protein expression levels of freshly prepared poly(ethylene imine) (PEI) polyplexes, highlighting the potential of this thixotropic and *in situ* gelling system without solvent as an injectable vehicle for long-term gene delivery.[93] PpRX-based supramolecular hydrogels have been studied as durable scaffolds for delivering recombinant adeno-associated virus (rAAV) vectors in cartilage regeneration.[72] Gels containing polysaccharides (HA or chondroitin sulfate) with α-CD demonstrated reinforced viscoelasticity and resistance to autoclaving. The specific gels exhibited higher transgene expression levels and sustained release of rAAV vectors compared to free vectors, with the specific gel compositions influencing release kinetics and interactions with viral vectors. These results demonstrate the possibility of PpRX gels as promising tools for tissue engineering and regenerative medicine strategies by acting as a sustained delivery vehicle.[72] A study successfully developed injectable supramolecular gels based on PpRXs, combining α-CD with temperature-responsive copolymers. These gels exhibited gelling *in situ* at physiological temperature and demonstrated the ability to accommodate large amounts of microspheres. Furthermore, the gels served as 3D scaffolds for MSCs, promoting osteogenic differentiation and displaying resilience to lyophilization and reconstitution with minimal changes in rheological and structural properties.[94] Ohshita et al. reported a PpRX gel composed of CDs and PEG-PPG-PEG triple block copolymers (Pluronics F108, F87, F68, and L44) and reported noteworthy benefits of stabilizing human immunoglobulin G (IgG), surpassing CD/PEG and generic gels. Based on these results, CD/Pluronic gels have great potential as medicinal materials for antibody compositions.[95]

5.3. Peptide-based supramolecular hydrogels

5.3.1. Amino acid-based supramolecular hydrogels

To overcome the cytotoxicity and non-biocompatibility issues associated with polymer-based hydrogels, supramolecular hydrogels assembled from oligonucleotides, carbohydrates, proteins, and peptides have been utilized as cell-friendly alternatives.[99] Supramolecular hydrogels composed of LMW ingredients, like functionalized amino acids and dipeptides, have emerged as alternatives to peptide assemblies in recent years. Specifically, N-fluorenylmethoxycarbonyl phenylalanine (Fmoc-Phe) constituents are a notable group of molecules that possess self-assembling properties and exhibit the necessary characteristics for drug delivery applications.[100] A study conducted by Jagrosse et al. introduced proteins being encapsulated in and released from supramolecular hydrogels made of perfluorinated Fmoc-modified phenylalanine (Fmoc-F5-Phe-DAP). They demonstrated the release of four model proteins, namely RNase A, TI, BSA, and IgG, from these hydrogels, emphasizing the active and time-sensitive characteristics of protein release. Depending on the molecular weight and isoelectric point of the protein, the release profile can be optimized. These findings substantiate the possibility of this supramolecular LMW hydrogel as a viable approach for sustained and localized therapeutic protein release.[14,100,101] In an effort to enhance mechanical rigidity and comprehend the effects of hydrophobicity and conformational freedom, researchers designed modified aromatic amino acid-based building blocks, Fmoc-γ-Phe and Fmoc-(3-hydroxy)-γ-Phe. Fmoc-γ-Phe formed a stable hydrogel possessing remarkable mechanical and thermal characteristics, while Fmoc-(3-hydroxy)-γ-Phe exhibited transient fibrillar hydrogel formation, followed by microcrystalline aggregation, shedding light on the structure–assembly relationship of amino acid-based hydrogels.[102] A novel approach was employed by Li and his team[103] to overcome the fragility of hydroxyapatite (HAP) by integrating it with supramolecular hydrogels. The resulting hybrid supramolecular N-(9-Fmoc)-L-Phe/nano-HAP (Fmoc-L-Phe/nHAP) hydrogels exhibited enhanced mechanical strength due to the intermolecular interaction between Fmoc-L-Phe and nHAP. Furthermore, these hybrid hydrogels demonstrated inherent antibacterial properties, cytocompatibility, and promising potential as drug delivery carriers, as indicated by the successful release of chlorogenic acid with significant inhibition effects on *S. aureus*.[103] The tuning of viscoelastic properties of supramolecular hydrogels for tissue engineering has gained relevance due to their influence on cell fate. To enhance stability and mechanical properties, polysaccharide dextran derivatives were incorporated into a C2-phenylalanine gelator (LPF) through π–π stacking and hydrogen bonding. The resulting hybrid hydrogels, LPF-ADx and LPF-CMDHx, [C2-phenylalanine gelator (LPF), carboxymethyl dextran (CMDH), aminodextran (AD), x represents the amount of AD and CMDH] exhibited dense highly-branched fibers and improved mechanical properties, with LPF-CMDH3 displaying the best elastic modulus at 11,654 Pa. The incorporation of biodegradable additives into these hydrogels offers opportunities to

enhance the strength of weak gelators and expand their applicability in tissue engineering.[104]

5.3.2. Short peptide-based supramolecular bioinks

Peptide-based supramolecular hydrogels are formed when peptides self-assemble into 3D networks in a solvent, usually water. The non-covalent interactions that bind the peptide molecules in these gels include van der Waals forces, hydrogen bonding, and electrostatic interactions. In the context of bioinks for 3D bioprinting, their flexibility and capacity to mimic the ECM render them appealing for creating bioprinted structures that closely resemble natural tissues. Peptide-derived hydrogels within supramolecular assemblies exhibit enhanced properties, including gel formation in both aqueous phosphate buffers and aromatic organic solvents.[105,106] The biocompatible amphiphilic properties of γ-peptide-injectable hydrogels enable the formation of hydrogels and organogels (in the form of nanofibrils).[106] The subsequently formed gel can load large amounts of drug with improved solubility,[107] the peptide-based backbone is relatively flexible, and the resulting gel has higher hydrophobicity.[106,108] The nanofiber structure of the D/L-peptide of NapGDFDFDYGYSV (D-YSV) demonstrated superior resistance to proteinase digestion compared to its control peptide NapGFFYGYSV (L-YSV). The gel also demonstrated enhanced anticancer efficiency *in vitro*, attributed to improved cellular uptake, biocompatibility, and notable tumor inhibition capacity.[108,109] Non-covalent interactions between peptides and fullerenes in peptide-modulated self-assembled fullerene gels successfully inhibited multi-antibiotic resistant *S. aureus* and promoted wound healing with excellent thermodynamic stability.[110] Furthermore, peptide-based supramolecular hydrogels possess robustness, pH responsiveness, tunable stiffness, viscoelastic properties, self-healing properties, shear-thinning behavior, cell media durability, antimicrobial activity, and controllable biodegradability.[96,105,111] These properties are highly essential for a bioink to be successfully used in 3D bioprinting.

Tert-butoxycarbonyl (Boc)-(S)-β-Phe was developed using Arndt–Eistert homologation of Boc-Phe. Similarly, Boc-(S)-γ-Phe can also be produced from Boc-Phe via the Wittig reaction, followed by catalytic hydrogenation, saponification, and coupling with N-ethyl-N'-(3-dimethylaminopropyl) carbodiimide hydrochloride (EDC) and 1-hydroxybenzotriazole (HOBt). Peptide synthesis was performed using conventional solution phase chemistry or solid phase peptide synthesis methods.[106,107,112] Hydrogen bonding and π–π stacking among peptides are commonly observed interactions during hydrogel formation.[105,106,110,111,113] Similar observations were noted for a supramolecular hydrogel consisting of a monodisperse PEG and an aromatic hexapeptide containing Phe and Tyr residues. Due to their amphipathic nature, peptides can self-assemble in hydrated conditions at a very low concentration (critical aggregation concentration = 1.5×10^{-5} mol/L, 22.8 μg/mL) forming a fibril amyloid-like network. A dry interface is formed by the network of π–π stacking between all the hydrophobic side chains of Phe, whereas a wet interface is generated by the solvent entangling water in extending hydrogen-bond networks that link the Tyr residues. By altering either the wet interface, the dry interface, or both, three different peptides, (Nal-Y)3, (F-Dopa)3, and (Nal-Dopa)3, have been reported.[112] However, peptide-based hydrogels can also be formed by cleaving the disulfide bonds between the hydrogelator and peptide molecule.[107] In utilizing Phe dipeptide (FF) as the supramolecular hydrogelator to form the hydrogel, the presence of hydrophilic diglutamic acid helps maintain a balanced hydrophilicity–hydrophobicity ratio, facilitating water solubility of the delivered compound.[107] In contrast, non-covalent functionalization of peptide occurs when a supramolecular polymer (Fmoc-RGD) and a covalent polymer (chitosan) are combined to form a biopolymer gel. This is because a hydrogen bond is formed between the carboxylic acid group of Fmoc-RGD and the -NH_2/-OH groups of chitosan and the α-carboxyl group of Fmoc-RGD.[105] Similarly, another di-Fmoc-based RGD hydrogel was reported by the same group for efficient cell adhesion, where they further incorporated polyaniline (PAnil) to mimic electrogenic tissue engineering.[114]

Peptides can self-assemble into a stable hydrogel via a heating-cooling procedure.[108] Contrastingly, peptides formed from aliphatic amino acids, such as isoleucine (Ile), have a high propensity to form β-sheets in the self-assembled hydrogels upon protonation or charge recognition/hydrogen bonding. In addition, these amino acids can improve water solubility by combining two aspartic acids (Asp).[111] Falcone et al. utilized an innovative PA, myristyl-Phe-Phe (C14-FF), to form hydrogels with a β-sheet aggregate-composed nanofiber matrix morphology. It was distinguished by a novel solvent-dependent helical switching and a record-low gelation concentration.[115] Interestingly, Frémy's salt, an inorganic stable source of free radicals, can modulate the mechanical properties of tyrosine-based self-assembled β-hairpin peptides.[116] *In situ* gelation can also be utilized for a supramolecular hydrogel stabilized by electrostatic interactions between two peptides with opposite charges without the addition of any crosslinkers. Jian et al. developed two 9-Fmoc-dipeptides with opposing charges on their end residues,[96] and *in situ* gelation was accomplished using a layer-wise alternate printing technique (Figure 5A). The resulting gel exhibited adjustable mechanical characteristics

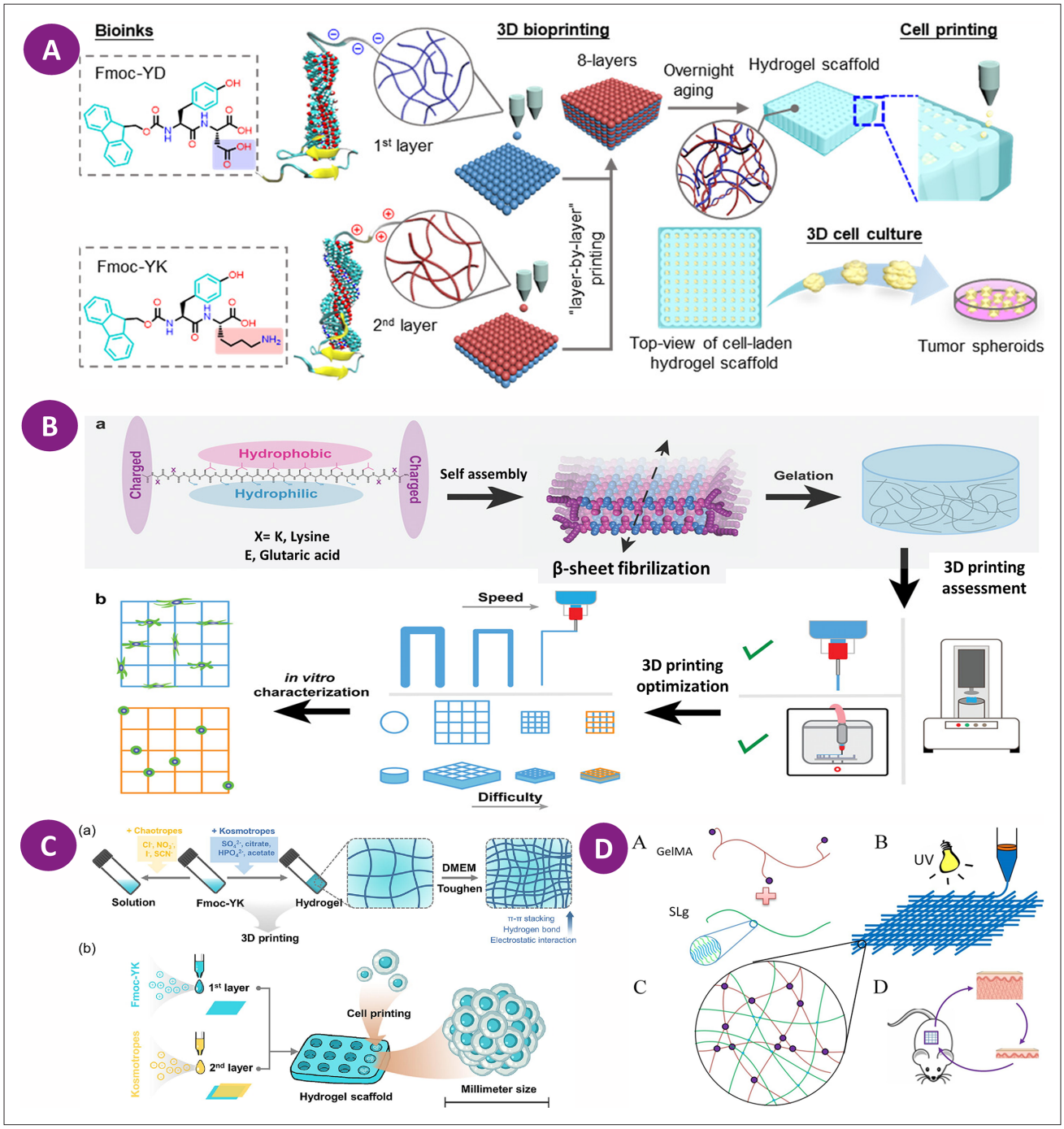


Figure 5. Peptide-based supramolecular hydrogel as advanced bioinks in 3D bioprinting applications. (A) Illustrations of fluorenylmethoxycarbonyl (Fmoc)-dipeptide-based bioink synthesis method for creating tumor spheroid models *in vitro* via 3D bioprinting. Adapted with permission from.[96] (B - *a*) Multidomain peptide-based gelation due to self-assembly of peptides with opposite charges for *β*-sheet fibrillization. (B - *b*) 3D printing of different structures using multidomain peptide gels and their *in vitro* characterization. Adapted with permission from.[97] (C) Diagrams of 3D bioprinting anionic dipeptide gels and anion-induced Fmoc-L-tyrosine-L-lysine (Fmoc-YK) gelation. (C - *a*) Anions induce Fmoc-YK gelation via the Hofmeister effect, and Dulbecco's Modified Eagle Medium (DMEM)-soaked anionic dipeptide hydrogel exhibits a toughening effect. (C - *b*) 3D bioprinting is used to create hydrogel scaffolds for 3D cell culture, which are based on the ionic action of Fmoc-YK gelation. Adapted with permission from.[51] (D - *A*) Gelatin methacrylate (GelMA) and proangiogenic self-assembling peptide nanofiber hydrogel (SLg) are the two components of 3D-printed slurries. (D - *B*) With ultraviolet (UV) light, a 3D-printed scaffold is constructed. (D - *C*) Chemical and physical crosslinks in 3D-printed scaffolds. (D - *D*) Epidermal detachment and recovery to regenerate the dermis in rats. Adapted with permission from.[98]

(e.g., elastic modulus: 4–62 kPa), resulting in the development, growth, and customary release of HepaRG spheroids. Since no crosslinkers have been used, it is expected that there will be a decrease in cell damage attributed to chemical reactions.[96] In addition, the N-terminal is essential if the two peptides are short and contain Lys-Cys residues at the C-terminal. Such highly thixotropic gels were found to be effective for 3D cell proliferation.[117] A coupling reaction could also be adopted to fabricate peptide-based supramolecular hydrogels as in normal hydrogel synthesis. Through a thiourea-catechol (TU-Cat) coupling reaction, a catechol-modified peptide (Cat-RGD) can bioactivate a mechanically inert hydrogel. The engineered peptide (Cat-RGD) with host thiourea-linked (TU) monoacrylated β-CDs monomers were used to create robust hydrogels, leading to enhanced cell and tissue adhesion.[109]

Additionally, the amalgamation of magnetic NPs (MNPs) into a gel matrix expanded its applications in the biomedical field. Embedded MNPs enabled remote modulation of the hydrogel's physical properties via an exterior magnetic field, leading to long-lasting changes in mechanical properties and adjustments in the 3D structure, potentially inducing anisotropy. Mañas-Torres et al.[118] developed biocompatible and biodegradable Fmoc-FF and Fmoc-RGD short peptide hydrogels (7:3 ratio) incorporated with MNPs. This hybrid hydrogel, serving as a 3D scaffold, demonstrated improved self-healing properties, mechanical stability, good biocompatibility, and injectability. It was confirmed that the use of MNPs with the supramolecular peptide hydrogel improved its physical properties.[118]

With similar objectives, Farsheed et al. established the printability of a multidomain peptide (MDPs)-based supramolecular nanofibrous hydrogel at low concentrations.[97] The precursors, N'-acetylated cationic MDP (K2[SL]6E2) and C'-amidated anionic MDP (E2[SL]6E2), formed dynamic nanofibers through supramolecular forced assembly (Figure 5B). The temperature-independent extrusion-based 3D-bioprinted MDP structures displayed variations in cellular activity that were charge-dependent *in vitro*, such as fast proliferation and high viability. Overall, the work has generated an enhanced version of self-assembled peptide (SAP)-based 3D bioprinting bioink. Dankers et al. reported a UPy moieties-based supramolecular hydrogel for corneal stromal construct development. The hybrid hydrogels revealed striking similarities, positioning the fully synthetic hydrogel as a promising candidate for mimicking the stromal ECM and demonstrating potential as a minimally invasive tool for tissue defect filling or corneal cell introduction for self-regeneration.[119]

Researchers made efforts to improve the mechanical properties, cell adhesion, and proliferation, thereby providing a native ECM-like environment for 3D-bioprinted scaffolds using bioinks containing peptides (Figure 5C). An *in situ* gelled dipeptide, Fmoc-YK bioink, based on the Hofmeister sequence in the presence of sulfate ions, was developed to achieve adjustable mechanical strength and controllable degradation properties.[51] Fmoc-YK contributed to hydrophobic and π–π interactions, while lysine provided electrostatic interactions and hydrogen bonding. The DMEM-toughened scaffold was prepared using a layer-wise 3D printing method without any crosslinking agent, ensuring cell culture stability, biocompatibility, and biosafety for organoid culture.

In a study by Chu et al.,[98] it was reported that a 20% proangiogenic self-assembling peptide nanofiber hydrogel (SLg)-based 3D-printed framework (in combination with UV-crosslinking GelMA) established the best collagenous fibrous structure for fast revascularization and dermal regeneration (Figure 5D). The hydrogel's nanofibrous structure, formed through hydrophilic and hydrophobic interactions between alternating amino acids, resembled the native ECM. The loose porous structure of the nanofibrous hydrogel 3D scaffolds was conducive to cell migration, infiltration, and growth, especially those of endothelial origin.[98] In another approach, Zhou et al.[120] developed a lysine peptide–dendrimer-reinforced bioink (HC-PDN) containing the peptide–dendrimer-branched PEG with end-grafted norbornene (PDN) and cysteine-modified HA (HC). The addition of ethylene end-groups extensively promoted the attaching of abundant moieties, leading to enhanced thiol-ene-promoted crosslinking in HC-PDN. This subsequently increased the rheological and mechanical characteristics of HC-PDN and significantly reduced the accumulation of reactive oxygen species (ROS) compared to methacrylated HA (HAMA). As a result, a diverse and biomimetic hepatic tissue was created by co-culturing HepG2-C3As, LX-2s, and EA.hy.926s cells in 3D-bioprinted scaffolds of HC-PDN, demonstrating the vital roles of the native liver.[120]

Chiesa et al.[121] attempted to predict biomaterial printability with respect to extrudability and long-term mechanical stability of the scaffold using finite element (FE) simulation. An SAP hydrogel containing β-sheet-forming F9 peptide (FEFKFEFKK; F: Phe; E: Glu; K: Lys) underwent piston-driven extrusion 3D bioprinting, showcasing versatility in printing complex structures, such as the human ear.[121] Furthermore, a specific peptide folding-mediated interaction-based 3D printable hydrogel was developed by Aronsson et al. using a tunable covalent biorthogonal crosslinking strategy.[122] In this case, strain-promoted alkyne-

azide cycloaddition was employed, utilizing multi-arm PEG, to crosslink the hyaluronan-based hydrogel. This hydrogel was synthesized *de novo* using helix-loop-helix peptide conjugation. The fabrication process involved bicyclo[6.1.0] nonyne (BCN)-modified HA via carbodiimide chemistry. Additionally, the modified HA was then crosslinked via both covalent and supramolecular means with an azide-modified helix-loop-helix polypeptide (JR2EK[N3]), which folded and dimerized into four-helix bundles. Cell–hydrogel interactions and biomineralization can be regulated through supramolecular tuning by utilizing a variety of complimentary peptides with diverse functions. Notably, an inexpensive osteogenic growth peptide (OGP) delivery system for sustained release, focusing on long-term bone regeneration, was reported based on the SAP strategy.[123] In addition to demonstrating biocompatibility and promoting cell proliferation, the OGP-dimer hydrogel displayed promise as both a therapeutic option and a bioink for 3D bioprinting, particularly in the context of bone regeneration.

Peptide amphiphiles (PAs) are a useful supramolecular material with customizable biochemical and nano-structural characteristics. PAs have been extensively applied in tissue engineering, including angiogenesis, neurogenesis, and bone regeneration. Yan et al.[124] established a thiolated gelatin 3D-printable bioink augmented with PAs to modify its nanostructure and bioactivity, thereby facilitating cell incorporation. The bioink was developed through a double secondary crosslinking approach, involving homo-bi-functional maleimide PEG (MAL-PEG-MAL) and Ca^{2+}. This method enabled multi-layered bioprinting, exemplified by the use of a laminin-mimetic IKVAV ($CH_3[CH_2]_{15}$VVAAEEIKVAV)-based PA system with biliary epithelial cells (SV40SM) that displayed remarkable rheological properties.[124] Additionally, Sather et al.[125] utilized supramolecular polymer aqueous inks, composed of PAs and chromophore amphiphile (CA), in direct ink writing (DIW) to construct macroscopic ionically crosslinked liquid crystalline hydrogels with modifiable nanoscale arrangement. Intermolecular interactions among the self-assembled structures were determined by the pH and salt concentrations in the system. For example, charge density affected the viscosity of the bioink. Nonetheless, these hierarchical interactions enhance the printability and nanoscale alignment of the hydrogel.[125]

Notably, the formation of π–π stacking and hydrogen bonds between the precursors of a peptide-based supramolecular hydrogel is dependent on the nature of the precursors. The formation of the stackings and bonds can be attained via chemical reactions, such as homologation, wittig, catalytic hydrogenation, and coupling reactions. The stacking and bonds impart key characteristics to the hydrogel, such as solubility, hydrophobicity, and flexibility. In summary, the remarkable versatility, biocompatibility, and widespread acceptance of peptide-based supramolecular hydrogels position them as promising bioink candidates for effective 3D bioprinting of tissues. Several comprehensive reviews have previously been published[15,126,127] that elucidated the diverse applications and versatility of peptide and polypeptide-based supramolecular hydrogels.

5.4. DNA-based supramolecular hydrogels

DNA supramolecular hydrogels refer to hydrogels that are interconnected through DNA hybridization. These hydrogels have garnered significant interest, owing to their exceptional molecular permeability, compatibility with biological systems, degradability, thixotropy, and ability to self-repair. Consequently, they are highly useful in different fields, including tissue engineering, cell culture, and 3D printing. The inherent design flexibility and stimuli-responsiveness of DNA further broaden the applications for DNA-based hydrogels,[134] such as the development of detection apparatuses and materials with shape-memory properties.[135] These hydrogels could be hybridized with other materials, such as polyacrylamide, polypeptide, protein, poly(phenylenevinylene), graphene oxide (GO), and carbon nanotube, via ester-amine click reaction, conjugation, or π–π interactions. Moreover, DNA-based hydrogels can be dual-crosslinked with more than one DNA molecule. Pure DNA hydrogels were also formed by branched and linear DNA scaffolds, either via self-assembly or pH-triggered crosslinking.[136]

DNA supramolecular hydrogels are responsive to environmental stimuli (physical and chemical), leading to alterations in the assembly of crosslinking and subsequent phase transitions. The dynamic response to these triggers enhances the versatility of DNA hydrogels, rendering them suitable for a range of applications. Various DNA hydrogels have unique responsive behaviors to environmental stimuli, such as a pH-sensitive DNA hydrogel with a high cytosine content. Similarly, a pH-sensitive hybrid hydrogel made of DNA and polyacrylamide would exhibit shape-memory behavior. Furthermore, when exposed to visible and UV light, a polyacrylamide–DNA hybrid hydrogel treated with Azo exhibits reversible volume changes. A carboxymethylcellulose (CMC)–DNA hybrid hydrogel with dual crosslinking networks and Azo functionalization exhibits shape-memory characteristics in both visible and UV light. Temperature variations induce gel–sol conversion in a polyacrylamide–DNA hybrid hydrogel through reversible DNA hybridization. Likewise, a comprehensive DNA hydrogel undergoes phase confirmations in response to temperature changes. Another type of DNA gel network would respond to temperature changes by releasing doxorubicin (Dox) and gold NPs (AuNPs)

upon dissociation. A DNA MNP-functionalized all-DNA hydrogel exhibits diverse behaviors under the influence of a magnetic field, including phase changes, shape distortion, physical movements, and neutralized gravitational effects.[135,137-139]

A two-component mixing technique was used by Li et al.[128] to demonstrate a rapidly-formed supramolecular polypeptide–DNA hydrogel, enabling *in situ* multi-layer inkjet 3D bioprinting (Figure 6A). The hydrogel rapidly forms under physiological conditions, facilitating the merging of printed structures, maintaining the shape without deformation, and enabling cell printing for tissue engineering applications.[128] These hydrogels offer significant advantages specifically in the following areas: (i) facilitate stem cell differentiation by regulating matrix mechanical strength alone; (ii) facilitate cell migration within the hydrogel and establish a realistic *in vivo* model for observing cancer cell migration; (iii) synergize with 3D printing technology to enhance the creation of artificial organs and 3D tissues.

Zhang et al.[129] reported a 3D-nanostructured supramolecular hydrogel containing G-quartet/hemin (G4/H) motifs, GO, and poly(vinyl alcohol) (PVA), synthesized using a direct self-assembly method (Figure 6B). The resulting GO/PVA/G4/H hydrogel displayed remarkable mechanical strength and a strong 3D GO network that resembles a honeycomb. Notably, the hydrogel can be utilized as an injectable ink and for 3D printing a variety of patterns due to its reversible pH-induced phase shifts. Enzymes can be used to create responsive binary AND/OR logic gates and can also be used to detect H_2O_2 with extreme sensitivity by exhibiting remarkable peroxidase-like activity. This adaptable hydrogel architecture could advance intelligent soft materials across various biological and medicinal applications.[129]

In another recent study, 3D-printed PCL scaffolds were integrated with dynamic vascular endothelial growth factor (VEGF)–DNA hydrogel and reinforced using black phosphorus (BP) nanosheets (BPNSs). The scaffolds were used to improve bone regeneration and angiogenesis.[140] BPNSs were employed to form a dynamic polymer network, ensuring sufficient mechanical strength while preserving the protein binding surface. In addition, the interaction of BPNSs further increased the storage modulus. Additional crosslinking further stabilized the scaffolds into a denser nano-composite. The DNA gel also facilitated long-term retention and delivery of biologically active VEGF, thereby promoting angiogenesis and osteoinductivity.[141] A versatile supramolecular hydrogel incorporating chemically branched DNA on self-complimentary linkers (Figure 6C) and a K^+ ion-responsive pure DNA hydrogel with intermolecular G-quadruplex were developed for 3D cell culture applications.[130] The hydrogels rapidly formed under physiological conditions, exhibiting excellent mechanical properties, shear-thinning behavior, and injectability. A dendritic DNA-based hydrogel (DDH) was developed with enhanced mechanical stiffness for the *in situ* incorporation of live cells and thermolabile factors. The hydrogel was formulated with four single-stranded DNAs at nanomolar concentrations crosslinked to a tetraethylene glycol core without any crosslinkers in isothermal conditions.[131] The hydrogel offers good mechanical support, high cell viability, and good cell proliferation (Figure 6D).

The incorporation of G-quadruplex, a guanine-rich region, in DNA/RNA-based hydrogels was reported by Aderito et al.[132] The group created an injectable, conductive, thermo-reversible, and self-healing G-quadruplex hydrogel by combining guanosine (G), potassium chloride, and 3-aminophenylboronic acid-functionalized HA (HA-PBA) in a dynamic co-assembling multicomponent system (Figure 6E). The K^+-stabilized gel was created between G-coupled dynamic covalent boronate ester bonds and HA-PBA through hydrogen bonding and π–π interaction. The HA-functionalized GelMA microchannel-embedded 3D hydrogel displayed enhanced cell viability, subsequently applied as artificial blood vessels.[132] The incorporation of nanoforms or nanostructures in DNA hydrogel will reinforce the polymer network and enhance its physical characteristics. A study detailed that an injectable 3D-bioprinted scaffold, containing GelMA and self-assembled tetrahedral DNA nanostructure (TDN), successfully delivered an antibiotic, clindamycin (CLI), for treating osteomyelitis.[142] The antibiotic was electrostatically complexed to the TDN network nanocarrier. As a result, the TDN nanocarrier-loaded GelMA scaffold is biocompatible and suitable for bone tissue regeneration with significant antibacterial activity.

Low molecular weight gelators (LMWG) with nucleoside/nucleotide precursors are also considered DNA-based hydrogels. A self-assembled metallo-nucleoside injectable hydrogel was reported for wound repair.[133] In this study, cytidine (C) along with $B(OH)_3$ and $AgNO_3$ were used as precursors, where C formed orthogonal diester bonds with borate, while Ag^+ stabilized the C-C base pairs through dimers (Figure 6F). The formed hydrogel was stable with high water content, stimuli-responsive, self-supporting, and elastic. Its sol–gel transition upon applied shear stress enabled a 3D-printed and flexible wound healing patch with antibacterial activity induced by the incorporated Ag^+.

These studies demonstrate the versatile applications of DNA-based supramolecular hydrogels in 3D bioprinting,

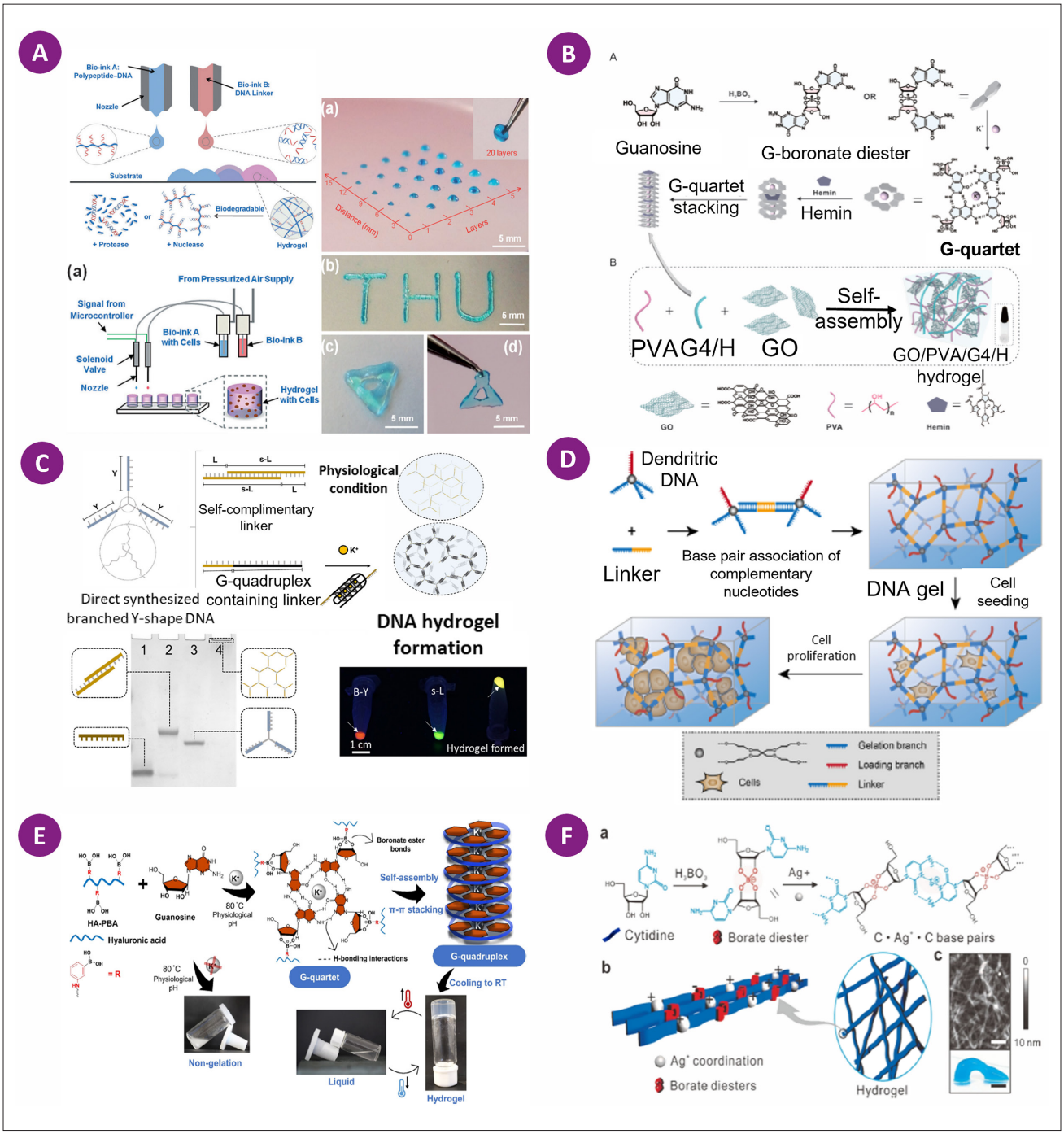


Figure 6. DNA-based supramolecular hydrogels as advanced bioinks in 3D printing. (A) 3D-printed polypeptide–DNA hydrogel embedded into 3D structures via hybridization crosslinking. Adapted with permission from.[128] (B) Self-assembly of a graphene oxide (GO)-poly(vinyl alcohol) (PVA)-guanosine (G4)-hemin (GO/PVA/G4/H) hydrogel using a simple mixing method. Adapted with permission from.[129] (C) Formation of a responsive supramolecular DNA hydrogel based on Y-shaped branched DNA. Native PAGE was used to characterize the hydrogel matrix and linker synthesis, in a molar ratio of 1:3. Lanes 1–4 correlate to the 32 nucleotide (nt) control sequence, s-L, B-Y, and B-Y + s-L, respectively. Images of the DNA hydrogel stained with SYBR-gold and SYBR-green, respectively, were used to stain the B-Y and s-L samples. Adapted with permission from.[130] (D) Self-assembly of the dendritic DNA hydrogel (DDH) for 3D cell culture. Adapted with permission from.[131] (E) Self-assembly mechanism of a hyaluronic acid (HA)-functionalized G-quadruplex thermoresponsive hydrogel. Adapted from.[132] (F) Formation of injectable metallo-nucleoside nanofibrous hydrogel. Adapted with permission from.[133]

Table 1. Examples of supramolecular hydrogels and their applications in different areas

Polymer/ combination	Crosslinkage/ type	*In vivo* studies	*In vitro* studies	Reported injectability	Rheological/ mechanical properties Mechanical testing	Drug loading/ release	Self-healing property	Application	3D printing method
Nor-seco-CB[10] and adamantylamine terminated-4-PEG[65]	Non-covalent	No	No	No	Rheological analysis: storage modulus: -4.01 ± 0.01 kPa; loss modulus: 0.49 ± 0.13 kPa	No	Self-healable	Drug delivery; cell therapy; tissue engineering	N/A
CB[7] and PEG[61]	Host–guest chemistry; Click reaction	Mice; subcutaneous implant	No	No	Stress relaxation modulus: ~1 × 10^4–1 × 10^5 s (~3–30 h); shear thinning	Controlled release study of 70 kDa dextran encapsulation	Self-healable	Synthetic ECM; stem cell biology; biomimetic; bioinspired synthetic materials	N/A
CB[8]-Pluronic F-127 polymers[170]	Host–guest chemistry; photo-induced covalent dimerization	Hairless, immunocompetent SKH1-E mice; encapsulation and release of a model macromolecule by *in vivo* imaging	NIH-3T3 fibroblasts; cell viability studies	Yes	Shear thinning	Controlled release study of 70 kDa dextran encapsulation and hydrogel erosion	Self-healable	Biomedical applications	N/A
α-CD and binary-drug-loaded micelles (self-assembled 8-PEG-BA-HCPT)[85]	Host–guest inclusion complexation	*In vivo* antitumor activity on mice	Hemolysis assay and *in vitro* cytotoxicity test (CCK-8 assay); LLC cells	Yes, but not tested	Viscoelastic behavior: storage modulus and loss modulus	Temperature-mediated *in vitro* release kinetics studies of HCPT	No	Drug delivery	N/A
β-CD-AOI2 and A-TEG-Ad[42]	Three-arm host–guest chemistry; UV-initiated polymerization	No	Biocompatibility test; mBMSC and MDSC	No	Rheological analysis and mechanical properties (compression, tensile, cyclic compression, and anti-slicing experiments)	No	Self-healable	Biomedical materials in regenerative medicine (e.g., cartilage repair)	N/A
4-PEG and α-CD[84]	Host–guest chemistry	No	Cytotoxicity studies; NIH3T3 fibroblasts	Yes	Thixotropic shear thinning; reversible gel–sol transition	*In vitro* drug release kinetics (brimonidine in PBS)	No	Controlled drug release	N/A

(*Continued...*)

Table 1. (*Continued...*)

Polymer/ combination	Crosslinkage/ type	*In vivo* studies	*In vitro* studies	Reported injectability	Rheological/ mechanical properties Mechanical testing	Drug loading/ release	Self-healing property	Application	3D printing method
AAP-modified pentapeptide gelator Nap-GFFYS and β-CDV with superparamagnetic cobalt ferrite NPs embedded in their membrane[83]	Host–guest chemistry	No	No	No	Magneto-responsive storage modulus; reversible-magneto-rheological and photo-rheological properties	No	No	Soft robotics; tissue engineering; life-like materials	N/A
AGP3[171]	Non-covalent interactions (ionic and H-bonding)	Intraneural implant study; *in vivo* functional and histological studies	Biocompatibility test; NSCs; IF analysis of NSC differentiation and growth	Yes	Soft mechanical properties; storage modulus: 560 Pa at 37°C; mechanical strength: 1470 Pa	No	No	Biomaterial for spinal cord injury correction	N/A
Fmoc-FF and Fmoc-RGD short peptides with MNPs[118]	Peptide bond	*Ex vivo* evaluation using osteoblasts: cell proliferation, cell adhesion and differentiation; *in vivo* biocompatibility in mice; subcutaneous implant	No	Yes	Anisotropic mechanical properties; stronger storage modulus	No	Self-healable	Biomedical applications	N/A
NAGA and nanoclay[172]	Hydrogen bonding; UV crosslinking	*In vivo* evaluation on rat tibia model; implant placed in tibia bone	Proliferation, differentiation, and cytotoxicity assays; primary ROBs	Yes	Mechanical evaluation (tensile test) and rheology	No	No	Repair of bone defects and degeneration	Extrusion-type 3D printing with a precision three-axis positioning system
HA-CD and HA-Ad[173]	Host–guest interaction	*In vivo* assessment of cartilage defect repair in rat on one side of the knee joint	Cytocompatibility tests; MSCs; *in vitro* chondrogenic differentiation (qPCR, IF)		Shear thinning	No	Self-healable	Cartilage regeneration; tissue engineering	N/A
N-alkyl-D-galactonamides[174]	Low energy bonds (H-bonds, π–π stacking)	No	No	Yes	Mechanically fragile	No	Self-healable	3D bioprinting; 3D printing applications	Liquid-in-liquid direct writing (hydrogel in a water bath)

(*Continued...*)

Table 1. (*Continued...*)

Polymer/ combination	Crosslinkage/ type	*In vivo* studies	*In vitro* studies	Reported injectability	Rheological/ mechanical properties Mechanical testing	Drug loading/ release	Self-healing property	Application	3D printing method
GelMA and acrylated β-CD[52]	Host–guest crosslinking	*In vivo* experiment on SCI model rat for neuronal regeneration and axonal growth	Cytotoxicity test; adhesion and proliferation assays; NnSCs	Yes	Stable mechanical properties; fast gelation	Sustained delivery of OSMI-4 molecule	Self-healable	Neuronal repair in the spinal cord	Extrusion-based bioprinting and 405 nm UV-crosslinking
Laponite nanosheets and guanidinylated chitosan[175]	H bonding; electrostatic interaction	No	Cell viability assay; mBMSCs; ALP expression; mineralization assay	Yes	Shear thinning; storage modulus (G'): ~215 Pa; loss modulus (G"): ~183 Pa	As polymeric carriers for DBM to enhance handling properties and osteogenic potential	Self-healable	Bone regeneration; clinical bone repair	N/A
HPMC-modified with hydrophobic lipid C12 chains and RGD-functionalized PEG–PLA NPs[28]	Isocyanate coupling chemistry; multivalent, non-covalent interactions	*In vivo* cell retention and immunoprotection tests; subcutaneous injection in SKH1E mice	Cell viability; hMSCs; tissue integration test	Yes	Shear thinning; tunable; viscoelastic	No	Self-healable	Therapeutic and clinical applications	Extrusion-based 3D bioprinting for cell administration in hydrogel
PEG block and temperature-responsive PNIPAM block with pH-sensitive A6ACA[160]	H bonding	*In vivo* gastric perforation repair in rat model	Biocompatibility test; HeLa and MRC-5 cells	Yes	Thermo-reversibility; mechanical stability; extended lifespan	No	Self-healable	Carrier of nano/ microelectronics; disease diagnosis/ therapy; health monitoring	N/A
Polypeptide–DNA conjugate (6 wt%) and bio-ink DNA linker (2 mM)[128]	Click chemistry; complementary hybridization	No	*In vitro* viability test; AtT-20 cell (an anterior pituitary cell line) and HEK-293 cells; biological function of printed cells (LysoTracker Red staining); biodegradability	Yes, but not detailed	Suitable viscosity and surface tension; high mechanical strength; non-swelling/ shrinking properties	No	Self-healable	Complex 3D tissue-like constructs in tissue engineering	Microvalve-based inkjet *in situ* multilayer 3D bioprinting

(*Continued...*)

Table 1. (*Continued...*)

Polymer/ combination	Crosslinkage/ type	*In vivo* studies	*In vitro* studies	Reported injectability	Rheological/ mechanical properties Mechanical testing	Drug loading/ release	Self-healing property	Application	3D printing method
HDI-Upy-HDI and amino-telechelic (C_6H_{12}, C_8H_{16}, and $C_{10}H_{20}$ spacers) PEG4k and -ONH_2-capped PEG-C8-Upy-C8-PEG copolymers[176]	Hydrophobic and quadruple H-bonding; oxime bond	No	*In vitro* adhesion stress test using porcine skin model; *in vitro* cytotoxicity; L929 fibroblast cells	Yes	Non-swellable; excellent stretchability of 750–1000%; enhanced fracture strength; 90% compressive strain; fatigue and self-recovery; compressive strength: 4 MPa	No	No	Biomedical application	N/A
Borax-guar gum[177]	Borate/didiol bonds	No	No	Yes	85% compressibility; highest storage modulus and compressive stress at 2 wt% guar gum	No	Self-healable	Biomedical application	N/A
N-acryloyl glycinamide and 1-vinyl-1,2,4-triazole[64]	H-bond interactions between dual amide motifs	*In vivo* gel disk (5 x 1 mm) implantation study on C57BL/6 6-week-old male mice	Antimicrobial (*E. coli* and *S. aureus*) and anti-inflammatory activities; *in vitro* cytotoxicity assay	Yes	High tensile strength (≈ 1.2 MPa); large stretchability (≈ 1300%); outstanding compressive strength (≈ 11 MPa) at a swelling equilibrium state	No	Self-healable; remoldable	Clinical and biomedical applications	N/A

Abbreviations: β-CD-AOI: Isocyanatoethyl acrylate-modified β-cyclodextrin; 4-PEG: Four-armed poly(ethylene glycol); 8-PEG: Eight-armed poly(ethylene glycol); A6ACA: Acryloyl-6-aminocaproic acid; AAP: Arylazopyrazole; Ad: Adamantane; AGP3: Agarose/gelatin/polypyrrole; A-TEG-Ad: 2-(2-{2-[2-(Adamantyl-1-oxy)ethoxy]ethoxy} ethoxy)ethanol acrylate; BA: Betulinic acid; CB[*n*]: Cucurbit[*n*]uril; CD: Cyclodextrin; CDV: Cyclodextrin vesicles; ECM: Extracellular matrix; FF: Diphenylalanine; Fmoc: Fluorenylmethoxycarbonyl; GelMA: Methacrylated gelatin; HA: Hyaluronic acid; HCPT: Hydroxycamptothecin; hMSCs: Human mesenchymal stem cells; HPMC: Hydroxypropyl methylcellulose; IF: Immunofluorescence; mBMSCs: Mouse bone marrow stromal cells; MDSCs: Myeloid-derived suppressor cells; MNPs: Magnetic nanoparticles; MSCs: Mesenchymal stem cells; N/A: Not available; NAGA: N-acryloyl glycinamide; NnSCs: Neuronal stem cells; NPs: Nanoparticles; NSCs: Neural stem cells; PEG: Poly(ethylene glycol); PLA: Poly(lactic acid); PNIPAM: Poly(N-isopropyl acrylamide); qPCR: Quantitative polymerase chain reaction; RGD: Arginine-glycine-aspartic acid; ROB: Rat osteoblast; SCI: Spinal cord injury; UPy: Ureido pyrimidinone; UV: Ultraviolet.

highlighting their potential to revolutionize tissue engineering. Table 1 presents several specific examples of supramolecular hydrogels and their application in different areas. These hydrogels, with their unique structural properties, contribute to the precision and intricacy required for creating complex biological structures. The combination of DNA technology and bioprinting offers new possibilities for advanced regenerative medicine. Additional insights into DNA-based hydrogels and their varied applications have been extensively examined by previous studies,[135,137-139] highlighting the programmable and responsive nature of these hydrogels in 3D bioprinting.

6. Other applications of supramolecular hydrogels

6.1. Supramolecular hydrogels for drug delivery applications

Supramolecular hydrogels, known for their exceptional adaptability and tunability, prove indispensable in drug delivery. Figure 7 displays the different interactions within supramolecular hydrogels and their biomedical

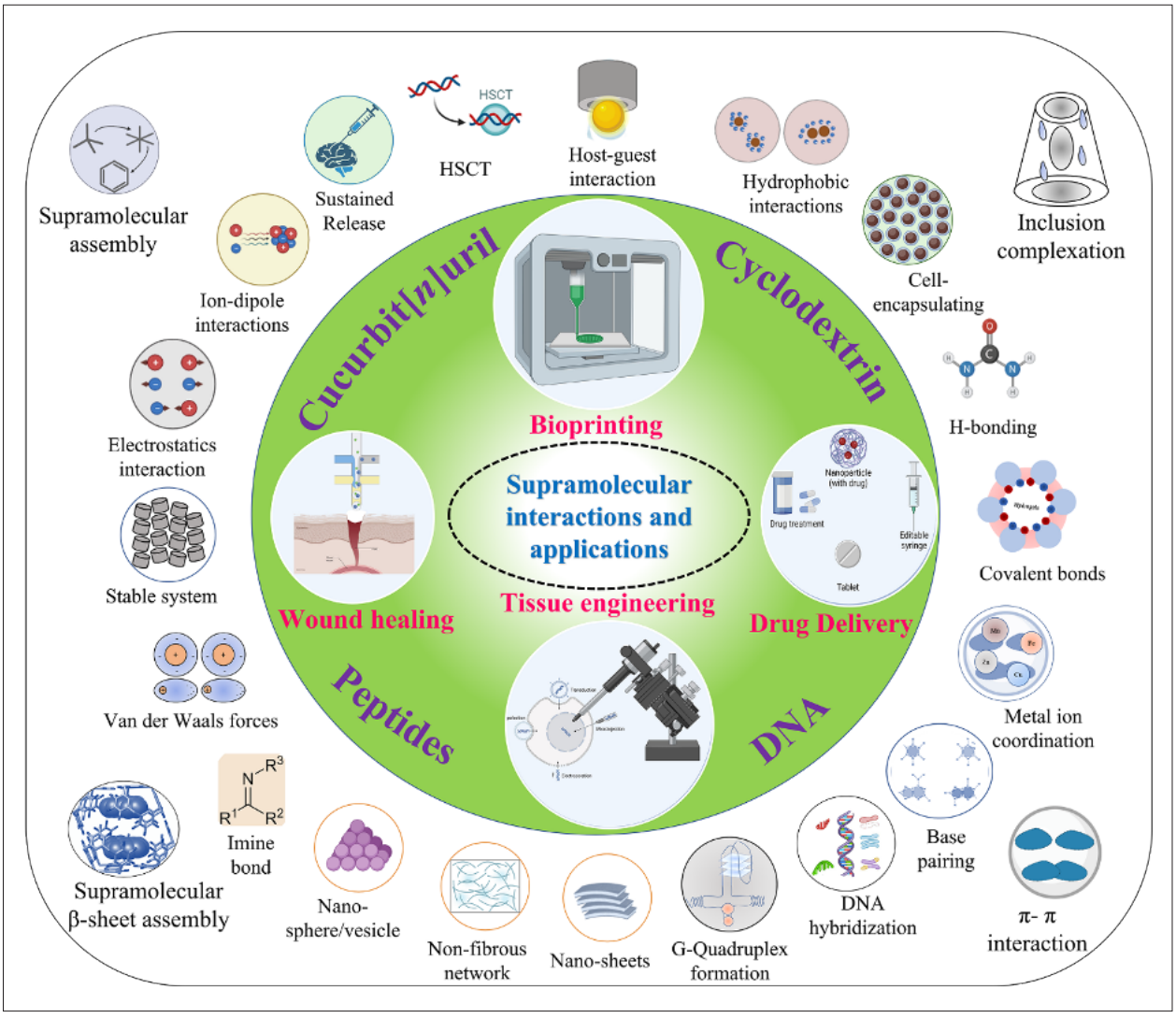


Figure 7. Interactions of different supramolecular hydrogels and their biomedical applications. Abbreviation: HSCT: Host-stabilized charge transfer.

applications. Their diverse crosslinking possibilities, particularly with biologically relevant biomacromolecules, further broaden their applications. Supramolecular hydrogels enhance drug delivery precision, ensuring targeted release and optimizing therapeutic efficacy for improved medical treatments. Supramolecular hydrogel formation typically utilizes precursors such as dexamethasone sodium phosphate,[143] ketoprofen hydrogelator (peptide),[144] α-CD,[145,146] cationic MPEG-b-PCL-b-PEI (MPEG-PCL-PEI),[145] and monofunctional cationic UPy amine.[147]

A gel composition containing Ca^{2+} and dexamethasone sodium phosphate (Dex) could transition between liquid and gel states, contingent upon the concentrations of Ca^{2+} and Dex, for tunable thixotropic properties. Additionally, the gel could regulate the rate of drug release by altering the concentration of Ca^{2+}. These hydrogels are self-assembled through intermolecular aromatic–aromatic interactions, facilitated by the ionic interactions between Ca^{2+} and the phosphate groups of Dex. Higher concentrations of Ca^{2+} ions lead to increased crosslinking density, resulting in a macroscopic sol–gel transition.[143] The covalent translation of ketoprofen (drug) into self-assembling prodrugs enabled the formation of supramolecular drug-loaded hydrogels.[144] The interface of α-CD and MPEG-PCL-PEI, a copolymer that can bond with anionic pDNA for gene transfer, was employed to produce a similar hydrogel.[145] To create Dox-loaded micelles, a glycol chitosan-Pluronic F127 copolymer (GC-PF127) was utilized.[146] The micelles exhibited pH-sensitive surface charges and were capable of forming an injectable hydrogel when α-CD was added. The hydrogel demonstrated the prolonged release of Dox-loaded micelles and was supported with remarkable injectability, shear responsiveness, and rapid recovery.[146] The gel was well-tolerated when injected into the eyes of rats, effectively reducing inflammation compared to the traditional Dex solution. Hence, Dex supramolecular hydrogel may be a good alternative for treating non-infectious uveitis, with a low risk of adverse effects such as lens opacity and problems with blood vessels in the eye.[143] A ketoprofen hydrogelator reportedly increased cyclooxygenase 2 (COX-2) selectivity over COX-1, reduced inflammatory cytokine concentration, and induced cell death in fibroblast-like synoviocytes. These hydrogels, when injected into a joint cavity, demonstrated sustained release and retention of the therapeutic agent, making them a promising candidate for localized treatment strategies for conditions like rheumatoid arthritis.[144] The MPEG-PCL-PEI copolymers exhibit improved gene transfection efficiency and lower cytotoxicity compared to a standard gene transfection agent. The hydrogel system demonstrates controlled release of the therapeutic Bcl-2 conversion gene for up to a week, successfully inhibiting tumor expansion in an animal model of therapeutic-resistant hepatocarcinoma. This work presented the injectable MPEG-PCL-PEI/α-CD supramolecular hydrogels as a versatile platform for on-demand gene delivery and personalized medicine applications.[146] In a mice model, a Dox/GC-PF127 hydrogel significantly increased Dox buildup in tumor tissue while minimizing accumulation in normal tissues, leading to effective tumor growth inhibition. This research highlights the potential of the injectable Dox/GC-PF127 hydrogel as a promising system for localized tumor chemotherapy.[146] A local RNAi delivery method was developed with an amine-PEG supramolecular gel that regulates the release of microRNAs and anti-miRs in their respective therapies. Effective ways for controlled RNAi therapy were achieved by the modification of cholesterol, which regulates the release of microRNA. Additionally, the introduction of positively charged additive molecules into the gel controls the release mechanism.[147] Supramolecular hydrogels are vastly used in numerous drug delivery applications because of their versatility and tunability.[148] Recently, an injectable hydrogel depot technology was developed for the treatment of type 2 diabetes. This hydrogel-based therapy sustained glucagon-like peptide (GLP)-1 receptor agonists (RA) delivery over 42 days with a single injection, promising a once-every-four-months therapy for type 2 diabetes management.[149]

Supramolecular hydrogels have advanced as versatile vehicles for therapeutic delivery, allowing the regulated release of medicines, genes, and proteins into pathological tissues.[7] The high water content and mechanical characteristics similar to tissue, coupled with their ability for *in situ* gel formation and responsiveness to bio-related stimuli, render these hydrogels highly relevant for therapeutic applications.[150,151] Moreover, these hydrogels have demonstrated potential for pH-controlled drug delivery in cancer therapy, as well as efficient gene delivery and protein encapsulation.[152,153] Supramolecular hydrogels offer promising strategies to enhance therapeutic efficacy, reduce side effects, and improve targeted delivery in several biomedical applications.

6.2. Supramolecular hydrogels for wound healing applications

Insufficient vascularization and an extended inflammatory response lead to a poor and delayed healing process, warranting the need for fast and better wound management. Hydrogels can mediate or assist the healing process by acting as a reservoir for anti-inflammatory, anti-bacterial, and vascular regenerative substances, apart from providing mechanical support at the wound site. In general, the *in situ* injectability and shear-thinning properties of hydrogels

make them suitable for complex wounds. Furthermore, the regulated release of specific molecules, such as basic fibroblast growth factor (bFGF) and epidermal growth factor (EGF), was reported to promote angiogenesis *in vitro*.[154,155]

Hybrid supramolecular hydrogels, composed of PEG methacrylate (PEGMA) and PEGylated silver NPs (AgNPs), possess superior antibacterial properties. By utilizing host–guest inclusion chemistry between α-CD and PEGMA side chains in an aqueous solution, Niu et al.[156] were able to electrostatically complex the materials, resulting in a physically crosslinked, strain-driven, temperature-responsive, and self-healing injectable polymer that is well-suited for wound healing applications.[156] Similar to this work, Zheng et al.[157] postulated the treatment of skin burns using a host–guest supramolecular chemistry-based gelatin hydrogel filled with resveratrol (Res) and histatin-1 (His-1).[157]

Zhai et al.[158] formulated a supramolecular hydrogel that facilitates rapid hemostasis and efficient wound healing. The hydrogel was formed with a cell adhesive peptide (Pept-1) and alginate, and it was mechanically stable and aided wound healing without any growth factors.[158] The hydrogel's dense nanofibrillar structure, which was created through metal chelation-mediated co-assembly, and its electrostatic interactions effectively increased mechanical stability. Additionally, the hydrogel was able to reduce bleeding without any hemolytic effects and increase the rate of cell adhesion and migration when used as wound dressing. Preman et al.[159] created a temperature-pH dual-responsive, degradable supramolecular gel structure based on sodium alginate/poly(N-vinyl caprolactam) (AG/PVCL) and tannic acid to speed up wound healing.[159] Free radical polymerization was used to form the hydrogel scaffold, which was then crosslinked chemically and ionically. Through this method, tannic acid was able to strengthen the crosslinking and mechanical toughness of the gel by securing polymer chains through multiple interactions with their polyphenol arm. The hydrogel effectively regulated the release of tannic acid under physiological conditions and demonstrated capabilities to scavenge free radicals, reduce inflammation, inhibit microbial growth, and promote cell proliferation. Recently, a gastric environment-adaptive supramolecular self-healing hydrogel with ABA triblock polymer was reported with outstanding anti-biofouling properties, which promises better internal wound healing and reduces post-operative complications in surgery.[160] The hydrogel assembly was made up of pH-sensitive acryloyl-6-aminocaproic acid (A6ACA) moieties that were randomly integrated into the terminal poly(N-isopropylacrylamide) (PNIPAM) (thermosensitive) block and the middle PEG (hydrophilic) block. These polymers were able to adapt to the acidic environment, attributed to the hydrophobic and hydrogen bonding synergetic interactions in the gel.[160] As evident from various reports, supramolecular hydrogels have displayed significant promise for wound healing due to their exceptional properties, positioning them as effective agents for promoting healing.

6.3. Supramolecular hydrogels for biosensing and bioimaging applications

Supramolecular hydrogels can also be used in bioimaging and biosensing applications.[7,8,161] Bioimaging plays a crucial role in visualizing specific molecular pathways *in vivo*, enabling the rapid visualization of complex biological processes at the molecular level, such as cancer diagnosis and therapy.[162,163] Supramolecular polymer hydrogel-based bioimaging probes hold great promise for the diagnosis of cancer due to their smart responsiveness to physiological stimuli, biodegradability, biocompatibility, and 3D crosslinked structure. These probes, such as supramolecular nanohydrogels, have been successfully utilized as carriers for versatile bioimaging agents, facilitating both *in vivo* and *in vitro* bioimaging for several applications, including lymph node trafficking, tumor targeting, and simultaneous delivery of therapeutic agents and imaging probes.[7,164]

Biosensors integrate components for signal transduction and biomolecule recognition and have emerged as valuable tools for the rapid and convenient detection of disease-related biomarkers. Supramolecular hydrogels, with their high biocompatibility and responsive behavior to biological stimuli, hold great potential for biosensor applications.[165,166] They have been utilized to construct optical and mechanical sensors capable of detecting various bio-relevant molecules or species, including cancer cells and bacteria. Additionally, supramolecular hydrogel-based biosensors have been developed for naked-eye detection, offering portable and user-friendly solutions for biomedical and environmental applications, such as detecting ultralow concentrations of analytes. These advances in supramolecular hydrogel-based biosensors contribute to the development of rapid, sensitive, and cost-effective diagnostic systems.[7,8,167]

7. Challenges and future research in supramolecular synthesis and applications

Supramolecular synthesis involves the non-covalent interactions that assemble molecular monomers to create larger functional structures, thereby presenting both exciting opportunities and unique challenges. Achieving precise control over the desired supramolecular structures

can be challenging in developing advanced bioinks. Designing functional building polymer blocks that can assemble in a predictable and programmable manner requires in-depth knowledge of non-covalent interactions and their influence on the assembly process. However, as previously indicated, weak non-covalent interactions, typically responsible for maintaining supramolecular groups, could influence bioink stability and reversibility. Ensuring the stability of these assemblies in different environments, such as in solution or at interfaces, can be a challenge. Additionally, controlling the reversibility of the assembly/disassembly processes is crucial for their practical applications.

Achieving the desired supramolecular structure often involves a balance between kinetic and thermodynamic factors. Kinetic control directs the assembly pathway, while thermodynamic control stabilizes the most favorable structure. Striking this balance can be challenging and requires careful consideration when selecting the bioink composition. Scaling up supramolecular bioink synthesis to produce larger quantities of functional structures and maintaining reproducibility across batches pose additional difficulties.

Supramolecular hydrogels hold great potential in tissue engineering, yet they face several challenges. The comparatively feeble mechanical properties of supramolecular hydrogels compared to other hydrogels can restrict their use in load-bearing applications.[168] Additionally, devising novel and efficient methods to regulate hydrogel degradation is essential, as supramolecular hydrogels are often more susceptible to degradation than covalently crosslinked hydrogels.[169]

Characterizing supramolecular hydrogel bioinks can be technically challenging due to their dynamic nature and transient interactions. Traditional characterization techniques, such as X-ray crystallography and nuclear magnetic resonance (NMR) spectroscopy, may not always be applicable. Combining different techniques or adapting existing methods to study the structural and dynamic properties of supramolecular assemblies is an ongoing challenge. Optimization is needed for compatibility with various physiological environments and systems, as incorporating supramolecular structures into bioprinted constructs requires addressing stability, processability, and interface compatibility challenges. Ensuring the desired functional performance with properties, such as selectivity, responsiveness, and stability over extended periods, is critical for their successful implementation in real-world applications, especially in tissue engineering and regenerative medicine.

Advancing the clinical translation of supramolecular hydrogels and related complexes presents numerous obstacles, including biocompatibility and safety concerns, production scale constraints, regulatory compliance, understanding *in vivo* behavior, and ensuring therapeutic efficacy. Addressing these challenges necessitates rigorous review, efficient manufacturing processes, clear regulatory requirements, a better understanding of biological interactions, and optimization methodologies for consistent therapeutic outcomes. Interdisciplinary approaches are essential for overcoming these challenges. Hence, continued research and innovation are necessary to unlock the full potential of supramolecular hydrogel bioink synthesis and translate it into clinical applications across various biomedical fields.

8. Conclusion

In summary, this review has explored advancements in supramolecular hydrogels, emphasizing their crucial role in tissue engineering, especially in the context of 3D bioprinting. The formulation of adaptable supramolecular polymer-NP hydrogels represents a significant stride, providing versatile features like biodegradability, cytocompatibility, and customizable composition. Positioned as promising bioinks, these hydrogels demonstrate cytocompatibility, fostering cell growth and differentiation, thereby making them attractive for 3D bioprinting applications. These hydrogels have the capability to confer self-healing properties, shear-thinning behavior, tunable mechanical properties, and adjustable degradability. The incorporation of relevant biological macromolecules further enhances the usefulness of these materials. The exploration of different chemistries, such as CB[*n*]-based, CD-based, peptide-based, and DNA-based hydrogels, reveals a diverse landscape. These hydrogels, extending beyond tissue engineering, demonstrate applications in drug delivery, wound healing, and other innovative uses, highlighting their broad potential and versatility. Despite these advancements, challenges remain in characterizing the dynamic nature of supramolecular assemblies and addressing compatibility issues for seamless integration into devices or materials. Nevertheless, the future of supramolecular hydrogel synthesis and applications appears promising. As we venture into this exciting frontier, interdisciplinary research will be essential to shape the trajectory of supramolecular hydrogel development and utilization. Future research may focus on precision in tuning hydrogel properties for specific

applications, exploring diverse chemistries, addressing compatibility challenges, and ensuring functional performance through interdisciplinary collaborations, underscoring the promising trajectory of supramolecular hydrogel synthesis and applications.

Acknowledgments

The authors acknowledge the licensed service from BioRender software for illustrating Figure 7.

Funding

This research did not receive any specific grant from funding agencies in the public, commercial, or not-for-profit sectors. S.V. was supported by the start-up funds from the New York University, Abu Dhabi.

Conflict of interest

The authors declare no conflicts of interest.

Author contributions

Conceptualization: Gopinathan Janarthanan, Shyam Kokkattunivarthil Uthaman, Sanjairaj Vijayavenkataraman
Formal analysis: Gopinathan Janarthanan, Shyam Kokkattunivarthil Uthaman
Funding acquisition: Sanjairaj Vijayavenkataraman
Investigation: Gopinathan Janarthanan, Shyam Kokkattunivarthil Uthaman
Methodology: Gopinathan Janarthanan, Shyam Kokkattunivarthil Uthaman, Karthik Murugesh
Project administration: Sanjairaj Vijayavenkataraman
Supervision: Sanjairaj Vijayavenkataraman
Validation: Gopinathan Janarthanan, Shyam Kokkattunivarthil Uthaman
Visualization: Gopinathan Janarthanan, Shyam Kokkattunivarthil Uthaman, Karthik Murugesh
Writing – original draft: Gopinathan Janarthanan, Shyam Kokkattunivarthil Uthaman, Karthik Murugesh
Writing – review & editing: Sanjairaj Vijayavenkataraman

Ethics approval and consent to participate

Not applicable.

Consent for publication

Not applicable.

Availability of data

Not applicable.

References

1. Xiang T, Guo Q, Jia L, et al. Multifunctional hydrogels for the healing of diabetic wounds. *Adv Healthc Mater*. 2023:2301885.
doi: 10.1002/adhm.202301885

2. Gelmi A, Schutt CE. Stimuli-responsive biomaterials: scaffolds for stem cell control. *Adv Healthc Mater*. 2021;10(1):2001125.
doi: 10.1002/adhm.202001125

3. Lim J, Lin Q, Xue K, Loh X. Recent advances in supramolecular hydrogels for biomedical applications. *Mater Today Adv*. 2019;3:100021.
doi: 10.1016/j.mtadv.2019.100021

4. Karoyo AH, Wilson LD. Physicochemical properties and the gelation process of supramolecular hydrogels: a review. *Gels*. 2017;3(1):1.
doi: 10.3390/gels3010001

5. Skopinska-Wisniewska J, De la Flor S, Kozlowska J. From supramolecular hydrogels to multifunctional carriers for biologically active substances. *Int J Mol Sci*. 2021;22(14):7402.
doi: 10.3390/ijms22147402

6. Saunders L, Ma PX. Self-healing supramolecular hydrogels for tissue engineering applications. *Macromol Biosci*. 2019;19(1):1800313.
doi: 10.1002/mabi.201800313

7. Dong R, Zhou Y, Huang X, Zhu X, Lu Y, Shen J. Functional supramolecular polymers for biomedical applications. *Adv Mater*. 2015;27(3):498-526.
doi: 10.1002/adma.201402975

8. Dong R, Pang Y, Su Y, Zhu X. Supramolecular hydrogels: synthesis, properties and their biomedical applications. *Biomater Sci*. 2015;3(7):937-954.
doi: 10.1039/C4BM00448E

9. Malík M, Velechovský J, Tlustoš P. Natural pentacyclic triterpenoid acids potentially useful as biocompatible nanocarriers. *Fitoterapia*. 2021;151:104845.
doi: 10.1016/j.fitote.2021.104845

10. Xu C, Yu B, Qi Y, Zhao N, Xu FJ. Versatile types of cyclodextrin-based nucleic acid delivery systems. *Adv Healthc Mater*. 2021;10(1):2001183.
doi: 10.1002/adhm.202001183

11. Cai Y, Zheng C, Xiong F, et al. Recent progress in the design and application of supramolecular peptide hydrogels in cancer therapy. *Adv Healthc Mater*. 2021;10(1):2001239.
doi: 10.1002/adhm.202001239

12. Ayoubi-Joshaghani MH, Seidi K, Azizi M, et al. Potential applications of advanced nano/hydrogels in biomedicine: static, dynamic, multi-stage, and bioinspired. *Adv Funct Mater*. 2020;30(45):2004098.
doi: 10.1002/adfm.202004098

13. Hu J-H, Huang Y, Redshaw C, Tao Z, Xiao X. Cucurbit [n] uril-based supramolecular hydrogels: synthesis, properties and applications. *Coord Chem Rev*. 2023;489:215194. doi: 10.1016/j.ccr.2023.215194

14. Raymond DM, Abraham BL, Fujita T, et al. Low-molecular-weight supramolecular hydrogels for sustained and localized in vivo drug delivery. *ACS Appl Bio Mater*. 2019;2(5): 2116-2124. doi: 10.1021/acsabm.9b00125

15. Hao Z, Li H, Wang Y, et al. Supramolecular peptide nanofiber hydrogels for bone tissue engineering: from multihierarchical fabrications to comprehensive applications. *Adv Sci*. 2022;9(11):2103820. doi: 10.1002/advs.202103820

16. Dong RJ, Pang Y, Su Y, Zhu XY. Supramolecular hydrogels: synthesis, properties and their biomedical applications. *Biomater Sci*. 2015;3(7):937-954. doi: 10.1039/c4bm00448e

17. Wang X, Wang J, Yang YY, Yang F, Wu DC. Fabrication of multi-stimuli responsive supramolecular hydrogels based on host-guest inclusion complexation of a tadpole-shaped cyclodextrin derivative with the azobenzene dimer. *Polym Chem-Uk*. 2017;8(26):3901-3909. doi: 10.1039/c7py00698e

18. Chen Y, Pang XH, Dong CM. Dual stimuli-responsive supramolecular polypeptide-based hydrogel and reverse micellar hydrogel mediated by host-guest chemistry. *Adv Funct Mater*. 2010;20(4):579-586. doi: 10.1002/adfm.200901400

19. Ghosh G, Barman R, Sarkar J, Ghosh S. pH-responsive biocompatible supramolecular peptide hydrogel. *J Phys Chem B*. 2019;123(27):5909-5915. doi: 10.1021/acs.jpcb.9b02999

20. Wang Q, Zhang YY, Dai XY, Shi XH, Liu WG. A high strength pH responsive supramolecular copolymer hydrogel. *Sci China Technol Sc*. 2017;60(1):78-83. doi: 10.1007/s11431-016-0698-0

21. Zhu CN, Zheng SY, Qiu HN, et al. Plastic-like supramolecular hydrogels with polyelectrolyte/surfactant complexes as physical crosslinks. *Macromolecules*. 2021;54(17): 8052-8066. doi: 10.1021/acs.macromol.1c00835

22. Bernhard S, Tibbitt MW. Supramolecular engineering of hydrogels for drug delivery. *Adv Drug Deliv Rev*. 2021;171:240-256. doi: 10.1016/j.addr.2021.02.002

23. Raina N, Pahwa R, Bhattacharya J, et al. Drug delivery strategies and biomedical significance of hydrogels: translational considerations. *Pharmaceutics*. 2022;14(3):574. doi: 10.1002/btm2.10147

24. O'Connor JP, Kanjilal D, Teitelbaum M, Lin SS, Cottrell JA. Zinc as a therapeutic agent in bone regeneration. *Materials*. 2020;13(10). doi: 10.3390/ma13102211

25. Chandramohan Y, Jeganathan K, Sivanesan S, et al. Assessment of human ovarian follicular fluid derived mesenchymal stem cells in chitosan/PCL/Zn scaffold for bone tissue regeneration. *Life Sci*. 2021;264. doi: 10.1016/j.lfs.2020.118502

26. Wahid F, Zhou Y-N, Wang H-S, Wan T, Zhong C, Chu L-Q. Injectable self-healing carboxymethyl chitosan-zinc supramolecular hydrogels and their antibacterial activity. *Int J Biol Macromol*. 2018;114:1233-1239. doi: 10.1002/adhm.201900847

27. Xu J, Feng Q, Lin S, et al. Injectable stem cell-laden supramolecular hydrogels enhance in situ osteochondral regeneration via the sustained co-delivery of hydrophilic and hydrophobic chondrogenic molecules. *Biomaterials*. 2019;210:51-61. doi: 10.1016/j.biomaterials.2019.04.031

28. Grosskopf AK, Roth GA, Smith AA, Gale EC, Hernandez HL, Appel EA. Injectable supramolecular polymer–nanoparticle hydrogels enhance human mesenchymal stem cell delivery. *Bioeng Transl Med*. 2020;5(1):e10147. doi: 10.1186/s40824-018-0122-1

29. Aguado BA, Mulyasasmita W, Su J, Lampe KJ, Heilshorn SC. Improving viability of stem cells during syringe needle flow through the design of hydrogel cell carriers. *Tissue Eng Part A*. 2012;18(7-8):806-815. doi: 10.1021/acs.chemrev.0c00015

30. Lopez Hernandez H, Grosskopf AK, Stapleton LM, Agmon G, Appel EA. Non-Newtonian polymer–nanoparticle hydrogels enhance cell viability during injection. *Macromol Biosci*. 2019;19(1):1800275. doi: 10.1016/j.polymer.2018.08.029

31. Mol EA, Lei Z, Roefs MT, et al. Injectable supramolecular ureidopyrimidinone hydrogels provide sustained release of extracellular vesicle therapeutics. *Adv Healthc Mater*. 2019;8(20):1900847. doi: 10.1002/anie.201804400

32. Meis CM, Grosskopf AK, Correa S, Appel EA. Injectable supramolecular polymer-nanoparticle hydrogels for cell and drug delivery applications. *J Vis Exp: JoVE*. 2021;(168). doi: 10.1002/anie.201804400

33. Zhao Y, Song S, Ren X, Zhang J, Lin Q, Zhao Y. Supramolecular adhesive hydrogels for tissue engineering applications. *Chem Rev*. 2022;122(6):5604-5640. doi: 10.1021/acs.chemrev.1c00815

34. Morwood AJ, El-Karim IA, Clarke SA, Lundy FT. The role of extracellular matrix (ECM) adhesion motifs in functionalised hydrogels. *Molecules*. 2023;28(12):4616. doi: 10.3390/molecules28124616

35. Zhang ZP, Hu J, Ma PX. Nanofiber-based delivery of bioactive agents and stem cells to bone sites. *Adv Drug Deliv*

Rev. 2012;64(12):1129-1141.
doi: 10.1016/j.addr.2012.04.008

36. Luo ZL, Zhang SG. Designer nanomaterials using chiral self-assembling peptide systems and their emerging benefit for society. *Chem Soc Rev*. 2012;41(13):4736-4754.
doi: 10.1039/c2cs15360b

37. Yang YL, Khoe U, Wang XM, Horii A, Yokoi H, Zhang SG. Designer self-assembling peptide nanomaterials. *Nano Today*. 2009;4(2):193-210.
doi: 10.1016/j.nantod.2009.02.009

38. Shi L, Ding P, Wang Y, Zhang Y, Ossipov D, Hilborn J. Self-healing polymeric hydrogel formed by metal–ligand coordination assembly: design, fabrication, and biomedical applications. *Macromol Rapid Commun*. 2019;40(7):1800837.
doi: 10.1002/marc.201800837

39. Gopinathan J, Noh I. Recent trends in bioinks for 3D printing. *Biomater Res*. 2018;22(1):11.
doi: 10.1186/s40824-018-0122-1

40. Lee SC, Gillispie G, Prim P, Lee SJ. Physical and chemical factors influencing the printability of hydrogel-based extrusion bioinks. *Chem Rev*. 2020;120(19):10834-10886.
doi: 10.1021/acs.chemrev.0c00015

41. Li H, Wang H, Zhang D, Xu Z, Liu W. A highly tough and stiff supramolecular polymer double network hydrogel. *Polymer*. 2018;153:193-200.
doi: 10.1016/j.polymer.2018.08.029

42. Wang Z, Ren Y, Zhu Y, et al. A rapidly self-healing host–guest supramolecular hydrogel with high mechanical strength and excellent biocompatibility. *Angew Chem Int Ed*. 2018;57(29):9008-9012.
doi: 10.1002/anie.201804400

43. Wu Q, Wei J, Xu B, et al. A robust, highly stretchable supramolecular polymer conductive hydrogel with self-healability and thermo-processability. *Sci Rep*. 2017;7(1):1-11.
doi: 10.1002/anie.201804400

44. Zhu S, Wang J, Yan H, et al. An injectable supramolecular self-healing bio-hydrogel with high stretchability, extensibility and ductility, and a high swelling ratio. *J Mater Chem B*. 2017;5(34):7021-7034.
doi: 10.1039/C7TB01183K

45. Lorson T, Jaksch S, Lübtow MM, et al. A thermogelling supramolecular hydrogel with sponge-like morphology as a cytocompatible bioink. *Biomacromolecules*. 2017;18(7): 2161-2171.
doi: 10.1021/acs.biomac.7b00481

46. Li L, Tian X, Yu X, Dong S. Effects of acute and chronic heavy metal (Cu, Cd, and Zn) exposure on sea cucumbers (*Apostichopus japonicus*). *Biomed Res Int*. 2016;2016:4532697.
doi: 10.1155/2016/4532697

47. Hu T, Cui X, Zhu M, et al. 3D-printable supramolecular hydrogels with shear-thinning property: fabricating strength tunable bioink via dual crosslinking. *Bioact Mater*. 2020;5(4):808-818.
doi: 10.1016/j.bioactmat.2020.06.001

48. Gao F, Xu Z, Liang Q, et al. Osteochondral regeneration with 3D-printed biodegradable high-strength supramolecular polymer reinforced-gelatin hydrogel scaffolds. *Adv Sci*. 2019;6(15):1900867.
doi: 10.1002/advs.201900867

49. Godoy-Gallardo M, Merino-Gómez M, Mateos-Timoneda MA, Eckhard U, Gil FJ, Perez RA. Advanced binary guanosine and guanosine 5'-monophosphate cell-laden hydrogels for soft tissue reconstruction by 3D bioprinting. *ACS Appl Mater Interfaces*. 2023;15(25):29729-29742.
doi: 10.1021/acsami.2c23277

50. Yang J, Fatima K, Zhou X, He C. Meticulously engineered three-dimensional-printed scaffold with microarchitecture and controlled peptide release for enhanced bone regeneration. *Biomater Trans*. 2024;5(1):69.
doi: 10.12336/biomatertransl.2024.01.007

51. Li X, Jian H, Han Q, et al. Three-dimensional (3D) bioprinting of medium toughened dipeptide hydrogel scaffolds with Hofmeister effect. *J Colloid Interface Sci*. 2023;639:1-6.
doi: 10.1016/j.jcis.2023.02.033

52. Liu X, Song S, Chen Z, et al. Release of O-GlcNAc transferase inhibitor promotes neuronal differentiation of neural stem cells in 3D bioprinted supramolecular hydrogel scaffold for spinal cord injury repair. *Acta Biomater*. 2022;151:148-162.
doi: 10.1016/j.actbio.2022.08.031

53. Shim J-H, Jang K-M, Hahn SK, et al. Three-dimensional bioprinting of multilayered constructs containing human mesenchymal stromal cells for osteochondral tissue regeneration in the rabbit knee joint. *Biofabrication*. 2016;8(1):014102.
doi: 10.1088/1758-5090/8/1/014102

54. Chen H, Hou S, Ma H, Li X, Tan Y. Controlled gelation kinetics of cucurbit[7]uril-adamantane crosslinked supramolecular hydrogels with competing guest molecules. *Sci Rep*. 2016;6(1):20722.
doi: 10.1038/srep20722

55. Gao W, Chao H, Zheng Y-C, et al. Ionic carbazole-based water-soluble two-photon photoinitiator and the fabrication of biocompatible 3D hydrogel scaffold. *ACS Appl Mater Interf*. 2021;13(24):27796-27805.
doi: 10.1021/acsami.1c02227

56. Madl AC, Madl CM, Myung D. Injectable cucurbit [8] uril-based supramolecular gelatin hydrogels for cell encapsulation. *ACS Macro Lett*. 2020;9(4):619-626.
doi: 10.1021/acsmacrolett.0c00184

57. Zou H, Liu J, Li Y, Li X, Wang X. Cucurbit [8] uril-based polymers and polymer materials. *Small*. 2018;14(46):1802234.
doi: 10.1002/smll.201802234

58. Liu YH, Zhang YM, Yu HJ, Liu Y. Cucurbituril-

based biomacromolecular assemblies. *Angew Chem*. 2021;133(8):3914-3924.
doi: 10.1002/anie.202009797

59. Wang Z, Shui M, Wyman IW, Zhang Q-W, Wang R. Cucurbit [8] uril-based supramolecular hydrogels for biomedical applications. *RSC Med Chem*. 2021;12(5):722-729.
doi: 10.3390/molecules28083566

60. Meng Z-J, Liu J, Yu Z, et al. Viscoelastic hydrogel microfibers exploiting cucurbit [8] uril host–guest chemistry and microfluidics. *ACS Appl Mater Interfaces*. 2020;12(15): 17929-17935.
doi: 10.1021/acsami.9b21240

61. Zou L, Braegelman AS, Webber MJ. Dynamic supramolecular hydrogels spanning an unprecedented range of host–guest affinity. *ACS Appl Mater Interfaces*. 2019;11(6):5695-5700.
doi: 10.1021/acsami.8b22151

62. Madl AC, Myung D. Supramolecular host–guest hydrogels for corneal regeneration. *Gels*. 2021;7(4):163.
doi: 10.3390/gels7040163

63. Wang Y, Zhang X, Wan K, Zhou N, Wei G, Su Z. Supramolecular peptide nano-assemblies for cancer diagnosis and therapy: from molecular design to material synthesis and function-specific applications. *J Nanobiotechnol*. 2021;19(1):1-31.
doi: 10.1186/s12951-021-00999-x

64. Wang H, Zhu H, Fu W, et al. A high strength self-healable antibacterial and anti-inflammatory supramolecular polymer hydrogel. *Macromol Rapid Commun*. 2017;38(9):1600695.
doi: 10.1002/marc.201600695

65. Park KM, Roh JH, Sung G, Murray J, Kim K. Self-healable supramolecular hydrogel formed by nor-seco-cucurbit [10] uril as a supramolecular crosslinker. *Chem Asian J*. 2017;12(13):1461-1464.
doi: 10.1002/asia.201700386

66. Xiao T, Xu L, Zhou L, Sun X-Q, Lin C, Wang L. Dynamic hydrogels mediated by macrocyclic host–guest interactions. *J Mater Chem B*. 2019;7(10):1526-1540.
doi: 10.1039/C8TB02339E

67. Zhou Y, Zhang Y, Dai Z, Jiang F, Tian J, Zhang W. A super-stretchable, self-healing and injectable supramolecular hydrogel constructed by a host–guest crosslinker. *Biomater Sci*. 2020;8(12):3359-3369.
doi: 10.1039/D0BM00290A

68. Miller B, Hansrisuk A, Highley CB, Caliari SR. Guest–host supramolecular assembly of injectable hydrogel nanofibers for cell encapsulation. *ACS Biomater Sci Eng*. 2021;7(9): 4164-4174.
doi: 10.1021/acsbiomaterials.1c00275

69. Dai W, Zhang L, Yu Y, et al. 3D bioprinting of heterogeneous constructs providing tissue-specific microenvironment based on host–guest modulated dynamic hydrogel bioink for osteochondral regeneration. *Adv Funct Mater*. 2022;32(23):2200710.
doi: 10.1002/adfm.202200710

70. Wei W, Liu W, Kang H, et al. A one-stone-two-birds strategy for osteochondral regeneration based on a 3D printable biomimetic scaffold with kartogenin biochemical stimuli gradient. *Adv Healthc Mater*. 2023;12(15):2300108.
doi: 10.1002/adhm.202300108

71. Jain M, Nowak BP, Ravoo BJ. Supramolecular hydrogels based on cyclodextrins: progress and perspectives. *Chem Nano Mat*. 2022;8(5):e202200077.
doi: 10.1002/cnma.202200077

72. Rey-Rico A, Babicz H, Madry H, Concheiro A, Alvarez-Lorenzo C, Cucchiarini M. Supramolecular polypseudorotaxane gels for controlled delivery of rAAV vectors in human mesenchymal stem cells for regenerative medicine. *Int J Pharm*. 2017;531(2):492-503.
doi: 10.1016/j.ijpharm.2017.05.050

73. Alvarez-Lorenzo C, Garcia-Gonzalez CA, Concheiro A. Cyclodextrins as versatile building blocks for regenerative medicine. *JCR*. 2017;268:269-281.
doi: 10.1016/j.jconrel.2017.10.038

74. Xia D, Wang P, Ji X, Khashab NM, Sessler JL, Huang F. Functional supramolecular polymeric networks: the marriage of covalent polymers and macrocycle-based host–guest interactions. *Chem Rev*. 2020;120(13):6070-6123.
doi: 10.1021/acs.chemrev.9b00839

75. Harada A, Okada M, Li J, Kamachi M. Preparation and characterization of inclusion complexes of poly (propylene glycol) with cyclodextrins. *Macromolecules*. 1995;28(24):8406-8411.
doi: 10.1021/ma00128a060

76. Simões S, Veiga F, Torres-Labandeira J, et al. Syringeable pluronic–α-cyclodextrin supramolecular gels for sustained delivery of vancomycin. *Eur J Pharm Biopharm*. 2012;80(1):103-112.
doi: 10.1016/j.ejpb.2011.09.017

77. Li J, Li X, Ni X, Wang X, Li H, Leong KW. Self-assembled supramolecular hydrogels formed by biodegradable PEO–PHB–PEO triblock copolymers and α-cyclodextrin for controlled drug delivery. *Biomaterials*. 2006;27(22): 4132-4140.
doi: 10.1016/j.biomaterials.2006.03.025

78. Khodaverdi E, Heidari Z, Tabassi SAS, et al. Injectable supramolecular hydrogel from insulin-loaded triblock PCL-PEG-PCL copolymer and γ-cyclodextrin with sustained-release property. *AAPS Pharm Sci Tech*. 2015;16:140-149.
doi: 10.1208/s12249-014-0198-4

79. Rey-Rico A, Cucchiarini M. Supramolecular cyclodextrin-based hydrogels for controlled gene delivery. *Polymers*. 2019;11(3):514.
doi: 10.3390/polym11030514

80. Kauscher U, Stuart MCA, Drücker P, Galla H-J, Ravoo BJ.

Incorporation of amphiphilic cyclodextrins into liposomes as artificial receptor units. *Langmuir*. 2013;29(24):7377-7383.
doi: 10.1021/la3045434

81. Redondo-Gómez C, Abdouni Y, Becer CR, Mata A. Self-assembling hydrogels based on a complementary host–guest peptide amphiphile pair. *Biomacromolecules*. 2019;20(6):2276-2285.
doi: 10.1021/acsbiomaterials.0c00549

82. Redondo-Gómez C, Padilla-Lopategui S, Azevedo HS, Mata A. Host–guest-mediated epitope presentation on self-assembled peptide amphiphile hydrogels. *ACS Biomater Sci Eng*. 2020;6(9):4870-4880.
doi: 10.1021/acsbiomaterials.0c00549

83. Nowak BP, Ravoo BJ. Magneto-and photo-responsive hydrogels from the co-assembly of peptides, cyclodextrins, and superparamagnetic nanoparticles. *Farad Disc*. 2019;219:220-228.
doi: 10.1039/C9FD00012G

84. Wang J, Williamson GS, Yang H. Branched polyrotaxane hydrogels consisting of alpha-cyclodextrin and low-molecular-weight four-arm polyethylene glycol and the utility of their thixotropic property for controlled drug release. *Colloids Surf B Biointerfaces*. 2018;165:144-149.
doi: 10.1016/j.colsurfb.2018.02.032

85. Dai L, Liu K, Wang L, et al. Injectable and thermosensitive supramolecular hydrogels by inclusion complexation between binary-drug loaded micelles and α-cyclodextrin. *Mater Sci Eng C*. 2017;76:966-974.
doi: 10.1002/adfm.202200710

86. Zohreband Z, Adeli M, Zebardasti A. Self-healable and flexible supramolecular gelatin/MoS2 hydrogels with molecular recognition properties. *Int J Biol Macromol*. 2021;182:2048-2055.
doi: 10.1016/j.ijbiomac.2021.05.106

87. Singh A, Zhan J, Ye Z, Elisseeff JH. Modular multifunctional poly (ethylene glycol) hydrogels for stem cell differentiation. *Adv Funct Mater*. 2013;23(5):575-582.
doi: 10.1002/adfm.201201902

88. Aramoto H, Osaki M, Konishi S, et al. Redox-responsive supramolecular polymeric networks having double-threaded inclusion complexes. *Chem Sci*. 2020;11(17):4322-4331.
doi: 10.1039/C9SC05589D

89. Arisaka Y, Tonegawa A, Tamura A, Yui N. Terminally cross-linking polyrotaxane hydrogels applicable for cellular microenvironments. *J Appl Polym Sci*. 2021;138(3):49706.
doi: 10.1002/app.49706

90. Arisaka Y, Yui N. Polyrotaxane-based biointerfaces with dynamic biomaterial functions. *J Mater Chem B*. 2019;7(13):2123-2129.
doi: 10.1039/C9TB00256A

91. Cho IS, Ooya T. Cell-encapsulating hydrogel puzzle: polyrotaxane-based self-healing hydrogels. *Chem A Eur J*. 2020;26(4):913-920.
doi: 10.1002/chem.201904446

92. Uekama K, Hirayama F, Irie T. Cyclodextrin drug carrier systems. *Chem Rev*. 1998;98(5):2045-2076.
doi: 10.1021/cr970025p

93. Li Z, Yin H, Zhang Z, Liu KL, Li J. Supramolecular anchoring of DNA polyplexes in cyclodextrin-based polypseudorotaxane hydrogels for sustained gene delivery. *Biomacromolecules*. 2012;13(10):3162-3172.
doi: 10.1021/bm300936x

94. Segredo-Morales E, Martin-Pastor M, Salas A, et al. Mobility of water and polymer species and rheological properties of supramolecular polypseudorotaxane gels suitable for bone regeneration. *Bioconjug Chem*. 2018;29(2):503-516.
doi: 10.1021/acs.bioconjchem.7b00823

95. Ohshita N, Motoyama K, Iohara D, et al. Polypseudorotaxane-based supramolecular hydrogels consisting of cyclodextrins and Pluronics as stabilizing agents for antibody drugs. *Carbohydr Polym*. 2021;256:117419.
doi: 10.1016/j.carbpol.2020.117419

96. Jian H, Wang M, Dong Q, et al. Dipeptide self-assembled hydrogels with tunable mechanical properties and degradability for 3D bioprinting. *ACS Appl Materi Inter*. 2019;11(50):46419-46426.
doi: 10.1021/acsami.9b13905

97. Farsheed AC, Thomas AJ, Pogostin BH, Hartgerink JD. 3D printing of self-assembling nanofibrous multidomain peptide hydrogels. *Adv Materi*. 2023;35(11):2210378.
doi: 10.1002/adma.202210378

98. Chu B, He J-m, Wang Z, et al. Proangiogenic peptide nanofiber hydrogel/3D printed scaffold for dermal regeneration. *Chem Eng J*. 2021;424:128146.
doi: 10.1016/j.cej.2020.128146

99. Li Y, Wang F, Cui H. Peptide-based supramolecular hydrogels for delivery of biologics. *Bioeng Transl Med*. 2016;1(3):306-322.
doi: 10.1002/btm2.10041

100. Jagrosse ML, Agredo P, Abraham BL, Toriki ES, Nilsson BL. Supramolecular phenylalanine-derived hydrogels for the sustained release of functional proteins. *ACS Biomater Sci Eng*. 2023;9(2):784-796.
doi: 10.1021/acsbiomaterials.2c01299

101. Rajbhandary A, Raymond DM, Nilsson BL. Self-assembly, hydrogelation, and nanotube formation by cation-modified phenylalanine derivatives. *Langmuir*. 2017;33(23):5803-5813.
doi: 10.1021/acs.langmuir.7b00686

102. Misra R, Tang Y, Chen Y, et al. Exploiting minimalistic backbone engineered γ-phenylalanine for the formation of supramolecular co-polymer. *Macromol Rapid Commun*. 2022;43(19):2200223.
doi: 10.1002/marc.202200223

103. Li W, Hu X, Chen J, Wei Z, Song C, Huang R. N-(9-Fluorenylmethoxycarbonyl)-L-phenylalanine/nano-hydroxyapatite hybrid supramolecular hydrogels as drug delivery vehicles with antibacterial property and cytocompatibility. *J Mater Sci: Mater Med*. 2020;31:1-9. doi: 10.1007/s10856-020-06410-9

104. Dang-i AY, Kousar A, Liu J, et al. Mechanically stable C2-phenylalanine hybrid hydrogels for manipulating cell adhesion. *ACS Appl Mater Interfaces*. 2019;11(32): 28657-28664. doi: 10.1021/acsami.9b08655

105. Chakraborty P, Ghosh M, Schnaider L, et al. Composite of peptide-supramolecular polymer and covalent polymer comprises a new multifunctional, bio-inspired soft material. *Macromol Rapid Commun*. 2019;40(18):1900175. doi: 10.1002/marc.201900175

106. Misra R, Sharma A, Shiras A, Gopi HN. Backbone engineered γ-peptide amphitropic gels for immobilization of semiconductor quantum dots and 2D cell culture. *Langmuir*. 2017;33(31):7762-7768. doi: 10.1021/acs.langmuir.7b01283

107. Wu C, Li R, Yin Y, Wang J, Zhang L, Zhong W. Redox-responsive supramolecular hydrogel based on 10-hydroxy camptothecin-peptide covalent conjugates with high loading capacity for drug delivery. *Mater Sci Eng C*. 2017;76: 196-202. doi: 10.1016/j.msec.2017.03.103

108. Ren C, Gao Y, Liu J, et al. Anticancer supramolecular hydrogel of D/L-peptide with enhanced stability and bioactivity. *J Biomed Nanotechnol*. 2018;14(6):1125-1134. doi: 10.1166/jbn.2018.2564

109. Wei K, Chen X, Zhao P, et al. Stretchable and bioadhesive supramolecular hydrogels activated by a one-stone–two-bird postgelation functionalization method. *ACS Appl Mater Interfaces*. 2019;11(18):16328-16335. doi: 10.1021/acsami.9b03029

110. Zhang Y, Zhang H, Zou Q, Xing R, Jiao T, Yan X. An injectable dipeptide–fullerene supramolecular hydrogel for photodynamic antibacterial therapy. *J Mater Chem B*. 2018;6(44):7335-7342. doi: 10.1039/C8TB01487F

111. Clarke DE, Parmenter CD, Scherman OA. Tunable pentapeptide self-assembled β-sheet hydrogels. *Angew Chem Int Ed*. 2018;57(26):7709-7713. doi: 10.1002/anie.201801001

112. Diaferia C, Netti F, Ghosh M, et al. Bi-functional peptide-based 3D hydrogel-scaffolds. *Soft Matter*. 2020;16(30): 7006-7017. doi: 10.1039/D0SM00825G

113. Dorishetty P, Dutta NK, Choudhury NR. Bioprintable tough hydrogels for tissue engineering applications. *Adv Colloid Interface Sci*. 2020;281:102163. doi: 10.1016/j.cis.2020.102163

114. Chakraborty P, Oved H, Bychenko D, et al. Nanoengineered peptide-based antimicrobial conductive supramolecular biomaterial for cardiac tissue engineering. *Adv Mater*. 2021;33(26):2008715. doi: 10.1002/adma.202008715

115. Falcone N, Shao T, Andoy NMO, et al. Multi-component peptide hydrogels–a systematic study incorporating biomolecules for the exploration of diverse, tuneable biomaterials. *Biomater Sci*. 2020;8(20):5601-5614. doi: 10.1039/D0BM01104E

116. Fichman G, Schneider JP. Utilizing Frémy's salt to increase the mechanical rigidity of supramolecular peptide-based gel networks. *Fbioe*. 2021;8:594258. doi: 10.3389/fbioe.2020.594258

117. Chowdhuri S, Saha A, Pramanik B, et al. Smart thixotropic hydrogels by disulfide-linked short peptides for effective three-dimensional cell proliferation. *Langmuir*. 2020;36(50):15450-15462. doi: 10.1021/acs.langmuir.0c03324

118. Mañas-Torres MC, Gila-Vilchez C, Vazquez-Perez FJ, et al. Injectable magnetic-responsive short-peptide supramolecular hydrogels: *ex vivo* and *in vivo* evaluation. *ACS Appl Mater Interfaces*. 2021;13(42):49692-49704. doi: 10.1021/acsami.1c13972

119. Vrehen AF, Rutten MGTA, Dankers PYW. Development of a fully synthetic corneal stromal construct via supramolecular hydrogel engineering. *Adv Healthc Mater*. 2023;12(32):2301392. doi: 10.1002/adhm.202301392

120. Zhou K, Ding R, Tao X, et al. Peptide-dendrimer-reinforced bioinks for 3D bioprinting of heterogeneous and biomimetic in vitro models. *Acta Biomater*. 2023;169:243-255. doi: 10.1016/j.actbio.2023.08.008

121. Chiesa I, Ligorio C, Bonatti AF, et al. Modeling the three-dimensional bioprinting process of β-sheet self-assembling peptide hydrogel scaffolds. *Fmedt*. 2020;2:571626. doi: 10.3389/fmedt.2020.571626

122. Aronsson C, Jury M, Naeimipour S, et al. Dynamic peptide-folding mediated biofunctionalization and modulation of hydrogels for 4D bioprinting. *Biofabrication*. 2020;12(3):035031. doi: 10.1088/1758-5090/ab9490

123. Zhao Y, Xing Y, Wang M, et al. Supramolecular hydrogel based on an osteogenic growth peptide promotes bone defect repair. *ACS Omega*. 2022;7(13):11395-11404. doi: 10.1021/acsomega.2c00501

124. Yan M, Lewis P, Shah R. Tailoring nanostructure and bioactivity of 3D-printable hydrogels with self-assemble peptides amphiphile (PA) for promoting bile duct formation. *Biofabrication*. 2018;10(3):035010. doi: 10.1088/1758-5090/aac902

125. Sather NA, Sai H, Sasselli IR, et al. 3D printing of supramolecular polymer hydrogels with hierarchical structure. *Small*. 2021;17(5):2005743. doi: 10.1002/smll.202005743

126. Das AK, Gavel PK. Low molecular weight self-assembling peptide-based materials for cell culture, antimicrobial, anti-inflammatory, wound healing, anticancer, drug delivery, bioimaging and 3D bioprinting applications. *Soft Matter*. 2020;16(44):10065-10095. doi: 10.1039/D0SM01136C

127. Cai L, Liu S, Guo J, Jia Y-G. Polypeptide-based self-healing hydrogels: design and biomedical applications. *Acta Biomater*. 2020;113:84-100. doi: 10.1016/j.actbio.2020.07.001

128. Li C, Faulkner-Jones A, Dun AR, et al. Rapid formation of a supramolecular polypeptide–DNA hydrogel for in situ three-dimensional multilayer bioprinting. *Angew Chem Int Ed*. 2015;54(13):3957-3961. doi: 10.1002/anie.201411383

129. Zhang J, Lu N, Peng H, et al. Multi-triggered and enzyme-mimicking graphene oxide/polyvinyl alcohol/G-quartet supramolecular hydrogels. *Nanoscale*. 2020;12(8): 5186-5195. doi: 10.1039/C9NR10779G

130. Yang B, Zhao Z, Pan Y, et al. Shear-thinning and designable responsive supramolecular DNA hydrogels based on chemically branched DNA. *ACS Appl Mater Interfaces*. 2021;13(41):48414-48422. doi: 10.1021/acsami.1c15494

131. Wu J, Liyarita BR, Zhu H, Liu M, Hu X, Shao F. Self-assembly of dendritic DNA into a hydrogel: application in three-dimensional cell culture. *ACS Appl Mater Interfaces*. 2021;13(42):49705-49712. doi: 10.1021/acsami.1c14445

132. Sousa V, Amaral AJ, Castanheira EJ, *et al.* Self-supporting hyaluronic acid-functionalized G-quadruplex-based perfusable multicomponent hydrogels embedded in photo-crosslinkable matrices for bioapplications. *Biomacromolecules*. 2023;24(7):3380-3396. doi: 10.1021/acs.biomac.3c00433

133. Tang Q, Plank TN, Zhu T, et al. Self-assembly of metallo-nucleoside hydrogels for injectable materials that promote wound closure. *ACS Appl Mater Interfaces*. 2019;11(22):19743-19750. doi: 10.1021/acsami.9b02265

134. Shen CY, Wang J, Li GF, et al. Boosting cartilage repair with silk fibroin-DNA hydrogel-based cartilage organoid precursor. *Bioact Mater*. May 2024;35:429-444. doi: 10.1016/j.bioactmat.2024.02.016

135. Shi J, Shi Z, Dong Y, Wu F, Liu D. Responsive DNA-based supramolecular hydrogels. *ACS Appl Bio Mater*. 2020;3(5):2827-2837. doi: 10.1021/acsabm.0c00081

136. Shao Y, Jia H, Cao T, Liu D. Supramolecular hydrogels based on DNA self-assembly. *Acc Chem Res*. 2017;50(4):659-668. doi: 10.1021/acs.accounts.6b00524

137. Wei Y, Wang K, Luo S, et al. Programmable DNA hydrogels as artificial extracellular matrix. *Small*. 2022;18(36):2107640. doi: 10.1002/smll.202107640

138. Budharaju H, Zennifer A, Sethuraman S, Paul A, Sundaramurthi D. Designer DNA biomolecules as a defined biomaterial for 3D bioprinting applications. *Mater Horiz*. 2022;9(4):1141-1166. doi: 10.1039/D1MH01632F

139. Wang D, Duan J, Liu J, et al. Stimuli-responsive self-degradable DNA hydrogels: design, synthesis, and applications. *Adv Healthc Mater*. 2023;12(16):2203031. doi: 10.1002/adhm.202203031

140. Tang M, Zhong Z, Ke C. Advanced supramolecular design for direct ink writing of soft materials. *Chem Soc Rev*. 2023;52(5):1614-1649. doi: 10.1039/D2CS01011A

141. Miao Y, Chen Y, Luo J, et al. Black phosphorus nanosheets-enabled DNA hydrogel integrating 3D-printed scaffold for promoting vascularized bone regeneration. *Bioact Mater*. 2023;21:97-109. doi: 10.1016/j.bioactmat.2022.08.005

142. Li J, Lai Y, Li M, et al. Repair of infected bone defect with clindamycin-tetrahedral DNA nanostructure complex-loaded 3D bioprinted hybrid scaffold. *Chem Eng J*. 2022;435:134855. doi: 10.1016/j.cej.2022.134855

143. Wu W, Zhang Z, Xiong T, et al. Calcium ion coordinated dexamethasone supramolecular hydrogel as therapeutic alternative for control of non-infectious uveitis. *Acta Biomater*. 2017;61:157-168. doi: 10.1016/j.actbio.2017.05.024

144. Chen Z, Xing L, Fan Q, et al. Drug-bearing supramolecular filament hydrogels as anti-inflammatory agents. *Theranostics*. 2017;7(7):2003. doi: 10.7150/thno.19404

145. Liu X, Chen X, Chua MX, Li Z, Loh XJ, Wu YL. Injectable supramolecular hydrogels as delivery agents of Bcl-2 conversion gene for the effective shrinkage of therapeutic resistance tumors. *Adv Healthc Mater*. 2017;6(11):1700159. doi: 10.1002/adhm.201700159

146. Liu Z, Xu G, Wang C, Li C, Yao P. Shear-responsive injectable supramolecular hydrogel releasing doxorubicin loaded micelles with pH-sensitivity for local tumor chemotherapy. *Int J Pharm*. 2017;530(1-2):53-62. doi: 10.1016/j.ijpharm.2017.07.063

147. Bakker MH, van Rooij E, Dankers PY. Controlled release of RNAi molecules by tunable supramolecular hydrogel carriers. *Chem Asian J*. 2018;13(22):3501-3508. doi: 10.1002/asia.201800582

148. Liu X, Chen X, Chua MX, Li Z, Loh XJ, Wu Y-L. Injectable supramolecular hydrogels as delivery agents of Bcl-2 conversion gene for the effective shrinkage of therapeutic resistance tumors. *Adv Healthc Mater*. 2017;6(11):1700159. doi: 10.1002/adhm.201700159

149. d'Aquino AI, Maikawa CL, Nguyen LT, et al. Use of a biomimetic hydrogel depot technology for sustained delivery of GLP-1 receptor agonists reduces burden of diabetes management. *Cell Rep Med*. 2023;4(11): 101292. doi: 10.1016/j.xcrm.2023.101292

150. Davis ME, Brewster ME. Cyclodextrin-based pharmaceutics: past, present and future. *Nat Rev Drug Discov*. 2004;3(12):1023-1035. doi: 10.1038/nrd1576

151. Ma D, Zhang L-M. Novel biosensing platform based on self-assembled supramolecular hydrogel. *Mater Sci Eng C*. 2013;33(5):2632-2638. doi: 10.1016/j.msec.2013.02.023

152. Li J, Kuang Y, Gao Y, Du X, Shi J, Xu B. D-amino acids boost the selectivity and confer supramolecular hydrogels of a nonsteroidal anti-inflammatory drug (NSAID). *J Am Chem Soc*. 2013;135(2):542-545. doi: 10.1021/ja310019x

153. Li X, Li J, Gao Y, Kuang Y, Shi J, Xu B. Molecular nanofibers of olsalazine form supramolecular hydrogels for reductive release of an anti-inflammatory agent. *J Am Chem Soc*. 2010;132(50):17707-17709. doi: 10.1021/ja109269v

154. Xuan X, Zhou Y, Chen A, et al. Silver crosslinked injectable bFGF-eluting supramolecular hydrogels speed up infected wound healing. *J Mater Chem B*. 2020;8(7): 1359-1370. doi: 10.1039/C9TB02331C

155. Zhao W, Li Y, Zhang X, et al. Photo-responsive supramolecular hyaluronic acid hydrogels for accelerated wound healing. *JCR*. 2020;323:24-35. doi: 10.1016/j.jconrel.2020.04.014

156. Niu Y, Guo T, Yuan X, Zhao Y, Ren L. An injectable supramolecular hydrogel hybridized with silver nanoparticles for antibacterial application. *Soft Matter*. 2018;14(7):1227-1234. doi: 10.1039/C7SM02251D

157. Zheng Y, Yuan W, Liu H, Huang S, Bian L, Guo R. Injectable supramolecular gelatin hydrogel loading of resveratrol and histatin-1 for burn wound therapy. *Biomater Sci*. 2020;8(17):4810-4820. doi: 10.1039/D0BM00391C

158. Zhai Z, Xu K, Mei L, et al. Co-assembled supramolecular hydrogels of cell adhesive peptide and alginate for rapid hemostasis and efficacious wound healing. *Soft Matter*. 2019;15(42):8603-8610. doi: 10.1039/C9SM01296F

159. Preman NK, ES SP, Prabhu A, et al. Bioresponsive supramolecular hydrogels for hemostasis, infection control and accelerated dermal wound healing. *J Mater Chem B*. 2020;8(37):8585-8598. doi: 10.1039/D0TB01468K

160. Wang W, Zeng Z, Xiang L, et al. Injectable self-healing hydrogel via biological environment-adaptive supramolecular assembly for gastric perforation healing. *ACS Nano*. 2021;15(6):9913-9923. doi: 10.1021/acsnano.1c01199

161. Li Y, Zhu C, Dong Y, Liu D. Supramolecular hydrogels: mechanical strengthening with dynamics. *Polymer*. 2020;210:122993. doi: 10.1016/j.polymer.2020.122993

162. Kim J-H, Park K, Nam HY, Lee S, Kim K, Kwon IC. Polymers for bioimaging. *Prog Polym Sci*. 2007;32(8-9): 1031-1053. doi: 10.1016/j.progpolymsci.2007.05.016

163. Zhu Q, Qiu F, Zhu B, Zhu X. Hyperbranched polymers for bioimaging. *Rsc Adv*. 2013;3(7):2071-2083. doi: 10.1039/C2RA22210H

164. Mehwish N, Dou X, Zhao Y, Feng C-L. Supramolecular fluorescent hydrogelators as bio-imaging probes. *Mater Horiz*. 2019;6(1):14-44. doi: 10.1039/C8MH01130C

165. Gao F, Yang X, Song W. Bioinspired supramolecular hydrogel from design to applications. *Small Methods*. 2023:2300753. doi: 10.1002/smtd.202300753

166. Völlmecke K, Afroz R, Bierbach S, et al. Hydrogel-based biosensors. *Gels*. 2022;8(12):768. doi: 10.3390/gels8120768

167. Li F, Lyu D, Liu S, Guo W. DNA hydrogels and microgels for biosensing and biomedical applications. *Adv Mater*. 2020;32(3):1806538. doi: 10.1002/adma.201806538

168. Lin X, Zhao X, Xu C, Wang L, Xia Y. Progress in the mechanical enhancement of hydrogels: fabrication strategies and underlying mechanisms. *J Polym Sci*. 2022;60(17): 2525-2542. doi: 10.1002/pol.20220154

169. Omar J, Ponsford D, Dreiss CA, Lee TC, Loh XJ. Supramolecular hydrogels: design strategies and contemporary biomedical applications. *Chem Asian J*. 2022;17(9):e202200081. doi: 10.1002/asia.202200081

170. Zou L, Su B, Addonizio CJ, Pramudya I, Webber MJ. Temperature-responsive supramolecular hydrogels by ternary complex formation with subsequent photo-crosslinking to alter network dynamics. *Biomacromolecules*. 2019;20(12):4512-4521.

doi: 10.1021/acs.biomac.9b01267

171. Yang B, Liang C, Chen D, et al. A conductive supramolecular hydrogel creates ideal endogenous niches to promote spinal cord injury repair. *Bioact Mater*. 2022;15:103-119. doi: 10.1016/j.bioactmat.2021.11.032

172. Zhai X, Ma Y, Hou C, et al. 3D-printed high strength bioactive supramolecular polymer/clay nanocomposite hydrogel scaffold for bone regeneration. *ACS Biomater Sci Eng*. 2017;3(6):1109-1118. doi: 10.1021/acsbiomaterials.7b00224

173. Jeong SH, Kim M, Kim TY, Kim H, Ju JH, Hahn SK. Supramolecular injectable hyaluronate hydrogels for cartilage tissue regeneration. *ACS Appl Bio Mater*. 2020;3(8):5040-5047. doi: 10.1021/acsabm.0c00537

174. Andriamiseza F, Peters S, Roux C, Dietrich N, Coudret C, Fitremann J. Wet spinning and 3D printing of supramolecular hydrogels in acid-base and dynamic conditions. *Colloids Surf A Physicochem Eng Asp*. 2023;673:131765. doi: 10.1016/j.colsurfa.2023.131765

175. Zhang X, Fan J, Lee C-S, Kim S, Chen C, Lee M. Supramolecular hydrogels based on nanoclay and guanidine-rich chitosan: injectable and moldable osteoinductive carriers. *ACS Appl Bio Mater Interf*. 2020;12(14):16088-16096. doi: 10.1021/acsami.0c01241

176. Qin Z, Yu X, Wu H, Li J, Lv H, Yang X. Nonswellable and tough supramolecular hydrogel based on strong micelle crosslinkings. *Biomacromolecules*. 2019;20(9): 3399-3407. doi: 10.1021/acs.biomac.9b00666

177. Li N, Liu C, Chen W. Facile access to guar gum based supramolecular hydrogels with rapid self-healing ability and multistimuli responsive gel–sol transitions. *J Agric Food Chem*. 2018;67(2):746-752. doi: 10.1021/acs.jafc.8b05130

ACCSCIENCE PUBLISHING

International Journal of Bioprinting

REVIEW ARTICLE

Techniques, mechanisms, and application of 3D-printed biodegradable metals for bone regeneration

Lingxiao Wang[1,2†], Yang Liu[1†], and Zhipeng Fan[1,3,4*]

[1]Laboratory of Molecular Signaling and Stem Cells Therapy, Beijing Key Laboratory for Tooth Regeneration and Function Reconstruction of Oral Tissues, School of Stomatology, Beijing Stomatological Hospital, Capital Medical University, Beijing, China

[2]Department of Dental Implant Center, School of Stomatology, Beijing Stomatological Hospital, Capital Medical University, Beijing, China

[3]Beijing Laboratory of Oral Health, Capital Medical University, Beijing, China

[4]Research Unit of Tooth Development and Regeneration, Chinese Academy of Medical Sciences, Beijing, China

Abstract

Repairing severe bone defects and restoring complete bone tissue morphology are major challenges in clinical practice. Biodegradable metals (BMs) are bioactive materials with active degradation properties. The gradual improvement of three-dimensional (3D) printing technology holds tremendous potential for development and has spurred on the growing utilization of 3D-printed BM materials in the clinical applications of bone regeneration. In this paper, we review the application of three BM (magnesium, iron, and zinc) materials for use in 3D-printed bone regeneration; define the principle of 3D-printed bone regeneration, including the method and selection of materials; and summarize the characteristics and uses of various printing technologies and the properties, advantages, and disadvantages of BMs. Compared to traditional nondegradable implants, 3D-printed degradable metal implants have the advantages of not leaving residue, avoiding stress shielding, promoting osteogenesis and vascularization, and exhibiting antimicrobial ability. In addition, we summarize the clinical applications of 3D-printed BMs. 3D-printed BMs can be used not only for fracture fixation and bone defect repair but also for osteoporotic fracture repair, cartilage repair, maxillofacial surgery, and other processes. In this article, we discuss the advantages and limitations of the current 3D printing degradable metallic materials and describe future development prospects.

Keywords: Three-dimensional printing; Biodegradable metals; Bone regeneration; Bone tissue engineering

†These authors contributed equally to this work.

***Corresponding author:**
Zhipeng Fan
(zpfan@ccmu.edu.cn)

Citation: Wang L, Liu Y, Fan Z. Techniques, mechanisms, and application of 3D-printed biodegradable metals for bone regeneration. *Int J Bioprint*. 2024;10(3):2460.
doi: 10.36922/ijb.2460

Received: December 17, 2023
Accepted: January 19, 2024
Published Online: February 12, 2024

Copyright: © 2024 Author(s). This is an Open Access article distributed under the terms of the Creative Commons Attribution License, permitting distribution, and reproduction in any medium, provided the original work is properly cited.

Publisher's Note: AccScience Publishing remains neutral with regard to jurisdictional claims in published maps and institutional affiliations.

1. Introduction

Bone tissue is widely distributed, large, structurally complex, and functionally diverse in the human body; simultaneously, as a rare tissue with regenerative properties in the human body, bone tissue can be periodically regenerated through bone healing,

vascularization, matrix deposition, etc. to restore the structural and mechanical strength of the bone tissue and restore its function. However, when large bone defects occur as a result of severe damage, it is difficult to repair without external intervention to restore the original shape and structure.[1,2] Therefore, repair of severe bone defects is an important challenge in clinical practice. Currently, the main solutions for treatment include autologous bone grafting, allogeneic bone grafting, artificial bone material grafting, bone repair materials, and three-dimensional (3D) printing technology.[3-5] The use of autologous and allogeneic bone grafts is still affected by many challenges, including an insufficient supply of raw materials, rejection reactions, and infectious diseases.[3,6,7] In contrast, the use of artificial bone materials and bone repair materials, including bioceramics, hydrogels, and bionic nanoscaffolds, has led to many advances in severe bone defect repair.[8-10] Additive manufacturing, or 3D printing, can be used to construct 3D components that mimic the biostructural properties of bone through layer-by-layer fine positioning of biological and biochemical materials and living cells, thereby replacing bone tissues and applying them to either *in situ* or xenotransplantation.[11,12] To further the development of printing bone tissues with biomimetic effects, the selection of raw materials for 3D printing is particularly important; these materials should have specific porous properties to facilitate cellular colonization and serve as scaffolds and templates for regeneration of new tissues, while the components must maintain certain mechanical support properties to maintain the enrichment and delivery of important bone regeneration elements in the implanted area.[4,13,14]

To date, 3D printing has been widely used in the clinical treatment of bone defects, and a wide selection of materials, which are mainly categorized into synthetic materials and natural polymers, has been used.[15,16] Natural polymers, including chitosan, alginate, collagen, gelatin, cellulose, hyaluronic acid, sericin, fibrinogen, and starch, are mostly used to manufacture composite scaffolds by combination with calcium phosphate due to their bioactivity and resorbability; however, these materials are not easily amenable to fabrication and suffer from issues such as difficult removal of residual reagents in the polymer matrix and poor compatibility as a result of the utilization of toxic organic solvents.[15,17] Inorganic materials are categorized into metallic materials, bioceramics, poly(ether-ether-ketone) (PEEK), polycaprolactone (PCL), etc., of which metallic materials are most widely used.[18-20] Among metallic materials, nondegradable metals such as titanium and cobalt–chromium alloys have established clinical applications, but leave implant residues in the patient's body after applications. Because the stiffness of metallic materials is greater than that of bone tissues, residual implants may lead to stress shielding and cause separation of the implant from bone tissues; therefore, biodegradable metal (BM) materials have garnered increasing attention from scholars.[16,21-24]

The definition of a BM material is as follows: "A metal that is expected to gradually corrode in the body, and the released corrosion products cause appropriate host reactions; these corrosion products can be metabolized by cells and/or assimilated by cells and/or tissues and then completely dissolved after completing the task, assisting in tissue healing without implant residues."[25] There are three main categories of BM materials: magnesium, zinc, and iron. Moreover, biodegradable materials, including biodegradable medical sutures, bolts for fracture fixation, and biological scaffolds, have long been applied in the biomedical field. With the development of 3D printing technology, BM materials have gradually shown great advantages in terms of 3D printing characteristics, especially in the field of bone regeneration. In orthopedic clinical practice, 3D-printed BM technology has important application value. Preparing components that are suitable for the shape of bone defects is a major challenge in the repair of severe bone defects. Bone replacement materials must also have good biocompatibility, an elastic modulus, and antibacterial and osteogenic properties. 3D printing can personalize the shape of bone defects before surgery, and BM printing materials have physical and chemical properties that match those of bone tissue. An effective combination of these two materials is more conducive to the repair of bone tissue.[26,27] In this paper, we review the progress of research on various degradable metallic materials for bone regeneration reported in recent years and show the application of 3D-printed degradable metallic materials in bone regeneration in combination with various 3D printing methods (Figure 1). We also discuss key issues and challenges and provide suggestions for future research.

2. Mechanisms of bone regeneration by BMs

The bone regeneration principle of BMs involves three main steps: osteogenic differentiation, antimicrobial activity, and vascularization. The bone regeneration mechanism involving magnesium, iron, and zinc is demonstrated in Figure 2.

2.1. Osteogenic differentiation induced by BMs

Magnesium is an important component of bone, and its deficiency can lead to systemic osteoporosis and inflammatory bone resorption.[28,29] Magnesium can induce local neurons to produce calcitonin gene-related

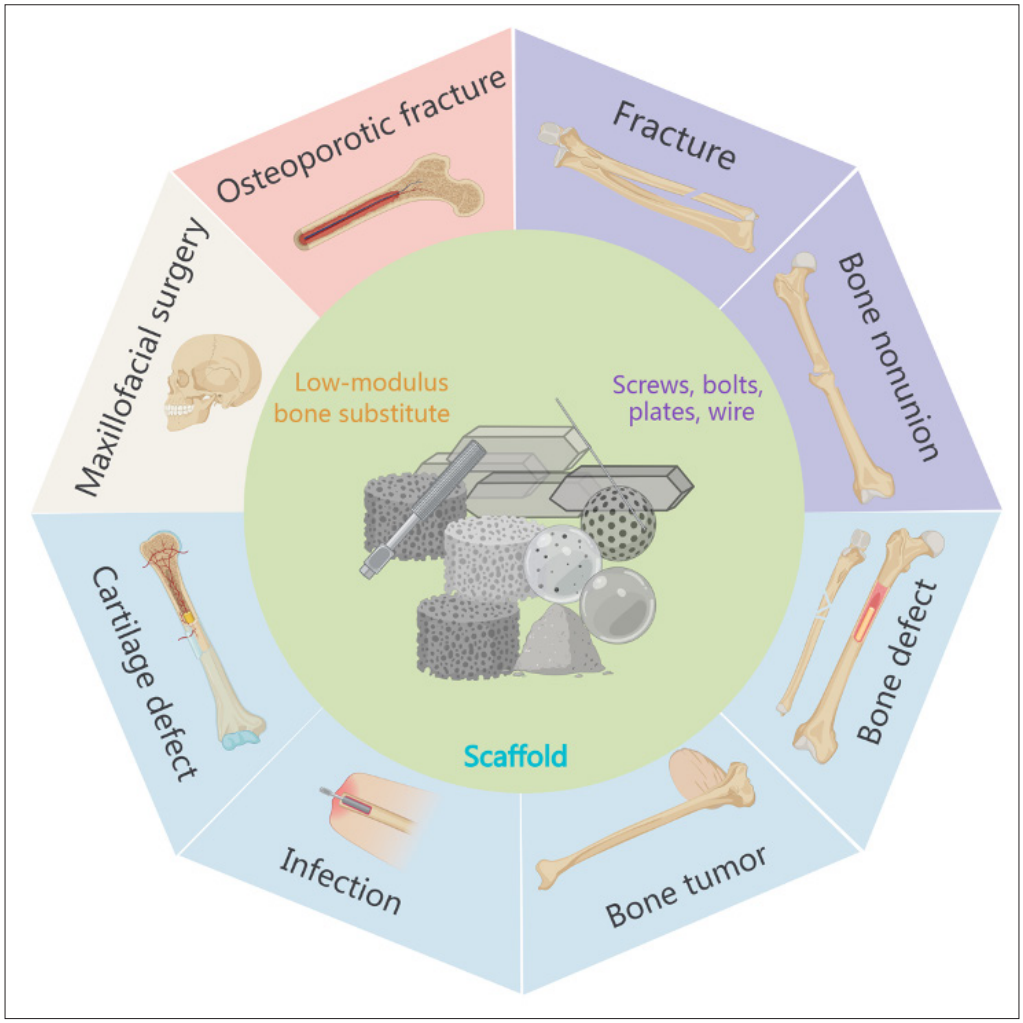


Figure 1. Illustration of the application of 3D-printed biodegradable metallic materials. Screws, bolts, plates, and wires can be used for fractures and bone nonunion; scaffolds can be used to treat trauma-induced bone defects, bone tumors, infection-induced bone defects, and cartilage defects; low-modulus bone substitution materials can be used for maxillofacial surgeries; and a full range of implants can be used to treat osteoporotic fractures.

peptide (CGRP) to promote osteogenesis through the CGRP–FAK–VEGF signaling pathway and improve the calcium-to-phosphorus ratio and mechanical properties of regenerated bone.[23,30] Animal experiments have demonstrated that magnesium ions can also promote bone formation and angiogenesis by promoting the secretion of platelet-derived growth factor BB (PDGF-BB) from mouse embryonic osteoblast precursor cells (MC3T3-E1).[31] In addition, magnesium ions can upregulate the expression of the transforming receptor potential cation channel subfamily M member 7 (TRPM7), forming an immune microenvironment favorable for osteogenesis. Magnesium ions also exhibit synergistic effects with low-dose bone morphogenetic protein 2 (BMP2) to promote osteogenesis.[32,33] However, prolonged exposure to magnesium ions leads to overactivation of NF-κB signaling in macrophages and an increase in the number of osteoclast-like cells and slows bone production by inhibiting hydroxyapatite precipitation.[34]

Zinc is another bone component; zinc deficiency can lead to slow bone growth and anemia, and zinc supplementation can prevent osteoporosis.[35,36] Zrt and Irt-like proteins (ZIPs) and zinc transporters (ZnTs) encoded by the metal transporter proteins SLC39A and SLC30A are present in the human body, and the zinc homeostasis mediated by these transporters plays an important regulatory role in bone homeostasis.[37,38] Zinc activates Runt-related transcription factor 2 (Runx2) and its downstream target gene Osterix.[36] Runx2 is the earliest osteogenic differentiation determinant and effectively promotes osteogenesis, whereas Osterix not only plays an important role in intramembranous bone formation

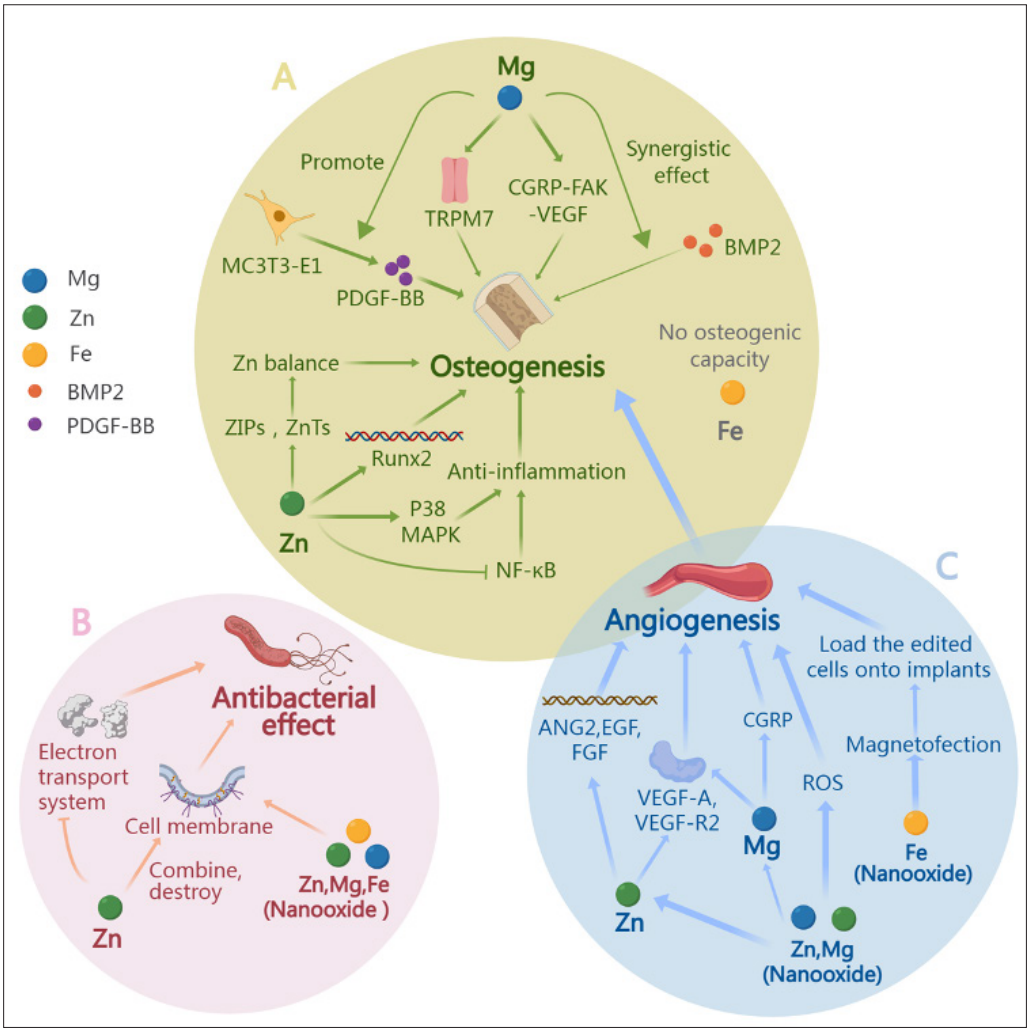


Figure 2. Mechanisms of bone regeneration by biodegradable metals. (A) Magnesium promotes osteogenesis by inducing MC3T3-E1 cells to secrete platelet-derived growth factor BB (PDGF-BB), activating the CGRP–FAK–VEGF signaling pathway, exerting synergistic effects with bone morphogenetic protein 2 (BMP2), and upregulating the expression of transforming receptor potential cation channel subfamily M member 7 (TRPM7); Zrt and Irt-like proteins (ZIPs) and zinc transporters (ZnTs) maintain zinc homeostasis; zinc can activate the Runt-related transcription factor 2 (Runx2) and P38 MAPK pathways, inhibit the nuclear factor kappa B (NF-κB) pathway, and promote osteogenesis and inflammation; and iron has no osteogenic effect. (B) The antimicrobial effect of zinc originates from its ability to inhibit oxidoreductase activity in the electron transport system and its ability to bind and destroy bacterial cell membranes and membrane proteins; zinc oxide nanoparticles, magnesium oxide, and iron oxide exhibit antimicrobial effects by destroying cell membranes. (C) Vascularization promotes osteogenesis; zinc ions upregulate angiopoietin-2 (*ANG2*), epidermal growth factor (*EGF*), and fibroblast growth factor (*FGF*) gene expression and increase vascular endothelial growth factor-A (VEGF-A) and vascular endothelial growth factor-R2 (VEGF-R2) protein levels, which in turn promote angiogenesis; magnesium increases VEGF protein levels and promotes calcitonin gene-related peptide (CGRP)-mediated angiogenesis; zinc nanooxide and magnesium oxide generate reactive oxygen species (ROS) and slowly and stably release metal ions to promote vascularization; and iron nanooxide promotes vascularization by performing magnetic transfection for gene modification, indirectly promoting vascularization.

but also influences intrachondral osteogenesis through its involvement in terminal cartilage differentiation.[39] Zinc also promotes the accumulation and deposition of citrate in bone apatite.[40] In bone tissue, the zinc content is positively correlated with whole-body bone mineral density (BMD) and bone mineral content (BMC).[41] Additionally, zinc inhibits stimulation of RANKL (receptor activator of NF-KB ligand) and suppresses osteoclastogenesis through the RANKL/RANK/OPG signaling pathway in osteoclast precursors.[42] Zinc can also exert anti-inflammatory effects by activating the P38 MAPK pathway and inhibiting the nuclear factor kappa B (NF-κB) pathway, but a high concentration of zinc ions leads to overactivation of NF-κB signaling and thus induces osteoclastogenesis.[43-45]

Iron is an essential trace element. Although iron in implants undergoes *in vivo* degradation, cells possess a

mechanism to maintain iron homeostasis, and the slow degradation of iron-based scaffolds and the difficulty in metabolizing the products prevent large changes in plasma iron levels.[46-48] If an implant is not loaded with other substances or if alloying elements with osteogenic effects are added, iron-based implants have a weak osteogenic effect *in vivo*.[49,50]

Among the three BM materials tested, magnesium has a strong and stable osteogenic differentiation effect, zinc is slightly inferior due to its ability to inhibit osteogenesis at higher concentrations and cytotoxicity, and the osteogenic differentiation effect of iron *in vivo* has rarely been reported.

2.2. Antibacterial effects of BMs

In addition to antibiotics, metals are a focus of current research seeking antibacterial substances. The antimicrobial effect of zinc originates from its ability to bind and disrupt bacterial cell membranes and membrane proteins, alter cellular permeability to calcium ions, and disrupt oxidoreductase enzymes in the electron transport system, and the antimicrobial effect of free zinc ions shows a dose-dependent effect.[51] The zinc ions released from pure zinc implants during degradation have significant antimicrobial effects, and the antimicrobial capacity of implants can be further strengthened by adding silver and lithium to form alloys.[52,53] The addition of zinc or zinc ions to nonbiodegradable metal scaffolds has also been shown to confer antimicrobial activity to the components.[54-56] In addition to zinc ions, metals that form nanoparticles can also exert antimicrobial effects. NPs can interact with bacterial cell membranes, leading to leakage, inducing oxidative stress, and ultimately leading to bacterial death.[57] Zinc nanooxide, magnesium nanooxide, and iron nanooxide have strong antibacterial effects.[58-60] Among the three degradable metallic materials, magnesium, iron, and zinc have the most prominent antimicrobial activity, while magnesium and iron are slightly inferior and exert antimicrobial activity only when used as nanooxides.

2.3. Vascularization induced by BMs

Both magnesium and zinc can promote vascularization. Magnesium can promote endothelial cell migration in a dose-dependent manner, upregulate vascular endothelial growth factor, and promote CGRP-mediated angiogenesis to promote neovascularization and prevent vascular leakage.[61,62] The use of magnesium-based implants or the addition of magnesium to implants can promote vascularization and thus accelerate bone regeneration.[63-65] Zinc ions can upregulate the gene expression of angiopoietin-2 (ANG2), epidermal growth factor (EGF), and fibroblast growth factor (FGF) and increase the protein levels of vascular endothelial growth factor-A (VEGF-A) and vascular endothelial growth factor-R2 (VEGF-R2), which in turn promote angiogenesis.[66,67] The production of reactive oxygen species (ROS) and the slow and steady release of metal ions from magnesium oxide or zinc oxide nanoparticles can promote vascularization, but importantly, an excessive concentration of zinc ions can instead inhibit angiogenesis.[68,69] Iron itself has no pro-vascularization activity, but iron oxide nanoparticles can be used in conjunction with electromagnetic fields to magnetically transfect the *miR-21* gene into bone marrow mesenchymal stem cells (BMSCs) and human umbilical cord endothelial cells (HUVECs), and the transfected cells can be loaded onto implants to promote vascularization and osteogenesis.[70] In general, magnesium has a stronger ability to promote vascular activity than zinc does, while the effect of iron is weaker than that of both.

3. Common 3D printing techniques for BMs

Three-dimensional printing techniques for BM materials can be broadly categorized into 3D printing of BMs and their alloys, and 3D printing of nonmetallic materials mixed with BM materials. The two manufacturing methods used were pure metal scaffolds and hybrid material scaffolds. The 3D printing methods commonly used for metals can be categorized into four main groups: powder bed fusion (PBF), direct energy deposition (DED), material extrusion (ME), and binder jetting (BJ).[71,72] The most commonly used and most effective method for implant fabrication is PBF, which is more accurate than the other methods, can print highly complex components, can generate finished products with strong mechanical properties, and is better suited to the needs of clinical implants.[73,74] Table 1 displays the advantages and disadvantages of each 3D printing method.

3.1. Three-dimensional printing of BMs by powder bed fusion

Powder bed fusion is an additive manufacturing process in which metal powders in a powder bed are bonded and sintered using thermal energy, with the energy source usually being a laser or an electron beam. The material is preheated in a vacuum or inert gas environment, and a laser or electron beam is used to selectively sinter a portion of the powder in the powder bed to form a crystalline metal layer, followed by a drop of the powder bed, where the new metal powder covers the sintered metal layer, on which sintering is performed again, and the procedure is repeated until the metal component is printed.[75,76] The advantages of PBF include high precision, control, suitability for metallic materials, and the ability to create porous structures by adding other substances (e.g., diamond).[77,78] The disadvantages of PBF include sputtering and metal vaporization. Especially for magnesium alloys,

Table 1. Comparison of the advantages and disadvantages of 3D printing methods

Materials	Name of technology	Advantages	Disadvantages	References
Biodegradable metal	Powder bed fusion	High precision, high controllability, suitable for metallic materials	Metal oxidation, sputtering, and vaporization in the manufacturing process	77-80
	Direct energy deposition	High efficiency, material saving, low cost	Need to add auxiliary support structure, low precision, lack of heat dissipation media caused by stress build up	84,85
	Material extrusion	Printing process can be carried out at room temperature	Need to add auxiliary support structure, low mechanical strength, adhesive residue may exist	98-100
	Binder jetting	Printing process can be carried out at room temperature, can be used without adhesives, can print larger components	Low mechanical strength	102-105
	3D weaving	No heat treatment required	High cost and manufacturing difficulty	109
Hybrid materials	Fused deposition modeling, cryogenic deposition 3D printing, etc.	Wide range of materials, have both plasticity and bioactivity	Lower mechanical strength than metals	133,186,188-190

due to the high melting point of magnesium at 650°C, which is close to its boiling point (1091°C), vaporization is highly likely to occur during fabrication using PBF.[77]

Scaffolds fabricated using PBF have high fineness and a wide variety of materials to achieve excellent fabrication effects.[79,80] The high precision and controllability of PBF are essential for controlling the pore size of porous scaffolds, where pores larger than 100 μm promote osteogenesis and angiogenesis, and micropores smaller than 20 μm can be utilized to achieve a more homogeneous distribution of neoplastic bone through capillary action and, by facilitating cellular recruitment and attachment, stimulate mineralization.[81] Scaffolds with both macropores and micropores have optimal bone-enhancing effects.[82] In addition, scaffolds with high fidelity can provide more adequate support for bone defect healing, and the precise arrangement of cells and drugs loaded in the scaffolds can also result in superior bone regeneration promotion.[83]

3.2. Three-dimensional printing of BMs by direct energy deposition

Direct energy deposition is used to manufacture parts by melting powdered materials as they are deposited; the most commonly used method is wire arc additive manufacturing (WAAM). A metal powder is ejected from a nozzle into a vacuum or inert gas environment, while an electron beam is used as a heat source to melt the powder and sinter it, thus printing components layer by layer.[84,85] Scaffolds fabricated using DED can be added to modify the structure several times during the fabrication process, avoiding material waste and decreasing costs.[86,87] The advantages of DED include the high density mechanical properties of the finished product, high efficiency, material savings, low cost, and suitability for printing large components.[87] Furthermore, DED can be used to add structures to existing components, such as by adding hard surfaces to enhance the mechanical strength of the component.[88] The disadvantages of these methods include the need to add auxiliary support structures during the printing process, lower precision, rough surface structures, and the lack of a heat dissipation medium (e.g., loose metal powder) around the component, which can easily lead to stress buildup.[85,87,89]

The higher density and lower porosity allow the fabrication of components with higher mechanical strength when using DED than when using other printing methods; for instance, DED-printed 316L stainless steel components are similar in strength to those prepared by conventional fusion casting.[90] These properties allow DED to retain the high mechanical properties of the material while incorporating a flexible shape that can provide more adequate support for bone regeneration.[91,92] Moreover, although the surface of DED-produced components is rough, a smooth surface can be obtained by treating the components, and the components can also be endowed with a microscopic rough texture by specific means to increase the levels of osteoprotegerin, transforming growth factor beta 1 (TGF-β1), VEGF-A, FGF-2, and angiopoietin-1 in osteoblasts, which can promote bone regeneration.[93-96]

3.3. Three-dimensional printing of BMs by material extrusion

Material extrusion is also commonly known as 3D plotting or 3D gel printing. When applied to metals, the "ink" made by mixing a metal powder with a binder is extruded through a nozzle during printing and stacked layer by layer to obtain the initial finished product. The preliminary product is then degreased and heat-treated to remove the binder, resulting in a metal component.[85] The most obvious benefit of ME over other approaches is that products can be processed and printed at room temperature; this not only reduces vaporization, sputtering, and oxidation of the metal but also allows the incorporation of materials that are not resistant to high temperatures into the component. The equipment costs for ME are also lower than those for other printing methods. The disadvantages of ME include the poor mechanical properties of the components, rough surface of the products, possible distortion of the component structure during subsequent heat treatment, possible presence of adhesive residues, and limited material selection. By choosing a lower extrusion temperature and layer thickness, it is possible to achieve a relatively smooth component surface and improve the precision.[97]

Material extrusion can use high-purity magnesium powder as a raw material, while other printing methods, such as PBF and DED, cannot easily be applied to pure magnesium due to vaporization during the printing process. The use of appropriate binders and methods such as short-term liquid-phase sintering can create porous magnesium scaffolds with high porosity and high structural fidelity to support the regeneration of bone tissue.[98] Furthermore, surface modification of porous magnesium scaffolds can reduce the degradation rate.[99,100] A high porosity provides a pathway for bone growth into the scaffold, and a reduced degradation rate provides time for bone regeneration, while magnesium has properties such as osteogenic activity and pro-vascularization that can enhance the effect of bone regeneration.[23,30,31]

3.4. Three-dimensional printing of BMs by a binder jet

The BJ manufacturing process is similar to that of PBF in that both use a powder bed for feeding; the difference is that PBF uses a laser or electron beam to sinter the metal powder, whereas BJ binds the metal powder by directional spraying of a liquid binder or by relying on capillary forces. After the initial printing, the constructs are heat-treated to remove the adhesive and increase their mechanical strength.[85] Binder jetting has the following advantages: (i) printing can be performed at room temperature, (ii) the components are supported during the printing process, and (iii) the components can be printed without the use of adhesives.[101,102] In addition, the wide selection of materials suitable for BJ enables the fabrication of components with appropriate mechanical strength by adjusting the materials used, such as magnesium–zinc alloy, magnesium phosphate, and 316L stainless steel.[103-105] The microstructure and mechanical properties of the components fabricated using BJs change with respect to the sintering temperature. By using the appropriate heat treatment temperature and holding time, components with a density, compressive properties, and an elastic modulus similar to those of human cortical bone and with appropriate porosity can be obtained.[102] Physical properties similar to those of human bone tissue can provide support while minimizing stress shielding for bone regeneration.[106-108]

3.5. Three-dimensional printing of BMs by 3D weaving

In addition to traditional 3D printing methods, several new printing techniques have achieved excellent results. For example, 3D weaving magnesium wires, in which magnesium alloy filaments are woven in a fixed sequence and structure supplemented by filler wires, can create magnesium implants with porous structures.[109] This method does not require heat treatment, and the mechanical properties of the components are significantly improved after being covered with a polylactic acid (PLA) coating with appropriate mechanical strength. The structural properties, including porosity, pore size, and connectivity, of the components fabricated using 3D braiding are more controllable than those of components fabricated by any other printing method, but this method has the disadvantages of difficult fabrication and high cost.[109] The excellent connectivity of 3D woven components provides excellent support for cell attachment and spreading and provides pathways for neovascularization, which in turn promotes bone regeneration.[110]

4. Selection of BM materials for 3D printing

The main BM materials that can be used as implants are magnesium, zinc, iron, and their alloys. Table 2 and Figure 3 show the advantages, disadvantages, mainstream 3D printing technologies, common alloys, implants, and applications of these three BMs.

4.1. Magnesium and its alloys

The Young's modulus of magnesium-based alloys is similar to that of bone cancellous mass, and the density of magnesium and its alloys is also close to that of human bone, which is favorable for eliminating the stress masking of magnesium implants.[111,112] Moreover, the degradation products of magnesium *in vivo*, magnesium ions, are biologically active and can directly induce osteoblast proliferation while promoting CGRP release from

Table 2. Advantages and disadvantages of biodegradable metallic materials

Materials	Advantages	Disadvantages	Mainstream 3D printing technologies	Common alloys	Implants	Applications	References
Magnesium and its alloys	Density and Young's modulus close to those of bone tissue, magnesium ions promote osteogenesis and vascularization	Excessive biodegradation rate, hydrogen precipitation and alkalization during degradation	PBF, ME, BJ, 3D weaving	Magnesium phosphate, polycaprolactone/ magnesium, Mg–Nd–Zn–Zr alloys	Magnesium phosphate implant, JDBM implant	Osteoarthritis of the hip, oral implant, bone defect repair, osteoporosis bone defect	23,111-113,116-118,127-130,132-134
Zinc and its alloys	Moderate biodegradation rate, zinc ions promote bone formation and vascularization, good antimicrobial activity	Low biocompatibility with cytotoxicity, high manufacturing difficulty, uneven alloy phase causing pitting, low mechanical strength	PBF, DED, BJ	ZnO, ZnO-AgHAP, Zn–xMg alloys	Implants modified with zinc coating	Oral implant, antimicrobial coating	137-146,165
Iron and its alloys	High tensile and mechanical strength, excellent biocompatibility, low cost	Low degradation rate, high modulus of elasticity, degradation produces nonmetabolizable iron oxides	L-PBF, BJ	Fe–Mn–Ca/Mg, Fe–Mn, Fe–Si	Fe–Si implant	Bone defect repair	46,47,49,166-168,181-183

Abbreviations: BJ, binder jetting, DED, direct energy deposition; L-PBF, laser powder bed fusion; ME, material extrusion; PBF, powder bed fusion.

neuronal cells, which in turn promotes the osteoblast proliferation and neovascularization and accelerates the healing of bone defects.[23,113] By converting magnesium components into porous structures, the voids in the components can support the growth of mineralized tissues, and the connectivity of the voids can guarantee the flow of nutrients and metabolic waste to the new tissues.[113-115] The voids can also be filled with bioactive drugs to promote bone regeneration. Considerable experience has been achieved in the manufacture of porous magnesium with a variety of manufacturing options.[79,80]

The most significant disadvantage of magnesium alloys is their rapid rate of biodegradation, which makes these materials likely to corrode completely before the patient's fracture heals; thus, they fail to provide adequate mechanical support at a later stage, and other means are required to retard the *in vivo* degradation of magnesium alloys.[116-118] To control the rate of magnesium corrosion, components are usually surface-modified, alloyed, purified, or converted into porous structures. Specific methods of surface modification include the addition of coatings and nanodiamonds, mesoporous silica (MS), etc. to magnesium alloys to retard magnesium degradation corrosion.[80,119,120] Coatings may break down after several weeks or months due to cracking, inhomogeneous degradation, etc., resulting in the loss of coating protection for the component, and the survival time may not be sufficient to support magnesium alloy implants safely through the recovery period of bone defects in the patient.[72,121] When other substances are added to magnesium to form magnesium alloys, the corrosion precipitation of the alloying elements (e.g., Al and Mn) may be cytotoxic, and the proportion of the alloying elements added will affect the corrosion rate of the components, which is different for different patients in the clinic; moreover, the addition of rare earth elements may be potentially biotoxic to a certain extent, and their biocompatibility is still uncertain.[116,122,123] Increasing the purity of magnesium does not cause biotoxicity but has a limited effect on the magnesium degradation rate.[124,125] Converting building blocks into porous structures is limited by the problems of uneven pore distribution, the presence of residues, and the high cost of the technology.[80,126]

Additionally, the degradation of magnesium *in vivo* that occurs via a protocell reaction generates magnesium ions and hydroxide ions, ultimately producing magnesium hydroxide and hydrogen gas. The magnesium hydroxide generated by the reaction is loose and does not provide protection for the components, while the precipitated hydrogen creates gas cavities that hinder tissue growth, and the hydroxide released during the corrosion process is also cytotoxic.[127-130] The human body can slowly absorb precipitated hydrogen and neutralize alkalinity, so delaying the degradation of magnesium is an effective way to prevent gas cavity generation and alkalization. For example, Mg–Zn alloys exhibit increased corrosion resistance and reduced hydrogen precipitation and

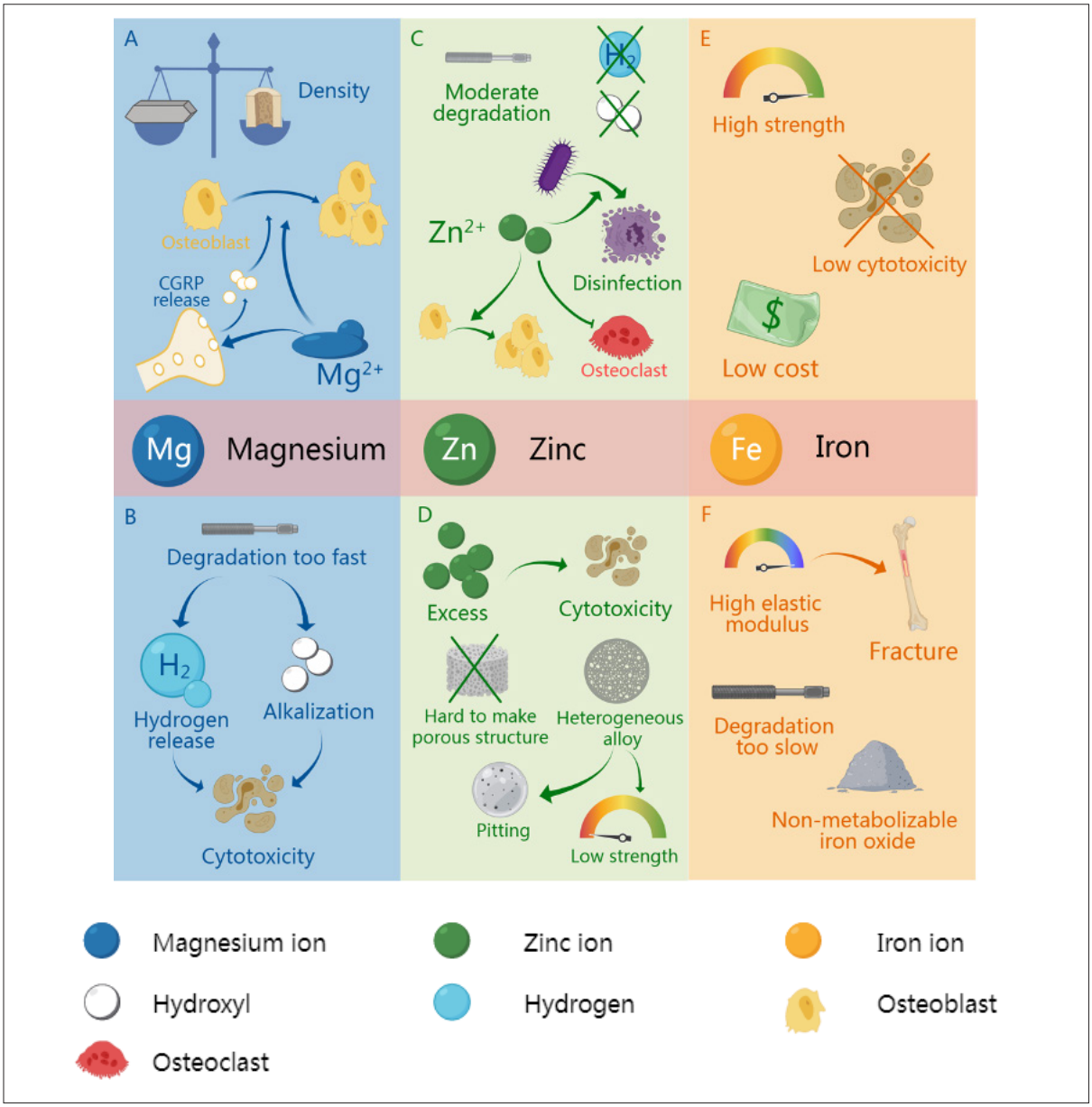


Figure 3. Schematic diagram of the advantages and disadvantages of 3D-printed biodegradable metallic materials. (A) The density of magnesium is comparable to that of human bone; magnesium degradation results in the production of Mg^{2+} cations, which can directly promote osteoblast proliferation and can also promote calcitonin gene-related peptide (CGRP) release from neuronal cells to indirectly promote osteoblast proliferation. (B) Rapid degradation of magnesium produces H_2 bubbles and OH^- ions, leading to localized air pockets and alkalization, which cause cytotoxicity and impede healing. (C) Zinc is degraded at an appropriate rate; it does not produce gas cavities or cause alkalization; Zn^{2+} ions are produced after zinc degradation and have bactericidal effects, inhibit osteoclast activity, and promote osteoblast proliferation. (D) Excess Zn^{2+} ions exert cytotoxic effects; zinc-based alloys cannot easily form porous structures; zinc-based alloys have an inhomogeneous alloying phase, resulting in alloys with low mechanical strength that are prone to pitting. (E) Iron-based alloys have high mechanical strength, low cytotoxicity, and low cost. (F) Iron-based alloys with an excessively high modulus of elasticity have stress interruptions and are prone to fracture; degradation rates are too slow; and degradation leads to the buildup of nonmetabolizable iron oxides.

alkalization while retaining the mechanical properties of magnesium close to bone tissue.[123] In terms of *in vivo* implants, the degradation of Mg implants mainly results in the production of Mg ions. Although we know that cells have a certain physiological range of tolerance to Mg ions, the Mg ions produced by the degradation of Mg implants do not change the concentration of Mg ions in the serum, as excessive Mg ions can be excreted from the body through the urinary system. Therefore, Mg implants have a certain degree of biological safety.[131] The mainstream 3D

printing methods for magnesium and magnesium alloys mainly include PBF, ME, BJ, and 3D weaving. 3D-printed regenerated magnesium phosphate implants can ensure the stability and recovery of hip joint dysplasia,[132] and 3D-printed polycaprolactone/magnesium porous scaffolds can promote bone defect repair in the early stages and have good cell compatibility.[133] Porous 3D-printed Mg Nd Zn Zr (referred to as JDBM) implants possess good mechanical properties, are compatible with MC3T3-E1 and RAW267.4 cells, and prevent implant infections.[134]

4.2. Zinc and its alloys

While pure zinc has a low tensile strength (20 MPa) and is usually not used in the manufacture of implants, zinc alloys can achieve tensile strengths of 200–600 MPa, which satisfy the requirements for bone implants.[16,135,136] The main advantage of zinc alloys is that their biodegradation rate is between that of magnesium- and iron-based alloys and is closest to the ideal biodegradation rate; this allows zinc alloys to provide effective support for bone defect healing before complete degradation and to avoid secondary damage from stress interruption after healing. Second, zinc ions are involved in bone formation and mineralization and can accelerate bone defect healing by activating Runx2 and Osterix to promote osteoblast differentiation, inhibiting RANKL to reduce osteoclastogenesis, and promoting citrate deposition.[137-139] Zinc also has a proangiogenic effect, which guarantees good blood circulation during bone regeneration. Moreover, zinc has strong antimicrobial activity with some anti-infective effects, providing a stable immune microenvironment for bone regeneration.[140]

The disadvantages of zinc include its low biocompatibility and high manufacturing difficulty. Excessive release of zinc ions during degradation results in cytotoxicity and attenuates osteoblastic activity, decelerating the healing of bone defects.[141-144] Furthermore, zinc has a lower melting point than magnesium, and although zinc does not react with air, it is difficult to convert into porous structures due to vaporization and sputtering during processing.[145,146] Retarding the corrosion of zinc-based alloys by surface modification, adding different elements or improving the alloy manufacturing process can improve the properties of these alloys. Surface modifications such as microarc oxidation (MAO) can regulate the oxidation of zinc and improve its biocompatibility, but there is still a certain degree of cytotoxicity, and the degradation rate is far greater than that of pure zinc, deviating from the ideal biodegradation rate.[142] Additionally, biomimetic deposition can improve biocompatibility. Immersing the components in SBF solution for 14 days can result in the formation of a protective layer of corrosion products, which can delay corrosion and improve cytocompatibility.[147] The remaining methods, such as atomic layer deposition (ALD), magnetron sputtering, or sandblasting, may delay degradation while decreasing biocompatibility as well as cracking and uneven degradation.[148,149]

The addition of other elements and the choice of different manufacturing methods can also improve the properties of alloys. For example, the addition of aluminum to zinc-based alloys enhances the antimicrobial activity of the components, but aluminum is also cytotoxic and may cause inflammation.[150,151] The addition of titanium, copper, magnesium, manganese, lithium, and other metal elements to zinc can delay component corrosion. Currently, the most studied zinc-based alloys are Zn–xMg and Zn–xAl alloys, which, when prepared by appropriate fabrication methods, such as plasma sintering (MASPS) to control the porosity of the components, can improve the mechanical properties while reducing the degradation rate.[152-154] Zn–Mg alloy scaffolds have great potential in the treatment of load-bearing bone defects. On the one hand, zinc and magnesium play important roles in bone metabolism and are conducive to cell proliferation and bone tissue regeneration; on the other hand, Zn–Mg alloys can avoid the production of hydrogen gas, severe pH fluctuations, and rapid corrosion after injection. Moreover, Mg is added to the Zn matrix to provide nucleation sites and promote the production of secondary Mg2Z11 phases, leading to grain refinement and strengthening. The synergistic effect of solid solution strengthening and precipitation strengthening endows Zn–Mg alloys with unique advantages in the treatment of orthopedic diseases, helps avoid chronic inflammatory reactions caused by permanent implantation, and removes the need for additional surgeries.[155] At present, scholars have focused mainly on the mechanical properties, wear resistance, fatigue resistance, corrosion resistance, degradation behavior, microstructure, and other directions of Zn–Mg alloys. By introducing specific metals or nonmetal elements, improving preparation methods, programming degradation behavior, etc., Zn–Mg alloys can be modified to improve their bone regeneration potential.[156,157]

Magnesium–zinc alloys are the most biocompatible, and the mechanical properties of these alloys can be significantly improved by adjusting the Zn–Mg ratio. The Mg–Zn alloy components molded by hot extrusion using a casting process have a low degradation rate and good mechanical strength.[158] However, whether the alloy phase of a component is uniformly distributed has an important impact on its mechanical properties and corrosion form, and if a uniform distribution cannot be achieved during the manufacturing process, the component may suffer from mechanical strength degradation, localized pitting corrosion, and other problems.[159-162] However, how to

enhance the precision of these components through 3D printing while ensuring the uniform distribution of the alloy phase is yet to be studied. Zinc is an essential trace element for humans. The dietary allowance for zinc in the United States is 8–11 milligrams per day. In terms of implants, the degradation products of zinc implants are mainly zinc oxide, zinc hydroxide, and zinc phosphate. The high biocompatibility of degradable zinc metal mainly comes from zinc phosphate, which is a common dental adhesive.[163] The mainstream 3D printing methods for zinc and zinc alloys mainly include PBF, DED, and BJ. Doping strontium (Sr) and zinc (Zn) into hydroxyapatite nanoparticle (HANPs) and incorporating them into 30 wt.% polyether ether ketone (PEEK) can produce skull implants with good mechanical properties.[164] Furthermore, 3D-printed titanium-based implants modified with ZnO coatings have efficient antibacterial properties and can play a role in repairing severe bone defects.[165]

4.3. Iron and its alloys

The promotion of bone regeneration by iron alloy implants is mainly reflected in the provision of adequate physical support and connectivity as a result of the porous structure. In addition, the good biocompatibility of iron leads to a stable immune microenvironment for the healing of bone defects. A representative iron alloy commonly used in bone regeneration is 316L austenitic stainless steel.[49] While 316L steel has excellent tensile and mechanical strengths, making it the gold standard for orthopedic implants, its austenitic morphology is MRI-compatible, thus facilitating subsequent medical treatment; it is also biocompatible, as no hydrogen is generated during degradation. The high tensile and mechanical strength of 316L steel enable greater mechanical support and utilization for larger bone defects.[166-168]

The disadvantages of iron and iron alloy implants include their extremely low degradation rate and excessively high modulus of elasticity. The slow degradation allows iron-based implants to remain in the body after the patient has healed, and their modulus of elasticity does not match that of the bone tissue, which can lead to stress interruptions similar to those experienced by nondegradable metal implants. Additionally, due to the presence of certain amounts of chromium and nickel in some ferrous alloys, these materials may cause allergic reactions in some patients.[169]

The *in vivo* degradation process of ferrous alloys is complex and slows the *in vitro* degradation process, with a dense layer of iron oxide degradation products being formed on the surface of the implant, which prevents oxygen transport and considerably slows the degradation of the implant, resulting in no significant difference among the *in vivo* degradation rates of various iron-based alloys.[170] Furthermore, iron oxides are difficult to metabolize *in vivo* and are prone to buildup, hindering bone defect healing.[46,47] Therefore, the main way to improve the rate of iron degradation is to convert iron into porous structural alloy components.[171] The main Fe-based alloys that have been studied are Fe–Mn alloys and Fe–Cu alloys, such as Fe-35Mn, Fe-30Mn, Fe-Mn-Pd, and Fe-xCu.[171-175] The mechanical properties of these alloys are weaker than or comparable to those of 316L steel; additionally, these alloys exhibit good biocompatibility, higher corrosion rates, and more homogeneous corrosion types but still fall short of ideal biodegradation rates.[171,172,174-176] The addition of copper to the alloys led to antimicrobial activity, but the density and Young's modulus decreased with increasing copper content.[50,177] Adding manganese, however, may adversely affect the cytocompatibility of the alloy.[178] Another unique alloying method is to form a powder with a copper shell over an iron core by electroplating, where the powder particles are alloyed on the outer periphery and pure iron exists on the inside.[179] This powder can be used to generate macroscopically homogeneous and biodegradable sintered parts composed of iron and copper alloys. However, this powder has the disadvantage of microscopic copper precipitation during the sintering process, resulting in an uneven distribution of copper in the components, a high content of the outer layer, and precipitated subnanometer copper blockage in the pores of the components, which may adversely affect the degradation of the components. In terms of *in vivo* implants, the degradation rate of iron implants is extremely low, which may cause negative effects similar to permanent implants. The degradation products of iron mainly include Fe^{2+} and Fe^{3+}, which may catalyze the generation of reactive oxygen species and free radicals. Therefore, some scholars do not recognize iron as a safe and BM material.[180] The mainstream 3D printing methods for iron and iron alloys mainly include laser powder bed fusion (L-PBF) and BJ. Common iron-based alloys include Fe, Mn, and Ca/Mg alloys, which can be used for skull repair. A porous biodegradable Fe–Mn alloy, as a mesh scaffold, is used for severe bone defect repair. The Fe–Si implant can be used as a solid implant for bone transplantation and as a temporary implant for fracture fixation.[181-183]

4.4. Hybrid materials

In addition to pure metal scaffolds, it is also possible to promote vascularization, enhance osteogenesis, and strengthen the mechanical properties of new bone by adding degradable metal components, such as magnesium oxide nanoparticles, to other nonmetallic materials and releasing them through slow degradation, which can significantly enhance the mechanical properties of some materials.[184] Hybrid material scaffolds have the advantage

of combining the good biocompatibility and plasticity of nonmetallic materials with the bioactivity of BMs.[185-187] These scaffolds are usually prepared by fused deposition modeling, in which metal powders are mixed with PEEK, PCL, etc. to form fused filaments, which are heated and extruded through a nozzle during printing and stacked layer by layer to generate the finished product.[133,186,188] Depending on the material used, cryogenic deposition 3D printing, material extrusion printing, and other methods may also be used.[189,190] In addition, composite 3D printing technology for multiple materials has important potential in harsh environments, such as high temperatures, high loads, and high corrosion conditions, and is applied in fields such as aerospace, nuclear energy, marine, and offshore operations; among them, the multimaterial structure represented by NiTi/Ti6Al4V is suitable for personalized biomedical orthopedic implants and has a stiffness similar to that of human bone and excellent wear and corrosion resistance. Moreover, the precise processing of various materials can adapt to various characteristics required by human bone, such as biocompatibility, stiffness, wear resistance, and corrosion resistance, and has controllable drug delivery potential.[191]

5. 3D-printed BMs

3D-printed BM materials have a wide range of applications, such as in orthopedics and maxillofacial surgery. Table 3 displays the applications of 3D-printed BMs in various diseases.

For fractures with small bone defects or no bone defects, screws composed of BM materials and bolts can be used for fixation, and when weight-bearing skeletal sites are involved, a plate-screw hybrid fixation system can be applied for support.[192] For fractures located in the curved part of the skeleton, the application of 3D printing enables the implant to fit more closely to the fracture site and provide better support. Animal experiments have shown that BM materials perform well and provide adequate support for fracture healing, and compared to conventional titanium nails, they undergo significant degradation, eliminating the need for secondary surgical removal.[124,193-195] The bone-enhancing properties of magnesium ions can also lead to a significant increase in the healing rate of osteoporotic fractures.[196] In recent years, successful treatment of fractures using BM materials has been achieved in the clinic, and good therapeutic results have been obtained.[197-201]

For injuries involving large bone defects, scaffolds composed of BM materials can temporarily replace bone tissue to provide mechanical support and simultaneously provide attachment points for bone regeneration. For example, when performing bone tumor surgery, which can cause defects in a patient's bone tissue, 3D-printed BM scaffolds can be used to support the bone structure and promote bone regeneration; these scaffolds can closely fit the bone defect site to prevent fracture and bone collapse and can work in conjunction with medication to prevent infection.[202-204] Figure 4 shows an example of a porous magnesium scaffold prepared by Cheng et al.[125] However, due to the unresolved application difficulties of each metallic material, degradable metallic stents still remain in the cell and animal experimental stage and have not been clinically applied.[125,201,205,206] Only stainless steel materials have been used as permanent scaffolds in clinical applications.[207,208]

In addition to bone tissue, BM materials are also expected to be useful for cartilage and ligament repair. Cartilage tissue is entirely nourished by the subchondral bone plate, and conventional permanent scaffolds cannot provide access to nutrients if the bone defect extends to the subchondral bone plate. 3D-printed BM scaffolds can provide mechanical support for 2 months and then gradually degrade to allow growth of cells and blood vessels that provide nutrients for cartilage tissue regeneration.[209,210] Porous scaffolds can also carry growth factors and immunoactive drugs to promote cartilage regeneration.[211,212]

In the field of maxillofacial surgery, BM materials have higher biocompatibility, osteoinductivity, and biodegradability than traditional calcium phosphate

Table 3. Applications of 3D-printed biodegradable metals

Application	Disease	Implant	References
Orthopedics	Fractures with little or no bone defect	Screws, bolts, plates	124,193-195,197-201
	Osteoporotic fracture	Screws, bolts, scaffolds, low-modulus bone substitutes	196
	Bone defect, bone tumor	Scaffolds	125,201-206
	Cartilage defect		
Maxillofacial surgery	Maxillofacial surgery	Low-modulus bone substitutes	215
	Dental implant	Scaffolds	216

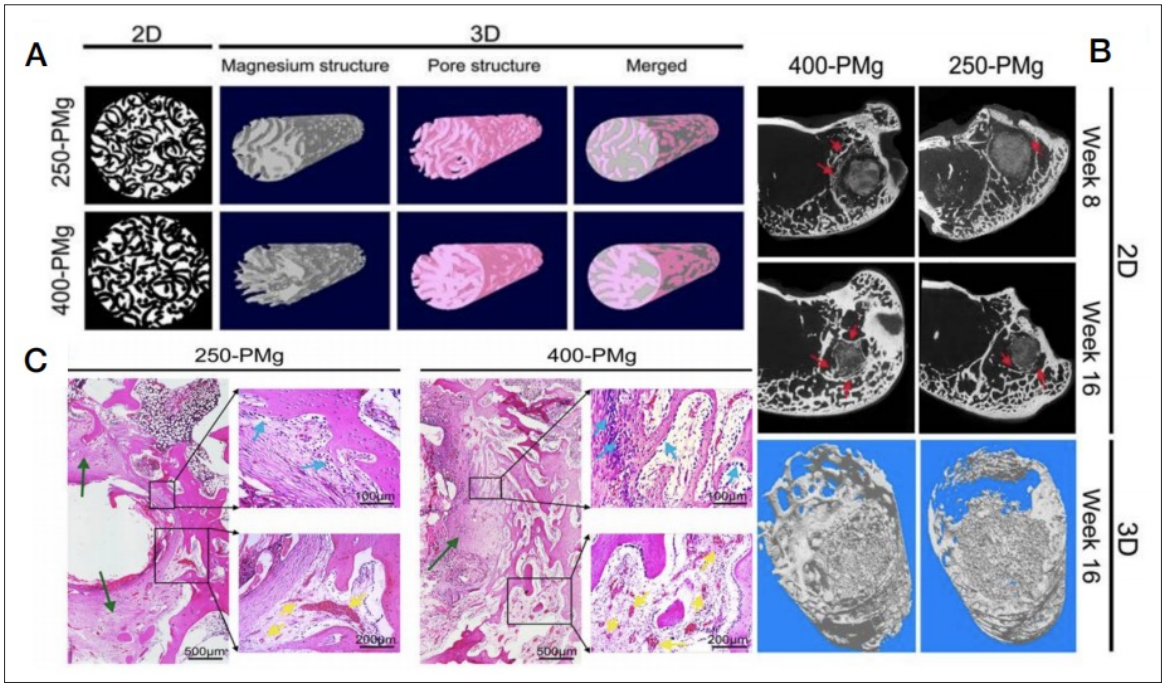


Figure 4. Porous magnesium scaffolds were applied to rabbit bone defects. (A) 2D and 3D images of 250 μm and 400 μm pore size porous magnesium scaffolds (250-PMg, 400-PMg) obtained by micro-computed tomography (micro-CT), (B) 2D micro-CT (red arrows pointing to newly formed bone) showing the status of response of the new bone (white) at 8 and 16 weeks post-surgery, and the 3D reconstructed model showing the status of the response at 16 weeks postsurgery. (C) Representative histological analysis (H&E staining) of bone formation in the 250-PMg and 400-PMg scaffold groups. Green arrows indicate regular dense fibrous tissue, blue arrows indicate cuboidal osteoblasts, and yellow arrows indicate neovascularization. Both scaffolds promoted bone regeneration and angiogenesis, with the 400-PMg scaffold having a milder inflammatory response, more new bone, and more neovascularization.[125]

and magnesium phosphate bone cements.[213,214] The incorporation of magnesium particles into the PCL matrix enables the production of low-modulus bone substitute composites.[215] These materials degrade to generate magnesium ions while filling the supporting bone defect site, thus promoting bone regeneration and enhancing bone quality; these materials are expected to replace bone cement for bone regeneration in the maxillofacial area and other parts of the body and can simultaneously be used for the treatment of osteoporotic fractures. High-modulus metal components can be used as dental implants. Porous structures converted from scaffolds can provide support and simultaneously promote the function of osteoporosis, thus increasing the load-bearing capacity of dental implants.[216] These implants are precisely designed and printed to achieve closer contact with the bone surface, thus accelerating the healing of bone defects and providing better aesthetic results for patients.[217] Additionally, stainless steel has been used for crown restorations in children.[218,219]

6. Future perspectives and outlooks

3D-printed BMs demonstrate enormous potential in the field of bone regeneration. However, the application of 3D printing technology for BMs still remains a challenge, attributable to problems such as vapor sputtering, low mechanical strength, and material selection limitations that occur during the printing process, depending on the method chosen. Printing with magnesium results in an excessive degradation rate, hydrogen precipitation, and alkalization; printing with zinc results in cytotoxicity, an uneven alloy phase that affects the mechanical strength, pitting corrosion, and porous structure manufacturing difficulties; the iron elastic modulus is too high; and its degradation rate is too slow, resulting in the accumulation of nonmetabolizable iron oxides. In addition, improving the mechanical properties, antibacterial properties, fatigue resistance, biocompatibility, and degradation behavior of BMs are important research directions. Further studies on these problems for resolution are warranted.

A list of 3D-printed BMs for use in the field of bone regeneration is shown in Table 4.

7. Conclusion

3D printing technology, as a common tool for tissue regeneration and repair, offers unprecedented possibilities for producing complex customized structures, and porous implants prepared by 3D printing have excellent potential

Table 4. Applications of 3D-printed biodegradable metals in the field of bone regeneration

Materials	Mechanisms for bone regeneration	Advantages and disadvantages in application	Medical applications
Magnesium and its alloys	Secreting osteogenic cytokines, synergizing with cytokines, promoting osteogenic gene expression, and activating related pathways	Density and Young's modulus close to those of bone tissue, but excessively high biodegradation rate, hydrogen precipitation and alkalization during degradation	Fracture, bone defect, cartilage repair, bone substitution composite material additives, *etc.*
Zinc and its alloys	Zinc homeostasis, redox effect, antibacterial ability, vascularization	Good antibacterial effect, but low biocompatibility and difficult processing	Osteoporotic fractures, bone defect repair and dentistry, etc.
Iron and its alloys	Vascularization	Strong mechanical support, but low degradation rate and high elastic modulus	Nanoparticle coating, etc.

for bone tissue regeneration. The advancement of 3D printing technology and materials leads to the continuous improvement of BM materials. 3D-printed BMs are used not only for fracture fixation and bone defect repair but also for osteoporotic fractures, cartilage repair, maxillofacial surgery, and other processes. We anticipate more research contributions regarding further applications of 3D printing with BMs and their expansion to unexplored fields.

Acknowledgments

None.

Funding

This work was supported by the Young Scientist Program of Beijing Stomatological Hospital, Capital Medical University (No. YSP202208); the National Key Research and Development Program (No. 2022YFA1104401); the CAMS Innovation Fund for Medical Sciences (No. 2019-I2M-5-031); and grants from the Innovation Research Team Project of Beijing Stomatological Hospital, Capital Medical University (No. CXTD202204).

Conflict of interest

The authors declare no conflicts of interest.

Author contributions

Conceptualization: Zhipeng Fan, Lingxiao Wang
Supervision: Zhipeng Fan
Writing – original draft: Yang Liu, Lingxiao Wang
Writing – review & editing: Lingxiao Wang, Yang Liu, Zhipeng Fan

Ethics approval and consent to participate

Not applicable.

Consent for publication

Not applicable.

Availability of data

Not applicable.

References

1. Wildemann B, Ignatius A, Leung F, et al. Non-union bone fractures. *Nat Rev Dis Primers*. 2021;7(1):57. doi: 10.1038/s41572-021-00289-8

2. Megas P. Classification of non-union. *Injury*. 2005;36 (Suppl 4):S30-37. doi: 10.1016/j.injury.2005.10.008

3. Dimitriou R, Jones E, McGonagle D, Giannoudis PV. Bone regeneration: current concepts and future directions. *BMC Med*. 2011;9:66. doi: 10.1186/1741-7015-9-66

4. Daly AC, Freeman FE, Gonzalez-Fernandez T, Critchley SE, Nulty J, Kelly DJ. 3D bioprinting for cartilage and osteochondral tissue engineering. *Adv Healthc Mater*. 2017;6(22):1700298. doi: 10.1002/adhm.201700298

5. Liao J, Wu S, Li K, Fan Y, Dunne N, Li X. Peptide-modified bone repair materials: factors influencing osteogenic activity. *J Biomed Mater Res A*. 2019;107(7):1491-1512. doi: 10.1002/jbm.a.36663

6. Sanz-Sanchez I, Sanz-Martin I, Ortiz-Vigon A, Molina A, Sanz M. Complications in bone-grafting procedures: classification and management. *Periodontology 2000*. 2022;88(1):86-102. doi: 10.1111/prd.12413

7. Graham SM, Leonidou A, Aslam-Pervez N, et al. Biological therapy of bone defects: the immunology of bone allo-transplantation. *Expert Opin Biol Ther*. 2010;10(6):885-901. doi: 10.1517/14712598.2010.481669

8. Bavya Devi K, Lalzawmliana V, Saidivya M, Kumar V, Roy M, Nandi SK. Magnesium phosphate bioceramics for bone tissue engineering. *Chem Rec*. 2022;22(11):e202200136. doi: 10.1002/tcr.202200136

9. Sordi MB, Cruz A, Fredel MC, Magini R, Sharpe PT. Three-dimensional bioactive hydrogel-based scaffolds for bone

regeneration in implant dentistry. *Mater Sci Eng C Mater Biol Appl*. 2021;124:112055.
doi: 10.1016/j.msec.2021.112055

10. Funda G, Taschieri S, Bruno GA, et al. Nanotechnology scaffolds for alveolar bone regeneration. *Materials (Basel)*. 2020;13(1).
doi: 10.3390/ma13010201

11. Murphy SV, Atala A. 3D bioprinting of tissues and organs. *Nat Biotechnol*. 2014;32(8):773-785.
doi: 10.1038/nbt.2958

12. Wang S, Zhao S, Yu J, Gu Z, Zhang Y. Advances in translational 3D printing for cartilage, bone, and osteochondral tissue engineering. *Small*. 2022;18(36):e2201869.
doi: 10.1002/smll.202201869

13. Qu M, Wang C, Zhou X, et al. Multi-dimensional printing for bone tissue engineering. *Adv Healthc Mater*. 2021;10(11):e2001986.
doi: 10.1002/adhm.202001986

14. Ashammakhi N, Hasan A, Kaarela O, et al. Advancing frontiers in bone bioprinting. *Adv Healthc Mater*. 2019;8(7):e1801048.
doi: 10.1002/adhm.201801048

15. Thrivikraman G, Athirasala A, Twohig C, Boda SK, Bertassoni LE. Biomaterials for craniofacial bone regeneration. *Dent Clin North Am*. 2017;61(4):835-856.
doi: 10.1016/j.cden.2017.06.003

16. Liu Y, Zheng Y, Chen XH, et al. Fundamental theory of biodegradable metals—definition, criteria, and design. *Adv Funct Mater*. 2019;29(18).
doi: 10.1002/adfm.201805402

17. Bose S, Koski C, Vu AA. Additive manufacturing of natural biopolymers and composites for bone tissue engineering. *Mater Horizons*. 2020;7(8):2011-2027.
doi: 10.1039/d0mh00277a

18. Panayotov IV, Orti V, Cuisinier F, Yachouh J. Polyetheretherketone (PEEK) for medical applications. *J Mater Sci Mater Med*. 2016;27(7):118.
doi: 10.1007/s10856-016-5731-4

19. Siddiqui N, Asawa S, Birru B, Baadhe R, Rao S. PCL-based composite scaffold matrices for tissue engineering applications. *Mol Biotechnol*. 2018;60(7):506-532.
doi: 10.1007/s12033-018-0084-5

20. Pina S, Rebelo R, Correlo VM, Oliveira JM, Reis RL. Bioceramics for osteochondral tissue engineering and regeneration. *Adv Exp Med Biol*. 2018;1058:53-75.
doi: 10.1007/978-3-319-76711-6_3

21. Rahmanian R, Moghaddam NS, Haberland C, Dean D, Miller M, Elahinia M. Load bearing and stiffness tailored NiTi implants produced by additive manufacturing: a simulation study. *In: Proceedings of the SPIE 9058, Behavior and Mechanics of Multifunctional Materials and Composites 2014*; 2014: 905814.
doi: 10.1117/12.2048948

22. Jing Z, Zhang T, Xiu P, et al. Functionalization of 3D-printed titanium alloy orthopedic implants: a literature review. *Biomed Mater*. 2020;15(5):052003.
doi: 10.1088/1748-605X/ab9078

23. Zhang Y, Xu J, Ruan YC, et al. Implant-derived magnesium induces local neuronal production of CGRP to improve bone-fracture healing in rats. *Nat Med*. 2016;22(10):1160-1169.
doi: 10.1038/nm.4162

24. Qin Y, Wen P, Guo H, et al. Additive manufacturing of biodegradable metals: current research status and future perspectives. *Acta Biomater*. 2019;98:3-22.
doi: 10.1016/j.actbio.2019.04.046

25. Xia D, Yang F, Zheng Y, Liu Y, Zhou Y. Research status of biodegradable metals designed for oral and maxillofacial applications: a review. *Bioact Mater*. 2021;6(11):4186-4208.
doi: 10.1016/j.bioactmat.2021.01.011

26. Feng Y, Zhu S, Mei D, et al. Application of 3D printing technology in bone tissue engineering: a review. *Curr Drug Deliv*. 2021;18(7):847-861.
doi: 10.2174/1567201817999201113100322

27. Putra NE, Leeflang MA, Taheri P, et al. Extrusion-based 3D printing of ex situ-alloyed highly biodegradable MRI-friendly porous iron-manganese scaffolds. *Acta Biomater*. 2021;134:774-790.
doi: 10.1016/j.actbio.2021.07.042

28. Belluci MM, de Molon RS, Rossa Jr C, et al. Severe magnesium deficiency compromises systemic bone mineral density and aggravates inflammatory bone resorption. *J Nutr Biochem*. 2020;77:108301.
doi: 10.1016/j.jnutbio.2019.108301

29. Erem S, Atfi A, Razzaque MS. Anabolic effects of vitamin D and magnesium in aging bone. *J Steroid Biochem Mol Biol*. 2019;193:105400.
doi: 10.1016/j.jsbmb.2019.105400

30. Ye L, Xu J, Mi J, et al. Biodegradable magnesium combined with distraction osteogenesis synergistically stimulates bone tissue regeneration via CGRP-FAK-VEGF signaling axis. *Biomaterials*. 2021;275:120984.
doi: 10.1016/j.biomaterials.2021.120984

31. Liu W, Guo S, Tang Z, et al. Magnesium promotes bone formation and angiogenesis by enhancing MC3T3-E1 secretion of PDGF-BB. *Biochem Biophys Res Commun*. 2020;528(4):664-670.
doi: 10.1016/j.bbrc.2020.05.113

32. Gillman CE, Jayasuriya AC. FDA-approved bone grafts and bone graft substitute devices in bone regeneration. *Mater Sci Eng C Mater Biol Appl*. 2021;130:112466.
doi: 10.1016/j.msec.2021.112466

33. Lin S, Yin S, Shi J, et al. Orchestration of energy metabolism and osteogenesis by Mg(2+) facilitates low-dose BMP-2-driven regeneration. *Bioact Mater*. 2022;18:116-127.
doi: 10.1016/j.bioactmat.2022.03.024

34. Qiao W, Wong KHM, Shen J, et al. TRPM7 kinase-mediated immunomodulation in macrophage plays a central role in magnesium ion-induced bone regeneration. *Nat Commun*. 2021;12(1):2885.
doi: 10.1038/s41467-021-23005-2

35. Jeng SS, Chen YH. Association of zinc with anemia. *Nutrients*. 2022;14(22).
doi: 10.3390/nu14224918

36. Skalny AV, Aschner M, Silina EV, et al. The role of trace elements and minerals in osteoporosis: a review of epidemiological and laboratory findings. *Biomolecules*. 2023;13(6).
doi: 10.3390/biom13061006

37. Kraus VB. Osteoarthritis: the zinc link. *Nature*. 2014;507(7493):441-442.
doi: 10.1038/507441a

38. Kambe T, Tsuji T, Hashimoto A, Itsumura N. The physiological, biochemical, and molecular roles of zinc transporters in zinc homeostasis and metabolism. *Physiol Rev*. 2015;95(3):749-784.
doi: 10.1152/physrev.00035.2014

39. Liu Q, Li M, Wang S, et al. Recent advances of osterix transcription factor in osteoblast differentiation and bone formation. *Front Cell Dev Biol*. 2020;8:601224.
doi: 10.3389/fcell.2020.601224

40. Fu X, Li Y, Huang T, et al. Runx2/osterix and zinc uptake synergize to orchestrate osteogenic differentiation and citrate containing bone apatite formation. *Adv Sci (Weinh)*. 2018;5(4):1700755.
doi: 10.1002/advs.201700755

41. Rył A, Miazgowski T, Szylińska A, et al. Bone health in aging men: does zinc and cuprum level matter? *Biomolecules*. 2021;11(2).
doi: 10.3390/biom11020237

42. Park KH, Park B, Yoon DS, et al. Zinc inhibits osteoclast differentiation by suppression of Ca2+-Calcineurin-NFATc1 signaling pathway. *Cell Commun Signal*. 2013;11:74.
doi: 10.1186/1478-811x-11-74

43. Wang S, Gu R, Wang F, et al. 3D-printed PCL/Zn scaffolds for bone regeneration with a dose-dependent effect on osteogenesis and osteoclastogenesis. *Mater Today Bio*. 2022;13:100202.
doi: 10.1016/j.mtbio.2021.100202

44. Wang S, Li R, Xia D, et al. The impact of Zn-doped synthetic polymer materials on bone regeneration: a systematic review. *Stem Cell Res Ther*. 2021;12(1):123.
doi: 10.1186/s13287-021-02195-y

45. Li C, Sun F, Tian J, et al. Continuously released Zn(2+) in 3D-printed PLGA/β-TCP/Zn scaffolds for bone defect repair by improving osteoinductive and anti-inflammatory properties. *Bioact Mater*. 2023;24:361-375.
doi: 10.1016/j.bioactmat.2022.12.015

46. Pierson D, Edick J, Tauscher A, et al. A simplified in vivo approach for evaluating the bioabsorbable behavior of candidate stent materials. *J Biomed Mater Res B Appl Biomater*. 2012;100(1):58-67.
doi: 10.1002/jbm.b.31922

47. Sikora-Jasinska M, Paternoster C, Mostaed E, et al. Synthesis, mechanical properties and corrosion behavior of powder metallurgy processed Fe/Mg(2)Si composites for biodegradable implant applications. *Mater Sci Eng C Mater Biol Appl*. 2017;81:511-521.
doi: 10.1016/j.msec.2017.07.049

48. Ru Q, Li Y, Xie W, et al. Fighting age-related orthopedic diseases: focusing on ferroptosis. *Bone Res*. 2023;11(1):12.
doi: 10.1038/s41413-023-00247-y

49. Adeyemi A, Akinlabi ET, Mahamood RM. Powder bed based laser additive manufacturing process of stainless steel: a review. *Mate Today Proc*. 2018;5(9):18510-18517.
doi: 10.1016/j.matpr.2018.06.193

50. Sotoudehbagha P, Sheibani S, Khakbiz M, Ebrahimi-Barough S, Hermawan H. Novel antibacterial biodegradable Fe-Mn-Ag alloys produced by mechanical alloying. *Mater Sci Eng C Mater Biol Appl*. 2018;88:88-94.
doi: 10.1016/j.msec.2018.03.005

51. Rewak-Soroczynska J, Dorotkiewicz-Jach A, Drulis-Kawa Z, Wiglusz RJ. Culture media composition influences the antibacterial effect of silver, cupric, and zinc ions against *Pseudomonas aeruginosa*. *Biomolecules*. 2022;12(7).
doi: 10.3390/biom12070963

52. Chen K, Zhou G, Li Q, et al. In vitro degradation, biocompatibility and antibacterial properties of pure zinc: assessing the potential of Zn as a guided bone regeneration membrane. *J Mater Chem B*. 2021;9(25):5114-5127.
doi: 10.1039/D1TB00596K

53. Jia B, Zhang Z, Zhuang Y, et al. High-strength biodegradable zinc alloy implants with antibacterial and osteogenic properties for the treatment of MRSA-induced rat osteomyelitis. *Biomaterials*. 2022;287:121663.
doi: 10.1016/j.biomaterials.2022.121663

54. Zhang Y, Wu H, Yuan B, et al. Enhanced osteogenic activity and antibacterial performance in vitro of polyetheretherketone by plasma-induced graft polymerization of acrylic acid and incorporation of zinc ions. *J Mater Chem B*. 2021;9(36):7506-7515.
doi: 10.1039/D1TB01349A

55. Mutlu N, Liverani L, Kurtuldu F, Galusek D, Boccaccini AR. Zinc improves antibacterial, anti-inflammatory and cell motility activity of chitosan for wound healing applications. *Int J Biol Macromol*. 2022;213:845-857.
doi: 10.1016/j.ijbiomac.2022.05.199

56. Rodwihok C, Suwannakeaw M, Charoensri K, et al. Alkali/zinc-activated fly ash nanocomposites for dye

removal and antibacterial applications. *Bioresour Technol.* 2021;331:125060.
doi: 10.1016/j.biortech.2021.125060

57. Vimbela GV, Ngo SM, Fraze C, Yang L, Stout DA. Antibacterial properties and toxicity from metallic nanomaterials. *Int J Nanomed.* 2017;12:3941-3965.
doi: 10.2147/ijn.S134526

58. He Y, Ingudam S, Reed S, et al. Study on the mechanism of antibacterial action of magnesium oxide nanoparticles against foodborne pathogens. *J Nanobiotechnol.* 2016;14(1):54.
doi: 10.1186/s12951-016-0202-0

59. Coelho CC, Padrão T, Costa L, et al. The antibacterial and angiogenic effect of magnesium oxide in a hydroxyapatite bone substitute. *Sci Rep*. 2020;10(1):19098.
doi: 10.1038/s41598-020-76063-9

60. Ye Q, Chen W, Huang H, et al. Iron and zinc ions, potent weapons against multidrug-resistant bacteria. *Appl Microbiol Biotechnol.* 2020;104(12):5213-5227.
doi: 10.1007/s00253-020-10600-4

61. Zheng LZ, Wang JL, Xu JK, et al. Magnesium and vitamin C supplementation attenuates steroid-associated osteonecrosis in a rat model. *Biomaterials*. 2020;238:119828.
doi: 10.1016/j.biomaterials.2020.119828

62. Zhu WY, Guo J, Yang WF, et al. Biodegradable magnesium implant enhances angiogenesis and alleviates medication-related osteonecrosis of the jaw in rats. *J Orthop Translat*. 2022;33:153-161.
doi: 10.1016/j.jot.2022.03.004

63. Gao P, Fan B, Yu X, et al. Biofunctional magnesium coated Ti6Al4V scaffold enhances osteogenesis and angiogenesis in vitro and in vivo for orthopedic application. *Bioact Mater*. 2020;5(3):680-693.
doi: 10.1016/j.bioactmat.2020.04.019

64. Zhang X, Huang P, Jiang G, et al. A novel magnesium ion-incorporating dual-crosslinked hydrogel to improve bone scaffold-mediated osteogenesis and angiogenesis. *Mater Sci Eng C*. 2021;121:111868.
doi: 10.1016/j.msec.2021.111868

65. Gu Y, Zhang J, Zhang X, et al. Three-dimensional printed Mg-doped β-TCP bone tissue engineering scaffolds: effects of magnesium ion concentration on osteogenesis and angiogenesis in vitro. *Tissue Eng Regen Med.* 2019;16(4):415-429.
doi: 10.1007/s13770-019-00192-0

66. Li Y, Ma T, Zhu X, et al. Zinc improves neurological recovery by promoting angiogenesis via the astrocyte-mediated HIF-1α/VEGF signaling pathway in experimental stroke. *CNS Neurosci Ther*. 2022;28(11):1790-1799.
doi: 10.1111/cns.13918

67. Yu L, Yin Y, Guo Z, et al. A functional study of zinc–titanium coatings and exploration of the intrinsic correlation between angiogenesis and osteogenesis. *J Mater Chem B*. 2023;11(14):3236-3251.
doi: 10.1039/D3TB00119A

68. Hassan A, Elebeedy D, Matar ER, Fahmy Mohamed Elsayed A, Abd El Maksoud AI. Investigation of angiogenesis and wound healing potential mechanisms of zinc oxide nanorods. *Front Pharmacol*. 2021;12:661217.
doi: 10.3389/fphar.2021.661217

69. Chen Y, Sheng W, Lin J, et al. Magnesium oxide nanoparticle coordinated phosphate-functionalized chitosan injectable hydrogel for osteogenesis and angiogenesis in bone regeneration. *ACS Appl Mater Interfaces*. 2022;14(6):7592-7608.
doi: 10.1021/acsami.1c21260

70. Wang T, Zhao H, Jing S, et al. Magnetofection of miR-21 promoted by electromagnetic field and iron oxide nanoparticles via the p38 MAPK pathway contributes to osteogenesis and angiogenesis for intervertebral fusion. *J Nanobiotechnol.* 2023;21(1):27.
doi: 10.1186/s12951-023-01789-3

71. Salmi M. Additive manufacturing processes in medical applications. *Materials*. 2021;14(1).
doi: 10.3390/ma14010191

72. Hornberger H, Virtanen S, Boccaccini AR. Biomedical coatings on magnesium alloys - a review. *Acta Biomater*. 2012;8(7):2442-2455.
doi: 10.1016/j.actbio.2012.04.012

73. Liu J, Wei B, Chang H, Li J, Yang G. Review of visual measurement methods for metal vaporization processes in laser powder bed fusion. *Micromachines.* 2023;14(7).
doi: 10.3390/mi14071351

74. Ng CC, Savalani MM, Lau ML, Man HC. Microstructure and mechanical properties of selective laser melted magnesium. *Appl Surf Sci.* 2011;257(17):7447-7454.
doi: 10.1016/j.apsusc.2011.03.004

75. Hossain N, Chowdhury MA, Shuvho MBA, Kashem MA, Kchaou M. 3D-printed objects for multipurpose applications. *J Mater Eng Perform*. 2021;30(7):4756-4767.
doi: 10.1007/s11665-021-05664-w

76. Milewski JO. *Additive Manufacturing of Metals*. Springer; 2017:258.
doi: 10.1007/978-3-319-58205-4

77. Li Y, Zhou J, Pavanram P, et al. Additively manufactured biodegradable porous magnesium. *Acta Biomater*. 2018;67:378-392.
doi: 10.1016/j.actbio.2017.12.008

78. Ma P, Ji P, Jia Y, et al. Effect of substrate plate heating on the microstructure and properties of selective laser melted Al-20Si-5Fe-3Cu-1Mg alloy. *Materials*. 2021;14(2).
doi: 10.3390/ma14020330

79. Kirkland NT, Kolbeinsson I, Woodfield T, Dias GJ, Staiger MP. Synthesis and properties of topologically ordered porous magnesium. *Mater Sci Eng B*. 2011;176(20): 1666-1672.
doi: 10.1016/j.mseb.2011.04.006

80. Zhang X, Li XW, Li JG, Sun XD. Preparation and mechanical property of a novel 3D porous magnesium scaffold for bone tissue engineering. *Mater Sci Eng C Mater Biol Appl*. 2014;42:362-367.
doi: 10.1016/j.msec.2014.05.044

81. Murphy CM, Duffy GP, Schindeler A, O'Brien FJ. Effect of collagen-glycosaminoglycan scaffold pore size on matrix mineralization and cellular behavior in different cell types. *J Biomed Mater Res A*. 2016;104(1):291-304.
doi: 10.1002/jbm.a.35567

82. Rustom LE, Boudou T, Lou S, et al. Micropore-induced capillarity enhances bone distribution in vivo in biphasic calcium phosphate scaffolds. *Acta Biomater*. 2016;44:144-154.
doi: 10.1016/j.actbio.2016.08.025

83. Zhang J, Wehrle E, Rubert M, Müller R. 3D bioprinting of human tissues: biofabrication, bioinks, and bioreactors. *Int J Mol Sci*. 2021;22(8).
doi: 10.3390/ijms22083971

84. Takagi H, Sasahara H, Abe T, et al. Material-property evaluation of magnesium alloys fabricated using wire-and-arc-based additive manufacturing. *Addit Manuf*. 2018;24:498-507.
doi: 10.1016/j.addma.2018.10.026

85. Bar-Cohen Y. *Advances in Manufacturing and Processing of Materials and Structures*. Boca Raton: CRC Press; 2018.
doi: 10.1201/b22020

86. Gao C, Wang C, Jin H, et al. Additive manufacturing technique-designed metallic porous implants for clinical application in orthopedics. *RSC Adv*. 2018;8(44):25210-25227.
doi: 10.1039/c8ra04815k

87. Ni J, Ling H, Zhang S, et al. Three-dimensional printing of metals for biomedical applications. *Mater Today Bio*. 2019;3:100024.
doi: 10.1016/j.mtbio.2019.100024

88. Elshazli AM, Elshaer RN, Hussein AHA, Al-Sayed SR. Laser surface modification of TC21 (α/β) titanium alloy using a direct energy deposition (DED) process. *Micromachines*. 2021;12(7).
doi: 10.3390/mi12070739

89. Liu Y, Liu Z, Zhou G, He C, Zhang J. Microstructures and properties of Al-Mg alloys manufactured by WAAM-CMT. *Materials*. 2022;15(15).
doi: 10.3390/ma15155460

90. Ron T, Dolev O, Leon A, Shirizly A, Aghion E. Effect of phase transformation on stress corrosion behavior of additively manufactured austenitic stainless steel produced by directed energy deposition. *Materials*. 2020;14(1).
doi: 10.3390/ma14010055

91. Rodrigues TA, Duarte V, Miranda RM, Santos TG, Oliveira JP. Current status and perspectives on wire and arc additive manufacturing (WAAM). *Materials*. 2019;12(7).
doi: 10.3390/ma12071121

92. Soni R, Jhavar S, Tyeb S, et al. Wire arc additive manufacturing of zinc as a degradable metallic biomaterial. *J Funct Biomater*. 2022;13(4).
doi: 10.3390/jfb13040212

93. Le Guéhennec L, Soueidan A, Layrolle P, Amouriq Y. Surface treatments of titanium dental implants for rapid osseointegration. *Dent Mater*. 2007;23(7):844-854.
doi: 10.1016/j.dental.2006.06.025

94. Lukaszewska-Kuska M, Wirstlein P, Majchrowski R, Dorocka-Bobkowska B. Osteoblastic cell behaviour on modified titanium surfaces. *Micron*. 2018;105:55-63.
doi: 10.1016/j.micron.2017.11.010

95. Souza JCM, Sordi MB, Kanazawa M, et al. Nano-scale modification of titanium implant surfaces to enhance osseointegration. *Acta Biomater*. 2019;94:112-131.
doi: 10.1016/j.actbio.2019.05.045

96. Majhy B, Priyadarshini P, Sen AK. Effect of surface energy and roughness on cell adhesion and growth - facile surface modification for enhanced cell culture. *RSC Adv*. 2021;11(25):15467-15476.
doi: 10.1039/d1ra02402g

97. Bouzaglou O, Golan O, Lachman N. Process design and parameters interaction in material extrusion 3D printing: a review. *Polymers*. 2023;15(10).
doi: 10.3390/polym15102280

98. Dong J, Li Y, Lin P, et al. Solvent-cast 3D printing of magnesium scaffolds. *Acta Biomater*. 2020;114:497-514.
doi: 10.1016/j.actbio.2020.08.002

99. Zhang Y, Lin T, Meng H, et al. 3D gel-printed porous magnesium scaffold coated with dibasic calcium phosphate dihydrate for bone repair in vivo. *J Orthop Transl*. 2022;33: 13-23.
doi: 10.1016/j.jot.2021.11.005

100. Dong J, Tümer N, Putra NE, et al. Extrusion-based 3D printed magnesium scaffolds with multifunctional MgF(2) and MgF(2)-CaP coatings. *Biomater Sci*. 2021;9(21):7159-7182.
doi: 10.1039/d1bm01238j

101. Mirzababaei S, Pasebani S. A review on binder jet additive manufacturing of 316L stainless steel. *J Manuf Mater Process*. 2019;3(3).
doi: 10.3390/jmmp3030082

102. Salehi M, Maleksaeedi S, Sapari MAB, et al. Additive manufacturing of magnesium–zinc–zirconium (ZK) alloys via capillary-mediated binderless three-dimensional printing. *Mater Des*. 2019;169.
doi: 10.1016/j.matdes.2019.107683

103. Meininger S, Mandal S, Kumar A, et al. Strength reliability and in vitro degradation of three-dimensional powder

printed strontium-substituted magnesium phosphate scaffolds. *Acta Biomater*. 2016;31:401-411.
doi: 10.1016/j.actbio.2015.11.050

104. Meininger S, Moseke C, Spatz K, et al. Effect of strontium substitution on the material properties and osteogenic potential of 3D powder printed magnesium phosphate scaffolds. *Mater Sci Eng C Mater Biol Appl*. 2019;98:1145-1158.
doi: 10.1016/j.msec.2019.01.053

105. Verlee B, Dormal T, Lecomte-Beckers J. Density and porosity control of sintered 316L stainless steel parts produced by additive manufacturing. *Powder Metall*. 2013;55(4):260-267.
doi: 10.1179/0032589912z.00000000082

106. Dutta S, Roy M. Recent developments in engineered magnesium scaffolds for bone tissue engineering. *ACS Biomater Sci Eng*. 2023;9(6):3010-3031.
doi: 10.1021/acsbiomaterials.2c01510

107. Hériveaux Y, Le Cann S, Fraulob M, et al. Mechanical micromodeling of stress-shielding at the bone-implant interphase under shear loading. *Med Biol Eng Comput*. 2022;60(11):3281-3293.
doi: 10.1007/s11517-022-02657-2

108. Raffa ML, Nguyen VH, Hernigou P, Flouzat-Lachaniette CH, Haiat G. Stress shielding at the bone-implant interface: Influence of surface roughness and of the bone-implant contact ratio. *J Orthop Res*. 2021;39(6):1174-1183.
doi: 10.1002/jor.24840

109. Xue J, Singh S, Zhou Y, et al. A biodegradable 3D woven magnesium-based scaffold for orthopedic implants. *Biofabrication*. 2022;14(3).
doi: 10.1088/1758-5090/ac73b8

110. Persson M, Lehenkari PP, Berglin L, et al. Osteogenic differentiation of human mesenchymal stem cells in a 3D woven scaffold. *Sci Rep*. 2018;8(1):10457.
doi: 10.1038/s41598-018-28699-x

111. Karunakaran R, Ortgies S, Tamayol A, Bobaru F, Sealy MP. Additive manufacturing of magnesium alloys. *Bioact Mater*. 2020;5(1):44-54.
doi: 10.1016/j.bioactmat.2019.12.004

112. Lavery NP, Cherry J, Mehmood S, et al. Effects of hot isostatic pressing on the elastic modulus and tensile properties of 316L parts made by powder bed laser fusion. *Mater Sci Eng A*. 2017;693:186-213.
doi: 10.1016/j.msea.2017.03.100

113. de Baaij JH, Hoenderop JG, Bindels RJ. Magnesium in man: implications for health and disease. *Physiol Rev*. 2015;95(1):1-46.
doi: 10.1152/physrev.00012.2014

114. Langer R, Vacanti JP. Tissue engineering. *Science*. 1993;260(5110):920-926.
doi: 10.1126/science.8493529

115. Hollister SJ. Porous scaffold design for tissue engineering. *Nat Mater*. 2005;4(7):518-524.
doi: 10.1038/nmat1421

116. Agarwal S, Curtin J, Duffy B, Jaiswal S. Biodegradable magnesium alloys for orthopaedic applications: a review on corrosion, biocompatibility and surface modifications. *Mater Sci Eng C*. 2016;68:948-963.
doi: 10.1016/j.msec.2016.06.020

117. Martinez Sanchez AH, Luthringer BJ, Feyerabend F, Willumeit R. Mg and Mg alloys: how comparable are in vitro and in vivo corrosion rates? A review. *Acta Biomater*. 2015;13:16-31.
doi: 10.1016/j.actbio.2014.11.048

118. Xu L, Zhang E, Yin D, Zeng S, Yang K. In vitro corrosion behaviour of Mg alloys in a phosphate buffered solution for bone implant application. *J Mater Sci Mater Med*. 2008;19(3):1017-1025.
doi: 10.1007/s10856-007-3219-y

119. Ansari MAA, Golebiowska AA, Dash M, et al. Engineering biomaterials to 3D-print scaffolds for bone regeneration: practical and theoretical consideration. *Biomater Sci*. 2022;10(11):2789-2816.
doi: 10.1039/d2bm00035k

120. Yang Y, Guo X, He C, Gao C, Shuai C. Regulating degradation behavior by incorporating mesoporous silica for Mg bone implants. *ACS Biomater Sci Eng*. 2018;4(3):1046-1054.
doi: 10.1021/acsbiomaterials.8b00020

121. Sarian MN, Iqbal N, Sotoudehbagha P, et al. Potential bioactive coating system for high-performance absorbable magnesium bone implants. *Bioact Mater*. 2022;12:42-63.
doi: 10.1016/j.bioactmat.2021.10.034

122. Hanzi AC, Gunde P, Schinhammer M, Uggowitzer PJ. On the biodegradation performance of an Mg-Y-RE alloy with various surface conditions in simulated body fluid. *Acta Biomater*. 2009;5(1):162-171.
doi: 10.1016/j.actbio.2008.07.034

123. Bîrcă AC, Neacşu IA, Vasile OR, et al. Mg-Zn alloys, most suitable for biomedical applications. *Rom J Morphol Embryol*. 2018;59(1):49-54.

124. Han P, Cheng P, Zhang S, et al. In vitro and in vivo studies on the degradation of high-purity Mg (99.99wt.%) screw with femoral intracondylar fractured rabbit model. *Biomaterials*. 2015;64:57-69.
doi: 10.1016/j.biomaterials.2015.06.031

125. Cheng MQ, Wahafu T, Jiang GF, et al. A novel open-porous magnesium scaffold with controllable microstructures and properties for bone regeneration. *Sci Rep*. 2016;6:24134.
doi: 10.1038/srep24134

126. Seyedraoufi ZS, Mirdamadi S. Synthesis, microstructure and mechanical properties of porous Mg--Zn scaffolds. *J Mech Behav Biomed Mater*. 2013;21:1-8.
doi: 10.1016/j.jmbbm.2013.01.023

127. Jung O, Porchetta D, Schroeder ML, et al. In vivo simulation of magnesium degradability using a new fluid dynamic bench testing approach. *Int J Mol Sci*. 2019;20(19). doi: 10.3390/ijms20194859

128. Tan Q, Atrens A, Mo N, Zhang M-X. Oxidation of magnesium alloys at elevated temperatures in air: a review. *Corros Sci*. 2016;112:734-759. doi: 10.1016/j.corsci.2016.06.018

129. Cao F, Song G-L, Atrens A. Corrosion and passivation of magnesium alloys. *Corros Sci*. 2016;111:835-845. doi: 10.1016/j.corsci.2016.05.041

130. Ghali E, Dietzel W, Kainer K-U. General and localized corrosion of magnesium alloys: a critical review. *J Mater Eng Perform*. 2013;22(10):2875-2891. doi: 10.1007/s11665-013-0730-9

131. Draxler J, Martinelli E, Weinberg AM, et al. The potential of isotopically enriched magnesium to study bone implant degradation in vivo. *Acta Biomater*. 2017;51: 526-536. doi: 10.1016/j.actbio.2017.01.054

132. Golafshan N, Willemsen K, Kadumudi FB, et al. 3D-printed regenerative magnesium phosphate implant ensures stability and restoration of hip dysplasia. *Adv Healthc Mater*. 2021;10(21):e2101051. doi: 10.1002/adhm.202101051

133. Zhao S, Xie K, Guo Y, et al. Fabrication and biological activity of 3D-printed polycaprolactone/magnesium porous scaffolds for critical size bone defect repair. *ACS Biomater Sci Eng*. 2020;6(9):5120-5131. doi: 10.1021/acsbiomaterials.9b01911

134. Xie K, Wang N, Guo Y, et al. Additively manufactured biodegradable porous magnesium implants for elimination of implant-related infections: an in vitro and in vivo study. *Bioact Mater*. 2022;8:140-152. doi: 10.1016/j.bioactmat.2021.06.032

135. Qin Y, Yang H, Liu A, et al. Processing optimization, mechanical properties, corrosion behavior and cytocompatibility of additively manufactured Zn-0.7Li biodegradable metals. *Acta Biomater*. 2022;142:388-401. doi: 10.1016/j.actbio.2022.01.049

136. Mostaed E, Sikora-Jasinska M, Drelich JW, Vedani M. Zinc-based alloys for degradable vascular stent applications. *Acta Biomater*. 2018;71:1-23. doi: 10.1016/j.actbio.2018.03.005

137. Toledano M, Vallecillo-Rivas M, Osorio MT, et al. Zn-containing membranes for guided bone regeneration in dentistry. *Polymers*. 2021;13(11). doi: 10.3390/polym13111797

138. Levaot N, Hershfinkel M. How cellular Zn(2+) signaling drives physiological functions. *Cell Calcium*. 2018;75: 53-63. doi: 10.1016/j.ceca.2018.08.004

139. Molenda M, Kolmas J. The role of zinc in bone tissue health and regeneration-a review. *Biol Trace Elem Res*. 2023;201(12):5640-5651. doi: 10.1007/s12011-023-03631-1

140. Zhao C, Wu H, Hou P, et al. Enhanced corrosion resistance and antibacterial property of Zn doped DCPD coating on biodegradable Mg. *Mater Lett*. 2016;180:42-46. doi: 10.1016/j.matlet.2016.04.035

141. Yang H, Qu X, Lin W, et al. In vitro and in vivo studies on zinc-hydroxyapatite composites as novel biodegradable metal matrix composite for orthopedic applications. *Acta Biomater*. 2018;71:200-214. doi: 10.1016/j.actbio.2018.03.007

142. Yuan W, Li B, Chen D, et al. Formation mechanism, corrosion behavior, and cytocompatibility of microarc oxidation coating on absorbable high-purity zinc. *ACS Biomater Sci Eng*. 2019;5(2):487-497. doi: 10.1021/acsbiomaterials.8b01131

143. Ma J, Zhao N, Zhu D. Endothelial cellular responses to biodegradable metal zinc. *ACS Biomater Sci Eng*. 2015;1(11):1174-1182. doi: 10.1021/acsbiomaterials.5b00319

144. Ma J, Zhao N, Zhu D. Bioabsorbable zinc ion induced biphasic cellular responses in vascular smooth muscle cells. *Sci Rep*. 2016;6:26661. doi: 10.1038/srep26661

145. Katarivas Levy G, Goldman J, Aghion E. The prospects of zinc as a structural material for biodegradable implants—a review paper. *Metals*. 2017;7(10). doi: 10.3390/met7100402

146. Kim J, Oh S, Ki H. Effect of keyhole geometry and dynamics in zero-gap laser welding of zinc-coated steel sheets. *J Mater Process Technol*. 2016;232:131-141. doi: 10.1016/j.jmatprotec.2016.01.028

147. Jablonská E, Vojtěch D, Fousová M, et al. Influence of surface pre-treatment on the cytocompatibility of a novel biodegradable ZnMg alloy. *Mater Sci Eng C Mater Biol Appl*. 2016;68:198-204. doi: 10.1016/j.msec.2016.05.114

148. Yuan W, Xia D, Wu S, et al. A review on current research status of the surface modification of Zn-based biodegradable metals. *Bioact Mater*. 2022;7:192-216. doi: 10.1016/j.bioactmat.2021.05.018

149. Yuan W, Xia D, Zheng Y, et al. Controllable biodegradation and enhanced osseointegration of ZrO2-nanofilm coated Zn-Li alloy: In vitro and in vivo studies. *Acta Biomater*. 2020;105:290-303. doi: 10.1016/j.actbio.2020.01.022

150. Bakhsheshi-Rad HR, Hamzah E, Low HT, et al. Fabrication of biodegradable Zn-Al-Mg alloy: Mechanical properties, corrosion behavior, cytotoxicity and antibacterial activities. *Mater Sci Eng C Mater Biol Appl*. 2017;73:215-219.

doi: 10.1016/j.msec.2016.11.138

151. Bowen PK, Seitz JM, Guillory RJ, 2nd, et al. Evaluation of wrought Zn-Al alloys (1, 3, and 5 wt % Al) through mechanical and in vivo testing for stent applications. *J Biomed Mater Res B Appl Biomater*. 2018;106(1):245-258. doi: 10.1002/jbm.b.33850

152. Lin J, Tong X, Shi Z, et al. A biodegradable Zn-1Cu-0.1Ti alloy with antibacterial properties for orthopedic applications. *Acta Biomater*. 2020;106:410-427. doi: 10.1016/j.actbio.2020.02.017

153. Prakash C, Singh S, Verma K, Sidhu SS, Singh S. Synthesis and characterization of Mg-Zn-Mn-HA composite by spark plasma sintering process for orthopedic applications. *Vacuum*. 2018;155:578-584. doi: 10.1016/j.vacuum.2018.06.063

154. Wen P, Voshage M, Jauer L, et al. Laser additive manufacturing of Zn metal parts for biodegradable applications: processing, formation quality and mechanical properties. *Mater Des*. 2018;155:36-45. doi: 10.1016/j.matdes.2018.05.057

155. Zhao D, Han C, Peng B, et al. Corrosion fatigue behavior and anti-fatigue mechanisms of an additively manufactured biodegradable zinc-magnesium gyroid scaffold. *Acta Biomater*. 2022;153:614-629. doi: 10.1016/j.actbio.2022.09.047

156. Campos Becerra LH, Hernandez Rodriguez MAL, Esquivel Solis H, Lesso Arroyo R, Torres Castro A. Bio-inspired biomaterial Mg-Zn-Ca: a review of the main mechanical and biological properties of Mg-based alloys. *Biomed Phys Eng Express*. 2020;6(4):042001. doi: 10.1088/2057-1976/ab9426

157. Zhang S, Tang C, Feng J, et al. The in vivo and in vitro corrosion behavior of MgO/Mg-Zn-Ca composite with different Zn/Ca ratio. *Front Bioeng Biotechnol*. 2023;11:1222722. doi: 10.3389/fbioe.2023.1222722

158. Mostaed E, Sikora-Jasinska M, Mostaed A, et al. Novel Zn-based alloys for biodegradable stent applications: design, development and in vitro degradation. *J Mech Behav Biomed Mater*. 2016;60:581-602. doi: 10.1016/j.jmbbm.2016.03.018

159. Gong H, Wang K, Strich R, Zhou JG. In vitro biodegradation behavior, mechanical properties, and cytotoxicity of biodegradable Zn-Mg alloy. *J Biomed Mater Res B Appl Biomater*. 2015;103(8):1632-1640. doi: 10.1002/jbm.b.33341

160. Vojtěch D, Kubásek J, Serák J, Novák P. Mechanical and corrosion properties of newly developed biodegradable Zn-based alloys for bone fixation. *Acta Biomater*. 2011;7(9):3515-3522. doi: 10.1016/j.actbio.2011.05.008

161. Katarivas Levy G, Leon A, Kafri A, et al. Evaluation of biodegradable Zn-1%Mg and Zn-1%Mg-0.5%Ca alloys for biomedical applications. *J Mater Sci Mater Med*. 2017;28(11):174. doi: 10.1007/s10856-017-5973-9

162. Guleryuz LF, Ipek R, Arıtman I, Karaoglu S. Microstructure and mechanical properties of Zn-Mg alloys as implant materials manufactured by powder metallurgy method. *AIP Conf. Proc*. 2017;1809:020020. doi: 10.1063/1.4975435

163. Livingstone C. Zinc: physiology, deficiency, and parenteral nutrition. *Nutr Clin Pract*. 2015;30(3):371-382. doi: 10.1177/0884533615570376

164. Manzoor F, Golbang A, Dixon D, et al. 3D printed strontium and zinc doped hydroxyapatite loaded PEEK for craniomaxillofacial implants. *Polymers*. 2022;14(7). doi: 10.3390/polym14071376

165. Milivojevic M, Chen K, Radovanovic Z, et al. Enhanced antimicrobial properties and bioactivity of 3D-printed titanium scaffolds by multilayer bioceramic coating for large bone defects. *Biomed Mater*. 2023;18(6). doi: 10.1088/1748-605X/ad02d2

166. Pound BG. The use of electrochemical techniques to evaluate the corrosion performance of metallic biomedical materials and devices. *J Biomed Mater Res B Appl Biomater*. 2019;107(4):1189-1198. doi: 10.1002/jbm.b.34212

167. Gotman I. Characteristics of metals used in implants. *J Endourol*. 1997;11(6):383-389. doi: 10.1089/end.1997.11.383

168. Seitz JM, Durisin M, Goldman J, Drelich JW. Recent advances in biodegradable metals for medical sutures: a critical review. *Adv Healthc Mater*. 2015;4(13):1915-1936. doi: 10.1002/adhm.201500189

169. Chen Q, Thouas GA. Metallic implant biomaterials. *Mater Sci Eng R Rep*. 2015;87:1-57. doi: 10.1016/j.mser.2014.10.001

170. Kraus T, Moszner F, Fischerauer S, et al. Biodegradable Fe-based alloys for use in osteosynthesis: outcome of an in vivo study after 52 weeks. *Acta Biomater*. 2014;10(7):3346-3353. doi: 10.1016/j.actbio.2014.04.007

171. Hermawan H, Dubé D, Mantovani D. Degradable metallic biomaterials: design and development of Fe-Mn alloys for stents. *J Biomed Mater Res A*. 2010;93(1):1-11. doi: 10.1002/jbm.a.32224

172. Schinhammer M, Hanzi AC, Loffler JF, Uggowitzer PJ. Design strategy for biodegradable Fe-based alloys for medical applications. *Acta Biomater*. 2010;6(5):1705-1713. doi: 10.1016/j.actbio.2009.07.039

173. Hermawan H, Dubé D, Mantovani D. Development of degradable Fe-35Mn alloy for biomedical application. *Adv Mater Res*. 2006;15-17:107-112. doi: 10.4028/www.scientific.net/AMR.15-17.107

174. Guo Y, Zhao M-C, Xie B, et al. In vitro corrosion resistance and antibacterial performance of novel Fe–xCu biomedical alloys prepared by selective laser melting. *Adv Eng Mater.* 2021;23(4).
doi: 10.1002/adem.202001000

175. Schinhammer M, Hänzi AC, Löffler JF, Uggowitzer PJ. Design strategy for biodegradable Fe-based alloys for medical applications. *Acta Biomater*. 2010;6(5):1705-1713.
doi: 10.1016/j.actbio.2009.07.039

176. Mandal S, Kishore V, Bose M, Nandi SK, Roy M. In vitro and in vivo degradability, biocompatibility and antimicrobial characteristics of Cu added iron-manganese alloy. *J Mater Sci Technol.* 2021;84:159-172.
doi: 10.1016/j.jmst.2020.12.029

177. Huang T, Cheng J, Bian D, Zheng Y. Fe-Au and Fe-Ag composites as candidates for biodegradable stent materials. *J Biomed Mater Res B Appl Biomater*. 2016;104(2):225-240.
doi: 10.1002/jbm.b.33389

178. Schinhammer M, Gerber I, Hänzi AC, Uggowitzer PJ. On the cytocompatibility of biodegradable Fe-based alloys. *Mater Sci Eng C Mater Biol Appl*. 2013;33(2):782-789.
doi: 10.1016/j.msec.2012.11.002

179. Kupková M, Kupka M, Morovská Turoňová A, Oriňaková R. Microstructural, mechanical and corrosion characteristics of degradable PM biomaterials made from copper-coated iron powders. *Materials.* 2022;15(5).
doi: 10.3390/ma15051913

180. Scarcello E, Lison D. Are Fe-based stenting materials biocompatible? a critical review of in vitro and in vivo studies. *J Funct Biomater*. 2019;11(1).
doi: 10.3390/jfb11010002

181. Bondareva JV, Dubinin ON, Kuzminova YO, et al. Biodegradable iron-silicone implants produced by additive manufacturing. *Biomed Mater*. 2022;17(3).
doi: 10.1088/1748-605X/ac6124

182. Hong D, Chou DT, Velikokhatnyi OI, et al. Binder-jetting 3D printing and alloy development of new biodegradable Fe-Mn-Ca/Mg alloys. *Acta Biomater.* 2016;45:375-386.
doi: 10.1016/j.actbio.2016.08.032

183. Nie Y, Chen G, Peng H, et al. In vitro and 48 weeks in vivo performances of 3D printed porous Fe-30Mn biodegradable scaffolds. *Acta Biomater*. 2021;121:724-740.
doi: 10.1016/j.actbio.2020.12.028

184. Shuai C, Zan J, Qi F, et al. nMgO-incorporated PLLA bone scaffolds: enhanced crystallinity and neutralized acidic products. *Mater Des.* 2019;174.
doi: 10.1016/j.matdes.2019.107801

185. Anita Lett J, Sagadevan S, Léonard E, et al. Bone tissue engineering potentials of 3D printed magnesium-hydroxyapatite in polylactic acid composite scaffolds. *Artif Organs*. 2021;45(12):1501-1512.
doi: 10.1111/aor.14045

186. Wei X, Zhou W, Tang Z, et al. Magnesium surface-activated 3D printed porous PEEK scaffolds for in vivo osseointegration by promoting angiogenesis and osteogenesis. *Bioact Mater*. 2023;20:16-28.
doi: 10.1016/j.bioactmat.2022.05.011

187. Liu X, Li X, Huo S, et al. Magnesium bioactive glass hybrid functionalized polyetheretherketone with immunomodulatory function to guide cell fate and bone regeneration. *Colloids Surf B.* 2023;230:113523.
doi: 10.1016/j.colsurfb.2023.113523

188. Xu D, Xu Z, Cheng L, et al. Improvement of the mechanical properties and osteogenic activity of 3D-printed polylactic acid porous scaffolds by nano-hydroxyapatite and nano-magnesium oxide. *Heliyon*. 2022;8(6):e09748.
doi: 10.1016/j.heliyon.2022.e09748

189. Lai Y, Li Y, Cao H, et al. Osteogenic magnesium incorporated into PLGA/TCP porous scaffold by 3D printing for repairing challenging bone defect. *Biomaterials*. 2019;197:207-219.
doi: 10.1016/j.biomaterials.2019.01.013

190. Eugen G, Claus M, Anna-Maria S, et al. Degradation of 3D-printed magnesium phosphate ceramics in vitro and a prognosis on their bone regeneration potential. *Bioact Mater*. 2023;19:376-391.
doi: 10.1016/j.bioactmat.2022.04.015

191. Wang D, Liu L, Deng G, et al. Recent progress on additive manufacturing of multi-material structures with laser powder bed fusion. *Virtual Phys Prototyp.* 2022;17(2):329-365.
doi: 10.1080/17452759.2022.2028343

192. Huang S, Wang B, Zhang X, et al. High-purity weight-bearing magnesium screw: translational application in the healing of femoral neck fracture. *Biomaterials*. 2020;238:119829.
doi: 10.1016/j.biomaterials.2020.119829

193. Rossig C, Angrisani N, Helmecke P, et al. In vivo evaluation of a magnesium-based degradable intramedullary nailing system in a sheep model. *Acta Biomater*. 2015;25:369-383.
doi: 10.1016/j.actbio.2015.07.025

194. Jahn K, Saito H, Taipaleenmaki H, et al. Intramedullary Mg2Ag nails augment callus formation during fracture healing in mice. *Acta Biomater*. 2016;36:350-360.
doi: 10.1016/j.actbio.2016.03.041

195. Ali W, Mehboob A, Han M-G, Chang S-H. Experimental study on degradation of mechanical properties of biodegradable magnesium alloy (AZ31) wires/poly(lactic acid) composite for bone fracture healing applications. *Compos Struct.* 2019;210:914-921.
doi: 10.1016/j.compstruct.2018.12.011

196. Ran Z, Wang Y, Li J, et al. 3D-printed biodegradable magnesium alloy scaffolds with zoledronic acid-loaded ceramic composite coating promote osteoporotic bone defect repair. *Int J Bioprint*. 2023;9(5):769.
doi: 10.18063/ijb.769

197. Acar B, Kose O, Turan A, et al. Comparison of bioabsorbable magnesium versus titanium screw fixation for modified distal chevron osteotomy in hallux valgus. *BioMed Res Int*. 2018;2018:5242806.
doi: 10.1155/2018/5242806

198. Chen L, Lin Z, Wang M, et al. Treatment of trauma-induced femoral head necrosis with biodegradable pure Mg screw-fixed pedicle iliac bone flap. *J Orthop Transl*. 2019;17:133-137.
doi: 10.1016/j.jot.2019.01.004

199. Lee J-W, Han H-S, Han K-J, et al. Long-term clinical study and multiscale analysis of in vivo biodegradation mechanism of Mg alloy. *Proc Natl Acad Sci*. 2016;113(3): 716-721.
doi: doi:10.1073/pnas.1518238113

200. Zhao D, Huang S, Lu F, et al. Vascularized bone grafting fixed by biodegradable magnesium screw for treating osteonecrosis of the femoral head. *Biomaterials*. 2016;81:84-92.
doi: 10.1016/j.biomaterials.2015.11.038

201. Zhao D, Witte F, Lu F, et al. Current status on clinical applications of magnesium-based orthopaedic implants: a review from clinical translational perspective. *Biomaterials*. 2017;112:287-302.
doi: 10.1016/j.biomaterials.2016.10.017

202. Mou H, Qu H, Li B, et al. Can "domino" therapy effectively treat the infection around the prosth esis after the limb salvage surgery of bone tumor? - A study of sequential therapy. *Int J Surg*. 2022;101:106630.
doi: 10.1016/j.ijsu.2022.106630

203. Hill D, Williamson T, Lai CY, et al. Automated elaborate resection planning for bone tumor surgery. *Int J Comput Assist Radiol Surg*. 2023;18(3):553-564.
doi: 10.1007/s11548-022-02763-4

204. Park JW, Kang HG, Lim KM, et al. Bone tumor resection guide using three-dimensional printing for limb salvage surgery. *J Surg Oncol*. 2018;118(6):898-905.
doi: 10.1002/jso.25236

205. Amukarimi S, Mozafari M. Biodegradable magnesium-based biomaterials: an overview of challenges and opportunities. *MedComm*. 2020;2(2):123-144.
doi: 10.1002/mco2.59

206. Zhang X, Li X-W, Li J-G, Sun X-D. Preparation and mechanical property of a novel 3D porous magnesium scaffold for bone tissue engineering. *Mater Sci Eng C*. 2014;42:362-367.
doi: 10.1016/j.msec.2014.05.044

207. Disegi JA, Eschbach L. Stainless steel in bone surgery. *Injury*. 2000;31(Suppl 4):2-6.
doi: 10.1016/s0020-1383(00)80015-7

208. Sing SL, An J, Yeong WY, Wiria FE. Laser and electron-beam powder-bed additive manufacturing of metallic implants: a review on processes, materials and designs. *J Orthop Res*. 2016;34(3):369-385.
doi: 10.1002/jor.23075

209. Witte F, Reifenrath J, Müller PP, et al. Cartilage repair on magnesium scaffolds used as a subchondral bone replacement. *Materwiss Werksttech*. 2006;37(6):504-508.
doi: 10.1002/mawe.200600027

210. Newman AP. Articular cartilage repair. *Am J Sports Med*. 1998;26(2):309-324.
doi: 10.1177/03635465980260022701

211. Coutts RD, Healey RM, Ostrander R, et al. Matrices for cartilage repair. *Clin Orthop Relat Res*. 2001;391:S271-279.
doi: 10.1097/00003086-200110001-00025

212. Zhang Y, Pizzute T, Pei M. Anti-inflammatory strategies in cartilage repair. *Tissue Eng Part B Rev*. 2014;20(6): 655-668.
doi: 10.1089/ten.TEB.2014.0014

213. Xu HH, Wang P, Wang L, et al. Calcium phosphate cements for bone engineering and their biological properties. *Bone Res*. 2017;5:17056.
doi: 10.1038/boneres.2017.56

214. Gelli R, Ridi F. An overview of magnesium-phosphate-based cements as bone repair materials. *J Funct Biomater*. 2023;14(8).
doi: 10.3390/jfb14080424

215. Wong HM, Wu S, Chu PK, et al. Low-modulus Mg/PCL hybrid bone substitute for osteoporotic fracture fixation. *Biomaterials*. 2013;34(29):7016-7032.
doi: 10.1016/j.biomaterials.2013.05.062

216. Zhang X, Mao J, Zhou Y, Ji F, Chen X. Mechanical properties and osteoblast proliferation of complex porous dental implants filled with magnesium alloy based on 3D printing. *J Biomater Appl*. 2021;35(10):1275-1283.
doi: 10.1177/0885328220957902

217. Salah M, Tayebi L, Moharamzadeh K, Naini FB. Three-dimensional bio-printing and bone tissue engineering: technical innovations and potential applications in maxillofacial reconstructive surgery. *Maxillofac Plast Reconstr Surg*. 2020;42(1):18.
doi: 10.1186/s40902-020-00263-6

218. Zafar S, Siddiqi A. Biological responses to pediatric stainless steel crowns. *J Oral Sci*. 2020;62(3):245-249.
doi: 10.2334/josnusd.20-0083

219. Leal SC, Takeshita EM. Pediatric restorative dentistry. *Pediatr Dent*. 2017;39(6):312-324.

ACCSCIENCE PUBLISHING

International Journal of Bioprinting

REVIEW ARTICLE

The promising applications of 3D printing technology in neurotrauma

Wenbo He[1,2†], Chongxi Xu[1,2†], Wenbi Wu[3†], Yuchen Chen[2], Jingxuan Hou[2], Zhouhaoran Chen[2], Jianguo Xu[1], Maling Gou[3*], and Yu Hu[1*]

[1]Department of Neurosurgery, West China Hospital, Chengdu, Sichuan, China

[2]West China School of Medicine, Sichuan University, Chengdu, Sichuan, China

[3]Department of Biotherapy, Cancer Center and State Key Laboratory of Biotherapy, West China Hospital, Sichuan University, Chengdu, Sichuan, China

Abstract

Neurotrauma mainly includes brain injury, spinal cord injury, and peripheral nerve injury, which are characterized by high morbidity and disability rates, and involve costly treatments. Currently, various strategies have been applied for the treatment of neurotrauma, but their efficacy is unsatisfactory. New effective strategies are needed to be developed to promote recovery after neurotrauma. In recent years, three-dimensional (3D) printing technology has been used to manufacture customized and complex constructs in tissue engineering applications, exhibiting great potential in repairing nervous system injuries. In this review, we introduce the principles and advantages of 3D printing and 3D bioprinting technologies that have been applied to repair injured nervous system. In particular, we summarize the current strategies in the aspects of biomaterials, physical stimulation, bioactive substances, cell transplantation, and their combination that have been considered in fabricating 3D-printed devices for neurotrauma treatment. Additionally, the challenges and prospects of 3D printing for neurotrauma treatment were also presented.

Keywords: Neurotrauma; Traumatic brain injury; Spinal cord injury; Peripheral nerve injury; Bioprinting; Neural tissue regeneration

†These authors contributed equally to this work.

***Corresponding authors:**
Yu Hu
(huyu0304@scu.edu.cn)

Maling Gou
(goumaling@scu.edu.cn)

Citation: He W, Xu C, Wu W, et al. The promising applications of 3D printing technology in neurotrauma. *Int J Bioprint*. 2024;10(3):2311. doi: 10.36922/ijb.2311

Received: November 24, 2023
Accepted: January 15, 2024
Published Online: February 12, 2024

Copyright: © 2024 Author(s). This is an Open Access article distributed under the terms of the Creative Commons Attribution License, permitting distribution, and reproduction in any medium, provided the original work is properly cited.

Publisher's Note: AccScience Publishing remains neutral with regard to jurisdictional claims in published maps and institutional affiliations.

1. Introduction to neurotrauma and three-dimensional (3D) printing

1.1. Components of nervous system

The nervous system consists of the central nervous system (CNS) and the peripheral nervous system (PNS). The brain and spinal cord are the main components of the CNS.[1] The cerebrum, diencephalon, cerebellum, and brainstem are the four major regions of the brain, which are in charge of a series of fundamental and higher functions, such as sensorimotor, cognitive, memory, and emotion. The spinal cord is located within the spinal canal and consists of white and gray matter, serving as a connection for transferring information between the brain and the PNS.[2] The PNS mainly comprises afferent sensory fibers and efferent motor fibers, which control the body movement, conduct sensation, and regulate internal organ homeostasis.[3]

In terms of cellular composition, the nervous system is characterized by functionally specialized neurons and unique glial cell types.[4] Neurons act to conduct electrical signals, and glial cells are mainly responsible for the stability and development of the nervous system, which are arranged alongside neurons. In addition, glial cells can provide metabolic support to neurons and promote the survival, differentiation, and outgrowth of neurons.[5] Furthermore, the extracellular matrix (ECM), synthesized and secreted by cells, is indispensable in the nervous system. The ECM of the nervous system is made up of three parts: the basement, a diffuse interstitial portion, and perineuronal net (PNN).[6] PNN is a special component of ECM in the nervous system, contributing to maintaining the newly appointed neuronal connections and neuronal protection while concurrently inhibiting synaptic plasticity and neural regeneration with certain components like CSPGs.[7,8] Besides, there are other crucial components, such as chemotropic and neurotrophic factors, in the ECM of the nervous system.[9]

1.2. Neurotrauma

Neurotrauma is an emergency situation and refers to injuries that involve the CNS and PNS. CNS injuries mainly include traumatic brain injury (TBI) and spinal cord injury (SCI). TBI is defined as an alteration in brain function, or other evidence of brain pathology, caused by an external force. It can be divided into mild, moderate, and severe injuries.[10] With 50 million new cases of mild TBI and 2 million new cases of moderate and severe TBI being reported every year worldwide, TBI has emerged as a global public health problem.[11] The absence of effective treatments poses a challenge to the management of TBI. Despite advances in preoperative measures and intensive care, TBI still results in high mortality and long-term neurological deficits.[12] In addition to the primary injury, secondary injuries such as inflammatory reaction, reduction of neural cells, and glial scar formation may occur after TBI.[13] In recent years, the emergence of stem cell therapy and tissue engineering has provided new strategies for neural network reconstruction after TBI.[14,15] However, the delivery and survival of stem cells to the injured sites still face significant challenges. SCI is characterized by damage to the spinal cord, which breaks nerve contact between the brain and the rest of the body, leading to temporary or permanent functional impairment.[16] Approximately 500,000 individuals suffer from SCI worldwide every year, resulting in a huge socioeconomic burden.[17] Currently, treatment options for SCI encompass surgical interventions, pharmaceutical approaches, hypothermia, and rehabilitative medical care.[18] Nevertheless, the effectiveness of these treatments is limited, and the prognosis for individuals with SCI is poor.[19]

Peripheral nerve injury (PNI) is one of the most common neuropathies, which is often caused by diseases, accidents, and natural disasters.[20] It has been reported that there are more than 20 million patients diagnosed with PNI every year in the United States and more than 300,000 patients diagnosed with PNI every year in Europe.[21,22] PNI often affects neural signal transduction, leading to the loss of sensory and motor function and even causing disability in patients. Unlike the CNS, the PNS has an intrinsic ability of regeneration.[23,24] After an injury, Wallerian degeneration occurred at the distal end of the injured sites, and the debris was cleared by Schwann cells and phagocytes.[25,26] Meanwhile, Schwann cells would proliferate and migrate rapidly to form the Bungner band, and the growth cone could advance toward the distal end. However, in severe cases of PNI, especially long-segmental PNI, the self-regeneration of the peripheral nerves is unable to realize the re-connection of the injured nerves.[27,28] At present, the functional recovery of long-segmental PNI remains challenging in regenerative medicine. Autografts have been considered the gold standard for the clinical treatment of PNI,[29] but this strategy is still restricted by inadequate nerve donors, donor site morbidity, and secondary trauma. Recently, nerve guide conduits derived from synthetic and/or natural materials have been developed as promising alternatives for PNI treatment.[30] With a tube-like structure, a conduit can provide physical support and directional guidance for nerve regeneration. Currently, several conduits have been approved by the Food and Drug Administration (FDA) for PNI repair.[21,30] However, the therapeutic efficacy of these conduits for long-segmental PNI is still unsatisfactory and needs to be improved.

Recently, some new treatment approaches, including gene therapy, electrical stimulation, electrochemical neuromodulation therapy, and stem cell therapy, have been used for neurotrauma treatment.[31] However, these strategies can still not provide an ideal microenvironment for repairing nervous system injuries, which can resemble the physical and biological characteristics of natural tissues, such as the anatomical structure, the diversities of cells and bioactive substances, and the spatial distribution of the bioactive components.

1.3. 3D printing and 3D bioprinting technology

3D printing is an additive manufacturing process that creates unique 3D constructs by building 3D structures layer by layer from computer-aided design (CAD) models. 3D printing combined with 3D imaging technology and robot-based precision biofabrication

are compatible with a variety of materials, capable of creating constructs with high resolution and highly controllable spatial structures. It allows customization according to the characteristics of different diseases.[32-34] 3D bioprinting is an extended application of the additive manufacturing process or rapid prototyping (RP) systems to print various cells, bioactive substances, and biomaterials in the form of layers, which can produce biological constructs that highly mimic the properties of innate tissues and organs.[35] Bioink is an important component in bioprinting. Bioinks are composed of biomaterials that encapsulate cells or bioactive substances, allowing the creation of mimetic 3D tissue constructs by different printing principles such as extrusion, inkjet, stereolithography, and digital light processing.[36]

1.4. Advantages of 3D printing in neurotrauma

3D printing technology has many unique advantages in treating neurotrauma. First, 3D printing can customize personalized constructs based on different nervous system injuries. Constructs designed based on 3D topological data of patients using 3D imaging technology are highly matched to the patient's injured site, facilitating nerve regeneration and neurological function recovery.[34] Secondly, 3D printing can directly print cells and bioactive substances by various bioinks at precise and optimal locations, such as in specific areas of a layered or multi-channel scaffold, to better facilitate the survival of transplanted cells and nerve regeneration.[37] Thirdly, the nervous system is composed of complex cells and ECM components. 3D printing allows different types of cells (e.g., nerve cells, glial cells, and immune cells) and different bioactive substances (e.g., neurotrophic factors and cytokines) to be combined with various biomaterials and printed simultaneously to better restore the neural microenvironment of the injured site.[38,39] Finally, the nervous system is fragile and mainly located within bony structures, making it difficult to be accessible for examination. 3D printing enables long-term, non-invasive visualization of implanted constructs by adding contrast agents to bioinks.[40]

Herein, we introduce 3D printing and bioprinting technologies based on different principles that have been applied to neurotrauma treatment, and summarize the current strategies in the aspects of biomaterials, physical stimulation, bioactive substances, cell transplantation, and their combination that have been considered in the fabrication of 3D-printed devices for neurotrauma treatment. Finally, the challenges and prospects of combining 3D printing to treat neurotrauma are discussed.

2. Three-dimensional printing technologies for neurotrauma treatment

The 3D printing technologies currently used for neurotrauma treatment can be divided into two categories. The first category is cell-free printing, like fused deposition modeling, near-field electrospinning, and two-photon printing. This type of 3D printing technology usually requires high temperatures, lasers, and other cell-harmful environments. Such printed constructs usually exploit their physical properties or are used to carry drugs to treat neurotrauma. The other type is bioprinting, which uses bioink to directly print constructs, like inkjet, extrusion, stereolithography, and digital light processing. This type of 3D printing technology enables more accurate arrangement of cells, bioactive components, and biomaterials, thereby better simulating the microenvironment for repairing nervous system injuries. The principles, advantages, and disadvantages of various 3D printing methods used for neurotrauma treatment are summarized in Figure 1 and Table 1, respectively.

2.1. 3D printing technology

2.1.1. Fused deposition modeling

Fused deposition modeling (FDM) is a 3D printing technique based on the controlled, layer-by-layer deposition of thermoplastic materials. FDM printing process involves heating a filament of thermoplastic material until it becomes molten and extruding it through a fine nozzle onto a build platform. The material quickly solidifies, forming a layer, and the platform is lowered for the next layer. The process is repeated until the entire 3D structure is fabricated. FDM is well-suited for material fabrication and the production of highly porous constructs and fully interconnected channel networks.[41,42] It enables localized and targeted drug delivery within the nervous system, reducing systemic side effects and optimizing treatment effectiveness.[43] One of the primary applications of FDM in the field of regeneration medicine is the fabrication of constructs with porous structures and controllable pore sizes, into which cells can be seeded to repair injured tissue. Channels and cavities within the constructs can facilitate nutrient and oxygen exchange for growing cells.[44] Besides, the 3D construct with gaps obtained through FDM makes it easier to induce cells to differentiate into neural cells.[42] However, the disadvantages of FDM include poor mechanical properties, limited availability of thermoplastic polymers, substandard surface properties, and the inability to directly print cells.[45] The layer-by-layer construction in FDM may result in visible layer lines on the final construct, potentially affecting biocompatibility and surface quality. FDM typically offers lower resolution than high-precision

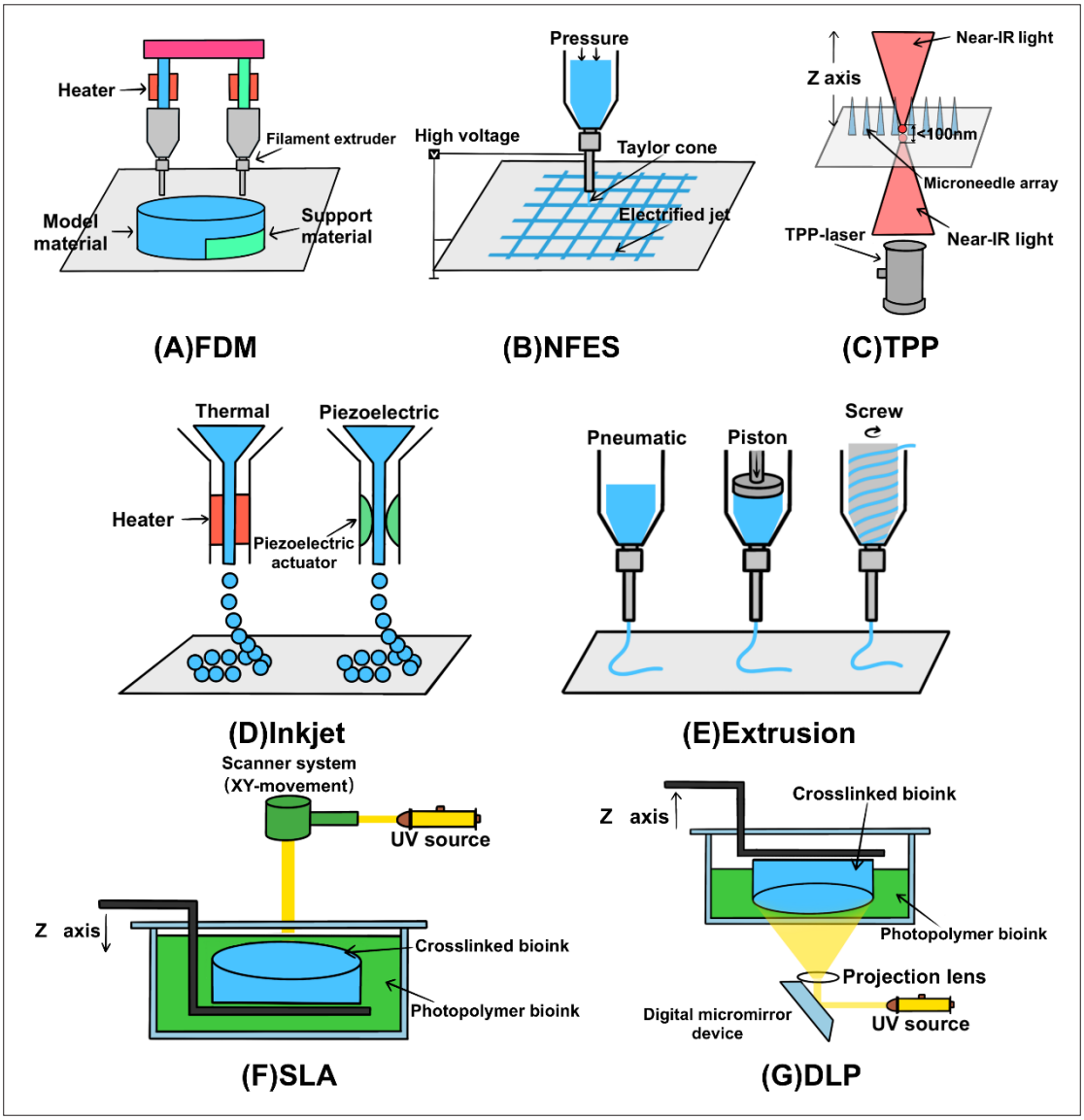


Figure 1. The principles of various 3D printing and bioprinting methods used for neurotrauma treatment.

3D printing technologies like inkjet 3D printing, which can affect the fabrication of intricate neural structures. Complex FDM designs may require additional support structures, which can be challenging to remove without damaging delicate neural structures.

2.1.2. Near-field electrospinning

Near-field electrospinning (NFES) is a micro- or nanofiber production technology based on jetting molten polymer or polymer solution.[46] Sun et al. designed the NFES device for the first time, which has the characteristics of high precision and high resolution.[47] The NFES setup includes a high-voltage power supply, nozzle, and collector, similar to conventional far-field electrospinning setups. However, fiber deposition is poorly controlled with conventional electrospinning (FFES) techniques, inevitably resulting in random pore distribution and morphology.[47,48] In comparison, NFES can produce aligned and patterned fibers by eliminating irregular movement of the nozzle, which has more advantages in scaffold design.[49] NFES technology has been applied to neurotrauma. The near-field direct-writing melt electrospinning involves heating and melting a polymer, then precisely ejecting it through a fine nozzle while an electrical field is applied. The result is the deposition of nanofibers onto a substrate with high precision and control, making it particularly suitable for tissue engineering and regenerative medicine applications. Zhao et al. used this technology to make

Table 1. Different types of 3D printing and bioprinting technologies for neurotrauma treatment

Technology	Suitable materials	Advantages	Disadvantages
FDM	Thermoplastic filaments, e.g., polyurethane, ABS, PCL, and PLA	High speed; low cost; environmental protection	Poor mechanical features; poor surface properties; limited availability of suitable thermoplastic polymer
NFES	Thermoplastic and functional polymer materials, e.g., PCL and PLA	Micron/Nanoscale resolution; low cost; compatible with various materials	Possible cytotoxicity of solvents and the electric field
TPP	Photopolymer, e.g., polypyrrole, GelMA, and PEGDA	Highest resolution; directly perform photopolymerization at any point	Cumbersome printing process; high cost
Inkjet	Thermoplastic and functional polymer materials, e.g., collagen, PCL, and PLA	High resolution; low cost; high fabrication speed	Low mechanical strength; low droplet accuracy; relatively low cell viability
Extrusion	Thermoplastic and functional polymer materials, e.g., alginate dialdehyde, GelMA, PLLA, and PLGA	Low cost; multiple materials mixed printing; higher cell viability	Lower resolution than inkjet; low fabrication speed; nozzle clogging
SLA	Photopolymer, e.g., GelMA, HAMA, and PEGDA	Higher resolution; high fabrication speed; personalization	High cost; limited availability of suitable hydrogels; possible cytotoxicity of photoinitiator and uncured resin
DLP	Photopolymer, e.g., GelMA, HAMA, and PEGDA	Higher resolution; no limitation on cell viscosity; no artificial interfaces	High cost; limited availability of suitable hydrogels

Abbreviations: ABS, acrylonitrile butadiene styrene; DLP, digital light processing; FDM, fused deposition modeling; GelMA, gelatin methacrylate; HAMA, hyaluronic acid methacrylate; NFES, near-field electrospinning; PEGDA, poly (ethylene glycol) diacrylate; PLA, poly lactic acid; PLGA, poly lactic-co-glycolic acid; PLLA, poly-L-lactic acid; PCL, polycaprolactone; TPP, two-photon polymerization; SLA, stereolithography.

poly-e-caprolactone (PCL) scaffolds, which can serve as guidance cues for regenerating nerve fibers and facilitating functional recovery. These scaffolds allow therapeutic agents and biomaterials to be incorporated directly into the printed constructs.[50] In addition, Song et al. used NFES based on polymer solutions to fabricate scaffolds, and loaded ECM hydrogel with drugs on the scaffolds to promote the differentiation of neural stem cells (NSCs).[51] However, this technique cannot directly print cells because the electric field can be deleterious, and most solvents exhibit cytotoxicity.

2.1.3. Two-photon polymerization

The two-photon polymerization (TPP) technology involves the photopolymerization process initiated by two-photon absorption at the high-intensity laser focal point generated by a near-infrared femtosecond pulsed laser beam, which was initially introduced by Japanese scholars in recent years.[52,53] Notably, two-photon absorption only occurs at the focal point, distinguishing it from the traditional stereolithography method. This unique characteristic enables TPP to complete photopolymerization anywhere in the 3D space, transcending surface limitations.[54,55] One of the most remarkable aspects of TPP is its potential for solidification resolutions below the diffraction limit of the applied light, allowing for 3D printing at a nanoscale and achieving a lateral spatial resolution of less than 100 nm.[56] This resolution makes it particularly suitable for fabricating delicate structures for applications in neurotrauma. Accardo et al. produced an intricate 3D scaffold from polyethylene glycol diacrylate (PEGDA) using the TPP method. These 3D scaffolds proved conducive to the survival of Neuro 2A cells and nerve regeneration.[57] Similarly, Marino et al. applied the TPP method to create high-resolution scaffolds, revealing that neurons exhibited better shape when cultured on the scaffold.[58] Besides, the TPP method can also print other forms of delicate constructs such as microneedle arrays to carry drugs to treat neurotrauma.[59] In summary, TPP is an advanced technology offering the highest resolution and the capability to fabricate intricate structures that show potential in neurotrauma. However, TPP also has the disadvantages of a cumbersome printing process, high cost, and inability to print cells directly.

2.2. 3D bioprinting technology

2.2.1. Inkjet 3D printing

Inkjet 3D printing, an evolved version of traditional two-dimensional (2D) inkjet printing, operates on the foundational principle of controlled material deposition within a 3D space. This technology employs print heads equipped with nozzles to dispense minute droplets of material onto a substrate. By systematically layering these droplets, intricate 3D structures are meticulously constructed.[60] Notably, the flexibility of inkjet 3D printing

extends to a variety of materials, including biocompatible polymers, living cells, and therapeutic compounds.[61,62] In nervous system injuries, inkjet 3D printing plays an important role, offering notable advantages such as precision and customization. Inkjet 3D printing provides a high degree of precision in the deposition of cells, growth factors, and biomaterials within 3D constructs. This precision allows for the accurate replication of the intricate nervous system microenvironment and the customization of treatments to suit individual patients' needs.[63] Empirical evidence also underscores the effectiveness of inkjet 3D-printed constructs in promoting neural tissue regeneration.[64] A hallmark feature of inkjet 3D printing is the precision in delivering therapeutic agents, thereby minimizing side effects and optimizing therapeutic outcomes.[61,63] Biocompatible scaffolds created through inkjet 3D printing faithfully replicate the native CNS environment, providing essential support for cell growth, differentiation, and the formation of neural connections, all crucial aspects of CNS repair.[63,65,66] Compared to other 3D printing technologies, inkjet 3D printing excels in terms of precision and resolution, and thus is crucial for constructing intricate neural structures.[60,63] However, inkjet 3D printing may have limited material compatibility. Additionally, it is worth noting that inkjet 3D printing may have limitations in terms of speed, which can be a drawback for high-volume printing.[67]

2.2.2. Extrusion 3D printing

Extrusion 3D printing, a versatile additive manufacturing technique, distinguishes itself from inkjet printing by fabricating 3D structures line-by-line through a movable nozzle driven by pneumatic or mechanical dispensing systems. This method provides a resolution typically ranging from 100 to 500 μm, making it ideal for a wide range of applications.[68,69] In the field of regenerative medicine, custom 3D printing systems based on micro-extrusion have been developed, enabling the creation of constructs that significantly enhance functional recovery after neurotrauma. For instance, 3D-printed collagen/chitosan scaffolds based on micro-extrusion have shown promise in repairing nerve defects after TBIs.[70] In the realm of bioprinting, it has been applied to develop scaffolds laden with various cell types, such as NSCs and ectomesenchymal stem cells (EMSCs), fostering the recovery of injured CNS.[71,72] Compared to other 3D printing methods, it offers several advantages and disadvantages. On the positive side, it is cost-effective and suitable for projects with limited budgets, allowing for the creation of highly customized bioscaffolds and tissue engineering solutions tailored to individual patient needs. It also provides versatility in material choices, including bioceramics and biopolymers. Additionally, extrusion-based 3D printing can manufacture high-density cell structures at a relatively fast production rate.[73,74] On the negative side, it has a lower resolution, making it less suitable for applications requiring fine details. Besides, cell viability may be influenced by pressure in pressure-based systems, necessitating careful control. The layer-by-layer stacking characteristic of extrusion-based 3D printing can result in visible layer lines that may affect surface quality and biocompatibility. Therefore, while it excels in customization and cost-effectiveness, extrusion 3D printing may not be ideal for high-precision applications and may require special attention to pressure-sensitive cell viability.

2.2.3. Stereolithography

Stereolithography (SLA) has emerged as a remarkably precise and adaptable technology across various domains. It functions based on the principle of photopolymerization, employing a laser crosslinking mode. The process involves the incremental layer-by-layer construction of 3D objects by selectively solidifying liquid resin or photopolymer materials with a laser beam, following a 2D image of the intended cross-section, until the entire 3D structure is formed. SLA technology offers distinct advantages compared to other 3D printing methods. Its remarkable features include:

(i) *High precision.* SLA stands out for its ability to achieve high-resolution printing, boasting a remarkable resolution of approximately 100 μm.[75] It makes it a preferred choice for crafting intricate and finely detailed structures.

(ii) *Complex geometrical capabilities.* SLA excels in producing objects with intricate and highly complex geometrical features. This capability allows for customization and precise design, offering versatility in meeting diverse requirements.

(iii) *No restrictions on cell viscosity.* Unlike other techniques, SLA imposes no constraints on the viscosity of cells, rendering it adaptable to various bioink formulations.[76]

(iv) *Reduced toxicity with visible light.* In response to concerns about cell safety, visible light photopolymerization has been explored in SLA.[77] Compared with traditional ultraviolet light, this approach proves to be less harmful to cells.

In the sphere of regenerative medicine, SLA technology holds substantial promise for neurotrauma treatment. It facilitates the meticulous creation of scaffolds characterized by controlled structures, including multi-channels, oriented fibers, and the incorporation of cells and neurotrophic factors. These elements play a pivotal role in promoting the regeneration of nerves.[78] But SLA technology also has some shortcomings, such as limited

proper bioinks for SLA-based 3D printing due to special photocuring characteristics of printed biomaterials, and possible cytotoxicity of photoinitiator and uncured resin.

2.2.4. Digital light processing

Digital light processing (DLP) is an advanced 3D printing technology that utilizes digital micromirror devices (DMD) to construct 3D objects by selectively solidifying light-sensitive polymers or other materials in a layer-by-layer fashion.[79] The object is systematically built layer by layer, with each layer solidified by the DMD projecting a 2D image of the desired cross-section onto the liquid resin. When exposed to the light pattern, the photopolymer undergoes solidification, resulting in the formation of that specific layer of the object. After each layer is solidified, the build platform incrementally moves upward, creating space for the subsequent layer. This process iterates until the entire 3D structure is fully realized. DLP technology boasts numerous advantages, including rapid production, high precision, no artificial interfaces, absence of nozzles, and suitability for crafting intricate structures. DLP technology shows great promise in the neurotrauma. On the one hand, DLP technology enables the customization of patient-specific constructs with finely tuned structures. Its ability to create intricate hierarchal branched geometries and achieve printing resolutions as fine as 1 μm represents a significant advancement in bioprinting technology.[80] On the other hand, DLP can be leveraged to create constructs that integrate nanoparticles and drugs, facilitating sustained drug release to enhance nerve repair. For example, microgel with sustained drug release can be prepared by the DLP method. In addition, cells can be printed into microgel with high survival and proliferation.[81] This approach offers a compelling alternative to conventional methods for the neurotrauma. In summary, the DLP technology has garnered significant attention due to its precision, speed, and versatility, finding applications across fields of the neurotrauma. Nonetheless, it has limitations, such as material compatibility and potential requirements for post-processing.

3. Three-dimensional printing strategies for neurotrauma treatment

External intervention is usually required to repair the damage following neurotrauma. Current 3D printing strategies for neurotrauma treatment mainly include biomaterials, physical regulation, bioactive substances, and cell transplantation. 3D printing can prepare corresponding bulk hydrogels, microspheres, conduits, or microneedles to treat neurotrauma in combination with the above strategies. Figure 2 summarizes current 3D printing strategies for neurotrauma treatment. Besides, Tables 2 and 3 list the detailed studies related to 3D printing for neurotrauma treatment.

3.1. Biomaterials

Biomaterials can bridge damaged areas of the nervous system, promote axon extension and cell migration, and be used as carriers of neurotrophic or regulatory drugs.

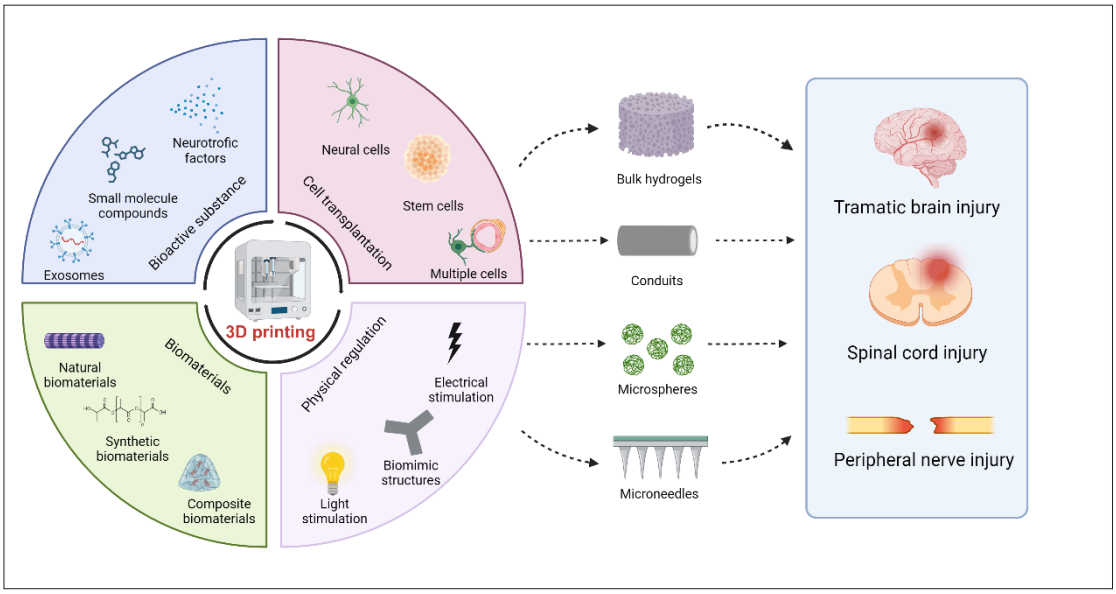


Figure 2. Schematic diagram of various treatment strategies for neurotrauma using 3D printing technology. Strategies such as biomaterial, physical regulation, bioactive substance, and cell transplantation are combined with various constructs of 3D printing from different angles to treat neurotrauma. At the same time, combinations of these strategies are increasingly common. The figure is generated with BioRender.com.

Table 2. Studies related to 3D printing combined with cell-free therapy applications for neurotrauma treatment

Applications	Biomaterials	Additives	Printing method	Design	*In vitro/In vivo*	Strategies	Ref.
Traumatic brain injuries	GelMA	Genipin	Extrusion	Scaffold	*In vitro*	Nat. bm + Small molecule	[142]
Peripheral nerve injuries	GelMA	XMU-MP-1	DLP	Conduit	*In vitro + In vivo*	Nat. bm + Small molecule	[81]
Peripheral nerve injuries	GelMA	RGFP966	DLP	Conduit	*In vitro +I n vivo*	Nat. bm + Small molecule	[145]
Peripheral nerve injuries	GelMA-DBCO/ GelMA-N3	XMU-MP-1	DLP	Conduit	*In vitro + In vivo*	Nat. bm + Small molecule + Physical regulation	[146]
Peripheral nerve injuries	Silicone	NGF/GDNF	Extrusion	Conduit	*In vitro + In vivo*	Nat. bm + Neurotrophic factors + Physical regulation	[39]
Spinal cord injuries	Polypyrrole	Dexa	TPP	Microneedle	*In vitro*	Syn. bm + Small molecule	[59]
Peripheral nerve injuries	PCL	Melatonin	Extrusion	Conduit	*In vitro + In vivo*	Syn. bm + Small molecule	[144]
Nervous system injuries	Graphene-polyurethane	/	Extrusion	Scaffold	*In vitro*	Syn. bm + Physical regulation	[112]
Peripheral nerve injuries	PCL	PDA/RGD/GO	Extrusion	Conduit	*In vitro + In vivo*	Syn. bm + Physical regulation	[134]
Peripheral nerve injuries	PCL	GO	Extrusion	Conduit	*In vitro + In vivo*	Syn. bm + Physical regulation	[109]
Peripheral nerve injuries	PEGDA	/	SLA	Conduit	*In vitro + In vivo*	Syn. bm +Physical regulation	[65]
Spinal cord injuries	Collagen/Chitosan	/	Extrusion	Scaffold	*In vivo*	Com. bm	[98]
Spinal cord injuries	Collagen/Silk fibroin	/	Extrusion	Scaffold	*In vivo*	Com. bm	[91]
Spinal cord injuries	Collagen/Heparin sulfate	/	Extrusion	Scaffold	*In vivo*	Com. bm	[171]
Spinal cord injuries	GelMA	/	DLP	Scaffold	*In vivo*	Com. bm	[101]
Spinal cord injuries	PLGA/PLLA	/	Extrusion	Scaffold	*In vitro + In vivo*	Com. bm	[108]
Traumatic brain injuries	Collagen/Heparin sulfate	/	Extrusion	Scaffold	*In vitro + In vivo*	Com. bm	[87]
Spinal cord injuries	Gel/CNF/HA/N-Cad-Alg	MnTBAP	Extrusion	Scaffold	*In vitro + In vivo*	Com. bm + Small molecule	[37]
Spinal cord injuries	ASCM/G-CD-PEGDA/PCL	Way-316606	FDM/SLA	Scaffold	*In vitro + In vivo*	Com. bm + Small molecule	[50]
Spinal cord injuries	dECM/PCL	OMT	NFES	Scaffold	*In vitro + In vivo*	Com. bm + Small molecule	[137]
Traumatic brain injuries	PEGDA/Me-Gel+Me-HA	SDF-1	DLP	Scaffold	*In vitro*	Com. bm + Small molecule	[140]
Peripheral nerve injuries	GelMA/SF-MA	7,8-DHF	DLP	Conduit	*In vitro + In vivo*	Com. bm + Small molecule	[93]
Nervous system injuries	Collagen/Fibrin	VEGF	Extrusion	Scaffold	*In vitro*	Com. bm + Neurotrophic factors	[150]

(Continued.....)

Table 2. *(Continued.....)*

Applications	Biomaterials	Additives	Printing method	Design	*In vitro/In vivo*	Strategies	Ref.
Spinal cord injuries	Collagen/Chitosan	BDNF	Extrusion	Scaffold	*In vitro* + *In vivo*	Com. bm + Neurotrophic factors	[149]
Peripheral nerve injuries	GelMA/PEGDA	Platelet	DLP	Conduit	*In vitro* + *In vivo*	Com. bm + Neurotrophic factors	[151]
Traumatic brain injuries	Collagen/Silk fibroin	MExos	Extrusion	Scaffold	*In vitro* + *In vivo*	Com. bm + Exosomes	[155]
Traumatic brain injuries	Collagen/Chitosan	MExos	Extrusion	Scaffold	*In vitro* + *In vivo*	Com. bm + Exosomes	[70]
Traumatic brain injuries	Collagen/Chitosan	INExos	Extrusion	Scaffold	*In vitro* + *In vivo*	Com. bm + Exosomes	[154]
Nervous system injuries	GelMA/PEGDA	/	SLA	Scaffold	*In vitro*	Com. bm + Physical regulation	[122]
Nervous system injuries	GelMA/Graphene	/	SLA	Scaffold	*In vitro*	Com. bm + Physical regulation	[116]
Peripheral nerve injuries	GelMA/PEGDA	/	DLP	Conduit	*In vivo*	Com. bm + Physical regulation	[135]

Abbreviations: ABS, acrylonitrile butadiene styrene; ASCM, acellularized spinal cord matrix; BDNF, brain-derived neurotrophic factor; CNF; cellulose nanofiber; 7,8-DHF, 7,8-Dihydroxyflavone; com.bm, composite biomaterial; DBCO, dibenzyl cyclooctyne; Dexa, dexamethasone; G-CD, gelatin-acrylated-β-cyclodextrin; dECM, decellularized extracellular matrix; GDNF, glial cell line-derived neurotrophic factor; Gel, gelatin; GelMA, gelatin methacryloyl; GO, graphene oxide; HA, hyaluronic acid; INExos, exosomes derived from neural stem cells pretreated with insulin-like growth factor-1; LAP, lithium phenyl-2,4,6-trimethylbenzoylphosphinate; Me-HA, methacrylated hyaluronic acid; Me-Gel, methacrylated gelatin; MExos, human umbilical cord mesenchymal stem cells-derived exosomes; N3, azide; N-Cad-Alg, N-Cadherin functionalized sodium alginate; NT-3, Neurotrophin-3; NGF, nerve growth factor; nat.bm, natural biomaterial; OMT, oxymatrine; PCL, polycaprolactone; PDA, polydopamine; PEGDA, poly (ethylene glycol) diacrylate; PLGA, poly lactic-co-glycolic acid; PLLA, poly-L-lactic acid; RGD, arginine-glycine-aspartic acid; SDF-1, stromal-derived factor 1; SF-MA, silk fibroin glycidyl methacrylate; syn.bm, synthetic biomaterial; VEGF, vascular endothelial growth factor; XMU-MP-1, 4-((5,10-dimethyl-6-oxo-6,10-dihydro-5H-pyrimido[5,4-b]thieno[3,2-e][1,4]diazepin-2-yl)amino) benzenesulfonamide.

Table 3. Studies related to 3D printing combined with cell transplantation applications for neurotrauma treatment

Applications	Biomaterials	Cell type	Printing method	Design	*In vitro/In vivo*	Strategies	Ref.
Nervous system injuries	SAMA	EMSCs	Extrusion	Scaffold	*In vitro*	Nat. bm + Stem cell	[72]
Nervous system injuries	GelMA	DPSCs	DLP	Microsphere	*In vitro*	Nat. bm + Stem cell	[172]
Spinal cord injuries	GelMA	hAECs	DLP	Scaffold	*In vivo*	Nat. bm + Stem cell	[173]
Spinal cord injuries	Matrigel	iPSCs	Extrusion	Scaffold	*In vitro*	Nat. bm + Stem cell	[38]
Peripheral nerve injuries	GelMA	ADSCs	Inkjet	Conduit	*In vitro* + *In vivo*	Nat. bm + Stem cell	[174]
Traumatic brain injuries	dECM	NSCs	Extrusion	Scaffold	*In vitro* + *In vivo*	Nat. bm + Stem cell	[102]
Traumatic brain injuries	Polyurethane	NSCs	FDM	Scaffold	*In vitro* + *In vivo*	Syn. bm + Stem cell	[113]
Spinal cord injuries	PLGA	SCs	LDM	Conduit	*In vitro* + *In vivo*	Syn. bm + Neural cell	[178]
Peripheral nerve injuries	PDA-gold/PCL	BMSCs/SCs	Extrusion	Conduit	*In vitro* + *In vivo*	Syn. bm + Multiple cells	[183]
Nervous system injuries	PEDOT:PSS	DRG cells	SLA	Scaffold	*In vitro*	Syn. bm + Neural cell + Physical regulation	[128]

(Continued.....)

Table 3. ***(Continued.....)***

Applications	Biomaterials	Cell type	Printing method	Design	*In vitro/In vivo*	Strategies	Ref.
Spinal cord injuries	HBC/HA/MA	NSCs	Extrusion	Scaffold	*In vitro + In vivo*	Com. bm + Stem cell	[164]
Spinal cord injuries	GelMa/PEGDA	NPCs	μCPP	Scaffold	*In vivo*	Com. bm + Stem cell	[163]
Spinal cord injuries	GelMA/HAMA	NSCs	Extrusion	Scaffold	*In vitro + In vivo*	Com. bm + Stem cell	[165]
Spinal cord injuries	Collagen/Silk fibroin	NSCs	Extrusion	Scaffold	*In vitro + In vivo*	Com. bm + Stem cell	[71]
Spinal cord injuries	Collagen/Silk fibroin	EMSCs	Extrusion	Scaffold	*In vitro + In vivo*	Com. bm + Stem cell	[171]
Nervous system injuries	Al-CMC-Ag	NSCs	Extrusion	Scaffold	*In vitro*	Com. bm + Stem cell	[63]
Spinal cord injuries	SPCL/Gellan gum	OLGs	Extrusion	Scaffold	*In vitro + In vivo*	Com. bm + Neural cell	[180]
Peripheral nerve injuries	Sodium alginate/ Gelatin	SCs	Extrusion	Scaffold	*In vitro + In vivo*	Com. bm + Neural cell	[179]
Spinal cord injuries	Sodium alginate/ Gelatin	NSCs/OLGs	Extrusion	Scaffold	*In vivo*	Com. bm + Multiple cells	[181]
Spinal cord injuries	GelMA	BMSCs/SCs	Extrusion	Scaffold	*In vitro + In vivo*	Com. bm + Multiple cells	[182]
Spinal cord injuries	PEDOT: CSMA, TA/GP	NSCs	Extrusion	Scaffold	*In vitro + In vivo*	Com. bm + Stem cell + Physical regulation	[129]
Spinal cord injuries	GelMA/Ac-β-CD/OSMI-4	NSCs	Extrusion	Scaffold	*In vitro + In vivo*	Com. bm + Stem cell + Small molecule	[184]

Abbreviations: Ac-β-CD, acrylated β-cyclodextrins; ADSCs, Adipose-derived mesenchymal stem cells; Al-CMC-Ag, alginate-carboxymethyl chitosan-agarose; BMSCs, bone marrow mesenchymal stem cells ; DPSCs, dental pulp stem cells; dECM, decellularized extracellular matrix; EMSCs, ectomesenchymal stem cells; GelMA, gelatin methacryloyl; GP, gelatin/polyethylene glycol; HA, hyaluronic acid; HAMA, hyaluronic acid methacrylate; HBC, hydroxypropyl chitosan; iPSCs, Induced pluripotent stem cells; LDM, low temperature deposition manufacturing; MA, Matrigel; NSCs, neural stem cells; PCL, polycaprolactone; PDA-gold/PCL, gold/polycaprolactone nanocomposite coated with polydopamine; PEDOT:CSMA, TA, a novel polyphenol-doped conductive polymer; PEDOT:PSS, poly(3,4-ethylenedioxythiophene): polystyrene sulfonate; PEGDA, poly (ethylene glycol) diacrylate; PLGA, poly lactic-co-glycolic acid; syn.bm, synthetic biomaterial; SAMA, Sodium alginate-Matrigel; SCs, Schwann cells; SPCL, starch/poly-e-caprolactone; μCPP, microscale continuous projection printing.

In addition, when combined with cells to treat neurotrauma, they have a specific nutritional and protective effect on transplanted cells.[82] In the study of neurotrauma, many natural biomaterials and synthetic biomaterials have been combined with 3D printing methods, including collagen, silk fibroin, chitosan, gelatin poly lactic-co-glycolic acid, poly-e-caprolactone, etc. Biomaterials for use in the nervous system need to be biocompatible, degradable, and have appropriate mechanical properties. Biocompatibility ensures low immune reactivity and cytotoxicity, degradability ensures that the constructs can be removed from injured tissue at a rate suitable for tissue regeneration, and appropriate mechanical properties ensure that the injured area will not collapse during normal activities, nor will it generate excessive stress that affects normal tissues.[18] The challenges for biomaterials in neurotrauma include reducing inflammation, reducing scar formation, improving nerve regeneration and axonal growth, and guiding axons to the damaged area.[83]

Here, we reviewed several natural and synthetic biomaterials used in 3D printing for neurotrauma treatment.

3.1.1. Natural biomaterials

Natural materials come from substances that exist in nature and could be classified into polysaccharides, such as hyaluronic acid, chitosan, and alginate, and protein/peptides, such as collagen, gelatin, and silk fibroin.[84] Besides, hydrogels based on natural ECM, such as Matrigel and decellularized extracellular matrix (dECM), can also be classified as natural biomaterials. Many of these materials have been applied to treat neurotrauma by 3D printing technology.

3.1.1.1. Collagen

Serving as the main protein component of the ECM, collagen is highly flexible and is an important natural protein-based biomaterial. Collagen is involved in the morphological maintenance of the ECM, so it is significant for the morphological reconstruction of the ECM and the

regeneration of the whole tissue. In addition, the arginine-glycine-aspartic acid (RGD) sequence in collagen is able to influence stem cells, and the collagen scaffold could promote cell adhesion, proliferation, and differentiation.[85] However, the scaffolds made of collagen alone face several problems, such as insufficient mechanical strength and too rapid degradation. Chen et al. crosslinked collagen and heparin sulfate, a kind of linear polysaccharide of the glycosaminoglycan family, and produced a 3D-collagen/heparin sulfate by extrusion printing.[86] They found that implanting this scaffold into SCI rats could increase the number of neurofilament-positive cells, reduce cavities, and restore motor function. Similarly, Jiang et al. applied a collagen scaffold made by extrusion bioprinting into beagle TBI models.[87] The scaffold exhibited good physical properties and biocompatibility and promoted structural and functional reconstruction after brain injury in beagles. Wang et al. constructed a multichannel collagen scaffold with a multi-nozzle 3D printing technology and found that the mechanical properties of the conduit could vary with the concentration of collagen.[88] They reported that 5% collagen was optimal for nerve scaffold fabrication based on the mechanical properties and printing performances.[88]

3.1.1.2. Silk fibroin

Silk fibroin (SF) is a natural macromolecular protein polymer with inherent advantages, such as good mechanical properties, biocompatibility, biodegradability, and low immunogenicity when forming different materials.[89,90] SF has the characteristics of high mechanical strength, good elasticity, and good environmental stability, which can improve the shortcomings of collagen. Li et al. used the extrusion bioprinting method to make a biomaterial scaffold made of SF and collagen, which combines the advantages of high mechanical strength and SF stability, simulating white matter tracts in the spinal cord. Moreover, the biomimetic scaffold containing SF can guide nerve regeneration and reconstruct neural functional networks in SCI rats.[91] Kim et al. synthesized silk fibroin glycidyl methacrylate (SF-MA) able to form hydrogels through DLP printing, which is promising for fabricating hydrogel conduits with good mechanical properties.[92] However, the *Bombyx mori* SF lacks cell-adhesive motifs and is not beneficial for the adhesion and proliferation of Schwann cells.[93] Meanwhile, Zhang et al. reported a bioink based on *Antheraea pernyi* silk fibroin (ASF) which contains cell-attachable sequence RGD for DLP printing.[94] The developed ASF hydrogel displayed good mechanical properties and positive effects on Schwann cell's adhesion, proliferation, and migration, and holds potential for application in PNI treatment.

3.1.1.3. Chitosan

Chitosan is a natural polysaccharide extracted from the exoskeleton of crustaceans, squid cartilage, or fungal cell walls. It has good mechanical strength and can carry bioactive substances to treat neurotrauma. In the field of peripheral nerve regeneration, it has been proven that chitosan can be used for nerve regeneration and reduction of fibrous scar tissue.[95,96] Chitosan may be beneficial to neurotrauma because its degradation product chitooligosaccharides can promote the migration of macrophages to the injured site and reshape the microenvironment of the injured nerve.[97] Sun et al. designed a chitosan-containing scaffold to repair SCI by a 3D extrusion printing method. Histologically, this scaffold reduced glial scar and promoted axonal regeneration. Functionally, it promoted the recovery of motor function in rats.[98]

3.1.1.4. Gelatin

Gelatin is obtained from collagen and converted into gelatin through high temperature, chemical denaturation, or enzymatic treatment.[99] Gelatin is a biocompatible and degradable polymer that is easily soluble in water and can form hydrogels with heat-sensitive retention properties. Raising the temperature can turn it into a liquid by weakening hydrogen bonds. Therefore, the gelatin material can be formed into various shapes suitable for nervous system.[100] Tran et al. synthesized gelatin methacrylate (GelMA) by adding methacrylic anhydride to gelatin in a carbonate/bicarbonate buffer.[101] Next, they used an improved digital light processing (DLP) technique to prepare GelMA scaffolds with heterogeneous mechanical properties, and simulate the gray and white matter structures of the spinal cord for SCI repair. Regarding peripheral nerve injuries, Tao et al. used GelMA to fabricate hydrogel conduits in a continuous DLP printing process.[78] They found that the GelMA hydrogel conduits were compatible with HUVECs and Schwann cells.

3.1.1.5. Decellularized extracellular matrix

Decellularized extracellular matrix is derived from natural tissue and is prepared by removing cells from the tissue while retaining functional ECM components. It has a good function of promoting cell adhesion and is easy to form a hydrogel by thermal crosslinking.[102] These characteristics make it particularly suitable for preparing constructs by 3D printing to treat neurotrauma. For example, Bae et al. prepared brain dECM to carry NSCs and fabricated scaffolds through 3D printing for implantation in TBI rats.[103] The results showed that NSCs proliferated and differentiated well in dECM, and the scaffold was helpful in reducing neuroinflammation in TBI rats. Similarly, Kong et al. used porcine CNS tissue to prepare dECM

and found that it was beneficial to the growth of motor neuron axons.[104]

3.1.2. Synthetic biomaterials

Synthetic biomaterials have better physical properties and controllable degradation rates than natural biomaterials and have been used in many fields of biomedicine.[105] Synthetic biocompatible polymers such as PCL, poly lactic acid (PLA), poly-L-lactic acid (PLLA), and poly lactic-co-glycolic acid (PLGA) have diverse chemical properties, controllable degradation rate, and high-water absorption.[106,107] Various synthetic biomaterials have been adopted for 3D printing of nervous system injury repair. Kaplan et al. produced polyester scaffolds composed of PLGA and PLLA for nerve tissue regeneration based on 3D printing.[108] This customized scaffold closely simulates the morphology of neural tissue and is beneficial to the survival and proliferation of iPSCs-derived neurons and axon regeneration. Besides, Qian et al. developed PCL conduit loading with GO nanoparticles through an extrusion method.[109] They found that the conduit exhibited uniform nanoparticle dispersion, porous structure, strong mechanical strength, and high electrical conductivity. They also demonstrated that the PCL/GO scaffolds positively affect the proliferation, adhesion, and functions of Schwann cells, and the conduits could promote angiogenesis and functional recovery of a 15 mm sciatic nerve defect. In addition to the polyesters introduced above, there are many synthetic hydrogel constructs that have been used in neurotrauma, such as PEGDA and polyurethane (PU) hydrogels. PEGDA is modified with polyethylene glycol (PEG) terminal hydroxyl groups, and polyethylene glycol dimethacrylate (PEGDMA) is also formed similarly. They form hydrogels through photo-crosslinking, making them suitable for 3D printing methods such as SLA and DLP. For example, Pateman et al. produced PEGDA hydrogel conduits, which promote the dorsal root ganglion to proliferate, differentiate, and orientate *in vitro* and support nerve re-connection *in vivo*.[65] Biodegradable PU is an emerging synthetic biomaterial because of its biocompatibility, elasticity, mechanical properties, and flexibility.[110,111] Polyurethane is a copolymer formed by the polymerization of polyols, small-molecule chain extenders, and isocyanates. Huang et al. synthesized a new biodegradable waterborne PU and mixed graphene with PU to produce a graphene-based composite bioink for 3D bioprinting.[112] The rheological properties of the bioink facilitate NSCs survival and printing. Hsieh et al. prepared thermoresponsive water-based PU dispersions and demonstrated that the NSCs had good proliferation and differentiation capabilities in the dispersions.[113] After implanting the scaffold made of this dispersion by the FDM method into the adult zebrafish TBI model, the neurological function of the zebrafish was restored.

3.1.3. Composite biomaterials

Natural biomaterials and synthetic biomaterials can be further compounded for 3D printing to treat neurotrauma. Composite biomaterials refer to biomaterials composed of two or more materials with different physicochemical properties.[114] For example, various materials can combine with natural biomaterials to form composite biomaterials, such as microspheres, conductive polymers, and electrospun fibers.[115] Wei et al. synthesized GelMA and graphene nanoplatelets into composite biomaterials and made them into 3D scaffolds through the SLA method.[116] *In vitro* experiments have confirmed that this scaffold benefits the survival and differentiation of NSCs and the repair of neural tissue.[116] To develop biomaterials with biocompatibility and proper mechanical strength for PNI, Wu et al. developed composite hydrogels by combining GelMA and SF-MA, in which GelMA is beneficial for cell adhesion while SF-MA can provide mechanical strength.[93] They found that GelMA/SF-MA with a ratio of 1:1 was optimal for Schwann cell behaviors including cell adhesion, proliferation, spreading, and migration. In addition, they also designed and prepared photopolymerizable plasma by a mild one-pot method.[117] This composite biomaterial derived from plasma contains various proteins and growth factors, and the formulation of the composite biomaterial is similar to that of physiological conditions. They found that the plasma hydrogel could sustainedly release growth factors and promote the neurite elongation of PC12 cells, which is promising for fabricating personalized nerve guide conduits for PNI by DLP printing.

3.2. Physical regulation

3.2.1. Light stimulation

The role of light stimulation after neurotrauma is to rebuild lost neuronal circuits. In recent years, low-intensity light therapy (LLLT) has gradually become a new strategy to improve function through external stimulation of cells.[118,119] LLLT, also known as photo biomodulation, has been used to cure many clinical diseases, including promoting wound healing, reducing pain and inflammatory responses, accelerating tissue recovery, and treating certain neurological diseases.[120,121] Although the precise biochemical mechanism of LLLT regulation remains to be elucidated, it has been shown that LLLT is implicated at the molecular, cellular, and tissue levels.[119] Zhu et al. produced a transparent scaffold consisting of GelMA and PEGDA by SLA, which could combine with LLLT.[122] *In vitro* experiments have proven that this 3D-printed scaffold, combined with a light stimulation strategy, can promote

the differentiation of stem cells into neurons rather than glial cells.[122]

3.2.2. Electric stimulation

Electrical stimulation can regulate stem cell migration and differentiation through its polarity characteristics. Previous studies have found that pulsed DC stimulation of 1 V/cm effectively enhances the differentiation of NSCs into neurons.[123] Many studies have demonstrated regulating the electrical stimulation through conductive materials can promote the proliferation, differentiation, and neurite elongation of NSCs.[124,125] The effect of electrical stimulation is more significant in a 3D culture environment, specifically reflected in higher expression levels of neuron-related genes, and more stem cells differentiate into nerve cells under electrical stimulation.[126,127] Heo et al. combined dorsal root ganglion (DRG) cells and GelMA with a conductive structure (crystallized PEDOT: PSS) to create a 3D conductive scaffold, which can promote the differentiation of encapsulated DRG cells into neurons under electrical stimulation.[128] In a similar way, Song et al. prepared conductive scaffolds loaded with NSCs through 3D bioprinting and confirmed the differentiation of NSCs on the scaffolds into neurons.[129] The scaffolds can reduce glial scar formation when implanted in SCI rats.[129] Vijayavenkataraman et al. combined synthetic polymer PCL and conductive polymers (polypyrrole, poly (acrylic acid)) to fabricate conductive conduits through inkjet 3D printing. They found that the conductive conduits can promote neuronal cell proliferation and differentiation.[130-133] In addition, carbon-based conductive materials, such as graphene, also have the potential to be integrated into conduits for PNI. Qian et al. fabricated RGD and polydopamine (PDA)-coated PCL/GO conduits through an integrated 3D printing method.[134] The electrically conductive and cell-adhesive conduits could promote neural expression, axon regeneration, and remyelination for PNI *in vivo*.

3.2.3. Biomimic structures

For neurotrauma, the biomimetic structure is important for providing physical cues to build a favorable microenvironment for axon regeneration and remyelination. Generally, the structure design of conduits involves the specific architectures of the lumen, the wall, and the branch of conduits, which were biomimetic to the anatomical structures and properties of the natural nerves. 3D printing technology has provided an advanced tool for fabricating conduits with customized and complex structures. To mimic the structure of nerve fascicles and reduce the axon mismatch, Zhu et al. fabricated multi-channel conduits through a rapid continuous DLP printing process.[135] They demonstrated that the multi-channel conduits could effectively guide the proximal ends to regenerate directionally along the microchannel to connect with the distal ends in a mouse nerve defect model. The functional and histological assessments indicate that this conduit can promote axon regeneration and functional recovery. Meanwhile, Qian et al. prepared porous conduits using microneedles to generate multiple aligned macropores (50 μm) on the wall of the conduit,[109,134] to promote nutrient exchange during the regeneration process. Moreover, longitudinal topography of the inner wall of the conduit has also been reported to be beneficial for nerve regeneration.[136] For example, through laser-based micro SLA, Pateman et al. developed PEG-DA hydrogel conduits with inner microgroove structures (50 μm). This conduit could promote the dorsal root ganglion to proliferate, differentiate, and orientate *in vitro* and support nerve re-connection through a 3 mm defect.[65] When the PNI involves the loss of a branch point, the branch structure should be designed to match the anatomical structure. Johnson et al. fabricated a Y-shape conduit through an extrusion printing process based on the 3D models, designed by 3D scanning patients' nerve anatomies.[39] They also demonstrated that the bifurcating conduits with customized geometries and growth factor gradients could guide the injured stumps to regenerate across a complex nerve defect (10 mm, bifurcated) and result in improved functional recovery. Meanwhile, Zhu et al. also constructed a life-size triple-branched conduit based on the complex structure of the human facial nerve,[135] demonstrating the great potential of 3D printing for different nervous system injuries.

3.3. Bioactive substances

3.3.1. Small-molecule compounds

Small-molecule compounds have unique advantages such as high cell permeability, good reversibility, and easy control of cell fate. Combining them with 3D-printed constructs such as microneedle arrays, conduits, scaffolds, *etc.* has become a new strategy for regulating cell fate in nervous system injuries.

In the treatment of CNS injury, Huang et al. encapsulated the traditional anti-inflammatory drug dexamethasone (Dexa) in a polypyrrole-coated microneedle array using the TPP method to achieve electronically controlled release of dexamethasone.[59] This high-precision microneedle array can be placed under the dura mater to achieve electronically controlled sustained release of Dexa, thereby reducing the inflammatory response mediated by microglia. Some new anti-inflammatory drugs are also applied in 3D-printed scaffolds for CNS injury. Oxymatrine (OMT) is the main bioactive component of traditional Chinese medicine *Sophora flavescent* Ait. It has been proven to have anti-

tumor, anti-fibrotic, and anti-inflammatory effects. Song et al. precisely prepared PCL scaffolds similar to spinal cord shape by NFES technology, and loaded the ECM of rat spinal cord and OMT into hydrogel onto 3D scaffolds.[137] This scaffold exerts the anti-inflammatory and anti-fibrotic effects of OMT, alleviates secondary SCI and glial scar formation, promotes axonal growth at the injured site, and improves the motor score of SCI rats. Certain small-molecule cytokines can also be combined with 3D bioprinting to treat CNS injuries. Stromal cell-derived factor-1 (SDF-1), also known as chemokine CXCL12, is a small-molecule cytokine belonging to the chemokine protein family. It has been proven that SDF-1 recruits cells to ischemic sites, reconstructs the regional blood supply, and promotes the repair of ischemic injury.[138,139] Li et al. used the DLP printing method to create a scaffold made of hydrogel and SDF-1. The *in vitro* experiment showed that the SDF-1-loaded scaffold was beneficial to the survival and proliferation of NSCs, and guided cell migration from NSC spheroids inside microchannels.[140] Some antibiotics with crosslinking properties can also be used to treat CNS damage. Genipin was shown to reduce sepsis and have crosslinking properties, and therefore, was proposed to be a potential therapeutic agent for TBI.[141] Based on this, Da et al. provided a protein-based interpenetrating polymer network (IPN) scaffold encapsulated with genipin for treating TBI.[142]

In terms of PNI treatment, small-molecule drugs have been combined with nerve guide conduit to realize local drug delivery and conduit functionalization.[60] For example, 7,8-DHF prodrug nanoassemblies were developed and encapsulated into a nerve guide conduit by a DLP technology.[93] It was found that the prodrug nanoassemblies with high drug-loading capacities within the conduit could sustainably release the 7,8-DHF to promote neurite elongation. Meanwhile, 3D-printed PCL NGCs with melatonin have also been demonstrated to promote Schwann cell proliferation and upregulate neural-specific gene expression.[143,144] In addition, several small-molecule drugs have also been proven to have the potential to improve the functional recovery of injured nerves. Tao et al. found that the Hippo pathway inhibitor XMU-MP-1 could accelerate Schwann cell proliferation and migration and upregulate the gene expression of neurotrophic factors. The XMU-MP-1-loaded conduits fabricated by DLP printing exhibited improved efficacy for nerve regeneration.[78] Xu et al. also demonstrated that RGFP966 could promote Schwann cell remyelination through activating the PI3K-AKT-ERK signal pathway, and the sustained RGFP966 release from the 3D-printed conduits could significantly promote functional recovery after injury.[145] In a recent study, Zhang et al. fabricated a self-adhesive bandage made up of a grating inner layer and a lamellar outer layer by DLP printing. Through click reaction, the two layers can adhere to each other to form a tube-like scaffold that could wrap the injured nerve sites. The XMU-MP-1 nanoparticles were loaded in the grating layer, and the drug could be directionally released to the injured sites to promote functional recovery.[146]

3.3.2. Neurotrophic factors

Neurotrophic factors can promote the regeneration of nerve fibers and synapses, and has been used to treat neurotrauma for better neurological recovery. There are many types of neurotrophic factors. For example, nerve growth factor (NGF) and its receptors are widely distributed in the nervous system. They have neurotrophic effects under physiological conditions and can promote the development and maturation of neurons. They also have neuroprotective effects under pathological conditions, protect neurons from damage, improve survival rate, and promote the regeneration and functional recovery of damaged neurons.[147] For another example, brain-derived neurotrophic factor (BDNF) and its receptors are widely expressed in the nervous system and act through the high-affinity receptor tyrosine-protein kinase B (TrkB). BDNF has a neuroprotective effect on a variety of neurons after injury. This effect can extend to the cortical motor system and increase the survival rate of motor neurons.[148] Liu et al. applied a low-temperature extrusion 3D printer to create a collagen/chitosan scaffold encapsulated with BDNF.[149] *In vivo* experiments showed that a 3D printing scaffold combined with BDNF promoted nerve fiber regeneration, reduced the cavity area of the injured site, and promoted the recovery of motor function. Lee et al. produced a collagen and VEGF-releasing fibrin hydrogel scaffold by freeform fabrication (FF) technique.[150] Subsequent *in vitro* experiments confirmed that the VEGF-loading scaffold supported sustained release of the GF, and the C17.2 cells in the scaffold showed high viability. Meanwhile, neurotrophic growth factors have also been introduced into conduits to provide a beneficial microenvironment to improve peripheral nerve regeneration after PNI. Notably, Johnson et al. found that specific growth factor gradients and/or spatial distribution within conduits could guide branch nerve regeneration for complex PNIs.[39] It has also been reported that local delivery of multiple neurotrophic factors may display a better effect on nerve regeneration than a single neurotrophic factor. In a recent study, Tao et al. fabricated functional conduits by developing composite bioinks of photopolymerizable polymers and platelets isolated from whole blood.[151] They found that the DLP-printed conduits could prolong the survival of the platelets and sustainably release various neurotrophic factors. Thus, the conduits provided a regenerative microenvironment

for the long-term nerve regeneration and significantly improved peripheral nerve recovery *in vivo*.

3.3.3. Exosomes

Exosomes originate from endosomes and are extracellular vesicles with a diameter of 40–160 nm and an average diameter of 100 nm. The multivesicular bodies can fuse with the cell membrane and release the vesicles from the cell to the ECM, so exosomes often contain substances such as lipids, proteins, DNA, RNA, and microRNAs.[152] The function of exosomes depends on their cell or tissue source and can participate in multiple pathophysiological processes, such as immune response, antigen presentation, programmed cell death, angiogenesis, inflammation, and coagulation.[153] Liu et al. prepared low-temperature 3D-printed collagen/chitosan scaffolds loaded with exosomes derived from NSCs pretreated with insulin growth factor-1.[154] Their strategy of 3D printing scaffold combined with exosomes can improve the neurological function of TBI rats by recruiting stem cells, reducing inflammation, promoting angiogenesis, etc. Besides, they also designed a hypoxia-pretreated EMSC-derived exosomes-loaded bioprinting scaffold. In TBI beagle dogs, this exosomes-loaded scaffold plays an important role in anti-inflammation, promoting nerve regeneration and improving the motor ability.[155]

3.4. Cell transplantation

3.4.1. Stem cells

Stem cells are multipotent cells with the ability to self-replicate, differentiate, and repair damaged tissue. Stem cells have been incorporated in neurotrauma treatment because they release neurotrophic factors and promote neurovascular unit reconstruction in neural tissue repair.[156] The combination of 3D printing technology and stem cell transplantation can more effectively improve the function outcome after neurotrauma.[157] 3D printing combined with stem cell transplantation increases cell proliferation and neural differentiation. Besides, it reduces inflammatory response and shrinks the cavities after neurotrauma.[158] Stem cells such as neural stem/progenitor cells, induced pluripotent stem cells, and mesenchymal stem cells have been combined with 3D printing for neurotrauma treatment.

3.4.1.1. Neural stem cells/neural progenitor cells

Neural stem cells (NSCs)/neural progenitor cells (NPCs) are multipotent stem cells with the ability to self-renew. They can differentiate into neurons, astrocytes, and oligodendrocytes, and can pass through the blood–brain barrier, thereby replacing damaged cells at the injury site. Moreover, they can secrete a variety of chemokines and neurotrophic factors to benefit nerve regeneration.[159] After nerve injury, neural stem cell transplantation can reduce the inflammatory response, prevent cell apoptosis, inhibit the formation of glial scars, and shrink the injury cavity, thereby promoting the recovery of electrophysiological activities and sensorimotor functions after injury.[160,161] However, transplanting NSCs directly into damaged areas has limited therapeutic effect, which may be due to the difficulty of stem cells surviving and uncontrolled differentiation.[162] 3D-printed constructs can provide a conducive microenvironment for stem cells survival, proliferation, and differentiation in the injured areas. Koffler et al. printed a precision-tailored 3D scaffold via a microscale continuous projection printing technology (μCPP) ladened with NPCs.[163] In rat SCI model, the scaffold promoted axons extension into the 3D scaffold and regeneration to caudal side of the injured spinal cord, and significantly improved the functional outcomes.[163] Liu et al. fabricated NSC-laden scaffolds by 3D bioprinting. The 3D biomimetic scaffold is beneficial to the survival and differentiation of NSCs cells into neurons because it simulates the natural environment of the spinal cord, promoting nerve regeneration and motor function recovery.[164] Besides, Yang et al. created NSCs-laden scaffolds via extrusion-based 3D bioprinting.[165] NSCs were wrapped in an ECM-like hydrogel to form a 3D nerve fiber-like structure. The NCSs in the scaffold survived and improved the microenvironment in the injured site, and subsequently promoted nerve regeneration, the formation of nerve relay, and effective motor function recovery in rats.[165] As for PNI, Li et al. prepared a bionic scaffold with longitudinal fibers by a 3D printing technology and combined the scaffold with neural crest stem cells (NSCs)-derived Schwann cell progenitors.[166] They found that the cell-loading scaffold could promote directional cell growth and axonal myelination *in vitro*, and facilitate nerve regeneration and functional recovery *in vivo*.

3.4.1.2. Mesenchymal stem cells

Mesenchymal stem cells (MSCs) originate from mesoderm and ectoderm in the early stages of development and have various types, including bone (BMSCs), amniotic membrane (hAMSCs), adipose (ADSCs), and dental pulp (DP-MSCs). MSCs are also pluripotent stem cells and can replicate and differentiate themselves.[167,168] In addition, MSCs can secrete cytokines such as nerve growth factors.[169] MSCs have shown great potential in the field of tissue repair and regeneration due to their high availability, pleiotropic effects, immunomodulation, self-regeneration, easy isolation, and culture in damaged tissues.[170] Li et al. and Chen et al. fabricated EMSCs-loaded sodium alginate-Matrigel (SAMA) hydrogel and collagen/silk fibroin by 3D bioprinting, respectively.[72,171]

Their results showed that EMSCs-laden scaffolds can continuously release BDNF and improve neurological function by reconstructing the neural network after SCI in rats.[72,171] Qian et al. used the DLP 3D printing technology to print dental pulp stem cells (DPSCs) in microspheres for nerve tissue regeneration.[172] They found that the DPSCs-loaded microspheres were able to promote angiogenesis and repair nerve tissue structurally and functionally. Qiu et al. used the DLP technique to construct human amniotic epithelial cells (hAECs)-laden hydrogel for SCI, and their later *in vivo* experiments showed that the neural circuit and hindlimb locomotion were partly recovered in rats.[173] Hu et al. prepared a cryoGelMA conduit through indirect printing and seeded ADSCs on the scaffold to generate the bioconduit.[174] They found that the cryoGelMA conduit with porous structures could support the adhesion, proliferation, and viability of ADSCs and upregulate the mRNA expressions of neurotrophic factors *in vitro*. They also demonstrated that the ADSCs-loading conduit could promote axon regeneration and functional recovery in a 10 mm sciatic nerve defect model.

3.4.1.3. Induced pluripotent stem cells

Induced pluripotent stem cells (iPSCs) are a kind of pluripotent stem cells formed by reprogramming fully differentiated somatic cells by introducing specific transcription factors, which also have the ability to proliferate and differentiate into a variety of tissues and organs. Due to no ethical issues involved, iPSCs are more suitable for clinical application and are expected to be the preferred cell types in the field of tissue repair and regeneration. iPSCs can easily differentiate into precursor cells of all neural cell types at the injured site, such as neural precursor cells (NPCs) and oligodendrocyte precursor cells (OPCs).[175,176] Therefore, IPSCs may have great potential in repairing nervous system injury. Fan et al. embedded iPSC-derived NSCs in GelMA hydrogel for SCI, and found that the scaffold inhibited glial scars formation and facilitated axons regeneration.[158] Joung et al. prepared iPSC-derived NPCs- and OPCs-laden hydrogel by extrusion-based 3D bioprinting, which was beneficial to the survival of transplanted cells and the reconstruction of the nervous system after injury.[38]

3.4.2. Neural cells

3.4.2.1. Schwan cells

Schwann cells belong to glial cells, which play the role of structural support in the PNS and provide a favorable microenvironment for axon regeneration.[177] There are various neurotrophic factors and repair-promoting proteins in the extracellular stroma secreted by Schwann cells, which are beneficial to the survival of neurons and the regeneration of demyelinating axons. Sun et al. cultured Schwann cells on 3D-printed PLGA scaffold, and the construct was further applied for the treatment of SCI. The results showed that the cell-laden scaffolds relieved secondary injuries, promoted axonal growth, decreased neuronal apoptosis and demyelination, and improved functional neurological recovery.[178] Wu et al. developed a conduit by bioprinting with a composite bioink of gelatin, sodium alginate, and Schwann cells. The printed conduit was demonstrated to promote cell adhesion and upregulate the gene expression of neurotrophic factors when compared with 2D culture, providing a promising candidate for 3D-bioprinted cell-laden conduits.[179]

3.4.2.2. Oligodendrocytes

Oligodendrocytes also belong to glial cells, which are responsible for myelin formation in the CNS. Oligodendrocytes can myelinate axons, thereby protecting neurons. In addition, oligodendrocytes can secrete growth factors, such as BDNF, neurotrophic factor (NT-3), and NGF, which can mediate the interaction between oligodendrocytes and neurons, thereby promoting axon regeneration. Silva et al. printed a tubular scaffold using 3D bioplotting technique, and further filled it with oligodendrocyte-like cells. The oligodendrocytes-loaded scaffold did not cause significant inflammation, reduced secondary spinal cord injuries, and promoted axonal regeneration and the recovery of motor function in rat SCI model.[180]

3.4.3. Simultaneous transplantation of multiple types of cells

Stem and differentiated neural cells can simultaneously be loaded in 3D-printed constructs to treat neurotrauma. For example, simultaneous loading of NSCs and oligodendrocytes within 3D-printed scaffolds has been used for neurotrauma treatment from the point of view of nerve regeneration and neuron support, respectively. Liu et al. customized a 3D hydrogel scaffold with hyaluronic acid and gelatin and loaded NSCs and oligodendrocytes onto the scaffold.[181] After the scaffold was implanted into SCI rats, they found that neuronal degeneration and demyelination were reduced, and motor function was significantly restored in rats. In addition, some studies combined BMSCs and Schwann cells for facilitating neural regeneration. Wang et al. used BMSCs, Schwann cells, and GelMA hydrogels as bioink to fabricate 3D constructs.[182] They oriented the two types of cells to enable wrapping the outer layer of BMSCs with Schwann cells. The 3D scaffold, which precisely customizes the location of cells, plays an important role in differentiating BMSCs into neural cells. The scaffold with a precise combination of multi-cells acts as a bridge in the injury site of SCI rats and promotes the reconstruction of neural functional networks.[182] Besides,

Qian et al. fabricated a PCL conduit loading with PDA-coated gold nanoparticles by an extrusion printing process.[183] They found that the scaffold could provide a favorable microenvironment for BMSCs and Schwann cells *in vitro*. After loading with BMSCs and Schwann cells, they demonstrated that the conduit could promote axonal regeneration and remyelination in a sciatic nerve defect model.[183]

4. Conclusion and future outlook

The emerging 3D printing technology has the characteristics of design flexibility, personalized customization, and controllable manufacturing accuracy. Taking advantage of the advanced technology, we could fabricate functionalized neural constructs based on multiple strategies, such as biomaterials, physical stimulation, bioactive substances, cell transplantation, and their combination, for efficient neurotrauma treatment. At present, although significant progresses have been achieved in the application of 3D printing in neurotrauma treatment, challenges still remain. First, in order to accurately manufacture constructs with customized functions, the 3D printing system needs to be optimized, especially in terms of accuracy and speed. Second, the biomaterials available for printing are limited. The properties of printable biomaterials for neurotrauma, such as degradability, biocompatibility, and mechanical properties, could be further improved. Choosing a combination of various biomaterials may be an alternative option. Third, for the purpose of clinically translating 3D-printed devices into applications for neurotrauma treatment, it is still a huge challenge to fabricate constructs suitable for humans and test them on large animals or even conduct clinical trials. More importantly, exploring and elucidating the repair mechanism of a damaged nervous system is of great significance and can provide direction for the design of new 3D-printed products. Finally, 3D-printed constructs with synergetic combination of multiple neurotrauma treatment strategies to achieve multi-angle and sequential treatment are expected to lead to breakthroughs in the future.

Acknowledgments

None.

Funding

This work was supported by National Natural Science Foundation of China (grant number: 82001320), Key R&D projects in Sichuan Province (2022YFS0319), and Post-Doctor Research Project, West China Hospital, Sichuan University (No. 2023HXBH081).

Conflict of interest

The authors declare no conflicts of interest.

Author contributions

Conceptualization: Yu Hu
Funding acquisition: Yu Hu, Wenbi Wu
Supervision: Maling Gou
Visualization: Wenbo He
Writing – original draft: Wenbo He, Chongxi Xu, Wenbi Wu, Yuchen Chen, Jingxuan Hou, Zhouhaoran Chen
Writing – review & editing: Jianguo Xu, Yu Hu, Maling Gou

Ethics approval and consent to participate

Not applicable.

Consent for publication

Not applicable.

Availability of data

Not applicable.

References

1. Peppiatt CM, Howarth C, Mobbs P, Attwell D. Bidirectional control of CNS capillary diameter by pericytes. *Nature*. 2006;443(7112):700-704.
doi: 10.1038/nature05193

2. Bican O, Minagar A, Pruitt AA. The spinal cord: a review of functional neuroanatomy. *Neurol Clin*. 2013;31(1):1-18.
doi: 10.1016/j.ncl.2012.09.009

3. Catala M, Kubis N. Gross anatomy and development of the peripheral nervous system. *Handb Clin Neurol*. 2013;115:29-41.
doi: 10.1016/b978-0-444-52902-2.00003-5

4. Suter T, Jaworski A. Cell migration and axon guidance at the border between central and peripheral nervous system. *Science (New York, NY)*. 2019;365(6456).
doi: 10.1126/science.aaw8231

5. Lozano JCM, Gomez RM, Sanabria AGZ, Jubiz G, Valderrama S. Genetic aspects of glial cells regarding neurodegenerative diseases. *Curr Pharm Des*. 2018;24(15):1727-1735.
doi: 10.2174/1381612823666170828134055

6. Shafiee A, Ahmadi H, Taheri B, et al. Appropriate scaffold selection for CNS tissue engineering. *Avicenna J Med Biotechnol*. 2020;12(4):203-220.

7. Alilain WJ, Horn KP, Hu H, Dick TE, Silver J. Functional regeneration of respiratory pathways after spinal cord injury. *Nature*. 2011;475(7355):196-200.
doi: 10.1038/nature10199

8. Fawcett JW, Oohashi T, Pizzorusso T. The roles of perineuronal nets and the perinodal extracellular matrix in neuronal function. *Nat Rev Neurosci*. 2019;20(8):451-465. doi: 10.1038/s41583-019-0196-3

9. Reichardt LF, Tomaselli KJ. Extracellular matrix molecules and their receptors: functions in neural development. *Annu Rev Neurosci*. 1991;14:531-570. doi: 10.1146/annurev.ne.14.030191.002531

10. Menon DK, Schwab K, Wright DW, Maas AI. Position statement: definition of traumatic brain injury. *Arch Phys Med Rehabil*. 2010;91(11):1637-1640. doi: 10.1016/j.apmr.2010.05.017

11. Maas AIR, Menon DK, Adelson PD, et al. Traumatic brain injury: integrated approaches to improve prevention, clinical care, and research. *Lancet Neurol*. 2017;16(12):987-1048. doi: 10.1016/s1474-4422(17)30371-x

12. Wiles MD. Management of traumatic brain injury: a narrative review of current evidence. *Anaesthesia*. 2022; 77(Suppl 1):102-112. doi: 10.1111/anae.15608

13. Zhang J, Liu X, Ma K, et al. Collagen/heparin scaffold combined with vascular endothelial growth factor promotes the repair of neurological function in rats with traumatic brain injury. *Biomater Sci*. 2021;9(3):745-764. doi: 10.1039/c9bm01446b

14. Mukherjee N, Adak A, Ghosh S. Recent trends in the development of peptide and protein-based hydrogel therapeutics for the healing of CNS injury. *Soft Matter*. 2020;16(44):10046-10064. doi: 10.1039/d0sm00885k

15. Mahumane GD, Kumar P, Pillay V, Choonara YE. Repositioning N-acetylcysteine (NAC): NAC-loaded electrospun drug delivery scaffolding for potential neural tissue engineering application. *Pharmaceutics*. 2020;12(10). doi: 10.3390/pharmaceutics12100934

16. Spinal cord injury (SCI) 2016 facts and figures at a glance. *J Spinal Cord Med*. 2016;39(4):493-494. doi: 10.1080/10790268.2016.1210925

17. Zarepour A, Hooshmand S, Gökmen A, Zarrabi A, Mostafavi E. Spinal cord injury management through the combination of stem cells and implantable 3D bioprinted platforms. *Cells*. 2021;10(11). doi: 10.3390/cells10113189

18. Bedir T, Ulag S, Ustundag CB, Gunduz O. 3D bioprinting applications in neural tissue engineering for spinal cord injury repair. *Mater Sci Eng C Mater Biol Appl*. 2020;110:110741. doi: 10.1016/j.msec.2020.110741

19. Fehlings MG, Tetreault LA, Wilson JR, et al. A clinical practice guideline for the management of acute spinal cord injury: introduction, rationale, and scope. *Global Spine J*. 2017;7(3 Suppl):84s-94s. doi: 10.1177/2192568217703387

20. Carvalho CR, Reis RL, Oliveira JM. Fundamentals and current strategies for peripheral nerve repair and regeneration. *Adv Exp Med Biol*. 2020;1249:173-201. doi: 10.1007/978-981-15-3258-0_12

21. Kehoe S, Zhang XF, Boyd D. FDA approved guidance conduits and wraps for peripheral nerve injury: a review of materials and efficacy. *Injury*. 2012;43(5):553-572. doi: 10.1016/j.injury.2010.12.030

22. Petcu EB, Midha R, McColl E, Popa-Wagner A, Chirila TV, Dalton PD. 3D printing strategies for peripheral nerve regeneration. *Biofabrication*. 2018;10(3):032001. doi: 10.1088/1758-5090/aaaf50

23. Barnes DM. What makes nerves regenerate? *Science (New York, NY)*. 1985;230(4729):1024-1025. doi: 10.1126/science.4059920

24. Horner PJ, Gage FH. Regenerating the damaged central nervous system. *Nature*. 2000;407(6807):963-970. doi: 10.1038/35039559

25. Scheib J, Höke A. Advances in peripheral nerve regeneration. *Nat Rev Neurol*. 2013;9(12):668-676. doi: 10.1038/nrneurol.2013.227

26. Liu B, Xin W, Tan JR, et al. Myelin sheath structure and regeneration in peripheral nerve injury repair. *Proc Natl Acad Sci U S A*. 2019;116(44):22347-22352. doi: 10.1073/pnas.1910292116

27. Bridging the gap. *Science*. 2008;320(5878):851. doi: 10.1126/science.320.5878.851b

28. Vijayavenkataraman S. Nerve guide conduits for peripheral nerve injury repair: a review on design, materials and fabrication methods. *Acta Biomater*. 2020;106:54-69. doi: 10.1016/j.actbio.2020.02.003

29. Deumens R, Bozkurt A, Meek MF, et al. Repairing injured peripheral nerves: bridging the gap. *Prog Neurobiol*. 2010;92(3):245-276. doi: 10.1016/j.pneurobio.2010.10.002

30. Parker BJ, Rhodes DI, O'Brien CM, Rodda AE, Cameron NR. Nerve guidance conduit development for primary treatment of peripheral nerve transection injuries: a commercial perspective. *Acta Biomater*. 2021;135:64-86. doi: 10.1016/j.actbio.2021.08.052

31. Islamov R, Bashirov F, Fadeev F, et al. Epidural stimulation combined with triple gene therapy for spinal cord injury treatment. *Int J Mol Sci*. 2020;21(23). doi: 10.3390/ijms21238896

32. Ford S, Despeisse M. Additive manufacturing and sustainability: an exploratory study of the advantages and challenges. *J Clean Prod*. 2016;137:1573-1587. doi: 10.1016/j.jclepro.2016.04.150

33. Wang X, Jiang M, Zhou Z, Gou J, Hui D. 3D printing of polymer matrix composites: a review and prospective. *Compos B Eng*. 2017;110:442-458.

doi: 10.1016/j.compositesb.2016.11.034

34. Joung D, Lavoie NS, Guo SZ, Park SH, Parr AM, McAlpine MC. 3D printed neural regeneration devices. *Adv Funct Mater*. 2020;30(1). doi: 10.1002/adfm.201906237

35. Haring AP, Sontheimer H, Johnson BN. Microphysiological human brain and neural systems-on-a-chip: potential alternatives to small animal models and emerging platforms for drug discovery and personalized medicine. *Stem Cell Rev Rep*. 2017;13(3):381-406. doi: 10.1007/s12015-017-9738-0

36. Matai I, Kaur G, Seyedsalehi A, McClinton A, Laurencin CT. Progress in 3D bioprinting technology for tissue/organ regenerative engineering. *Biomaterials*. 2020;226:119536. doi: 10.1016/j.biomaterials.2019.119536

37. Li Y, Cheng S, Wen H, et al. Coaxial 3D printing of hierarchical structured hydrogel scaffolds for on-demand repair of spinal cord injury. *Acta Biomater*. 2023;168:400-415. doi: 10.1016/j.actbio.2023.07.020

38. Joung D, Truong V, Neitzke CC, et al. 3D printed stem-cell derived neural progenitors generate spinal cord scaffolds. *Adv Funct Mater*. 2018;28(39). doi: 10.1002/adfm.201801850

39. Johnson BN, Lancaster KZ, Zhen G, et al. 3D printed anatomical nerve regeneration pathways. *Adv Funct Mater*. 2015;25(39):6205-6217. doi: 10.1002/adfm.201501760

40. Oliveira EP, Malysz-Cymborska I, Golubczyk D, et al. Advances in bioinks and in vivo imaging of biomaterials for CNS applications. *Acta Biomater*. 2019;95:60-72. doi: 10.1016/j.actbio.2019.05.006

41. O'Brien CM, Holmes B, Faucett S, Zhang LG. Three-dimensional printing of nanomaterial scaffolds for complex tissue regeneration. *Tissue Eng Part B Rev*. 2015;21(1):103-114. doi: 10.1089/ten.TEB.2014.0168

42. Hsiao D, Hsu SH, Chen RS, Chen MH. Characterization of designed directional polylactic acid 3D scaffolds for neural differentiation of human dental pulp stem cells. *J Formos Med Assoc*. 2020;119(1 Pt 2):268-275. doi: 10.1016/j.jfma.2019.05.011

43. Wang J, Zhang Y, Aghda NH, et al. Emerging 3D printing technologies for drug delivery devices: current status and future perspective. *Adv Drug Deliv Rev*. 2021;174:294-316. doi: 10.1016/j.addr.2021.04.019

44. Wu GH, Hsu SH. Review: polymeric-based 3D printing for tissue engineering. *J Med Biol Eng*. 2015;35(3):285-292. doi: 10.1007/s40846-015-0038-3

45. Chen MY, Skewes J, Woodruff MA, Dasgupta P, Rukin NJ. Multi-colour extrusion fused deposition modelling: a low-cost 3D printing method for anatomical prostate cancer models. *Sci Rep*. 2020;10(1):10004. doi: 10.1038/s41598-020-67082-7

46. Nazemi MM, Khodabandeh A, Hadjizadeh A. Near-field electrospinning: crucial parameters, challenges, and applications. *ACS Appl Biomater*. 2022;5(2):394-412. doi: 10.1021/acsabm.1c00944

47. Sun D, Chang C, Li S, Lin L. Near-field electrospinning. *Nano Lett*. 2006;6(4):839-842. doi: 10.1021/nl0602701

48. He FL, Li DW, He J, et al. A novel layer-structured scaffold with large pore sizes suitable for 3D cell culture prepared by near-field electrospinning. *Mater Sci Eng C Mater Biol Appl*. 2018;86:18-27. doi: 10.1016/j.msec.2017.12.016

49. Chang C, Limkrailassiri K, Lin L. Continuous near-field electrospinning for large area deposition of orderly nanofiber patterns. *Appl Phys Lett*. 2008;93(12):123111. doi: 10.1063/1.2975834

50. Zhao X, Lu X, Li K, et al. Double crosslinked biomimetic composite hydrogels containing topographical cues and WAY-316606 induce neural tissue regeneration and functional recovery after spinal cord injury. *Bioact Mater*. 2023;24:331-345. doi: 10.1016/j.bioactmat.2022.12.024

51. Song S, Zhou J, Wan J, et al. Three-dimensional printing of microfiberreinforced hydrogel loaded with oxymatrine for treating spinal cord injury. *Int J Bioprint*. 2023;9(3). doi: 10.18063/ijb.692

52. Maruo S, Nakamura O, Kawata S. Three-dimensional microfabrication with two-photon-absorbed photopolymerization. *Opt Lett*. 1997;22(2):132-134. doi: 10.1364/ol.22.000132

53. Kawata S, Sun HB, Tanaka T, Takada K. Finer features for functional microdevices. *Nature*. 2001;412(6848):697-698. doi: 10.1038/35089130

54. Lee K-S, Kim RH, Yang D-Y, Park SH. Advances in 3D nano/microfabrication using two-photon initiated polymerization. *Prog Polym Sci*. 2008;33(6):631-681. doi: 10.1016/j.progpolymsci.2008.01.001

55. Liska R, Schuster M, Inführ R, et al. Photopolymers for rapid prototyping. *J Coat Technol Res*. 2007;4(4):505-510. doi: 10.1007/s11998-007-9059-3

56. Xing J-F, Dong X-Z, Chen W-Q, et al. Improving spatial resolution of two-photon microfabrication by using photoinitiator with high initiating efficiency. *Appl Phys Lett*. 2007;90(13):131106. doi: 10.1063/1.2717532

57. Accardo A, Blatché M-C, Courson R, Loubinoux I, Vieu C, Malaquin L. Two-photon lithography and microscopy of 3D hydrogel scaffolds for neuronal cell growth. *Biomed Phys Eng Express*. 2018;4(2):027009. doi: 10.1088/2057-1976/aaab93

58. Marino A, Ciofani G, Filippeschi C, et al. Two-photon polymerization of sub-micrometric patterned surfaces:

investigation of cell-substrate interactions and improved differentiation of neuron-like cells. *ACS Appl Mater Interfaces*. 2013;5(24):13012-13021.
doi: 10.1021/am403895k

59. Huang J, Yap N, Walter M, et al. 3D-printed polypyrrole microneedle arrays for electronically controlled transdural drug release. *ACS Biomater Sci Eng*. 2022;8(4):1544-1553.
doi: 10.1021/acsbiomaterials.1c01305

60. Huang Y, Wu W, Liu H, et al. 3D printing of functional nerve guide conduits. *Burns Trauma*. 2021;9:tkab011.
doi: 10.1093/burnst/tkab011

61. Gao B, Yang Q, Zhao X, Jin G, Ma Y, Xu F. 4D bioprinting for biomedical applications. *Trends Biotechnol*. 2016;34(9):746-756.
doi: 10.1016/j.tibtech.2016.03.004

62. Tse C, Whiteley R, Yu T, et al. Inkjet printing Schwann cells and neuronal analogue NG108-15 cells. *Biofabrication*. 2016;8(1):015017.
doi: 10.1088/1758-5090/8/1/015017

63. Gu Q, Tomaskovic-Crook E, Lozano R, et al. Functional 3D neural mini-tissues from printed gel-based bioink and human neural stem cells. *Adv Healthc Mater*. 2016;5(12):1429-1438.
doi: 10.1002/adhm.201600095

64. Lorber B, Hsiao WK, Hutchings IM, Martin KR. Adult rat retinal ganglion cells and glia can be printed by piezoelectric inkjet printing. *Biofabrication*. 2014;6(1):015001.
doi: 10.1088/1758-5082/6/1/015001

65. Pateman CJ, Harding AJ, Glen A, et al. Nerve guides manufactured from photocurable polymers to aid peripheral nerve repair. *Biomaterials*. 2015;49:77-89.
doi: 10.1016/j.biomaterials.2015.01.055

66. Choudary R, Saini N, Chopra DS, Singh D, Singh N. A comprehensive review of 3D bioprinting biomaterials: properties, strategies and wound healing application. *J Mater Res*. 2023;38(13):3264-3300.
doi: 10.1557/s43578-023-01078-7

67. Yan X, Tong Y, Wang X, Hou F, Liang J. Extrusion-based 3D-printed supercapacitors: recent progress and challenges. *Energy Environ Mater*. 2022;5(3):800-822.
doi: 10.1002/eem2.12260

68. Cui H, Nowicki M, Fisher JP, Zhang LG. 3D bioprinting for organ regeneration. *Adv Healthc Mater*. 2017;6(1).
doi: 10.1002/adhm.201601118

69. Wang R, Wang Y, Yao B, et al. Redirecting differentiation of mammary progenitor cells by 3D bioprinted sweat gland microenvironment. *Burns Trauma*. 2019;7:29.
doi: 10.1186/s41038-019-0167-y

70. Liu X, Zhang J, Cheng X, et al. Integrated printed BDNF-stimulated HUCMSCs-derived exosomes/collagen/chitosan biological scaffolds with 3D printing technology promoted the remodelling of neural networks after traumatic brain injury. *Regen Biomater*. 2023;10:rbac085.
doi: 10.1093/rb/rbac085

71. Jiang JP, Liu XY, Zhao F, et al. Three-dimensional bioprinting collagen/silk fibroin scaffold combined with neural stem cells promotes nerve regeneration after spinal cord injury. *Neural Regen Res*. 2020;15(5):959-968.
doi: 10.4103/1673-5374.268974

72. Li Y, Cao X, Deng W, et al. 3D printable sodium alginate-matrigel (SA-MA) hydrogel facilitated ectomesenchymal stem cells (EMSCs) neuron differentiation. *J Biomater Appl*. 2021;35(6):709-719.
doi: 10.1177/0885328220961261

73. Bishop ES, Mostafa S, Pakvasa M, et al. 3-D bioprinting technologies in tissue engineering and regenerative medicine: current and future trends. *Genes Dis*. 2017;4(4):185-195.
doi: 10.1016/j.gendis.2017.10.002

74. Sanz-Garcia A, Sodupe-Ortega E, Pernía-Espinoza A, Shimizu T, Escobedo-Lucea C. A versatile open-source printhead for low-cost 3D microextrusion-based bioprinting. *Polymers*. 2020;12(10).
doi: 10.3390/polym12102346

75. Gauvin R, Chen YC, Lee JW, et al. Microfabrication of complex porous tissue engineering scaffolds using 3D projection stereolithography. *Biomaterials*. 2012;33(15):3824-3834.
doi: 10.1016/j.biomaterials.2012.01.048

76. Mandrycky C, Wang Z, Kim K, Kim DH. 3D bioprinting for engineering complex tissues. *Biotechnol Adv*. 2016;34(4):422-434.
doi: 10.1016/j.biotechadv.2015.12.011

77. Wang Z, Abdulla R, Parker B, Samanipour R, Ghosh S, Kim K. A simple and high-resolution stereolithography-based 3D bioprinting system using visible light crosslinkable bioinks. *Biofabrication*. 2015;7(4):045009.
doi: 10.1088/1758-5090/7/4/045009

78. Tao J, Zhang J, Du T, et al. Rapid 3D printing of functional nanoparticle-enhanced conduits for effective nerve repair. *Acta Biomater*. 2019;90:49-59.
doi: 10.1016/j.actbio.2019.03.047

79. Derakhshanfar S, Mbeleck R, Xu K, Zhang X, Zhong W, Xing M. 3D bioprinting for biomedical devices and tissue engineering: a review of recent trends and advances. *Bioact Mater*. 2018;3(2):144-156.
doi: 10.1016/j.bioactmat.2017.11.008

80. Kim SH, Yeon YK, Lee JM, et al. Precisely printable and biocompatible silk fibroin bioink for digital light processing 3D printing. *Nat Commun*. 2018;9(1):1620.
doi: 10.1038/s41467-018-03759-y

81. Liu X, Tao J, Liu J, et al. 3D Printing enabled customization of functional microgels. *ACS Appl Mater Interfaces*. 2019;11(13):12209-12215.
doi: 10.1021/acsami.8b18701

82. Raspa A, Pugliese R, Maleki M, Gelain F. Recent therapeutic approaches for spinal cord injury. *Biotechnol Bioeng*. 2016;113(2):253-259. doi: 10.1002/bit.25689

83. Slotkin JR, Pritchard CD, Luque B, et al. Biodegradable scaffolds promote tissue remodeling and functional improvement in non-human primates with acute spinal cord injury. *Biomaterials*. 2017;123:63-76. doi: 10.1016/j.biomaterials.2017.01.024

84. Li J, Wu C, Chu PK, Gelinsky M. 3D printing of hydrogels: rational design strategies and emerging biomedical applications. *Mater Sci Eng R Rep*. 2020;140:100543. doi: 10.1016/j.mser.2020.100543

85. Kuo KC, Lin RZ, Tien HW, et al. Bioengineering vascularized tissue constructs using an injectable cell-laden enzymatically crosslinked collagen hydrogel derived from dermal extracellular matrix. *Acta Biomater*. 2015;27:151-166. doi: 10.1016/j.actbio.2015.09.002

86. Chen C, Zhao ML, Zhang RK, et al. Collagen/heparin sulfate scaffolds fabricated by a 3D bioprinter improved mechanical properties and neurological function after spinal cord injury in rats. *J Biomed Mater Res Part A*. 2017;105(5):1324-1332. doi: 10.1002/jbm.a.36011

87. Jiang J, Liu X, Chen H, et al. 3D printing collagen/heparin sulfate scaffolds boost neural network reconstruction and motor function recovery after traumatic brain injury in canine. *Biomater Sci*. 2020;8(22):6362-6374. doi: 10.1039/d0bm01116a

88. Wang Y, Zhang L, Guo K, Wang H. 3D printing of collagen nerve scaffold with multichannel characteristics. *J Phys Conf Ser*. 2023;2557(1):012058. doi: 10.1088/1742-6596/2557/1/012058

89. Rockwood DN, Preda RC, Yücel T, Wang X, Lovett ML, Kaplan DL. Materials fabrication from Bombyx mori silk fibroin. *Nat Protoc*. 2011;6(10):1612-1631. doi: 10.1038/nprot.2011.379

90. Qian KY, Song Y, Yan X, et al. Injectable ferrimagnetic silk fibroin hydrogel for magnetic hyperthermia ablation of deep tumor. *Biomaterials*. 2020;259:120299. doi: 10.1016/j.biomaterials.2020.120299

91. Li XH, Zhu X, Liu XY, et al. The corticospinal tract structure of collagen/silk fibroin scaffold implants using 3D printing promotes functional recovery after complete spinal cord transection in rats. *J Mater Sci Mater Med*. 2021;32(4):31. doi: 10.1007/s10856-021-06500-2

92. Kim SH, Yeon YK, Lee JM, et al. Precisely printable and biocompatible silk fibroin bioink for digital light processing 3D printing. *Nat Commun*. 2018;9(1):1620. doi: 10.1038/s41467-018-03759-y

93. Wu W, Dong Y, Liu H, et al. 3D printed elastic hydrogel conduits with 7,8-dihydroxyflavone release for peripheral nerve repair. *Mater Today Bio*. 2023;20:100652. doi: 10.1016/j.mtbio.2023.100652

94. Zhang X, Wu W, Huang Y, Yang X, Gou M. Antheraea pernyi silk fibroin bioinks for digital light processing 3D printing. *Int J Bioprint*. 2023;9(5):760. doi: 10.18063/ijb.760

95. Stenberg L, Kodama A, Lindwall-Blom C, Dahlin LB. Nerve regeneration in chitosan conduits and in autologous nerve grafts in healthy and in type 2 diabetic Goto-Kakizaki rats. *Eur J Neurosci*. 2016;43(3):463-473. doi: 10.1111/ejn.13068

96. Neubrech F, Sauerbier M, Moll W, et al. Enhancing the outcome of traumatic sensory nerve lesions of the hand by additional use of a chitosan nerve tube in primary nerve repair: a randomized controlled bicentric trial. *Plast Reconstr Surg*. Aug 2018;142(2):415-424. doi: 10.1097/prs.0000000000004574

97. Zhao Y, Wang Y, Gong J, et al. Chitosan degradation products facilitate peripheral nerve regeneration by improving macrophage-constructed microenvironments. *Biomaterials*. 2017;134:64-77. doi: 10.1016/j.biomaterials.2017.02.026

98. Sun Y, Yang C, Zhu X, et al. 3D printing collagen/chitosan scaffold ameliorated axon regeneration and neurological recovery after spinal cord injury. *J Biomed Mater Res Part A*. 2019;107(9):1898-1908. doi: 10.1002/jbm.a.36675

99. Lindberg D, Kristoffersen KA, Wubshet SG, et al. Exploring effects of protease choice and protease combinations in enzymatic protein hydrolysis of poultry by-products. *Molecules (Basel, Switzerland)*. 2021;26(17). doi: 10.3390/molecules26175280

100. Duan B, Hockaday LA, Kang KH, Butcher JT. 3D bioprinting of heterogeneous aortic valve conduits with alginate/gelatin hydrogels. *J Biomed Mater Res Part A*. 2013;101(5):1255-1264. doi: 10.1002/jbm.a.34420

101. Tran KA, DeOre BJ, Ikejiani D, et al. Matching mechanical heterogeneity of the native spinal cord augments axon infiltration in 3D-printed scaffolds. *Biomaterials*. 2023;295:122061. doi: 10.1016/j.biomaterials.2023.122061

102. Murphy SV, Atala A. 3D bioprinting of tissues and organs. *Nat Biotechnol*. 2014;32(8):773-785. doi: 10.1038/nbt.2958

103. Bae M, Hwang DW, Ko MK, et al. Neural stem cell delivery using brain-derived tissue-specific bioink for recovering from traumatic brain injury. *Biofabrication*. 2021;13(4). doi: 10.1088/1758-5090/ac293f

104. Kong JS, Huang X, Choi YJ, et al. Promoting long-term cultivation of motor neurons for 3D neuromuscular junction formation of 3D in vitro using central-nervous-tissue-derived bioink. *Adv Healthc Mater*. 2021;10(18):e2100581. doi: 10.1002/adhm.202100581

105. Gyles DA, Castro LD, Silva JOC, Ribeiro-Costa RM. A review of the designs and prominent biomedical advances of natural and synthetic hydrogel formulations. *Eur Polym J*. 2017;88:373-392.
doi: 10.1016/j.eurpolymj.2017.01.027

106. Assunção-Silva RC, Gomes ED, Sousa N, Silva NA, Salgado AJ. Hydrogels and cell based therapies in spinal cord injury regeneration. *Stem Cells Int*. 2015;2015:948040.
doi: 10.1155/2015/948040

107. Haggerty AE, Oudega M. Biomaterials for spinal cord repair. *Neurosci Bull*. 2013;29(4):445-459.
doi: 10.1007/s12264-013-1362-7

108. Kaplan B, Merdler U, Szklanny AA, et al. Rapid prototyping fabrication of soft and oriented polyester scaffolds for axonal guidance. *Biomaterials*. 2020;251:120062.
doi: 10.1016/j.biomaterials.2020.120062

109. Qian Y, Song J, Zhao X, et al. 3D fabrication with integration molding of a graphene oxide/polycaprolactone nanoscaffold for neurite regeneration and angiogenesis. *Adv Sci*. 2018;5(4):1700499.
doi: 10.1002/advs.201700499

110. Zhang C, Zhang N, Wen X. Synthesis and characterization of biocompatible, degradable, light-curable, polyurethane-based elastic hydrogels. *J Biomed Mater Res Part A*. 2007;82(3):637-650.
doi: 10.1002/jbm.a.30992

111. Yeganegi M, Kandel RA, Santerre JP. Characterization of a biodegradable electrospun polyurethane nanofiber scaffold: mechanical properties and cytotoxicity. *Acta Biomater*. 2010;6(10):3847-3855.
doi: 10.1016/j.actbio.2010.05.003

112. Huang CT, Kumar Shrestha L, Ariga K, Hsu SH. A graphene-polyurethane composite hydrogel as a potential bioink for 3D bioprinting and differentiation of neural stem cells. *J Mater Chem B*. 2017;5(44):8854-8864.
doi: 10.1039/c7tb01594a

113. Hsieh FY, Lin HH, Hsu SH. 3D bioprinting of neural stem cell-laden thermoresponsive biodegradable polyurethane hydrogel and potential in central nervous system repair. *Biomaterials*. 2015;71:48-57.
doi: 10.1016/j.biomaterials.2015.08.028

114. Lendlein A, Trask R. Multifunctional materials: concepts, function- structure relationships, knowledge-based design, translational materials research. *Multifunct Mater*. 2018;1.
doi: 10.1088/2399-7532/aada7b

115. Buwalda S. Bio-based composite hydrogels for biomedical applications. *Multifunct Mater*. 2020;3.
doi: 10.1088/2399-7532/ab80d6

116. Wei Z, Harris BT, Zhang LG. Gelatin methacrylamide hydrogel with graphene nanoplatelets for neural cell-laden 3D bioprinting. *Annu Int Conf IEEE Eng Med Biol Soc*. 2016;2016:4185-4188.
doi: 10.1109/embc.2016.7591649

117. Wu W, Dong Y, Liu H, et al. Modification of plasma protein for bioprinting via photopolymerization. *Chin Chem Lett*. 2023;109260.
doi: 10.1016/j.cclet.2023.109260

118. AlGhamdi KM, Kumar A, Moussa NA. Low-level laser therapy: a useful technique for enhancing the proliferation of various cultured cells. *Lasers Med Sci*. 2012;27(1):237-249.
doi: 10.1007/s10103-011-0885-2

119. Chung H, Dai T, Sharma SK, Huang YY, Carroll JD, Hamblin MR. The nuts and bolts of low-level laser (light) therapy. *Ann Biomed Eng*. 2012;40(2):516-533.
doi: 10.1007/s10439-011-0454-7

120. Pjrek E, Friedrich ME, Cambioli L, et al. The efficacy of light therapy in the treatment of seasonal affective disorder: a meta-analysis of randomized controlled trials. *Psychother Psychosom*. 2020;89(1):17-24.
doi: 10.1159/000502891

121. Hashmi JT, Huang YY, Osmani BZ, Sharma SK, Naeser MA, Hamblin MR. Role of low-level laser therapy in neurorehabilitation. *PM & R*. 2010;2(12 Suppl 2):S292-S305.
doi: 10.1016/j.pmrj.2010.10.013

122. Zhu W, George JK, Sorger VJ, Grace Zhang L. 3D printing scaffold coupled with low level light therapy for neural tissue regeneration. *Biofabrication*. 2017;9(2):025002.
doi: 10.1088/1758-5090/aa6999

123. Sordini L, Garrudo FFF, Rodrigues CAV, et al. Effect of electrical stimulation conditions on neural stem cells differentiation on cross-linked PEDOT:PSS films. *Front Bioeng Biotechnol*. 2021;9:591838.
doi: 10.3389/fbioe.2021.591838

124. Fu C, Pan S, Ma Y, Kong W, Qi Z, Yang X. Effect of electrical stimulation combined with graphene-oxide-based membranes on neural stem cell proliferation and differentiation. *Artif Cells Nanomed Biotechnol*. 2019;47(1):1867-1876.
doi: 10.1080/21691401.2019.1613422

125. Yang K, Yu SJ, Lee JS, et al. Electroconductive nanoscale topography for enhanced neuronal differentiation and electrophysiological maturation of human neural stem cells. *Nanoscale*. 2017;9(47):18737-18752.
doi: 10.1039/c7nr05446g

126. Heo DN, Acquah N, Kim J, Lee SJ, Castro NJ, Zhang LG. Directly induced neural differentiation of human adipose-derived stem cells using three-dimensional culture system of conductive microwell with electrical stimulation. *Tissue Eng Part A*. 2018;24(7-8):537-545.
doi: 10.1089/ten.TEA.2017.0150

127. Rahmani A, Nadri S, Kazemi HS, Mortazavi Y, Sojoodi M. Conductive electrospun scaffolds with electrical stimulation for neural differentiation of conjunctiva mesenchymal stem cells. *Artif Organs*. 2019;43(8):780-790.
doi: 10.1111/aor.13425

128. Heo DN, Lee SJ, Timsina R, Qiu X, Castro NJ, Zhang LG. Development of 3D printable conductive hydrogel with crystallized PEDOT:PSS for neural tissue engineering. *Mater Sci Eng C Mater Biol Appl*. 2019;99:582-590. doi: 10.1016/j.msec.2019.02.008

129. Song S, Li Y, Huang J, Cheng S, Zhang Z. Inhibited astrocytic differentiation in neural stem cell-laden 3D bioprinted conductive composite hydrogel scaffolds for repair of spinal cord injury. *Biomater Adv*. 2023;148:213385. doi: 10.1016/j.bioadv.2023.213385

130. Vijayavenkataraman S, Zhang S, Thaharah S, Sriram G, Lu WF, Fuh JYH. Electrohydrodynamic jet 3D printed nerve guide conduits (NGCs) for peripheral nerve injury repair. *Polymers*. 2018;10(7). doi: 10.3390/polym10070753

131. Vijayavenkataraman S, Kannan S, Cao T, Fuh JYH, Sriram G, Lu WF. 3D-printed PCL/PPy conductive scaffolds as three-dimensional porous nerve guide conduits (NGCs) for peripheral nerve injury repair. *Front Bioeng Biotechnol*. 2019;7:266. doi: 10.3389/fbioe.2019.00266

132. Vijayavenkataraman S, Thaharah S, Zhang S, Lu WF, Fuh JYH. 3D-printed PCL/rGO conductive scaffolds for peripheral nerve injury repair. *Artif Organs*. 2019;43(5):515-523. doi: 10.1111/aor.13360

133. Vijayavenkataraman S, Thaharah S, Zhang S, Lu WF, Fuh JYH. Electrohydrodynamic jet 3D-printed PCL/PAA conductive scaffolds with tunable biodegradability as nerve guide conduits (NGCs) for peripheral nerve injury repair. *Mater Des*. 2019;162:171-184. doi: 10.1016/j.matdes.2018.11.044

134. Qian Y, Zhao X, Han Q, Chen W, Li H, Yuan W. An integrated multi-layer 3D-fabrication of PDA/RGD coated graphene loaded PCL nanoscaffold for peripheral nerve restoration. *Nat Commun*. 2018;9(1):323. doi: 10.1038/s41467-017-02598-7

135. Zhu W, Tringale KR, Woller SA, et al. Rapid continuous 3D printing of customizable peripheral nerve guidance conduits. *Mater Today*. 2018;21(9):951-959. doi: 10.1016/j.mattod.2018.04.001

136. Liu K, Yan L, Li R, et al. 3D printed personalized nerve guide conduits for precision repair of peripheral nerve defects. *Adv Sci*. 2022;9(12):e2103875. doi: 10.1002/advs.202103875

137. Song S, Zhou J, Wan J, et al. Three-dimensional printing of microfiber- reinforced hydrogel loaded with oxymatrine for treating spinal cord injury. *Int J Bioprint*. 2023;9(3):692. doi: 10.18063/ijb.692

138. Jin DK, Shido K, Kopp HG, et al. Cytokine-mediated deployment of SDF-1 induces revascularization through recruitment of CXCR4+ hemangiocytes. *Nat Med*. 2006;12(5):557-567. doi: 10.1038/nm1400

139. Cheng X, Wang H, Zhang X, et al. The role of SDF-1/CXCR4/CXCR7 in neuronal regeneration after cerebral ischemia. *Front Neurosci*. 2017;11:590. doi: 10.3389/fnins.2017.00590

140. Li C, Kuss M, Kong Y, et al. 3D printed hydrogels with aligned microchannels to guide neural stem cell migration. *ACS Biomater Sci Eng*. 2021;7(2):690-700. doi: 10.1021/acsbiomaterials.0c01619

141. Kim TH, Yoon SJ, Lee SM. Genipin attenuates sepsis by inhibiting Toll-like receptor signaling. *Mol Med*. 2012;18(1):455-465. doi: 10.2119/molmed.2011.00308

142. Da Silva K, Kumar P, van Vuuren SF, Pillay V, Choonara YE. Three-dimensional printability of an ECM-based gelatin methacryloyl (GelMA) biomaterial for potential neuroregeneration. *ACS Omega*. 2021;6(33):21368-21383. doi: 10.1021/acsomega.1c01903

143. Chang HM, Liu CH, Hsu WM, et al. Proliferative effects of melatonin on Schwann cells: implication for nerve regeneration following peripheral nerve injury. *J Pineal Res*. 2014;56(3):322-332. doi: 10.1111/jpi.12125

144. Qian Y, Han Q, Zhao X, et al. 3D melatonin nerve scaffold reduces oxidative stress and inflammation and increases autophagy in peripheral nerve regeneration. *J Pineal Res*. 2018;65(4):e12516. doi: 10.1111/jpi.12516

145. Xu X, Tao J, Wang S, et al. 3D printing of nerve conduits with nanoparticle-encapsulated RGFP966. *Appl Mater Today*. 2019;16:247-256. doi: 10.1016/j.apmt.2019.05.014

146. Zhang J, Chen Y, Huang Y, et al. A 3D-printed self-adhesive bandage with drug release for peripheral nerve repair. *Adv Sci*. 2020;7(23):2002601. doi: 10.1002/advs.202002601

147. Holtzman DM, Sheldon RA, Jaffe W, Cheng Y, Ferriero DM. Nerve growth factor protects the neonatal brain against hypoxic-ischemic injury. *Ann Neurol*. 1996;39(1):114-122. doi: 10.1002/ana.410390117

148. Keefe KM, Sheikh IS, Smith GM. Targeting neurotrophins to specific populations of neurons: NGF, BDNF, and NT-3 and their relevance for treatment of spinal cord injury. *Int J Mol Sci*. 2017;18(3). doi: 10.3390/ijms18030548

149. Liu XY, Chen C, Xu HH, et al. Integrated printed BDNF/collagen/chitosan scaffolds with low temperature extrusion 3D printer accelerated neural regeneration after spinal cord injury. *Regen Biomater*. 2021;8(6):rbab047. doi: 10.1093/rb/rbab047

150. Lee YB, Polio S, Lee W, et al. Bio-printing of collagen and VEGF-releasing fibrin gel scaffolds for neural stem cell culture. *Exp Neurol*. 2010;223(2):645-652. doi: 10.1016/j.expneurol.2010.02.014

151. Tao J, Liu H, Wu W, et al. 3D-printed nerve conduits with live platelets for effective peripheral nerve repair. *Adv Funct Mater*. 2020;30(42):2004272. doi: 10.1002/adfm.202004272

152. Kalluri R, LeBleu VS. The biology, function, and biomedical applications of exosomes. *Science*. 2020;367(6478). doi: 10.1126/science.aau6977

153. Wen SW, Lima LG, Lobb RJ, et al. Breast cancer-derived exosomes reflect the cell-of-origin phenotype. *Proteomics*. 2019;19(8):e1800180. doi: 10.1002/pmic.201800180

154. Liu XY, Feng YH, Feng QB, et al. Low-temperature 3D-printed collagen/chitosan scaffolds loaded with exosomes derived from neural stem cells pretreated with insulin growth factor-1 enhance neural regeneration after traumatic brain injury. *Neural Regen Res*. 2023;18(9):1990-1998. doi: 10.4103/1673-5374.366497

155. Liu X, Wang J, Wang P, et al. Hypoxia-pretreated mesenchymal stem cell-derived exosomes-loaded low-temperature extrusion 3D-printed implants for neural regeneration after traumatic brain injury in canines. *Front Bioeng Biotechnol*. 2022;10:1025138. doi: 10.3389/fbioe.2022.1025138

156. Shinozaki M, Nagoshi N, Nakamura M, Okano H. Mechanisms of stem cell therapy in spinal cord injuries. *Cells*. 2021;10(10). doi: 10.3390/cells10102676

157. Yousefifard M, Nasseri Maleki S, Askarian-Amiri S, et al. A combination of mesenchymal stem cells and scaffolds promotes motor functional recovery in spinal cord injury: a systematic review and meta-analysis. *J Neurosurg Spine*. 2019;32(2):269-284. doi: 10.3171/2019.8.Spine19201

158. Fan L, Liu C, Chen X, et al. Directing induced pluripotent stem cell derived neural stem cell fate with a three-dimensional biomimetic hydrogel for spinal cord injury repair. *ACS Appl Mater Interfaces*. 2018;10(21):17742-17755. doi: 10.1021/acsami.8b05293

159. Pereira IM, Marote A, Salgado AJ, Silva NA. Filling the gap: neural stem cells as a promising therapy for spinal cord injury. *Pharmaceuticals*. 2019;12(2). doi: 10.3390/ph12020065

160. Younsi A, Zheng G, Riemann L, et al. Long-term effects of neural precursor cell transplantation on secondary injury processes and functional recovery after severe cervical contusion-compression spinal cord injury. *Int J Mol Sci*. 2021;22(23). doi: 10.3390/ijms222313106

161. Giraldo E, Nebot VJ, Đorđević S, et al. A rationally designed self-immolative linker enhances the synergism between a polymer-rock inhibitor conjugate and neural progenitor cells in the treatment of spinal cord injury. *Biomaterials*. 2021;276:121052. doi: 10.1016/j.biomaterials.2021.121052

162. Mothe AJ, Tam RY, Zahir T, Tator CH, Shoichet MS. Repair of the injured spinal cord by transplantation of neural stem cells in a hyaluronan-based hydrogel. *Biomaterials*. 2013;34(15):3775-3783. doi: 10.1016/j.biomaterials.2013.02.002

163. Koffler J, Zhu W, Qu X, et al. Biomimetic 3D-printed scaffolds for spinal cord injury repair. *Nat Med*. 2019;25(2):263-269. doi: 10.1038/s41591-018-0296-z

164. Liu X, Hao M, Chen Z, et al. 3D bioprinted neural tissue constructs for spinal cord injury repair. *Biomaterials*. 2021;272:120771. doi: 10.1016/j.biomaterials.2021.120771

165. Yang J, Yang K, Man W, et al. 3D bio-printed living nerve-like fibers refine the ecological niche for long-distance spinal cord injury regeneration. *Bioact Mater*. 2023;25:160-175. doi: 10.1016/j.bioactmat.2023.01.023

166. Li Y, Lv S, Yuan H, et al. Peripheral nerve regeneration with 3D printed bionic scaffolds loading neural crest stem cell derived schwann cell progenitors. *Adv Funct Mater*. 2021;31(16):2010215. doi: 10.1002/adfm.202010215

167. Cho SR, Kim YR, Kang HS, et al. Functional recovery after the transplantation of neurally differentiated mesenchymal stem cells derived from bone marrow in a rat model of spinal cord injury. *Cell Transplant*. 2009;18(12): 1359-1368. doi: 10.3727/096368909x475329

168. Luo H, Xu C, Liu Z, et al. Neural differentiation of bone marrow mesenchymal stem cells with human brain-derived neurotrophic factor gene-modified in functionalized self-assembling peptide hydrogel in vitro. *J Cell Biochem*. 2019;120(3):2828-2835. doi: 10.1002/jcb.26408

169. GBD 2016 Traumatic Brain Injury and Spinal Cord Injury Collaborators. Global, regional, and national burden of traumatic brain injury and spinal cord injury, 1990-2016: a systematic analysis for the Global Burden of Disease Study 2016. *Lancet Neurol*. 2019;18(1):56-87. doi: 10.1016/s1474-4422(18)30415-0

170. Ocansey DKW, Pei B, Yan Y, et al. Improved therapeutics of modified mesenchymal stem cells: an update. *J Transl Med*. 2020;18(1):42. doi: 10.1186/s12967-020-02234-x

171. Chen C, Xu HH, Liu XY, et al. 3D printed collagen/silk fibroin scaffolds carrying the secretome of human umbilical mesenchymal stem cells ameliorated neurological

dysfunction after spinal cord injury in rats. *Regen Biomater*. 2022;9:rbac014.
doi: 10.1093/rb/rbac014

172. Qian Y, Gong J, Lu K, et al. DLP printed hDPSC-loaded GelMA microsphere regenerates dental pulp and repairs spinal cord. *Biomaterials*. 2023;299:122137.
doi: 10.1016/j.biomaterials.2023.122137

173. Qiu C, Sun Y, Li J, et al. Therapeutic effect of biomimetic scaffold loaded with human amniotic epithelial cell-derived neural-like cells for spinal cord injury. *Bioengineering*. 2022;9(10).
doi: 10.3390/bioengineering9100535

174. Hu Y, Wu Y, Gou Z, et al. 3D-engineering of cellularized conduits for peripheral nerve regeneration. *Sci Rep*. 2016;6:32184.
doi: 10.1038/srep32184

175. Li Y, Shen PP, Wang B. Induced pluripotent stem cell technology for spinal cord injury: a promising alternative therapy. *Neural Regen Res*. 2021;16(8):1500-1509.
doi: 10.4103/1673-5374.303013

176. Moradi S, Mahdizadeh H, Šarić T, et al. Research and therapy with induced pluripotent stem cells (iPSCs): social, legal, and ethical considerations. *Stem Cell Res Ther*. 2019;10(1):341.
doi: 10.1186/s13287-019-1455-y

177. Gaudet AD, Fonken LK. Glial cells shape pathology and repair after spinal cord injury. *Neurotherapeutics*. 2018;15(3):554-577.
doi: 10.1007/s13311-018-0630-7

178. Sun F, Shi T, Zhou T, et al. 3D poly(lactic-co-glycolic acid) scaffolds for treating spinal cord injury. *J Biomed Nanotechnol*. 2017;13(3):290-302.
doi: 10.1166/jbn.2017.2348

179. Wu Z, Li Q, Xie S, Shan X, Cai Z. In vitro and in vivo biocompatibility evaluation of a 3D bioprinted gelatin-sodium alginate/rat Schwann-cell scaffold. *Mater Sci Eng C*. 2020;109:110530.
doi: 10.1016/j.msec.2019.110530

180. Silva NA, Salgado AJ, Sousa RA, et al. Development and characterization of a novel hybrid tissue engineering-based scaffold for spinal cord injury repair. *Tissue Eng Part A*. 2010;16(1):45-54.
doi: 10.1089/ten.TEA.2008.0559

181. Liu S, Yang H, Chen D, et al. Three-dimensional bioprinting sodium alginate/gelatin scaffold combined with neural stem cells and oligodendrocytes markedly promoting nerve regeneration after spinal cord injury. *Regen Biomater*. 2022;9:rbac038.
doi: 10.1093/rb/rbac038

182. Wang J, Kong X, Li Q, et al. The spatial arrangement of cells in a 3D-printed biomimetic spinal cord promotes directional differentiation and repairs the motor function after spinal cord injury. *Biofabrication*. 2021;13(4).
doi: 10.1088/1758-5090/ac0c5f

183. Qian Y, Song J, Zheng W, et al. 3D manufacture of gold nanocomposite channels facilitates neural differentiation and regeneration. *Adv Funct Mater*. 2018;28(14):1707077.
doi: 10.1002/adfm.201707077

184. Liu X, Song S, Chen Z, et al. Release of O-GlcNAc transferase inhibitor promotes neuronal differentiation of neural stem cells in 3D bioprinted supramolecular hydrogel scaffold for spinal cord injury repair. *Acta Biomater*. 2022;151:148-162.
doi: 10.1016/j.actbio.2022.08.031

ACCSCIENCE PUBLISHING

International Journal of Bioprinting

REVIEW ARTICLE

Vascularization strategies for human skin tissue engineering via 3D bioprinting

Arvind Kumar Shukla[1], Dongjun Lee[2], Sik Yoon[3,4], Minjun Ahn[5]*, and Byoung Soo Kim[1,5]*

[1]School of Biomedical Convergence Engineering, Pusan National University, Yangsan, Republic of Korea

[2]Department of Convergence Medicine, Pusan National University College of Medicine, Yangsan, Republic of Korea

[3]Department of Anatomy and Convergence Medical Sciences, Pusan National University College of Medicine, Yangsan, Republic of Korea

[4]Immune Reconstitution Research Center of Medical Research Institute, Pusan National University College of Medicine, Yangsan, Republic of Korea

[5]Medical Research Institute, Pusan National University, Yangsan, Republic of Korea

(This article belongs to the *Special Issue: 3D Printing for Tissue Engineering and Regenerative Medicine*)

Abstract

The skin is composed of many cells that are organized into different layers and connected by dense and complex vascular networks. This creates a dynamic microenvironment in which cells interact within the matrix. Significant advancements have been made in this field over the past decade, and various strategies have been developed for accelerating and enhancing skin regeneration. The primary challenge for successful skin grafts is the integration of the functional vasculature, which can supply essential nutrients and oxygen to cell-laden structures and damaged native tissues. An inadequate vascular network can lead to ischemia, which can cause slow wound healing—particularly in the case of chronic skin conditions. Therefore, blood vessel formation remains one of the most significant obstacles that skin tissue engineering must overcome to create vascularized skin tissue substitutes with specific living cells. Technological advances can augment effective vascularization. The three-dimensional (3D) bioprinting platform is a promising technology that allows precise deposition of living cells and bioactive materials. The application of this technology to skin tissue engineering can provide solutions for augmenting pre-vascularization in engineered *in vitro* skin models and *in vivo* skin substitutes. This review presents the significance of skin vascularization in *in vitro* modeling and *in vivo* wound healing. Various strategies and related applications involving 3D bioprinting technology are introduced for the biofabrication of enhanced vascularized skin *in vitro* and *in vivo*, followed by a discussion of their limitations and future research directions.

Keywords: Vascularization; Angiogenesis; Human skin; Biofabrication; 3D bioprinting; Regenerative medicine

***Corresponding authors:**
Minjun Ahn (mjahn@pusan.ac.kr)

Byoung Soo Kim (bskim7@pusan.ac.kr)

Citation: Shukla AK, Lee D, Yoon S, Ahn M, Kim BS. Vascularization strategies for human skin tissue engineering via 3D bioprinting. *Int J Bioprint*. 2024;10(3):1727. doi: 10.36922/ijb.1727

Received: August 31, 2023
Accepted: November 20, 2023
Published Online: January 28, 2024

Copyright: © 2024 Author(s). This is an Open Access article distributed under the terms of the Creative Commons Attribution License, permitting distribution, and reproduction in any medium, provided the original work is properly cited.

Publisher's Note: AccScience Publishing remains neutral with regard to jurisdictional claims in published maps and institutional affiliations.

1. Introduction

The skin accounts for 15% of an individual's total body weight and covers an area of 1.8 m^2. It is the largest organ in the body and has several essential functions.[1,2]

The skin consists of epidermis and dermis. The epidermis—the outermost layer of the skin—functions as a barrier that protects the skin from external chemical, physical, and biological risks. The dermis—the second layer—is a complex structure with many components that are crucial for proper skin function. It contains a network of blood vessels responsible for supplying oxygen and nutrients to the cells that constitute the skin tissue.[3,4]

Damage to dermal layer containing vascular networks impairs efficient wound-healing process, which involves a sequence of cellular functions such as hemostasis, inflammation, proliferation, maturation, and remodeling.[1,5] Vascular regeneration process, which facilitates the reconstruction of vascular networks in the wounded skin, can be slightly accelerated using wound dressings.[6] However, traditional dressings such as gauze and tulle are not suitable for patients who need continuous treatment and have significant exuding wounds.[7,8] Despite the development of advanced polymeric dressing devices utilizing materials such as poly (vinyl alcohol), chitosan, polyurethane, poly(ε-caprolactone) (PCL), and alginate, these devices have inherent limitations when it comes to promoting essential vascularization for effective wound skin treatment. This is because they primarily address moisture retention and the prevention of secondary infections.

Tissue engineering, which employs biomaterials, bioactive compounds, and cells, has recently emerged as a promising approach to tackle these challenges.[9] The supply of nutrients to engineered tissue is limited to a distance up to 200 μm, accomplished through diffusion from the surface in contact with the culture media.[10,11] Consequently, most tissue engineering scaffolds have been designed with high porosity to facilitate tissue reconstruction by allowing the infiltration of blood vessels from the host tissue. Nevertheless, this approach inherently results in sluggish vascularization.[12] Typically, vascularization processes at an average rate of about 5 μm/h, implying that it takes several months to achieve complete vascularization for larger wounds that span several millimeters in length.[13] Moreover, delayed vascularization can have adverse effects on cell viability and lead to uneven nutrient distribution within the scaffold, ultimately hindering cell growth and function.[14]

Hence, the establishment of vascularization from within the engineered construct itself is critically essential to ensure its survival, functionality, and integration. From this perspective, three-dimensional (3D) bioprinting has emerged as a promising solution to address this challenge. It accomplishes this by precisely depositing bioinks containing bioactive molecules and endothelial cells (ECs) into predetermined patterns, thereby enabling the creation of intricate vascular structures within the engineered tissue. Additionally, bioactive molecules like vascular endothelial growth factor (VEGF) can be incorporated into the construct at specific locations using 3D bioprinting. These growth factors play a pivotal role in stimulating ECs to form functional vascular network. In summary, the 3D bioprinting technique allows for the development of functional vascular networks through precise control over the distribution of relevant cells and growth factors. These advancements would not only enhance the functionality and integration of transplanted tissues and organs but also unlock the potential of regenerative medicine.

The purpose of this review is to introduce various aspects of vascularization strategies and important components of wound healing used to explore the development of engineered human functional vascular skin tissues. Through continuous development, 3D bioprinting techniques have become increasingly efficient for producing vascularized skin. Additionally, we discuss the advantages of different 3D bioprinting techniques and ideal candidates for bioinks used in vascular 3D skin bioprinting. We also address future perspectives and provide solutions in this highly dynamic field of research that involves 3D-bioprinted skin tissue for the successful formation of vascularized functional skin *in vitro* and *in vivo*.

2. Human skin structure and functions

Human skin is composed of several appendages (Table 1), each of which serves a distinct biological function and possesses a unique architecture and properties that collectively provide protection for the underlying organs.[15] In general, the skin comprises three layers: the epidermis, dermis, and hypodermis (Figure 1).

The epidermis serves as a vital protective barrier,[15] protecting against stress and regulating the absorption of water and chemicals.[16] An epidermis is composed of five sublayers, including the stratum corneum, stratum spinosum, stratum granulosum, stratum lucidum, and stratum basale.[17,18] In the stratum corneum, basal-layer keratinocyte stem cells are replenished by lower-layer keratinocytes.[19,20] Found in the stratum spinosum, Langerhans cells play a role in triggering immune responses.[21] Between the epidermis and dermis, a cutaneous basement membrane region integrates the underlying keratinocytes with collagen fibers.[22] Its primary function is to act as an adhesive between the two layers. Because the epidermis lacks blood vessels, the basement membrane zone facilitates the transfer of nutrients and oxygen from the vascular and non-vascular dermis to the epidermis.[23] The dermis is essential for providing structural support and cushioning for the body. It consists of connective tissue, including vascular structures, lymphatic vessels,

Table 1. Locations and functions of structural components of different skin layers

	Cellular/ECM components	Location	Function
Epidermis	Keratinocyte	Entire layers	As component of skin boundary, synthetic keratin
	Melanocyte	Stratum germinativum	For synthesis of melanosomes
	Merkel cell	Stratum germinativum	As sensor
	Langerhans cell	Spinous layer/prickle cell layer/ distinctive keratinocytes	Present antigens to the immune system
	Laminin	Basement membrane	Connect epidermis and dermis
Dermis	Fibroblast	Entire dermis layer	Synthesize ECM, secrete cytokines, and promote wound healing
	Collagen fiber	Entire dermis layer	For support and protection
	Blood vessel	Dermis of papillaries	Maintain the skin's oxygen and nutrient levels
	Elastic fiber	Reticular dermis	For the elasticity of skin
	Nerve	Venules and arterioles	Enable various sensations associated with touch, pressure, temperature, and itching
	Hair follicle	Dermis reticular	Form physical barrier, inhibit scar formation, and for antibacterial effect
	Sweat gland	Dermis reticular	Maintain body temperature

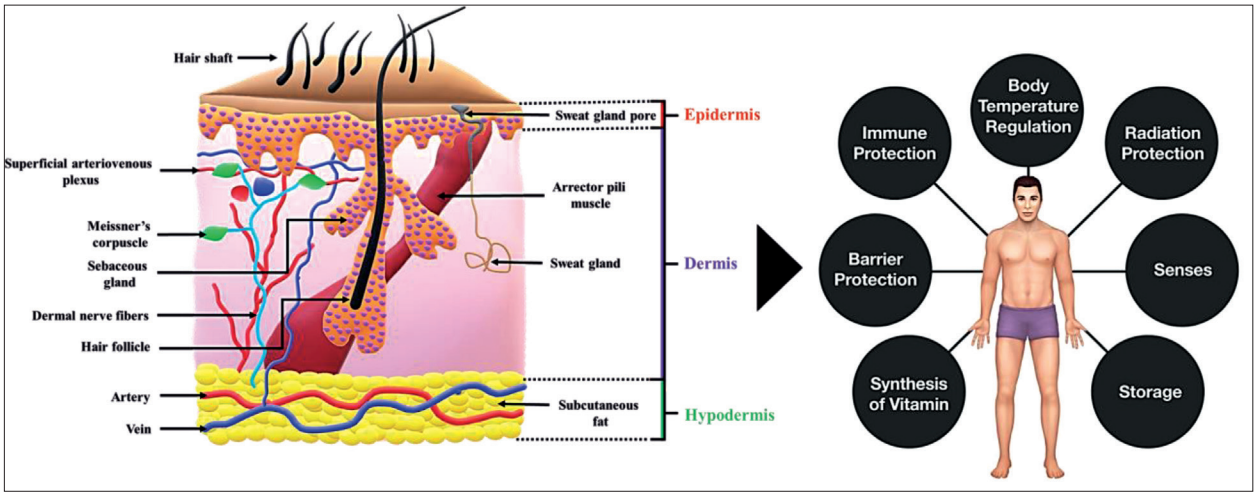


Figure 1. Schematic of the structure and function of human skin.

and mast cells organized in a network-like configuration.[23] Fibroblasts are the primary cells in connective tissue that produce collagen and elastin.[24] Elastin proteins help maintain skin elasticity and resilience, whereas collagen fibers provide tensile strength and stretchability.[25] Mast cells are responsible for the inflammatory response of the skin to pathogens, allergens, and physical damage.[26] The dermis includes an intricate vascular structure that supplies nutrients to maintain its homeostasis and function of the skin. The vascular network is mainly located at two primary dermal layers: the reticular and the papillary layers. There is a dense meshwork of blood vessels in the reticular layer, located beneath the papillary layer. Through these vessels, oxygen and essential nutrients are delivered to skin cells, while waste materials are removed from the dermis. This layer also contains collagen and elastin fibers, contributing to the skin's strength, elasticity, and structural integrity. Above the reticular layer lies the papillary layer, which features a more delicate arrangement of capillaries. These capillaries stimulate immunological responses and provide nutrition to the epidermis, the skin's upper layer. These two layers function in concert to form a highly complex vascular network whose function is essential for maintaining the health of the skin, controlling body temperature, and responding to numerous environmental stimuli. In dermatology, wound healing, and the development of skin care products and therapies all depend on an understanding of the complex dermal

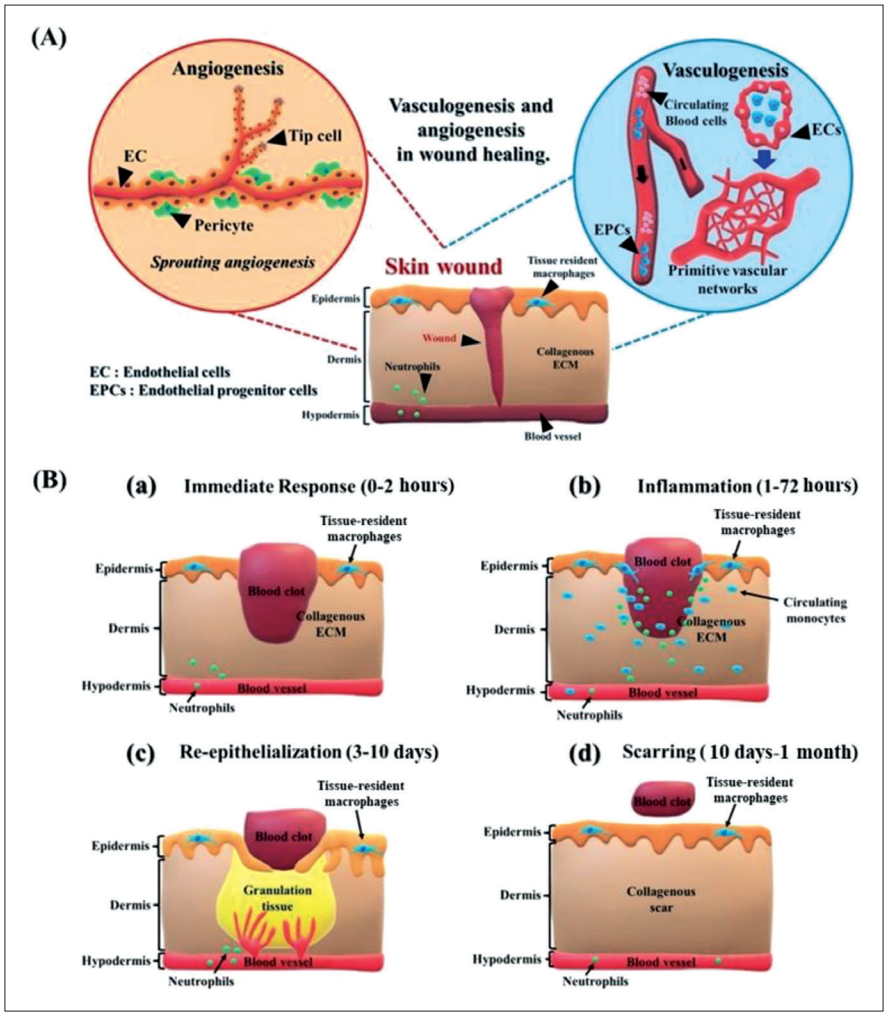


Figure 2. (A) The wound-healing process is influenced by both vasculogenesis and angiogenesis. (B) Four stages of cutaneous wound healing in mature mice: (a) immediate reactions, including blood-clot formation and neutrophil recruitment (0–2 h); (b) inflammatory responses involving the recruitment of neutrophils and monocytes from the peripheral bloodstream, as well as the activation of tissue-resident cells (1–72 h); (c) re-epithelialization, where keratinocytes proliferate and migrate to repair the wound, accompanied by the formation of fibrotic granulation tissue, collagen deposition, and angiogenic sprouting (3–10 days); and (d) contraction of the wound through myofibroblasts, wound closure, resolution of inflammatory processes, and scar remodeling (14 months).

vascular structure. The hypodermis—the innermost layer of the skin—is composed mostly of adipocytes. It serves as a connection between muscle tissue and the dermal layer. Damage to or loss of the hypodermis caused by deep wounds that extend to this layer presents a significant obstacle to the wound-healing process.[27,28]

3. Enhancing vascularization strategies in human skin tissue for effective *in vitro* skin modeling and *in vivo* wound healing

3.1. Importance of vascularization in human skin for *in vitro* modeling and *in vivo* wound healing

The clinical efficacy of tissue engineered skin transplantation depends on effective vascularization.[29] The limited blood flow can result in problems with necrosis. During skin implantation, improving vascularization is essential.[30] Vasculogenesis can be achieved by means of pre-vascularization and angiogenesis. Due to poor microvessel development (about 5 μm/h) in large skin implants, angiogenesis alone encounters challenges.[31] Before transplantation, pre-vascularization generates microvessels inside the tissue layers to ensure an increased supply of blood.[32] Table 2 presents an overview of various factors that may influence the vascularization of skin constructs.

The neovascularization in native skin (Figure 2A) involves the formation of new blood vessels by angiogenesis and vasculogenesis process.[33] These processes occur when endothelial progenitor cells (EPCs) differentiate into ECs, forming a complex vascular network where blood supply

Table 2. Factors that potentially have a significant influence on skin-construct vascularization

Vasculogenic factors	Significant results	Reference
Vascularization depends on a scaffold		
Films that replace artificial skin (**e.g.**, Integra® & Matriderm®)	Enhance neo-dermis structure with thick microvascular networks mimicking native dermal layer, triggering angiogenic tissue response, but with time-dependent clinical efficacy decrease, delayed vascularization, and increased infection risk	[143-148]
Scaffolds consisting of fibrin or/and hyaluronic acid	Do not help with the closure of the wound	[149]
Surface irradiation with plasma and argon	Increase angiogenesis; promote neovascularization	[146,150]
By using various biomolecules that promote angiogenesis		
VEGF nanocapsules that degrade by plasmin within hydrogels	Increase closure and regeneration of wounds; improve vessel maturation; reduced fibrotic activity	[149]
Combination of alginate microspheres filled with hydrogels containing basic fibroblast growth factor (bFGF) with carboxymethyl chitosan and polyvinyl alcohol, resulting in a scaffold	*In vitro*, increase bFGF bioactivity; enhance *in vivo* cell proliferation *In vivo*, increase healing of wounds; enhance dermal regeneration as well as re-epithelialization; trigger neovascularization; promote higher mature blood vessel density	[151]
By incorporating gene-activated matrices (GAMs)		
Combining VEGF plasmid DNA into the collagen–chitosan membrane scaffold	Enhance density of newly developed and mature blood vessels; increased dermis regeneration; the repaired skin showed tensile strength up to 80% of normal skin	[152,153]
Encoding of polyplexes of basic fibroblast growth factor within the plasmid (pbFGF) of transfected fibrous mats	Four weeks of continuous pbFGF release; higher rate of wound healing in diabetic rats; increase vascularization; increase collagen deposition as well as maturation; achieve complete re-epithelialization and develop appendages	[154]
VEGF gene vector-based transcription into the dermal scaffolds by copolymer encapsulation	Increase vascularization in nude mice in full-thickness skin wounds; develop fragile vessels within a scaffold	[155]
Based on biodegradable poly-N-acetyl-glucosamine nanofibers, a bioactive scaffold-like membrane	Increase healing of wounds; promote angiogenesis and blood vessel development in the newly formed tissue mediated by VEGF.	[156]
Stimulating agents for targeting angiogenic growth factor		
Bioactivated microfibers of glass with copper-doped borate	Enhance HUVEC migration and proliferation *in vitro*; facilitate long, tubular shape development; increase fibroblasts' VEGF production; promote efficient full-thickness skin wound healing with more developed wound bed vasculatures and collagen fiber deposition; (there are currently no findings on the *in vivo* duration of copper retention in the body)	[157]
Collagen–chitosan scaffold combined with poly L-lactide-co-glycolide meshed scaffolds	Enhance regeneration and closure of complete-depth mouse skin wounds through the synergy of thin split-thickness autografts, tissue regeneration, and vasculogenesis; after 8 weeks of transplantation, the repaired skin showed up to 73% of normal skin's tensile strength and enhanced microvascular network density, promoting angiogenesis	[158]
Specifically designed hydrogel scaffold consisting of dextran	Enhance angiogenic activity when used to treat full-thickness burns in mice models; hair follicles and sebaceous glands contributed to epithelial maturation or regeneration	[159]

Continued...

Table 2. ***Continued...***

Vasculogenic factors	Significant results	Reference
	By cell-mediated angiogenesis	
3D constructions integrating fetal fibroblasts with human dermal microvascular endothelial cells	Third- and second-degree burns in young children heal more rapidly without the use of autografts; excellent aesthetic and functional results were achieved	[160]
Endothelial cells (HUVECs) within hyaluronic acid-based scaffolds for artificial dermis	Increase endothelial cell organization and development of micro-capillaries	[161]
Use of collagen with and without glycosaminoglycan in the co-culture of HUVECs with fibroblasts and/or keratinocytes	Enhance *in vitro* capillary-like tube generation and increase formation of tubular structures interconnected with mesh-like capillary networks	[162-164]
Endothelial progenitor cell administration can be achieved with both local and systemic delivery	Cells were incorporated into the capillary wall at the location of the injury as well as by ischemia; contractile and vasomotor activity could be seen in the developing vessels.	[165-168]
Incorporation of endothelial cells into a dermal construct from human blood outgrowth	Achieve a more effective epithelialization of the matrix structure and effective revascularization and oxygenation of the wound bed	[169]
Micro-tissues constructed with fibrin, seeded by human microvascular endothelial cells	Higher endothelial sprouting occurs in larger vessels that spread out across a substantial distance (1–2 mm)	[170]
Conditioned medium for bone marrow-derived mesenchymal stem cells	Enhance migration and proliferation of endothelial cells in culture; local injections increased collateral perfusion and improved limb function *in vivo*	[171]
Biofabrication of scaffolds using mesenchymal stem cells derived from within the bone marrow	Improve repair or healing of wounds by cutaneous, fibrous, adipose, and especially vascular-endothelium tissues in mouse models	[172-174]
In vivo treatment of human adipose-derived mesenchymal stem cells	A higher density of microvascular tissue was seen	[175]
Human umbilical vein blood-derived mesenchymal stem cells	The engraftment of umbilical cord blood-derived mesenchymal stem cells (UCB-MSC) in a mouse model with an ischemic hind limb increased the regenerative ability of skeletal muscles, but its role in angiogenesis remains unclear	[176-178]

is needed.[34] During the wound-healing process, the new blood vessels must develop from pre-existing ones by an angiogenesis process.[35] ECs at vessel tips initiate the development of new vessels during angiogenic sprouting by degrading the interstitial proteins and basement membrane, resulting in branching.[34] While the role of angiogenesis in the healing of wounds in mature skin has been extensively studied, that of vasculogenesis remains up for debate.[33]

However, it is challenging to develop a microvasculature network in large tissue substitutes after transplantation.[36] For successful vascularization, the physiology of cells and viability after transplantation are essential for the formation of new blood vessels. Tissue substitutes with a general size of 0.1 to 10 cm experience oxygen and nutrition deficits compared to other existing vessels with a size of 100 to 200 μm. This sizable difference causes cell death along with the failure of the implant.[37-39] Considering effective vascularization both *in vitro* and *in vivo*, it is essential to comprehend three stages of human skin wound healing including immediate injury responses (clot formation), inflammation (recruitment of inflammatory cells), re-epithelialization, and scar deposition/remodeling (Figure 2B).[40]

3.2. Conventional approaches to enhance vascularization of skin for *in vivo* wound healing

Increased levels of proangiogenic factors in transplanted cells and physiological inflammation—particularly in the hypoxic environment of wounds—induce *in vivo* tissue engineering transplantation, promoting vascularization during wound healing. In the absence of a fully functional vasculature, cells seeded or encapsulated in bioink in the 3D construct develop hypoxic environments owing to insufficient nutrient supply. Blood vessel formation was observed in the surrounding host tissue growing in a 3D-bioprinted construct.[38,39] The biological process of angiogenesis occurs slowly, incorporating tens of micrometers of tissue each day. Large implants require an extended period for vascularization because of this delayed process, which can lead to the functional and structural loss of nutrient-starved cells and eventual cell death. However, in thin or avascular tissue implants, this timeframe may

be sufficient for vascularization owing to the adequate capillary proximity, which allows proper nutrition, gas exchange, and metabolite diffusion. The transplantation of large tissue constructs can be dangerous because of the risk of ischemia during implantation.[38,39,41-45] The effective growth and support of implanted tissue require a sufficient supply of nutrients and oxygen, as well as the removal of waste products through blood vessels. Cells and tissues in close proximity to capillaries or within a distance of 100–200 μm are required for long-term growth and support, as shown in Figure 3A.[38,39,41,42,44,46-53] Non-hypoxic and hypoxic groups have been developed using gelatin-based hydrogels for better understanding *in vivo* cluster-based angiogenesis mechanisms, including EPC functions. Hypoxic hydrogels allowed EPCs and endothelial colony-forming cells (ECFCs) to proliferate and stabilize, whereas non-hypoxic hydrogels prevented the formation of clusters. The GFP-ECFCs that were injected intravenously showed significant function. The *in vivo* oxygen levels were regulated by incorporating calcium hydroxide along with calcium

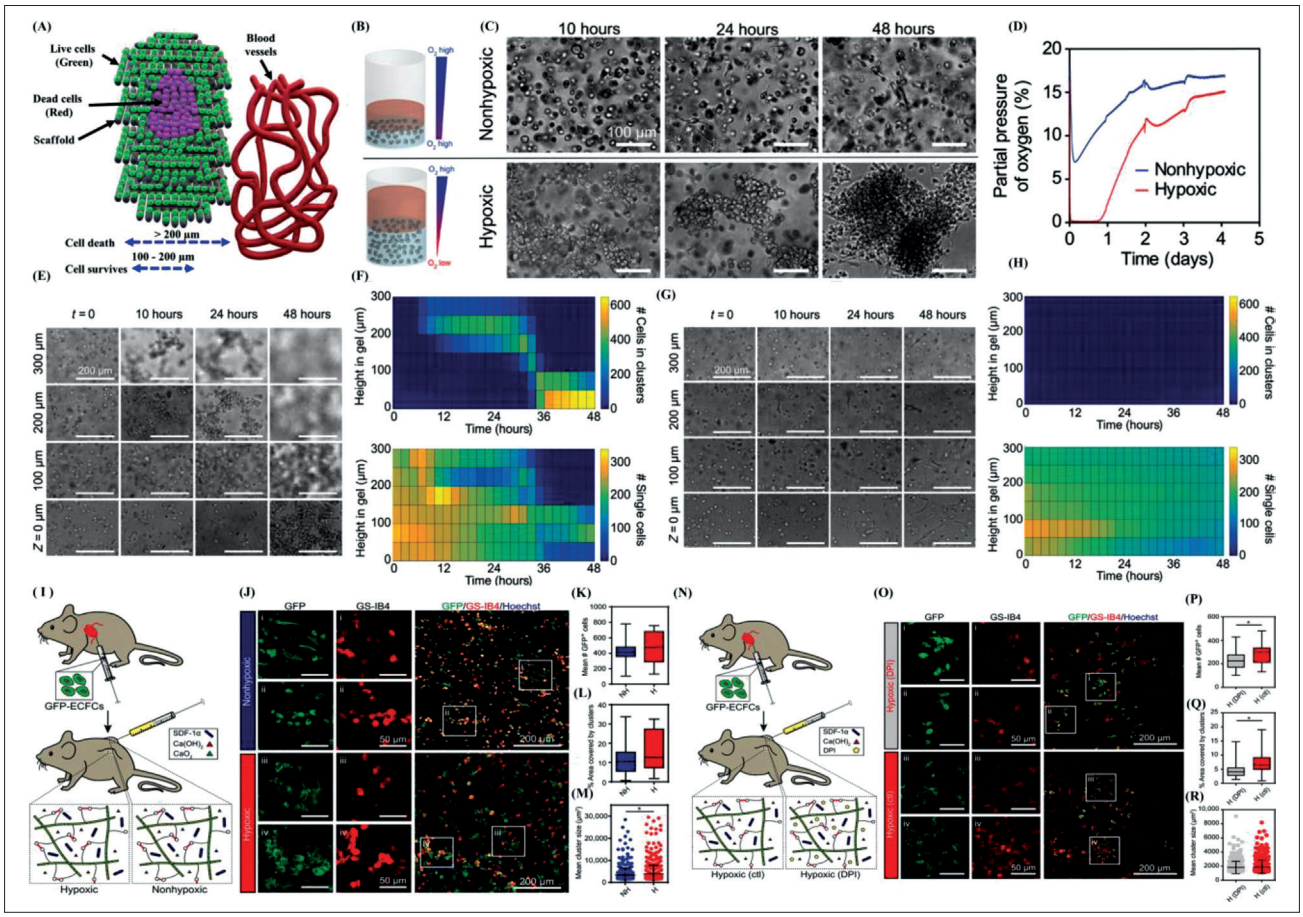


Figure 3. (A) Demonstration of cell viability at varying distances from a microvascular network in a thick scaffold. (B) Encapsulation of hypoxic and non-hypoxic cells. (C) Morphology of cells in hypoxic and non-hypoxic hydrogels for up to 48 h, captured by using bright-field photography. The clustering morphology of hypoxic hydrogels becomes clear after 6–12 h of culturing and can continue to grow for up to 48 h. In contrast, endothelial colony-forming cells (ECFCs) embedded in non-hypoxic hydrogels expand outward and sprout without forming clusters. (D) O_2 concentration measured at the bottom of the gel during 4 d of culturing. Cluster development dynamics in hypoxic hydrogels confirmed by performing (E) time-lapse microscopy and (F) later measurement of multiple cells within clusters (top) compared with individual cells (bottom). No clustering is observed in non-hypoxic hydrogels (G and H). (I) Injection of SDF-1-laden non-hypoxic and hypoxic hydrogels into the flanks of nude mice after intracardial injection of GFP-ECFCs. (J) GFP-ECFCs exhibiting single-cell spindle (i) and spherical (ii) shapes in non-hypoxic hydrogels 12 h after injection. Additionally, host cells (GS-IB4 lectin) are observed as solitary spherical cells. In hypoxic conditions, GFP-ECFCs form clusters (iii and iv) and exhibit sprouting cells (iii). Host cells also exhibit cluster structures under hypoxic conditions (iii and iv). (K) Measurements confirming that the total number of cells is comparable between the hypoxic and non-hypoxic conditions, whereas (L) the percentage of area occupied by clusters is slightly higher in the hypoxic setting. (M) Clusters in hypoxic environments are larger than those in normoxic environments. (N) GFP-ECFCs injected into the coronary arteries of nude mice's hearts, followed by injection of SDF-1-filled hypoxic (ctl) and non-hypoxic (DPI) hydrogels into the flanks of the mice. (O) GFP-ECFCs are observed as individual cells (ii and iii) and clusters (i and iv) in both conditions for 12 h after encapsulation. (P) The untreated (control) group has more GFP^+ cells than the DPI-treated group, while (Q) the percentage of area occupied by clusters is higher for the control group than for the DPI-treated group. (R) Average cluster sizes do not differ significantly between the two groups. Figure 3B–R were reprinted from[54] (Copyright © 2019, with permission from AAAS).

peroxide into hydrogels that were both hypoxic and non-hypoxic. Hydrogels that were hypoxic showed a higher level of cell independence when compared with those that were non-hypoxic. Larger cell clusters in both hydrogels showed the recruitment of host cells. In comparison to the diphenyleneiodonium chloride (DPI)-treated groups, there was a decrease in GFP^+ cell recruitment and cluster area, but there was no significant difference in cluster size as shown in Figure 3B–R.[54]

Common in all cases, a hypoxic microenvironment is an essential component wherein ECs interact to form networks of neovessels. By creating a regulated microenvironment to investigate clustered vasculogenesis, we observed the formation of clusters both *in vitro* and *in vivo* within an equivalent timeframe, which allowed us to confirm the significance of tightly controlling this mechanism. The formation of a vascular network is crucial in implanted tissues. Therefore, new functional vascular networks must be identified after transplantation. If the structure already contains blood vessels, increased perfusion and improved connectivity *in vivo* allow them to function more efficiently after implantation, thereby reducing hypoxia and cellular necrosis.[42,47-51,55]

3.3. Conventional pre-vascularization techniques for *in vitro* skin tissue modeling

In vitro vascularization involves multiple synergistic cooperative components among cells, multiple active factors, and different types of proteins.[56] Currently, the development of vascularized skin is improved by pre-vascularization and angiogenesis techniques.[29] Angiogenesis, which uses skin grafts to enhance the healing process, aids in the growth and maturation of host vasculature before implantation. However, this method results in blood vessel formation at an average speed of only 5 μm/h.[13] Delayed vascularization in the early stages of wound healing can negatively affect the healing process, leading to apoptosis, tissue necrosis, and compromised nutrient, oxygen, and waste supply at the injury site. In comparison, pre-vascularization methods are more suitable for developing vascular networks in *in vitro* skin models. Pre-vascularized skin grafts accelerate the wound-healing process by providing rapid connections with the host's vascular networks. Moreover, pre-vascularized skin models exhibit higher success rates in *in vitro* testing.[57]

In vitro, pre-vascularization methods play a crucial role in promoting vascularization in the skin and are key components of cell-based techniques for tissue engineering. They involve growing ECs on biomaterials, often in combination with different cell types, to promote proliferation. After *in vitro* vascularization, the tissue constructs undergo *in vivo* transplantation to create a favorable microenvironment for rapid incorporation and further vascularization.[58-62] Miyazaki et al.[63] developed 3D skin substitutes with vascular networks that did not require scaffolding. Dermal fibroblasts, vascular ECs, and epidermal keratinocytes were among these cells utilized to develop vascularized skin substitutes. In approximately 15 days, pre-vascularized 3D skin substitutes developed the desired morphology, and GFP-expressing human umbilical vein endothelial cells (HUVECs) showed a significantly high level of viability as well as an effective vasculature with a minimal amount of non-viable cells. Vascular network density and branching, vessel formation, and vascular area were all influenced by the optimum cell density ratio of HUVECs to FN-G-coated normal human dermal fibroblasts (NHDFs). The incorporation of keratinocytes produced fully vascularized 3D skin substitutes with a homogeneous dermis, a well-stratified epidermis, and a dermal lumenized vasculature (Figure 4A-a–d).[63]

Although ECs are the primary cell type responsible for angiogenesis, their survival in monocultures *in vitro* is insufficient for tissue engineering applications because of the irregular vascular structures formed in monocultures.[49,59,64] Monocultures cause ECs to lose their self-assembling ability, rendering them unable to form a lasting, functional cell-based vasculature.[39,49,61,65,66] For example, Ren et al.[67] reported high vascular networks on human mesenchymal stem cell (hMSC) sheets but no HUVEC vascular networks on culture plates. Using CD31 staining, HUVEC growth within hMSC sheets has been demonstrated to be network-like, with networks growing out of the inner layer. The O.C.T. mixture incorporating HUVEC/hMSC sheets showed capillary lumen formation along with network expansion. Using confocal microscopy, the study verified the presence of numerous vascular networks in cell sheet layers and HUVEC networks inside hMSC sheets. The image showed lumen development and upward network movement in 3D cell sheets *in vitro* (Figure 4B-a–f).[67] Currently, vascularized skin models are used to screen drugs and investigate disease conditions. 3D-bioprinted vascularized full-thickness skin was used as a substitute.[68] According to these models, the bioprinting approach is suitable for developing skin substitutes for various disease models, further demonstrating the construction of atopic dermatitis-like tissues.

3.4. Limitations of conventional approaches for *in vivo* wound healing and *in vitro* skin modeling

The limitations of conventional vascularization strategies for *in vitro* and *in vivo* skin applications pose significant challenges. These strategies often do not provide adequate functional vascular networks to support engineered skin tissue growth and survival. Monocultures of ECs

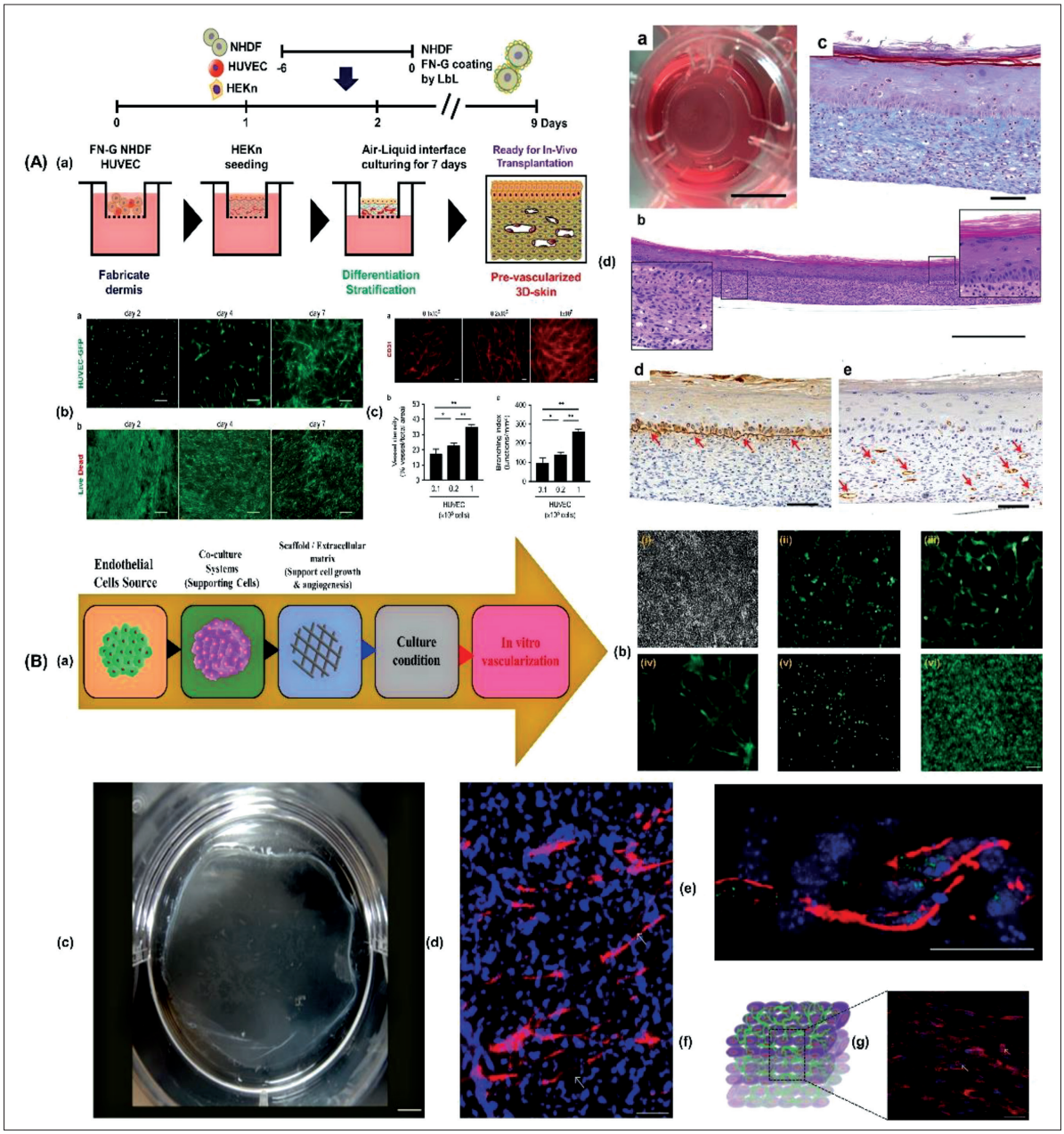


Figure 4. (A) Biofabrication of pre-vascularized scaffold-free 3D skin tissue. (a) Main method for producing vascular skin as a substitute *in vitro*; HEKn: neonatal human epidermal keratinocytes. (b) *In vitro* vascular network development in dermo-epidermal 3D skin replacements. HUVEC-expressing cells were co-cultured with normal human dermal fibroblasts (NHDF) and grown for up to 7 days before being covered with HEKn cells. (c) The 3D skin replacements developed an interconnected vascular network in 7 days because of epidermal differentiation. FN-G-coated NHDF was supported, while HUVECs were seeded at 0.1–1 × 10^5 cells per culture. Co-culturing of 1000:1, 500:1, or 100:1 FN-G-coated NHDFs with HUVECs was performed, followed by the addition of HEKn. (d) *In vitro* evaluation of 3D skin replacements with pre-vascularization was performed using HUVECs mixed with FN-G-coated NHDF and HEKn, which were maintained for up to 7 days. Figure 4A was reprinted from[63] (Copyright © 2019, with permission from Springer Nature). (B) (a) Schematic of 3D pre-vascularized skin replacement construction in the *in vitro* condition, showing the process and the morphology of human mesenchymal stem cells (hMSCs) after 14 days. (b) (i) Confluence was achieved, resulting in a thick cell layer. Fluorescent images ((ii)–(vi)) indicated the development of HUVEC networks on an hMSCs sheet after HUVECs were sown there for 2 h (ii), 1 day (iii), and 7 days (iv). The shape and size of HUVECs grown on tissue culture plates after 2 h (v) and 7 days (vi) are shown in fluorescent images. On the tissue culture plates, HUVECs proliferated but were not arranged into networks (scale bar: 100 μm). (c) A cell sheet in its entirety (scale bar: 3.4 mm). Following 7 days of growth, confocal microscopy images showed the development of HUVEC lumens on human mesenchymal stem cell (hMSC) sheets. Lumens developed on the hMSCs sheet (d) (scale bar: 100 μm) and moved within the surface of the sheet (e) (cross-sectional view; scale bar: 50 μm), as revealed by CD31 immunofluorescent staining images.[67] When a single cell sheet was folded into a 3D pre-vascularized construct, it was cryosectioned (f), and CD31 staining revealed that the structure had developed networks and lumens (g) (white arrows; scale bar: 100 μm). Figure 4B-b–g were reprinted from[67] (Copyright © 2014, with permission from Hindawi).

have exhibited a limited ability to self-assemble into proper vascular structures *in vitro*. The irregularity of these structures hinders the function of the vasculature, compromising the supply of nutrients and oxygen to the tissue.[57] The lack of sustained and stable vascularization in EC monocultures poses a barrier to successful tissue engineering outcomes.[57] Conventional *in vivo* angiogenesis techniques are limited in speed and efficiency. Blood vessels are formed slowly, at a rate of approximately 5 μm/h.[57] Delayed vascularization can slow wound healing, leading to apoptosis, tissue necrosis, and insufficient absorption of nutrients in the wound. Besides, sluggish angiogenesis makes it challenging to vascularize large tissue constructs effectively.[57] Furthermore, the pre-existing vasculature has a theoretical diffusion capacity of approximately 100–200 μm, which may result in inadequate nutrient and oxygen supply to the central regions of thick or avascular tissue implants.[57] Lack of vascularization can lead to tissue necrosis, compromised functionality, and failure of the implant.

To overcome these limitations, researchers have explored alternative approaches such as *in vitro* pre-vascularization techniques. These methods involve the cultivation of ECs on biomaterials—often in combination with other cell types—to promote vascular network formation.[57] Pre-vascularized skin constructs accelerate wound healing and improve *in vitro* testing outcomes.[57] Thus, conventional vascularization strategies for both *in vitro* and *in vivo* skin applications are limited by the inadequate self-assembly of ECs in monocultures, slow angiogenesis, and insufficient nutrient delivery to thicker or avascular tissue implants. Overcoming these limitations requires innovative approaches such as *in vitro* pre-vascularization techniques to achieve functional and sustained vascularization in engineered skin tissues.

4. 3D bioprinting techniques and bioinks for engineering skin tissue

4.1. Potential of 3D skin bioprinting

The precise deposition of living cells, biomaterials, and growth factors in a predefined manner is made possible by an advanced additive manufacturing technique known as bioprinting, which uses computer-aided design and employs an layer-by-layer printing process for high adaptability and reproducibility (Figure 5).[69,70] Creating intricate structures that closely resemble the extracellular matrix (ECM) using this technique has considerable potential for enhancing cell adhesion and proliferation simultaneously. The benefits of bioprinting include the ability to design graded macroscale structures that closely resemble the environment in real tissues, encouraging the attachment and growth of various cells. Additionally, the inclusion of microfeatures, such as ridges and modified

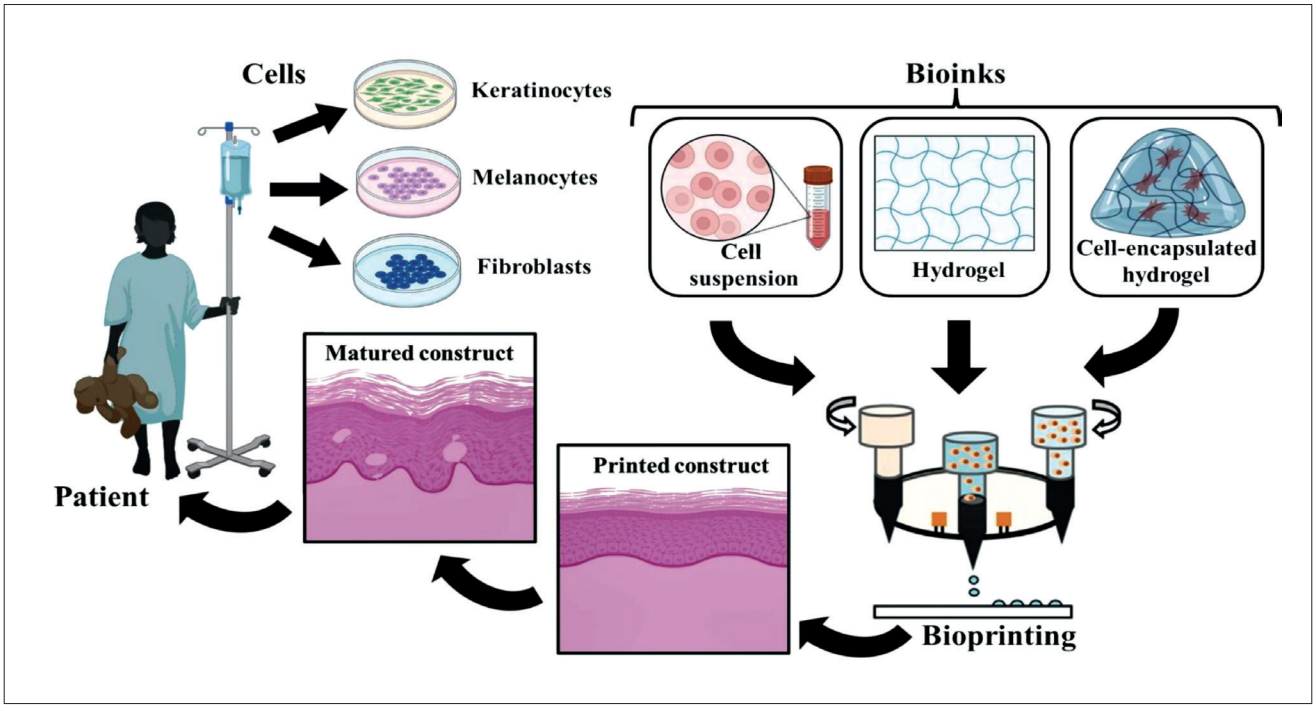


Figure 5. Schematic illustrating bioprinting technology. Skin biopsy cells from the patient are cultured *in vitro* to obtain a sufficient number of cells. Skin constructs are bioprinted with bioinks such as cell suspensions, hydrogels, or cell-encapsulated hydrogels. To obtain transplantable tissue constructs for skin transplants, the printed constructs are cultured under submerged conditions followed by an air–liquid interface (ALI).

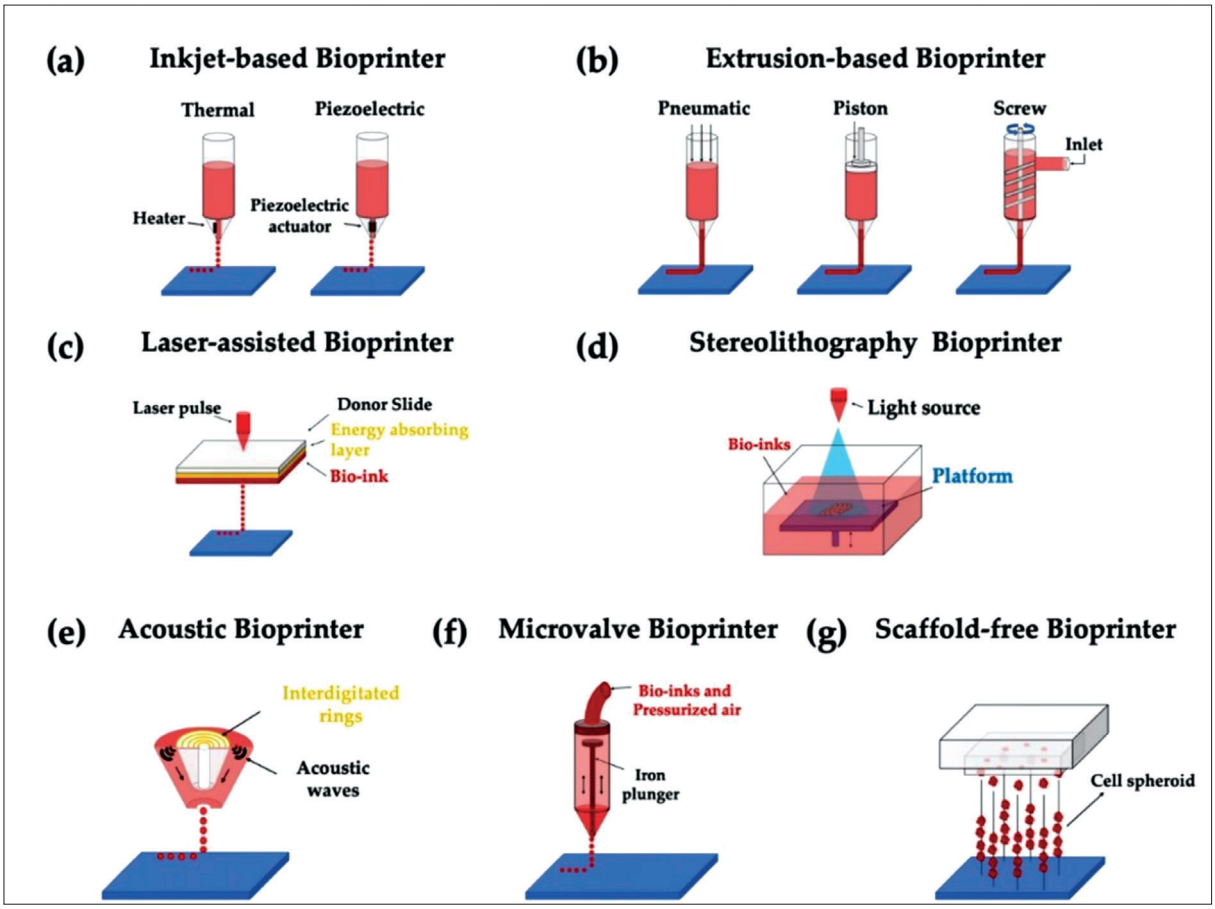


Figure 6. Different types of 3D bioprinters. (a) Inkjet- and (b) extrusion-based bioprinters. (c) Laser-assisted bioprinter. (d) Stereolithography-based bioprinter. (e) Acoustic and (f) microvalve bioprinters. (g) Scaffold-free bioprinter. Figure 6 was reprinted from[76] (Copyright © 2020, with permission from MDPI).

surfaces, is facilitated by bioprinting. The mechanical and biological signals provided by these microfeatures, which are dispensed through a variety of material substrates, guide and enhance cellular alignment and differentiation.[70,71] A pioneer in the field of bioprinting, Lee et al.[72] produced the first bioprinted skin model in 2009 using keratinocytes, fibroblasts, and type I collagen obtained from rat tails. Additional studies have shown that cells proliferated on both planar and non-planar surfaces, indicating that 3D bioprinting has promise for producing personalized skin constructions for skin graft transplantation. In 2011, Binder et al.[73] successfully showed wound healing in mice by testing a 3D inkjet-printed skin graft replacement with fibroblasts and keratinocytes in collagen and fibroin matrices. Using 3D bioprinting, Koch et al.[74] developed a bilayer skin patch that mimicked physiological skin function by promoting vascularization and tissue integration more effectively than *in vitro* constructs. These developments in vascularized skin tissue 3D bioprinting contribute to the wound healing of the skin.[30,75]

4.2. 3D bioprinting techniques for skin

As shown in Figure 6, 3D bioprinting techniques can be divided into seven categories: inkjet-based, extrusion-based, laser-assisted, stereolithography-based, acoustic-based, microvalve-based, and needle array-based.[76]

4.2.1. Inkjet-based bioprinting

In 1988, Klebe[77] published the first study on inkjet-based bioprinters. He used a hydrogel approach with a typical Hewlett-Packard thermal drop-on-demand inkjet-based printer. Subsequently, cells and biomaterials were efficiently distributed in droplets by inkjet printers using thermal chambers and piezoelectric transducers. Droplet printing and bubble formation were triggered by a heating coil adjacent to the nozzle.[78,79] Pressure pulses were produced by piezoelectric inkjet bioprinters, which allowed living cells to be printed in droplets.[78] Although

inkjet bioprinters are fast and affordable,[69] they have some limitations.[80] These bioprinters can disturb cell viability and result in significant damage during printing.[81] Despite the heat control program retrofitted in the printers, thermal inkjet printing would still inhibit cell viability at 89%.[82] Moreover, non-uniform droplet size and nozzle blockages are some of the challenges faced by inkjet-based bioprinters, necessitating a labor-intensive process for the preparation of proper biomaterial.[69] The development of vascular networks within skin tissue constructs using inkjet-based bioprinting precisely enables the deposition of bioink-encapsulating endothelial cells along with growth factors. This technique enables the functioning and formation of blood vessels, thereby improving the viability as well as integration of designed skin tissue for more effective tissue regeneration and wound healing.

4.2.2. Extrusion-based bioprinter

Extrusion-based bioprinters use mechanical hardware, such as pneumatic pressure, pistons, and screws, to extrude hydrogel-type bioink through a nozzle. They have several advantages, as compared to inkjet-based bioprinters, in terms of the ability to handle viscoelastic properties, high cell densities, and adaptive crosslinking mechanisms.[83]

In skin tissue engineering, conventional methods relying on manual seeding of epidermal keratinocytes on dermis inevitably generate multiple acellular places and cell clumps at unpredictable sites, resulting in poor productivity and repeatability.[84] The formation of these keratinocyte clusters not only hinders proper differentiation but also destabilizes the junction between the epidermal and dermal layers.[85] Although prolonged cultivation periods may eventually fill the acellular places, they can also result in the creation of additional clusters of keratinocytes in areas where a continuous cell layer has already been established. Therefore, it is of utmost importance to establish a uniform and contiguous monolayer across the entire surface before initiating keratinocyte differentiation. Extrusion-based 3D bioprinting system has emerged as a promising solution to address the limitations of conventional approaches. This fully automated system enables the precise and reproducible deposition of living cells and biomaterials in a layer-by-layer manner, facilitating the creation of biomimetic skin models with exceptional fidelity and accuracy. In particular, it has brought about significant advancements in the field of 3D skin bioprinting due to its ease of use and suitability for fabricating 3D tissue constructs.[86-88] Ma et al.[89] created a dermis scaffold with gradient stiffness using gelatin–alginate hydrogel containing adipose-derived stem cells. The scaffold showed physical relevance to native environment of the dermis and other subcutaneous layers. However, 3D skin extrusion bioprinting is still facing challenges in achieving an air-exposed cellular monolayer because cells are enclosed in a bioink to shield them from the shear stress resulting from mechanical forces during extrusion. In light of this limitation, like the conventional method, a few 3D skin bioprinting methods have opted for extruding only a dermal structure using ECM-based bioinks and subsequently seeding keratinocytes onto the dermis.[90] Recent study introduced a novel strategy to uniformly cover keratinocytes on dermis using a sacrificial gelatin-assisted 3D skin extrusion bioprinting.[91] The researchers used the thermosensitive characteristics of gelatin to ensure that keratinocyte-enclosing gelatin was evenly extruded onto the dermis, while it dissolved during the incubation at 37°C; this led to a uniform keratinocyte monolayer. The results demonstrated the successful establishment of a thicker and more natural epidermis, along with the increased expression of epidermal differentiation markers, following the application of sacrificial gelatin-assisted extrusion bioprinting.

Extrusion-based bioprinting systems have revolutionized the field of skin engineering, offering innovative solutions to long-standing challenges. Such breakthroughs not only improve the efficiency and repeatability of skin tissue engineering but also hold great promise for the development of biomimetic skin models with exceptional fidelity and accuracy. Therefore, extrusion-based bioprinting is poised to play a pivotal role in advancing our capabilities and understanding of skin regeneration and reconstruction.

4.2.3. Laser-assisted bioprinter

In 1999, Odde and Renn[92] introduced laser-assisted bioprinting using optical cell trapping. Three layers, namely, the energy-absorbing layer, donor ribbon, and bioink, comprise this system.[93] Droplets of bioink are produced when a high-pressure bubble is generated in the donor-ribbon layer through the use of a laser. The least amount of contamination is generated by maintaining printing dispensers along with separated bioinks.[94] By using this method, high precision can be achieved and high-viscosity bioinks can be deposited with excellent efficacy.[95] Additionally, since it is a nozzle-free method, laser-assisted bioprinting is not afflicted with problems such as nozzle blockages.[69] Using live/dead experiments, Catros et al.[96] evaluated the vitality of Ea. hy926 cells and found that viscosity, substrate height, and laser frequency influence viability. Cell viability is improved by higher viscosity and thicker substrates. However, this approach is challenging and expensive, and could damage the cells by its laser.[69,95,96] By precisely depositing bioinks and constructing complex

microvascular networks, laser-assisted bioprinters provide an effective technique for vascularizing skin tissue constructions. Given their excellent speed and precision, these bioprinters offer an avenue to improve the development of functional and perfusable skin tissue for regenerative medicine applications.

4.2.4. Stereolithography bioprinter

Stereolithography utilizes light for layer-by-layer crosslinking of light-responsive bioinks inside reservoirs. Stereolithography can reduce the fabrication time of 3D volumetric structures because it can polymerize the two-dimensional plane and stack them in layer-by-layer.[97] Choi et al.[98] irradiated methacrylated silk fibroin and gelatin bioinks to bioprint a 3D skin model with a digital light processing printer. The skin model exhibited excellent mechanical properties, promoted cellular growth, and demonstrated therapeutic effects, making them adaptable for various skin layer thicknesses. Another innovative approach involved the development of biocompatible gelatin methacrylamide- and hyaluronic acid methacrylamide-based scaffolds featuring a dermal layer that supports keratinocyte attachment and facilitates efficient vascularization.[99] The exploration of an optimal light-sensitive bioink and a practical stereolithography has laid a novel foundation for potential applications in skin tissue engineering, drug development, cosmetic testing, and future advancements in wound-healing strategies. Stereolithography enables the creation of intricate internal structure such as vascularized skin tissue. The development of intricate circulatory networks by this technique is crucial to ensure the availability of nutrition to the biofabricated skin, while improving regenerative medicine and developing applications for wound healing. A major drawback of stereolithography is that the reservoirs may be filled with photopolymerization materials, resulting in waste production and high research costs compared to alternative methods that use smaller amounts of bioinks.[97]

4.2.5. Other bioprinters

Acoustic and microvalve bioprinters are classified as droplet-based. An acoustic bioprinter discharges droplets when an acoustic wave generates force.[100] Gudapati et al. have compared the significant advancements in extrusion- and inkjet-based bioprinters and found that the presence of heat and high pressure, which can induce cellular damage, did not affect cell viability in bioinks.[101] A microvalve bioprinter uses a valve coil to generate an electromechanical microvalve that releases droplets. The valve coil produces a magnetic field that pushes the plunger higher, and the resulting pneumatic pressure pressurizes the bioinks in the barrel, which are subsequently discharged from the open barrel. However, the resolution is low because of the uniform nozzle diameter, which results in droplets larger than those produced by inkjet-based bioprinters.[101] In the Kenzan method, aggregated cells or spheroids are deposited onto a platform using a needle-array technique. LaBarge et al. developed a solution for depositing spheroids on needle arrays by simultaneously producing entire constructed layers, allowing one-by-one spherical deposition.[102] Utilizing microscale droplets of cells and bioinks, droplet-based bioprinting enables precise construction of vascular structures inside skin tissue constructs. By promoting the growth of functioning blood vessels, this ground-breaking method improves the viability and functionality of engineered skin tissues that enable regenerative medicine applications.

4.2.6. Handheld skin bioprinter

The revolutionary medical technology developed by Navid Hakimi—a portable skin printer—changed how skin transplantation and wound healing are performed. This bioprinter has been utilized by clinicians to treat burns, chronic wounds, and various other skin-related disorders. It exemplifies the convergence of biomedical engineering with cutting-edge medical applications. A handheld skin printer is a small portable tool that allows medical personnel to apply multiple layers of bioink directly to a patient's skin, accurately locating and curing damaged or diseased regions. A variety of bioinks, which are composed of specific mixtures of live cells, proteins, and growth factors that support skin regeneration and tissue healing, are included in this portable tool.[103] This type of portable skin bioprinter holds promise for improving vascularization in skin tissue constructions. Its precise bioink deposition can generate complex blood vessel networks that are essential for tissue survival. The technique might advance regenerative medicine and patient care by revolutionizing skin grafting and wound healing.

4.3. Bioink candidates for skin

In 3D bioprinting, biomaterials-based hydrogels utilized to encapsulate particular cells are known as bioinks, and they are essential to the replication of healthy and physiological microenvironments (Table 3).[104] It is difficult to replicate skin structure and function, and developing bioink entails a step for selecting appropriate cells and biomaterial.[105] The most commonly utilized biomaterials in 3D bioprinting are synthetic and natural polymers.[106,107] Although natural materials such as collagen, alginate, gelatin, fibrin, and chitosan have limited immunogenicity, biocompatibility, and biodegradability, they may have insufficient mechanical properties as well as present immunological risks.[104] The mechanical and structural properties of synthetic polymers can be controlled. They can be biodegradable, like PCL and PLA, or non-biodegradable, like PEG.[108] For skin

Table 3. Summary of the most significant natural and synthetic polymers used to develop skin bioinks for 3D bioprinting

Types of polymers	Bioprinting techniques	Gelation mechanism and combination of polymer	Targeted structure	Cells	Ref.
		Natural polymers			
Gelatin	Extrusion	Thermal (GelMA)	Only dermis	Only Fbs	[179]
		Chemical (alginate and gelatin)	Epidermis and dermis	Only AECs	[180]
Collagen	Droplet	Thermal (only collagen)		KCs, Fbs, and MCs	[134]
				KCs, and Fbs	[181]
		Thermal (collagen and GelMA)		KCs, Fbs, and MCs	[182]
Alginate	Extrusion	Ionic (alginate and gelatin)	Only sweat gland	Only Eps	[183]
		Ionic (alginate and PLGA)	Epidermis and dermis	KCs, and Fbs	[184]
		Ionic (alginate, NFC, and CMC)	Only dermis	Only Fbs	[185]
Chitosan	Extrusion	pH (only chitosan)	Epidermis and dermis	KCs, and Fbs	[186]
		pH (chitosan with gelatin)	Only dermis	Only Fbs	[187]
Fibrin	Extrusion	Thrombin (only found in fibrin)	Epidermis/dermis	KCs, and Fbs	[188]
		Synthetic polymers			
PEG	Extrusion	Thermoplastic (PEG, chitosan, and genipin)	Epidermis/dermis	KCs, and Fbs	[189]
	Droplet	Thermoplastic (silk fibroin with PEG)			[190]
PLA	Extrusion	Thermoplastic (PLA, chitosan and HA)	Only dermis	Only Fbs	[188,191]
PCL	Inkjet	Thermoplastic (PCL and collagen)	Epidermis and dermis	KCs, and Fbs	[84]

Abbreviations: AECs, amniotic epithelial cells; CMC, carboxymethyl cellulose; Eps, epidermal progenitors; Fbs, fibroblasts; GelMA, gelatin methacryloyl; HA, hyaluronic acid; KCs, keratinocytes; MCs, melanocytes; MSCs, mesenchymal stem cells; NFC, nanofibrillated cellulose; PCL, poly(e-caprolactone); PEG, polyethylene glycol; PLA, poly(lactic acid); PLGA, poly(lactic-co-glycolic acid).

engineering, modifications are usually achieved by mixing synthetic materials with natural materials and changing their required properties.[109] To enhance the characteristics of synthetic materials for potential implementation in skin engineering, they are often modified and combined with natural materials. A comprehensive review of the different types of natural and synthetic polymers and their combinations used in various 3D bioprinting techniques targeting different skin structures is presented in Table 3.

Moreover, owing to the constantly evolving wound-healing dynamics and diverse microenvironments that affect skin diseases, the demand for biomaterials is increasing.[110,111] Studies on bioinks incorporating decellularized extracellular matrix (dECM) to retain the structural and functional features of natural ECM have grown in recent years.[112] The most significant advantage of the dECM is that it offers a wider range of structural, chemical, and biological cues than other biomaterials because it originates from heterogeneous natural tissues.[113,114] In addition, it has excellent printability and biocompatibility.[115] Many dECM-based bioinks have proven to be effective in developing skin substitutes.[116-119] However, to prevent immune and rejection reactions after transplantation, physical, chemical, or biological removal of biocompatible complexes from native tissues, which may damage the microstructure and bioactive substances within the ECM, is necessary.[120] Decellularization and the optimization of these processes remain challenging.

5. 3D bioprinting-based applications for engineering vascularized skin tissue

Distinct challenges and objectives exist for bioprinting vascularization strategies in *in vitro* (outside the living body) and *in vivo* (inside the living body) settings. *In vitro* bioprinting focuses on creating functional microvasculature within engineered tissues. This is essential for applications such as drug testing, disease modeling, and tissue engineering, where accurate replication of the complex structural aspects of blood vessels is required. In this context,

bioprinters deposit bioinks, including endothelial cells, in a layer-by-layer fashion, forming intricate vascular networks within a controlled microenvironment. Challenges in this domain include maintaining cell viability, enhancing the biological properties of biomaterials, and developing suitable bioinks. On the other hand, *in vivo* bioprinting involves regenerating blood vessels within host organs to facilitate tissue repair and regeneration. Strategies for *in vivo* bioprinting may include the direct application of 3D bioprinting into wound sites or the transplantation of encapsulated endothelial cells in specific bioinks. This approach necessitates bioink materials being compatible with the host's immune system. Challenges in this context encompass managing immunological responses, ensuring integration within host tissues, and promoting functional vessel development. Table 4 summarizes the distinctions between *in vitro* and *in vivo* bioprinting vascularization strategies, highlighting the unique advantages and drawbacks associated with each approach and underscoring the importance of selecting the most suitable strategy based on research or therapeutic objectives.

In summary, *in vitro* bioprinting primarily serves tissue engineering and research purposes, while *in vivo* bioprinting is employed for therapeutic applications within living organisms. Each approach presents specific challenges related to biocompatibility and functional integration. Both *in vitro* and *in vivo* bioprinting for vascularization have their own advantages and disadvantages. *In vitro* models allow for the precise fabrication of complex vascular networks under controlled conditions, but they face challenges related to limited tissue maturation and integration post-transplantation. In contrast, *in vivo* bioprinting enables real-time integration and, potentially, immediate functionality, but involves challenges related to the immune system and ethical considerations. Selection of the suitable approach should be guided by specific research or therapeutic goals.

5.1. Development of *in vitro* vascularized skin models

Recently, there has been a rapidly growing demand for skin models designed *in vitro* to evaluate pharmaceutical and cosmetic products or regenerate skin function after damage.[121] In 2014, approximately USD 958.8 million was spent on tissue-engineered skin substitutes, and by 2023, the market is expected to reach approximately USD 3873.5 million. The cost of *in vitro* toxicological studies in 2016 reached USD 14.2 billion. Previously, it was a common practice to assess the efficacy and toxicity of skin-targeted compounds through *in vivo* animal testing, since many compounds could not be directly tested in humans.[122] However, in March 2013, the use of animal models to study cosmetic-related compounds was banned. Moreover, the failure of animal models to accurately predict human responses because of physiological differences between animals and humans often leads to expensive and unsuccessful clinical trials subsequently.[123] Thus, the European Parliament and the European Council passed an amendment (Directive 2003/15/EC) on February 27, 2013.[124] Currently, the "3 R" principle is emphasized, i.e., refining, reducing, and replacing animal tests whenever possible.[122,125] Several approaches have been investigated for the *in vitro* development of tissue-engineered constructs with stable, functional, and perfusable microvessels. The construct gradually vascularizes after being transplanted into the host as a result of the host body's immune response to foreign

Table 4. Comparison between *in vitro* and *in vivo* bioprinting strategies for vascularization

Aspect	*In vitro* bioprinting	*In vivo* bioprinting
Environment	Controlled lab conditions	Real biological environment
Vascular network complexity	Precise control possible	Limited control, natural networks
Tissue maturation	Limited maturation, may require further development before transplantation	Immediate integration, natural maturation
Integration	Transplantation challenges, potential for limited integration	Real-time integration, immediate functionality
Immune response	Reduced immune response *in vitro*, not representative of the immune system's role *in vivo*	May trigger immune responses, immune modulation needed
Ethical considerations	No ethical concerns	Ethical considerations due to the invasive nature
Applications	Suitable for drug testing, research, and disease modeling	Tissue regeneration, organ transplantation
Advantages	Precise control, no ethical concerns	Immediate functionality, natural integration
Disadvantages	Limited maturation, transplantation challenges	Potential immune responses, ethical considerations

materials. A few strategies to accelerate vascularization include enhancing wound healing, promoting blood vessel regeneration before transplantation, optimizing scaffold properties, and incorporating growth factor delivery systems. However, fast microvascular formation within the large construct presents challenges for the host immune response, which could reduce the duration required for effective vascularization. According to Yanez et al.,[126] pre-vascularization of constructs is a strategy to promote *in vivo* blood vessel formation after transplantation. By developing a 3D cell printing technique that develops mature, perfusable, and vascularized human skin substitutes, Kim et al.[127] successfully achieved a significant breakthrough. By precisely distributing cells with biomaterials, this technique provides structural complexity that mimics human skin, comprising the epidermis, dermis, and hypodermis. The vascularized dermal and hypodermal compartments combine to provide an ideal microenvironment, which leads to enhanced epidermal morphogenesis and skin recapitulation. The full-thickness skin model demonstrated superior performance in a comparison study compared to normal dermal and epidermal skin models, which showed the potential to enhance the *in vitro* platform for skin disease modeling, pathological research, and sustainable instruments for research.[127] For example, Yanez et al.[126] enhanced vascularization in 3D-bioprinted skin grafts implanted on mice by using inkjet printing technology with collagen and fibrinogen matrix containing fibroblasts from neonatal dermis, keratinocytes, and HUVECs as seeding cells. Within 2 weeks following surgery, the results showed improved wound healing and neovascularization in the skin graft.[126] Abaci et al.[128] developed a unique bioengineering method for creating micropatterned, spatially controlled, and perfusable vascular networks within 3D human skin substitutes using primary and induced pluripotent stem cell (iPSC)-derived ECs. They regulated the geometries of micropatterned vascular networks using 3D printing technology. Vascularized human skin equivalents (vHSEs) based on this approach can enhance neovascularization during wound healing[126] (Figure 7). 3D printing was utilized to develop molds for establishing vascular networks in human skin equivalents (HSEs), as well as the inlet and outlet tubes and ring-shaped holders (Figure 7A-a). Researchers investigated the formation of the epidermal layer along with the endothelial barrier in vHSEs using GFP-tagged HUVECs and induced endothelial cells (iECs). The HUVEC-lined hollow microchannels were observed in vHSE sections, including vasculature, with a physiological pattern. Histological and immunostaining investigations confirmed the development of an epidermal layer (Figure 7A-b). Proliferation of basal keratinocyte and blood perfusion were observed in vHSEs-transplanted immunodeficient mice, as compared to their counterparts transplanted with native HSEs. In grafts, vHSEs promoted host neovascularization. Neovascularization was directed by micropatterned vasculature by facilitating the perfusion of labeled dextran into host vessels, as shown in Figure 7A-c–g.[126] Taken together, the results indicate that the micropatterned vasculature in vHSEs promotes and directs neovascularization during graft integration into wounds, possibly improving the engraftment of engineered skin structures. A vascularized and pigmented dermoepidermal skin substitute (DESS) was developed *in vitro* by Pontiggia et al.[129] using a robotic 3D bioprinter called SkinFactory (Figure 7B-a). As shown in Figure 7B-b and c, the bioink, type I collagen hydrogel, was utilized to distribute different human skin-derived cells by patterned inkjet and extrusion-based bioprinting to develop *in vitro* blood and lymphatic vascular networks. Afterward, the biofabricated DESS was placed into a frame and inside a cell culture flask with the appropriate media, followed by the sealing of the lid. The two main parts of the DESS were fibroblasts mixed with melanocytes and keratinocytes to provide the necessary epidermal layer for skin substitute and fibroblasts integrated into collagen-based hydrogels for the dermal structure. One week later, the DESS showed satisfactory dermal motility and cell survival of the fibroblasts within the collagen matrix. Dense patterns of melanocytes and keratinocytes were jetted onto the hydrogel-based bioink using a 3D bioprinting process, developing layers with excellent skin structural organization. After 4 weeks, CD31 expression could be observed in a vascular network within the dermal layer, with CD90-positive mural cells and CD31-positive capillaries, as demonstrated by immunofluorescence staining. After 3 weeks, compression did not show any significant effect on the formation of vascular plexuses in lymphatic and blood capillaries (Figure 7B-d and e).[129]

The significance of vascularized skin construction requirements has been increasingly recognized owing to its progressive function in regulating the biological activities of implants, which is vital for the survival of implants in the host body.[130] The *in vitro* fabrication of vascularized networks of channels into 3D-bioprinted skin constructs is essential for providing nutrition to surrounding cells.[127] In addition, angiogenesis significantly contributes to the efficacy of skin grafts. However, adding layers may reduce the survivability of the graft in low-oxygen (hypoxic) environments because of the distance between the cell layers and the wound surface.[131] Pre-vascularization of 3D-bioprinted structures using HUVECs and fibroblasts, as well as mesenchymal stem cells (MSCs) and HUVECs, has been demonstrated in *in vivo* models to improve integration with the host tissue, enhance graft survival, and promote re-epithelialization after implant placement.[63,131] Several researchers conducted *in vitro* bioprinting experiments

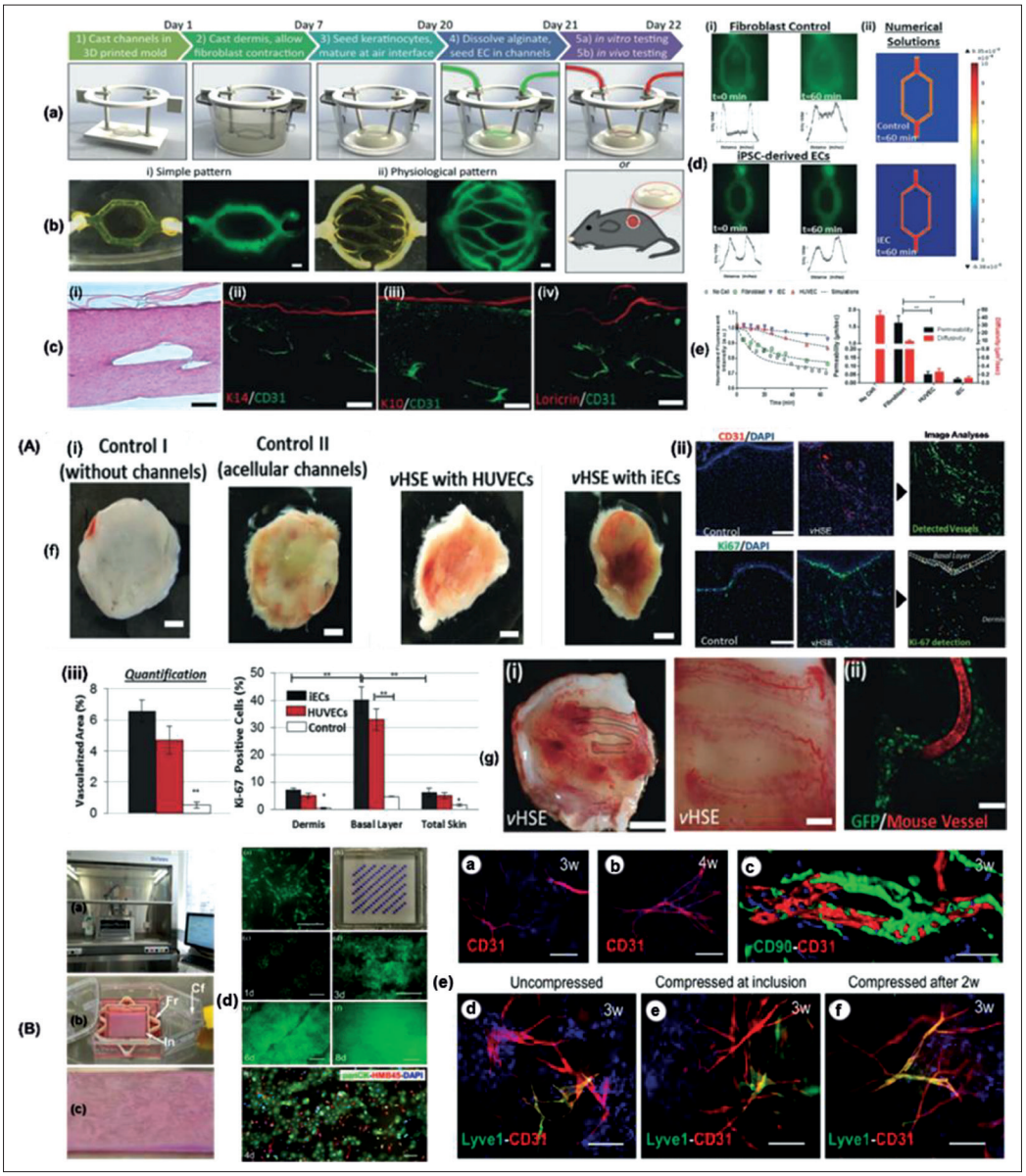


Figure 7. Development of vascularized HSEs. (A) (a) Alginate microchannels formed in 3D-printed molds, surrounded by dermal fibroblasts and collagen gel. Keratinocytes seeded over the dermal compartment, and sacrificial layer dissolved for endothelial cell (EC) seeding. (b) Fluorescently tagged alginate used to generate vasculature patterns; scale bar: 600 μm. Epidermal integrity and endothelial barrier function in vHSEs: (c) H&E and immunofluorescent staining of vascularized human skin equivalent (vHSE) sections generated with induced pluripotent stem cell (iPSC)-derived ECs, for evaluating the epidermal integrity and endothelial coating; scale bar: 250 μm. (d) Evaluation of endothelial barrier function via perfusion of fluorescently tagged dextran. The distribution is depicted in surface plots. (e) Quantification of the fluorescence intensity, permeability, and diffusivity in microchannels. (**$p < 0.005$, N = 3 HSEs). Implantation of vHSEs onto SCID mice: (f) Effect on host neovascularization. (i) Blood perfusion in Control I, Control II, vHSEs with HUVECs, and intestinal epithelial cells (iECs) after 2 weeks; scale bar: 2.5 mm. (ii) Immunostaining of human skin equivalents (HSEs) and vHSEs with CD31 and Ki67; scale bar: 250 μm. (iii) Quantification of host vasculature area and Ki-67-positive cells (*$p < 0.05$, **$p < 0.005$, $N = 4$). (g) Effect of vasculature pattern. (i) Pictures of host vasculature in vHSEs and HSEs with microchannels; scale bars: 2.5 mm and 500 μm. (ii) Confocal image showing perfused mouse vessels and GFP-tagged HUVECs ($N = 4$ for all conditions); scale bar: 500 μm. Figure 7A was reprinted from[142] (Copyright © 2016, with permission from WILEY). (B) *In vitro* 3D bioprinting of vascularized pigmented skin tissue. The biofabrication process involves the use of the regenHU "BioFactoryTM 3D bio-printer system" for (a) 3D bioprinting and (b) cell cultivation. (c) 6 cm^2 patch of pre-vascularized, pigmented human dermo-epidermal skin. (d) 3D bioprinting of human melanocytes and keratinocytes follows a predetermined pattern, with cells stained and immunofluorescently labeled. (e) Vasculature development is observed within collagen type I hydrogels via CD31 immunofluorescence imaging in human dermo-epidermal skin substitutes. (f) Human dermal microvascular endothelial cells (HDMECs) cultured under different conditions exhibit blood capillaries and lymphatics under CD31 and Lyve1 immunofluorescence imaging. The scale bars represent (d) 2 μm and (c, e, f) 100 μm. Figure 7B was reprinted from[129] (Copyright © 2022, with permission from SAGE Publications).

using ECs from placental pericytes and cord blood to print pre-vascularized biofabricated structures. In their latest vascularized skin grafts, Baltazar et al.[132] integrated keratinocytes with vascularized dermal fibroblasts, ECs, and pericytes using type I collagen bioink solutions. This resulted in the production of vasculature-like structures *in vitro* by ECs and pericytes, while keratinocytes produced stratified structures with multiple layers.[132] Yanez et al.[126] developed a skin graft by incorporating microvascular ECs into dermal compartments containing fibroblasts. To create a skin graft, keratinocytes were printed on top of dermal compartments and vascularized through the incorporation of microvasculature via 3D printing.[126]

Kolesky et al.[133] reported that approximately 1-cm-thick human vascularized and perfusable tissue was biofabricated using 3D bioprinting methods with different materials within 6 weeks. This tissue replaces the engineered ECM that is encapsulated in a variety of human cells, including hMSCs and human neonatal dermal fibroblasts (hNDFs). Additionally, HUVECs have been used to enhance normal endothelial-lining function. Initially, scientists created printable inks containing cells and a castable ECM using gelatin and fibrinogen. These materials were combined for the 3D bioprinting of tissue constructs. This approach satisfies important criteria such as ease of handling, ability to incorporate different components, and compatibility with living systems.

5.2. Enhancement of *in vivo* skin tissue regeneration

Several vascularization strategies have been studied to develop tissue-engineered constructs with stable and functionally perfusable microvessels *in vivo*. When the construct is transplanted into the host, it gradually vascularizes as the body responds to foreign substances. One strategy for expediting vascular development in constructs is to optimize the scaffold characteristics and incorporate growth factor delivery systems to enhance wound healing by promoting blood vessel regeneration before transplantation into the host.[38] However, this approach relies on the host response to rapid microvascular development and may face challenges in achieving prompt vascularization. Pre-vascularization of constructs, as reported by Heller et al.,[60] is a potential method for promoting blood vessel development *in vivo* after transplantation. For instance, Yanez et al.[126] developed artificial skin using inkjet printing technology with HUVECs as seed cells for bioprinting. Type I collagen and combined fibrinogen were employed as bioinks for building a supportive structure to enhance vascularization in bioprinted skin tissues. This 3D-bioprinted skin graft was implanted on the backs of nude mice in the absence of the thymus. Two weeks after surgery, the 3D-bioprinted skin transplants accelerated wound healing with sufficient neovascularization within the skin graft.[126] Utilizing 3D bioprinting, Ng et al.[134] developed pigmented human skin by incorporating ECs with other skin cells to promote vascularization. After 4 weeks of air–liquid interface (ALI) culture, they combined the manual casting process with a combined 3D bioprinting process to develop a functional skin substitute, as shown in Figure 8A.[134] The pre-vascularized 3D skin substitutes were treated with excisional full-thickness wounds in immunodeficient rats. However, wounds without blood vessels were less transparent, and treatments with pre-vascularized substitutes showed host tissue-integrated blood vessels. As seen in Figure 8B,[63] histological analysis after 7 days showed blood-perfused blood vessels in pre-vascularized substitute wounds, which were however absent in the control groups.

In this *in vivo* grafting model, under physical examination, the areas treated with control substitutes exhibited drying and detachment from the injured site by day 14. Among the 15 mice that received non-vascularized control substitutes, 11 exhibited skin blistering by day 7 after grafting. However, both the control-treated wounds and the pre-vascularized substitutes fully re-established the outer layer of the skin (re-epithelialization) by day 14. In contrast, pre-vascularized substitutes adhered to the wound tissue, resulting in remarkable healing with minimal wound contraction. Masson's trichrome staining revealed the presence of mature collagen fibers (bright blue and densely packed) within the pre-vascularized substitutes, with a collagen content similar to that of the host tissues. In contrast, wounds treated with control substitutes exhibited immature collagen (light blue and loosely packed) surrounding the fibroblasts. As demonstrated in Figure 8C,[63] human HLA-ABC expression in artificial human blood vessels and the Malpighian layer attests to the successful transplantation of human 3D skin substitutes in mice. A quantitative assessment of blood vessel density showed that the pre-vascularized substitutes had a higher vessel density compared with the control group. Figure 8C[63] shows angiogenesis in both control and pre-vascularized substitute-treated wounds, with both human- and host-derived endothelium present.

Several major bottlenecks exist in the tissue engineering of permanent skin substitutes, including insufficient induction of angiogenesis, ineffective graft–host anastomoses, and an inadequate vascular architecture. Ma et al.[135] synthesized homogeneous strontium silicate micropillars as stable angiogenesis-inducing factors in biomaterial inks. They employed these micropillars to print functional skin substitutes using multicellular cellular systems that were induced for angiogenesis. Strontium silicate microcylinders were incorporated into the bioink

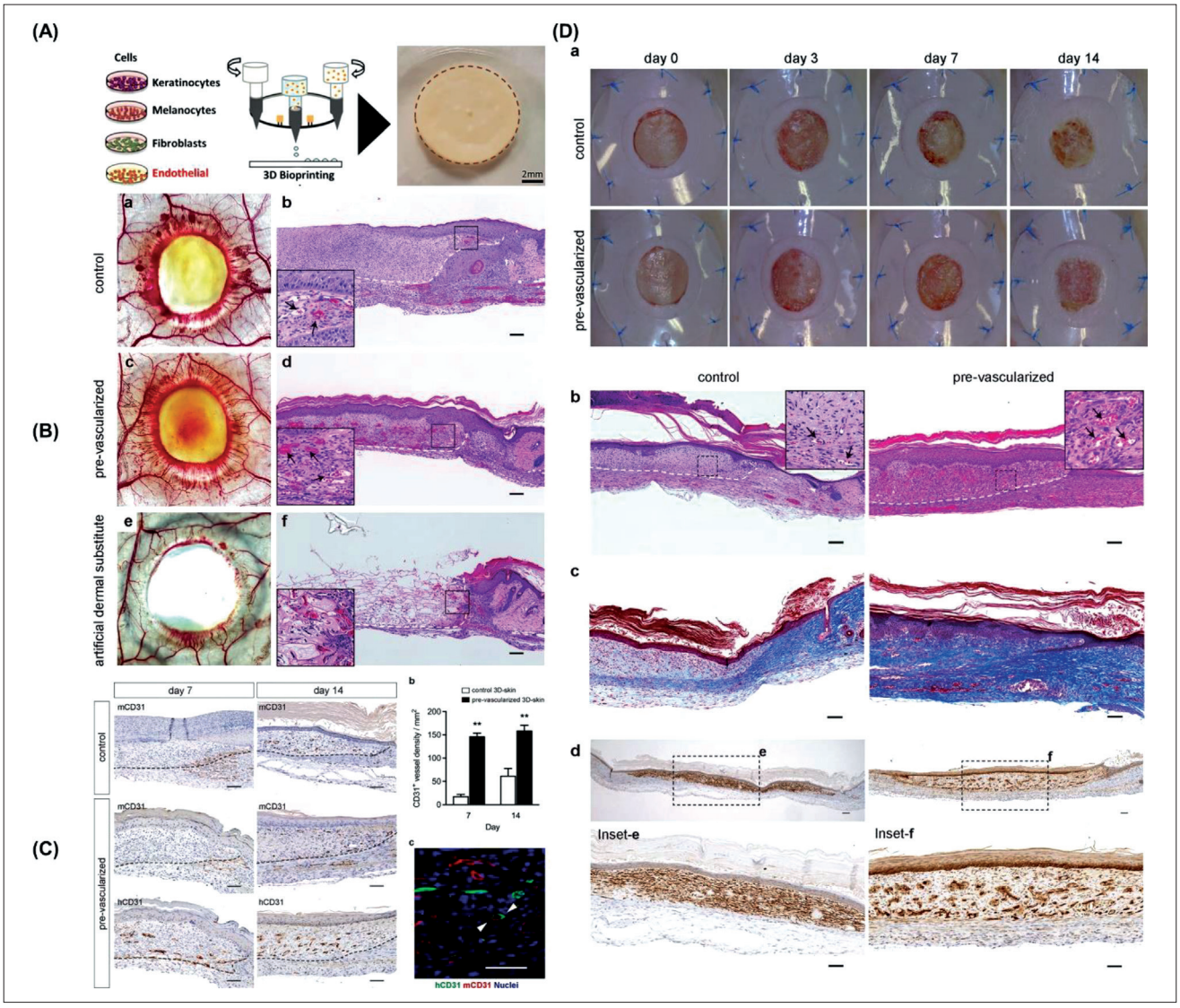


Figure 8. (A) Biofabrication of functionally vascularized skin. The construction and development of 3D vascularized skin with human tissues using a two-phase bioprinting process. (B) Rapid formation of functional vasculature *in vivo* inside pre-vascularized 3D skin tissue mimics.[63] (C) Evaluation of the *in vivo* wound vasculature. (a) Immunohistochemical identification of human-specific CD31 (hCD31) along with mouse-specific CD31 (mCD31) between day 7 and day 14 following grafting. Skin substitute–host interactions are represented by dashed lines; scale bar: 100 μm. (b) Evaluation of $CD31^+$ blood vessels in dermal areas of the transplants. The data represent the mean ± standard deviation ($n = 5$). $^{**}p < 0.01$ compared with the non-vascularized control (unpaired Student's *t*-test). (c) Immunofluorescence imaging of pre-vascularized wounds treated with substitutes on day 14 following grafting, based on mouse-CD31 (red) and human-CD31 (green). DAPI was used to label the nuclei (blue). Human–mouse hybrid vessels are indicated by white arrowheads; scale bar: 50 μm.[63] (D) Wound healing and remodeling accelerated by pre-vascularization. (a) Microscopic evaluation of transplanted controls and pre-vascularized skin substitutes on immunodeficient mice performed for a maximum of 14 days post-transplant. (b–f) Histopathological and immunohistochemical staining of control group wounds and pre-vascularized substitutes during the 14 days after transplantation by means of (b) hematoxylin and eosin, (c) Masson's trichrome, and (d–f) HLA-ABC. The interactions between the skin substitute and host are indicated by white dashed lines. Vascular indications from mice were used to illustrate blood veins with black arrows; scale bar: 100 μm. Figure 8 was reprinted from[63] (Copyright © 2019, with permission from Springer Nature).

to enhance vascularization, as recapitulating the dermal vasculature was believed to be a crucial step in developing effective bioprinted skin replacements.[135] In this context, incorporating therapeutic substances capable of stimulating blood vessel development into bioinks is crucial. Silica-based products promote the growth of blood vessels and collagen during the wound-healing process.[136-138] Similarly, strontium ions increase the expression of angiogenic transcription factors in cells, promoting angiogenesis.[139,140] Microparticles have a highly crystalline structure and a diameter of 15 μm, produced through a hydrothermal procedure, continuously releasing strontium and silicon

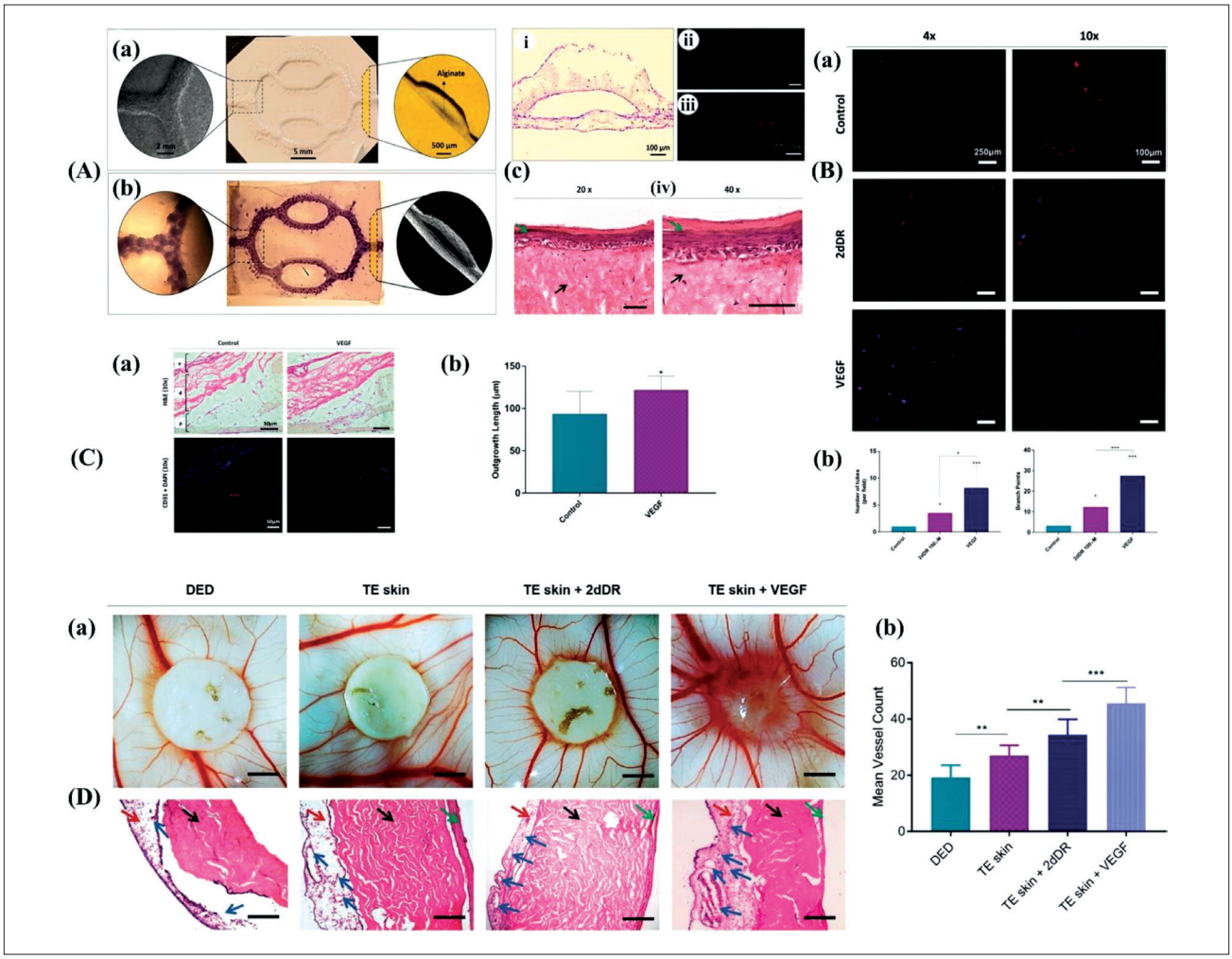


Figure 9. (A) PHBV SVN scaffolds were recellularized with human dermal microvascular endothelial cells (HDMECs) and human dermal fibroblasts (HDFs) in indirect contact, resulting in a well-recellularized structure. The scaffolds were labeled using CellTracker Red and Green, respectively, for visualization. Histological assessment of the tissue-engineered skin models was conducted after incubation in Green's media and at the air–liquid interface (ALI). The addition of HDMECs and HDFs during the recellularization process resulted in a larger cell population within the PHBV SVN scaffold. (B) PHBV channels were used for the growth of HDMECs, which were then subjected to vascular endothelial growth factor (VEGF) or 2dDR-loaded Matrigel experiments. Staining analysis revealed that the VEGF-loaded groups had more organized tubular structures than the 2dDR and control groups. (C) HDMECs expanded from PHBV channels and spread onto tissue-engineered skin models, primarily originating from two different electrospun sheets. A graph quantitatively illustrates the distance of HDMEC outgrowth, confirming that the addition of VEGF enhanced this outgrowth. (D) Macro-images depict the angiogenesis in the case of dry eye disease (DED), tissue-engineered skin without any supplementation, and tissue-engineered skin supplemented daily with 2dDR and VEGF. The middle row showcases the histological appearance, with arrows indicating the chorioallantoic membrane, dermal layer, epidermal layer, and blood vessels. Figure 9 was reprinted with permission from[141] (Copyright © 2020, with permission from ACS Publications).

ions. These ions have been shown to promote collagen formation and angiogenesis during wound healing. Using an *in vivo* 3D human skin mimic model developed by 3D bioprinting combined with electrospinning, Dikici et al.[141] investigated angiogenesis to study different aspects of angiogenesis using Matrigel. The objective was to precisely replicate a human skin model by developing a structure that physiologically functions as skin. As shown in Figure 9A-a,[141] a total of 12 PHBV SVN scaffolds have been efficiently developed. After adding methylene blue dye to the PHBV SVN and using scanning electron microscopy (SEM) to observe the open-channel structure (Figure 9A-b),[141] the removal of alginate was confirmed. A continuous EC monolayer was formed by co-culturing human dermal microvascular endothelial cells (HDMECs) and human dermal fibroblasts (HDFs) within artificial vascular channels, as Figure 9A-c-i–iii demonstrates. Anti-human CD31 antibody immunostaining observed evenly spaced single layers of HDMECs within the channels and HDFs on the outside surfaces (Figure 9A-c-i–iii). Histological analysis after 14 days showed a multilayer epithelium with normal skin morphology associated with the dermis (Figure 9A-c-iv).

As shown in Figure 9B,[141] HDMECs migrated out of the Matrigel by day 7, forming networked tube-like formations adjacent to the PHBV channel borders. More effective tube-like structures were formed through the addition of VEGF-loaded Matrigel; this effect was significantly identified when the proangiogenic compounds 2dDR and VEGF were added. About 20% of the Matrigel tested with VEGF loading and 13.3% of the Matrigel tested with 2dDR loading in the control group showed structures mimicking tubes. As shown in Figure 9C,[141] PHBV scaffolds with HDMECs and HDFs showed uniformly distributed channels with HDFs on the outside of the structure. High-magnification images of the reconstituted skin models, primarily constructed from electrospun sheets, showed that CD31-positive HDMECs were proliferating within the PHBV channels. An *in vivo* study showed that the dry eye disease (DED) group had the fewest blood vessels, while tissue-engineered skin analogs with 2dDR had the most significant vascularization. Figure 9D[141] shows that the function of proangiogenic chemicals and dermal cells markedly enhanced the vascular count. The PHBV SVN can be a useful platform for *in vitro* angiogenesis research for evaluating vascularization in human skin development, as this study demonstrates.

6. Conclusion and future perspectives

Multiple approaches can be used in skin tissue engineering to facilitate the biofabrication of vascular structures. The integration of specific cell types, application of growth factors, and use of biomaterials can promote the development of new blood vessels. In contrast to other organs where vascularization can occur from adjacent surfaces, proper vascularization from beneath is crucial for the absorption of any tissue construct in the skin. Achieving proper vascularization is challenging because all cells within the biofabricated construct typically require higher metabolic activity during the first transplantation phase. The physiological limitations of vascularization in normal skin represent the largest barrier to vascular neoformation, and they become less severe over time. Long-term preclinical investigations are necessary to assess the vascularization rate. Currently, a perfused construct developed using *in vitro* techniques must successfully integrate blood vessels within the construct to achieve complete vascularization under both *in vitro* and *in vivo* conditions. Further research is needed to achieve equilibrium in the implementation of large-scale regenerative skin treatment options. Despite extensive research, challenges remain in the field of tissue vascular engineering. Although significant advancements have been made in 3D bioprinting since the development of the first tissue-engineered blood vessel over 50 years ago, more effort is needed to fabricate therapeutically useful vascular structures. Increasing the complexity of the constructed objects and improving the physical composition of biomaterials relevant to different cell types are necessary.

Bioprinting holds tremendous promise for revolutionizing vascularization in tissue engineering. This advanced technology has the potential to significantly enhance the creation of functional blood vessels in engineered tissues, addressing critical challenges in regenerative medicine. Manufacturing processes in bioprinting enable precise control over the architecture of vascular networks. Bioprinters can deposit bioinks composed of living cells, growth factors, and biomaterials in intricate patterns that mimic natural blood vessel structures. This level of control allows for the customization of vessel size, shape, and branching, catering to the specific needs of different tissues. One key advantage of bioprinting is its ability to support the maturation of engineered blood vessels. Over time, printed vessels can develop into more functional and stable networks. As cells populate the bioink and self-organize, they can remodel the vascular structures that bear high resemblance to native vessels. This maturation potential is crucial for long-term tissue viability. Moreover, bioprinting is making strides in the development of functional trilayer blood vessels. In addition to the inner endothelial layer that interfaces with blood, bioprinters can deposit smooth muscle cells for the middle layer and fibroblasts for the outer layer. This trilayer configuration closely mimics natural blood vessels, contributing to better blood flow regulation and tissue integration. In the future, bioprinting may facilitate the creation of highly vascularized tissues and organs for transplantation, wound healing, and disease modeling. By harnessing the power of precise manufacturing, maturation potential, and trilayer vessel development, bioprinting promises to significantly advance the field of vascularization and improve the success of tissue-engineered products in clinical applications.

Acknowledgments

The schematics of Figures 1 and 5 were created by the authors using images provided by BioRender (https://biorender.com/).

Funding

This work was supported by Pusan National University Research Grant, 2021 and by National Research Foundation of Korea (NRF) grants funded by the Korean government (MSIT) (No. 2022R1A5A2027161, 2022R1C1C1004803, and RS-2023-00214149) and by the Institute of Civil-Military Technology Cooperation funded by the Defense Acquisition

Program Administration and Ministry of Trade, Industry, and Energy of the Korean government (No. 22-CM-BR-12).

Conflict of interest

The authors declare no conflicts of interest.

Author contributions

Conceptualization: Arvind Kumar Shukla, Dongjun Lee, Sik Yoon, Minjun Ahn, Byoung Soo Kim
Supervision: Minjun Ahn, Byoung Soo Kim
Visualization: Arvind Kumar Shukla, Dongjun Lee, Sik Yoon, Minjun Ahn
Writing – original draft: Arvind Kumar Shukla
Writing – review & editing: Byoung Soo Kim, Minjun Ahn

Ethics approval and consent to participate

Not applicable.

Consent for publication

Not applicable.

Availability of data

Not applicable.

References

1. Talikowska M, Fu X, Lisak G. Application of conducting polymers to wound care and skin tissue engineering: a review. *Biosens Bioelectron*. 2019;135:50-63. doi: 10.1016/j.bios.2019.04.001
2. Fenner J, Clark RAF. Anatomy, physiology, histology, and immunohistochemistry of human skin. In: *Skin Tissue Engineering and Regenerative Medicine*. New York: Elsevier; 2016:1-17. doi: 10.1016/B978-0-12-801654-1.00001-2
3. Pittman RN. *Regulation of Tissue Oxygenation*. San Rafael, CA:Morgan & Claypool Life Sciences; 2011:1-100. doi: 10.4199/c00029ed1v01y201103isp017
4. Arroyo JA, Winn VD. Vasculogenesis and Angiogenesis in the IUGR Placenta. In: *Seminars in Perinatology*. New York: Elsevier; 2008:172-177. doi: 10.1053/j.semperi.2008.02.006
5. Chouhan D, Dey N, Bhardwaj N, Mandal BB. Emerging and innovative approaches for wound healing and skin regeneration: current status and advances. *Biomaterials*. 2019;216:119267. doi: 10.1016/j.biomaterials.2019.119267
6. Winter GD. Effect of air exposure and occlusion on experimental human skin wounds. *Nature*. 1963;200:378-379. doi: 10.1038/200377a0
7. Dhivya S, Padma VV, Santhini E. Wound dressings–a review. *BioMedicine*. 2015;5(4):22. doi: 10.7603/s40681-015-0022-9
8. Kamoun EA, Kenawy E-RS, Chen X. A review on polymeric hydrogel membranes for wound dressing applications: PVA-based hydrogel dressings. *J Adv Res*. 2017;8(3):217-233. doi: 10.1016/j.jare.2017.01.005
9. Ahmed S, Ali A, Sheikh J. A review on chitosan centred scaffolds and their applications in tissue engineering. *Int J Biol Macromol*. 2018;116:849-862. doi: 10.1016/j.ijbiomac.2018.04.176
10. Carmeliet P, Jain RK. Angiogenesis in cancer and other diseases. *Nature*. 2000;407(6801):249-257. doi: 10.1038/35025220
11. Jain R, Au P, Tam J, Duda DG, Fukumura D. Engineering vascularized tissue. *Nat Biotechnol*. 2005;23(7):821. doi: 10.1038/nbt0705-821
12. Bouhadir KH, Mooney DJ. Promoting angiogenesis in engineered tissues. *J Drug Targeting*. 2001;9(6):397-406. doi: 10.3109/10611860108998775
13. Utzinger U, Baggett B, Weiss JA, Hoying JB, Edgar LT. Large-scale time series microscopy of neovessel growth during angiogenesis. *Angiogenesis*. 2015;18:219-232. doi: 10.1007/s10456-015-9461-x
14. Malda J, Rouwkema J, Martens D, et al. Oxygen gradients in tissue-engineered PEGT/PBT cartilaginous constructs: measurement and modeling. *Biotechnol Bioeng*. 2004;86(1):9-18. doi: 10.1002/bit.20038
15. Hsu Y-C, Li L, Fuchs E. Emerging interactions between skin stem cells and their niches. *Nat Med*. 2014;20(8):847-856. doi: 10.1038/nm.3643
16. Nguyen AV, Soulika AM. The dynamics of the skin's immune system. *Int J Mol Sci*. 2019;20(8):1811. doi: 10.3390/ijms20081811
17. Abdo JM, Sopko NA, Milner SM. The applied anatomy of human skin: A model for regeneration. *Wound Med*. 2020;28:100179. doi: 10.1016/j.wndm.2020.100179
18. Roger M, Fullard N, Costello L, et al. Bioengineering the microanatomy of human skin. *J Anat*. 2019;234(4):438-455. doi: 10.1111/joa.12942
19. Pincelli C, Marconi A. Keratinocyte stem cells: friends and foes. *J Cell Physiol*. 2010;225(2):310-315. doi: 10.1002/jcp.22275
20. Clayton K, Vallejo AF, Davies J, Sirvent S, Polak ME. Langerhans cells—programmed by the epidermis. *Front Immunol*. 2017;8:1676. doi: 10.3389/fimmu.2017.01676
21. Haeberle H, Lumpkin EA. Merkel cells in somatosensation. *Chemosens Percept*. 2008;1:110-118. doi: 10.1007/s12078-008-9012-6

22. Roig-Rosello E, Rousselle P. The human epidermal basement membrane: a shaped and cell instructive platform that aging slowly alters. *Biomolecules*. 2020;10(12):1607. doi: 10.3390/biom10121607

23. Prost-Squarcioni C, Fraitag S, Heller M, Boehm N. Functional histology of dermis. *Ann Dermatol Venereol*. 2008:1S5-20. doi: 10.1016/s0151-9638(08)70206-0

24. Grinnell F. Fibroblast biology in three-dimensional collagen matrices. *Trends Cell Biol*. 2003;13(5):264-269. doi: 10.1016/s0962-8924(03)00057-6

25. Muiznieks LD, Keeley FW. Molecular assembly and mechanical properties of the extracellular matrix: a fibrous protein perspective. *Biochim Biophys Acta*. 2013;1832(7):866-875. doi: 10.1016/j.bbadis.2012.11.022

26. Moon TC, Befus AD, Kulka M. Mast cell mediators: their differential release and the secretory pathways involved. *Front Immunol*. 2014;5:569. doi: 10.3389/fimmu.2014.00569

27. Driskell RR, Jahoda CA, Chuong CM, Watt FM, Horsley V. Defining dermal adipose tissue. *Exp Dermatol*. 2014;23(9):629-631. doi: 10.1111/exd.12450

28. Driskell RR, Jahoda CA, Chuong CM, Watt FM, Horsley V. Defining dermal adipose tissue. *Exp. Dermatol*. 2014; 23(9):629-631. doi: 10.1111/exd.12450

29. Frueh FS, Menger MD, Lindenblatt N, Giovanoli P, Laschke MW. Current and emerging vascularization strategies in skin tissue engineering. *Crit Rev Biotechnol*. 2016;37(5): 613-625. doi: 10.1080/07388551.2016.1209157

30. Hendrickx B, Vranckx JJ, Luttun A. Cell-based vascularization strategies for skin tissue engineering. *Tissue Eng Part B Rev*. 2011;17(1):13-24. doi: 10.1089/ten.teb.2010.0315

31. Laschke MW, Menger MD. Prevascularization in tissue engineering: current concepts and future directions. *Biotechnol Adv*. 2016;34(2):112-121. doi: 10.1016/j.biotechadv.2015.12.004

32. Laschke M, Menger M. Vascularization in tissue engineering: angiogenesis versus inosculation. *Eur Surg Res*. 2012;48(2):85-92. doi: 10.1159/000336876

33. Johnson KE, Wilgus TA. Vascular endothelial growth factor and angiogenesis in the regulation of cutaneous wound repair. *Adv Wound Care*. 2014;3(10):647-661. doi: 10.1089/wound.2013.0517

34. Kolte D, McClung JA, Aronow WS. Chapter 6 - Vasculogenesis and angiogenesis. In: *Translational Research in Coronary Artery Disease*. New York: Elsevier; 2016:49-65. doi: 10.1016/B978-0-12-802385-3.00006-1

35. Demidova-Rice TN, Durham JT, Herman IM. Wound healing angiogenesis: innovations and challenges in acute and chronic wound healing. *Adv Wound Care*. 2012;1(1):17-22. doi: 10.1089/wound.2011.0308

36. Heller M, Bauer HK, Schwab R, et al. The impact of intercellular communication for the generation of complex multicellular prevascularized tissue equivalents. *J Biomed Mater Res Part A*. 2020;108(3):734-748. doi: 10.1002/jbm.a.36853

37. Liew AWL, Zhang Y. In vitro pre-vascularization strategies for tissue engineered constructs–Bioprinting and others. *Int J Bioprint*. 2017;3(1). doi: 10.18063/iib.2017.01.008

38. Tomasina C, Bodet T, Mota C, Moroni L, Camarero-Espinosa S. Bioprinting vasculature: materials, cells and emergent techniques. *Materials*. 2019;12(17):2701. doi: 10.3390/ma12172701

39. Yang G, Mahadik B, Choi JY, Fisher JP. Vascularization in tissue engineering: fundamentals and state-of-art. *Prog Biomed Eng*. 2020;2(1):012002. doi: 10.1088/2516-1091/ab5637

40. Richardson RJ. Parallels between vertebrate cardiac and cutaneous wound healing and regeneration. *Npj Regener Med*. 2018;3(1):21. doi: 10.1038/s41536-018-0059-y

41. Chandra P, Atala A. Engineering blood vessels and vascularized tissues: technology trends and potential clinical applications. *Clin Sci*. 2019;133(9):1115-1135. doi: 10.1042/cs20180155

42. Min S, Ko IK, Yoo JJ. State-of-the-art strategies for the vascularization of three-dimensional engineered organs. *Vasc Spec Int*. 2019;35(2):77. doi: 10.5758/vsi.2019.35.2.77

43. Sharma D, Ross D, Wang G, Jia W, Kirkpatrick SJ, Zhao F. Upgrading prevascularization in tissue engineering: a review of strategies for promoting highly organized microvascular network formation. *Acta Biomater*. 2019;95:112-130. doi: 10.1016/j.actbio.2019.03.016

44. Takei T, Sakai S, Yoshida M. In vitro formation of vascular-like networks using hydrogels. *J Biosci Bioeng*. 2016;122(5):519-527. doi: 10.1016/j.jbiosc.2016.03.023

45. Wong HK, Lam CRI, Wen F, et al. Novel method to improve vascularization of tissue engineered constructs with biodegradable fibers. *Biofabrication*. 2016;8(1):015004. doi: 10.1088/1758-5090/8/1/015004

46. Datta P, Ayan B, Ozbolat IT. Bioprinting for vascular and vascularized tissue biofabrication. *Acta Biomater*. 2017; 51:1-20. doi: 10.1016/j.actbio.2017.01.035

47. Herrmann M, Binder A, Menzel U, Zeiter S, Alini M, Verrier S. CD34/CD133 enriched bone marrow progenitor cells

promote neovascularization of tissue engineered constructs in vivo. *Stem Cell Res*. 2014;13(3):465-477.
doi: 10.1016/j.scr.2014.10.005

48. Kniebs C, Kreimendahl F, Köpf M, Fischer H, Jockenhoevel S, Thiebes AL. Influence of different cell types and sources on pre-vascularisation in fibrin and agarose–collagen gels. *Organogenesis*. 2020;16(1):14-26.
doi: 10.1080/15476278.2019.1697597

49. Liu X, Chen W, Zhang C, et al. Co-seeding human endothelial cells with human-induced pluripotent stem cell-derived mesenchymal stem cells on calcium phosphate scaffold enhances osteogenesis and vascularization in rats. *Tissue Eng Part A*. 2017;23(11-12):546-555.
doi: 10.1089/ten.tea.2016.0485

50. Rouwkema J, Khademhosseini A. Vascularization and angiogenesis in tissue engineering: beyond creating static networks. *Trends Biotechnol*. 2016;34(9):733-745.
doi: 10.1016/j.tibtech.2016.03.002

51. Sarker M, Chen X, Schreyer D. Experimental approaches to vascularisation within tissue engineering constructs. *J Biomater Sci*. 2015;26(12):683-734.
doi: 10.1080/09205063.2015.1059018

52. Xiao X, Wang W, Liu D, et al. The promotion of angiogenesis induced by three-dimensional porous beta-tricalcium phosphate scaffold with different interconnection sizes via activation of PI3K/Akt pathways. *Sci Rep*. 2015;5(1):9409.
doi: 10.1038/srep09409

53. Xie R, Zheng W, Guan L, Ai Y, Liang Q. Engineering of hydrogel materials with perfusable microchannels for building vascularized tissues. *Small*. 2020;16(15):1902838.
doi: 10.1002/smll.201902838

54. Blatchley MR, Hall F, Wang S, Pruitt HC, Gerecht S. Hypoxia and matrix viscoelasticity sequentially regulate endothelial progenitor cluster-based vasculogenesis. *Sci Adv*. 2019;5(3):eaau7518.
doi: 10.1126/sciadv.aau7518

55. Auger FA, Gibot L, Lacroix D. The pivotal role of vascularization in tissue engineering. *Annu Rev Biomed Eng*. 2013;15:177-200.
doi: 10.1146/annurev-bioeng-071812-152428

56. Phua QH, Han HA, Soh B-S. Translational stem cell therapy: vascularized skin grafts in skin repair and regeneration. *J Transl Med*. 2021;19:1-11.
doi: 10.1186/s12967-021-02752-2

57. Gao C, Lu C, Qiao H, et al. Strategies for vascularized skin models in vitro. *Biomater Sci*. 2022;10(17):4724-4739.
doi: 10.1039/d2bm00784c

58. Baldwin J, Antille M, Bonda U, et al. In vitro pre-vascularisation of tissue-engineered constructs A co-culture perspective. *Vasc Cell*. 2014;6:1-16.
doi: 10.1186/2045-824x-6-13

59. Costa-Almeida R, Granja P, Soares R, Guerreiro S. Cellular strategies to promote vascularisation in tissue engineering applications. *Eur Cell Mater*. 2014;28:51-66.
doi: 10.22203/ecm.v028a05

60. Heller M, Frerick-Ochs E, Bauer H-K, et al. Tissue engineered pre-vascularized buccal mucosa equivalents utilizing a primary triculture of epithelial cells, endothelial cells and fibroblasts. *Biomaterials*. 2016;77:207-215.
doi: 10.1016/j.biomaterials.2015.10.073

61. Um Min Allah N, Berahim Z, Ahmad A, Kannan TP. Biological interaction between human gingival fibroblasts and vascular endothelial cells for angiogenesis: a co-culture perspective. *Tissue Eng Regener Med*. 2017;14:495-505.
doi: 10.1007/s13770-017-0065-y

62. Weinandy S, Laffar S, Unger RE, et al. Biofunctionalized microfiber-assisted formation of intrinsic three-dimensional capillary-like structures. *Tissue Eng Part A*. 2014;20(13-14):1858-1869.
doi: 10.1089/ten.tea.2013.0330

63. Miyazaki H, Tsunoi Y, Akagi T, Sato S, Akashi M, Saitoh D. A novel strategy to engineer pre-vascularized 3-dimensional skin substitutes to achieve efficient, functional engraftment. *Sci Rep*. 2019;9(1):7797.
doi: 10.1038/s41598-019-44113-6

64. Costa-Almeida R, Gomez-Lazaro M, Ramalho C, Granja PL, Soares R, Guerreiro SG. Fibroblast-endothelial partners for vascularization strategies in tissue engineering. *Tissue Eng Part A*. 2015;21(5-6):1055-1065.
doi: 10.1089/ten.tea.2014.0443

65. Morin KT, Tranquillo RT. In vitro models of angiogenesis and vasculogenesis in fibrin gel. *Exp Cell Res*. 2013;319(16):2409-2417.
doi: 10.1016/j.yexcr.2013.06.006

66. Wan X, Bovornchutichai P, Cui Z, O'Neill E, Ye H. Morphological analysis of human umbilical vein endothelial cells co-cultured with ovarian cancer cells in 3D: an oncogenic angiogenesis assay. *PLoS One*. 2017;12(7):e0180296.
doi: 10.1371/journal.pone.0180296

67. Ren L, Ma D, Liu B, et al. Preparation of three-dimensional vascularized MSC cell sheet constructs for tissue regeneration. *BioMed Res Int*. 2014;2014.
doi: 10.1155/2014/301279

68. Liu X, Michael S, Bharti K, Ferrer M, Song MJ. A biofabricated vascularized skin model of atopic dermatitis for preclinical studies. *Biofabrication*. 2020;12(3):035002.
doi: 10.1088/1758-5090/ab76a1

69. Murphy SV, Atala A. 3D bioprinting of tissues and organs. *Nat Biotechnol*. 2014;32(8):773-785.
doi: 10.1038/nbt.2958

70. Ng WL, Wang S, Yeong WY, Naing MW. Skin bioprinting: impending reality or fantasy? *Trends Biotechnol*. 2016;34(9):689-699.
doi: 10.1016/j.tibtech.2016.04.006

71. Guillotin B, Guillemot F. Cell patterning technologies for organotypic tissue fabrication. *Trends Biotechnol*. 2011;29(4):183-190. doi: 10.1016/j.tibtech.2010.12.008

72. Lee W, Debasitis JC, Lee VK, et al. Multi-layered culture of human skin fibroblasts and keratinocytes through three-dimensional freeform fabrication. *Biomaterials*. 2009;30(8):1587-1595. doi: 10.1016/j.biomaterials.2008.12.009

73. Binder KW, Zhao W, Aboushwareb T, Dice D, Atala A, Yoo JJ. In situ bioprinting of the skin for burns. *J Am Coll Surg*. 2010;211(3):S76. doi: 10.1016/j.jamcollsurg.2010.06.198

74. Koch L, Deiwick A, Schlie S, et al. Skin tissue generation by laser cell printing. *Biotechnol Bioeng*. 2012;109(7): 1855-1863. doi: 10.1002/bit.24455

75. Richards D, Jia J, Yost M, Markwald R, Mei Y. 3D bioprinting for vascularized tissue fabrication. *Ann Biomed Eng*. 2017;45:132-147. doi: 10.1007/s10439-016-1653-z

76. Yu J, Park SA, Kim WD, et al. Current advances in 3D bioprinting technology and its applications for tissue engineering. *Polymers*. 2020;12(12):2958. doi: 10.3390/polym12122958

77. Klebe RJ. Cytoscribing: a method for micropositioning cells and the construction of two-and three-dimensional synthetic tissues. *Exp Cell Res*. 1988;179(2):362-373. doi: 10.1016/0014-4827(88)90275-3

78. Zikulnig J, Kosel J. Fabrication technologies for flexible printed sensors. In: *Encyclopedia of Sensors and Biosensors*. New York: Elsevier; 2023:33–50. doi: 10.1016/b978-0-12-822548-6.00010-8

79. Cui X, Boland T. Human microvasculature fabrication using thermal inkjet printing technology. *Biomaterials*. 2009;30(31):6221-6227. doi: 10.1016/j.biomaterials.2009.07.056

80. Malda J, Visser J, Melchels FP, et al. 25th anniversary article: engineering hydrogels for biofabrication. *Adv Mater*. 2013;25(36):5011-5028. doi: 10.1002/adma.201302042

81. Cui X, Boland T, DD'Lima D, Lotz MK. Thermal inkjet printing in tissue engineering and regenerative medicine. *Recent Pat Drug Delivery Formulation*. 2012;6(2):149-155. doi: 10.2174/187221112800672949

82. Cui X, Dean D, Ruggeri ZM, Boland T. Cell damage evaluation of thermal inkjet printed Chinese hamster ovary cells. *Biotechnol Bioeng*. 2010;106(6):963-969. doi: 10.1002/bit.22762

83. Ning L, Chen X. A brief review of extrusion-based tissue scaffold bio-printing. *Biotechnol J*. 2017;12(8):1600671. doi: 10.1002/biot.201600671

84. Kim BS, Lee J-S, Gao G, Cho D-W. Direct 3D cell-printing of human skin with functional transwell system. *Biofabrication*. 2017;9(2):025034. doi: 10.1088/1758-5090/aa71c8

85. Ramasamy S, Davoodi P, Vijayavenkataraman S, et al. Optimized construction of a full thickness human skin equivalent using 3D bioprinting and a PCL/collagen dermal scaffold. *Bioprinting*. 2021;21:e00123. doi: 10.1016/j.bprint.2020.e00123

86. Park JH, Ahn M, Park SH, et al. 3D bioprinting of a trachea-mimetic cellular construct of a clinically relevant size. *Biomaterials*. 2021;279:121246. doi: 10.1016/j.biomaterials.2021.121246

87. Choi Y-J, Jun Y-J, Kim DY, et al. A 3D cell printed muscle construct with tissue-derived bioink for the treatment of volumetric muscle loss. *Biomaterials*. 2019;206:160-169. doi: 10.1016/j.biomaterials.2019.03.036

88. Kang H-W, Lee SJ, Ko IK, Kengla C, Yoo JJ, Atala A. A 3D bioprinting system to produce human-scale tissue constructs with structural integrity. *Nat Biotechnol*. 2016;34(3): 312-319. doi: 10.1038/nbt.3413

89. Ma Y, Wang Y, Chen D, et al. 3D bioprinting of a gradient stiffened gelatin–alginate hydrogel with adipose-derived stem cells for full-thickness skin regeneration. *J Mater Chem B*. 2023;11(13):2989-3000. doi: 10.1039/d2tb02200a

90. Pati F, Jang J, Ha D-H, et al. Printing three-dimensional tissue analogues with decellularized extracellular matrix bioink. *Nat Commun*. 2014;5(1):3935. doi: 10.1038/ncomms4935

91. Ahn M, Cho WW, Lee H, et al. Engineering of uniform epidermal layers via sacrificial gelatin bioink-assisted 3D extrusion bioprinting of skin. *Adv Healthc Mater*. 2023:2301015. doi: 10.1002/adhm.202301015

92. Odde DJ, Renn MJ. Laser-guided direct writing for applications in biotechnology. *Trends Biotechnol*. 1999;17(10):385-389. doi: 10.1016/s0167-7799(99)01355-4

93. Derakhshanfar S, Mbeleck R, Xu K, Zhang X, Zhong W, Xing M. 3D bioprinting for biomedical devices and tissue engineering: a review of recent trends and advances. *Bioact Mater*. 2018;3(2):144-156. doi: 10.1016/j.bioactmat.2017.11.008

94. Li H, Tan C, Li L. Review of 3D printable hydrogels and constructs. *Mater Des*. 2018;159:20-38. doi: 101016/jmatdes201808023

95. Donderwinkel I, Van Hest JC, Cameron NR. Bio-inks for 3D bioprinting: recent advances and future prospects. *Polym Chem*. 2017;8(31):4451-4471. doi: 10.1039/C7PY00826K

96. Catros S, Guillotin B, Bačáková M, Fricain J-C, Guillemot F. Effect of laser energy, substrate film thickness and bioink viscosity on viability of endothelial cells printed by laser-assisted bioprinting. *Appl Surf Sci*. 2011;257(12): 5142-5147.
doi: 10.1016/j.apsusc.2010.11.049

97. Magalhães LSS, Santos FEP, Elias CdMV, et al. Printing 3D hydrogel structures employing low-cost stereolithography technology. *J Funct Biomater*. 2020;11(1):12.
doi: 10.3390/jfb11010012

98. Choi KY, Ajiteru O, Hong H, et al. A digital light processing 3D-printed artificial skin model and full-thickness wound models using silk fibroin bioink. *Acta Biomater*. 2023;164:159-174.
doi: 10.1016/j.actbio.2023.04.034

99. Zhang G, Zhang Z, Cao G, et al. Engineered dermis loaded with confining forces promotes full-thickness wound healing by enhancing vascularisation and epithelialisation. *Acta Biomater*. 2023;170:464-478.
doi: 10.1016/j.actbio.2023.08.049

100. Xu T, Binder KW, Albanna MZ, et al. Hybrid printing of mechanically and biologically improved constructs for cartilage tissue engineering applications. *Biofabrication*. 2012;5(1):015001.
doi: 10.1088/1758-5082/5/1/015001

101. Gudapati H, Dey M, Ozbolat I. A comprehensive review on droplet-based bioprinting: past, present and future. *Biomaterials*. 2016;102:20-42.
doi: 10.1016/j.biomaterials.2016.06.012

102. LaBarge W, Morales A, Pretorius D, Kahn-Krell AM, Kannappan R, Zhang J. Scaffold-free bioprinter utilizing layer-by-layer printing of cellular spheroids. *Micromachines*. 2019;10(9):570.
doi: 10.3390/mi10090570

103. Hakimi N, Cheng R, Leng L, et al. Handheld skin printer: in situ formation of planar biomaterials and tissues. *Lab Chip*. 2018;18(10):1440-1451.
doi: 10.1039/c7lc01236e

104. Vijayavenkataraman S, Lu W, Fuh J. 3D bioprinting of skin: a state-of-the-art review on modelling, materials, and processes. *Biofabrication*. 2016;8(3):032001.
doi: 10.1088/1758-5090/8/3/032001

105. Matai I, Kaur G, Seyedsalehi A, McClinton A, Laurencin CT. Progress in 3D bioprinting technology for tissue/organ regenerative engineering. *Biomaterials*. 2020;226:119536.
doi: 10.1016/j.biomaterials.2019.119536

106. Ning L, Gil CJ, Hwang B, et al. Biomechanical factors in three-dimensional tissue bioprinting. *Appl Phys Rev*. 2020;7(4):041319.
doi: 10.1016/j.biomaterials.2019.119536

107. Zorlutuna P, Vrana NE, Khademhosseini A. The expanding world of tissue engineering: the building blocks and new applications of tissue engineered constructs. *IEEE Rev Biomed Eng*. 2012;6:47-62.
doi: 10.1109/rbme.2012.2233468

108. Wang Y, Kankala RK, Ou C, Chen A, Yang Z. Advances in hydrogel-based vascularized tissues for tissue repair and drug screening. *Bioact Mater*. 2022;9:198-220.
doi: 10.1016/j.bioactmat.2021.07.005

109. Bedell ML, Navara AM, Du Y, Zhang S, Mikos AG. Polymeric systems for bioprinting. *Chem Rev*. 2020;120(19): 10744-10792.
doi: 10.1021/acs.chemrev.9b00834

110. Nyström A, Bruckner-Tuderman L. Matrix molecules and skin biology. In: *Seminars in Cell & Developmental Biology*. New York: Elsevier; 2019;89:136-146.
doi: 10.1016/j.semcdb.2018.07.025

111. Wells A, Nuschke A, Yates CC. Skin tissue repair: matrix microenvironmental influences. *Matrix Biol*. 2016; 49:25-36.
doi: 10.1016/j.matbio.2015.08.001

112. Dzobo K, Motaung KSCM, Adesida A. Recent trends in decellularized extracellular matrix bioinks for 3D printing: an updated review. *Int J Mol Sci*. 2019;20(18):4628.
doi: 10.3390/ijms20184628

113. Kim BS, Das S, Jang J, Cho D-W. Decellularized extracellular matrix-based bioinks for engineering tissue-and organ-specific microenvironments. *Chem Rev*. 2020;120(19): 10608-10661.
doi: 10.1021/acs.chemrev.9b00808

114. Choudhury D, Tun HW, Wang T, Naing MW. Organ-derived decellularized extracellular matrix: a game changer for bioink manufacturing? *Trends Biotechnol*. 2018;36(8):787-805.
doi: 10.1016/j.tibtech.2018.03.003

115. Kim BS, Kim H, Gao G, Jang J, Cho D-W. Decellularized extracellular matrix: a step towards the next generation source for bioink manufacturing. *Biofabrication*. 2017;9(3):034104.
doi: 10.1088/1758-5090/aa7e98

116. Kim BS, Kwon YW, Kong J-S, et al. 3D cell printing of in vitro stabilized skin model and in vivo pre-vascularized skin patch using tissue-specific extracellular matrix bioink: A step towards advanced skin tissue engineering. *Biomaterials*. 2018;168:38-53.
doi: 10.1016/j.biomaterials.2018.03.040

117. Jorgensen AM, Chou Z, Gillispie G, et al. Decellularized skin extracellular matrix (dsECM) improves the physical and biological properties of fibrinogen hydrogel for skin bioprinting applications. *Nanomaterials*. 2020;10(8):1484.
doi: 10.3390/nano10081484

118. Zhang Q, Johnson JA, Dunne LW, et al. Decellularized skin/adipose tissue flap matrix for engineering vascularized composite soft tissue flaps. *Acta Biomater*. 2016;35:166-184.
doi: 10.1016/j.actbio.2016.02.017

119. Parmaksiz M, Elçin AE, Elçin YM. Decellularized bSIS-ECM as a regenerative biomaterial for skin wound repair. *Skin Stem Cell Methods Protoc*. 2019:175-185. doi: 10.1007/7651_2018_147

120. Abaci A, Guvendiren M. Designing decellularized extracellular matrix-based bioinks for 3D bioprinting. *Adv Healthc Mater*. 2020;9(24):2000734. doi: 10.1002/adhm.202000734

121. Velasco D, Quílez C, Garcia M, del Cañizo JF, Jorcano JL. 3D human skin bioprinting: a view from the bio side. *J 3D Print Med*. 2018:141-162. doi: 10.2217/3dp-2018-0008

122. Hayden P, Ayehunie S, Jackson G, et al. In vitro skin equivalent models for toxicity testing. In: *Alternative Toxicological Methods*. Boca Raton, FL: CRC Press; 2003:229-247. doi: 10.1201/9780203008799.ch20

123. Schmook FP, Meingassner JG, Billich A. Comparison of human skin or epidermis models with human and animal skin in in-vitro percutaneous absorption. *Int J Pharm*. 2001;215(1-2):51-56. doi: 10.1016/s0378-5173(00)00665-7

124. Almeida A, Sarmento B, Rodrigues F. Insights on in vitro models for safety and toxicity assessment of cosmetic ingredients. *Int J Pharm*. 2017;519(1-2):178-185. doi: 10.1016/j.ijpharm.2017.01.024

125. Liebsch M, Grune B, Seiler A, et al. Alternatives to animal testing: current status and future perspectives. *Arch Toxicol*. 2011;85:841-858. doi: 10.1007/s00204-011-0718-x

126. Yanez M, Rincon J, Dones A, De Maria C, Gonzales R, Boland T. In vivo assessment of printed microvasculature in a bilayer skin graft to treat full-thickness wounds. *Tissue Eng Part A*. 2015;21(1-2):224-233. doi: 10.1089/ten.tea.2013.0561

127. Kim BS, Gao G, Kim JY, Cho DW. 3D cell printing of perfusable vascularized human skin equivalent composed of epidermis, dermis, and hypodermis for better structural recapitulation of native skin. *Adv Healthc Mater*. 2019;8(7):1801019. doi: 10.1002/adhm.201801019

128. Abaci HE, Coffman A, Doucet Y, et al. Tissue engineering of human hair follicles using a biomimetic developmental approach. *Nat Commun*. 2018;9(1):5301. doi: 10.1038/s41467-018-07579-y

129. Pontiggia L, Van Hengel IA, Klar A, et al. Bioprinting and plastic compression of large pigmented and vascularized human dermo-epidermal skin substitutes by means of a new robotic platform. *J Tissue Eng*. 2022;13:20417314221088513. doi: 10.1177/20417314221088513

130. Naomi R, Ridzuan PM, Bahari H. Current insights into collagen type I. *Polymers*. 2021;13(16):2642. doi: 10.3390/polym13162642

131. Zhang X, Li J, Ye P, Gao G, Hubbell K, Cui X. Coculture of mesenchymal stem cells and endothelial cells enhances host tissue integration and epidermis maturation through AKT activation in gelatin methacryloyl hydrogel-based skin model. *Acta Biomater*. 2017;59:317-326. doi: 10.1016/j.actbio.2017.07.001

132. Baltazar T, Merola J, Catarino C, et al. Three dimensional bioprinting of a vascularized and perfusable skin graft using human keratinocytes, fibroblasts, pericytes, and endothelial cells. *Tissue Eng Part A*. 2020;26(5-6):227-238. doi: 10.1089/ten.tea.2019.0201

133. Kolesky DB, Homan KA, Skylar-Scott MA, Lewis JA. Three-dimensional bioprinting of thick vascularized tissues. *Proc Natl Acad Sci*. 2016;113(12):3179-3184. doi: 10.1073/pnas.1521342113

134. Ng WL, Qi JTZ, Yeong WY, Naing MW. Proof-of-concept: 3D bioprinting of pigmented human skin constructs. *Biofabrication*. 2018;10(2):025005. doi: 10.1088/1758-5090/aa9e1e

135. Ma J, Qin C, Wu J, et al. 3D printing of strontium silicate microcylinder-containing multicellular biomaterial inks for vascularized skin regeneration. *Adv Healthc Mater*. 2021;10(16):2100523. doi: 10.1002/adhm.202100523

136. Heinemann S, Coradin T, Desimone MF. Bio-inspired silica–collagen materials: applications and perspectives in the medical field. *Biomater Sci*. 2013;1(7):688-702. doi: 10.1039/c3bm00014a

137. Desimone MF, Hélary C, Mosser G, Giraud-Guille M-M, Livage J, Coradin T. Fibroblast encapsulation in hybrid silica–collagen hydrogels. *J Mater Chem*. 2010;20(4):666-668. doi: 10.1039/B921572G

138. Desimone MF, Hélary C, Rietveld IB, et al. Silica–collagen bionanocomposites as three-dimensional scaffolds for fibroblast immobilization. *Acta Biomater*. 2010;6(10):3998-4004. doi: 10.1016/j.actbio.2010.05.014

139. Pouroutzidou GK, Liverani L, Theocharidou A, et al. Synthesis and characterization of mesoporous mg-and sr-doped nanoparticles for moxifloxacin drug delivery in promising tissue engineering applications. *Int J Mol Sci*. 2021;22(2):577. doi: 10.3390/ijms22020577

140. Mao L, Xia L, Chang J, et al. The synergistic effects of Sr and Si bioactive ions on osteogenesis, osteoclastogenesis and angiogenesis for osteoporotic bone regeneration. *Acta Biomater*. 2017;61:217-232. doi: 10.1016/j.actbio.2017.08.015

141. Dikici S, Claeyssens F, MacNeil S. Bioengineering vascular networks to study angiogenesis and vascularization of

physiologically relevant tissue models in vitro. *ACS Biomater Sci Eng*. 2020;6(6):3513-3528.
doi: 10.1021/acsbiomaterials.0c00191

142. Abaci HE, Guo Z, Coffman A, et al. Human skin constructs with spatially controlled vasculature using primary and iPSC-derived endothelial cells. *Adv Healthc Mater*. 2016;5(14):1800-1807.
doi: 10.1002/adhm.201500936

143. Schneider J, Biedermann T, Widmer D, et al. Matriderm® versus Integra®: a comparative experimental study. *Burns*. 2009;35(1):51-57.
doi: 10.1016/j.burns.2008.07.018

144. Choi SW, Zhang Y, MacEwan MR, Xia Y. Neovascularization in biodegradable inverse opal scaffolds with uniform and precisely controlled pore sizes. *Adv Healthc Mater*. 2013;2(1):145-154.
doi: 10.1002/adhm.201200106

145. van Zuijlen PP, Vloemans JF, van Trier AJ, et al. Dermal substitution in acute burns and reconstructive surgery: a subjective and objective long-term follow-up. *Plast Reconstr Surg*. 2001;108(7):1938-1946.
doi: 10.1097/00006534-200112000-00014

146. Ring A, Langer S, Schaffran A, et al. Enhanced neovascularization of dermis substitutes via low-pressure plasma-mediated surface activation. *Burns*. 2010;36(8):1222-1227.
doi: 10.1016/j.burns.2010.03.002

147. Shaterian A, Borboa A, Sawada R, et al. Real-time analysis of the kinetics of angiogenesis and vascular permeability in an animal model of wound healing. *Burns*. 2009;35(6):811-817.
doi: 10.1016/j.burns.2008.12.012

148. Supp DM, Boyce ST. Engineered skin substitutes: practices and potentials. *Clin Dermatol*. 2005;23(4):403-412.
doi: 10.1016/j.clindermatol.2004.07.023

149. Cam C, Zhu S, Truong NF, Scumpia PO, Segura T. Systematic evaluation of natural scaffolds in cutaneous wound healing. *J Mater Chem B*. 2015;3(40):7986-7992.
doi: 10.1039/c5tb00807g

150. Griffin M, Naderi N, Kalaskar D, Seifalian A, Butler P. Argon plasma surface modification promotes the therapeutic angiogenesis and tissue formation of tissue-engineered scaffolds in vivo by adipose-derived stem cells. *Stem Cell Res Ther*. 2019;10:1-14.
doi: 10.1186/s13287-019-1195-z

151. Liu Q, Huang Y, Lan Y, et al. Acceleration of skin regeneration in full-thickness burns by incorporation of bFGF-loaded alginate microspheres into a CMCS–PVA hydrogel. *J Tissue Eng Regener Med*. 2017;11(5):1562-1573.
doi: 10.1002/term.2057

152. Guo R, Xu S, Ma L, Huang A, Gao C. Enhanced angiogenesis of gene-activated dermal equivalent for treatment of full thickness incisional wounds in a porcine model. *Biomaterials*. 2010;31(28):7308-7320.
doi: 10.1016/j.biomaterials.2010.06.013

153. Guo R, Xu S, Ma L, Huang A, Gao C. The healing of full-thickness burns treated by using plasmid DNA encoding VEGF-165 activated collagen–chitosan dermal equivalents. *Biomaterials*. 2011;32(4):1019-1031.
doi: 10.1016/j.biomaterials.2010.08.087

154. Yang Y, Xia T, Chen F, et al. Electrospun fibers with plasmid bFGF polyplex loadings promote skin wound healing in diabetic rats. *Mol Pharm*. 2012;9(1):48-58.
doi: 10.1021/mp200246b

155. Reckhenrich AK, Hopfner U, Krötz F, et al. Bioactivation of dermal scaffolds with a non-viral copolymer-protected gene vector. *Biomaterials*. 2011;32(7):1996-2003.
doi: 10.1016/j.biomaterials.2010.11.022

156. Scherer SS, Pietramaggiori G, Matthews J, et al. Poly-N-acetyl glucosamine nanofibers: a new bioactive material to enhance diabetic wound healing by cell migration and angiogenesis. *Ann Surg*. 2009;250(2):322-330.
doi: 10.1097/sla.0b013e3181ae9d45

157. Zhao S, Li L, Wang H, et al. Wound dressings composed of copper-doped borate bioactive glass microfibers stimulate angiogenesis and heal full-thickness skin defects in a rodent model. *Biomaterials*. 2015;53:379-391.
doi: 10.1016/j.biomaterials.2015.02.112

158. Wang X, You C, Hu X, et al. The roles of knitted mesh-reinforced collagen–chitosan hybrid scaffold in the one-step repair of full-thickness skin defects in rats. *Acta Biomater*. 2013;9(8):7822-7832.
doi: 10.1016/j.actbio.2013.04.017

159. Sun G, Zhang X, Shen Y-I, et al. Dextran hydrogel scaffolds enhance angiogenic responses and promote complete skin regeneration during burn wound healing. *Proc Natl Acad Sci*. 2011;108(52):20976-20981.
doi: 10.1073/pnas.1115973108

160. Hohlfeld J, de Buys Roessingh A, Hirt-Burri N, et al. Tissue engineered fetal skin constructs for paediatric burns. *Lancet*. 2005;366(9488):840-842.
doi: 10.1016/s0140-6736(05)67107-3

161. Tonello C, Zavan B, Cortivo R, Brun P, Panfilo S, Abatangelo G. In vitro reconstruction of human dermal equivalent enriched with endothelial cells. *Biomaterials*. 2003;24(7):1205-1211.
doi: 10.1016/s0142-9612(02)00450-7

162. Hudon V, Berthod F, Black A, Damour O, Germain L, Auger F. A tissue-engineered endothelialized dermis to study the modulation of angiogenic and angiostatic molecules on capillary-like tube formation in vitro. *Br J Dermatol*. 2003;148(6):1094-1104.
doi: 10.1046/j.1365-2133.2003.05298.x

163. Black AF, Berthod F, L'Heureux N, Germain L, Auger FA. In vitro reconstruction of a human capillary-like network in a tissue-engineered skin equivalent. *FASEB J*. 1998;12(13):1331-1340.
doi: 10.1046/j.1365-2133.2003.05298.x

164. Tremblay P-L, Hudon V, Berthod F, Germain L, Auger FA. Inosculation of tissue-engineered capillaries with the host's vasculature in a reconstructed skin transplanted on mice. *Am J Transplant*. 2005;5(5):1002-1010. doi: 10.1111/j.1600-6143.2005.00790.x

165. Asahara T, Murohara T, Sullivan A, et al. Isolation of putative progenitor endothelial cells for angiogenesis. *Science*. 1997;275(5302):964-966. doi: 10.1126/science.275.5302.964

166. Sander AL, Jakob H, Henrich D, et al. Systemic transplantation of progenitor cells accelerates wound epithelialization and neovascularization in the hairless mouse ear wound model. *J Surg Res*. 2011;165(1):165-170. doi: 10.1016/j.jss.2009.07.003

167. Ingram DA, Mead LE, Tanaka H, et al. Identification of a novel hierarchy of endothelial progenitor cells using human peripheral and umbilical cord blood. *Blood*. 2004;104(9):2752-2760. doi: 10.1182/blood-2004-04-1396

168. Kaushal S, Amiel GE, Guleserian KJ, et al. Functional small-diameter neovessels created using endothelial progenitor cells expanded ex vivo. *Nat Med*. 2001;7(9):1035-1040. doi: 10.1038/nm0901-1035

169. Hendrickx B, Verdonck K, Van den Berge S, et al. Integration of blood outgrowth endothelial cells in dermal fibroblast sheets promotes full thickness wound healing. *Stem Cell*. 2010;28(7):1165-1177. doi: 10.1002/stem.445

170. Tiruvannamalai Annamalai R, Rioja AY, Putnam AJ, Stegemann JP. Vascular network formation by human microvascular endothelial cells in modular fibrin microtissues. *ACS Biomater Sci Eng*. 2016;2(11):1914-1925. doi: 10.1021/acsbiomaterials.6b00274

171. Kinnaird T, Stabile E, Burnett M, et al. Marrow-derived stromal cells express genes encoding a broad spectrum of arteriogenic cytokines and promote in vitro and in vivo arteriogenesis through paracrine mechanisms. *Circ Res*. 2004;94(5):678-685. doi: 10.1161/01.res.0000118601.37875.ac

172. Yoshikawa T, Mitsuno H, Nonaka I, et al. Wound therapy by marrow mesenchymal cell transplantation. *Plast Reconstr Surg*. 2008;121(3):860-877. doi: 10.1097/01.prs.0000299922.96006.24

173. Moioli EK, Clark PA, Chen M, et al. Synergistic actions of hematopoietic and mesenchymal stem/progenitor cells in vascularizing bioengineered tissues. *PLoS One*. 2008;3(12):e3922. doi: 10.1371/journal.pone.0003922

174. Liu P, Deng Z, Han S, et al. Tissue-engineered skin containing mesenchymal stem cells improves burn wounds. *Artif Organs*. 2008;32(12):925-931. doi: 10.1111/j.1525-1594.2008.00654.x

175. Altman AM, Yan Y, Matthias N, et al. IFATS collection: human adipose-derived stem cells seeded on a silk fibroin-chitosan scaffold enhance wound repair in a murine soft tissue injury model. *Stem Cell*. 2009;27(1):250-258. doi: 10.1634/stemcells.2008-0178

176. Gang E, Jeong J, Han S, Yan Q, Jeon C, Kim H. In vitro endothelial potential of human UC blood-derived mesenchymal stem cells. *Cytotherapy*. 2006;8(3): 215-227. doi: 10.1080/14653240600735933

177. Koponen JK, Kekarainen T, Heinonen SE, et al. Umbilical cord blood–derived progenitor cells enhance muscle regeneration in mouse hindlimb ischemia model. *Mol Ther*. 2007;15(12):2172-2177. doi: 10.1038/sj.mt.6300302

178. Wang Z, Zheng L, Lian C, Qi Y, Li W, Wang S. Human umbilical cord-derived mesenchymal stem cells relieve hind limb ischemia by promoting angiogenesis in mice. *Stem Cell Dev*. 2019;28(20):1384-1397. doi: 10.1089/scd.2019.0115

179. Chen X, Yue Z, Winberg PC, Lou Y-R, Beirne S, Wallace GG. 3D bioprinting dermal-like structures using species-specific ulvan. *Biomater Sci*. 2021;9(7):2424-2438. doi: 10.1039/d0bm01784a

180. Liu P, Shen H, Zhi Y, et al. 3D bioprinting and in vitro study of bilayered membranous construct with human cells-laden alginate/gelatin composite hydrogels. *Colloid Surf B*. 2019;181:1026-1034. doi: 10.1016/j.colsurfb.2019.06.069

181. Lee V, Singh G, Trasatti JP, et al. Design and fabrication of human skin by three-dimensional bioprinting. *Tissue Eng Part C*. 2014;20(6):473-484. doi: 10.1089/ten.tec.2013.0335

182. Shi Y, Xing T, Zhang H, et al. Tyrosinase-doped bioink for 3D bioprinting of living skin constructs. *Biomed Mater*. 2018;13(3):035008. doi: 10.1088/1748-605x/aaa5b6

183. Huang S, Yao B, Xie J, Fu X. 3D bioprinted extracellular matrix mimics facilitate directed differentiation of epithelial progenitors for sweat gland regeneration. *Acta Biomater*. 2016;32:170-177. doi: 10.1016/j.actbio.2015.12.039

184. Wang S, Xiong Y, Chen J, et al. Three dimensional printing bilayer membrane scaffold promotes wound healing. *Front Bioeng Biotechnol*. 2019;7:348. doi: 10.3389/fbioe.2019.00348

185. Zidarič T, Milojević M, Gradišnik L, Stana Kleinschek K, Maver U, Maver T. Polysaccharide-based bioink formulation for 3D bioprinting of an in vitro model of the human dermis. *Nanomaterials*. 2020;10(4):733. doi: 10.3390/nano10040733

186. Intini C, Elviri L, Cabral J, et al. 3D-printed chitosan-based scaffolds: an in vitro study of human skin cell growth and an in-vivo wound healing evaluation in experimental diabetes in rats. *Carbohydr Polym*. 2018;199:593-602.
doi: 10.1016/j.carbpol.2018.07.057

187. Ng WL, Yeong WY, Naing MW. Development of polyelectrolyte chitosan-gelatin hydrogels for skin bioprinting. *Procedia Cirp*. 2016;49:105-112.
doi: 10.1016/j.procir.2015.09.002

188. Cubo N, Garcia M, Del Canizo JF, Velasco D, Jorcano JL. 3D bioprinting of functional human skin: production and in vivo analysis. *Biofabrication*. 2016;9(1):015006.
doi: 10.1088/1758-5090/9/1/015006

189. Hafezi F, Shorter S, Tabriz AG, et al. Bioprinting and preliminary testing of highly reproducible novel bioink for potential skin regeneration. *Pharmaceutics*. 2020;12(6):550.
doi: 10.3390/pharmaceutics12060550

190. Kwak H, Shin S, Lee H, Hyun J. Formation of a keratin layer with silk fibroin-polyethylene glycol composite hydrogel fabricated by digital light processing 3D printing. *J Ind Eng Chem*. 2019;72:232-240.
doi: 10.1016/j.jiec.2018.12.023

191. Azadmanesh F, Pourmadadi M, Zavar Reza J, Yazdian F, Omidi M, Haghirosadat BF. Synthesis of a novel nanocomposite containing chitosan as a three-dimensional printed wound dressing technique: Emphasis on gene expression. *Biotechnol Prog*. 2021;37(4):e3132.
doi: 10.1002/btpr.3132

ACCSCIENCE PUBLISHING

International Journal of Bioprinting

REVIEW ARTICLE

Challenges and perspectives of liver tissue engineering: From cell therapy to bioprinting

Julio Rodríguez-Fernández[1], M. Teresa Donato[2,3,4], Gloria Gallego-Ferrer[1,5]*, and Laia Tolosa[2,5]*

[1]Center for Biomaterials and Tissue Engineering (CBIT), Universitat Politècnica de València, Valencia, Spain

[2]Experimental Hepatology Unit, Health Research Institute La Fe (IISLAFE), Valencia, Spain

[3]Departament of Biochemistry and Molecular Biology, Faculty of Medicine, Universitat de València, Valencia, Spain

[4]Biomedical Research Networking Center on Hepatic and Digestive Diseases (CIBER-EHD), Valencia, Spain

[5]Biomedical Research Networking Center on Bioengineering, Biomaterials and Nanomedicine (CIBER-BBN), Valencia, Spain

(This article belongs to the *Special Issue: Innovative Tissue and Diseases Models - Novelties in Bioprinting/3D Bioprinting*)

Abstract

Liver tissue engineering offers a remarkable tool for toxicological screening and an approach to disease modeling, and provides an alternative solution to liver transplantation in treating end-stage liver diseases. As the liver is a highly specialized multicellular organ, distinctive features such as diversity of cell types, extracellular matrix composition, and three-dimensional architecture must be taken into consideration in recapitulating its physiology. Here, we review the current developments in liver tissue engineering approaches, focusing on their application to liver disease modeling and treatment, with special emphasis on bioprinting for high-throughput analysis. We also discuss the challenges encountered and the likely future developments in the area.

Keywords: Liver; Bioprinting; Disease modeling; Hepatotoxicity; Regenerative medicine

***Corresponding authors:**
Laia Tolosa
(laia_tolosa@iislafe.es)

Gloria Gallego-Ferrer
(ggallego@ter.upv.es)

Citation: Rodríguez-Fernández J, Donato MT, Gallego-Ferrer G, Tolosa L. Challenges and perspectives of liver tissue engineering: From cell therapy to bioprinting. *Int J Bioprint*. 2024;10(3):2706.
doi: 10.36922/ijb.2706

Received: January 10, 2024
Accepted: February 26, 2024
Published Online: March 29, 2024

Copyright: © 2024 Author(s). This is an Open Access article distributed under the terms of the Creative Commons Attribution License, permitting distribution, and reproduction in any medium, provided the original work is properly cited.

Publisher's Note: AccScience Publishing remains neutral with regard to jurisdictional claims in published maps and institutional affiliations.

1. Introduction

As the biggest internal organ in the human body, the liver plays a key role in more than 500 different functions, such as protein synthesis (i.e., albumin, transferrin), metabolism of carbohydrates, proteins and lipids, and detoxification of endogenous and foreign compounds. These functions can be altered by different disorders such as congenital metabolic diseases, toxic injury, viral infections, metabolic dysfunction-associated steatotic liver disease (MASLD, formerly known as non-alcoholic fatty liver disease), or hepatocellular carcinoma (HCC). The incidence of hepatic diseases is increasing worldwide and presents high morbidity and mortality rates.[1] Despite the intensive research in this area, there are limited therapies available in the clinical setting, and the only effective treatment for end-stage liver disease is liver transplantation, which is

limited by the scarcity of organs.[2] On the other hand, both animal models and the traditional cell-based systems often fail to adequately recapitulate human pathophysiology, a conundrum that hinders the development of suitable treatments and accounts for the limited number of currently available therapies.[3]

Several cell-based models have been proposed to study liver physiology and disease development. The traditional *in vitro* systems featuring monolayer cultures of primary human hepatocytes (PHHs) or hepatoma cell lines are still the predominant mode of research in this field,[4] but the new, more complex systems that consider that the three-dimensional (3D) organization have been on the rise, along with the fact that many different liver cell types contribute to hepatic functionality and participate in the development of diseases have been increasingly described. In this regard, the central objective of liver tissue engineering is to create models that mimic the *in vivo* liver functions. These models can be applied to unravel the mechanisms of different liver pathologies and to treat liver disorders. In these engineering approaches, both the cellular components and the extracellular matrix (ECM) organization that best reflect what happens *in vivo* should be considered.

Different biomaterials have been used in liver tissue engineering to provide a suitable microarchitecture, composition, and stiffness, among other attributes.[5] Finally, in recent decades, bioprinting has appeared as a method of increasing the throughput of the test systems that best mimic the environment and complexity of liver tissue.[6]

In this paper, we review the advanced materials used as hydrogels or scaffolds for 3D liver models, especially focusing on the cell type(s) used, since different cells can be used for *in vitro* models. We also provide an overview of the use of these strategies for drug screening, disease modeling, or regenerative medicine, indicating the challenges that need to be solved.

2. Liver disease and treatment

2.1. Liver disease

The liver has an extraordinary ability to restore its mass after loss or injury,[7] and liver regeneration has been shown to combine both hepatocyte proliferation (hyperplasia) and hypertrophy,[8] although certain conditions such as chronic liver injury can impair its regenerative properties.[9] Acute and chronic liver diseases are major reasons of mortality worldwide, accounting for approximately 2 million deaths per year, and pose a considerable economic problem. The main causes of liver disease are viral hepatitis, MASLD, and alcoholic liver disease.[1,10] Others include primary cholangitis, autoimmune hepatitis, and inherited metabolic disorders such as alpha-1-antitrypsin deficiency.[10] These trends are constantly changing, and the incidence of viral liver disease will probably be reduced in the future following the vaccination efforts and implementation of new treatments, while the incidences of drug-induced liver injury (DILI) and MASLD are expected to increase in Western countries.[10]

Alcohol consumption is a risk factor associated with multiple diseases, including cirrhosis and cancer.[1] There is an exponential correlation between alcohol consumption and the development of cirrhosis,[1,11] but it is also important to take into account the synergic effect of alcohol and other factors such as obesity or infection in developing the disease.[12] Alcoholic liver disease encompasses a range of liver pathologies, such as steatosis, liver injury, and inflammatory infiltrate, which usually appear associated to fibrosis and can progress to HCC.[13] Histologically, cirrhosis, which can also be precipitated by produced other diseases, e.g., hepatitis, causes an expansion of the ECM and the capillarization of the endothelium.[14]

MASLD is characterized by excessive lipid accumulation in the liver and can range from simple steatosis to steatohepatitis, also characterized by inflammation and necrosis of hepatocytes and fibrosis.[15] Hepatic fibrosis is defined as the accumulation of ECM proteins in the space of Disse that can even block the blood flow.[16] In liver fibrosis, in response to chronic liver injury, hepatic stellate cells (HSCs) are activated into proliferative fibrogenic fibroblasts, and several inflammatory mediators are upregulated, eventually resulting in ECM accumulation and progressive fibrosis.[17] The progression of steatohepatitis underlies cirrhosis and even HCC.[15,18] Different genetic, dietary, metabolic, and immunological factors have been implicated in MASLD.[15,18] Currently, there is no pharmacological therapy available, and the variation in lifestyle is the commonest therapeutic indication.[19]

Hepatitis B and C infections represent one of the primary factors for liver disease development in Europe.[1] The pathogenesis of hepatitis B and C viral infections is generally mediated by the immune system, even though both viruses can avoid immune removal and continue to replicate in the infected host for years. Chronic infection can result in oxidative stress induction and inflammation.[20] Vaccination programs have brought significant improvements to the reduction of advanced liver disease incidence caused by hepatitis B virus, but achieving complete eradication of the disease remains a monumental task.[21] On the other hand, hepatitis C is the leading cause of HCC, although antiviral therapies have reduced the burden of hepatitis C viral infection.[21]

HCC is the most common type of primary liver cancer that is often linked to other chronic liver diseases such as

MASLD or hepatitis. There seems to be a final pathway in the pathogenesis of HCC, regardless of the cause, wherein repetitive hepatocyte injury begins a vicious cycle of cell death and regeneration that eventually results in genomic instability and onset of the disease.[22] Different treatments are available for HCC, including surgical resection, liver transplantation, chemotherapy, and immunotherapy,[23] but most patients received the diagnosis of HCC when the disease has already progressed into an advanced phase or when their liver function become compromised, leaving them with limited number of therapeutic choices.

DILI is one of the principal factors contributing to acute liver failure (ALF) and a major cause of drug attrition in the preclinical and clinical phases of drug development or withdrawals after they have been commercialized.[24] It involves high costs to both the pharmaceutical companies working on the drug development process and healthcare organizations due to its associated morbidities and mortality.[25,26] DILI reactions are frequently intricate processes that involve multiple interactions between hepatocytes and non-parenchymal cells. Furthermore, drugs can induce DILI by different mechanisms such as immune-mediated responses, mitochondrial damage, oxidative stress induction, steatosis, or cholestasis.

Inherited metabolic liver diseases represent a heterogeneous group of rare disorders mostly characterized by a defect in a single enzyme or protein with metabolic functions, e.g., receptors or transporters.[27,28] Some examples of these disorders include urea cycle disorders due to defects of urea synthesis and related metabolic pathways; Crigler–Najjar syndrome type 1 caused by mutations of the UDP glucuronosyltransferase 1A1 that produce severe hyperbilirubinemia; Wilson disease due to mutations of the *ATP7B* gene, involved in copper transport; and glycogen storage diseases caused by mutations that alter the accumulation of glycogen.[27] Although these diseases, which are typically treated with organ transplantation, do not normally present changes in the liver architecture, the characteristics of these disorders underline the feasibility of using cell therapy treatment as the ideal therapy.[14]

2.2. Treatment of end-stage liver disease

Although liver transplantation is the only effective treatment for end-stage liver disease and presents a high survival rate (85% after 1 year),[29] the world is facing an organ scarcity problem, and many patients experience worsening disease condition or may even die while still being put on the waiting list.[30] New strategies have been explored to amplify the number of available organs or improve their quality (i.e., dynamic preservation, living donors).[30] Despite these efforts, the next-generation treatments such as cell transplantation or other bioengineering approaches have also been explored for the treatment of liver disease.[31] Liver cell transplantation using hepatocytes, macrophages, or stem cells has been suggested as an alternative or bridging technique to reduce liver disease mortality and morbidity. The first attempts at liver cell-based therapies focused on inherited metabolic disorders produced by the lack or dysfunction of a single enzyme, although cell transplantation has been also applied in different liver diseases.[32,33] Other approaches such as bioartificial liver support systems have also been proposed, and promising results have been obtained in animal models. However, more clinical studies are warranted to establish the safety and efficacy profile of the procedure.[34]

3. Liver microenvironment

The liver has a uniform anatomical structure,[35] and its structural unit is the hepatic lobule, which is hexagonal and consists of hepatocyte plates that radiate from the central vein in the center of the hexagon following a honeycomb-like pattern.[4] The portal triad is composed of a vein, an artery, and a bile duct, and is located at each vertex of the hexagon[4] (Figure 1). Blood rich in oxygen and different soluble factors enters through the portal vein and hepatic artery and flows concentrically toward the center of the lobule, whereas the bile flows outward from the center to the bile duct in the vertex of the lobule.[35] The areas surrounding the central vein are known as pericentral, while those close to the portal triad are called periportal. With an anatomically diverse and complex landscape, the liver functions are performed in parallel according to the zones, a phenomenon known as liver zonation.[35,36] Liver zonation has been implicated in the initiation and progression of liver disease;[36] therefore, new cell-based models have been created to simulate liver zonation, for instance, by modulating oxygen tension.[36]

3.1. Liver cells

The liver is formed by distinct cell types of different embryological origins that carry out unique functions.[37] Hepatocytes are the major liver cell type and perform most of its secretory and metabolic functions. Cholangiocytes are epithelial cells that form the bile duct. The non-parenchymal cells include Kupffer cells (KCs) which are liver-resident macrophages, HSCs, and liver sinusoidal endothelial cells (LSECs).[37] Figure 1 depicts the distribution of the different cell types in the hepatic lobule.

Hepatocytes account for approximately 80% of the total cell volume mass and are responsible for most of the liver functions. They express the greater part of circulating plasma proteins like albumin, transporters, blood clotting factors, and immune modulators. Hepatocytes synthesize different proteins such as albumin (involved in the maintenance of

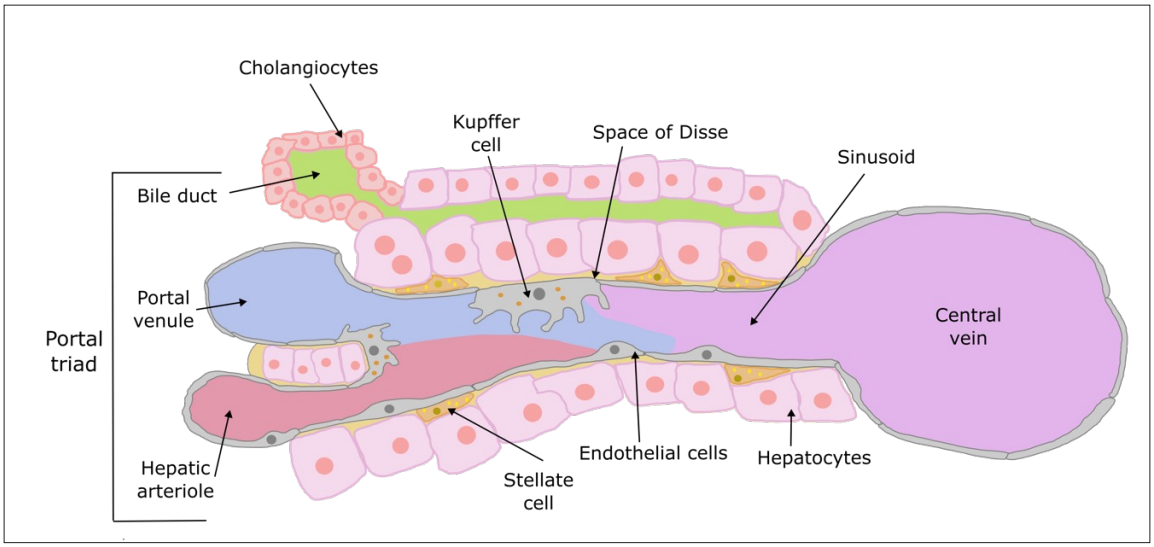


Figure 1. Schematic overview of the human liver structure and organization.

the transport of different molecules in the blood). They also play an important role in the metabolism of ammonia and endogenous and exogenous substances, and manage the homeostasis of bile acids, cholesterol, triglycerides, and glucose/glycogen.[4] They are polygonal epithelial cells that possess apical (canalicular) and basolateral (sinusoidal) domains.[38] This polarity and the fact that they simultaneously receive venous and arterial blood mean that they can combine the main liver functions: the production of plasma proteins and endocytic uptake of lipids and other substances, which also makes them susceptible to damage by drugs or other toxins. [38] Functional zonation of hepatocytes has been deeply studied, and it is mostly related to oxygen gradients and WNT signaling.[39] The energy-demanding functions (i.e., gluconeogenesis) are performed by periportal hepatocytes, while the pericentral hepatocytes are more involved in drug metabolism and glycolysis, which require less energy.[40]

Cholangiocytes, also known as biliary epithelial cells, comprise approximately 3% of the liver mass. They modify composition of the bile produced by the hepatocytes and also participate in detoxifying foreign compounds.[41] Like hepatocytes, cholangiocytes are polarized cells with basolateral and apical membranes that express different receptors and channels.[42] The cholangiocytes also help to regulate the bile flow, guaranteeing its appropriate release for digestion.

KCs are localized in the hepatic sinusoid and have been reported to play a key role in the systemic and hepatic response to pathogens.[43] They are also critical mediators in liver injury and repair and can show high plasticity, according to the microenvironment. KCs activation is a key factor in injuries or infections since their inflammatory response has a protective role and limits the injury.[44] However, in some conditions, such as MASLD, an uncontrolled activation of these cells can lead to chronic inflammation.[43]

LSECs are highly specialized endothelial cells that establish the wall of the hepatic sinusoid. Due to their location, they control the transfer of substances between blood and liver parenchyma and exhibit great endocytic activity.[45] LSECs carry out unique immune functions[46] and play an important role in regeneration and diseases like liver fibrosis.[47] On the other hand, RNAseq technology has also unveiled a significant zonation in LSEC.[40,48]

HSCs are located in the space of Disse, and a few of their major functions are vitamin A metabolism and lipid storage.[49] The space of Disse is a thin perisinusoidal area separating hepatocytes and endothelial cells that allows the bidirectional exchange between cells.[50] Another of their important roles is the production of ECM. Under pathological conditions such as fibrosis or cirrhosis, the HSCs proliferate and activate into myofibroblasts, which produce and secrete large amounts of different liver ECM components, mainly collagen type I or glycoproteins into the space of Disse, and increase inflammation and immunoregulation,[51] while modifications in the stiffness and constituents of liver ECM have also been shown to impact HSC responses.[51]

3.2. Liver extracellular matrix

ECM is the non-cellular part of a tissue that basically acts as a scaffold for the cells and releases critical biochemical signals needed for morphogenesis, homeostasis, and

survival.[52] Under normal conditions, liver ECM comprises less than 3% of the relative area and is mainly composed of collagens (types I, III, IV, and V being the most abundant); glycoproteins such as fibronectin, laminin, or nestin; and glycosaminoglycans such as hyaluronic acid, chondroitin, heparin, and dermatan sulfates.[53,54] Liver ECM is composed by two different structures (basement membrane and interstitial matrix) that differ in both morphology and biochemistry. The interstitial matrix is composed of collagen (types I and III) and fibronectin. The basement membrane mainly comprises laminin, heparan sulfate proteoglycan, and collagen IV and forms a thin acellular layer that facilitates diffusion. However, it is not present in the sinusoids and parenchyma of healthy livers.[55] Liver ECM has a critical role in the regulation of cell behavior, phenotype, migration, and proliferation.[56] Remodeling the liver ECM can help to maintain both the viability and functionality of the tissue and induce diseases.[56] For instance, in liver fibrosis, different chemicals or viruses can induce cell death, through which different mediators that can trigger HSC activation are liberated.[57] Activated HSCs deposit elastin and collagen, thus increasing stiffness.[56]

ECM modification is an extremely coordinated process that involves synthesis, secretion, degradation, and reorganization of the different components.[58] A pathological deposition of ECM would occur when there is an injury or the enzymes involved in modifying the ECM, such as the matrix metalloproteinases (MMPs), become malfunctioned.[58,59]

Several cell types are implicated in modifying the liver ECM, e.g., the cross-talk between HSCs, portal fibroblasts, LSECs, and KCs has been extensively discussed.[58] In this regard, Ramachandran et al. used RNAseq technology to identify pathogenic subpopulations of endothelial cells, macrophages (KCs, mononuclear phagocytes, and scar-associated macrophages), and myofibroblasts in fibrotic human tissues.[60]

4. *In vitro* models in hepatology

Animal models offer an indispensable tool for exploring the mechanisms underlying liver disease and deciphering the process of liver regeneration. However, different human *in vitro* models are now used to fully recapitulate human liver disease and develop safer and more efficacious treatments.[61] PHHs are the gold-standard cells used in liver cell-based assays[62-68] as they can be isolated and cultured, but the functionality and quality of the cells may significantly decline over long periods of culture in monolayer configuration.[4,62-64,68] One of the major advantages of cultured PHHs is that they can reflect inter-individual variability,[69] although this approach is fraught with several limitations, such as the scarcity of liver tissue and the vulnerability of PHHs to freezing and thawing procedures.[70-72] Researchers have recently focused on exploring new culture systems (3D cultures, co-culture systems, microfluidic devices) that maintain the cultures over longer periods and even improve their functionality.[4] Human liver cell lines (HepG2, Huh7, and HepaRG) are alternatives to PHHs, that are widely available and easy to handle,[73,74] despite their reduced metabolic performance and inability to reflect inter-individual differences.[73]

Stem cell research has driven a series of efforts leading to the generation of induced pluripotent stem cells (iPSC), reprogramming of distinct cell types, and thus, their differentiation toward a hepatocyte phenotype (hepatocyte-like cells, HLCs) by means of a sequential protocol that mimics liver development. The generation of HLCs would supply an unlimited cell source for cell-based assays and also as therapy for liver disease.[75-77] One of their major advantages is that these iPSC models could reflect inter-individual variability, offering more representative models,[78] while HLCs could be also a therapeutic alternative to organ transplants, although protocols that permit the differentiation of iPSCs into a more mature form are urgently needed.

Monolayer (two-dimensional [2D]) cultures have traditionally been used in hepatology; however, these systems do not accurately reproduce the liver's spatial organization or the cell–cell or cell–matrix interactions that improve and stabilize hepatocyte's functionality.[79,80] Co-cultures of hepatocytes and other liver cells have also been proposed to improve functionality and better recapitulate liver (patho)physiology.[81-83]

5. Hydrogels for liver tissue engineering

Tissue engineering approaches are utilized to simulate the functions of the target organs but not necessarily their architectures. These approaches entail the combination of cells, 3D scaffolds, and signals for the correct regeneration of the tissue/organ or the *in vitro* simulation of healthy and diseased tissues/organs. As the liver is a relatively soft organ, hydrogels or soft scaffolds have mostly been applied as synthetic ECM components for the cells. Great advances in liver tissue engineering techniques tailoring complex multicellular models to better recapitulate the liver functions, microarchitecture, and microenvironment have been achieved in recent years.

Hydrogels are polymeric hydrophilic networks that can absorb large amounts of water without dissolving. They maintain their integrity in the presence of an aqueous environment due to the crosslinking points between the polymeric chains.[84] These crosslinks can be chemical,

formed by covalent bonds, or physical, which imply non-covalent bonds such as hydrophobic interactions, hydrogen bonding, chains entanglements, crystallites of semi-crystalline polymers, or ionic interactions.[85] They can even form dual networks consisting of physical and chemical crosslinks that can sometimes be mechanically advantageous.[86] Chemical hydrogels are more stable than physical hydrogels in physiological environments in which the pH or ionic strength is subject to changes. They are good candidates for liver tissue engineering due to their water sorption capacity and softness in mimicking the liver's mechanical properties, their ability to mimic the composition of the liver ECM upon combination, and their capacity to deliver biomolecules.[87]

One of their major disadvantages is that many crosslinking reactions are cytotoxic, and thus, they are not able to be used with cells,[88] although mild reactions have been explored; these can take place together with the cells to form *in situ* gelling or injectable hydrogels.[89] They are advantageous because the precursor solution can be mixed with cells and bioactive components and be injected into the body where they become solid, homogeneously entrapping the cells, completely filling a tissue defect and being implantable by minimally invasive procedures. Our group has recently optimized a family of enzymatically gellable hydrogels of gelatin and hyaluronic acid for culturing liver cells.[90] These types of hydrogels can be used to form 3D construct structures by bioprinting through the development of bioinks (a solution of the precursor molecules of the hydrogel together with a suspension of cells).[91] Section 6 of this review contains a summary of the recent advances in this liver tissue engineering technique.

The main physical properties of hydrogels, their swelling capacity, and mechanical properties depend on different parameters, including crosslinking density, the chemical nature of the polymeric chains (through the Flory–Huggins interaction parameter), the activity of water in the environment, the concentration of polymers, the porosity of the hydrogel, etc. The network structure, characterized by its mesh size,[92] determines the diffusivity of water or other soluble species (growth factors or drugs) through the hydrogel. The rubber elasticity theory describes the mechanical behavior of hydrogels, and the Flory–Huggins equation describes their equilibrium swelling.[93] The elastic modulus of hydrogels increases with the crosslinking density, while the water sorption capacity and diffusivity of biomolecules decrease with it. A lower interaction parameter indicates that more water is absorbed by the hydrogel, and a higher water activity in the environment suggests that more water is retained by the hydrogel.

Table 1 summarizes the main hydrogels that have been used for different *in vitro* applications, classified according to their origin (natural or synthetic), together with the type of cells and the main outcomes of the studies.

5.1. Natural hydrogels for liver tissue engineering

Liver-derived hydrogels can be created with liver decellularized ECM (dECM) since they preserve many of the components of the natural matrix that can be beneficial for 3D liver cell culture. Willemse et al. used liver dECM hydrogels to culture and expand intrahepatic cholangiocyte organoids (ICO) as alternatives to tumor-derived basement membrane extracts.[94] Liver dECM allowed for successful culture of ICOs in dynamic spinner flasks, which was more efficient and faster than the classical culture in basement membrane extracts. Despite the promising results, as the liver ECM varies in different parts of the organ, the composition of the resulting hydrogels is difficult to control, so that chemically defined hydrogels are preferred in liver tissue engineering,[95] as in the case of alginate (Alg), which has been explored in many tissue engineering applications. In general, Alg has a bad interaction with cells, and when it is directly crosslinked with $CaCl_2$ salt, it becomes a non-injectable hydrogel due to the rapid crosslinking reaction. To make it injectable for liver tissue engineering, Tong et al.[87] developed a two-step method to ionically crosslink the hydrogel with Ca^{2+} through an insoluble calcium salt that progressively released the crosslinking ions. To improve the interaction with cells, the study used glycyrrhizin triterpene glycoside which provided the hydrogel with specific binding sites for hepatic cells. The authors demonstrated that the new GL-Alg-Ca hydrogel had suitable viscoelastic properties for the cell culture of hepatic cells (HepG2) with enhanced hepatic functionality and CYP450 expression in three dimensions rather than two dimensions.

Of the chemically defined hydrogels, collagen (Col) is probably the best for liver tissue engineering because it is one of the main components of the liver ECM.[53] It forms a viscous solution in acetic acid and forms a physical hydrogel when neutralized with NaOH.[96] Col bioinks and the resulting hydrogels possess mechanical properties inadequate for their usage in liver tissue engineering, so they are usually combined with other more rigid polymers, e.g., polycaprolactone grids in the form of scaffolds built in the melting head of an in-house bioprinter,[97] for the heterotypic culture of rat hepatocytes, human umbilical vein endothelial cells (HUVEC), and human lung fibroblasts encapsulated into collagen filaments. The authors described a vascular formation and an enhanced functionality of hepatocytes (albumin secretion and urea synthesis) in the case of the heterotypic interaction among hepatocytes and non-parenchymal cells compared to hepatocytes monoculture. Gelatin (Gel), the denaturalized version of Col, is an alternative hydrogel widely used in

Table 1. Natural and synthetic hydrogels for *in vitro* liver tissue engineering

Polymer	Crosslinking agent/ mechanism	Cells	Outcomes	Refs
Natural hydrogels				
Liver dECM	Neutralization	Intrahepatic cholangiocyte organoids (ICO)	– No differences in ICO viability or improvement in differentiation between liver dECM hydrogels and basement membrane extracts. – Lower proliferation rates for the ICO grown in dECM. – ICOs were successfully cultured in dynamic spinner flasks using human dECM, which was less time-consuming and more efficient compared to normal static culture in domes.	94
GL-Alg	Ca^{2+} ions	HepG2	– Injectable alginate hydrogels containing GL that promoted liver viability and functionality were produced. – The mechanical properties of the injectable hydrogel were suitable for hepatic cells culture. – Hepatic functionality and CYP450 expression were higher in the 3D hydrogel system than in 2D format.	87
Col	Neutralization	Rat hepatocytes, HUVEC and human lung fibroblasts	– Col containing the cells was alternatively bioprinted between printed polycaprolactone lines. A 3D scaffold was built layer-by-layer. – Vascular formation and enhanced functionality of hepatocytes (albumin secretion and urea synthesis) in co-cultures, among hepatocytes and non-parenchymal cells, were observed.	97
Gel	UV-light GelMA	HepG2 and fibroblasts	– GelMA hydrogel was used as a matrix to build 3D lobule-like microtissues for the co-culture of HepG2 cells and fibroblasts. – Urea synthesis and albumin secretion by HepG2 were significantly higher in co-culture than in monoculture.	98
HA	8-Arm PEG-azide/ alkyne-azide cycloaddition	HLC from human iPSC	– HA hydrogels crosslinked with PEG were successfully obtained by click chemistry with shear storage modulus between 100 Pa to 1 kPa. – The low viscosity of the hydrogel precursors allowed producing the hydrogels into liver-on-chip devices. – HLC required cell adhesion motifs to survive and function up to 13 days. – Cyclic RGD motifs grafted to HA formed large structures of viable HLC that migrated throughout the hydrogel. Albumin secretion was higher than in non-functionalized hydrogels.	100
Fibrin	Thrombin	Rat hepatocytes	– Hepatocytes were homogeneously distributed and in 3D within the fibrin hydrogel. – Hydrogel encapsulation allowed high cell density and cell-to-cell contacts during the *in vitro* experiments. – Cell number within the hydrogel remained stable till day 3 of culture. Cell loss was observed at day 7. – Hepatocytes cultured in hydrogels expressed CK-18, albumin, and the biliary epithelial cell marker CK-19 during the culture (3 and 7 days).	116

(*Continued...*)

Table 1. (*Continued...*)

Heparin	Michael-type addition reaction (thiol and diacrylate)	Rat hepatocytes	– Heparin hydrogel allowed encapsulation and culture of hepatocytes (single cells or spheroids) with and without HGF for 20 days. – Hepatocyte spheroids exhibited high levels of albumin and urea synthesis with increased hepatic function over time; single cells showed gradual loss of hepatic function. – Inclusion of HGF into the hydrogel reversed the loss of function in single hepatocytes and enhanced hepatic phenotype of spheroids.	101
HA-Col	UV-light/ hyaluronic acid methacrylated, imine bonds (HA-Col) and physical crosslinking (Col)	HepG2	– Col provided adhesion, fibrous network structure and viscoelastic mechanical basis. HA simulated ECM composition and provided rigidity. Imine bonds adjusted the viscoelasticity of the hydrogel. – Hydrogel Young's modulus was 2.5 kPa, and the half relaxation time ($\tau_{1/2}$) was 50 s, representing viscoelastic property of the hydrogel. – HepG2 cells proliferated and typically tend to cluster in hydrogels. – The *in vitro* system was useful to study alcoholic liver disease.	86
HA-Gel	PEGDA/thiolated HA and Gel	HepaRG	– Cells formed spheroids within the hydrogels, being better organized in the case of low cell density encapsulation than in high density. – Low- and high-cell-density encapsulation in 3D showed good viability. – Cells showed differentiation towards hepatocyte phenotype in hydrogels after 2 weeks of culture.	103
Pullulan-dextran	Sodium trimetaphosphate/ ionic	HepaRG	– Microindentation showed that hydrogel mimics the mechanical properties of healthy liver. – HepaRG cells exhibited long term viability when cultured for 21 days within the hydrogel. – Cells within the hydrogel displayed typical functions of mature hepatocytes: urea production, albumin synthesis, CYP450 activity, glycogen storage, bile acids transport, and excretion system.	117
Synthetic hydrogels				
PEG diacrylamide-peptide	UV-light	Rat hepatocytes, J2-3T3 fibroblasts, and a liver endothelial cell (LEC) line	– 85% of MMP-sensitive peptide reacted with the PEG diacrylamide and hydrogel degraded with collagenase, being stable for several weeks in aqueous environments. – Hepatocytes-embedded hydrogels produced albumin and secreted urea for at least 15 days of culture. – Co-culture of hepatocytes with LEC allowed the preservation of hepatic-specific function for at least 3 weeks of culture.	104
PEG glycol diacrylate (RGD or RGE peptide functionalized)	UV-light	Bipotential mouse embryonic liver cells and rat hepatoctytes co-cultured with fibroblasts	– Pre-aggregated bipotential embryonic cells showed a significant increase in viability compared to dispersed cells. – Differentiation occurred within the PEG hydrogels (albumin and alcohol dehydrogenase gene expression). – Fibroblasts co-culture with rat hepatocytes helped to maintain the hepatocyte function within PEG hydrogels. – Conjugation of hydrogels with RGD adhesion peptides improved hepatocyte functionality.	105

(*Continued...*)

Table 1. (*Continued...*)

PEG-tetra-norbornene	UV-light/dithiol crosslinker	HepG2 and Huh7	– Orthogonally crosslinked thiol-ene hydrogel PEG system was cytocompatible for culturing Huh7 and HepG2 cells. – The hydrogels that contained bio-active MMP-sensitive peptide linkers could better upregulate the expression of several hepatocyte-specific genes and enhance hepatocyte functions. – Inclusion of RGD motifs was also conducive for augmenting hepatic functionality.	[106]
PVA	Not described	HepG2	– Collagen-coated scaffolds allowed the attachment and viability of HepG2, while very few cells were observed in non-coated scaffolds. – Cell proliferation was significantly higher in the collagen-coated scaffolds than in pure PVA scaffolds. – Albumin secretion and urea synthesis were significantly higher in the collagen-coated scaffolds than in PVA.	[118]
PNIPAAm	Radical copolymerization with AIBN and TEMED	HL-7702 and HepG2	– The hydrogel was copolymerized with glycyrrhetic acid to better interact with hepatocytes. – Hydrogel promoted cell adhesion and proliferation. – Urea synthesis and albumin secretion were higher in copolymerized hydrogels.	[119]
Polyisocyanopeptides-based hydrogel	Temperature	$LGR5^+$ liver stem cells	– Organoids were formed when the hydrogels were modified by laminin–entactin complex. – Organoids proliferated within the hydrogels at rates very similar to that in Matrigel. – Hydrogels promoted stem cell differentiation confirmed by the upregulation of several hepatocyte markers.	[120]

Abbreviations: AIBN, azobisisobutyronitrile; Col, collagen; dECM, decellularized extracellular matrix; GelMA, gelatin methacryloyl; GL, glycyrrhizin; HA, Hyaluronic acid; HLC, hepatocyte-like cells; ICO, intrahepatic cholangiocyte organoids; iPSC: induced pluripotent stem cells; LEC, liver endothelial cell; PEG, polyethylene glycol; UV: ultraviolet.

tissue engineering because it is cheaper and possesses some of the advantages of Col. It is soluble in physiological buffers (not needing acetic acid) and forms a physical hydrogel by reducing the temperature. The problem is that the sol–gel transition happens below 37°C, forming liquid solutions in cell culture conditions. This has led to a search for alternative ways to crosslink Gel for use in tissue engineering. One of the most frequently used methods is UV light crosslinking of gelatin methacryloyl (GelMA), which has been tested in building 3D lobule-like microtissues for culturing hepatocytes and fibroblasts.[98] The study showed that urea synthesis and albumin secretion by HepG2 were significantly higher in co-culture than in monoculture.

In the group of glycosaminoglycans present in liver ECM, hyaluronic acid (HA) has been proposed as a suitable hydrogel for its high hydration capacity and mechanical stiffness, as well as the ability to interact with cells through the binding domains for the cell-surface receptors CD44 and RHAMM.[99] An example of its use in liver tissue engineering has been described,[100] in which HA was crosslinked using an 8-arm polyethylene glycol (PEG) by click chemistry, giving rise to hydrogels with a shear storage modulus that ranged from 100 Pa to 1 kPa. HepG2 cells and HLC derived from human iPSC were successfully cultured within the hydrogels, after grafting arginine-glycine-aspartic acid (RGD) adhesion motifs to HA, which secreted more albumin than non-functionalized HA hydrogels. Heparin is another abundant glycosaminoglycan in liver ECM, with the advantage that it binds ECM proteins such as the hepatic growth factor (HGF) thanks to the presence of the sulfated group in its structure. For instance, heparin hydrogels can be obtained by Michael-type addition reaction of thiolated heparin and diacrylated PEG crosslinker.[101] By the inclusion of HGF in heparin, single hepatocytes and hepatocyte spheroids showed excellent hepatic functions up to 20 days in culture.

In addition to applying pure hydrogels for *in vitro* systems in liver tissue engineering, combining different components of the ECM to produce hydrogels with improved characteristics, as described in a previous study that established a biomimetic difunctional HA-Col hydrogel matrix to mimic different properties of natural ECM, such as fast relaxation, a nanofibrillar structure, and rich adhesion domains,[102] is gaining traction. The same

authors propose this hydrogel mixture to build a viscoelastic approach with native adhesion domains and fibrillary architecture to provide a mimetic microenvironment for the cell culture of HepG2 cells, as an *in vitro* artificial liver model to study alcohol-induced liver disease.[86] HA has also been combined with Gel[103] for the culture of HepaRG cells.

5.2. Synthetic hydrogels for liver tissue engineering

PEG hydrogels are the most frequently used synthetic hydrogels in tissue engineering due to their biocompatibility, neutral charge, and precise control of the crosslinking density, and they form networks with reproducible mechanical properties. Compared to natural origin hydrogels, PEG hydrogels are limited by their disadvantages such as non-biodegradability and lack of recognition sites to interact with cells. These drawbacks can be solved, on the one hand, by providing PEG with MMP-sensitive peptides (as crosslinking agents or in the polymer backbone), allowing PEG degradation in cell microenvironment.[104] On the other hand, the chemical modification of PEG by including bioactive factors, such as the adhesion sequence RGD, permits the interaction with cells, in general, and modifications by incorporating hepatic cells, in particular, improve the hepatic functionality of hepatocytes (in co-culture with fibroblasts).[105] Orthogonally crosslinked thiol-ene hydrogel PEG systems have been synthesized[106] as a cytocompatible material for the culture of hepatic cells (Huh7 and HepG2) in three dimensions. When these hydrogels contained bioactive MMP-sensitive peptide linkers, they could better modulate the expression of different hepatocyte-specific genes and enhance hepatocyte functions than bioinert hydrogels of the same nature. Including RGD motifs was also conducive for augmenting hepatic functionality.

There are not many options of single-component hydrogels that can mimic mechanical and biological properties of the natural ECM. Thus, there is an increasing tendency to use multicomponent hydrogels, especially in the development of bioinks to improve printability at the same time as the hydrogels keep the biological performance. Of importance is the case of the use of dECM in combination with other components to enable its printability, as it has a slow gelation time and the preparation of complex or large structures with enough fidelity is quite difficult.[107] For example, Kim et al. combined a liver dECM bioink with gelatin and observed a significant increase in its viscosity, allowing the improvement of the printing resolution and enabling the preparation of higher structures in the case of using single-component dECM bioink.[108] Another study incorporated gelatin into the dECM bioink with the aid of silk fibronectin with promising results in hepatocyte functionality.[109] Incorporation of HA into dECM bioinks was also possible thanks to the modification of HA with tyramine.[110]

Hydrogels have achieved progress in the *in vitro* culture of hepatic cells since hepatic functionality and the culture time of 3D hepatocytes have improved in comparison to the traditional monolayer culture. However, hydrogels have also posed new challenges related to the construction of more physiologically relevant *in vitro* models. For instance, there is a need to recreate the native liver microarchitecture, with a heterogeneous ECM that can be recreated by building micropatterned hydrogels.[111,112] Although the hydrogels described have a good affinity for hepatic cells or have been decorated with biomolecules that provide cell–matrix interactions, the inclusion of growth factors presented by the hydrogel in synergy with the interaction domains can represent a step forward in hepatic functionality.[113] New hydrogel formulations that more accurately reproduce the viscoelastic behavior of the native tissue are expected in the future[114,115] to adequately mimic the *in vivo* situation in order to improve the current outcomes.

6. Bioprinting applied to designing hepatotoxicity assessment platforms and 3D *in vitro* disease models

6.1. Bioprinting methods and main control parameters

Bioprinting is the automatic 3D spatial deposition of cells (and other biological molecules such as growth factors) through a layer-by-layer process of a hydrogel that crosslinks by non-cytotoxic reactions. As the bioprinter automatically manufactures the samples, multiple samples can be produced in a very short time for scaling up, while complex tissue-like structures can also be formed. Bioink is a mixture of a hydrogel precursor solution, cells, and bioactive molecules. When it is injected onto the bioprinter plate, a crosslinking reaction takes place that keeps the shape of the printed structure, homogeneously entrapping the cells and biomolecules.[121] There are three main bioprinting strategies: inkjet-based, laser-assisted, and extrusion-based.[122] Inkjet bioprinting works by depositing microdroplets formed in the print head by a piezoelectric actuator onto the plate. In laser bioprinting, a bioink droplet is formed in a template material that is vaporized by the laser and transferred to the receiving substrate. During extrusion bioprinting, a continuous filament, produced in a syringe that can move in three directions, is deposited onto the collecting plate. The filament is formed by pneumatic or mechanical screw pressure in the syringe. Highly viscous materials with different cell densities can be extruded by this method, the most widely used bioprinting technique.[123] The printing resolution depends on the method used for obtaining the structure; the literature describes 50 μm for inkjet bioprinting, 10 μm for laser bioprinting, and 100 μm for extrusion bioprinting.[124] The ideal structure

to print for recreating the liver microenvironment is the liver lobule, and the majority of studies dedicated to build this structure have used extrusion bioprinting because the resulting constructs are more viable than when using the other techniques.[125] The designs have a central hollow zone with printed endothelial cells, with radiating endothelial cells separated from radiating hepatocytes, and a final surrounding structure with endothelial cells.[125] These structures combine the ECM comprising the ink together with the cells, which are desirably homogeneous, to better mimic the *in vivo* situation.

In extrusion-based bioprinting, bioink viscosity is one of the main parameters to be controlled for successful printing,[126] which depends on characteristics such as the polymer concentration, polymer molecular weight, polydispersity index, cell density, and processing temperature. Highly viscous materials produce stable structures after leaving the nozzle, although they can also produce high shear stresses in the print head, limiting cell survival. Low-viscosity materials are gentle on cells, but printing pressure and filament shape are difficult to control. Shear thinning materials can be used to obtain a balance between cell survival and shape fidelity. These materials reduce their viscosity in the presence of shear forces and facilitate bioink deposition without compromising the cells. Shape fidelity is guaranteed in this type of material because filament viscosity is recovered after exiting the nozzle.[126] Khati et al. developed a shear thinning bioink based on liver dECM, Gel, and PEG that enabled the extrusion of dECM at body temperature.[127] The nozzle diameter also influences cell viability; lower pressure is required to produce large-diameter filament than small diameters, and the cells demonstrated good viability after being exposed to lower shear stresses.[128] Hydrogel crosslinking needs to be fast enough to prevent the hydrogels from spreading out so that the filament keeps its shape. This better shape fidelity can be achieved in hydrogels which have undergone a high crosslinking degree. Shape fidelity also depends on the hydrogels' swelling properties after printing. A low degree of swelling, which can be regulated by the crosslinking degree of the hydrogel, is required to maintain the shape of the filament.

As bioprinting allows the automatic deposition of hydrogels and cells onto platforms with a precise and desired shape in a very short time, it has allowed the design of advanced 3D hepatotoxicity platforms to test the effect of multiple drugs in 3D-cultured hepatic cells. This field has been extended to the automatic preparation of 3D platforms to simulate *in vitro* liver diseases to allow for the mechanistical exploration of these diseases and the development of new drugs for treatment. Both of these applications are summarized in the following section.

6.2. Disease modeling using bioprinting

6.2.1. DILI

Bioprinting can also be used to assess drug-induced hepatotoxicity, as it allows reproducible high-throughput generation of 3D structures. Different systems with different materials in combination with hepatic cells have been proposed to build 3D platforms for this purpose (see Table 2).

Generally, different materials are combined to optimize bioprinting, as pure components are difficult to print, as in the case of Pluronic,[129] a material widely used for extrusion bioprinting due to its good printability and shape fidelity, although, despite these advantages, it has rather poor mechanical properties that compromise its applicability. A combination of Pluronic with Alg enhances the mechanical properties of the mixture, a method used by the authors to compare the material in supporting HepG2 cell line viability and metabolic activity with monolayer cultures, using the platform for high-throughput screening of hepatotoxic compounds. Compared to monolayer culture, cell viability was significantly reduced when the 3D liver models were exposed to a dose of acetaminophen, demonstrating the printed model's prediction of hepatotoxicity. In the case of Col, there were some difficulties in bioprinting.[130] This is a low-viscous liquid when dissolved in acidic conditions; however, when neutralized, it begins to assemble into fibers, forming a physical hydrogel that compromises its bioprinting.[130] The combination of methacrylated Col with thiolated HA produced a printable material with relevant components in liver ECM. When PHHs were bioprinted, they maintained hepatocyte functionality, which however declined when the systems were incubated with acetaminophen, demonstrating the adequate response to hepatotoxic drugs. Another approach used a combination of Alg and Gel as bioink to construct a hepatic tissue model based on encapsulated HLC derived from iPSC.[131] The cells within the 3D-printed model had significantly better hepatic functionality than the monolayer cultures and non-printed sandwich-cultured models. The 3D-printed model was used to evaluate acetaminophen's hepatotoxicity; the cells in the 3D-bioprinted model showed stronger resistance to the drug than the sandwich-cultured model. A three-component mixture is sometimes necessary to increase printability, retain shape after printing, and improve cell viability, as in the case of the 3D liver model proposed by Schmidt et al. in which Alg, Gel, and Matrigel were mixed to print scaffolds containing HepaRG cells.[132] The system allowed the culture of HepaRG cells for long periods, which would allow chronic treatments with toxic compounds such as albumin, suggesting that these hydrogels are suitable for repeated-dose assays.

Microfluidic systems allow the cells being physiologically stimulated under a continuous flow of cell culture media. As previously described,[133] a microfluidic bioreactor was interfaced with a bioprinter to fabricate 3D hepatic constructs of spheroids encapsulated in photocrosslinkable GelMA hydrogel. The cultured spheroids were viable and active for 30 days and responded to acetaminophen treatment in a similar way to those described in other published studies on animal or *in vitro* models.

Bioprinting can be used to build complex 3D structures that mimic the liver lobule microarchitecture for drug toxicity experiments. In a previous study,[134] the authors propose a physiologically relevant *in vitro* liver model formed by hepatic sinusoids with alternate cords of hepatocytes and non-parenchymal cells obtained by extrusion bioprinting. The bioink used was a mixture of Gel, silk fibroin, and liver dECM. The authors demonstrated that the co-culture of hepatocytes and non-parenchymal cells is more accurate than hepatocyte monoculture in predicting hepatotoxicity.

6.2.2. Other diseases

Bioprinting can be used to develop precise liver disease models to study the underlying mechanisms and test the potential of drugs under development (see the recent advances in Table 2). Bioprinted Gel-Alg hydrogels were used to culture primary HCC cells obtained from six different patients. The cells retained the expression of specific HCC biomarkers as well as the genetic alterations and expression profiles of their original tumors. The model was used to evaluate the efficacy of candidate drugs for HCC.[135] HCC models were also developed with photocrosslinkable liver dECM bioprinted through a rapid light-based process to tune the mechanical properties of the hydrogels.[136] The dECM was mixed with photocrosslinkable GelMA to produce the bioink. By changing the light exposure time, the mechanical properties of the hydrogel increased from healthy liver values (0.5 kPa) to those of cirrhotic liver (15 kPa). HepG2 cells were less viable in the stiff scaffolds and had a significantly reduced expression of liver-specific markers, indicating that the cirrhotic mechanical environment plays a significant role in liver function.

GelMa was used to model liver fibrosis for the co-culture of HepaRG and LX-2 cells.[137] The shear storage modulus of the hydrogels was controlled by the Gel concentration, from values ranging from 0.05 kPa to 2.12 kPa for 2.5% and 15% solutions, respectively. The printed structures were viable for 1 month, and HepaRG cells were able to differentiate in three dimensions in the absence of dimethylsulfoxide. HSCs activated in response to TGF-β, depositing fibrillar collagen, suggesting the system's suitability for modeling liver fibrosis.

Although 3D bioprinting has allowed the cost-effective rapid manufacture of 3D models, there are still limitations and challenges to address before they can be applied to clinical applications. For instance, current bioprinting resolution is not accurate enough to reproduce the complex hepatic microenvironment that includes abundant vascularization to ensure long-term hepatotoxic experiments or research on liver diseases.[121] Most of the studies reviewed proposed successful bioinks with cell lines. However, the bioink characteristics need to be improved to allow the survival of PHHs and the maintenance of the cells' original functionality and morphology, which is still a challenge with the current bioinks.[121] Many bioink crosslinking methods rely on UV exposure, which is suspected of being cytotoxic, so that there is a need to develop bioinks able to crosslink under visible light.[138] Additional research is needed before the optimal bioprinting method, composition, and crosslinking mechanism are obtained to put the technique into clinical practice.

Table 2. Applications of bioprinting for disease modeling

Ink composition	Cell source	Printing method	3D model	Outcomes	Refs
DILI					
Pluronic F127 and Alg	HepG2/C3A	Pneumatic extrusion	Square + inner grid	– 18.4 kPa of storage modulus after crosslinking. – Homogeneous cell distribution and maintenance of viability (>95%). – Increased urea and albumin production after 7 days. – Upregulation of CYP1A2 expression. – Increased sensitivity to APAP-induced hepatotoxicity.	[129]
Col I and HA	Lx2 cells/HSCs and PHHs	Pneumatic extrusion	Circle + inner grid	– Printable bioinks form stable constructs. – Maintenance of viability (>80%). – Col-I rich bioinks displayed improvements in cell morphology (Lx2 and HSCs). – Hepatotoxicity assessment of APAP-induced toxicity (urea and albumin production).	[130]

(*Continued...*)

Table 2. (*Continued...*)

Alg and Gel	hiPSC-HLCs	Pneumatic extrusion	Square + inner grid	– Increased cell density. – Integrated cell morphology, proliferation, and functionality. – Upregulation of CYP1A2 in bioprinted HLC after APAP treatment.	[139]
Gel, Alg and Matrigel	HepaRG	Pneumatic extrusion	Rectangular shape + inner grid	– Maintenance of viability up to 3 weeks. – Increased levels of albumin production. – Increased resistance to aflatoxin B1-induced hepatotoxicity (chronic treatment lasting 7 days). – Sensitive to doxorubicin-induced toxicity.	[132]
GelMA	HepG2/C3A	Hollow capillary and piston system	Dot array	– Increased levels of albumin, A1AT, transferrin, and ceruloplasmin on day 30. – Sustained expression of cytokeratin 18, ZO1, and MRP2 cellular proteins. – APAP treatment produced a decrease in cell metabolism and reduced levels of albumin, A1AT, transferrin, and ceruloplasmin.	[133]
Liver dECM, Silk and Gel	HLCs, HUVECs, and HSCs	Pneumatic extrusion	Hepatic lobule shape	– Increased viability 15 days after printing. – Upregulation of hepatic markers for HLC (albumin, phase I enzymes), HUVEC genes (CD31 and vWF), and HSC (desmin) genes. – HLCs were organized in aggregates with HSCs and HUVECs in a sinusoidal-like layer around them. – HSCs along HUVECs created a vascular network. – Hepatotoxicity was assessed by testing six different drugs, making this co-culture more sensitive and better at predicting hepatotoxic events than HLC monoculture.	[134]
Liver fibrosis					
Gel and Alg	HCC (from donor tissue)	Pneumatic extrusion	Cube	– Better viability than 2D culture. – HCC tumorigenic potential for individual patients, after *in vivo* implantation on mice was confirmed by AFP expression and Ki67 for proliferation rates. – Drug screening with four commonly used drugs in treatments showed a dose-dependent pattern in almost every case.	[135]
GelMA and porcine dECM	HepG2 cells	Digital micromirror device (DMD)	Hexagonal shape	– Reduced viability and proliferation in GelMA constructs. – Higher expression of hepatic markers (ALB and AFP) on the dECM-based constructs than others. – Study of fibrosis by exposure to different matrix stiffnesses, simulating fibrotic scenarios (soft, medium and stiff). Stiff hydrogels were associated with a significantly reduced expression of MKi67, ALB, and AFP. CASP8 apoptotic markers were also upregulated for the stiff matrix. – Genes related to angiogenesis (IGF2) and matrix metalloproteinases (MMP2 and MMP9) were upregulated in stiff matrix, indicating improved tumor progression (HCC).	[136]
GelMA	Huh7, HepaRG, LX-2, and HUVECs	Pneumatic extrusion	Cube and Square grid	– Long-term viability (up to 28 days). – Inducibility of metabolism enzymes – HepaRG showed markers related to polarization with E-cad and N-cad on the apico/lateral membranes, as well as functional transporter MRP2. – Co-cultures of HepaRG and LX-2 cells allow detecting collagen deposition and studying liver fibrosis.	[137]
Novogel 2.0	PHHs, HSCs, HUVECs,	Pneumatic extrusion		– Bioprinted constructs exhibit multicellular architecture of liver tissue. – HSCs exhibit quiescent states. – Chronic induction of fibrosis by methotrexate or thioacetamide for up to 14 days resulted in increased collagen deposition and pro-inflammatory cytokines.	[140]

(*Continued...*)

Table 2. (*Continued...*)

Novogel 2.0	PHHs, HSCs, HUVECs, and KCs	Pneumatic extrusion		– Incorporating KCs does not affect functionality (urea and albumin production). – The addition of KCs reduces the response to pro-fibrogenic drugs (TGF-b and methotrexate). – KCs salter cytokine responses in tissues with mild injuries.	[141]
GelMA	HepG2-C3A and LX-2 cells	DLP Bioprinting	Hexagonal shape	– HepG2/C3A and its co-culture with LX-2 cells were 90% viable 14 days after printing. – LX-2 cells tend to migrate to the peripheral parts of the hexagonal construct, mimicking the native tissue organization. – Co-culture showed a more efficient uptake of fatty acids. Complex models confirmed better outcomes in replicating the behavior of the native tissue. – Adding TGF-β1 enhanced the fibrotic state of the cells. Albumin and urea levels were reduced due to the growth factor.	[142]
Liver cancer					
Gel and Alg	HCC (from donor tissue)	Pneumatic extrusion	Cube	– Better viability than 2D culture. – HCC tumorigenic potential for individual patients, after *in vivo* implantation on mice, was confirmed by AFP expression and Ki67 for proliferation rates. – Drug screening with four commonly used drugs in treatments showed a dose-dependent pattern in almost every case.	[135]
Gel-Alg-Matrigel	Intrahepatic cholangiocarcinoma	Extrusion	Grid-like hydrogel	– High survival and proliferation. – Expression levels of tumor markers, cancer stem cell markers, matrix metalloproteinase protein, index of tumor fibrosis, index of liver function, and epithelial–mesenchymal transition regulatory proteins. – Bioprinted cells showed anti-cancer drug resistance.	[143]
Metabolic associated fatty liver disease					
Scaffold-free	Zucker rat hepatocytes		9×9 needle array	– Liver model maintained MASLD disease pathology for at least 3 weeks	[144]

Abbreviations: AFP, alpha-fetoprotein; ALB, albumin; Alg, alginate; APAP, acetaminophen; Col, collagen; dECM, decellularized extracellular matrix; Gel, gelatin; HCC, hepatocellular carcinoma; HLC, hepatocyte-like cells; HSC, hepatic stellate cells; HUVEC, human umbilical vein endothelial cells; KC, Kupffer cells; MMP, matrix metalloproteinase; PHH, primary human hepatocytes; vWF, von Willebrand factor.

7. Liver tissue engineering approaches for treating liver disease

Liver cell transplantation is an alternative to organ transplants and an option for patients with different types of liver disease, including inborn errors of metabolism and end-stage liver disease.[145,146] However, the low engraftment and repopulation of transplanted hepatocytes[72,147] have prompted the use of alternatives based on tissue engineering principles. Liver cell therapy enabled through tissue engineering involves creating functional liver tissue for regenerating diseased organs. Different strategies are used to produce liver tissue to restore the hepatic functions of a diseased liver, such as decellularized–recellularized tissue,[148] scaffolds,[149] or hydrogels.[95] Regarding cell types, although different researchers have used hepatocytes of human or animal origin to treat different diseased animal models, others have used multipotent stem cells (i.e., different mesenchymal stem cells). iPSCs differentiated into HLC have also been explored, generating interesting results. Since iPSCs offer an unlimited and available cell source that can be differentiated into any of the body's cell types, including hepatocytes, these cells could overcome one of the major limitations of liver cell therapy, or they could be also used as a personalized medicine approach with patient-derived cells.

Different animal models have been proposed to test the therapeutic potential of the developed strategies. Most of these involve ALF models induced by acetaminophen, thioacetamide, or D-galactosamine for testing the therapeutic efficacy of the engineered liver systems.[117,150-152] However, other disease models, such as the Wilson disease animal model, have also been used to show the clinical effects of the developed grafts.[153]

The different systems used and their major outcomes, organized by liver diseases, are detailed in Table 3.

Decellularized liver tissue is an ideal scaffold since it retains the natural liver ECM vascular network, microarchitecture, and components.[154] dECM could be used directly as a scaffold or as hydrogels for the treatment

of liver disease. For example, Vishwakarma et al. used rat dECM scaffolds seeded with human EpCAM+ cells to treat rats with ALF and achieved an improved survival rate and the maintenance of specific hepatic functions for up to 1 month,[155] while the decellularization of whole human liver lobes was first demonstrated in 2015.[148] The same authors seeded human liver cubic scaffolds with three distinct cell types (stellate cells, hepatocellular carcinoma, and hepatoblastoma) and demonstrated their biocompatibility by xenotransplantation into immunocompetent mice, although not their therapeutic effect.[148] To establish scalability to human-sized techniques, engineered liver grafts of pig dECM repopulated with endothelial cells and primary hepatocytes were used in pigs subjected to a 60% liver hepatectomy.[156] The study showed that dysfunction markers such as transaminases levels, bilirubin, or inflammation markers were lower in the transplanted animals, indicating that these bioengineered grafts functioned at clinical level.[156] Although using dECM is a potential tissue engineering approach for the treatment of end-stage liver disease, important issues related to possible risk of xenogeneic/allogeneic tissues, recellularization (cell sources, flow rate, migration and repopulation, etc.), or the enduring stability of the decellularized/recellularized tissues should be solved before its clinical translation.[154]

Other authors have explored using synthetic scaffolds seeded with different types of hepatic cells, since they not only provide a 3D microenvironment, but their interconnected pore structure also provides a suitable nutrient supply.[5] Some studies have used the scaffolds to improve the differentiation potential of multipotent stem cells before transplanting,[157] while others employed the scaffolds as a delivery method and studied the differentiation potential *in vivo*.[158,159] Alg scaffolds seeded with bone marrow MSC were shown to promote liver regeneration in rats after partial hepatectomy, and the transplanted cells[158] were endowed with specific hepatic functions such as glycogen production or albumin secretion and able to differentiate *in vivo* when transplanted within scaffolds.[158] While many studies used mesenchymal stem cells to recapitulate fully functional hepatic activity, certain authors utilized hepatocyte-laden scaffolds to treat liver disease, e.g., Alg scaffolds seeded with fetal liver cells were used to treat a Wilson's disease animal model, showing a significant therapeutic effect on the copper metabolism deficiency.[153] Biodegradable materials offer an advantage for clinical application over other strategies such as using Alg. We recently showed that Gel-HA scaffolds containing PHH improved hepatic functions in an acetaminophen-ALF animal model compared to intrasplenic injection of single cells.[90] Other natural polymers such as dextran and pullulan were recently used for encapsulating HepaRG cells and led to improved survival in mice with ALF.[117]

Regarding the use of hydrogels as a tissue engineering method to treat liver disease, different types of polymers, including chitosan, Alg, or natural-derived ECM molecules, have been used as hydrogels for regenerative medicine. For instance, rat hepatocytes encapsulated in Alg microbeads confer metabolic support in an animal liver failure model[150] and have been suggested as a promising therapy for children with ALF.[160] The authors used cryopreserved PHHs encapsulated into Alg microbeads, obtaining encouraging results, since four of the eight children tested avoided organ transplants.[160] Despite the promising results, the safety of the procedure continues to be uncertain since Alg is non-biodegradable in mammals and its lasting effects have not been thoroughly analyzed.[161] For this reason, other authors have used other approaches like Col-based hydrogels.[162-164] Zhao et al. used Col hydrogels seeded with neonatal and adult hepatocytes for the treatment of liver fibrosis in a multi-site injection strategy that enabled transplanting a huge number of liver cells into liver parenchyma in a single intervention, and they observed a reduction in fibrosis afterward.[163] Interestingly, Chiang et al. used an HGF-releasing hydrogels for the transplantation of iPSC-derived HLCs, which manifested increased antioxidant and anti-apoptotic potential after the procedure and improved the results in treating ALF.[152]

The use of cell-sheet engineering for treating liver disease has also been studied.[5] Nagamoto et al. showed that transplanting human iPSC-HLC sheets into animals with CCl_4-induced liver failure reduced lethality, and the siRNA experiments showed that the HGF produced from the HLC sheets played a key role in the HGF/c-met pathway.[165] Fibroblasts used as a feeder in combination with primary hepatocytes have been shown to be effective for treating radiation-induced liver failure in rats.[166]

8. Conclusions and future perspectives

Despite the key advances in the liver tissue engineering field, some major challenges must be overcome before they can be widely applied in both preclinical and clinical settings. One of the major limitations lies in the cell sources used, since, although PHHs are the gold standard, the shortage of liver tissue for isolating hepatocytes, their variability and instability, and the short length when in culture restrict their application. Of the different alternatives proposed, HLCs obtained from iPSCs present an unlimited self-renewal and proliferation capacity and reflect the patient's phenotype, although they have shown an immature phenotype after differentiation. The use of iPSCs could also help to expand the applications of the

Table 3. Liver cell transplantation for the treatment of liver disease

Biomaterial	Cell type	Animal model	Highlights	Refs
Inborn errors of metabolism				
HA scaffold	Fetal rat liver cells	Long Evans Cinnamon rat (Wilson's disease)	– Decrease in blood copper. – Significant reduction in total and direct bilirubin levels. – Increased albumin production.	[153]
Collagen-coated microcarriers	Rat hepatocytes	Gunn rat (Crigler–Najjar disease)	– Maintained decrease in serum total levels of bilirubin. – Presence and persistence of conjugated bilirubin after 3–4 weeks.	[167]
Acute liver failure				
Decellularized rat liver scaffolds	Human EpCAM+ cells	Wistar rats + ALF (D-GalN)	– Improved survival. – Improvements in ammonia, bilirubin, and albumin levels in transplanted animals. – Reduction of prothrombin time in transplanted animals.	[155]
Decellularized rat liver scaffolds	HLC-derived mouse mesenchymal stem cells	NOD-SCID mice + ALF (CCl_4)	– 3D microenvironment supported hepatic differentiation of MSCs. – Increased survival (63%) in transplanted animals. – Liver functions (albumin, transaminase, and bilirubin levels) improved after transplantation.	[168]
PCL-PLA-PAAm-IGF-1/TNF-α scaffolds	Rat bone marrow mesenchymal stem cells	Sprague–Dawley rats With ALF (D-GalN/LPS)	– Reduction of transaminases levels and total bilirubin in transplanted animals. – Histology of other relevant organs showed no toxicity associated to the scaffold. – *In vitro* studies showed the differentiation potential of MSCs cultured in the scaffolds.	[159]
Col I and chitosan printed scaffold	L02 cells	Nude mice + ALF (radiation + hepatectomy)	– Increased survival of transplanted animals after 14 days. – Decreased levels of ALT and AST.	[162]
Gel-HA scaffold	Primary human hepatocytes	NOD/SCID with ALF (APAP)	– Increased survival in transplanted animals. – Significant reduction of transaminases levels in animals transplanted with PHH-laden scaffolds compared to ALF animals and ALF animals only treated with cells. – Reduction of oxidative stress and proinflammatory cytokines in animals transplanted with PHH-scaffolds.	[90]
Pullulan and dextran scaffolds	HepaRG	NOD/SCID mice with ALF (APAP)	– Increased survival (37%) in transplanted animals. – Human albumin remained stable in sera for 28 days. – Successful engraftment and survival of transplanted cells.	[117]
Alg microbeads	Rat primary hepatocytes	Sprague–Dawley rat + ALF (D-GalN)	– Increased survival in transplanted animals. – Reduced levels of transaminases and bilirubin levels in animals transplanted with microbeads. – No sign of inflammation or adhesion was observed in treated animals. – Complete normal lobular architecture in transplanted animals after 1 week.	[150]
Carboxymethyl-hexanoyl chitosan HGF-releasing hydrogels	iPSC-HLC	BALB/c mice + ALF (thioacetamide overdose)	– Increased survival of transplanted animals; survival was higher in functionalized hydrogels containing HGF. – HLC delivered in hydrogels releasing HGF showed higher antioxidant and antiapoptotic activities that reduced necrosis.	[152]
Mebiol TGP (PNIPAAm-PEG) hydrogels	Rat hepatocytes	Wistar rat + ALF (D-GalN)	– Increased survival of transplanted animals. – Reduction of transaminases and bilirubin levels after transplantation.	[151]
Cell sheets	Human iPSC-HLC	Rag2/Il2rg double-knockout mice + partial hepatectomy (70%) + ALF (CCl_4)	– Higher survival of animals transplanted with cell-sheet HLC than those transplanted intrasplenically with HLC. – Increased albumin levels in transplanted animals. – Reduced transaminase levels in animals transplanted with cell-sheet HLC.	[165]

(*Continued...*)

Table 3. (*Continued...*)

Partial hepatectomy				
Decellularized rat liver coated with heparin	Primary rat hepatocytes	Lewis rats with hepatectomy (90%)	– Improved survival and functionality. – Absence of thrombosis.	[169]
Decellularized pig liver	Pig hepatocytes + endothelial cells	Pigs with hepatectomy (60%)	– Active blood flow through the graft. – Preservation of the architecture of the transplanted graft. – Reduction of injury markers (bilirubin, transaminases, inflammation markers).	[156]
Hydrolyzed tetra-ethylorthosilicate, chitosan, Alg, Col I scaffolds	Human mesenchymal stem cells	Wistar rats with partial hepatectomy (70%)	– Human MSCs were differentiated within scaffolds and then transplanted. – After transplantation, cells storage glycogen and showed the expression of hepatic markers (AFP, CK19, CK18, albumin, HNF-3b, and MRP-2).	[157]
Alg scaffolds	Bone marrow mesenchymal stem cells	Sprague–Dawley rats with partial hepatectomy (70%)	– Increased survival (80% vs. 50%, transplanted vs. control). – Improved liver function (reduced transaminase levels). – MSCs on Alg scaffolds secreted albumin and produced glycogen 4 weeks after transplantation.	[158]
Polyacrylonitrile sodium meth-ylallylsulfonate hydrogels	Pig hepatocytes (fresh and cryopreserved)	Lewis rats + hepatectomy (95%)	– Increased survival of transplanted animals. – Fresh or cryopreserved hepatocytes preserved their ultrastructure. – Partial maintenance of CYP3A4 activity in transplanted constructs.	[170]
Fibrosis/Cirrhosis				
Col I hydrogels	Rat neonatal and adult hepatocytes	Sprague–Dawley rat + cirrhosis (CCl_4)	– Implanted cells survived and hosted the native tissue. – Cells had characteristic hepatocyte morphology. – Reduction of fibrosis after multi-site injection of collagen hydrogels containing hepatocytes.	[163]
Col hydrogel	Rat liver cells + MSCs	Wistar rat + CCl_4-induced fibrosis	– Increased survival in treated animals. – Reduction of transaminases levels in transplanted animals. – Reduction of the fibrotic areas assessed by histology. – Reconstruction of transplanted tissue after 90 days.	[164]
Other models				
Decellularized human liver cubes	Sk-Hep-1, HepG2, and LX2	Immunocompetent mice	– Complete decellularization of whole human liver. – dECM human liver scaffolds were successfully repopulated with different human liver cell types. – Interspecies biocompatibility was demonstrated by transplanting dECM cubes into immunocompetent mice.	[148]

Abbreviations: ALF, acute liver failure; Alg, alginate; ALT, alanine transaminase; AST, aspartate transaminase; Col, collagen; dECM, decellularized extracellular matrix; EpCAM, epithelial cell adhesion molecule; Gel, gelatin; HA, hyaluronic acid; HGF, hepatocyte growth factor; HLC, hepatocyte-like cells; MSC, mesenchymal stem cells; PHH, primary human hepatocytes.

developed systems for disease modeling. Secondly, many studies focus on maintaining the hepatocyte phenotype without considering the liver's multicellularity. In fact, Takebe et al. attempted to recapitulate early organogenesis by creating liver buds that contain hepatic endoderm cells from iPSCs, HUVECs, and MSCs and demonstrated their increased functionality *in vitro,* along with their ability to rescue an animal model of drug-induced lethal failure and achieve human vascularization.[83] The development of an angiogenic response for regenerative medicine applications would thus be essential to achieve long-term effects. On the other hand, despite the fact that the co-culture of hepatocytes and other non-parenchymal cells in 3D configuration has been described as an optimal method that could better recapitulate liver physiology, the random distribution of the cells, their limited expansion capability, and the problems associated with maintaining functionality for longer periods remain as important challenges to be addressed.[171] Finally, most of the animal models used in the regenerative medicine approach are based on the use of partial hepatectomy or ALF; thus, more animal models that reflect other aspects of liver disease should be used to determine the efficacy of the developed systems.

On the other hand, future studies will be directed to searching for biomaterials with the appropriate mechanical

properties, printability, and functionality to promote hepatic functions. Dynamic culture in bioreactors or in microfluidic chip devices equipped with micro-physiological stimulation will play a key role in drug screening and liver disease modeling and could pave the way for clinical applications.[5]

Acknowledgments

None.

Funding

This work was funded by the Institute of Health Carlos III (ISCIII, Plan Estatal de I+D+i 2013-2016) and co-financed by the European Regional Development Fund "A way to achieve Europe" (FEDER) through Grant No. PI21/00223, and by Grants PID2022-136433OB-C21 and C-22 funded by MCIN/AEI/10.13039/501100011033 and Grant No. CNS2022-135425. The funders had no role in the design of the study; in the collection, analyses, or interpretation of data; in the writing of the manuscript; or in the decision to publish the results.

Conflict of interest

The authors declare no conflicts of interest.

Author contributions

Conceptualization: Gloria Gallego-Ferrer, Laia Tolosa
Formal analysis: Julio Rodríguez-Fernández, M. Teresa Donato, Gloria Gallego-Ferrer, Laia Tolosa
Funding acquisition: M. Teresa Donato, Gloria Gallego-Ferrer, Laia Tolosa
Visualization: Julio Rodríguez-Fernández, Gloria Gallego-Ferrer, Laia Tolosa
Writing – original draft: Julio Rodríguez-Fernández, M. Teresa Donato, Gloria Gallego-Ferrer, Laia Tolosa
Writing – review & editing: Julio Rodríguez-Fernández, M. Teresa Donato, Gloria Gallego-Ferrer, Laia Tolosa
All authors have read and agreed to the published version of the manuscript.

Ethics approval and consent to participate

Not applicable.

Consent for publication

Not applicable.

Availability of data

Not applicable.

References

1. Pimpin L, Cortez-Pinto H, Negro F, et al. Burden of liver disease in Europe: epidemiology and analysis of risk factors to identify prevention policies. *J Hepatol*. 2018;69(3):718-735. doi: 10.1016/j.jhep.2018.05.011
2. Karlsen TH, Sheron N, Zelber-Sagi S, et al. The EASL–Lancet Liver Commission: protecting the next generation of Europeans against liver disease complications and premature mortality. *Lancet*. 2022;399(10319):61-116. doi: 10.1016/S0140-6736(21)01701-3
3. Kaur S, Kidambi S, Ortega-Ribera M, et al. In vitro models for the study of liver biology and diseases: advances and limitations. *CMGH*. 2023;15(3):559-571. doi: 10.1016/j.jcmgh.2022.11.008
4. Godoy P, Hewitt NJ, Albrecht U, et al. Recent advances in 2D and 3D in vitro systems using primary hepatocytes, alternative hepatocyte sources and non-parenchymal liver cells and their use in investigating mechanisms of hepatotoxicity, cell signaling and ADME. *Arch Toxicol*. 2013;87(8):1315-1530. doi: 10.1007/s00204-013-1078-5
5. da Silva Morais A, Vieira S, Zhao X, et al. Advanced biomaterials and processing methods for liver regeneration: state-of-the-art and future trends. *Adv Healthc Mater*. 2020;9(5). doi: 10.1002/adhm.201901435
6. Ming Z, Tang X, Liu J, Ruan B. Advancements in research on constructing physiological and pathological liver models and their applications utilizing bioprinting technology. *Molecules*. 2023;28(9):3683. doi: 10.3390/molecules28093683
7. Michalopoulos GK, DeFrances MC. Liver regeneration. *Science*. 1997;276(5309):60-66. doi: 10.1126/science.276.5309.60
8. Kholodenko IV, Yarygin KN. Cellular mechanisms of liver regeneration and cell-based therapies of liver diseases. *Biomed Res Int*. 2017;2017:1-17. doi: 10.1155/2017/8910821
9. Chawla S, Das A. Preclinical-to-clinical innovations in stem cell therapies for liver regeneration. *Curr Res Transl Med*. 2023;71(1):103365. doi: 10.1016/j.retram.2022.103365
10. Asrani SK, Devarbhavi H, Eaton J, Kamath PS. Burden of liver diseases in the world. *J Hepatol*. 2019;70(1):151-171. doi: 10.1016/j.jhep.2018.09.014
11. Burton R, Henn C, Lavoie D, et al. A rapid evidence review of the effectiveness and cost-effectiveness of alcohol control policies: an English perspective. *Lancet*. 2017;389(10078):1558-1580. doi: 10.1016/S0140-6736(16)32420-5
12. Hart CL, Morrison DS, Batty GD, Mitchell RJ, Smith GD. Effect of body mass index and alcohol consumption on

liver disease: analysis of data from two prospective cohort studies. *BMJ*. 2010;340(7747):634.
doi: 10.1136/bmj.c1240

13. Bataller R, Cabezas J, Aller R, et al. Enfermedad hepática por alcohol. Guías de práctica clínica. Documento de consenso auspiciado por la AEEH. *Gastroenterol Hepatol*. 2019;42(10):657-676.
doi: 10.1016/j.gastrohep.2019.09.006

14. Bhatia SN, Underhill GH, Zaret KS, Fox IJ. Cell and tissue engineering for liver disease. *Sci Transl Med*. 2014;6(245).
doi: 10.1126/scitranslmed.3005975

15. Pelechá M, Villanueva-Bádenas E, Timor-López E, Donato MT, Tolosa L. Cell models and omics techniques for the study of nonalcoholic fatty liver disease: focusing on stem cell-derived cell models. *Antioxidants*. 2021;11(1):86.
doi: 10.3390/antiox11010086

16. Ströbel S, Kostadinova R, Fiaschetti-Egli K, et al. A 3D primary human cell-based in vitro model of non-alcoholic steatohepatitis for efficacy testing of clinical drug candidates. *Sci Rep*. 2021;11(1):22765.
doi: 10.1038/s41598-021-01951-7

17. Tsuchida T, Friedman SL. Mechanisms of hepatic stellate cell activation. *Nat Rev Gastroenterol Hepatol*. 2017;14(7):397-411.
doi: 10.1038/nrgastro.2017.38

18. EASL. EASL-EASD-EASO Clinical Practice Guidelines for the management of non-alcoholic fatty liver disease. *Obes Facts*. 2016;9(2):65-90.
doi: 10.1159/000443344

19. Diehl AM, Day C. Cause, pathogenesis, and treatment of nonalcoholic steatohepatitis. *N Engl J Med*. 2017;377(21):2063-2072.
doi: 10.1056/NEJMra1503519

20. Arzumanyan A, Reis HMGPV, Feitelson MA. Pathogenic mechanisms in HBV- and HCV-associated hepatocellular carcinoma. *Nat Rev Cancer*. 2013;13(2):123-135.
doi: 10.1038/nrc3449

21. Ray G. Management of liver diseases: current perspectives. *World J Gastroenterol*. 2022;28(40):5818-5826.
doi: 10.3748/wjg.v28.i40.5818

22. Dhanasekaran R, Bandoh S, Roberts LR. Molecular pathogenesis of hepatocellular carcinoma and impact of therapeutic advances. *F1000Res*. 2016;5:879.
doi: 10.12688/f1000research.6946.1

23. Ruff SM, Manne A, Cloyd JM, Dillhoff M, Ejaz A, Pawlik TM. Current landscape of immune checkpoint inhibitor therapy for hepatocellular carcinoma. *Curr Oncol*. 2023;30(6):5863-5875.
doi: 10.3390/curroncol30060439

24. Kaplowitz N. Idiosyncratic drug hepatotoxicity. *Nat Rev Drug Discov*. 2005;4(6):489-499.
doi: 10.1038/nrd1750

25. Björnsson ES, Gunnarsson BI, Gröndal G, et al. Risk of drug-induced liver injury from tumor necrosis factor antagonists. *Clin Gastroenterol Hepatol*. 2015;13(3):602-608.
doi: 10.1016/j.cgh.2014.07.062

26. EASL. EASL Clinical Practice Guidelines: drug-induced liver injury. *J Hepatol*. 2019;70(6):1222-1261.
doi: 10.1016/j.jhep.2019.02.014

27. Anand SK, Caputo M, Xia Y, et al. Inhibition of MAP4K4 signaling initiates metabolic reprogramming to protect hepatocytes from lipotoxic damage. *J Lipid Res*. 2022;63(7):100238.
doi: 10.1016/j.jlr.2022.100238

28. Pareja E, Gómez-Lechón MJ, Tolosa L. Induced pluripotent stem cells for the treatment of liver diseases: challenges and perspectives from a clinical viewpoint. *Ann Transl Med*. 2020;8(8):566-566.
doi: 10.21037/atm.2020.02.164

29. Adam R, Karam V, Delvart V, et al. Evolution of indications and results of liver transplantation in Europe. A report from the European Liver Transplant Registry (ELTR). *J Hepatol*. 2012;57(3):675-688.
doi: 10.1016/j.jhep.2012.04.015

30. Dutkowski P, Linecker M, DeOliveira ML, Müllhaupt B, Clavien PA. Challenges to liver transplantation and strategies to improve outcomes. *Gastroenterology*. 2015;148(2):307-323.
doi: 10.1053/j.gastro.2014.08.045

31. Bizzaro, Russo, Burra. New perspectives in liver transplantation: from regeneration to bioengineering. *Bioengineering*. 2019;6(3):81.
doi: 10.3390/bioengineering6030081

32. Smets F, Najimi M, Sokal EM. Cell transplantation in the treatment of liver diseases. *Pediatr Transplant*. 2008;12(1):6-13.
doi: 10.1111/j.1399-3046.2007.00788.x

33. Lysy PA, Najimi M, Stéphenne X, Bourgois A, Smets F, Sokal EM. Liver cell transplantation for Crigler-Najjar syndrome type I: update and perspectives. *World J Gastroenterol*. 2008;14(22):3464.
doi: 10.3748/wjg.14.3464

34. van de Kerkhove MP, Hoekstra R, Chamuleau RAFM, van Gulik TM. Clinical application of bioartificial liver support systems. *Ann Surg*. 2004;240(2):216-230.
doi: 10.1097/01.sla.0000132986.75257.19

35. Gebhardt R, Matz-Soja M. Liver zonation: novel aspects of its regulation and its impact on homeostasis. *World J Gastroenterol*. 2014;20(26):8491.
doi: 10.3748/wjg.v20.i26.8491

36. Panday R, Monckton CP, Khetani SR. The role of liver zonation in physiology, regeneration, and disease. *Semin Liver Dis*. 2022;42(01):001-016.
doi: 10.1055/s-0041-1742279

37. Trefts E, Gannon M, Wasserman DH. The liver. *Curr Biol*. 2017;27(21):R1147-R1151.

doi: 10.1016/j.cub.2017.09.019

38. Schulze RJ, Schott MB, Casey CA, Tuma PL, McNiven MA. The cell biology of the hepatocyte: a membrane trafficking machine. *J Cell Biol*. 2019;218(7):2096-2112. doi: 10.1083/jcb.201903090

39. Ramachandran P, Matchett KP, Dobie R, Wilson-Kanamori JR, Henderson NC. Single-cell technologies in hepatology: new insights into liver biology and disease pathogenesis. *Nat Rev Gastroenterol Hepatol*. 2020;17(8):457-472. doi: 10.1038/s41575-020-0304-x

40. Aizarani N, Saviano A, Sagar, et al. A human liver cell atlas reveals heterogeneity and epithelial progenitors. *Nature*. 2019;572(7768):199-204. doi: 10.1038/s41586-019-1373-2

41. Dianat N, Dubois-Pot-Schneider H, Steichen C, et al. Generation of functional cholangiocyte-like cells from human pluripotent stem cells and HepaRG cells. *Hepatology*. 2014;60(2):700-714. doi: 10.1002/hep.27165

42. Salas-Silva S, Simoni-Nieves A, Chávez-Rodríguez L, Gutiérrez-Ruiz MC, Bucio L, Quiroz LEG. Mechanism of cholangiocellular damage and repair during cholestasis. *Ann Hepatol*. 2021;26:100530. doi: 10.1016/j.aohep.2021.100530

43. Dixon LJ, Barnes M, Tang H, Pritchard MT, Nagy LE. Kupffer cells in the liver. *Compr Physiol*. 2013;3(2):785-797. doi: 10.1002/cphy.c120026

44. Han J, Ulevitch RJ. Limiting inflammatory responses during activation of innate immunity. *Nat Immunol*. 2005;6(12):1198-1205. doi: 10.1038/ni1274

45. Sørensen KK, Simon-Santamaria J, McCuskey RS, Smedsrød B. Liver sinusoidal endothelial cells. *Compr Physiol*. 2015;5:1751-1774. doi: 10.1002/cphy.c140078

46. Jenne CN, Kubes P. Immune surveillance by the liver. *Nat Immunol*. 2013;14(10):996-1006. doi: 10.1038/ni.2691

47. Ding B Sen, Cao Z, Lis R, et al. Divergent angiocrine signals from vascular niche balance liver regeneration and fibrosis. *Nature*. 2014;505(7481):97-102. doi: 10.1038/nature12681

48. Halpern KB, Shenhav R, Massalha H, et al. Paired-cell sequencing enables spatial gene expression mapping of liver endothelial cells. *Nat Biotechnol*. 2018;36(10):962. doi: 10.1038/nbt.4231

49. Senoo H. Structure and function of hepatic stellate cells. *Med Electron Microsc*. 2004;37(1):3-15. doi: 10.1007/s00795-003-0230-3

50. Sanz-García C, Fernández-Iglesias A, Gracia-Sancho J, Arráez-Aybar LA, Nevzorova YA, Cubero FJ. The space of Disse: the liver hub in health and disease. *Livers*. 2021;1(1):3-26. doi: 10.3390/livers1010002

51. Puche JE, Saiman Y, Friedman SL. Hepatic stellate cells and liver fibrosis. *Compr Physiol*. 2013;3:1473-1492. doi: 10.1002/cphy.c120035

52. Frantz C, Stewart KM, Weaver VM. The extracellular matrix at a glance. *J Cell Sci*. 2010;123(24):4195-4200. doi: 10.1242/jcs.023820

53. Baiocchini A, Montaldo C, Conigliaro A, et al. Extracellular matrix molecular remodeling in human liver fibrosis evolution. *PLoS One*. 2016;11(3). doi: 10.1371/journal.pone.0151736

54. Bedossa P, Paradis V. Liver extracellular matrix in health and disease. *J Pathol*. 2003;200(4):504-515. doi: 10.1002/path.1397

55. Allu I, Sahi AK, Koppadi M, Gundu S, Sionkowska A. Decellularization techniques for tissue engineering: towards replicating native extracellular matrix architecture in liver regeneration. *J Funct Biomater*. 2023;14(10):518. doi: 10.3390/jfb14100518

56. Ford AJ, Rajagopalan P. Extracellular matrix remodeling in 3D: implications in tissue homeostasis and disease progression. *Wiley Interdiscip Rev Nanomed Nanobiotechnol*. 2018;10(4). doi: 10.1002/wnan.1503

57. Mejias M, Gallego J, Naranjo-Suarez S, et al. CPEB4 increases expression of PFKFB3 to induce glycolysis and activate mouse and human hepatic stellate cells, promoting liver fibrosis. *Gastroenterology*. 2020;159(1):273-288. doi: 10.1053/j.gastro.2020.03.008

58. Arriazu E, Ruiz de Galarreta M, Cubero FJ, et al. Extracellular matrix and liver disease. *Antioxid Redox Signal*. 2014;21(7):1078-1097. doi: 10.1089/ars.2013.5697

59. Leroy V, Monier F, Bottari S, et al. Circulating matrix metalloproteinases 1, 2, 9 and their inhibitors TIMP-1 and TIMP-2 as serum markers of liver fibrosis in patients with chronic hepatitis C: comparison with PIIINP and hyaluronic acid. *Am J Gastroenterol*. 2004;99(2):271-279. doi: 10.1111/j.1572-0241.2004.04055.x

60. Ramachandran P, Dobie R, Wilson-Kanamori JR, et al. Resolving the fibrotic niche of human liver cirrhosis at single-cell level. *Nature*. 2019;575(7783):512-518. doi: 10.1038/s41586-019-1631-3

61. Yuan J, Li X, Yu S. Cancer organoid co-culture model system: novel approach to guide precision medicine. *Front Immunol*. 2023;13. doi: 10.3389/fimmu.2022.1061388

62. Soldatow VY, LeCluyse EL, Griffith LG, Rusyn I. In vitro models for liver toxicity testing. *Toxicol Res*. 2013;2(1):23-39. doi: 10.1039/C2TX20051A

63. Gomez-Lechon M, Donato M, Lahoz A, Castell J. Cell lines: a tool for in vitro drug metabolism studies. *Curr Drug Metab*. 2008;9(1):1-11. doi: 10.2174/138920008783331086

64. Hewitt NJ, Gómez Lechón MJ, Houston JB, et al. Primary hepatocytes: current understanding of the regulation of metabolic enzymes and transporter proteins, and pharmaceutical practice for the use of hepatocytes in metabolism, enzyme induction, transporter, clearance, and hepatotoxicity studies. *Drug Metab Rev*. 2007;39(1):159-234. doi: 10.1080/03602530601093489

65. O´Brien PJ, Chan K, Silber PM. Human and animal hepatocytes in vitro with extrapolation in vivo. *Chem Biol Interact*. 2004;150(1):97-114. doi: 10.1016/j.cbi.2004.09.003

66. O´Brien PJ, Irwin W, Diaz D, et al. High concordance of drug-induced human hepatotoxicity with in vitro cytotoxicity measured in a novel cell-based model using high content screening. *Arch Toxicol*. 2006;80(9):580-604. doi: 10.1007/s00204-006-0091-3

67. Tolosa L, Pareja-Ibars E, Donato MT, et al. Neonatal livers: a source for the isolation of good-performing hepatocytes for cell transplantation. *Cell Transplant*. 2014;23(10):1229-1242. doi: 10.3727/096368913X669743

68. Gomez-Lechon M, Donato M, Castell J, Jover R. Human hepatocytes in primary culture: the choice to investigate drug metabolism in man. *Curr Drug Metab*. 2004;5(5):443-462. doi: 10.2174/1389200043335414

69. Chowdhary V, Teng K yu, Thakral S, et al. miRNA-122 protects mice and human hepatocytes from acetaminophen toxicity by regulating cytochrome P450 family 1 subfamily A member 2 and family 2 subfamily e member 1 expression. *Am J Pathol*. 2017;187(12):2758-2774. doi: 10.1016/j.ajpath.2017.08.026

70. Fox IJ, Chowdhury JR. Hepatocyte transplantation. *Am J Transplant*. 2004;4:7-13. doi: 10.1111/j.1600-6135.2004.0340.x

71. Hansel MC, Davila JC, Vosough M, et al. The use of induced pluripotent stem cells for the study and treatment of liver diseases. *Curr Protoc Toxicol*. 2016;67(1). doi: 10.1002/0471140856.tx1413s67

72. Iansante V, Mitry RR, Filippi C, Fitzpatrick E, Dhawan A. Human hepatocyte transplantation for liver disease: current status and future perspectives. *Pediatr Res*. 2018;83(1-2):232-240. doi: 10.1038/pr.2017.284

73. Gómez-Lechón MJ, Tolosa L, Conde I, Donato MT. Competency of different cell models to predict human hepatotoxic drugs. *Expert Opin Drug Metab Toxicol*. 2014;10(11):1553-1568. doi: 10.1517/17425255.2014.967680

74. Donato MT, Tolosa L, Gómez-Lechón MJ. Culture and functional characterization of human hepatoma HepG2 cells. *Methods Mol Biol*. 2015;1250:77-93. doi: 10.1007/978-1-4939-2074-7_5

75. Forbes SJ, Gupta S, Dhawan A. Cell therapy for liver disease: from liver transplantation to cell factory. *J Hepatol*. 2015;62(1):S157-S169. doi: 10.1016/j.jhep.2015.02.040

76. Donato MT, Tolosa L. Stem-cell derived hepatocyte-like cells for the assessment of drug-induced liver injury. *Differentiation*. 2019;106(January):15-22. doi: 10.1016/j.diff.2019.02.004

77. Hannan NRF, Segeritz CP, Touboul T, Vallier L. Production of hepatocyte-like cells from human pluripotent stem cells. *Nat Protoc*. 2013;8(2):430-437. doi: 10.1038/nprot.2012.153

78. Takayama K, Morisaki Y, Kuno S, et al. Prediction of interindividual differences in hepatic functions and drug sensitivity by using human iPS-derived hepatocytes. *Proc Natl Acad Sci*. 2014;111(47):16772-16777. doi: 10.1073/pnas.1413481111

79. Bell CC, Dankers ACA, Lauschke VM, et al. Comparison of hepatic 2D sandwich cultures and 3d spheroids for long-term toxicity applications: a multicenter study. *Toxicol Sci*. 2018;162(2):655-666. doi: 10.1093/toxsci/kfx289

80. Lee JY, Han HJ, Lee SJ, et al. Use of 3D human liver organoids to predict drug-induced phospholipidosis. *Int J Mol Sci*. 2020;21(8):2982. doi: 10.3390/ijms21082982

81. Berger M, Neth O, Ilmer M, et al. Hepatoblastoma cells express truncated neurokinin-1 receptor and can be growth inhibited by aprepitant in vitro and in vivo. *J Hepatol*. 2014;60(5):985-994. doi: 10.1016/j.jhep.2013.12.024

82. Davidson MD, Pickrell J, Khetani SR. Physiologically inspired culture medium prolongs the lifetime and insulin sensitivity of human hepatocytes in micropatterned co-cultures. *Toxicology*. 2021;449. doi: 10.1016/j.tox.2020.152662

83. Takebe T, Sekine K, Enomura M, et al. Vascularized and functional human liver from an iPSC-derived organ bud transplant. *Nature*. 2013;499(7459):481-484. doi: 10.1038/nature12271

84. Peters JT, Wechsler ME, Peppas NA. Advanced biomedical hydrogels: molecular architecture and its impact on medical applications. *Regen Biomater*. 2021;8(6). doi: 10.1093/rb/rbab060

85. Annabi N, Tamayol A, Uquillas JA, et al. 25th anniversary article: rational design and applications of hydrogels in

regenerative medicine. *Adv Mater*. 2014;26(1):85-124.
doi: 10.1002/adma.201303233

86. Jiang J, Tan Y, Liu A, et al. Tissue engineered artificial liver model based on viscoelastic hyaluronan-collagen hydrogel and the effect of EGCG intervention on ALD. *Colloids Surf B Biointerfaces*. 2021;206.
doi: 10.1016/j.colsurfb.2021.111980

87. Tong X, Zhao F, Ren Y, Zhang Y, Cui Y, Wang Q. Injectable hydrogels based on glycyrrhizin, alginate, and calcium for three-dimensional cell culture in liver tissue engineering. *J Biomed Mater Res A*. 2018;106(12):3292-3302.
doi: 10.1002/jbm.a.36528

88. Lai JY. Biocompatibility of chemically cross-linked gelatin hydrogels for ophthalmic use. *J Mater Sci Mater Med*. 2010;21(6):1899-1911.
doi: 10.1007/s10856-010-4035-3

89. Tan H, Marra KG. Injectable, biodegradable hydrogels for tissue engineering applications. *Materials*. 2010;3(3): 1746-1767.
doi: 10.3390/ma3031746

90. Rodriguez-Fernandez J, Garcia-Legler E, Villanueva-Badenas E, et al. Primary human hepatocytes-laden scaffolds for the treatment of acute liver failure. *Biomater Adv*. 2023;153:213576.
doi: 10.1016/j.bioadv.2023.213576

91. Ramiah P, du Toit LC, Choonara YE, Kondiah PPD, Pillay V. Hydrogel-based bioinks for 3D bioprinting in tissue regeneration. *Front Mater*. 2020;7.
doi: 10.3389/fmats.2020.00076

92. Raghuwanshi VS, Garnier G. Characterisation of hydrogels: linking the nano to the microscale. *Adv Colloid Interface Sci*. 2019;274:102044.
doi: 10.1016/j.cis.2019.102044

93. Richbourg NR, Peppas NA. The swollen polymer network hypothesis: quantitative models of hydrogel swelling, stiffness, and solute transport. *Prog Polym Sci*. 2020;105:101243.
doi: 10.1016/j.progpolymsci.2020.101243

94. Willemse J, van Tienderen G, van Hengel E, et al. Hydrogels derived from decellularized liver tissue support the growth and differentiation of cholangiocyte organoids. *Biomaterials*. 2022;284:121473.
doi: 10.1016/j.biomaterials.2022.121473

95. Ye S, Boeter JWB, Penning LC, Spee B, Schneeberger K. Hydrogels for liver tissue engineering. *Bioengineering*. 2019;6(3):59.
doi: 10.3390/bioengineering6030059

96. Desimone MF, Hélary C, Rietveld IB, et al. Silica-collagen bionanocomposites as three-dimensional scaffolds for fibroblast immobilization. *Acta Biomater*. 2010;6(10): 3998-4004.
doi: 10.1016/j.actbio.2010.05.014

97. Lee JW, Choi YJ, Yong WJ, et al. Development of a 3D cell printed construct considering angiogenesis for liver tissue engineering. *Biofabrication*. 2016;8(1):015007.
doi: 10.1088/1758-5090/8/1/015007

98. Cui J, Wang H, Shi Q, Sun T, Huang Q, Fukuda T. Multicellular co-culture in three-dimensional gelatin methacryloyl hydrogels for liver tissue engineering. *Molecules*. 2019;24(9).
doi: 10.3390/molecules24091762

99. An S, Choi S, Min S, Cho SW. Hyaluronic acid-based biomimetic hydrogels for tissue engineering and medical applications. *Biotechnol Bioprocess Eng*. 2021;26(4):503-516.
doi: 10.1007/s12257-020-0343-8

100. Christoffersson J, Aronsson C, Jury M, Selegård R, Aili D, Mandenius CF. Fabrication of modular hyaluronan-PEG hydrogels to support 3D cultures of hepatocytes in a perfused liver-on-a-chip device. *Biofabrication*. 2019;11(1).
doi: 10.1088/1758-5090/aaf657

101. Kim M, Lee JY, Jones CN, Revzin A, Tae G. Heparin-based hydrogel as a matrix for encapsulation and cultivation of primary hepatocytes. *Biomaterials*. 2010;31(13):3596-3603.
doi: 10.1016/j.biomaterials.2010.01.068

102. Chen S, Liu A, Wu C, et al. Static–dynamic profited viscoelastic hydrogels for motor-clutch-regulated neurogenesis. *ACS Appl Mater Interfaces*. 2021;13(21):24463-24476.
doi: 10.1021/acsami.1c03821

103. Malinen MM, Kanninen LK, Corlu A, et al. Differentiation of liver progenitor cell line to functional organotypic cultures in 3D nanofibrillar cellulose and hyaluronan-gelatin hydrogels. *Biomaterials*. 2014;35(19):5110-5121.
doi: 10.1016/j.biomaterials.2014.03.020

104. Stevens KR, Miller JS, Blakely BL, Chen CS, Bhatia SN. Degradable hydrogels derived from PEG-diacrylamide for hepatic tissue engineering. *J Biomed Mater Res A*. 2015;103(10):3331-3338.
doi: 10.1002/jbm.a.35478

105. Underhill GH, Chen AA, Albrecht DR, Bhatia SN. Assessment of hepatocellular function within PEG hydrogels. *Biomaterials*. 2007;28(2):256-270.
doi: 10.1016/j.biomaterials.2006.08.043

106. Lin TY, Ki CS, Lin CC. Manipulating hepatocellular carcinoma cell fate in orthogonally cross-linked hydrogels. *Biomaterials*. 2014;35(25):6898-6906.
doi: 10.1016/j.biomaterials.2014.04.118

107. Kim D, Kim M, Lee J, Jang J. Review on multicomponent hydrogel bioinks based on natural biomaterials for bioprinting 3D liver tissues. *Front Bioeng Biotechnol*. 2022;10.
doi: 10.3389/fbioe.2022.764682

108. Kim MK, Jeong W, Kang HW. Liver dECM–gelatin composite bioink for precise 3D printing of highly functional liver tissues. *J Funct Biomater*. 2023;14(8).
doi: 10.3390/jfb14080417

109. Liu H, Gong Y, Zhang K, et al. Recent advances in decellularized matrix-derived materials for bioink and 3D bioprinting. *Gels*. 2023;9(3).
doi: 10.3390/gels9030195

110. Monteiro MV, Henriques-Pereira M, Neves BM, Duarte ID, Gaspar VM, Mano JF. Photo-compartmentalized decellularized matrix-hyaluronan hybrid units for pancreatic tumor-stroma modeling. *Adv Funct Mater*. 2023;34(6):2305473.
doi: 10.1002/adfm.202305473

111. Agarwal T, Subramanian B, Maiti TK. Liver tissue engineering: challenges and opportunities. *ACS Biomater Sci Eng*. 2019;5(9):4167-4182.
doi: 10.1021/acsbiomaterials.9b00745

112. Huang D (Danielle), Gibeley SB, Xu C, et al. Engineering liver microtissues for disease modeling and regenerative medicine. *Adv Funct Mater*. 2020;30(44).
doi: 10.1002/adfm.201909553

113. Trujillo S, Dobre O, Dalby MJ. Salmeron-Sanchez M. Mechanotransduction and Growth Factor Signaling in Hydrogel-Based Microenvironments. Reis RL, eds. *In Encyclopedia of Tissue Engineering and Regenerative Medicine*. Oxford: Academic Press. 2019:87-101.
doi: 10.1016/B978-0-12-801238-3.11141-9

114. Cantini M, Donnelly H, Dalby MJ, Salmeron-Sanchez M. The plot thickens: the emerging role of matrix viscosity in cell mechanotransduction. *Adv Healthc Mater*. 2020;9(8).
doi: 10.1002/adhm.201901259

115. Rizwan M, Ling C, Guo C, et al. Viscoelastic notch signaling hydrogel induces liver bile duct organoid growth and morphogenesis. *Adv Healthc Mater*. 2022;11(23).
doi: 10.1002/adhm.202200880

116. Bruns H, Kneser U, Holzhüter S, et al. Injectable liver: a novel approach using fibrin gel as a matrix for culture and intrahepatic transplantation of hepatocytes. *Tissue Eng*. 2005;11(11-12):1718-1726.
doi: 10.1089/ten.2005.11.1718

117. Le Guilcher C, Merlen G, Dellaquila A, et al. Engineered human liver based on pullulan-dextran hydrogel promotes mice survival after liver failure. *Mater Today Bio*. 2023;19:100554.
doi: 10.1016/j.mtbio.2023.100554

118. Meng D, Lei X, Li Y, Kong Y, Huang D, Zhang G. Three dimensional polyvinyl alcohol scaffolds modified with collagen for HepG2 cell culture. *J Biomater Appl*. 2020; 35(4-5):459-470.
doi: 10.1177/0885328220933505

119. He XL, Ge LL, Liu ZL, et al. Glycyrrhetinic acid-based thermoresponsive hydrogel as a synthetic extracellular matrix for hepatocyte culture and recovery. *Ind Eng Chem Res*. 2014;53(26):10618-10628.
doi: 10.1021/ie404417u

120. Ye S, Boeter JWB, Mihajlovic M, et al. A chemically defined hydrogel for human liver organoid culture. *Adv Funct Mater*. 2020;30(48).
doi: 10.1002/adfm.202000893

121. Ma L, Wu Y, Li Y, et al. Current advances on 3D-bioprinted liver tissue models. *Adv Healthc Mater*. 2020;9(24).
doi: 10.1002/adhm.202001517

122. Naranjo-Alcazar R, Bendix S, Groth T, Gallego Ferrer G. Research progress in enzymatically cross-linked hydrogels as injectable systems for bioprinting and tissue engineering. *Gels*. 2023;9(3):230.
doi: 10.3390/gels9030230

123. Naghieh S, Chen X. Printability–a key issue in extrusion-based bioprinting. *J Pharm Anal*. 2021;11(5):564-579.
doi: 10.1016/j.jpha.2021.02.001

124. Li W, Liu Z, Tang F, et al. Application of 3D bioprinting in liver diseases. *Micromachines*. 2023;14(8).
doi: 10.3390/mi14081648

125. Wang Q, Liu J, Yin W, et al. Microscale tissue engineering of liver lobule models: advancements and applications. *Front Bioeng Biotechnol*. 2023;11.
doi: 10.3389/fbioe.2023.1303053

126. Xie M, Su J, Zhou S, Li J, Zhang K. Application of hydrogels as three-dimensional bioprinting ink for tissue engineering. *Gels*. 2023;9(2):88.
doi: 10.3390/gels9020088

127. Khati V, Ramachandraiah H, Pati F, Svahn HA, Gaudenzi G, Russom A. 3D bioprinting of multi-material decellularized liver matrix hydrogel at physiological temperatures. *Biosensors*. 2022;12(7):521.
doi: 10.3390/bios12070521

128. Unagolla JM, Jayasuriya AC. Hydrogel-based 3D bioprinting: a comprehensive review on cell-laden hydrogels, bioink formulations, and future perspectives. *Appl Mater Today*. 2020;18:100479.
doi: 10.1016/j.apmt.2019.100479

129. Gori M, Giannitelli SM, Torre M, et al. Biofabrication of hepatic constructs by 3D bioprinting of a cell-laden thermogel: an effective tool to assess drug-induced hepatotoxic response. *Adv Healthc Mater*. 2020; 9(21).
doi: 10.1002/adhm.202001163

130. Mazzocchi A, Devarasetty M, Huntwork R, Soker S, Skardal A. Optimization of collagen type I-hyaluronan hybrid bioink for 3D bioprinted liver microenvironments. *Biofabrication*. 2018;11(1):015003.
doi: 10.1088/1758-5090/aae543

131. He J, Wang J, Pang Y, et al. Bioprinting of a hepatic tissue model using humaninduced pluripotent stem cell-derived hepatocytes for drug-induced hepatotoxicity evaluation. *Int J Bioprint*. 2022;8(3):581.
doi: 10.18063/ijb.v8i3.581

132. Schmidt K, Berg J, Roehrs V, Kurreck J, Al-Zeer MA. 3D-bioprinted HepaRG cultures as a model for testing long term aflatoxin B1 toxicity in vitro. *Toxicol Rep*. 2020;7:1578-1587.
doi: 10.1016/j.toxrep.2020.11.003

133. Bhise NS, Manoharan V, Massa S, et al. A liver-on-a-chip platform with bioprinted hepatic spheroids. *Biofabrication*. 2016;8(1).
doi: 10.1088/1758-5090/8/1/014101

134. Janani G, Priya S, Dey S, Mandal BB. Mimicking native liver lobule microarchitecture in vitro with parenchymal and non-parenchymal cells using 3D bioprinting for drug toxicity and drug screening applications. *ACS Appl Mater Interfaces*. 2022;14(8):10167-10186.
doi: 10.1021/acsami.2c00312

135. Xie F, Sun L, Pang Y, et al. Three-dimensional bio-printing of primary human hepatocellular carcinoma for personalized medicine. *Biomaterials*. 2021;265:120416.
doi: 10.1016/j.biomaterials.2020.120416

136. Ma X, Yu C, Wang P, et al. Rapid 3D bioprinting of decellularized extracellular matrix with regionally varied mechanical properties and biomimetic microarchitecture. *Biomaterials*. 2018;185:310-321.
doi: 10.1016/j.biomaterials.2018.09.026

137. Cuvellier M, Ezan F, Oliveira H, et al. 3D culture of HepaRG cells in GelMa and its application to bioprinting of a multicellular hepatic model. *Biomaterials*. 2021;269:120611.
doi: 10.1016/j.biomaterials.2020.120611

138. Kim D, Kim M, Lee J, Jang J. Review on multicomponent hydrogel bioinks based on natural biomaterials for bioprinting 3D liver tissues. *Front Bioeng Biotechnol*. 2022;10.
doi: 10.3389/fbioe.2022.764682

139. He J, Wang J, Pang Y, et al. Bioprinting of a hepatic tissue model using human-induced pluripotent stem cell-derived hepatocytes for drug-induced hepatotoxicity evaluation. *Int J Bioprint*. 2022;8(3):176-190.
doi: 10.18063/ijb.v8i3.581

140. Norona LM, Nguyen DG, Gerber DA, Presnell SC, LeCluyse EL. Editor's highlight: modeling compound-induced fibrogenesis *in vitro* using three-dimensional bioprinted human liver tissues. *Toxicol Sci*. 2016;154(2):354-367.
doi: 10.1093/toxsci/kfw169

141. Norona LM, Nguyen DG, Gerber DA, Presnell SC, Mosedale M, Watkins PB. Bioprinted liver provides early insight into the role of Kupffer cells in TGF-β1 and methotrexate-induced fibrogenesis. *PLoS One*. 2019;14(1):e0208958.
doi: 10.1371/journal.pone.0208958

142. Maharjan S, Bonilla D, Sindurakar P, et al. 3D human nonalcoholic hepatic steatosis and fibrosis models. *Biodes Manuf*. 2021;4(2):157-170.
doi: 10.1007/s42242-020-00121-4

143. Mao S, He J, Zhao Y, et al. Bioprinting of patient-derived in vitro intrahepatic cholangiocarcinoma tumor model: establishment, evaluation and anti-cancer drug testing. *Biofabrication*. 2020;12(4).
doi: 10.1088/1758-5090/aba0c3

144. Kizawa H, Nagao E, Shimamura M, Zhang G, Torii H. Scaffold-free 3D bio-printed human liver tissue stably maintains metabolic functions useful for drug discovery. *Biochem Biophys Rep*. 2017;10:186-191.
doi: 10.1016/j.bbrep.2017.04.004

145. Dhawan A, Mitry RR, Hughes RD, et al. Hepatocyte transplantation for inherited factor VII deficiency. *Transplantation*. 2004;78(12):1812-1814.
doi: 10.1097/01.TP.0000146386.77076.47

146. Meyburg J, Das AM, Hoerster F, et al. One liver for four children: first clinical series of liver cell transplantation for severe neonatal urea cycle defects. *Transplantation*. 2009;87(5):636-641.
doi: 10.1097/TP.0b013e318199936a

147. Anderson TN, Zarrinpar A. Hepatocyte transplantation: past efforts, current technology, and future expansion of therapeutic potential. *J Surg Res*. 2018;226:48-55.
doi: 10.1016/j.jss.2018.01.031

148. Mazza G, Rombouts K, Rennie Hall A, et al. Decellularized human liver as a natural 3D-scaffold for liver bioengineering and transplantation. *Sci Rep*. 2015;5(1):13079.
doi: 10.1038/srep13079

149. Hammond JS, Beckingham IJ, Shakesheff KM. Scaffolds for liver tissue engineering. *Expert Rev Med Devices*. 2006;3(1):21-27.
doi: 10.1586/17434440.3.1.21

150. Jitraruch S, Dhawan A, Hughes RD, et al. Alginate microencapsulated hepatocytes optimised for transplantation in acute liver failure. *PLoS One*. 2014;9(12):1-23.
doi: 10.1371/journal.pone.0113609

151. Parveen N, Khan AA, Baskar S, et al. Intraperitoneal transplantation of hepatocytes embedded in thermoreversible gelation polymer (Mebiol Gel) in acute liver failure rat model. *J Hepatol*. 2008;48:S71.
doi: 10.1016/S0168-8278(08)60166-X

152. Chiang CH, Wu WW, Li HY, et al. Enhanced antioxidant capacity of dental pulp-derived iPSC-differentiated hepatocytes and liver regeneration by injectable HGF-releasing hydrogel in fulminant hepatic failure. *Cell Transplant*. 2015;24(3):541-559.
doi: 10.3727/096368915X686986

153. Katsuda T, Teratani T, Ochiya T, Sakai Y. Transplantation of a fetal liver cell-loaded hyaluronic acid sponge onto the mesentery recovers a Wilson's disease model rat. *J Biochem*. 2010;148(3):281-288.
doi: 10.1093/jb/mvq063

154. Zhang W, Du A, Liu S, Lv M, Chen S. Research progress in decellularized extracellular matrix-derived hydrogels. *Regen Ther*. 2021;18:88-96.
doi: 10.1016/j.reth.2021.04.002

155. Vishwakarma SK, Bardia A, Lakkireddy C, et al. Intraperitoneal transplantation of bioengineered humanized liver grafts supports failing liver in acute condition. *Mater Sci Eng C*. 2019;98:861-873.
doi: 10.1016/j.msec.2019.01.045

156. Higashi H, Yagi H, Kuroda K, et al. Transplantation of bioengineered liver capable of extended function in a preclinical liver failure model. *Am J Transplant*. 2022;22(3):731-744.
doi: 10.1111/ajt.16928

157. Tai BCU, Du C, Gao S, Wan ACA, Ying JY. The use of a polyelectrolyte fibrous scaffold to deliver differentiated hMSCs to the liver. *Biomaterials*. 2010;31(1):48-57.
doi: 10.1016/j.biomaterials.2009.09.022

158. Lin J, Meng L, Yao Z, et al. Use an alginate scaffold-bone marrow stromal cell (BMSC) complex for the treatment of acute liver failure in rats. *Int J Clin Exp Med*. 2015;8(8):12593-12600.

159. Zhang LK, Wang H, Yang R, et al. Bone marrow stem cells combined with polycaprolactone-polylactic acid-polypropylene amine scaffolds for the treatment of acute liver failure. *Chem Eng J*. 2019;360:1564-1576.
doi: 10.1016/j.cej.2018.10.230

160. Dhawan A, Chaijitraruch N, Fitzpatrick E, et al. Alginate microencapsulated human hepatocytes for the treatment of acute liver failure in children. *J Hepatol*. 2020;72(5):877-884.
doi: 10.1016/j.jhep.2019.12.002

161. McKiernan PJ, Squires RH. Bridging transplantation with beads in paediatric acute liver failure. *Nat Rev Gastroenterol Hepatol*. 2020;17(4):197-198.
doi: 10.1038/s41575-020-0281-0

162. Zhong C, Xie HY, Zhou L, Xu X, Zheng SS. Human hepatocytes loaded in 3D bioprinting generate mini-liver. *Hepatobiliary Pancreat Dis Int*. 2016;15(5):512-518.
doi: 10.1016/S1499-3872(16)60119-4

163. Zhao Y, Xu B, Liang W, et al. Multisite injection of bioengineered hepatic units from collagen hydrogel and neonatal liver cells in parenchyma improves liver cirrhosis. *Tissue Eng Part A*. 2019;25(15-16):1167-1174.
doi: 10.1089/ten.tea.2018.0107

164. Shagidulin M, Onishchenko N, Sevastianov V, et al. Experimental correction and treatment of chronic liver failure using implantable cell-engineering constructs of the auxiliary liver based on a bioactive heterogeneous biopolymer hydrogel. *Gels*. 2023;9(6):456.
doi: 10.3390/gels9060456

165. Nagamoto Y, Takayama K, Ohashi K, et al. Transplantation of a human iPSC-derived hepatocyte sheet increases survival in mice with acute liver failure. *J Hepatol*. 2016;64(5):1068-1075.
doi: 10.1016/j.jhep.2016.01.004

166. Baimakhanov Z, Yamanouchi K, Sakai Y, et al. Efficacy of multilayered hepatocyte sheet transplantation for radiation-induced liver damage and partial hepatectomy in a rat model. *Cell Transplant*. 2016;25(3):549-558.
doi: 10.3727/096368915X688669

167. Demetriou AA, Levenson SM, Novikoff PM, et al. Survival, organization, and function of microcarrier-attached hepatocytes transplanted in rats. *Proc Natl Acad Sci U S A*. 1986; 83:7475-7479.
doi: 10.1073/pnas.83.19.7475

168. Jiang WC, Cheng YH, Yen MH, Chang Y, Yang VW, Lee OK. Cryo-chemical decellularization of the whole liver for mesenchymal stem cells-based functional hepatic tissue engineering. *Biomaterials*. 2014;35(11):3607-3617.
doi: 10.1016/j.biomaterials.2014.01.024

169. Bao J, Wu Q, Sun J, et al. Hemocompatibility improvement of perfusion-decellularized clinical-scale liver scaffold through heparin immobilization. *Sci Rep*. 2015;5(1):10756.
doi: 10.1038/srep10756

170. Sarkis R, Honiger J, Chafai N, et al. Semiautomatic macroencapsulation of fresh or cryopreserved porcine hepatocytes maintain their ability for treatment of acute liver failure. *Cell Transplant*. 2001;10(7):601-607.
doi: 10.3727/000000001783986314

171. Segovia-Zafra A, Di Zeo-Sánchez DE, López-Gómez C, et al. Preclinical models of idiosyncratic drug-induced liver injury (iDILI): moving towards prediction. *Acta Pharm Sin B*. 2021;11(12):3685-3726.
doi: 10.1016/j.apsb.2021.11.013

ACCSCIENCE PUBLISHING

International Journal of Bioprinting

REVIEW ARTICLE

3D-bioprinted bone for regenerative medicine: Current concepts and future perspectives

Borbála Lovászi[1,2,3], Diána Szűcs[1,2,3], Tamás Monostori[1,3], Lajos Kemény[1,3,4,5], and Zoltán Veréb[1,3,4]*

[1]Regenerative Medicine and Cellular Pharmacology Laboratory, Department of Dermatology and Allergology, University of Szeged, Szeged, Hungary

[2]Doctoral School of Clinical Medicine, University of Szeged, Szeged, Hungary

[3]Interdisciplinary Research Development and Innovation, Center of Excellence, University of Szeged, Szeged, Hungary

[4]Research Institute of Translational Biomedicine, Department of Dermatology and Allergology, University of Szeged, Szeged, Hungary

[5]Hungarian Centre of Excellence for Molecular Medicine-University of Szeged Skin Research Group (HCEMM-USZ Skin Research Group), University of Szeged, Szeged, Hungary

Abstract

The shortages in human tissue and organ donors have made clinical therapy relatively challenging. Therefore, research has been initiated over the last decades to develop artificial tissues and organs, particularly from cell and tissue cultures. Three-dimensional (3D) bioprinting is a recent technology capable of building structures for implantation, and these constructs closely resemble native tissues, such as skin, liver, connective tissues, and supportive tissues (bone and cartilage). In this review, we briefly introduce the structure, function, and development of bone tissues, followed by a detailed discussion on 3D bioprinting techniques, materials, and their recent advancements for clinical applications.

Keywords: Bone; 3D bioprinting; Transplantation; Therapy; Clinical use; Regenerative medicine

***Corresponding author:**
Zoltán Veréb
(vereb.zoltan@med.u-szeged.hu)

Citation: Lovászi B, Szűcs D, Monostori T, Kemény L, Veréb Z. 3D-bioprinted bone for regenerative medicine: current concepts and future perspectives. *Int J Bioprint*. 2024;10(3):2056.
doi: 10.36922/ijb.2056

Received: October 17, 2023
Accepted: February 21, 2024
Published Online: June 12, 2024

Copyright: © 2024 Author(s). This is an Open Access article distributed under the terms of the Creative Commons Attribution License, permitting distribution, and reproduction in any medium, provided the original work is properly cited.

Publisher's Note: AccScience Publishing remains neutral with regard to jurisdictional claims in published maps and institutional affiliations.

1. Introduction

Bone is a vital organ that constitutes the body's skeletal framework, enabling movement and providing essential protection for internal organs. Bone replacement and supplementation are indispensable in treating various bone-related physical injuries and pathological conditions (e.g., tumors and autoimmune diseases). However, the complexity of bone structures and their physicomechanical properties convolutes the therapeutic efficacy of general bone replacement procedures.[1-4] Three-dimensional (3D) bioprinting has emerged as a promising technology in tissue engineering to synthesize biologically similar tissue structures from suitable materials (e.g., hydrogels and cells) (Figure 1).[5,6] The printed constructs initially undergo incubation and maintenance to induce tissue formation, followed by rigorous morphological, mechanical, and biological tests for standardization. Thereafter, successfully 3D-bioprinted tissues may

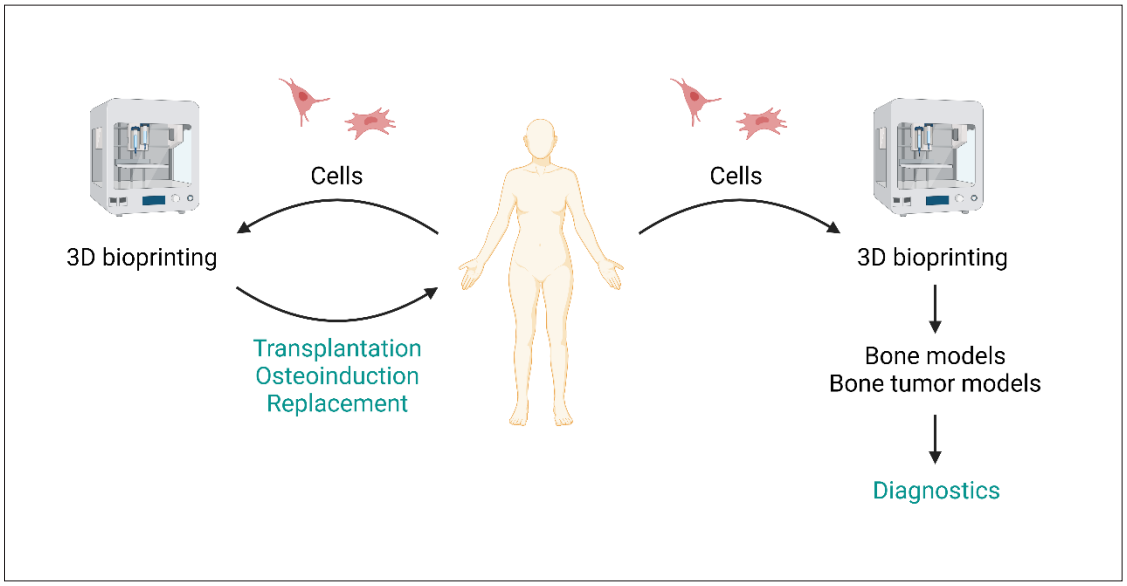


Figure 1. 3D-bioprinted bone in regenerative medicine. This figure was created using BioRender.

be reproduced for further evaluation in clinical trials prior to clinical applications and human transplantations (Figure 2).

Despite the clinical potential of 3D bioprinting, the process is challenged by the complex biological aspects and technological limitations that impact the biological function of tissue structures.[3] Nonetheless, bioprinting is anticipated to be an effective tool in bone tissue engineering that is capable of constructing 3D constructs to replicate bone microstructure and potentially enhance clinical outcomes in bone repair (e.g., by mitigating current adverse effects of bone grafts).[4] Hydrogel-based matrices garner significant interest as tissue scaffolds, owing to their biocompatibility and structural similarity to the natural extracellular matrix (ECM). Additionally, composite materials, such as polymers, ceramics, and nano-materials,

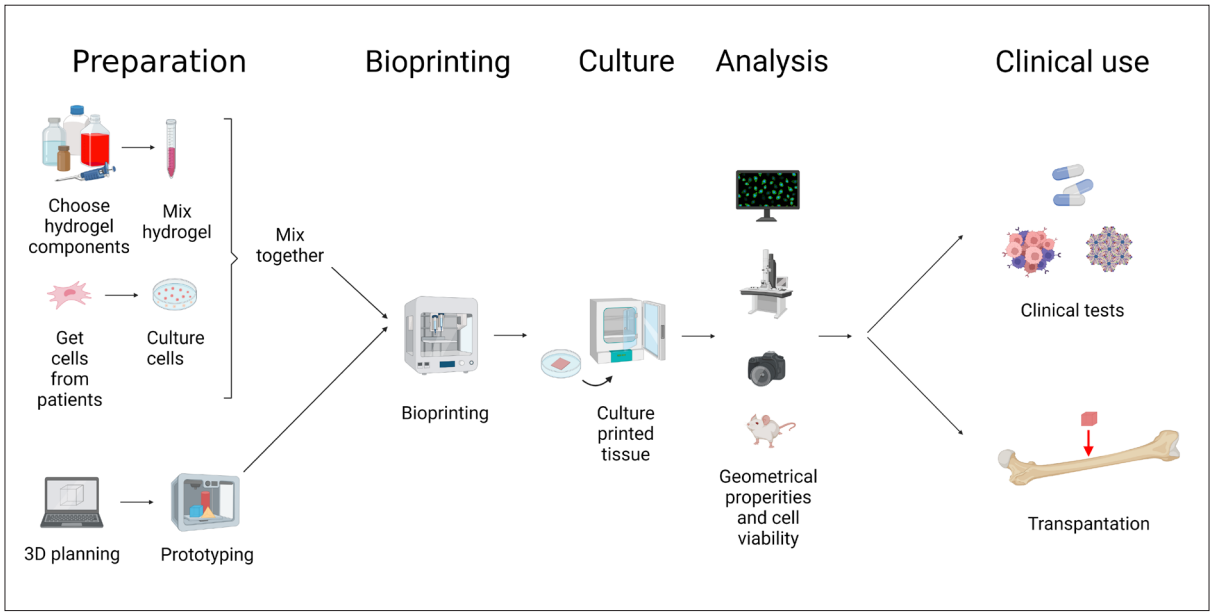


Figure 2. The process of 3D bioprinting. This figure was created using BioRender.

have displayed promising enhancements in biomaterial strength and biodegradability, while eliciting an adequate host immune response. Furthermore, there is currently an increasing utilization of decellularized ECM (dECM) in scaffolds, hydrogels, and bioinks due to its resemblance to native ECM. Mesenchymal stem cells (MSCs) derived from bone marrow and adipose tissue are among the widely and successfully bioprinted cell types used in bioinks.[7,8]

Several studies have reported the clinical application of 3D-bioprinted bone tissues as replacements and implants, but the number of related clinical trials remains low, warranting further research and development in the field. Herein, this article briefly introduces the structure, function, and development of bone tissues, followed by a detailed discussion on 3D bioprinting techniques, materials, and their recent advancements for clinical applications.

2. Structure, function, and development of bone tissues

2.1. Structure and composition of bone tissues

Bone is the only tissue type in the body with a mineralized intercellular matrix, resulting in a tough and resistant tissue that constitutes the body's skeletal framework. Bones can be divided into four groups according to their morphology:

(i) The tubular or long bone group refers to most limbs, where the epiphysis (end of the bone) has an ironlike cartilaginous articular surface and the diaphysis (middle part of the bone) is tubular. The cavities (interior) of the epiphysis are filled with spongy bone tissues, corresponding to the red bone marrow in young bones. Likewise, the diaphysis has a strong cortex with a cavity of yellow bone marrow.

(ii) The short bone group is found in the wrists, knees, and ankles. These bones resemble the epiphyseal part of the long bones and are filled with spongy bone tissues without a medullary cavity.

(iii) The flat bone group includes the cranial and pelvic bones, as well as the scapulae, sternum, and ribs. These bones are typically shaped like a blade or shell and are fitted together to enclose a cavity, thereby protecting essential organs from mechanical stress and providing a large muscle contact surface. Like tubular bones, flat bones have a robust cortical structure and are filled with spongy bone tissues without large cavities.

(iv) Irregularly shaped bones are found in the face, vertebrae, patella, feet, and hands. These bones usually have a thin cortex with an interior of spongy bone tissues.

The human body comprises 206–208 bones, which can be tubular, flat, or irregularly shaped. The outer layer of bones is made of a dense fibrous connective tissue, called the periosteum, which functions to protect and nourish the bones and also plays a vital role in bone regeneration. The periosteum layer comprises an outer fibrous layer (stratum fibrosum) and an inner cellular layer (stratum osteoblasticum). The layers comprise parallel plates composed of collagen fibrils with intervening proteoglycans. The plates are arranged in a few layers parallel to the outer and inner surfaces of the solid bone (i.e., lamina generales externae and lamina generales internae, respectively); in the other parts of the bone, they form columnar units called osteons (or Haversian plate systems).[9] Haversian canals are cavities within the osteons, through which veins and nerves pass. These canals are interconnected with the periosteal (outer) and endosteal (inner) spaces via Volkmann canals, which radiate outward from the bone's surface. Extensions of these canals connect neighboring cells through tiny channels called canaliculi within the bone plates. Their extensions are connected to the wings of adjacent cells by tiny canaliculi through the plates. A trabecular bone has a similar structure to a solid bone but has smaller and larger cavities that resemble a sponge. Hence, the trabecular bone is both strong and light. Moreover, the cavities contain part of the bone marrow, an essential tissue for blood formation.[9] In the case of tubular bones, the spongy substance is reduced in the diaphysis, and the large marrow cavity is filled with yellow marrow, fatty tissue, and a few large vessels (Figure 3).[9]

The mechanical properties of bone tissue are essential for its function and overall health. The unique composition and hierarchical structure of bones imbue the ability to withstand external forces, resist fractures, and adapt to changes in response to mechanical stress. Bone strength refers to the ability of the bone to withstand stress without breaking and is determined by the bone composition and structure. The inorganic component of bone, mainly calcium phosphate, provides compressive strength, while the organic component, mostly collagen fibers, provides tensile strength. The unique arrangement of these components in a hierarchical structure allows for a balance between strength and flexibility and simultaneously increases the fracture resistance of bones.

Bone stiffness refers to the resistance of bone to deformation when a force is applied. Stiffness is directly related to the elastic modulus of bone that measures its ability to return to its original shape after being deformed. Bone tissue has a high elastic modulus to withstand large forces without permanent deformation, maintaining the shape and stability of bones and preventing them from bending or breaking easily. In contrast, bone toughness

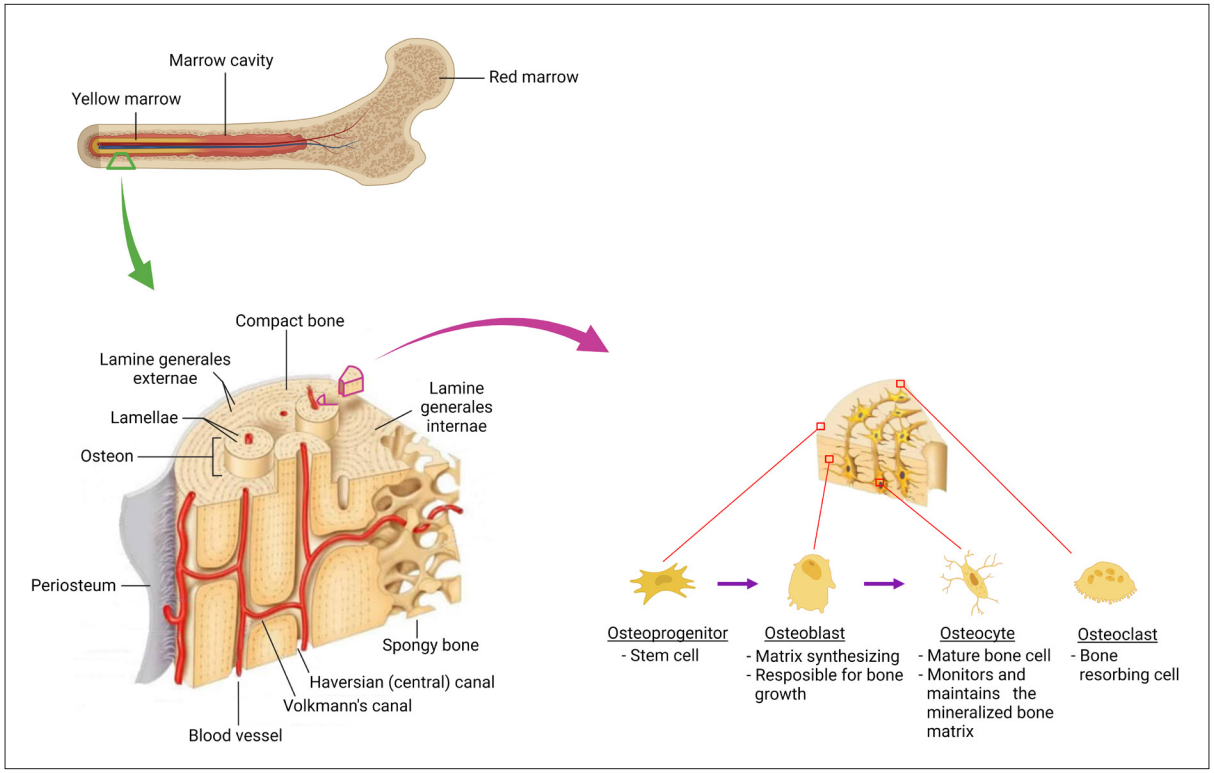


Figure 3. The structure of a long bone and the cells of the bone. This figure was created using BioRender.

refers to the ability of bones to absorb energy before breaking, i.e., when bones are subjected to sudden impacts or high forces, such as during physical activities or accidents. The toughness of bone is primarily influenced by the amount and orientation of collagen fibers and the quality and distribution of calcium phosphate crystals. A higher amount of collagen and a more organized structure would result in increased toughness, making bone tissue more resistant to fracture.

While all bone types serve imperative functions in providing support and protection, they have distinct differences in their mechanical properties that can be observed from both the macroscopic and microscopic levels. In compact bones, the arrangement of osteons induces compressive force resistance, making it strong and rigid. These bones are commonly found in areas of the body that require strength and support, such as the shafts of long bones. In contrast, spongy bones are naturally porous and strong and can resist forces from multiple directions. One of the critical differences between compact and spongy bones is their response to mechanical stress. Compact bones can withstand compressive forces due to their dense and organized structure, as well as bending and twisting forces, making them ideal for supporting the body's weight and movement. Likewise, spongy bones are better suited for dissipating forces as their porous structure allows for the redistribution of forces, reducing the strain on the bone and preventing fractures. This is particularly important for bones in joints that are subjected to various forces during movement. At the microscopic level, lamellar bones are known for their strength and stiffness, while woven bones are used in bone remodeling and have poorer mechanical properties. Accordingly, fibrolamellar bones combine the properties of both lamellar and woven bones, and the secondary osteons provide high resistance to bending and torsional forces.[10]

The mechanical properties of bones can be determined from bone specimens, i.e., samples cut from the bones. However, the measured mechanical properties of bones may differ due to non-standardized procedures, different sample sites, and other conditions. While these properties may vary along the bone structure due to the non-homogeneity and varied geometry, they are relevant for 3D bioprinting (Table 1).[11,12]

2.1.1. Bone cells

There are four types of bone cells: osteoprogenitors, osteoblasts, osteocytes, and osteoclasts (Figure 3). Osteoprogenitor cells, commonly found in the periosteum and endosteum, are derived from MSCs and can subsequently differentiate into osteoblasts.[13] These cells are

Table 1. Mechanical properties of bone tissues

Material property	Compact bone	Spongy bone
Compressive strength (MPa)	130–200	0.1–16
Tensile strength (MPa)	50–151	5–10
Compressive modulus (GPa)	11.5–17	0.12–1.1
Young's modulus (GPa)	7–30	0.05–0.5
Fracture toughness ($MPa \cdot m^{0.5}$)	2–12	0.1–0.2

responsible for producing the bone matrix, which plays a significant role in bone regeneration. As the ECM builds around them and mineralizes, osteoblasts mature into osteocytes. Although osteocytes have reduced synthetic activity and cannot undergo mitotic division (similar to osteoblasts), they are actively involved in remodeling the bone matrix.[13] Additionally, nodules of mineralization of hydroxyapatite (HA), calcium carbonate, and calcium phosphate mineralization are commonly found surrounding the osteocytes.[13] In contrast, osteoclasts are phagocytotic cells of bone tissues and are responsible for removing degraded bone materials (i.e., erosion by osteocytes). Osteoclasts are usually found on the surface of the bone in cavities, called Howship lacunae.[9,13]

2.1.2. Bone extracellular matrix

The bone ECM is a unique composite material that contains approximately 65–70% inorganic minerals and 30–35% organic compounds (Table 2), the ratio of which varies with age or physiological state.[14] The main component of the inorganic phase is HA ($Ca_{10}[PO_4]_6[OH]_3$), which is made up of two mineral salts: calcium phosphate and calcium hydroxide. In addition to these two components, trace elements (calcium, magnesium, fluorine, sodium, and sulfate) are often bound into the inorganic crystals. Calcification is a process whereby the inorganic crystals are deposited around collagen fibrils.[13]

In contrast, the organic phase is composed of approximately 90% type I collagen and 10% type III and V collagen and non-collagen proteins.[14,15] Collagens are coiled into triple-stranded helices to form fibers, providing both a mechanically stable structure and a scaffold for bone cells.[16] Likewise, the non-collagen proteins can be subdivided into four groups: γ-carboxyglutamic acid (Gla) proteins, proteoglycans, glycoproteins, and small integrin-binding ligand N-linked glycoproteins (SIBLINGs).[17] Proteoglycans consist of polysaccharide fibers and proteins, and some small leucine-rich proteoglycans (SLRP) play a crucial role in bone tissue homeostasis and bone tissue formation.[15,16] Proteoglycans interact with cell surface receptors to regulate their pathological functions and are also involved in all stages of bone formation, including cell proliferation, osteogenesis, mineral deposition, remodeling, and collagen fibrillogenesis.[14,15,17] Gla is an amino acid with a dicarboxylic acid side chain and is found in several forms in the body with different functions (e.g., as blood clotting factors and plasma proteins). Gla is located in bone and other mineralized tissues, such as osteocalcin (OCN), bone matrix Gla protein (MGP), and periostin.[18] OCN binds to calcium and is stored in bones. It acts as a glucose and energy metabolism regulator, and its increased serum concentration stimulates bone formation. In addition, OCN is released into the blood through bone resorption processes. Conversely, MGPs are responsible for inhibiting bone mineralization, while periostin is an adhesion molecule that promotes osteoblast aggregation, adhesion, proliferation, and differentiation, as well as collagen fibrillogenesis.[18] Glycoproteins, such as osteonectin, thrombospondins, and R-spondins, are composed of a protein chain and several different carbohydrate linkages and are typically found in bone ECM. Osteonectin regulates calcium release by binding to HA crystals and collagen fibers, and high concentrations of osteonectin can cause osteoporosis; thrombospondins are essential in skeletal development, bone cell differentiation, and bone mass maintenance; R-spondins regulate embryonic bone development and adult bone remodeling. SIBLINGs are a family of glycoproteins and commonly include bone sialoprotein (BSP), osteopontin (OPN), dentin matrix protein-1 (DMP1), dentin sialophosphoprotein (DSPP), and matrix extracellular phosphoglycoprotein (MEPE). BSP plays a vital role in the regulation of osteoblast differentiation and the initiation of matrix mineralization, while OPN, DMP1, and MEPE are involved in the regulation of matrix mineralization. In teeth, DSPP plays a similar role to BSP. Additionally, DMP1 and MEPE also regulate the binding of phosphate to bones.

2.2. Functions of bone tissues

Bone tissues provide the skeletal framework that protects the body. Additionally, bone tissues are a passive component of movement, function as a mineral store, and play an essential role in hematopoiesis (protecting the red and yellow bone marrow during hematopoiesis).[9,13] In the body, many organs (e.g., lungs, kidneys, liver, skin, and intestines) can serve as buffer systems to maintain an ideal pH of 7.2–7.4. Bones are also considered a buffer system, owing to their phosphate storage. Besides that, bones can rapidly bind to and accumulate heavy metals and subsequently release them in smaller doses for efficient removal. Therefore, bones can protect the other tissues from heavy metal poisoning by absorbing toxic metals in the body. Notably, some heavy metals can also damage

Table 2. Components of the bone extracellular matrix (ECM) and their function

Material	Protein	ECM component	Origin	Function
Inorganic	N/A	Hydroxyapatite	Bone	Mineralization
Organic	Collagenous	Type I collagen	Osteoblast	Scaffold for bone cells; strengthen bone; promote bone formation; regulate collagen fibrillogenesis
		Type III collagen	Bone	Promote bone formation
		Type IV collagen	Bone	Promote bone formation
	Non-collagenous	Proteoglycans		
		Biglycan	Osteoblast	Promote collagen fibrillogenesis; promote bone formation
		Decorin	Osteoblast	Promote collagen fibrillogenesis; promote bone formation
		Keratocan	Osteoblast	Promote mineral deposition rates
		Asporin	Articular cartilage; periodontal tissue	Promote collagen mineralization
		γ-Carboxyglutamic acid-containing proteins		
		Osteocalcin	Osteoblast	Regulate calcium metabolism; indicate bone formation
		MGP	Osteoblast; osteocyte; chondrocyte	Inhibit bone formation; mineralization
		Periostin	Osteoblast; precursor cells	Regulate collagen fibrillogenesis; strengthen bone
		Glycoproteins		
		Osteonectin	Osteoblast	Promote bone formation; mineralization; regulate collagen fibrillogenesis; maintain biomechanical properties
		Thrombospondins	Osteoblast	Promote bone formation; regulate collagen fibrillogenesis
		R-spondins	Bone	Promoter Wnt/β-catenin signaling; regulate bone development
		SIBLINGs		
		BSP	Mineralized tissue	Promote bone formation; mineralization
		OPN	Osteoblast; odontoblast; osteocyte	Promote bone formation; mineralization; regulate bone remodeling
		DMP1	Osteoblast	Regulate phosphate metabolism; promote bone mineralization
		MEPE	Bone	Regulate phosphate metabolism; promote bone mineralization

Abbreviations: BSP: Bone sialoprotein; DMP1: Dentin matrix protein-1; MEPE: Matrix extracellular phosphoglycoprotein; MGP: Matrix Gla protein; N/A: Not applicable; OPN: Osteopontin; SIBLINGs: Small integrin-binding ligand N-linked glycoproteins.

bone tissues, such as cadmium (when bound to calcium) causing severe osteoporosis.

2.3. Development of bone tissues

Osteogenesis or ossification is defined as the formation of bone tissues and starts from week eight of the embryonic age.[19] Most bones are already formed by birth, after which new bone cells and tissues are formed only for bone growth, regeneration, and renewal.[9] Primary ossification refers to the direct differentiation of MSCs into bone-forming cells and can occur in the periosteum, the fibrous membrane of the bone (intramembranous ossification), or in the perichondrium, the fibrous membrane of the cartilage (perichondral ossification), where the newly formed bone tissues do not replace the existing tissues. In secondary ossification, MSCs first

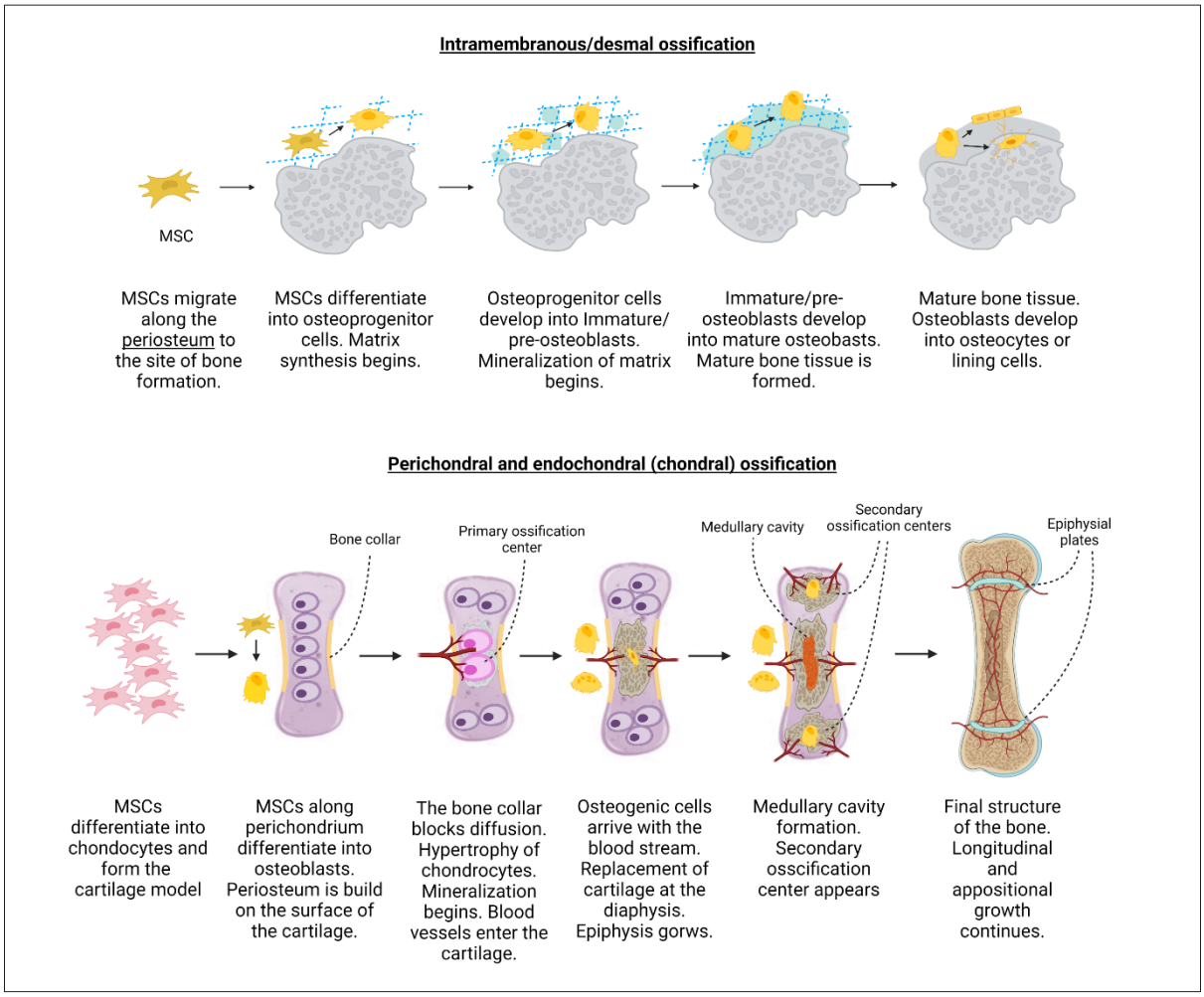


Figure 4. Types of bone formation and participating cells. Abbreviation: MSC: Mesenchymal stem cell. This figure was created using BioRender.

differentiate into hyaline cartilage tissues, which are then gradually replaced with bone tissues from other MSCs (endochondral ossification).[19,20] Conversely, ossification processes based on the initial tissue can be distinguished, such that intramembranous ossification is called desmal ossification while perichondrial and endochondral ossifications are called chondral or endochondral ossification. Intramembranous or desmal ossification is primarily associated with the growth of the cranial bones, mandible, and clavicles and regeneration after bone fracture. The base of the skull and all other bones develop through chondral ossification (Figure 4).[8,9,19]

2.3.1. Cells involved in the development of bone tissues

Bone formation and regeneration are dependent on the differentiation of MSCs into cell types that build or break down bone, cartilage, or connective tissue (Figure 4).[20] In the case of intramembranous ossification, MSCs migrate along the periosteum to the site of bone formation and differentiate into osteoblasts by settling on the surface of existing bone tissues (e.g., at the end of a fracture or the edge of a cranial suture).[8,21] Osteoblasts are responsible for producing bone ECM,[9] and as the matrix mineralizes, the osteoblasts become embedded in the hardened tissue and develop into mature osteocytes. MSCs differentiate into chondrocytes in chondral bone formation and shape the cartilage model of the bone.[20] Along the perichondrium, at the diaphysis part of the bone, other MSCs differentiate into osteoblasts and create periosteum on the surface of the cartilage (perichondral ossification), forming the bone collar. The bone collar does not allow diffusion into the cartilage model, causing the chondrocytes to swell and change their physiology and gene expression. These altered chondrocytes secrete alkaline phosphatase (ALP), which stimulates cartilage calcification. Consequently, the tissues

become impervious to nutrients, and the chondrocytes inside the cartilage begin to die, thereby allowing blood vessels to enter the empty cavity (primary ossification center) through the periosteum.[20] Osteoprogenitor cells are transported through blood vessels from the primary ossification center toward the ends of the bones and replace the cartilage tissues with bone tissues (endochondral ossification), forming a spongy bone.[19,20] After the cartilage model is completely replaced in the diaphysis, the osteoclasts open the medullary cavity inside the bone.[19] Meanwhile, in the epiphyses, chondrocytes proliferate and the cartilages continue to grow, forming a secondary ossification center. At the end of the process, the entire cartilage model is replaced by bone tissues except for the epiphyseal plate, located between the epiphysis and the diaphysis, and this facilitates subsequent longitudinal bone growth by endochondral ossification. While the interior of the cartilage model is replaced by spongy bone, the perichondrium transforms into the periosteum and the surface osteoblasts form the compact bone. These two types of bone growth continue until about 20–25 years, after which only bone regeneration occurs.

2.3.2. Stem cells and bone differentiation

Stem cells are undifferentiated cells that develop into specific cells of other tissues through specific differentiation pathways.[22] These cells can be either embryonic, adult, or induced pluripotent stem cells, and based on their developmental potential, they can be divided into five groups: totipotent, pluripotent, multipotent, oligopotent, and unipotent stem cells (Figure 5). After fertilization, the zygote of a single cell begins to divide (barring). Totipotent stem cells refer to actively dividing undifferentiated stem cells (i.e., less than 16 cells [morula]) and are capable of forming cells of any tissue. The morula then develops into a blastocyte, where the cells are pluripotent. Consequently, these cells can no longer form extraembryonic tissue but can form germinal cells and gametes.

In the next stage of development, the monolayer blastoderm differentiates into the three germ layers: the endoderm (inner germ layer), the mesoderm (middle germ layer), and the ectoderm (outer germ layer). These cells are also pluripotent and form the cells of the different tissues. The endoderm comprises epithelial cells from the

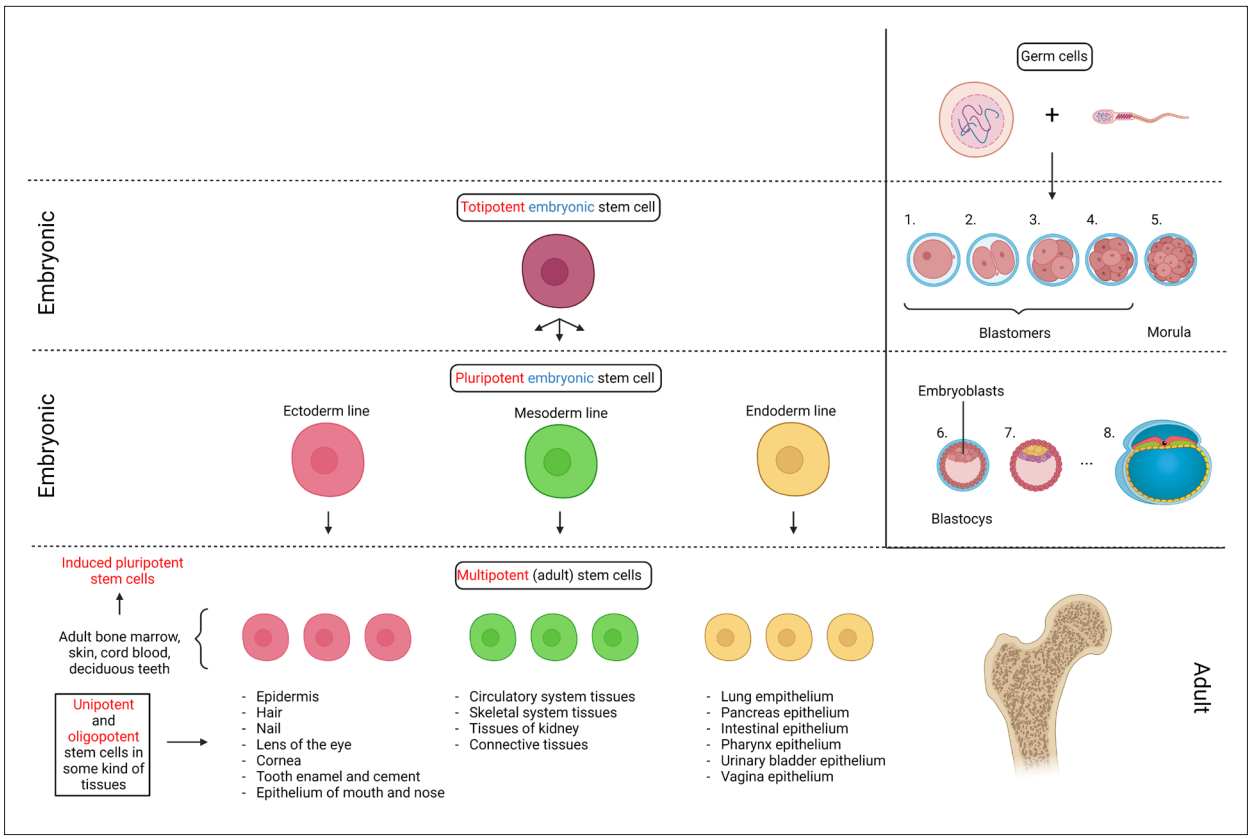


Figure 5. Types of embryonic stem cells. This figure was created using BioRender.

urogenital, gastrointestinal, respiratory, pharyngeal, and thyroid glands. The mesoderm contributes to most circular skeletal systems and the kidneys. The ectoderm forms the dermis of the skin, the nervous system, tooth enamel, dental cement, dentin, the epithelium of the esophagus, the lens of the eye, and the cornea.[23] Upon differentiation, these multipotent adult stem cells can no longer be used to develop stem cells of other tissues. In contrast, oligopotent and unipotent stem cells (e.g., osteoprogenitor cells) refer to the differentiation into a few types and one type of cells, respectively.[21] Induced pluripotent stem cells are stem cells that can be produced directly from somatic cells.[21,23-25]

MSCs are a type of stem cell commonly found in the adult body (e.g., in the umbilical cord, bone marrow, and adipose tissue) and can differentiate into cells from a variety of tissues, such as bones (i.e., via osteogenesis), cartilages (i.e., via chondrogenesis), and the bone marrow (Figure 6).[8] MSCs initially adopt a specific differentiation pathway, forming transitional osteoblasts in bones and transitional chondrocytes in cartilages. These transition

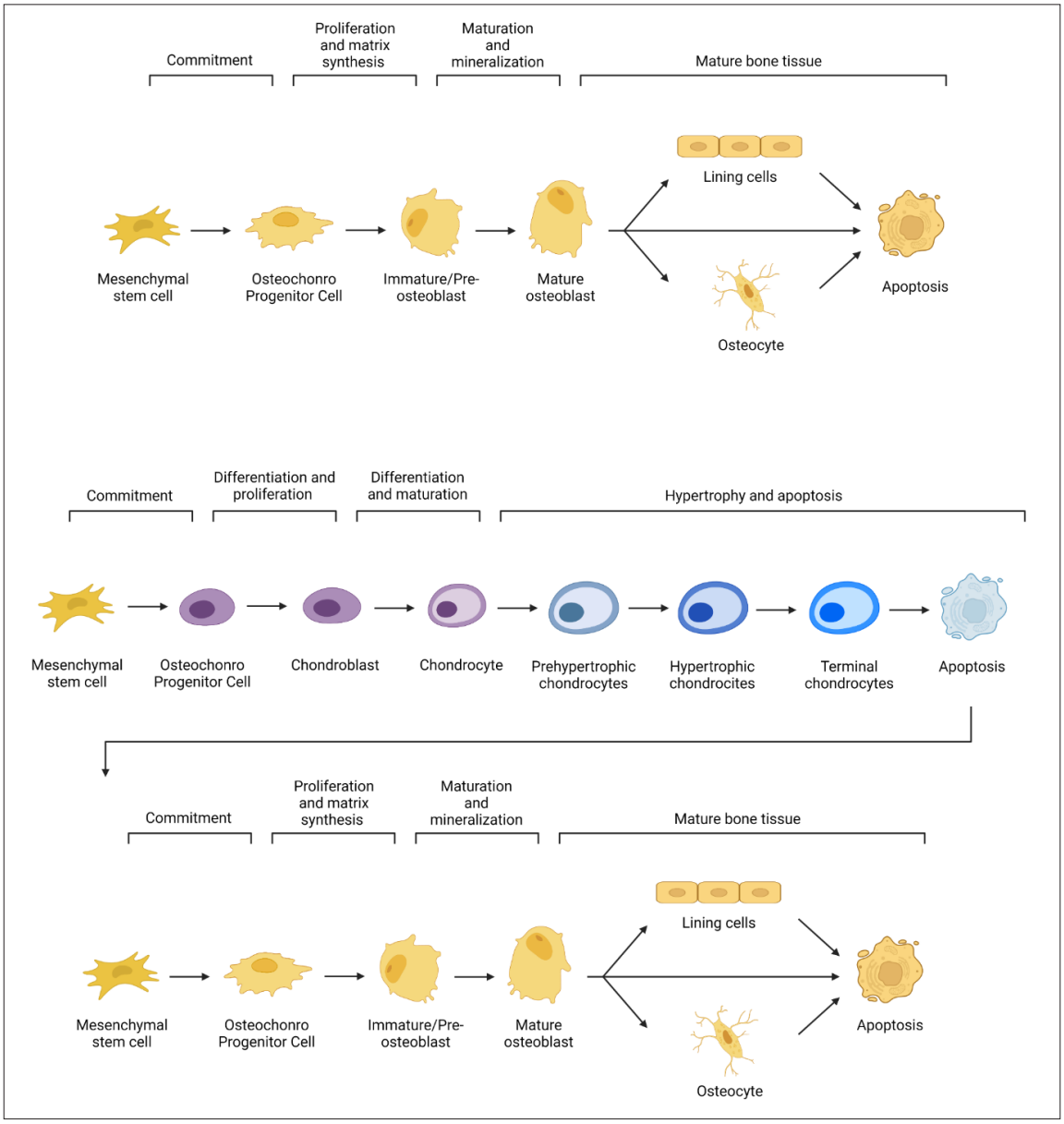


Figure 6. Cells involved in bone generation. This figure was created using BioRender.

cells (i.e., in bone and cartilage tissues) then develop into osteoblasts and chondrocytes,[8,24] where the osteoblasts then divide and produce bone matrix, while the chondrocytes mature into hypertrophic chondrocytes. The final step of differentiation is maturation, where bone cells develop into osteocytes and the chondrocytes mineralize the cartilage tissues around them. MSCs are usually extracted for research and therapeutic purposes.[8,22,24]

2.3.3. Growth factors and cytokines in the development of bone tissues

Bone generation is regulated by several integrated signaling pathways, such as the bone morphogenic protein (BMP), transforming growth factor (TGF), Wingless/int1 (WNT), fibroblast growth factor (FGF), hedgehog (HH), Notch, and parathyroid hormone-related protein (PTHrP) signaling pathways. These signaling pathways regulate the expressions of different genes and transcription factors,

Table 3. Signaling pathways, growth factors, cytokines, and expressed genes in bone generation

Ossification	Cells	Signaling molecules (i.e., growth factors and cytokines)	Effect of signals	Gene markers
Intramembranous	Cranial neural crest cells	SHH, SOX10, FGF8, FGF9, BMP4	Differentiation	*Selective markers: SOX10, B3GAT1, BARX1, FRZB* (Sfrp3), *GEMIN2, HAND2, LHX6, LHX8* (Lhx7), *MSX1* (Hox7), *MSX2* (Hox8), *PITX1* (Ptx1), *SATB2, SOX9, TFAP2A* (AP2alpha) *Selectively unexpressed marker: HOXA2 Expressed markers: AP3D1, COL1A2, DLX1, DLX2, DLX3, DLX4, DLX5, DLX6, EZH2, FBLN5* (Fibulin 5), *FOXC1* (Mf1), *FOXC2, FOXD1* (BF-2), *FOXD2, FOXF1* (HFH-8), *FOXF2* (forkhead box F2), *HAPLN1* (Crtl1), *LIX1, LMAN1, MARVELD1, MIR129, MIR149, MIR18, MIR184, MIR185, MIR214, MIR290A, MIR292, MIR296, MIR299A, MIR30A, MIR320, MIR341, MIR342, MIR346, MIR351, MIR370, MIR376B, MIR376C, MIR423, MIR429, MIR452, MIR468, MIR483, MIRLET7A-1, MIRLET7B, MIRLET7E, MRC2, NOG, NRP2* (Npn2), *PAX3* (splotch), *PF4, SLC39A7, SPRY1, STEAP1, TNFAIP6, TNFRSF19* (Troy), *TSPAN14, WNT1, WNT5A*
		BMP4, ET1, FGF8, miR452	Uncategorized	
	Osteochondroprogenitor cells	FGF18	Proliferation	*Selective markers: EZH2, RUNX2* (Cbfa-1), *SOX9, TAZ* *Selectively unexpressed markers: HOXA2, HOXA3, HOXB4, PPARG* (PPAR-gamma) *Expressed markers: COL2A1, DLX5, DLX6, FGFR2* (Fgfr-2), *PAX1, PAX9, PKD1, TGFBR2* (TbetaRII), *TWIST1* (Twist)
		BMPs, EZH2	Differentiation	
		Twist1, WNTs	Inhibition of differentiation	
	Immature/pre-osteoblasts	BMPs	Proliferation	*Selective markers: COL1A1, COL1A2, SP7* (Osx), *ALPL* (Akp-2), *MSX1 (HOX7), MSX2* (Hox8), *POSTN* (Osf2), *PTH1R* (Pthr1), *RUNX2* (Cbfa-1), *SATB2, SPARC, SPP1* (BSPI), *TNC* (tenascin-C) *Selectively unexpressed markers: HOXA2, SOX9 Expressed markers: BGLAP* (OC), *DLX5, FGF18, FGFR1* (Flt-2), *FN1* (Fn-1), *GATA3, TAZ, TWIST1* (Twist)
		BMP2, FGF18, RUNX2/Cbfa-1, WNTs	Differentiation	
		BMP4	Uncategorized	
	Mature osteoblasts	ATF4, BMP2, BMPs, FGF18, RUNX2/ Cbfa-1, SATB2	Differentiation	*Selective markers: SP7* (Osx), *ALPL* (Akp-2), *ATF4, BGLAP* (OC), *MSX1* (Hox7), *MSX2* (Hox8), *PTH1R* (Pthr1), *RUNX2* (Cbfa-1), *SATB2, SPARC, TAZ, TNC* (tenascin-C) *Selectively unexpressed markers: HOXA2, SOX9 Expressed markers: FN1* (Fn-1), *SMO, SPP1* (BSPI)
	Osteocytes	FGF18	Uncategorized	*Selective markers: SP7* (Osx), *ATF4, BGLAP* (OC), *MSX2* (Hox8), *SPARC, SPP1* (BSPI) *Expressed markers: FGFR2* (Fgfr-2), *FN1* (Fn-1), *RUNX2* (Cbfa-1)

(*Continued*)

Table 3. ***Continued...***

Ossification	Cells	Signaling molecules (i.e., growth factors and cytokines)	Effect of signals	Gene markers
Endochondral	Osteochondral MSCs	SOX9, Twist1, WNTs	Differentiation	*Selective markers: RUNX2* (Cbfa-1), *SOX9* *Selectively unexpressed markers: COL1A1, COL1A2, HAS2, HAS3* *Expressed markers: CCN2, CDH2* (N-cadherin), *CHAD, CTNNB1* (Catnb), *DPP6, DPT* (Dermatopontin), *FGF10, FGFR2* (Fgfr-2), *FN1* (Fn-1), *GDF5, GREM1* (Grem), *HOXA10, HOXD8, ITGA1, KLK10, LHX2* (Lim2), *LHX9, LMX1B* (LMX1.1), *LRP5, MATN3, NDNF, NIPBL, NKX3-1, NKX3-2* (Bapx1), *OGN* (Osteoglycin), *PAMR1, PCDH8, PLOD1, PTCH1, RARG* (RARgamma2), *SLC35E3, SOX11, SOX9, TGFB1, TGFB2* (Tgfb-2), *TGFBR2* (TbetaRII), *TNC* (tenascin-C), *TWIST1* (Twist), *ZFP521, 4930555G01RIK*
	Osteochondroprogenitor cells	FGF18	Proliferation	*Selective markers: EZH2, RUNX2* (Cbfa-1), *SOX9, TAZ* *Selectively unexpressed markers: HOXA2, HOXA3, HOXB4, PPARG* (PPAR-gamma) *Expressed markers*: COL2A1, DLX5, DLX6, FGFR2 (Fgfr-2), *PAX1, PAX9, PKD1, TGFBR2* (TbetaRII), TWIST1 (Twist)
		BMPs, EZH2	Differentiation	
		Twist1, WNTs	Inhibition of differentiation	
	Chondroblasts	IHH	Proliferation	*Selective markers: NCAM1* (Ncam), *SOX5, SOX6, SOX9, TNC* (tenascin-C) *Expressed markers: CDH2* (N-cadherin*), DLX5, DLX6, FGFR3, IGF1, PKD1, PTCH1, PTHLH* (Pthrp)
	Chondrocytes	IHH, SOX5, SOX6, SOX9	Proliferation	*Selective markers: ACAN, COL2A1, COL11A1, COL11A2, COMP, HAPLN1* (Crtl1), *MATN1* (Crtm), *NKX3-2* (Bapx1), *PTH1R* (Pthr1), *PTHLH* (Pthrp), *SOX5, SOX6, SOX9* *Selectively unexpressed marker: IHH* *Expressed markers: ATF2, EVC, FGFR3, NOG, PKD1, PTCH1, SMO*
		FGF18	Cell cycle arrest	
		SOX9	Differentiation	
		NOG	Inhibition of differentiation	
	Pre-hypertrophic chondrocytes	IHH, RUNX2/Cbfa-1	Differentiation	*Selective markers: ACAN, COL10A1, COL2A1, COMP, IHH, MATN1* (Crtm), *PTH1R* (Pthr1), *PTHLH* (Pthrp), *RUNX2* (Cbfa-1), *RUNX3* (Cbfa3) *Expressed markers: ALPL* (Akp-2), *DLX5, DLX6, FGFR3, HAPLN1* (Crtl1)
	Hypertrophic chondrocytes	IHH, RUNX2/Cbfa-1	Differentiation	*Selective markers: COL10A1, IHH, PTH1R* (Pthr1), *PTHLH* (Pthrp), *RUNX2* (Cbfa-1), *RUNX3* (Cbfa3), *SPP1* (BSPI) *Selectively unexpressed markers: SOX5, SOX6, SOX9* *Expressed markers: DLX5, DLX6, MAF* (c-maf), *MMP13, MMP14, VEGFA*
		VEGF	Uncategorized	
	Terminal chondrocytes	RUNX2/Cbfa-1, VEGF	Uncategorized	*Selective markers: MAF* (c-maf), *MMP13, MMP14, RUNX2* (Cbfa-1) *Expressed markers: SPP1* (BSPI), *VEGFA*

(*Continued*)

Table 3. ***Continued...***

Ossification	Cells	Signaling molecules (i.e., growth factors and cytokines)	Effect of signals	Gene markers
Endochondral	Cranial neural crest cells	SHH, SOX10, FGF8, FGF9, BMP4	Differentiation	*Selective markers: SOX10, B3GAT1, BARX1*, *FRZB* (Sfrp3), *GEMIN2, HAND2, LHX6, LHX8* (Lhx7), *MSX1* (Hox7), *MSX2* (Hox8), *PITX1* (Ptx1), *PTCH1, SATB2, SOX9, TFAP2A* (AP2alpha) *Selectively unexpressed marker: HOXA2* *Expressed markers: AP3D1, COL1A2, DLX1, DLX2, DLX3, DLX4, DLX5, DLX6, EZH2, FBLN5* (Fibulin 5), *FOXC1* (Mf1), *FOXC2, FOXD1* (BF-2), *FOXD2, FOXF1* (HFH-8), *FOXF2* (forkhead box F2), *HAPLN1* (Crtl1), *LIX1, LMAN1, MARVELD1, MIR129, MIR149, MIR18, MIR184, MIR185, MIR214, MIR290A, MIR292, MIR296, MIR299A, MIR30A, MIR320, MIR341, MIR342, MIR346, MIR351, MIR370, MIR376B, MIR376C, MIR423, MIR429, MIR452, MIR468, MIR483, MIRLET7A-1, MIRLET7B, MIRLET7E, MRC2, NOG, NRP2* (Npn2), *PAX3* (splotch), *PF4, SLC39A7, SPRY1, STEAP1, TNFAIP6, TNFRSF19* (Troy), *TSPAN14, WNT1, WNT5A*
		BMP4, ET1, FGF8, miR452	Uncategorized	
	Osteochondroprogenitor cells	FGF18	Proliferation	*Selective markers: EZH2, RUNX2* (Cbfa-1), *SOX9, TAZ* *Selectively unexpressed markers: HOXA2, HOXA3, HOXB4, PPARG* (PPAR-gamma) *Expressed markers: COL2A1, DLX5, DLX6, FGFR2* (Fgfr-2), *PAX1, PAX9, PKD1, TGFBR2* (TbetaRII), *TWIST1* (Twist)
		BMPs, EZH2	Differentiation	
		Twist1, WNTs	Inhibition of differentiation	
	Immature/pre-osteoblasts	BMP2, IGF1, IHH, RUNX2/Cbfa-1	Differentiation	*Selective markers: COL1A1, COL1A2, SP7* (Osx), *ALPL* (Akp-2), *IGF1R* (IGF-1R), *MSX2* (Hox8), *POSTN* (Osf2), *PTH1R* (Pthr1), *RUNX2* (Cbfa-1), *SATB2, SPARC, TNC* (tenascin-C) *Selectively unexpressed markers: HOXA2, SOX9* *Expressed markers*: *FGF18, PTCH1, TAZ, TWIST1* (Twist)
		BMP4	Uncategorized	
	Mature osteoblasts	ALF4, BMP2, IHH, RUNX2/Cbfa-1, SATB2	Differentiation	*Selective markers: COL1A1, COL1A2, SP7* (Osx), *ALPL* (Akp-2), *BGLAP* (OC), *DCN, IBSP* (BSP), *IGF1R* (IGF-1R), *PTH1R* (Pthr1), *RUNX2* (Cbfa-1), *SATB2, SPP1* (BSPI) *Selectively unexpressed markers: HOXA2, SOX9* *Expressed markers: ATF4, BMP2* (Bmp2a), *BMP4, FGFR2* (Fgfr-2), *FN1* (Fn-1), *IGF1, MSX2* (Hox8), *PTCH1, TAZ, VTN* (Vitronectin)
	Osteocytes	FGF18, BMP2	Uncategorized	*Selective markers: SP7* (Osx), *MSX2* (Hox8), *SPARC, SPP1* (BSPI) *Expressed markers: ATF4, FGFR2* (Fgfr-2), *FN1* (Fn-1), *MEPE, VTN* (Vitronectin)

thereby altering cell metabolism and the secretion of ECM components (Table 3). The main factors associated with ossification are Runt-related transcription factors (RUNX), osterix (OSX), sex-determining region Y (Sry)-related high mobility group (HMG)-related box factors (SOX), and several other factors responsible for collagen production.[26,27] In primary ossification, the transformation of MSCs into mature bone tissue consists four main steps: (i) attachment of MSCs to osteoprogenitor cells; (ii) proliferation and differentiation of osteoprogenitor cells into immature osteoblasts/pre-osteoblasts and subsequent ECM secretion; (iii) maturation of osteoblasts and ECM mineralization; and (iv) transformation of osteoblasts into osteocytes and/or lining cells, or apoptotic cell death. These factors can be stimulating or inhibiting at various stages. In secondary ossification, cartilage formation also has its distinct mechanisms: (i) differentiation of MSCs into chondroprogenitors and subsequent formation of the cartilage model; (ii) differentiation of chondroprogenitors into chondroblasts and chondrocytes; and (iii) cell swelling and apoptotic cell death during endochondral ossification. The dead cells are then replaced by MSC-derived bone cells from the initial steps.[28-30]

3. Bone deformities and corresponding treatments

In the event of injury, disease, or abnormal bone development, bone tissues may need to be replaced. The donor bone tissue may come from another (healthy) part of the individual (autogenous transplantation), another human (allogeneic transplantation), or animal species (xenogeneic transplantation).[1] Alternatively, bone replacement can be performed with non-tissue bone substitutes of human origin,[5] and these non-tissue substitutes usually contain growth factors and cell-based bone substitutes. Besides that, bone grafting is a personalized alternative, and ceramic-based bone grafts are mainly used in dentistry, i.e., to treat traumatic injury, disease, abnormal development, or dental surgery.[1]

3.1. Bone fractures and injuries

In bone fractures and injuries, it is often sufficient to adequately fix a part of the body while the damaged bone regenerates.[20] This is achieved by external non-invasive fixation methods or surgically implanting elements to the bone surface. However, there are cases where bone tissue cannot regenerate or the bones fuse poorly, leading to bone deformation and anatomical dysfunction. In such cases, the bone needs to be reshaped with implants or bone grafts.

3.2. Regenerative medicine and bone replacement

Intensive bone tissue formation stops at the age of 20–25, after which new bone cells are formed only for renewal and regeneration, indicating that the body cannot naturally replace a damaged bone in the event of a significant injury. Regenerative medicine repairs damaged tissues and organs (e.g., from trauma, disease, or congenital problems) through the artificial production (differentiation) and replacement of cells. The healing process is rapid and biologically similar to natural mechanisms. In addition, it has the advantage of circumventing the lack of ideal transplant donors and can be fully personalized. Some tissues (e.g., skin and liver tissues) are continuously regenerated, and replacing these tissues could facilitate the healing process.[1,22]

The production of artificial tissues should approximate the native tissue or organ in both structural (physicomechanical and chemical properties) and biological functions.[5,6,31] Biologically functional artificial tissues require cells that can be primary, differentiated, or highly potent stem cells. In this regard, hydrogels are used as an ECM to provide an exceptional environment for cells, and in some cases, a hard skeleton (e.g., bone) may be required.[5,32,33] 3D scaffolds can be created in several ways (e.g., casting), but the best method to generate structures that most closely resemble native tissue is 3D bioprinting (tissue printing).[5,6]

Nonetheless, the performance of 3D bioprinting is dpendent on several critical requirements such as good biocompatibility, cell dispersion capability,[32] efficient nutrient and oxygen diffusion, and suitable material printability. For example, a gel must not be too fluid or have an inherently cross-linked structure. 3D-bioprinted tissues generally do not have a vascular network in the structures. Therefore, a crosslinking design should be integrated into the overall structure prior to 3D bioprinting.[6,31]

4. 3D bioprinting

3D bioprinting is an additive manufacturing technology used in tissue engineering to create the most native-like artificial living tissues from a mixture of living cells and biomaterial-containing hydrogels, called bioinks. Since organs have a complex structure, spatial location, and cell type presence, imitation of the characteristics of tissues is essential for appropriate function. In contrast to conventional tissue engineering techniques (e.g., 2D tissue culture), 3D bioprinting can develop complex tissue-specific constructs. A general 3D-bioprinted tissue contains cells and an ECM to provide the cells with a native-like microenvironment. In addition, different types of tissue-

specific cells can be incorporated into a particular location. Therefore, 3D-bioprinted tissues are commonly used in *in vitro* testing and clinical implantations. Nonetheless, the technology faces limitations and challenges, such as the intricacies of printing vascularized tissue, selecting and engineering suitable hydrogels, and maintaining cell viability while printing larger tissue constructs. To achieve the most biologically similar artificial tissue, the initial stages of the 3D bioprinting process focus on precisely designing and evaluating hydrogels, cells, and 3D models. In the design process, desired structures are conceptualized using 3D computer-aided design (CAD) design software and then translated into G-code (the computer numerical control (CNC) programming language for 3D printers) via cutting programs. Likewise, the selection of hydrogel components should consider the ECM composition of the target tissue, the biocompatibility of the hydrogel with the cells, and its printability. After printing, the cell-hydrogel construct should be cultured accordingly to promote the development of functional tissues.

4.1. Types of 3D bioprinting techniques

In 3D printing, structures are built layer-wise from a wide array of printing techniques. According to ISO/ASTM 52900:2021, additive manufacturing can be classified into six categories: material extrusion, direct energy deposition, material jetting, sheet lamination, powder bed fusion, and vat photopolymerization. Among these, three main categories are relevant to 3D bioprinting: material extrusion, material jetting, and vat polymerization (Figure 7). Additionally, the powder bed fusion technique can also be used to print rigid scaffolds.[34]

4.1.1. Material extrusion-based bioprinting

Material extrusion-based bioprinting is mainly performed with either fused deposition modeling (FDM) or direct ink writing (DIW) (Figure 8). With FDM, thermoplastic materials can be printed for daily and industrial purposes, but this technique is used for fast prototyping and bioprinting hard scaffolds. In contrast, bioinks are printed with DIW printers, which apply pneumatic (compressed air flow) or mechanical (axial pistons or screws) pressure or a solenoid system to eject the bioink through a nozzle or needle into one or more cartridges fixed to the print head.

Most extrusion-based bioprinters are cartesian-type 3D printers, i.e., assigning the movements according to the *X*, *Y*, and *Z* axes. Usually, the print head moves in the *X* and *Y* directions, while the bed or build plate moves in the *Z* direction. Most printers have temperature-controlled print heads and platforms to maintain an optimal temperature for the cells and the hydrogel. Extrusion-based bioprinters have some drawbacks, such as poor cell viability, low resolution, and slow printing speed. Nonetheless, these bioprinters are the most widely used as they can handle various hydrogels, have high cell density, are cost-effective, and are easy to operate (Table 4).[35-37]

4.1.2. Material jetting-based bioprinting

Material jetting-based bioprinting refers to droplet-based bioprinting, whereby the hydrogel is ejected dropwise to build the final construct. All material jetting-based bioprinters are drop-on-demand printers, where only one drop of material leaves the printer head at a time. Based on their droplet formation mechanism, material jetting-based bioprinting can be categorized into inkjet,

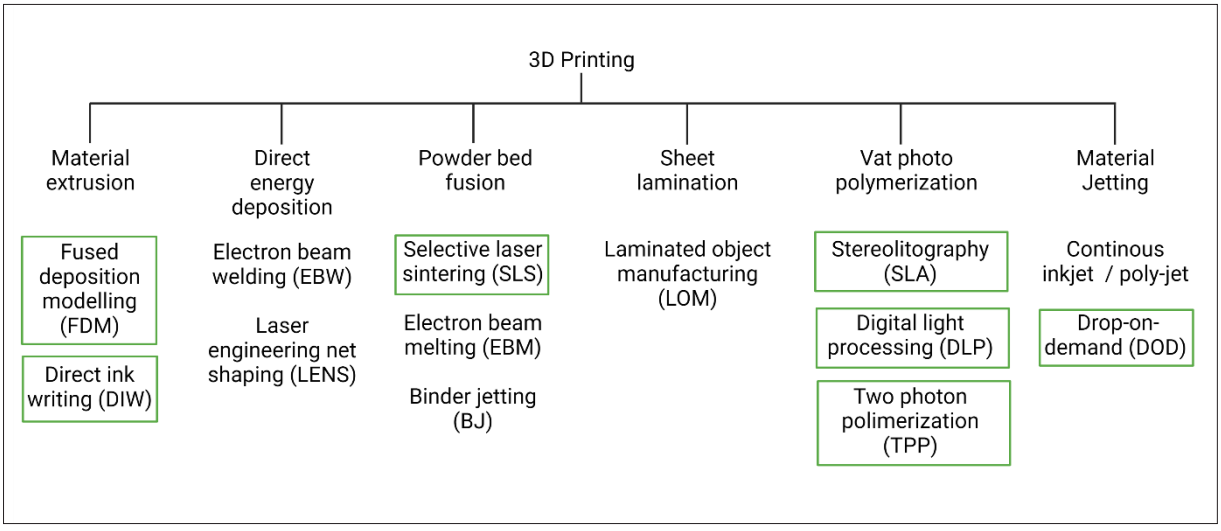


Figure 7. Classification of 3D printing techniques. Green boxes indicate the techniques used in bioprinting. This figure was created using BioRender.

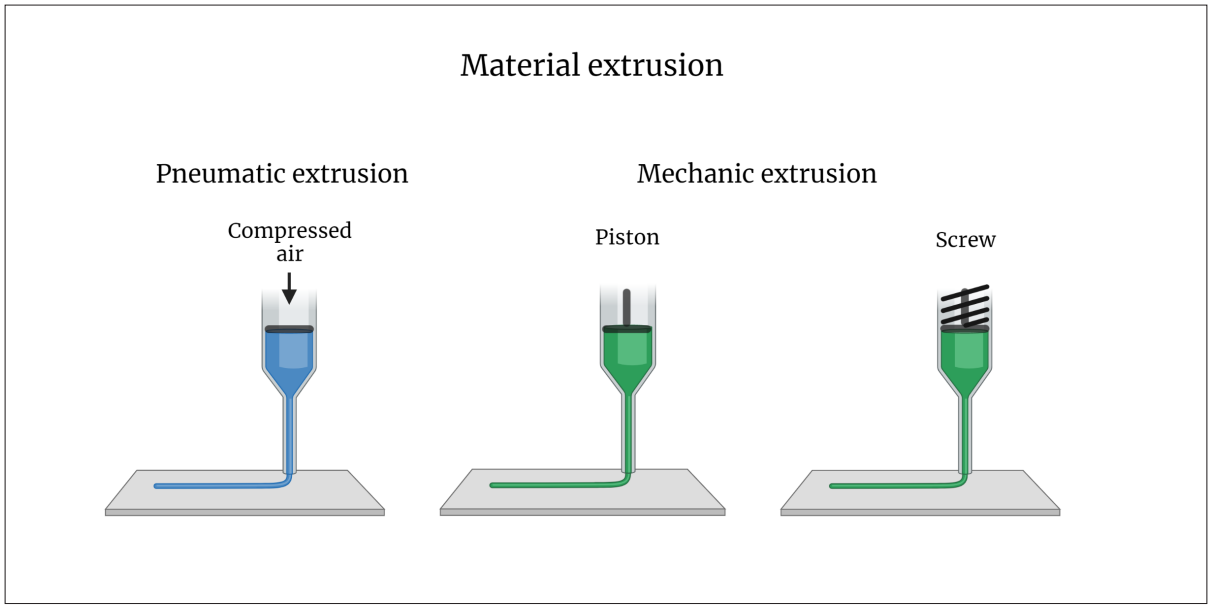


Figure 8. Material extrusion-based 3D bioprinting techniques. This figure was created using BioRender.

Table 4. Comparison of 3D bioprinting techniques

Parameter/category	Material extrusion	Material jetting	Laser	VAP
Resolution	Medium	High	High	High
Material viscosity (mPa·s)	30–36 × 10^7	3.5–12	1–300	No limitation
Cell density	High	Low	Medium	High
Materials	Wide range of materials printed via several crosslinking methods	Wide range of materials printed via several crosslinking methods	Wide range of materials printed via ionic crosslinking methods	Only photocurable materials
Print speed	Slow	Fast	Medium	Fast
Cost	Medium	Low	High	Low
Advantages	Wide range of bioinks; low cost; high cell density	Fast printing process; less cell damage; low cost; precise cell positioning	High resolution; wide range of bioinks	Fast printing process; high cell density; no specific limitation in hydrogel rheological properties
Disadvantages	Limited resolution; slow printing process; limited hydrogel rheology	Limited cell density	High cost; complicated operation	Limited hydrogel possibilities

Abbreviation: VAP: Vat polymerization.

electrohydrodynamic, microvalve-operated, acoustic, and laser-assisted bioprinting (LAB) (Figure 9).[38] The main advantages of material jetting-based bioprinting are its low cost, fast printing speed, and high resolution. However, the cell density and viscosity of the hydrogels are limited (Table 4).[39] The categories of material jetting-based bioprinting are described as follows:

(i) Inkjet bioprinting: Inkjet bioprinting uses the drop-on-demand technique,[40] where the layers are printed dropwise.[41] The hydrogel is loaded into a cartridge or syringe, from which droplets are generated at a nozzle using an actuator driven by thermal, piezoelectric, or electrostatic forces. Inkjet bioprinting is favored due to its affordability among droplet bioprinting techniques. Additionally, commercial bioprinters can be equipped with thermal, piezoelectric, or electrostatic heads. However, a major drawback of this technology is the frequent occurrence of nozzle clogging. In thermal inkjet bioprinters, a small heating unit raises the temperature to 100–300°C

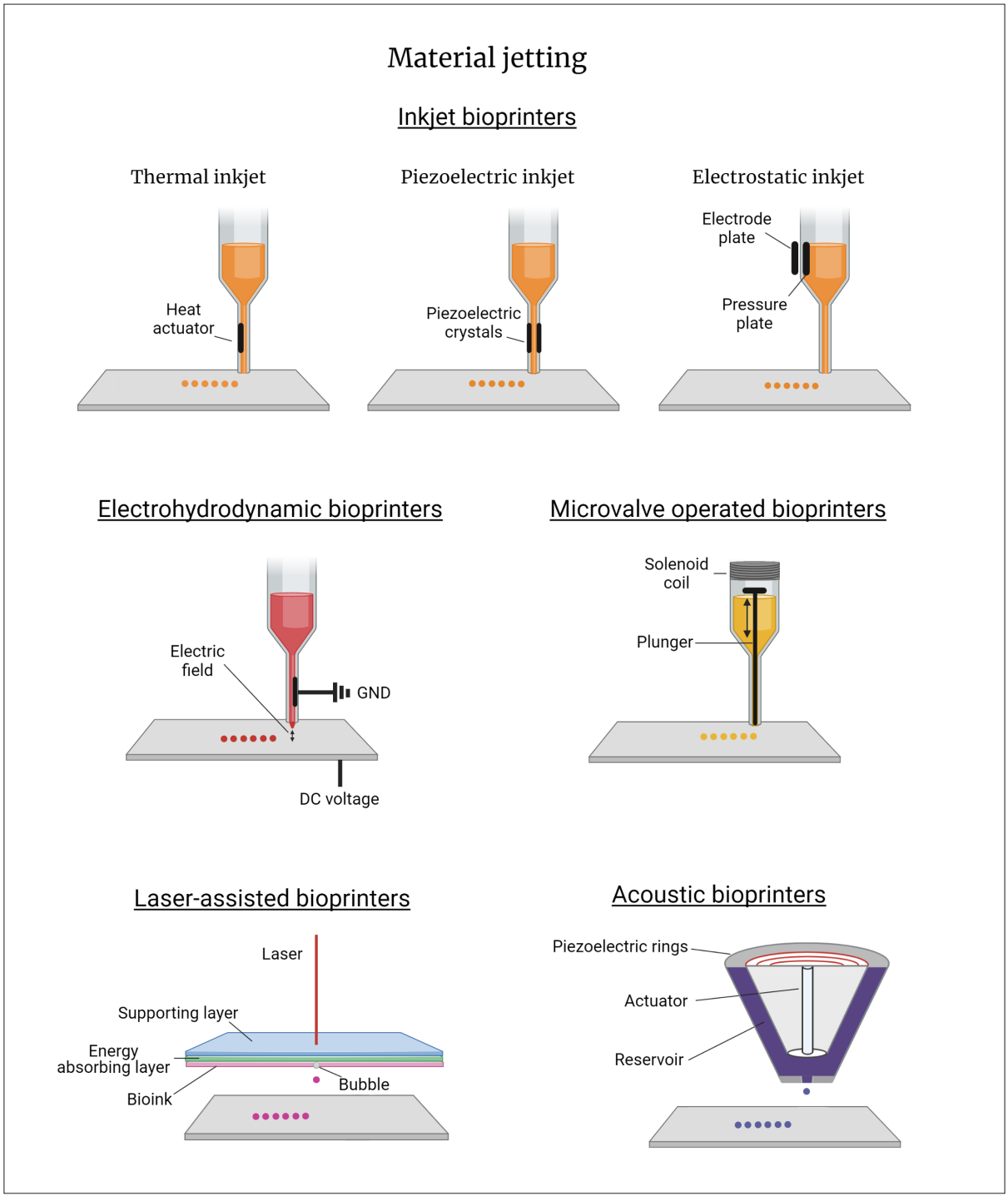


Figure 9. Material jetting-based 3D bioprinting techniques. This figure was created using BioRender.

to momentarily create a bubble in the hydrogel, resulting in the ejection of a droplet. Piezoelectric inkjet printers generate pressure using piezoelectric crystals, where a brief voltage pulse is applied to a piezoelectric actuator located on the inner wall of the hydrogel chamber, altering its shape and exerting pressure on the hydrogel.[39,42]

(ii) Electrohydrodynamic bioprinting: Similarly to inkjet bioprinting, the hydrogel is filled into a

cartridge. However, the force required for droplet formation is not generated from within but between the nozzle and the surface of the build plate. Additionally, pressure is applied to the hydrogel using a piston similar to extrusion techniques by electrohydrodynamic bioprinters. As a result, a constant meniscus of the hydrogel is formed on the aperture of the nozzle. A high DC voltage power source is applied to the collector substrate while the nozzle is grounded, creating a strong electromagnetic field between the substrate and the nozzle and leading to an accumulation of electrical charges in the meniscus. When the electrical charges exceed the surface tension, a drop leaves the nozzle through the wide-operated electrohydrodynamic jet printers. Therefore, a single drop is produced by low electric voltage, field strength, and flow rate. Likewise, a continuous stream can be achieved with high electric field strength and flow rate via electrospinning. Due to the strong driving force and ability to create droplets smaller than the nozzle size, this technique enables single-cell printing.[43]

(iii) Microvalve-operated bioprinting: Similar to inkjet and electrohydrodynamic bioprinting, the bioink is filled in a cartridge and pushed out through a nozzle, and microvalve-operated bioprinting also uses drop-on-demand type printers. However, droplet formation does not occur due to force on the hydrogel, but instead with a mechanical valve. The valve comprises a solenoid coil and a plunger that blocks the aperture of the nozzle. An applied voltage creates a magnetic field in the coil that pulls the plunger upward. Similar to the electrohydrodynamic method, pressure is applied to the hydrogel to leave the nozzle as a droplet when the valve opens. The main advantages of this printing technique are the adjustable droplet size and high cell viability.[39,44]

(iv) LAB: LAB is based on the laser-induced forward transfer method. The main parts of laser-assisted bioprinters are the optical system, donor ribbon, and receiving substrate. The ribbon is typically covered with an absorbing metal layer on the upper side and an adhesive layer with bioink on the lower side. The optical system produces and focuses a laser beam on the top of the donor substrate, resulting in localized evaporation and bubble formation. Subsequently, the high-energy bubble ejects a droplet from the hydrogel layer that lands on the substrate. Laser-assisted bioprinters are advantageous in many aspects, such as print speed and high resolution, and they can handle high cell-content bioinks. In addition, this technique provides the best cell viability rate among all bioprinting methods. However, the cost of these bioprinters is high and has an approximately small build volume.[45]

(v) Acoustic bioprinting: Acoustic bioprinting is an ultrasound-based nozzle-free droplet printing technique. The hydrogel is loaded into a microfluidic reservoir with piezoelectric rings that generate circular ultrasound waves. These waves form an acoustic focal plane at the air–ink interface at the opening of the channels. The channels are open from the bottom, but the bioink drips only when the force of the ultrasound exceeds the surface tension. A substrate, closely placed under the holes, collects the droplets. As this technique does not apply any electric charge, heat, excessive pressure, shear stress, or shocks, it can avoid nozzle damage to the cells. However, the timing of the droplets may be affected by external movements or forces due to the wide gap between the substrate and the fluid surface.[39,46]

4.1.3. Vat polymerization-based bioprinting

Vat polymerization-based bioprinting utilizes a vat of photocurable liquid to construct a 3D model layerwise with a digitally controlled light source (i.e., ultraviolet [UV] or blue light as a focused beam or projection). The only physical movement present is the table along the *Z* axis. The bioresin can be polymerized via top-down and bottom-up methods. However, vat polymerization-based bioprinting requires additional materials for printing and post-processing. Moreover, the number of suitable materials is limited, and cell viability is reportedly lower. Despite the limitations, the technology features a high resolution and may not require a support system (Table 4), suggesting its application in printing cell-free hard supporting scaffolds and experimental devices, such as microvascular vessels and channels.[47,48] Vat polymerization-based bioprinting techniques can be further categorized depending on the photo-crosslinking mechanism: stereolithography (SLA), digital light processing (DLP), and two-photon polymerization (Figure 10). These types of vat polymerization-based bioprinting are discussed as follows:

(i) SLA: SLA uses a laser source to cure bioresins via bottom-up or top-down order. In top-down printers, the optical system is located above the vat, and the building platform is submerged in the bioresin from below. The laser unit directs a UV beam to a movable mirror, where a Galvo motor system steers the focused beam to the resin surface, drawing the layer by scanning. After a layer is imaged, an elevator system moves the building platform down, and a recorder blade moves across the platform to apply

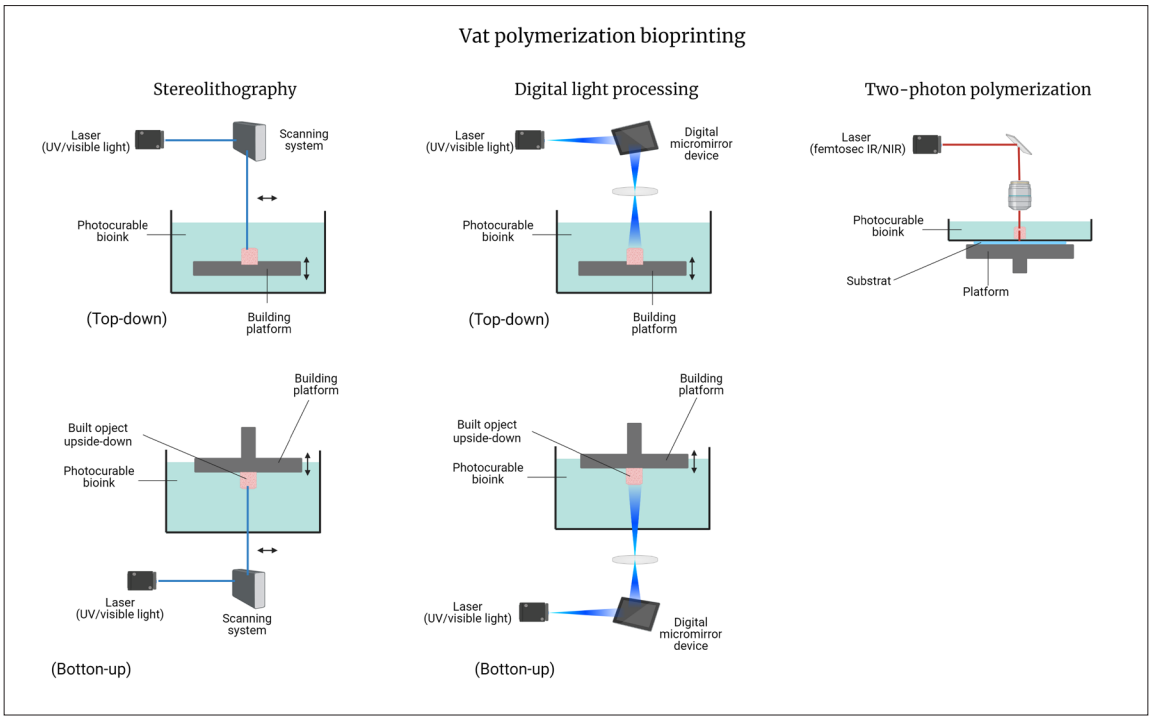


Figure 10. Vat polymerization-based 3D bioprinting techniques. Abbreviations: IR: Infrared; NIR: Near-infrared; UV: Ultraviolet. This figure was created using BioRender.

the next resin layer. Bottom-up printers are based on the same principle, with the difference that the optical system is located below the vet, and the platform pad descends into the resin from above. The finished construct is built upside down on the platform. SLA is a fast, flexible, and accurate printing method, but requires supports made from the same material for post-processing.[48]

(ii) DLP: DLP differs from SLA such that DLP utilizes light (UV or visible blue light) from a projector. The light source remains stationary and simultaneously cures the resin layer. Depending on the applied biocompatible resin, the layer height and exposure time must be controlled to ensure strong interface bonding. The most significant advantage of using this technique is the ability to print vessels and microchannels without a support system. In addition, blue light damages cells less than UV light, making it even more reliable for printing cell-laden bioinks. Additionally, DLP features fast printing speed, low cost, and high accuracy, but the printed construct may have poor mechanical properties.[48]

(iii) Two-photon polymerization: Two-photon polymerization is an ultraprecise micro- or nanoscale 3D printing technique. While SLA and DLP use a single photon to polymerize the resin, two-photon polymerization requires the absorption of two photons. The light source is typically a high-intensity ultrashort femtosecond infrared or near-infrared laser. The 3D structures are built pointwise, but the fabrication is not limited to the layerwise method. Multiple laser beams are directed to the same point and operated simultaneously during printing. When the simultaneous energy of two photons exceeds the absorption energy threshold of the photosensitive material, photo-crosslinking occurs. As with other vat polymerization techniques, two-photon polymerization requires post-processing, as the waste material must be washed off the structure. However, no support systems can be removed, suggesting its suitability to print porous microstructures, vessels, and microfluidic systems. The main advantage of this technique is the very high resolution, which comes at the expense of printing speed and printing volume (limited to a few mm).[48,49]

4.1.4. Selective laser sintering

Selective laser sintering (SLS) is a powder bed fusion 3D printing technique that is not commonly used in 3D bioprinting but occasionally in bone bioprinting. SLS 3D printers work on a similar principle to SLA, except that the raw material is in powder form instead of resin, and the laser light does not bind the material chemically but

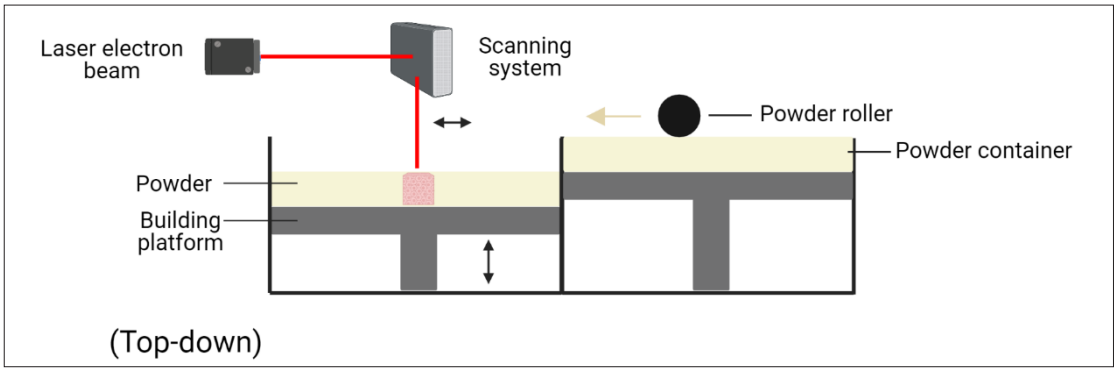


Figure 11. Powder bed fusion 3D printing. This figure was created using BioRender.

fuses the powder particles at high temperatures. SLS does not require a support system, making it possible to print channels and pores with different materials (e.g., metals, ceramics, and composites) (Figure 11).

4.2. Materials used in bone bioprinting

Bioprinting bone tissues requires both soft and hard scaffolds. The former provides the appropriate microenvironment for cells, and the latter offers the shape and mechanical strength of the tissue. Soft scaffolds are commonly hydrogels, while hard scaffolds are usually thermoplastic polymers. All components of the scaffolds need to be biocompatible and biodegradable. In addition, it is advisable to use bioactive substances for the hydrogel to provide binding sites for the cells and support their growth and differentiation. Likewise, the physical and chemical properties of the materials are also important in regulating the printability and mechanical stability of the 3D construct (Table 5).

4.2.1. Hard scaffold materials

Hard scaffold materials are essential for bone printing as hard supporting tissues. The common synthetic polymers used to create hard scaffolds include polycaprolactone (PCL), polylactic acid (PLA), polyglycolide (PGA), and polylactide-coglycolide (PLGA). These materials ensure the appropriate mechanical properties of the scaffold and are also biocompatible and biodegradable. PCL and PLGA are suitable for creating a rigid scaffold of bone tissue, as they are osteoconductive. In addition, they are approved by the US Food and Drug Administration (FDA) as biopolymer materials that can be used for clinical purposes.[50,51] These materials are discussed in detail as follows:

(i) PCL: PCL is a biocompatible and biodegradable synthetic thermoplastic polymer widely used for medicinal purposes. It has a low melting point at 60°C and good thermal stability with a decomposition temperature of approximately 350°C. In 3D printing, PCL is used as pellets in DIW extrusion printers and as filaments in FDM printers. PCL is usually heated to 60–120°C before the printing process at room temperature. When the extruded material leaves the nozzle, it solidifies rapidly and maintains its shape. Its mechanical properties are excellent for making a hard bone frame. Although the tensile strength and modulus of PCL are relatively low, its elongation at break is between 300% and 600% (can even reach 1000%), and its flexural modulus is also high. When PCL is printed in a suitable structure, it retains the hydrogel. However, PCL may not be suited for cell detachment due to its hydrophobic nature, and PCL features a slow biodegradation rate. Nonetheless, PCL is easy to print with and is low cost.[52-54]

(ii) PLGA: PLGA, also called hyperelastic bone, is a biocompatible and biodegradable organic polymer synthesized from lactic acid and glycolic acid. The ratios of these two components affect the properties, including the biodegradation rate. Higher lactic acid content would speed up the degradation and increase the mechanical strength of the scaffold. However, PLGA alone is not sufficient for hard bone scaffolds, as it is not osteoconductive and has weak mechanical properties. Therefore, PLGA is usually combined with other materials, such as PCL, HA, ceramics, or bioglass, to improve the mechanical properties.[55,56]

4.2.2. Hydrogels

Hydrogels are mixtures of several biopolymers. For bones, the base components are typically alginate, gelatin, gelatin methacryloyl (GelMA), chitosan, collagen, hyaluronic acid, silk, dECM, cellulose, and polyethylene glycol (PEG) diacrylate (PEGDA). Additionally, inorganic substances, such as HA, calcium, and phosphate, are often added to hydrogels to support bone generation (Table 5).[50,51,57] The different hydrogel materials are discussed as follows:

(i) Alginate: Alginate is one of the most commonly used natural polysaccharides as a hydrogel component. Alginate is derived from alginic acid, also called algin, which is a polysaccharide naturally produced by brown algae. Algin is hydrophilic and forms a viscous non-bioactive gel in an aqueous solution that does not provide ligands to the cells for adhesion. Algin salts formed with sodium and calcium are called alginates, which are considered an excellent hydrogel base for tissue engineering and bioprinting when combined with other bioactive components. Alginates can crosslink rapidly and easily with ionic solutions, most commonly with calcium chloride. Additionally, alginates are low-cost and have low immunogenicity. However, they have poor mechanical properties and weak bone conductivity. Alginate-based hydrogels are commonly used with DIW, inkjet, and LAB bioprinters.[58]

(ii) Gelatin: Gelatin is a natural protein produced by the irreversible hydrolysis of collagen extracted from the connective tissue of animals. Gelatin is commonly reversibly crosslinked by temperature and has a melting point between 30 and 37°C. Therefore, it is soluble at body temperature, limiting its applications. Likewise, temperature regulation is crucial when printing with gelatin, and its slow gelation makes it challenging to precisely create complex 3D structures. Besides that, gelatin has a fast degradation and poor mechanical characteristics. However, gelatin is inexpensive and has excellent biological properties. Therefore, it is the second most commonly used hydrogel component after alginate. Gelatin is usually mixed with other materials, such as alginate or collagen, and is used in DIW, inkjet, and LAB printing techniques.[59,60]

(iii) GelMA: GelMa is a modified gelatin engineered with methacrylamide and methacrylate groups. In contrast to gelatin, GelMa is irreversibly photo-crosslinkable by adding photo-initiator groups, thus preventing gel dissolution at body temperature. In addition, the photo-crosslinking process is fast, and the crosslinked structures are very stable. However, photo-initiators usually bind to blue or UV light, which could damage the cells, and GelMA is also more expensive than alginate and gelatin. GelMA is most often used in DIW, DLP, and electrospun printing.[61,62]

(iv) Chitosan: Chitosan is a polysaccharide obtained from the deacetylation of chitin by substituting half of the acetyl groups with amine groups, thereby making chitosan soluble in acidic solutions. Due to its poor mechanical properties, chitosan is usually modified by adding or changing different side groups. These groups can be subjected to different crosslinking mechanisms, such as ionic, enzymatic, and photo-crosslinking. In contrast, the basic chitosan structure can only be crosslinked via chemical methods. With these modifications, the mechanical properties of chitosan can be improved, broadening its applicability. However, chitosan-based hydrogels have rapid biodegradation and high cost. To address these issues, chitosan is usually mixed with different materials, such as gelatin, collagen, and GelMa. Nonetheless, chitosan-based hydrogels can be used in DIW, inkjet, LAB, and DLP bioprinting.[63]

(v) Collagen: Collagen is an essential organic constituent of the ECM. Type I collagen is most commonly used for hydrogels in 3D bioprinting. Like gelatin, collagen self-assembly is also temperature-dependent, occurring at 20–37°C. Higher temperatures result in faster bonding and less ordered fibers, thereby affecting the mechanical and functional properties of the construct. When 3D bioprinting with collagen, temperature regulation is crucial to standardize the properties of collagen and the resultant hydrogel. The gelation of collagen is very slow, and collagen has a low viscosity, indicating that the printed constructs could not maintain their shapes. Additionally, collagen degrades rapidly, complicating its cultivation after printing. Nonetheless, collagen-based hydrogels are commonly used in DIW, inkjet, and laser-assisted bioprinters.

(vi) Hyaluronic acid: Hyaluronic acid is a glycosaminoglycan found in the ECM of several tissue types. Its hydrophilic nature and high molecular weight enable the absorption of large amounts of water, highlighting its excellent biocompatibility and bioactivity. However, the solubility and mechanical properties of hyaluronic acid are weak, thereby requiring chemical modifications (ionic, enzymatic, temperature-based, and photo-crosslinking) to be effectively used in hydrogels. Hyaluronic acid-based hydrogels are mainly used in DIW, inkjet, and LAB bioprinting techniques.[64]

(vii) Silk: Silk is a natural polyamide extracted from silkworms. Its main ingredients are silk fibroin and sericin. Due to the structure of the former, silk can absorb mechanical shocks, making it an extremely resistant material. Besides that, silk has excellent biocompatibility, low immunotoxicity, and adjustable degradation, highlighting its suitability for tissue engineering. However, the crosslinking of silk alone in a cellular environment is challenging, and silk is high-cost. Nonetheless, silk-based

hydrogels are often used in DIW, inkjet, LAP, and DLP bioprinting technologies.[65]

(viii) dECM: dECM provides the most native-like microenvironment for cells as a hydrogel material. It contains all the components of the ECM and growth factors commonly found in native tissues; therefore, it can promote cell proliferation and differentiation.[7] The production of dECM is tissue-specific, but the tissue is generally exposed to physical, chemical, or enzymatic stressors to remove the cellular components. These methods can oftentimes be complicated and expensive. In addition, dECM-based hydrogels are challenging to use for 3D bioprinting, as they have low viscosity and poor mechanical properties, making it difficult to regulate their temperature-dependent crosslinking and rapid degradation. As such, dECM is usually mixed with other hydrogel materials for use in DIW, LAB, and electrospun bioprinters.[66-69]

(ix) Cellulose: Cellulose is a biocompatible and bioactive natural hydrophilic polymer. Due to the abundance of hydroxyl groups and its poor biodegradability, cellulose is used not in its natural form but in different chemically modified forms in hydrogels. In this regard, modified cellulose hydrogels have good mechanical properties, and cellulose is an affordable material.[70]

(x) PEG and its derivatives: PEG is a synthetic biocompatible polymer that is highly hydrophilic and has a high water-absorbing capacity. Additionally, its aqueous solution has a low viscosity. In 3D bioprinting, PEGDA and PEG methacrylate (PEGDMA) are often used as they are highly photocurable. PEGDA features rapid and stable crosslinking, good mechanical properties, good shape retention, high resolution, and high resistance to swelling in the aqueous environment. However, PEGDA and PEGMA have low degradation rates and poor cell adhesion, and they are often combined with other organic hydrogel components (e.g., GelMA) or inorganic components (e.g., HA) to improve their properties. PEG-based hydrogels are commonly used in DIW, inkjet, and DLP bioprinters.[39,71]

4.2.3 Additional inorganic components

Bone tissue is a complex mineralized tissue with a rigid ECM that is mainly composed of HA. Additionally, the two

Table 5. Materials used in bone 3D bioprinting

Type of material	Material	Benefits	Drawbacks	Crosslinking mechanism	3D printing technique
Hard scaffold	Polycaprolactone (PCL)[89,90]	Good biocompatibility; biodegradable; easy to print	Slow degradation; poor cell adhesion	N/A	Extrusion
	PEGDA[89,91-94]	Biocompatible; fast degradation; easy to print	Poor mechanical properties	Photo-crosslinking	Extrusion; SLA; DLP
	Polylactic acid (PLA)	Biodegradable; biocompatible; easy to print; good mechanical strength	Slow degradation; poor cell adhesion	N/A	Extrusion
Hydrogel	Alginate	Low cost; good biocompatibility; biodegradable; low immunogenicity; shear-thinning behavior	Low bioactivity; poor cell adhesion; poor mechanical properties; limited stability in the presence of antioxidants.; poor bone conductivity; poor 3D shape maintenance	Ionic crosslinking	Extrusion; inkjet; laser-assisted
	Gelatin	Biocompatible; biodegradable; reversible gelation; low cost	Fast degradation; poor mechanical properties; slow gelation	Thermal crosslinking	Extrusion; inkjet; laser-assisted
	Gelatin methacryloyl (GelMA)	Biocompatible; biodegradable; easy to crosslink with photo-initiators; fast crosslinking; 3D shape maintenance	High cost; cell damage by blue or UV light	Photo-crosslinking	Extrusion; DLP; electrospun
	Chitosan[63]	Good biocompatibility; good cell adhesion; osteogenic potential	Fast degradation; poor mechanical properties; high cost	Ionic crosslinking; photo-crosslinking; self-assembly	Extrusion; DLP; laser-assisted

(*Continued*)

Table 5. ***Continued...***

Type of material	Material	Benefits	Drawbacks	Crosslinking mechanism	3D printing technique
Hydrogel	Chitosan[63]	Good biocompatibility; good cell adhesion; osteogenic potential	Fast degradation; poor mechanical properties; high cost	Ionic crosslinking; photo-crosslinking; self-assembly	Extrusion; DLP; laser-assisted
	Collagen	Good biocompatibility; biodegradable; low immunogenicity; good cell adhesion; regulates cell differentiation	Fast degradation; poor mechanical properties; low viscosity; slow gelation; inconsistent 3D structure; poor 3D shape maintenance	Thermal crosslinking	Extrusion; inkjet; laser-assisted
	Hyaluronic acid[64]	Good biocompatibility; good viscoelastic properties; highly hydrophilic; anti-microbial	Low mechanical strength; high cost	Chemical crosslinking; enzymatic crosslinking; thermal crosslinking; ionic crosslinking; photo-crosslinking	Extrusion; laser-assisted
	Decellularized ECM[66-69]	Good bioactivity; native-like tissue microenvironment; high maintenance of growth and differentiation factors	Poor mechanical properties; low viscosity; fast degradation	Thermal crosslinking	Extrusion; laser-assisted; electrospun
	Cellulose	Already approved for biomedical applications; good bioprintability	Some derivatives could elicit immune responses or cytotoxic effects; highly hydrophilic; limited osteoconductivity	Chemical crosslinking; enzymatic crosslinking	Extrusion
Additional non-organic materials	Hydroxyapatite	Supports bone formation; improves mechanical properties, osteoconductivity, and bioactivity	Complicated to use with ionically cross-linked hydrogels; mesh size must be controlled; tends to be quite rigid and brittle; prone to cracking or fracturing	Does not undergo crosslinking as polymers	Extrusion; laser-assisted
	Biphasic calcium phosphate (BCP)[95-98]	Supports bone formation; improves mechanical properties and biodegradability; has controlled degradation	May elicit an inflammatory response when implanted; bioprinting is challenging; mechanical strength limitations	Biphasic calcium phosphate does not undergo crosslinking as polymers	Extrusion
	Calcium carbonate	Naturally biodegradable; can act as a buffer; facilitates ECM deposition	Infrequently employed in bone bioprinting; limited osteoconductivity; weak mechanical strength; poor biocompatibility	Calcium carbonate does not undergo crosslinking as polymers	Extrusion

Abbreviations: DLP: Digital light processing; ECM: Extracellular matrix; PEGDA: Polyethylene glycol diacrylate; SLA: Stereolithography; UV: Ultraviolet.

main inorganic components of the ECM are calcium and phosphorus, both of which are essential for bone formation. Bone tissues also contain calcium, magnesium, fluorine, sodium, and sulfate ions in crystalline form. Hence, these materials should be provided to the culture medium or scaffold materials for cells to effectively build the tissues of the artificial bone. Calcium phosphate bioceramics, such as synthetic HA, tricalcium phosphates (TCPs), and biphasic calcium phosphate, provide calcium and phosphorus. Likewise, the other trace elements and silicon that support bone formation are provided by bioactive glass. These particles retain the biological properties of the constructs and simultaneously enhance the mechanical properties of hydrogels. The different inorganic components are discussed as follows:

(i) HA: HA is the naturally occurring mineral form of calcium apatite. It accounts for up to half the volume and more than two-thirds the weight of a human bone. Its components are 39.68% calcium and 18% phosphorus by weight and hydroxyl groups. Synthetic HA has a relatively similar composition and crystallography as natural HA and is used for bone tissue engineering (e.g., bone and teeth repair filler). 3D bioprinting has made it possible to develop

3D scaffolds made of HA-containing composites with good biological and mechanical properties. HA is often mixed with microparticles or nanoparticles when producing hard scaffold materials or hydrogels and is used in FDM, DIW, SLA, SLS, inkjet, DLP, and LAB techniques.[72-74]

(ii) TCP: TCP is a preferred material for developing bioceramic-containing scaffolds. Its chemical formula is $Ca_3(PO_4)_2$ and has three polymorphic forms, *β*-TCP, *α*-TCP, and *α*'-TCP. Among these, *β*-TCP is stable with a melting temperature of approximately 1150°C. At higher temperatures, *β*-TCP transforms into *α*-TCP and subsequently to the unstable *α*'-TCP above 1400°C. Hence, only *α*-TCP and *β*-TCP are used in bone replacement and tissue engineering. Both forms of TCP have excellent bioactivity and biocompatibility and degrade faster than HA. *β*-TCP is chemically more stable, but *α*-TCP displayed faster bone formation *in vivo* due to its better solubility in an aqueous solution. Like HA, TCP can be used to produce hard scaffold materials and hydrogels, and TCP composites can be employed with the same printing techniques.[75,76]

(iii) Biphasic calcium phosphate: Both HA and TCP have their advantages and disadvantages in terms of bone formation and 3D bioprinting. Biphasic calcium phosphate is a mixture of HA and *β*-TCP in different proportions, thereby enabling precise regulation of their individual properties. Solubility is the most important parameter that affects bone formation. Free calcium and phosphate ions can initiate bone formation, such that calcium ions have a direct effect on osteoblasts. The calcium and phosphate ions also regulate the bone-oriented differentiation of MSCs. Furthermore, inorganic phosphate ions regulate the expression of mineralization-related genes, and the long-term release of inorganic phosphate ions enhances the collagen mineralization process. Higher solubility speeds up the bone formation process, but excessive calcium levels might be deleterious to the bone cells. In this regard, the solubility of ceramics could be optimized based on the HA/*β*-TCP ratio.[77]

(iv) Bioactive glass: Bioactive glass is a surface-reactive glass-ceramic biomaterial. When implanted into the body, the material forms a layer similar to that of HA on the surface. The basis of bioactive glass is silicon dioxide (SiO_2), calcium oxide (CaO), sodium oxide (Na_2O), and phosphorus tetraoxide (P_2O_5), but may also contain calcium, magnesium, copper, zinc, and silver ions. Bioactive glass can be used for implants, fabricated with SLS or SLA 3D printing technology. Bioactive glass can also be added to thermoplastic materials of a hard scaffold or even mixed into hydrogels as nanoparticles, both of which can be used in DIW and DLP bioprinters.[78,79]

5. Recent advances in 3D bone tissue bioprinting

Although 3D bioprinting appears to be the future of tissue engineering, we are still far from producing functional tissues of relevant size that are suitable for human transplantation. For example, 3D printing of blood vessels is a great challenge as we are currently unable to create tissues of a size that exceeds the diffusion distance of nutrients and oxygen supply. Likewise, the clinical translation of cell-based strategies faces legal and regulatory limitations, as well as the risk of immune reactions and uncontrolled cell differentiation in the recipient's body. In addition, the optimization of hydrogels used for bioprinting can be complicated. Due to the challenges of 3D bioprinting, there have been no successful studies on 3D-bioprinted active, cell-containing human bone transplantation.[2,80-85] Despite the *in vitro* and *in vivo* experiments conducted (Table 6), more studies are warranted before 3D-printed tissues can be implemented for human transplantation.

Nonetheless, the transplantation of cell-free 3D-printed rigid scaffolds and injectable bone replacement materials has long been used in regenerative medicine, particularly in dental repairs and bone replacement. These scaffolds are primarily printed with SLS 3D printers from bioceramics,[74] bioglass, or metals. According to the ClinicalTrials.gov database, there are less than 30 cases related to 3D-printed bone implants in humans (Tables 7 and 8). Recently, Hao et al. developed a bioink from a patient's autologous platelet-rich plasma (PRP) and PCL/*β*-TCP composites. The active scaffold was bioprinted and transplanted into the patient with a good outcome.[86]

6. Conclusion

The dynamic advancement of 3D bioprinting is encouraging for the future of tissue engineering. Due to the interdisciplinary aspect of 3D bioprinting, the current limitations (i.e., in human transplantation) can be addressed by technological advancements and a better understanding of the underlying biological processes.

A major obstacle in clinically implementing 3D bioprinting lies in the intricate structure of bone tissues, which makes it challenging to replicate the complex microarchitecture, including hierarchical organization and vascular networks. Future studies should emphasize refining bioink formulations for more sophisticated

Table 6. 3D-bioprinted bone *in vivo* experiments

Experiment	Materials	Cells	Printing technique	Reference
3D-printed Ch/MSC-laden grafts consisting of alginate and BCP transplanted into female nude mice	Alginate	hMSCs; hChs	DIW	[99]
3D-printed β-TCP scaffolds implanted into rats	β-TCP; pluronic	Primary bone marrow MSCs	Unspecified	[100]
3D-bioprinted PCL-reinforced gene-activated bioinks for bone tissue engineering	RGD-γ-irradiated alginate and nHA complexed to pDNA; PCL	hMSCs	FDM	[101]
Nanoclay-based 3D-printed scaffolds implanted into nude mice	Alginate-methylcellulose bioink	hBMSCs; HUVECs	Extrusion-based	[102]
Calvarial defect model in DM rats	GelMA; gelatin; PEG; MSNs	BMSCs	DIW	[103]
Calvarial bone reconstruction in rats	PCL; TCP; unspecified hydrogel components	hAFSCs	DIW	[104]
Pre-vascularized bone tissue implanted into mice	Fibrin; gelatin; HA; glycerol; hydroxyapatite; VEGF; bFGF; aprotinin	HUVECs; ASCs	DIW	[105]
Porous bioprinted constructs in BMP-2 nonviral gene therapy for bone tissue engineering in the dorsal pockets of mice	Alginate	MG-63 cells; goat MSCs	DIW	[106]
Critical-size rat calvarial defect treatment with ECM/magnesium phosphate-based 3D-printed craniomaxillofacial bone tissue	ECM; amorphous magnesium phosphate	DPSCs	Inkjet	[107]
In vivo tibia repair and ectopic osteoinduction experiments	PEGDA; Laponite XLG nanoclay; HA sodium salt	ROBs	DIW	[108]
Hyperelastic bone scaffolds with MSCs implants in mouse and rat	Hyperelastic bone	MSCs	DIW	[55]
Bilateral calvarial bone defect in mice	Collagen; HA nanoparticles	Mesenchymal stromal cells	LAB	[109]
Subcutaneous implantation in mice	Alginate; gelatin; collagen	DPSCs	DIW	[110]
Chitosan-based scaffolds implanted in nude mice for osteogenesis and vascularization	Chitosan; SiO_2 nanoparticles	Human osteoblasts		[111]
Calcium phosphate scaffold seeded with MSCs in rats	Calcium phosphate paste	Rat MSCs	DIW	[112]
β-TCP-seeded MSC and HUVEC scaffolds in rats	β-TCP	Mouse bone MSCs; HUVECs	DIW	[113]
Pre-vascularized PCL-hydrogel-cell 3D-printed bone implanted into rats	PCL; fibrin; modified alginate; GelMA	HUVECs; hBMSCs	DIW	[114]
Hybrid scaffolds with HUVECs and MSCs implanted into rats	PCL; fibrin	HUVECs; hMSCs	Extrusion-based	[115]
Micro-channeled MSC-GelMA scaffolds implanted into rats	GelMA; pluronic	MSCs	DIW	[116]

Abbreviations: ASC: Adipose-derived stem cell; BCP: Biphasic calcium phosphate particle; bFGF: Basic fibroblast growth factor; BMP-2: Bone morphogenetic protein 2; BMSCs: Bone marrow stromal cells; DIW: Direct ink writing; DM: Diabetes mellitus; DPSC: Dental pulp stem cells; ECM: Extracellular matrix; FDM: Fused deposition modeling; GelMA: Gelatin methacryloyl; HA: Hyaluronic acid; hAFSCs: Human amniotic fluid stem cells; hBMSC: Human bone marrow stromal cells; hChs: Human articular chondrocytes; hMSC: Human mesenchymal stem cell; HUVECs: Human umbilical vein endothelial cells; LAB: Laser-assisted bioprinting; MSC: Mesenchymal stem cell; MSN: Mesoporous silica nanoparticles; nHA: Nanohydroxyapatite; PCL: Polycaprolactone; pDNA: Plasmid DNA; PEG: Polyethylene glycol; PEGDA: Polyethylene glycol diacrylate; RGD: Radiation generating device; ROBs: Rat osteoblasts; TCP: Tricalcium phosphate; VEGF: Vascular endothelial growth factor.

Table 7. 3D bioprinting-related clinical trials based on keywords from ClinicalTrials.gov

Searched keywords	Number of clinical trials	Number of targeted clinical trials
3D-printed bone	88	24
Tissue engineering bone	75	2
Bioprinted bone	0	0
Bone bioprinting	5	0

applications, such as improving cell behavior and tissue regeneration with adjustable mechanical properties, bioactive molecules, and growth factors. Additionally, the materials used in bioprinting, such as hydrogels, dECM, and minerals, should be biocompatible (e.g., avert inflammatory responses) and have relatively similar biological (e.g., cell growth and differentiation) and mechanical properties as native bone tissues.

Minimizing immune reactions and ensuring sustained integration of bioprinted constructs within the host tissue are crucial for successful clinical translation. Maintaining high cell viability throughout the printing process and preserving the biological functions and phenotypic traits are imperative for effective tissue integration and regeneration. It is also important to incorporate specific cells into the bone, particularly for vascularization.[74] Nonetheless, the incorporation of functional vascular networks within bioprinted constructs to facilitate nutrient and oxygen exchange and waste removal remains a significant challenge.

Table 8. 3D bioprinting-related clinical trials found on ClinicalTrials.gov

NCT number	Study title
NCT03185286	3D-printed personalized metal implant in surgical treatment of ankle bone defects
NCT05550285	3D-printed titanium mesh vs. guided autogenous graft
NCT05241548	BMAC on PCL scaffold for ridge augmentation
NCT05057143	3D-printed implants for defect reconstruction in patients with chest wall tumors
NCT04271137	Correction of enophthalmos and orbital volume using pre-bent mesh versus 3D-printed onlay in orbital fracture cases
NCT04466397	Repair of large bone defects through 3D-printed individualized porous implant
NCT04773847	The clinical and radiographic outcomes of a 3D-printed patient-specific biomimetic bone substitute in maxillofacial indications: An interventional, multicentered, open-label, post-market clinical investigation
NCT05291754	3D-printed PEEK implants for cranioplasty
NCT03292679	Craniofacial applications of 3D printing
NCT05700526	Customized bone allografts by 3D-printing
NCT04167878	Exploratory study of 3D-printed biodegradable cervical interbody fusion cage
NCT04000672	Patient-specific instrumentation (PSI) referencing osteotomy technological transfer—a randomized control trial (RCT)
NCT05348434	Evaluation of using 3D-printed PEEK facial implants in repairing maxillofacial deformities
NCT03608280	Efficiency of 3D-printed implant versus autograft for orbital reconstruction (TOR-3D)
NCT03735199	3D-printed scaffold device for ridge preservation after tooth extraction
NCT05616195	Application of 3D-printed prosthesis in limb salvage surgery for bone tumors
NCT04566874	SPIRA™-A 3D and HCT/p DBM vs. Medtronic Divergent™-L/Perimeter™ and recombinant BMP-2
NCT04086784	3D-printed porous titanium alloy cages versus PEEK cages in patients with osteoporosis
NCT04635865	3D-printed patient-specific surgical plates versus conventional surgical plates in jaw reconstruction
NCT05023733	Clinical and radiographic outcomes of TLIF with 3D-printed cellular implant
NCT03647501	Lumbar fusion with Nexxt spine 3D-printed titanium interbody cages
NCT03941028	Clinical effects of large segmental bone defects with 3D-printed titanium implant
NCT05696470	Fusion rates of 3D-printed porous titanium cages in three and four-level ACDFs
NCT04449211	The effectiveness in the treatment of long bone defects using 3D-printed implant
NCT03185286	3D-printed personalized metal implant in surgical treatment of ankle bone defects

Abbreviations: ACDF: Anterior cervical discectomy with fusion; BMAC: Bone marrow aspirate concentrate; BMP: Bone morphogenic protein; DBM: Demineralized bone matrix; HCT/p: Human cells, tissues, and cellular and tissue-based product; PCL: Polycaprolactone; PEEK: Polyether ether ketone; TLIF: Transforaminal lumbar interbody fusion.

Various methods can be explored to overcome these challenges, such as employing multi-material bioprinting techniques for the creation of intricate structures with precise control over the mechanical properties, cell distribution, and concentration of bioactive molecules. Recently, computer vision was utilized for bone bioprinting, encompassing common tasks such as controlling bone scaffold processes, implementing deep learning techniques, and assessing cell viability. The findings revealed the capability of artificial intelligence to overcome current limitations and expedite advancements within this domain.[87] Besides that, integrating pre-vascularization methods, such as co-culturing endothelial cells with other cell types or using sacrificial materials, promotes the formation of functional vascular networks within bioprinted constructs.[74]

External factors, such as mechanical forces, biochemical signals, and electrical impulses, can significantly affect the formation of bone tissues. Bioreactors and other external stimuli can augment cell viability, specialization, and tissue maturation within printed biological constructs. Furthermore, the advancement of programmable biomaterials adds a temporal dimension, suggesting that four-dimensional (4D)-printed constructs can adapt their shape or function over time in response to environmental changes.[88] In this regard, 4D bioprinting is anticipated to be the next frontier in bone regeneration technology.[87]

By addressing these hurdles and exploring innovative approaches, bone bioprinting can progress toward developing functional tissue constructs with superior regenerative capabilities for clinical applications in bone repair and regeneration. It should be mentioned that producing engineered tissues for therapeutic purposes also has its legal proceedings prior to market entry, such as medical device regulation (MDR) and good manufacturing practice (GMP).[86]

Acknowledgments

All figures were generated by Borbála Lovászi using BioRender (www.app.biorender.com).

Funding

This work was supported by GINOP_PLUSZ-2.1.1-21-2022-00043 (co-financed by the European Union and the European Regional Development Fund) and the National Research, Development, and Innovation Office (NKFIH PD 132570 to ZV). ZV is a recipient of the János Bolyai Research Scholarship of the Hungarian Academy of Sciences (BO/00190/20/5) and the NPP-22-5 Bolyai+ Fellowship (NKP-22-5-SZTE-319), financed by the New National Excellence Program of the Hungarian Ministry of Innovation and Technology from the National Research Development and Innovation Fund. The projects (TKP2021-EGA-28 and TKP2021-EGA-32) were funded by the Ministry of Innovation and Technology of Hungary from the National Research, Development and Innovation Fund, financed under the TKP2021-EGA funding scheme.

Conflict of interest

The authors declare no conflicts of interest.

Authors' contributions

Conceptualization: Borbála Lovászi, Zoltán Veréb
Funding acquisition: Zoltán Veréb
Methodology: Borbála Lovászi
Supervision: Zoltán Veréb
Visualization: Diána Szűcs
Writing – original draft preparation: Borbála Lovászi
Writing – reviewing and editing: Diána Szűcs, Tamás Monostori, Lajos Kemény, Zoltán Veréb

Ethics approval and consent to participate

Not applicable.

Consent for publication

Not applicable.

Availability of data

Not applicable.

References

1. Oryan A, Alidadi S, Moshiri A, Maffulli N. Bone regenerative medicine: classic options, novel strategies, and future directions. *J Orthop Surg Res.* 2014;9(1):18. doi: 10.1186/1749-799X-9-18

2. Maresca JA, DeMel DC, Wagner GA, Haase C, Geibel JP. Three-dimensional bioprinting applications for bone tissue engineering. *Cells.* 2023;12(9). doi: 10.3390/cells12091230

3. Masaeli R, Zandsalimi K, Rasoulianboroujeni M, Tayebi L. Challenges in three-dimensional printing of bone substitutes. *Tissue Eng Part B Rev.* 2019;25(5):387-397. doi: 10.1089/ten.TEB.2018.0381

4. Mirkhalaf M, Men Y, Wang R, No Y, Zreiqat H. Personalized 3D printed bone scaffolds: a review. *Acta Biomater.* 2023;156:110-124. doi: 10.1016/j.actbio.2022.04.014

5. Do AV, Khorsand B, Geary SM, Salem AK. 3D printing of scaffolds for tissue regeneration applications. *Adv Healthc Mater.* 2015;4(12):1742-1762.

doi: 10.1002/adhm.201500168

6. Jariwala SH, Lewis GS, Bushman ZJ, Adair JH, Donahue HJ. 3D printing of personalized artificial bone scaffolds. *3D Print Addit Manuf.* 2015;2(2):56-64. doi: 10.1089/3dp.2015.0001
7. Stanco D, Urban P, Tirendi S, Ciardelli G, Barrero J. 3D bioprinting for orthopaedic applications: current advances, challenges and regulatory considerations. *Bioprinting.* 2020;20:None. doi: 10.1016/j.bprint.2020.e00103
8. Wang X, Wang Y, Gou W, Lu Q, Peng J, Lu S. Role of mesenchymal stem cells in bone regeneration and fracture repair: a review. *Int Orthop.* 2013;37(12):2491-2498. doi: 10.1007/s00264-013-2059-2
9. Florencio-Silva R, Sasso GR, Sasso-Cerri E, Simoes MJ, Cerri PS. Biology of bone tissue: structure, function, and factors that influence bone cells. *Biomed Res Int*. 2015;2015:421746. doi: 10.1155/2015/421746
10. Sander PM, Klein N, Stein K, Wings O. Sauropod bone histology and its implications for sauropod biology. In: Klein N, Remes K, Sander M, Gee C, eds. Biology of the Sauropod Dinosaurs: Understanding the Life of Giants. Indiana University Press; 2011:276-302.
11. Gerhardt LC, Boccaccini AR. Bioactive glass and glass-ceramic scaffolds for bone tissue engineering. *Materials (Basel)*. 2010;3(7):3867-3910. doi: 10.3390/ma3073867
12. Datta HK, Ng WF, Walker JA, Tuck SP, Varanasi SS. The cell biology of bone metabolism. *J Clin Pathol.* 2008;61(5):577-587. doi: 10.1136/jcp.2007.048868
13. Lin X, Patil S, Gao YG, Qian A. The bone extracellular matrix in bone formation and regeneration. *Front Pharmacol.* 2020; 11:757. doi: 10.3389/fphar.2020.00757
14. Kirby DJ, Young MF. Isolation, production, and analysis of small leucine-rich proteoglycans in bone. *Methods Cell Biol*. 2018;143:281-296. doi: 10.1016/bs.mcb.2017.08.016
15. Nikitovic D, Aggelidakis J, Young MF, Iozzo RV, Karamanos NK, Tzanakakis GN. The biology of small leucine-rich proteoglycans in bone pathophysiology. *J Biol Chem*. 2012;287(41):33926-33933. doi: 10.1074/jbc.R112.379602
16. Burnier JP, Borowski M, Furie BC, Furie B. Gamma-carboxyglutamic acid. *Mol Cell Biochem*. 1981;39:191-207. doi: 10.1007/BF00232574
17. Wen L, Chen J, Duan L, Li S. Vitamin K-dependent proteins involved in bone and cardiovascular health (Review). *Mol Med Rep*. 2018;18(1):3-15. doi: 10.3892/mmr.2018.8940
18. Berendsen AD, Olsen BR. Bone development. *Bone*. 2015;80:14-18. doi: 10.1016/j.bone.2015.04.035
19. Salhotra A, Shah HN, Levi B, Longaker MT. Mechanisms of bone development and repair. *Nat Rev Mol Cell Biol*. 2020;21(11):696-711. doi: 10.1038/s41580-020-00279-w
20. Walmsley GG, Ransom RC, Zielins ER, et al. Stem cells in bone regeneration. *Stem Cell Rev Rep*. 2016;12(5):524-529. doi: 10.1007/s12015-016-9665-5
21. Kolios G, Moodley Y. Introduction to stem cells and regenerative medicine. *Respiration*. 2013;85(1):3-10. doi: 10.1159/000345615
22. Vereb Z, Mazlo A, Szabo A, et al. Vessel wall-derived mesenchymal stromal cells share similar differentiation potential and immunomodulatory properties with bone marrow-derived stromal cells. *Stem Cells Int*. 2020;2020:8847038. doi: 10.1155/2020/8847038
23. Han Y, Li X, Zhang Y, Han Y, Chang F, Ding J. Mesenchymal stem cells for regenerative medicine. *Cells*. 2019;8(8). doi: 10.3390/cells8080886
24. Vereb Z, Poliska S, Albert R, et al. Role of human corneal stroma-derived mesenchymal-like stem cells in corneal immunity and wound healing. *Sci Rep*. 2016;6:26227. doi: 10.1038/srep26227
25. Galea GL, Zein MR, Allen S, Francis-West P. Making and shaping endochondral and intramembranous bones. *Dev Dyn*. 2021;250(3):414-449. doi: 10.1002/dvdy.278
26. Kozhemyakina E, Lassar AB, Zelzer E. A pathway to bone: signaling molecules and transcription factors involved in chondrocyte development and maturation. *Development*. 2015;142(5):817-831. doi: 10.1242/dev.105536
27. Park IK, Cho CS. Stem cell-assisted approaches for cartilage tissue engineering. *Int J Stem Cells*. 2010;3(2):96-102. doi: 10.15283/ijsc.2010.3.2.96
28. Guasto A, Cormier-Daire V. Signaling pathways in bone development and their related skeletal dysplasia. *Int J Mol Sci*. 2021;22(9). doi: 10.3390/ijms22094321
29. Martin V, Bettencourt A. Bone regeneration: Biomaterials as local delivery systems with improved osteoinductive properties. *Mater Sci Eng C Mater Biol Appl*. 2018;82:363-371. doi: 10.1016/j.msec.2017.04.038
30. Yan L, Cinar A, Ma S, Abel R, Hansen U, Marrow TJ. A method for fracture toughness measurement in trabecular bone using computed tomography, image correlation and finite element methods. *J Mech Behav Biomed Mater*. 2020;109:103838. doi: 10.1016/j.jmbbm.2020.103838

31. Haleem A, Javaid M, Khan RH, Suman R. 3D printing applications in bone tissue engineering. *J Clin Orthop Trauma*. 2020;11(Suppl 1):S118-S124. doi: 10.1016/j.jcot.2019.12.002

32. Yi S, Ding F, Gong L, Gu X. Extracellular matrix scaffolds for tissue engineering and regenerative medicine. *Curr Stem Cell Res Ther.* 2017;12(3):233-246. doi: 10.2174/1574888X11666160905092513

33. Zhu W, Ma X, Gou M, Mei D, Zhang K, Chen S. 3D printing of functional biomaterials for tissue engineering. *Curr Opin Biotechnol.* 2016;40:103-112. doi: 10.1016/j.copbio.2016.03.014

34. Szűcs D, Fekete Z, Guba, et al. Toward better drug development: three-dimensional bioprinting in toxicological research. *Int J Bioprint.* 2023;9(2):663. doi: 10.18063/ijb.v9i2.663

35. Xu J, Zheng S, Hu X, et al. Advances in the research of bioinks based on natural collagen, polysaccharide and their derivatives for skin 3D bioprinting. *Polymers (Basel)*. 2020;12(6). doi: 10.3390/polym12061237

36. Lee VK, Dai G. Three-dimensional bioprinting and tissue fabrication: prospects for drug discovery and regenerative medicine. *Adv Healthcare Technol.* 2015;1:23-35. doi: 10.2147/AHCT.S69191

37. Sundaramurthi D, Rauf S, Hauser CAE. 3D bioprinting technology for regenerative medicine applications. *Int J Bioprint*. 2016;2(2):9-26. doi: 10.18063/IJB.2016.02.010

38. Vijayavenkataraman S, Yan WC, Lu WF, Wang CH, Fuh JYH. 3D bioprinting of tissues and organs for regenerative medicine. *Adv Drug Deliv Rev.* 2018;132:296-332. doi: 10.1016/j.addr.2018.07.004

39. Zhou D, Chen J, Liu B, Zhang X, Li X, Xu T. Bioinks for jet-based bioprinting. *Bioprinting.* 2019;16:e00060. doi: 10.1016/j.bprint.2019.e00060

40. He Y, Gu Z, Xie M, Fu J, Lin H. Why choose 3D bioprinting? Part II: methods and bioprinters. *Bio-Des Manuf.* 2020;3:1-4. doi: 10.1007/s42242-020-00064-w

41. Fontes A, Marcomini RF. 3D bioprinting: a review of materials, processes and bioink properties. *J Eng Exact Sci.* 2020;6(5):0617-0639. doi: 10.18540/jcecvl6iss5pp0617-0639

42. Chowdhury SR, Lokanathan Y, Xian LJ, et al. 3D printed bioscaffolds for developing tissue-engineered constructs. In: Yasa E, Mhadhbi M, Santecchia E, eds. *Design and Manufacturing*. 2020. doi: 10.5772/intechopen.92418

43. Gao D, Zhou JG. Designs and applications of electrohydrodynamic 3D printing. *Int J Bioprint.* 2019;5(1):172. doi: 10.18063/ijb.v5i1.172

44. Gudapati H, Dey M, Ozbolat I. A comprehensive review on droplet-based bioprinting: past, present and future. *Biomaterials.* 2016;102:20-42. doi: 10.1016/j.biomaterials.2016.06.012

45. Ventura RD. An overview of laser-assisted bioprinting (LAB) in tissue engineering applications. *Med Lasers.* 2021;10(2):76-81. doi: 10.25289/ML.2021.10.2.76

46. Leberfinger AN, Ravnic DJ, Dhawan A, Ozbolat IT. Concise review: bioprinting of stem cells for transplantable tissue fabrication. *Stem Cells Transl Med.* 2017;6(10):1940-1948. doi: 10.1002/sctm.17-0148

47. Lee JM, Sing SL, Zhou M, Yeong WY. 3D bioprinting processes: a perspective on classification and terminology. *Int J Bioprint.* 2018;4(2):151. doi: 10.18063/IJB.v4i2.151

48. Ng WL, Lee JM, Zhou M, et al. Vat polymerization-based bioprinting-process, materials, applications and regulatory challenges. *Biofabrication*. 2020;12(2):022001. doi: 10.1088/1758-5090/ab6034

49. Faraji Rad Z, Prewett PD, Davies GJ. High-resolution two-photon polymerization: the most versatile technique for the fabrication of microneedle arrays. *Microsyst Nanoeng.* 2021;7:71. doi: 10.1038/s41378-021-00298-3

50. Liu F, Chen Q, Liu C, et al. Natural polymers for organ 3D bioprinting. *Polymers (Basel)*. 2018;10(11):1278. doi: 10.3390/polym10111278

51. Wang C, Huang W, Zhou Y, et al. 3D printing of bone tissue engineering scaffolds. *Bioact Mater.* 2020;5(1):82-91. doi: 10.1016/j.bioactmat.2020.01.004

52. Eshraghi S, Das S. Mechanical and microstructural properties of polycaprolactone scaffolds with one-dimensional, two-dimensional, and three-dimensional orthogonally oriented porous architectures produced by selective laser sintering. *Acta Biomater*. 2010;6(7):2467-2476. doi: 10.1016/j.actbio.2010.02.002

53. Lu L, Zhang Q, Wootton DM, et al. Mechanical study of polycaprolactone-hydroxyapatite porous scaffolds created by porogen-based solid freeform fabrication method. *J Appl Biomater Funct Mater.* 2014;12(3):145-154. doi: 10.5301/JABFM.5000163

54. Koch F, Thaden O, Conrad S, et al. Mechanical properties of polycaprolactone (PCL) scaffolds for hybrid 3D-bioprinting with alginate-gelatin hydrogel. *J Mech Behav Biomed Mater*. 2022;130:105219. doi: 10.1016/j.jmbbm.2022.105219

55. Jakus AE, Rutz AL, Jordan SW, et al. Hyperelastic "bone": a highly versatile, growth factor-free, osteoregenerative, scalable, and surgically friendly biomaterial. *Sci Transl Med.* 2016;8(358):358ra127.

doi: 10.1126/scitranslmed.aaf7704

56. Gentile P, Chiono V, Carmagnola I, Hatton PV. An overview of poly(lactic-co-glycolic) acid (PLGA)-based biomaterials for bone tissue engineering. *Int J Mol Sci.* 2014;15(3): 3640-3659.
doi: 10.3390/ijms15033640

57. Petros S, Tesfaye T, Ayele M. A review on gelatin based hydrogels for medical textile applications. *J Eng.* 2020;2020:8866582.
doi: 10.1155/2020/8866582

58. Sanchez-Fernandez JA, Presbitero-Espinosa G, Pena-Paras L, et al. Characterization of sodium alginate hydrogels reinforced with nanoparticles of hydroxyapatite for biomedical applications. *Polymers (Basel).* 2021; 13(17).
doi: 10.3390/polym13172927

59. Tan JJY, Lee CP, Hashimoto M. Preheating of gelatin improves its printability with transglutaminase in direct ink writing 3D printing. *Int J Bioprint.* 2020;6(4):296.
doi: 10.18063/ijb.v6i4.296

60. Mancha Sanchez E, Gomez-Blanco JC, Lopez Nieto E, et al. Hydrogels for bioprinting: a systematic review of hydrogels synthesis, bioprinting parameters, and bioprinted structures behavior. *Front Bioeng Biotechnol*. 2020;8:776.
doi: 10.3389/fbioe.2020.00776

61. Yue K, Trujillo-de Santiago G, Alvarez MM, Tamayol A, Annabi N, Khademhosseini A. Synthesis, properties, and biomedical applications of gelatin methacryloyl (GelMA) hydrogels. *Biomaterials*. 2015;73:254-271.
doi: 10.1016/j.biomaterials.2015.08.045

62. Piao Y, You H, Xu T, et al. Biomedical applications of gelatin methacryloyl hydrogels. *Eng Regener.* 2021;2:47-56.
doi: 10.1016/j.engreg.2021.03.002

63. Lazaridou M, Bikiaris DN, Lamprou DA. 3D bioprinted chitosan-based hydrogel scaffolds in tissue engineering and localised drug delivery. *Pharmaceutics*. 2022;14(9):1978.
doi: 10.3390/pharmaceutics14091978

64. Khunmanee S, Jeong Y, Park H. Crosslinking method of hyaluronic-based hydrogel for biomedical applications. *J Tissue Eng*. 2017;8:2041731417726464.
doi: 10.1177/2041731417726464

65. Zheng H, Zuo B. Functional silk fibroin hydrogels: preparation, properties and applications. *J Mater Chem B*. 2021;9(5):1238-1258.
doi: 10.1039/d0tb02099k

66. Amirazad H, Dadashpour M, Zarghami N. Application of decellularized bone matrix as a bioscaffold in bone tissue engineering. *J Biol Eng.* 2022;16(1):1.
doi: 10.1186/s13036-021-00282-5

67. Boso D, Maghin E, Carraro E, Giagante M, Pavan P, Piccoli M. Extracellular matrix-derived hydrogels as biomaterial for different skeletal muscle tissue replacements. *Materials (Basel)*. 2020;13(11):2483.
doi: 10.3390/ma13112483

68. Kim YS, Majid M, Melchiorri AJ, Mikos AG. Applications of decellularized extracellular matrix in bone and cartilage tissue engineering. *Bioeng Transl Med.* 2019;4(1):83-95.
doi: 10.1002/btm2.10110

69. Pati F, Jang J, Ha DH, et al. Printing three-dimensional tissue analogues with decellularized extracellular matrix bioink. *Nat Commun*. 2014;5:3935.
doi: 10.1038/ncomms4935

70. Hickey RJ, Pelling AE. Cellulose biomaterials for tissue engineering. *Front Bioeng Biotechnol.* 2019;7:45.
doi: 10.3389/fbioe.2019.00045

71. Choi JR, Yong KW, Choi JY, Cowie AC. Recent advances in photo-crosslinkable hydrogels for biomedical applications. *Biotechniques.* 2019;66(1):40-53.
doi: 10.2144/btn-2018-0083

72. Kumar A, Kargozar, Baino F, Han SS. Additive manufacturing methods for producing hydroxyapatite and hydroxyapatite-based composite scaffolds: a review. *Front Mater.* 2019;6:313.
doi: 10.3389/fmats.2019.00313

73. Habibah TU, Amlani DV, Brizuela M. *Hydroxyapatite Dental Material*. Treasure Island (FL): StatPearls; 2022.

74. Zhang M, Lin R, Wang X, et al. 3D printing of Haversian bone-mimicking scaffolds for multicellular delivery in bone regeneration. *Sci Adv.* 2020;6(12):eaaz6725.
doi: 10.1126/sciadv.aaz6725

75. Brazete D, Torres PMC, Abrantes JCC, Ferreira JMF. Influence of the Ca/P ratio and cooling rate on the allotropic α↔β-tricalcium phosphate phase transformations. *Ceram Int.* 2018;44(7):8249-8256.
doi: 10.1016/j.ceramint.2018.02.005

76. Kim WJ, Yun HS, Kim GH. An innovative cell-laden alpha-TCP/collagen scaffold fabricated using a two-step printing process for potential application in regenerating hard tissues. *Sci Rep.* 2017;7(1):3181.
doi: 10.1038/s41598-017-03455-9

77. Bouler JM, Pilet P, Gauthier O, Verron E. Biphasic calcium phosphate ceramics for bone reconstruction: a review of biological response. *Acta Biomater*. 2017;53:1-12.
doi: 10.1016/j.actbio.2017.01.076

78. Dukle A, Murugan D, Nathanael AJ, Rangasamy L, Oh TH. Can 3D-printed bioactive glasses be the future of bone tissue engineering? *Polymers (Basel)*. 2022;14(8).
doi: 10.3390/polym14081627

79. Heid S, Boccaccini AR. Advancing bioinks for 3D bioprinting using reactive fillers: a review. *Acta Biomater.* 2020;113:1-22.
doi: 10.1016/j.actbio.2020.06.040

80. Alawi SA, Matschke J, Muallah D, Gelinksy M, Dragu A. 3D bioprinting in plastic and reconstructive surgery: current concepts, progress, and clinical application. *Eur J Plast Surg*. 2023;46:833-843.
doi: 10.1007/s00238-023-02108-7

81. Yazdanpanah Z, Johnston JD, Cooper DML, Chen XB. 3D bioprinted scaffolds for bone tissue engineering: state-of-the-art and emerging technologies. *Front Bioeng Biotech*. 2022;10:824156.
doi: 10.3389/fbioe.2022.824156

82. Lim W, Kim B, Moon YL. Three-dimensional bioprinting for bone and cartilage transplantation. *Ann Joint*. 2019;4(1).
doi: 10.21037/aoj.2018.12.06

83. Genova T, Roato I, Carossa M, Motta C, Cavagnetto D, Mussano F. Advances on bone substitutes through 3D bioprinting. *Int J Mol Sci*. 2020;21(19).
doi: 10.3390/ijms21197012

84. Abu Owida H. Developments and clinical applications of biomimetic tissue regeneration using 3D bioprinting technique. *Appl Bionics Biomech*. 2022;2022: 2260216.
doi: 10.1155/2022/2260216

85. Su X, Wang T, Guo S. Applications of 3D printed bone tissue engineering scaffolds in the stem cell field. *Regen Ther*. 2021;16:63-72.
doi: 10.1016/j.reth.2021.01.007

86. Hao Y, Cao B, Deng L, et al. The first 3D-bioprinted personalized active bone to repair bone defects: a case report. *Int J Bioprint*. 2023;9(2):654.
doi: 10.18063/ijb.v9i2.654

87. Liu C, Wang L, Lu W, et al. Computer vision-aided bioprinting for bone research. *Bone Res*. 2022;10(1):21.
doi: 10.1038/s41413-022-00192-2

88. Wan Z, Zhang P, Liu Y, Lv L, Zhou Y. Four-dimensional bioprinting: current developments and applications in bone tissue engineering. *Acta Biomater*. 2020;101:26-42.
doi: 10.1016/j.actbio.2019.10.038

89. Kotturi H, Abuabed A, Zafar H, et al. Evaluation of polyethylene glycol diacrylate-polycaprolactone scaffolds for tissue engineering applications. *J Funct Biomater*. 2017;8(3).
doi: 10.3390/jfb8030039

90. Khalaf AT, Wei Y, Wan J, et al. Bone tissue engineering through 3D bioprinting of bioceramic scaffolds: a review and update. *Life (Basel)*. 2022;12(6).
doi: 10.3390/life12060903

91. Liu W, Jing X, Xu Z, Teng C. PEGDA/HA mineralized hydrogel loaded with Exendin4 promotes bone regeneration in rat models with bone defects by inducing osteogenesis. *J Biomater Appl*. 2021;35(10):1337-1346.
doi: 10.1177/088532822098704

92. Yang F, Williams CG, Wang DA, Lee H, Manson PN, Elisseeff J. The effect of incorporating RGD adhesive peptide in polyethylene glycol diacrylate hydrogel on osteogenesis of bone marrow stromal cells. *Biomaterials*. 2005;26(30): 5991-5998.
doi: 10.1016/j.biomaterials.2005.03.018

93. Sousa AC, Biscaia S, Alvites R, et al. Assessment of 3D-printed polycaprolactone, hydroxyapatite nanoparticles and diacrylate poly(ethylene glycol) scaffolds for bone regeneration. *Pharmaceutics*. 2022;14(12):2643.
doi: 10.3390/pharmaceutics14122643

94. Stillman ZS, Jarai BM, Raman N, Patel P, Fromen CA. Degradation profiles of poly(ethylene glycol) diacrylate (PEGDA)-based hydrogel nanoparticles. *Polym Chem*. 2020;11(2):568-580.
doi: 10.1039/c9py01206k

95. Thrivikraman G, Athirasala A, Twohig C, Boda SK, Bertassoni LE. Biomaterials for craniofacial bone regeneration. *Dent Clin North Am*. 2017;61(4):835-856.
doi: 10.1016/j.cden.2017.06.003

96. Ahmed AG, Awartani FA Niazy AA, Jansen JA, Alghamdi HS. A combination of biphasic calcium phosphate (Maxresorb®) and hyaluronic acid gel (Hyadent®) for repairing osseous defects in a rat model. *Appl Sci*. 2020;10(5):1651.
doi: 10.3390/app10051651

97. Genova T, Roato I, Carossa M, Motta C, Cavagnetto D, Mussano F. Advances on bone substitutes through 3D bioprinting. *Int J Mol Sci*. 2020;21(19):7012.
doi: 10.3390/ijms21197012

98. Beheshtizadeh N, Azami M, Abbasi H, Farzin A. Applying extrusion-based 3D printing technique accelerates fabricating complex biphasic calcium phosphate-based scaffolds for bone tissue regeneration. *J Adv Res*. 2022;40:69-94.
doi: 10.1016/j.jare.2021.12.012

99. Fedorovich NE, Schuurman W, Wijnberg HM, et al. Biofabrication of osteochondral tissue equivalents by printing topologically defined, cell-laden hydrogel scaffolds. *Tissue Eng Part C Methods*. 2012;18(1):33-44.
doi: 10.1089/ten.TEC.2011.0060

100. Jiao X, Sun X, Li W, et al. 3D-printed beta-tricalcium phosphate scaffolds promote osteogenic differentiation of bone marrow-deprived mesenchymal stem cells in an N6-methyladenosine-dependent manner. *Int J Bioprint*. 2022;8(2):544.
doi: 10.18063/ijb.v8i2.544

101. Cunniffe GM, Gonzalez-Fernandez T, Daly A, et al. (*) Three-dimensional bioprinting of polycaprolactone reinforced gene activated bioinks for bone tissue engineering. *Tissue Eng Part A*. 2017;23(17-18):891-900.
doi: 10.1089/ten.tea.2016.0498

102. Cidonio G, Glinka M, Kim YH, et al. Nanoclay-based 3D printed scaffolds promote vascular ingrowth ex vivo and generate bone mineral tissue in vitro and in vivo. *Biofabrication*. 2020;12(3):035010.
doi: 10.1088/1758-5090/ab8753

103. Sun X, Ma Z, Zhao X, et al. Three-dimensional bioprinting of multicell-laden scaffolds containing bone morphogenic protein-4 for promoting M2 macrophage polarization and accelerating bone defect repair in diabetes mellitus. *Bioact Mater.* 2021;6(3):757-769.
doi: 10.1016/j.bioactmat.2020.08.030

104. Kang HW, Lee SJ, Ko IK, Kengla C, Yoo JJ, Atala A. A 3D bioprinting system to produce human-scale tissue constructs with structural integrity. *Nat Biotechnol.* 2016;34(3):312-319.
doi: 10.1038/nbt.3413

105. Rukavina P, Koch F, Wehrle M, et al. In vivo evaluation of bioprinted prevascularized bone tissue. *Biotechnol Bioeng.* 2020;117(12):3902-3911.
doi: 10.1002/bit.27527

106. Loozen LD, Wegman F, Oner FC, Dhert WJA, Alblas J. Porous bioprinted constructs in BMP-2 non-viral gene therapy for bone tissue engineering. *J Mater Chem B.* 2013;1(48):6619-6626.
doi: 10.1039/c3tb21093f

107. Dubey N, Ferreira JA, Malda J, Bhaduri SB, Bottino MC. Extracellular matrix/amorphous magnesium phosphate bioink for 3D bioprinting of craniomaxillofacial bone tissue. *ACS Appl Mater Interfaces*. 2020;12(21):23752-23763.
doi: 10.1021/acsami.0c05311

108. Zhai X, Ruan C, Ma Y, et al. 3D-bioprinted osteoblast-laden nanocomposite hydrogel constructs with induced microenvironments promote cell viability, differentiation, and osteogenesis both in vitro and in vivo. *Adv Sci (Weinh).* 2018;5(3):1700550.
doi: 10.1002/advs.201700550

109. Keriquel V, Oliveira H, Remy M, et al. In situ printing of mesenchymal stromal cells, by laser-assisted bioprinting, for in vivo bone regeneration applications. *Sci Rep.* 2017;7(1):1778.
doi: 10.1038/s41598-017-01914-x

110. Park JY, Shim JH, Choi SA, et al. 3D printing technology to control BMP-2 and VEGF delivery spatially and temporally to promote large-volume bone regeneration. *J Mater Chem B.* 2015;3(27):5415-5425.
doi: 10.1039/c5tb00637f

111. Keller L, Regiel-Futyra A, Gimeno M, et al. Chitosan-based nanocomposites for the repair of bone defects. *Nanomedicine.* 2017;13(7):2231-2240.
doi: 10.1016/j.nano.2017.06.007

112. Korn P, Ahlfeld T, Lahmeyer F, et al. 3D printing of bone grafts for cleft alveolar osteoplasty - in vivo evaluation in a preclinical model. *Front Bioeng Biotechnol.* 2020; 8:217.
doi: 10.3389/fbioe.2020.00217

113. Liu X, Miao Y, Liang H, et al. 3D-printed bioactive ceramic scaffolds with biomimetic micro/nano-HAp surfaces mediated cell fate and promoted bone augmentation of the bone-implant interface in vivo. *Bioact Mater.* 2022;12:120-132.
doi: 10.1016/j.bioactmat.2021.10.016

114. Nulty J, Freeman FE, Browe DC, et al. 3D bioprinting of prevascularised implants for the repair of critically-sized bone defects. *Acta Biomater*. 2021;126:154-169.
doi: 10.1016/j.actbio.2021.03.003

115. Piard C, Baker H, Kamalitdinov T, Fisher J. Bioprinted osteon-like scaffolds enhance in vivo neovascularization. *Biofabrication*. 2019;11(2):025013.
doi: 10.1088/1758-5090/ab078a

116. Daly AC, Pitacco P, Nulty J, Cunniffe GM, Kelly DJ. 3D printed microchannel networks to direct vascularisation during endochondral bone repair. *Biomaterials*. 2018;162:34-46.
doi: 10.1016/j.biomaterials.2018.01.057

ACCSCIENCE PUBLISHING

International Journal of Bioprinting

REVIEW ARTICLE

Current advances of 3D-bioprinted microfluidic models with hydrogel bioinks and their applications in drug screening

Jianing Li[1], Na Li[1,2], Bo Liu[1,2], Shen Li[2,3]*, and Hangyu Zhang[1,2]*

[1]School of Biomedical Engineering, Liaoning Key Lab of Integrated Circuit and Biomedical Electronic System, Dalian University of Technology, Dalian, Liaoning, China

[2]Faculty of Medicine, Dalian University of Technology, Dalian, Liaoning, China

[3]Department of Endocrinology, Central Hospital of Dalian University of Technology, Dalian, Liaoning, China

(This article belongs to the *Special Issue: Novel Hydrogels/Bioinks Formulations Prepared from Naturally Derived Components for 3D Bioprinting*)

Abstract

Microenvironments of tumor and organ models dictate the accuracy of drug screening results. The advancement of technologies and hydrogel bioinks has significantly increased the representation of tumor and organs models in the armada of drug testing tools. Hydrogel bioinks, characterized by their high water content and efficient substance transport, facilitate the reconstruction of human tissues by acting as functional carriers for cells. The molding and cell culture function of hydrogels are preserved and optimized through rational engineering techniques. Furthermore, previous studies have often focused on fabrication of supporting constructs by means of three-dimensional (3D) bioprinting or microfluidic technology for dynamic cultures. Nevertheless, the combination of bioprinting and microfluidic technologies offers advantages in terms of dynamic response and automation, which enable the creation of artificial tumor or organ models to represent actual microenvironments. In this review, we discuss the components and physical features of tumor microenvironments (TMEs), most of which have been reproduced in artificial models widely by different researchers. We also classify bioink-simulating extracellular matrix (ECM) in TMEs, explain their crosslinking principles, and introduce their manifestations, including artificial disease or organ models in tissue engineering application. Technologies, such as 3D bioprinting and microfluidic technology, used to create these models are also outlined. At last, we summarize disease models and organ microarchitectures fabricated by these two technologies and offer application prospects of these models in the realm of precision medicine.

Keywords: 3D bioprinting; Bioinks; Tissue engineering; Drug screening; Microfluidic

***Corresponding authors:**
Hangyu Zhang
(hangyuz@dlut.edu.cn)

Shen Li
(lishen2010@dlut.edu.cn)

Citation: Li J, Li N, Liu B, Li S, Zhang H. Current advances of 3D-bioprinted microfluidic models with hydrogel bioinks and their applications in drug screening. *Int J Bioprint.* 2024;10(3):1951. doi: 10.36922/ijb.1951

Received: September 29, 2023
Accepted: December 6, 2023
Published Online: March 4, 2024

Copyright: © 2024 Author(s). This is an Open Access article distributed under the terms of the Creative Commons Attribution License, permitting distribution, and reproduction in any medium, provided the original work is properly cited.

Publisher's Note: AccScience Publishing remains neutral with regard to jurisdictional claims in published maps and institutional affiliations.

1. Introduction

The diagnosis and treatment of emerging, highly infective, and fatal diseases continue to pose a global challenge in the clinical scene. Cancer is a highly representative disease due to the complexity of its treatment and the rather comprehensive delineation

of tumor pathogenic mechanisms, composition, and physical properties, contributing to one-sixth of the deaths worldwide.[1] It is pathologically heterogeneous between affected individuals. Cancer, subject to multiple factors, including cellular components, non-cellular components (e.g., cytokines and signaling pathways), and their interactions, undergoes relentless evolution. Aside from eradicating tumor cells, cancer treatments have a bearing on factors in the entire tumor microenvironment, which are related to tumor growth.[2] As the most common cancer therapy, chemotherapy acts directly on the deoxyribonucleic acid (DNA) in tumor cells to prevent cell growth or impede specific signaling pathways. Difficulty in targeting specific signaling pathways spurs on the development of drugs from complicated sources that have a potential to impact various mechanisms. Drug development involves a long study cycle, high costs, and a high failure rate of up to 50% in preclinical studies.[3,4] Drug screening is a crucial component of drug research and runs throughout the drug research process. The primary objective of drug screening is to identify any potential side effects of the drug to assess its safety profile and evaluate its therapeutic efficacy in animal or human subjects. Moreover, persistent drug exposure will give rise to drug resistance, which warrants more in-depth investigations in drug screening models.

Traditional methods for drug screening include two-dimensional (2D) cell culture, which features monolayer cells having strong proliferative capacity with applanate and stretched shapes. 2D cell culture cannot accurately reflect the real cell–cell and cell–matrix interactions, and, thus, is unable to portray various microenvironments within the human body. The culture conditions offered by the existing 2D culture methods cannot sufficiently support the maturation of cultured cells into models that closely recapitulate the physical characteristics of lesions or organs *in vivo,* thus decreasing the representativeness of the *in vivo* tissues. The 2D-cultured cells may not exhibit resistance to the applied drugs, yielding inaccurate data in drug resistance studies.[5,6]

Animal models stand as the gold standard method for preclinical drug screening. On the one hand, these models enable the exploration of disease mechanisms and lesion status, which aids the assessment of drug potential. On the other hand, animal models can be utilized to evaluate toxicity, efficacy, and pharmacokinetics of new treatments, for confirming their eligibility for the subsequent clinical studies. However, there are limitations to using animal models in drug screening. Tumor-implanted animals cannot accurately replicate the effects seen in humans with tumors because of genetic, immunological, and cellular variations. Additionally, orthotopic mice models transplanted with human tumors are unable to faithfully recapitulate tumor characteristics. These transplanted tumors differ not only from those in humans, but also from those in the same batch of individual mice. The discrepancy in transplanted tumors poses a challenge to researches of drug properties. Separately, genetic intervention in knockout mice may promote tumor growth, which adds a layer of ambiguity with regard to the pathological outcome stemming from the transplanted human tumor.[7] Therefore, these obstacles pose a hindrance to accurate prediction of drug toxicity and safety using animal models. Of note, only a measly 8% of the drugs tested in animal experiments successfully entered clinical trial phase I for further evaluation, and most positive results stemming from animal experiments do not necessarily translate into the same success rate in human trials.[8] Animal models that are easily mutable and ethically challenging in experimental settings do not represent an ideal approach in drug discovery process.

Given these drawbacks, the amalgamation of extracorporal manufacturing technologies and internal tissue simulations becomes the focus of research. Three-dimensional (3D) bioprinting, one of the additive manufacturing technologies, precisely deposits bioink from animal or non-mammal sources in a layer-by-layer fashion. This technique enables the fabrication of organ or disease models with microenvironment features, which will gradually replace 2D culture and animal models.[9] The arrangement and geometry of organ-like or disease-like models are automatically finished through 3D bioprinters controlled by a computing system. Genetic information, cells, and factors capable of performing internal functions are incorporated to enhance physiological relevance. Most importantly, 3D culture integrates the crosstalk between biological components, tumor metastasis, and vascular formation, providing more accurate insights through drug resistance studies and presenting complex responses to anti-tumor drugs.[10] Nevertheless, a limitation of 3D-bioprinted constructs is that they are unable to remove metabolic waste efficiently, and the nutrients they possess are not evenly distributed, resulting in lower cell viability and shorter culture times.[11]

"Lab-on-a-chip" based on microfluidic technologies recapitulates all laboratory operations on a micrometer-level chip. The constructs on a chip can also mimic tissue or organ microenvironments equipped with mechanical features such as blood flow, heartbeat, and breathing. Controlled perfusion in microfluidic channels overcomes the issue of uneven nutrient diffusion in 3D bioprinting, and various organs can be connected on a chip. The interactions between organs are developed on this basis. Furthermore, the voluntary deposition of bioink on microfluidic chips lessens the tedious steps of microprocessing and increases the possibility of automation in microfluidic chips.[12,13]

Bioink, derived from biocompatible and natural sources, is a bridge that connects 3D bioprinting and microfluidic chips, enabling the creation of hierarchical tissue constructions and facilitating communication among cells, molecules, and artificial stimulations.[14] Hydrogel-based bioinks with high water content have garnered a growing interest in cell proliferation and differentiation studies. The popularity of bioink in 3D bioprinting can be attributed to the ease of adjusting their performance through factors such as pH, temperature, concentration, or chemical modification. Besides, these bioinks are compatible with biological substances and can establish the overall characteristics of organ or tissue microenvironments. Moreover, hydrogel-based bioinks exhibit a transition from a liquid to a gel state via physical and chemical actions.[15] This property, along with shear thinning behavior, makes bioinks well-suited for the construction of entities with the help of bioprinting. Once bioprinted, microarchitectures created by bioinks are perfused and stimulated by microfluidic systems with precise control.

3D bioprinting and microfluidic technology have been used to co-produce external models. The application of 3D-bioprinted organoids and organ-on-a-chip made by microfluidic technology has been reviewed. However, the 3D-bioprinted organ-on-a-chip for drug screening, which is the advanced manifestation of bioink, is rarely summarized. Therefore, in this review, we focus on the advantages and applications of combining these two technologies and illustrate the traits of the tumor microenvironment, such as cell components, physical properties, and bionic behaviors. Bioinks of various classes, which can recapitulate extracellular matrix (ECM) functions, are also presented in this review. The advantages of the combined technologies are elaborated following a brief narrative for 3D bioprinting and microfluidic technology. Moreover, relevant studies on drug screening are summarized to explain key concepts. In the end, we discuss the application prospects of 3D constructs fabricated by combined technologies in the field of precision medicine.

The fabrication process of disease/organ-on-a-chip and their applications are depicted in Figure 1.

2. Tumor microenvironment

The most critical problem solved by functional hydrogels in tissue engineering is their ability to provide a water-rich microenvironment for targeted cells, facilitating the development of artificial tumor microenvironment (TME) or organ models. Hydrogel-based bioinks serve

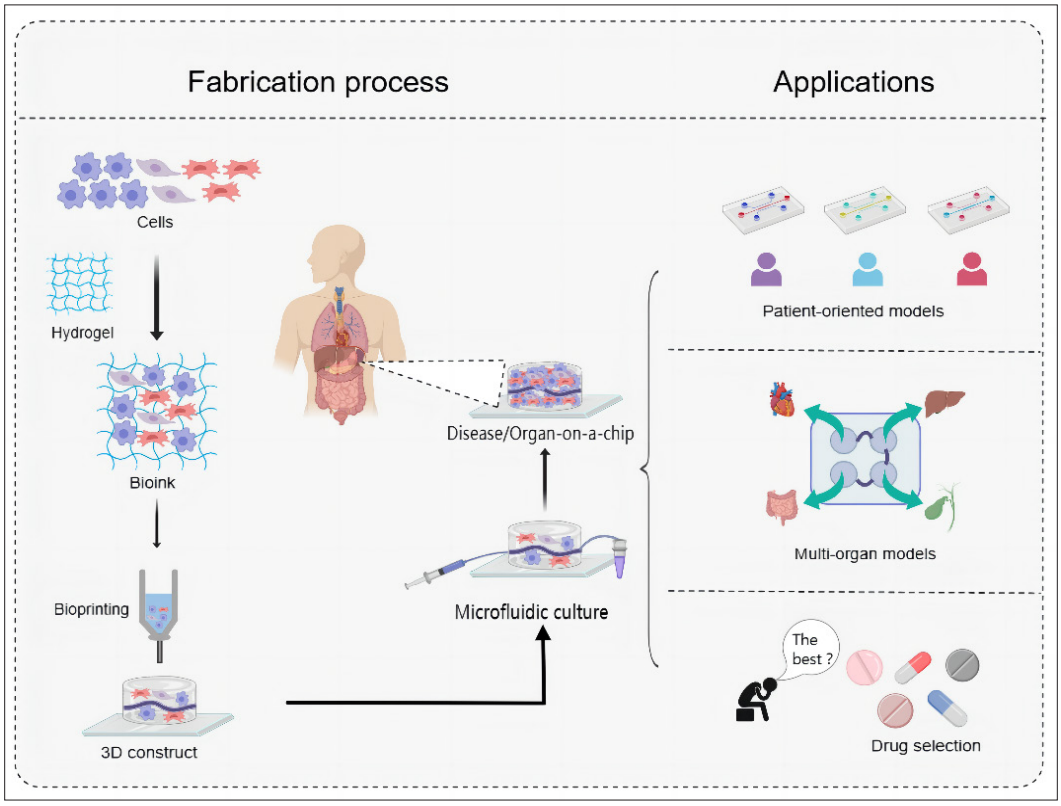


Figure 1. Schematic diagram of the fabrication process of disease/organ-on-a-chip and their applications.

as a support and delivery foundation for mimicking the physical properties and biomimetic behaviors in TMEs or organs. These strategies used to imitate other tissue microenvironments are similar to those employed for tumors, which are also relevant to the study of their cell compositions and physical properties. Since the characteristics of TMEs are well-established and extensively researched, we selected TMEs as representative examples for different disease and tissue environments to avoid unnecessary and redundant descriptions.

A comprehensive study of the components and behaviors in TMEs is essential for creating realistic and vibrant artificial tissues. Furthermore, TMEs encompass various cells, non-cellular components, and even microorganisms.[16,17]

2.1. Cell components

Cell selection is the starting point in the fabrication of *in vitro* 3D construct. Target lesion cells and the cells they interact with are selected to ensure better maturity in subsequent cell culture and higher expression of tissue-like or organ-like molecules. TME is composed of immunocytes such as thymus-dependent lymphocytes/bursa-dependent lymphocytes (T/B lymphocytes), tumor-associated macrophages (TAMs), natural killer cells (NK cells), and stroma cells, including cancer-associated fibroblasts (CAFs), pericytes, and mesenchymal stromal cells. These cells interact with the ECM and interconnect with other secretory molecules, including growth factors and chemotactic factors, contributing to the complex mechanisms of TMEs.[18] The maturity of 3D constructs that precisely recapitulate the physiological and pathological processes of tissues of interest is dependent on cell proliferation and differentiation. Moreover, the cell introduction is not limited to tumor cells but involves cells with various functions. Fibroblasts, macrophages, and other immunocytes are research hotspots in the realm of 3D bioprinting.

2.1.1. Cancer-associated fibroblasts

Mesothelial cells covering the entire coelom are differentiated into fibroblasts or other cells for promoting organ development through epithelial–mesenchymal transition (EMT) during embryonic growth.[19] A motif enrichment analysis by Huang et al. for up-regulated genes in antigen-presenting CAF demonstrated that the signaling pathways of interleukin (IL)-1 and transforming growth factor beta (TGF-β) induced the transformation from mesothelial cells into fibroblasts.[20] Furthermore, fibroblasts regulate epithelial cell differentiation, participate in wound healing, and excrete growth factors to maintain the stability of the epithelial microenvironment. Fibroblasts also control the synthesis of the ECM and its degrading protease to adjust the ECM activity.[21] The fibroblasts around healing wounds and under some pathological conditions have stronger proliferation ability and secrete more ECM than counterparts in normal tissues. This phenomenon is known as fibroblast activation.

Activated fibroblasts relevant to tumor microenvironment were discovered as CAFs in 2006.[20] CAFs that were defined by Kobayashi et al.[22] locate in or around TME, encompassing both natural fibroblasts and fibroblasts that activate, proliferate, and gather in response to cancer stimulation. However, the novel definition and biomarkers to represent CAFs are still evolving due to their high heterogeneity and variation.[23] ECM is modulated by CAFs to control tumor stromal properties and secrete growth factors, thereby regulating the formation of vessels that provide nutrients for tumors. Simultaneously, CAFs are implicated in tumor invasion, metastasis, and drug resistance.[24]

2.1.2. Tumor-associated macrophages

Tumor-associated macrophages (TAMs), which are derived from the marrow and affiliated to immunomodulatory cells, are divided into anti-tumor M1 and pro-tumor M2 phenotypes. The definition and mutual transformations of the two phenotypes depend on environmental signaling stimulation from immunocytes and ECM.[25] The M2 phenotype is constantly differentiated into other subtypes upon the stimulation of different cytokines.[26] TAMs with the M2 phenotype contribute to tissue remodeling, angiogenesis, and immune responses. TAMs cannot activate NK and T cells but release relevant factors and enzymes to control immune response.[27] TAM-induced inflammation also affects tumor growth.[28]

2.1.3. Immune cells

Innate immune cells contain monocytes, neutrophils, eosinophils, basophils, and NK cells, all of which restrict tumor progression. However, the proliferation and maturation of immune cells are negatively regulated by soluble modulators in TME. This explains why immune cells are not abundant in TME.[29] Tumor cells exert a significant inhibitory effect on immunocytes. Tumor cells compete with immunocytes for essential nutrients and glucose uptake, which are heavily relied on by tumor cells and necessary for immunocyte growth and function activity.[30] More research on immunocytes in 3D constructs is needed.

2.2. Physiological characteristics

Tissues under an oxygen partial pressure of less than 10–15 mmHg are defined as hypoxic tissues. Hypoxia-inducible factor (HIF) is a transcription factor that binds to DNA and triggers reactions to reduce oxygen partial pressure.[31]

It has been reported that partial tumor environments do exist with permanent or temporary hypoxia. Pericytes surrounding endothelial cells control vasoconstriction. Hypoxia and ischemia in TME are promoted by pericyte abscission, increased permeability of vessel, as well as abnormal angiogenesis, thereby promoting tumor metastasis and invasion.[32] The energy metabolism pathway of tumors is affected by HIF activity in a hypoxic state. In an attempt to help tumor cells adapt to hypoxic conditions, glycolysis serves as a common energy metabolism pathway in tumor cells. Glycolysis with great glucose consumption and significant lactate formation is accompanied by the generation of pyruvic acid and hydrion, which gives rise to low potential of hydrogen (pH) that is regarded as another characteristic of TME. In addition, one of the critical mechanisms undermining tumor immunity is the restriction of immunocyte functions by hypoxia.[33] Thus, physiological characteristics, including hypoxia/oxygen gradient, acidity, and abnormal vessel formation, should be recapitulated in tumor models (Figure 2).

2.3. Tumor behaviors

Relentless proliferation (replication immortality), drug resistance, abnormal vessel formation, invasion, and metastasis are fundamental tumor behaviors. Research confirmed that reprogramming of tumor energy metabolism and immune evasion are also tumor behaviors.[34] Some of these behaviors have been reproduced *in vitro* via 3D bioprinting and microfluidic technology.

2.3.1. Metastasis and invasion

Invasion and metastasis are the most representative behaviors of therioma in comparison with benign tumors.[35] Invasion and metastasis are inextricably linked, but in general, tumors should acquire an invasive phenotype first. Tumor cells internally infiltrate into blood vessels after migrating on the tumor–stromal surface. Although most cells will succumb to death in blood stream, a minority of the cells survive and successfully exosmose from blood vessels to target organs, where metastatic cells spoliate nutrients from target organs for proliferation and

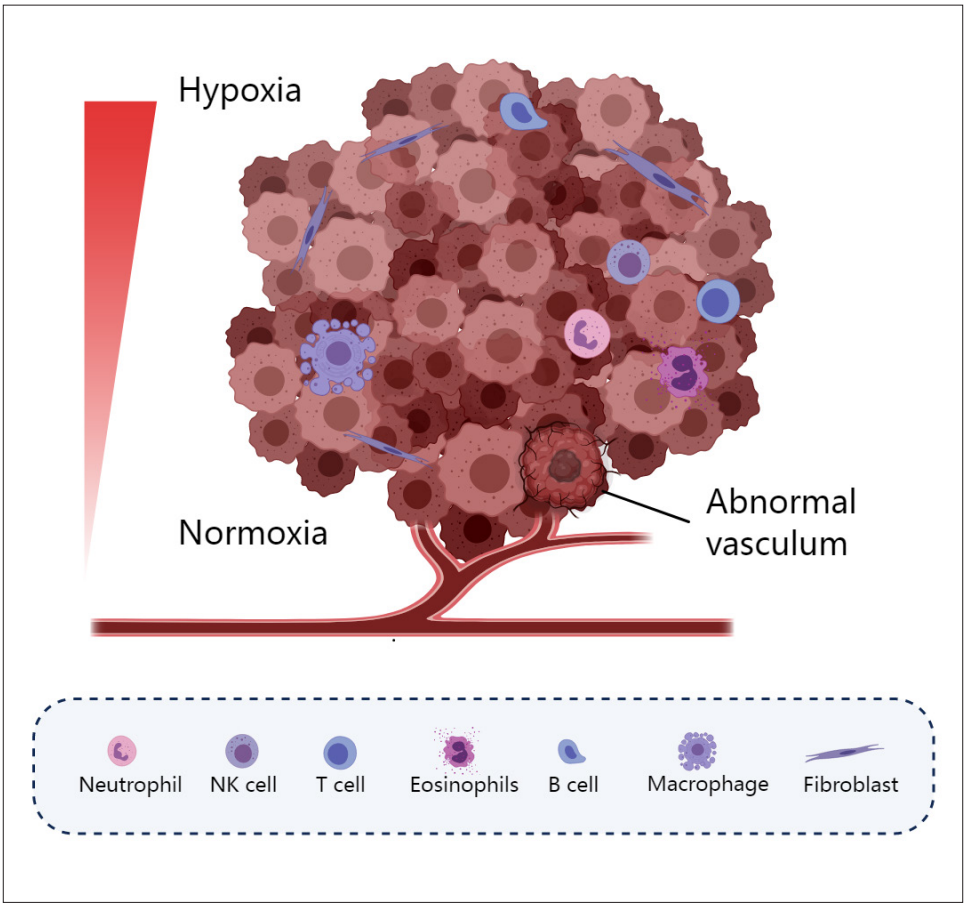


Figure 2. Schematic diagram depicting various cell types (neutrophil, NK cell, T cell, B cell, macrophage, fibroblast) and physiological features (hypoxia, oxygen gradient, abnormal vasculum) associated with tumor microenvironment. Abbreviations: NK cell, natural killer cells; T cell, thymus-dependent lymphocyte; B cell, bursa-dependent lymphocyte.

development.[36] Moreover, proteases, especially matrix metalloproteases (MMPs), acting as an indispensable contributor in tumor metastasis, not only degrade ECM to provide transfer channels for migrating cells but also release factors relevant to metastasis during degradation.[37]

2.3.2. Vascularization and co-culture

Vascularization is the generation of vascular system for tumor growth, under the influence of vascular regulators from host cells and tumor cells.[38] The endothelial cell (EC)–TME interaction and angiogenin contribute to vascularization. A review[39] illustrates that the progress of vascularization cannot rely only on vessel induction. The two mechanisms of vascularization are: (i) occupation of pre-existing blood vessels by tumor cells; and (ii) formation of vessel-like structures made of tumor cells to enable bloodstream passage.

TME with cell–cell and cell–matrix interactions has a collective influence on tumor growth. 3D constructs featuring interactions of components in the TME, rather than single cell type, assure greater *in vivo* relevance than 2D models. Co-culture models that recapitulate crosstalks among components in TME are superior to single tumor cell models due to the existence of interactions between components within the TME. There are some instances of co-culture: the communication between cancer stem cells (CSCs) and ECM enhances the performance of stem cells; immunocytes and tumor cells inhibit each other; the matrix metalloproteinase secreted by CAFs creates room for abnormal vessels to grow; TAMs and ECs both have effect on the tumor growth and vasculogenesis.[40] Tumor cells activate CAFs to release factors that induce tumor progression, and apoptotic cancer cells influence the invasion of CAFs.[41] Jeong et al. demonstrated that tumor cells co-cultured with CAFs were much larger than those in monocultures, and they could also activate CAFs.[42] TAMs that exchange more with tumor cells may contribute to chemotherapeutic resistance and tumor recurrence.[43]

2.3.3. Immune evasion and limitless proliferation

Anti-tumor immunity encompasses three stages: clearance, balance, and escape. The congenital immune system is the initial coping mechanism of our body encountering tumors, namely the stage of immune clearance with the cooperation between congenital and acquired immune cells. There is no obvious clinical manifestation in this stage. When the immunity is at a balanced state, tumor cells and the immune system do not significantly affect each other. However, surviving tumor cells with good proliferative capacity and viability may escape the recognition of the immune system, producing manifestations that can be clinically detected during the balance stage.[44] Immune escape occurs in malignant tumors because of the declining autoimmunogenicity of immune cells.[45] Moreover, metabolic characteristics of tumor cells help impel immune escape. Lactate, the metabolic reprogramming product, impairs the capability of immune cells to produce cytokines and hinders their activation and killing ability.[46] Telomere, a protein complex, controls cell survival and accelerates cell aging until cell death caused by injury. Telomerase, abundant in tumor cells, allows the cells to proliferate infinitely.[47]

2.3.4. Drug resistance

The refractory nature after chemotherapy stems from the tumor metastasis and drug resistance. Drug resistance is manifested by inadequate drug response at the site of treatment during early administration or prolonged drug exposure. Persistent exposure to drugs engenders drug resistance in various tumor cells, thereby circumventing drug-induced apoptosis and reducing the clinical efficacy of drugs.[48] Drug resistance stemming from TME is caused by ECM reconstruction and vessel generation, which alter drug distribution and metabolism. Furthermore, Taylor et al.[49] proved that weak alkaline drugs to neutralize the acidity in the TME served as an effective and well-tolerated therapy to reverse acquired resistance to chemotherapeutic drugs, insinuating that acidity in the TME is one of the crucial factors contributing to drug resistance. Although TME is not the leading cause of drug resistance in tumors, it directly affects the treatment effect. In non-small cell lung carcinoma (NSCLC), carbon materials are metabolized through the Embden-Meyerhof-Parnas pathway, producing metabolites that activate RAS proteins. On this basis, PI3K/AKT and MAPK/ERK signaling pathways are triggered to contribute to drug resistance, which indirectly restricts drug efficiency.[50] Therefore, research on TME-driven resistance in 3D constructs for drug screening is necessary.[51,52]

3. Simulating components in 3D bioprinting

3.1. Bio-based polymers as bioinks

Bioinks, whose rheological and mechanical properties resemble those of internal tissues, refer to the printed stock solutions that are compatible with cell culture. Generally, cell-laden bioinks are used to print tissue-like structures directly, while cell-free bioinks are employed in structure printing prior to cell inoculation. Bioink materials, derived from natural and synthetic polymers, can fuse functional proteins and genes.[14] Bioinks with excellent properties, such as non-toxicity, biocompatibility, and biomechanic properties, can be applied in tissue engineering. In addition, compared with 2D culture and animal models, 3D culture models that are dependent on the abilities of

bioink to diffuse are superior in the visual investigation of cell–cell and cell–matrix crosstalks.

3.1.1. Natural polymers

Natural polymers are extracted or separated from natural substances, such as alginate, gelatin, hyaluronic acid, collagen, and fibrin.

Alginate with non-Newtonian fluid properties composed of β-D-mannuronic acid (M section) and α-L-glucuronic acid (G section) is a negatively charged linear polysaccharide extracted from brown seaweed. The G section in sodium alginates crosslinks with polyvalent cations (Ca^{2+}, Ba^{2+}) to form the gel network, and the high content of G section contributes to alginate stiffness. After being printed out of the bioprinter, rapid gelation is required for bioinks. Alginate is difficult to mold at room temperature. Alginate often crosslinks in non-covalent manners by ion crosslinking and self-assembly, which are dependent on hydrogen bonds or electrostatic interactions. The hydrogel network produced by these methods has a weak internal force, while the intensity is expediently regulated by concentration, pH, and temperature.[53] The mechanical property of bioink refers to the ability to support scaffolds embedded with cells as long as possible during culture time. Alginate gel at lower concentrations tends to have less aperture and total areas, and higher concentrations with good mechanical properties have the lowest cell viability and almost no cell spreading.[54] Additionally, alginate contains abundant carboxyl (-COOH) and hydroxyl (-OH) groups, which are covalently connected through various processes such as polymerization, condensation, click chemistry, and radiation. These linkages lead to constructs with high mechanical strength and integrity.[55] When mixed with other bioinks, alginate is used as the constituent to improve the mechanical properties of the bioink.

Mammal-derived gelatin, similar to the amino acid composition of collagen in humans, is the hydrolysis product of collagen from pig skin, cowhide, and bone.[56] The bionic nature of gelatin provides appropriate conditions for cell differentiation. In the construct composed of oxidized alginate and gelatin, Distler et al.[57] achieved the proliferation of mouse myoblast cells and the directed differentiation of ordered myotube clusters. During the gelation process, molecules in gelatin are interconnected by non-specific bonds, such as hydrogen and electrostatic bonds, which are easily depolymerized under high temperatures.[58] Gelatin with poor mechanical and unique thermo-reversible properties dissolves at 37°C; thus, its side chains are often modified.[59] The most used modified gelatin is gelatin methacrylate (GelMA), obtained through the reaction of methacrylic anhydride with amino groups in gelatin, which maintains a stable hydrogel state at 37°C.[60] Moreover, another significant advantage of GelMA is the simplicity of stiffness regulation. In photocrosslinked printing, the structure with high resolution is formed by GelMA at low concentrations by means of simple optimizations.[61] The concentration of GelMA and photoinitiator are critical determinants of structural integrity.

Components of ECM such as collagen, hyaluronic acid, and fibrin are applied as bioink to enhance functional relevance. Collagen that belongs to the insoluble fibrin preserves the stiffness and integrity of ECM, supporting the morphological structures of the skin.[62] Collagen is compatible with other biotic components due to its pervasiveness *in vivo*. More than 90% of the cell viability was maintained in collagen without photo-crosslinking at high concentrations, indicating that this bioink has lower toxicity and immunogenicity.[63] Collagen as bioink has been used to construct liver and neurological models.[64,65] However, the mechanical properties of collagen, composed of triple helices, are too weak to allow individual printing of construct. Three solutions are available for addressing this issue: (i) chemical modifications; (ii) changing the printing carrier and using collagen as the support bath or removing sacrificial ink after printing in collagen; and (iii) using collagen as an adhesive in the bioink. In addition, since animal-derived collagen bioink is not conducive to the fabrication of complex structures and triggers immune response from human-derived cells, Wang et al.[66] replaced the traditional collagen with recombinant human collagen, which was modified by methacrylic anhydride and later crosslinked by 1-ethyl-3-(3-dimethylaminopropyl) carbodiimide hydrochloride/N-hydroxysuccinimide (EDC/NHS). This crosslinking bioink with biocompatibility, high porosity, and long degradation time was proven to provide potential microenvironments for cultured cells.

Decellularized extracellular matrix (dECM) can be derived from animal tissues. Considering heterogeneity and residual interfering substances from animal-derived ECM, human-derived ECM is gradually applied for drug screening models.[67] There are three extraction methods for dECM: physical methods suitable for small tissues, chemical methods, and enzymic methods. Except for cells and genes, acquired dECM with similar organizational integrity and components to the original ECM can induce the corresponding stem cell differentiation and tissue regeneration.[68,69] Except for the cells, the structural components of original organs are retained in dECM. In theory, in the condition that the degradation of dECM does not affect the mechanical properties of the bioprinted construct, as long as it does not collapse, the degradation rate of dECM may equal to the rate at which cells produce the new ECM.[70] The degradation products of dECM may

not trigger an immune response from encapsulated cells, leading to the reserved biocompatibility of dECM. In contrast, non-animal-derived bioink causes an immune response as well as the change of pH and temperature in microenvironments.[71]

Like other bioinks, the addition of dECM enables bioprinted bioinks to regulate viscosities, reduce shear stress, and help cells proliferate after printing and form a self-supporting structure.[72] However, the mechanical properties of dECM do not meet the requirements of supporting 3D constructs. Moreover, dECM fails to be perfectly copied *in vitro* because of the differences between individuals, organs, and even tissues. dECM is extracted from ECM via methods of cell removal. Uncontrolled and unstandardized methods lead to degradation of dECM at different degrees during extraction processes, contributing to differences between batches. The strong specificity of dECM could explain why popularizing dECM on a large scale remains challenging.

3.1.2. Examples of hydrogel bioinks

The single-component natural bioink cannot simultaneously meet the requirements for molding during the printing process and the suitability of viscosity on the growth of cells encapsulated in bioinks, so two-component and even multi-component hydrogels are applied to break the mutual limitation of molding and cell culture. Moreover, the mechanical properties of bioink may be improved through crosslinking. The alginate component in the alginate/GelMA bioink enabled the initial consolidation of the bioink, and GelMA formed the covalent bonds after photocrosslinking to conglutinate the interlayer bioink. This process completed the entity construction of a cell-friendly bioink at a low concentration.[73] Soltan et al.[74] investigated the synthesis of alginate dialdehyde because the human body lacked alginate sodium enzymes, and the increased oxidation degree of alginate dialdehyde promoted biodegradation. The oxidized and methacrylate alginate (OMA) bioink also underwent ion crosslinking and photocrosslinking. However, the methacrylate bonds for photocrosslinking were obtained by the esterification of the groups in alginate rather than the involvement of GelMA. On the premise of ensuring mechanical stability, this bioink showed a high resolution and rapid recovery capability, simultaneously supporting a high survival rate of cultured stem cells.[75] Cui et al.[76] developed a three-component bioink using natural proteins/polyphenols/polysaccharides. The hydrogel construct was shaped through hydrogen bonding and electrostatic interactions after the ion crosslinking of alginate. The addition of polyphenols disrupted the protein structure in gelatin, exposing more reactive sites for crosslinking. The initial hydrogel had structural features in the form of sheets and lines, and the restored bioink after the shear thinning state retained most of the structural features, demonstrating its self-healing ability. The pore structure within the microarchitecture plays a crucial role in material diffusion and cell migration. Wang et al.[77] developed a bioink with an emulsion system, which facilitated the generation of multiple interconnected micropores. These micropores in bioink were beneficial for the proliferation and distribution of cells in deep structures. When taking GelMA as the dispersed phase and dextran as the continuous phase, methacrylated galactoglucomannan, acting as the emulsifier in this system, was added to enhance cell viability promote intercellular communication (Figure 3A). Two-component bioink is subjected to oxidation or modification to obtain specific chemical groups that interact with groups in other components, resulting in more stable covalent bonds. Biological substances, such as polypeptides, are introduced to enhance cell adhesion and biomimetic properties. In general, bioinks mimicking functions of ECM provide gas exchange, facilitate material transport and removal, and offer physical support for experimental cultures. Moreover, advanced hydrogels can selectively enrich or deplete molecules. For example, Zhang et al.[78] exploited a functional hydrogel system that consumed reactive oxygen, thus protecting cells from oxidative stimulation (Figure 3B).

3.1.3. Synthetic polymers

Despite non-natural sources, research certified that synthetic bioink has biological correlations in cell culture. Synthetic polymers with high inertness and resistance are artificially produced for specific purposes. Synthetic polymers are blended with natural bioink to promote the mechanical properties of the mixed bioink and offset the disadvantages of natural bioink.[79] Since the polymers are non-animal and non-human derived, their toxicity may restrict cell viability. Moreover, the targeted cells can not adhere to the synthetic polymers, contributing to cell loss at the beginning of model constructions.

Polyethylene glycol (PEG) is an ethylene oxide polymer with high cytocompatibility, commonly seen as a constituent of capsules. It is used in wound dressing for hemostasis and pharmaceutic preparations to enhance the stability of the drug-loaded nanoparticles.[80-82] The ability of PEG to support cell adhesion allows for its further application in tissue engineering.[83] Aliphatic polyester, polycaprolactone (PCL) consisting of acetate, has a melting point of 56–66°C. Notwithstanding that PCL is degraded by most natural microorganisms, it is difficult to be enzymatically degraded *in vivo*.[84] Liu et al.[85] printed the gelatin solution between PCL bands for cell support (Figure 3C-I). Notably, 92% cell viability was maintained after a 7-day culture (Figure 3C-II). Furthermore, the

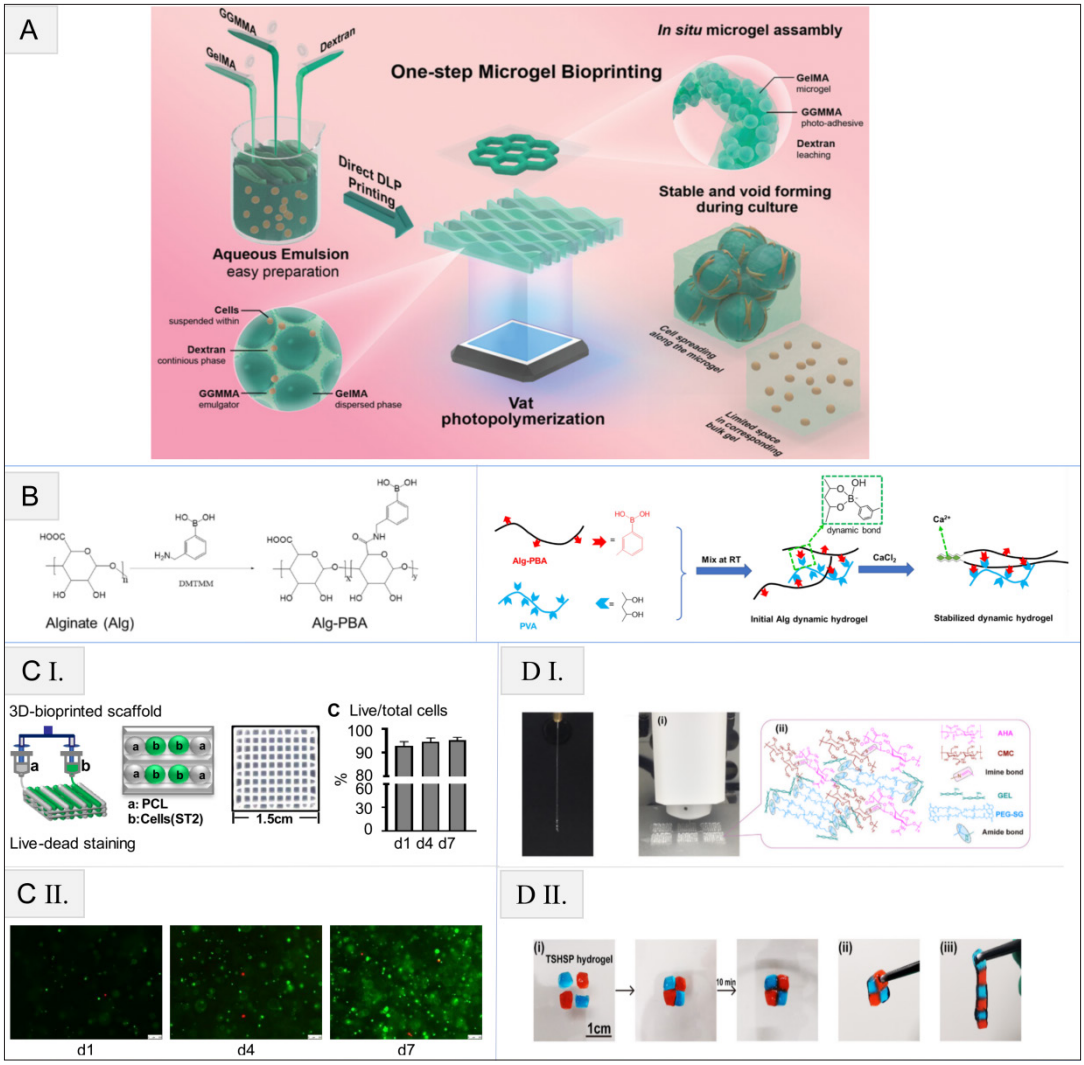


Figure 3. Schematic illustrations of different properties of bioinks. (A) The gel state during fabrication and cell culture. Reproduced with permission from ref.[77] (B) Chemical structure of antioxidant ink and its crosslinking process [from ref.[78] licensed under Creative Commons Attribution (CC BY)]. (C) The printed scaffold and the viability of encapsulated cells: (I) the printed process of the bioink, and (II) the photographs of live/dead staining [from ref.[85] licensed under Creative Commons Attribution (CC BY)]. (D) Structure and crosslinking process of this bioink [from ref.[87] licensed under Creative Commons Attribution (CC BY)].

remarkable mechanical properties of PCL make it a popular choice for cardiac tissue engineering. The rebound characteristic of PCL allows it to withstand the great pressure from ventricular systole, and the degradation of PCL lasts for 2–3 years.[86] Synthetic polymers with lower gelation temperatures can be more easily modified to improve cell adhesion. Although these polymers with both toxicity and lower cell adhesion may go against cell growth, they are widely used in osteogenic manufacturing.

3.1.4. An example of the multi-component bioink

Multi-component bioinks are mixed after successive combinations, acquiring a stable and complementary hydrogel network. This approach may synchronously enhance the mechanical properties and physiological relevance of the resulting bioinks. Each component in these bioinks retains its functionality without interfering with others. Khati et al.[87] employed succinimidyl valerate-polyethylene glycol-succinimidyl valerate to connect gelatin and dECM. Gelatin enhanced the rheological properties, and dECM promoted the physiological correlation of the final bioink. The covalent linkage was based on the reaction between the succinimidyl valerate group and the amino group. To ensure the stability of the construct, the enzyme tyrosinase was used to facilitate secondary crosslinking. Moreover, the entire fabrication

process was carried out under 37°C, meeting the requirement for cell survival without abrupt temperature change (Figure 3D). Chen et al.[88] proposed a new method for mixing four materials in pairs in a complementary manner. One was composed of aldehyde hyaluronic acid (AHA)/N-carboxymethyl chitosan (CMC) bioink, which rapidly gelled through Schiff base bonds. The other bioink utilized here was the combination of gelatin and 4-arm poly(ethyleneglycol) succinimidyl glutarate (PEG-SG), connected by amide bonds. The addition of the latter hindered the excessive fusion of the AHA/CMC bioink. As a result, the four-component bioink could be directly printed without extra crosslinking agents and exhibited remarkable self-healing ability.

3.2. Technical basis of bioink models: 3D bioprinting and microfluidic technologies

When cell sources and biological materials are ready, the precision of model design and bioink delivery is determined by 3D bioprinting, which is an indispensable technological medium. The universal 3D bioprinting technologies and applications are presented in the following chapters.

Twenty years ago, inkjet bioprinting was used to deliver cell suspension as the bioink to the gel-based scaffolds, setting a precedent for organ models produced rapidly and repeatedly.[89] Since then, multiple types of cells encapsulated in bioink can be printed to form 3D constructs, where the bioink imitates the functions of ECM rather than a simple support. Cultured models with pre-designed shapes, such as organs or tissues, possess the interactions of cell–cell and cell–ECM and physiological characteristics, which allow for comprehensive understanding of the physiological models.

Vasculature is responsible for delivering nutrients and removing metabolites in the human body. Although vascular endothelial cells are integrated, there are only disordered vessels without perfusion ability in some 3D-bioprinted vascular models. Attempts have been made to mimic blood vessels using physical molds such as microacupuncture needles, but the products in a single form do not match the shape and structure of physiological vasculature.[90] To overcome this, the combination of 3D bioprinting and microfluidic technology has emerged to fabricate blood vessels with dynamic perfusion, thereby improving the culture efficiency.[91]

3.2.1. Droplet-based bioprinting

Inkjet-based bioprinting is a popular method for model construction because of its precise deposition and low cell damage.[92] Bioink in droplet form is directly injected onto base materials, forming arrays or depositing in a layer-by-layer manner to create sandwich-like structures with functional cells. Inkjet-based bioprinting has advanced to drop-on-demand (DOD) inkjet bioprinting, categorized into thermal bioprinting, piezoelectric bioprinting, and electrostatic bioprinting based on driving mechanisms, as shown in Figure 4A.[93] Generally, natural bioinks with low viscosity are suitable for inkjet-based bioprinting.[94] Stratesteffen et al.[95] demonstrated that droplet-based bioprinting allowed the bioink to improve physiological relevance and the mechanical property simultaneously, although the addition of collagen increased the viscosity of the GelMA blend.

Inkjet-based bioprinting can form tubular structures, but there have been no reports on 3D perfusable constructs using solely inkjet bioprinting because of the complex production process and the ineligible quality of the hollow vessel tissue that fails to meet perfusion standards. However, inkjet bioprinting is well-suited for creating 3D organ or disease models and generating cell-embedded hydrogel blocks without intricate designs. Therefore, its advantages in precise cell delivery and creating homogeneous 3D constructs have been extensively investigated, leading to its wide application in high-throughput drug screening. Droplet-based bioprinting is good at maintaining cell viability and precise deposition, but it fails in not only reproducing vascular filaments, but also restructuring the integrity of tissue or organ microenvironments.

3.2.2. Light-assisted bioprinting

Stereolithography (SLA) and digital light processing (DLP) bioprinting are two types of light-assisted bioprinting that use laser radiation to solidify the bioinks, improving efficiency, resolution, and repetitiveness in the fabrication process. The laser beam controlled by computers scans the bioink, thereby realizing light curing of each layer in constructs. During the construction of each layer structure, the preset pattern is solidified by the laser beam movement in SLA. DLP with higher efficiency can emit lights that disposably solidifies the bioink in each layer throughout the entire construct (Figure 4B).[96] Natural bioink has the risk of non-forming and excessive softness in light-assisted bioprinting. Moreover, the introduction of human-derived cells affects the viscosity and pellucidity of bioink. Bioinks, possessing functional groups that act as crosslinks under light, should also exhibit acceptable mechanical properties and transparency.[96] Although lights at different wavelengths may be toxic to encapsulated cells, light-assisted bioprinting in tissue engineering has been developed owing to its excellent resolution (10 μm). Similar to inkjet bioprinting, the fabrication of tube structures alone cannot completely replicate tissue microenvironments, even if perfusion capacity was not taken into consideration.

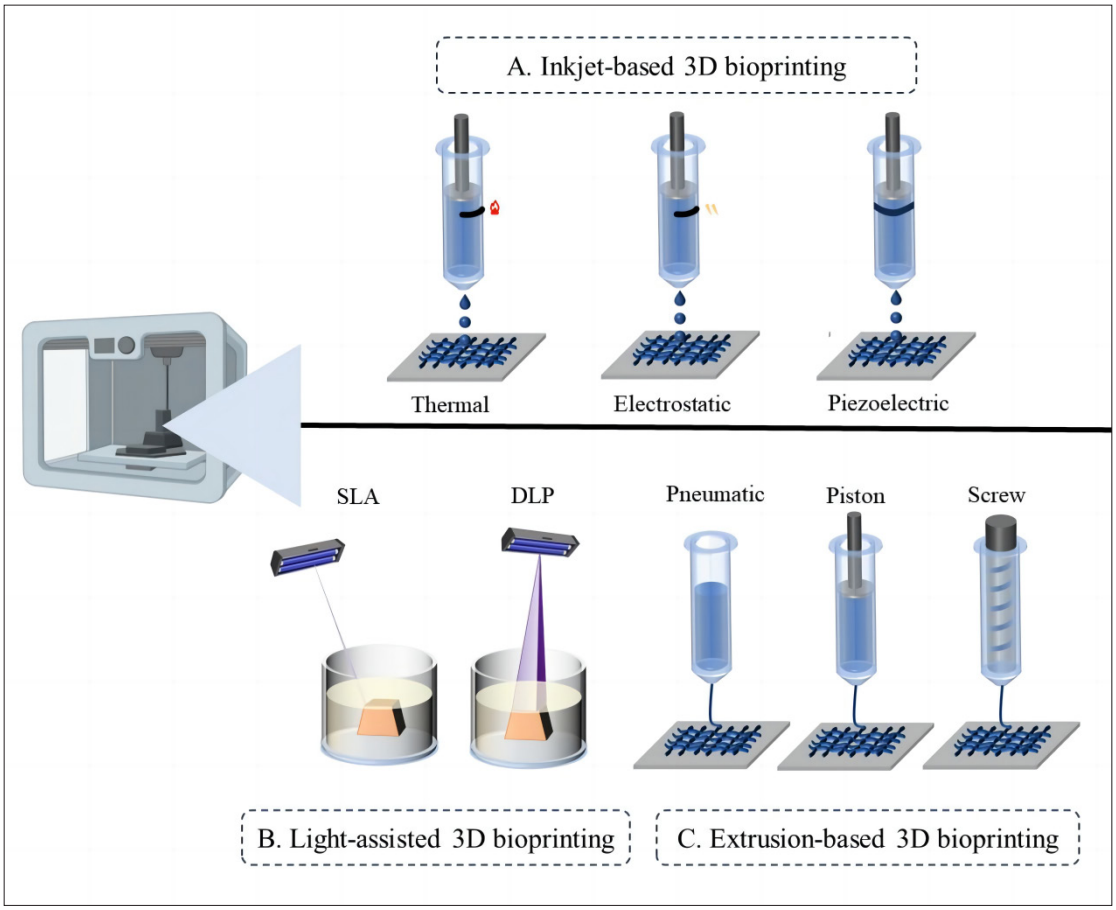


Figure 4. Diagrams of 3D bioprinting technologies with different mechanisms: (A) inject-based bioprinting, (B) light-assisted bioprinting, (C) extrusion-based bioprinting. Abbreviations: SLA, stereolithography; DLP, digital light processing.

3.2.3. Extrusion-based bioprinting

Most heterogeneous tissue or organ models with relatively larger volumes and vascularized models with inner circulation structures are printed by extrusion-based bioprinting. This technique enables the printing of bioinks with a wider range of viscosities compared to inkjet-based bioprinting.[97] Prepared bioinks are usually extruded as continuous filaments, which influence the performance of the bioprinted microarchitectures (Figure 4C). Printability, referring to the ability of bioinks to maintain the integrity and reproducibility of bioprinted constructs, is mainly evaluated by mechanical properties relevant to filament collapse, wastage, storage modulus tests, as well as biological correlations.[98] There is an inverse relationship between mechanical property and biological relevance in 3D constructs agglomerated by bioink.[99] High mechanical properties lead to the obstruction of substance diffusion, which is important for nutrient delivery and drug screening. Bioinks with various physical properties showed different biological correlations by regulating cell adhesion and substance diffusion, which further influence whether inoculated or encapsulated cells in 3D constructs can survive during cultivation and mature with tissue specificity. Nevertheless, focusing on bioink cannot solve the diffusion problem completely in extrusion-based bioprinting since simple bioink diffusion contributes to the extremely uneven distribution of matters due to spatial distance.

Artificial vessels generated with endothelial cells that are constructed by conventional extrusion-based bioprinting technology are not only disordered and unpredictable, but also unable to reflect the effect of blood flow on tissues. 3D bioprinting has the potential to fabricate vasculature with high biomimicry and even the infused property. New strategies based on extrusion-based bioprinting have been developed, such as coaxial bioprinting and embedded bioprinting. In coaxial bioprinting, the bioinks with the crosslinking solution as the core and the alginate as the outer shell were printed simultaneously to form tubular vessels.[100] In another example, two small adjacent nozzles were embedded into the printing nozzle in coaxial

bioprinting system; one was filled with the calcium chloride ($CaCl_2$) solution for perfusion, and the other was inoculated with two types of cells to study their interaction. Compared with non-perfusion models, this construct had a longer culture duration and better biological relevance.[101]

Embedded bioprinting based on extrusion-based bioprinting enables the construction of biocompatible entities without introducing heterogeneous components to enhance the mechanical properties. It is manifested in two construction ways. The cell-laden bioink with poor mechanical behaviors is bioprinted in a high-density solution (supporting bath) without biological cells to assist in the consolidation of microarchitectures. The supporting bath is replaced by culture mediums after the printed constructs are gelated. The GelMA construct printed into Kapom bath had significantly improved fidelity compared to air printing.[102] The other case is the opposite. The sacrificial bioink is printed in the support bath that helps the bioink still during printing and maintain its structure afterward. The latter method is beneficial for creating perfusable microarchitectures. Embedded bioprinting breaks through the traditional bottom-to-top order of model construction, thereby enabling its flexibility in printing and model constructing.[103,104] Unlike coaxial bioprinting, which supports the perfusion fluid with bioprinted thin tubes, hollow tubes in embedded bioprinting are perfused with the support of the entire construct, reducing the risk of collapse. Embedded bioprinting also eliminates the gravity effects found in traditional extrusion bioprinting. However, bioprinted bioinks and supporting materials are difficult to match since support materials with non-Newtonian fluid properties should liquify when subjected to shear stress from moving nozzles, but present increased viscosity to support bioprinted bioink upon stress removal.[105] Shao et al.[106] developed a new strategy that combined coaxial and embedded bioprinting. The endothelial cells were encapsulated in gelatin and adhered to the GelMA walls after the gelatin dissolved. The problems for nutrient distribution and metabolite removal caused by non-perfusion were significantly represented in this research, underlining the importance of integrating perfusion into bioprinted constructs.

Interlaced vasculature and numerous substance transport routes exist in the 3D-printed construct with hierarchical grid, adding uncertainty to the experimental results. Although bioprinting can mimic vessels like hollow tubes with perfusable ability, it is still inefficient in dynamic culture, highlighting the need to incorporate microfluidic technology.

3.2.4. Microfluidic technology

The model that is fully constructed on a chip should be cultured for maturation under microfluidic technology. To fabricate microfluidic chips, it is essential to integrate a meticulously designed structure, a propulsion system, a module for cell culture, and a monitoring unit.[107] Fluid-driven systems are categorized into two types: (i) mechanical force, such as flow micropump and pneumatic micropump, and (ii) non-mechanical force, such as gravity and surface tension.[108] The base materials for supporting artificial tissues or organs, such as polydimethylsiloxane (PDMS) and polymethyl methacrylate (PMMA), enable the generation of fluid channels and the insertion of tissue cultures. PDMS, known for its inexpensive and excellent performance, is used in soft lithography, which is the mainstream in chip fabrication.[109] The manufacturing microprocesses for chips containing the pre-fabricating molds, material curing, and plasma treatments are tedious. 3D bioprinting that regulates bore size and microstructure in bioprinted models may simplify the complexity of microfluidic chip fabrication. The combination of 3D bioprinting and microfluidic technology offers certain advantages: (i) It allows for the creation of biomimetic structures, as common polymers like PDMS cannot culture cells and replicate organ or tissue microenvironments. The use of hydrogels, popular materials in 3D bioprinting, can replace PDMS and enable the culture of biomimetic structures by combining these two technologies. (ii) Automated cell seeding can be efficiently achieved on a large scale without requiring manual seeding. This technique has the potential to construct organ or tumor chips with complex structures.[110] (iii) Controllability can be achieved by manually regulating physical factors such as material delivery and velocity of fluid flow, thereby increasing experimental reproducibility.

3D bioprinting can be applied in every step during the fabrication of microfluidic chips, such as mold designs, cell inoculations, and perfusable channel manufacture that is imbued with perfusates.[111] Colosi et al.[73] combined these two technologies prior to printing, thereby successfully printing the construct with high resolution and porosity *via* bioink of lower viscosity. Two different bioinks were converged on a microfluidic chip into a needle for bioprinting.

4. Applications: 3D-bioprinted perfusable models for drug screening

Mature bioink microarchitectures are constructed using 3D bioprinting and microfluidic technologies, which serve as efficient and convenient models for conducting drug screening.

Drug screening, divided into preclinical and clinical screening based on experimental types, plays an essential role in drug development. Although 3D-bioprinted microfluidic models can express the associated growth

Table 1. Summarized previous disease/organ-on-a-chip involving 3D bioprinting

Bioprinting technology	Hydrogel bioinks and functions	Materials for fabrications of microfluidic parts	Organ or tissue	Culture duration	Characteristics	Reference
Extrusion bioprinting	• Collagen encapsulates HepG2 • Gelatin encapsulates HUVECs	PCL	Liver	6 days	One-step bioprinting with no additional adhesion	[118]
Extrusion bioprinting	• The liver dECM encapsulates HepaRG cells • Gelatin encapsulates HUVECs	PEVA, PMMA	Liver and biliary passage	7 days	The introduction of biliary tract enabling crosstalk between organs	[119]
Extrusion (coaxial) bioprinting	The GelMA and alginate blend encapsulates HUVECs and adheres cardiomyocytes after consolidation	PDMS, PMMA	Heart	15 days	Cardiomyocytes in this construct spontaneously contracting in one direction	[120]
Extrusion bioprinting	The gelatin and fibrin blend act as ECM to adhere to cells		Kidney	7 days	The connection between blood vessels and renal tubes	[121]
Extrusion bioprinting	dECM derived from porcine tracheal mucosa encapsulates endothelial cells and fibroblasts	PCL, PDMS	Airway	3 months	The interaction of airway epithelial and endothelial cells	[122]
Extrusion bioprinting	• Gelatin encapsulates hepatic stellate cells and HUVECs • The liver dECM encapsulates HepaRG cells	PEVA	Liver fibrosis		The accurate deposition of three cell types	[127]
Extrusion bioprinting	• Collagen encapsulates neuroblastoma tumor spheroids • GelMA supports the structure	PMMA	Neuroblastoma	14 days	Endothelial cells were distributed evenly by an orbital oscillator	[128]
Extrusion (sacrificial) bioprinting	The GelMA and gelatin blend encapsulates fibroblasts	PDMS	Thrombosis	14 days	Thrombus in the perfusion state via a branch model	[129]

Abbreviations: ECM, extracellular matrix; GelMA, gelatin methacrylate; HepG2, human hepatocellular carcinoma; HUVECs, human umbilical vein endothelial cells; PCL, polycaprolactone; PEVA, poly-(ethylene/vinyl acetate); PMMA, polymethylmethacrylate; PDMS, polydimethylsiloxane.

factors and proteins, they cannot completely replicate drug efficiency in the human body. However, these models have the potential to substitute for animal models in the preclinical screening phase for new drugs (Figure 5). Models with physiological or pathological organ characteristics have been used for drug metabolism analysis and drug toxicity evaluation.

Disease models are broadly employed in different aspects of drug screening, such as comparing drug efficiency underlying different mechanisms and at varying concentrations, as well as studying drug-drug interactions and determining the feasibility of combined administration.

In vitro models are superior to animal experiments that are pretty limited due to ethical issues. The technologies in 3D-bioprinted microfluidic models complement each other, enabling *in vitro* cultures to be cultivated and stimulated artificially in miniature form accurately. 3D-bioprinted microfluidic models have successfully eliminated the errors and time consumption associated with manual labor and automatically created multiple models with uniform structures and components. Compared to the pure cell microarrays for drug screening, these models offer more complex and bionic characteristics.[112,113] 3D-bioprinted microfluidic models allow for improved interactions among cells, ECM, and relevant signaling pathways, enabling the replication of cell behaviors and disease features *in vivo*. These models in which drug reactions are observed directly can be manufactured in an automated and controlled manner, reducing randomness and enhancing the reliability of drug screening results.

4.1. 3D-bioprinted organ-on-a-chip

3D-bioprinted organ-on-a-chip (OOC), a complex but more physiologically related model, is based on microfluidic technology containing perfusable microfluidics, reaction parts, and drug delivery channels. 3D-bioprinted OOCs, as an advancement in the integration of 3D bioprinting technology with microfluidic technology, are figurative and momentous applications of hydrogel. When combined with bioprinting, it enables the printing of live cells in functional hydrogel constructs that have similar spatial distributions to physiological microenvironments.[114] Since functional cells are bioprinted and perfused, the hydrogel constructs could express specific factors and enzymes, possessing features of the mimicked microenvironments, such as the oxygen gradient, acidity, abnormal vessels, and dynamic perfusion. Once the cells have differentiated to be mature, drug solutions are applied for testing efficiency.

Given their organ-like properties, OOCs are used to explore drug toxicity for the organs by evaluating cell viability, metabolic activity, and biomarker expressions.[115] Moreover, many studies have confirmed that liver injury caused by hepatotoxicity from drugs is one of the factors contributing to the numerous challenges associated with drug diagnosis and management.[116] The renal system is also necessary for drug screening and metabolism. Hepatotoxicity and nephrotoxicity slow down the drug development from discovery to the clinic, increasing the risk of failure.[117]

Lee et al.[118] selected PCL with low protein adsorption and hydrophobicity as the printed channel shells to support the internal reaction regions. Collagen hydrogel encapsulated

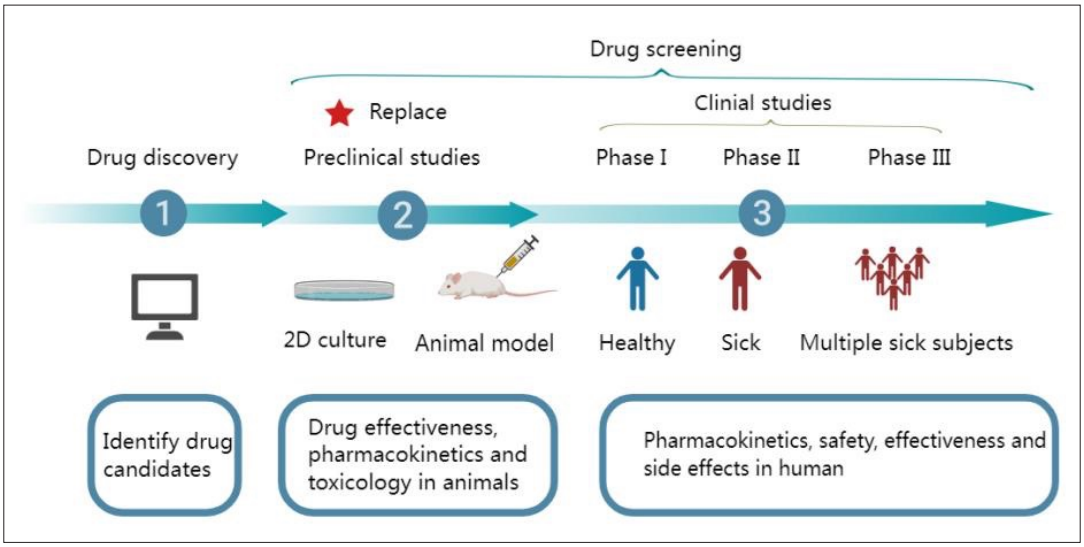


Figure 5. The process of drug development from discovery to clinical experiments. The red star represents 3D-bioprinted chips discussed in this review, which may replace animal models and 2D cultures in preclinical drug screening.

hepatocytes and gelatin containing human umbilical vein endothelial cells (HUVECs) were printed at the bottom of the channel, accomplishing the one-step construction without additional bonding and adhesion (Figure 6A). In this study, 3D bioprinting is employed in the fabrication of the whole tissue model, including microfluidic channels and tissue-culture chambers, which allowed higher liver activity than static culture. Furthermore, the biliary system excreting the bile acids that were toxic to the hepatocytes was incorporated into the novel model developed by Lee et al.,[119] which contained two chambers separated by a porous membrane. The upper chamber supported culture cells and was perfused by fluids while metabolic waste leaked into the bottom chamber. The expression of specific proteins to biliary duct demonstrated the successful construction of liver model with the biliary duct. The physiological and structural characteristics of hepatobiliary interdependence were embodied in the model. This dual-channel system embodying two-organ features also provided the potential for integration into multi-organ chips.

Heart tissues, with structural complexity and physiological importance, attract significant interest from many investigators. Zhang et al.[120] utilized coaxial bioprinting with nozzles that are designed in a concentric circle shape. The inner nozzle was filled with a crosslinked solution, and a blend of GelMA and alginate was printed in the outer nozzle as shells. This structure that was printed on PDMS carried myocardial endothelial cells, which were guided into the bioprinted filament surface to form a tubular cavity. A cardiomyocyte suspension was then perfused for cell inoculation in this construct. The resulting endothelialized cardiac model facilitated cell growth aligned along the long axis to replicate the cardiomyocyte bundle architecture *in vivo*. The drug azithromycin exhibited dose-dependent effects and significantly reduced the beat rate of cardiomyocytes, indicating the reliable potential of the cardiac model for drug screening. Nevertheless, it should be noted that this model, which could be perfused, has no hollow tubular structures.

Proximal renal tubules, the chief reabsorbing structures, reabsorb most glucose and protein back into the blood. Lin et al.[121] introduced vasculature into renal tubules in their model, which was used to study the crosstalk between epithelium and endothelium. Original sacrificial ink added with high-molecular-weight poly (ethylene oxide) (PEO) was printed between the two modified ECM casting layers. The vascular templates were removed at a low temperature, and then the cultured cells were inoculated by perfusion. At the junction of the two tubes, the adhesion and increased expression of transport proteins were observed, indicating the crosstalk between epithelium and endothelium. The administration and subsequent withdrawal of dapagliflozin reduced and restored the rate at which glucose was reabsorbed in the kidney tubule model. In addition, the state of the constructed model could be regulated through applying different perfusable materials. In the hyperglycemic state, this model with notable changes in cell morphology and drug effects offered a solid basis for further pathological and drug research.

Park et al.[122] utilized PCL to assemble three communicating chambers, containing bioink with endothelial cells as the central chamber and the bioink with pulmonary fibrocytes as chambers on both sides. The two chambers were separated from the central chamber to ensure media flow. The capillary network was generated in the central chamber. Marino et al.[123] fabricated blood–brain barrier-on-a-chip (BBB-on-a-chip) with two-photolithography. The bioprinted vessels with well-distributed micropores were arranged in parallel, mimicking the microcapillaries in BBB for brain tumor and lesions research. Similarly, Mandt et al.[124] designed the x-shaped microfluidic chamber with wave-shaped condensates and printed it on the interface via two-photolithography. It reproduced the placental barrier to investigate the permeability of glucose molecules (Figure 6B).

Pulmonary alveoli directly exposed to the environment are used for gas exchange between inhaled air and blood. The epithelium and the endothelium in blood–air barrier are located on each side of the basement membrane. This micron-thick structure with three-layered cells was constructed by drop-on-demand piezoelectric bioprinting. The printer with multi-jet nozzles was utilized to fabricate mold containing four cylinders for supporting tissue-embedded inserts. The upper layer of the 3D structure was obtained by casting the PDMS into the printed mold and then assembled with a flattened PDMS layer. Subsequently, the inserts were transplanted into cylindrical holes of the PDMS model (Figure 6C).[125] The chip was able to replicate physiological microenvironments to investigate influenza viruses and respiratory diseases. Furthermore, this chip with flexible insert could conveniently integrate cultured cells from various organs. These chip models would be composed of repeated building blocks with high uniformity and resolution.

4.2. 3D-bioprinted disease-on-a-chip

The OOCs and disease-on-a-chip (DOCs) are distinguished by cell sources, and the latter accommodates lesion cells instead of organ cells. DOCs allow for the reconstruction of TME or lesion organs in the laboratory setting.[126] The liver disease model was further developed based on previous

studies on liver models. Gelatin-based bioink dissolved afterward was used to encapsulate activated stellate cells that induced liver fibrosis. The human HepaRG cells were laid in the dECM of the liver. Two adjacent chambers were printed with poly-(ethylene/vinyl acetate) (PEVA), and the upper chamber was filled with dECM. Secondly, PEVA was added again on the first-printed chamber walls to deepen the volume of the chamber. After consolidation, bioinks were printed and subsequently dissolved in order to inoculate cells and form the upper channel. The structure possessed two channels compartmentalized by printed bioinks. It was known that activated stellate cells generated excessive ECM due to the increased expression of key components in ECM, demonstrating that this pathological model was successfully fabricated and could be used to evaluate drug efficiency for inhibiting stellate cell activation[127] (Figure 6D).

Nothdurfter et al.[128] fabricated the chamber and perfusable channels on PMMA through laser etching, which addressed the shedding problem of the vascular

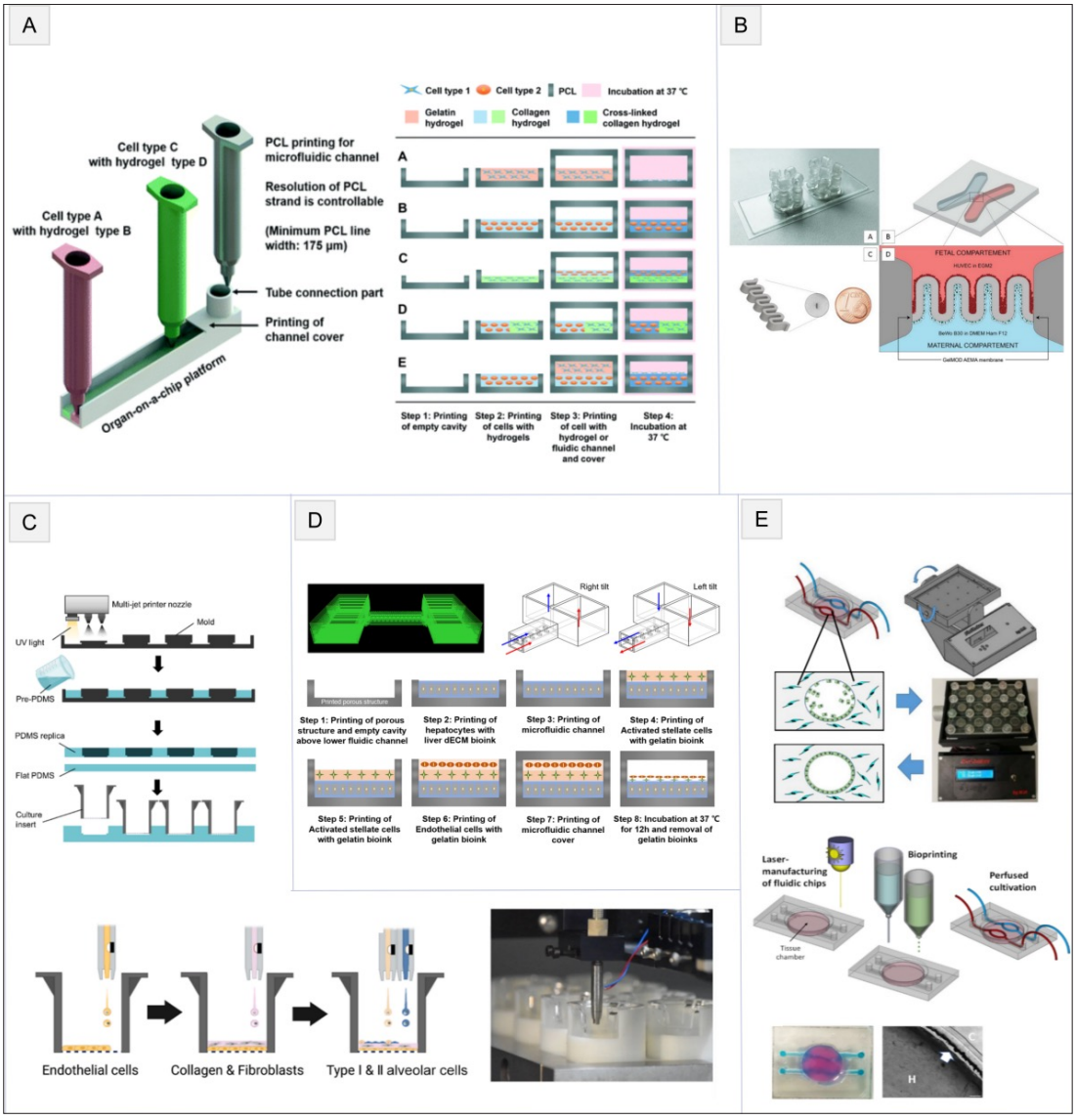


Figure 6. Fabrication processes of microfluidic chips for mimicking disease or organ microenvironments. (A) Cell-bioprinted liver-on-a-chip in one-step fabrication (reproduced with permission from ref.[118]). (B) Placental barrier-on-a-chip under two-photon polymerization (reproduced with permission from ref.[124]). (C) Inkjet-bioprinting lung-on-a-chip (Reproduced with permission from ref.[125]). (D) 3D liver fibrosis-on-a-chip (reproduced with permission from ref.[127]). (E) Micro-vascularized neuroblastoma-on-a-chip in medium throughput (from ref.[128] licensed under Creative Commons Attribution 4.0 license).

neuroblastoma tissue on the chip. The bioink was printed on the central groove, and the above procedures were repeated after printing vessels with sacrificial bioink (Pluronic). In order to distribute the ECs evenly on the channel walls, an orbital oscillator was integrated to form the vascular wall. The fully automated process eliminated the manual steps of the traditional tumor-on-a-chip and was expected to enable high-throughput screening (Figure 6E).

Zhang et al.[129] printed the vessel model with branches in GelMA hydrogel, and inoculated erythrocytes following perfusion with whole blood for a while. The coagulant was added in one branch to enable the thrombus formation to ensure perfusability of another branch. The addition of thrombolytic agents and co-culture with fibroblasts confirmed the potential application in pathological models, including thrombus, thrombolysis, fibrosis, and related drug studies.

The disease-on-a-chip will no longer be limited to reproducing the lesion locations. Taking the artificial tumor model as an example, the interaction between tumor and vessels that plays a role in tumor metastasis gives impetus to developing a vascularized tumor-on-a-chip, which enhances physiological correlation and exhibits the potential to screen drugs for inhibiting angiogenesis and tumor metastasis.[130]

4.3. 3D-bioprinted microfluidic arrays

Microfluidic arrays with multiple reaction sites require repeated manual operations. Nevertheless, inkjet-based bioprinting provides a solution that fully automates both cell inoculation and model formation, thereby realizing high-throughput analysis.

Microarrays have ten-fold reaction sites generated by pre-mixed bioinks. This program realizes high-throughput drug screening and minimal reagent consumption. Multiple microarrays in which an ejected droplet is a reaction site are always incorporated with automated 3D inkjet-based bioprinting. Inkjet-based bioprinting is effective in printing droplets with cells, whereas the resulting bioprinted constructs are simple at the cellular level.

In this study, 400 single-cell microreactors were created using inkjet bioprinting on a microfluidic chip after the printing parameters were optimized. However, each microreactor contained cancer cells with weak migration ability, and the reaction in each microreactor was unable to recapitulate that in organs. Ultimately, paclitaxel at varying concentrations, which was found to be dose-dependent, was applied on this chip.[131]

Several issues need to be addressed to obtain predictive and cogent results from microarrays: (i) The appropriate quantity of cells required in microdroplets needs to be determined. (ii) Consistent culture conditions should be maintained in different microdroplets. (iii) Taking high throughput as the prerequisite, further development of structural complexity is necessary.

5. Prospects in precision medicine

The 3D-bioprinted microfluidic model can be used not only in preclinical stages but also in the evaluation of drug therapy effects on different patients. To provide effective treatment options for different patients, it is important for the model to incorporate more characteristics from patient microenvironments. Drug treatment can be tailored based on specific pathogenesis and dosage for each person. The inaccurately predictive results of animal models, the gap between animal models and humans, and the high experimental cost promote the advancement of human-derived *in vitro* models using emerging manufacturing technologies. Precision medicine utilizes pathological information such as genetic materials to distinguish specific patients from other patients with similar disease characteristics and match them with personalized treatment options. These individual-based treatments result in lower dosages, fewer side effects, and less toxicity.[132] Personalized human-derived *in vitro* models are the perfect solution for the implementation of personalized medicine. The research of patient-derived models, multi-organ chips, and drug therapy lays a solid foundation for precision medicine.

5.1. Patient-oriented models

In the fabrication of bioprinted OOCs, ordinary functional hydrogels and animal-derived bioinks are replaced by human-derived bioinks, such as dECM extracted from human tissues.[133] The quality of prepared bioink is critical for the maturation of the models. When the bioink exhibits significant individual differences, it contains individual genetic information and expresses functional protein. As a result, the patient-derived models constructed from such bioink have more individual specificity. Consequently, optimal treatment can be identified to achieve the goal of precision medicine. Moreover, the cultured cells could be substituted by tissues excised from each patient. Constructs from patients with the same disease are fabricated to explore the individual variability according to their drug response. Although patient-derived chips may not fully replicate genetic information, the parental tumor phenotype and the heterogeneity that decide the variation of drug resistance are retained.[134] As a result, the models have high accuracy

in predicting chemotherapy and specific targeted therapy responses, providing distinctive treatments for individual patients. Hu et al.[135] utilized patient-derived tumor tissues to develop the superhydrophobic microfluidic chip. The morphology and stable mutation of tumors were maintained with passaging, which was consistent with clinical observations. Moreover, this construct generated clinically relevant drug responses after being cultured for 7 days, showing that patient-derived models have great potential for drug screening.

5.2. Multi-organ microfluidic chips

Drug metabolism is a crucial factor that determines the value of the drug development and the drug toxicity to organs. The liver that houses the enzyme system (CYP450) is responsible for about 70% of drug metabolism, and the intestinal tract is also the primary organ for drug metabolism. The metabolic transformations of drugs involving hepato-enteric circulation and first-pass metabolism are accomplished by multiple organs. A single-organ model is inadequate to reproduce these physiological processes. As the further expansion of the organ-on-a-chip, multi-organ chips have not only been utilized to reveal the crosstalk in tissue or organ microenvironments and related mechanisms, but also study drug metabolism and tumor metastasis among organs due to their capabilities of connecting different organ microarchitectures *via* perfusion channels that resemble blood vessels.[136]

In addition, the pharmacokinetics for drugs includes four processes: absorption, distribution, metabolism, and elimination (ADME). Data collected from multi-organ chips can be used to construct the pharmacokinetic-pharmacodynamic (PK-PD) mathematical model, which can predict the ADME processes for different administration routes and metabolic pathways.[137] To study the uptake and metabolism characteristics of anti-cancer prodrugs in the liver, Shinha et al.[138] inoculated hepatocytes and cancer-associated cells in two blocks on a chip, respectively, constituting the disease-targeted model. In another example, tissues from heart, bone, liver, and skin were selected owing to their distinctive properties and significance. The mature models were cultured and transplanted onto the tissue chip and connected by the flow of blood vessels. Not only did this construct express more biomarkers, but it also allowed the establishment of PK-PD models and study on treatment regimens as well as drug metabolism. This construct was found to be superior to simple mixed multi-tissue models.[139]

Human-on-a-chip refers to human tissue cultures connected in series by a vascular analog on a single chip. This approach enables the study of complex interactions among multiple organs, facilitating the exploration of pathological process and drug metabolism in human.[140] One of the key advantages of this chip is the use of human-derived cells for each tissue culture. By collecting and analyzing blood mimics in the connected tube, valuable drug metabolism data can be easily obtained. This data can be used to construct a metabolic model of drugs in the human body, which can improve the efficiency of first-phase clinical experiments. Furthermore, once the data obtained from the chip are comparable to that in human experiments, it will be possible to study disease characteristics in different genders and age groups in a relatively safe manner. The application of human-on-a-chip can help overcome the challenge of finding diverse types of experimental individuals for human experiments.[141] Additionally, the chip has the potential to expand the scope of clinical research, including rare diseases and complications with individual differences.

5.3. Personalized administration

The emergence of diseases such as cancer often arises from dysfunctions in multiple signaling pathways and abnormalities in multiple organs. Personalized administration refers to the selection of drugs with different mechanisms or administration models for different individuals to achieve the best treatment effect. Combinative administration, from the perspective of the whole microenvironment, combines two or more drugs that act on different signaling pathways and organs rather than using a single drug. Moreover, combinative administration can reduce the dose of a single drug, thereby attenuating drug toxicity and the potential for drug resistance.[142] Nevertheless, combinative administration has the disadvantage of drug–drug interactions. The bioprinted microfluidic models can also study the interaction among drugs with different mechanisms through toxicity evaluation. Wan et al.[143] testified the difference between single and combined administrations and analyzed synergistic effect of drugs in combined administration. Therefore, bioprinted chips can not only verify the optimal therapy regimen for each patient but also analyze the interactions among drugs with different mechanisms.

6. Conclusion

The integration of 3D bioprinting and microfluidic technologies has become a megatrend for accurately modeling tissues or organs *in vivo*. In the case of tumors, the *in vitro* microarchitecture is based on the interactions between different cell types, which reproduce physical features and even bionic behaviors of TME. This combined engineering technology is crucial for implementing these characteristics. Gel-based bioinks that imitate the material composition in the microenvironment are deposited into

representative structures with the help of 3D bioprinting technologies and then dynamically cultured through microfluidic technologies. The combination of these two technologies has the potential to eliminate biological limitations and produce more standardized and persuasive results for drug screening. Furthermore, integrated chips will significantly influence personalized medicine and drug administration. In the future, tissue chips can be universal, providing a model that satisfies different patients and even different types of cancers.

Acknowledgments

None.

Funding

This work was supported by the National Key R&D Program of China (2018AAA0100300) and the Fundamental Research Funds for the Central Universities (DUT22YG238).

Conflict of interest

The authors declare no conflicts of interest.

Author contributions

Conceptualization: Hangyu Zhang, Jianing Li
Funding acquisition: Hangyu Zhang, Shen Li
Supervision: Hangyu Zhang
Writing – original draft: Jianing Li
Writing – review & editing: Na Li, Bo Liu, Shen Li, Hangyu Zhang

Ethics approval and consent to participate

Not applicable.

Consent for publication

Not applicable.

Availability of data

Not applicable.

References

1. Dawood AA, Yousif WI. The main reasons why cancer is so difficult to treatment. *AJOAIMS*. Philadelphia: Elsevier; 2020;2(2):20-22.
2. DeBerardinis RJ. Tumor microenvironment, metabolism, and immunotherapy. *N Engl J Med*. 2020;382(9):869-871. doi: 10.1056/NEJMcibr1914890
3. Advancing cancer therapy. *Nat Cancer*. 2021;2(3):245-246. doi: 10.1038/s43018-021-00192-x
4. Bains W. Failure rate in drug discovery and development: will we ever get any better? *Drug Discov World*. 2004;5.
5. Imamura Y, Mukohara T, Shimono Y, et al. Comparison of 2D- and 3D-culture models as drug-testing platforms in breast cancer. *Oncol Rep*. 2015;33(4):1837-1843. doi: 10.3892/or.2015.3767
6. Jensen C, Teng Y. Is it time to start transitioning from 2D to 3D cell culture? *Front Mol Biosci*. 2020;7:33. doi: 10.3389/fmolb.2020.00033
7. de Jong M, Maina T. Of mice and humans: are they the same?--Implications in cancer translational research. *J Nucl Med*. 2010;51(4):501-504. doi: 10.2967/jnumed.109.065706
8. Mak IW, Evaniew N, Ghert M. Lost in translation: animal models and clinical trials in cancer treatment. *Am J Transl Res*. 2014;6(2):114-118.
9. Dey M, Ozbolat IT. 3D bioprinting of cells, tissues and organs. *Sci Rep*. 2020;10:14023. doi: 10.1038/s41598-020-70086-y
10. Staros R, Michalak A, Rusinek K, Mucha K, Pojda Z, Zagożdżon R. Perspectives for 3D-bioprinting in modeling of tumor immune evasion. *Cancers (Basel)*. 2022;14(13):3126. doi: 10.3390/cancers14133126
11. Xie F, Sun L, Pang Y, et al. Three-dimensional bio-printing of primary human hepatocellular carcinoma for personalized medicine. *Biomaterials*. 2021;265:120416. doi: 10.1016/j.biomaterials.2020.120416
12. Jia X, Yang X, Luo G, Liang Q. Recent progress of microfluidic technology for pharmaceutical analysis. *J Pharm Biomed Anal*. 2022;209:114534. doi: 10.1016/j.jpba.2021.114534
13. Yu F, Choudhury D. Microfluidic bioprinting for organ-on-a-chip models. *Drug Discov Today*. 2019;24(6):1248-1257. doi: 10.1016/j.drudis.2019.03.025
14. Tiwari AP, Thorat ND, Pricl S, Patil RM, Rohiwal S, Townley H. Bioink: a 3D-bioprinting tool for anticancer drug discovery and cancer management. *Drug Discov Today*. 2021;26(7):1574-1590. doi: 10.1016/j.drudis.2021.03.010
15. Ji S, Guvendiren M. Recent advances in bioink design for 3D bioprinting of tissues and organs. *Front Bioeng Biotechnol*. 2017;5:23. doi: 10.3389/fbioe.2017.00023
16. Nejman D, Livyatan I, Fuks G, et al. The human tumor microbiome is composed of tumor type-specific intracellular bacteria. *Science*. 2020;368(6494):973-980. doi: 10.1126/science.aay9189

17. Galeano Niño JL, Wu H, LaCourse KD, et al. Effect of the intratumoral microbiota on spatial and cellular heterogeneity in cancer. *Nature*. 2022;611(7937):810-817. doi: 10.1038/s41586-022-05435-0

18. Bejarano L, Jordão MJC, Joyce JA. Therapeutic targeting of the tumor microenvironment. *Cancer Discov*. 2021;11(4):933-959. doi: 10.1158/2159-8290

19. Marconi GD, Fonticoli L, Rajan TS, et al. Epithelial-mesenchymal transition (EMT): the type-2 EMT in wound healing, tissue regeneration and organ fibrosis. *Cells*. 2021;10(7):1587. doi: 10.3390/cells10071587

20. Huang H, Wang Z, Zhang Y, et al. Mesothelial cell-derived antigen-presenting cancer-associated fibroblasts induce expansion of regulatory T cells in pancreatic cancer. *Cancer Cell*. 2022;40(6):656-673. doi: 10.1016/j.ccell.2022.04.011

21. Kalluri R, Zeisberg M. Fibroblasts in cancer. *Nat Rev Cancer*. 2006;6(5):392-401. doi: 10.1038/nrc1877

22. Kobayashi H, Enomoto A, Woods SL, Burt AD, Takahashi M, Worthley DL. Cancer-associated fibroblasts in gastrointestinal cancer. *Nat Rev Gastroenterol Hepatol*. 2019;16(5):282-295. doi: 10.1038/s41575-019-0115-0

23. Nurmik M, Ullmann P, Rodriguez F, Haan S, Letellier E. In search of definitions: cancer-associated fibroblasts and their markers. *Int J Cancer*. 2020;146(4):895-905. doi: 10.1002/ijc.32193

24. Chen X, Song. Turning foes to friends: targeting cancer-associated fibroblasts. *Nat Rev Drug Discov*. 2019;18(2):99-115. doi: 10.1038/s41573-018-0004-1

25. Wu K, Lin K, Li X, et al. Redefining tumor-associated macrophage subpopulations and functions in the tumor microenvironment. *Front Immunol*. 2020;11:1731. doi: 10.3389/fimmu.2020.01731

26. Pan Y, Yu Y, Wang X, Zhang T. Tumor-associated macrophages in tumor immunity. *Front Immunol*. 2020;11:583084. doi: 10.3389/fimmu.2020.583084

27. Fukuda K, Kobayashi A, Watabe K. The role of tumor-associated macrophage in tumor progression. *Front Biosci*. 2012;4(2):787-798. doi: 10.2741/s299

28. Qian BZ, Pollard JW. Macrophage diversity enhances tumor progression and metastasis. *Cell*. 2010;141(1):39-51. doi: 10.1016/j.cell.2010.03.014

29. Melaiu O, Lucarini V, Cifaldi L, Fruci D. Influence of the tumor microenvironment on NK cell function in solid tumors. *Front Immunol*. 2020;10:3038. doi: 10.3389/fimmu.2019.03038

30. Xia L, Oyang L, Lin J, et al. The cancer metabolic reprogramming and immune response. *Mol Cancer*. 2021;20(1):28. doi: 10.1186/s12943-021-01316-8

31. Greer SN, Metcalf JL, Wang Y, Ohh M. The updated biology of hypoxia-inducible factor. *EMBO J*. 2012;31(11):2448-2460. doi: 10.1038/emboj.2012.125

32. Jiang Z, Zhou J, Li L, et al. Pericytes in the tumor microenvironment. *Cancer Lett*. 2023;216074. doi: 10.1016/j.canlet.2023.216074

33. Li Y, Zhao L, Li XF. Hypoxia and the tumor microenvironment. *Technol Cancer Res Treat*. 2021;20:15330338211036304. doi: 10.1177/15330338211036304

34. Hanahan D, Weinberg RA. Hallmarks of cancer: the next generation. *Cell*. 2011;144(5):646-674. doi: 10.1016/j.cell.2011.02.013

35. Meirson T, Gil-Henn H, Samson AO. Invasion and metastasis: the elusive hallmark of cancer. *Oncogene*. 2020;39(9):2024-2026. doi: 10.1038/s41388-019-1110-1

36. Majidpoor J, Mortezaee K. Steps in metastasis: an updated review. *Med Oncol*. 2021;38(1):3. doi: 10.1007/s12032-020-01447-w

37. Duffy MJ, McGowan PM, Gallagher WM. Cancer invasion and metastasis: changing views. *J Pathol*. 2008;214(3):283-293. doi: 10.1002/path.2282

38. Jain RK, Martin JD, Chauhan VP, Duda DG. Tumor microenvironment: vascular and extravascular compartment. In: Niederhuber JE, Armitage JO, Kastan MB, Doroshow JH, Tepper JE, eds. *Abeloff's Clinical Oncology*. 6th ed. Elsevier; 2020:108-126. doi: 10.1016/B978-0-323-47674-4.00008-6

39. Ribatti D, Pezzella F. Overview on the different patterns of tumor vascularization. *Cells*. 2021;10(3):639. doi: 10.3390/cells10030639

40. Najafi M, Goradel NH, Farhood B, et al. Tumor microenvironment: interactions and therapy. *J Cell Physiol*. 2019;234(5):5700-5721. doi: 10.1002/jcp.27425

41. Farhood B, Najafi M, Mortezaee K. Cancer-associated fibroblasts: secretions, interactions, and therapy. *J Cell Biochem*. 2019;120(3):2791-2800. doi: 10.1002/jcb.27703

42. Jeong SY, Lee JH, Shin Y, Chung S, Kuh H-J. Co-culture of tumor spheroids and fibroblasts in a collagen matrix-incorporated microfluidic chip mimics reciprocal activation in solid tumor microenvironment. *PLoS One*. 2016;11(7):e0159013. doi: 10.1371/journal.pone.0159013

43. Melcher V, Graf M, Interlandi M, et al. Macrophage-tumor cell interaction promotes ATRT progression

and chemoresistance. *Acta Neuropathol*. 2020;139(5): 913-936.
doi: 10.1007/s00401-019-02116-7

44. Mortezaee K. Immune escape: a critical hallmark in solid tumors. *Life Sci*. 2020;258:118110.
doi: 10.1016/j.lfs.2020.118110

45. Elmusrati A, Wang J, Wang CY. Tumor microenvironment and immune evasion in head and neck squamous cell carcinoma. *Int J Oral Sci*. 2021;13(1):24.
doi: 10.1038/s41368-021-00131-7

46. Tang H, Fu YX. Immune evasion in tumor's own sweet way. *Cell Metab*. 2018;27(5):945-946.
doi: 10.1016/j.cmet.2018.03.013

47. Shay JW. Role of telomeres and telomerase in aging and cancer. *Cancer Discov*. 2016;6(6):584-593.
doi: 10.1158/2159-8290.CD-16-0062

48. Cabanos HF, Hata AN. Emerging insights into targeted therapy-tolerant persister cells in cancer. *Cancers*. 2021;13(11):2666.
doi: 10.3390/cancers13112666

49. Taylor S, Spugnini EP, Assaraf YG, Azzarito T, Rauch C, Fais S. Microenvironment acidity as a major determinant of tumor chemoresistance: proton pump inhibitors (PPIs) as a novel therapeutic approach. *Drug Resist Updat*. 2015;23:69-78.
doi: 10.1016/j.drup.2015.08.004

50. Icard P, Simula L, Fournel L, et al. The strategic roles of four enzymes in the interconnection between metabolism and oncogene activation in non-small cell lung cancer: therapeutic implications. *Drug Resist Updat*. 2022;63:100852.
doi: 10.1016/j.drup.2022.100852

51. Sun Y. Tumor microenvironment and cancer therapy resistance. *Cancer Lett*. 2015;380(1):205-215.
doi: 10.1016/j.canlet.2015.07.044

52. Seebacher NA, Krchniakova M, Stacy AE, Skoda J, Jansson PJ. Tumour microenvironment stress promotes the development of drug resistance. *Antioxidants*. 2021;10(11):1801.
doi: 10.3390/antiox10111801

53. Axpe E, Oyen ML. Applications of alginate-based bioinks in 3D bioprinting. *Int J Mol Sci*. 2016;17(12):1976.
doi: 10.3390/ijms17121976

54. Zhang J, Wehrle E, Vetsch JR, Paul GR, Rubert M, Müller R. Alginate dependent changes of physical properties in 3D bioprinted cell-laden porous scaffolds affect cell viability and cell morphology. *Biomed Mater*. 2019;14(6):065009.
doi: 10.1088/1748-605X/ab3c74

55. Zhang M, Zhao X. Alginate hydrogel dressings for advanced wound management. *Int J Biol Macromol*. 2020; 162:1414-1428.
doi: 10.1016/j.ijbiomac.2020.07.311

56. Thakur S, Govender PP, Mamo MA, Tamulevicius S, Thakur VK. Recent progress in gelatin hydrogel nanocomposites for water purification and beyond. *Vacuum*. 2017;146:396-408.
doi: 10.1016/j.vacuum.2017.05.032

57. Distler T, Solisito AA, Schneidereit D, Friedrich O, Detsch R, Boccaccini AR. 3D printed oxidized alginate-gelatin bioink provides guidance for C_2C_{12} muscle precursor cell orientation and differentiation *via* shear stress during bioprinting. *Biofabrication*. 2020;12(4):045005.
doi: 10.1088/1758-5090/ab98e4

58. Wang X, Ao Q, Tian X, et al. Gelatin-based hydrogels for organ 3D bioprinting. *Polymers*. 2017;9(9):401.
doi: 10.3390/polym9090401

59. Bertlein S, Brown G, Lim KS, et al. Thiol-ene clickable gelatin: a platform bioink for multiple 3D biofabrication technologies. *Adv Mater*. 2017;29(44):201703404.
doi: 10.1002/adma.201703404

60. Leu Alexa R, Iovu H, Ghitman J, et al. 3D-printed gelatin methacryloyl-based scaffolds with potential application in tissue engineering. *Polymers*. 2021;13(5):727.
doi: 10.3390/polym13050727

61. Kumar H, Sakthivel K, Mohamed MGA, et al. Designing gelatin methacryloyl (GelMA)-based bioinks for visible light stereolithographic 3D biofabrication. *Macromol Biosci*. 2021;21(1):e2000317.
doi: 10.1002/mabi.202000317

62. Stepanovska J, Supova M, Hanzalek K, Broz A, Matejka R. Collagen bioinks for bioprinting: a systematic review of hydrogel properties, bioprinting parameters, protocols, and bioprinted structure characteristics. *Biomedicines*. 2021;9(9):1137.
doi: 10.3390/biomedicines9091137

63. Osidak EO, Karalkin PA, Osidak MS, et al. Viscoll collagen solution as a novel bioink for direct 3D bioprinting. *J Mater Sci Mater Med*. 2019;30(3):31.
doi: 10.1007/s10856-019-6233-y

64. Lee JM, Suen SKQ, Ng WL, Ma WC, Yeong WY. Bioprinting of collagen: considerations, potentials, and applications. *Macromol Biosci*. 2021;21(1):e2000280.
doi: 10.1002/mabi.202000280

65. Osidak EO, Kozhukhov VI, Osidak MS, Domogatsky SP. Collagen as bioink for bioprinting: a comprehensive review. *Int J Bioprint*. 2020;6(3):270.
doi: 10.18063/ijb.v6i3.270

66. Wang Z, Yang Y, Gao Y, Xu Z, Yang S, Jin M. Establishing a novel 3D printing bioinks system with recombinant human collagen. *Int J Biol Macromol*. 2022;211:400-409.
doi: 10.1016/j.ijbiomac.2022.05.088

67. Zhang W, Du A, Liu S, Lv M, Chen S. Research progress in decellularized extracellular matrix-derived hydrogels. *Regen Ther*. 2021;18:88-96.
doi: 10.1016/j.reth.2021.04.002

68. Wang H, Yu H, Zhou X, et al. An overview of extracellular matrix-based bioinks for 3D bioprinting. *Front Bioeng Biotechnol*. 2022;10:905438. doi: 10.3389/fbioe.2022.905438

69. Liu C, Pei M, Li Q, Zhang Y. Decellularized extracellular matrix mediates tissue construction and regeneration. *Front Med*. 2022;16(1):56-82. doi: 10.1007/s11684-021-0900-3

70. Rana D, Kumar TS, Ramalingam M. Cell-laden hydrogels for tissue engineering. *J Biomater Tissue Eng*. 2014;4. doi: 10.1166/jbt.2014.1206

71. Liu H, Gong Y, Zhang K, et al. Recent advances in decellularized matrix-derived materials for bioink and 3D bioprinting. *Gels*. 2023;9(3):195. doi: 10.3390/gels9030195

72. Abaci A, Guvendiren M. Designing decellularized extracellular matrix-based bioinks for 3D bioprinting. *Adv Healthc Mater*. 2020;9(24):e2000734. doi: 10.1002/adhm.202000734

73. Colosi C, Shin SR, Manoharan V, et al. Microfluidic bioprinting of heterogeneous 3D tissue constructs using low-viscosity bioink. *Adv Mater*. 2016;28(4):677-684. doi: 10.1002/adma.201503310

74. Soltan N, Ning L, Mohabatpour F, Papagerakis P, Chen X. Printability and cell viability in bioprinting alginate dialdehyde-gelatin scaffolds. *ACS Biomater Sci Eng*. 2019;5(6):2976-2987. doi: 10.1021/acsbiomaterials.9b00167

75. Jeon O, Lee YB, Lee SJ, Guliyeva N, Lee J, Alsberg E. Stem cell-laden hydrogel bioink for generation of high resolution and fidelity engineered tissues with complex geometries. *Bioact Mater*. 2021;15:185-193. doi: 10.1016/j.bioactmat.2021.11.025

76. Cui R, Li S, Li T, et al. Natural polymer derived hydrogel bioink with enhanced thixotropy improves printability and cellular preservation in 3D bioprinting. *J Mater Chem B*. 2023;11(17):3907-3918. doi: 10.1039/d2tb02786k

77. Wang Q, Karadas Ö, Backman O, et al. Aqueous two-phase emulsion bioresin for facile one-step 3D microgel-based bioprinting. *Adv Healthc Mater*. 2023;12(19):e2203243. doi: 10.1002/adhm.202203243

78. Zhang W, Kuss M, Yan Y, Shi W. Dynamic alginate hydrogel as an antioxidative bioink for bioprinting. *Gels*. 2023;9(4):312. doi: 10.3390/gels9040312

79. Sachdev A 4th, Acharya S, Gadodia T, et al. A review on techniques and biomaterials used in 3D bioprinting. *Cureus*. 2022;14(8):e28463. doi: 10.7759/cureus.28463

80. Zhu J, Li F, Wang X, Yu J, Wu D. Hyaluronic acid and polyethylene glycol hybrid hydrogel encapsulating nanogel with hemostasis and sustainable antibacterial property for wound healing. *ACS Appl Mater Interfaces*. 2018;10(16):13304-13316. doi: 10.1021/acsami.7b18927

81. Shi L, Zhang J, Zhao M, et al. Effects of polyethylene glycol on the surface of nanoparticles for targeted drug delivery. *Nanoscale*. 2021;13(24):10748-10764. doi: 10.1039/d1nr02065j

82. Wang J, Williamson GS, Yang H. Branched polyrotaxane hydrogels consisting of alpha-cyclodextrin and low-molecular-weight four-arm polyethylene glycol and the utility of their thixotropic property for controlled drug release. *Colloids Surf B Biointerfaces*. 2018;165:144-149. doi: 10.1016/j.colsurfb.2018.02.032

83. Liu P, Chen W, Liu C, Tian M, Liu P. A novel poly (vinyl alcohol)/poly (ethylene glycol) scaffold for tissue engineering with a unique bimodal open-celled structure fabricated using supercritical fluid foaming. *Sci Rep*. 2019;9(1):9534. doi: 10.1038/s41598-019-46061-7

84. Labet M, Thielemans W. Synthesis of polycaprolactone: a review. *Chem Soc Rev*. 2009;38(12):3484-504. doi: 10.1039/b820162p

85. Liu G, Chen J, Wang X, Liu Y, Ma Y, Tu X. Functionalized 3D-printed ST2/gelatin methacryloyl/polcaprolactone scaffolds for enhancing bone regeneration with vascularization. *Int J Mol Sci*. 2022;23(15):8347. doi: 10.3390/ijms23158347

86. Schmitt PR, Dwyer KD, Coulombe KLK. Current applications of polycaprolactone as a scaffold material for heart regeneration. *ACS Appl Bio Mater*. 2022;5(6):2461-2480. doi: 10.1021/acsabm.2c00174

87. Khati V, Ramachandraiah H, Pati F, Svahn HA, Gaudenzi G, Russom A. 3D bioprinting of multi-material decellularized liver matrix hydrogel at physiological temperatures. *Biosensors*. 2022;12(7):521. doi: 10.3390/bios12070521

88. Chen H, Fei F, Li X, et al. A structure-supporting, self-healing, and high permeating hydrogel bioink for establishment of diverse homogeneous tissue-like constructs. *Bioact Mater*. 2021;6(10):3580-3595. doi: 10.1016/j.bioactmat.2021.03.019

89. Xu T, Jin J, Gregory C, Hickman JJ, Boland T. Inkjet printing of viable mammalian cells. *Biomaterials*. 2005;26(1):93-99. doi: 10.1016/j.biomaterials.2004.04.011

90. Mandrycky CJ, Howard CC, Rayner SG, Shin YJ, Zheng Y. Organ-on-a-chip systems for vascular biology. *J Mol Cell Cardiol*. 2021;159:1-13. doi: 10.1016/j.yjmcc.2021.06.002

91. Kolesky DB, Truby RL, Gladman AS, Busbee TA, Homan KA, Lewis JA. 3D bioprinting of vascularized, heterogeneous cell-laden tissue constructs. *Adv Mater*. 2014;26(19):3124-3130. doi: 10.1002/adma.201305506

92. Cui X, Dean D, Ruggeri ZM, Boland T. Cell damage evaluation of thermal inkjet printed Chinese hamster ovary cells. *Biotechnol Bioeng*. 2010;106(6):963-969. doi: 10.1002/bit.22762

93. Gudapati H, Dey M, Ozbolat I. A comprehensive review on droplet-based bioprinting: past, present and future. *Biomaterials*. 2016;102:20-42. doi: 10.1016/j.biomaterials.2016.06.012

94. Angelopoulos I, Allenby MC, Lim M, Zamorano M. Engineering inkjet bioprinting processes toward translational therapies. *Biotechnol Bioeng*. 2020;117(1): 272-284. doi: 10.1002/bit.27176

95. Stratesteffen H, Köpf M, Kreimendahl F, Blaeser A, Jockenhoevel S, Fischer H. GelMA-collagen blends enable drop-on-demand 3D printablility and promote angiogenesis. *Biofabrication*. 2017;9(4):045002. doi: 10.1088/1758-5090/aa857c

96. Li W, Wang M, Ma H, Chapa-Villarreal FA, Lobo AO, Zhang YS. Stereolithography apparatus and digital light processing-based 3D bioprinting for tissue fabrication. *iScience*. 2023;26(2):106039. doi: 10.1016/j.isci.2023.106039

97. Ozbolat IT, Hospodiuk M. Current advances and future perspectives in extrusion-based bioprinting. *Biomaterials*. 2016;76:321-343. doi: 10.1016/j.biomaterials.2015.10.076

98. Naghieh S, Chen X. Printability-a key issue in extrusion-based bioprinting. *J Pharm Anal*. 2021;11(5):564-579. doi: 10.1016/j.jpha.2021.02.001

99. Benwood C, Chrenek J, Kirsch RL, et al. Natural biomaterials and their use as bioinks for printing tissues. *Bioengineering*. 2021;8(2):27. doi: 10.3390/bioengineering8020027

100. Mohan TS, Datta P, Nesaei S, Ozbolat V, Ozbolat IT. 3D coaxial bioprinting: process mechanisms, bioinks and applications. *Prog Biomed Eng*. 2022;4(2):022003. doi: 10.1088/2516-1091/ac631c

101. Yu Y, Xie R, He Y, et al. Dual-core coaxial bioprinting of double-channel constructs with a potential for perfusion and interaction of cells. *Biofabrication*. 2022;14(3). doi: 10.1088/1758-5090/ac6e88

102. Ning L, Mehta R, Cao C, et al. Embedded 3D bioprinting of gelatin methacryloyl-based constructs with highly tunable structural fidelity. *ACS Appl Mater Interfaces*. 2020;12(40):44563-44577. doi: 10.1021/acsami.0c15078

103. Zhou K, Sun Y, Yang J, Mao H, Gu Z. Hydrogels for 3D embedded bioprinting: a focused review on bioinks and support baths. *J Mater Chem B*. 2022;10(12): 1897-1907. doi: 10.1039/d1tb02554f

104. Zeng X, Meng Z, He J, et al. Embedded bioprinting for designer 3D tissue constructs with complex structural organization. *Acta Biomater*. 2022;140:1-22. doi: 10.1016/j.actbio.2021.11.048

105. Li Q, Ma L, Gao Z, et al. Regulable supporting baths for embedded printing of soft biomaterials with variable stiffness. *ACS Appl Mater Interfaces*. 2022; 14(37):41695-41711. doi: 10.1021/acsami.2c09221

106. Shao L, Gao Q, Xie C, et al. Directly coaxial 3D bioprinting of large-scale vascularized tissue constructs. *Biofabrication*. 2020;12(3):035014. doi: 10.1088/1758-5090/ab7e76

107. Zheng W, Xie R, Liang X, Liang Q. Fabrication of biomaterials and biostructures based on microfluidic manipulation. *Small*. 2022;18(16):e2105867. doi: 10.1002/smll.202105867

108. Fan XY, Deng ZF, Yan YY, et al. Application of microfluidic chips in anticancer drug screening. *Bosn J Basic Med Sci*. 2022;22(3):302-314. doi: 10.17305/bjbms.2021.6484

109. Torino S, Corrado B, Iodice M, Coppola G. PDMS-based microfluidic devices for cell culture. *Inventions*. 2018;3:65. doi: 10.3390/inventions3030065

110. Yu F, Choudhury D. Microfluidic bioprinting for organ-on-a-chip models. *Drug Discov Today*. 2019;24(6):1248-1257. doi: 10.1016/j.drudis.2019.03.025

111. Yi HG, Jeong YH, Kim Y, et al. A bioprinted human-glioblastoma-on-a-chip for the identification of patient-specific responses to chemoradiotherapy. *Nat Biomed Eng*. 2019;3(7):509-519. doi: 10.1038/s41551-019-0363-x

112. Xu F, Wu J, Wang S, Durmus NG, Gurkan UA, Demirci U. Microengineering methods for cell-based microarrays and high-throughput drug-screening applications. *Biofabrication*. 2011;3(3):034101. doi: 10.1088/1758-5082/3/3/034101

113. Liang Y, Pan J, Fang Q. Research advances of high-throughput cell-based drug screening systems based on microfluidic technique. *Se Pu*. 2021;39(6):567-577. doi: 10.3724/SP.J.1123.2020.07014

114. Wu Q, Liu J, Wang X, et al. Organ-on-a-chip: recent breakthroughs and future prospects. *Biomed Eng Online*. 2020;19(1):9. doi: 10.1186/s12938-020-0752-0

115. Knowlton S, Tasoglu S. A bioprinted liver-on-a-chip for drug screening applications.*Trends Biotechnol.* 2016; 34(9):681-682. doi: 10.1016/j.tibtech.2016.05.014

116. Hoofnagle JH, Björnsson ES. Drug-induced liver injury - types and phenotypes. *N Engl J Med*. 2019;381(3):264-273. doi: 10.1056/NEJMra1816149

117. Yin L, Du G, Zhang B, et al. Efficient drug screening and nephrotoxicity assessment on co-culture microfluidic kidney chip. *Sci Rep*. 2020;10(1):6568. doi: 10.1038/s41598-020-63096-3

118. Lee H, Cho DW. One-step fabrication of an organ-on-a-chip with spatial heterogeneity using a 3D bioprinting technology. *Lab Chip*. 2016;16(14):2618-2625. doi: 10.1039/c6lc00450d

119. Lee H, Chae S, Kim JY, et al. Cell-printed 3D liver-on-a-chip possessing a liver microenvironment and biliary system. *Biofabrication*. 2019;11(2):025001. doi: 10.1088/1758-5090/aaf9fa

120. Zhang YS, Arneri A, Bersini S, et al. Bioprinting 3D microfibrous scaffolds for engineering endothelialized myocardium and heart-on-a-chip. *Biomaterials*. 2016;110:45-59. doi: 10.1016/j.biomaterials.2016.09.003

121. Lin NYC, Homan KA, Robinson SS, et al. Renal reabsorption in 3D vascularized proximal tubule models. *Proc Natl Acad Sci U S A*. 2019;116(12):5399-5404. doi: 10.1073/pnas.1815208116

122. Park JY, Ryu H, Lee B, et al. Development of a functional airway-on-a-chip by 3D cell printing. *Biofabrication*. 2018;11(1):015002. doi: 10.1088/1758-5090/aae545

123. Marino A, Tricinci O, Battaglini M, et al. A 3D real-scale, biomimetic, and biohybrid model of the blood-brain barrier fabricated through two-photon lithography. *Small*. 2018;14(6). doi: 10.1002/smll.201702959

124. Mandt D, Gruber P, Markovic M, et al. Fabrication of biomimetic placental barrier structures within a microfluidic device utilizing two-photon polymerization. *Int J Bioprint*. 2018;4(2):144. doi: 10.18063/IJB.v4i2.144

125. Kim W, Lee Y, Kang D, Kwak T, Lee H-R, Jung S. 3D inkjet-bioprinted lung-on-a-chip. *ACS Biomater Sci Eng*. 2023;9(5):2806-2815. doi: 10.1021/acsbiomaterials.3c00089

126. Li W, Zhou Z, Zhou X, et al. 3D biomimetic models to reconstitute tumor microenvironment in vitro: spheroids, organoids, and tumor-on-a-chip. *Adv Healthc Mater*. 2023;e2202609. doi: 10.1002/adhm.202202609

127. Lee H, Kim J, Choi Y, Cho D-W. Application of gelatin bioinks and cell-printing technology to enhance cell delivery capability for 3D liver fibrosis-on-a-chip development. *ACS Biomater Sci Eng*. 2020;6(4):2469-2477. doi: 10.1021/acsbiomaterials.9b01735

128. Nothdurfter D, Ploner C, Coraça-Huber DC, et al. 3D bioprinted, vascularized neuroblastoma tumor environment in fluidic chip devices for precision medicine drug testing. *Biofabrication*. 2022;14(3). doi: 10.1088/1758-5090/ac5fb7

129. Zhang YS, Davoudi F, Walch P, et al. Bioprinted thrombosis-on-a-chip. *Lab Chip*. 2016;16(21):4097-4105. doi: 10.1039/c6lc00380j

130. Huang CBX, Tu TY. Recent advances in vascularized tumor-on-a-chip. *Front Oncol*. 2023;13:1150332. doi: 10.3389/fonc.2023.1150332

131. Mi S, Yang S, Liu T, et al. A novel controllable cell array printing technique on microfluidic chips. *IEEE Trans Biomed Eng*. 2019;66(9):2512-2520. doi: 10.1109/TBME.2019.2891016

132. Jameson JL, Longo DL. Precision medicine--personalized, problematic, and promising. *N Engl J Med*. 2015;372(23):2229-2234. doi: 10.1056/NEJMsb1503104

133. van Riet S, van Schadewijk A, Khedoe PPSJ, et al. Organoid-based expansion of patient-derived primary alveolar type 2 cells for establishment of alveolus epithelial lung-chip cultures. *Am J Physiol Lung Cell Mol Physiol*. 2022;322(4):L526-L538. doi: 10.1152/ajplung.00153.2021

134. Haque MR, Wessel CR, Leary DD, Wang C, Bhushan A, Bishehsari F. Patient-derived pancreatic cancer-on-a-chip recapitulates the tumor microenvironment. *Microsyst Nanoeng*. 2022;8:36. doi: 10.1038/s41378-022-00370-6

135. Hu Y, Sui X, Song F, et al. Lung cancer organoids analyzed on microwell arrays predict drug responses of patients within a week. *Nat Commun*. 2021;12(1):2581. doi: 10.1038/s41467-021-22676-1

136. Fan H, Demirci U, Chen P. Emerging organoid models: leaping forward in cancer research. *J Hematol Oncol*. 2019;12(1):142. doi: 10.1186/s13045-019-0832-4

137. Lee SH, Sung JH. Organ-on-a-chip technology for reproducing multiorgan physiology. *Adv Healthc Mater*. 2018;7(2). doi: 10.1002/adhm.201700419

138. Shinha K, Nihei W, Ono T, Nakazato R, Kimura H. A pharmacokinetic-pharmacodynamic model based on multi-organ-on-a-chip for drug-drug interaction studies. *Biomicrofluidics*. 2020;14(4):044108. doi: 10.1063/5.0011545

139. Ronaldson-Bouchard K, Teles D, Yeager K, et al. A multi-organ chip with matured tissue niches linked by vascular flow. *Nat Biomed Eng*. 2022;6(4):351-371. doi: 10.1038/s41551-022-00882-6

140. Li ZA, Tuan RS. Towards establishing human body-on-a-chip systems. *Stem Cell Res Ther*. 2022;13(1):431. doi: 10.1186/s13287-022-03130-5

141. Ingber DE. Human organs-on-chips for disease modelling, drug development and personalized medicine. *Nat Rev Genet*. 2022;23(8):467-491.

doi: 10.1038/s41576-022-00466-9

142. van Hasselt JGC, Iyengar R. Systems pharmacology: defining the interactions of drug combinations. *Annu Rev Pharmacol Toxicol*. 2019;59:21-40.
doi: 10.1146/annurev-pharmtox-010818-021511

143. Wan L, Yin J, Skoko J, et al. 3D collagen vascular tumor-on-a-chip mimetics for dynamic combinatorial drug screening. *Mol Cancer Ther*. 2021;20(6):1210-1219.
doi: 10.1158/1535-7163.MCT-20-0880

ACCSCIENCE PUBLISHING

International Journal of Bioprinting

RESEARCH ARTICLE

Polydopamine chelating strontium on graphene oxide enhances the mechanical and osteogenic induction properties of PLLA/PGA bone scaffold

Feng Yang[1†], Yun Lin[1†], Saipu Shen[1], Yulong Gu[1], Cijun Shuai[1,2,3*], and Pei Feng[1*]

[1]State Key Laboratory of Precision Manufacturing for Extreme Service Performance, College of Mechanical and Electrical Engineering, Central South University, Changsha, Hunan, China

[2]Institute of Additive Manufacturing, Jiangxi University of Science and Technology, Nanchang, Jiangxi, China

[3]College of Mechanical Engineering, Xinjiang University, Urumqi, Xinjiang, China

Abstract

Poly (lactic acid)/poly (glycolic acid) (LG) bone scaffold exhibits good biocompatibility for bone defect regeneration but lacks satisfactory mechanical and osteogenic induction properties. Here, graphene oxide (GO) was encapsulated by polydopamine (PDA) via self-polymerization of dopamine, and strontium (Sr) was loaded onto GO by the chelation of PDA. The modified GO was added to the LG scaffold prepared via selective laser sintering as a reinforcing phase to improve the mechanical properties and osteogenic induction properties. The results indicated that the tensile and compressive strengths of the scaffold with 1.5 wt% modified GO were 9.49 MPa and 19.22 MPa, respectively, representing 67.08% and 95.33% improvement compared to the LG scaffold. The enhancement mechanisms of the modified GO in the scaffold included crack branching, crack deflection, crack pinning, crack bridging, and pulling out. More importantly, the scaffold with modified GO exhibited superior bioactivity and osteogenic induction properties compared to the LG scaffold, because PDA could chelate calcium ions derived from the surrounding physiological environment, and the calcium ions attracted phosphate ions through electrostatic interactions to promote the apatite layer deposition. Additionally, the presence of Sr in the scaffold promoted the proliferation and differentiation of osteoblasts, thereby improving osteogenic induction properties.

Keywords: Graphene oxide; Polydopamine, Strontium; Mechanical properties; Osteogenic induction properties

[†]These authors contributed equally to this work.

***Corresponding authors:**
Cijun Shuai
(shuai@csu.edu.cn)

Pei Feng
(fengpei@csu.edu.cn)

Citation: Yang F, Lin Y, Shen S, Gu Y, Shuai C, Feng P. Polydopamine chelating strontium on graphene oxide enhances the mechanical and osteogenic induction properties of PLLA/PGA bone scaffold. *Int J Bioprint*. 2024;10(3):1829. doi: 10.36922/ijb.1829

Received: September 13, 2023
Accepted: November 17, 2023
Published Online: January 12, 2024

Copyright: © 2024 Author(s). This is an Open Access article distributed under the terms of the Creative Commons Attribution License, permitting distribution, and reproduction in any medium, provided the original work is properly cited.

Publisher's Note: AccScience Publishing remains neutral with regard to jurisdictional claims in published maps and institutional affiliations.

1. Introduction

Graphene oxide (GO) as a reinforcing material of biopolymer bone scaffold has attracted extensive attention because of its excellent mechanical properties as well as good biocompatibility for cell adhesion and proliferation.[1-5] Poly (lactic acid) (PLLA)/poly (glycolic acid) (PGA) (named LG) composite bone scaffold obtained by blending PLLA with PGA is endowed with good biocompatibility and a suitable degradation rate.[6-10] Besides, the mechanical properties of the LG scaffold can be enhanced by

adding GO.[11,12] In addition to mechanical properties, bone scaffolds should possess the ability of osteogenic induction, which is instrumental for promoting bone regeneration and remodeling.[13-16] However, the LG scaffold lacks the osteogenic induction ability, which limits further application in bone defect repair.[17,18]

Bioactive substances, such as bone morphogenetic proteins and fibroblast growth factors, have been directly added into bone scaffold to enhance the osteogenic induction properties because of their ability to promote osteoblast proliferation and differentiation.[19,20] Jarrar et al. have demonstrated that the released osteogenic protein from the chitosan/hydroxyapatite scaffold doped with osteogenic protein and melatonin induced the differentiation of undifferentiated mesenchymal stem cells to osteogenic cells, enhancing their proliferation capacity and promoting osteogenic cell maturation.[21] The released melatonin facilitated the differentiation of osteoblast progenitor cells and inhibited osteoclast differentiation by increasing the expression of bone protective factors. Nevertheless, the utilization of these bioactive substances is subject to certain limitations, including high cost, short half-life, and potential side effects.[22]

Certain metallic elements existing in natural bone, such as zinc, copper, calcium, magnesium, and strontium (Sr), can endow straightforward therapeutic signals for bone regeneration and play a decisive role in the regulation of osteogenic induction properties.[23-25] It has been reported that magnesium could promote osteoblast differentiation, while high concentrations of magnesium ions could impair osteoblast activity and contribute to bone disease, thus limiting its application.[26] Zinc and copper possess both antibacterial and osteogenic effects but are toxic to cells.[27,28] Sr has been found to promote osteogenic cell differentiation and exert stimulatory effect on bone formation and inhibitory effect on bone resorption.[29] Some of the Sr compounds, such as strontium citrate and strontium ranelate, are currently employed in osteoporosis treatment due to their desirable therapeutic efficacy.[30-32] The incorporation of Sr into bone tissue engineering materials can enhance the osteogenic activity of scaffold.[30,33] For example, Zhao et al. demonstrated that strontium-doped three-dimensional (3D) hydroxyapatite whiskers exhibited better bone regeneration compared with pure hydroxyapatite.[33] Polydopamine (PDA), a biomimetic polymer formed by the spontaneous oxidation and self-polymerization of dopamine (DA) in alkaline conditions, can chelate metal ions owing to the phenolic hydroxyl groups. Using PDA with excellent adhesion ability and excellent biocompatibility as a bridge to immobilize metal ions on GO has been shown to be an effective and suitable approach.[34,35] In another example, Xie et al. improved the antibacterial ability of cellulose by coating PDA, and then loading silver ions through the chelation of PDA.[36] Therefore, Sr^{2+} can be loaded onto GO by encapsulating PDA on GO and utilizing the chelating properties of PDA.

In this study, GO was encapsulated by PDA (named GP) in order to immobilize Sr (named GPSr), and then added into the LG scaffold prepared via selective laser sintering (SLS) to enhance both mechanical properties and osteogenic induction properties. Fourier transform infrared spectroscopy (FTIR) and X-ray photoelectron spectroscopy (XPS) were conducted to characterize the chemical structure and functional groups of the modified GO. Tensile and compression tests were carried out on composite scaffolds with different proportions of modified GO, and the mechanical enhancement mechanism of the scaffolds was analyzed. Finally, the bioactivity, cytocompatibility, and osteogenic induction properties of the scaffolds with and without the addition of modified GO were evaluated by simulated body fluid (SBF) immersion test and *in vitro* biological experiments.

2. Materials and methods

2.1. Materials

PGA (Mw: 150 kDa) was procured from Shenzhen Polymtek Biomaterial Co., Ltd. (Shenzhen, China). PLLA (Mw: 260 kDa) was supplied by Jinan Daigang Biomaterial Co., Ltd. (City, Country). GO (TNGO-3) was obtained from Chengdu Organic Chemicals Co., Ltd. (Chengdu, China). DA hydrochloride (Mw: 189.64 Da, purity: >99%), $SrCl_2 \cdot 6H_2O$ (Mw: 266.62 Da), penicillin/streptomycin antibiotics, glutaraldehyde, calcein-AM, propidium iodide, diaminidine phenyl indole (DAPI), and deionized water were purchased from Aladdin Technology Co., Ltd. (Shanghai, China). Tris-HCl buffer (1 mol/L) and NaOH standard solution (1 mol/L) were obtained from Phygene Biotechnology Co., Ltd. (Fuzhou, China). Bone marrow stromal cells (BMSCs) were obtained from Xiangya Medical College (Changsha, China). Simulated body fluid, Dulbecco's Modified Eagle's Medium (DMEM), fetal bovine serum (FBS), and phosphate-buffered saline (PBS) were supplied by Mediatech, Inc. (Virginia, USA).

2.2. Preparation of GPSr powder

The process for preparing GPSr powder is displayed in Figure 1a. First, 50 mg GO was dispersed in 50 mL diluted Tris-HCl buffer (10 mmol/L) by ultrasound for 1 h for obtaining a homogeneous suspension. DA hydrochloride (200 mg) was then mixed into the suspension, and pH was controlled at 8.5 followed by magnetic stirring for 24 h. At this time, DA would undergo self-polymerization reaction to form PDA, and there was π-π interaction between PDA and GO, which caused PDA to encapsulate GO.[37,38] The

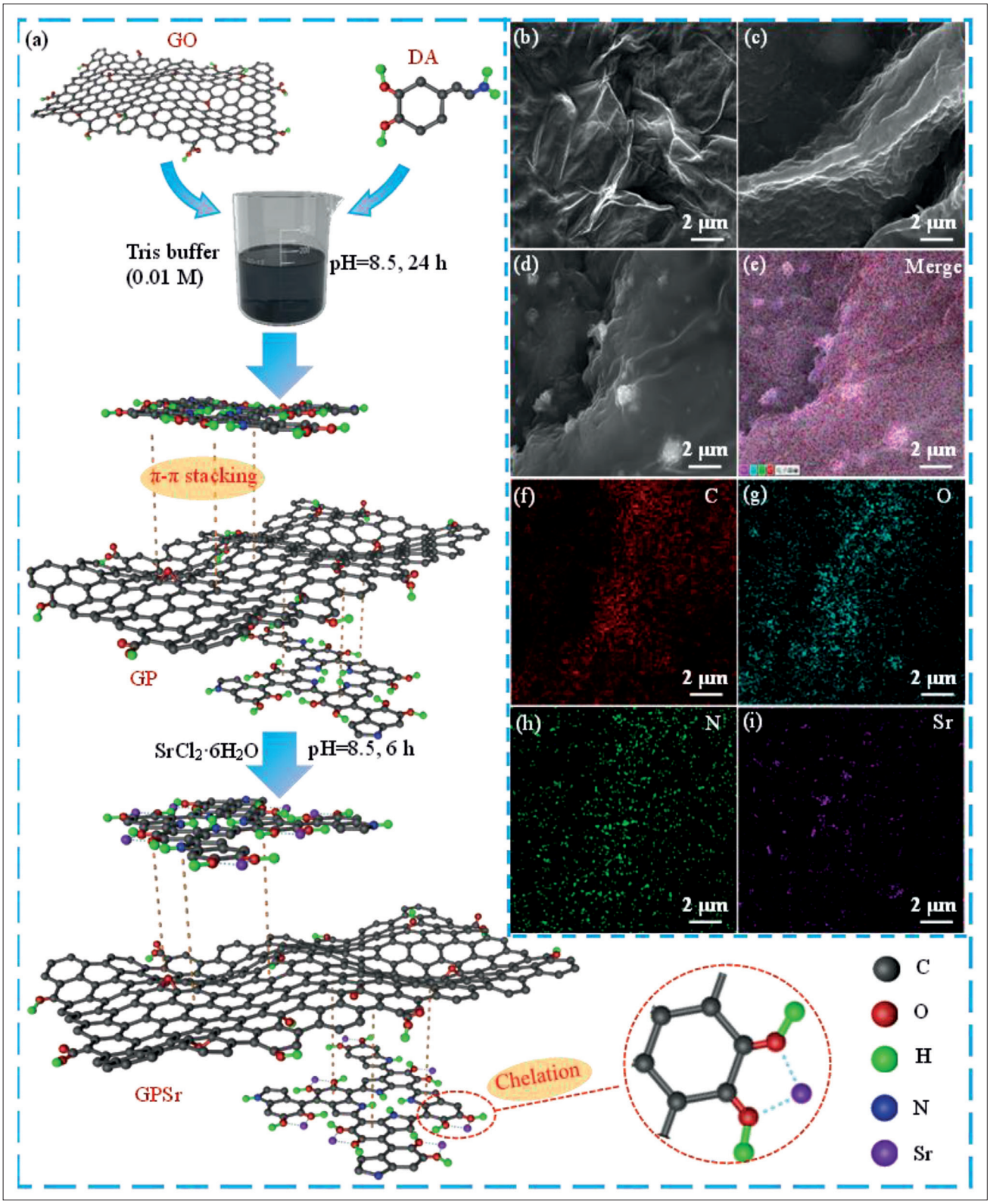


Figure 1. Schematic diagram of the preparation process and mechanism of GPSr (a); SEM images of GO (b), GP (c), and GPSr (d); EDS element mapping of C, O, N, and Sr in GPSr (e–i).

suspension was fully stratified after being centrifuged to obtain a solid product. The product was rinsed five times with deionized water for removing excess DA, and then the GO encapsulated in PDA (i.e., GP) was harvested by drying at 50°C. Subsequently, 50 mg GP was dispersed in 100 mL deionized water to obtain a homogeneous suspension. $SrCl_2 \cdot 6H_2O$ (2 g) was added with pH controlled at 8.5 followed by magnetic stirring for 6 h, and Sr was loaded onto GO by the chelation of phenolic hydroxyl groups in PDA.[39,40] The suspension was subjected to centrifugation followed by rinsing five times to remove the excess $SrCl_2$. Finally, the GPSr powder was harvested after drying at 50°C for 48 h.

2.3. Fabrication of GO-PDA-Sr/PLLA/PGA scaffold

The composite scaffolds with different GPSr contents (0% GPSr, 0.5% GPSr, 1% GPSr, 1.5% GPSr, and 2% GPSr) were fabricated, with PLLA and PGA in a weight proportion of 70:30. Take scaffold with 0.5% GPSr as an example, 0.5% GPSr was ultrasonically dispersed in deionized water for 30 min, and then PLLA and PGA were added, followed by stirring. The composite powder was obtained after the mixture had been filtered and dried, and was denoted as LG/GPSr0.5 powder.

LG/GPSr0.5 scaffold was prepared using laser sintering of the LG/GPSr0.5 composite powder according to the geometry of the layers using the SLS system built in the laboratory.[41-46] The preparation parameters of the scaffold were as follows: the thickness of the powder layer of 200 μm, laser power of 6.0 W, scanning speed of 80 mm/s, and scanning distance of 80 μm. Several other composite scaffolds with the addition of the 0% GPSr, 1% GPSr, 1.5% GPSr, and 2% GPSr were fabricated according to a similar procedure, and were denoted as LG, LG/GPSr1, LG/GPSr1.5, and LG/GPSr2, respectively. Accordingly, the scaffolds produced in this work were categorized, based on the GPSr contents, into five groups: LG, LG/GPSr0.5, LG/GPSr1, LG/GPSr1.5, and LG/GPSr2.

2.4. Characterization of specimens

The micromorphologies of the GO and GPSr and their distribution in the scaffold were observed using scanning electron microscopy (SEM) coupled to an energy dispersive spectrometer (EDS) (Tescan Mira4, Tescan, Brno, the Czech Republic) at 20 kV. The chemical structures of the GO, GP, and GPSr were characterized by FTIR (Nicolet iS50, Nicolet, Wisconsin, USA) in the range of 500–4000 cm^{-1}. The surface elemental characterization was recorded by XPS (Thermo ESCALAB 250XI, Thermo Fisher Scientific, Massachusetts, USA). The tensile and compressive properties of the scaffolds containing different amounts of GPSr were investigated according to GB/T 528-2009 and GB/T 7757-2009 standards, respectively.[47,48] The crack in the specimens was made by an automatic Vickers hardness tester (Tukon 2500, Massachusetts) at the load of 9.8 N, and then observed with SEM to study the crack propagation.

2.5. Evaluation of *in vitro* bioactivity

The *in vitro* bioactivity of the scaffolds containing GP and GPSr, respectively, was tested by immersing the specimens in SBF solution and compared with the original LG scaffold. The square specimens of 10 × 10 × 3 mm^3 were fabricated for *in vitro* bioactivity testing. The temperature of the specimens in the SBF solution, which was replaced daily, maintained at 36.5°C. After being soaked for 21 days, the specimens were removed from the SBF solution and immediately rinsed with deionized water, followed by vacuum drying for 24 h. The surface morphologies and chemical compositions of the specimens after immersion in SBF were examined by means of SEM-EDS analysis.

2.6. Evaluation of *in vitro* cytocompatibility and osteogenic properties

Adhesion and proliferation of BMSCs on the scaffolds were investigated. They were cultured in DMEM supplemented with 10% FBS and 1% penicillin/streptomycin in an atmosphere of 5% CO_2 at 37°C for 7 days, with medium changes occurring every 2 days. The specimens were placed horizontally in 24-well culture plates after being sterilized by using 70% ethanol for 30 min combined with exposure to ultraviolet light for another 20 min. BMSCs were seeded on the specimens at a density of 4 × 10^4 cells/mL in an atmosphere of 5% CO_2 at 37°C. After cultivation for 1, 3, and 5 days, the inoculated scaffolds were fixed in 2.5% glutaraldehyde and then dehydrated in graded ethanol. All five specimens in each scaffold group were subjected to cell morphology examination performed with the use of SEM, and the relative cell adhesion area was calculated for each specimen by determining the ratio of cell adhesion area to the image area, which was measured using Photoshop software.

After culturing for 1, 3, and 5 days, each specimen was added with calcein-AM and propidium iodide for analyzing cell viability and visualized using a fluorescence microscope (TE2000U, Nikon). Cell density of five specimens per group containing was calculated by determining the ratio of the number of viable cells to the image area.

For the evaluation of the *in vitro* osteogenic properties of scaffolds, the BMSCs were seeded into 24-well plates and co-cultured with LG and LG/GPSr1.5 scaffolds in an osteogenic induction medium containing 10 nmol dexamethasone, 10 mmol sodium glycerophosphate, and 50 μg/mL ascorbic acid, with medium changes occurring every 2 days. Alkaline phosphatase (ALP) staining was performed after culturing for 7 days, and then the optical density (OD) value

was determined. In addition, BMSCs were fixed with 4% paraformaldehyde, washed with PBS, and permeated with 0.1% v/v Triton X-100. After washing, non-specific binding was blocked by 10% goat serum solution (Invitrogen, Massachusetts, USA).)Osteocalcin polyclonal antibody (OCN; 1:200 dilution; no. PA5-96529, Thermo Fisher Scientific, Massachusetts, USA) and osteopontin (OPN; 1:1000 dilution; ab8448, Abcam, Cambridge, England) were added and incubated overnight. Subsequently, a fluorescent secondary antibody (ab150115, Abcam, Cambridge, England) was added, and the nuclei were stained with DAPI. Finally, BMSCs were observed with laser scanning confocal microscopy (LSCM; Zeiss, Jena, Germany) followed by qualitative analysis using Image 6.0 software.

2.7. Statistical analysis

In this study, all experiments were repeated five times, unless otherwise noted, and the obtained data are expressed as mean ± standard deviation. The Statistical Product and Service Solutions (SPSS) software was employed to analyze the experimental data. Differences with $p < 0.05$ and $p < 0.01$ were regarded as statistically significant and very significant, respectively.

3. Results and discussion

The surface morphologies of GO, GP, and GPSr were visualized using SEM at the accelerated voltage of 20 kV. As shown in Figure 1b–d, the smooth surface of GO was accompanied by an obvious wrinkled structure, while the GP surface was rough due to a layer of PDA attachment. Numerous particles were observed on the surface of GPSr, possibly being the chelated Sr by PDA. In order to further confirm the existence of PDA and Sr on GO, the element analysis of GPSr was carried out by EDS. The corresponding element mappings of C, O, N, and Sr elements were recorded, and the results are shown in Figure 1e–i. It could be found that N and Sr elements appeared in addition to C and O elements, which GO originally had, and were uniformly distributed in GPSr. This indicated that the Sr were successfully loaded on GO encapsulated by PDA.

The chemical structures of GO, GP, and GPSr were evaluated by FTIR spectroscopy, as shown in Figure 2a. For the spectrum of GO, a strong band at 3407 cm^{-1} could be indicative of O-H in GO, while peaks at 1728, 1630, 1406, and 1080 cm^{-1} correspond to C=O, C=C, C-OH, and C-O in GO, respectively.[49,50] Regarding the spectrum of GP, the peak of C=O in GO disappeared, indicating that the carboxyl group in GO was consumed during the encapsulation process of PDA.[51] Two new peaks emerged at 1574 and 1192 cm^{-1}, indicating N-H shear vibration and C-N stretching vibration in PDA, respectively.[52] This proved that GO had been successfully encapsulated by PDA. The spectrum of GPSr was similar to that of GP, which indicated that some functional groups, including N-H and C-N, still existed after Sr was chelated onto GP. However, the peak of C-OH at 1406 cm^{-1} almost disappeared, probably caused by the chelation of Sr^{2+}.[53] XPS was employed to study the elemental compositions and chemical structures of GO, GP, and GPSr, and the results are demonstrated in Figure 2b–f. Two typical peaks of GO, i.e., C1s and O1s, could be observed in the full spectrum. Compared with GO, the full spectrum of GP and GPSr revealed a new peak of N1s and two of N1s and Sr3d, respectively. The C1s spectrum was fitted, and the binding energies were determined at 289.68, 288.60, 286.73, 284.74, and 283.58 eV for GO, which correlated with C(O)OH, C=O, C-O, C=C/C-C, and C-H, respectively.[54,55] A new peak was found at 287.44 eV, corresponding to C-N, which was formed due to the attached PDA for GPSr. The N1s in GPSr could be fitted to three peaks with binding energies at 401.85, 400.10, and 398.68 eV. The first two were associated with NH-C=O and N-H, respectively, which were generated by the amine group in PDA.[56] The peak at 398.68 eV corresponded to -N=, which was generated by the pyridine-like structure in PDA.[57] The above results indicated that PDA was attached to GO in GPSr. In addition, high-resolution XPS scans of Sr3d region in GPSr displayed $Sr3d_{3/2}$ and $Sr3d_{5/2}$ peaks at 135.94 and 134.17 eV, respectively, which further demonstrated the presence of GPSr.[58]

The scaffolds were fabricated by SLS, and the designed model with the fabricated scaffold is displayed in Figure 3a–c. The scaffolds were designed based on the hierarchical porous structure of natural bone.[59,60] Specifically, the scaffold presented as a cylinder with a dimension of 11 mm (Φ) × 3 mm (h) combined with the interpenetrating pores in a size ranging from 0.7 to 1.2 mm, which has been reported to be beneficial for cell adhesion and growth.[61] Tensile and compressive properties of LG scaffolds with different content of GPSr were tested, as demonstrated in Figure 3c–h. LG scaffold exhibited 5.68 MPa in tensile strength and found that LG/GPSr0.5 scaffold exhibited significantly higher tensile strength than the LG scaffold. As the GPSr content increased, the tensile strength of scaffolds gradually increased until the GPSr content reached 1.5 wt%. The LG/GPSr1.5 exhibited 9.49 MPa in tensile strength, surpassing that of LG scaffold by 67.08%. But the tensile strength of LG/GPSr2 scaffold was 8.59 MPa in tensile strength, which was lower compared with that of LG/GPSr 1.5 scaffold. Compressive properties of scaffolds with different content of GPSr showed a similar trend to that of tensile properties. The LG/GPSr1.5 exhibited 19.22 MPa in compressive strength, which was 95.33% higher than that of the LG scaffold. It could be concluded from the above test results that the addition of GPSr to the LG scaffold could significantly improve its

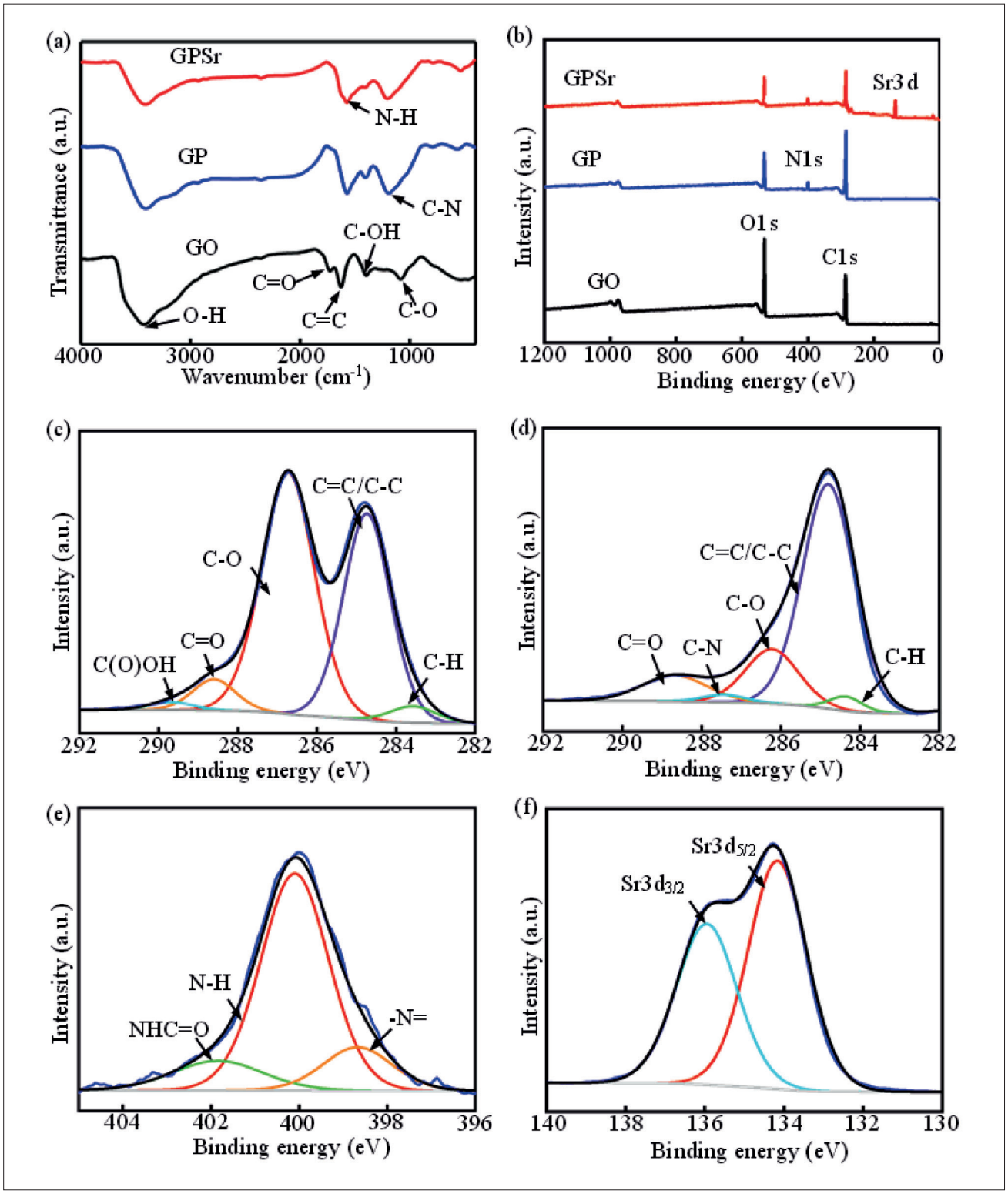


Figure 2. FTIR spectra of GO, GP, and GPSr (a); full XPS spectra of GO, GP, and GPSr (b); C1s XPS spectra of GO (c); C1s (d), N1s (e), and Sr3d (f) XPS spectra of GPSr.

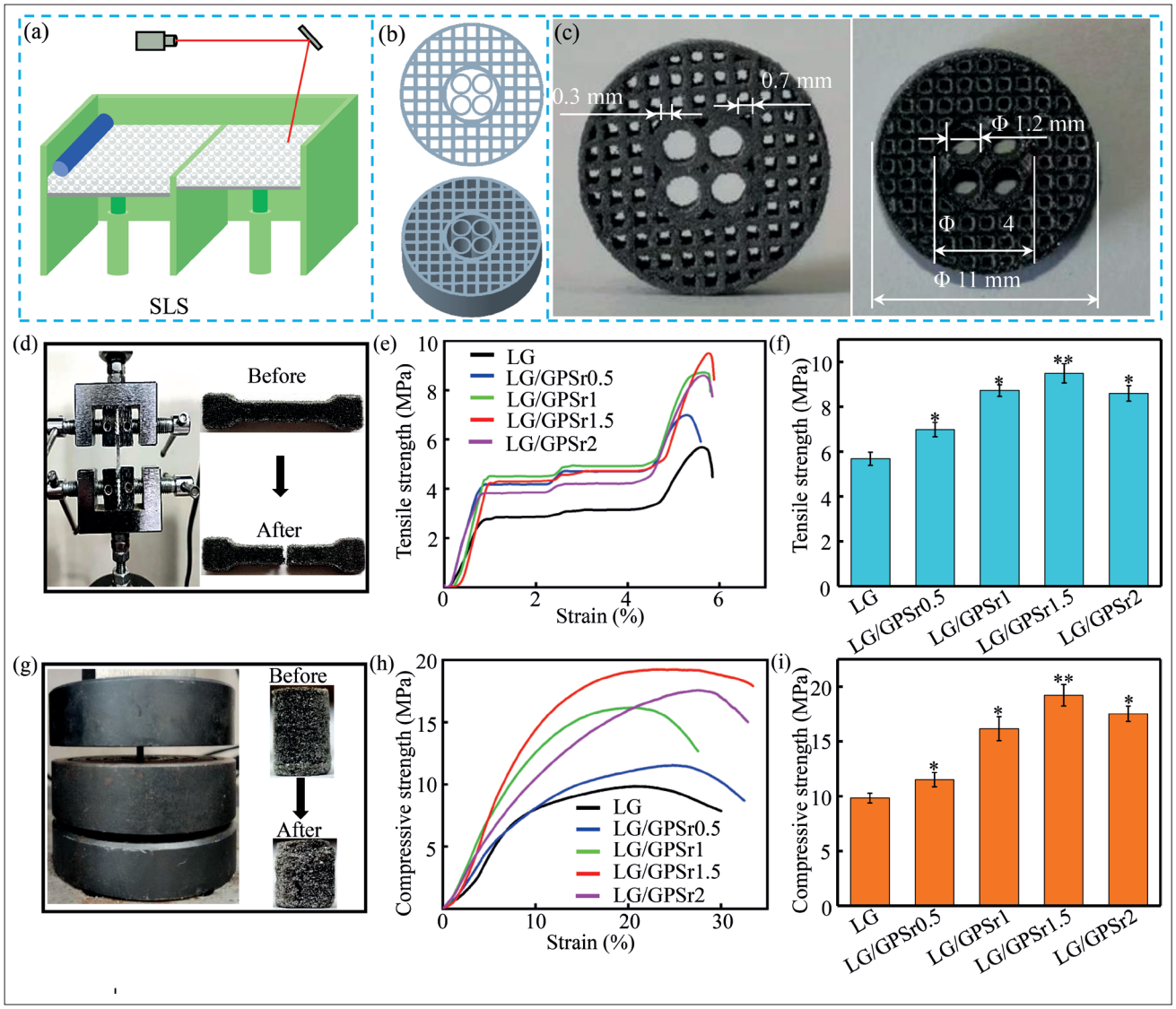


Figure 3. Schematic illustration of SLS (a), the designed model (b), and the scaffold fabricated by SLS (c). Tensile testing (d), tensile strength–strain curves (e), and tensile strengths of all tested scaffold groups (f). Compression testing (g), compressive strength–strain curves (h), and compressive strengths of all tested scaffold groups (i).

mechanical properties, which was mainly attributed to the excellent mechanical properties of GO.[62] Meanwhile, the improvement of mechanical properties was associated with the content of GPSr.

The enhancement in mechanical properties of the scaffold resulting from the nanofiller was also related to its dispersion in the matrix. As depicted in Figure 4a–e, the dispersion of different contents of GPSr in the LG scaffold was explored using SEM. The LG scaffold exhibited a smooth and clean surface, while GPSr was found on the surfaces of the LG/GPSr0.5, LG/GPSr1, and LG/GPSr1.5 scaffolds. GPSr was well dispersed on these scaffolds without agglomeration, and the observed GPSr increased with increasing content of GPSr in the scaffolds. However, GPSr observed on the LG/GPSr2 scaffold showed obvious aggregation, which justifies the weakening mechanical properties of the LG/GPSr2 scaffold.[63]

To further study the mechanism underlying the enhancement of scaffold mechanical properties by GPSr, LG and LG/GPSr1.5 scaffolds were subjected to crack expansion induced by an automatic Vickers hardness tester at the load of 9.8 N, and the generated crack expansion was observed by SEM. As shown in Figure 4f–i, the crack generated in the LG scaffold passed straight through the scaffold, while the crack was hindered by GPSr in the LG/GPSr1.5 scaffold. Phenomena such as

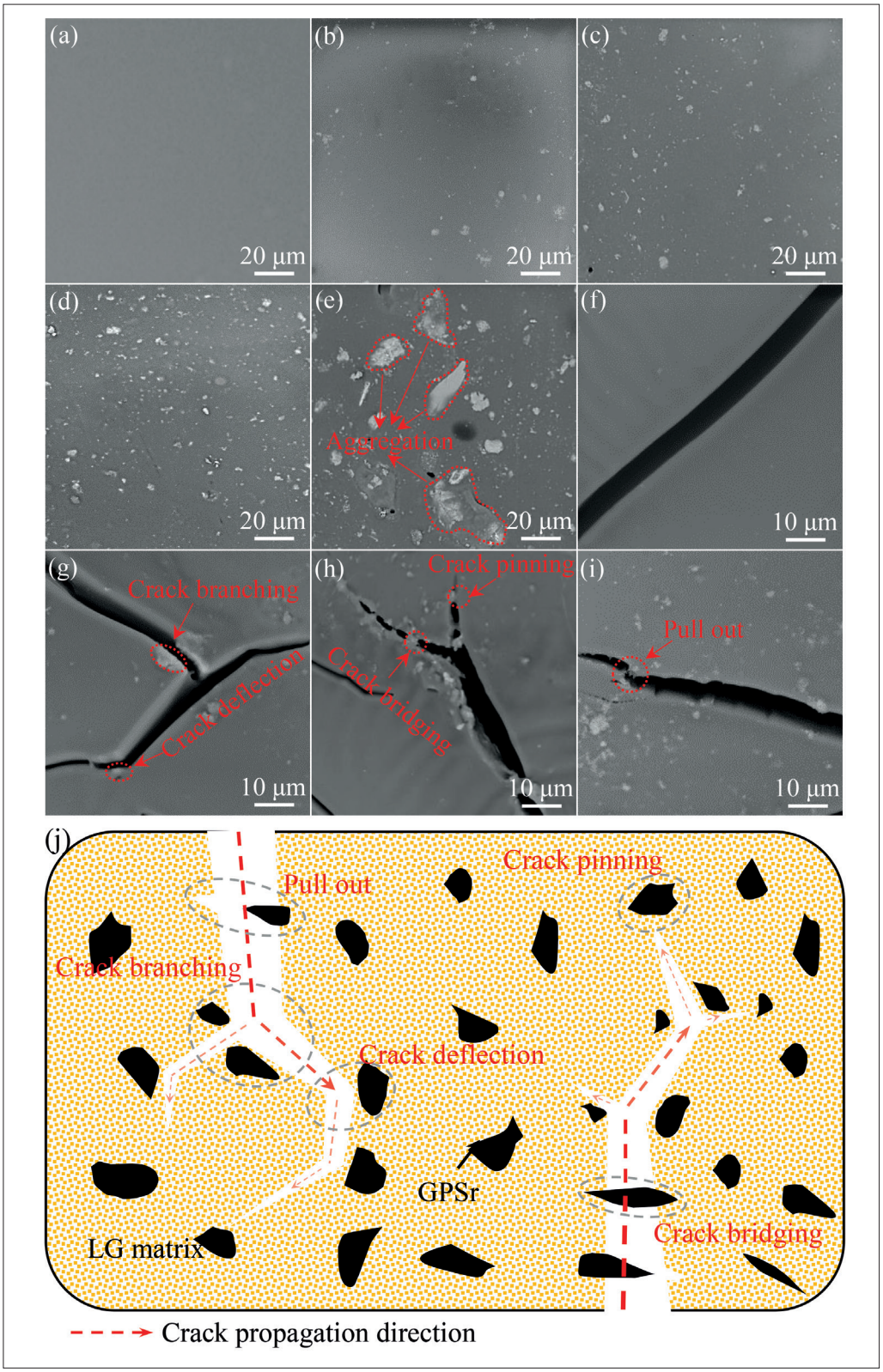


Figure 4. The dispersion of GPSr in the LG (a), LG/GPSr0.5 (b), LG/GPSr1 (c), LG/GPSr1.5 (d), and LG/GPSr2 (e) scaffolds observed under SEM; SEM images showing crack propagation in LG scaffold (f) and LG/GPSr1.5 scaffold (g–i); schematic diagram of crack propagation model in the LG/GPSr1.5 scaffold (j).

crack branching, crack deflection, crack pinning, crack bridging, and pulling out also occurred, eventually preventing the crack from expanding further.[64-67] The specific enhancement mechanism was shown in Figure 4j. Crack bridging and pulling out occurred when the crack passed through GPSr, which could slow down the rupture of the LG scaffold. When the crack propagated in the LG/GPSr1.5 scaffold, the crack was deflected and branched due to the blocking of GPSr in the LG scaffold. The zigzag path for crack propagation was created by crack deflection, which could significantly increase the energy dissipation; however, more energy is required to further propagate the crack after branching. At the same time, GPSr could prevent further crack propagation by pinning at the crack propagation tip. Ultimately, the above mechanism effectively slowed down the fracture of the LG scaffold and improved mechanical properties.

SBF immersion experiment was conducted to investigate the *in vitro* biological activity of the LG/GP and LG/GPSr1.5 scaffolds, which was compared with that

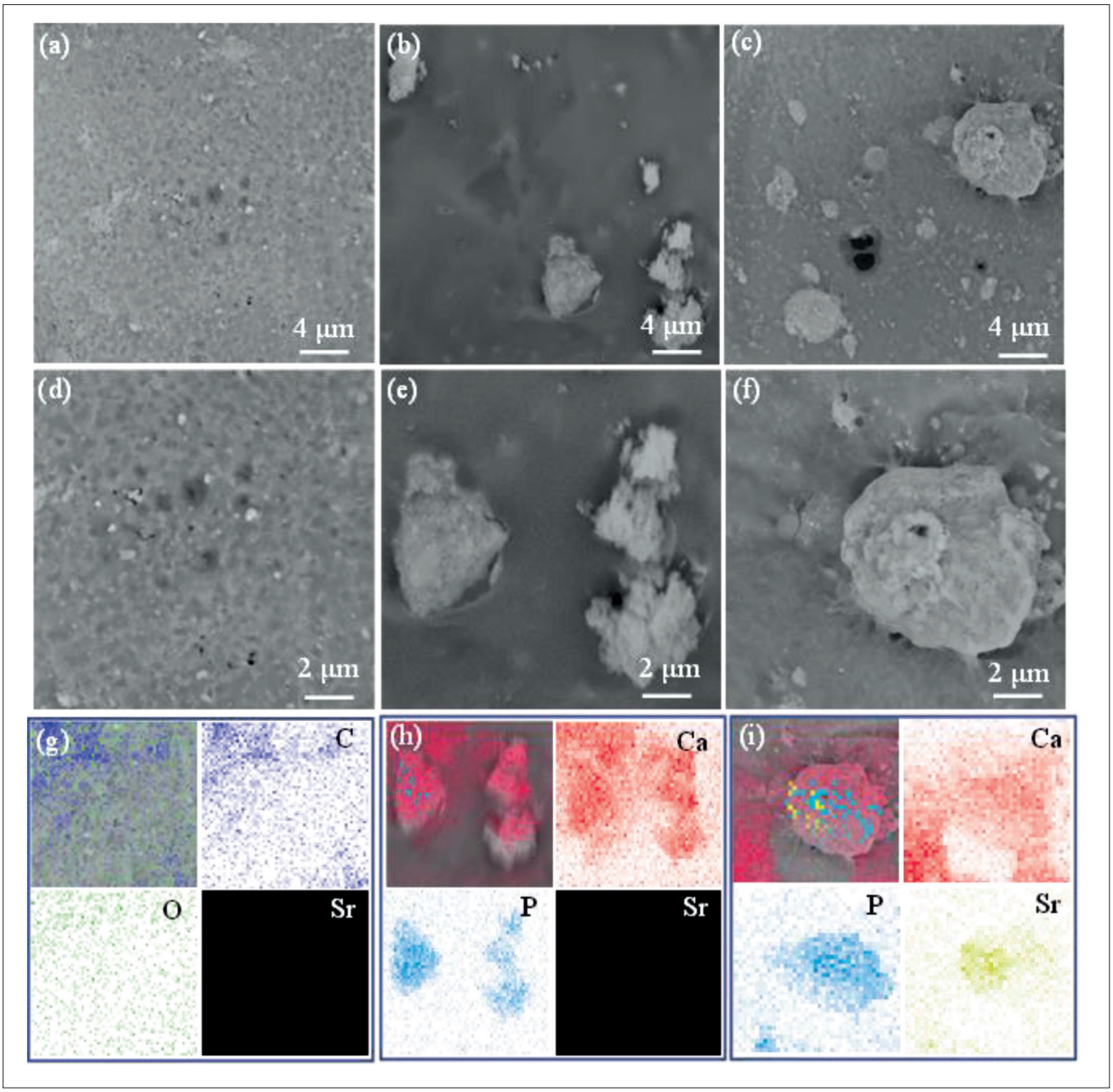


Figure 5. Surface morphology of the LG (a), LG/GP (b), and LG/GPSr1.5 scaffolds (c) immersed in SBF for 21 days, and their corresponding high-magnification images (d, e); EDS element mapping of the LG (g), LG/GP (h), and LG/GPSr1.5 (i) scaffolds.

of the LG scaffold. As shown in Figure 5a–f, the surface of the scaffolds showed small holes due to degradation. There were a number of particles on the surface of the LG/GP and LG/GPSr1.5 scaffolds, which might be the apatite layer deposition generated during immersion in SBF. The elemental composition of the scaffolds after SBF immersion was analyzed by EDS, as shown in Figure 5g–i. It was found that the deposition on the surface of the LG/GP and LG/GPSr1.5 scaffolds was mainly composed of Ca and P elements. This indicated that calcium and phosphorus crystals grew on the surface of the LG/GP and LG/GPSr1.5 scaffolds after immersion in SBF, because of the presence of PDA in scaffold, which was considered to be an effective promoting factor for apatite deposition under physiological conditions.[68,69] The phenolic hydroxyl groups in PDA could sequester Ca^{2+} from SBF solution and subsequently attract PO_4^{3-} to form the apatite layer deposition.[70] At the same time, Sr element was also detected in the apatite layer deposition on the surface of the LG/GPSr1.5 scaffold, indicating that Sr partially replaced Ca in the apatite layer.[71] The above results showed that the LG/GPSr1.5 scaffold had good bioactivity.

A scaffold should have good cytocompatibility, an attribute important for promoting cell growth and proliferation without triggering an immune response. The cytocompatibility of the LG/GPSr1.5 scaffold was tested and compared with that of the LG scaffold. BMSCs were inoculated on the two kinds of scaffolds, and morphology of the cells cultured for 1, 3, and 5 days was visualized using SEM. The cells had good adhesion and extension on the surface of both LG and LG/GPSr1.5 scaffolds, as shown

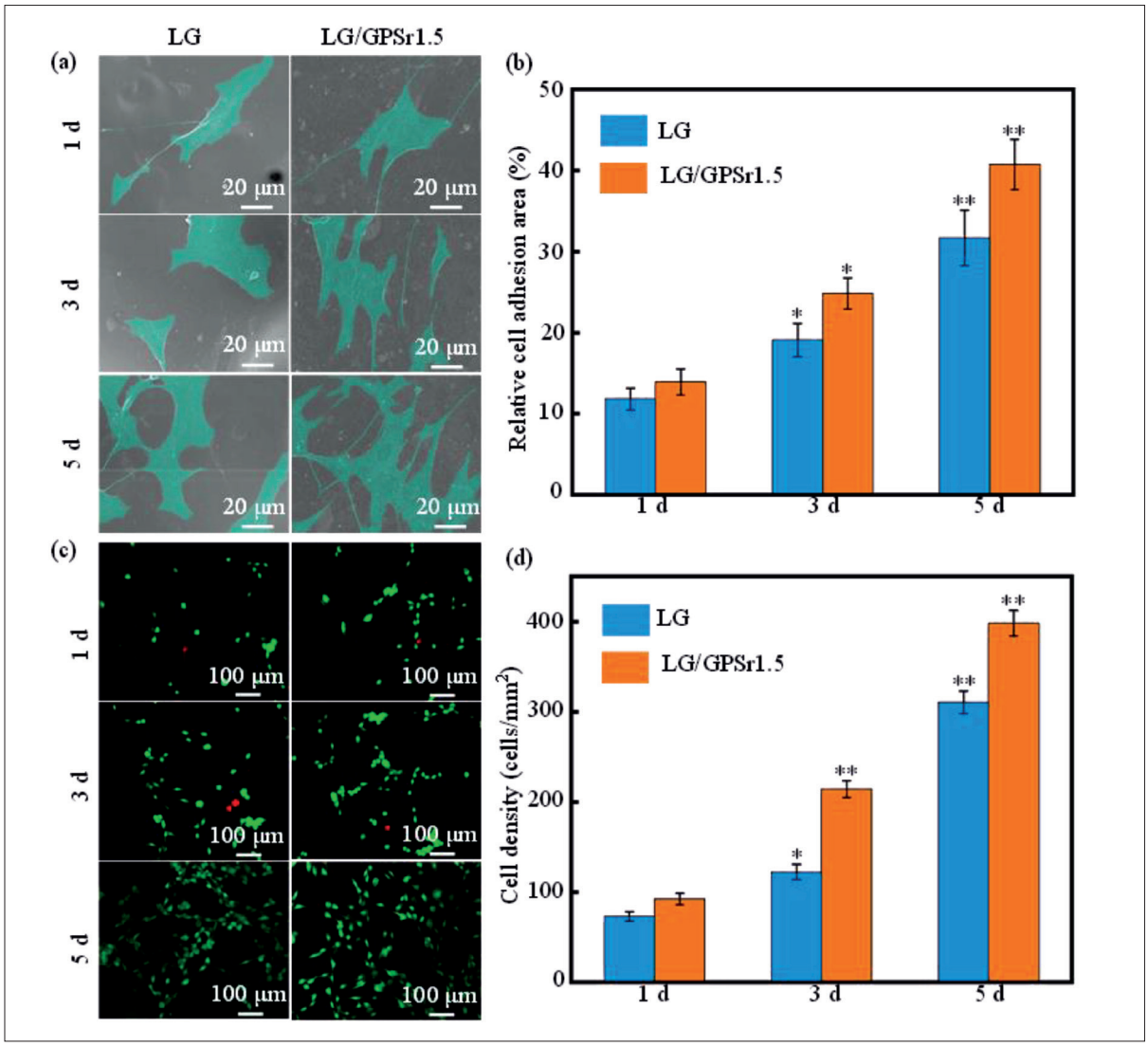


Figure 6. BMSCs adhesion on the LG and LG/GPSr1.5 scaffolds (a); statistical results of relative cell adhesion area (b); live/dead cell staining for BMSCs on the LG and LG/GPSr1.5 scaffolds (c); statistical results of cell density (d).

in Figure 6a. As time elapsed, the cells expanded and were accompanied by a large number of prominent pseudopodia on both scaffolds.[72,73] The quantitative analysis of relative cell adhesion area was carried out, and the results are presented in Figure 6b. As time prolonged, the relative cell adhesion area on the surface of the LG and LG/GPSr1.5 scaffolds gradually increased and reached 31.68% and 40.72% on day 5, respectively. The LG/GPSr1.5 scaffold exhibited a larger relative cell adhesion area than the LG scaffold at each period.

The results of live/dead cell staining experiments after BMSCs being cultured on the LG and LG/GPSr1.5 scaffolds for 1, 3, and 5 days are shown in Figure 6c; the live and dead cells were stained in green and red, respectively. Both scaffolds were able to maintain survival of almost all inoculated cells, and it has been found that the number of live cells gradually increased with the culture time.[74,75] As shown in Figure 6d, the cell densities on the LA and LG/GPSr1.5 scaffolds were 310.52 cells/mm^2 and 398.32 cells/mm^2, respectively, on day 5, which were much higher than that on day 1. LG/GPSr1.5 exhibited a higher BMSCs density than the LG scaffold when cultured for the same period of time. This might be due to the fact that the GPSr in the LG/GPSr1.5 scaffold increased surface roughness of the scaffold, providing more adhesion sites for BMSCs and thus promoting cell adhesion and growth.[76,77] The results of living/dead cell staining and cell adhesion showed that the LG/GPSr1.5 scaffold possessed good cytocompatibility.

Since osteoblast differentiation was a prerequisite for bone regeneration, the role of the LG/GPSr1.5 scaffold in inducing osteogenic differentiation of BMSCs was studied, with the LG scaffold as the control group. ALP staining test was conducted to evaluate the activity of ALP which reflected the early mature osteoblasts.[78,79] The secretions of OCN and OPN were generally considered to be the main markers of late differentiation of osteoblasts, so the expression of osteogenesis-related genes was evaluated by

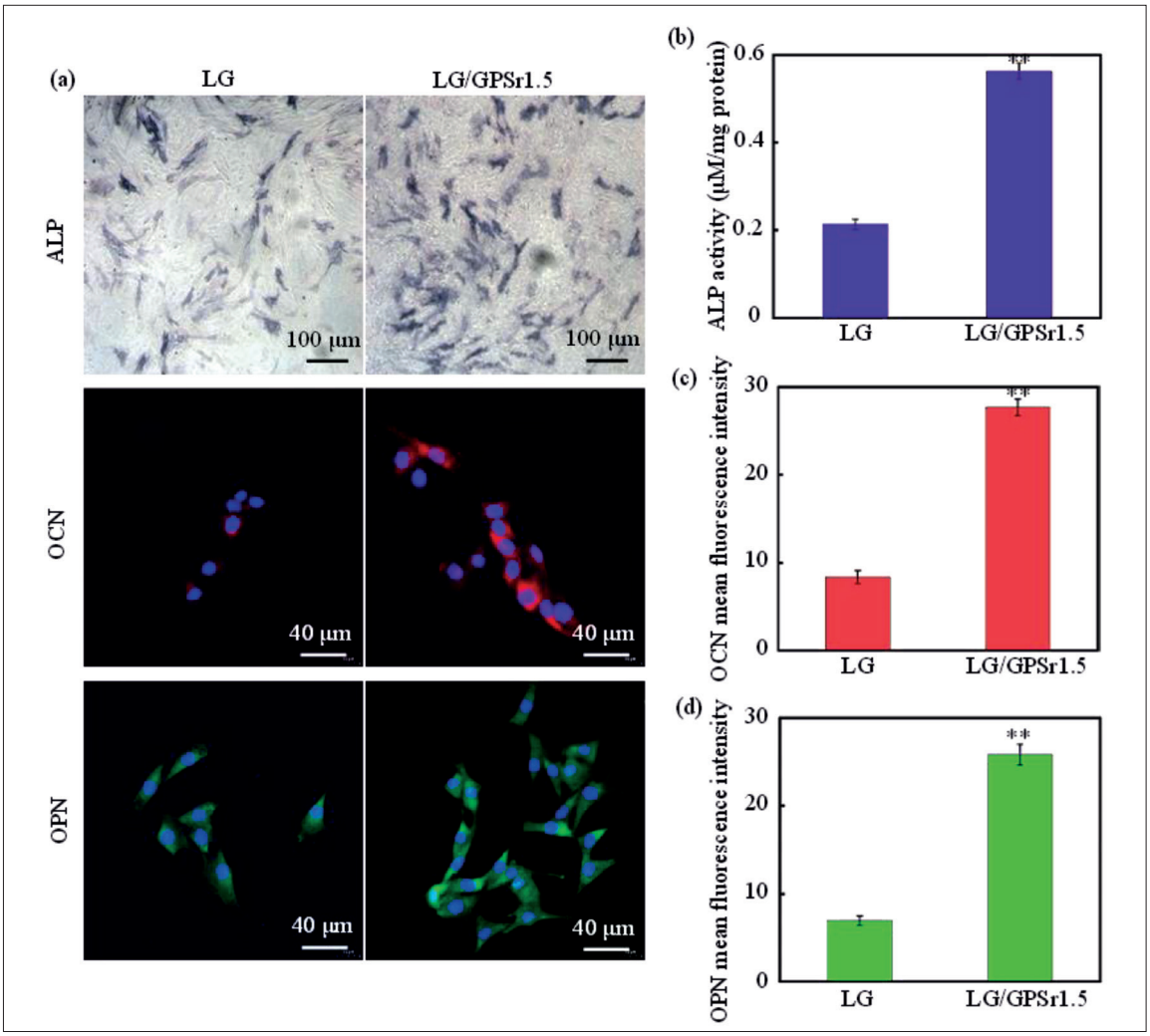


Figure 7. ALP staining, immunofluorescence staining of OCN and OPN on day 7 (a); statistical results of ALP activity (b); mean fluorescence intensity of OCN (c) and OPN (d).

means of immunofluorescence staining.[80,81] The staining results are shown in Figure 7, in which the ALP was stained dark blue while OCN and OPN were red and green, respectively. BMSCs in the LG/GPSr1.5 group showed obvious dark blue changes after ALP staining, indicating a higher activity of ALP in this group than that in the LG group. Through quantitative analysis, it was found that the expression of ALP in the LG/GPSr1.5 group increased to 0.56 μM/mg protein, which was in sharp contrast to the LG group. The fluorescence intensities of OCN and OPN in the LG/GPSr1.5 group were 27.68 and 25.83, respectively, which were significantly higher than those in the LG group. These results suggested that the LG/GPSr1.5 scaffold was superior to the LG scaffold in inducing osteogenesis owing to the presence of Sr in the LG/GPSr1.5 scaffold, which is gradually released when the scaffold degrades. Both Sr and Ca are elements of the same group, thus sharing very similar physical and chemical properties. Sr can bind to calcium-sensitive receptors on the cell membrane of osteoblasts and initiate intracellular signal transduction pathways to promote osteogenesis.[82] In addition, it has been found that Sr may regulate the expression of osteoblast-related genes, such as *OCN* and *ALP*, which can promote osteoblast proliferation and differentiation and promote bone formation.[83-85]

Previous reports have demonstrated that Sr could promote bone regeneration by inhibiting osteoclast differentiation and promoting bone substance absorption.[86-89] For example, Sun et al. revealed the inhibitory effect of strontium on osteoclast differentiation, as evidenced by the reduction in levels of key biomarkers associated with receptor activators of nuclear factor kappa-B ligand (RANKL).[86] In fact, the concentration of released Sr ions must be considered when evaluating the reparative potential of Sr. However, to the best of our knowledge, there are no referable universal concentration ranges for Sr concentrations that have a positive effect on osteogenesis, and thus, more extensive and in-depth studies are required. In addition, it is essential to take into account the impact of both GPSr content and scaffold design on the release of Sr in future work, as the interplay of these parameters may affect the mechanical strength of scaffold,[90-92] and this will become an important strategy to balance the mechanical and bioactive properties of scaffold for future work.

4. Conclusion

In this study, GO was encapsulated by PDA formed by self-polymerization of DA in alkaline solution, and Sr was loaded onto GO by the chelation of PDA. Then, the obtained GP and GPSr were added into LG, and the scaffold was fabricated by SLS. The mechanical properties of the LG scaffold were improved by adding GPSr. Our results showed that the LG/GPSr1.5 scaffold had better mechanical properties, evidenced by the tensile strength and compressive strength of 9.49 and 19.22 MPa, respectively, which were 67.08% and 95.33% higher than those of the LG scaffold. GPSr enhances the mechanical properties of the scaffold through crack branching, crack deflection, crack pinning, crack bridging, and pulling out. In addition, the LG/GPSr1.5 scaffold could induce osteogenic differentiation of BMSCs.

Acknowledgments

The authors would like to thank Shiyanjia Lab (www.shiyanjia.com) for the SEM test.

Funding

This work was supported by the following funds: (1) The Natural Science Foundation of China (52275393, 51935014, 82072084); (2) Hunan Provincial Natural Science Foundation of China (2021JJ20061, 2020JJ3047, 2019JJ50588); (3) Jiangxi Provincial Natural Science Foundation of China (20224ACB204013); (4) The Project of State Key Laboratory of Precision Manufacturing for Extreme Service Performance; (5) Technology Innovation Platform Project of Shenzhen Institute of Information Technology 2020 (PT2020E002); (6) Guangdong Province Precision Manufacturing and Intelligent production education Integration Innovation Platform (2022CJPT019).

Conflict of interest

The authors declare no conflicts of interest.

Author contributions

Conceptualization: Pei Feng
Data curation: Feng Yang, Yun Lin
Methodology: Feng Yang, Yun Lin, Saipu Shen, Cijun Shuai
Supervision: Cijun Shuai
Validation: Saipu Shen, Yulong Gu
Writing – original draft: Feng Yang, Saipu Shen, Yun Lin
Writing – review & editing: Pei Feng

Ethics approval and consent to participate

Not applicable.

Consent for publication

Not applicable.

Availability of data

All data are available in the main text.

References

1. Sun H, Ling L, Ren Z, Memon SA, Xing F. Effect of graphene oxide/graphene hybrid on mechanical properties of cement mortar and mechanism investigation. *Nanomaterials (Basel)*. 2020;10(1):113. doi: 10.3390/nano10010113
2. Chathuranga H, Wasalathilake KC, Marriam I, et al. Preparation of bioinspired graphene oxide/PMMA nanocomposite with improved mechanical properties. *Compos Sci Technol.* 2021;216:109046. doi: 10.1016/j.compscitech.2021.109046
3. Qu H, Huang L, Han Z, et al. A review of graphene-oxide/metal–organic framework composites materials: characteristics, preparation and applications. *J Porous Mat.* 2021; 28:1837-1865. doi: 10.1007/s10934-021-01125-w
4. Yan L, Wang L, Wu J, et al. Multi-biofunctional graphene oxide-enhanced poly-L-lactic acid composite nanofiber scaffolds for ovarian function recovery of transplanted-tissue. *NPJ Regen Med.* 2022;7(1):52. doi: 10.1038/s41536-022-00236-5
5. Ju J, Peng X, Huang K, et al. High-performance porous PLLA-based scaffolds for bone tissue engineering: preparation, characterization, and in vitro and in vivo evaluation. *Polymer.* 2019;180:121707. doi: 10.1016/j.polymer.2019.121707
6. Murakami T, Otsuki S, Nakagawa K, et al. Establishment of novel meniscal scaffold structures using polyglycolic and poly-l-lactic acids. *J Biomater Appl.* 2017;32:150-161. doi: 10.1177/0885328217713631
7. Cantón I, Mckean R, Charnley M, et al. Development of an Ibuprofen-releasing biodegradable PLA/PGA electrospun scaffold for tissue regeneration. *Biotechnol Bioeng.* 2010;105:396-408. doi: 10.1002/bit.22530
8. Hua W, Shi W, Mitchell K, et al. 3D printing of biodegradable polymer vascular stents: a review. *Chin J Mech Eng Addit Manuf Front*. 2022;1(2):100020. doi: 10.1016/j.cjmeam.2022.100020
9. Shuai C, Shi X, Yang F, Tian H, Feng P. Oxygen vacancy boosting Fenton reaction in bone scaffold towards fighting bacterial infection. *Int J Extreme Manuf.* 2023;6: 015101. doi: 10.1088/2631-7990/ad01fd
10. Storck JL, Ehrmann G, Uthoff J, Diestelhorst E, Blachowicz T, Ehrmann A. Investigating inexpensive polymeric 3D printed materials under extreme thermal conditions. *Mater Futures*. 2022;1:015001. doi: 10.1088/2752-5724/ac4beb
11. Najafinezhad A, Bakhsheshi-Rad HR, Saberi A, et al. Graphene oxide encapsulated forsterite scaffolds to improve mechanical properties and antibacterial behavior. *Biomed Mater.* 2022;17:035011. doi: 10.1088/1748-605X/ac62e8
12. Abzan N, Kharaziha M, Labbaf S. Development of three-dimensional piezoelectric polyvinylidene fluoride-graphene oxide scaffold by non-solvent induced phase separation method for nerve tissue engineering. *Mater Design*. 2019;167:107636. doi: 10.1016/j.matdes.2019.107636
13. Wang W, Wei J, Lei D, et al. 3D printing of lithium osteogenic bioactive composite scaffold for enhanced bone regeneration. *Compos Part B Eng.* 2023;256:110641. doi: 10.1016/j.compositesb.2023.110641
14. Zhang X, He J, Qiao L, et al. 3D printed PCLA scaffold with nano-hydroxyapatite coating doped green tea EGCG promotes bone growth and inhibits multidrug-resistant bacteria colonization. *Cell Prolif.* 2022;55(10):e13289. doi: 10.1111/cpr.13289
15. Chen A, Wang W, Mao Z, et al. Multi-material 3D and 4D bioprinting of heterogeneous constructs for tissue engineering. *Adv Mater*. 2023:2307686. doi: 10.1002/adma.202307686
16. Askari E, Rasouli M, Darghiasi SF, Naghib SM, Zare Y, Rhee KY. Reduced graphene oxide-grafted bovine serum albumin/bredigite nanocomposites with high mechanical properties and excellent osteogenic bioactivity for bone tissue engineering. *Bio-Des Manuf.* 2021;4:243-257. doi: 10.1007/s42242-020-00113-4
17. Soraya Z, Ghollasi M, Halabian R, Eftekhari E, Tabasi A, Salimi A. Donepezil hydrochloride as a novel inducer for osteogenic differentiation of mesenchymal stem cells on PLLA scaffolds in vitro. *Biotechnol J.* 2021;16:2100112. doi: 10.1002/biot.202100112
18. Toosi S, Naderi-Meshkin H, Kalalinia F, et al. Bone defect healing is induced by collagen sponge/polyglycolic acid. *J Mater Sci Mater Med.* 2019;30:1-10. doi: 10.1007/s10856-019-6235-9
19. Bai H, Zhao Y, Wang C, et al. Enhanced osseointegration of three-dimensional supramolecular bioactive interface through osteoporotic microenvironment regulation. *Theranostics.* 2020;10:4779. doi: 10.7150/thno.43736
20. Wang J, Wang H, Wang Y, et al. Endothelialized microvessels fabricated by microfluidics facilitate osteogenic differentiation and promote bone repair. *Acta Biomater.* 2022;142:85-98. doi: 10.1016/j.actbio.2022.01.055
21. Jarrar H, Altındal DÇ, Gümüşderelioğlu M. Scaffold-based osteogenic dual delivery system with melatonin and BMP-2 releasing PLGA microparticles. *Int J Pharmaceut.* 2021;600:120489. doi: 10.1016/j.ijpharm.2021.120489

22. Wu X, Tang Z, Wu K, et al. Strontium-calcium phosphate hybrid cement with enhanced osteogenic and angiogenic properties for vascularised bone regeneration. *J Mater Chem B.* 2021;9(2021):5982-5997. doi: 10.1039/D1TB00439E

23. Zhang W, Tian Y, He H, et al. Strontium attenuates rhBMP-2-induced osteogenic differentiation via formation of Sr-rhBMP-2 complex and suppression of Smad-dependent signaling pathway. *Acta Biomater.* 2016;33:290-300. doi: 10.1016/j.actbio.2016.01.042

24. Li S, Cui Y, Liu H, et al. Application of bioactive metal ions in the treatment of bone defects. *J Mater Chem B.* 2022;10(45):9369-9388. doi: 10.1039/D2TB01684B

25. Luo Y, Liu H, Zhang Y, et al. Metal ions: the unfading stars of bone regeneration-from bone metabolism regulation to biomaterial applications. *Biomater Sci.* 2023;11(22): 7268-7295. doi: 10.1039/D3BM01146A

26. Yuan Z, Wei P, Huang Y, et al. Injectable PLGA microspheres with tunable magnesium ion release for promoting bone regeneration. *Acta Biomater*. 2019;85:294-309. doi: 10.1016/j.actbio.2018.12.017

27. Yu Y, Liu K, Wen Z, Liu W, Zhang L, Su J. Double-edged effects and mechanisms of Zn^{2+} microenvironments on osteogenic activity of BMSCs: osteogenic differentiation or apoptosis. *RSC Adv.* 2020;10(25):14915-14927. doi: 10.1039/D0RA01465F

28. Xue Y, Zhang L, Liu F, et al. Alkaline "nanoswords" coordinate ferroptosis-like bacterial death for antibiosis and osseointegration. *ACS Nano.* 2023;17(3):2711-2724. doi: 10.1021/acsnano.2c10960

29. Kołodziejska B, StępieńN, Kolmas J. The influence of strontium on bone tissue metabolism and its application in osteoporosis treatment. *Int J Mol Sci.* 2021;22:6564. doi: 10.3390/ijms22126564

30. Zhang C, Xu G, Han L, Hu X, Zhao Y, Li Z. Bone induction and defect repair by true bone ceramics incorporated with rhBMP-2 and Sr. *J Mater Sci Mater Med.* 2021;32:107. doi: 10.1007/s10856-021-06587-7

31. Lakhkar NJ, Lee IH, Kim HW, Salih V, Wall IB, Knowles JC. Bone formation controlled by biologically relevant inorganic ions: role and controlled delivery from phosphate-based glasses. *Adv Drug Deliver Rev.* 2013;65(4):405-420. doi: 10.1016/j.addr.2012.05.015

32. Schatkoski VM, Larissa do Amaral Montanheiro T, Canuto de Menezes, et al. Current advances concerning the most cited metal ions doped bioceramics and silicate-based bioactive glasses for bone tissue engineering. *Ceram Int.* 2021;47(3):2999-3012. doi: 10.1016/j.ceramint.2020.09.213

33. Zhao R, Chen S, Zhao W, et al. A bioceramic scaffold composed of strontium-doped three-dimensional hydroxyapatite whiskers for enhanced bone regeneration in osteoporotic defects. *Theranostics.* 2020;10(4):1572. doi: 10.7150/thno.40103

34. Szewczyk J, Aguilar-Ferrer D, Coy E. Polydopamine films: electrochemical growth and sensing applications. *Eur Polym J.* 2022;174:111346. doi: 10.1016/j.eurpolymj.2022.111346

35. Wang LS, Xu S, Gopal S, et al. Facile fabrication of antibacterial and antiviral perhydrolase-polydopamine composite coatings. *Sci Rep.* 2021;11:12410. doi: 10.1038/s41598-021-91925-6

36. Xie Y, Yue L, Zheng Y, et al. The antibacterial stability of poly (dopamine) in-situ reduction and chelation nano-Ag based on bacterial cellulose network template. *Appl Surf Sci.* 2019;491:383-394. doi: 10.1016/j.apsusc.2019.06.096

37. Yang Z, Fan WH, Ding YJ, Xiao Z-L. Preparation and thermal performance of nitrocellulose coated by polydopamine. *J Appl Polym Sci.* 2022;139:51809. doi: 10.1002/app.51809

38. Zhou S, Yan J, Chen J, et al. Polydopamine/polyethyleneimine co-crosslinked graphene oxide for the enhanced tribological performance of epoxy resin coatings. *J Mater Sci Technol.* 2023;136:13-20. doi: 10.1016/j.jmst.2022.07.019

39. Gao T, Zhang J, Zhang N, Wang Y, He J, Wu F. Dopamine assisted incorporation of Sr ions in porous titanium alloy and its in-vitro bioactivity and cellular responses. *Mater Lett.* 2021;287:129308. doi: 10.1016/j.matlet.2021.129308

40. Zhou X, Cheng X, Xing D, et al. Ca ions chelation, collagen I incorporation and 3D bionic PLGA/PCL electrospun architecture to enhance osteogenic differentiation. *Mater Design.* 2021;198:109300. doi: 10.1016/j.matdes.2020.109300

41. Qi F, Liao R, Wu P, et al. An electrical microenvironment constructed based on electromagnetic induction stimulates neural differentiation. *Mater Chem Front.* 2023;7: 1671-1683. doi: 10.1039/D2QM01193J

42. Gao C, Yao X, Deng Y, Pan H, Shuai C. Laser-beam powder bed fusion followed by annealing with stress: a promising route for magnetostrictive improvement of polycrystalline $Fe_{81}Ga_{19}$ alloys. *Addit Manuf.* 2023;68:103516. doi: 10.1016/j.addma.2023.103516

43. Ling C, Li Q, Zhang Z, et al. Influence of heat treatment on microstructure, mechanical and corrosion behavior of WE43 alloy fabricated by laser-beam powder bed fusion. *Int J Extreme Manuf.* 2024;6:015001.

doi: 10.1088/2631-7990/acfad5

44. Han W, Kong L, Xu M. Advances in selective laser sintering of polymers. *Int J Extreme Manuf.* 2022;4:042002. doi: 10.1088/2631-7990/ac9096

45. Feng J, Fu J, Yao X, He Y. Triply periodic minimal surface (TPMS) porous structures: from multi-scale design, precise additive manufacturing to multidisciplinary applications. *Int J Extreme Manuf.* 2022;4:022001. doi: 10.1088/2631-7990/ac5be6

46. Hou Y, Wang W, Bartolo P. Application of additively manufactured 3D scaffolds for bone cancer treatment: a review. *Bio Des Manuf.* 2022;5:556-579. doi: 10.1007/s42242-022-00182-7

47. Cui ZW, Jing YR, Liu SS, Liu GY. Systematic investigation on the effect of crosslinking agent type and dosage on the performance of TPU/MVQ based thermoplastic vulcanizates. *J Appl Polym Sci.* 2021;138:50630. doi: 10.1002/app.50630

48. Liu Y, Qian L, Xia C, Zou J, Lian Z, Yi X. Failure analysis and structural optimization of rubber core and support rib of full-size spherical blowout preventer. *Eng Fail Anal.* 2023;143:106865. doi: 10.1016/j.engfailanal.2022.106865

49. Goel P, Mandal P, Bhuvanesh E, Shahi VK, Chattopadhyay S. Temperature resistant cross-linked brominated poly phenylene oxide-functionalized graphene oxide nanocomposite anion exchange membrane for desalination. *Sep Purif Technol.* 2021;255:117730. doi: 10.1016/j.seppur.2020.117730

50. Qiblawey H. Development of novel composite membranes in water/wastewater treatment. *Membranes (Basel).* 2022;12:260. doi: 10.3390/membranes12030260

51. Kou Y, Zhou W, Xu L, et al. Surface modification of GO by PDA for dielectric material with well-suppressed dielectric loss. *High Perform Polym.* 2019;31:1183-1194. doi: 10.1177/0954008319837744

52. Alkhouzaam A, Qiblawey H, Khraisheh M. Polydopamine functionalized graphene oxide as membrane nanofiller: spectral and structural studies. *Membranes (Basel).* 2021;11:86. doi: 10.3390/membranes11020086

53. Song H, Wang Z, Yang J, Jia X, Zhang Z. Facile synthesis of copper/polydopamine functionalized graphene oxide nanocomposites with enhanced tribological performance. *Chem Eng J.* 2017;324:51-62. doi: 10.1016/j.cej.2017.05.016

54. Ren Y, Peng D, Wu H, et al. Enhanced carbon dioxide flux by catechol-Zn^{2+} synergistic manipulation of graphene oxide membranes. *Chem Eng J.* 2019;195:230-238. doi: 10.1016/j.ces.2018.11.055

55. Zhao Z, Guo L, Feng L, et al. Polydopamine functionalized graphene oxide nanocomposites reinforced the corrosion protection and adhesion properties of waterborne polyurethane coatings. *Eur Polym J.* 2019;120:109249. doi: 10.1016/j.eurpolymj.2019.109249

56. Ye W, Chen Y, Zhou Y, et al. Enhancing the catalytic activity of flowerike Pt nanocrystals using polydopamine functionalized graphene supports for methanol electrooxidation. *Electrochim Acta.* 2014;142:18-24. doi: 10.1016/j.electacta.2014.06.161

57. Wang S, Zhu J, Rao Y, et al. Polydopamine modified graphene oxide-TiO_2 nanofiller for reinforcing physical properties and anticorrosion performance of waterborne epoxy coatings. *Appl Sci.* 2019;9:3760. doi: 10.3390/app9183760

58. Wang R, Song F, Li S, et al. Polydopamine-assisted Sr immobilization to improve the osteogenesis of a three-dimensional reduced graphene oxide/polypyrrole composite scaffold. *Mater Lett.* 2019;246:182-185. doi: 10.1016/j.matlet.2019.03.065

59. Jia Z, Xu X, Zhu D, Zheng Y. Design, printing, and engineering of regenerative biomaterials for personalized bone healthcare. *Prog Mater Sci.* 2023;134:101072. doi: 10.1016/j.pmatsci.2023.101072

60. Tan X, Tan Y, Chow C, Tor SB, Yeong WY. Metallic powder-bed based 3D printing of cellular scaffolds for orthopaedic implants: a state-of-the-art review on manufacturing, topological design, mechanical properties and biocompatibility. *Mat Sci Eng C Mater.* 2017;76:1328-1343. doi: 10.1016/j.msec.2017.02.094

61. Zhu H, Li M, Huang X, et al. 3D printed tricalcium phosphate-bioglass scaffold with gyroid structure enhance bone ingrowth in challenging bone defect treatment. *Appl Mater Today.* 2021;25:101166. doi: 10.1016/j.apmt.2021.101166

62. Ibrahim A, Klopocinska A, Horvat K, Hamid ZA. Graphene-based nanocomposites: synthesis, mechanical properties, and characterizations. *Polymers (Basel).* 2021;13:2869. doi: 10.3390/polym13172869

63. Wang M, Ma L, Shi L, et al. Chemical grafting of nano-SiO_2 onto graphene oxide via thiol-ene click chemistry and its effect on the interfacial and mechanical properties of GO/epoxy composites. *Compos Sci Technol.* 2019;182:107751. doi: 10.1016/j.compscitech.2019.107751

64. Hu Y, Xie Y, Xin H, et al. Nano/microstructures and mechanical properties of Al_2O_3-TiC ceramic composites reinforced with Al_2O_3@RGO nanohybrids. *Ceram Int.* 2022;48:27536-27549. doi: 10.1016/j.ceramint.2022.06.047

65. Li B, Ying P, Gao Y, et al. Heterogeneous diamond-cBN composites with superb toughness and hardness. *Nano Lett.* 2022;22:4979-4984.

doi: 10.1021/acs.nanolett.2c01716

66. Peng J, Huang C, Cao C, et al. Inverse nacre-like epoxy-graphene layered nanocomposites with integration of high toughness and self-monitoring. *Matter.* 2020;2:220-232. doi: 10.1016/j.matt.2019.08.013

67. Gholinezhad F, Golhosseini R, Moini Jazani O. Synthesis, characterization, and properties of silicone grafted epoxy/acrylonitrile butadiene styrene/graphene oxide nanocomposite with high adhesion strength and thermal stability. *Polym Composite.* 2022;43:1665-1684. doi: 10.1002/pc.26487

68. Mehwish N, Xu M, Zaeem M, Lee BH. Mussel-inspired surface functionalization of porous albumin cryogels supporting synergistic antibacterial/antioxidant activity and bone-like apatite formation. *Gels.* 2022;8:679. doi: 10.3390/gels8100679

69. Deng Y, Yang WZ, Shi D, et al. Bioinspired and osteopromotive polydopamine nanoparticle-incorporated fibrous membranes for robust bone regeneration. *NPG Asia Mater.* 2019;11:39. doi: 10.1038/s41427-019-0139-5

70. Ghorbani F, Zamanian A, Behnamghader A, Joupari MD. A facile method to synthesize mussel-inspired polydopamine nanospheres as an active template for in situ formation of biomimetic hydroxyapatite. *Mat Sci Eng C Mater.* 2019;94:729-739. doi: 10.1016/j.msec.2018.10.010

71. Arepalli SK, Tripathi H, Hira SK, Manna PP, Pyare R, Singh SP. Enhanced bioactivity, biocompatibility and mechanical behavior of strontium substituted bioactive glasses. *Mat Sci Eng C Mater Biol Appl.* 2016;69:108-116. doi: 10.1016/j.msec.2016.06.070

72. Ge J, Wang F, Xu Z, et al. Influences of niobium pentoxide on roughness, hydrophilicity, surface energy and protein absorption, and cellular responses to PEEK based composites for orthopedic applications. *J Mater Chem B.* 2020;8:2618-2626. doi: 10.1039/C9TB02456E

73. Mi X, Su Z, Fu Y, Li S, Mo A. 3D printing of Ti_3C_2-MXene-incorporated composite scaffolds for accelerated bone regeneration. *Biomed Mater.* 2022;17:035002. doi: 10.1088/1748-605X/ac5ffe

74. Qi F, Wang Z, Yang L, et al. A collaborative CeO_2@metal-organic framework nanosystem to endow scaffolds with photodynamic antibacterial effect. *Mater Today Chem.* 2023;27:101336. doi: 10.1016/j.mtchem.2022.101336

75. Guo W, Wang X, Yang C, Huang R, Wang H, Zhao Y. Microfluidic 3D printing polyhydroxyalkanoates-based bionic skin for wound healing. *Mater Futures.* 2022;1:015401. doi: 10.1088/2752-5724/ac446b

76. Ng JY, Obuobi S, Chua ML, et al. Biomimicry of microbial polysaccharide hydrogels for tissue engineering and regenerative medicine: a review. *Carbohyd Polym.* 2020;241:116345. doi: 10.1016/j.carbpol.2020.116345

77. Abdollahiyan P, Baradaran B, de la Guardia M, Oroojalian F, Mokhtarzadeh A. Cutting-edge progress and challenges in stimuli responsive hydrogel microenvironment for success in tissue engineering today. *J Control Release.* 2020; 328:514-531. doi: 10.1016/j.jconrel.2020.09.030

78. Dong P, Zhu D, Deng X, et al. Effect of hydroxyapatite nanoparticles and wedelolactone on osteoblastogenesis from bone marrow mesenchymal stem cells. *J Biomed Mater Res A.* 2019;107:145-153. doi: 10.1002/jbm.a.36541

79. Su Y, Li Z, Zhu H, He J, Wei B, Li D. Electrohydrodynamic fabrication of triple-layered polycaprolactone dura mater substitute with antibacterial and enhanced osteogenic capability. *Chin J Mech Eng Addit Manuf Front.* 2022;1(2):100026. doi: 10.1016/j.cjmeam.2022.100026

80. Han X, Sun M, Chen B, et al. Lotus seedpod-inspired internal vascularized 3D printed scaffold for bone tissue repair. *Bioact Mater.* 2021;6:1639-1652. doi: 10.1016/j.bioactmat.2020.11.019

81. Yan Y, Chen H, Zhang H, et al. Vascularized 3D printed scaffolds for promoting bone regeneration. *Biomaterials.* 2019;190:97-110. doi: 10.1016/j.biomaterials.2018.10.033

82. Li Z, Wang S, Xu G, Hu X, Han L, Zhao Y. Synergy effect of Sr and rhBMP-2: a potential solution to osteolysis caused by rhBMP-2. *Med Hypotheses.* 2020;144:109895. doi: 10.1016/j.mehy.2020.109895

83. Yi Q, Liang P, Liang D, Shi J-F, Sha S, Chang Q. Multifunction Sr doped microporous coating on pure magnesium of antibacterial, osteogenic and angiogenic activities. *Ceram Int.* 2021;47:8133-8141. doi: 10.1016/j.ceramint.2020.11.168

84. Chen A, Su J, Li Y, et al. 3D/4D printed bio-piezoelectric smart scaffolds for next-generation bone tissue engineering. *Int J Extreme Manuf.* 2023;5(3):032007. doi: 10.1088/2631-7990/acd88f

85. Lee NH, Kang MS, Kim TH, et al. Dual actions of osteoclastic-inhibition and osteogenic-stimulation through strontium-releasing bioactive nanoscale cement imply biomaterial-enabled osteoporosis therapy. *Biomaterials.* 2021;276:121025. doi: 10.1016/j.biomaterials.2021.121025

86. Sun T, Li Z, Zhong X, et al. Strontium inhibits osteoclastogenesis by enhancing LRP6 and β-catenin-mediated OPG targeted by miR-181d-5p. *J Cell Commun Signal.* 2019;13:85-97. doi: 10.1007/s12079-018-0478-y

87. Wu Q, Hu L, Yan R, et al. Strontium-incorporated bioceramic scaffolds for enhanced osteoporosis bone regeneration. *Bone Res.* 2022;10(1):55.
doi: 10.1038/s41413-022-00224-x

88. Jiang S, Wang X, Ma Y, et al. Synergistic effect of micro-nano-hybrid surfaces and Sr doping on the osteogenic and angiogenic capacity of hydroxyapatite bioceramics scaffolds. *Int J Nanomed*. 2022;17:783-797.
doi: 10.2147/IJN.S345357

89. Quade M, Vater C, Schlootz S, et al. Strontium enhances BMP-2 mediated bone regeneration in a femoral murine bone defect model. *J Biomed Mater Res B.* 2020;108(1):174-182.
doi: 10.1002/jbm.b.34376

90. Cheng D, Liang Q, Li Y, et al. Strontium incorporation improves the bone-forming ability of scaffolds derived from porcine bone. *Colloids Surf B Biointerfaces*. 2018; 162:279-287.
doi: 10.1016/j.colsurfb.2017.11.070

91. Meininger S, Mandal S, Kumar A, Groll J, Basu B, Gbureck U. Strength reliability and in vitro degradation of three-dimensional powder printed strontium-substituted magnesium phosphate scaffolds. *Acta Biomater.* 2016; 31:401-411.
doi: 10.1016/j.actbio.2015.11.050

92. Denry I, Goudouri OM, Fredericks DC, Akkouch A, Acevedo MR, Holloway JA. Strontium-releasing fluorapatite glass-ceramic scaffolds: structural characterization and in vivo performance. *Acta Biomater.* 2018;75: 463-471.
doi: 10.1016/j.actbio.2018.05.047

ACCSCIENCE PUBLISHING

International Journal of Bioprinting

RESEARCH ARTICLE

Preparation and characterization of angled dual- and multi-branched nerve guidance conduits

Yinchu Dong†, Wenbi Wu†, Haofan Liu†, Xuebing Jiang, Li Li, Li Zhang, Yi Zhang, Jing Luo, and Maling Gou*

Department of Biotherapy, Cancer Center and State Key Laboratory of Biotherapy, West China Hospital, Sichuan University, Chengdu 610041, China

(This article belongs to the *Special Issue: Special Issue of International Journal of Bioprinting in the BDMC 2023 Conference*)

Abstract

Branched nerve guidance conduit (NGC) provides a promising alternative to autografts for the effective treatment of severe peripheral nerve injuries. Despite this, the impact of branched architecture on nerve regeneration remains unclear, particularly concerning branch angle and number in multi-branched NGCs. In this study, we investigated the effects of branch angle and number on nerve regeneration by preparing and characterizing multi-angled and multi-branched NGCs. We designed and fabricated dual-branched NGCs (DBNs) with various branch angles and multi-branched NGCs (MBNs) through a digital light processing (DLP) printing process. When branched NGCs were implanted to bridge the linear sciatic nerve gap, nerve dual branches with acute (45°), right (90°), or obtuse (120°) branch angles were formed in DBNs, while nerve multi-branches were generated in MBNs. The regenerated nerves in DBNs with various angles exhibited comparable electrophysiological conduction and histological morphologies, indicating that the branch angle of dual-branched NGCs may not affect nerve branch regeneration. In contrast, the diameter of the regenerated nerve branches in MBNs decreased with increasing distance from the scaffold center, highlighting the potential significance of branch number in the design of branched NGCs. This study contributes valuable insights for designing, preparing, and applying branched NGCs, offering potential assistance in advancing nerve regeneration strategies.

Keywords: 3D printing; Nerve regeneration; Branched nerve conduit; Nerve graft substitute

†These authors contributed equally to this work.

***Corresponding author:**
Maling Gou
(goumaling@scu.edu.cn)

Citation: Dong Y, Wu W, Liu H, et al. Preparation and characterization of angled dual- and multi-branched nerve guidance conduits. *Int J Bioprint*. 2024;10(3):1750.
doi: 10.36922/ijb.1750

Received: September 2, 2023
Accepted: October 30, 2023
Published Online: January 15, 2024

Copyright: © 2024 Author(s). This is an Open Access article distributed under the terms of the Creative Commons Attribution License, permitting distribution, and reproduction in any medium, provided the original work is properly cited.

Publisher's Note: AccScience Publishing remains neutral with regard to jurisdictional claims in published maps and institutional affiliations.

1. Introduction

The peripheral nervous system (PNS) consists of extensively branching nerves, serving as a crucial interface between the central nervous system (CNS) and target tissues. The anatomical structures of a branched peripheral nerve are essential for PNS functions. Severe segmental peripheral nerve injuries, involving the loss of branch points, commonly occur in facial, arm, or leg nerve injuries. These injuries can lead to de-innervation of target tissues and organs through multiple pathways, resulting in

abnormal motor, sensory, and autonomic functions, and even functional disability.[1-4] Currently, segmental defects in branch nerves, such as femoral branch nerve,[5] sciatic branch nerve,[6] facial branch nerve,[7-9] musculocutaneous branch nerve,[10] and pronator teres branch nerve,[11,12] pose challenges in peripheral nerve repair.

Bypassing branch and nerve transfer are frequently employed strategies for branched nerve repair, yet they are limited by permanent functional loss in tissues innervated by the bypassed branches and the scarcity of autografts, respectively.[1] Nerve guidance conduit (NGC), a tube-like exogenous alternative to autografts, has been widely applied to provide physical support and directional guidance for nerve regeneration.[13-15] In recent studies, various functional NGCs with biomimetic structures have been developed to create a favorable microenvironment for nerve regeneration. For instance, NGCs with aligned micro/nano-structures can promote axon regeneration and myelination, while multi-lumen NGCs can effectively control axon dispersion and mismatch.[16-22] However, the traditional straight design of these NGCs may lead to unsatisfactory recovery in branched peripheral nerve injuries since the linear structure may damage the branch points crucial for nerve function.[23]

The use of branched NGC may offer a novel therapeutic approach for treating branched nerve injury.[6] A previous study has suggested that a specific type of dual-branched conduit has the potential to repair the peroneal nerve while preserving partial functionality of the donor tibial nerve.[24] Meanwhile, another study reported multi-channel NGCs enhanced with a four-channel structural design, demonstrating the functionalization of NGCs through special structural design.[25] Moreover, Chen et al. have reported on a life-sized branched NGC for human facial nerve repair, designed based on magnetic resonance imaging (MRI) scanning.[26] Building on these studies, branched NGCs could be designed to reconstruct the anatomical and fascicular organization of trunk and branch nerves. While the ideal design for branched nerve repair involves reconstructing personalized anatomical structures, this approach is hindered by its inherent expensiveness, inefficiency, and the difficulties of achieving large-scale production through traditional means. However, in the realm of industrial manufacturing, the architectural design of branched NGCs faces limitations imposed by various factors that can affect nerve regeneration, including the diameter, angle, and number of nerve branches. Previous studies have proved that inapposite inner diameters of NGCs are unfavorable for nerve regeneration.[21,22,24,27-31] Still, there is a notable absence of studies addressing the influence of branch angle and number on nerve regeneration, necessitating further elucidation. Additionally, the fabrication of complex structures for branched NGCs remains challenging.

The emerging three-dimensional (3D) printing technology, facilitating the manufacturing of sophisticated and customized scaffolds, finds widespread applications in tissue engineering through various methodologies, including inkjet printing, extrusion printing, and stereolithography-based printing.[26,32-37] Notably, a recent study has employed an extrusion-based 3D printing process to develop a bifurcating nerve pathway in a "Y" shape for branched nerve injury, guiding the regeneration of injured branch nerves.[38] In a previous study, our group utilized digital light processing (DLP)-based 3D printing to fabricate a complex multi-branched scaffold resembling a tree.[25] This multi-branched scaffold formed an intricate network of nerves from a single stump *in vivo*, indicating that multi-angle branched NGCs may be effective for regeneration of nerve tissues across multiple nerve paths. 3D printing technologies provide an advanced tool for fabricating branched NGCs and a novel platform for researching branched NGC structural design.[26,39-41] In this study, we investigated the effects of branch angle and number on nerve regeneration by preparing and characterizing multi-angled and multi-branched (NGCs). Firstly, dual-branched (DBNs) with various branch angles and multi-branched NGC (MBN) were designed and fabricated using DLP 3D printing. Subsequently, the branched NGCs were implanted to bridge linear sciatic nerve gaps and harvested after 16 weeks to evaluate nerve regeneration. The results indicated that the branch angle of DBNs did not significantly affect nerve regeneration, as most injured nerve stumps were successfully connected. Moreover, the efficiency of nerve regeneration in branch channels gradually decreased from the center to the side within the MBN. This study provides valuable insights for designing and applying novel branched NGCs to promote branched peripheral nerve regeneration.

2. Materials and methods

2.1. Material

Type A gelatin from porcine skin, poly(ethylene glycol) diacrylate (PEGDA), and methacrylic anhydride (MAA) were purchased from Sigma-Aldrich. Lithium phenyl-2,4,6-trimethyl-benzoylphosphinate (LAP) was synthesized following the procedures outlined in the previous study.[42] All chemical reagents were of analytical grade and used as received.

Sprague–Dawley (SD) rats (200–220 g, male) were bought from Chengdu Dossy Experimental Animals Co., Ltd., and they were housed under specific pathogen-free conditions. All the animal experimental studies were performed in compliance with the guidelines and

regulations set forth by the Sichuan University Committee on Animal Research and Ethics.

2.2. Mechanical property and degradation of GelMA/PEGDA hydrogel

Gelatin methacryloyl (GelMA) was synthesized via the reaction of Type A gelatin and methacrylic anhydride (MMA), following the procedures outlined in the previous study.[43] To investigate the mechanical property of GelMA/PEGDA hydrogels, we prepared a series of prepolymer solutions by mixing 15% (w/v) PEGDA and 10% (w/v) GelMA at ratios of 4:1, 3:2, 1:1, 0:1, and blending 15% (w/v) PEGDA and 20% (w/v) GelMA at a ratio of 4:1. Subsequently, the resulting hydrogel discs with a diameter of 25 mm and a thickness of 1 mm were photo-crosslinked under 405 nm light exposure. The hydrogels were then immersed in normal saline to achieve a state of swelling equilibrium. Finally, a penetration test was performed using the MCR 302e (Anton Paar) to determine the Young's modulus of the hydrogels.

The hybrid hydrogel containing 12% PEGDA and 4% GelMA was incubated in a 1 mg/mL collagenase I solution at 37°C with a 60 rpm shaker to investigate degradation properties *in vitro*. The enzyme solution was refreshed at predetermined time points, and the hydrogels were weighed. The degradation rate was calculated as the ratio of the final weight to the original weight.

2.3. 3D-printed micropatterned hydrogel scaffolds

To assess the biocompatibility of GelMA/PEGDA hydrogel, we designed micropatterned scaffolds for *in vitro* cell culture. The micropatterned hydrogel scaffolds were fabricated using DLP printing, following the procedures outlined in our previous reports.[44] Firstly, the prepolymer solution was prepared by dissolving PEGDA (15% w/v), GelMA (20% w/v), LAP (0.75% w/v), and tartrazine (0.05% w/v) in deionized water, sterilized using a 0.22 μm filter membrane. Tartrazine was used as the photo-absorber to absorb scattered light and improve printing fidelity. Subsequently, two-dimensional (2D) structures of scaffolds, such as the loop, arc, and strip channels, were designed using Adobe Photoshop software. These designs were then uploaded to the digital micromirror device (DMD) chip to generate 405 nm visual light patterns. The prepolymer solution was applied to methacrylated glass coverslips, and after an 8-second exposure to 405 nm light, micropatterned scaffolds were formed through photo-polymerization. The bottom of the scaffold was exposed for an additional 2 s. Finally, the obtained scaffolds were immersed in sterilized phosphate-buffered saline (PBS) to remove the initiator, photo-absorber, and un-crosslinked polymers.

2.4. Culture of PC12 cells in micropatterned scaffolds

The proliferation, migration, and orientation of PC12 cells were evaluated to investigate the effect of micropatterned scaffolds on cell behaviors. PC12 cells (2000 cells) were seeded onto the scaffolds and cultured in the IncuCyte® imaging system at 37°C within a 5% CO_2 humidified environment. Cell images were taken every 2 h for 1 week. The proliferation of PC12 cells was evaluated through cell counts, with the number of cells within specific rectangular areas on days 1, 2, and 4 of culture determined using ImageJ software. The migration distance and migration rate of PC12 cells were calculated and analyzed over 20 h using manual tracking plugins in ImageJ software. After 4 days of culture, the orientation angle (θ) of PC12 cells, which represents the angle between the extension direction of cells and the microchannel, was measured using ImageJ software. In addition, fluorescence staining of F-actin was performed to observe the morphology of PC12 cells. After 3 days of culture, cells were fixed with 4% paraformaldehyde and incubated with rhodamine-phalloidin (Cytoskeleton Inc.) and DAPI (Invitrogen). Images were captured using the Delta Vision Ultra live cell workstation (GE Healthcare).

2.5. Preparation of the branched NGCs

As described in previous reports, the fabrication of branched NGCs utilized a continuous DLP printing process.[45,46] The prepolymer solution, comprising PEGDA (15% w/v), GelMA (20% w/v), LAP (0.75% w/v), and tartrazine (0.05% w/v), was prepared. The 3D structures of the branched NGCs were designed using Creo 5.0 software (PTC Inc.) and sliced into a series of 2D images using CreationWorkshop software. These 2D images were then imported into the DMD chip. For NGC fabrication, the prepolymer solution underwent sterilization by filtration through a 0.22 μm filter membrane and was added to the building platform. The designed branched NGCs were fabricated by exposing them to a sequentially patterned visual light (405 nm, 130 mW/cm^2) while continuously elevating the Z-stage under aseptic conditions. The Z-stage elevation proceeded at a rate of 0.06 mm per second, and each layer's exposure time was set at 2.5 s for 16 images (with the first two images exposed *in situ* for stabilized construction). The resulting branched NGCs were obtained through a 40-s printing process. Finally, the NGCs were immersed in sterilized PBS to remove unreacted polymers, photo-absorbers, and initiators.

2.6. Surgical process

The SD rats were randomly divided into six groups: dual-branched NGCs groups (0°, 45°, 90°, and 120°), multi-

branched NGCs group, and sham group. Anesthesia was induced in all rats via intraperitoneal injection of 10% chloral hydrate. Subsequently, the sciatic nerve was exposed, and a 6 mm nerve defect was created by surgically excising a segment of the nerve for conduit implantation. For dual-branched NGC groups, the 8-0 absorbable Vicryl sutures were used to suture the proximal nerve ends, which were then connected with a soft silicone guider. The sutures were guided to the contralateral side through the inner channel and sutured with the distal stumps at the connector of branched NGCs. For the multi-branched NGCs group, the proximal and distal stumps were placed into the two connectors of the NGCs, and the nerve stumps within the conduits were stabilized by coaptating 8-0 absorbable surgical sutures (Vicryl) around the outsides of conduits. For the sham group, no treatment was administered to the sciatic nerve. Finally, the muscle and skin layers were sutured with 2-0 nylon sutures.

2.7. Functionality assessment of regenerated nerves

Sixteen weeks post-surgery, SD rats were anesthetized, and the injured sites were exposed to observe nerve regeneration within branched NGCs. An electrophysiology assessment was performed to evaluate the functional recovery of regenerated nerves. Bipolar electrodes were used to stimulate the proximal and distal ends of the regenerated sciatic nerves, with a monopolar recording electrode placed in the gastrocnemius muscle. After surgically removing the dual-branched NGCs, the regenerated nerve dual branches, denoted Branch 1 (B1) and Branch 2 (B2), were exposed. Meanwhile, the electrophysiological conduction of each nerve branch was tested by attaching the bipolar stimulating electrodes to the proximal and distal ends of the branched nerves. Nerve conduction velocity (NCV), the latency of compound muscle action potential (CMAP), and the peak amplitude of CMAP were measured using an electromyography machine (Nuocheng, Shanghai, China).

Following the electrophysiology assessment, gastrocnemius muscles on both sides of the rats were harvested. The wet weight of the gastrocnemius muscle was immediately measured, and the wet weight ratio was calculated based on the mass ratio of the injured side to the normal side. Subsequently, the muscles were preserved in 10% formalin overnight and dehydrated with an automated tissue processer (ASP300s, Leica), followed by embedding in paraffin. Tissue sections of 7 μm were prepared using a rotary microtome (RM2125 RTS, Leica). Finally, hematoxylin and eosin (H&E) staining was performed, and images were acquired via a digital slide scanner (Pannoramic MIDI). The diameter of muscle fibers was measured using ImageJ software.

2.8. Histological analysis of the regenerated nerves

Following the electrophysiology assessment, the regenerated sciatic nerves were harvested. The nerve tissues were fixed in 10% formalin, dehydrated in ethanol, and embedded in paraffin to prepare paraffin sections (7 μm). Subsequently, the tissue sections were stained with H&E and luxol fast blue (LFB) and observed using a digital slide scanner (Pannoramic MIDI).

2.9. Statistical analysis

Statistical analysis was performed using GraphPad Prism 7 software. The data were expressed as mean values ± standard deviation (SD). Significance was determined utilizing the one-way ANOVA method, with $p < 0.05$ considered statistically significant.

3. Results

3.1. Design and fabrication of the branched NGCs

The scaffold material is the basic component of conduits, and an ideal scaffold for nerve repair should possess characteristics of biodegradability, biocompatibility, and mechanical properties aligned with the injured sites. In this study, GelMA and PEGDA were combined as a composite prepolymer for NGC fabrication. GelMA, containing cell-binding motifs, fosters cell adhesion and proliferation, albeit hindered by its poor mechanical properties. PEGDA, a synthetic polymer, has received FDA approval for various human applications. The mechanical properties of PEGDA hydrogel can be fine-tuned to provide favorable mechanical strength for NGC. Thus, we integrated GelMA and PEGDA to formulate a composite prepolymer that is both biocompatible and mechanically strong for nerve repair.[47-49] Notably, hydrogels containing GelMA have been reported to be beneficial for cell adhesion, a benefit not dependent on GelMA concentration in a linear relationship.[50] Therefore, our optimization of the composite prepolymer mainly focused on hydrogel mechanical properties. We fabricated various scaffolds using a series of composite prepolymers, varying the concentrations of GelMA and PEGDA. As shown in **Figure S1** (Supplementary File), the composition of 4% GelMA: 12% PEGDA yielded Young's modulus of 0.318 MPa, a value relatively optimal for matching the elastic modulus of peripheral nerves (0.5–13 MPa).

To investigate the biocompatibility of GelMA/PEGDA hydrogel and elucidate the effects of scaffold structures on neuron growth *in vitro*, we employed a DLP 3D printing process to fabricate a micropatterned scaffold (**Figure S2a** in Supplementary File). The centrosymmetric scaffold was designed, featuring circular microchannels at the center, along with several central strip channels and two side loops (**Figure S2b** in Supplementary File). Rhodamine-phalloidin staining revealed that PC12 cells exhibited

oriented and elongated growth along the direction of microchannels after 3 days (**Figure S2c–d** in Supplementary File). The calculated PC12 cell orientation angle (θ)[21] in the linear channels was 1.799°, significantly different from that observed for cells on a flat surface (**Figure S2e** in Supplementary File). Moreover, we observed that PC12 cells proliferated rapidly and filled the microchannels on day 6 (**Figure S2f** in Supplementary File), although the number of proliferated cells within the scaffolds was less than those outside the micropatterned scaffolds (**Figure S3a–b** in Supplementary File). Additionally, PC12 cells within the scaffold displayed directional migration along the linear microchannels (**Figure S3a** in Supplementary File). No significant differences were noted in migration displacement and velocity between cells inside and outside the scaffold (**Figure S3c–d** in Supplementary File). These results underscored the biocompatibility of the hybrid hydrogel, emphasizing the efficacy of its micropatterned structure in guiding cell proliferation, orientation, and migration. Subsequently, the GelMA/PEGDA composite prepolymer was further used for the construction of branched NGCs.

To explore the effect of branch angle and number on nerve regeneration, we utilized continuous DLP 3D printing technology to design and fabricate a variety of DBNs and MBNs (Figure 1a). The DBNs were designed as cuboid-like scaffolds (Figure 1b–i), characterized by dimensions of 12 mm in length, 9 mm in width, and 2.1 mm in height, with channel diameters set at 1.3 mm. These scaffolds consisted of a proximal connector, a distal connector at each end, and inner bifurcated branches connecting the two connectors. The two connectors were configured as hollow straight channels (3 mm in length). The branches symmetrically bifurcated from the proximal end and converged at the distal end, forming a loop. Various DBNs were printed with varying branch angles (0°, 45°, 90°, and 120°). Specifically, the branch angle denoted the angle between the branch channel and the central axis of the connectors. These DBNs were designed for implantation to bridge linear nerve gaps. This approach allowed us to circumvent the impact of selectively regeneration of distinct nerve stumps, thereby enabling a pure assessment of the effect of NGC architectures on nerve regeneration.

Meanwhile, the MBNs took the form of cuboid scaffolds, sharing the same dimensions as the DBNs (Figure 1b[ii]). These multi-branched scaffolds featured two straight connectors at both ends, connected to internal triangular structures. In the middle, nine tiny straight channels converged. The two connectors both measured 3 mm in length and 1.3 mm in diameter. The inner tiny straight branches were 1.8 mm in length, and their cross-section was oval-shaped with a short diameter of 0.5 mm and a long diameter of 1.3 mm. The separation distance between each tiny branch was 0.3 mm. The number of branches was designed based on comprehensive considerations, including NGC's inner diameter, volume, and mechanical properties, surpassing the number of natural nerve branches (e.g., five branches in the facial nerve).

To observe the channels of the branched conduits, a dye solution was injected into the channels. As shown in

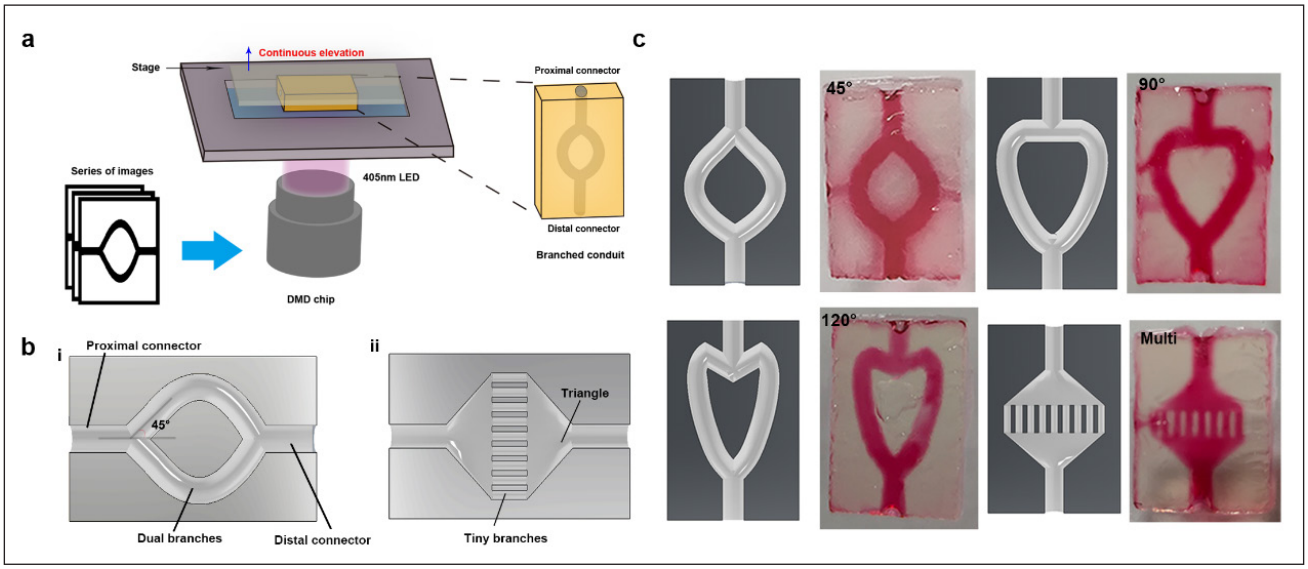


Figure 1. Fabrication of branched NGCs. (a) The continuous 3D printing process for branched NGC fabrication. A series of images for varying NGC designs were imported into the DMD chip, and the prepolymers were crosslinked under exposure to visible light (405 nm). (b) The design of (i) dual-branched NGCs (45°) and (ii) multi-branched NGCs. (c) The representative photographs of branched NGCs filled with dye (red). Abbreviations: DMD: digital micromirror device; NGC: nerve guidance conduit.

Figure 1c, all the DBNs and MBNs were unobstructed and could be filled with the dye solution. Meanwhile, the degradable behaviors of the conduits were also evaluated *in vitro*. The results indicated that the degradation rate of the hybrid hydrogel was 10% in 144 h in a 1% collagenase I solution (**Figure S4** in Supplementary File). In our previous study, we demonstrated that GelMA/PEGDA conduits exhibit biodegradability.[51] In this study, with a higher concentration of PEGDA, the GelMA/PEGDA hydrogel was biodegradable, although the degradation rate was slower.

3.2. Nerve regeneration in dual-branched NGCs

DBNs with predetermined angles were surgically implanted into the sciatic nerve gap of rats to investigate the *in vivo* effects of different branch angles on branched nerve regeneration (Figure 2a). The rat sciatic nerve defect serves as a primary model for peripheral nerve regeneration research. This model is chosen due to its appropriate length, diameter, elongated direction, and adequate space for implanting bulk nerve grafts, making it an ideal fit for our study. However, it has been reported that using a silicone Y-shaped chamber may result in selective regeneration of motor and sensory nerves.[52,53] When a branched conduit is implanted to bridge a branched nerve gap, the bifurcating pathways connect to different distal nerve stumps, potentially resulting in varied outcomes in nerve regeneration due to differences in the microenvironment between

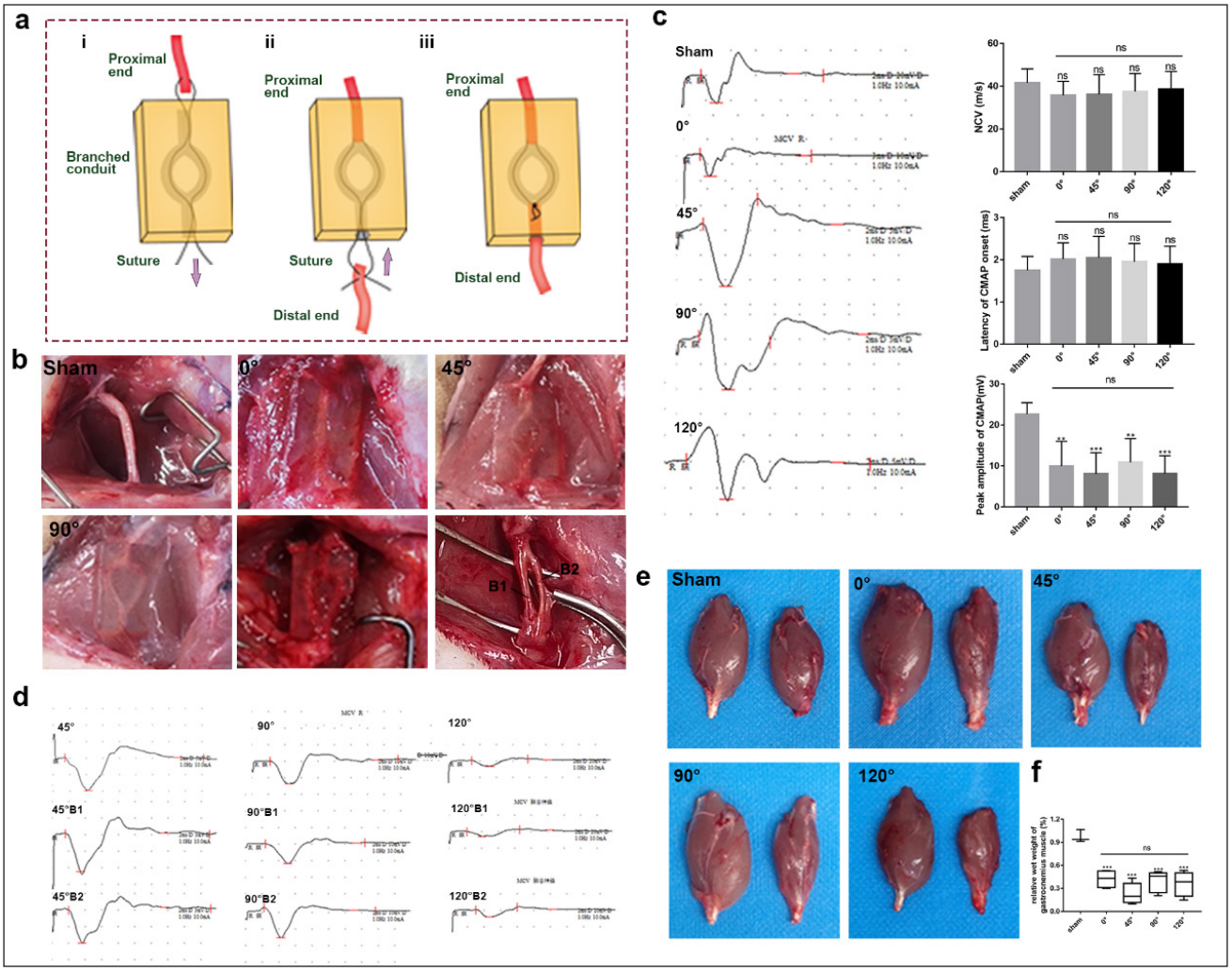


Figure 2. DBNs-guided nerve regeneration in the predesigned angled channels. (a) During the surgical process, DBNs were implanted to bridge the injured nerve stumps through connectors. For the fragile NGCs, the absorbable suture was introduced to prevent the stumps from sliding out of the channels. (b) The injured sites with/without NGCs were exposed 16 weeks post-surgery. (c) Representative CMAP recordings of the nerves 16 weeks after implantation, and the corresponding NCV value, latency of CMAP onset, and the peak amplitude of CMAP. (d) Representative CMAP recordings of the regenerated branch nerves in MBNs, namely branch 1 and branch 2 (B1, B2). (e) The images of gastrocnemius muscles on the normal side (left) and surgical side (right). (f) The relative wet weight ratio of gastrocnemius muscles. Abbreviations: CMAP: compound muscle action potential; DBN: dual-branched NGC; MBN: multi-branched NGCs; NCV: nerve conduction velocity; NGC: nerve guidance conduit.

the two pathways.[54,55] To eliminate the influence of different nerve stumps, a linear sciatic nerve defect model was established in this study, creating a single microenvironment induced by a single injured distal stump for nerve regeneration.

At the 16-week postoperative mark, the functional recovery of the implanted sites and NGCs was evaluated. The distal and proximal stumps of the injured nerves were successfully reconnected in all groups (Figure 2b), and nerve regeneration along the branched channels with various angles was observed in all DBNs. In the DBNs with a branch angle of 120°, a segment of the regenerated nerves even displayed an elongating direction that was reversed to the distal stumps to a certain degree (**Figure S5** in Supplementary File). Electrophysiology examinations were performed to assess the physiological functions of the regenerated nerves. As shown in Figure 2c, no significant difference was observed in NCV and CMAP latency among all DBN groups. However, the peak amplitude of CMAP in the sham group exhibited a significantly lower value than that of the DBN groups. The recovery of CMAP amplitude indirectly reflects the number of regenerated motor nerve fibers, while a reduced level of CMAP amplitude may suggest the incomplete innervation of target tissues.[56,57] Besides, the electrophysiological assessment was also performed on the branched nerves (B1 and B2) (Figure 2d). Unexpectedly, there were no significant differences in electrophysiological function among the trunk and branches, specifically B1 and B2. The result hinted that the branched nerves within dual-branched channels exhibit comparable electrophysiological conduction. Our findings suggested that branch angles did not significantly impact nerve regeneration within DBN when the branched conduits were implanted to bridge linear sciatic nerve gaps. Furthermore, we assessed the gastrocnemius muscle's relative wet weight ratios (i.e., the weight of the right side divided by that of the left side). The results showed no significant differences among DBN groups (Figure 2e–f). Histological analysis of gastrocnemius muscle cross-sections was also performed. The mean diameters of muscle fibers were similar among all the branched NGC groups (Figure 3g; **Figure S7** in Supplementary File). These results were consistent with electrophysiology assessments.

The regenerated branched nerves, bifurcating from the proximal stump and converging toward the distal stumps, were observed (Figure 3a). Histological examination through H&E staining confirmed the regenerated nerves, showcasing the presence of newly formed capillaries (Figure 3b). Concurrently, LFB staining of myelin sheaths served to further validate the remyelination

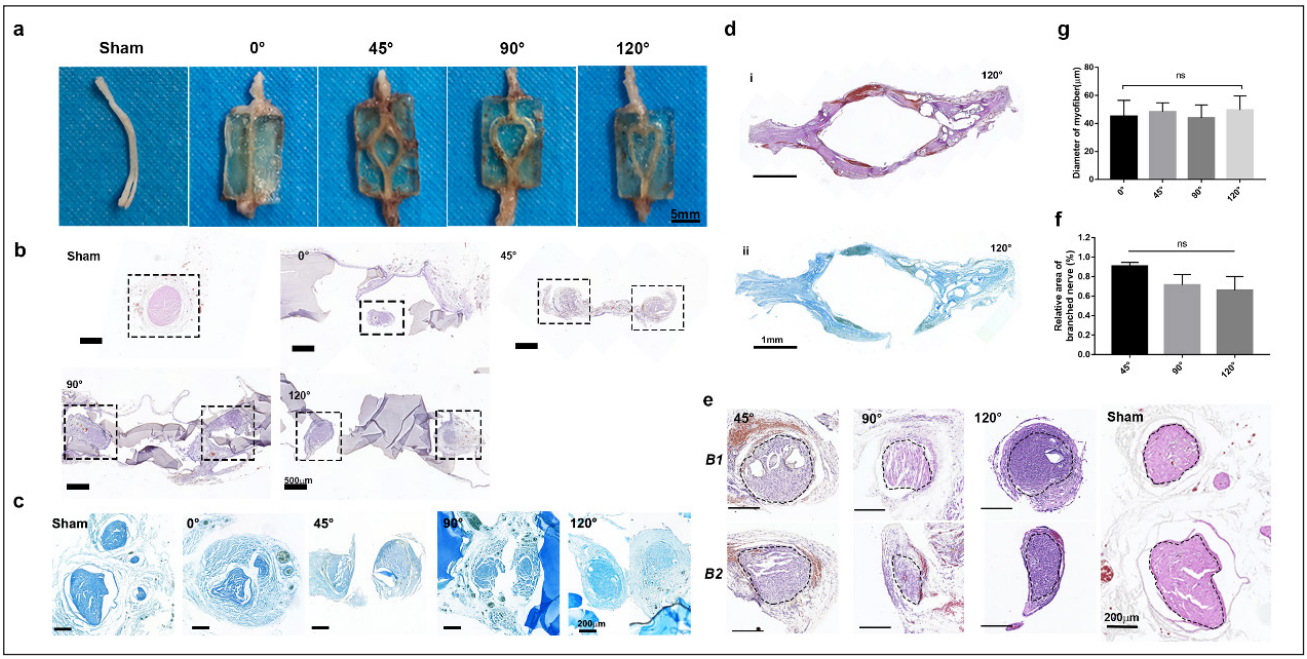


Figure 3. Histological analysis of nerves in DBNs. (a) Representative photographs of the fixed nerves with DBNs (scale bar = 5 mm). (b) H&E staining (scale bar = 500 μm) and (c) LFB staining of the regenerated nerve tissues in conduits (scale bar = 200 μm). (d) H&E staining and LFB staining of the longitudinal section of the regenerated branched nerves in DBNs (120°) (scale bar = 1 mm). (e) H&E staining of the regenerated branched nerves (B1, B2) (scale bar = 200 μm). (f) The relative cross-section area ratio of regenerated branched nerves. (g) The diameter of muscle fibers. Abbreviations: DBN: dual-branched NGC; H&E: hematoxylin and eosin; LFB: luxol fast blue.

of the regenerated axons (Figure 3c; **Figure S6** in Supplementary File). Notably, myelination was observed in the DBN groups and the sham group. The histological analysis of nerve longitudinal sections in DBN (120°) further indicated the formation of myelinated nerve branches (Figure 3d). In addition, the assessment of the relative cross-section area ratio, calculated in terms of the cross-section area of nerve B1 to that of nerve B2, yielded results indicating no significant differences among all the branched NGC groups (Figure 3e–f). In summary, the results demonstrated that peripheral nerves exhibit the capability to elongate into dual branches in DBNs. Furthermore, these nerves exhibited growth patterns at acute, right, and even obtuse angles to establish connections with the distal end.

3.3. Nerve regeneration in multi-branched NGCs

To investigate the effect of branch number on branched nerve regeneration, we utilized MBN implantation to bridge a linear defect of rat sciatic nerve (Figure 4a). Following a 16-week period, the two injured nerve stumps were reconnected. Electrophysiology analysis (Figure 4c and d) revealed no significant differences in the NCV and the latency of CMAP between the MBN group and the single-channel NGC group (0°). Meanwhile, the wet weight ratio of the gastrocnemius muscle demonstrated a

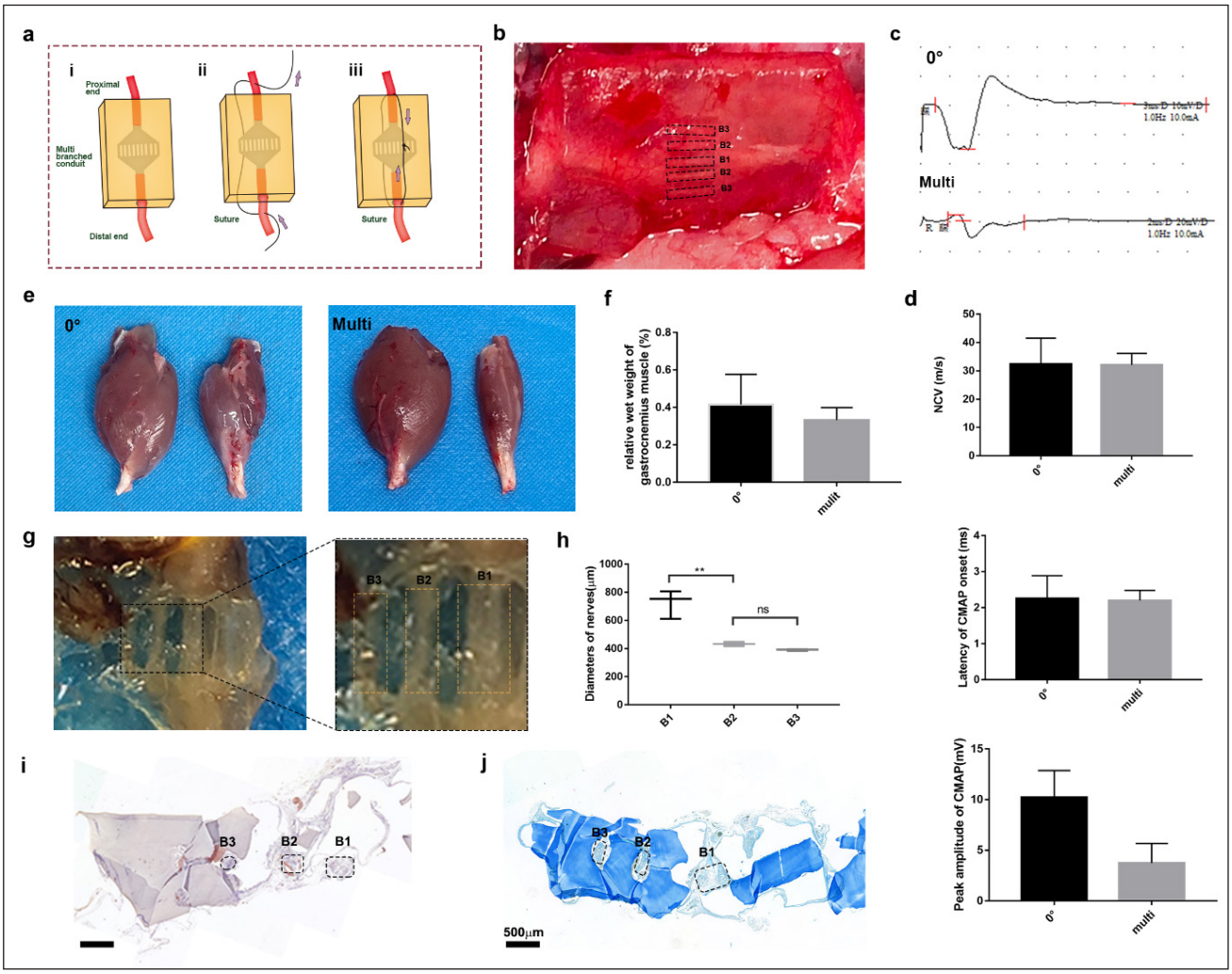


Figure 4. Nerve multi-branches were generated in MBNs. (a) The surgical process for implanting the multi-branched NGCs to bridge a linear gap of the sciatic nerve. (b) Photographs of the regenerated nerve branches in the multi-branched NGC. Dotted boxes represent newly regenerated nerve branches, including the middle one (B1), the second side (B2), and the third side (B3). (c) Representative CMAP recordings 16 weeks post-implantation. (d) Measurements of NCV, latency of CMAP onset, and peak amplitude of CMAP for each group. (e) The images of gastrocnemius muscles on the normal side (left) and surgical side (right). (f) The relative wet weight ratio of gastrocnemius muscles. (g) The representative photographs of the harvested regenerated multi-branched nerve with NGC. (h) The diameter of the regenerated branched nerves (B1, B2, and B3). (i) The H&E (scale bar = 500 μm) and (j) LFB staining of the regenerated branched nerves with NGC (scale bar = 500 μm). Abbreviations: CMAP: compound muscle action potential; H&E: hematoxylin and eosin; LFB: luxol fast blue; MBN: multi-branched NGCs; NCV: nerve conduction velocity; NGC: nerve guidance conduit.

similar trend in both groups. These results indicated that the regenerated nerves in MBNs exhibited a functional recovery comparable to that observed in the traditional NGC (Figure 4e and f).

Meanwhile, morphological observations of the regenerated nerves in the MBN group revealed that they filled the triangular area of the proximal connector and elongated into branch channels, forming tiny branches (Figure 4b and g). The average number of regenerated nerve branches was 6 across all rats, smaller than the pre-designed MBN channels. In the central channels of MBN, nerves regenerated into tiny nerve branches spanning the entire channel, while in side channels, no tiny nerve branches formed across the channel. The regenerated branched nerves formed within the channels extending from the center of the conduit exhibited a gradual reduction in diameter as they progressed toward both sides. The middle segment possessed the largest diameter, denoted as B1, while those on both sides were labeled B2 and B3, respectively, as shown in Figure 4b. Specifically, a statistically significant difference in diameter was observed between B1 and B2/B3 (Figure 4h), suggesting that nerve regeneration within the scaffold channel is influenced by the distance from the channel to the center axis of the NGC.

Furthermore, histological analysis was conducted to assess the regenerated multi-branched nerves using H&E and LFB staining (Figure 4i and j). H&E staining revealed the formation of inner branches within the regenerated nerves, while LFB staining provided evidence of myelination in these regenerated nerves. The results also suggested variations in nerve regeneration status among different tiny channels within the multi-branched NGC. These findings underscore the notion that the branch array within NGC may contribute to the formation of nerve branches and influence nerve branch regeneration.

Together, our investigation reveals that the architectural design of branched NGCs affects the nerve branching patterns and functions (Figure 5). The myelinated nerve branches exhibited comparable electrophysiological conduction within the channels of DBNs but demonstrated distinct electrophysiological conduction in MBN. The number of branched channels may be implicated in this disparity, suggesting that an excess number of branches could potentially lead to a decrease in nerve conduction. However, further investigation is warranted in the subsequent studies.

4. Discussion

Severe peripheral nerve injuries often result in the disruption of nerve tissues across multiple nerve paths, leading to functional disabilities in extremities such as the arms or legs. While traditional linear NGCs are effective in promoting nerve regeneration, they may damage the branch points, thereby inadequately addressing denervated tissue atrophy.[58,59] In contrast, branched NGCs present a novel approach to clinically treating peripheral nerve injuries by eliminating the impact of branch points. Recent studies have reported various branched NGCs for branched peripheral nerve regeneration.[60] However, the architectural design principles governing branched NGCs warrant further exploration.

Consequently, our study aims to promote the rational design of branched NGCs by investigating the effect of branch angle and number on nerve regeneration. In this study, we established a linear sciatic nerve defect model, marking the first exploration of the design of the branch angle and number for branched NGCs. By eliminating the influence of different nerve stumps, this method proves beneficial for investigating additional architecture parameters for branched NGC design. Within the scope of dual-branched NGCs featuring varying branch angles, we observed comparable histological morphologies and physiological functions of the regenerated branched nerves. These findings suggest that the branch angle of NGCs has minimal impact on nerve regeneration. While previous studies have often designed branched NGCs with a branch angle replicating the anatomical structure of injured nerves, our study suggests that the branch angle design may not be limited to anatomical considerations, offering potential flexibility to meet surgical needs. This aspect needs to be further explored in future studies.

Furthermore, reconstructing nerve branch points in branched nerve regeneration remains a challenge.[61,62] Our study presents a novel approach to reconstructing nerve branch points, demonstrating equivalent functionality in both branched channels irrespective of the angle. However, it should be noted that the number of branches also plays a crucial role in nerve regeneration. In multi-branched NGCs, we observed that excessive branching may lead to limited nerve regeneration in channels on the side of NGCs. Our findings may be helpful in promoting the rational design of the branch number of branched NGCs.

The fabrication of branched NGCs with complex architectural design holds significance for their further application in addressing branched peripheral nerve injuries. Traditional fabrication techniques for branched NGCs, such as electrospinning, lyophilization, and molding, face limitations in precision control and architectural replication.[13,14,32,63] Leveraging the advantages of fabricating scaffolds with delicate structures, 3D printing emerges as an advanced tool for the fabrication of branched NGCs.[64]

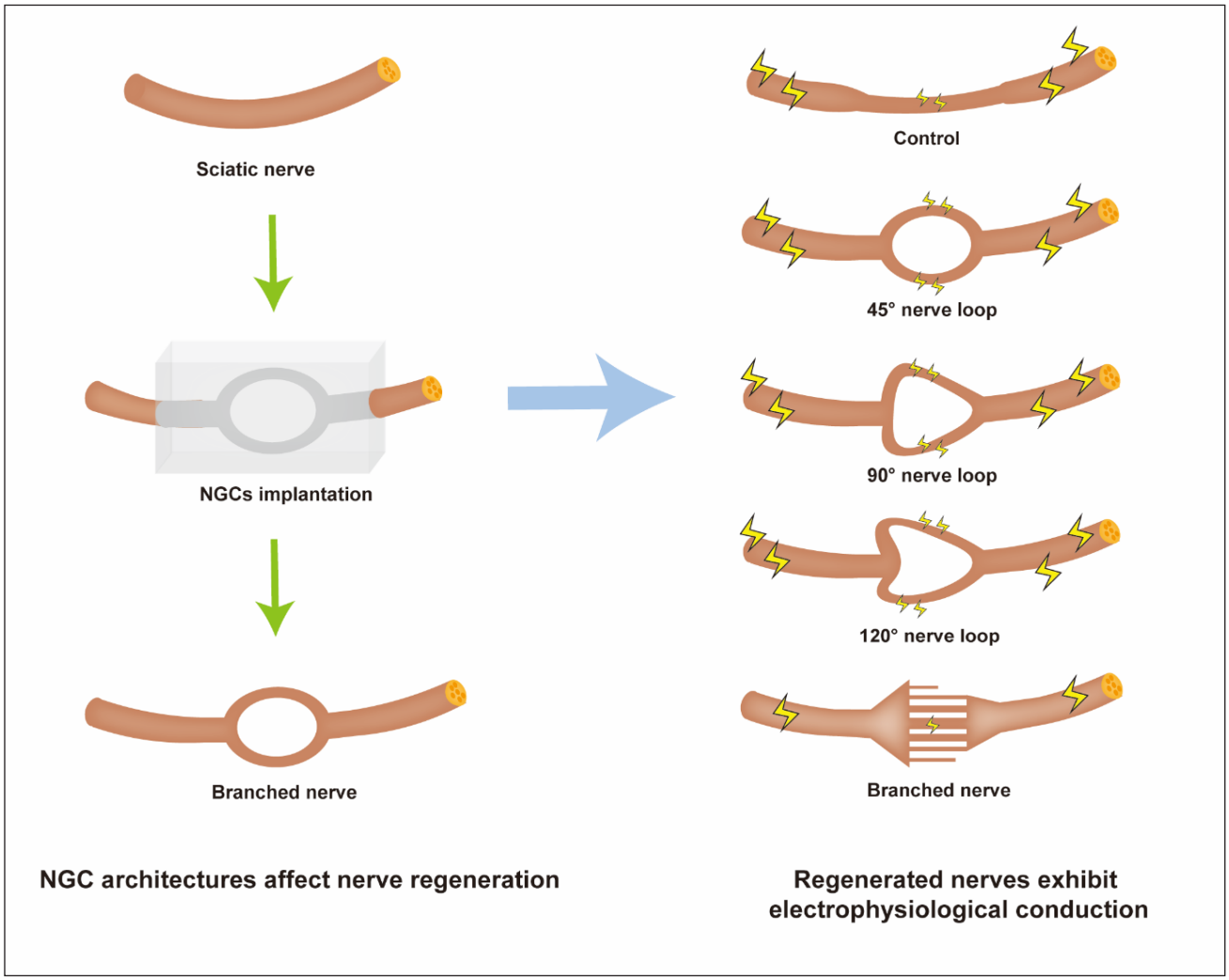


Figure 5. The designed branched NGC architectures could affect nerve regeneration, and the regenerated branched nerves exhibit comparable electrophysiology conduction.

Previous attempts by Johnson *et al.* involved the fabrication of a "Y"-shaped branched conduit using an extrusion-based 3D printing process.[39] However, extrusion-based techniques, with their relatively low printing precision, fall short of meeting the requirements for fabricating multi-branched NGCs.[65] Additionally, the reported branched conduit was composed of non-biodegradable silicone, potentially compromising the creation of a conducive microenvironment for nerve regeneration. In our study, DLP 3D printing exhibited excellent resolution, speed, and flexibility in constructing branched NGCs.[26,50,66,67] Additionally, the GelMA/PEGDA hydrogel NGC developed was both biodegradable and biocompatible, featuring high water content. This composition provides an enhanced biomimetic microenvironment for nerve regeneration when compared to silicone,[68] resin,[69] or polylactic acid (PLA)[70] and poly(lactide-co-caprolactone) PCL.[16]

The distal stump has been documented to exhibit a guiding effect on regenerated nerves within branched conduits, akin to a neurotropic effect.[71] Moreover, another study has found that nerve segments could grow along a bifurcation pathway even in the absence of a connection to a distal segment. However, the extent of outgrowth is significantly augmented in a pathway connected to a distal stump as opposed to an empty pathway.[72] In our study, the two regenerated branches in dual-branched NGCs exhibited similarities, attributed to the symmetrical nature of the two pathways within the scaffold. Both pathways shared identical lengths and a homogeneous microenvironment. However, the mechanisms underlying comparable nerve regeneration in various DNB configurations warrant further exploration. Meanwhile, different nerve branch regenerations observed in MBNs may be related to different neurotrophic effects and varying regenerated

pathway lengths within each channel. This aspect should also be further investigated in future studies.

Through the fabrication and characterization of branched NGCs, our work delved into the effect of branch angle and number on branch nerve regeneration. Our findings hold the potential to advance the design and fabrication of branched NGCs and, in turn, facilitate their application in cases of branched nerve injuries, such as those affecting the facial,[7,73] arm,[74] or leg[75] nerves. Furthermore, the implications of our findings on branch angle may open avenues for innovative surgical approaches that are otherwise challenging to perform. For instance, the utilization of branched conduits to create short-circuit connections presents a feasible strategy to decrease the sensory perception in the glans, thereby preventing erectile dysfunction arising from sensory deficits.[76,77]

5. Conclusion

In this study, we designed and prepared a series of dual-branched and multi-branched NGCs using DLP printing. Our aim was to investigate the effect of the branch angle and number of NGCs on nerve regeneration. Upon implanting these branched NGCs into a linear sciatic nerve defect model, we observed the regeneration of proximal nerve stumps along the designed channels, resulting in the formation of nerve dual branches with varying angles or multi-branches. Contrary to our expectations, our findings revealed that the electrophysiological conduction and histological morphologies of the regenerated nerve dual branches with various angles were similar. Meanwhile, the regenerated nerve branches in MBNs presented a decreasing diameter with an increasing distance from the scaffold center. These results suggest that the branched angle of branched NGCs may exert limited effects on nerve regeneration. Conversely, an excessive branch number in branched NGCs could potentially impede the reconstruction of nerve pathways. In summary, our study contributes valuable insights into the construction and application of functional multi-branched nerve conduits.

Acknowledgments

We would like to express our gratitude to Hao Cheng for his invaluable guidance and assistance in conducting the animal experiments. We also extend our thanks to Xiong Yang and Congrui Li for their technical support throughout the experiment. Additionally, we are grateful to Boya Li for her meticulous editing of this article.

Funding

The work is supported by the National Natural Science Foundation (32271468), the Sichuan Science and Technology Program (2021JDTD0001), the Fundamental Research Funds for the Central Universities (2022SCU12046), and Post-Doctor Research Project, West China Hospital, Sichuan University (2023HXBH081).

Conflict of interest

The authors declare that they have no known competing financial interests or personal relationships that could have appeared to influence the work reported in this paper.

Author contributions

Conceptualization: Maling Gou, Yinchu Dong, Wenbi Wu
Formal analysis: Yinchu Dong, Wenbi Wu, Haofan Liu, Xuebing Jiang, Li Li, Li Zhang , Yi Zhang, Jing Luo, Maling Gou
Investigation: Haofan Liu, Xuebing Jiang, Li Li, Li Zhang, Yi Zhang, Jing Luo
Methodology: Maling Gou, Yinchu Dong, Wenbi Wu
Supervision: Maling Gou
Writing – original draft: Yinchu Dong, Wenbi Wu
Writing – review & editing: Wenbi Wu, Yinchu Dong

Ethics approval and consent to participate

Animal experiments were approved by the Animal Care and Management Committee of West China Hospital, Sichuan University (Approval ID: 2021425A) and were performed in accordance with the guidelines and regulations of the Animal Research and Ethics Committee of Sichuan University.

Consent for publication

Not applicable.

Availability of data

The datasets used and/or analyzed during the current study are available from the corresponding author upon reasonable request.

References

1. Rodríguez FJ, Valero-Cabré A, Navarro X. Regeneration and functional recovery following peripheral nerve injury. *Drug Discov Today Dis Models*. 2004;1(2):177-185. doi: 10.1016/j.ddmod.2004.09.008
2. Scheib J, Hoke A. Advances in peripheral nerve regeneration. *Nat Rev Neurol*. 2013;9(12):668-676. doi: 10.1038/nrneurol.2013.227
3. Sunderland S. The anatomy and physiology of nerve injury. *Muscle Nerve*. 1990;13(9):771-784. doi: 10.1002/mus.880130903

4. Flores AJ, Lavernia CJ, Owens PW. Anatomy and physiology of peripheral nerve injury and repair. *Am J Orthop*. 2000;29(3):167-173.

5. Muheremu A, Sun JG, Wang XY, Zhang F, Ao Q, Peng J. Combined use of Y-tube conduits with human umbilical cord stem cells for repairing nerve bifurcation defects. *Neural Regen Res*. 2016;11(4):664-669. doi: 10.4103/1673-5374.180755

6. Allgood JE, Roballo KCS, Sparks BB, Bushman JS. The effects of graft source and orientation on outcomes after ablation of a branched peripheral nerve. *Front Cell Neurosci*. 2022;16:1055490. doi: 10.3389/fncel.2022.1055490

7. Bengur FB, Stoy C, Binko MA, et al. Facial nerve repair: Bioengineering approaches in preclinical models. *Tissue Eng Part B Rev*. 2022;28(2):364-378. doi: 10.1089/ten.TEB.2020.0381

8. Haller JR, Shelton C. Medial antebrachial cutaneous nerve: A new donor graft for repair of facial nerve defects at the skull base. *Laryngoscope*. 1997;107(8):1048-1052. doi: 10.1097/00005537-199708000-00008

9. White WM, McKenna MJ, Deschler DG. Use of the thoracodorsal nerve for facial nerve grafting in the setting of pedicled latissimus dorsi reconstruction. *Otolaryngol Head Neck Surg*. 2006;135(6):962-964. doi: 10.1016/j.otohns.2005.09.017

10. McKee D, Osemwengie B, Cox C. Distal digital nerve repair using nerve allograft with a dermal substitute: A case report. *Hand (N Y)*. 2020;15(4):Np47-np50. doi: 10.1177/1558944719854169

11. Leechavengvongs S, Witoonchart K, Uerpairojkit C. Penetrating injury to the terminal branches of the posterior interosseous nerve with nerve grafting. *J Hand Surg*. 2001;26(6):593-595. doi: 10.1054/jhsb.2001.0609

12. Terzis JK, Kostas I. Vein grafts used as nerve conduits for obstetrical brachial plexus palsy reconstruction. *Plast Reconstr Surg*. 2007;120(7):1930-1941. doi: 10.1097/01.prs.0000287391.12943.00

13. Stocco E, Barbon S, Emmi A, et al. Bridging gaps in peripheral nerves: From current strategies to future perspectives in conduit design. *Int J Mol Sci*. 2023;24(11). doi: 10.3390/ijms24119170

14. Wu S, Shen W, Ge X, et al. Advances in large gap peripheral nerve injury repair and regeneration with bridging nerve guidance conduits. *Macromol Biosci*. 2023:e2300078. doi: 10.1002/mabi.202300078

15. de Ruiter GC, Spinner RJ, Verhaagen J, Malessy MJ. Misdirection and guidance of regenerating axons after experimental nerve injury and repair. *J Neurosurg*. 2014;120(2):493-501. doi: 10.3171/2013.8.JNS122300

16. Fang Y, Wang C, Liu Z, et al. 3D printed conductive multiscale nerve guidance conduit with hierarchical fibers for peripheral nerve regeneration. *Adv Sci (Weinh)*. 2023;10(12):e2205744. doi: 10.1002/advs.202205744

17. Semmler L, Naghilou A, Millesi F, et al. Silk-in-silk nerve guidance conduits enhance regeneration in a rat sciatic nerve injury model. *Adv Healthc Mater*. 2023;12(11):e2203237. doi: 10.1002/adhm.202203237

18. Hasiba-Pappas S, Kamolz LP, Luze H, et al. Does electrical stimulation through nerve conduits improve peripheral nerve regeneration?-A systematic review. *J Pers Med*. 2023;13(3). doi: 10.3390/jpm13030414

19. Jin B, Yu Y, Chen X, et al. Microtubes with gradient decellularized porcine sciatic nerve matrix from microfluidics for sciatic nerve regeneration. *Bioact Mater*. 2023;21:511-519. doi: 10.1016/j.bioactmat.2022.08.027

20. Lin Y, Yu J, Zhang Y, et al. 4D printed tri-segment nerve conduit using zein gel as the ink for repair of rat sciatic nerve large defect. *Biomater Adv*. 2023;151:213473. doi: 10.1016/j.bioadv.2023.213473

21. Zhang D, Yao Y, Duan Y, et al. Surface-anchored graphene oxide nanosheets on cell-scale micropatterned poly(d,l-lactide-co-caprolactone) conduits promote peripheral nerve regeneration. *ACS Appl Mater Interfaces*. 2020;12(7):7915-7930. doi: 10.1021/acsami.9b20321

22. Zhang DM, Suo HR, Qian J, Yin J, Fu JZ, Huang Y. Physical understanding of axonal growth patterns on grooved substrates: Groove ridge crossing versus longitudinal alignment. *Biodes Manuf*. 2020;3(4):348-360. doi: 10.1007/s42242-020-00089-1

23. Allgood JE, Bittner GD, Bushman JS. Repair and regeneration of peripheral nerve injuries that ablate branch points. *Neural Regen Res*. 2023;18(12):2564-2568. doi: 10.4103/1673-5374.373679

24. Zhang J, Tao J, Cheng H, et al. Nerve transfer with 3D-printed branch nerve conduits. *Burns Trauma*. 2022;10:tkac010. doi: 10.1093/burnst/tkac010

25. Yao L, de Ruiter GC, Wang H, et al. Controlling dispersion of axonal regeneration using a multichannel collagen nerve conduit. *Biomaterials*. 2010;31(22):5789-5797. doi: 10.1016/j.biomaterials.2010.03.081

26. Zhu W, Tringale KR, Woller SA, et al. Rapid continuous 3D printing of customizable peripheral nerve guidance conduits. *Mater Today (Kidlington)*. 2018;21(9):951-959. doi: 10.1016/j.mattod.2018.04.001

27. Isaacs J, Mallu S, Yan W, Little B. Consequences of oversizing: Nerve-to-nerve tube diameter mismatch. *J Bone Joint Surg Am*. 2014;96(17):1461-1467. doi: 10.2106/JBJS.M.01420

28. Ma Y, Gao H, Wang H, Cao X. Engineering topography: Effects on nerve cell behaviors and applications in peripheral nerve repair. *J Mater Chem B*. 2021;9(32):6310-6325. doi: 10.1039/d1tb00782c

29. Moore AM, Kasukurthi R, Magill CK, Farhadi HF, Borschel GH, Mackinnon SE. Limitations of conduits in peripheral nerve repairs. *Hand (N Y)*. 2009;4(2):180-186. doi: 10.1007/s11552-008-9158-3

30. Giusti G, Shin RH, Lee JY, Mattar TG, Bishop AT, Shin AY. The influence of nerve conduits diameter in motor nerve recovery after segmental nerve repair. *Microsurgery*. 2014;34(8):646-652. doi: 10.1002/micr.22312

31. Hoffman-Kim D, Mitchel JA, Bellamkonda RV. Topography, cell response, and nerve regeneration. *Annu Rev Biomed Eng*. 2010;12:203-231. doi: 10.1146/annurev-bioeng-070909-105351

32. Petcu EB, Midha R, McColl E, Popa-Wagner A, Chirila TV, Dalton PD. 3D printing strategies for peripheral nerve regeneration. *Biofabrication*. 2018;10(3):032001. doi: 10.1088/1758-5090/aaaf50

33. Sarker M, Naghieh S, McInnes AD, Schreyer DJ, Chen XB. Strategic design and fabrication of nerve guidance conduits for peripheral nerve regeneration. *Biotechnol J*. 2018;13(7):1700635. doi: 10.1002/biot.201700635

34. Vijayavenkataraman S, Zhang S, Thaharah S, Sriram G, Lu WF, Fuh JYH. Electrohydrodynamic jet 3D printed nerve guide conduits (NGCs) for peripheral nerve injury repair. *Polymers*. 2018;10(7):753. doi: 10.3390/polym10070753

35. Kim JH, Kim I, Seol YJ, et al. Neural cell integration into 3D bioprinted skeletal muscle constructs accelerates restoration of muscle function. *Nat Commun*. 2020;11(1):1025. doi: 10.1038/s41467-020-14930-9

36. Zhang J, Hu Q, Wang S, Tao J, Gou M. Digital light processing based three-dimensional printing for medical applications. *Int J Bioprint*. 2020;6(1):242. doi: 10.18063/ijb.v6i1.242

37. Akbari M, Khademhosseini A. Tissue bioprinting for biology and medicine. *Cell*. 2022;185(15):2644-2648. doi: 10.1016/j.cell.2022.06.015

38. Johnson BN, Lancaster KZ, Zhen G, et al. 3D printed anatomical nerve regeneration pathways. *Adv Funct Mater*. 2015;25(39):6205-6217. doi: 10.1002/adfm.201501760

39. Johnson BN, Jia X. 3D printed nerve guidance channels: computer-aided control of geometry, physical cues, biological supplements and gradients. *Neural Regen Res*. 2016;11(10):1568-1569. doi: 10.4103/1673-5374.193230

40. Jain P, Kathuria H, Dubey N. Advances in 3D bioprinting of tissues/organs for regenerative medicine and in-vitro models. *Biomaterials*. 2022;287:121639. doi: 10.1016/j.biomaterials.2022.121639

41. Suri S, Han LH, Zhang W, Singh A, Chen S, Schmidt CE. Solid freeform fabrication of designer scaffolds of hyaluronic acid for nerve tissue engineering. *Biomed Microdevices*. 2011;13(6):983-993. doi: 10.1007/s10544-011-9568-9

42. Fairbanks BD, Schwartz MP, Bowman CN, Anseth KS. Photoinitiated polymerization of PEG-diacrylate with lithium phenyl-2,4,6-trimethylbenzoylphosphinate: Polymerization rate and cytocompatibility. *Biomaterials*. 2009;30(35):6702-6707. doi: 10.1016/j.biomaterials.2009.08.055

43. Shirahama H, Lee BH, Tan LP, Cho NJ. Precise tuning of facile one-pot gelatin methacryloyl (GelMA) synthesis. *Sci Rep*. 2016;6:31036. doi: 10.1038/srep31036

44. Liu X, Tao J, Liu J, et al. 3D printing enabled customization of functional microgels. *ACS Appl Mater Interfaces*. 2019;11(13):12209-12215. doi: 10.1021/acsami.8b18701

45. Tao J, Zhang J, Du T, et al. Rapid 3D printing of functional nanoparticle-enhanced conduits for effective nerve repair. *Acta Biomater*. 2019;90:49-59. doi: 10.1016/j.actbio.2019.03.047

46. Xu X, Tao J, Wang S, et al. 3D printing of nerve conduits with nanoparticle-encapsulated RGFP966. *Appl Mater Today*. 2019;16:247-256. doi: 10.1016/j.apmt.2019.05.014

47. Gu Y, Ji Y, Zhao Y, et al. The influence of substrate stiffness on the behavior and functions of Schwann cells in culture. *Biomaterials*. 2012;33(28): 6672-6681. doi: 10.1016/j.biomaterials.2012.06.006

48. Dalamagkas K, Tsintou M, Seifalian A. Advances in peripheral nervous system regenerative therapeutic strategies: A biomaterials approach. *Mater Sci Eng C Mater Biol Appl*. 2016;65:425-432. doi: 10.1016/j.msec.2016.04.048

49. Zhu W, Ma X, Gou M, Mei D, Zhang K, Chen S. 3D printing of functional biomaterials for tissue engineering. *Curr Opin Biotechnol*. 2016;40:103-112. doi: 10.1016/j.copbio.2016.03.014

50. Wu W, Dong Y, Liu H, et al. 3D printed elastic hydrogel conduits with 7,8-dihydroxyflavone release for peripheral nerve repair. *Mater Today Bio*. 2023;20:100652. doi: 10.1016/j.mtbio.2023.100652

51. Tao J, Liu H, Wu W, et al. 3D-printed nerve conduits with live platelets for effective peripheral nerve repair. *Adv Funct Mater*. 2020;30(42):2004272. doi: 10.1002/adfm.202004272

52. Politis MJ. Specificity in mammalian peripheral nerve regeneration at the level of the nerve trunk. *Brain Res*. 1985;328(2):271-276. doi: 10.1016/0006-8993(85)91038-8

53. Brushart TM, Seiler WAt. Selective reinnervation of distal motor stumps by peripheral motor axons. *Exp Neurol*. 1987;97(2):289-300.
doi: 10.1016/0014-4886(87)90090-2

54. Robinson GA, Madison RD. Motor neurons can preferentially reinnervate cutaneous pathways. *Exp Neurol*. 2004;190(2):407-413.
doi: 10.1016/j.expneurol.2004.08.007

55. Brushart TM, Gerber J, Kessens P, Chen YG, Royall RM. Contributions of pathway and neuron to preferential motor reinnervation. *J Neurosci*. 1998;18(21):8674-8681.
doi: 10.1523/jneurosci.18-21-08674.1998

56. Lacomis D. Electrophysiology of neuromuscular disorders in critical illness. *Muscle Nerve*. 2013;47(3):452-463.
doi: 10.1002/mus.23615

57. Wolthers M, Moldovan M, Binderup T, Schmalbruch H, Krarup C. Comparative electrophysiological, functional, and histological studies of nerve lesions in rats. *Microsurgery*. 2005;25(6):508-519.
doi: 10.1002/micr.20156

58. Vijayavenkataraman S. Nerve guide conduits for peripheral nerve injury repair: A review on design, materials and fabrication methods. *Acta Biomater*. 2020;106:54-69.
doi: 10.1016/j.actbio.2020.02.003

59. Conforti L, Gilley J, Coleman MP. Wallerian degeneration: An emerging axon death pathway linking injury and disease. *Nat Rev Neurosci*. 2014;15(6):394-409.
doi: 10.1038/nrn3680

60. Evangelista MS, Perez M, Salibian AA, et al. Single-lumen and multi-lumen poly(ethylene glycol) nerve conduits fabricated by stereolithography for peripheral nerve regeneration in vivo. *J Reconstr Microsurg*. 2015;31(5):327-335.
doi: 10.1055/s-0034-1395415

61. Zhai QK, Wang XK, Tan XX, Li L. Reconstruction for facial nerve defects of zygomatic or marginal mandibular branches using upper buccal or cervical branches. *J Craniofac Surg*. 2015;26(1):245-247.
doi: 10.1097/scs.0000000000001196

62. Chowdhry S, Yoder EM, Cooperman RD, Yoder VR, Wilhelmi BJ. Locating the cervical motor branch of the facial nerve: Anatomy and clinical application. *Plast Reconstr Surg*. 2010;126(3):875-879.
doi: 10.1097/PRS.0b013e3181e3b374

63. Tao J, Hu Y, Wang S, et al. A 3D-engineered porous conduit for peripheral nerve repair. *Sci Rep*. 2017;7:46038.
doi: 10.1038/srep46038

64. Yao Z, Yan L-W, Qiu S, et al. Customized scaffold design based on natural peripheral nerve fascicle characteristics for biofabrication in tissue regeneration. *Biomed Res Int*. 2019;20193845780.
doi: 10.1155/2019/3845780

65. Park JH, Jang J, Lee JS, Cho DW. Three-dimensional printing of tissue/organ analogues containing living cells. *Ann Biomed Eng*. 2017;45(1):180-194.
doi: 10.1007/s10439-016-1611-9

66. You S, Xiang Y, Hwang HH, et al. High cell density and high-resolution 3D bioprinting for fabricating vascularized tissues. *Sci Adv*. 2023;9(8):eade7923.
doi: 10.1126/sciadv.ade7923

67. Huang Y, Wu W, Liu H, et al. 3D printing of functional nerve guide conduits. *Burns Trauma*. 2021;9:tkab011.
doi: 10.1093/burnst/tkab011

68. Maki Y, Yoshizu T, Tsubokawa N. Selective regeneration of motor and sensory axons in an experimental peripheral nerve model without endorgans. *Scand J Plast Reconstr Surg Hand Surg*. 2005;39(5):257-260.
doi: 10.1080/0284431051006510

69. Bolleboom A, de Ruiter GCW, Coert JH, Tuk B, Holstege JC, van Neck JW. Novel experimental surgical strategy to prevent traumatic neuroma formation by combining a 3D-printed Y-tube with an autograft. *J Neurosurg*. 2019;130(1):184-196.
doi: 10.3171/2017.8.Jns17276

70. Shahriari D, Loke G, Tafel I, et al. Scalable fabrication of porous microchannel nerve guidance scaffolds with complex geometries. *Adv Mater*. 2019;31(30):e1902021.
doi: 10.1002/adma.201902021

71. Chiu DT, Smahel J, Chen L, Meyer V. Neurotropism revisited. *Neurol Res*. 2004;26(4):381-387.
doi: 10.1179/016164104225013815

72. Abernethy DA, Thomas PK, Rud A, King RH. Mutual attraction between emigrant cells from transected denervated nerve. *J Anat*. 1994;184(Pt 2):239-249.

73. Hu M, Xiao H, Niu Y, Liu H, Zhang L. Long-term follow-up of the repair of the multiple-branch facial nerve defect using acellular nerve allograft. *J Oral Maxillofac Surg*. 2016;74(1):218.e1-11.
doi: 10.1016/j.joms.2015.08.005

74. Cheesborough JE, Smith LH, Kuiken TA, Dumanian GA. Targeted muscle reinnervation and advanced prosthetic arms. *Semin Plast Surg*. 2015;29(1):62-72.
doi: 10.1055/s-0035-1544166

75. Szwedowski D, Ambrozy J, Grabowski R, Dallo I, Mobasheri A. Diagnosis and treatment of the most common neuropathies following knee injuries and reconstructive surgery - A narrative review. *Heliyon*. 2021;7(9):e08032.
doi: 10.1016/j.heliyon.2021.e08032

76. Liu Q, Li S, Zhang Y, et al. Anatomic basis and clinical effect of selective dorsal neurectomy for patients with lifelong premature ejaculation: A randomized controlled trial. *J Sex Med*. 2019;16(4):522-530.
doi: 10.1016/j.jsxm.2019.01.319

77. Moon du G. Is there a place for surgical treatment of premature ejaculation? *Transl Androl Urol*. 2016;5(4):502-507.
doi: 10.21037/tau.2016.05.06

ACCSCIENCE PUBLISHING

International Journal of Bioprinting

RESEARCH ARTICLE

Increased stiffness of extracellular matrix enhanced chemoresistance in 3D-bioprinted ovarian cancer model

Ying Shan[1†], Mingchang Pang[2†], Liqian Wang[3†], Yixin Mao[4†], Ruiyi Yan[2], Chang Zhou[5], Jingyuan Ji[5], Yilei Mao[2], Ying Jin[1*], and Huayu Yang[2*]

[1] Department of Obstetrics and Gynecology, National Clinical Research Center for Obstetric & Gynecologic Diseases, Peking Union Medical College Hospital, Chinese Academy of Medical Sciences & Peking Union Medical College, Beijing, China

[2] Department of Liver Surgery, Peking Union Medical College Hospital, Chinese Academy of Medical Sciences & Peking Union Medical College, Beijing, China

[3] Department of Gynecology, The Affiliated Yantai Yuhuangding Hospital of Qingdao University, Yantai, China

[4] Department of Geriatrics, Shanghai Eighth Peoples Hospital, Shanghai, China

[5] Biomanufacturing Center, Department of Mechanical Engineering, Tsinghua University, Beijing, China

(This article belongs to the *Special Issue: Bioprinting process for tumor model development*)

Abstract

Ovarian cancer is a gynecological malignancy with a high mortality rate. The ovarian cancer microenvironment is a crucial factor affecting the overall and progression-free survival rates of patients with ovarian cancer. The biophysical factors of the tumor microenvironment, such as stiffness, can affect the gene expression and behavior of tumor cells. In this study, we utilized 3D bioprinting technology to construct ovarian cancer tumor models with varying levels of stiffness *in vitro* to investigate the effect of extracellular matrix stiffness on drug resistance of tumor cells. Our findings indicate that increasing the stiffness of extracellular matrix can attenuate the sensitivity of tumor cells to chemotherapeutic agents. Additionally, the increased stiffness of 3D tumor model may promote malignant phenotypes, such as tumor stemness and tumor progression.

Keywords: 3D bioprinting technology; Ovarian cancer; Tumor microenvironment; Stiffness; Drug resistance

†These authors contributed equally to this work.

***Corresponding authors:**
Huayu Yang (dolphinyahy@hotmail.com)

Ying Jin (jinying@pumch.cn)

Citation: Shan Y, Pang M, Wang L, et al. Increased stiffness of extracellular matrix enhanced chemoresistance in 3D-bioprinted ovarian cancer model. *Int J Bioprint*. 2024;10(3):1673.
doi: 10.36922/ijb.1673

Received: August 24, 2023
Accepted: November 21, 2023
Published Online: January 18, 2024

Copyright: © 2024 Author(s). This is an Open Access article distributed under the terms of the Creative Commons Attribution License, permitting distribution, and reproduction in any medium, provided the original work is properly cited.

Publisher's Note: AccScience Publishing remains neutral with regard to jurisdictional claims in published maps and institutional affiliations.

1. Introduction

Ovarian cancer is the most fatal gynecological malignancy with a high mortality/morbidity ratio primarily attributed to the lack of specific symptoms and effective early screening strategies.[1] Despite advances in cancer treatment, survival rates for ovarian cancer have remained largely unchanged, even in medically advanced countries such as the United States and Canada, where only about 47% of patients survive five years after diagnosis.[2] Currently, cytoreductive surgery and cisplatin-based chemotherapy remain the preferred treatment options,[3,4] while the continuous development and updates in immunotherapy, targeted therapy, and combinatorial chemotherapy offer

new opportunities for clinical treatment.[5] Nevertheless, the efficacy of these treatments varies considerably among patients with ovarian cancer. This can be partly ascribed to the heterogeneity of individual tumors. As a matter of fact, personalized precision therapy for patients holds promise for improving overall survival rates.[6]

In recent years, the rapid advancement of 3D bioprinting technology has created a powerful platform for achieving patient-specific precision therapy. In contrast to other common 3D culture methods such as organoids and patient-derived xenografts, 3D bioprinting is extensively utilized in the development of functional tissues and organs,[7-10] construction of *in vitro* tumor models,[11-13] screening of anti-tumor drugs[14-16] and oncotherapy,[17] owing to its simplicity, low cost, and high stability. In addition, traditional screening tools for anti-tumor drugs are typically focused on two-dimensional planar cultures, which lack the inherent characteristics of the 3D environment *in vivo*, such as cell-cell interactions and cell-matrix interactions.[18,19] Therefore, 2D models may produce inaccurate results in the screening of anti-tumor drugs. In our previous study, we successfully created *in vitro* tumor models of hepatocellular carcinoma and cholangiocarcinoma using 3D bioprinting technology and assessed the effectiveness of anti-tumor drugs.[20-22] More importantly, a growing body of research confirms that 3D bioprinting technology is undoubtedly a promising approach to produce *in vitro* cancer model, thus allowing identification of patient-specific sensitive drugs.[23-25]

As previously described, the tumor microenvironment (TME) is a complex ecosystem that supports cancer initiation, progression, and invasion.[26] Undoubtedly, the ovarian cancer microenvironment is a crucial factor affecting the overall and progression-free survival of patients with ovarian cancer.[27,28] To be specific, the components of the TME, including the neighboring stromal cells and the extracellular matrix (ECM) secreted by tumors, interact with tumor cells in a complex and multifaceted manner to regulate chemotherapy resistance.[29-31] There is growing evidence that the biophysical properties of TME, such as stiffness, have implications for gene expression and behaviors of tumor cells. For instance, Wei *et al.* quantitatively confirmed that omental metastases are rich in desmoplasia and stiffer than paired primary tumors, and further demonstrated that matrix rigidity can modulate ovarian cancer progression.[32] Additionally, an interesting study by Kim *et al.* described a mechanically enhanced bioink that mimics the biochemical microenvironment characteristics of gastric cancer and exhibits more aggressive cancer-related traits, such as cell aggregation, cell interactions, and drug resistance.[33] Moreover, Tang *et al.* employed rapid 3D bioprinting to create multizone glioblastoma models with different stiffness, revealing that a rigid ECM microenvironment induces mesenchymal phenotypes that are linked to patient recurrence and unfavorable treatment results.[34] Another study conducted by Yang *et al.* identified many stiffness-sensing genes and genes enriched in cancer-related pathways by RNA-seq analysis of ovarian cancer cells grown in matrix of different stiffness, confirming that ovarian cancer is a mechanically responsive tumor.[35] At the same time, Pietilä *et al.* found that matrix hardness altered ECM signaling in high-grade serous cancer (HGSC) cells and that increased ECM stiffness protected HGSC cells from cisplatin therapy.[36] While these studies provide insights into matrix stiffness and tumor biological behavior, the approaches to model tumors with different levels of stiffness described above are complicated. Consequently, a simple and high-efficiency modeling method is urgently needed to simulate ovarian cancer tissues with various rigidity.

In this study, we fabricated *in vitro* models of ovarian cancer with various levels of stiffness in a more efficient and flexible way using 3D bioprinting technology. By modifying the hydrogel concentration, we simulated ovarian cancer tissues with various levels of stiffness and investigated the potential impact of ECM rigidity on pharmacodynamics. Accordingly, our study may provide practical guidance for oncologists to adjust drug regimens appropriately according to the stiffness of tumor tissue. In addition, we proved that 3D bioprinting technology is also an effective technique paving the way for investigating the correlation between tumor stiffness and biological activity, facilitating further exploration of disease mechanisms and new drugs.

2. Materials and methods

2.1. Cell culture

Human ovarian cancer cell line SKOV3 was purchased from Procell Life Science & Technology Co., Ltd. (Wuhan, Hubei, China). The cells were cultured in SKOV3 cell-specific medium (ProCell, Wuhan, China). Cells were cultured in a 5% CO_2 incubator at 37°C and passaged using trypsin (0.25%; Invitrogen, Carlsbad, USA) after reaching ~80% confluence. The culture medium was replaced every two days.

2.2. Rheological measurements

Rheological measurements were performed using a Physica MCR 302 rheometer (Anton Paar, Germany) with a cone-plate geometry measuring system (25 mm diameter, 2° cone angle, 99 truncation gap). The storage modulus (G') and loss modulus (G'') were recorded as a function of time through oscillatory measurements under a strain of 0.1% and frequency of 1.5 Hz. Besides that, temperature sweep

oscillatory tests were also conducted through cooling process with the rate of 5°C/min. The intersection of the G' and G'' curves is generally considered the gel point of the material. Different concentrations (6% and 8%) of GelMA were incubated at 37°C before testing and the temperature-controlled testing plate was also set at 37°C as the initial temperature. The time dependence of G' and G'' of GelMA hydrogels with different concentrations were measured according to a set measurement temperature (21.5°C), which corresponded to the setting of the printing temperature.

2.3. Semi-quantification of printability

When GelMA is in the ideal gelation state, the extruded filaments will show a clear morphology, marked by regular grids and square holes in the manufactured structure. We utilized the following formula to calculate GelMA printability (Pr) based on the square shape:[37]

$$\mathrm{Pr}=\frac{L^2}{16A} \quad \text{(I)}$$

where L means perimeter, and A means area. For an acceptable printability state, the interconnected channels of the 3D-bioprinted model would be square shape, and the Pr value was 1. To determine the Pr value of each concentration of GelMA at printing temperature, optical images of printed models were analyzed in ImageJ software (version 1.8.0) to calculate the perimeter and area of interconnected channels (n = 4).

2.4. Construction of 3D-bioprinted ovarian cancer model

A 3D cellular bioprinter BIOMAKER (SUNP Biotech, Beijing, China) was used to construct *in vitro* ovarian cancer models according to previously reported procedures.[22,23,38] Briefly, 10% gelatin methacryloyl (GelMA) hydrogels (EFL-GM-30, Engineering for Life, China) were prepared with phosphate-buffered saline (PBS) containing 0.25% (w/v) lithium phenyl(2,4,6-trimethylbenzoyl) phosphinate (EFL-GM-30, Engineering for Life, China). SKOV3 cells cultured in a 2D environment were collected and prepared as a suspension. The cell suspension was then mixed with 10% GelMA in a volume ratio of 2:3 (6%-3DP) or 1:4 (8%-3DP), with a final cell density of 5×10^6/mL. The cell/hydrogel mixture was pumped into a sterile syringe with a 23G needle and placed in a 3D bioprinter at a controlled temperature. The temperature of nozzle and molding chamber was 21.5°C and 10°C, respectively. The cell/hydrogel mixture was squeezed at a rate of 1 mm^3/s to fabricate the model and then exposed to a blue laser (wavelength 405 nm) for 20 s to modify the GelMA. Afterward, 1 mL SKOV3 cell-specific medium was added to each well of the 24-well plate. The culture medium was changed every two days.

2.5. Young's modulus tests

For each concentration of samples, the same 3D bioprinter was used to construct cuboids, which were 2 cm long, 1 cm wide and 0.6 cm high. Young's modulus tests were also performed on 3D models containing 6% GelMA and 8% GelMA but without tumor cells, in addition to 3D tumor models. Prior to the determination of Young's modulus, all samples were measured with vernier caliper to determine their actual sizes, including length, width, and height. Three samples of each condition were loaded and compressed until rupture at the rate of 0.05 mm/s using a mechanical test instrument (Bose ElectroForce 3200, Bose Corp.). The elastic part (10% to 20% strain) of the stress-strain curve was used to calculate the Young's modulus.

2.6. Cell survival assay

Cell survival in the 3D-bioprinted models was assessed on days 1, 3, 5, 7, and 10 after printing. Cell survival was measured using a live/dead fluorescence assay. Briefly, a mixture of calcein-AM (C-AM, 1 μmol/L; Sigma-Aldrich, Burlington, USA) and propidium iodide (PI, 2 μmol/L; Sigma-Aldrich, Burlington, USA) was prepared and passed through a 0.22-μm filter prior to staining. The 3D-bioprinted model was gently washed with PBS and incubated in a C-AM/PI mixture at 37°C for 30 minutes in the dark. After incubation, the 3D-bioprinted model was gently washed with PBS and observed using a laser-scanning confocal microscope (C2/C2si; Nikon, Tokyo, Japan). Five random fields were captured for each sample, and the cells in the five samples were counted using the ImageJ software (Version 1.8.0). Cell survival (%) was calculated using the following formula:

$$Cell\,survival(\%)=\frac{Number\,of\,live\,cells}{Total\,number\,of\,cells}\times100 \quad \text{(II)}$$

2.7. Cell proliferation assay

The 2D-Ov cells and 3D-bioprinted cells on days 1, 3, 5, 7,10 after printing were incubated in a mixture of culture medium and Cell Counting Kit 8 (CCK8; Dojindo, Kumamoto, Japan) at a volume ratio of 9:1. After 2 h of incubation at 37°C, the absorbance of the culture medium at 450/620 nm was measured (AMR-100; ALLSHENG, Hangzhou, China).

2.8. Evaluation of protein and mRNA expression

The expression of ovarian cancer-associated proteins and multidrug resistance genes was evaluated using several methods. Ki-67 and p53 protein expression were detected by immunofluorescence, and the mRNA expression of *p53*,

IL-6, *CD133*, *ALDH1*, *CD44*, *ABCA1*, *MRP-1*, and *MDR-1* was detected by real-time quantitative polymerase chain reaction. The antibody details and primer sequences are shown in Tables 1 and 2, respectively.

2.9. Pharmacodynamic evaluation of antitumor drugs

On day 7 after printing, 3D-bioprinted cells were treated with a range of concentrations of carboplatin (1 μM, 10μ M, 30 μM, 50 μM, 70 μM, 100 μM), paclitaxel (0.1 nM, 1 nM, 10 nM, 1000 nM, 50000 nM) and olaparib (1 μM, 10 μM, 30 μM, 50 μM, 100 μM, 150 μM). When 2D-Ov cells reached approximately 70–80% confluence, they were treated with different concentrations of the antitumor drugs listed above. Cell growth was measured using the CCK8 assay, and dose-response curves were plotted using GraphPad Prism (Version 9.0.0, San Diego, CA, USA).

2.10. RNA sequencing and bioinformation analysis

RNA was extracted using the TRIzol method (Invitrogen, CA, USA) and treated with RNase-free DNase I (Takara, Kusatsu, Japan). A total amount of 1.5 μg RNA per sample was used as input material for the RNA sample preparations. Sequencing libraries were generated using NEBNext® Ultra™ RNA Library Prep Kit for Illumina® (NEB, USA) following recommendations of manufacturer and index codes were added to attribute sequences to each sample. The library preparations were sequenced on an Illumina Novaseq 6000 platform by the Beijing Allwegene Technology Company Limited (Beijing, China), and paired-end 150 bp reads were generated. Differential expression analysis of two conditions/groups was performed using the DESeq R package (1.10.1). Genes with an adjusted *p*-value <0.05 found by DESeq were assigned as "differentially expressed." Gene Ontology (GO) enrichment analyses of differentially expressed genes (DEGs) were implemented using the cluster Profiler R package. GO terms with corrected p <0.05 were considered significantly enriched by DEGs.

2.11. Statistical analysis

Data are expressed as mean ± standard deviation. Student's *t*-test was used to determine whether there was a statistically significant difference between groups. Statistical significance was defined as $^{*}p$ <0.05, $^{**}p$ <0.01, $^{***}p$ <0.001, $^{****}p$ <0.0001.

3. Results

3.1. Rheological evaluation

For assessment of printability, we conducted rheological evaluation for two concentrations of GelMA. As shown in Figure 1A, temperature sweep oscillatory tests were performed through cooling process, the temperature to reach G' and G'' crossover of 6% GelMA and 8% GelMA were about 18.8°C and 20.7°C, respectively. When temperature is higher than crosslinking temperature, G'' is greater than G', and the GelMA hydrogels would be in a fluid or sol state. In addition, the results of time sweep tests demonstrated that the different concentrations of GelMA showed time-dependence properties when operating from

Table 1. Antibodies used in immunofluorescence experiment

Antibodies	Concentration	Source
Rabbit anti--human Ki-67	1:100	Abcam, Cambridge, UK
Mouse anti-human p53	1:100	Abcam, Cambridge, UK
Goat anti-Rabbit (Alexa Fluor® 594)	1:300	Abcam, Cambridge, UK
Goat anti-Mouse (Alexa Fluor® 488)	1:300	Abcam, Cambridge, UK

Table 2. Primers used in quantitative polymerase chain reaction (qPCR)

Gene	Forward (5'-3')	Reverse (5'-3')
p53	ACTTGTCGCTCTTGAAGCTAC	GATGCGGAGAATCTTTGGAACA
IL-6	GCCAGAGCTGTGCAGATGAG	CAGTGGACAGGTTTCTGACC
CD133	AGTCGGAAACTGGCAGATAGC	GGTAGTGTTGTACTGGGCCAAT
ALDH1	CCCTGGAGACGATGGATACAG	TCTGAGGGTTCTAATACAGCCC
CD44	CTGCCGCTTTGCAGGTGTA	CATTGTGGGCAAGGTGCTATT
ABCA1	TCTCACCACTTCGGTCTCCATG	CCTCGCCAAACCAGTAGGACTT
MRP-1	TCTACCTCCTGTGGCTGAATCTG	CCGATTGTCTTTGCTCTTCATG
MDR-1	TTGCTGCTTACATTCAGGTTTCA	AGCCTATCTCCTGTCGCATTA
GAPDH	CGAGATCCCTCCAAAATCAA	TTCACACCCATGACGAACAT

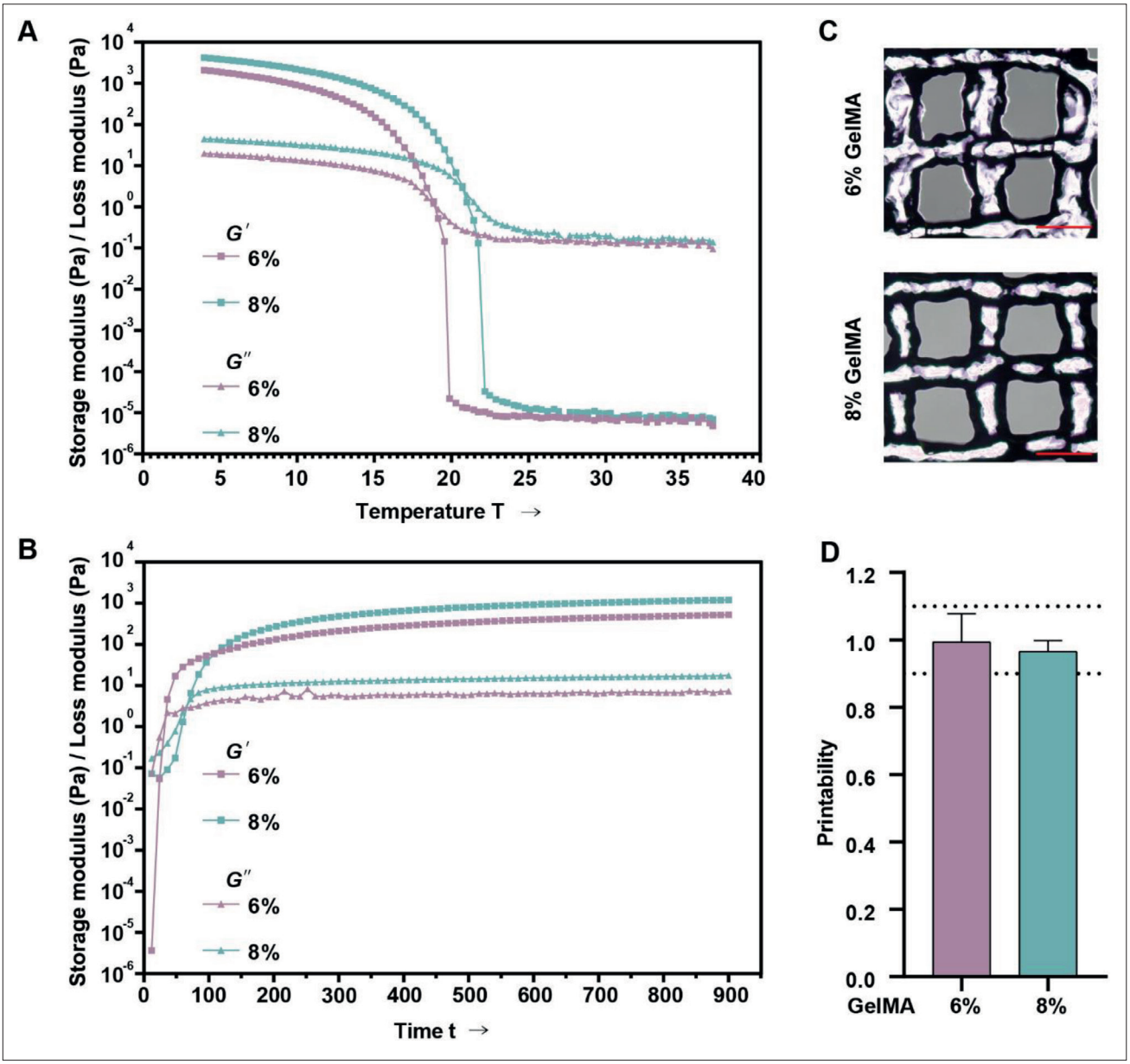


Figure 1. Rheological measurement and Young's modulus for different 3D-bioprinted models. (A) Temperature sweep tests showing storage modulus (G') and loss modulus (G'') with cooling rate of 5°C/min for 6% GelMA and 8% GelMA. (B) Time sweep tests showing G' and G'' under 21.5°C for 6% GelMA and 8% GelMA. (C) Optical images of 3D-printed models with different concentrations of GelMA. Scale bar: 500 μm. (D) Semi-quantitation of Pr values of 3D-printed models with different concentrations of GelMA.

initial temperature of 37°C to the measured temperature of 21.5°C. To be specific, 8% GelMA had a relatively higher modulus compared to 6% GelMA (Figure 1B). In our study, in order to evaluate the printability of bioinks semi-quantitatively, the Pr values of each concentration of GelMA were calculated by **Equation I**. According to previous study,[37] 3D-bioprinted models will exhibit satisfying morphology when Pr is in the range of 0.9 to 1.1. Figure 1D show that Pr values of 6% GelMA and 8% GelMA are 0.994±0.083 and 0.966±0.032, respectively.

3.2. Construction of 3D-bioprinted ovarian cancer model

To simulate the TME *in vivo*, a 3D-bioprinted ovarian cancer tumor model with a lattice structure was constructed *in vitro* (Figure 2A). The 3D bioprinting technology allows for the quick generation of various fine structures with

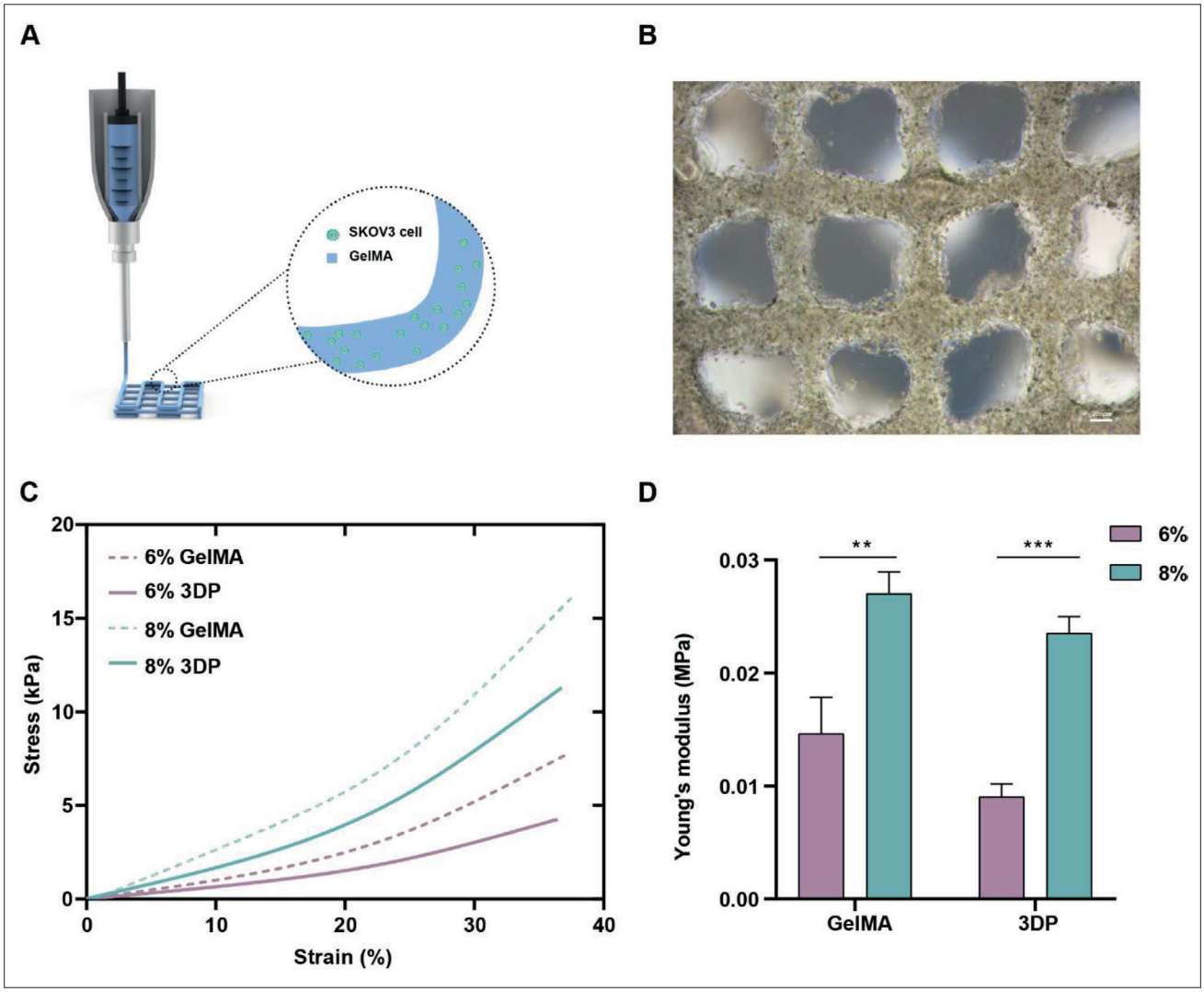


Figure 2. Fabrication of 3D-bioprinted ovarian cancer model. (A) Schematic illustration of the 3D bioprinting process. (B) An image of the 3DP-Ov model. Scale bar: 200 μm. (C) Representative stress-strain curves of 3D models under different conditions. (D) Young's modulus of 3D models under different conditions.

high resolution tailored for research purposes. Figure 2B shows the resulting 3D-bioprinted ovarian cancer model. Our preliminary study involved exploring suitable bioink materials and 3D bioprinting technologies for cell growth and proliferation.[23] We used GelMA, a hydrogel containing ovarian cancer cells, to print a 3D lattice structure measuring 6 mm in length, 6 mm in width, and 1 mm in height, according to a preset procedure.

To investigate the impact of ECM stiffness on tumor cells, we mixed tumor cell suspensions with 10% GelMA hydrogel in suitable proportions to create tumor models with GelMA concentrations of 6% (*i.e.*, 6%-3DP) and 8% (*i.e.*, 8%-3DP). As presented in Figure 2C, stress-strain curves of 3D models under various conditions were obviously different. To be specific, the Young's moduli of 6%-3DP and 8%-3DP tumor models were 0.009±0.001 MPa and 0.024±0.001 MPa with a significant difference. Additionally, for the 3D-bioprinted models without tumor cells, the Young's modulus of 6% GelMA and 8% GelMA were 0.015±0.003 MPa and 0.027±0.002 MPa, respectively (Figure 2D).

The 3D-bioprinted ovarian cancer model was cultured in SKOV3 cell medium with medium changes every two days. C-AM/PI staining was used to evaluate the viability of tumor cells in 3D ovarian cancer model. The results revealed that cell viability of 6%-3DP was approximately 82% on the first day after printing. With the extension of culture time after printing, cell viability gradually increased

and remained stable at over 90% from the fifth day after printing (Figure 3A).

Compared to ovarian cancer cells grown under traditional 2D conditions (2D-Ov), tumor cells cultured under 3D conditions exhibited strong proliferative capability. Specifically, the growth rate of 6%-3DP cells was lower on the first to third day. However, on day 4, the cell proliferation rates in both cultures became equal.

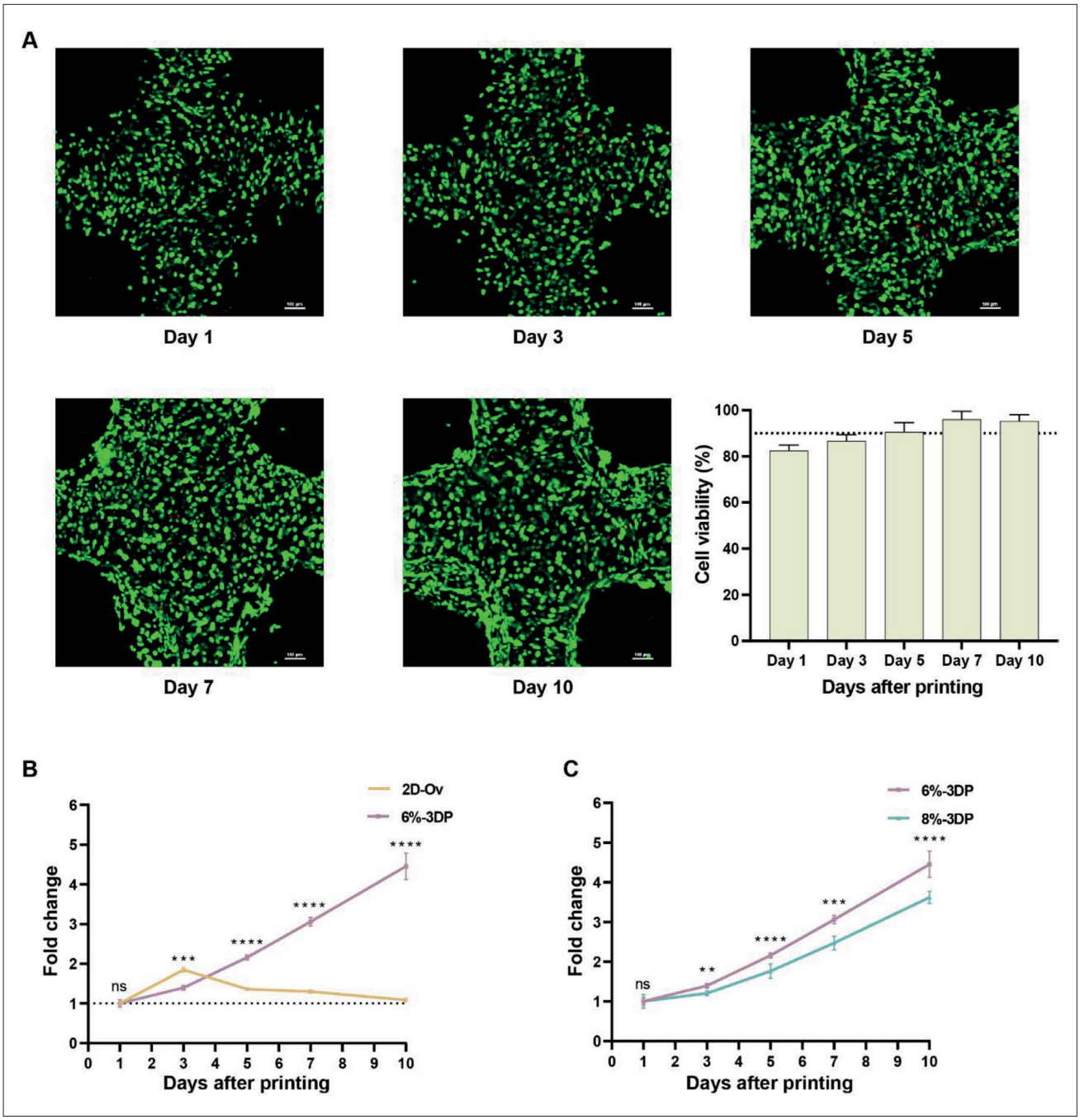


Figure 3. Cell survival and proliferation in 3D-bioprinted ovarian cancer model. (A) Representative live-dead staining images of 6%-3DP model captured on days 1, 3, 5, 7, and 10, and cell viability of 6%-3DP model at different time points after printing. Live and dead cells were labeled with calcein-AM (green) and PI (red), respectively. Scale bar: 500 μm. (B) Proliferation rates of 2D-Ov and 6%-3DP cells at different time points after printing. (C) Proliferation rates of 6%-3DP and 8%-3DP cells at different time points after printing. The results are expressed as fold change compared to day 1. ns, not significant; $^{**}p$ <0.01; $^{***}p$ <0.001; $^{****}p$ <0.0001.

Since then, the 6%-3DP model maintained a high growth rate, while because there was not enough room to grow, the number of cells in the 2D model gradually decreases. Moreover, the amount of cells in the 6%-3DP model increased approximately four times by day 10, while the number of cells on day 10 in the 2D model was similar to that on day 1 (Figure 3B). Notably, in both 3D models, the cells maintained a high growth rate. Nevertheless, differences in the rate of proliferation between the two models began to appear starting day 3, and by day 10, the number of cells in the 6%-3DP and 8%-3DP models had approximately quadrupled and tripled, respectively, as compared to the cell number on day 1 (Figure 3C).

3.3. Tumor-related protein and mRNA expression

To assess the biological activity of tumor cells in the 3D-bioprinted models, we used immunofluorescence to detect the expression of ovarian cancer-related proteins in 6%-3DP and 8%-3DP models. Our findings revealed that Ki-67 and p53 proteins were expressed in both models, indicating high activity of tumor cells in these models (Figure 4).

To investigate whether ECM stiffness affects tumor-related genes, we extracted mRNA from cells in 6%-3DP and 8%-3DP models 10 days after printing. We evaluated the expression of *p53*, *IL-6*, *ALDH1*, *CD44* and *CD133* genes. Our findings indicate that the levels of *p53* and *IL-6* mRNA were approximately eight- and three-fold higher, respectively, in 8%-3DP group than in 6%-3DP group. Additionally, as the stiffness of 3D tumor model increased, the expression of tumor stemness markers ALDH1 and CD44 was upregulated, whereas the expression of CD133 did not change significantly (Figure 5).

3.4. Effects of antitumor drugs on 2D-Ov and 3D-bioprinted model

Initially, we evaluated the response of 2D-Ov and 6%-3DP cells to anti-tumor drugs by treating both models with carboplatin, paclitaxel, and olaparib for 72 h. Our results revealed that the IC_{50} values of carboplatin, paclitaxel, and olaparib in the 6%-3DP models were significantly higher compared to those in 2D-Ov models (62.85 vs. 9.921 μM, 3.305 vs. 0.004 μM, 27.17 vs. 8.119 μM, respectively) (Figure 6).

3.5. Effects of antitumor drugs on 3D-bioprinted models with different stiffness

To further investigate the impact of the structural stiffness of 3D tumor models on pharmacodynamics, we treated 6%-3DP and 8%-3DP models with carboplatin, paclitaxel, and olaparib for 72 h. Our findings indicated that the IC_{50} values of the three anti-tumor drugs measured in the 8%-3DP model were higher than those measured in the 6%-3DP model (127.6 vs. 62.85 μM, 4.997 vs. 3.305 μM, 39.59 vs. 27.17 μM, respectively) (Figure 7A–C).

To investigate the mechanism underlying the differences in the pharmacodynamics of 3D ovarian cancer models with different stiffness, we collected RNA from 6%-3DP and 8%-3DP cells after 10 days of culture and evaluated the expression of multidrug resistance genes. Our results revealed that the stiffness of ECM affects the expression of drug resistance genes. In 8%-3DP model, the expression of *MDR1* and *MRP1* genes were obviously increased, and their mRNA levels were approximately four and two times higher than those in 6%-3DP model, respectively. However, there was no significant difference in ABCA1 expression between the two groups (Figure 7D–F).

3.6. Transcriptional profiling of 3D-bioprinted models with different stiffness

Next, we found significant differences in transcriptional profile between the 6%-3DP and 8%-3DP models. A total of 217 DEGs were identified, including 145 upregulated genes and 72 downregulated genes (Figure 8A and 8B). To explore the functional characteristics of DEGs, we performed GO pathway enrichment analysis. GO analysis results demonstrated that the upregulated genes were obviously enriched in "metabolic process," "response to chemical," "phosphorus metabolic process," "response to organic substance," and "response to endogenous stimulus." For the downregulated DEGs, the most enriched GO terms included "immune system process," "interspecies interaction between organisms," "response to external stimulus," "regulation of response to stress," and "response to biotic stimulus" (Figure 9).

Additionally, bioinformatics analysis also revealed that elevating the stiffness of the 3D-bioprinted ovarian cancer model led to increased expression of key genes associated with chemotherapy resistance, namely *EGR1*, *FOS*, *CRYAB*, *G6PD*, *DUSP1*, *PIM1*, *PPDPF*, *HDAC5*, and *FGFR4* (Figure 8C). These findings align with previous research that has confirmed the correlation between overexpression of these genes and enhanced chemoresistance, which has implication on shortening the overall survival durations.[39-47]

4. Discussion

In this study, we used 3D bioprinting technology to construct *in vitro* ovarian cancer tumor models and generated ovarian cancer models with varying degrees of stiffness by adjusting GelMA hydrogel content. Thus, we were able to simulate ovarian cancer tissues with different levels of stiffness that closely resembled those observed in clinical settings. Compared with traditional 2D models,

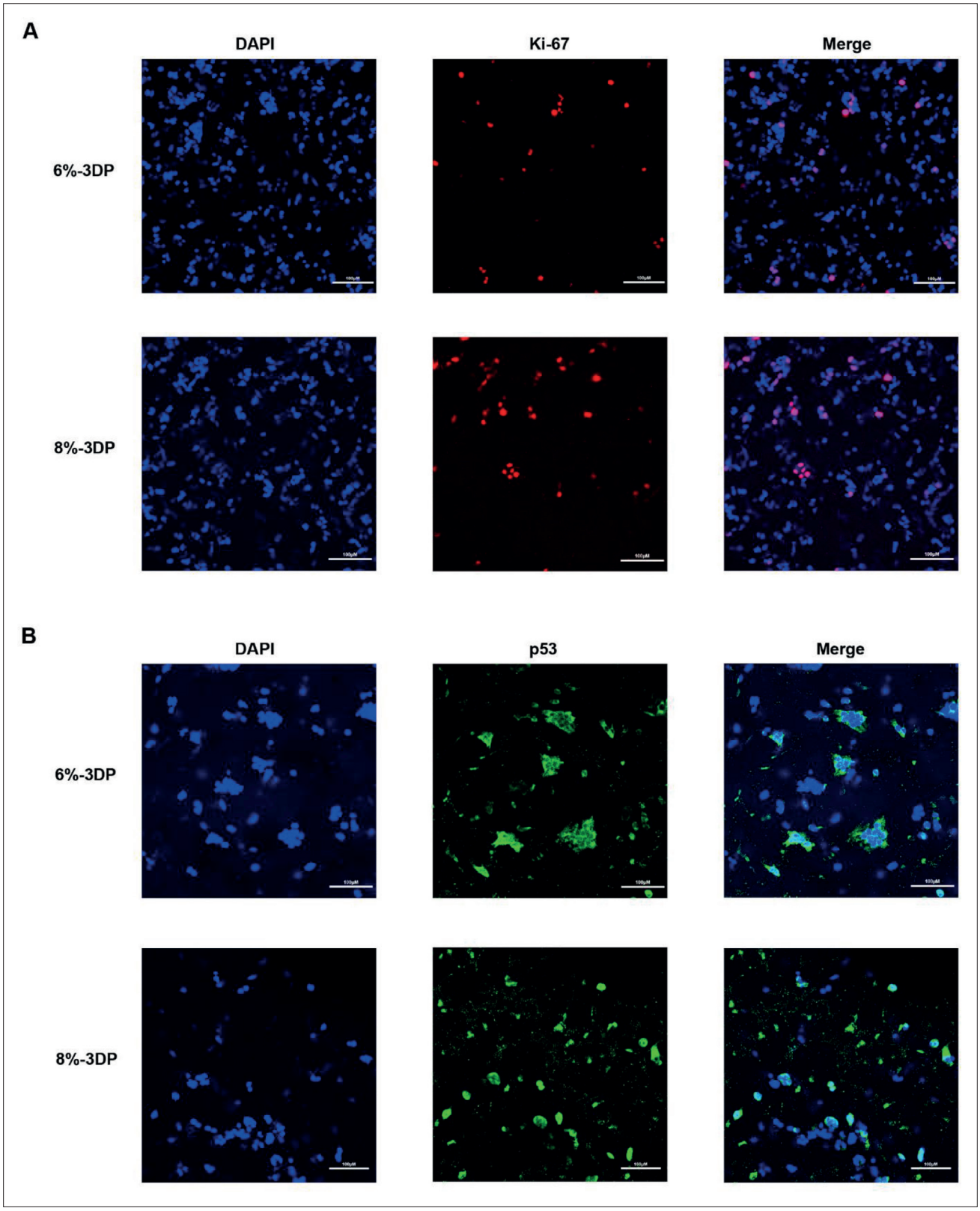


Figure 4. Ovarian cancer-related protein expression in 3D-bioprinted ovarian cancer models with different stiffness. (A) The expression of Ki-67 in 6%-3DP and 8%-3DP models. (B) The expression of p53 in 6%-3DP and 8%-3DP models.

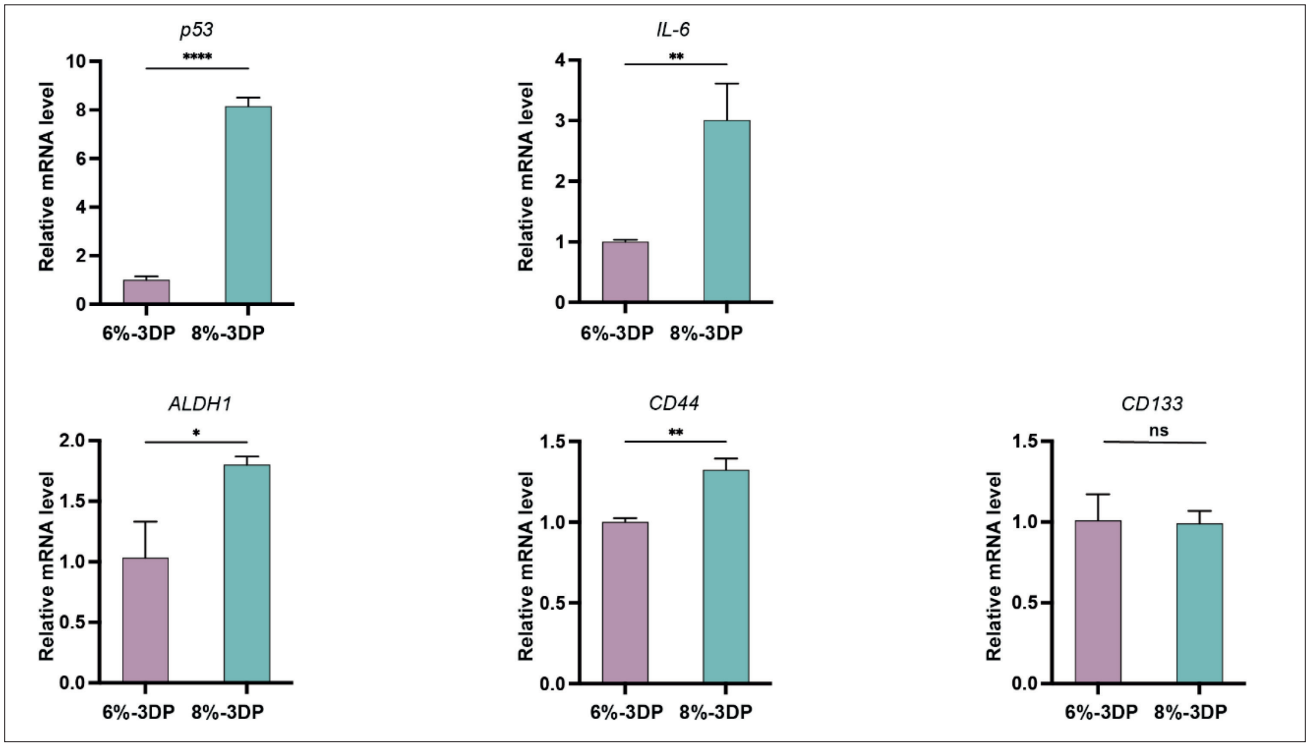


Figure 5. Ovarian cancer-related mRNA expression in 3D-bioprinted ovarian cancer models. The expression of tumor-related genes, including *p53*, *IL-6*, *ALDH1*, *CD44* and *CD133* in 6%-3DP and 8%-3DP models. ns, not significant; **p* <0.05; ***p* <0.01; *****p* <0.0001.

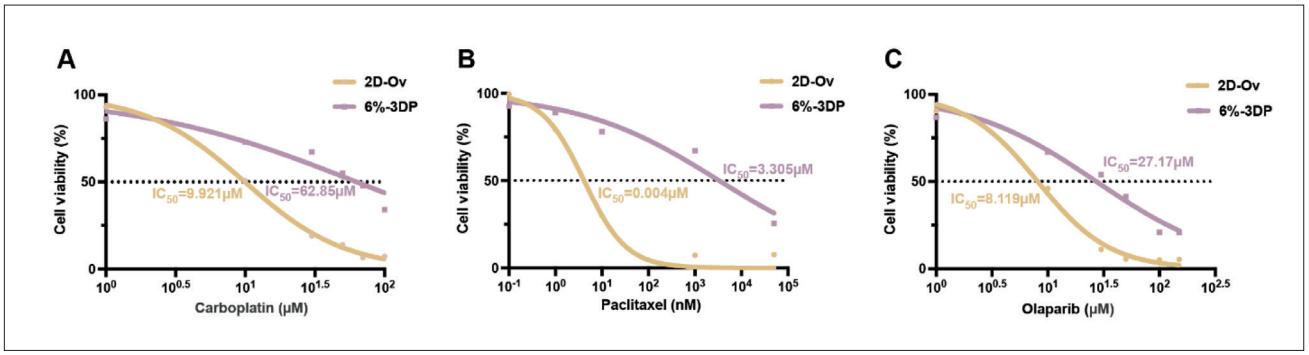


Figure 6. Characteristics of drug metabolism across various ovarian cancer models. Dose-effect curves of carboplatin (A), paclitaxel (B), and Olaparib (C) in the 2D-Ov and 6%-3DP models after 72 h of treatment.

3D models provide tumor cells in a microenvironment that bear greater resemblance to the one found *in vivo*, especially in the aspects of specific cell size, spatial distribution of cells, cell geometry, and ECM components.[48,49] These factors significantly affect the functional state of and interactions between tumor cells. Previous studies have shown that increased matrix stiffness can promote the malignant phenotype of tumors during progression.[50] Furthermore, evidence suggests that stiffness, an important characteristic of the ECM, can significantly influence cancer cell responses to treatment and chemotherapy resistance.[51] Consistent with these findings, we observed that increasing the stiffness of the tumor ECM reduced the sensitivity of tumor cells to antitumor drugs.

Three-dimensional tumor models, particularly those developed through 3D bioprinting, hold great promise for advancing next-generation precision therapies.[52] These models have garnered global support, and the most recent milestone was marked by the United States passing a law in December 2022 that enables new drugs to be approved by the U.S. Food and Drug Administration (FDA) without

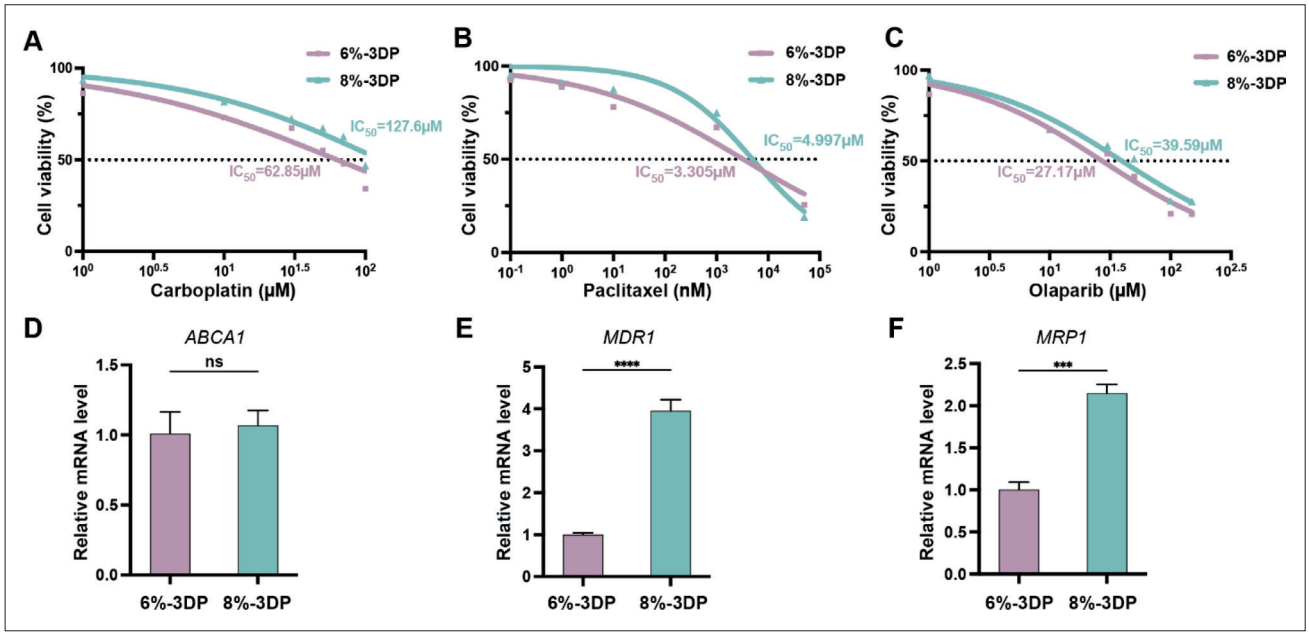


Figure 7. Profiles of drug metabolism of 3D-bioprinted ovarian cancer models with different stiffness. (A–C) Dose-effect curves of carboplatin (A), paclitaxel (B), and olaparib (C) in 6%-3DP and 8%-3DP models after 72 h of treatment. (D–F) mRNA expression of drug resistance genes, including *ABCA1* (D), *MDR1*(E), and *MRP1*(F) in 6%-3DP and 8%-3DP models. ns, not significant; ***p <0.001; ****p <0.0001.

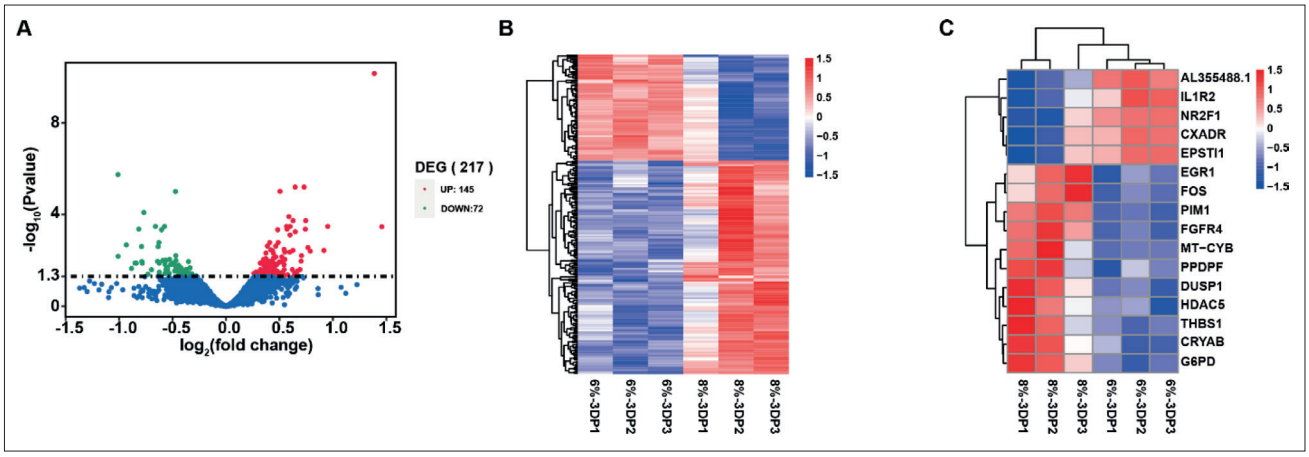


Figure 8. Transcriptional profiling of 3D-bioprinted ovarian cancer models with varying stiffness. (A) Volcano plot of 217 differentially expressed genes (DEGs), including 145 significantly upregulated DEGs (red spots) and 72 significantly downregulated DEGs (green spots). (B) Cluster analysis of DEGs of the 6%-3DP and 8%-3DP models. Rows represent genes, and columns represent samples. (C) The heatmap of 16 significantly DEGs. Red represents upregulated genes, and green represents downregulated genes.

requiring animal testing. This legislation also permits the FDA to progress from drug or biological testing to human testing after conducting non-animal testing. An increasing number of researchers have recognized the value of non-animal methods such as computer modeling and organ chips in drug testing and development. 3D bioprinting offers a unique opportunity to test novel drugs that currently lack clinical data. As a result, tumor models constructed *in vitro* using 3D bioprinting technology can facilitate preclinical prediction, which conforms to the new trend of tumor research in the era of precision medicine.

Our team constructed an ovarian cancer tumor model using straightforward, time-saving, and economical extrusion-based bioprinting techniques. The tumor model demonstrated structural stability in culture post-printing, maintained high cell vitality and proliferation

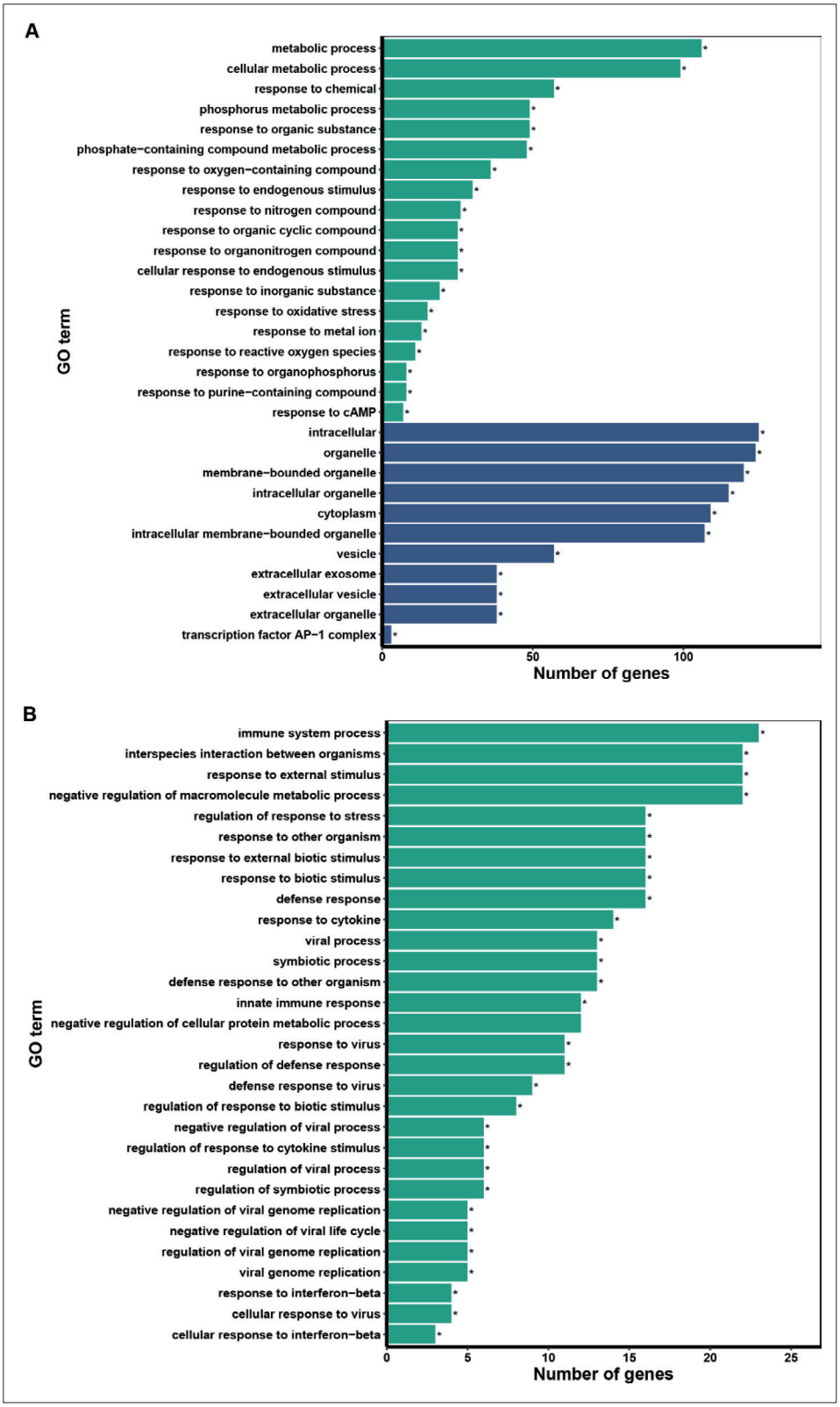


Figure 9. GO enrichment analysis of differentially expressed genes (DEGs) in 3D-bioprinted ovarian cancer models with varying stiffness. (A) Gene Ontology (GO) enrichment analysis of upregulated genes. (B) GO enrichment analysis of downregulated genes. Green color indicates biological process, and blue color indicates cellular component.

ability, and provided a solid foundation for later-stage pharmacodynamic research on antitumor drugs. In addition to extrusion-based bioprinting, other 3D culture methods, such as organoids and patient-derived xenografts (PDXs), are gaining attention. Despite the utilization of organoids in studying various diseases, including cancer, the cost factor and a lack of standardization in terms of establishment and quality control are still a matter of concern.[53] On the other hand, PDXs belong to a type of tumor tissue that is extracted from biopsies or surgical excisions and propagated in mice via implants and explants.[54] To some extent, the propagation of this tissue via culturing method can still accurately retain the genomic and transcriptomic characteristics of the parental tumor tissue, and the resultant cultures can be used for measuring tumor response to treatment; however, it has several shortcomings, such as the time-consuming and costly culturing process, and the likelihood of intratumoral heterogeneity and genome evolution. Additionally, the existing PDX models, which are constructed with tissues acquired from immunodeficient mice, are not feasible for use in immuno-oncology research.[55] Therefore, the development of new 3D tumor models for preclinical studies is imperative.

Before the construction of 3D tumor models, we first performed rheological analysis for both concentrations of GelMA hydrogels. Temperature sweep oscillatory tests indicated that the temperature at which 6% GelMA and 8% GelMA reached the intersection of G' and G'' was about 18.8°C and 20.7°C, respectively. Therefore, in the subsequent experiments, we set the printing temperature at 21.5°C to avoid extrusion needle clogging, to reduce the damage of shear stress on tumor cells during the printing process and ensure good formability of printed structure. Furthermore, the results of semi-quantification of printability showed that the Pr values of 6% GelMA and 8% GelMA were both close to 1. As a result, smooth and uniform filaments could be continuously extruded, resulting in a standard grid structure with obvious layering.

When examining the biological behavior of tumor cells in 3D tumor models, we observed that 8%-3DP model exhibited a lower rate of cell proliferation than 6%-3DP model. However, we also noted a higher expression level of p53, an ovarian cancer cell marker, in 8%-3DP model. Additionally, increasing the stiffness of the tumor model resulted in a significant increase in the expression levels of the tumor stemness markers like ALDH1[56] and CD44,[57] whereas the level of CD133[58] remained unchanged. Notably, the rigid model also showed higher expression levels of IL-6, a factor associated with poor prognosis and chemotherapy resistance in patients with ovarian cancer.[59] These findings suggest that appropriately increasing the stiffness of 3D tumor models may promote malignant phenotypes such as tumor stemness and tumor progression.

In pharmacodynamic research, it is widely accepted that pharmacodynamic results obtained from 3D culture conditions are more reliable than those obtained from 2D planar cultures. Our findings demonstrate that cell proliferation in 3D model (6%-3DP) was higher than that in 2D model. Furthermore, the IC_{50} values obtained using 3D model (6%-3DP) were more closely aligned with the clinically effective blood concentrations. Additionally, the responses of the two tumor models with different matrix stiffness to antitumor drugs also varied, with the IC_{50} values of the three tested drugs in 8%-3DP model being notably higher than those in 6%-3DP model. The expression of several common drug resistance genes, such as *MDR1* and *MRP1*, except for *ABCA1*, was upregulated in rigid model, partly accounting for the distinct responses of the two tumor models to the three tested chemotherapy drugs. Hence, 3D models offer a superior platform for preclinical drug testing, and matrix stiffness plays a critical role in modulating the sensitivity of tumor cells to chemotherapy drugs.

We also identified unique transcriptomic characteristics in the stiffer 3D-bioprinted ovarian cancer model. Specifically, 3D models with different levels of stiffness were found to manifest varied transcriptional expression profiles. In comparison to the 6%-3DP model, the 8%-3DP model showed elevated expression of 145 genes and attenuated expression of 72 genes. Notably, among these DEGs, we discovered several significant ones associated with enhanced chemotherapy resistance, including *FOS*, *CRYAB*, *G6PD*, and *DUSP1*. According to Javellana *et al.*, *FOS* was particularly upregulated in chemotherapy-resistant specimens obtained from a cohort of patients with advanced stage IIIC or IV high-grade serous ovarian cancer.[40] Another research confirmed that *CRYAB* overexpression was associated with acquired drug tolerance and poor patient prognosis.[41] Through a correlation analysis between chemoresistance data and gene expression profiles of ovarian cancer patient-derived spheroids, Yamawaki *et al.* proved that cisplatin resistance was significantly related with increased expression levels of *G6PD*.[42] In addition, Kang *et al.* demonstrated that *DUSP1* overexpression impaired chemotherapy response in ovarian cancer, whereas silencing the gene *in vivo* significantly enhanced sensitivity to paclitaxel and increased apoptosis.[43] Consistent with these findings, our study revealed that an increase in ECM stiffness can promote the expression of related genes, which collectively contributes to enhanced chemoresistance.

However, several limitations of this study need to be addressed. The TME is composed of various cellular

and noncellular components that drive tumor growth, invasion, metastasis, and response to therapy in a concerted manner.[31] Instead of using the typical set of ingredients including fibroblasts, endothelial cells, immune cells, *etc.*, we only utilized tumor cells, which constitute only part of the actual tumor environment in the human body, in this study. Secondly, the application of cell lines in preclinical studies suffer from several shortcomings, including reduced heterogeneity, potential of gene modification, and faster growth rates, as compared to primary tumors.[60] Therefore, tumor specimens obtained from surgical resection should be used to extract primary tumor cells, which are then printed into 3D tumor models for the investigations of mechanisms underlying tumor development and the individualized drug screening. Tumor models fabricated from actual human tissues allow for more realistic analysis of the correlation between primary tumor stiffness and drug sensitivity.

5. Conclusion

In conclusion, compared to traditional planar cultures, 3D tumor models have significant advantages in providing accurate preclinical drug testing results. Having biophysical characteristics, such as stiffness, equivalent to those of the natural TME, 3D *in vitro* tumor model holds promise as a more efficient and powerful platform for drug research.

Acknowledgments

None.

Funding

This work was supported by the National Natural Science Foundation of China (Grant No. 32271470), National High Level Hospital Clinical Research Funding (2022-PUMCH-C-045), Beijing Natural Science Foundation (7212077), and CAMS Innovation Fund for Medical Sciences (CIFMS) (No.2021-I2M-1-058).

Conflict of interest

The authors declare that the research was carried out without any commercial or financial relationships that could be perceived as a potential conflict of interest.

Author contributions

Conceptualization: Ying Shan, Yilei Mao, Ying Jin, Huayu Yang
Formal analysis: Liqian Wang, Ruiyi Yan
Funding acquisition: Yilei Mao, Huayu Yang
Investigation: Ying Shan, Mingchang Pang
Methodology: Ying Shan, Mingchang Pang, Liqian Wang, Yixin Mao, Chang Zhou, Jingyuan Ji
Resources: Yilei Mao
Supervision: Huayu Yang
Writing–original draft: Ying Shan, Mingchang Pang, Chang Zhou, Yixin Mao
Writing–review & editing: Huayu Yang
All authors participated in the research and approved the final version of the article.

Ethics approval and consent to participate

Not applicable.

Consent for publication

Not applicable.

Availability of data

Data used in this work are available from the corresponding authors upon reasonable request.

References

1. Alkmin, S., Patankar, M. S. & Campagnola, P. J., 2022, Assessing the roles of collagen fiber morphology and matrix stiffness on ovarian cancer cell migration dynamics using multiphoton fabricated orthogonal image-based models. *Acta Biomater*, 153:342-354.
doi: 10.1016/j.actbio.2022.09.037

2. Lheureux, S., Braunstein, M. & Oza, A. M., 2019, Epithelial ovarian cancer: Evolution of management in the era of precision medicine. *CA Cancer J Clin*, 69(4):280-304.
doi: 10.3322/caac.21559

3. Vescarelli, E., Gerini, G., Megiorni, F. *et al.*, 2020, MiR-200c sensitizes Olaparib-resistant ovarian cancer cells by targeting Neuropilin 1. *J Exp Clin Cancer Res*, 39(1):3.
doi: 10.1186/s13046-019-1490-7

4. Wang, M., Zhou, J., Zhang, L. *et al.*, 2019, Surgical treatment of ovarian cancer liver metastasis. *Hepatobiliary Surg Nutr*, 8(2):129-137.
doi: 10.21037/hbsn.2018.12.06

5. Herrera, F. G., Irving, M., Kandalaft, L. E. *et al.*, 2019, Rational combinations of immunotherapy with radiotherapy in ovarian cancer. *Lancet Oncol*, 20(8):e417-e433.
doi: 10.1016/s1470-2045(19)30401-2

6. Raghavan, S., Mehta, P., Ward, M. R. *et al.*, 2017, Personalized Medicine-Based Approach to Model Patterns of Chemoresistance and Tumor Recurrence Using Ovarian Cancer Stem Cell Spheroids. *Clin Cancer Res*, 23(22): 6934-6945.
doi: 10.1158/1078-0432.CCR-17-0133

7. Lee, A., Hudson, A. R., Shiwarski, D. J. *et al.*, 2019, 3D bioprinting of collagen to rebuild components of the human heart. *SCIENCE*, 365(6452):482-487.
doi: 10.1126/science.aav9051

8. Lee, S., Sani, E. S., Spencer, A. R. *et al.*, 2020, Human-Recombinant-Elastin-Based Bioinks for 3D Bioprinting of Vascularized Soft Tissues. *Adv Mater*, 32(45):e2003915. doi: 10.1002/adma.202003915

9. Li, C., Jiang, Z. & Yang, H., 2022, Advances in 3D bioprinting technology for liver regeneration. *Hepatobiliary Surg Nutr*, 11(6):917-919. doi: 10.21037/hbsn-22-531

10. Zhang, J., Yang, H. & Yang, H., 2022, Highlights of constructing liver-relevant in vitro models with 3D bioprinting. *Hepatobiliary Surg Nutr*, 11(6):896-898. doi: 10.21037/hbsn-22-486

11. Neufeld, L., Yeini, E., Pozzi, S. *et al.*, 2022, 3D bioprinted cancer models: from basic biology to drug development. *Nat Rev Cancer*, 22(12):679-692. doi: 10.1038/s41568-022-00514-w

12. Tang, M., Xie, Q., Gimple, R. C. *et al.*, 2020, Three-dimensional bioprinted glioblastoma microenvironments model cellular dependencies and immune interactions. *Cell Res*, 30(10):833-853. doi: 10.1038/s41422-020-0338-1

13. Park, W., Bae, M., Hwang, M. *et al.*, 2021, 3D Cell-Printed Hypoxic Cancer-on-a-Chip for Recapitulating Pathologic Progression of Solid Cancer. *J Vis Exp,* (167). doi: 10.3791/61945

14. Hong, S. & Song, J. M., 2022, 3D bioprinted drug-resistant breast cancer spheroids for quantitative in situ evaluation of drug resistance. *Acta Biomater*, 138:228-239. doi: 10.1016/j.actbio.2021.10.031

15. Mei, Y., He, C., Gao, C. *et al.*, 2021, 3D-Printed Degradable Anti-Tumor Scaffolds for Controllable Drug Delivery. *Int J Bioprint*, 7(4):418. doi: 10.18063/ijb.v7i4.418

16. Yi, H. G., Jeong, Y. H., Kim, Y. *et al.*, 2019, A bioprinted human-glioblastoma-on-a-chip for the identification of patient-specific responses to chemoradiotherapy. *Nat Biomed Eng*, 3(7):509-519. doi: 10.1038/s41551-019-0363-x

17. Shim, I. K., Yi, H. J., Yi, H. G. *et al.*, 2017, Locally-applied 5-fluorouracil-loaded slow-release patch prevents pancreatic cancer growth in an orthotopic mouse model. *Oncotarget*, 8(25):40140-40151. doi: 10.18632/oncotarget.17370

18. Hirschhaeuser, F., Menne, H., Dittfeld, C. *et al.*, 2010, Multicellular tumor spheroids: an underestimated tool is catching up again. *J Biotechnol*, 148(1):3-15. doi: 10.1016/j.jbiotec.2010.01.012

19. Abhinand, C. S., Raju, R., Soumya, S. J. *et al.*, 2016, VEGF-A/VEGFR2 signaling network in endothelial cells relevant to angiogenesis. *J Cell Commun Signal*, 10(4):347-354. doi: 10.1007/s12079-016-0352-8

20. Sun, L., Yang, H., Wang, Y. *et al.*, 2020, Application of a 3D Bioprinted Hepatocellular Carcinoma Cell Model in Antitumor Drug Research. *Front Oncol*, 10:878. doi: 10.3389/fonc.2020.00878

21. Mao, S., He, J., Zhao, Y. *et al.*, 2020, Bioprinting of patient-derived in vitro intrahepatic cholangiocarcinoma tumor model: establishment, evaluation and anti-cancer drug testing. *Biofabrication*, 12(4):045014. doi: 10.1088/1758-5090/aba0c3

22. Xie, F., Sun, L., Pang, Y. *et al.*, 2021, Three-dimensional bio-printing of primary human hepatocellular carcinoma for personalized medicine. *BIOMATERIALS*, 265:120416. doi: 10.1016/j.biomaterials.2020.120416

23. Yang, H., Sun, L., Pang, Y. *et al.*, 2021, Three-dimensional bioprinted hepatorganoids prolong survival of mice with liver failure. *GUT*, 70(3):567-574. doi: 10.1136/gutjnl-2019-319960

24. Tebon, P. J., Wang, B., Markowitz, A. L. *et al.*, 2023, Drug screening at single-organoid resolution via bioprinting and interferometry. *Nat Commun*, 14(1):3168. doi: 10.1038/s41467-023-38832-8

25. Mazzocchi, A., Soker, S. & Skardal, A., 2019, 3D bioprinting for high-throughput screening: Drug screening, disease modeling, and precision medicine applications. *Appl Phys Rev*, 6(1). doi: 10.1063/1.5056188

26. Wang, M., Zhao, J., Zhang, L. *et al.*, 2017, Role of tumor microenvironment in tumorigenesis. *J Cancer*, 8(5):761-773. doi: 10.7150/jca.17648

27. Yang, M., Lu, J., Zhang, G. *et al.*, 2021, CXCL13 shapes immunoactive tumor microenvironment and enhances the efficacy of PD-1 checkpoint blockade in high-grade serous ovarian cancer. *J Immunother Cancer*, 9(1). doi: 10.1136/jitc-2020-001136

28. Ding, Q., Dong, S., Wang, R. *et al.*, 2020, A nine-gene signature related to tumor microenvironment predicts overall survival with ovarian cancer. *Aging (Albany NY)*, 12(6):4879-4895. doi: 10.18632/aging.102914

29. Di Modugno, F., Colosi, C., Trono, P. *et al.*, 2019, 3D models in the new era of immune oncology: focus on T cells, CAF and ECM. *J Exp Clin Cancer Res*, 38(1):117. doi: 10.1186/s13046-019-1086-2

30. Hinshaw, D. C. & Shevde, L. A., 2019, The Tumor Microenvironment Innately Modulates Cancer Progression. *Cancer Res*, 79(18):4557-4566. doi: 10.1158/0008-5472.CAN-18-3962

31. Elhanani, O., Ben-Uri, R. & Keren, L., 2023, Spatial profiling technologies illuminate the tumor microenvironment. *CANCER CELL*, 41(3):404-420. doi: 10.1016/j.ccell.2023.01.010

32. Wei, X., Lou, H., Zhou, D. *et al.*, 2021, TAGLN mediated stiffness-regulated ovarian cancer progression via RhoA/ROCK pathway. *J Exp Clin Cancer Res*, 40(1):292. doi: 10.1186/s13046-021-02091-6

33. Kim, J., Jang, J. & Cho, D. W., 2021, Controlling Cancer Cell Behavior by Improving the Stiffness of Gastric Tissue-Decellularized ECM Bioink With Cellulose Nanoparticles. *Front Bioeng Biotechnol*, 9:605819. doi: 10.3389/fbioe.2021.605819

34. Tang, M., Tiwari, S. K., Agrawal, K. *et al.*, 2021, Rapid 3D Bioprinting of Glioblastoma Model Mimicking Native Biophysical Heterogeneity. *Small*, 17(15):e2006050. doi: 10.1002/smll.202006050

35. Yang, X., Wang, G., Huang, X. *et al.*, 2020, RNA-seq reveals the diverse effects of substrate stiffness on epidermal ovarian cancer cells. *Aging (Albany NY)*, 12(20):20493-20511. doi: 10.18632/aging.103906

36. Pietilä, E. A., Gonzalez-Molina, J., Moyano-Galceran, L. *et al.*, 2021, Co-evolution of matrisome and adaptive adhesion dynamics drives ovarian cancer chemoresistance. *Nat Commun*, 12(1):3904. doi: 10.1038/s41467-021-24009-8

37. Ouyang, L., Yao, R., Zhao, Y. *et al.*, 2016, Effect of bioink properties on printability and cell viability for 3D bioplotting of embryonic stem cells. *Biofabrication*, 8(3):035020. doi: 10.1088/1758-5090/8/3/035020

38. Li, C., Jin, B., Sun, H. *et al.*, 2022, Exploring the function of stromal cells in cholangiocarcinoma by three-dimensional bioprinting immune microenvironment model. *Front Immunol*, 13:941289. doi: 10.3389/fimmu.2022.941289

39. Singha, B., Gatla, H. R., Manna, S. *et al.*, 2014, Proteasome inhibition increases recruitment of IκB kinase β (IKKβ), S536P-p65, and transcription factor EGR1 to interleukin-8 (IL-8) promoter, resulting in increased IL-8 production in ovarian cancer cells. *J Biol Chem*, 289(5):2687-2700. doi: 10.1074/jbc.M113.502641

40. Javellana, M., Eckert, M. A., Heide, J. *et al.*, 2022, Neoadjuvant Chemotherapy Induces Genomic and Transcriptomic Changes in Ovarian Cancer. *Cancer Res*, 82(1):169-176. doi: 10.1158/0008-5472.CAN-21-1467

41. du Manoir, S., Delpech, H., Orsetti, B. *et al.*, 2022, In high-grade ovarian carcinoma, platinum-sensitive tumor recurrence and acquired-resistance derive from quiescent residual cancer cells that overexpress CRYAB, CEACAM6, and SOX2. *J Pathol*, 257(3):367-378. doi: 10.1002/path.5896

42. Yamawaki, K., Mori, Y., Sakai, H. *et al.*, 2021, Integrative analyses of gene expression and chemosensitivity of patient-derived ovarian cancer spheroids link G6PD-driven redox metabolism to cisplatin chemoresistance. *Cancer Lett*, 521:29-38. doi: 10.1016/j.canlet.2021.08.018

43. Kang, Y., Nagaraja, A. S., Armaiz-Pena, G. N. *et al.*, 2016, Adrenergic Stimulation of DUSP1 Impairs Chemotherapy Response in Ovarian Cancer. *Clin Cancer Res*, 22(7):1713-1724. doi: 10.1158/1078-0432.Ccr-15-1275

44. Andreoli, M., Persico, M., Kumar, A. *et al.*, 2014, Identification of the first inhibitor of the GBP1:PIM1 interaction. Implications for the development of a new class of anticancer agents against paclitaxel resistant cancer cells. *J Med Chem*, 57(19):7916-7932. doi: 10.1021/jm5009902

45. Xiao, Y., Lai, Y., Yu, Y. *et al.*, 2021, The Exocrine Differentiation and Proliferation Factor (EXDPF) Gene Promotes Ovarian Cancer Tumorigenesis by Up-Regulating DNA Replication Pathway. *Front Oncol*, 11:669603. doi: 10.3389/fonc.2021.669603

46. Zhang, Y., Qiu, J. G., Jia, X. Y. *et al.*, 2023, METTL3-mediated N6-methyladenosine modification and HDAC5/YY1 promote IFFO1 downregulation in tumor development and chemo-resistance. *Cancer Lett*, 553:215971. doi: 10.1016/j.canlet.2022.215971

47. Zaid, T. M., Yeung, T. L., Thompson, M. S. *et al.*, 2013, Identification of FGFR4 as a potential therapeutic target for advanced-stage, high-grade serous ovarian cancer. *Clin Cancer Res*, 19(4):809-820. doi: 10.1158/1078-0432.Ccr-12-2736

48. Brancato, V., Oliveira, J. M., Correlo, V. M. *et al.*, 2020, Could 3D models of cancer enhance drug screening? *BIOMATERIALS*, 232:119744. doi: 10.1016/j.biomaterials.2019.119744

49. Zanoni, M., Cortesi, M., Zamagni, A. *et al.*, 2020, Modeling neoplastic disease with spheroids and organoids. *J Hematol Oncol*, 13(1): 97. doi: 10.1186/s13045-020-00931-0

50. Fan, Y., Sun, Q., Li, X. *et al.*, 2021, Substrate Stiffness Modulates the Growth, Phenotype, and Chemoresistance of Ovarian Cancer Cells. *Front Cell Dev Biol*, 9:718834. doi: 10.3389/fcell.2021.718834

51. Paradiso, F., Lenna, S., Gazze, S. A. *et al.*, 2022, Mechanomimetic 3D Scaffolds as a Humanized In Vitro Model for Ovarian Cancer. *Cells*, 11(5). doi: 10.3390/cells11050824

52. Barroso, M., Chheda, M. G., Clevers, H. *et al.*, 2022, A path to translation: How 3D patient tumor avatars enable next generation precision oncology. *CANCER CELL*, 40(12):1448-1453. doi: 10.1016/j.ccell.2022.09.017

53. Kim, J., Koo, B. K. & Knoblich, J. A., 2020, Human organoids: model systems for human biology and medicine. *Nat Rev Mol Cell Biol*, 21(10):571-584. doi: 10.1038/s41580-020-0259-3

54. Zanella, E. R., Grassi, E. & Trusolino, L., 2022, Towards precision oncology with patient-derived xenografts. *Nat Rev Clin Oncol*, 19(11):719-732.
doi: 10.1038/s41571-022-00682-6

55. Zhuo, J., Su, R., Tan, W. *et al.*, 2020, The ongoing trends of patient-derived xenograft models in oncology. *Cancer Commun (Lond)*, 40(11):559-563.
doi: 10.1002/cac2.12096

56. Zong, X., Wang, W., Ozes, A. *et al.*, 2020, EZH2-Mediated Downregulation of the Tumor Suppressor DAB2IP Maintains Ovarian Cancer Stem Cells. *Cancer Res*, 80(20):4371-4385.
doi: 10.1158/0008-5472.Can-20-0458

57. Sacks Suarez, J., Gurler Main, H., Muralidhar, G. G. *et al.*, 2019, CD44 Regulates Formation of Spheroids and Controls Organ-Specific Metastatic Colonization in Epithelial Ovarian Carcinoma. *Mol Cancer Res*, 17(9):1801-1814.
doi: 10.1158/1541-7786.Mcr-18-1205

58. Zhao, Y., He, M., Cui, L. *et al.*, 2020, Chemotherapy exacerbates ovarian cancer cell migration and cancer stem cell-like characteristics through GLI1. *Br J Cancer*, 122(11):1638-1648.
doi: 10.1038/s41416-020-0825-7

59. Wang, Y., Niu, X. L., Qu, Y. *et al.*, 2010, Autocrine production of interleukin-6 confers cisplatin and paclitaxel resistance in ovarian cancer cells. *Cancer Lett*, 295(1):110-123.
doi: 10.1016/j.canlet.2010.02.019

60. Klinghammer, K., Walther, W. & Hoffmann, J., 2017, Choosing wisely - Preclinical test models in the era of precision medicine. *Cancer Treat Rev*, 55:36-45.
doi: 10.1016/j.ctrv.2017.02.009

ACCSCIENCE PUBLISHING

International Journal of Bioprinting

RESEARCH ARTICLE

Distinct toxicity of microplastics/TBBPA co-exposure to bioprinted liver organoids derived from hiPSCs of healthy and patient donors

Shaojun Liang[1†], Yixue Luo[1†], Yijun Su[1], Dawei Zhang[2], Shi-jie Wang[3], Mingen Xu[4,5], and Rui Yao[1*]

[1]Biomanufacturing and Rapid Forming Technology Key Laboratory of Beijing, Department of Mechanical Engineering, Tsinghua University, Beijing, China

[2]Senior Department of Infectious Diseases of the 5th Medical Center, PLA General Hospital, Beijing, China

[3]National Translational Science Center for Molecular Medicine & Department of Cell Biology, Fourth Military Medical University, Xi'an, China

[4]Key Laboratory of Medical Information and 3D Biological of Zhejiang Province, Hangzhou Dianzi University, Hangzhou, China

[5]Hangzhou Institute of Medicine (HIM), Chinese Academy of Sciences, Hangzhou, China

(This article belongs to the *Special Issue: Special Issue of International Journal of Bioprinting in the BDMC 2023 Conference*)

Abstract

Bioprinted tissues derived from human-induced pluripotent stem cells (hiPSCs) can provide precise information on disease mechanisms and toxicity. The detection of microplastics (MPs) in the liver tissues of patients with liver cirrhosis has raised concerns about their hepatotoxicity. MPs could absorb endocrine disruptors, such as tetrabromobisphenol A (TBBPA) that is widely present in the environment, thereby complicating their toxic behaviors. To investigate their toxic mechanisms in liver tissues, we used the electro-assisted inkjet printing technology to fabricate healthy donor or patient-sourced hiPSC-derived Disse space organoids (DOs) that resembled the cell types and transcriptional features of Disse space. We observed an accumulation of polystyrene MP microbeads in the DOs, and TBBPA exacerbated the process. Neither MPs and TBBPA alone nor the co-exposure at non-cytotoxicity dosages could affect the liver functions of healthy donor hiPSC-derived DOs, as revealed by transcriptomic and biochemical analyses, whereas alcoholic liver disease (ALD) patient hiPSC-derived DOs exhibited the ALD disease transcriptional profiles. We found that MPs/TBBPA co-exposure significantly influenced the patient organoids in terms of the pathological transcription expression and biochemical profiles. These results suggested that both hereditary factors and pollutants contribute to susceptibility to environmental toxicants. This study exemplified the value of bioprinting hiPSC-derived organoids in environmental toxicology, offering a powerful strategy to advance the personalized environmental toxicology paradigm.

Keywords: Disse space organoids; Induced pluripotent stem cells; Bioprinting; Microplastics; Toxicology

†These authors contributed equally to this work.

***Corresponding author:**
Rui Yao
(yaorui@tsinghua.edu.cn)

Citation: Liang S, Luo Y, Su Y, et al. Distinct toxicity of microplastics/TBBPA co-exposure to bioprinted liver organoids derived from hiPSCs of healthy and patient donors. *Int J Bioprint*. 2024;10(3):1403.
doi: 10.36922/ijb.1403

Received: July 27, 2023
Accepted: September 19, 2023
Published Online: January 18, 2024

Copyright: © 2024 Author(s). This is an Open Access article distributed under the terms of the Creative Commons Attribution License, permitting distribution, and reproduction in any medium, provided the original work is properly cited.

Publisher's Note: AccScience Publishing remains neutral with regard to jurisdictional claims in published maps and institutional affiliations.

1. Introduction

Human health is threatened by various pollutants in the living environment. Small-sized (<5 mm in diameter) plastics, known as microplastics (MPs), have been widely detected in the environment, including marine, drinking water, air, and food.[1] Polyethylene, polypropylene, polystyrene, and polyvinyl chloride MPs are predominant in aquatic environments.[2] Recently, MPs have been found in human blood,[3] the placenta,[4] and the liver tissue of liver cirrhosis patients,[5] raising increasing global concerns about its potential effects on human health. Danopoulos *et al*. systematically reviewed the scientific data from studies regarding MP effects on human cells and attempted to establish thresholds of MP toxicity in human risk assessment.[6] However, they pointed out that the overall certainty of collected evidence was graded as low. Large-scaled biomimetic human tissue models with physiological relevance for evaluating MP toxicity are missing.

The substantial surface area and hydrophobic nature of MPs make them ideal vectors for transporting environmental xenobiotics.[1] Tetrabromobisphenol A (TBBPA), an emerging environmental xenobiotic, is one of the most widely used brominated flame retardants.[7,8] It can reach relatively high concentrations (850–4870 ng/L) in rivers and has been frequently detected in aquatic food.[9] TBBPA has been detected in breast milk and umbilical cord blood of human owing to continuous exposure.[7] Studies have demonstrated that TBBPA disrupts thyroid homeostasis and liver metabolism.[10] Due to their high propensity to accumulate in environmental media, both MPs and TBBPA can co-exist in the same system. Xu *et al.* found that TBBPA could be adsorbed onto the surface of polystyrene MPs (PS-MPs), inhibiting its biotransformation.[11] This process may lead to unexpected and complex toxic effects. A recent study has found that compared with single exposure, co-exposure to MPs and TBBPA resulted in a more severe disruption of the hepatic redox status of zebrafish, increasing the risk of liver fibrosis and cirrhosis.[12] However, due to species differences between zebrafish and human liver, there is a need for models capable of accurately simulating human liver toxicity responses to conduct further research on the toxic effects and mechanisms of MPs and TBBPA co-exposure.

Human liver Disse space composed of hepatocytes, endothelial cells, and hepatic stellate cells (HSCs) plays a crucial regulatory role in the pathogenesis of liver fibrosis and cirrhosis.[13] A recent study has demonstrated that a three-dimensional (3D)-bioprinted *in vitro* model composed of the three types of cells could recapitulate the critical features involved in fibrogenesis.[14] Due to compatibility limitations between cell assembly and extrusion printing techniques, the three cell lines in the extruded hydrogel were not able to assemble into a liver Disse space-like microstructure. Organoids are considered a strategy of biomimetic tissue microstructures. Human-induced pluripotent stem cells (hiPSCs), reprogramed from adult somatic cells, can differentiate into multitype of cells with the intrinsic ability to self-assemble into organoids *in vitro*. This avoids ethical issues associated with using human stem cells and primary human cells, providing multiple cell sources for establishing *in vitro* human artificial organs.[15] Moreover, hiPSCs carry individual genetic information, and 3D-bioprinted hiPSC can provide a personalized genetic background for toxicological studies.[16] Nonetheless, the efficient production of hiPSC-derived liver Disse space organoids (DOs) suitable for complex environmental toxicology assessment remains challenging.

Here, we mass-produced multicellular DOs based on healthy donor and patient-derived hiPSCs using electro-assisted inkjet bioprinting. The chemically defined alginate/laminin bioink and 3D microenvironment of microspheres facilitated multicellular crosstalk and mutually enhanced the maturation of hiPSC-derived progenitor cells, thus generating DOs mimicking Disse space features. PS-MPs (1 μm) crossed the barrier of the hydrogel matrix and were preferentially taken up by endothelial cells followed by dispersing throughout the whole organoids. Additionally, co-exposure to MPs and TBBPA enhanced the accumulation of pollutants within DOs at the tested time points. The alcoholic liver disease (ALD) patient-derived hiPSCs efficiently formed DOs with specific disease transcriptional profiles. Transcriptional and biochemical evaluations showed that co-exposure to MPs and TBBPA severely impacted patient-derived DOs over healthy donor organoids, suggesting that both hereditary factors and pollutants could strengthen the susceptibility of organisms to environmental toxicants (Figure 1A). This study provided the proof of concept that hiPSC-derived *in vitro* models fabricated by bioprinting technologies offer a potential platform for investigating personalized toxicology.

2. Materials and methods

2.1. Cell culture

hiPSCs-N, reprogrammed from the peripheral blood cells of a healthy male, were purchased from Nuwacell Biotechnologies Co., Ltd. (RC01001-A). hiPSCs-AC19 were reprogrammed from the peripheral blood mononuclear cells of a 64-year-old male patient with ALD. The patient provided written consent, and ethical approval was obtained from the Institution Review Board of Tsinghua University. The reprogramming of hiPSCs-AC19 was performed with Sendai virus-based reprogramming

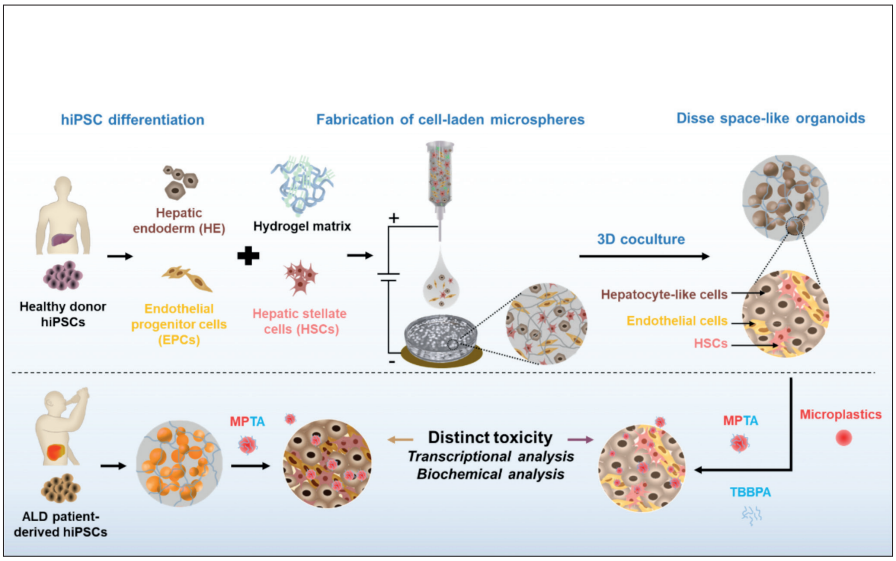


Figure 1. Schematic illustration of the study.

vectors. Both hiPSCs expressed pluripotent stem cell markers, maintained normal karyotypes, and formed teratomas *in vivo*. hiPSCs were cultured in Matrigel-coated (Matrigel, BD, 354277) tissue culture plates in ncTarget medium (Nuwacell Biotechnologies Co., Ltd., RP01020). The medium was refreshed daily. A human hepatic stellate cell line LX-2 (Procell, CL-0560) was cultured in Dulbecco's Modified Eagle's Medium (DMEM; Gibco, 11965175) supplemented with 5% fetal bovine serum (FBS) and 1% antibodies. The culture medium was refreshed every 2 days.

2.2. Differentiation of hiPSCs into hepatic endoderm cells and endothelial progenitor cells

2.2.1. Specification and expansion of hepatic endoderm cells

hiPSCs were dissociated into single cells by Nuwacell® Solase (Nuwacell Biotechnologies Co., Ltd., RP01021), and 1×10^5 cells/mL were seeded onto Matrigel (BD, 354230)-coated 12-well plates with ncTarget medium plus 10 μM Y27632 (Selleck, S6390). On days 0–1, RPMI 1640 (Thermo Fisher, 11875119) was supplemented with 1× B27 insulin minus (Gibco, A1895601) and 3 μM CHIR99021 (Selleck, S1263). On days 2–3, the medium was supplemented with 100 ng/mL activin A (R&D, 338-AC). On days 4–7, the optimized hepatic endoderm cell (HE) induction medium included RPMI 1640, 1× B27 (Gibco, A1486701), 20 ng/mL BMP4 (PeproTech, 96-120), and 10 ng/mL fibroblast growth factor 2 (FGF2; PeproTech, 96-100-18B). HE cells were obtained on day 8.

On day 8, the cells were counted as HE_P0. Then, the HE_P0 cells were dissociated in a defined medium composed of DMEM-F12 (Gibco, 11320033), 1× ITS (Merck, I3146), 500 μM monothioglycerol (Sigma-Aldrich, M6145), 1× GlutaMax (Gibco, 35050061), 50 μg/mL ascorbic acid (Sigma-Aldrich, A8960), 0.1% bovine serum albumin (BSA; Sigma-Aldrich, V900933), 5 ng/mL FGF2, 10 ng/mL vascular endothelial growth factor (VEGF; R&D Systems, 293-VE), 20 ng/mL epidermal growth factor (EGF; PeproTech, AF-100), 3 μM CHIR99021, and 5 μM A83-01 (Selleck, S7692). The medium was refreshed every day.

2.2.2. Specification and expansion of endothelial progenitor cells

Endothelial progenitor cells (EPCs) were derived from hiPSCs according to protocol.[17] Briefly, hiPSCs at 4×10^5/mL were seeded onto Matrigel-coated 12-well plates and cultured overnight in ncTarget medium supplemented with 1 μM CHIR99021 and 10 μM Y27632. On days 0–1, RPMI 1640 was supplemented with 1× B27 insulin minus, 50 ng/mL Activin A, and 1/60 Matrigel (BD, Growth Factor Reduced, 354230). On days 1–2, RPMI 1640 was supplemented with 1× B27 insulin minus, 40 ng/mL BMP4, and 1 μM CHIR99021. On days 2–5, the optimized basal medium included Vivo15 (Lonza X-VIVO15, 04-418Q), 1× ITS, 500 μM monothioglycerol, 1× GlutaMax, 50 μg/mL ascorbic acid, and 0.1% BSA; the optimized basal medium was supplemented with 300 ng/mL VEGF, 5 ng/mL FGF2, and 10 ng/mL BMP4. On day 5, the cells were obtained and continuously cultured in optimized basal medium supplemented with 20 ng/mL FGF2, 20 ng/mL VEGF, and 1 μM CHIR99021. When confluent, the cells were counted as EPC_P0 and split at a ratio of 1:3. The medium was refreshed daily.

2.3. Fabrication of DOs-laden microspheres by electro-assisted inkjet printing

The printing procedure conducted in this experiment was similar to that reported in our previous study.[18] The bioink was composed of 3.5% alginate (Sigma, 919373), 2 μg/mL ncLaminin 511 (Nuwacell Biotechnologies Co., Ltd., RP01025), and a cell mixture of hPSC-HE, hiPSC-EPCs, and LX-2 at 10:7:2[19] with a total density of 3×10^6 cells/mL.

The electro-assisted inkjet printing device consisted of a static electricity power supply, a syringe pump (Longer Pump Ltd.), and a grounded collecting device. A disposable sterile syringe loaded with bioink was fixed to the syringe pump. Cell-laden microspheres were printed at a 10 mL/h propulsion speed, 2 cm electrode distance, and 12 kV voltage. Microspheres were crosslinked with 300 mM calcium chloride solution and washed with DMEM-F12 basal medium three times.

The post-printed cell-laden microspheres were cultured in organoid culture medium composed of DMEM-F12/M199/William (1:1:1), 500 μM monothioglycerol, 1× B27 with insulin, 1% ITS, 50 μg/mL ascorbic acid, 0.1% BSA, 2% FBS, 1% v/v sodium pyruvate (Sigma, P2256), 1% v/v NEAA (Sigma, M7145), 1% v/v GlutaMAX, 100 μM ascorbic acid, 20 ng/mL VEGF, 20 ng/mL hepatocyte growth factor (HGF; R&D, 294-HG-025), and 5 ng/mL FGF2. The medium was refreshed daily. DOs-laden microspheres were formed after 5 days of culture.

2.4. Pollution exposure

The spherical polystyrene MPs (Wuxi Ruige Biotechnology Co., Ltd.) were monodispersed particles with a diameter of 1 μm in water at a concentration of 25 mg/mL. The stock solutions were pasteurized before utilization. TBBPA (purity > 98.0%, TCI, Shanghai Development Co., Ltd., China) was dissolved in dimethyl sulfoxide (DMSO; Amresco, USA, 0231). Polystyrene MPs and TBBPA were diluted according to the manufacturer's protocols. The MPTA complex was obtained by incubating 6 μg/mL PS-MPs and 10 μM TBBPA in medium at 37°C overnight.

The exposure dosage of PS-MPs was 600 ng/mL, TBBPA was 100 nM, and MPTA was 600 ng/mL/100 nM. The vehicle control was 0.01% DMSO. DOs-laden microspheres were incubated with MPs, TBBPA, MPTA, and vehicle control for 3 days. The media were changed every day.

2.5. Tracing MPs in DOs

The cell membranes of hiPSC-derived HE, EPC, and LX-2 cells were labeled with a PKH67 Green Fluorescent Cell Linker Kit (Merck, PKH67GL) according to the manufacturer's protocols. We printed three types of microspheres with cell mixtures: (i) PKH67-labeled HE, unlabeled EPC, and LX-2; (ii) PKH67-labeled EPC, unlabeled HE, and LX-2; and (iii) PKH67-labeled LX-2, unlabeled HE, and EPC. After 5 days of co-culture, the three types of DOs-laden microspheres were obtained.

To allow clearer observation of the microplastic entry into cells within a short period, we used MPs in dosages higher than the environmental concentrations. The DOs-laden microspheres were exposed to 100 μg/mL red fluorescence-labeled MPs (for better visualization) (Wuxi Ruige Biotechnology Co., Ltd.) and MPTA at 100 μg/mL/100 nM. The DOs-laden microspheres were placed in a sterile chamber at 5% CO_2 and 37°C.

The diffusion of MPs in the DOs was visualized and recorded with a laser scanning confocal microscope (LSCM; Nikon, Z2). The fluorescence signal distribution of MPs and PKH67 at the specified locations was analyzed and graphed with Nikon NIS-Elements Advanced Research (AR). The fluorescence intensities and areas of the more than 10 microspheres were analyzed by Nikon NIS-Elements AR. The fluorescence intensity of the MPs ($n > 10$) was the average of the normalized fluorescence intensity of MPs, which was divided by the area of the microsphere.

2.6. Cell live/dead staining

The cell viability in the post-printed microspheres, DOs within microspheres, and DOs with pollutant treatments was analyzed by *in situ* staining of microspheres for live/dead cells. The live/dead cells were stained with the Calcein-AM/PI Kit (Merck, 04511-1KT-F) according to the manufacturer's instructions. The staining was incubated for 10 min in the dark and observed using an LSCM (Nikon, Z2).The cell viabilities were the averages of the ratio of green fluorescence intensity to total cell fluorescence intensity ($n > 3$).

2.7. Determination of liver function

Bile salt transport was examined with cholyl-lysyl-fluorescein (CLF) staining. DOs-laden microspheres were incubated with Williams' E medium (BasalMedia, L660KJ) supplemented with 5 μM cholyl-lysyl-fluorescein (CLF; BD Biosciences, BD-451041) for 15 min at 37°C and 5% CO_2. After washing, CLF internalization was visualized with confocal microscopy. The fluorescence intensity of CLF was analyzed by Nikon NIS-Elements AR. More than 20 DOs-laden microspheres from three independent experiments were included in the calculation. The CLF intensities were calculated as the average fluorescence intensity of the CLF divided by the microsphere area.

2.7.1. Neutral lipid staining

Lipid accumulation was detected using neutral lipid staining. DOs were harvested from microspheres, fixed

in 4% formaldehyde for 30 min, washed, and stained with red neutral lipid dye (Invitrogen, H34476) according to the manufacturer's instructions. The nucleus was stained with DAPI. The DOs were visualized by means of confocal microscopy. The fluorescence intensity of neutral lipids was analyzed using Nikon NIS-Elements AR. The fluorescence intensity of neutral lipid dye in each slide was normalized to the DAPI area. Then, the fluorescence intensity of neutral lipid staining was counted by finding the average of all the slides in three independent experiments.

2.7.2. Indocyanine green uptake assay

The indocyanine green (ICG) uptake assay was performed by adding 1 mg/mL ICG to the medium for 30 min. ICG was wholly released from the cells after 7 h. ICG uptake and release images were captured from over 20 microspheres using an inverted optical microscope. Image-Pro software was used to calculate the uptake ratio as the Integrated Optical Density (IOD) of the microsphere divided by the area of the microsphere.

2.8. Immunofluorescence staining

2.8.1. Staining of cultured planner cells

hiPSC-derived HE and EPC were fixed with 4% paraformaldehyde for 15 min and blocked with Dulbecco's phosphate-buffered saline (DPBS; Solarbio, D1040) containing 5% goat serum (Solarbio, China, SL038) and 0.1% Triton X-100 (Amresco, USA, 0694-1 L) for 1 h at room temperature. Then, the cells were incubated with primary antibodies for 1 h and secondary antibodies for 30 min at room temperature.

2.8.2. Staining of DOs

The DOs-laden microspheres were incubated in a de-crosslinking solution (150 mM sodium chloride containing 55 mM sodium citrate and 20 mM EDTA), and DOs were harvested by gravitational settlement.

The harvested DOs or DOs-laden microspheres were fixed with 4% paraformaldehyde for 45 min at 4°C, washed three times with 0.1% v/v Hanks (Solarbio, H1025)-Tween-20, and blocked with Hanks containing 2% BSA and 0.1% Triton X-100 for 15 min at 4°C. Then, the samples were incubated with primary antibodies overnight at 4°C. After being washed three times, the DOs were continuously incubated with secondary antibodies overnight at 4°C. Fluorescent images were taken with an LSCM (Nikon, Z2).

The fluorescent intensities of COL1A1, αSMA, and F-actin were analyzed by Nikon NIS-Elements AR. The fluorescence intensity in each slide was normalized to the DAPI area. The fluorescence intensity of each target protein was calculated by determining the average of all the slides in three independent experiments.

The following antibodies and dilution ratios were employed: HNF4α (1:200, Abcam, ab92378), FOXA2 (1:200, Abcam, ab256493), ALB (1:100, Abcam, ab83465), CD31 (1:100, Cell Signaling Technology, 89C2), MRP2 (1:100, Abcam, ab3373), αSMA (1:100), COL1A1 (1:100, Cell Signaling Technology, 72026), F-actin (Invitrogen, A12379), Alexa Fluor® 594-conjugated secondary antibody (1:1000, Abcam, ab150080), and Alexa Fluor® 488-conjugated secondary antibody (1:1000, Abcam, ab150113). The nuclei were stained with DAPI (Sigma, D9542).

2.9. Total RNA isolation and qRT-PCR analysis

The DOs were harvested from microspheres with a de-crosslinking solution. The DOs were resolved in TRIzol (Life Technologies, USA, 15596018). Total RNA samples were isolated according to the TRIzol manufacturer's specifications. RNA (2 μg) was reverse-transcribed into cDNA with the RT Reagent Kit with gDNA Eraser (Takara, Japan, RR047A). Quantitative polymerase chain reaction (qPCR) was performed using a SYBR Premix Ex Taq kit (Takara, Japan, RR420A) on a QuantStudio 6 Flex System (Thermo, USA). The PCR primers are listed in Table S1 (Supplementary File).

2.10. RNA-seq

The samples for RNA-seq were collected in TRIzol. RNA isolation, cDNA library construction, sequencing, and primary analysis were performed at Novogene (Tianjin, China). Briefly, 1 μg of RNA per sample was used as input material for the RNA sample preparations. Following the manufacturer's recommendations, sequencing libraries were generated using the NEBNext® UltraTM RNA Library Prep Kit for Illumina® (NEB, USA), and index codes were added to attribute sequences to each sample. After being analyzed with an Agilent 2100 Bioanalyzer, the RNA was found to be of good standard quality.

Sequencing was performed with an Illumina NovaSeq platform, and 150 bp paired-end reads were generated. Reads were filtered and mapped to the reference genome sequence with HISAT2 v2.0.5. Feature Counts v1.5.0-p3 was used to count the read numbers mapped to each gene. The fragments per kilobase of exon per million fragments mapped (FPKM) method was used to calculate gene expression levels. Differentially expressed genes (DEGs) with fold change ≥ 1.25 and FDR q-value <0.05 were calculated using the DESeq2 R package (1.16.1).

Gene Ontology (GO), Kyoto Encyclopedia of Genes and Genomes (KEGG), Reactome, and DisGeNET enrichment analyses of DEGs were implemented using the clusterProfiler R package. Significantly enriched GO and KEGG terms were determined based on a corrected P <0.05. Based on KEGG, Reactome, and DisGeNET datasets, gene

set enrichment analysis (GSEA) was conducted using the local version of the GSEA tool (http://www.broadinstitute.org/gsea/index.jsp). A protein–protein interactions (PPI) network of representative GSEA GO terms from the whole clusters was constructed with Cytoscape EnrichmentMap. The Pearson correlation heatmap, volcanic map, and gene heatmap were calculated and graphed using R (version 3.0.3) ggplot2 and pheatmap packages. The chord plot was graphed with R GOplot v1.0.2. R (version 3.0.3). The parallel set was graphed using the Origin 2021 software. All original sequence datasets were submitted to the GEO database under the accession number GSE212099.

2.11. Statistical analysis

All values are expressed as the means ± standard deviations (SD) and were analyzed using Prism software (GraphPad Inc.). Statistical analysis was performed using Student's *t*-test or one-way analysis of variance (ANOVA).

3. Results and discussion

3.1. Fabrication of hiPSC-derived multicellular DOs

We sought to tackle the challenges of large-scale biofabrication of biomimetic DOs from two main aspects: (i) obtaining sufficient hiPSC-derived progenitor cells that facilitate the assembly of 3D structures and co-culturing them with multiple cell types; and (ii) developing bioink and biofabrication methods considering the survival and subsequent multilineage maturation of hiPSC-derived cells.

3.1.1. Specification of hiPSCs into progenitor cells

We differentiated hiPSCs derived from healthy donors (hiPSC-N) into HEs and EPCs, which retained the ability to self-assemble into liver organoids and showed synergistic development toward maturation.[19] To obtain sufficient cells for biofabrication, HEs were sub-cultured after differentiation into FOXA2+/HNF4A+ HEs (counted as passage 0; HE-P0) (Figure S1A in Supplementary File). Within the first three passages, HE-P3 positively expressed cell identity markers (Figure S1B and S1D in Supplementary File) and maintained their capacity for differentiating into hepatoblasts (HBs) and hepatocyte-like cells (HCs) with the positive expression of ALB/AFP expression (Figure S1C and S1F in Supplementary File). Beyond three passages, above markers exhibited decreased expression (Figure S1D in Supplementary File); therefore, HE-P3 was used for organoid biofabrication. Besides, hiPSCs-N differentiated EPCs (EPC-P0) (Figure S1G in Supplementary File) underwent planar expansion and further matured into endothelial-like cells with upregulated expression of endothelial markers (Figure S1J in Supplementary File). A tube formation assay demonstrated EPC-P4 cells' capacity for *in vitro* angiogenesis on the Matrigel layer and embedding conditions (Figure S1I in Supplementary File). Beyond four passages, the doubling time became prolonged (Figure S1K in Supplementary File); thus, EPC-P4 cells were used for subsequent organoid biofabrication.

3.1.2. Electro-assisted bioprinting of hiPSC-derived DOs

While 3D bioprinting has been integrated with iPSCs to 3D-print biomimetic tissues, it is crucial to select an appropriate printing method based on the research objectives due to the distinct features associated with each technique.[20] Extrusion-based bioprinting enables the fabrication of hierarchical biomimetic models by controlling spatial positioning of cell-laden bioinks. However, the high shear stresses involved in the printing process can impair the cellular viability of iPSCs, which are sensitive to mechanical damage.[21,22] While the current vat polymerization-based bioprinting technologies have achieved superior bioprinting resolution and accuracy, there is still a shortage of cell-compatible materials that can be used with these technologies.The thermal inkjet bioprinting technology is only applicable to a narrower range of biomaterials characterized by low viscosity.[23] The electro-assisted inkjet printing of hydrogel microspheres demonstrates compatibility with a wide range of biomaterials, high printing throughput, and exceptional structural stability.[24,25] Our previous study demonstrated that alginate-based microspheres generated by electro-assisted inkjet printing maintained high cell viability of mesenchymal stem cells and hepatic stem cells in the printing process, and facilitated uniform cell aggregation and differentiation.[18,26] Thus, utilizing electro-assisted inkjet printing technology and a blend of alginate and laminin, we were able to generate a large amount of reproducible cell-laden microspheres measuring approximately 500 μm in diameter (Figure 2A; Figure S2A in Supplementary File). After 5 days of culture, the cell viability was almost fully recovered (Figure 2A). The three types of cells (HE/EPC/human HSC cell line LX-2) self-organized into multicellular organoids (DOs) with averaged diameters of 35 ± 13 μm, the diameter of 90% of the organoids is within the range of 25–45 μm, and no necrosis was observed within the center of the core (Figure 2A; Figure S2B in Supplementary File). These results suggested that electro-assisted inkjet printing was suitable for printing monodispersed hiPSC-derived cells that were sensitive to mechanical disturbance.[27]

These DOs positively expressed hepatocyte typical markers (ALB+/CYP3A4+), endothelial markers (CD31), and HSC markers (vimentin, VIM) (Figure 2B). We fabricated DOs-laden microspheres labeled with EPC-RFP, LX-2-EGFP, and nuclear staining. The results indicated that the three types of cells closely interacted

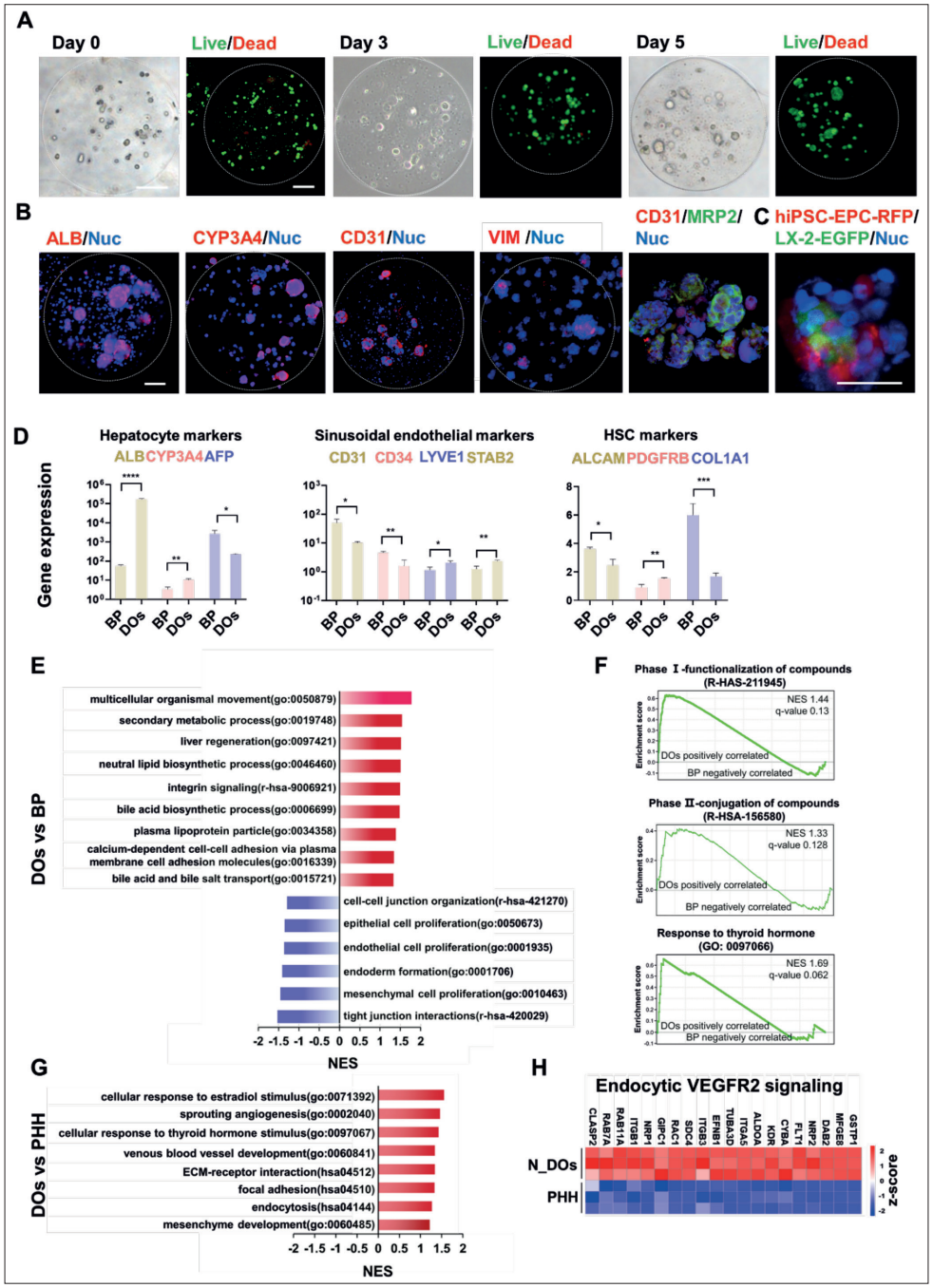


Figure 2. Biofabrication and analysis of DOs from healthy donor-derived hiPSCs. (A) Optical images and fluorescent live/dead images of cell-laden microspheres on day 0, day 3, and day 5. Day 0 refers to the day of biofabrication. (B) Immunofluorescence staining of hepatocyte markers (ALB, CYP3A4, and MRP2), endothelial marker (CD31), and HSC marker (VIM) in DOs within the microspheres or harvested DOs. Nucleus (Nuc) was stained by DAPI. The dashed circles in (A) and (B) indicate the outline of the microspheres; scale bars in (A) and (B): 100 μm. (C) Fluorescence images of DOs composed of hiPSCs-EPC-RFP, LX2-EGFP, and DAPI staining; scale bar: 50 μm. (D) qRT-PCR of hepatic markers (*ALB*, *CYP3A4*, *AFP*), endothelial markers (*CD31*, *CD34*, *LYVE1*, *STAB2*), and HSC markers (*ALCAM*, *PDGFRB*, *COL1A1*) of planar cultured cells before printing (BP) and DOs, normalized to hiPSCs. Data are presented as the mean ± SD. Statistical significance was analyzed using the unpaired two-tailed *t*-test, $^{*}P < 0.05$, $^{**}P < 0.01$, $^{***}P < 0.001$, $^{****}P < 0.0001$, $n = 3$. (E) GSEA of GO/Reactome terms based on the differential expression between DOs and BP. (F) Representative plots of GSEA for the comparison of DOs and BP. (G) GSEA of GO/Reactome terms based on the differential expression between DOs and PHHs. In (E) and (G), the *X* axes represent the NES (normalized enrichment score); the numbers next to the columns represent the FDR q-value. (H) Heatmaps of gene expression in DOs and PHHs; the bar stands for z score values, $n = 3$.

with each other in the DOs (Figure 2C). Compared with cultured planner cells before printing (BP), DOs showed hepatocyte maturation with upregulation of ALB and CYP3A4 and downregulation of the fetal gene *AFP* (Figure 2D). DOs exhibited transcriptional features of sinusoidal endothelial cells, with reduced expression of *CD31* and *CD34*, while elevated expression of *LYVE1* and *STAB2* (Figure 2D). Additionally, the activation markers of HSC, such as *ALCAM* and *COL1A1*, were downregulated in the DOs[28] (Figure 2D). These results suggested that the hydrogel microspheres provided an appropriate microenvironment that facilitated the assembly of multiple hiPSC-derived cells into organoids, as well as mutual maturation with tissue-specific features. Mechanically, RNA-seq analysis comparing DOs and BP revealed upregulation of integrin signaling and calcium-dependent cell–cell interactions as well as downregulation of cell proliferation and tight junction interactions (Figure 2E). Presumably, these shifts in gene clusters contributed to the morphogenesis and maturation of liver functions, including phase I/II metabolism, hormone response, VEGF production, and bile acid biosynthetic processes (Figure 2F; Figure S2C in Supplementary File).

To figure out the advantages of DOs in practical applications, we compared DOs with primary human hepatocytes (PHH) which were considered the gold standard for evaluating *in vitro* hepatotoxicity. The results indicated that DOs exhibit higher transcriptional levels associated with sprouting angiogenesis and response to thyroid hormone stimulus and endothelial endocytosis (Figure 2G and H). These results indicated that DOs were more representative than PHH in the context of morphogenesis and response to toxicants. Taken together, we developed a biofabrication workflow for the stable generation of liver Disse-like organoids from hiPSC-derived monodispersed progenitor cells. The biomimetic multicellular interaction, liver morphogenesis, and diverse liver functions laid the foundation for testing the multifaceted hepatotoxicity of exogenous toxicants.

3.2. Entry and diffusion of the MPs and TBBPA in DOs

PS-MPs microbeads have been detected in human liver tissue samples[5]; however, the diffusion behaviors of MPs in liver tissue are not yet clarified. Fluorescently labeled microplastics allow for non-destructive visualization of the distribution and accumulation of MPs in 3D structures due to their minimal leakage of fluorescent groups in DPBS or culture media.[29,30] We observed and recorded the diffusion of fluorescently labeled PS-MPs microbeads in DOs-laden hydrogel microspheres. After incubating 1 μm red fluorescence-labeled MPs for 1800 s, fluorescence was gradually detected in the DOs, while no substantial increase was observed in empty microspheres (Figure 3A and B), implying that the dynamics for the adsorption of microplastics into organoids are closely related to the presence of organoids.

To investigate whether PS-MPs diffuse in a targeted manner into specific cell types, we labeled the cell membranes of HEs, EPCs and LX-2 cells, respectively, and generated three kinds of DOs: HE-Green, EPC-Green, and LX-2-Green. After an exposure for 8 h, the red signaling of PS-MPs appeared within the range of EPCs but disappeared from hepatocyte-like cells and LX-2 cells, indicating that endothelial cells internalized PS-MPs more preferentially than other cell types (Figure 3C). We reasoned that the mechanisms of cellular internalization differ among the three cell types.[31,32] For example, PS-MPs larger than 1 μm could be internalized in human umbilical vein endothelial cells,[31] but could rarely enter planar cultured hepatocytes.[33] We extended the exposure duration to 48 h and observed MP signaling outside the region of endothelial cells, which indicates the diffusion of PS-MPs throughout the organoids (Figure 3D).

To study the influence of endocrine disruptors on PS-MPs accumulation in liver tissue, we added TBBPA at environmental-relevant concentration (100 nM)[34] to the fluorescence-labeled PS-MPs culture media to simulate PS-MPs/TBBPA co-exposure (henceforth MPTA) (Figure 3D).We found that TBBPA significantly aggravated the accumulation of PS-MPs in DOs at both 8 and 48 h (Figure 3Eand F). This effect was likely due to TBBPA altering the protein corona on the surface of the microplastic, which as a result impacted its cellular internalization.[32] These results probably explained the synergistic toxicity of PS-MPs and TBBPA in a previous study[12] and provoked a further exploration of the synergistic toxicity of PS-MPs and TBBPA in multicellular organoids.

3.3. Co-exposure to PS-MPs and TBBPA showed limited toxicity on healthy donor-derived DOs

While the hepatic toxicity of microplastics and TBBPA has garnered significant attention, there remains controversy regarding the effects on human liver health at low-dose exposures. Herein, utilizing DOs derived from a healthy donor, we assessed the hepatic toxicity of low-dose PS-MPs (600 ng/mL), TBBPA (100 nM), and their composite MPTA (600 ng/mL/100 nM) via the evaluation of cellular toxicity, transcriptome vibration, and hepatic functional impairment under short-term (3 days) exposure conditions.

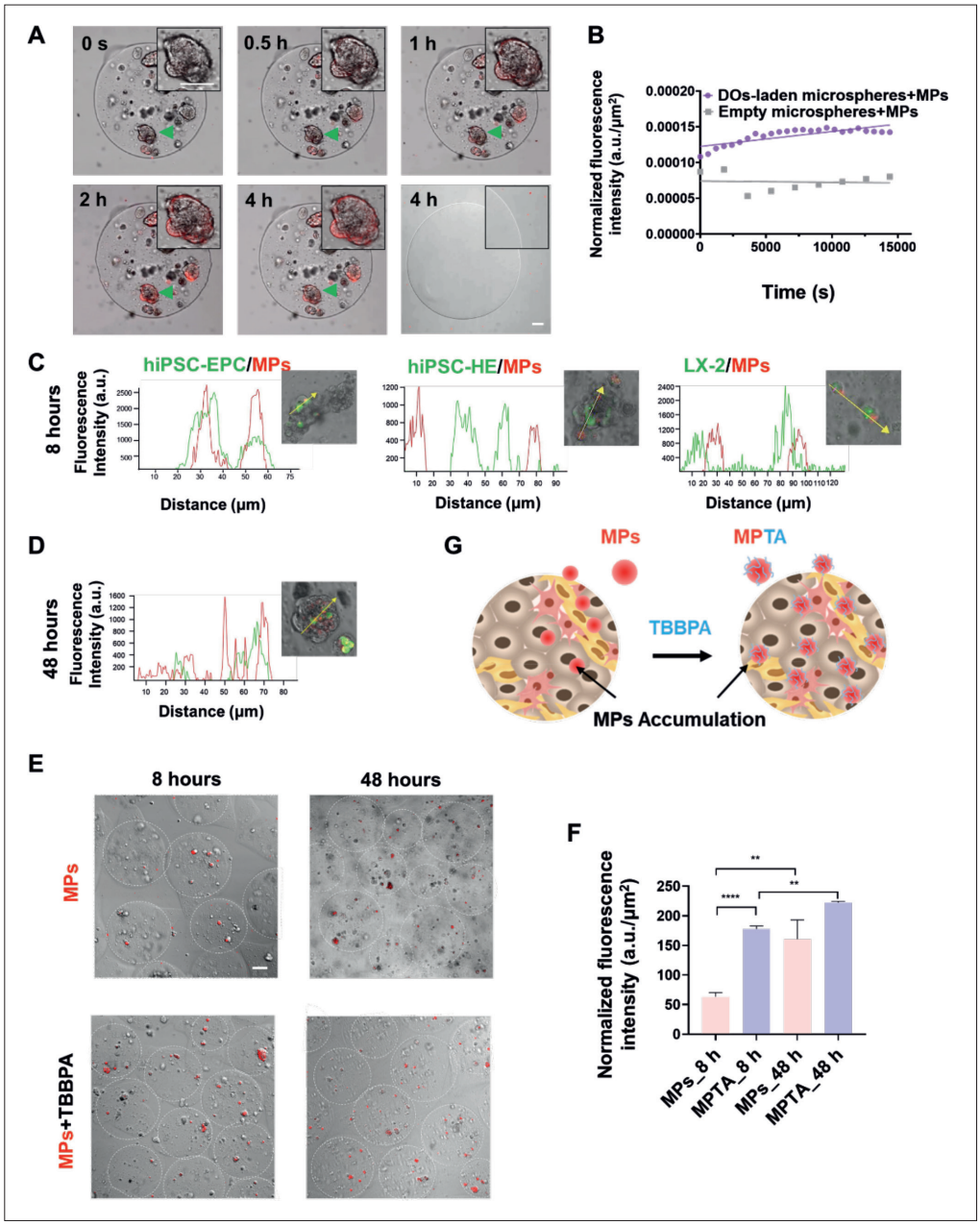


Figure 3. Diffusion of PS-MPs and MPTA in the DOs. (A) Time-lapse brightfield and fluorescence-merged images of DOs treated with fluorescent PS-MPs (red) or empty microspheres; scale bar: 50 μm. (B) The curves depict the time-lapse fluorescence intensity of PS-MPs in the DOs-laden microsphere (pink curve) and the empty microspheres (gray), normalized to the area of microsphere (μm²); the data are presented as mean ± SD, $n = 3$. (C, D) The curves depict the localization of fluorescent signals of PS-MPs (red) and PKH67 (green) in the positions of arrows in the merged images. PKH67 (green) labels cell membranes of hiPSCs_EPC, HE, and LX-2, respectively. (E) Merged images of PS-MPs signals and brightfield image of DO-laden microspheres. The dashed circles mark the outline of the microspheres; scale bar: 100 μm. (F) Quantification of (E) was calculated as the fluorescence intensity (a.u.) of PS-MPs normalized by the areas of microspheres (μm²); over 20 microspheres were counted. The data are presented as mean ± SD. Statistical significance was analyzed using a two-tailed *t*-test, $^{*}P < 0.05$, $^{**}P < 0.01$, $^{***}P < 0.001$, $n = 3$.

Live/dead staining showed that the three groups of contaminants did not impact cell viability after 3 days of repeated exposure (Figure 4A), consistent with most studies showing that PS-MPs at concentrations below 1 μg/mL and TBBPA at nanomolar dosages rarely caused cytotoxicity.[35,36] Additionally, PS-MPs, TBBPA, and MPTA did not cause apoptosis and cellular senescence in the DOs (Figure S3A and S3B in Supplementary File).

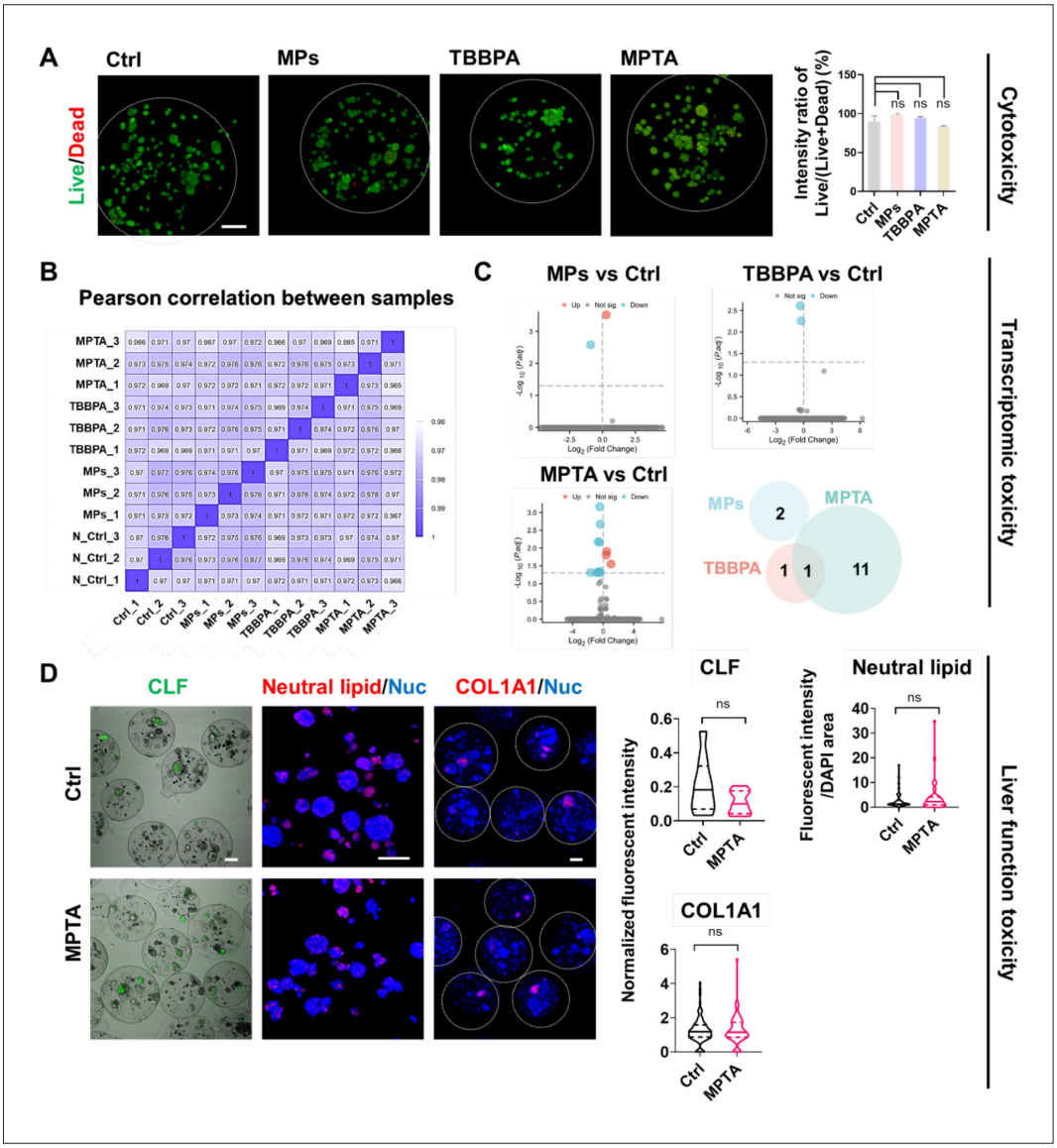


Figure 4. The effects of PS-MPs, TBBPA, and MPTA on hiPSC-N_DOs. (A) Maximal projection of the *in situ* staining of Live/Dead in N_DOs within microspheres treated with PS-MPs, TBBPA, and MPTA for 3 days; scale bar: 100 μm. The dashed circles mark the outline of the microspheres. The right panel is the ratio of Live/Dead calculated based on the three fields of Live/Dead staining. (B) The Pearson correlation heatmap of gene expression levels between all samples. (C) The volcano plots of DEGs. (D) Merged images of *in situ* staining of CLF merged with brightfield images of N_DOs within microspheres; maximal projection of neutral lipid staining and *in situ* staining of COL1A1 and DAPI in N_DOs within the microspheres; scale bar: 100 μm. Nucleus (Nuc) was stained by DAPI. The quantification of CLF, neutral lipids, and COL1A1 based on the images is shown in the lower panels. The statistical significance was determined by Student's *t*-test; "ns" indicates no significant difference.

In order to gain a more comprehensive understanding of the toxic effects, we conducted RNA-seq analysis to compare PS-MPs, TBBPA, and MPTA to Ctrl and found no significant difference in the Pearson correlation of transcriptomes within and between groups (values approximately 0.97) (Figure 4B). Moreover, PS-MPs, TBBPA, and MPTA only affected the expression of a minimal number of genes, which was almost negligible (Figure 4C).

Functional toxicity analysis through staining showed that MPTA, which induced most changes in gene transcription, did not affect the pathological signature of liver metabolic diseases in DOs, in terms of bile acid transportation (CLF), accumulation of neutral lipids, COL1A1 accumulation, αSMA activation, and polymerization of F-actin (Figure 4D; Figure S3C in Supplementary File). These results demonstrated that the hepatotoxicity of PS-MPs, TBBPA,

and MPTA at low dosages was tolerable in DOs derived from healthy donor hiPSC, suggesting that PS-MPs and TBBPA at environmental concentrations lower than those used in this study might be tolerable for healthy individuals. These findings were distinct from those reported in a prior study that utilized human embryonic stem cell-derived hepatocyte organoids, which showed cytotoxicity, lipid metabolism, and gene transcriptional toxicity even at lower concentrations of 250 ng/mL.[37] We speculated that hydrogel encapsulation and multicellular constituents might have altered the toxic response of organoids.

3.4. DOs with ALD genetic backgrounds exhibited disease-related gene phenotypes

Pollutants, along with genetic susceptibility to the disease and alcohol stimulation, may contribute to the development of ALD through their synergistic effects.[38] hiPSCs from patients with liver diseases carry a personalized genetic and epigenetic background of the diseases.[39] In order to further investigate the effects of PS-MPs and TBBPA on patients susceptible to ALD, we adopted hiPSC-AC19, derived from an ALD patient, to fabricate AC19_DOs and verify the representativeness of the genetic characteristics of ALD.

Briefly, hiPSC-AC19-derived AC19_HE-P3 and AC19_EPC-P4, together with LX-2, were printed and assembled into highly viable AC19_DOs with increasing expression of respective specific gene in the hydrogel microspheres (Figure S4A–C). After co-culture, multicellular AC19_DOs maturely expressed endothelial cell and hepatocyte markers (CD31/MRP2) (Figure S4D in Supplementary File).

To investigate whether AC19_DOs represented an inherited feature of ALD, we conducted qRT-PCR and RNA-seq analysis to compare the transcriptional expression levels of ALD biomarkers between AC19_DOs and DOs derived from healthy donor hiPSCs (N_DOs) without exogenous stimulation (Figure 5A).[40-42] Compared with N_DOs, AC19_DOs showed a pathologically relevant tendency of gene expression of ALD biomarkers. Specifically, downregulation of specific marker expression of liver sinusoidal endothelial cells (LSECs) (i.e., *STAB2*, *LYVE1*) and upregulation of *CD31* expression suggested a pathological gene phenotype of LSECs.[43] RNA-seq analysis revealed that these biomarkers were significantly enriched

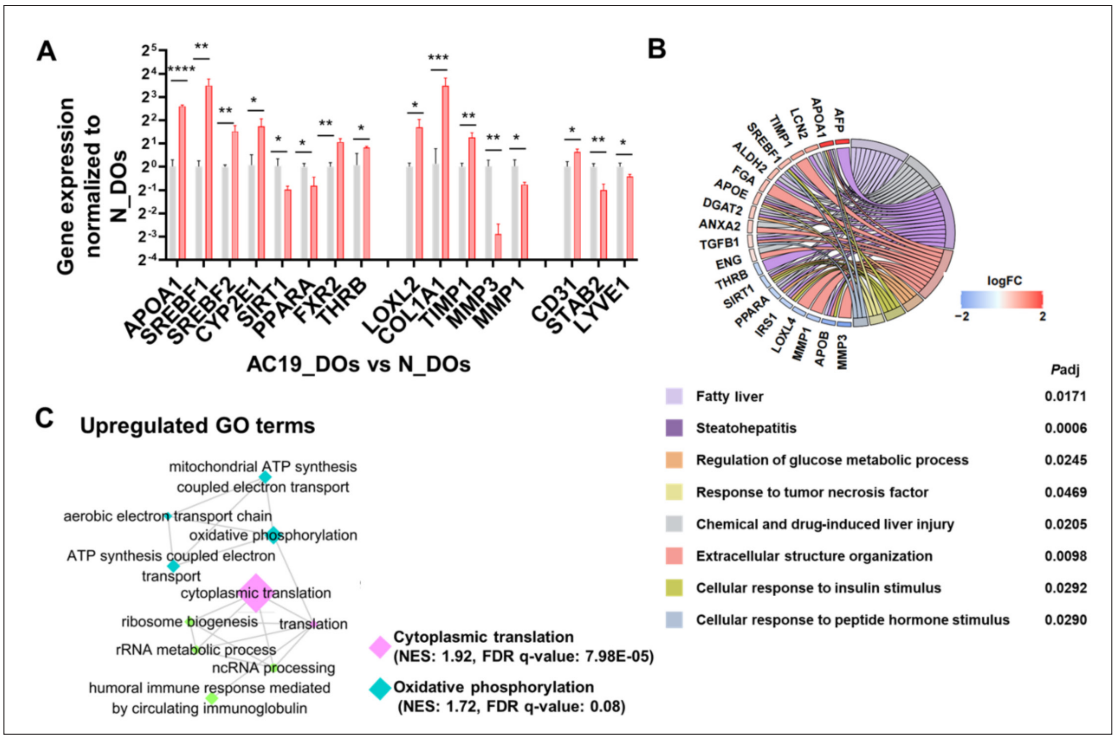


Figure 5. AC19_DOs have ALD transcriptional phenotypes. (A) qPCR of ALD pathological hallmark genes in N_DOs and AC19_DOs normalized to *GAPDH* and N_DOs; the data are presented as mean ± SD; statistical significance was calculated by Student's *t*-test. $^{*}P < 0.05$, $^{**}P < 0.01$, $^{***}P < 0.001$, $^{****}P < 0.0001$, $n = 3$. (B) Chord plot illustrating the relationships between ALD pathological hallmark genes (left) and the terms enriched by DEGs of AC19_DOs vs. N_DOs (right). The bar represents the changed folds (log10 scale) of DEGs. (C) PPI network of representative upregulated GO terms enriched by GSEA. Circle nodes represent terms, and the size is inversely proportional to FDR q-values (all <0.25). The colors represent cluster identities.

in terms related to metabolic liver diseases (Figure 5B). Furthermore, gene terms of cytoplasmic translation and mitochondrial oxidative phosphorylation were upregulated (Figure 5C), consistent with the established ALD hallmark that was mitochondrial stress.[40]

Similarly, organoids derived from hiPSCs of nonalcoholic steatohepatitis (NASH) patients exhibited increased lipid accumulation, a hallmark of NASH, compared to those from healthy controls without inducer.[39] We upgraded patient iPSC-derived organoids from single to multicellular compositions and from naked to encapsulated hydrogel microsphere. Furthermore, the close interaction between ALD biomarkers and extracellular structural organization suggested that 3D microstructure contributed to the transcriptional characteristics of ALD (Figure 5B).

3.5. MP-TBBPA complexes exhibited hepatotoxicity to ALD patient-derived DOs

Given the experimental results obtained from the N_DOs model indicating that MPTA affected a relevant more number of transcriptional genes compared to TBBPA and PS-MPs, this study opted to employ MPTA to examine the hepatotoxicity associated with AC19_DOs in the context of cytotoxicity, transcriptomic, and functional toxicities (Figure 6A).

MPTA did not impair cell viability of AC19_DOs at 600 ng/mL/100 nM with 3-day repeated exposure (Figure 6B), consistent with the results obtained with N_DOs (Figure 4A). RNA-seq analysis revealed the significant differentiation of transcriptomic correlation between AC19_MPTA and AC19_ctrl (Figure S5A and S5B in Supplementary File). Compared to AC19_ctrl, MPTA upregulated 2865 genes and downregulated 2122 genes (Figure 6C; Figure S5C in Supplementary File), distinctly different from the transcriptional data based on the N_DOs model that showed only a small number of genetic changes (Figure 4C). The DEGs were involved in the ribosome, mitochondrial functions, antioxidant activity, cell–substrate junction, and extracellular matrix components (Figure S5D and S5E in Supplementary File).

We clustered the DEGs between AC19_MPTA and AC19_ctrl into the disease-specific database DisGeNET. The results showed that inherited metabolic disease, biliary tract disease, and hepatitis were significantly upregulated (Figure 6D). Functional analysis by immunostaining corroborated results of the RNA-seq analysis that MPTA aggravated neutral lipid accumulation, impaired bile acid transport, and caused hepatic fibrosis associated with upregulation of αSMA and F-actin despite the lack of alteration of collagen I (Figure 6E). This finding was consistent with previous studies showing elevated αSMA by MPs in rats[44] and deteriorated lipid metabolism-related oxidative stress in the liver of zebrafish by co-exposure of MPs and TBBPA.[12]

Mechanistically, liver disease-related terms by MPTA were closely correlated with the cell–substrate interaction-related GO terms in the three levels of biology process, cell component, and molecular functions, like regulation of cell–substrate adhesion, cell–substrate adhesion junctions, cell cadherin molecule binding, etc. (purple in Figure 6F). This speculated mechanism was exemplified by the *in vivo* and *in vitro* findings that 1 μm MPs affected adhesion protein expression in endothelial cells and heterogeneous cell adhesion.[45] Specifically, the upregulation of inherited metabolic disorder by MPTA (green in Figure 6F) was correlated with mitochondria-related GO terms in the three levels like ATP metabolic process, mitochondrial membrane part, and NADH dehydrogenase activity (green in Figure 6F), which were hallmarks of metabolic liver diseases.[46] Therefore, these results suggested that MPTA resulted in liver diseases mainly by disrupting cell–cell/matrix interactions and mitochondrial functions.

Further, we found that MPTA interrupted the expression of ALD susceptibility-related genes in AC19_DOs in a pathologically relevant manner (AC19_MPTA vs. AC19_ctrl, Figure 6G) while not disrupting their expression in N_DOs (N_MPTA vs. N_ctrl, Figure 6G). For example, ALD susceptibility-related genes (such as *ALDH2*[38]) were specifically enhanced in AC19_DOs but not in N_DOs. Therefore, MPTA played a critical role in regulating the gene expression related to ALD susceptibility. Conversely, we analyzed the contribution of ALD susceptibility-related genes to MPTA hepatotoxicity by means of transcriptomic analysis. Transcriptome comparison of AC19_MPTA against AC19_ctrl represented the MPTA hepatotoxicity (Group MPTA); AC19_DOs against N_DOs represented the ALD susceptibility-related genes (Group models) (Figure S5F in Supplementary File). Approximately 80% of DEGs in the terms of Group models overlapped with Group MPTA (Figure S5G and S5H in Supplementary File), indicating a major contribution of ALD susceptibility-related genes to MPTA hepatotoxicity. Therefore, these results suggested that MPTA led to hepatotoxicity probably by regulating gene expression related to ALD susceptibility.

4. Conclusions

In this study, we delineated the hepatotoxicity of PS-MPs and endocrine disruptor TBBPA using hiPSC-derived DOs with healthy and ALD genetic backgrounds. The

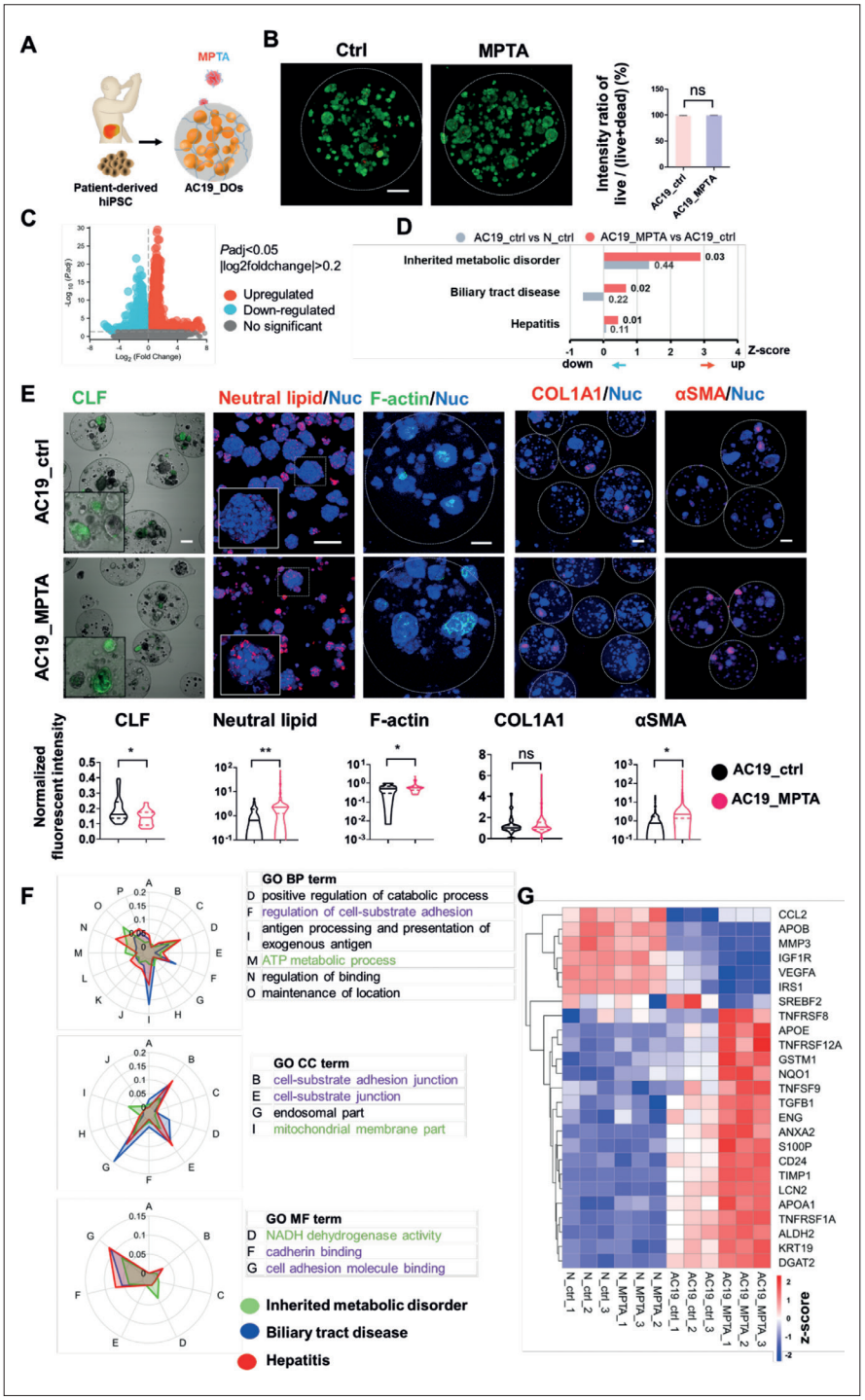


Figure 6. Hepatotoxicity of MPTA to AC19_DOs. (A) Schematic of the toxicity assessment of MPTA with AC19_DOs. (B) Maximal projection of the in situ staining of Live/Dead in N_DOs within microspheres; scale bar: 100 μm. The dashed circles mark the outline of the microspheres. (C) The volcano plot depicts the DEGs of AC19_MPTA vs. AC19_ctrl. (D) GSEA of DisGeNET terms between AC19_DOs and N_DOs. The numbers are FDR q-values. (E) In situ staining of CLF (slides), neutral lipid staining in harvested AC19_DOs (the maximal projection), in situ staining of F-actin, COL1A1 and αSMA (the maximal projection), with treatments of vehicle and MPTA; nucleus (Nuc) was stained by DAPI; scale bar: 100 μm. The lower panels show the quantification based on the staining images. The statistical significance was determined by Student's t-test. *P < 0.05, **P < 0.01. (F) Heatmaps of ALD-related gene expression in N_DOs and AC19_DOs treated with vehicle (Ctrl) and MPTA; the bar represents z score values calculated based on FPKM, n = 3. (G) The radar chart plots the similarity scores between the GO terms and disease-related terms of hepatitis, biliary tract disease, and inherited metabolic disorder. The similarity scores are calculated based on shared gene numbers.

DOs laden in microspheres had Disse space-specific cell phenotypes and outperformed PHHs in terms of endocytosis, cell–ECM interactions, and hormone responses. Promoted by TBBPA, PS-MPs could accumulate in the DOs. Low doses of PS-MPs, TBBPA, and the co-exposure to MPTA did not reduce the cell viability and had limited hepatotoxicity to N_DOs with the healthy genetic background. However, MPTA significantly increased the risks of liver diseases in AC19_DOs with ALD genetic backgrounds such as inherited metabolic disease, biliary tract disease, and hepatitis, possibly disrupting the cell–cell/matrix interactions and mitochondrial functions. Transcriptomic analysis demonstrated that ALD susceptibility-related genes play a critical role in the susceptibility of MPTA hepatotoxicity. This study provided a proof of concept that co-exposure to PS-MPs and endocrine disruptors engenders higher level of toxicity to ALD patients than to healthy individuals, which could be determined in personalized assessments using hiPSC-derived organoids.

Acknowledgments

None.

Funding

The authors were sincerely grateful for funding from the National Key Research and Development Program of China (2022YFA1104600 and 2018YFA0109000).

Conflict of interest

The authors declare no conflicts of interest.

Author contributions

Conceptualization: Rui Yao, Shaojun Liang
Formal analysis: Shaojun Liang, Yixue Luo, Yijun Su
Funding acquisition: Rui Yao, Mingen Xu, Shi-jie Wang
Investigation: Shaojun Liang, Yixue Luo, Dawei Zhang, Shi-jie Wang
Resources: Dawei Zhang, Shi-jie Wang, Mingen Xu
Writing – original draft: Shaojun Liang, Yixue Luo
Writing – review & editing: Rui Yao, Shaojun Liang, Yixue Luo

Ethics approval and consent to participate

Ethics approval was obtained from the Institution Review Board of Tsinghua University (Project No. 20220097). Written consent was obtained from the 64-year-old male patient with ALD who donated peripheral blood mononuclear cells for the experiments.

Consent for publication

Written consent was obtained from the patient for using his cells and data in preclinical researches.

Availability of data

The bulk RNA-seq data were submitted to the GEO database (GEO GSE212099).

References

1. Vethaak AD, Legler J. Microplastics and human health. *Science*. 2021;371:672-674.
doi: 10.1126/science.abe5041

2. Li S, Ma R, Zhu X, et al. Sorption of tetrabromobisphenol A onto microplastics: Behavior, mechanisms, and the effects of sorbent and environmental factors. *Ecotoxicol Environ Safety*. 2021;210:111842.
doi: 10.1016/j.ecoenv.2020.111842

3. Leslie HA, van Velzen MJM, Brandsma SH, et al. Discovery and quantification of plastic particle pollution in human blood. *Environ Int*. 2022;163:107199.
doi: 10.1016/j.envint.2022.107199

4. Ragusa A, Svelato A, Santacroce C, et al. Plasticenta: First evidence of microplastics in human placenta. *Environ Int*. 2021;146:106274.
doi: 10.1016/j.envint.2020.106274

5. Horvatits T, Tamminga M, Liu B, et al. Microplastics detected in cirrhotic liver tissue. EBioMedicine. 2022;82:104147.
doi: 10.1016/j.ebiom.2022.104147

6. Danopoulos E, Twiddy M, West R, et al. A rapid review and meta-regression analyses of the toxicological impacts of microplastic exposure in human cells. *J Hazard Mater*. 2022;427:127861.
doi: 10.1016/j.jhazmat.2021.127861

7. Colnot T, Kacew S, Dekant W. Mammalian toxicology and human exposures to the flame retardant 2,2',6,6'-tetrabromo-4,4'-isopropylidenediphenol (TBBPA): Implications for risk assessment. *Arch Toxicol*. 2014;88:553-573.
doi: 10.1007/s00204-013-1180-8

8. Lai DY, Kacew S, Dekant W. Tetrabromobisphenol A (TBBPA): Possible modes of action of toxicity and carcinogenicity in rodents. *Food Chem Toxicol*. 2015;80:206-214.
doi: 10.1016/j.fct.2015.03.023

9. Liu K, Li J, Yan S, et al. A review of status of tetrabromobisphenol A (TBBPA) in China. *Chemosphere*. 2016;148:8-20.
doi: 10.1016/j.chemosphere.2016.01.023

10. Zhou H, Yin NY, Faiola F. Tetrabromobisphenol A (TBBPA): A controversial environmental pollutant. *J Environ Sci*. 2020;97:54-66.
doi: 10.1016/j.jes.2020.04.039

11. Xu S, Wu C, Guo WB, et al. Polystyrene nanoplastics inhibit the transformation of Tetrabromobisphenol A by the bacterium Rhodococcus jostii. *Acs Nano*. 2022;16: 405-414.
doi: 10.1021/acsnano.1c07133

12. Yu Y, Ma R, Qu H, et al. Enhanced adsorption of tetrabromobisphenol a (TBBPA) on cosmetic-derived plastic microbeads and combined effects on zebrafish. *Chemosphere*. 2020;248:126067.
doi: 10.1016/j.chemosphere.2020.126067

13. Lua I, Li Y, Zagory JA, et al. Characterization of hepatic stellate cells, portal fibroblasts, and mesothelial cells in normal and fibrotic livers. *J Hepatol*. 2016;64:1137-1146.
doi: 10.1016/j.jhep.2016.01.010

14. Cuvellier M, Ezan F, Oliveira H, et al. 3D culture of HepaRG cells in GelMa and its application to bioprinting of a multicellular hepatic model. *Biomaterials*, 2021;269:120611.
doi: 10.1016/j.biomaterials.2020.120611

15. Rowe RG, Daley GQ. Induced pluripotent stem cells in disease modelling and drug discovery. *Nat Rev Genet*, 2019;20:377-388.
doi: 10.1038/s41576-019-0100-z

16. Soman SS, Vijayavenkataraman S. Applications of 3D bioprinted-induced pluripotent stem cells in healthcare. *Int J Bioprint*. 2020;6:280.
doi: 10.18063/ijb.v6i4.280

17. Palpant NJ, Pabon L, Friedman CE, et al. Generating high-purity cardiac and endothelial derivatives from patterned mesoderm using human pluripotent stem cells. *Nat Protoc*. 2017;12:15-31.
doi: 10.1038/nprot.2016.153

18. Yao R, Alkhawtani AYF, Chen R, Luan J, Xu M. Rapid and efficient in vivo angiogenesis directed by electro-assisted bioprinting of alginate/collagen microspheres with human umbilical vein endothelial cell coating layer. *Int J Bioprint*. 2019;5:194.
doi: 10.18063/ijb.v5i2.1.194

19. Takebe T, Sekine K, Enomura M, et al. Vascularized and functional human liver from an iPSC-derived organ bud transplant. *Nature*. 2013;499:481-484.
doi: 10.1038/nature12271

20. Li Y, Jiang X, Li L, et al. 3D printing human induced pluripotent stem cells with novel hydroxypropyl chitin bioink: scalable expansion and uniform aggregation. *Biofabrication*. 2018;10:044101.
doi: 10.1088/1758-5090/aacfc3

21. Ouyang L, Yao R, Zhao Y, Sun W. Effect of bioink properties on printability and cell viability for 3D bioplotting of embryonic stem cells. *Biofabrication*. 2016;8:035020.
doi: 10.1088/1758-5090/8/3/035020

22. Feng L, Liang S, Zhou Y, et al. Three-Dimensional Printing of Hydrogel Scaffolds with Hierarchical Structure for Scalable Stem Cell Culture. *ACS Biomater Sci Eng*. 2020;6: 2995-3004.
doi: 10.1021/acsbiomaterials.9b01825

23. Suntornnond R, Ng WL, Huang X, et al. Improving printability of hydrogel-based bio-inks for thermal inkjet bioprinting applications via saponification and heat treatment processes. *J Mater Chem B*. 2022;10:5989-6000.
doi: 10.1039/d2tb00442a

24. Below CR, Kelly J, Brown A, et al. A microenvironment-inspired synthetic three-dimensional model for pancreatic ductal adenocarcinoma organoids. *Nat Mater*. 2022;21: 110-119.
doi: 10.1038/s41563-021-01085-1

25. Kanninen LK, Harjumaki R, Peltoniemi P, et al. Laminin-511 and laminin-521-based matrices for efficient hepatic specification of human pluripotent stem cells. *Biomaterials*. 2016;103:86-100.
doi: 10.1016/j.biomaterials.2016.06.054

26. Huo H, Liu F, Luo Y, et al. Triboelectric nanogenerators for electro-assisted cell printing. *Nano Energy*. 2020;67:104150.
doi: 10.1016/j.nanoen.2019.104150

27. Horiguchi I, Torizal FG, Nagate H, et al. Protection of human induced pluripotent stem cells against shear stress in suspension culture by Bingham plastic fluid. *Biotechnol Prog*. 2021;37:e3100.
doi: 10.1002/btpr.3100

28. Xu L, Hui AY, Albanis E, et al. Human hepatic stellate cell lines, LX-1 and LX-2:New tools for analysis of hepatic fibrosis. *Gut*. 2005;54:142-151.
doi: 10.1136/gut.2004.042127

29. Caldwell J, Lehner R, Balog S, et al. Fluorescent plastic nanoparticles to track their interaction and fate in physiological environments. *Environ Sci Nano*. 2021;8:502-513.
doi: 10.1039/D0EN00944J

30. Caldwell J, Taladriz-Blanco P, Lehner R, et al. The micro-, submicron-, and nanoplastic hunt: A review of detection methods for plastic particles. *Chemosphere*. 293:133514.
doi: 10.1016/j.chemosphere.2022.133514

31. Zauner W, Farrow NA, Haines AMR. In vitro uptake of polystyrene microspheres: effect of particle size, cell line and cell density. *J Control Release*. 2001;71:39-51.
doi: 10.1016/s0168-3659(00)00358-8

32. Lunov O, Syrovets T, Loos C, et al. Differential uptake of functionalized polystyrene nanoparticles by human macrophages and a monocytic cell line. *Acs Nano*. 2011;5:1657-1669.
doi: 10.1021/nn2000756

33. Shen R, Yang K, Cheng X, et al. Accumulation of polystyrene microplastics induces liver fibrosis by activating cGAS/STING pathway. *Environ Pollut*. 2022;300:118986.
doi: 10.1016/j.envpol.2022.118986

34. Wang X, Wei L, Zhu JB, et al. Environmentally relevant doses of tetrabromobisphenol A (TBBPA) cause immunotoxicity in murine macrophages. *Chemosphere*, 2019;236: 124413.
doi: 10.1016/j.chemosphere.2019.124413

35. Banerjee A, Shelver WL. Micro- and nanoplastic induced cellular toxicity in mammals: A review. *Sci Total Environ*. 2021;755:142518.
doi: 10.1016/j.scitotenv.2020.142518

36. Yin N, Liang S, Liang S, et al. TBBPA and its alternatives disturb the early stages of neural development by interfering with the NOTCH and WNT pathways. *Environ Sci Technol*. 52:5459-5468.
doi: 10.1021/acs.est.8b00414

37. Cheng W, Li X, Zhou Y, et al. Polystyrene microplastics induce hepatotoxicity and disrupt lipid metabolism in the liver organoids. *Sci Total Environ*. 2021;806:150328.
doi: 10.1016/j.scitotenv.2021.150328

38. Roman S, Zepeda-Carrillo EA, Moreno-Luna LE, et al. Alcoholism and liver disease in Mexico: Genetic and environmental factors. *World J Gastroenterol*. 2013;19: 7972-7982.
doi: 10.3748/wjg.v19.i44.7972

39. Gurevich I, Burton SA, Munn C, et al. iPSC-derived hepatocytes generated from NASH donors provide a valuable platform for disease modeling and drug discovery. *Biol Open*. 2020;9:bio055087.
doi: 10.1242/bio.055087

40. Ceni E, Mello T, Galli A. Pathogenesis of alcoholic liver disease: Role of oxidative metabolism. *World J Gastroenterol*. 2014;20:17756-17772.
doi: 10.3748/wjg.v20.i47.17756

41. Purohit V, Gao B, Song BJ. Molecular mechanisms of alcoholic fatty liver. *Alcohol Clin Exp Res*. 2009;33:191-205.
doi: 10.1111/j.1530-0277.2008.00827.x

42. Affo S, Dominguez M, Lozano JJ, et al. Transcriptome analysis identifies TNF superfamily receptors as potential therapeutic targets in alcoholic hepatitis. *Gut*. 2013;62:452-460.
doi: 10.1136/gutjnl-2011-301146

43. Chaparro M, Sanz-Cameno P, Trapero-Marugán M, García-Buey L, Moreno-Otero R, et al. Mechanisms of angiogenesis in chronic inflammatory liver disease. *Annals of Hepatology*. 2007;6:208-213.
doi: 10.1016/S1665-2681(19)31900-3

44. An R, Wang X, Yang L, et al. Polystyrene microplastics cause granulosa cells apoptosis and fibrosis in ovary through oxidative stress in rats. *Toxicology*. 2021;449:152665.
doi: 10.1016/j.tox.2020.152665

45. Vlacil AK, Banfer S, Jacob R, et al. Polystyrene microplastic particles induce endothelial activation. *Plos One*. 2021;16:e0260181.
doi: 10.1371/journal.pone.0260181

46. Mansouri A, Gattolliat CH, Asselah T. Mitochondrial dysfunction and signaling in chronic liver diseases. *Gastroenterology*. 2018;155:629-647.
doi: 10.1053/j.gastro.2018.06.083

ACCSCIENCE PUBLISHING

International Journal of Bioprinting

RESEARCH ARTICLE

3D-bioprinted bone scaffolds incorporating SR1 nanoparticles enhance blood vessel regeneration in rat calvarial defects

KyeongWoong Yang[1,2], Donghyun Lee[1], Kyoung Ho Lee[1], Woong Bi Jang[2], Hye Ji Lim[2], Eun Ji Lee[2], Hojun Jeon[3], Donggu Kang[3], Gi Hoon Yang[3], KyeongHyeon Lee[4], Yong-Il Shin[4,5], Sang-Cheol Han[6], SangHyun An[1]*, and Sang-Mo Kwon[2]*

[1]Preclinical Research Center, Daegu-Gyeongbuk Medical Innovation Foundation (K-MEDI Hub), Dong-gu, Daegu, Republic of Korea

[2]Laboratory of Regenerative Medicine and Stem Cell Biology, Department of Physiology, Medical Research Institute, School of Medicine, Pusan National University, Yangsan, Republic of Korea

[3]Research Institute of Additive Manufacturing and Regenerative Medicine, Baobab Healthcare Inc., Ansan, Gyeonggi-Do, Republic of Korea

[4]Science of Convergence, School of Medicine, Pusan National University, Yangsan, Republic of Korea

[5]Department of Rehabilitation Medicine, Pusan National University Yangsan Hospital, Yangsan, Republic of Korea

[6]CEN Co., Ltd. Nano-Convergence Center, Miryang, Republic of Korea

(This article belongs to the *Special Issue: 3D Printing of Bioinspired Materials*)

Abstract

The inherent limitations of bone grafting in the treatment of critical-sized bone defects have led to a growing demand for bone repair implants. Three-dimensional (3D) bioprinting has emerged as a promising manufacturing technique for implants, offering flexibility in their structural design and the use of applicable materials. Although numerous 3D-bioprinted bone scaffolds have been developed to enhance osteogenesis, angiogenesis remains a challenge. Angiogenesis is crucial for successful bone healing because the process forms blood vessels to deliver essential nutrients and oxygen. Endothelial progenitor cells (EPCs) play a pivotal role in the early stages of vascularization. These cells, capable of differentiating into endothelial cells (ECs), are recruited from the bone marrow to the injured area during the healing process. $CD34^+$ cells, a subset of EPCs, have gained attention because of their neovascularization potential and ability to contribute to bone regeneration. The incorporation of $CD34^+$ cell-enhancing factors into 3D-printed bone scaffolds may facilitate successful bone healing in critical defects. StemRegenin-1 (SR1), a molecule that promotes $CD34^+$ cell expansion, has shown promising results in increasing $CD34^+$ hematopoietic stem and progenitor cell populations. This study aimed to investigate the sustained release of SR1 from a collagen-based scaffold integrated with mesoporous silica nanoparticles (MSNs) to promote angiogenesis and enhance bone healing. The sustained release of SR1 from the collagen scaffold is hypothesized to promote angiogenesis, thereby facilitating bone repair. *In vitro* studies have demonstrated the angiogenic potential of SR1; however, further *in vivo* investigations are required to establish its clinical efficacy. This study contributes to the development of novel therapies targeting $CD34^+$ cells and demonstrates the potential of SR1 as a promising agent for promoting angiogenesis and enhancing bone healing in critical defects.

Keywords: 3D printing; Bone scaffold; Angiogenesis; Calvarial defect; Bone regeneration

***Corresponding authors:**
SangHyun An
(ash4235@kmedihub.re.kr)

Sang-Mo Kwon
(smkwon323@pusan.ac.kr)

Citation: Yang K, Lee D, Lee KH, et al. 3D-bioprinted bone scaffolds incorporating SR1 nanoparticles enhance blood vessel regeneration in rat calvarial defects. *Int J Bioprint*. 2024;2024;10(3):1931. doi: 10.36922/ijb.1931

Received: September 27, 2023
Accepted: November 3, 2023
Published Online: January 19, 2024

Copyright: © 2024 Author(s). This is an Open Access article distributed under the terms of the Creative Commons Attribution License, permitting distribution, and reproduction in any medium, provided the original work is properly cited.

Publisher's Note: AccScience Publishing remains neutral with regard to jurisdictional claims in published maps and institutional affiliations.

1. Introduction

The treatment of critical-sized defects caused by serious injury is often rendered unsuccessful due to the inherent limitations of bone grafting, despite the excellent healing capacity of bones.[1] Therefore, there is an increasing demand for bone-repairing implants to circumvent the limitations of bone grafting, which is generally used to treat extensive bone loss.[1] Other than the traditional methods, three-dimensional (3D) bioprinting can be used as a manufacturing technique to produce bone-repairing implants with structural flexibility from a range of applicable materials.[2,3] Several 3D-bioprinted bone scaffolds have been developed using various materials to enhance osteogenesis in previous studies.[4,5] However, the failure to promote angiogenesis, an essential step in the repair and regeneration of damaged bone, remains a weak point for 3D-printed bone scaffolds. Without angiogenesis, bone healing would fail due to a lack of essential nutrients and oxygen.[6] Therefore, promoting local vascularization is a crucial step for the successful healing of extensive bone loss.[7]

Endothelial progenitor cells (EPCs) play an important role in the early stages of vascularization.[8] During the healing process, bone marrow-derived EPCs circulating in the peripheral blood are recruited to injured areas. The recruited EPCs then form new vessels by differentiating into endothelial cells (ECs).[9] Asahara et al. were the first to identify EPCs that can differentiate into ECs.[10] Notably, $CD34^+$ cells have received considerable attention because of their neovascularization potential.[11] Previous studies have demonstrated increased vascularization in myocardial ischemia models and human clinical trials using $CD34^+$ cells.[12-14] Additionally, $CD34^+$ cells play an important role in bone regeneration because of their ability to promote vascularization. Previous studies have shown that $CD34^+$ cells contribute not only to vascularization, but also to bone healing, as demonstrated by *in vivo* experiments that locally supplied $CD34^+$ cells in rat models of critical-sized femoral defect.[15-18] Many studies have underscored the potential of $CD34^+$ cells in promoting vascularization, signifying that this cell type can be used as an endothelial cell source for bone scaffold construction. Therefore, 3D-printed bone scaffolds incorporating an angiogenic factor that can enhance $CD34^+$ populations may lead to successful bone healing in critical defects. StemRegenin-1 (SR1), a purine derivative molecule promoting $CD34^+$ cell expansion, was first identified by Boitano et al.[19] Co-culturing of monoclonal peripheral blood cells with SR1 led to a significant increase in $CD34^+$ hematopoietic stem and progenitor cell populations under *ex vivo* conditions by directly binding to and inhibiting aryl hydrocarbon receptor (AhR) signaling, which plays a role in the regulation of pluripotency and stemness of hematopoietic stem cells under normal condition.[19-21] A previous study demonstrated a 50-fold increase in $CD34^+$ cells in human cord blood $CD34^+$ cell-transplanted immunodeficient mice.[19] Many studies using $CD34^+$ cells have shown a successful promotion of angiogenesis and osteogenesis.[11] However, the number of $CD34^+$ cells available for therapeutic purposes is often limited, particularly in adult tissues. Therefore, evaluating the ability of SR1 to expand the $CD34^+$ cell population *in vivo* is required, to allow further studies examining the development of clinical therapies targeting $CD34^+$ cells.

In the early stages of 3D-printed bone scaffold development, some scaffolds were printed with bioink that was directly mixed with growth factors, such as the vascular endothelial growth factor (VEGF) or fibroblast growth factor. Recently, scaffolds capable of sustained release were developed to circumvent the limitations of the early-stage scaffolds, which have short half-life and subject to swift loss of growth factors.[22,23] In this study, mesoporous silica nanoparticles (MSNs) were added to a 3D-printed scaffold to enable the sustained local release of SR1. The components of the bone scaffold were selected considering the advantages of the polymers. Recently, natural polymers have been recognized as promising materials for constructing bone scaffolds because of their favorable biocompatibility, biodegradability, and osteoconductivity.[24] On the other hand, harboring the capacities to form extracellular matrix and create porous structures,[25] collagen can be used to manufacture scaffolds, i.e., collagen-based scaffolds, which possess the desirable characteristics, such as cell attachment and osteogenic differentiation.[26-28] Although existing results indicate that SR1 is a promising material for promoting angiogenesis *in vitro*, the lack of *in vivo* studies remains a challenge in demonstrating the clinical efficacy of SR1. Therefore, we aimed to address this gap in the literature by examining whether the sustained release of SR1 from collagen scaffolds promoted angiogenesis and ultimately increased bone healing using *in vivo* studies.

2. Materials and methods

2.1. *In vitro* studies

In the *in vitro* studies, the cells were divided into three groups: (i) negative control (CT) group, in which no treatment was given; (ii) SR1 nanoparticle (SNP) group, in which the cells were treated with SR1 nanoparticles (final concentration = 1 μM); and (iii) blank nanoparticle

(NP) group, in which the cells were treated with blank nanoparticles (final concentration = 1 μM).

2.1.1. Isolation and culture of human endothelial progenitor cells

Human umbilical cord blood cells (HUCBC) used in this study were generously provided by Pusan National University Yangsan Hospital (PNUYH, IRB No. 05-2017-053). Mononuclear cells (MNCs) were isolated from HUCBC using density gradient centrifugation with Ficoll (GE Healthcare, Buckinghamshire, UK). Freshly isolated MNCs were seeded in dishes coated with 1% gelatin (Sigma-Aldrich, St. Louis, MO, USA) and cultured in endothelial growth medium-2 (EGM-2; Lonza, Walkersville, MD, USA). EGM-2 comprises endothelial cell basal medium, 5% fetal bovine serum (FBS), 1% penicillin–streptomycin, human basic fibroblast growth factor, human vascular endothelial growth factor, human insulin-like growth factor-1, ascorbic acid, human epidermal growth factor, and gentamicin sulfate-amphotericin. Cells were incubated at 37°C in 5% CO_2. After 5 days, non-adherent cells were removed, and the attached cells were continuously cultured. Cultures were maintained to allow the development of spindle-shaped colonies. EGM-2 was replaced daily, and the colonies were replaced and cultured further. To ensure that the cells were in optimal condition, cells from passages 7–9 were selected for subsequent experiments.[29]

2.1.2. Flow cytometry analysis

Cells were seeded on 100 mm plates at a density of 1×10^6 cells/plate and grown at 37°C with 5% CO_2 for 48 h in EGM-2 culture medium with different treatments for each group. Cells were suspended in fluorescence-activated cell sorter (FACS) buffer (2% FBS, 2 mM ethylenediaminetetraacetic acid [EDTA] in phosphate-buffered saline [PBS]) and stained with antibodies against CD34, CXCR4, VEGFR2, VE-cadherin (555821, 555976, 560494, and 560410; BD Biosciences, New Jersey, USA), and c-Kit (130-091-733; Miltenyi Biotec, Bergisch Gladbach, Germany). The cells were incubated at 4°C for 30 min in the dark followed by washing and resuspension with FACS buffer. Samples were analyzed using flow cytometry (Accuri C6, BD Biosciences, New Jersey, USA).

2.1.3. CCK-8 assay

Cells were seeded in 96-well plates at a density of 3000 cells per well and grown at 37°C with 5% CO_2 for 48 h in EGM-2 with different treatments for each group. The cells were incubated with 10 μL of D-Plus™ CCK reagent (CCK-3000; Dongin, Seoul, Republic of Korea) and 90 μL media for an hour at 37°C. The cultured cells were then subjected to cell viability measurement. Absorbance was measured at 450 nm using a microplate reader (TECAN, Mannedorf, Switzerland).

2.1.4. 5-Ethynyl-2´-deoxyuridine (EdU) cell proliferation assay

Cells were seeded on coverslips in a 6-well plate at a density of 5×10^4 cells per well and grown at 37°C with 5% CO_2 for 48 h in EGM-2 with different treatments for each group. EdU staining was conducted using the Click-iT™ Plus EdU Alexa Fluor™ 488 Imaging Kit (C10637; Invitrogen, Waltham, Massachusetts, USA). Cells were incubated in medium containing a final concentration of 10 μM EdU for 5 h at 37°C under 5% CO_2. Subsequently, cells were fixed with 4% paraformaldehyde at room temperature for 15 min and permeabilized with 0.5 % Triton X-100 in PBS at room temperature for 20 min. Cells were then washed with PBS and reacted with EdU solution at room temperature for 30 min. Nuclei staining and mounting were performed using ProLong™ Diamond Antifade Mountant with 4',6-diamidino-2-phenylindole (DAPI) (P36962, Invitrogen, Waltham, Massachusetts, USA). An automated microscope (Lionheart FX; BioTek, Winooski, Vermont, USA) was used to capture the images.

2.1.5. Wound healing assay

Finally, a wound healing assay was conducted on EPCs to verify that SR1 improved their migration ability. Passage-8 EPCs were chosen for the migration assay to ensure appropriate cell conditions. The assay was conducted using the CytoSelect™ 24-well Wound Healing Assay Kit (CBA-120; Cell Biolabs, Inc., San Diego, California, USA). To initiate the assay, the desired number of inserts was oriented in the plate wells with their "wound field" aligned in the same direction using sterile forceps after warming up the 24-well plate with CytoSelect™ 24-well Wound Healing Inserts for 10 min. Cell suspension (500 μL) containing 0.5×10^6 cells/mL in media was added to each well. The cells were incubated for 24 h until a monolayer was formed. Following monolayer formation, the culture medium was replaced with the same volume of fresh medium. For the SNP group, the medium was exchanged with media containing SR1 nanoparticles (final concentration of SR1 = 1 μM). Similarly, the NP group was treated with media containing an equivalent number of blank nanoparticles as used in the SNP group. After 48 h of treatment, the inserts were removed, and the images were captured using an automated microscope (IX83, Olympus, Shinjuku City, Tokyo, Japan).

2.2. Characterization of MSNs

Mesoporous silica nanoparticles (SMB™3 Property) were obtained from CENNANO Co., Ltd., Ulsan, Korea. Nanoparticles encapsulating 25 wt.% of SR1 were

generated by following procedures; 75 mL of ethanol was dissolved with 75 mg of blank nanoparticles. Additionally, 1 mL of dimethyl sulfoxide (DMSO) was dissolved with 25 mg of SR1. The above-prepared mixture of ethanol and blank nanoparticles was combined with the DMSO and SR1 solution. The resulting mixture was incubated for 3 h under a vacuum state at a pressure of 100 bar. Then, the pressure was lowered to 60 bar for a 30 min incubation. Finally, 100 mg of SR1-laden nanoparticles were generated after drying for 12 h at a vacuum state. Characteristics of SMB™3, according to the manufacturer's description, are as follows: a SiO_2 content of 99%, an average pore diameter of 3.45 nm, an average BET surface area of >750 m^2/g, a pore volume of >1.0 cm^3/g, and a tap density of ~0.12 g/cm^3. Scanning electron microscopy (SEM; SU8010, Hitachi, Chiyoda, Tokyo, Japan) was used to visualize the morphology and analyze the diameter of the nanoparticles.

2.3. Liquid chromatography-mass spectrometry (LC-MS) release test of nanoparticles

A QTRAP 6500+ low-mass LC-MS system (SCIEX, Toronto, Canada) was used to analyze the cumulative release of SR1-laden nanoparticles. Calibration standard solutions were prepared by soaking SR1-laden nanoparticles in deionized water (10 mg/mL) and diluting them with methanol to final concentrations of 10, 50, and 100 part per billion. Samples were prepared by soaking SR1-laden nanoparticles in deionized water (10 mg/mL) and releasing them after 2, 4, and 6 days. SR1-released samples were filtered with a pore filter (pore size: 0.22 μm) to remove the nanoparticles. The filtered solutions were subjected to centrifugation (10,000 × *g*, 10 min) to ensure complete elimination of the remaining nanoparticles; after centrifugation, the supernatants were diluted using methanol to a final concentration of 0.01 mg/mL.

2.4. Scaffold fabrication

Core-shell scaffolds were constructed using a coaxial nozzle (inner needle 19 G, outer needle 14 G; Ramé-hart, Succasunna, New Jersey, USA) equipped with a 3D bioprinter (Root 1, Baobab Healthcare, Ansan, Republic of Korea). For the shell, bioinks were prepared by combining 3 w/v% neutralized atelocollagen (4°C; Baobab Healthcare, Ansan, Republic of Korea) and 3 w/v% alginate (viscosity >2000 cP, 20°C; Sigma-Aldrich, Burlington, Massachusetts, USA) at a ratio of 3:1. Then, either SR1-laden nanoparticles or nanoparticles alone were mixed with the bioinks at a final concentration of 1 μM (SR1) or an equivalent weight (nanoparticles only), respectively.

Bioinks were prepared for the core by combining 40 w/v% Pluronic F-127 (P2443, Sigma-Aldrich, Burlington, Massachusetts, USA) with 100 mM calcium chloride, which served as a crosslinking agent for the alginate. The core-shell bioinks were printed at 60 kPa (core) and 40 kPa (shell) on a 37°C printing base with a crosshead speed of 800 mm/min. The resulting sample dimensions were approximately 40 × 40 × 0.6 mm, and it was incubated at 37°C for an hour to allow the atelocollagen to gel. Subsequently, the sample was trimmed to a 5 mm diameter and immersed in PBS at 4°C to remove the Pluronic F-127.

2.5. *In vivo* studies

2.5.1. Experimental animals

Twenty-eight female Sprague-Dawley rats (age of 3 months, body weight of 240 ± 20 g) were purchased from Koatech (Pyeongtaek, Republic of Korea) and housed in a Sun Protection Factor environment of a 12 h light/12 h dark cycle. The animals had free access to water and food. Animal experiments were approved by the Institutional Animal Care and Use Committee of Daegu-Gyeongbuk Medical Innovation Foundation (Approval number: KMEDI-22080801-01).

2.5.2. Surgery and treatment

After a week of adaptation, the 28 rats were divided into three groups according to body weight: CT group (no treatment, n = 8), scaffold with blank nanoparticles (NP@Sc) group (implanted scaffolds incorporated with blank nanoparticles, n = 8), and scaffolds with SR1-laden nanoparticles (SNP@Sc) group (implanted scaffolds incorporated with SR1 nanoparticles, n = 12). The animals were anesthetized by intraperitoneal injection of Zoletil (tiletamine/zolazepam) (30 mg/kg) and xylazine (10 mg/kg). The rats then underwent surgery to create defects in their cranial bone (diameter = 5 mm) using a trephine bur and implant the scaffolds. Postoperatively, the rats were given subcutaneous injection of meloxicam (0.2 mg/kg) as an analgesic.[30] The animals were sacrificed for evaluation at 2 and 4 weeks after surgery.

2.5.3. Micro-computerized tomography analysis

Half of the animals in each group were anesthetized and subjected to micro-computerized tomography (MCT) scanning to evaluate bone regeneration and to visualize the whole cranial bone. The Quantum FX (PerkinElmer, Waltham, Massachusetts, USA) was used to perform MCT scanning 2 and 4 weeks after implantation.

2.5.4. Microfil perfusion

Four weeks after implantation, half of the animals in each group were perfused with Microfil compound (MICROFIL® MV-122; Flow Tech, Cheonan, Republic of Korea) to evaluate blood vessel formation using MCT scanning. The animals were anesthetized, and 0.2 mL of heparin (5000 IU/mL) was injected intravenously into their tail vein. The animals were then fixed on a polystyrene plate, and the

heart was exposed by vertically incising along their bodies' midline. An incision (<1 cm) was made in the left ventricle, and a feeding tube was inserted into their aorta. Afterward, the following procedures were conducted: First, the blood vessels were flushed by cardiac perfusion using 200 mL of heparin (1 IU/mL)-containing normal saline, and the right atrium was incised to allow the perfused normal saline to flow out. Next, 20 mL of Microfil solution (prepared by mixing 10.5 mL of Microfil compound, 13.2 mL of specific diluent, and 1.3 mL of specific curing agent) was used to perfuse the blood vessels in the same manner with an initial pressure of 120 mmHg and a perfusion rate of 2 mL/min. Following this, the animals were stored overnight at 4°C to facilitate the primary setting of visualizing the vasculature system of whole cranial region by MCT scanning Eventually, the animals were fixed in 10% buffered formaldehyde solution for a week and were soaked in 14% EDTA for decalcification for 3 weeks before scanning. Quantum FX (PerkinElmer, Waltham, Massachusetts, USA) was used to perform MCT scanning of the Microfil compound-perfused and decalcified rat calvarial samples.

2.6. Histological analysis

All animals were sacrificed immediately after MCT scanning, and cranial bone samples were extracted from the sacrificed animals. Harvested samples were fixed in 10% buffered formaldehyde solution for a week and were also decalcified with 14% EDTA for 3 weeks. Next, the samples were cut horizontally, dehydrated, embedded in paraffin, and trimmed into sections of 4 μm thickness. The sections were stained with hematoxylin–eosin (H&E) and Masson's trichrome (MT). Quantitative evaluation of the percentage area of new bone to the total defective area was conducted according to the results of the H&E- and MT-stained slides at 2 and 4 weeks after implantation.

2.7. Immunohistochemistry and immunofluorescence

Immunohistochemical analysis was conducted on the sectioned slides to detect the expression of CD31 and α-smooth muscle actin (α-SMA) using the following procedures: The sectioned slides were deparaffinized and rehydrated using a series of ethanol and xylene solutions. The slides were then labeled with elastin and biotin-conjugated secondary antibodies. Labeled slides were visualized using the Vector Nova RED substrate kit after incubation with an ABC complex kit. The nuclei were counterstained with hematoxylin. The slides were probed overnight at 4°C with the following antibodies: anti-CD31 (#ab182981, Abcam, Cambridge, England) and anti-α-SMA (#ab5694, Abcam, Cambridge, England). Afterward, the slides were washed with PBS and incubated for an hour with proper Alexa Fluor-coupled secondary antibodies at 25°C. Moreover, the nuclei were counterstained with DAPI. Finally, the slides were observed using a motorized fluorescence microscope (Eclipse Ti-E, Nikon, Minato City, Tokyo, Japan).[31] In this study, the regions of interest (ROIs) were defined as areas within the tissue sections that exhibited distinct staining patterns indicative of specific markers or characteristics. These areas were identified based on staining intensity, color, and patterns observed in the histological sections, particularly those stained with MT and H&E. The positive areas were quantified using image analysis software, which allowed us to measure the extent of marker expression or tissue characteristics within the defined ROIs. This approach facilitated the evaluation of various parameters, including angiogenesis, tissue regeneration, and cellular responses within the treated samples.[32-34]

2.8. Statistical analysis

All experimental data were processed and plotted using GraphPad Prism version 9.3 (GraphPad Software, Inc., Boston, MA, US). Data are expressed as mean ± standard deviation (SD). Analysis of variance (ANOVA) was used to test whether the obtained data had a statistical difference, and significance levels were set at $^{*}p < 0.05$, $^{**}p < 0.01$, and $^{***}p < 0.001$.

3. Results

3.1. *In vitro* studies

3.1.1. Flow cytometry analysis

Figure 1A shows the result of flow cytometry analysis using biomarkers (CD34, c-kit, CXCR4, VEGFR2, and VE-cadherin) on the differently treated groups. The histogram for CD34 revealed that 26.6%, 24.6%, and 35.3% of $CD34^{+}$ cells were present in CT, NP, and SNP groups, respectively. Among the $CD34^{+}$ cells of each group, the percentage values of expressing c-kit (CD117), CXCR4 (CD184), VEGFR2, and VE-cadherin (CD144) were 13.6%, 21.4%, 23%, and 23.9% for the CT group; 12.2%, 20.6%, 18.5%, and 24.8% for the NP group; and 17.9%, 27.2%, 32.4%, and 34.6% for the SNP group, respectively. In summary, SR-1-laden nanoparticles significantly boosted $CD34^{+}$ cell presence and enhanced EPC marker expressions, suggesting their potential to promote angiogenesis and tissue regeneration.

3.1.2. CCK-8 assay

A CCK-8 assay was conducted to evaluate the effect of the SR1 nanoparticle on EPC proliferation. The results (Figure 1B) clearly demonstrate a substantial difference in the relative optical intensity among the three groups. The SNP group revealed a significantly higher proliferation rate compared to that of the CT ($p < 0.001$) and NP groups ($p < 0.05$); the proliferation rates were 100.00 ± 5.04, 105.23

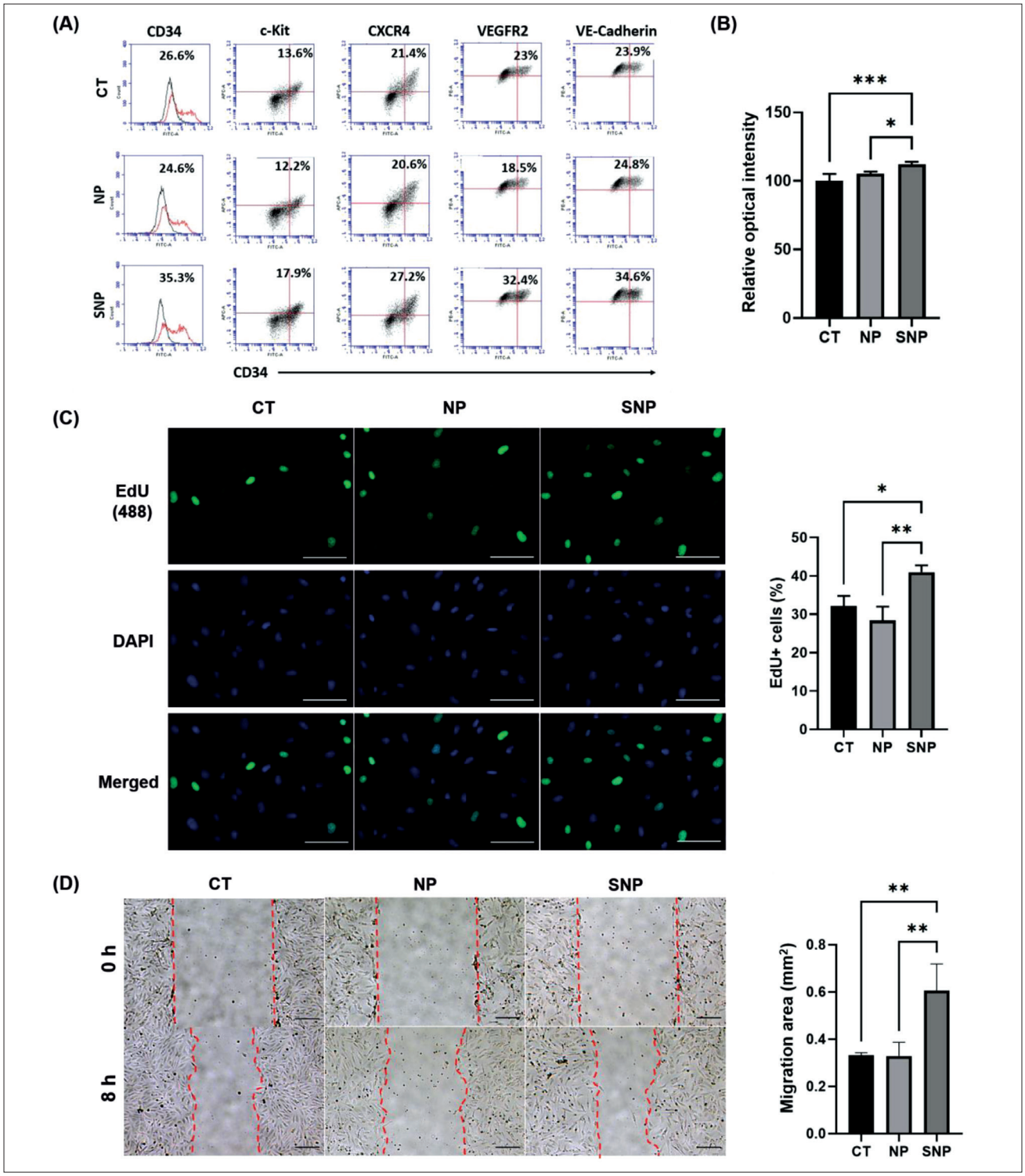


Figure 1. Results of *in vitro* experiments conducted 48 h after treatment. (A) Flow cytometry analysis using antibodies such as CD34, CD117 (c-kit), CD184 (CXCR4), CD144 (VE-cadherin), and VEFGR2 (KDR). (B) CCK-8 assay for evaluating cell proliferation. (C) Resulting images after 5-ethynyl-2'-deoxyuridine (EdU) cell proliferation assay under 200× magnification. Scale bar = 100 μm. (D) Migration of endothelial progenitor cells 8 h after removing gap-inducing inserts. Scale bar = 250 μm. (A–D) Values are expressed as mean ± standard deviation and analyzed using ordinary one-way ANOVA. Differences between groups were analyzed using Dunnett's multiple comparisons test, and significance levels were set at $^{*}p < 0.05$, $^{**}p < 0.01$, and $^{***}p < 0.001$. Abbreviations: CT, negative control; NP, blank nanoparticle; SNP; SR1-laden nanoparticle.

± 1.56, and 112.08 ± 1.92 for the CT, NP, and SNP groups, respectively. These findings strongly indicate that SR1 nanoparticles promote EPC proliferation, with the SNP group showing the most pronounced effect.

3.1.3. EdU cell proliferation assay

Cell proliferation in cultured EPCs was analyzed via EdU cell proliferation assay. Green signals indicate EdU-positive cells, while the nuclei were counterstained with DAPI. Figure 1C shows the results of the EdU assay and the quantitative evaluation of the experimental groups. Remarkably, the SNP group exhibited a significantly higher percentage of EdU-positive cells compared to that of the CT ($p < 0.05$) and NP groups ($p < 0.01$). The specific percentages of EdU-positive cells for all three groups are as follows: 32.17 ± 2.60, 28.40 ± 3.58, and 40.98 ± 1.76 for CT, NP, and SNP groups, respectively. These results strongly support the conclusion that SR1 nanoparticles exert a substantial stimulatory effect on EPC proliferation, with the SNP group displaying the most pronounced enhancement.

3.1.4. Wound healing assay

A wound healing assay was performed to examine the role of SR1 nanoparticles in cell migration, a fundamental process essential for vasculogenesis—the formation of new blood vessels. The scratched area was partially re-filled by the migrating cells 8 h after taking out the insert that was previously placed to induce the scratching. Figure 1D shows the migration area and the results of quantitative analysis on CT, NP, and SNP groups. The results demonstrated that the migrated area of the SNP group was approximately twice the size of the CT and NP groups, measuring at 0.61 ± 0.11 mm^2 ($p < 0.01$). These findings highlight the crucial role of SR1 nanoparticles in enhancing the migration capacity of EPCs, a key factor in facilitating vasculogenesis.

3.2. Scaffold fabrication and morphology

A schematic illustration of the scaffold manufacturing process is shown in Figure 2A.

3.2.1. Scaffold morphology

Figure 3A displays SEM images of the SNP@Sc and NP@Sc scaffolds. The appearance of the entire scaffold was revealed in the 30× **magnification** SEM images. A porous structure was observed in the 500× **magnification** SEM images, and a detailed one was observed in the 15,000× magnification images. No difference in appearance was detected between NP and SNP groups.

3.2.2. Nanoparticle size distribution assay

SEM was used to analyze the size distribution of SR1-laden nanoparticles. Figure 3B shows an image of the nanoparticles. After measurement, their diameter was found to be 189.34 ± 99.23 nm (Figure 3C).

3.3. LC/MS release test of nanoparticles

The cumulative release tendency of SR1-laden nanoparticles is shown in Figure 3D. Percentage values of released SR1 were 0.6%, 2.7%, and 3.3% for the nanoparticles released for 2, 4, and 6 days, respectively.

3.4. *In vivo* studies

None of the experimental animals died before sacrifice, and no significant loss of body weight was observed among the experimental animals during the investigation. Schematic illustration of the surgery and expected results are shown in Figure 2B. Figure 4A shows the outline of the *in vivo* experimental design.

3.4.1. Bone formation analysis

Figure 4B shows MCT images of the defected sites in the rats 2 and 4 weeks after scaffold implantation. Quantitative evaluations of the MCT results are presented in Figure 4C and D. MCT images indicated that new bone had partially regenerated in the defect, and differences between the groups were observed. The bone volume fraction (BV/TV%) and bone mineral density (BMD) of the CT, NP@Sc, and SNP@Sc groups were analyzed. At 2 weeks postoperatively, the BV/TV% values were recorded as 13.01 ± 2.51%, 11.30 ± 1.23%, and 15.75 ± 2.61% area/ROI for the CT, NP@Sc, and SNP@Sc groups, respectively. Similarly, the BMD values were 102.53 ± 16.83%, 92.60 ± 12.08%, and 125.27 ± 15.68%, showing trends of increasing bone area in the order of SNP@Sc > CT > NP@Sc. However, these differences were not statistically significant ($p > 0.05$) at this early time point.

Nevertheless, this trend persisted in the three groups, and the differences became more pronounced ($p < 0.01$) at 4 weeks after implantation, particularly for the SNP@Sc group. At this later time point, the BV/TV% values were 17.00 ± 1.87%, 15.54 ± 2.83%, and 23.91 ± 4.57% area/ROI, respectively, while the BMD values were 134.40 ±13.89%, 128.51 ± 19.97%, and 189.75 ± 21.15%. In summary, these findings strongly suggest that SR1 significantly accelerated new bone formation within the rat calvarial defects, with the most notable effects observed at 4 weeks after implantation. This underscores the role of SR1 in promoting bone regeneration, particularly in the later stages of healing.

3.4.2. Histological analysis

For additional evaluation, histological analysis was performed using H&E and MT staining on sections of rat calvaria after sacrifice. Figure 5A and B shows the H&E and MT staining results of the rat calvarial samples obtained at 2 and 4 weeks after implantation. Figure 5C clearly illustrates that new bone formation in the SNP@Sc group significantly surpassed that of the CT and NP@Sc

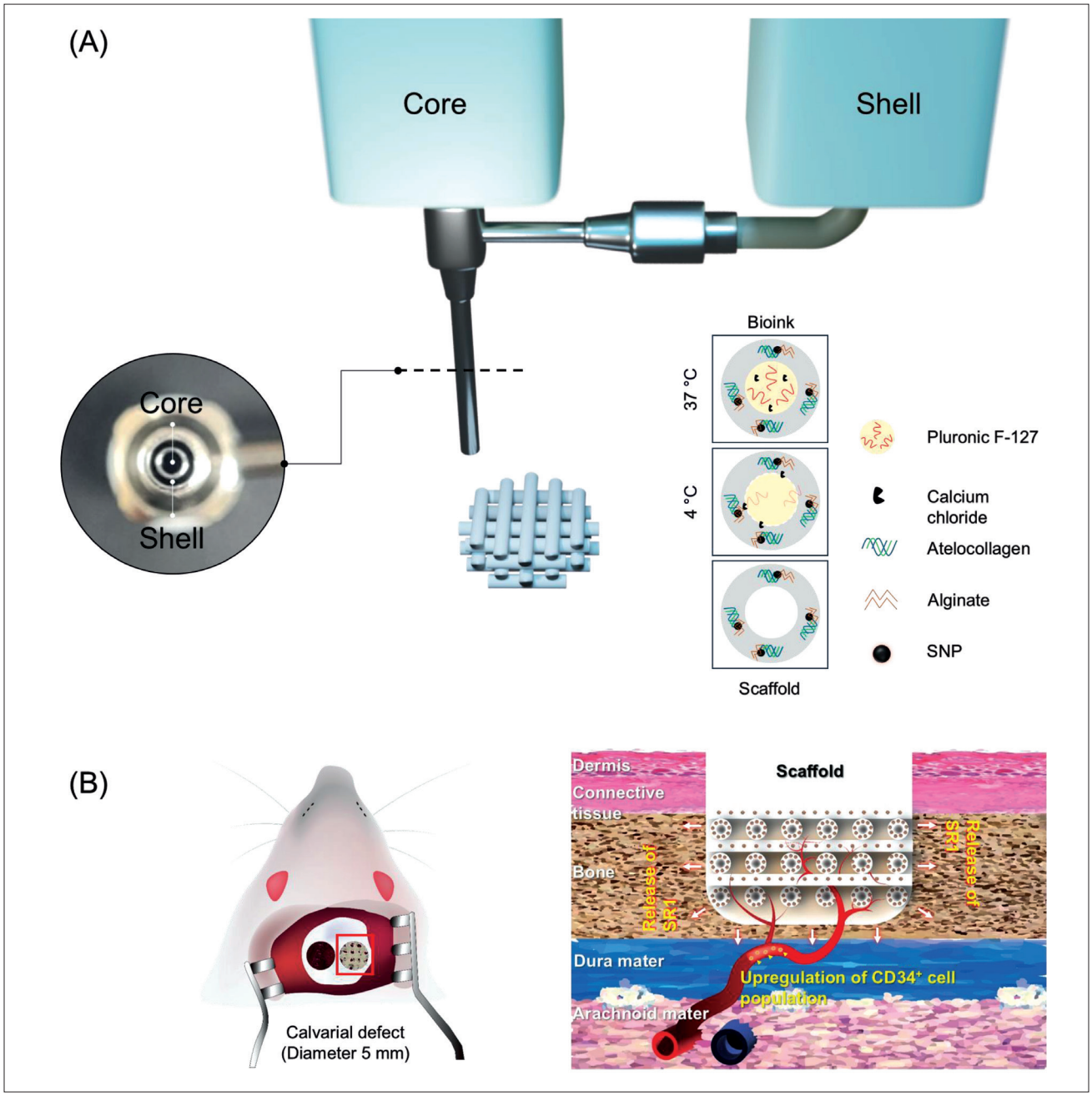


Figure 2. Schematic illustration of the experimental process. (A) StemRegenin-1 (SR1)-laden nanoparticle and collagen were applied to produce bioink which was used to prepare collagen scaffold using a 3D bioprinting system. (B) Outline of the operation and main expected effects of surgery. Abbreviation: SNP, SR1-laden nanoparticle.

groups at both the 2- and 4-week post-implantation time points. At 2 weeks after implantation, the area of newly formed bone was approximately five times larger in the SNP@Sc group (11.29 ± 1.72 mm^2) than in the CT group and nearly 4.5 times larger than in the NP@Sc group. Similarly, at 4 weeks after implantation, the newly formed bone in SNP@Sc group accounted for 29.75 ± 4.25 mm^2, which was approximately twice the area of the CT and NP@Sc groups. These results not only reinforce the significant role of SR1 in enhancing bone regeneration but also emphasize the sustained and increasingly beneficial effects over time.

3.4.3. Immunofluorescence staining

Immunofluorescence staining was performed on the paraffin-sectioned slides to analyze CD31 and α-SMA

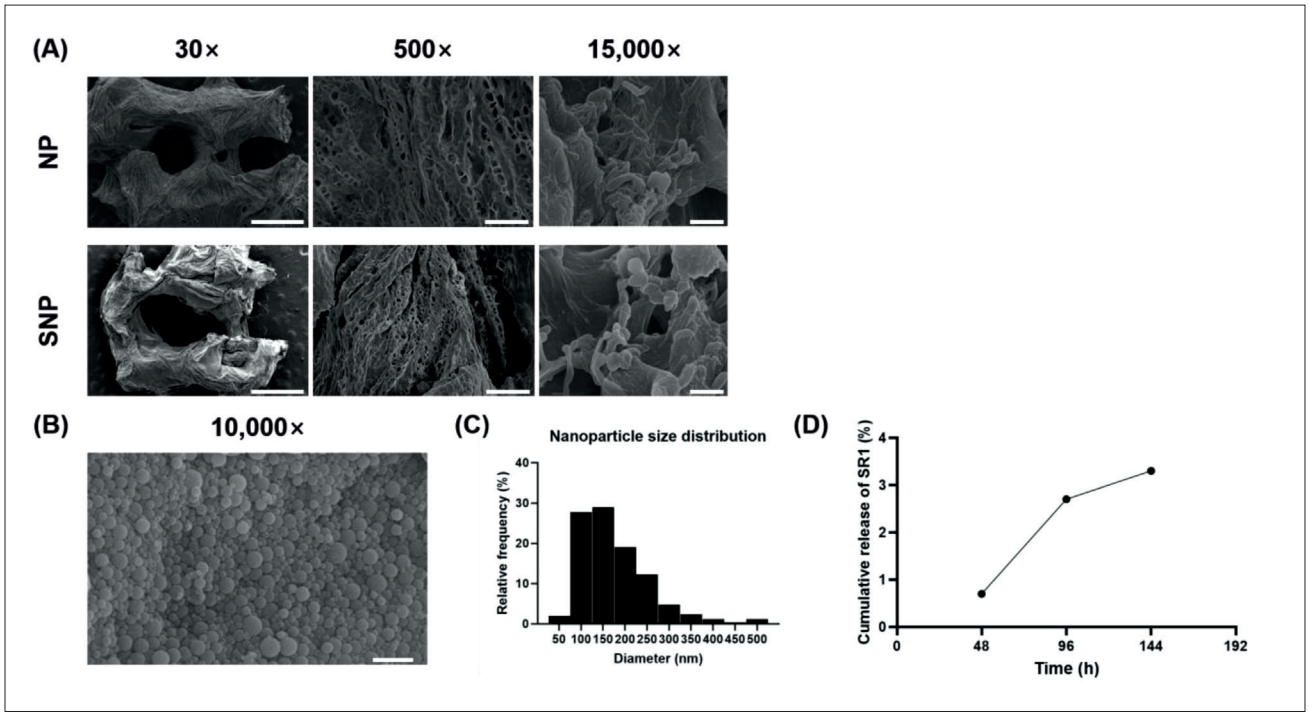


Figure 3. (A) Scanning electron microscopy (SEM) images of collagen scaffold. The 30× image visualizes the morphology of the scaffold. The 500× image reveals the porous structure of the scaffold, and the 15,000× image revealed the detailed structure inside the pores. Scale bars = 1.0 mm, 50 μm, and 1.5 μm for the 30×, 500×, and 15,000× magnified images, respectively. (B) A 10,000× SEM image of nanoparticles. Scale bar = 1 μm. (C) Nanoparticle size distribution. The average size is 189.34 ± 99.23 nm. Data are expressed as mean ± standard deviation. (D) Cumulative release of StemRegenin-1 (SR1) in nanoparticles analyzed by liquid chromatography-mass spectrometry (LC-MS). Abbreviations: NP, blank nanoparticle; SNP, SR1 nanoparticle.

expression in the newly regenerated bone areas (Figure 5D and E), which were confirmed using the MT-stained slides (Figure 5B). On the other hand, the quantitative indices of CD31-positive and α-SMA-positive sections are shown in Figure 5F and G. Expression levels of CD31 and α-SMA exhibited no significant difference between the CT and NP@Sc groups. However, the SNP@Sc group displayed significantly higher expression levels of CD31, with values of 1.06 ± 0.18% at 2 weeks and 2.04 ± 0.36% at 4 weeks after implantation, in contrast to the rather low values observed in the CT group (0.07 ± 0.07% at 2 weeks and 0.05 ± 0.03% at 4 weeks) and NP@Sc group (0.07 ± 0.03% at 2 weeks and 0.10 ± 0.06% at 4 weeks) ($p < 0.0001$). A similar trend was observed for α-SMA expression, with the SNP@Sc group showing significantly higher levels (0.83 ± 0.26% at 2 weeks and 1.08 ± 0.12% at 4 weeks) than the CT group (0.33 ± 0.27% at 2 weeks and 0.53 ± 0.08% at 4 weeks) and NP@Sc group (0.23 ± 0.15% at 2 weeks and 0.40 ± 0.31% at 4 weeks) ($p < 0.05$ when compared to CT; $p < 0.01$ when compared to NP@Sc).

These findings underscore the potent pro-angiogenic effects of SR1, particularly when delivered via the SNP@Sc scaffold. The significant upregulation of CD31 and α-SMA expression highlights the enhanced formation of blood vessels within the SNP@Sc group compared to other groups. This outcome supports our earlier observations on increased bone regeneration and reinforces the pivotal role of SR1 in promoting vascularization in the rat calvarial defects.

3.4.4. Evaluation of angiogenesis

Images were obtained using the MCT system after cardiac perfusion with a Microfil compound to observe the vasculature at the defect site. The defect site and cranial vessels are shown in Figure 6A. More capillaries were observed in the SNP@Sc group than in the other groups. However, no significant difference in the number of vessels formed was observed between the CT and NP@Sc groups. Quantitative analysis was performed using MCT images for all groups (Figure 6B). The vascular volume/total volume (percentage area) (VV/TV%) was analyzed, giving values of 15.94 ± 4.62%, 19.05 ± 2.64%, and 32.67 ± 6.51% for the CT, NP@Sc, and SNP@Sc groups at 4 weeks after implantation, respectively. A significantly higher volume of the vascular network was observed in the SNP@Sc group than in other groups ($p < 0.01$ when compared to CT; $p < 0.05$ when compared to NP@Sc).

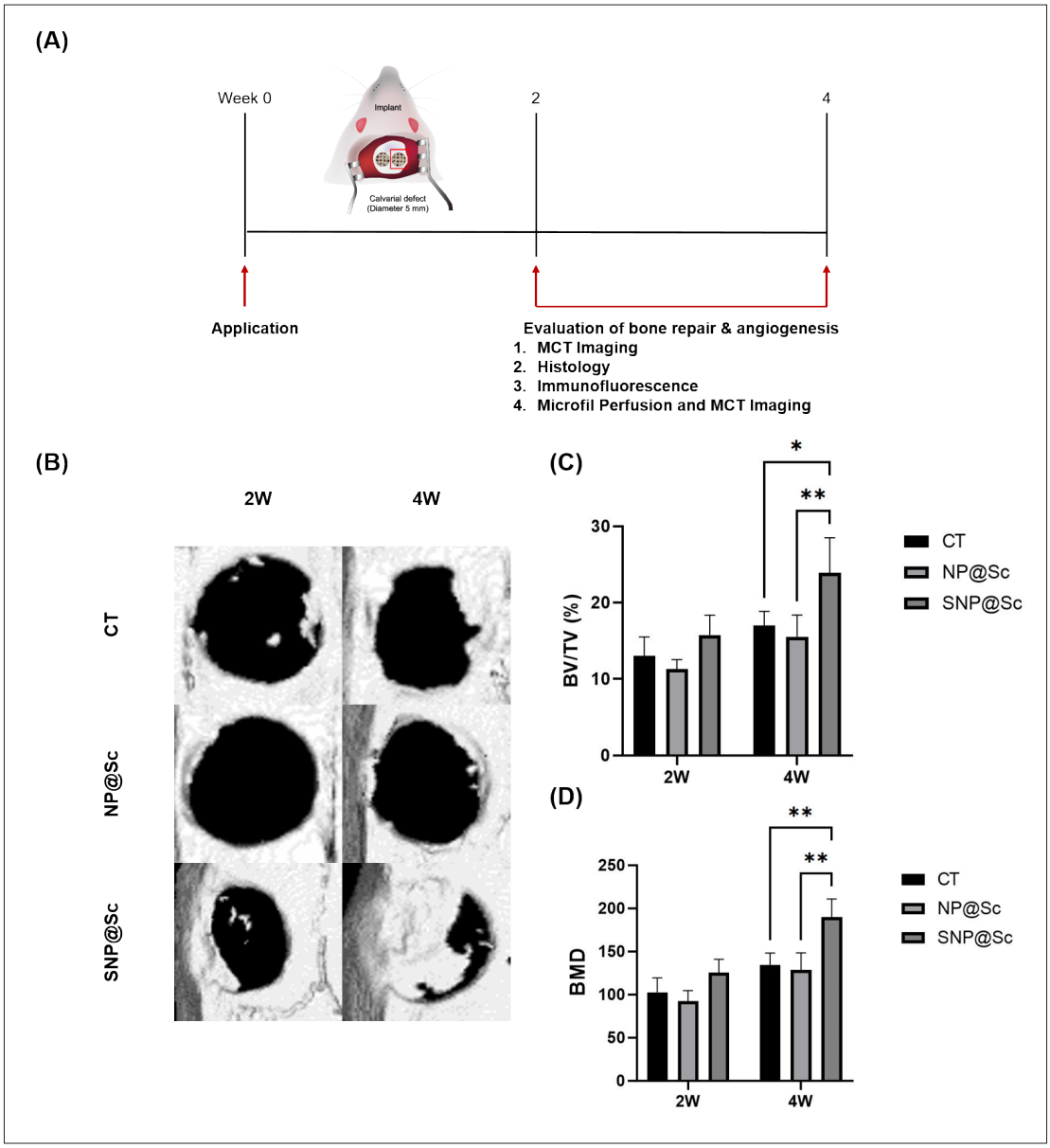


Figure 4. (A) Outline of the *in vivo* experiments. Three groups were analyzed with the following experiments for bone regeneration and angiogenesis: micro-computerized tomography (MCT) imaging, histology, immunofluorescence, and MCT imaging after cardiac perfusion with Microfil compound. Twenty-eight rats were used to conduct animal experiments. (B–D) MCT images and quantitative evaluation index 2 and 4 weeks after implantation. The values are expressed as mean ± standard deviation and analyzed using ordinary two-way ANOVA. Differences between the groups were analyzed using Sidak's multiple comparisons test, and significance levels were set at $*p < 0.05$ and $**p < 0.01$. Abbreviations: BV/TV%, bone volume fraction; BMD, bone mineral density; CT, negative control; NP@Sc, blank nanoparticle-encapsulated scaffold; SNP@Sc, SR1-laden nanoparticle-encapsulated scaffold.

Our vasculature analysis strongly suggests that SR1 treatment, delivered via the SNP@Sc scaffolds, substantially enhances neovascularization within rat calvarial defects. These findings align with our previous results, which showcased that SR1 treatment increased bone regeneration, reinforcing its critical role in promoting angiogenesis in these defects.

4. Discussion

Without blood supply by newly formed blood vessels, the repair and reconstruction for extensive bone loss prove to be a challenging endeavor.[7] Studies have shown that $CD34^+$ cells are responsible for vasculogenesis, and expansion of $CD34^+$ cell population can enhance angiogenesis and therefore bone regeneration.[11,35] As SR1 has been shown to

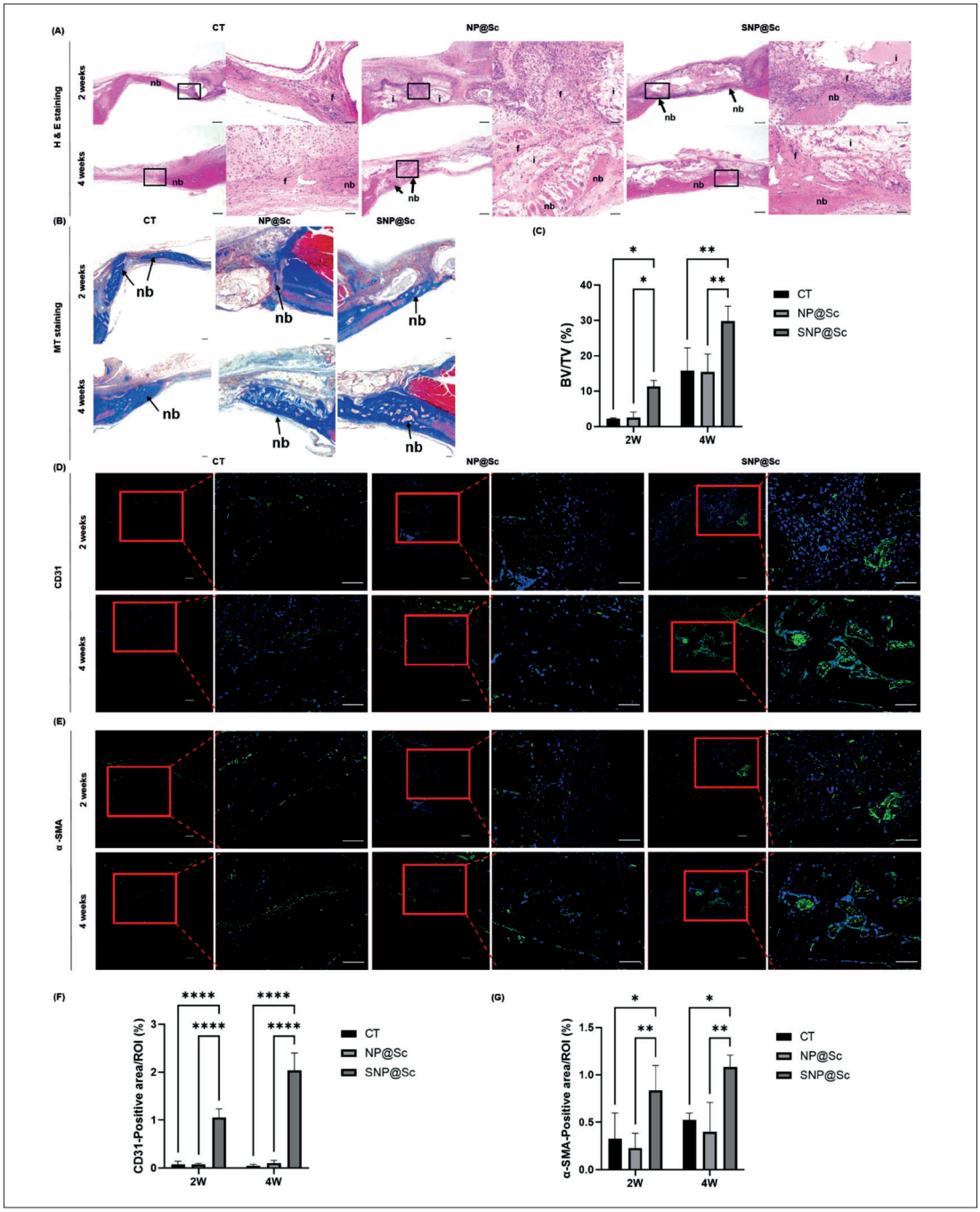


Figure 5. (A) Histological features of the cranial defective areas, stained by hematoxylin–eosin, 2 and 4 weeks after the implantation. The rectangles in the left figures correspond to the magnified areas in the right figures (nb = newly formed bone tissue; f = fibroblastic connective tissue; I = implanted material). Scale bars = 250 μm for left figures and 50 μm for right figures. (B) New bone formation (nb) in the defective areas of cranial bones, stained by Masson's trichrome, 2 and 4 weeks after the implantation. Scale bar = 100 μm. (C) Percentage of new bone to the total defective area. The values are expressed as mean ± standard deviation and analyzed using two-way ANOVA. Differences between the groups were analyzed using Sidak's multiple comparisons test. (D–G) Immunofluorescence analysis of the defective areas of cranial bones 2 and 4 weeks after implantation to assess the expression of vascular markers. Immunofluorescence staining of (D) CD31 (green) and (E) α-SMA (green). The nuclei were counterstained with 4',6-dianidino-2-phenylindole. Scale bar = 100 μm. (F–G) Quantitative analysis of (D) CD31 and (E) α-smooth muscle actin (α-SMA). All data are presented as mean ± standard deviation of the percentage of positively stained areas from the region of interest (%ROI), and analyzed using two-way ANOVA. Differences between the groups were analyzed by (F) Sidak's multiple comparisons test and (G) Dunnett's multiple comparisons test. Significance levels were set at $^{*}p < 0.05$, $^{**}p < 0.01$, and $^{****}p < 0.0001$. Abbreviations: BV/TV%, bone volume fraction; CT, negative control; NP@Sc, blank nanoparticle-encapsulated scaffold; SNP@Sc, SR1-laden nanoparticle-encapsulated scaffold.

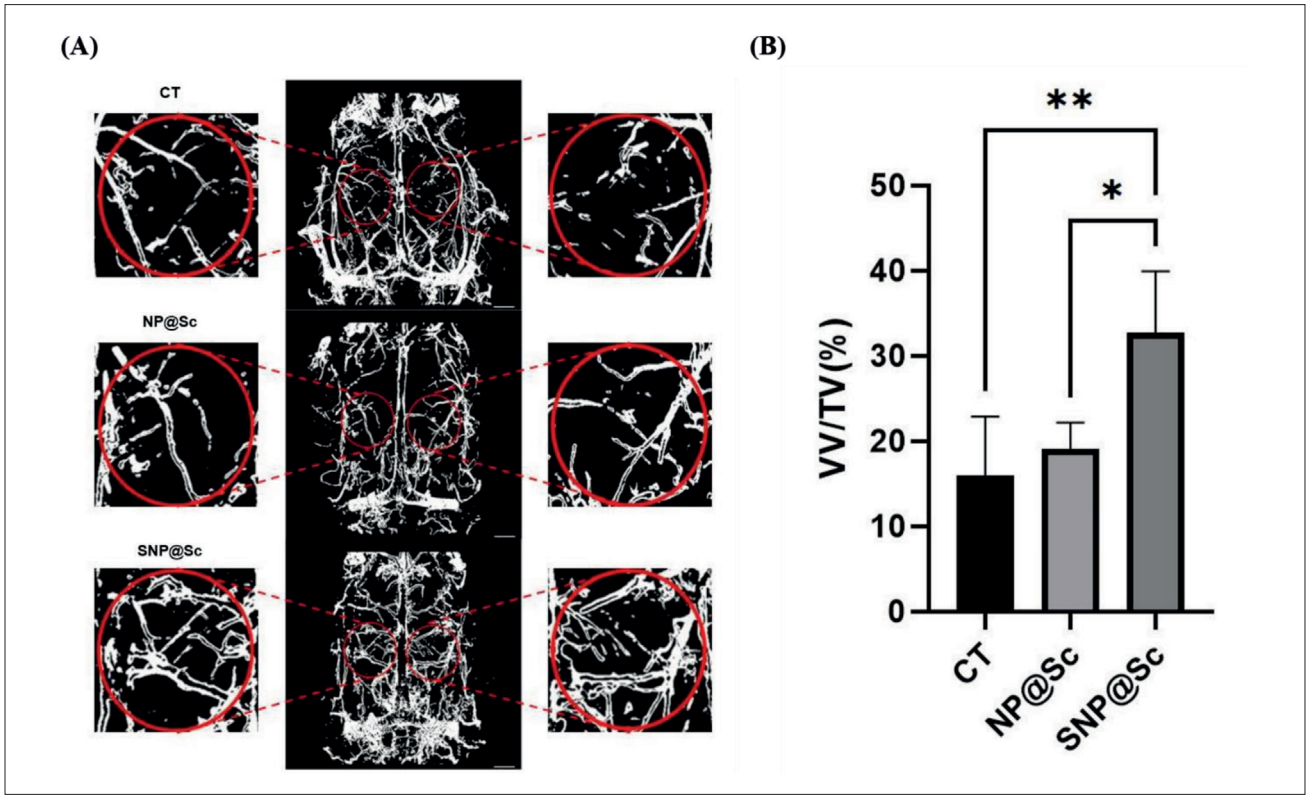


Figure 6. (A) Images showing the vascular network of the whole rat calvaria and their interior using micro-computerized tomography and Microfil perfusion at 4 weeks postoperatively. (B) Vascular volume/total volume (percentage area) (VV/TV [%]) was analyzed among three groups. Expressed as mean ± standard deviation, the data were analyzed using ordinary one-way ANOVA. Differences between the groups were analyzed using Tukey's multiple comparisons test, and significance levels were set at $*p < 0.05$ and $**p < 0.01$. Scale bar = 2.0 mm. Abbreviations: CT, negative control; NP@Sc, blank nanoparticle-encapsulated scaffold; SNP@Sc, SR1-laden nanoparticle-encapsulated scaffold.

expand $CD34^+$ hematopoietic progenitors, the aim of this study was to determine whether the sustained and topical release of SR1 could improve angiogenesis and bone regeneration *in vivo*.

The present study investigated the efficacy of SR1, an AhR inhibitor that expands $CD34^+$ cell populations. We encapsulated SR1 within MSNs, which were then incorporated into a 3D-printed scaffold used to promote angiogenesis and bone regeneration in a rat model of critical-sized bone defect. In this study, 3D scaffolds were produced using a core-shell printing system with a coaxial nozzle. This technique has been used to combine collagen and nanoparticles with different mechanical properties.[36,37] This system also allows the simultaneous extrusion of collagen and nanoparticles, with the former as the shell while the latter the core, a design that enables the incorporation of nanoparticles in the scaffolds.[38] This core-shell printing method helps with the topical release of SR1 by avoiding loss of nanoparticles from the scaffold. SEM imaging validated the structure of scaffold, while cumulative release analysis confirmed sustained release capability of SR1. Despite the evidence for sustained release, further examination on different SR1 concentrations is warranted in future.

The cumulative release of SR1-laden nanoparticles was meticulously analyzed using the LC-MS system, with samples carefully filtered and centrifuged to confirm the removal of the nanoparticles. As shown in Figure 3D, the release profile exhibited an intriguing trend over the course of 6 days. Notably, the release tendency displayed an acceleration as time elapsed, demonstrating the controlled and gradual nature of the release process. Of significant importance, the percentage of SR1 released from the nanoparticles on day 6 was observed to be only 4%. This finding underscores the unique sustained-release capability of the encapsulated nanoparticles, which allows for controlled and prolonged delivery of the therapeutic agent. The low release percentage at this time point aligns with the observed increase in the regenerated bone area at 4 weeks after implantation, suggesting a correlation between sustained SR1 release and enhanced bone healing. Taken together, the drug release experiment, coupled with the MCT results, sheds

light on the controlled and sustained release of SR1 from the nanoparticles. This dynamic release profile, in conjunction with the observed bone regeneration outcomes, presents promising avenues for advancing our understanding of the therapeutic potential of SR1 in promoting effective bone healing.

In vitro studies revealed significant insights into the mechanisms underlying the observed outcomes. Flow cytometry analysis demonstrated that SR1 treatment led to a higher percentage of $CD34^+$ cells, particularly in the SNP groups, accompanied by notable increases in expression of c-kit, CXCR4, VEGFR2, and VE-cadherin—the representative markers of EPCs. CD34 is a transmembrane phosphoglycoprotein that is widely known as a marker of hematopoietic stem cells and progenitor cells. Additionally, CD34 is a known marker of many other cell types, including mesenchymal stromal cells, epithelial progenitors, and vascular endothelial progenitors.[39] According to a previous study showing that SR1 enhances $CD34^+$ cell expansion.[40] $CD34^+$ cell populations in the three groups of EPCs were evaluated using flow cytometry. Furthermore, angiogenic biomarkers were double-labeled with CD34 and analyzed by means of flow cytometry analysis, which used CD117 (also known as c-kit; stem cell growth factor receptor) for stemness, VEGFR2 (KDR) for evaluating endothelial maturity,[41,42] CD184 (also known as homing receptor chemokine C-X-C receptor-4, CXCR4) for migration ability,[43] and CD144 (also known as VE-cadherin) for vascular epithelia (i.e., nascent blood vessels) forming ability.[44] Additionally, two cell proliferation assays (CCK-8 and EdU assays) and wound healing assays were conducted to evaluate the effect of SR1 on EPCs (Figure 1A, C, and D). To summarize the *in vitro* results, we concluded that SR1 may upregulate the functional abilities of EPCs and maybe effective in expanding the $CD34^+$ population in EPCs.

In the current study, the sustained release of SR1 in rat calvarial defects was successful. However, there was no statistically significant difference between the groups at 2 weeks after the operation in MCT data (Figure 4B–D). The reason for this result can be found in the histological analysis data; semi-quantitative scoring evaluation of cell type and tissue response in the cranial defective area 2 and 4 weeks after implantation was conducted according to the International Organization for Standardization 10993-6 for local biological effects (**Table S1** in Supplementary File). Regarding the features of the cranial defective area 2 weeks after implantation (Figure 5A), heavy infiltration of inflammatory cells, mainly composed of macrophages, multinucleated giant cells, and lymphocytes, occurred in the scaffold-implanted groups (NP@Sc and SNP@Sc) with fibroblastic connective tissue surrounding the implanted material. In contrast, the infiltration of inflammatory cells was decreased in every experimental group 4 weeks after implantation. Inflammation is a typical response at the injury site and a necessary process in wound healing. Regardless of the location and type of injury, the series of inflammation, regeneration, and remodeling occurs in the process of bone tissue regeneration.[45] In the current study, the acute inflammatory response after surgery was completed in 7 days and peaked within 24 h.[46] However, the infiltration of inflammatory cells, which was observed in the NP@Sc and SNP@Sc groups 2 weeks after implantation, appeared to have been triggered by the implanted materials. Prolonged inflammation after an acute inflammatory response delayed bone healing 2 weeks after implantation in the scaffold-implanted groups.[47] Finally, the timely termination of inflammation accelerated bone regeneration, and the percentage of the area of newly formed bone in the SNP@Sc group was significantly higher than that of the other groups 4 weeks after the operation.

In general, proliferation of ECs and fibroblasts induces angiogenesis. Furthermore, CD31 and α-SMA are widely known markers of ECs and pericytes or smooth muscle cells, respectively, which are the constituent cells in the mature blood vessels. Thus, vessels can be distinguished with immunofluorescence staining of anti-CD31 and anti-α-SMA antibodies, through which $CD31^+$ and $\alpha\text{-SMA}^+$ indicate mature blood vessels, while $CD31^+$ and $\alpha\text{-SMA}^-$ indicate immature ones.[48]

The current *in vivo* studies showed that SR1 is effective in bone regeneration and angiogenesis 4 weeks after surgery. Therefore, MCT scanning after Microfil compound perfusion was conducted to visualize the vascular network with a special focus on that time period. Immunofluorescence staining revealed that SR1 contributed to the formation of both immature and mature blood vessels, suggesting its potential to enhance angiogenesis. The Microfil compound perfusion experiment reinforced this notion, highlighting the capacity of SR1 to enhance angiogenesis in both defect sites and surrounding areas.

While this study presents promising outcomes regarding the beneficial impact of SR1 on bone regeneration and angiogenesis, further research encompassing a wider range of released SR1 concentrations is necessary. This is instrumental for optimizing the release method and for ensuring the long-term treatment implications from the eventual clinical application of sustained SR1 release.

5. Conclusion

Through the sustained release of SR1, 3D-printed scaffolds successfully promoted angiogenesis and bone regeneration. *In vitro* studies showed that SR1-loaded MSNs released SR1 sustainably, which led not only to the expansion of $CD34^+$ cell populations, but also promoted the migration and angiogenic differentiation of ECs. In animal studies, sustained topical release of SR1 increased vasculogenesis at the defect site. With an increased blood supply through the regenerated vessels, spontaneous bone healing could be promoted. Overall, SR1 loaded in 3D-printed bone scaffolds can promote angiogenesis *in vivo*.

Acknowledgments

None.

Funding

This work was supported by a grant from the National Research Foundation (NRF2020R1A2C2101297 and 2022R1A5A2027161) funded by the Korean government, the Korea Medical Device Development Fund grant funded by the Korea government (the Ministry of Science and ICT, the Ministry of Trade, Industry and Energy, the Ministry of Health & Welfare, the Ministry of Food and Drug Safety) (Project number: 1711179402, RS-2022-00140622), and South Korean Ministry of Trade, Industry, and Energy via the 2021 Outstanding Company Research Center Promotion Project (ATC+).

Conflict of interest

The authors declare no conflicts of interest.

Author contributions

Conceptualization: KyeongWoong Yang, Sang-Mo Kwon, SangHyun An

Formal analysis: KyeongWoong Yang, Eun Ji Lee, Donggu Kang, KyeongHyeon Lee

Investigation: KyeongWoong Yang, Kyoung Ho Lee, Woong Bi Jang

Methodology: KyeongWoong Yang, Donghyun Lee, Hye Ji Lim, Sang-Cheol Han, Yong-Il Shin

Writing – original draft: KyeongWoong Yang

Writing – review & editing: Hojun Jeon, Gi Hoon Yang

Ethics approval and consent to participate

Animal experiments were approved by the local animal ethics committee (approval number: KMEDI-22080801-01).

Consent for publication

Not applicable.

Availability of data

Data used in this work are available from the corresponding author upon reasonable request.

References

1. Roberts TT, Rosenbaum AJ. Bone grafts, bone substitutes and orthobiologics: the bridge between basic science and clinical advancements in fracture healing. *Organogenesis*. 2012;8(4):114-124.
doi: 10.4161/org.23306

2. Zhang L, Yang G, Johnson BN, Jia X. Three-dimensional (3D) printed scaffold and material selection for bone repair. *Acta Biomater*. 2019;84:16-33.
doi: 10.1016/j.actbio.2018.11.039

3. Wang H, Su K, Su L, Liang P, Ji P, Wang C. The effect of 3D-printed Ti(6)Al(4)V scaffolds with various macropore structures on osteointegration and osteogenesis: a biomechanical evaluation. *J Mech Behav Biomed Mater*. 2018;88:488-496.
doi: 10.1016/j.jmbbm.2018.08.049

4. Pei X, Ma L, Zhang B, et al. Creating hierarchical porosity hydroxyapatite scaffolds with osteoinduction by three-dimensional printing and microwave sintering. *Biofabrication*. 2017;9(4):045008.
doi: 10.1088/1758-5090/aa90ed

5. Dadhich P, Das B, Pal P, et al. A simple approach for an eggshell-based 3D-printed osteoinductive multiphasic calcium phosphate scaffold. *ACS Appl Mater Interfaces*. 2016;8(19):11910-11924.
doi: 10.1021/acsami.5b11981

6. Raisian S, Fallahi HR, Khiabani KS, Heidarizadeh M, Azdoo S. Customized titanium mesh based on the 3D printed model vs. manual intraoperative bending of titanium mesh for reconstructing of orbital bone fracture: a randomized clinical trial. *Rev Recent Clin Trials*. 2017;12(3):154-158.
doi: 10.2174/1574887112666170821165206

7. Kuttappan S, Mathew D, Jo JI, et al. Dual release of growth factor from nanocomposite fibrous scaffold promotes vascularisation and bone regeneration in rat critical sized calvarial defect. *Acta Biomater*. 2018;78:36-47.
doi: 10.1016/j.actbio.2018.07.050

8. Rouwkema J, Rivron NC, van Blitterswijk CA. Vascularization in tissue engineering. *Trends Biotechonol*. 2008;26(8):434-441.
doi: 10.1016/j.tibtech.2008.04.009

9. Urbich C, Dimmeler S. Endothelial progenitor cells: characterization and role in vacular biology. *Circ Res*. 2004;95(4):343-353.
doi: 10.1161/01.RES.0000137877.89448.78

10. Asahara T, Murohara T, Sullivan A, et al. Isolation of putative progenitor endothelial cells for angiogenesis. *Science*. 1997;275(5302):964-967.
doi: 10.1126/science.275.5302.964

11. Hertweck J, Ritz U, Götz H, Schottel PC, Rommens PM, Hofmann A. CD34(+) cells seeded in collagen scaffolds promote bone formation in a mouse calvarial defect model. *J Biomed Mater Res B Appl Biomater*. 2018;106(4):1505-1516. doi: 10.1002/jbm.b.33956

12. Kawamoto A, Iwasaki H, Kusano K, et al. CD34-positive cells exhibit increased potency and safety for therapeutic neovascularization after myocardial infarction compared with total mononuclear cells. *Circulation*. 2018;114(20): 2163-2169. doi: 10.1161/CIRCULATIONAHA.106.644518

13. Musialek P, Tekieli L, Kostkiewicz M, et al. Randomized transcoronary delivery of CD34(+) cells with perfusion versus stop-flow method in patients with recent myocardial infarction: early cardiac retention of (9)(9)(m)Tc-labeled cells activity. *J Nucl Cardiol*. 2011;18(1):104-116. doi: 10.1007/s12350-010-9326-z

14. Pasquet S, Sovalat H, Hénon P, et al. Long-term benefit of intracardiac delivery of autologous granulocyte-colony-stimulating factor-mobilized blood CD34+ cells containing cardiac progenitors on regional heart structure and function after myocardial infarct. *Cytotherapy*. 2009;11(8): 1002-1015. doi: 10.3109/14653240903164963

15. Sivan-Loukianova E, Awad OA, Stepanovic V, Bickenbach J, Schatteman GC. CD34+ blood cells accelerate vascularization and healing of diabetic mouse skin wounds. *J Vasc Res*. 2003;40(4):368-377. doi: 10.1159/000072701

16. O E, Lee BH, Ahn HY, et al. Efficient nanadhesive *ex vivo* expansion of early endothelial progenitor cells derived from CD34+ human cord blood fraction for effective therapeutic vascularization. *FASEB J*. 2011;25(1):159-169. doi: 10.1096/fj.10-162040

17. Mifune Y, Matsumoto T, Kawamoto A, et al. Local delivery of granulocyte colony stimulating factor-mobilized CD34-positive progenitor cells using bioscaffold for modality of unhealing bone fracture. *Stem Cells*. 2008;26(6):1395-1405. doi: 10.1634/stemcells.2007-0820

18. Matsumoto T, Kawamoto A, Kuroda R, et al. Therapeutic potential of vasculagenesis and osteogenesis promoted by peripheral blood CD34-positive cells for functional bone healing. *Am J Pathol*. 2006;169(4):1440-1457. doi: 10.2353/ajpath.2006.060064

19. Boitano AE, Wang J, Romeo R, et al. Aryl hydrocarbon receptor antagonists promote the expansion of human hematopoietic stem cells. *Science*. 2010;329(5997):1345-1348. doi: 10.1126/science.1191536

20. Wagner JE Jr, Brunstein CG, Boitano AE, et al. Phase I/II trial of StemRegenin-1 expanded umbilical cord blood hematopoietic stem cells supports testing as a stand-alone graft. *Cell Stem Cell*. 2016;18(1):144-155. doi: 10.1016/j.stem.2015.10.004

21. Smith KJ, Murray IA, Tanos R, et al. Identification of a high-affinity ligand that exhibits complete aryl hydrocarbon receptor antagonism. *J Pharmacol Exp Ther*. 2011;338(1):318-327. doi: 10.1124/jpet.110.178392

22. Cao L, Mooney DJ. Spatiotemporal control over growth factor signaling for therapeutic neovascularization. *Adv Drug Deliv Rev*. 2007;59(13):1340-1350. doi: 10.1016/j.addr.2007.08.012

23. Fahimipour F, Rasoulianboroujeni M, Dashtimoghadam E, et al. 3D printed TCP-based scaffold incorporating VEGF-loaded PLGA microspheres for craniofacial tissue engineering. *Dent Mater*. 2017;33(11):1205-1216. doi: 10.1016/j.dental.2017.06.016

24. Matassi F, Nistri L, Chicon Paez D, Innocenti M. New biomaterials for bone regeneration. *Clin Cases Miner Bone Metab*. 2011;8(1):21-24.

25. Jafari M, Paknejad Z, Rad MR, et al. Polymeric scaffolds in tissue engineering: a literature review. *J Biomed Mater Res B Appl Biomater*. 2017;105(2):431-459. doi: 10.1002/jbm.b.33547

26. Kim SC, Heo SY, Oh GW, Yi M, Jung W-K. A 3D-printed polycaprolactone/marine collagen scaffold reinforced with carbonated hydroxyapatite from fish bones for bone regeneration. *Mar Drugs*. 2022;20(6):344. doi: 10.3390/md20060344

27. Murphy CM, Haugh MG, O'Brien FJ. The effect of mean pore size on cell attachment, proliferation and migration in collagen-glycosaminoglycan scaffolds for bone tissue engineering. *Biomaterials*. 2010;31(3):461-466. doi: 10.1016/j.biomaterials.2009.09.063

28. Momot KI. Hydrated collagen: where physical chemistry, medical imaging, and bioengineering meet. *J Phys Chem B*. 2022;126(49):10305-10316. doi: 10.1021/acs.jpcb.2c06217

29. Lim HJ, Jang WB, Rethineswaran VK, et al. StemRegenin-1 attenuates endothelial progenitor cell senescence by regulating the AhR pathway-mediated CYP1A1 and ROS generation. *Cells*. 2023;12(15):2005. doi: 10.3390/cells12152005

30. Kang D, Lee YB, Yang GH, et al. FeS(2)-incorporated 3D PCL scaffold improves new bone formation and neovascularization in a rat calvarial defect model. *Int J Bioprint*. 2023;9(1):636. doi: 10.18063/ijb.v9i1.636

31. Jang MJ, Bae SK, Jung YS, et al. Enhanced wound healing using a 3D printed VEGF-mimicking peptide incorporated hydrogel patch in a pig model. *Biomed Mater*. 2021;16(4). doi: 10.1088/1748-605X/abf1a8

32. Gurcan MN, Boucheron LE, Can A, Madabhushi A, Rajpoot NM, Yener B. Histopathological image analysis: a review. *IEEE Rev Biomed Eng*. 2009;2:147-171. doi: 10.1109/RBME.2009.2034865

33. Gavet O, Pines J. Progressive activation of CyclinB1-Cdk1 coordinates entry to mitosis. *Dev Cell*. 2010;18(4): 533-543.
doi: 10.1016/j.devcel.2010.02.013

34. Bancroft JD, Gamble M. *Theory and Practice of Histological Techniques*. 6th ed. Churchill Livingstone; 2008:105-134.

35. Hankenson KD, Dishowitz M, Gray C, Schenker M. Angiogenesis in bone regeneration. *Injury*. 2011;42(6): 556-561.
doi: 10.1016/j.injury.2011.03.035

36. Kim JH, Park M, Shim JH, Yun W-S, Jin S. Multi-scale vascularization strategy for 3D-bioprinted tissue using coaxial core-shell pre-set extrusion bioprinting and biochemical factors. *Int J Bioprint*. 2023;9(4):726.
doi: 10.18063/ijb.726

37. Nasehi F, Karshenas M, Nardi S, Barati G, Salim A. Core-shell fibrous scaffold as a vehicle for sustained release of retinal pigmented epithelium-derived factor (PEDF) for photoreceptor differentiation of conjunctiva mesenchymal stem cells. *J Biomed Mater Res A*. 2017;105(12): 3514-3519.
doi: 10.1002/jbm.a.36182

38. Milojević M, Vihar B, Banović L, et al. Core/shell printing scaffolds for tissue engineering of tubular structures. *J Vix Exp*. 2019;(151).
doi: 10.3791/59951

39. Hassanpour M, Salybekov AA, Kobayashi S, Asahara T. CD34 positive cells as endothelial progenitor cells in biology and medicine. *Front Cell Dev Biol*. 2023;11:1128134.
doi: 10.3389/fcell.2023.1128134

40. Singh J, Chen ELY, Xing Y, Stefanski HE, Blazar BR, Zúñiga-Pflücker JC. Generation and function of progenitor T cells from StemRegenin-1-expanded CD34+ human hematopoietic progenitor cells. *Blood Adv*. 2019;3(20):2934-2948.
doi: 10.1182/bloodadvances.2018026575

41. Rakkar K, Othman OA, Sprigg N, Bath PM, Bayraktutan U. Evaluation of endothelial progenitor cell characteristics as clinical biomarkers for elderly patients with ischaemic stroke. *Stem Cell Rev Rep*. 2023;19(6):1856-1869.
doi: 10.1007/s12015-023-10544-y

42. Kamata S, Miyagawa S, Fukushima S, et al. Improvement of cardiac stem cell sheet therapy for chronic ischemic injury by adding endothelial progenitor cell transplantation: analysis of layer-specific regional cardiac function. *Cell Transplant*. 2014;23(10):1305-1319.
doi: 10.3727/096368913X665602

43. Wang X, Cooper S, Broxmeyer HE, Kapur R. Transient regulation of RNA methylation in human hematopoietic stem cells promotes their homing and engraftment. *Leukemia*. 2023;37(2):453-464.
doi: 10.1038/s41375-022-01761-4

44. Lewalle JM, Bajou K, Desreux J, et al. Alteration of interendothelial adherens junctions following tumor cell-endothelial cell interaction in vitro. *Exp Cell Res*. 1997;237(2):347-356.
doi: 10.1006/excr.1997.3799

45. Newman H, Shih YV, Varghese S. Resolution of inflammation in bone regeneration: from understandings to therapeutic applications. *Biomaterials*. 2021;277:121114.
doi: 10.1016/j.biomaterials.2021.121114

46. Marsell R, Einhorn TA. The biology of fracture healing. *Injury*. 2011;42(6):551-555.
doi: 10.1016/j.injury.2011.03.031

47. Schmidt-Bleek K, Schell H, Lienau J, et al. Initial immune reaction and angiogenesis in bone healing. *J Tissue Eng Regen Med*. 2014;8(2):120-130.
doi: 10.1002/term.1505

48. Usuda K, Iwai S, Funasaki A, et al. Expression and prognostic impact of VEGF, CD31 and alphaSMA in resected primary lung cancers. *Anticancer Res*. 2018;38(7):4057-4063.
doi: 10.21873/anticancers.12695

ACCSCIENCE PUBLISHING

International Journal of Bioprinting

RESEARCH ARTICLE

Design and optimization of 3D-bioprinted cell-laden scaffolds in dynamic culture

Jing Li[1†], Feng Chen[1†], Meixia Wang[2], Xiaolong Zhu[1], Ning He[1], Na Li[3], Haotian Zhu[1], and Xiaoxiao Han[1*]

[1]National Engineering Research Centre for High Efficiency Grinding, Hunan University, Changsha, Hunan, China

[2]Department of Pharmacy, College of Biology, Hunan University, Changsha, Hunan, China

[3]Radiology Department, The Third Xiangya Hospital of Central South University, Changsha, Hunan, China

(This article belongs to the *Special Issue: Special Issue of International Journal of Bioprinting in the BDMC 2023 Conference*)

Abstract

Light-based 3D printing enables the fabrication of biological scaffolds with high precision, versatility and biocompatibility, particularly the cell-laden scaffolds with architecturally complex geometric features. However, many bioprinted tissue scaffolds suffer from low cell viability due to insufficient oxygen and nutrient supply, which is heavily influenced by scaffold structure and cultivation conditions. Current practice relies mainly on resource-intensive trial-and-error methods to optimize scaffolds' structures and cultivation parameters. In this study, we developed a comprehensive multi-physics model integrating fluid dynamics, oxygen mass transfer, cell oxygen consumption, and cell growth processes to capture cell growth behaviors in scaffolds, establishing a robust theoretical foundation for scaffold structure optimization. The modeling results showed that a large number of parameters, such as system inlet flow rate, geometric feature size, cell parameters, and material properties, significantly impact oxygen concentration and cell growth within the scaffold. A two-step optimization strategy is proposed in this paper and was applied to obtain optimal geometric parameters of channeled scaffolds to demonstrate the model's effectiveness for scaffold optimization. The model can be employed for scaffolds with arbitrary shapes and various materials, facilitating the optimal design of sophisticated scaffolds for more advanced tissue engineering.

Keywords: Multi-physics model; Cell-laden scaffolds; Light-based bioprinting; Dynamic culturing; Scaffold structural design

[†]These authors contributed equally to this work.

***Corresponding author:**
Xiaoxiao Han
(xiaoxiaohan@hnu.edu.cn)

Citation: Li J, Chen F, Wang M, et al. Design and optimization of 3D-bioprinted cell-laden scaffolds in dynamic culture. *Int J Bioprint*. 2024;10(3):1838.
doi: 10.36922/ijb.1838

Received: September 14, 2023
Accepted: November 29, 2023
Published Online: January 25, 2024

Copyright: © 2024 Author(s). This is an Open Access article distributed under the terms of the Creative Commons Attribution License, permitting distribution, and reproduction in any medium, provided the original work is properly cited.

Publisher's Note: AccScience Publishing remains neutral with regard to jurisdictional claims in published maps and institutional affiliations.

1. Introduction

Three-dimensional (3D) bioprinting, also known as cell printing, is an advanced technology that allows the precise assembling of biocompatible materials, cells, or bioactive factors, offering great capability in fabricating artificial constructs with complex features that are necessary to achieve biomimetic morphology and microenvironments, and therefore appropriate biological functions.[1-8] Light-cured 3D printing technology

(such as digital light processing [DLP]) has been widely used in tissue engineering due to its advantages of high precision, rapid printing speed, and biocompatibility, and has been upgraded as a specialized "light-cured bioprinting technology" for biofabrication.[9-11] Significant progress has been made in manufacturing complex organ constructs and tissue scaffolds with biomimetic functions using light-cured bioprinting technology, such as cardiovascular networks, lung systems, and other organ models.[12-15] However, most bioprinted tissue scaffolds and organ models reported to date face several obstacles (such as poor vascularization) that hinder their progress toward clinical application. The *in vitro* biocompatibility and functions of tissue scaffolds and organ models still do not meet expected requirements.[16,17] A fundamental issue is the hypoxia within biofabricated constructs, leading to insufficient cell viability and thus deteriorated biological functions.[18]

Mechanistically, cell growth in scaffolds is a complex multi-physical-biological process involving oxygen diffusion and convection, nutrient consumption, and cell proliferation; each is influenced by a large number of parameters. During *in vitro* cultivation, the effective diffusion length of oxygen in the biocompatible materials is generally within the range of 100 μm to 200 μm; such a short diffusion distance creates significant challenges for cells encapsulated in scaffolds to survive without adequate nutrient channels.[19,20] When the cell density of the engineered structure is high, localized hypoxia can occur, resulting in cellular inactivation and uneven distribution that cause the loss of overall activity and functionality of cells.[21] To enhance the cell activity of scaffolds, perfusion bioreactors are generally employed to facilitate oxygen uptake by means of the fluid convection effect.[22] However, the structural characteristics, material properties, and *ex vivo* cultivation parameters of 3D-printed cell-laden scaffolds with diverse topological structures can significantly impact oxygen mass transfer and subsequently influence cell growth behaviors within the scaffold.[23,24] Changes in initial cell densities in bioinks may disturb the oxygen distribution within scaffolds, resulting in variations in final cell count and density. Nevertheless, a purely trial-and-error approach is considered problematic because it is not only time-consuming and expensive but also challenging to obtain an optimal design of a scaffold.[11]

Mathematical modeling can be adopted not only for investigating underlying oxygen transfer mechanisms in dynamic cultivation processes but also as an efficient tool to optimize the design of the scaffolds for achieving optimal cell viability. Many models,[25-30] particularly mechanistically realistic modeling, have been developed to capture the phenomena observed during the dynamic cultivation process or to predict the spatiotemporal evolution of the physical fields, enabling analysis of oxygen distribution within the scaffold under various physical conditions, prediction of cell growth patterns, guidance for optimizing experimental parameters, and optimization of architectural parameters of scaffolds. Allen and Bhatia[25] developed a two-dimensional (2D) steady-state model to predict oxygen distribution in a biodegradable scaffold with mouse liver cells, which was later expanded by Brown et al.[26] for cultivating cardiac tissue scaffolds *in vitro* and validated through hypoxia experiments. Yu et al.[27] incorporated fluid dynamics into their oxygen distribution model, emphasizing the importance of fluid dynamics on oxygen transport within the scaffold. However, coupling with a cell growth model was absent, and its impact on cell viability was thus not investigated. Mokhtari-Jafari et al.[28] simplified the fluid dynamics model based on the previous steady-state model, which was then successfully coupled with cell growth and oxygen consumption to simulate bone tissue engineering scaffolds. The 2D modeling has limitations for architecturally complex scaffolds that possess strong anisotropy, and 3D modeling is needed for accurate simulation of cell growth and oxygen transport in bioreactors. Coletti et al.[29] simplified the spatial dimensionality by using 2D axisymmetric theory and integrated processes of oxygen mass transfer, cell growth, and oxygen consumption, attempting to achieve multi-physics modeling of cell growth in 3D space. Ioana et al.[30] focused on the control solver for the cell growth model and described spatiotemporal evolution of cell density within 3D polymer scaffolds in perfusion bioreactors. Most scaffold optimization studies have focused on designing microchannels or biomimetic vascular networks.[31-34] Fang et al.[20] optimized the fractal vascular network of a 2D cardiac tissue by coupling the cellular oxygen consumption model with an oxygen distribution model. However, these optimization methods were based mainly on manually adjusting the number of microchannels or the tiers of the vascular network. On the one hand, a comprehensive model able to account for the multi-physical-biological processes of cell growth and the geometric complexity of the scaffold is needed as bioengineering scaffolds or models are becoming increasingly sophisticated due to the emergence of 3D printing.[35-39] On the other hand, further research on linking models with actual bioprinting process parameters and establishing optimization criteria is required to guide the structural design and optimization of bioprinted constructs.

In this paper, we propose a 3D multi-physics coupling modeling system based on the Contois cell growth equations that incorporate oxygen mass transfer, fluid dynamics, and cellular oxygen consumption, in order to

analyze and simulate light-cured 3D-bioprinted scaffolds under dynamic *in vitro* cultivation conditions. The model was validated by comparing the predicted results with those observed in experiments of C2C12 cell culture, demonstrating high capability in modeling cell growth behaviors. Utilizing this multi-physics model, parametric scanning simulations of nutrient flow rate were conducted to determine appropriate wall shear stress levels that promote C2C12 cell growth. Furthermore, the impact of different dynamic parameters, such as inlet flow rate, geometric feature size, and initial cell density, on scaffold-based tissue engineering outcomes was examined. Lastly, based on the modeling system proposed in this study, a two-step optimization strategy is proposed for structural optimization of scaffolds and applied for designing channeled scaffold with maximum cell proliferation. This strategy offers a novel framework for designing and optimizing multi-channel bioprinted scaffolds encapsulated with cells for advanced tissue engineering.

2. Model physics and implementation

2.1. Model assumptions

The multi-physics coupling model for cell growth considers fluid convection, oxygen mass transfer, cellular oxygen consumption, and cell growth involved in the dynamic cultivation process of DLP 3D-printed scaffolds. In practice, the physical processes involved in the entire cultivation process are more complex. To reduce the complexities of the modeling process while maintaining satisfactory prediction results, the following assumptions are made:

- The pores within the scaffold are assumed to be uniformly distributed.
- The entire system is assumed to contain sufficient nutrients, considering only oxygen as the sole substrate for cell metabolism and growth.
- Oxygen molecules are considered to be uniformly dissolved in the nutrient solution at a specific concentration.
- The system environment is maintained at 37°C and 5% carbon dioxide, an optimal condition for cell survival.
- The maximum absorption rate of oxygen by cells linearly increases from zero until a certain time point, where it remains constant.
- The cells within the scaffold experience an initial adhesion phase for the first 3 hours of cultivation, during which their maximum growth rate is zero, followed by linear growth until a certain time point where it remains constant.
- The influence of cell death is not considered in the model.
- The effects of material swelling are ignored.

2.2. Computational domain

In the geometric assembly of the multi-physics model, as shown in Figure 1a, the entire geometric space is divided into two domains: Ω_1 representing the uniform medium flow region of the nutrient solution, and Ω_2 expressing the porous medium flow region of the scaffold. The scaffold structure in the model is a circular block with a diameter of 4 mm and a thickness of 2 mm. The chamber is a hollow cylindrical structure with an inner diameter D_1 of 5 mm and a total length L of 10 mm. The scaffold is placed at the

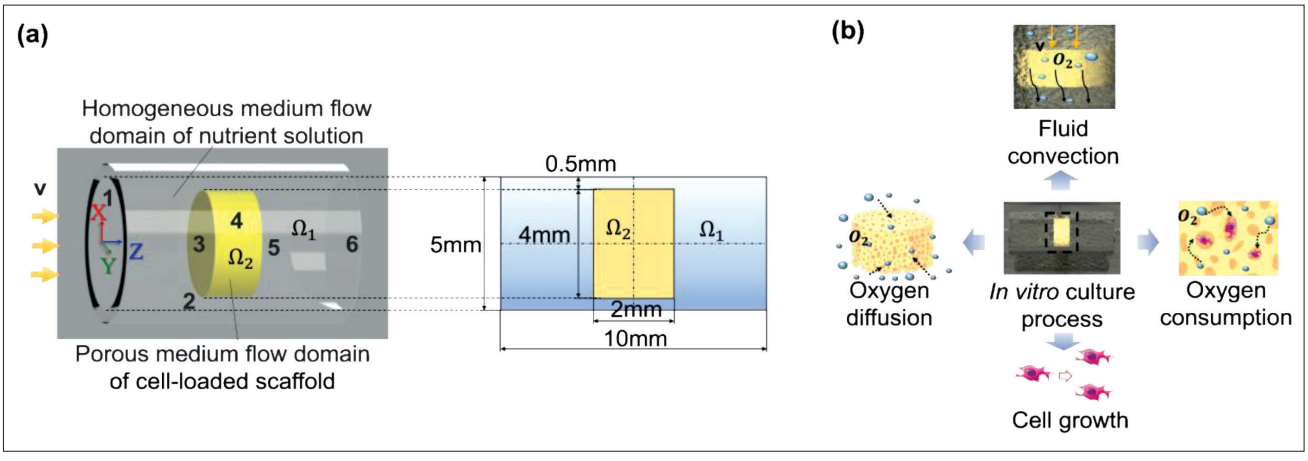


Figure 1. Geometric assembly of the scaffold in dynamic *in vitro* cultivation and physical processes of cell growth to be modeled. (a) Schematic diagram showing the geometry of the computational domain for model simulation. Ω_1 represents the homogeneous medium flow region of the nutrient solution, and Ω_2 is the porous medium flow region of the scaffold. (b) Physical processes incorporated in the model, including fluid convection occurred in domain Ω_1 and Ω_2, oxygen diffusion in the scaffold, oxygen consumption by cells, and cell growth.

chamber's center, with a distance (d) of 0.5 mm from the chamber wall. The fluid flows from left to right, where the center of the inlet boundary 1 is the origin of the geometric coordinate system. Boundary 2 represents the wall boundary of the chamber; boundaries 3 and 5 indicate the bottom contact boundaries between the scaffold and the nutrient solution; boundary 4 expresses the side contact boundary between the scaffold and the nutrient solution; boundary 6 is the fluid outlet boundary.

2.3. Modeling process and model physics

The physical processes considered in the multi-physics model for cell growth in the scaffold are illustrated in Figure 1b, including fluid convection, oxygen diffusion, nutrient consumption, and cell growth. Due to the velocity changes induced by fluid flow, the scaffold experiences fluid-induced oxygen convection. Oxygen dissolved in the nutrient solution undergoes spontaneous diffusion due to concentration gradients. Additionally, cellular absorption and consumption of oxygen occur within the scaffold. Furthermore, the quantity of cells within the scaffold changes in response to variations in oxygen concentration, scaffold porosity, and other parameters. The four processes are coupled to establish the multi-physics model for cell growth in the scaffold under dynamic cultivation conditions.

2.3.1. Fluid dynamics process

The fluid flows into region Ω_1 with the initial velocity v_0, which satisfies the Navier–Stokes equation (Equation 1):

$$\rho \cdot \frac{\partial v_1}{\partial t} + \rho \cdot (v_1 \cdot \nabla) v_1 = -\nabla P + \mu \cdot \nabla^2 v_1 + \rho \cdot g \quad (1)$$

where ρ is the fluid density; v_1 is the flow velocity of the nutrient solution in the chamber; P is the pressure within the fluid; μ is the dynamic viscosity of the fluid, and g is the acceleration due to gravity. The left-hand side of Equation 1 represents the inertial force term, while the right-hand side consists of the pressure term (the first term), the viscous force term (the second term), and the gravity term (the third term). Assuming that the fluid is incompressible, the following equation is used:

$$\frac{\partial \rho}{\partial t} + \nabla \cdot (\rho v) = 0 \quad (2)$$

Both velocity and pressure are functions of time and space, as shown in Equations 3 and 4. ∇ in Equations 1 and 2 represents the Hamiltonian operator, with its specific form given by Equation 5, and ∇^2 is the Laplacian operator, with its specific form given by Equation 6.

$$v_1 = f_1(x, y, z, t) \quad (3)$$

$$P = p(x, y, z, t) \quad (4)$$

$$\nabla f_i = \frac{\partial f_i}{\partial x} + \frac{\partial f_i}{\partial y} + \frac{\partial f_i}{\partial z} \quad (5)$$

$$\nabla f_i = \frac{\partial^2 f_i}{\partial x^2} + \frac{\partial^2 f_i}{\partial y^2} + \frac{\partial^2 f_i}{\partial z^2} \quad (6)$$

The cell-laden scaffold fabricated using DLP-based bioprinting in this study possesses porous characteristics, and the fluid flow within this structure (domain Ω_1) involves complex processes. To describe this process, the Brinkman equation for porous media flow is employed, and it incorporates material properties such as porosity, tortuosity, and permeability. The specific form of the model is given by Equation 7:

$$\rho \cdot \frac{\partial v_B}{\partial t} + \rho \cdot (v_B \cdot \nabla) v_B = -\nabla P - \frac{\mu}{\kappa} \cdot v_B + \mu \cdot \nabla^2 v_B + \rho \cdot g \quad (7)$$

Compared to the Navier–Stokes equation, the Brinkman equation introduces the variable of permeability κ to describe porous media. Additionally, the symbols representing the velocity variables are replaced with their corresponding counterparts, denoted by v_B. The permeability, denoted by κ, is expressed in terms of porosity and tortuosity. The permeability and tortuosity are governed by Equations 8 and 9, respectively.

$$\kappa(t) = \frac{1}{4.26 \times 10^9} \cdot \frac{\varepsilon^3(t)}{\Gamma^2(t)} \quad (8)$$

$$\Gamma(t) = \left(\frac{2 - \varepsilon(t)}{\varepsilon(t)} \right)^2 \quad (9)$$

where Γ represents tortuosity; ε represents porosity. These variables vary with time due to cell growth. To maintain the incompressibility of the fluid within the porous media, it satisfies Equation 10, where v_B is time and space dependent (Equation 11).

$$\frac{\partial \rho}{\partial t} + \nabla \cdot (\rho v_B) = 0 \quad (10)$$

$$v_B = f_2(x, y, z, t) \quad (11)$$

2.3.2. Oxygen transport process

Oxygen serves as the sole substrate for cell growth. As the flow velocity within the system changes, the oxygen transport transitions from a single diffusion to a coupled convection–diffusion process. The oxygen diffusion–convection process in region Ω_1 is governed by Equation 12:

$$\frac{\partial C_1}{\partial t} = \nabla \cdot \left[D \nabla C_1(t) \right] - v_1 \cdot \nabla C_1(t) \tag{12}$$

where C_1 represents the dissolved oxygen concentration in Ω_1, and D indicates the diffusion coefficient of oxygen in the nutrient solution. This equation describes the oxygen concentration changes due to the combined effects of spontaneous oxygen diffusion (the first term on the right-hand side) and convection caused by fluid flow (the second term on the right-hand side). Under different spatial and temporal conditions, C_1 should satisfy the corresponding boundary conditions as in Equation 13:

$$C_1 = c_1(x, y, z, t) \tag{13}$$

In the porous medium region Ω_2 of the scaffold, the oxygen transport should satisfy Equation 14:

$$\frac{\partial C_2(t)}{\partial t} = \nabla \cdot \left[D_e(t) \nabla C_2(t) \right] - v_B \cdot \nabla C_2(t) - R_0(t) \tag{14}$$

where C_2 expresses the oxygen concentration within the biological scaffold; D_e is the effective diffusion coefficient of oxygen within the scaffold; and R_0 denotes the oxygen consumption rate by cells. C_2 should satisfy Equation 15 within the region.

$$C_2 = c_2(x, y, z, t) \tag{15}$$

The effective diffusion coefficient of oxygen D_e varies due to changes in porosity caused by cell growth, and this process satisfies Equation 16.

$$D_e = \frac{\varepsilon(t)}{\Gamma(t)} \cdot D \tag{16}$$

2.3.3. Oxygen consumption process

Oxygen enters the scaffold (region Ω_2) and is then absorbed and consumed by the cells. The cell oxygen consumption term in Equation 14 is calculated by the Michaelis–Menten equation (Equation 17).

$$R_0(t) = \frac{Vo_{max} C_2(t)}{K_m + C_2(t)} \rho_c(t) \tag{17}$$

where R_0 is the oxygen consumption rate; C_2 is the oxygen concentration in the porous domain; Vo_{max} is the maximum oxygen absorption rate by the cells; K_m denotes the oxygen concentration value at which the absorption rate reaches half of its maximum; and ρ_c is the cell density. Additionally, it is necessary to consider the adaptation process, cell spreading, and deformation within the scaffold. In this model, it is assumed that Vo_{max} increases from zero at the beginning to a maximum value at a certain time, as expressed in Equation 18:

$$V_{o_{\max}} \begin{cases} \frac{V_r \cdot t}{3} & (0 \le t < t_1) \\ V_r & (t_1 \le t) \end{cases} \tag{18}$$

where Vo_{max} represents the actual maximum oxygen absorption rate, and t_1 is the nodal time.

2.3.4. Cell growth kinetics

After oxygen consumption, cell proliferation and division occur. The cell growth kinetics described by the first-order growth process is simulated by utilizing the modified Contois model, as expressed in Equation 19:

$$\mu_c(t) = \frac{\mu_{c\max} \cdot C_2(t)}{K_c \cdot \rho_m \cdot V_c \cdot \rho_c(t) + C_2(t)} \tag{19}$$

where μ_c indicates the specific growth rate of cells; μ_{cmax} denotes the maximum specific growth rate of cells during the growth process; C_2 is the oxygen concentration within the porous medium domain; K_c is the Contois parameter; ρ_m represents the mass density of cells; V_c is the volume of an individual cell; and ρ_c represents the density of cells. The change in cell density can be expressed using the Contois equation as follows:

$$\frac{\partial \rho_c(t)}{\partial t} = \mu_c(t) \cdot \rho_c(t) \tag{20}$$

In reality, the growth process of cells in the scaffold should consider an initial phase lag due to cell adhesion and spreading. Therefore, a step-wise profile for the maximum specific growth rate μ_{cmax} is necessary in the model:

$$\begin{cases} 0 & (0 \le t < t_0) \\ \dfrac{\mu_r \cdot (t - t_0)}{t_1 - t_0} & (t_0 \le t < t_1) \\ \mu_r & (t_1 < t) \end{cases} \tag{21}$$

where μ_r represents the actual input of the maximum specific growth rate in the model, and t represents time. t_0 is the cell adhesion time, while t_1 indicates the spreading

time. This model provides an intuitive description of the relationship between cell density changes over time and the cell growth rate. Such a step-wise profile is not only suitable for describing the logarithmic phase of cell growth but also can effectively incorporate the phase lag.

Furthermore, to take into account the variation in the scaffold's porosity resulting from the increase in cell number, the following relation is coupled to the model:

$$\varepsilon(t) = \varepsilon_0 - V_c \cdot \rho_c(t) \quad (22)$$

where ε_0 represents the initial porosity of the medium; V_c denotes the volume of a single cell; and ρ_c is the number of cells per unit volume.

2.4. Initial values and boundary conditions

The initial values of oxygen concentration (C_0), cell density (ρ_0), scaffold porosity (ε_0), and oxygen diffusivity (D_0) in the system and model boundary conditions are summarized in Table 1. Boundary 1 is the inlet of the nutrient solution flow, as depicted in Figure 1a. Both the initial flow rate of the fluid and oxygen concentration at boundary 1 were chosen to be constant, being Q_0 = 600 μL/min and C_{in} = 222.5 μM, respectively. The velocities and oxygen concentrations should be continuous at the interfaces (boundaries 3, 4, and 5) between the scaffold and nutrient solution flow, as indicated by the relation in Table 1. At boundary 2 where the flow is in contact with the chamber wall, the boundary was set to be a no-slip condition, while the oxygen concentration was set to be a no-flux condition. At outlet boundary 6, the fluid satisfies a zero gauge pressure condition.

2.5. Numerical method

A single timestep solution procedure for the multi-physics model is illustrated in Figure 2. Specifically, the parameters, such as flow rate (velocity), oxygen diffusion coefficient, initial cell density, initial oxygen concentration and initial porosity, were fed into the model. Computational fluid dynamics (CFD) simulations for the laminar and porous media flow were then performed to predict the oxygen mass transfer in the system where oxygen convection and diffusion occurred. Subsequently, the obtained oxygen concentration results, such as the oxygen concentration, cell density, and other parameters of each node in the structure, as the inputs, were fed to the cell oxygen consumption model to calculate the oxygen consumption, yielding new oxygen concentration values for simulating cell proliferation. These steps were repeated to obtain continuous results for the parameters within the target time interval.

To solve the multi-physics model more efficiently and conveniently, COMSOL Multi-physics software was used in this study. Given that various physical fields, such as fluid dynamics, mass transport, and cell kinetics, were coupled, appropriate finite element mesh generation should be obtained to balance solution accuracy and computational efficiency. Due to the different physical processes involved in each domain, a partitioned mesh approach was adopted for mesh generation, as illustrated in Figure 3a. Region 3 indicates the porous media flow domain in the channels of the biological scaffold, which is coupled additionally with oxygen consumption and cell growth processes. Hence, the mesh density and refinement in Region 3 must be higher to resolve the underlying physics adequately, while the mesh in regions 1, 2, and 4, where laminar flow

Table 1. Initial values and boundary conditions for model set-up

Initial values	Boundary conditions
C_0=222.5 μM	$v_1\|_{Boundary\ i} = v_B\|_{Boundary\ i}$ (i = 3, 4, 5)
ρ_0=3 × 10^6 cells/cm^3	$C_1\|_{Boundary\ i} = C_2\|_{Boundary\ i}$ (i = 3, 4, 5)
ε_0= 0.7	$v_1\|_{Boundary\ 2} = 0$
D_0=3.10 × $10^{(-9)}$ m^2/s	$\hat{n} \cdot (D \cdot \nabla C_1\|_{Boundary\ 2}) = 0$
	$Q_0 = Q\|_{Boundary1} = 2\pi\left(\frac{D}{2}\right)^2 \cdot v_0$
	$C_{in} = C\|_{Boundary\ 1}$ = 222.5 μM
	$P_0 = P\|_{Boundary\ 6} = 0$

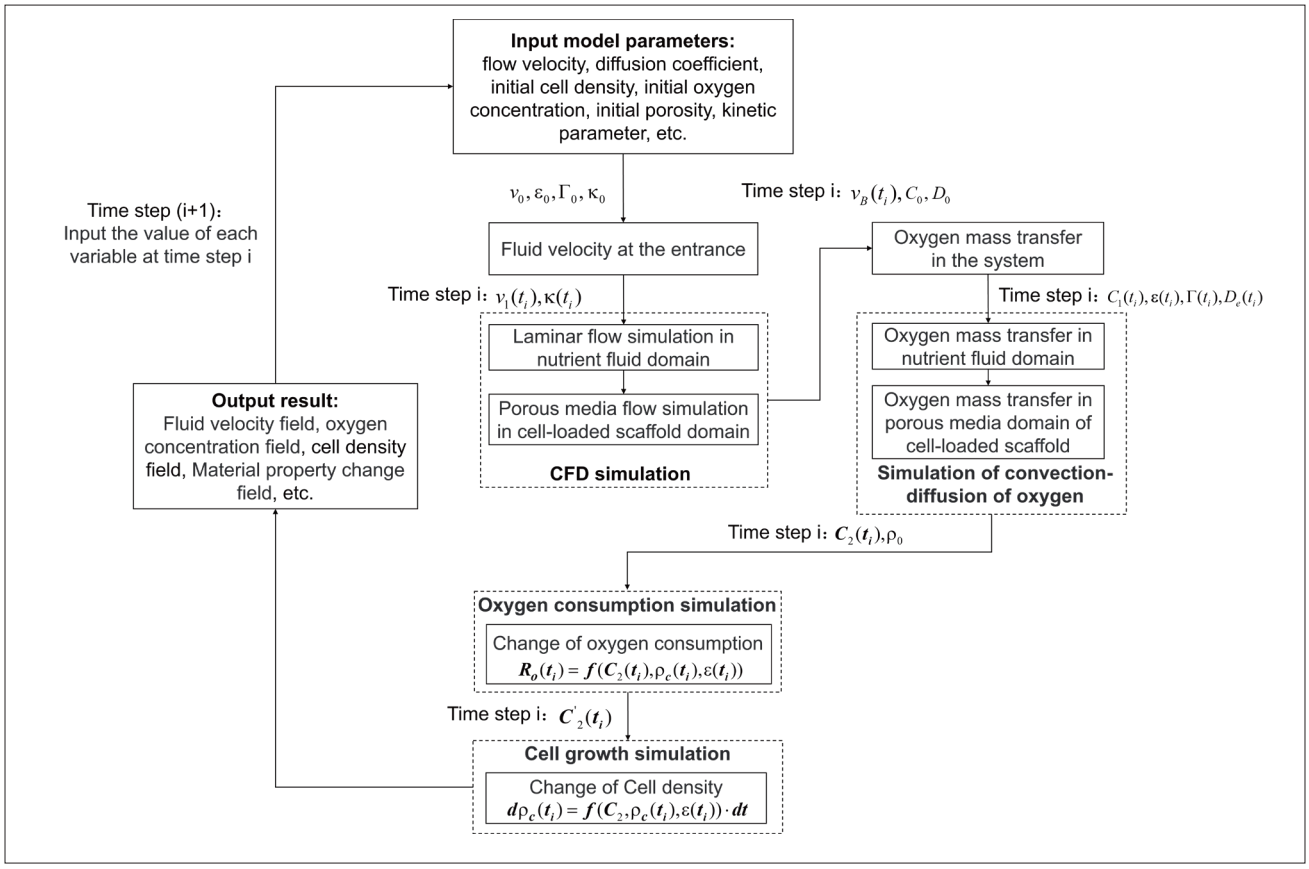


Figure 2. Computational procedure for solving the model within a single timestep.

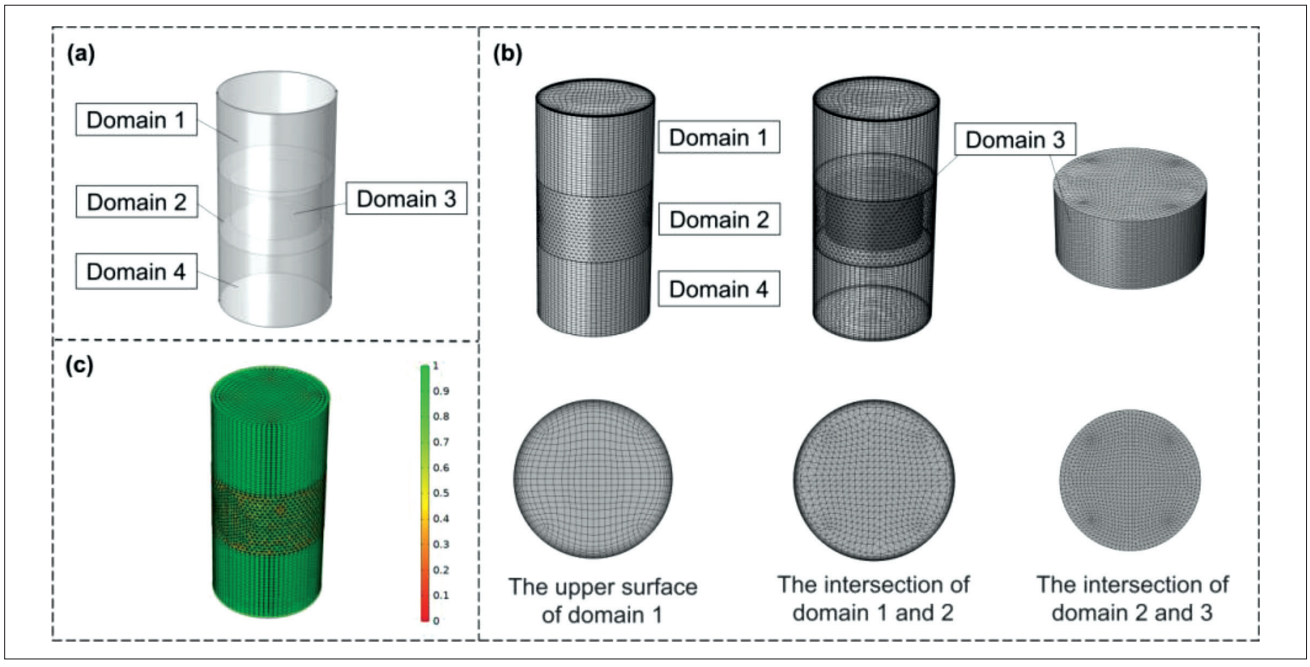


Figure 3. Finite element mesh partitioning. (a) Division of geometric regions. (b) Mesh configuration for each region. The mesh for domain 3, where the porous scaffold is located and the porous media flow is coupled with oxygen consumption and cell growth, was refined to resolve the physics correctly. (c) Quality assessment of the mesh, which shows relatively high values.

Table 2. Grid partitioning settings

Grid setting	Domain 1	Domain 2	Domain 3	Domain 4
Element type	Hexahedral	Tetrahedral	Hexahedral	Hexahedral
Maximum element size	1.000	0.189	0.800	1.000
Minimum element size	0.1800	0.0204	0.100	0.1800
Maximum element growth rate	1.5	1.1	1.45	1.5
Curvature factors	0.6	0.4	0.5	0.6
Resolution of narrow regions	0.5	0.9	0.6	0.5
Number of sweep units	30	-	40	30
Number of boundary layers	8	8	5	8
Boundary layer stretching factors	1.2	1.2	1.1	1.2
Thickness of the first layer	1	1	1	1
Thickness adjustment factors	0.10	0.10	0.08	0.10

and convection–diffusion mass transfer dominate, can be sparser and coarser. Furthermore, boundary layers were introduced during mesh generation to enhance the model's convergence for the fluid calculation processes, and transition smoothing was required at the interfaces between different domains. Figure 3b showcases the mesh results, and the detailed mesh parameters for each domain are summarized in Table 2. Although finer meshing is preferable for the porous media flow, it significantly lowers the computational efficiency. The mesh generation quality was tuned by adjusting the computational accuracy and efficiency balance. Figure 3c shows the quantitative depiction of mesh quality, demonstrating relatively high values. The time step for the model was set at interval of (0, 0.01, 7) days, where 0 is the start time, 0.01 is a time step length, and 7 is the finial time.

3. Materials and methods

3.1. Materials

The C2C12 mouse myoblast cell line was obtained from the School of Biology, Hunan University. The materials for generating the scaffold were gelatin methacryloyl (GelMA) and polyethylene glycol diacrylate (PEGDA). The tartrazine dye was purchased from Shanghai Aladdin Biochemical Technology Co., Ltd. High glucose DMEM culture medium, 1% antibiotic solution, 2 mM L-glutamine, and 10% fetal bovine serum (FBS) were obtained from Gibco Life Technologies (Waltham, MA, USA). 4',6-Diamidino-2-phenylindole (DAPI) and Cell Counting Kit-8 (CCK-8) were purchased from Beyotime Biotechnology (Shanghai, China) Co., Ltd. Phosphate-buffered saline (PBS) was obtained from Thompson Biological Technology Co., Ltd. (Hangzhou, China). The photoinitiator LAP (Bide Pharmaceutical Technology Co., Ltd., Shanghai, China), pipette tips (Corning Life Sciences, Suzhou, China), 0.22 μm sterile syringe filters (Dragon Lab, Beijing, China), cell culture dishes (Corning Life Sciences, Suzhou, China), and 15 mL centrifuge tubes (Corning Life Sciences, Suzhou, China) were also used in the experiments.

3.2. Preparation of bioink

The bioink consisted of 5% w/v PEGDA, 5% w/v GelMA, 0.5% w/v LAP, 0.03% w/v tartrazine, and cells at a concentration of 300,000 cells/mL. Specifically, GelMA, PEGDA, LAP powder, and tartrazine powder were individually weighed and added sequentially into a PBS solution to prepare the hydrogel solution. The solution was then heated in a 37°C water bath for 15 min and mixed thoroughly using a vortex mixer. Once the above process was completed, the pH of the hydrogel solution was adjusted to 7.4 using standard sodium bicarbonate titration solution and hydrochloric acid titration solution. The hydrogel solution was then filtered using a filter. The C2C12 cells that had grown to a high level of confluence in the culture dish were added. First, the culture medium (high-glucose DMEM: FBS: penicillin: streptomycin = 100:10:1:1) in the culture dish was removed. The dish was washed twice with 2 mL of PBS solution for 5 min. Then, the cells were digested with trypsin for 4 min to ensure both cell viability and complete detachment. The digestion was terminated by adding double the volume of trypsin-containing medium. The cells were counted using a cell counting plate, and the cell suspension was centrifuged at 1000 rpm to remove the supernatant. The cells were resuspended in the prepared hydrogel solution to obtain a cell density of 300,000 cells/mL for the bioink.

3.3. *In vitro* culturing

Cylindrical scaffolds with a radius of 2 mm and height of 2 mm were designed and printed using a nanoArch S140 printer (BMF Precision Tech Inc.) using the bioink prepared previously. The printing process is illustrated

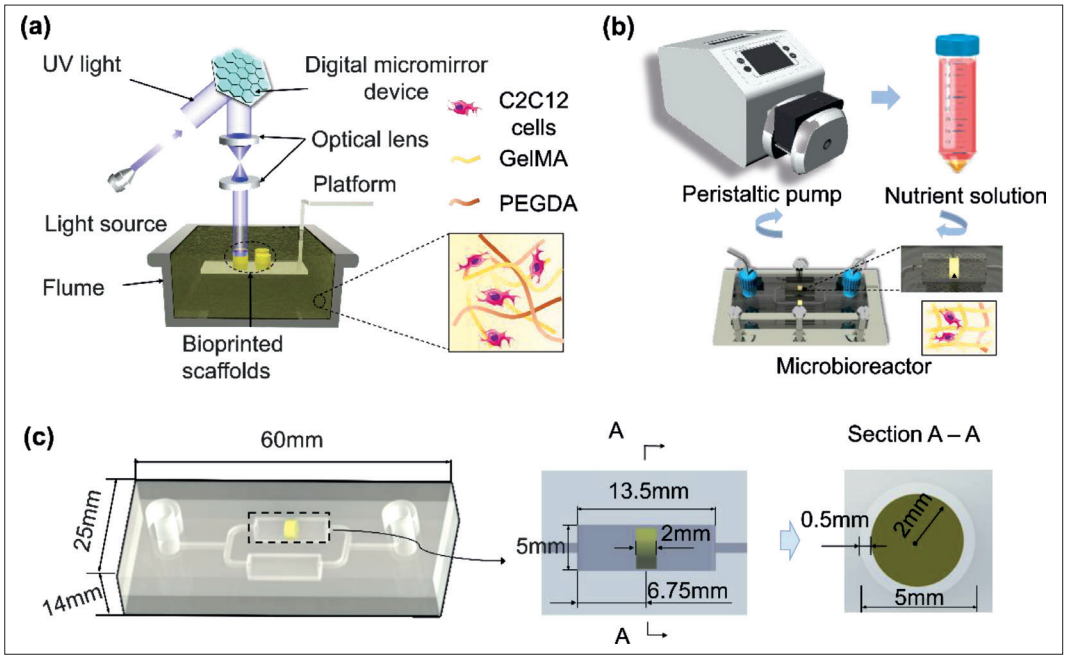


Figure 4. Manufacturing of the cell-laden scaffold and *in vitro* cultivation process. (a) Digital light processing (DLP) fabrication of the scaffold where a 405 nm light source was used. (b) *In vitro* cultivation process of the bioprinted scaffold. (c) Structure and assembly diagram of the perfusable micro-bioreactor with the scaffold. Abbreviation: GelMA, gelatin methacryloyl; PEGDA, polyethylene glycol diacrylate; UV, ultraviolet.

in Figure 4a, where a 405 nm light source was used to solidify the photocurable material. The printing parameters are listed in Table 3. The formulation of bioink and process parameters used in this study is similar to those described in the study by He et al.,[15] which were optimized to produce high-fidelity objects (geometric error less than 5%). The *in vitro* culturing system, as shown in Figure 4b, consists of a peristaltic pump (purchased from Lefu Fluid Technology Co., Ltd., Baoding, Hebei, China), centrifuge tubes with exchange effects, filters, a perfusable micro-bioreactor, and a holder (Wuhan Mesobio Technology Co., Ltd., Wuhan, Hubei, China) connected to a silicone tubing with a diameter of 1.5 mm. The bioprinted scaffold was placed into the perfusable micro-bioreactor; its dimensions are shown in Figure 4c. The scaffold was positioned in the middle of a cylindrical chamber, with a length of 13.5 mm, a diameter of 5 mm, and a 0.5 mm gap between the scaffold and the chamber walls, as depicted in the diagram (see Figure 4c). The flow rate was adjusted to the upper limit of the pump system (600 μL/min), although the optimal value obtained from modeling is greater than that. The entire system was placed in a CO_2 incubator at a temperature of 37°C and a CO_2 concentration of 5%. The culture medium was changed daily.

3.4. Cell proliferation assay

Multiple bioprinted scaffolds were printed and subjected to *in vitro* cultivation. Cell proliferation was assessed using CCK-8 assay on days 0, 1, 3, 5, and 7. Specifically, a test reagent was prepared by mixing CCK-8 solution

Table 3. DLP printing process parameters

DLP printing parameters	Parameter value
Wavelength of light	405 nm
Number of printing layers	20 layers
Thickness of each layer	100 μm
Light intensity	15 W · cm^{-2} per layer for the first 10 layers
	10 W · cm^{-2} per layer for the last 10 layers
Print time	10 s per layer for the first 10 layers
	8 s per layer for the last 10 layers

and culture medium at a volume ratio of 1:9. The scaffolds were placed in a 48-well plate, washed with PBS, and then immersed in an adequate amount of CCK-8 solution to cover the samples fully. The plate was incubated in a CO_2 incubator for 2 h. After incubation, the CCK-8 solution was transferred to a new plate, and the absorbance of the solution was measured using an ELISA reader at a wavelength of 450 nm. The cells were enumerated by converting the absorbance readings using standard equation. The cell proliferation data were primarily used to validate the model.

3.5. Optimization of channeled scaffold

Scaffolds featuring multiple channels play an essential role in tissue engineering as they are able to guide cell growth (such as nerve cells used for spinal cord injury repair) or facilitate nutrient transportation necessary for vascularization and tissue regeneration.[14,15] A two-step optimization strategy based on the multi-physics model was proposed for optimizing the structural parameters of channeled scaffolds so that the cell quantity and the averaged cell density were optimal simultaneously, while keeping hypoxia lower than the threshold C <14 μM.[20] The first step of the optimization method was to find the optimal volume fraction of a

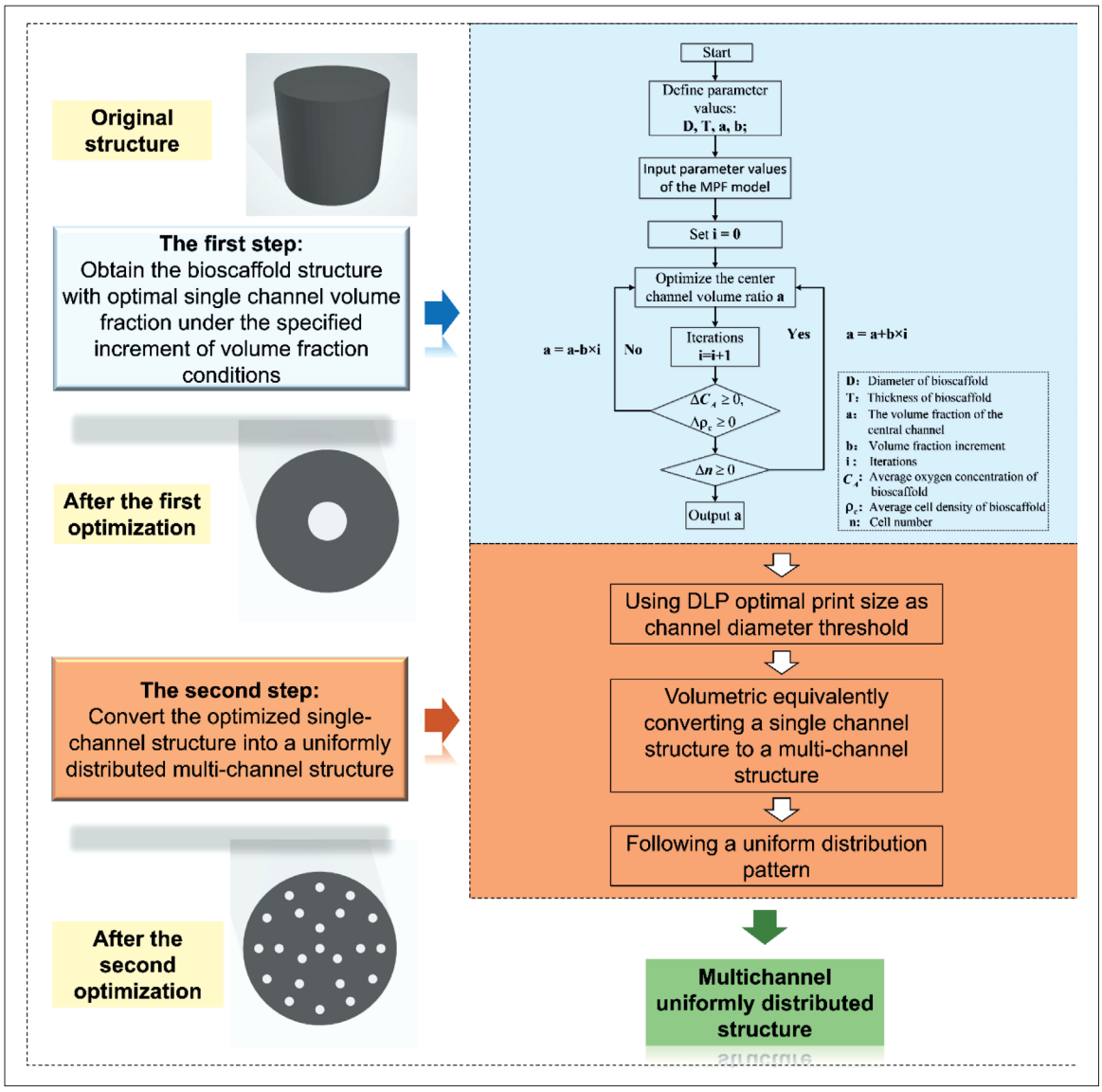


Figure 5. Flowchart of the "two-step optimization method" for optimizing channeled scaffolds. The first step is to find an appropriate volume fraction of a single channel in the scaffold to ensure that the cell quantity and average cell density are optimal simultaneously. In the second step, the volume of the single channel is spread evenly to the scaffold to form a multi-channeled structure. Abbreviation: DLP, digital light processing.

single channel in the scaffold. Specifically, as shown in the flowchart (see Figure 5), the initial volume fraction of the central channel in the scaffold was set to 2.5%. Iterative calculations were performed using the multi-physics model with an increment of volume fraction. The optimal volume fraction of the channel was then obtained when the average cell density and the total amount of cells in the scaffold no longer increased. In the second step, the single-channel scaffold was transformed into a uniformly distributed multi-channel structure with equivalent void volume fraction, where the optimal channel diameter and number values were obtained by iterative calculations.

4. Results and discussion

The modeling system was validated by comparing the modeled data to those observed to demonstrate its ability to predict cell growth and then applied to analyze the spatiotemporal behaviors of the associated physical fields. The parametric study was subsequently performed to gain insight into the mechanism of how geometric and culturing parameters influence cell growth. Finally, a showcase of optimizing the design of channeled scaffolds was presented to demonstrate the effectiveness of the two-step optimization method proposed in this study.

4.1. Model validation and modeled physical fields

To examine the accuracy of the multi-physics model in predicting cell growth, a series of experiments involving C2C12 cell cultivation, bioink preparation, DLP manufacturing of cell-laden scaffolds, dynamic cultivation of scaffolds, and cell proliferation assays were conducted. The C2C12 mouse myoblast cell line was selected because it is often used in pharmaceutical science and biomedical research to examine tissue metabolism and cell growth, and is widely used for validating cell growth models.[22,29] In addition, the cell kinetic parameters of C2C12 required to drive the model have been well-established in many studies (see Table 4). The comparison between the simulated and experimental cell growth trends in cylindrical scaffolds without channels within 7 days is depicted in Figure 6, exhibiting reasonably good agreement. Cell proliferation was increased by 4 times on day 7, as shown by both model and experimental results. The maximum discrepancy between the model and experiments was 4.38%, which occurred on day 4, likely due to the sensitivity issues of the detection reagents or the simplified model physics, such as the exclusion of biological forces and cell death factors. The selection of the model parameters can also contribute to the observed discrepancy (see section 4.2). Based on its well-modeled cell growth trend and relatively small error,

Table 4. Model parameters

Parameters	Values	Description	Sources
Q_0	600 μL · min^{-1}	Initial flow rate	Set
μ	8.4 × 10^{-4} Pa·s	Dynamic viscosity of culture medium	[36]
ρ	1009 kg·m^{-3}	Nutrient density	[36]
ε_0	0.7	Initial porosity	[20]
Γ_0	3.45	Initial tortuosity	[30]
κ_0	6.76 ×10^{-12} m^2	Initial permeability	[30]
P_0	0Pa	Outlet static pressure	Set
C_0	222.5 μM	Initial oxygen concentration	[20]
C_{in}	222.5 μM	Inlet oxygen concentration	[20]
D_0	3.10 × 10^{-9} m^2·s^{-1}	Initial diffusion coefficient	[30]
K_m	0.006 mol·m^{-3}	M-M equation constant	[37]
V_r	3.0 × 10^{-17} mol·cell^{-1}·s^{-1}	Actual maximum oxygen uptake rate	[20]
ρ_0	3.0 × 10^{-6} cells·cm^3	Initial cell density	Set
ρ_m	1020 kg·m^{-3}	Cell volume density	[30]
K_c	0.006	Contois equation constant	[38]
V_c	7.24 × 10^{-15} m^3	Cell volume	[39]
μ_r	1.53 × 10^{-5} cells·s^{-1}	Actual maximum specific growth rate	[30]
t_0	3 h	Cell adhesion period	[40]
t_1	72 h	Cell spreading period	[41]

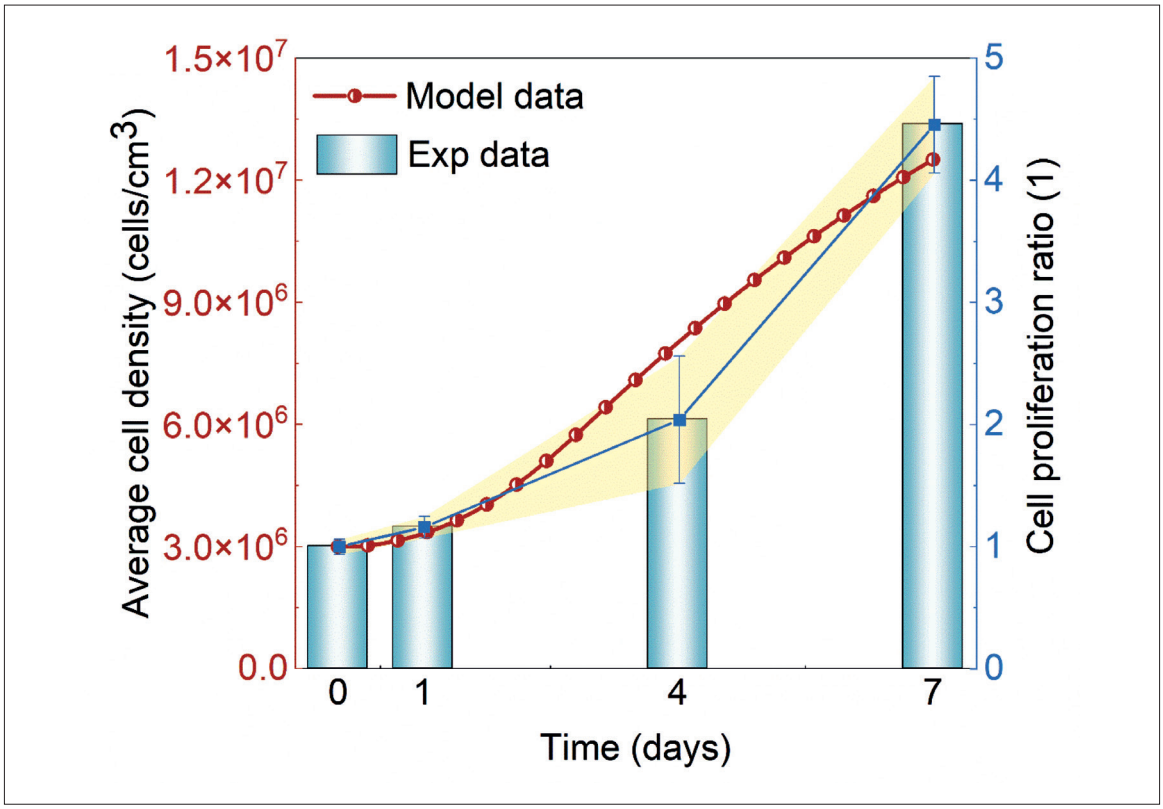


Figure 6. Comparison of simulated and experimental cell growth behaviors. The maximum discrepancy between the model and experiments is 4.38%, which occurred on day 4.

the modeling system proves to be a valuable tool for either studying the cell growth behaviors or guiding the scaffold design.

Although the model is able to predict cell growth properly at the early stage of cell growth, it may fail to simulate the long-term cell growth behaviors as the model ignores the effects of material swelling. The swelling can change the geometry and physical properties of the scaffolds, which may reshape the microenvironment of scaffolds to facilitate the migration, adhesion, and proliferation of cells.[40,41] Its impact on cell growth increases gradually as the cell culturing process proceeds. It is worthwhile incorporating the effect of material swelling to expand the capability of the modeling system, which will be addressed in future. In addition, the cell growth behavior is governed by the modified Contois equation (Equation 19) that does not consider the differentiation mechanism and the cell agglomeration behaviors. Therefore, the model may not be applicable to cells whose growing process entails agglomeration phenomena (such as cancer cells), and to culturing cases where cell differentiation occurs. In this situation, the cell growth model used in this study should be replaced by others, such as the Michaelis–Menten Kinetics model.[42]

The velocity field of the nutrient fluid for dynamic culturing is crucial as it affects the local refreshment rate of the nutrient that determines the amount of nutrients diffusing into the scaffold. Figure 7 depicts the velocity field of the nutrient fluid in the dynamic cultivation system on days 0, 1, 4, and 7, exhibiting weak variations in time. The maximum velocities (4.16× of the inlet velocity) occur at the gaps between the scaffold and the chamber due to a narrowed passing path that can cause fluid accumulation and enlarged internal forces. The modeling system takes into account the material porosity of the hydrogel scaffold that depends on molecular weight and degree of curing. Figure 7e–h shows the velocity of a magnified 2D cross-section in the porous media region of the scaffold for days 0, 1, 4, and 7, respectively. The velocity magnitude decreases gradually over time, and the maximum velocity is reduced from 1.07×10^{-4} m/s to 1.92×10^{-5} m/s from days 0 to 7. Such a reduction is attributed to the occupation by proliferating cells in the pores, leading to a decrease in fluid permeability and thus hindering fluid infiltration. The scaffold acts as a strong barrier in the system, and the fluid

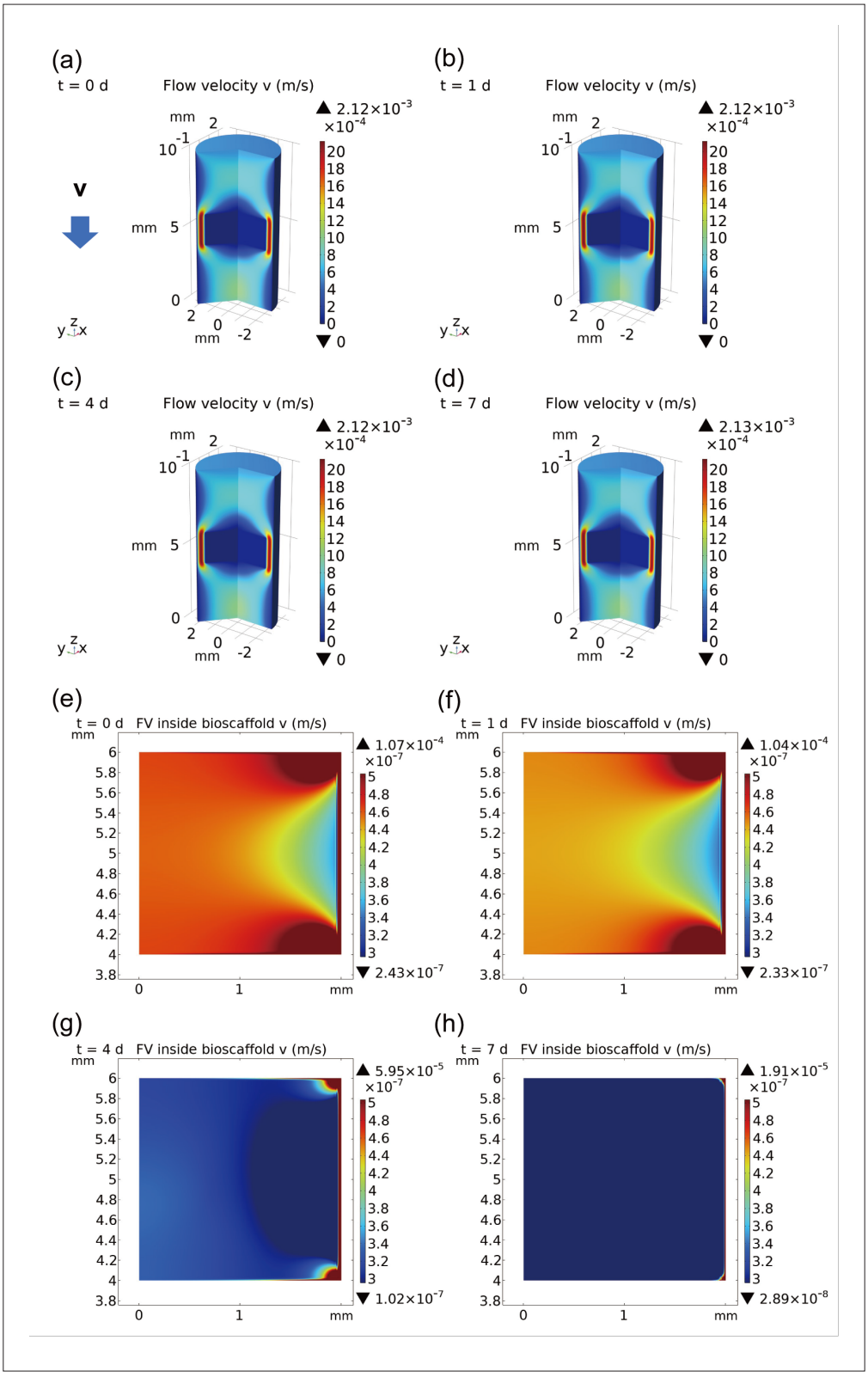


Figure 7. Simulation results of the velocity field in the cell-laden scaffold under dynamic cultivation. Panels a, b, c, and d show the velocity field maps in the dynamic cultivation device on days 0, 1, 4, and 7, respectively. Panels e, f, g, and h depict two-dimensional cross-sectional velocity field maps within the porous region of the scaffold on days 0, 1, 4, and 7, respectively.

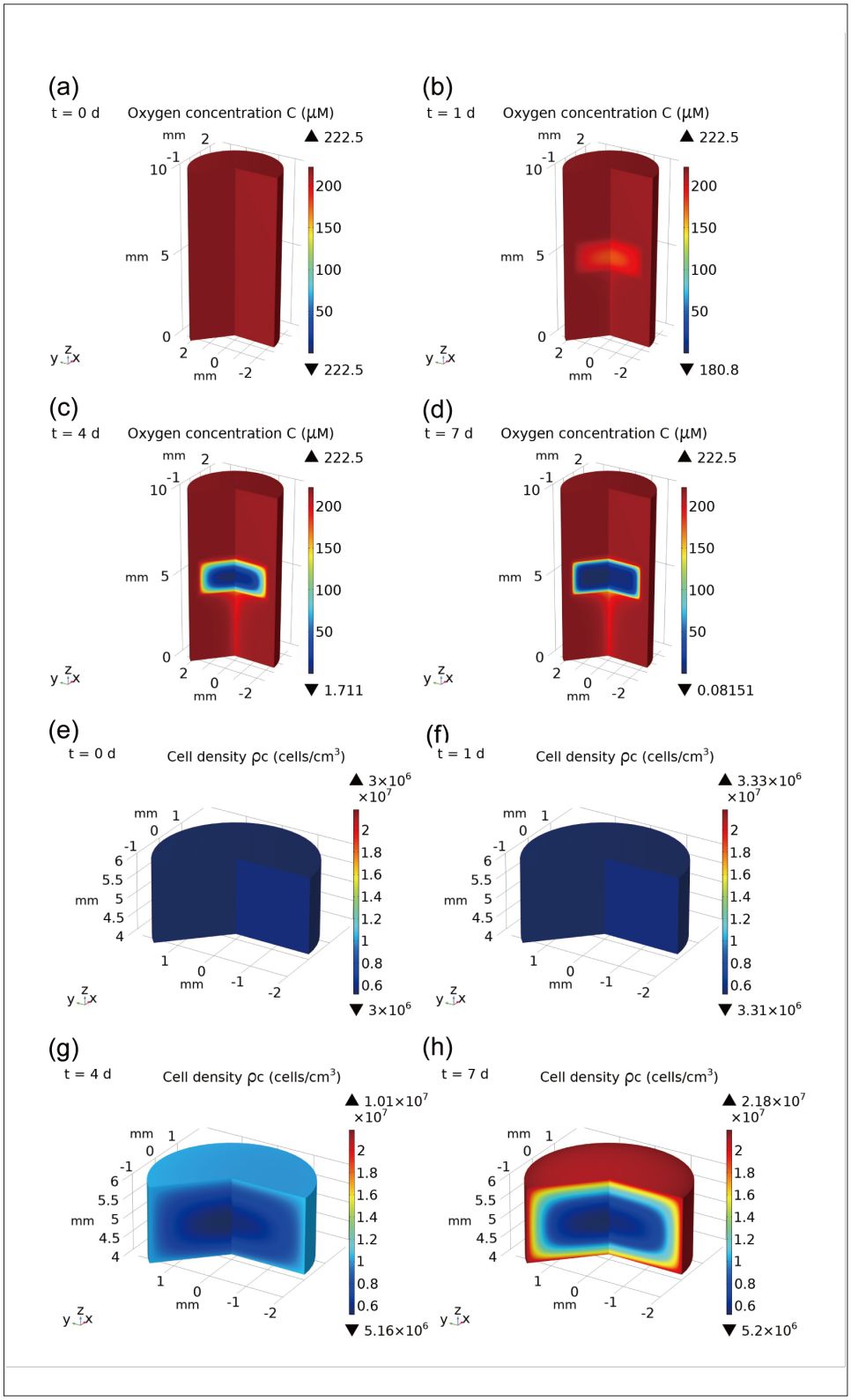


Figure 8. Simulation results of oxygen concentration and cell density in the cell-laden scaffold under dynamic cultivation. Panels a, b, c, and d illustrate the oxygen concentration field of the culturing system on days 0, 1, 4, and 7, respectively. Panels e, f, g, and h represent the cell density distribution of the cell-laden scaffold on days 0, 1, 4, and 7, respectively.

in the middle of the bioreactor will flow slowly from the middle of the scaffold. The results revealed that a constant inflow may not be suitable for dynamic culturing because the nutrient flow in the porous scaffold becomes slower as cell proliferation proceeds. In addition, using a material with a higher degree of microporosity (softer materials) is also beneficial for cell proliferation.

Oxygen concentration in the scaffold is a critical indicator for cell activities and is driven by both the convective action of the fluid and its diffusion. Figure 8a–d shows the simulation results of the bioreactor's oxygen concentration field, presenting the spatial distribution from days 1 to 7. It can be observed that the oxygen concentration in the non-scaffold area is uniform, while it changes significantly inside the scaffold. The magnitude of oxygen concentration reduces gradually from the surface of the scaffold to the center, where the oxygen consumed by cells is not compensated adequately via the diffusion process due to the lengthened diffusion path. A similar trend was observed for cell density, as shown in Figure 8e–h. At the initial stage of cultivation, the cell density distribution was set to be uniform with a density of 3.0×10^6 cell/cm^3. On day 4, the cell density in the center regions of the scaffold was lowered approximately by half compared to the outer areas, while the discrepancy was further amplified on day 7. To enhance the transportation of oxygen, macro channels or voids are commonly added to solid scaffolds to promote permeability.[14,15,20] However, excessive channels or voids can decline the cell loading of the scaffold, resulting in adverse effects on cell proliferation. Determining optimal geometric parameters of scaffolds is somewhat arbitrary or based on a trial-and-error approach currently. For example, structures with different geometric parameters are repeatedly used in cell culturing. This greatly increases the cost of experimentation and time, but the results obtained are still uncertain as to whether they are optimal. It is possible to use the modeling system developed in this study to optimize the architecture of the scaffold to maximize its cell activities (see section 4.3).

4.2. Parametric study

Prior to optimizing the scaffold, it is necessary to gain an understanding of how material, geometrical, and culturing parameters impact cell growth. The parameters, including the inlet flow of the bioreactor, scaffold's diameter and height, initial cell density, initial material porosity, maximum oxygen uptake rate, and maximum cell growth rate, were varied in the model to investigate the changes in oxygen concentration and cell growth.

4.2.1. Inlet flow

The impact of inlet flow rates (60 μL/min, 600 μL/min, and 6000 μL/min) on oxygen distribution in scaffolds was investigated, as shown in Figure 9a. Increasing the flow rate from 600 to 6000 μL/min resulted in a relatively large elevation in oxygen concentration, while it was minor when the flow rate changed from 60 to 600 μL/min. Accordingly, the average cell density in the scaffold was increased with a higher flow rate, mainly after 4 days (see Figure 9b). However, it should be noted that the flow rate cannot be increased indefinitely, as this can increase wall shear stress at the edges of the scaffold. C2C12 cells require a specific range of wall shear stress (1.6–3.3 dyn/cm^2) for growth stimulation,[20] and excessive or insufficient wall shear stress can lead to cell death or failure to grow. For this reason, the model was adopted to explore the relationship between flow rate and wall shear stress to obtain the optimal flow rate range. Figure 9c displays the shear stress variation against flow rate, demonstrating a strong linear correlation. When the wall shear stress was constrained within the range of 1.6–3.3 dyn/cm^2, it yielded the optimal values of inlet flow rates, being 2249 to 4515 μL/min.

4.2.2. Geometric parameters

Figure 10 illustrates the impact of the scaffold's diameter and thickness on the average oxygen concentration, cell density, and cell count. Changes in scaffold diameter had minimal impact on oxygen diffusion and cell density (see Figure 10a and b). The cell count was enlarged by approximately 4 times from day 0 to day 7 (Figure 10c). The scaffolds with a larger diameter demonstrated a greater proliferation rate primarily due to the higher degree of initial cell count since the initial density remained consistent, highlighting the importance of initial cell count on cell growth. In contrast, changes in thickness demonstrated a remarkable influence on cell proliferation behaviors (see Figure 10d and f). Oxygen mass transfer efficiency decreased significantly as the thickness increased from 0.3 mm to 1.5 mm, beyond which it remained stable at a particularly low level (~30%). As the effective diffusion length of oxygen in the biocompatible materials is generally within a few hundred microns,[19,20] the oxygen concentration was lowered by only ~13% after 7 days for the 0.3 mm scaffold in this study; however, the reduction reached 75% when the thickness was increased to 5 mm (see Figure 10d). Cell density exhibited a minor correlation to the thickness from days 0 to 3, while the difference in cell density between various scaffolds was more pronounced afterward (Figure 10e). Due to enhanced oxygen transportation for thinner scaffolds, the cell density was amplified by 7 times on day 7, while it was 4.5 times for a thickness of 3.0 mm. For the cases of cell count, the cell number on day 7 increased proportionally to the increase in thickness due to the enlarged volume of scaffolds. The results of the sensitivity study indicate that the oxygen concentration and average cell density are more sensitive to the axial dimension that

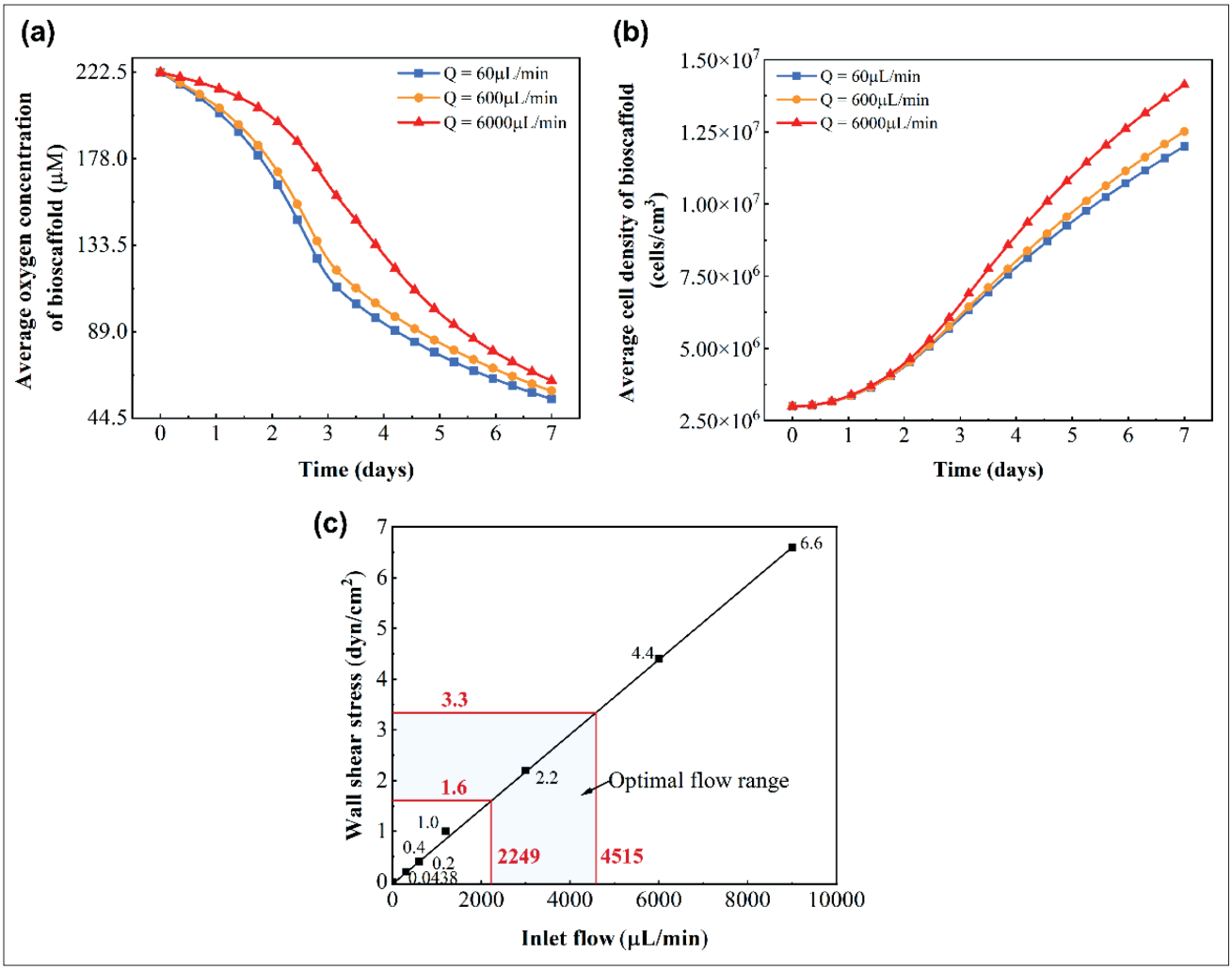


Figure 9. Impact of the bioreactor's inlet flow rate on (a) average oxygen concentration within the scaffold, (b) average cell density, and (c) wall shear stress at the outer edge of the scaffold.

is parallel to the direction of nutrient flow. Although the oxygen concentration and cell density were the highest for the 0.3 mm scaffold, its cell loading on day 7 was only one-eighth of the 3.0 mm scaffold. The cell population is vital for intercellular signaling that is of great importance to viability and proliferation.[43] A balance between oxygen permeability and cell loading should be thus considered during the design of scaffolds.

4.2.3. Material and cell parameters

Figure 11 presents the effects of initial material porosity, initial cell density, maximum oxygen uptake rate, and maximum cell growth rate on oxygen transportation and cell growth, where the normalized average oxygen concentration and cell density were presented with a factor of 222.5 and 3×10^6 cells/mL, respectively. As shown in Figure 11a, the average oxygen concentration decreased over time due to cell consumption, and the reduction rate was significantly augmented when the initial cell density (ρ_0) was increased. The oxygen concentration was lowered by ~50% for an initial cell density of 3×10^6 cells/mL after a 7-day culturing, while it was utterly hypoxic when the initial density tripled, leading to a discrepancy in the cell density on day 7 as high as ~13 times (see Figure 11e). On the 7th day of culture, the cells had proliferated by ~31 times from an initial density of 3×10^5 cells/mL, while extremely low cell proliferation was observed for the scaffold with 9×10^6 cells/mL density. In cell culturing, a low initial density will weaken cell-to-cell interaction and communication, leading to slow cell growth and eventually death. Conversely, excessive initial density brings about overcrowding and insufficient nutrients, resulting in local metabolic waste accumulation. Therefore, optimal initial cell density is required to maximize cell growth.

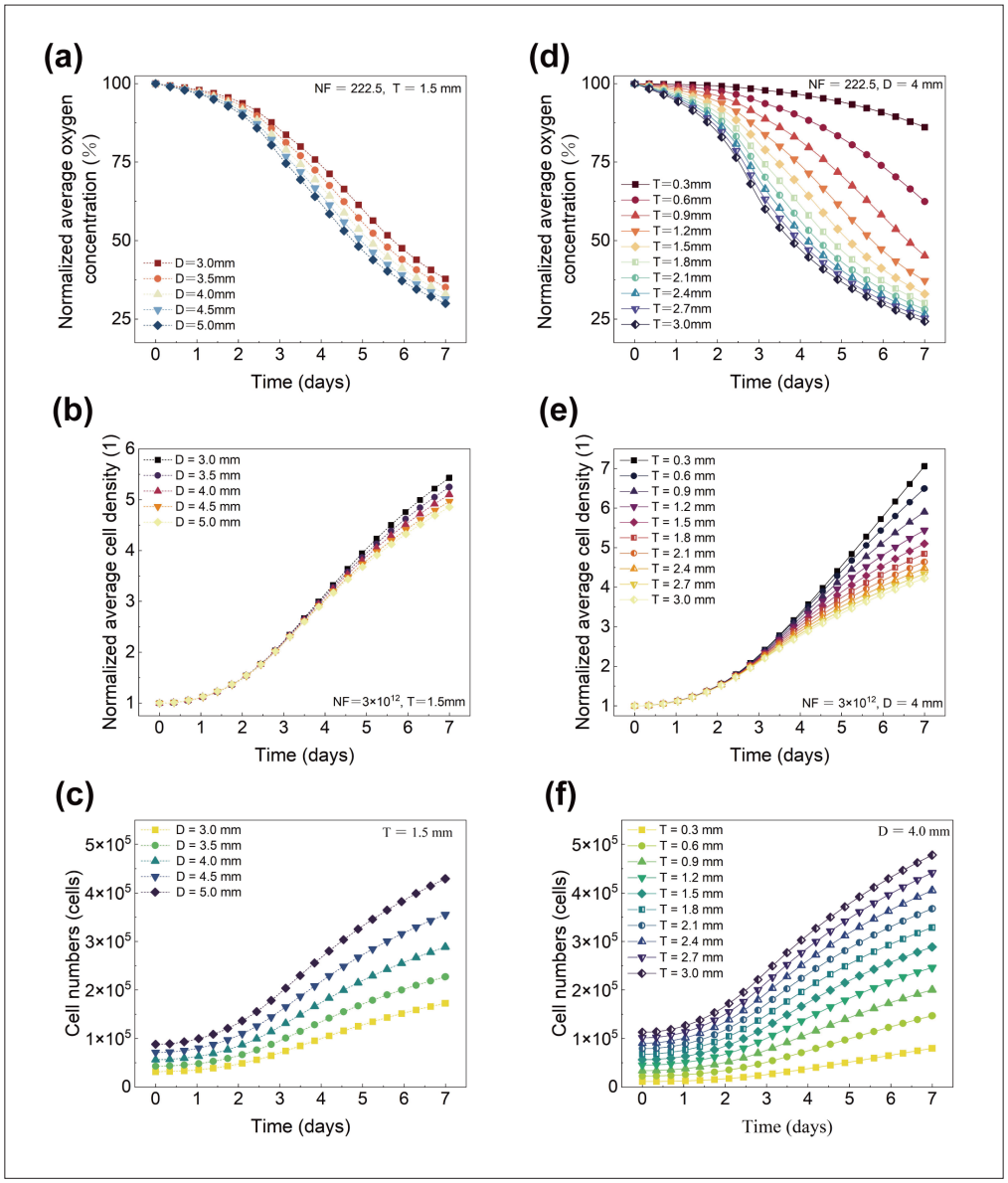


Figure 10. Impact of geometric dimensions on the performance of scaffolds. Panels a, b, and c depict the effect of diameter variations on the average oxygen concentration, cell density, and cell count, respectively, with a fixed thickness of 1.5 mm. Panels d, e, and f show the influence of thickness variations on the average oxygen concentration, cell density, and cell count, respectively, with a diameter of 4 mm.

The effects of initial material porosity (ε) on average oxygen concentration and cell density are presented in Figure 11b and f. Increasing the material porosity can significantly promote the oxygen concentration in the scaffold due to the enhanced diffusion. The percentage on day 7 was raised from approximately 10% to 70% when increasing the porosity from 0.3 to 0.9. Accordingly, the cell proliferation was improved by ~3 times (see Figure 11f). Materials with high porosity not only offer adequate space for cell interaction and thus facilitate intercellular signaling, but also enhance nutrient and waste transport via convection and diffusion.[44] It is feasible to modulate the porosity by tuning the concentration or molecular weight of the hydrogel materials. As expected, a higher value of the maximum oxygen uptake rate (V_r) led to faster oxygen consumption, resulting in a significant reduction in oxygen concentration as well as cell density (Figure 11c and g). Similarly, the actual maximum cell growth rate (μ_r) greatly impacts the average oxygen concentration and cell density (Figure 11d and h). V_r and μ_r are cell-type-dependent and vary among different types of cells, suggesting that an optimized scaffold for a specific type

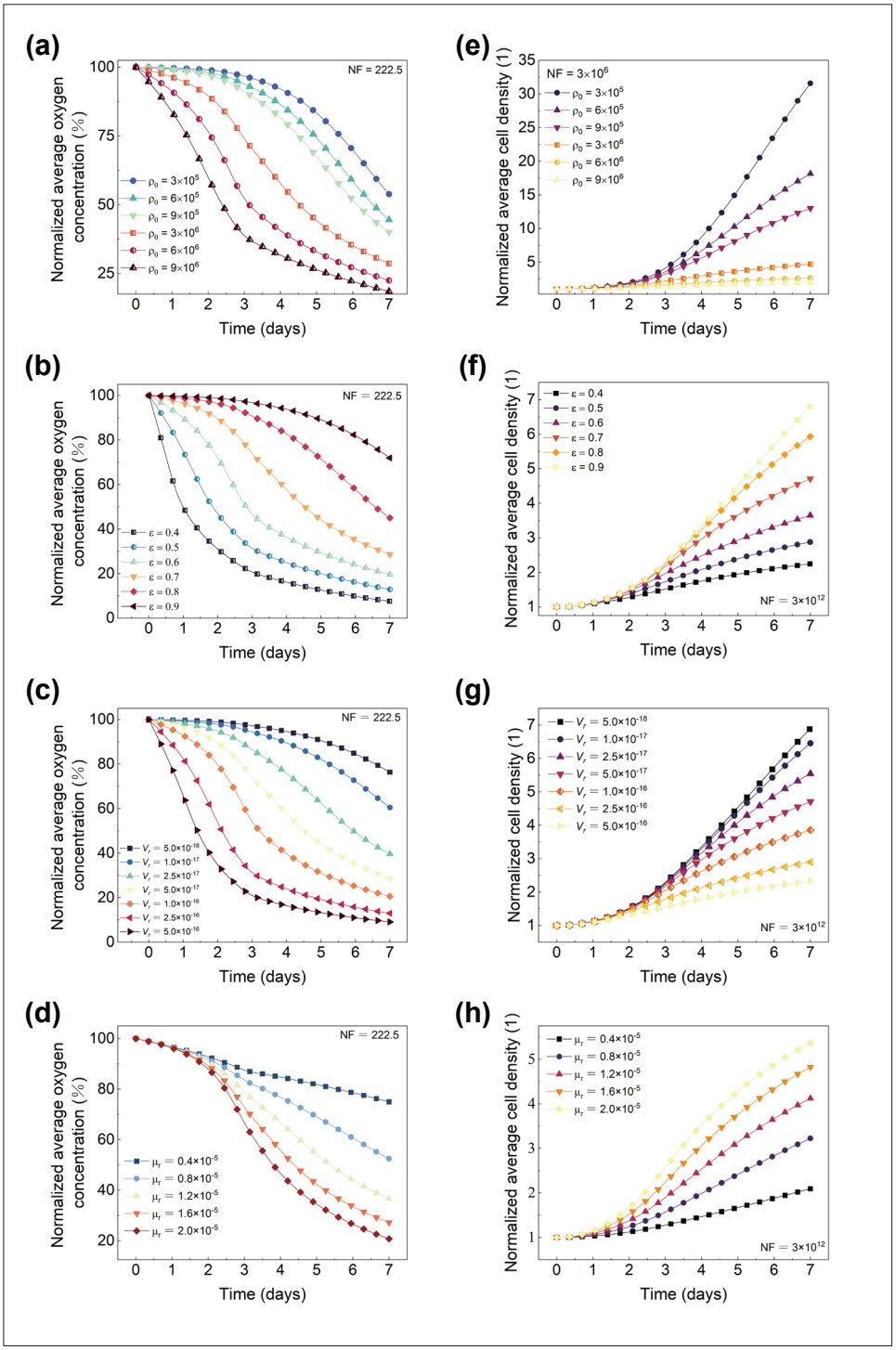


Figure 11. Sensitivity of average oxygen concentration to parameters including (a) initial cell density, (b) initial porosity, (c) maximum oxygen absorption rate, and (d) maximum cell growth rate. Panels e to h depict the sensitivity of average cell density to the same parameters aforementioned.

of cell may not be suitable for another cell type, and re-designing and optimization are thus needed. For example, tumor cells easily aggregate into balls, and its growth trend is completely different from that of C2C12, so the structure optimized based on the parameters in this study may not be suitable for tumor cell growth.

These results indicated that initial material porosity, initial cell density, maximum oxygen uptake rate,

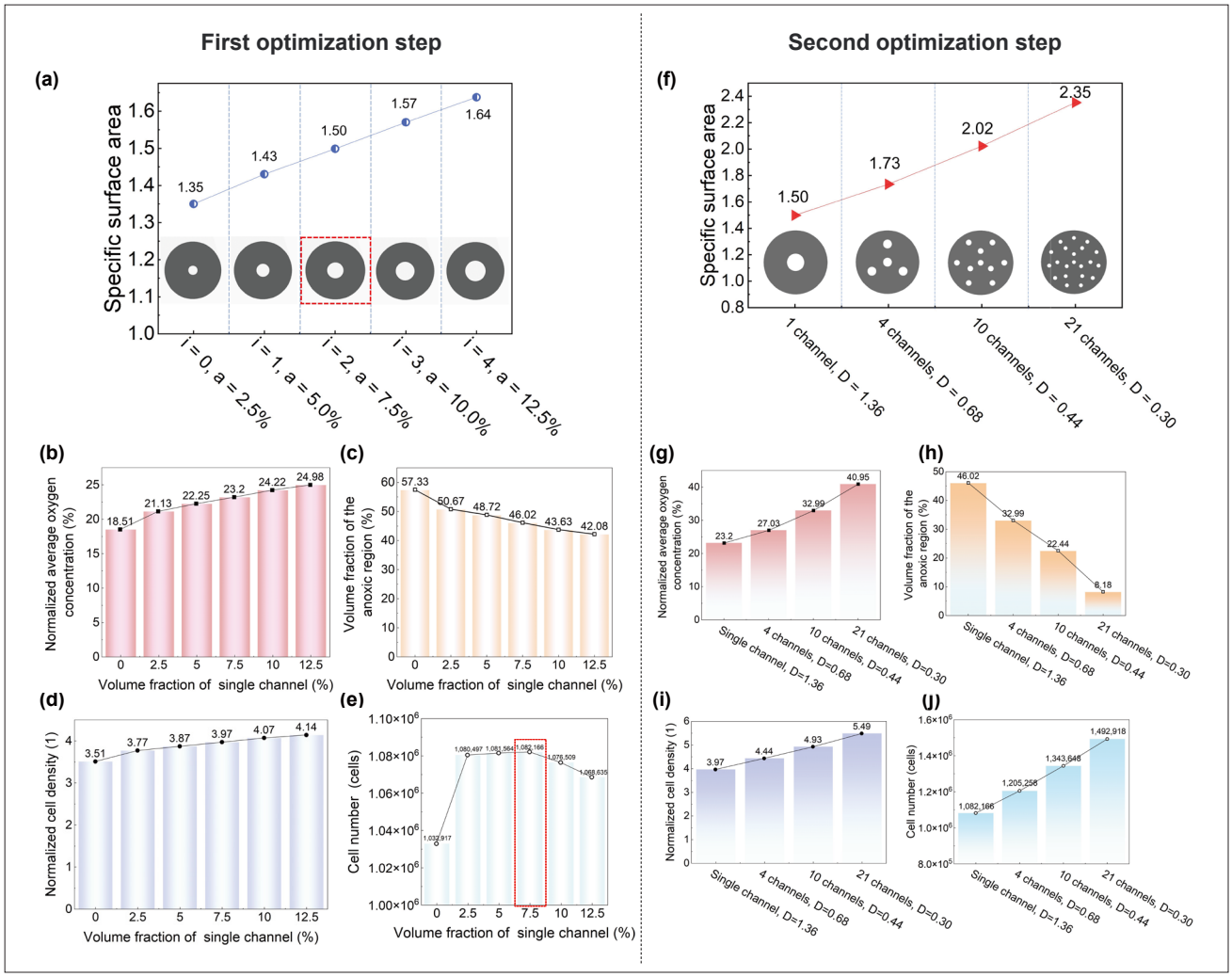


Figure 12. Optimization process of the channeled scaffold. (a) The structures used for model simulation in the first optimization step. The channel volume fraction increased by 2.5% in each step. The dotted line indicates the specific surface area ratio between channeled and solid structures. Panels b, c, d, and e illustrate the normalized average oxygen concentration, hypoxic region volume fraction, normalized average cell density, and cell count after five iterations of calculation, respectively. The red dashed rectangles indicate the optimal channel volume fraction where the cell count is maximum. (f) Structures adopted for model simulations in the second optimization step. The dotted line expresses the specific surface area ratio. Panels g, h, i, and j depict the normalized average oxygen concentration, hypoxic region volume fraction, normalized average cell density, and cell count for structures with various channels, respectively.

and maximum cell growth rate influence the oxygen concentration and cell growth. A purely trial-and-error approach is thus problematic for obtaining the optimal values of these parameters simultaneously. The modeling system can help find the desired parameter values prior to conducting actual experiments, or narrow the range of the values for testing.

4.3. Structural optimization

To further demonstrate the capability of the modeling system in optimizing the design of a cell-laden scaffold, the optimization for a channeled scaffold, as an example, was carried out (Figure 12). The optimal channel size, number and distribution ensuring maximum cell growth after a 7-day culturing were obtained using a two-step method assisted with the model. Figure 12a shows the process of finding the threshold of the void volume fraction with the maximum cell number while the oxygen concentration and cell density are high. Commencing from a solid cylindrical scaffold, the channel volume fraction increased up to 12.5% with an increment of 2.5%. The average oxygen concentration and cell density ascended gradually within such a volume fraction range (Figure 12b and d). However, the cell count reached the peak when the channel volume

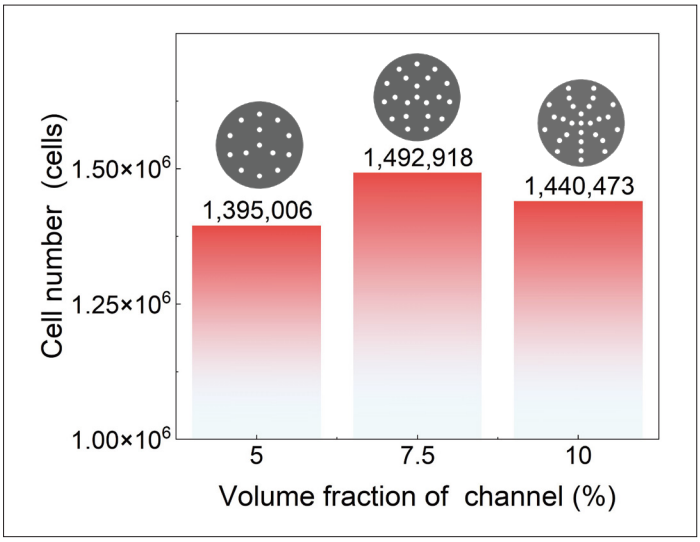


Figure 13. Cell counts for the multi-channel scaffolds with different volume fraction of channel on day 7.

fraction equaled to 7.5% (Figure 12e). This is attributed to the interplay between the increase in cell density and the reduction of scaffold materials for carrying cells. Note that this value may vary when other parameters differ, such as the height and diameter of the scaffold, cell type, scaffold material, and nutrient flow conditions. The second step is to spread the single-channel volume fraction (7.5% for this case) to the scaffold to form a multi-channeled scaffold with optimal geometric parameters, including channel diameter and number (see Figure 12f). When the number of channels increased from 1 to 21, the normalized average oxygen concentration rose from 23.2% to 40.95% (Figure 12g). The volume fraction of the hypoxic region, where the oxygen concentration was lower than the threshold C <14 μM,[20] decreased from 46.02% to only 8.18% (Figure 12h). As a result, the number of cells elevated from 1,082,166 to 1,492,918, showing an increment of 37.96% (Figure 12i and j). The specific surface area is a critical indicator to characterize the performance of scaffold as it influences the rate of oxygen and nutrients exchange significantly. The specific surface area increases when increasing the void volume fraction (Figure 12a) or splitting the empty phase into more tiny channels (Figure 12f). The specific surface area is enlarged from 1.5 to 2.35 when the number of channels increases from 1 to 21 (Figure 12f), indicating that scaffolds featuring more tiny channels possess better permeability and therefore higher cell growth rates. This is consistent with the modeled cell density (Figure 12i), further verifying the correctness of the model. To validate that the structure with multiple channels was optimal, a similar procedure was applied for scaffolds with channel volume fractions of 5% and 10% for comparison. As shown in Figure 13, the scaffolds with a volume fraction of 7.5% exhibited the highest cell numbers on day 7 compared to others, confirming the effectiveness of this optimization method.

Channels or voids are key architectural features in scaffolds, providing a passageway to guide cell growth and facilitating nutrient and waste exchange.[11,14,15] The degree of cellularity in scaffolds is critical to ensure the biological functionalities of the engineering tissue, and highly cellularized scaffolds can enhance intercellular and cell–material interactions, therefore improving cellular behaviors.[45] During the design of porous scaffolds, adding more empty phases can improve the permeability and thus cell proliferation; however, it reduces the solid volume for carrying cells. The correct geometric parameters of scaffolds yielding maximum cell number should be determined, in order to maximize the cellularity degree of the scaffolds. However, the selection of channel parameters is somewhat arbitrary in current practice or based on experiments, and the current design rules are insufficient to obtain the most optimal parameters. The results showed that the channel number and size significantly impact cell proliferation. Simply adding channels improves oxygen transportation and cell density. However, excessive channels will reduce the scaffold materials and thus the final cell number. The modeling-based optimization strategy proposed in this study can determine the optimal channel parameters that ensure maximum cell number after culturing. For this case, the optimal scaffold features 21 uniformly distributed channels with a diameter of 0.3 mm. Theoretically, the cell count can be further improved by increasing the channel number to more than 21. Scaffolds with desired permeability and cell proliferation are usually geometrically complex and feature microsized channels and thin walls,

such as the triply periodic minimal surface structures.[46] It creates significant challenges to the fabrication process due to the light scattering effect, an intrinsic defect of light-based 3D printing that can deviate propagating light to unilluminated regions (voids and channels, for instance) and thus result in deformation and blockage of channeled structures. To address this issue, He et al.[15] proposed a new photoinhibition approach that can effectively suppress the light scattering effect via a mechanism of simultaneous photoabsorption and free-radical reaction, thereby improving the printing resolution (~1.2 to ~2.1 pixels depending on swelling) and shape fidelity (geometric error of less than 5%) of DLP printing. This approach promotes the capability of DLP in patterning soft hydrogels to a new level at which functional porous scaffolds with microsized features (such as voids, channels, and thin walls) can be fabricated successfully. Although a cylindrical scaffold was used for demonstration in this study, the model and the optimization method can be applied to optimize other scaffolds' geometric parameters, such as the gyroid structure with a triply periodic minimal surface.

5. Conclusion

Light-based 3D printing enables the patterning of hydrogel materials in the formation of architecturally sophisticated scaffolds that can better biomimic native tissue microenvironments. However, it is a challenge to determine the optimal parameters using a purely trial-and-error method during the designing process of a scaffold, as many parameters need to be optimized simultaneously. To gain a better understanding of the cell growth behaviors of scaffolds designed with various parameters and facilitate the designing process of complex scaffolds, a multi-physics model incorporating oxygen mass transfer, fluid mechanics, cellular oxygen consumption, and cell growth is proposed in this study for modeling cell growth in bioprinted scaffolds under dynamic culturing. The model takes into account material, geometry, cell, and culturing parameters and is able to output many physical fields, such as cell density, oxygen concentration, and hypoxic region. Therefore, it is a useful tool to guide the design of scaffolds. The model's accuracy was verified by comparing the simulated results with those of cell proliferation experiments, which demonstrated good agreement. The parametric study showed that a large number of parameters greatly influence oxygen transportation and cell growth behaviors. We then showcased its effectiveness in promoting scaffold performance by optimizing the geometric parameters of channeled scaffolds, where the interplay between an increase in cell density and a reduction in cell count occurred when channel volume fraction rose. Although a cylindrical scaffold with channels, as an example, was utilized in this study, the model can be applied to design and optimize scaffolds with arbitrary shapes (e.g., lattice and gyroid) to achieve enhanced biological functions (e.g., vascularization and spinal cord repair), which will be demonstrated in forthcoming works.

Acknowledgments

None.

Funding

The authors acknowledge the financial support received from the National Natural Science Foundation of China (52075158) and the Natural Science Foundation of Hunan Province (2021JJ30109).

Conflict of interest

The authors declare no conflicts of interest.

Author contributions

Conceptualization: Xiaoxiao Han, Feng Chen
Data curation: Jing Li, Xiaolong Zhu, Ning He, Haotian Zhu
Formal analysis: Jing Li, Na Li
Funding acquisition: Xiaoxiao Han
Methodology: Jing Li, Feng Chen, Meixia Wang
Project administration: Xiaoxiao Han, Feng Chen
Software: Jing Li, Feng Chen
Supervision: Xiaoxiao Han
Validation: Jing Li, Xiaolong Zhu, Meixia Wang
Visualization: Jing Li, Na Li
Writing – original draft: Jing Li
Writing – review & editing: Feng Chen, Xiaoxiao Han

Ethics approval and consent to participate

Not applicable.

Consent for publication

Not applicable.

Availability of data

Data used in this work are available from the corresponding authors upon reasonable request.

Further disclosure

Part of or the entire set of findings has been presented in a conference: International Journal of Bioprinting in the BDMC 2023 Conference.

References

1. Ventola CL. Medical applications for 3D printing: current and projected uses. *P&T*. 2014;39(10):704-711.
2. Reddy VS, Ramasubramanian B, Telrandhe VM, Ramakrishna S. Contemporary standpoint and future of 3D bioprinting in tissue/organs printing. *Curr Opin Biomed Eng*. 2023;27:100461. doi: 10.1016/j.cobme.2023.100461
3. Murphy SV, Atala AJ. 3D bioprinting of tissues and organs. *Nat Biotechnol*. 2014;32:773-785. doi: 10.1038/nbt.2958
4. Muskan, Gupta D, Negi NP. 3D bioprinting: printing the future and recent advances. *Bioprinting*. 2022;27:2405-8866. doi: 10.1016/j.bprint.2022.e00211
5. Matai I, Kaur G, Seyedsalehi A, McClinton A, Laurencin CT. Progress in 3D bioprinting technology for tissue/organ regenerative engineering. *Biomaterials*. 2020;226:119536. doi: 10.1016/j.biomaterials.2019.119536
6. Li T, Chang J, Zhu Y, Wu C. 3D printing of bioinspired biomaterials for tissue regeneration. *Adv Healthc Mater*. 2020;9(23):2000208. doi: 10.1002/adhm.202000208
7. Javaid M, Haleem A. 3D printing applications towards the required challenge of stem cells printing. *Clin Epidemiol Global Health*. 2020;8:862-867. doi: 10.1016/j.cegh.2020.02.014
8. Cidonio G, Glinka M, Dawson JI, Oreffo ROC. The cell in the ink: improving biofabrication by printing stem cells for skeletal regenerative medicine. *Biomaterials*. 2019;20910-24. doi: 10.1016/j.biomaterials.2019.04.009
9. Sun Y, Yu K, Gao Q, He Y. Projection-based 3D bioprinting for hydrogel scaffold manufacturing. *Bio-Des Manuf*. 2022;5:633-639. doi: 10.1007/s42242-022-00189-0
10. He Y-X, Wang F, Wang X, Zhang J, Wang D, Huang X. A photocurable hybrid chitosan/acrylamide bioink for DLP based 3D bioprinting. *Mater Des*. 2021;202:109588. doi: 10.1016/j.matdes.2021.109588
11. Tao J-L, Zhu S, Liao X, et al. DLP-based bioprinting of void-forming hydrogels for enhanced stem-cell-mediated bone regeneration. *Mater Today Bio*. 2022;17:100487. doi: 10.1016/j.mtbio.2022.100487
12. Lee A, Hudson AR, Shiwarski DJ, et al. 3D bioprinting of collagen to rebuild components of the human heart. *Science*. 2019;365:482-487. doi: 10.1126/science.aav9051
13. Lei D, Yang Y, Liu Z, et al. 3D printing of biomimetic vasculature for tissue regeneration. *Mater Horiz*. 2019;6(6):1197-1206. doi: 10.1039/C9MH00174C
14. Grigoryan B, Paulsen SJ, Corbett DC, et al. Multivascular networks and functional intravascular topologies within biocompatible hydrogels. *Science*. 2019;364:458-464. doi: 10.1126/science.aav9750
15. He N, Wang X, Shi L, et al. Photoinhibiting via simultaneous photoabsorption and free-radical reaction for high-fidelity light-based bioprinting. *Nat Commun*. 2023;14(1):3063. doi: 10.1038/s41467-023-38838-2
16. Bernal PN, Bouwmeester MC, Madrid-Wolff J, et al. Volumetric bioprinting of organoids and optically tuned hydrogels to build liver-like metabolic biofactories. *Adv Mater*. 2022;34(15):2110054. doi: 10.1002/adma.202110054
17. Wang M, Li W, Hao J, et al. Molecularly cleavable bioinks facilitate high-performance digital light processing-based bioprinting of functional volumetric soft tissues. *Nat Commun*. 2022;13(1):3317. doi: 10.1038/s41467-022-31002-2
18. Kolesky DB, Homan KA, Skylar-Scott MA, Lewis JA. Three-dimensional bioprinting of thick vascularized tissues. *Proc Natl Acad Sci*. 2016;113:3179-3184. doi: 10.1073/pnas.1521342113
19. Han X, Courseaus J, Khamassi J, et al. Optimized vascular network by stereolithography for tissue engineered skin. *Int J Bioprint*. 2018;4(2). doi: 10.18063/ijb.v4i2.134
20. Fang Y, Ouyang L, Zhang T, Wang C, Lu B, Sun W. Optimizing bifurcated channels within an anisotropic scaffold for engineering vascularized oriented tissues. *Adv Healthc Mater*. 2020;9(24):2000782. doi: 10.1002/adhm.202000782
21. Margolis EA, Friend NE, Rolle MW, Alsberg E, Putnam AJ. Manufacturing the multiscale vascular hierarchy: progress toward solving the grand challenge of tissue engineering. *Trends Biotechnol*. 2023;41(11):P1400-1416. doi: 10.1016/j.tibtech.2023.04.003
22. Nascu I, Sebastia-Saez D, Chen T, Nascu I, Du W. Global sensitivity analysis for a perfusion bioreactor based on CFD modelling. *Comput Chem Eng*. 2022;163:107829. doi: 10.1016/j.compchemeng.2022.107829
23. Capuana E, Pavia FC, Lombardo ME, et al. Mathematical and numerical modeling of an airlift perfusion bioreactor for tissue engineering applications. *Biochem Eng J*. 2021;178:108298. doi: 10.1016/j.bej.2021.108298
24. Zhu X, Chen F, Cao H-Q, Li L, He N, Han X. Design and fused deposition modeling of triply periodic minimal surface scaffolds with channels and hydrogel for breast reconstruction. *Int J Bioprint*. 2023;9(2). doi: 10.18063/ijb.685
25. Allen JW, Bhatia SN. Formation of steady-state oxygen gradients in vitro: application to liver zonation. *Biotechnol Bioeng*. 2003;82(3):253-262. doi: 10.1002/bit.10569

26. Brown DA, MacLellan WR, Laks H, Dunn JCY, Wu BM, Beygui RE. Analysis of oxygen transport in a diffusion-limited model of engineered heart tissue. *Biotechnol Bioeng*. 2007;97(4):962-975.
doi: 10.1002/bit.21295

27. Yu P, Lee T-S, Zeng Y, Low HT. Fluid dynamics and oxygen transport in a micro-bioreactor with a tissue engineering scaffold. *Int J Heat Mass Transfer*. 2009;52:316-327.
doi: 10.1016/j.ijheatmasstransfer.2008.06.021

28. Mokhtari-Jafari F, Amoabediny G, Haghighipour N, et al. Mathematical modeling of cell growth in a 3D scaffold and validation of static and dynamic cultures. *Eng Life Sci*. 2016;16(3):290-298.
doi: 10.1002/elsc.201500047

29. Coletti F, Macchietto S, Elvassore N. Mathematical modeling of three-dimensional cell cultures in perfusion bioreactors. *Ind Eng Chem Res*. 2006;45:8158-8169.
doi: 10.1016/S1570-7946(06)80292-0

30. Nascu I, Sebastia-Saez D, Chen T, Du W. A combined computational-fluid-dynamics model and control strategies for perfusion bioreactor systems in tissue engineering. *IFAC-PapersOnLine*. 2021;54(3):324-329.
doi: 10.1016/j.ifacol.2021.08.262

31. Han X, Bibb R, Harris RA. Design of bifurcation junctions in artificial vascular vessels additively manufactured for skin tissue engineering. *J Vis Lang Comput*. 2015;28:238-249.
doi: 10.1016/j.jvlc.2014.12.005

32. Han X, Bibb R, Harris RA. Engineering design of artificial vascular junctions for 3D printing. *Biofabrication*. 2016;8(2):025018.
doi: 10.1088/1758-5090/8/2/025018

33. Nie J, Gao Q, Xie C, et al. Construction of multi-scale vascular chips and modelling of the interaction between tumours and blood vessels. *Mater Horiz*. 2020;7:82-92.
doi: 10.1039/C9MH01283D

34. Soltani M, Maleki MA, Kaboodrangi AH, Mosadegh B. Optimization of oxygen transport within a tissue engineered vascular graft model using embedded micro-channels inspired by vasa vasorum. *Chem Eng Sci*. 2018;184:1-13.
doi: 10.1016/j.ces.2018.02.044

35. Poon C. Measuring the density and viscosity of culture media for optimized computational fluid dynamics analysis of in vitro devices. *J Mech Behav Biomed Mater*. 2022; 126:105024.
doi: 10.1016/j.jmbbm.2021.105024

36. Haselgrove JC, Shapiro IM, Silverton SF. Computer modeling of the oxygen supply and demand of cells of the avian growth cartilage. *Am J Physiol*. 1993;265 2 Pt 1:C497-506.
doi: 10.1152/ajpcell.1993.265.2.C497

37. Acevedo CA, Weinstein-Oppenheimer CR, Brown DI, Huebner H, Buchholz R, Young ME. A mathematical model for the design of fibrin microcapsules with skin cells. *Bioprocess Biosyst Eng*. 2009;32:341-351.
doi: 10.1007/s00449-008-0253-1

38. McMahon D, Anderson PA, Nassar R, et al. C2C12 cells: biophysical, biochemical, and immunocytochemical properties. *Am J Physiol*. 1994;266 6 Pt 1:C1795-802.
doi: 10.1152/ajpcell.1994.266.6.c1795

39. Schlie S, Gruene M, Dittmar H, Chichkov BN. Dynamics of cell attachment: adhesion time and force. *Tissue Eng Part C, Methods*. 2012;18(9):688-696.
doi: 10.1089/ten.tec.2011.0635

40. Ricotti L, Taccola S, Pensabene V, et al. Adhesion and proliferation of skeletal muscle cells on single layer poly(lactic acid) ultra-thin films. *Biomed Microdevices*. 2010;12:809-819.
doi: 10.1007/s10544-010-9435-0

41. Zhou B, Yang B, Liu Q, et al. Effects of univariate stiffness and degradation of DNA hydrogels on the transcriptomics of neural progenitor cells. *J Am Chem Soc*. 2023;145(16): 8954-8964.
doi: 10.1021/jacs.2c13373

42. Jarrett AM, Lima EABF, Hormuth DA, et al. Mathematical models of tumor cell proliferation: a review of the literature. *Expert Rev Anticancer Ther*. 2018;18:1271-1286.
doi: 10.1080/14737140.2018.1527689

43. Kim K, Dean D, Mikos AG, Fisher JP. Effect of initial cell seeding density on early osteogenic signal expression of rat bone marrow stromal cells cultured on cross-linked poly(propylene fumarate) disks. *Biomacromolecules*. 2009;10(7):1810-1817.
doi: 10.1021/bm900240k

44. Yin J, Yan M, Wang Y-c, Fu J, Suo H. 3D bioprinting of low-concentration cell-laden gelatin methacrylate (GelMA) bioinks with a two-step cross-linking strategy. *ACS Appl Mater Interfaces*. 2018;10(8):6849-6857.
doi: 10.1021/acsami.7b16059

45. Cámara-Torres M, Sinha R, Mota C, Moroni L. Improving cell distribution on 3D additive manufactured scaffolds through engineered seeding media density and viscosity. *Acta Biomater*. 2020;101:183-195.
doi: 10.1016/j.actbio.2019.11.020

46. Su J, Hua S, Chen A, et al. Three-dimensional printing of gyroid-structured composite bioceramic scaffolds with tuneable degradability. *Biomater Adv*. 2022;133: 112595.
doi: 10.1016/j.msec.2021.112595

ACCSCIENCE PUBLISHING

International Journal of Bioprinting

RESEARCH ARTICLE

3D-bioprinted hydrogels with instructive niches for dental pulp regeneration

Nazi Zhou[1], Shunyao Zhu[1], Xinlin Wei[2], Xueyuan Liao[1], Yu Wang[1], Yue Xu[1], Liyun Bai[1], Haoyuan Wan[1], Li Liu[1], Jiumeng Zhang[3], Ling Zeng[4], Jie Tao[1]*, and Rui Liu[1]*

[1]Department of Stomatology, Daping Hospital, Army Medical University (The Third Military Medical University), Chongqing, China

[2]College of Materials Science and Engineering, Sichuan University, Chengdu, China

[3]Chongqing Key Laboratory of Natural Product Synthesis and Drug Research, School of Pharmaceutical Sciences, Chongqing University, Chongqing, China

[4]Department of Trauma Medical Center, Daping Hospital, State Key Laboratory of Trauma, Burns and Combined Injury, Army Medical University, Chongqing, China

(This article belongs to the *Special Issue: Special Issue of International Journal of Bioprinting in the BDMC 2023 Conference*)

Abstract

Infections to dental pulp commonly result in pulpitis and pulp necrosis, and surgical removal of the infected tissues is the only therapeutic approach. Dental pulp injury remains a challenging medical issue due to the limited regenerative capability of dental pulp. In this work, a dental pulp guidance construct (DPGC) with the instructive niche was bioprinted to mimic native teeth for dentin and neovascular-like structure reconstruction. GelMA-Dextran aqueous emulsion was used as an ink for *in situ* printing of porous DPGC to induce predominant nuclear localization of Yes-associated protein (YAP) in the encapsulated dental pulp stem cells (DPSCs) and enhance their stemness properties. Furthermore, the DPSCs encapsulated in DPGC with microporous structures exhibited enhanced viability, migration, and spreading. Meanwhile, we found that DPGC could promote capillary tube formation and induce neurogenesis. In a mouse subcutaneous implant model, the DPGC consisted of porous structures, such as odontoblasts and newly formed vascular structures, that mimic dental pulp characteristics. This study demonstrated a new strategy to design DPGC with instructive niche for dental pulp regeneration, presenting a potential treatment alternative to root canal therapy.

Keywords: Dental pulp guidance construct; Dental pulp stem cells; Porous hydrogel; Dental pulp regeneration

***Corresponding authors:**
Jie Tao
(taojietanker@sina.com)

Rui Liu
(liurui123@tmmu.edu.cn)

Citation: Zhou N, Zhu S, Wei X, et al. 3D-bioprinted hydrogels with instructive niches for dental pulp regeneration. *Int J Bioprint*. 2024;10(3):1790.
doi: 10.36922/ijb.1790

Received: September 11, 2023
Accepted: December 21, 2023
Published Online: February 5, 2024

Copyright: © 2024 Author(s). This is an Open Access article distributed under the terms of the Creative Commons Attribution License, permitting distribution, and reproduction in any medium, provided the original work is properly cited.

Publisher's Note: AccScience Publishing remains neutral with regard to jurisdictional claims in published maps and institutional affiliations.

1. Introduction

Dental pulp injury—a common outcome of trauma or bacterial infection affecting caries—emerges as a pressing medical issue with far-reaching consequences, including loss of nourishing dentin and sensing external stimuli.[1] In 2006, more than 400,000 patients in the USA were diagnosed with dental pulp disease and required to undergo removal of the diseased pulp or even the tooth.[2] Root canal treatment (RCT) is a standard

clinical therapy for dental pulp disease, encompassing pulpectomy and inorganic materials filling into the canals.[3] Usually, the tooth becomes brittle and easily fractures after RCT, setting the stage for reinfections and tooth loss eventually.[4,5]

Stem cell-based therapy has become a promising strategy in the field of tissue regenerative medicine.[6] In the field of dental pulp regeneration, vast studies have demonstrated the pulp-regenerative potential of stem cells, particularly for dental pulp stem cells (DPSCs).[7,8] The implanted DPSCs assist the dentin and neovascular-like structure reconstruction by differentiating into odontoblasts and secreting growth factors.[9] Yet, delivery of DPSCs in the absence of an instructive microenvironment presents limited efficacy due to the low cell retention, poor graft survival, and non-maintenance of a pro-regenerative mechanical property. The delivery of DPSCs on hydrogels that are hydrophilic three-dimensional (3D) polymer networks can replicate the extracellular matrix to alter cell behavior, such as proliferation, spreading, and paracrine activity, which are essential for pulp tissue regeneration.[10,11] Despite substantial advancements in past decades, biomaterials available for this purpose are still limited. Also, a research platform that can promote DPSCs-mediated pulp tissue regeneration has yet to be developed.

Continuous production of cell and bioactive factors hinges on two significant properties of transplanted stem cells: self-renewal and the capability to produce differentiated progenies by biophysical or biochemical stimulations.[12,13] Utilizing stem cells with these unique properties to repair diseased tissues has attracted extensive attention. However, in the long-term *in vitro* culture process, stem cells gradually lose the capacity of self-renewal and differentiation, resulting in the weakening of stemness. To maintain and facilitate stemness, the chemical/physical signals (e.g., melatonin, hypoxia, hepatocyte growth factor, and nanoparticle) can be added to tune the stemness of the cultured stem cells for regenerative medicine.[14,15] The porous structure could provide favorable space to promote the metabolism of substances and improve the bioactivity of stem cells, thus enhancing the differentiation potentials of stem cells.[16] Recently, Yuan et al. showed that GelMA-based cryogel microspheres with porous structure favored stemness maintenance of mesenchymal stem cells, compared to original bulk hydrogel microspheres.[17] Furthermore, Ying et al. also demonstrated that the mesenchymal stem cells encapsulated in the 3D-bioprinted porous hydrogels showed obvious superiority in osteogenic differentiation under the differentiation condition, demonstrating the capacity of porous structure in maintaining the stemness of encapsulated stem cells.[18] Moreover, enabling the spheroid of stem cells can also realize enhanced stemness maintenance. Guo et al. found that muse cell spheroid fabricated by the dynamic rotary cell culture system displayed a higher differentiation ratio than those in the static group.[19] *In vivo* testing revealed that muse cell spheroid reduced the severity of corneal inflammation and neovascularization, thus preventing the corneal scarring of stem cell-based therapy. However, the additives in the implants not only influence the stemness of the encapsulated stem cells, but also can be released into surrounding tissues and may cause adverse side effects. Meanwhile, it is critical to maintain the concentration of the additives to promote stemness. Although the functional scaffolds with the property of promoted stemness have proven effective in promoting regeneration of tissues such as bone,[17] skin,[20] and nerve,[21] their application in dental pulp repair remains limited.

Digital light processing (DLP)-based 3D bioprinting technology has emerged as a powerful tool to engineer customized tissues in the fields of biomedicine, tissue engineering, and regenerative medicine.[22-24] In this study, a dental pulp guidance construct (DPGC) with an instructive niche to maintain and facilitate the stemness of the encapsulated DPSCs was bioprinted for dental pulp regeneration (Figure 1). The gelatin methacryloyl (GelMA)-Dextran mixture solution led to an aqueous emulsion, in which dextran solution dispersed into spheroids within the GelMA solution. After bioprinting of the GelMA phase, the dextran was removed by diffusion into incubation media, resulting in a porous structure. *In vitro* studies demonstrated that the bioprinted DPGC with microporous structure enhanced the stemness properties of encapsulated DPSCs and facilitated Yes-associated protein (YAP) nuclear localization. Moreover, we also studied the biological properties of DPGC in promoting pulp regeneration potential of DPSCs *in vitro*. The results revealed that our DPGC could promote the proliferation, spreading, and migration of the encapsulated DPSCs. Meanwhile, the DPSCs with facilitated stemness could enhance the reconstruction of vascular networks and induce neurogenesis. In the subcutaneous implantation model of mice, the DPGC replicated dentin and neovascular-like structure that mimics the native teeth *in vivo*. Taken together, our study provides an advanced strategy to design DPGC with the dental pulp-specific niche, which has great potential for dental pulp regeneration.

2. Materials and methods

2.1. Materials and chemicals

Materials used in this study include gelatin (Sigma Aldrich, St. Louis, MO, USA), methacrylic anhydride

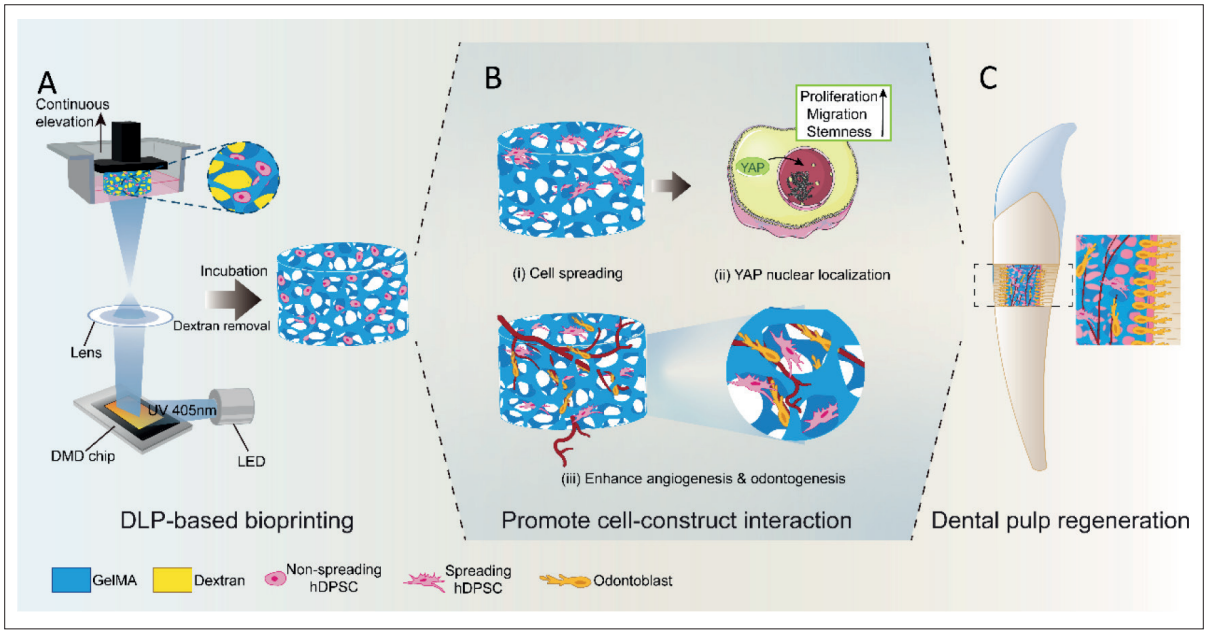


Figure 1. Schematic illustration. (A) The 3D-bioprinted DPGC was fabricated using DLP-based bioprinting technique. (B) The 3D-bioprinted DPGC with highly hierarchical, interconnected pores could promote cell–construct interaction, including (i) facilitating cell spreading; (ii) improving the proliferation, migration and stemness of hDPSCs via YAP nuclear location; and (iii) enhancing angiogenesis and odontogenesis. (C) Consequently, more persistent hDPSCs respond to the regulation of the highly hierarchical, interconnected porous structure to facilitate dental pulp regeneration.

(Sigma Aldrich, St. Louis, MO, USA), dextran (average Mw = 500,000; J&K Scientific, Beijing, China), phosphate-buffered saline (PBS; Sangon Biotech, Shanghai, China), alpha-Minimum Essential Medium (α-MEM; VivaCell, Shanghai, China), fetal bovine serum (FBS; Gibco, Waltham, MA, USA), penicillin–streptomycin (P/S; VivaCell, Shanghai, China), collagenase type I (Solarbio, Beijing, China), dispase II (Solarbio, Beijing, China), trypsin-EDTA (VivaCell, Shanghai, China), Endothelial Growth Medium-2 (EGM-2, Lonza, Basel, Switzerland), Cell Counting Kit-8 (CCK-8, MCE, New Jersey, USA), Live/Dead assay kit (KeyGEN BioTECH, Jiangsu, China), Alexa Fluor 488 Phalloidin (Thermo Fisher, Waltham, MA, USA), iFluor 555 Phalloidin (Abcam), 4',6-diamidino-2-phenylindole (DAPI; Thermo Fisher, Waltham, MA, USA), and 4% paraformaldehyde (PFA; Boster, Wuhan, China). Gelatin methacryloyl (GelMA) and lithium phenyl-2,4,6-trimethyl-benzoylphosphinate (LAP) were synthesized according to procedures described in a previous study.[23]

Animals utilized in this study were purchased from Charles River Laboratories (Beijing, China). Balb/C-NU mice were acclimatized to the environment of the animal facility for at least 7 days prior to the experiments. The animal experimental procedures were approved by the Institutional Animal Care and Use Committee (IACUC) of the Army Medical University (AMUWEC20212172).

2.2. Cell isolation and culture

2.2.1. Isolation and culture of human dental pulp stem cells (hDPSCs)

This study was approved by the institutional review boards of Daping Hospital, Third Military Medical University. As described previously,[10] human dental pulp tissues were isolated from the extracted healthy permanent teeth after obtaining informed consent of donors (aged 18–25 years). The isolated dental pulp tissues were rinsed repeatedly with PBS, and then digested in 3 mg/mL collagenase type I and 4 mg/mL dispase II for 30 min at 37°C in a humidified atmosphere containing 5% CO_2. Subsequently, digested hDPSCs were cultured in α-MEM medium supplemented with 10% FBS and 1% P/S. At a confluence of 80%, human dental pulp stem cells (hDPSCs) were trypsinized with trypsin-EDTA and subcultured. hDPSCs of passages 3–6 were used in subsequent studies. About 10 days after the dental pulp tissue culture, hDPSCs were completely expanded in culture flasks and maintained mesenchymal morphology during passage (Figure S3A in Supplementary File).

2.2.2. Human umbilical vein endothelial cells (HUVECs) culture

Human umbilical vein endothelial cells (HUVECs) were purchased from Procell (China) and expanded in EGM-2. Cells of passages 3–6 were used in the experiments.

2.3. Flow cytometry

For identification of specific cell-surface molecules, hDPSCs were trypsinized and subsequently incubated with anti-CD3, anti-CD31, anti-CD34, anti-CD73, and anti-CD105 (1:100 dilutions; BioLegend, San Diego, CA, USA) antibodies on ice for 30 min. Cell populations were resolved on a NovoCyte Flow cytometer (ACEA Biosciences, San Diego, CA, USA).

In flow cytometric analyses (Figure S3B in Supplementary File), the obtained hDPSCs were positive for the putative mesenchymal stem cell markers, CD73 (99.99%) and CD105 (99.86%), but negative for T-cell marker CD3 (0.01%), and hematopoietic stem cell marker CD31 (8.7%) and CD34 (0.09%). In summary, these results exhibited that the isolated hDPSCs were of mesenchymal origin and had stem cell characteristics.

2.4. Preparation of the emulsion ink

To fabricate DPGC, an aqueous emulsion was prepared by gently mixing 15% w/v GelMA solution with different concentrations of dextran solution. Briefly, the LAP (0.5% w/v) and lyophilized GelMA (15% w/v) were dissolved in PBS solution at 60°C for 30 min. The dextran powder was dispersed in the PBS solution with different final concentrations of 1%, 2%, 3%, 4%, 5%, 10%, and 15%. Then, the GelMA solution and the dextran solution were mixed in a predefined volume ratio of 2:1 to generate the GelMA-Dextran emulsion,[25] which was sterilized with 1 mL syringe and filters (0.22 μm in pore size) at 37°C.

2.5. Physicochemical characterization of the emulsion ink

To observe the microstructure of the porous constructs, the 3D-printed DPGCs were labeled with rhodamine and observed under confocal laser scanning microscopy (CLSM; TCS SP8, Leica, Wetzlar, Germany). The dextran drop size was analyzed by ImageJ software. The mechanical properties of the ultraviolet (UV)-curing cylindrical hydrogel constructs were tested with a mechanical testing machine (Model 5576, Instron Instruments, Boston, MA, USA) in compression mode at room temperature until 50% of the sample was deformed. The micromorphology of the 3D-printed DPGCs in their dehydrated state was observed by means of scanning electron microscopy (SEM; Inspect F, Waltham, MA, USA) to determine their pore distribution and size. DPGCs were washed three times with PBS and then dehydrated with graded ethanol solutions (35%, 50%, 65%, 80%, 95%, and 100% ethanol/water ratio) for 1 h each. The samples were critically dried and subsequently sputter-coated with gold before being scanned.

To test the size stability of the swollen DPGC with complex structure, constructs with honeycomb structure were printed using 3D printer, and emulsion inks of different formulations were prepared as follows: 15% GelMA, 15% GelMA + 5% dextran, 15% GelMA + 10% dextran, and 15% GelMA + 15% dextran. The 3D bioprinting of DPGC was performed using a DLP-based printing system as shown in Figure 1. This DLP-based bioprinter consisted of a computer-based control system, a 405 nm UV light source, a digital micromirror device (DMD) chip for optical patterning, a projection lens assembly, and a build plate for continuous elevation. The DPGCs were crosslinked by UV exposure (405 nm, 10 s) and then incubated at 37°C in PBS solution. Optical microscopy (Olympus, Tokyo, Japan) was used to image the constructs after 0 h, 2 h, and 24 h of incubation.

2.6. Fabrication of 3D-bioprinted hDPSCs-laden DPGC

For cell encapsulation, hDPSCs were trypsinized and mixed with GelMA pre-gel solution (15%, containing 0.5% LAP). Then, bioink in the DPGC group was prepared by mixing dextran solution with pre-gel GelMA solution in a volume ratio of 1:2. Next, the 3D-bioprinted microporous hydrogel constructs were fabricated using the DLP-based bioprinter mentioned in section 2.5. The bulk GelMA constructs in the control group were 3D-bioprinted using only GelMA pre-gel solution and the same DLP-based bioprinter. The cell-laden DPGC or bulk constructs were immersed in PBS to remove the LAP and were cultured in a humidified incubator.

2.7. Evaluation of cell pluripotency

In order to explore the effect of 3D-bioprinted DPGC on the pluripotency of hDPSCs, hDPSCs were separately encapsulated in the 3D-bioprinted DPGCs or bulk hydrogel constructs and placed into 12-well plates, while those directly seeded on the tissue culture plates (TCPs). The 3D-bioprinted hDPSCs-laden constructs were cultured in complete medium for 3 and 5 days. In the TCP group, hDPSCs were cultured in a complete medium and grew to a confluence of 70–80%.

Afterward, the total cellular RNA for each sample was extracted using the Trizol method (Takara, Shiga, Japan). Reverse transcription was conducted to synthesize cDNA using the Prime Script™ RT reagent Kit with gDNA Eraser (Takara) according to the manufacturer's instructions. cDNA templates from genes of interest were then amplified and quantified by quantitative real-time polymerase chain reaction (qPCR/RT-PCR) using the TB Green Premix Ex Taq™ II (Takara). The qPCR was performed to examine the expression of pluripotent genes on a CFX96 real-time PCR system (Bio-Rad Laboratories, Hercules, California, USA) using the following program: 95°C for 30 s, followed by 40 cycles at 95°C for 10 s and 60°C for 30 s. The housekeeping

gene *GAPDH* was used as the endogenous control. Changes in gene expression were measured using the $2^{-\Delta\Delta CT}$ method, and the final results were presented as fold change relative to the two-dimensional (2D) group. The primer sequences used are listed in **Table S1** (Supplementary File). For validation, the experiment was repeated for at least three times.

2.8. Immunofluorescent staining of YAP

Immunofluorescent staining of YAP was performed for the hDPSCs encapsulated in the 3D-bioprinted constructs after 3 days of culture. The primary antibodies against YAP (1:100 dilutions; GeneTex, Irvine, CA, USA) were used, and the fluorescent signal of YAP was detected using CLSM.

2.9. Evaluation of odontogenesis

2.9.1. Odontogenic differentiation

For the odontoblastic differentiation assay, hDPSCs were separately encapsulated in 3D-bioprinted DPGC and bulk hydrogel constructs in 12-well plates, and directly seeded on the TCPs. The hDPSCs-laden constructs were first cultured in a complete medium for 24 h for cell attachment. Afterward, the constructs were treated with odontogenic media (Cyagen Biosciences, Guangzhou, China) for 7 and 14 days.

2.9.2. Alkaline phosphatase (ALP) activity

Alkaline phosphatase (ALP) activity was detected using the Alkaline Phosphatase Assay Kit (Beyotime Institute of Biotechnology, Jiangsu, China) according to the manufacturer's protocol. Briefly, the 3D-bioprinted cell-laden hydrogel constructs were homogenized in GelMA lysis buffer (EFL) at 37°C for 30 min. Lysate was centrifuged at 1000 rpm at room temperature for 5 min. After removal of the supernatants, the deposits were lysed with RIPA buffer without the inhibitors (Beyotime Institute of Biotechnology) on ice for 1 h. Lysates were centrifuged at 1000 rpm at 4°C for 5 min. The supernatant was obtained for ALP assay using p-nitrophenyl phosphate (p-NPP) as a phosphatase substrate and alkaline phosphatase standard supplied with the kit. The absorbance was measured at 405 nm, and the amount of ALP in the cells was normalized against total protein content. The total protein amount was quantified using an Enhanced BCA Protein Assay Kit (Beyotime Institute of Biotechnology) in adherence with the manufacturer's instructions.

2.9.3. Gene expression analysis

After 7 and 14 days of culture, qPCR was performed to measure the expression of dentin-related genes, such as *ALP*, *RUNX2*, *OCN*, *OPN*, and *DSPP*, for hDPSCs in different groups based on the protocols provided in section 2.7. The experiments were repeated 3 times. Primer sequences used for qPCR are listed in Table S1 (Supplementary File).

2.10. Cell viability assay

The viability of encapsulated cells in the 3D-bioprinted hydrogel constructs *in vitro* was examined by Live/Dead assay.[26] Briefly, the hDPSCs-laden DPGC or bulk hydrogel constructs were cultured in 6-well plates (Corning Inc., Kennebunk, ME, USA) and maintained in full culture medium for different durations (1, 5, and 7 days). Before the examination, the constructs were immersed in the calcein acetoxymethyl ester (calcein-AM) and propidium iodide (PI) reagent following the manufacturer's instructions, and were visualized using fluorescent microscopy.

The viability of cells in the constructs was examined on a mouse subcutaneous implantation model. hDPSCs were encapsulated in the 3D-bioprinted DPGC or bulk hydrogel constructs and implanted subcutaneously into 3-week-old immunodeficient mice. The samples were harvested on days 7 and 14 after implantation. Then, these samples were immediately fixed in 4% PFA for 24 h, embedded in paraffin blocks, and sectioned at a thickness of 5–10 μm. Paraffin tissue sections were deparaffinized in xylene and rehydrated through graded ethanol solutions. Finally, the sections were stained with hematoxylin–eosin (H&E; Sigma Aldrich, St. Louis, MO, USA) according to the manufacturer's instructions.

2.11. Cell proliferation assay

The proliferation of hDPSCs encapsulated in the 3D-bioprinted hydrogel constructs was examined using Cell Counting Kit-8 according to the manufacturer's instructions. Briefly, the 3D-bioprinted hDPSCs-laden DPGC or bulk constructs were cultured in 12-well plates and maintained in complete culture medium for different durations (1, 5, and 7 days). Before examination, the hDPSCs-laden constructs were incubated with CCK-8 reagent at 37°C for 2.5 h. The absorbance at 405 nm was detected with the spectrophotometer (BioTek Instrumentals, Winooski, VT, USA) on days 1, 5, and 7 after culture.

2.12. Cell migration assay

Cell migration assay was performed in a 6.5 mm transwell with 8.0 μm pore polycarbonate membrane inserts in a 24-well format (Corning Inc.). The 3D-bioprinted hDPSCs-laden DPGC or bulk constructs were placed into the upper chambers of transwell plates and cultured in serum-free medium. The lower chambers were filled with 10% FBS. The samples were incubated at 37°C for 7 days, and then washed with PBS. After fixation with 4% PFA and staining with crystal violet (BBI, Shanghai, China), hDPSCs of each filter were counted in five random regions from three

replicates of each group under an optical microscope (200× magnification; Olympus), and the data were analyzed using ImageJ and GraphPad software.

2.13. Examination of cell spreading

To assess the spreading of the encapsulated cells within 3D-bioprinted DPGC or bulk hydrogel constructs on day 7 after culture, the samples were fixed and processed for immunofluorescent staining and SEM observation, respectively. The cytoskeleton and nuclei were counterstained with Alexa 488-phalloidin and DAPI, respectively, and imaged using CLSM. The cell spreading area was measured based on the acquired fluorescent images using ImageJ software.

2.14. Evaluation of angiogenesis

2.14.1. Collection of conditioned medium

For paracrine measurement, the 3D-bioprinted hDPSCs-laden DPGC and bulk hydrogel constructs were prepared in 24-well plates and maintained in complete culture medium for 7 days. Afterward, the supernatants were removed, and the culture medium was switched to serum-free α-MEM. The conditioned medium (CM) from the hDPSCs-laden constructs was collected 48 h later, centrifuged at 4°C at 3000 × g for 3 min followed by 1500 × g for 5 min, filtered through 0.22-μm filters, and stored in aliquots at -80°C.

2.14.2. Tube-formation assay

For the tube formation assay, HUVECs at a density of 2×10^4 cells/well were seeded in 96-well plates pre-coated with Matrigel (BD Biosciences, San Jose, CA, USA) and incubated with medium consisting of EGM-2 and CM (volume ratio of 2:1). After 6 h, HUVECs were fixed in 4% PFA and stained with iFluor 555-phalloidin, and the formed tubes were imaged under a fluorescence microscope (Olympus). The total number of branches, junctions, and nodes and total vessel length were measured based on three images randomly selected for each sample using ImageJ software.

2.15. Neurite extension

For paracrine measurement, the 3D-bioprinted rat dental pulp stem cells (rDPSCs)-laden DPGC and bulk hydrogel constructs were prepared in 24-well plates and maintained in complete culture medium for 5 days. Afterward, the supernatants were removed, and the culture medium was switched to serum-free medium. The CM from the rDPSCs-laden constructs were collected 48 h later, centrifuged at 4°C at 3000 × g for 3 min followed by 1500 × g for 5 min, filtered through 0.22-μm filters, and stored in aliquots at -80°C.

To evaluate the effect of DPGC on neurite extension, PC12 cells at a density of 1×10^4 cells/mL were seeded in 96-well plates and incubated in RPMI-1640 supplemented with 10% FBS for 24 h. Then, PC12 cells were cultured in the fresh culture medium containing 50% v/v CM. After 48 h, the cells were fixed in 4% PFA and stained with iFluor 555-phalloidin and DAPI. The stained PC12 cells were imaged in three randomly selected fields under a fluorescence microscope. Ten PC12 cells were randomly selected per field. Afterward, the neurite length of PC12 cells was measured using ImageJ software.[27]

2.16. Design and fabrication of the customized DPGC with microporous structures

The treated dentin matrix (TDM) was prepared based on an established protocol.[7] Briefly, the human TDMs were obtained from the extracted healthy premolars. Periodontal ligament tissues were carefully scraped away along with partial removal of the outer cementum, inner dental pulp tissue, and predentin. A high-speed air turbine handpiece was used to cut the root canal into pieces of about 5–6 mm in length. Next, the root canal pieces were concussed three times (5 to 6 min each time) by an ultrasonic cleaner before being further exposed to a series of decreasing EDTA solutions (17% for 5 min, 10% for 5 min, and 5% for 10 min) and washed with deionized water for 5 min (three times). TDMs were scanned using a Trios scanner (3 shapes) to obtain digital molds. According to the architectures of the TDM cavity, root canals were 3D-reconstructed using 3-matic software. Finally, customized DPGC matched the root canals of TDMs fabricated by the DLP-based bioprinter.

2.17. Implantation in an immunodeficient nude mouse model

TDMs were obtained from the mandible medial incisors of Sprague-Dawley rats and processed according to steps described in section 2.16, followed by a sterilization process. For subcutaneous implantation, the TDMs were filled with three groups of samples: (i) empty (n = 3), (ii) hDPSCs-laden bulk construct (n = 3), and (iii) hDPSCs-laden porous construct (n = 3). Ten microliters of mixture containing approximately 1×10^6 hDPSCs and GelMA-Dextran emulsion (15% GelMA, 0.01% LAP; 10% Dextran) were injected into TDMs and crosslinked by UV light for 30 s. For each mouse, TDMs from three different groups were inserted into the dorsal subcutaneous site of 3-week-old immunodeficient mice. Stent implantation was performed under deep anesthesia. After 8 weeks, the samples were collected and subjected to histological analysis.

2.18. Histology analysis and immunohistochemistry

The samples were fixed in 4% PFA for 24 h, decalcified in 10% EDTA (pH 7.0) for 4 weeks, and embedded in paraffin blocks. Samples were sectioned at 5–10 μm thickness. Paraffin tissue sections were deparaffinized in xylene and

rehydrated through graded ethanol solutions. Then, the sections were H&E-stained according to the manufacturer's instructions. For immunohistochemistry (IHC) staining, primary antibodies against dentin sialophosphoprotein (DSPP; Santa Cruz Biotechnology, Dallas, Texas, USA) and CD31 (Abcam) were used to evaluate the odontogenesis and angiogenesis. IHC images in each group were randomly captured at 20× magnification for quantitative measurement. DSPP- and CD31-positive expression rates were measured using Image J software.

2.19. Statistical analysis

Data are presented as the means ± SD from at least three independent experiments. Independent sample *t*-test and one-way analysis of variance (ANOVA) followed by Tukey's test were used for inter-group comparisons. Statistical significance was analyzed using GraphPad Prism 7 (GraphPad Software Inc., Boston, MA, USA). $P < 0.05$ was considered as a criterion of statistical significance.

3. Results

3.1. Characterization and optimization of DLP-based 3D-bioprinted DPGC

To assure the appropriate mechanical property of DPGC, 15% (w/v for all expressions unless otherwise indicated) GelMA solution was selected in this study as the base for all bioink formulations to be mixed with dextran solution in the volume ratio of 2:1.[25] In order to determine the proper concentration of dextran solution, the different size distributions of the dextran droplets in the GelMA-Dextran emulsion were visualized in confocal fluorescence field photographs (Figure 2Ai–iii and Figure S1 in Supplementary File). When the concentration of the dextran phase was lower than 5% in the mixture, phase separations were poorly formed; when the concentration of the dextran phase was higher than 15%, the inversion of the two phases occurred. Considering the structure stability of the microporous constructs, no statistical analysis was performed for the distribution of dextran droplets in the 15% dextran group. The average size (16.5 ± 0.7 μm) of the 5% dextran group was lower than that (49.1 ± 2.4 μm) of the 10% dextran group. The size distribution of the dextran droplets became more extensive, and the average size increased to 49.1 ± 2.4 μm as the concentration of dextran increased to 10% (Figure 2B). These data indicated that the pore size (the dextran droplet size) of the GelMA-Dextran emulsion could be optimized through this method to offer an advanced bioink for the subsequent 3D bioprinting procedure.

After the emulsions were photo-crosslinked by UV light, DPGC with a hierarchically microporous structure was prepared through a DLP-based 3D bioprinting process.[28] Compared to extrusion and inkjet printing, DLP-based printing could prevent the lysis of the encapsulated stem cells in hydrogels due to the high mechanical stresses caused by the nozzles, and also rescue the viability of encapsulated stem cells, which can be decimated due to prolonged printing in a line-by-line or drop-by-drop fashion.[29,30] Upon unconfined compression, DPGC showed a lower mechanical strain for a certain compression stress, compared with the bulk hydrogel (Figure 2C). For instance, under 50% deformation of the DPGCs before fracture, the average compression stress on bulk hydrogel constructs was 72.5 kPa, while the average stress on DPGCs was less than 39.8 kPa. In fact, the mechanical strengths of materials can be divided into macroscopic mechanical strength and microscopic contact strength. It should be noted that this experiment explored the macroscopic mechanical property, while mechanotransduction is mainly affected by mechanical cues from the surrounding microenvironment of cells at the microscale. Given the undiluted dextran phase and the same crosslinking degree, cells experienced the same microscopic mechanical properties of surrounding environments within DPGCs or bulk hydrogels. The shape stability evaluation demonstrated that, over the course of 2 h and 24 h, and then 48 h, the structural shape of the hydrogel constructs in all groups still retained its original form during the study (Figure 2D and Figure S2 in Supplementary File). Considering the pore size (dextran droplet size) and mechanical property of the DPGC, 10% concentration of dextran was chosen as the appropriate setting for the subsequent cell culture and *in vivo* experiments in the experimental group. The microscopic morphology of DPGC in the 10% dextran group was evaluated by using SEM. As shown in Figure 2E, DPGC exhibited a 3D hierarchical microporous sponge-like structure with highly interconnected micropores.

3.2. Stemness properties and YAP nuclear transduction of hDPSCs under the influence of 3D-bioprinted DPGC

Stemness properties play a pivotal role in the functions of stem cells, both *in vitro* and *in vivo*. Therefore, the pluripotent stem cell markers (OCT4, NANOG, and SOX2) of the hDPSCs cultured in DPGCs and bulk GelMA hydrogel constructs (control group) and on TCPs were evaluated. The expression levels of OCT4, NANOG, and SOX2 of hDPSCs encapsulated in DPGC significantly increased compared to that of the other two groups at 3 and 5 days (Figure 3A and B). In addition, the expression of OCT4, NANOG, and SOX2 increased in the DPGC and the control group, which exhibited a gradually increasing trend overall and peaked at day 5. These results

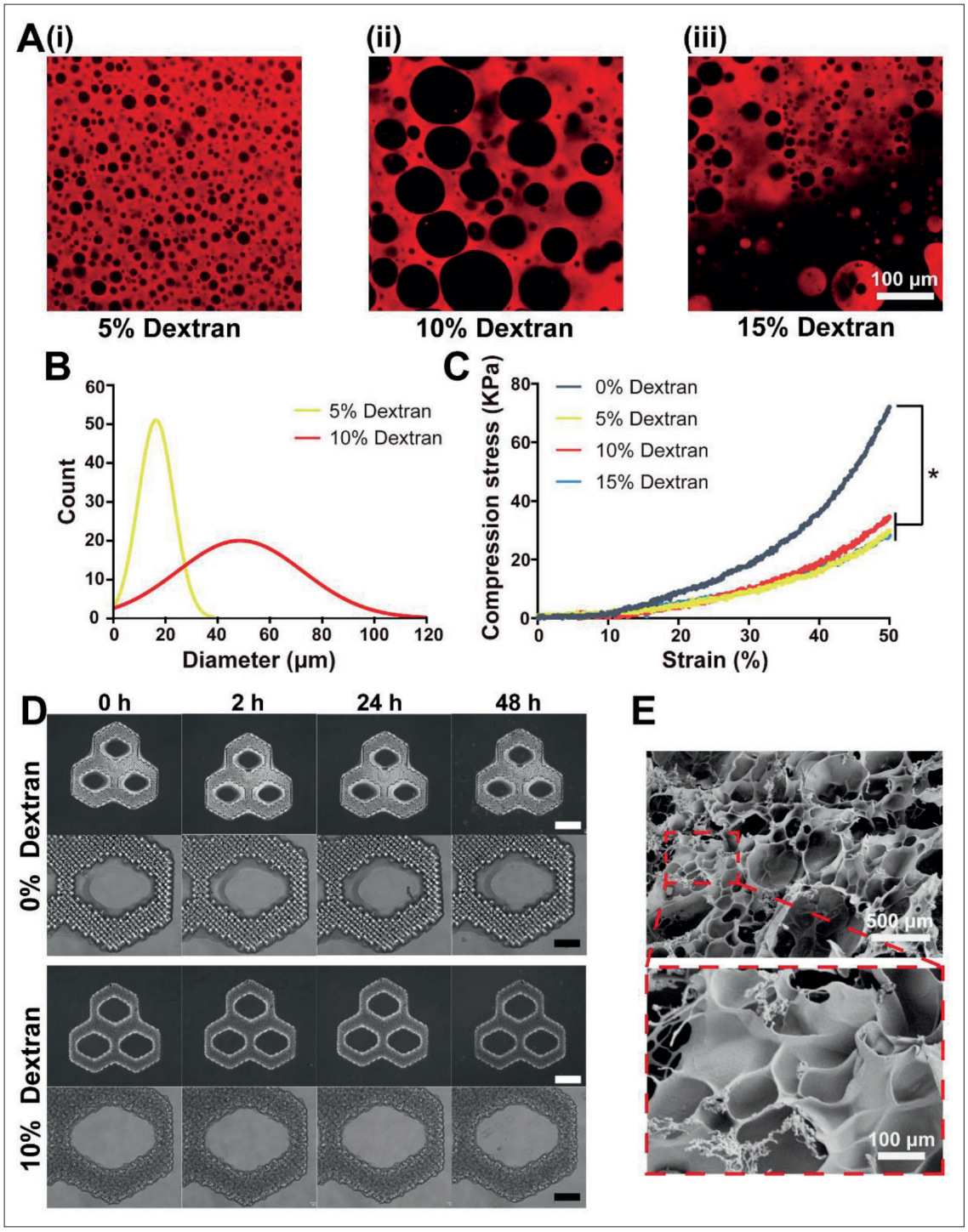


Figure 2. Characterization and optimization of the DLP-based 3D-bioprinted DPGC. (A) Fluorescence micrographs of the DPGC with different dextran concentrations at (i) 5%, (ii) 10%, and (iii) 15% w/v. (B) Pore size distribution of dextran droplets dispersed in the GelMA phase with different dextran concentrations at 5% and 10%. One hundred random droplets in each case were analyzed. (C) Stress–strain curves of the 3D-bioprinted DPGCs with different dextran concentrations at 5% and 10%, compared to bulk hydrogels with 0% dextran (*$p < 0.05$ for 0% dextran group vs. 5%, 10%, and 15% dextran group at specified strain points). (D) Micrographs showing size stability of 3D-printed DPGC with 10% dextran and the bulk hydrogel with 0% dextran during 48-h incubation. White scale bar: 500 μm; black scale bar: 200 μm. (E) SEM micrographs showing the 3D-printed DPGC with a dextran concentration of 10%.

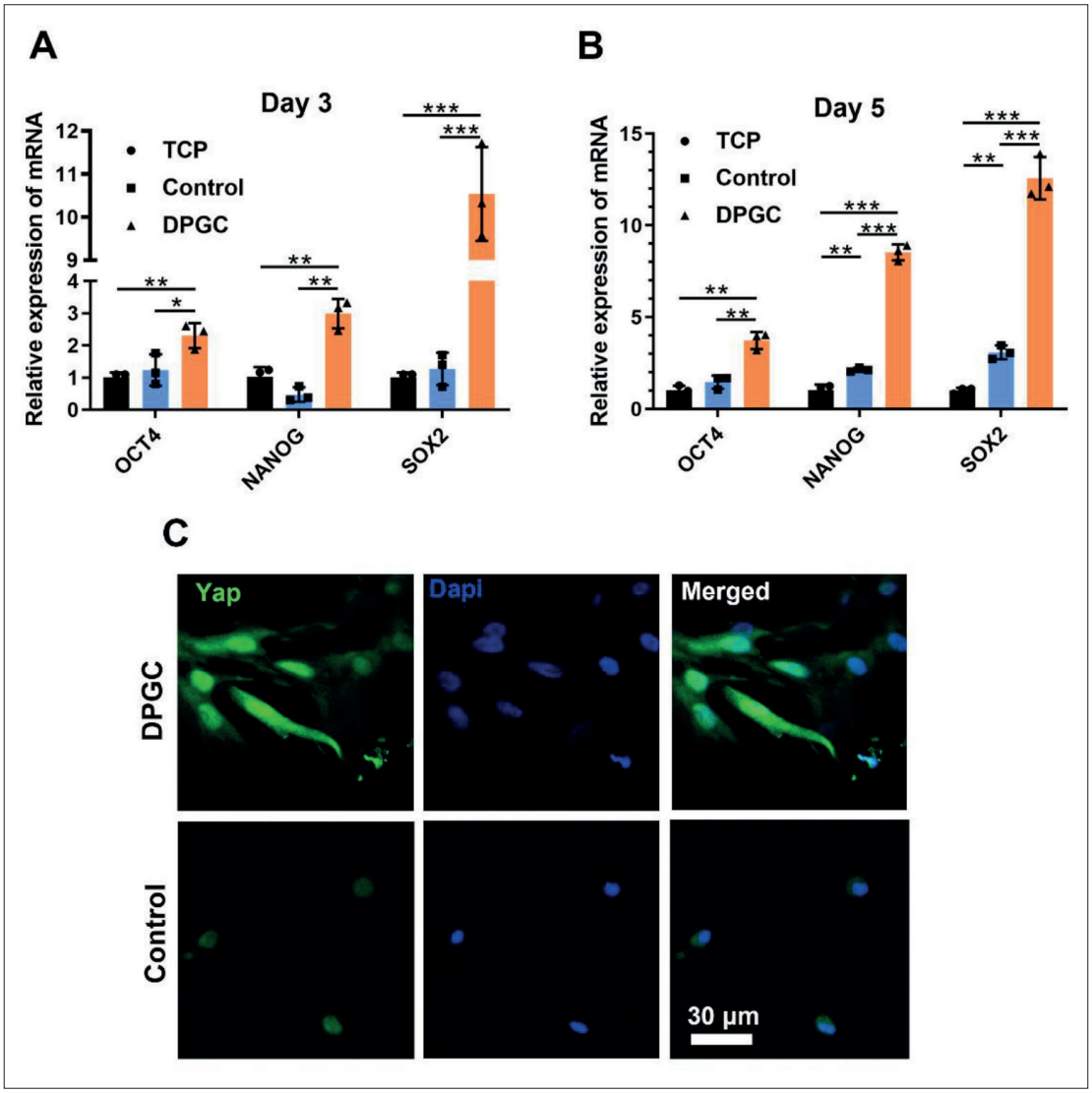


Figure 3. DLP-based 3D-bioprinted DPGCs enhance the pluripotency and YAP nuclear transduction of hDPSCs *in vitro*. (A, B) The pluripotency markers expression of hDPSCs encapsulated in DPGCs and bulk GelMA hydrogel constructs after being cultured for 3 and 5 days. *$p < 0.05$, **$p < 0.01$, ***$p < 0.001$. (C) Fluorescence micrographs of hDPSCs encapsulated in 3D-bioprinted DPGC were stained for YAP (green) and nuclei (blue).

corroborated that the hierarchy and interconnected porous structure favored the stemness maintenance of the hDPSC and promoted the differentiation potential of stem cells.

The spatial features of a material, including porous structures, could affect the cell behavior and orientation.[31-33] Several studies revealed that surface topography and spatial features could regulate cell behaviors through mechanotransduction signaling pathways.[34] Moreover, the YAP activity has recently been demonstrated to be related to the nuclear transduction of extracellular matrix (ECM) mechanical signals and to serve as an imperative contributor in cell fate determination, immunomodulation, and tissue regeneration.[35,36] Hence, the YAP activity and localization in hDPSCs encapsulated in 3D-printed DPGCs and bulk constructs were detected by immunofluorescent staining. As illustrated in Figure 3C, in the DPGC group, the accumulation of YAP protein in the nuclei was higher than that in the cytoplasm, whereas the YAP protein in the control group was uniformly distributed throughout the cytoplasm and nucleoplasm of hDPSCs. Our results are consistent with recent studies,[37,38] which indicate that YAP proteins are commonly expressed in the nuclei of porous constructs, highlighting the mechanosensitivity of YAP translocation to the tension of the actomyosin cytoskeleton. A growing line of evidence also supports the critical role of YAP translocation in regulating tissue regeneration.[36,39] Strikingly, the nuclear localization of YAP initiated direct

gene expression to support robust cell self-renewal and stimulate the secretion of regeneration-associated bioactive factors,[37,40] which is beneficial for dental pulp regeneration mediated by dental pulp stem cells.

To further analyze the aforementioned results, DLP-based 3D-bioprinted DPGCs were fabricated to evaluate the odontogenesis of hDPSCs cultured in an odontogenic induction medium. ALP plays a critical role in the early

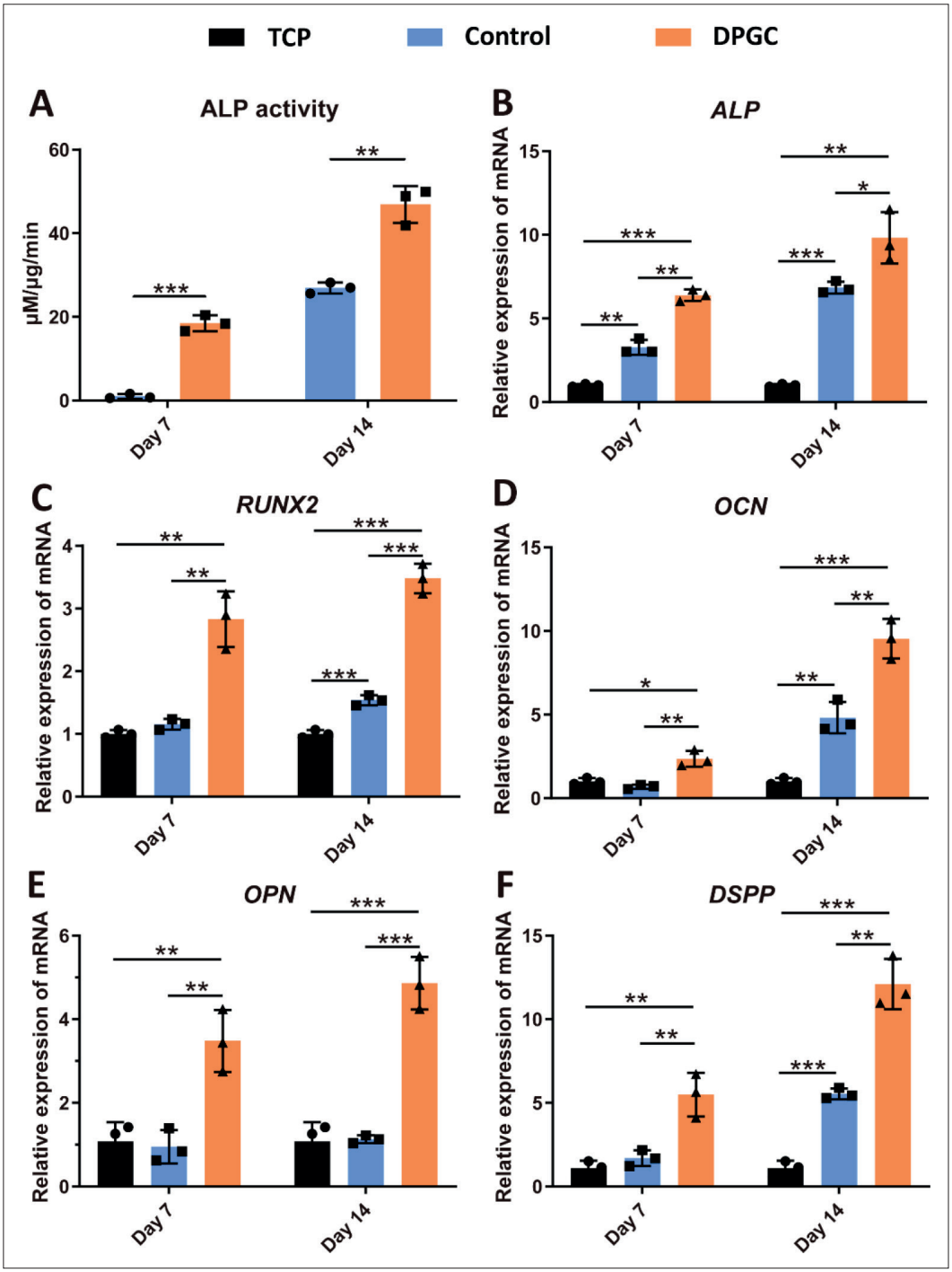


Figure 4. DLP-based 3D-bioprinted DPGCs improve the odontogenesis of hDPSCs *in vitro*. (A) ALP activity quantification and (B–F) odontogenesis-related gene expression of hDPSCs encapsulated in DPGCs and bulk GelMA hydrogel constructs after culturing for 7 and 14 days. $^{*}p < 0.05$, $^{**}p < 0.01$, $^{***}p < 0.001$.

phase of odontoblast differentiation. Figure 4A shows that substantial increases in ALP activity were noted both in the DPGC and control groups after 7–14 days of culture. There were significantly higher levels of ALP activity in the DPGC group on days 7 and 14. Furthermore, the expression of odontogenesis-related genes exhibited a similar increasing trend, as shown in Figure 4B–F. Although a slight decrease or increase in the gene expression levels of *RUNX2*, *OCN*, *OPN,* and *DSPP* of hDPSCs was observed in the control group at day 7 compared to the TCP group, no significant difference was noted for these genes. These results showed that the expression of all tested odontogenesis-related genes in the DPGC group gradually increased during culture period and peaked at day 14. These genes were prominently upregulated in hDPSCs of the DPGC group compared to those of the other two groups at different time points. In summary, these data indicate that the 3D-bioprinted DPGCs could enhance the differentiation potential of stem cells and promote hDPSCs differentiation into odontoblast-like cells, thereby displaying the superior capacity to induce odontogenesis through the hierarchically microporous structure.

3.3. Biological properties of 3D-bioprinted DPGC for promoting *in vitro* pulp regeneration potential of DPSCs

The hierarchical, interconnected porous structure provided an adequate nutrient supply to the encapsulated cell and a broad space for cell distribution, which was deemed to benefit cell survival, migration, and spreading.[41] To examine the biological properties of DPGC beneficial for promoting DPSCs, 3D-bioprinted DLP-based DPGCs were prepared *in vitro*. Since high cell viability was considered a precondition for successful bioprinted constructs in tissue regeneration, live/dead and biocompatibility assays were performed. As shown in Figure 5A, most of the hDPSCs were alive in both the DPGCs and bulk constructs (control group) after being incubated for 7 days. Interestingly, hDPSCs in the DPGC group aggregated and adhered along the inner surface of micropores to form a ring shape. In comparison, hDPSCs encapsulated in the bulk constructs were uniformly distributed. The result also indicated that there was no evident cytotoxicity in the dextran removal-based pore-creating process. Encapsulated stem cells might be protected from the physical forces in harsh

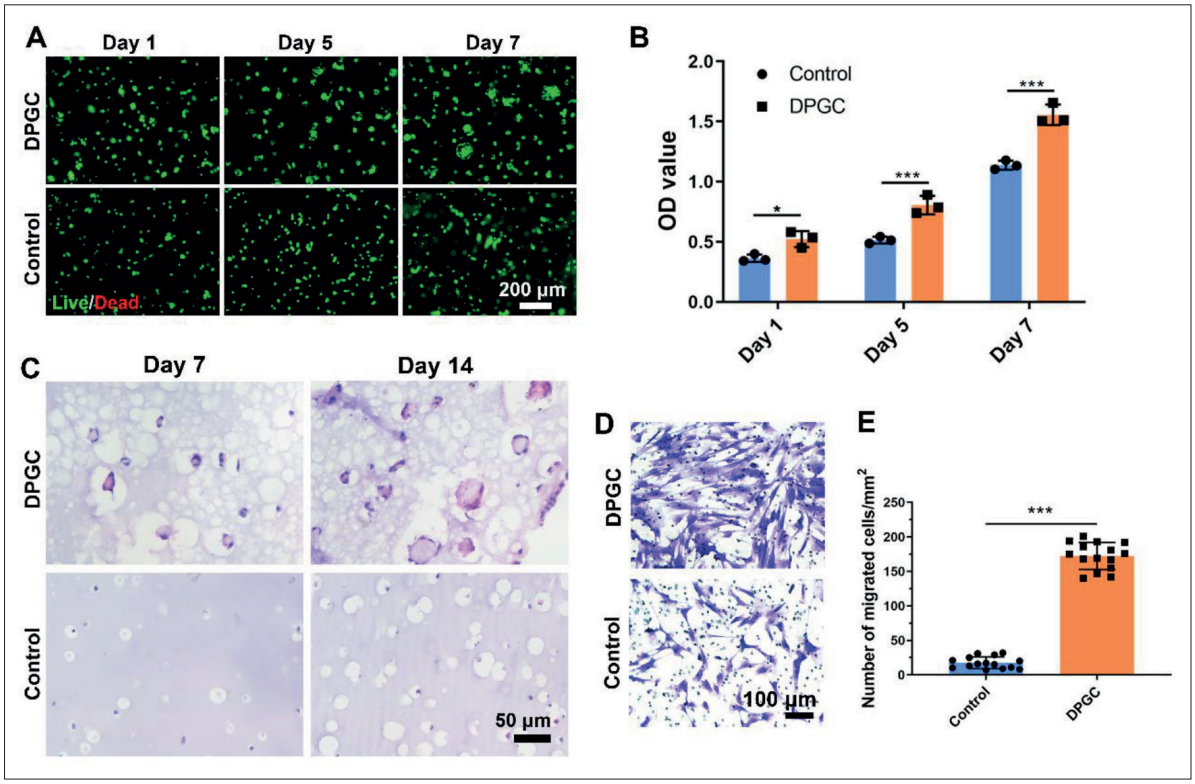


Figure. 5. Bioactivity of hDPSCs encapsulated in the DLP-based 3D-bioprinted DPGCs. Bulk GelMA hydrogel constructs were chosen as the control. (A) Fluorescence micrographs showing the viability of hDPSCs encapsulated in DPGC on days 1, 5, and 7, where live hDPSCs were stained in green and dead hDPSCs in red. (B) Quantification of the proliferation of hDPSCs within DPGC on days 1, 5, and 7 using the CCK-8 assay. $^{*}p < 0.05$, $^{***}p < 0.001$. (C) H&E staining of the DPGCs and control hydrogel constructs at days 7 and 14 post-implantation for biocompatibility evaluation. (D, E) Migration of hDPSCs encapsulated in DPGC assessed via transwell assay. $^{***}p < 0.001$.

environmental conditions.[42] In the preclinical evaluation of biocompatibility (Figure 5C), hDPSCs-laden DPGCs were implanted subcutaneously into immunodeficient mice. After 7 and 14 days of implantation, no inflammatory response, necrosis, or metaplasia was found within the constructs in both DPGC and control groups, demonstrating the high biosafety and biocompatibility of the GelMA hydrogel constructs. The *in vivo* results were also consistent with the *in vitro* findings, showing that the high viability and survival of hDPSCs in DPGC were promoted by the interconnected porous structures. Notably, in the DPGC group, hDPSCs adjacent to pores exhibited extended spread morphology, accompanied by the secretion of more ECM, implying an increase in cell proliferation and survival as well as spreading of the cultured hDPSCs. In addition, a CCK8 assay was conducted to evaluate the proliferation of hDPSCs encapsulated in DPGC. As a result, the optical density (OD) value in the DPGC group was significantly higher than that in the control group after 7 days of incubation (Figure 5B). Furthermore, the migration of hDPSCs encapsulated in the DPGCs or bulk GelMA hydrogel constructs was detected with a transwell assay. As shown in Figure 5D and E, the result suggested that the number of migrated hDPSCs in the DPGC group was approximately significantly 2.6-fold higher than that in the control group.

To investigate the spreading morphology of hDPSCs cultured in the microporous constructs, CLSM and SEM observations were performed. As shown in Figure 6A, hDPSCs encapsulated in DPGC displayed relatively more typical polygonal and stretched morphology. For hDPSCs in the control group, rounded shapes with few cellular protrusions were observed. Quantitative analysis of hDPSCs morphology demonstrated that the mean

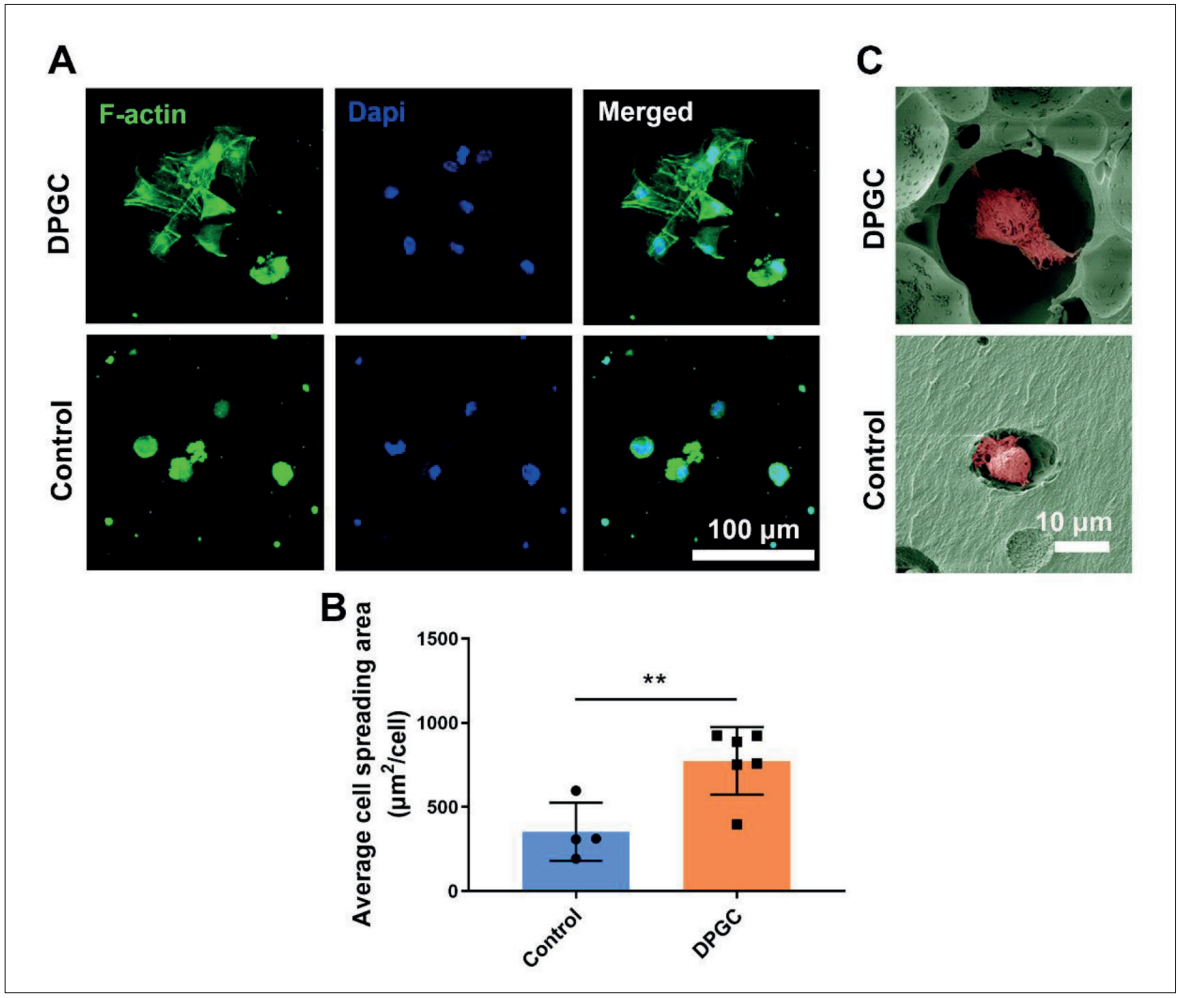


Figure 6. Cell morphology of hDPSCs encapsulated in the DLP-based 3D-bioprinted DPGCs. (A) Fluorescence images of spreading hDPSCs encapsulated in DPGC on day 7. Merged images integrate the fluorescence staining of F-actin (green) and nuclei (blue). (B) Calculated hDPSCs spreading areas on day 7. $^{**}p < 0.01$. (C) SEM images of spreading hDPSC encapsulated in DPGC on day 7.

spreading area in DPGC increased 2.2-fold compared to that in the bulk constructs (Figure 6B). The morphology of hDPSCs encapsulated in constructs was further evaluated by SEM. As shown in Figure 6C, similar to the fluorescent images, the SEM images show that the hDPSC adjacent to pores exhibited elongated and extended spread morphology, with relatively more cellular protrusions closely connecting to the microporous structure, whereas the hDPSC in the control construct maintained a near spherical morphology, giving rise to less intimate cell–construct interaction. As the main downstream effector of the Hippo signaling pathway, YAP mechanotransduction plays a vital role in a number of biological outcomes dictated by mechanical strains.[43-45] It was reported that YAP activity relies on actin cytoskeletal tension and regulates the fate of stem cells. In this study, the hydrogels made by a void-forming process not only provide a porous structure for cell spreading, but also exhibit stress relaxation. These mechanical cues increase YAP nuclear accumulation in the DPGC group, while confinement provided by dense hydrogel leads to YAP turn-off.

In short, hDPSCs encapsulated in the DPGCs through the DLP-based bioprinting process demonstrated increased cell growth, migration, and spreading. These results demonstrated that the biological properties of 3D-bioprinted hierarchical DPGC lend themselves to induce and support the behaviors of hDPSCs through their highly interconnected porous structure.

3.4. Pro-angiogenesis and neurogenesis evaluation of DPSCs-laden 3D-bioprinted DPGC *in vitro*

Rapid pro-angiogenesis is deemed as a precondition for dental pulp regeneration to support nutrient and oxygen exchange, recruitment of multiple cells, and circulating factor delivery.[43] Hence, the modulation and evaluation of angiogenesis are critical procedures for hDPSC-based therapies. Based on the above-mentioned finding of stemness properties and YAP in this study, the angiogenic effects of the hDPSC-encapsulated DPGCs and bulk GelMA hydrogel constructs were investigated (Figure 7A). *In vitro* tube formation experiment (Figure 7B–D) showed that the CM in the DPGC group exhibited a stronger ability to induce tubule formation in HUVECs. Specifically, the parameters of tubule formation (branches, junctions, nodes, and total length) showed similar trends, with the higher values detected in the DPGC group. For example, the total number of nodes of newly formed blood vessels was 254.7 ± 29.7 in the DPGC group, which was significantly higher than the number in the control group (118.8 ± 23.8).

Neurogenesis is considered one of the significant challenges in endodontic regeneration therapy.[46]. Studies have demonstrated the distinctive ability of DPSCs to secrete neurotrophic factors that regulate neurite outgrowth and neuroprotection.[47,48] Therefore, we further evaluated the neuroinductive capacity of DPSCs encapsulated in the 3D-bioprinted DPGC. PC12 cells (rat pheochromocytoma cells) were chosen in the study, as they possess neuron-like physiological properties.[49] PC12 cells displayed a distinctly neuron-like morphology with longer neurite elongation from the cell bodies in the DPGC group, as shown in Figure 8A. The length of the axon extending from the bodies of cells was further analyzed with ImageJ software (Figure 8B). In the DPGC group, PC12 cells exhibited significantly enhanced axonal outgrowth with the measured axon length of 106.0 ± 29.26 μm, compared to the control group (37.71 ± 15.54 μm), indicating that the CM in the DPGC group was more capable of inducing neurite elongation.

Overall, these results reflect that 3D-bioprinted DPGC possibly promotes cellular paracrine activity, formation of blood vessels, and rapid growth of axons through the hierarchical, interconnected porous structure.

3.5. *In vivo* pulp-like tissue regeneration promoted by 3D-bioprinted DPGC

Having an appropriate microstructure is one of the crucial features of tissue-engineered constructs.[23] Hydrogel constructs can be well designed and printed by a DLP-based printer to match tissue defects with complex shape, and offer an artificial extracellular matrix and proper macrostructural support to promote tissue regeneration.[50] We used digital scanned data of the TDM to fabricate the conformal DPGC with the microporous structure according to the irregular shape of root canal (TDM cavitary contour) using DLP-based 3D printer (Figure 9Ai–iii). As shown in Figure 9Aiv, after being inserted into the TDM to mimic the real environment of the root canal,[7] the 3D-printed DPGC was precisely matched with the irregularly shaped root canal of the TDM. Subsequently, the endodontic repair efficacy of DPGC was further explored *in vivo*. hDPSCs-laden DPGCs were combined with TDMs before subcutaneous implantation into immunodeficient mice for 8 weeks (Figure 9B). Based on the H&E staining images, dental pulp-like structures containing rich microvessel formation (black arrow) and an odontoblast-like layer (yellow triangle) can be found in the DPGC group (Figure 9C). In marked contrast, only a small amount of neotissue was observed near the open ends of the TDM combined with the bulk hydrogel construct (control group), and there was almost no soft tissue formed in the empty TDM group. Interestingly, unlike in the DPGC group, the neotissue mostly distributed at the open ends of the TDM and little neotissue was formed in

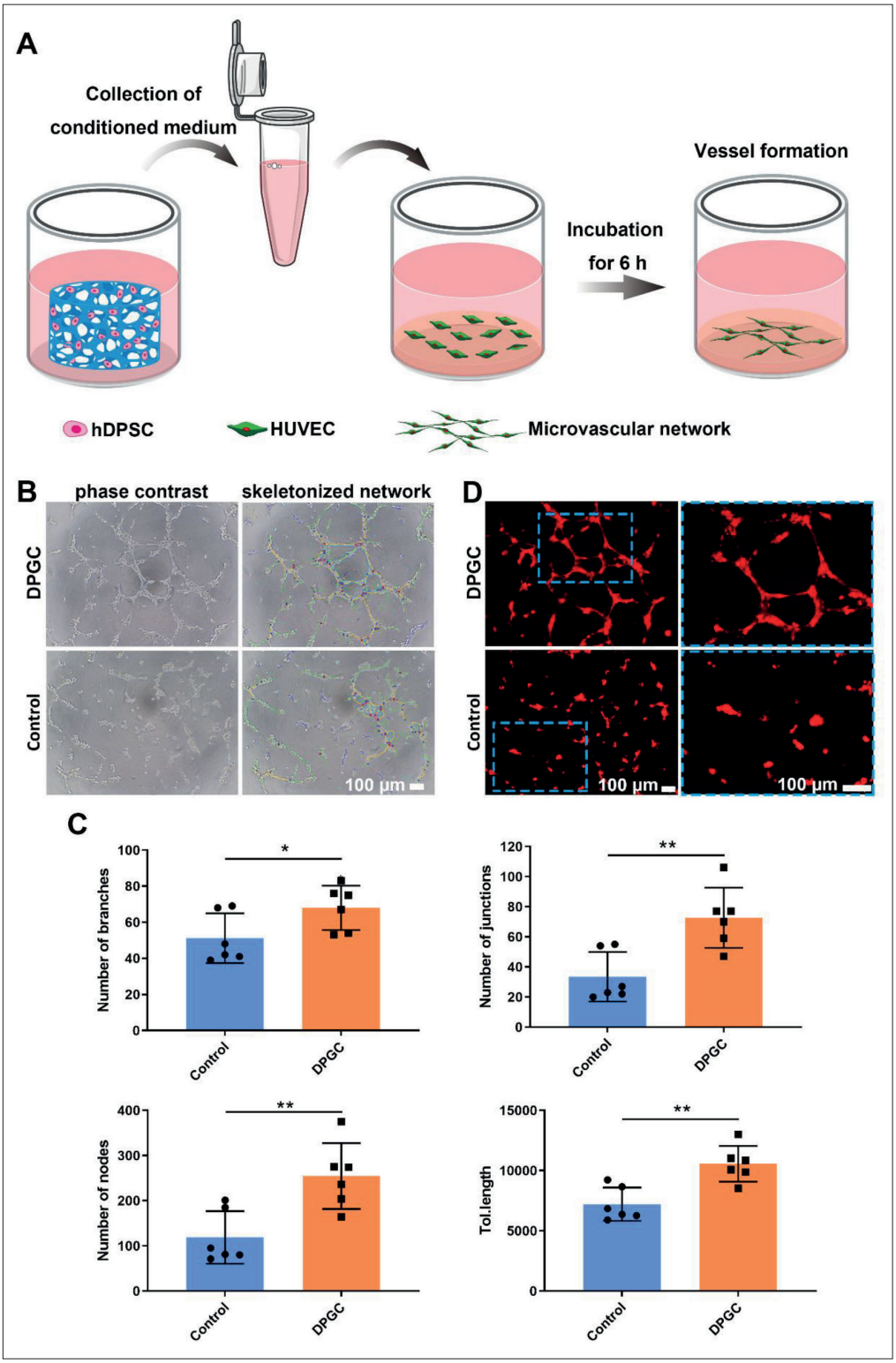


Figure 7. DLP-based 3D-bioprinted DPGCs enhance the angiogenesis capability of hDPSCs *in vitro*. (A) Schematic diagram of the tube-formation assay for examining the angiogenesis capability of hDPSCs. (B) Phase-contrast and analytical tube formation images of HUVECs incubated in different conditioned mediums. (C) Corresponding qualitative analysis of vascular network organization indexes, including branches, junctions, nodes, and total length. *p < 0.05, **p < 0.01. (D) Immunofluorescent tube formation images of HUVECs incubated in different conditioned media.

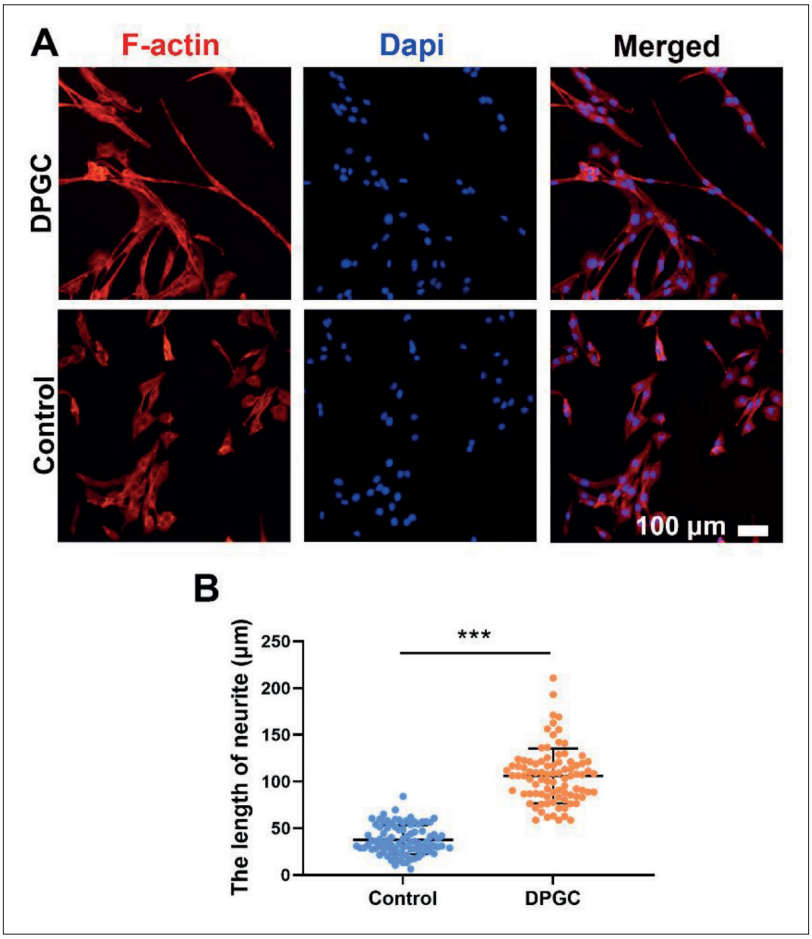


Figure 8. DLP-based 3D-bioprinted DPGCs enhance the neurogenesis capability of DPSCs *in vitro*. (A) Immunofluorescent images of neuronal cells induced in different conditioned media. (B) Corresponding quantitative analysis of the axon length of neuronal cells. ***$p < 0.001$.

the center zone in the bulk group, which led to a "hollow" TDM. This discrepancy could be attributed to the limited diffusion depth of oxygen, which is only 150–200 μm from the surface of the bulk constructs.[51] This limited diffusion depth of oxygen made the encapsulated cells located at the core of the bulk constructs more susceptible to hypoxia-induced cell death,[18] especially in the long-length root canals. Furthermore, the IHC staining images and quantitative analyses demonstrated higher expression of odontoblast-related protein DSPP in the porous group, further confirming the formation of the odontoblast-like layer (Figure 9D and E). Moreover, the IHC staining results of CD31 showed that the positive expression of CD31 was higher in the DPGC group than in the control group (Figure 9D and F), indicating the formation of more microvessels in the DPGC group. Overall, *in vivo* experiment further confirmed the feasibility of the DLP-based bioprinted DPGC to match the irregular shape of the root canal. Moreover, the results also indicated that the 3D-bioprinted hDPSCs-laden DPGCs were able to avoid pathophysiologically hostile cavitary microenvironment, and effectively deliver stem cells to the surrounding dental tissue for dental pulp regeneration.

4. Discussion

Stem cell-based transplantation has emerged as a promising strategy for the treatment of dental pulp diseases.[8,52,53] The stemness of stem cells is crucial for the cellular functions, both *in vitro* and *in vivo*.[54,55] Considering the stemness properties, we proposed a feasible approach in that the GelMA-Dextran aqueous emulsion was treated as ink for *in situ* printing of a DPGC with stem cell-adaptable microporous structure that exhibited favorable advantages. The acquired DPGC promoted stemness properties and YAP nuclear translocation of hDPSCs compared to the bulk GelMA hydrogel. Further analysis revealed that DPGC with facilitated stemness not only enhanced proliferation, spreading, and migration of the encapsulated

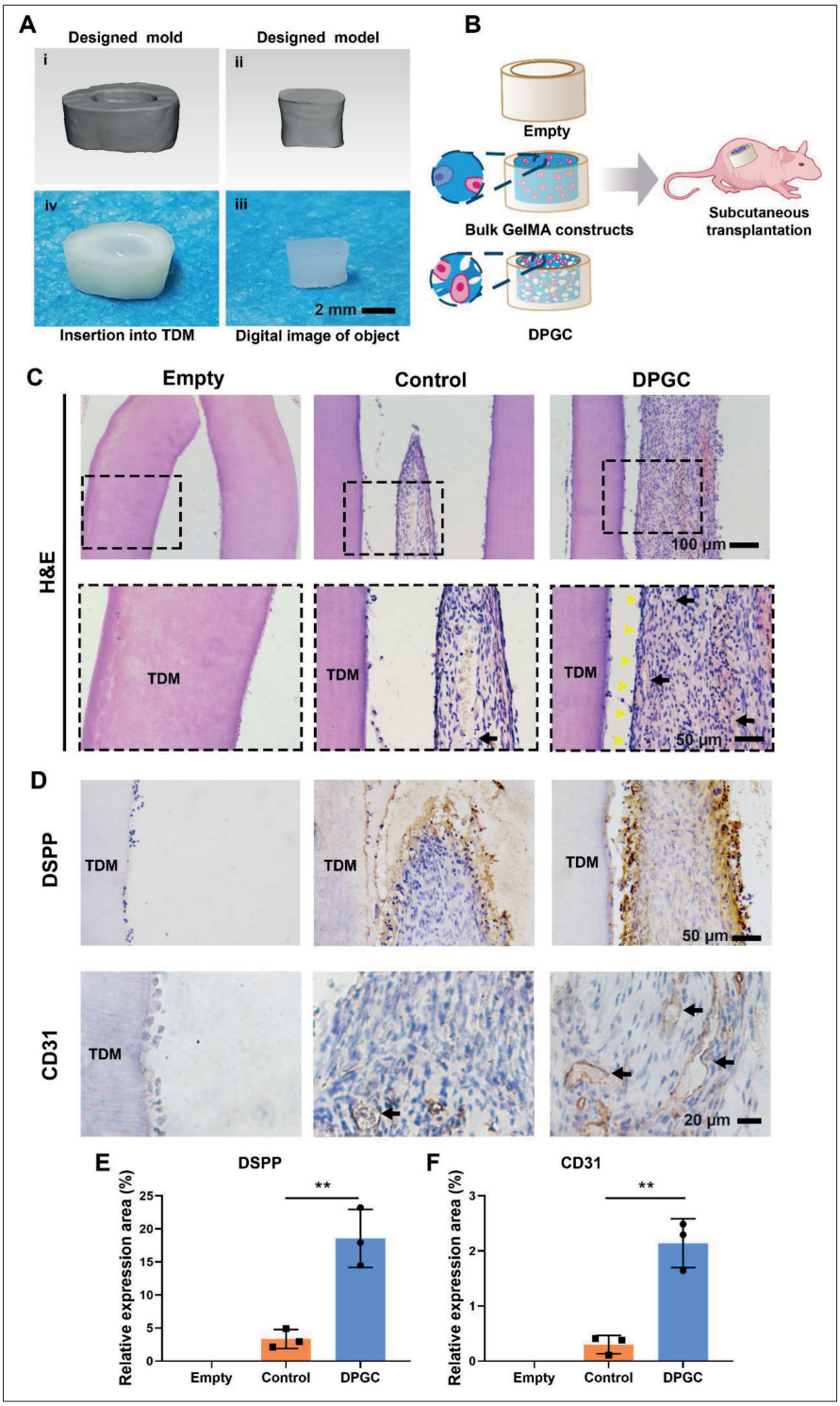


Figure 9. DLP-based 3D-bioprinted DPGCs promote dental pulp regeneration *in vivo*. (A) Design and fabrication of the customized DPGC. (B) Schematic diagram of TDM transplantation in immunodeficient mice. hDPSCs-laden DPGCs and bulk GelMA hydrogel constructs were combined with rat TDM, and then subcutaneously transplanted into immunodeficient mice for 2 months. Empty TDM, as negative control, was directly transplanted into recipient immunodeficient mice. (C) H&E staining images used for evaluating the newly regenerated tissue in each group. Dental pulp-like tissue containing more microvessels (black arrow) and an odontoblast-like layer (yellow triangles) was regenerated in the DPGC group. (D) Immunohistological detection of DSPP and CD31 protein. The black arrows denote that more microvessels were formed in the DPGC group. (E, F) Quantitative analysis of the DSPP- and CD31-positive area for each group. $^{**}p < 0.01$.

hDPSCs, but also boosted the capillary tube formation and neurogenesis. *In vivo* experiments confirmed the porous DPGC regenerated dental pulp with a dentin-like and microvascular structure.

GelMA is regarded as a good candidate for tissue engineering due to its similarity to natural ECM and possession of tunable mechanical properties to mimic 3D microenvironment for regulating cell fates and steering tissue regeneration.[56] However, bulk GelMA hydrogels generally own dense structural networks that limit robust cytoskeleton extension and the diffusion of oxygen and nutrients, leading to a relatively low survival of seed cells following their engraftment into the host tissue.[11,57] To address these restrictions, one strategy to improve cell viability and therapeutic efficacy of tissue regeneration is to enhance the porosity of biomaterials. Microporous structures in hydrogels have been produced by various techniques, which include freeze-drying, electrospinning, porogen leaching, and so on.[58,59] However, it is impossible to encapsulate any live cells during the manufacture of scaffolds using these methods to generate porous structures. In addition, after the accomplishment of porous scaffolds, most cells are loaded on the surface of scaffolds, and a precise 3D cell distribution within the construct can hardly be achieved. The water-in-water emulsion is composed of two aqueous phases, and the droplets of one aqueous phase (dispersed phase) are dispersed into the other aqueous phase (continuous phase) to reach a thermodynamic equilibrium state.[60] After the aqueous continuous phase is polymerized around the dispersed droplets, the *in situ* pore-forming material is mildly produced following the removal of dispersed phase. Dextran is a biocompatible, biodegradable, and non-immunogenic biological substance.[61] In the present study, dextran was mixed with GelMA solution to generate GelMA-Dextran emulsion where dextran droplets were dispersed within GelMA, the continuous phase (Figure 2A). In addition, as reported in our previous study,[25] the microporous hydrogel constructs prepared by the GelMA-Dextran emulsion could enhance the viability of chondrocytes and regulate cartilage tissue rebuilding. Hence, we hypothesize that the GelMA-Dextran emulsion is applicable as a bioink of DLP-based 3D bioprinting, and *in situ* 3D-bioprinted DPGC can steer DPSCs fates and functions for enhanced dental pulp regeneration.

Stemness maintenance is an indispensable factor for functional tissue regeneration essential in stem cell therapy. Enhanced stemness properties of stem cells can promote the potential of these stem cells to replenish diverse types of cells within injured sites and contribute pro-regenerative paracrine factors.[62] However, long-term 2D culture would result in alterations of phenotypes or even loss of stemness. According to recent studies, numerous strategies have been proposed to tune the stemness properties of stem cells, via the regulation of biomechanical/bioelectrical/biochemical factors.[63,64] For example, Kong et al. fabricated a ZnO nanorod array to sustain Zn^{2+} release and synergistically promote cellular stemness with its nanotopography.[65] However, extreme culture conditions (e.g., hypoxia and low temperature) and biomaterial additives released into surrounding tissues would heighten the risk of adverse side effects. To date, although the properties of promoted stemness commonly display desired outcomes in vast biomedical applications (e.g., bone, nerve, and muscle),[66,67] the research in dental pulp regeneration is still limited. In this study, the *in situ*-bioprinted DPGC provided a favorable 3D microenvironment to promote stemness properties and nuclear translocation of YAP (Figure 3). We speculate that the stemness-promoting effect on DPGC might be attributed to the microporous structure. The microporous structure within DPGC could provide enough space to promote the metabolism of substances and improve the bioactivity of stem cells, thus enhancing the differentiation potentials of stem cells.[16] Furthermore, the nuclear transcriptional activity of YAP relies on cell extension and spreading. Interconnected pores within DPGC offer adequate 3D space to promote DPSCs spreading in DPGC (Figure 6), which may result in nuclear flattening and nuclear pores stretching, facilitating YAP nuclear translocation.[44] This process could be regulated by Rho GTPase and the tensile forces.[43] In this study, the YAP activity in DPGC may play a pivotal role in the stemness maintenance of stem cells. Similarly, Bhattacharya et al. also confirmed that undifferentiated limbal stem cells enhanced YAP nuclear translocation.[68] In contrast, a confining environment would lead to the inhibition of YAP activity within intestinal stem cells by reducing cellular tension, thus restricting further growth and morphogenesis.[69] Further *in vitro* odontogenic differentiation assays showed that nuclear accumulation of YAP proteins promoted ALP activity and the upregulation of odontogenesis-related genes when DPSCs were cultured in odontogenic differentiation medium, confirming the potential of DPSCs in dental pulp regeneration (Figure 4).

Promoting angiogenesis and neurogenesis remains a prime challenge in dental pulp regeneration.[46] Angiogenesis could assist in the exchange of nutrition, cell recruitment, and circulating factor delivery.[37] *In vitro* tube formation assay showed that DPGC significantly promoted robust vessel formation (Figure 7). This is probably related to angiogenesis-related growth factors such as vascular endothelial growth factor (VEGF), which is secreted by DPSCs encapsulated in DPGC.[70,71] *In vitro* experiments further verified that DPGC embedded with

DPSCs could significantly facilitate the robust neurite growth of PC12 cells (Figure 8). This might be modulated by the neurotrophic factors (e.g., nerve growth factors [NGFs]). NGFs possess the ability to trigger the receptor tyrosine kinase, initiate signaling cascades, and promote cytoskeletal arrangements for the growth and extension of neurites.[72] Our results support previous studies that DPSCs have neurotrophic effect on PC12 cells through paracrine regulation.[47,48] Taken together, we hypothesize that the angiogenesis- and neurogenesis-enhancing ability of DPGC might be regulated by the enhanced paracrine function of DPSC via the microporous structure of bioprinted DPGC.

In this study, *in vivo* experiment revealed that the bioprinted DPGC regenerated the dental pulp-like tissue containing new dentin and neovascular-like structure (Figure 9). The significant difference between DPGC and other groups indicates that customized DPGC with controlled microporosity fabricated by DLP-based 3D printing technology provides accurate control over its macro geometry to match the specific anatomical structure of dental pulp and offer 3D physiological microenvironment favorable to a uniform spatial distribution of hDPSCs on microscale.[23,73,74] Furthermore, compared with bulk hydrogel constructs, DPGC allowed more rapid exchanges of oxygen and nutrients to regulate the behaviors of DPSCs (e.g., survival, migration and spreading).[11,75] Moreover, the niches created by the microporous constructs facilitated capillary invasion *in vitro*. Our approach not only provides new biomaterials for tissue-engineered pulp, but also a potential strategy for dental pulp personalized treatment. However, in further clinical applications, complete insertion of 3D-printed microporous hydrogel constructs into more complex root canal structures, such as full-length tooth canals, may not be feasible. Therefore, integrating injectable shape-memory property with DLP-based 3D-printed microporous hydrogel should be carried out in future for enhancing optimal efficacy of dental pulp regeneration.

5. Conclusion

In summary, we developed a customized DPGC with an instructive niche via the integration of GelMA-Dextran emulsion bioink with DLP-based bioprinting technology for dental pulp regeneration. In this research, the porous DPGC was *in situ* bioprinted to induce the nuclear translocation of YAP protein in the encapsulated DPSCs and promote their stemness properties. Further experiments confirmed that DPGC exhibited enhanced viability, migration, and spreading of the encapsulated DPSCs and angiogenesis. *In vivo* experiments showed the DPGC with the microporous structure potently reconstructs dental pulp tissue with orderly aligned dentin and neovascular-like structure that mimics the native teeth. The approach proposed in this study presents an advanced strategy for utilizing tissue-specific regenerative biomaterials in regenerative endodontic treatment.

Acknowledgments

The authors of this work are deeply appreciative of the assistance received from professionals and personnel.

Funding

This study was supported by grants from the National Natural Science Foundation of China (82201087), Science and Technology Innovation Capability Enhancement Project of Army Medical University (2022XJS30), Direct Train Research Project of Chongqing Doctor (CSTB2022BSM-C0027), and National Natural Science Foundation of China (82100306).

Conflict of interest

The authors declare no potential conflicts of interest with respect to the research, authorship, and/or publication of this article.

Author contributions

Conceptualization: Nazi Zhou, Jie Tao, Rui Liu
Formal analysis: Nazi Zhou, Shunyao Zhu, Xinlin Wei
Investigation: Nazi Zhou, Shunyao Zhu, Xinlin Wei, Xueyuan Liao, Yu Wang, Yue Xu, Liyun Bai, Haoyuan Wan, Li Liu, Jiumeng Zhang
Writing – original draft: Nazi Zhou
Writing – review & editing: Ling Zeng, Jie Tao, Rui Liu

Ethics approval and consent to participate

All animal experimental procedures were approved by the Institutional Animal Care and Use Committee (IACUC) of the Army Medical University, China (AMUWEC20212172). The procedure involving cell collection from human patients was approved by The Ethics Committee of Daping Hospital, Third Military Medical University, China (No. 2021-306). The patients gave informed consent to donate extracted healthy permanent teeth following tooth extraction surgery.

Consent for publication

Written consent was obtained from each of the subjects.

Availability of data

All reported data are available upon reasonable request to the corresponding authors.

References

1. Zhang W, Yelick PC. Tooth repair and regeneration: potential of dental stem cells. *Trends Mol Med*. 2021;27(5):501-511. doi: 10.1016/j.molmed.2021.02.005
2. Nalliah RP, Allareddy V, Elangovan S, et al. Hospital emergency department visits attributed to pulpal and periapical disease in the United States in 2006. *J Endod*. 2011;37(1):6-9. doi: 10.1016/j.joen.2010.09.006
3. Siddiqui Z, Acevedo-Jake AM, Griffith A, et al. Cells and material-based strategies for regenerative endodontics. *Bioact Mater*. 2022;14:234-249. doi: 10.1016/j.bioactmat.2021.11.015
4. Goldberg F, Cantarini C, Alfie D, Macchi RL, Arias A. Relationship between unintentional canal overfilling and the long-term outcome of primary root canal treatments and nonsurgical retreatments: a retrospective radiographic assessment. *Int Endod J*. 2020;53(1):19-26. doi: 10.1111/iej.13209
5. Wigsten E, Kvist T, Jonasson P, Davidson T. Comparing quality of life of patients undergoing root canal treatment or tooth extraction. *J Endod*. 2020;46(1):19-28.e1. doi: 10.1016/j.joen.2019.10.012
6. Zipser CM, Cragg JJ, Guest JD, et al. Cell-based and stem-cell-based treatments for spinal cord injury: evidence from clinical trials. *Lancet Neurol*. 2022;21(7):659-670. doi: 10.1016/s1474-4422(21)00464-6
7. Chen H, Fu H, Wu X, et al. Regeneration of pulpo-dentinal-like complex by a group of unique multipotent CD24a(+) stem cells. *Sci Adv*. 2020;6(15):eaay1514. doi: 10.1126/sciadv.aay1514
8. Xuan K, Li B, Guo H, et al. Deciduous autologous tooth stem cells regenerate dental pulp after implantation into injured teeth. *Sci Transl Med*. 2018;10(455). doi: 10.1126/scitranslmed.aaf3227
9. Liu S, Sun J, Yuan S, et al. Treated dentin matrix induces odontogenic differentiation of dental pulp stem cells via regulation of Wnt/β-catenin signaling. *Bioact Mater*. 2022;7:85-97. doi: 10.1016/j.bioactmat.2021.05.026
10. Zhang R, Xie L, Wu H, et al. Alginate/laponite hydrogel microspheres co-encapsulating dental pulp stem cells and VEGF for endodontic regeneration. *Acta Biomater*. 2020;113:305-316. doi: 10.1016/j.actbio.2020.07.012
11. Yang T, Zhang Q, Xie L, et al. hDPSC-laden GelMA microspheres fabricated using electrostatic microdroplet method for endodontic regeneration. *Mater Sci Eng C Mater Biol Appl*. 2021;121:111850. doi: 10.1016/j.msec.2020.111850
12. Kim SW, Im GB, Jeong GJ, et al. Delivery of a spheroids-incorporated human dermal fibroblast sheet increases angiogenesis and M2 polarization for wound healing. *Biomaterials*. 2021;275:120954. doi: 10.1016/j.biomaterials.2021.120954
13. Soman SS, Vijayavenkataraman S. Applications of 3D bioprinted-induced pluripotent stem cells in healthcare. *Int J Bioprint*. 2020;6(4):280. doi: 10.18063/ijb.v6i4.280
14. Yang L, Liu X, Song L, et al. Melatonin restores the pluripotency of long-term-cultured embryonic stem cells through melatonin receptor-dependent m6A RNA regulation. *J Pineal Res*. 2020;69(2):e12669. doi: 10.1111/jpi.12669
15. Kim Y, Jin HJ, Heo J, et al. Small hypoxia-primed mesenchymal stem cells attenuate graft-versus-host disease. *Leukemia*. 2018;32(12):2672-2684. doi: 10.1038/s41375-018-0151-8
16. Huebsch N, Lippens E, Lee K, et al. Matrix elasticity of void-forming hydrogels controls transplanted-stem-cell-mediated bone formation. *Nat Mater*. 2015;14(12):1269-1277. doi: 10.1038/nmat4407
17. Yuan Z, Yuan X, Zhao Y, et al. Injectable GelMA cryogel microspheres for modularized cell delivery and potential vascularized bone regeneration. *Small*. 2021;17(11):e2006596. doi: 10.1002/smll.202006596
18. Ying G, Jiang N, Parra C, et al. Bioprinted injectable hierarchically porous gelatin methacryloyl hydrogel constructs with shape-memory properties. *Adv Funct Mater*. 2020;30(46):2003740. doi: 10.1002/adfm.202003740
19. Guo Y, Xue Y, Wang P, et al. Muse cell spheroids have therapeutic effect on corneal scarring wound in mice and tree shrews. *Sci Transl Med*. 2020;12(562):eaaw1120. doi: 10.1126/scitranslmed.aaw1120
20. Zhou L, Zeng Z, Liu S, et al. Multifunctional DNA hydrogel enhances stemness of adipose-derived stem cells to activate immune pathways for guidance burn wound regeneration. *Adv Funct Mater*. 2022;32(46). doi: 10.1002/adfm.202207466
21. Han M, Yang H, Lu X, et al. Three-dimensional-cultured MSC-derived exosome-hydrogel hybrid microneedle array patch for spinal cord repair. *Nano Lett*. 2022;22(15):6391-6401. doi: 10.1021/acs.nanolett.2c02259
22. Zhang J, Hu Q, Wang S, Tao J, Gou M. Digital light processing based three-dimensional printing for medical applications. *Int J Bioprint*. 2020;6(1):242. doi: 10.18063/ijb.v6i1.242

23. Levato R, Jungst T, Scheuring RG, Blunk T, Groll J, Malda J. From shape to function: the next step in bioprinting. *Adv Mater*. 2020;32(12):e1906423. doi: 10.1002/adma.201906423

24. Tao J, Liu H, Wu W, et al. 3D-printed nerve conduits with live platelets for effective peripheral nerve repair. *Adv Funct Mater*. 2020;30(42). doi: 10.1002/adfm.202004272

25. Tao J, Zhu S, Zhou N, et al. Nanoparticle-stabilized emulsion bioink for digital light processing based 3D bioprinting of porous tissue constructs. *Adv Healthc Mater*. 2022;11(12):e2102810. doi: 10.1002/adhm.202102810

26. Shi S, Cui M, Sun F, et al. An innovative solvent-responsive coiling-expanding stent. *Adv Mater*. 2021;33(32):e2101005. doi: 10.1002/adma.202101005

27. Lu X, Xu G, Lin Z, et al. Engineered exosomes enriched in netrin-1 modRNA promote axonal growth in spinal cord injury by attenuating inflammation and pyroptosis. *Biomater Res*. 2023;27(1):3. doi: 10.1186/s40824-023-00339-0

28. Zhang X, Wu W, Huang Y, Yang X, Gou M. Antheraea pernyi silk fibroin bioinks for digital light processing 3D printing. *Int J Bioprint*. 2023;9(5):760. doi: 10.18063/ijb.760

29. Zhang M, Yang F, Han D, et al. 3D bioprinting of corneal decellularized extracellular matrix: GelMA composite hydrogel for corneal stroma engineering. *Int J Bioprint*. 2023;9(5). doi: 10.18063/ijb.774

30. Wu Y, Li M, Su H, Chen H, Zhu Y. Up-to-date progress in bioprinting of bone tissue. *Int J Bioprint*. 2023;9(1):628. doi: 10.18063/ijb.v9i1.628

31. Zhang C, Ren Y, Kong W, et al. Photocurable 3D-printed PMBG/TCP biphasic scaffold mimicking vasculature for bone regeneration. *Int J Bioprint*. 2023;9(5):767. doi: 10.18063/ijb.767

32. Tang Z, Zhou Y, Ma L, Li J. Flow performance of porous implants with different geometry: line, surface, and volume structures. *Int J Bioprint*. 2023;9(3):700. doi: 10.18063/ijb.700

33. Yu C, Zhu W, Sun B, Mei D, Gou M, Chen S. Modulating physical, chemical, and biological properties in 3D printing for tissue engineering applications. *Appl Phys Rev*. 2018;5(4). doi: 10.1063/1.5050245

34. Seetharaman S, Vianay B, Roca V, et al. Microtubules tune mechanosensitive cell responses. *Nat Mater*. 2022;21(3): 366-377. doi: 10.1038/s41563-021-01108-x

35. Li C, Jin Y, Wei S, et al. Hippo signaling controls NLR family pyrin domain containing 3 activation and governs immunoregulation of mesenchymal stem cells in mouse liver injury. *Hepatology*. 2019;70(5):1714-1731. doi: 10.1002/hep.30700

36. Moya IM, Halder G. Hippo-YAP/TAZ signalling in organ regeneration and regenerative medicine. *Nat Rev Mol Cell Biol*. 2019;20(4):211-226. doi: 10.1038/s41580-018-0086-y

37. Lian M, Sun B, Han Y, et al. A low-temperature-printed hierarchical porous sponge-like scaffold that promotes cell-material interaction and modulates paracrine activity of MSCs for vascularized bone regeneration. *Biomaterials*. 2021;274:120841. doi: 10.1016/j.biomaterials.2021.120841

38. Liu S, Tang L, Zhao X, et al. Yap promotes noncanonical Wnt signals from cardiomyocytes for heart regeneration. *Circ Res*. 2021;129(8):782-797. doi: 10.1161/CIRCRESAHA.121.318966

39. Dey A, Varelas X, Guan KL. Targeting the Hippo pathway in cancer, fibrosis, wound healing and regenerative medicine. *Nat Rev Drug Discov*. 2020;19(7):480-494. doi: 10.1038/s41573-020-0070-z

40. Jeanette H, Marziali LN, Bhatia U, et al. YAP and TAZ regulate Schwann cell proliferation and differentiation during peripheral nerve regeneration. *Glia*. 2021;69(4): 1061-1074. doi: 10.1002/glia.23949

41. Liang H, Wang Y, Chen S, Liu Y, Liu Z, Bai J. Nano-hydroxyapatite bone scaffolds with different porous structures processed by digital light processing 3D printing. *Int J Bioprint*. 2022;8(1):502. doi: 10.18063/ijb.v8i1.502

42. Hasturk O, Kaplan DL. Cell armor for protection against environmental stress: advances, challenges and applications in micro- and nanoencapsulation of mammalian cells. *Acta Biomater*. 2019;95:3-31. doi: 10.1016/j.actbio.2018.11.040

43. Brusatin G, Panciera T, Gandin A, Citron A, Piccolo S. Biomaterials and engineered microenvironments to control YAP/TAZ-dependent cell behaviour. *Nat Mater*. 2018;17(12):1063-1075. doi: 10.1038/s41563-018-0180-8

44. Chaudhuri O, Gu L, Darnell M, et al. Substrate stress relaxation regulates cell spreading. *Nat Commun*. 2015;6:6364. doi: 10.1038/ncomms7365

45. Tang S, Ma H, Tu HC, Wang HR, Lin PC, Anseth KS. Adaptable fast relaxing boronate-based hydrogels for probing cell-matrix interactions. *Adv Sci*. 2018;5(9): 1800638. doi: 10.1002/advs.201800638

46. Qian Y, Gong J, Lu K, et al. DLP printed hDPSC-loaded GelMA microsphere regenerates dental pulp and repairs spinal cord. *Biomaterials*. 2023;299. doi: 10.1016/j.biomaterials.2023.122137

47. Guo S, Redenski I, Landau S, Szklanny A, Merdler U, Levenberg S. Prevascularized scaffolds bearing human

dental pulp stem cells for treating complete spinal cord injury. *Adv Healthc Mater*. 2020;9(20). doi: 10.1002/adhm.202000974

48. Sultan N, Amin LE, Zaher AR, Grawish ME, Scheven BA. Dental pulp stem cells stimulate neuronal differentiation of PC12 cells. *Neural Regen Res*. 2021;16(9):1821-1828. doi: 10.4103/1673-5374.306089
49. Liu C, Fan L, Tian Z, et al. Self-curling electroconductive nerve dressing for enhancing peripheral nerve regeneration in diabetic rats. *Bioact Mater*. 2021;6(11):3892-3903. doi: 10.1016/j.bioactmat.2021.03.034
50. Fang W, Yang M, Wang L, et al. Hydrogels for 3D bioprinting in tissue engineering and regenerative medicine: current progress and challenges. *Int J Bioprint*. 2023;9(5):759. doi: 10.18063/ijb.759
51. Rodenhizer D, Gaude E, Cojocari D, et al. A three-dimensional engineered tumour for spatial snapshot analysis of cell metabolism and phenotype in hypoxic gradients. *Nat Mater*. 2016;15(2):227-234. doi: 10.1038/nmat4482
52. Liu Y, Graves DT, Wang S. Development and clinical application of human mesenchymal stem cell drugs. *Sci Bull*. 2023;68(9):860-863. doi: 10.1016/j.scib.2023.03.050
53. Rodriguez-Salvador M, Ruiz-Cantu L. Revealing emerging science and technology research for dentistry applications of 3D bioprinting. *Int J Bioprint*. 2019;5(1):170. doi: 10.18063/ijb.v5i1.170
54. Chang PH, Chao HM, Chern E, Hsu SH. Chitosan 3D cell culture system promotes naïve-like features of human induced pluripotent stem cells: A novel tool to sustain pluripotency and facilitate differentiation. *Biomaterials*. 2021;268:120575. doi: 10.1016/j.biomaterials.2020.120575
55. Lu X, Sun C, Chen L, et al. Stemness maintenance and massproduction of neural stem cells on poly L-lactic acid nanofibrous membrane based on piezoelectric effect. *Small*. 2022;18(13):e2107236. doi: 10.1002/smll.202107236
56. Gao J, Wang H, Li M, et al. DLP-printed GelMA-PMAA scaffold for bone regeneration through endochondral ossification. *Int J Bioprint*. 2023;9(5):754. doi: 10.18063/ijb.754
57. Salvador T, Oliveira MB, Mano JF. Leachable-free fabrication of hydrogel foams enabling homogeneous viability of encapsulated cells in large-volume constructs. *Adv Healthc Mater*. 2020;9(20):e2000543. doi: 10.1002/adhm.202000543
58. Silvestro I, Sergi R, Scotto d'Abusco A, et al. Chitosan scaffolds with enhanced mechanical strength and elastic response by combination of freeze gelation, photo-crosslinking and freeze-drying. *Carbohydr Polym*. 2021;267:118156. doi: 10.1016/j.carbpol.2021.118156
59. Yang XY, Chen LH, Li Y, Rooke JC, Sanchez C, Su BL. Hierarchically porous materials: synthesis strategies and structure design. *Chem Soc Rev*. 2017;46(2):481-558. doi: 10.1039/c6cs00829a
60. Esquena J. Water-in-water (W/W) emulsions. *Curr Opin Colloid Interface Sci*. 2016;25:109-119. doi: 10.1016/j.cocis.2016.09.010
61. Hu Q, Lu Y, Luo Y. Recent advances in dextran-based drug delivery systems: from fabrication strategies to applications. *Carbohydr Polym*. 2021;264:117999. doi: 10.1016/j.carbpol.2021.117999
62. Wu X, Zhu H, Che J, Xu Y, Tan Q, Zhao Y. Stem cell niche-inspired microcarriers with ADSCs encapsulation for diabetic wound treatment. *Bioact Mater*. 2023;26:159-168. doi: 10.1016/j.bioactmat.2023.02.031
63. Wilson KL, Pérez SCL, Naffaa MM, Kelly SH, Segura T. Stoichiometric post-modification of hydrogel microparticles dictates neural stem cell fate in microporous annealed particle scaffolds. *Adv Mater*. 2022;34(33):e2201921. doi: 10.1002/adma.202201921
64. Zhao Y, Shi Y, Yang H, et al. Stem cell microencapsulation maintains stemness in inflammatory microenvironment. *Int J Oral Sci*. 2022;14(1):48. doi: 10.1038/s41368-022-00198-w
65. Kong Y, Ma B, Liu F, et al. Cellular stemness maintenance of human adipose-derived stem cells on ZnO nanorod arrays. *Small*. 2019;15(51):e1904099. doi: 10.1002/smll.201904099
66. Kim J, Kim YM, Song SC. One-step preparation of an injectable hydrogel scaffold system capable of sequential dual-growth factor release to maximize bone regeneration. *Adv Healthc Mater*. 2023;12(4):e2202401. doi: 10.1002/adhm.202202401
67. Madl CM, LeSavage BL, Khariton M, Heilshorn SC. Neural progenitor cells alter chromatin organization and neurotrophin expression in response to 3D matrix degradability. *Adv Healthc Mater*. 2020;9(18):e2000754. doi: 10.1002/adhm.202000754
68. Bhattacharya S, Mukherjee A, Pisano S, et al. The biophysical property of the limbal niche maintains stemness through YAP. *Cell Death Differ*. 2023;30(6):1601-1614. doi: 10.1038/s41418-023-01156-7
69. Gjorevski N, Sachs N, Manfrin A, et al. Designer matrices for intestinal stem cell and organoid culture. *Nature*. 2016;539(7630):560-564. doi: 10.1038/nature20168
70. Atlas Y, Gorin C, Novais A, et al. Microvascular maturation by mesenchymal stem cells in vitro improves blood perfusion in implanted tissue constructs. *Biomaterials*. 2021;268:120594. doi: 10.1016/j.biomaterials.2020.120594
71. Gorin C, Rochefort GY, Bascetin R, et al. Priming dental pulp stem cells with fibroblast growth factor-2 increases angiogenesis of implanted tissue-engineered constructs through hepatocyte

growth factor and vascular endothelial growth factor secretion. *Stem Cells Transl Med*. 2016;5(3):392-404. doi: 10.5966/sctm.2015-0166

72. Xu D, Wu D, Qin M, et al. Efficient delivery of nerve growth factors to the central nervous system for neural regeneration. *Adv Mater*. 2019;31(33):e1900727. doi: 10.1002/adma.201900727

73. Jiang S, Lyu C, Zhao P, et al. Cryoprotectant enables structural control of porous scaffolds for exploration of cellular mechano-responsiveness in 3D. *Nat Commun*. 2019;10(1). doi: 10.1038/s41467-019-11397-1

74. Zhang J, Chen Y, Huang Y, et al. A 3D-printed self-adhesive bandage with drug release for peripheral nerve repair. *Adv Sci*. 2020;7(23):2002601. doi: 10.1002/advs.202002601

75. Khayat A, Monteiro N, Smith EE, et al. GelMA-encapsulated hDPSCs and HUVECs for dental pulp regeneration. *J Dent Res*. 2017;96(2):192-199. doi: 10.1177/0022034516682005

ACCSCIENCE PUBLISHING

International Journal of Bioprinting

RESEARCH ARTICLE

Frequency response analysis and *in vitro* verification of 3D-printed ossicular replacement materials

Jingbin Hao[1,2]*, Yin Zhu[1], Ding Shen[1], Md Thowfiqure Rahman[1], Yinxin Kou[1], and Houguang Liu[1,2]

[1]School of Mechanical and Electrical Engineering, China University of Mining and Technology, Xuzhou, Jiangsu, China

[2]Jiangsu Engineering Technology Research Centre on Intelligent Equipment for Fully Mining and Excavating, China University of Mining and Technology, Xuzhou, Jiangsu, China

Abstract

As a bridge that transmits airborne sound signals to the auditory receptors of the inner ear, the eardrum and ossicular chain of the middle ear convert sound through two types of conversions: gas–solid (airborne sound signal–eardrum and ossicular chain) and solid–liquid (eardrum and ossicular chain–internal and external lymphatic fluid in the cochlea). This process concentrates and amplifies the sound to the inner ear through the lever principle structure formed by the three ossicles. However, diseases, hereditary factors, or trauma can reduce the sound transmission function of the middle ear. The effectiveness of middle ear replacement prostheses depends on their vibration response to the human auditory perception frequency, from the eardrum to the stapes plate. This response is influenced by the materials, geometry, and design of the replacement prosthesis and eardrum. This study explores the effects of different materials on hearing after artificial ossicular replacement. Usually, human temporal bone models are used for testing and validating numerical results. However, obtaining specimens from living humans is not always feasible. Therefore, we used three-dimensional printing technology to build a model of the middle ear to test the ossicular bone. Titanium alloy TC4, stainless steel 316L, and composite HA/PCL are chosen as materials for ossicular replacement. Using finite element analysis and an *in vitro* verification experiment, individual replacements of the ossicles and three bone material replacements were conducted for frequency response analysis. The combination of the malleus made of TC4, the incus made of TC4, and the stapes made of HA/PCL were found to bear higher resemblance to a real normal ear ossicular model.

Keywords: Ossicular replacement materials; 3D printing; frequency response analysis; Finite element modeling; *In vitro* verification experiment

***Corresponding author:**
Jingbin Hao
(jingbinhao@cumt.edu.cn)

Citation: Hao J, Zhu Y, Shen D, Rahman MT, Kou Y, Liu H. Frequency response analysis and *in vitro* verification of 3D-printed ossicular replacement materials. *Int J Bioprint*. 2024;10(3):2040. doi: 10.36922/ijb.2040

Received: October 14, 2023
Accepted: December 14, 2023
Published Online: February 5, 2024

Copyright: © 2024 Author(s). This is an Open Access article distributed under the terms of the Creative Commons Attribution License, permitting distribution, and reproduction in any medium, provided the original work is properly cited.

Publisher's Note: AccScience Publishing remains neutral with regard to jurisdictional claims in published maps and institutional affiliations.

1. Introduction

The ossicular chain plays a crucial role in facilitating normal hearing, and any deformity in this chain can lead to conductive deafness. Chronic suppurative otitis media often results in varying degrees of hearing loss, along with damage and loss of

auditory ossicles. Ossicular chain reconstruction through tympanoplasty offers a solution for addressing these issues, with five categorized approaches based on the following:[1] all three ossicles are intact and functioning well and thus no reconstruction is needed; the tympanic membrane is transplanted to the undamaged incus and stapes; the stapes structure remains unaffected, allowing for direct attachment of the membrane or graft; there is a defect above the stapes, connecting the membrane or graft to the stapes floor; and fenestration of the external semicircular canal is involved. While recent advancements have been made to enhance these techniques, the core principles of ossicular chain reconstruction remain unchanged.

Autogenous materials, including autogenous residual ossicular bone, cortical bone, and cartilage, are considered ideal for ossicular chain reconstruction due to their excellent biocompatibility and lack of rejection in the body.[2] The residual auditory ossicles left after treatment are lightweight and rigid natural materials, often utilized in 75% to 100% of the hammer–stirrup connections.[3] In a study, autologous costal cartilage was used to reconstruct the ossicular chain in 102 ears. After a follow-up period ranging from 6 months to 6 years, 88 ears (86.3%) showed hearing improvement of more than 15 dB or reached an acceptable level of functionality.[4,5] Autologous cortical bone is a suitable material for ossicular reconstruction due to its density and structure being similar to natural ossicular bone, allowing easy sculpting without fracturing the material. Postoperative hearing outcomes are comparable to ossicular bone grafts. However, drawbacks include small residual lesions leading to infection recurrence and the soft nature of autologous cartilage, potentially reducing acoustic conductivity.[6] Allogeneic materials, like auditory ossicles, cartilage, and teeth, have been used for ossicular transplantation. Allogeneic ossicular bone shows good biocompatibility and acoustic conductivity, integrating into the host tissue without rejection or absorption. However, its limited availability and stringent storage requirements limit its utility given the infection transmission concerns (e.g., AIDS and Creutzfeldt–Jakob disease).[7]

Plastic prostheses, such as high-density porous polyethylene (HDPE) and high-density polyethylene sponge (plastipore), are commonly used in middle ear surgery due to their hardness, ease of shaping, and good biocompatibility. However, their most significant drawback is postoperative discharge and sensorineural deafness, with a discharge rate ranging from 6% to 39%.[8] To address this issue, it has been suggested to place a cartilage piece between the transplanted fascia and the prosthesis, which can reduce the ejection rate to 3% to 5%. Nonetheless, the long-term effect of this method is still being determined, and adding human cartilage may increase the instability of the entire structure, making it susceptible to dislocation.[9] Plastipore prostheses maintain their shape even after 7–10 years of implantation and are surrounded by fibrous tissue with some tissue invasion and giant cells at the margins. However, the micro-decomposition of the microporous wall raises concerns about potential foreign body rejection, limiting its application.[10] Ceramic prosthesis, particularly hydroxyapatite (HA), is a promising material known for its biocompatibility, low extraction rate, and stability, even in the presence of infection or eustachian tube dysfunction. However, HA is brittle and difficult to shape, which restricts its ideal characteristics.[11]

Metal prostheses have been employed in middle ear reconstruction since the 1960s, primarily for treating otosclerosis. The commonly used Teflon platinum wire piston, however, may lead to necrosis of the long process of the incus. In contrast, titanium, known for its lightweight (density 4.5 g/cm^3, 57% of stainless steel), hardness, non-toxicity, and non-magnetic properties, chemical stability, and corrosion resistance, is widely utilized as an anvil prosthesis or anvil stirrup prosthesis. Compatibility in the unique environment of the middle ear has been demonstrated in animal experiments.[12] In addition to its excellent biocompatibility and tissue affinity, the titanium ossicular prosthesis offers numerous advantages, such as being lightweight, facilitating sound conduction, providing suitable strength, allowing for fine processing, offering good stability, and demonstrating good plasticity.[13] It proves effective for reconstructing the ossicular chain in various types of chronic suppurative otitis media and shows promising postoperative outcomes.[14]

In China, an average postoperative air conduction hearing threshold increase of 10–15 dB at 500, 1000, and 2000 frequencies is defined as surgical success. In foreign countries, the success rate is assessed based on the closure of bone-conducted hearing. Many scholars consider the closure of the bone–air conduction difference within 20 dB as the criterion for success.[15,16]

The key to ossicular chain repair is to restore the normal function of the human ear. However, human specimens for experiments are not always readily available, so we built an artificial middle ear to test the performance of the ossicles. The model was prepared using a three-dimensional (3D) printing method to accurately acquire data from the human middle ear using a computed tomography (CT) scan.[17]

This study aims to explore the effects of different materials on hearing after artificial bone replacement. To achieve this, a 3D model of the ossicular chain was established using CT data. In order to verify the reliability and accuracy of the model, a finite element analysis of the ossicular chain was conducted. To compare the mechanical

properties of artificial bones made of different materials, the printed models underwent a series of tests, including tensile tests, hardness tests, friction and wear tests, roughness profile tests, sample density tests, and electrochemical corrosion tests. Additionally, biocompatibility was assessed through cell death staining experiments. In order to create a testing environment similar to that of the human temporal bone, a middle ear model that resembles the actual anatomy and function of the structure was created. This model includes a tympanic membrane made of silicone rubber and an ear canal prepared using a 3D printing method and filled with fluid in the inner ear to act as a lymphatic fluid. Furthermore, to verify the acoustic performance of artificial hearing bones made of different materials, laser vibration experiments were conducted on the printed model. Through a comparative analysis of the experimental data, three hearing bone materials that closely resemble the human ear model were analyzed to investigate the influence of different material combinations.

2. Materials and methods

Based on the established finite element model of the middle ear ossicular chain, this study simulates the replacement of auditory ossicles with different materials. It involves modifying the Poisson's ratio, Young's modulus, and density of the materials. Specifically, different materials such as titanium alloy, stainless steel, hydroxyapatite, and polycaprolactone composite were used for modeling the same parts (stapes, malleus, and incus) under replacement. The principle of dynamic conduction vibration was applied, and the mechanical behavior was compared with the normal ossicular chain to analyze the influence of different material combinations on various index parameters.

The middle ear model comprising the tympanic membrane, ossicles (malleus, incus, and stapes), joints, ligaments, and tendons is depicted in Figure 1. This model is based on a fresh human temporal bone specimen (male, 60-year-old, right ear) and was established using micro-CT scanning and reverse molding technology.

In this study, the finite element model of the human ear was used, where each part is simplified as a homogeneous and isotropic material with a Poisson's ratio of 0.3. During the dynamic analysis, two different forms of energy loss were considered. The tension part of the tympanic membrane (both the inner and outer layers), the relaxation part of the tympanic membrane, the ligament of the tympanic membrane ring, and the ligament of the stapes ring were all modeled using viscoelastic material properties (as shown in Table 1). The dynamic energy dissipation is represented by the viscous part, and its relaxation modulus $E(t)$ is defined by Equation I.

$$E(t)=E_0+E_1 e^{-\frac{t}{\tau_1}} \quad \text{(I)}$$

where E_1 is the first-order relaxation modulus; τ_1 is the first-order relaxation time; and Young's modulus is shown in Table 2.

Except for the human ear soft tissues mentioned above, the energy loss of other parts is in the form of Rayleigh damping, and the damping coefficient is set as $\alpha = 0\ s^{-1}$, $\beta = 0.000$.

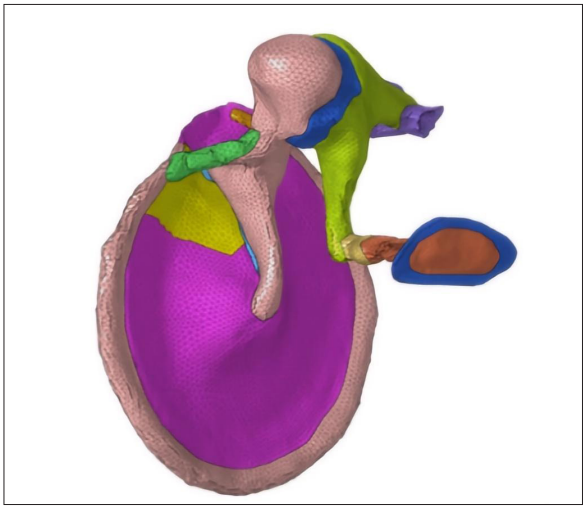


Figure 1. Finite element model of the middle ear.

Table 1. Viscoelastic parameters of tissue materials of various parts of the tympanic chamber

Structure	e_1	τ_1
Ligamentum annuli tympani	3.2	28
Tensor of tympanic membrane	2.8	25
Flaccid part of tympanic membrane	2.29	25
Anvil hammer joint	3.0	20
Incudo stapes joint	50	20
Ligaments of stapes ring	2.4	25

We conducted verification of the displacement of the stapes floor and tympanic umbilicus using the established middle ear finite element model. We then compared the displacement and phase angle results with the experimental findings from Gan et al.[9] According to our results, the displacements were found to be very small, falling in the micrometer to nanometer range. To clearly illustrate the trend and behavior of these displacements, we utilized a logarithmic scale for plotting. The exported model demonstrated sufficient capability to simulate the dynamic behavior of the human middle ear. Through the comparison with experimental data, we confirmed that the established ossicular chain model is reliable and accurate, as shown in Figures 2 and 3.

2.1. Performance test of materials

Titanium alloys, stainless steels, hydroxyapatite, and polycaprolactone composite (HA/PCL) materials are orthopedic materials with good biocompatibility. Therefore, we used these materials for research and analysis to compare the performance of different ossicular materials using 3D printing. We replaced the corresponding positions with these materials and conducted steady-state dynamic analysis on the ossicular chain model. Laser powder metal sintering (SLM) was employed for titanium alloys and stainless steels, while fused deposition (FDM) was used for HA/PCL materials. The mechanical property and biocompatibility of the printed samples were tested.

2.2. Mechanical property test

A series of mechanical property tests on the molded 3D-printed samples were performed to identify relevant parameters, and these mechanical property parameters between the three materials were compared. These tests included tensile tests, hardness tests, friction and wear tests, roughness profile tests, sample density tests, and electrochemical corrosion tests. Hardness testing is based

Table 2. Material properties used for the finite element modeling

Structure component	Density (kg/m^3)	Young's modulus/Bulk modulus (Pa)
Tympanic membrane (pars tensa)	1.20×10^3	3.00×10^7
Tympanic membrane (pars flaccida)	1.20×10^3	1.00×10^7
Ligamentum annuli tympani	1.20×10^3	3.00×10^5
Malleus (head)	2.55×10^3	1.41×10^{10}
Malleus (neck)	4.53×10^3	1.41×10^{10}
Malleus (handle)	3.70×10^3	1.41×10^{10}
Incus (long process)	5.08×10^3	1.41×10^{10}
Incus (short process)	2.26×10^3	1.41×10^{10}
Incus (body)	2.36×10^3	1.41×10^{10}
Stapes	2.20×10^3	1.41×10^{10}
Stapes muscle	1.20×10^3	5.20×10^5
Manubrium	1.00×10^3	4.70×10^9
Incudomalleolar joint	3.20×10^3	1.41×10^{10}
Incudostapedial joint	1.20×10^3	4.40×10^5
Stapedial annular ligament	1.20×10^3	1.50×10^4
Superior suspensory ligament of malleus	1.20×10^3	4.90×10^6
Anterior malleolar ligament	1.20×10^3	2.1×10^7
Ligamentum mallei lateralis	1.20×10^3	6.7×10^6
Superior suspensory ligament of incus	1.20×10^3	4.9×10^6
Posterior incus ligament	1.20×10^3	6.5×10^6

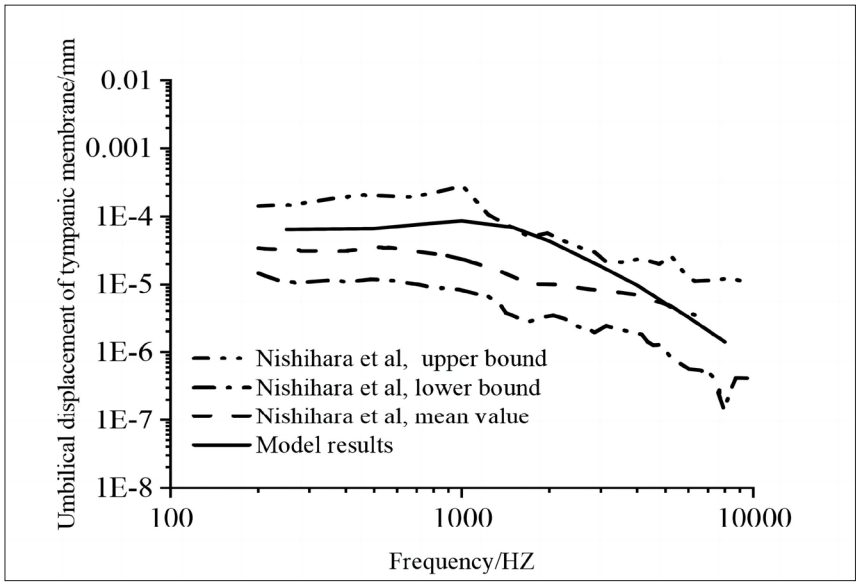


Figure 2. Verification of umbilicus displacement of tympanic membrane.

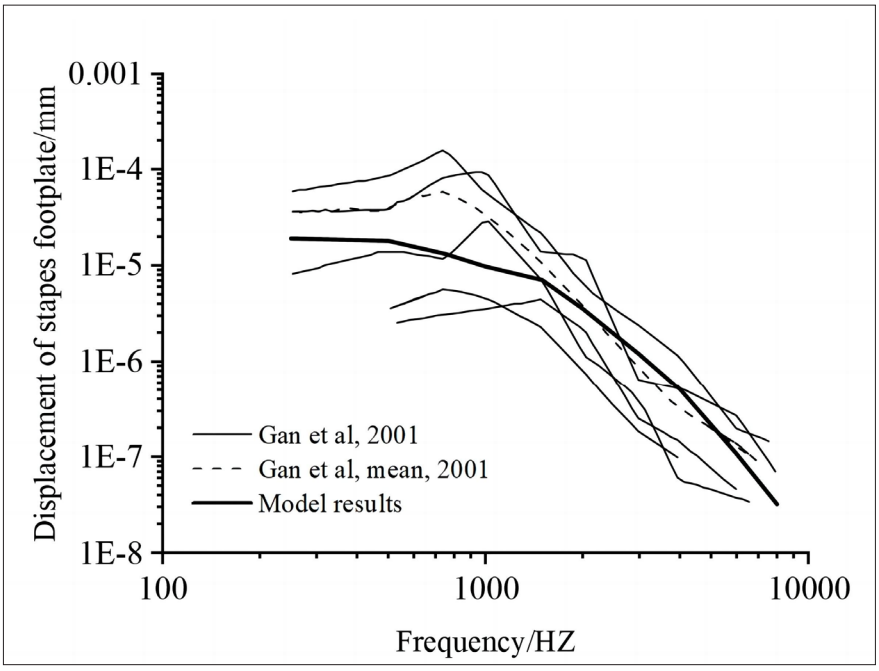


Figure 3. Verification of stapes floor displacement.

on the Vickers hardness test. The unit of the Vickers hardness test is HV. The unit of friction and wear test is the wear volume in mm^3. The unit of density test is g/cm^3. The tensile test of titanium alloy was TC4 prepared via SLM, and stainless steel 316L and FDM-prepared HA/PCL molded parts were measured with an electronic universal testing machine. The tensile test can determine the elongation, elastic modulus, yield strength, proportional limit, area reduction, and other performance indicators of the material. The unit of the tensile test is MPa.

2.3. *In vitro* detection models

The middle ear is a delicate and intricate structure that serves multiple purposes. Researchers with backgrounds in medicine and technology have long been intrigued by the challenge of understanding and replicating its function. The numerical results are often tested and validated using human temporal bones. However, obtaining fresh specimens from living human is challenging, and their mechanical characteristics may vary with time and from person to person. To overcome this challenge, we developed a fully functional, anatomically accurate middle ear model, providing a reliable and repeatable testing environment. The auxiliary model for detecting the vibration effect of the ossicular chain in the middle ear was manufactured with the help of 3D printing technology. Segmentation of essential functional elements was carried out using micro-CT data of individual temporal bones. The ossicles were 3D-printed using SLM and FDM, and the soft tissues were cast into 3D-printed molds with silicone rubber. The ear canal, middle ear cavity, and inner ear were artificially designed, and caution was exercised to ensure that the tympanic membrane, ossicle, and oval window were printed at the correct anatomical position. Since 3D printing technology is unable to manufacture various soft tissues directly, the silicone rubber molding molds are first printed to enable replication of soft tissues using a variety of elastic materials through die molding method.

To detect vibration of different ossicular materials, we used an *in vitro* auxiliary test to measure the frequency response of the stapes floor plate at the end of the ossicular chain to sound. Pure-tone audiometry is perhaps the most important standard hearing test in clinical practice, but it was not applied in this study since patient feedback is required. Thus, the response of the stapes to sound was measured according to the American Society for Testing and Materials (ASTM) standard (F2504.24930-1), which is used to determine the output of implantable middle ear hearing devices (IMEHDs) in the human temporal bone (ASTM, 2014). With reference to this, the following laser vibration measurement system was built, which can convert the frequency signal into the displacement signal of the object vibration. Laser vibration measurement system (Polytec, Karlsruhe, Germany) containing laser Doppler vibrometer, a laser head (OFV-525 SENSOR; Polytec, Karlsruhe, Germany), and a controller (OFV-5000 VIBROMETER; Polytec, Karlsruhe, Germany; running at the maximum power of 100 W) was utilized to acquire the displacement and velocity. The system frequency range was from DC to 24 MHz. The system displacement resolution was up to 0.1 pm. VibSoft 4.81 software was used for signal generation and data acquisition. A laptop was used to output a pure tone signal, and a headphone was used to collect signals. The laser vibration measuring device used in the experiments is shown in Figure 4.

3. Results

The service life and hardness of the molded parts made of titanium alloy TC4, stainless steel 316L, and HA/PCL are directly related, and hardness serves as a crucial indicator in evaluating the mechanical properties of these materials. For each of the three materials, five molded parts were selected for testing, and the experimental data are presented in Table 3. The results indicate that the hardness of HA/PCL formed using FDM is lower than that of titanium alloy TC4 and stainless steel 316L formed using SLM. Among the three materials, titanium alloy TC4 exhibits the highest

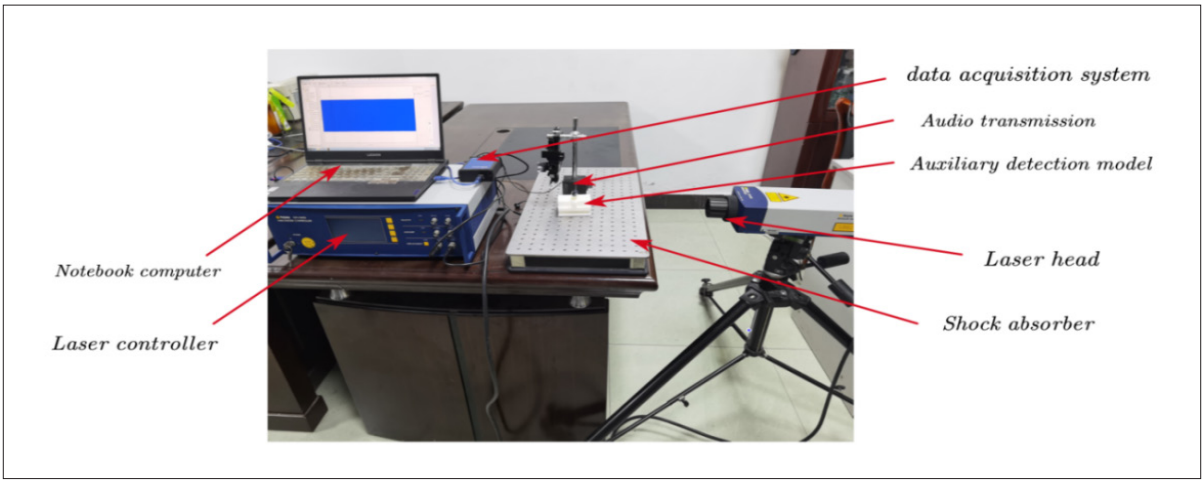


Figure 4. Experiment involving laser vibrometer.

hardness, with an average hardness value of 406 HV, while stainless steel 316L and HA/PCL have average hardness values of 246 HV and 107 HV, respectively.

Notably, the average hardness values of titanium alloy TC4 and stainless steel 316L produced via laser selective melting are significantly higher compared with those produced through traditional manufacturing methods. This can be attributed to the presence of dislocation structures embedded in coarse grains, resulting in a higher dislocation density than in traditionally manufactured materials. Consequently, the strength of the materials increases, leading to a 5% and 8% increase in hardness for titanium alloy TC4 and stainless steel 316L, respectively. Moreover, when comparing HA/PCL composites with pure PCL, the hardness of the HA/PCL composites also increases by 8%.

The prepared sample blocks were subjected to rubbing and wear at elevated temperatures, which produced an appearance of circular arc gullies on the contact surface. The cross-sectional contour of the worn gullies was extracted using a roughness profilometer, and the wear volume of the sample blocks was calculated through integral operations. The actual contours of the two opposite sections of the arc gullies were scanned, and their respective cross-sectional areas were calculated to determine the average value. The obtained data for the actual wear volume (WR) of the sample blocks are shown in Table 3.

$$WR = 2\pi R\bar{S} \quad \text{(II)}$$

In Equation II, $\bar{S}$ is the average value of the two opposite cross-sectional areas; and R is the friction radius (3 mm).

The test results of the sample blocks, yielded in the density detection method, are presented in Table 3. The SLM TC4 sample block has an average density of 4.416 g/cm^3, which is 97.91% of the theoretical value of 4.51 g/cm^3. The SLM 316L sample block has an average density of 7.819 g/cm^3, which is 97.98% of the theoretical value of 7.98 g/cm^3. However, both samples have slightly lower average densities compared with those produced by traditional methods due to instability during printing, which leads to incomplete melting of the powder on the surface. Defects were observed under the metallographic microscope after polishing. The density of HA is 3.076 g/cm^3, and PCL has a density of 1.146 g/cm^3. When combined in the HA/PCL composite, the density is 1.26 g/cm^3. These values indicate the influence of material composition on the final density of the composite.

The middle ear model was created using the 3D printing process. Initially, the main functional components were segregated from a single temporal bone micro-CT data set.

As depicted in Figure 5, the soft tissues were molded using silicone rubber into 3D-printed molds, while the ossicles were 3D-printed using SLM technology. Additionally, artificial constructions were implemented for the inner ear, tympanic chamber, and ear canal. However, special attention was given to ensuring that the oval window, ossicular ligaments, and tympanic membrane were placed in their anatomically correct positions within the model.

The difference between the experimental group and the simulation group lies in the model of the auditory ossicular chain. In the experimental group, the printed auditory ossicular chain omits the ligaments (malleus ligament, incus ligament, and stapes ligament). To account for the impedance posed by the inner ear lymph, normal saline was used as a substitute in the experiment. The 3D-printed small bones were assembled using glue, and the eardrum was replaced with a silicone rubber turnover mold. The

Table 3. Mechanical test parameters of materials

Sample number	Sample features		
	Hardness, HD (HV)	Wear volume, WR (mm^3)	Density, p (g/cm^3)
TC4 1	401.32	3.684	4.431
TC4 2	394.73	3.264	4.471
TC4 3	412.28	3.157	4.496
316L 1	247.94	5.542	7.974
316L 2	246.31	5.854	7.962
316L 3	251.18	5.674	7.976
HA/PCL 1	107.46	1.261	1.249
HA/PCL 2	106.72	1.236	1.256
HA/PCL 3	108.64	1.272	1.284

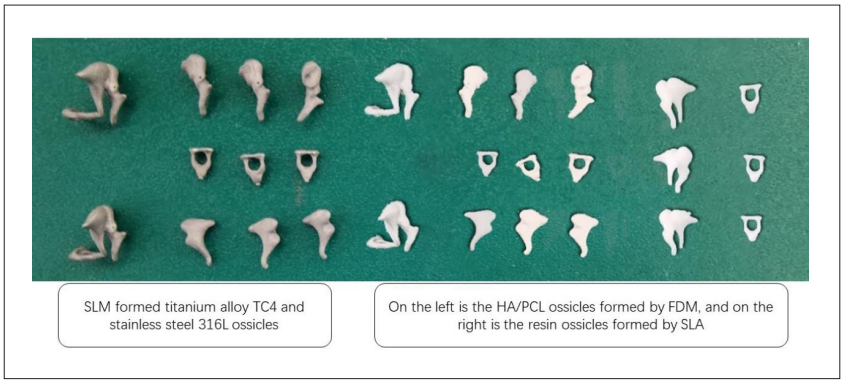


Figure 5. 3D-printed artificial ossicles.

overall trend was verified in the pre-experiment stage, and *in vitro* auxiliary detection was conducted. The procedure was repeated for the later-described combination. The *in vitro* test results are presented in Figure 6.

In order to determine the auditory characteristics, tests were carried out to measure the response of the stapes footplate to sound. Sound transmission experiments demonstrated that the model exhibits behavior similar to that of the human middle ear.

After conducting the mechanical testing of the materials mentioned earlier, the actual property parameters, including density, elastic modulus, and Poisson's ratio, were obtained. Figure 7 illustrates the comparison between the finite element numerical simulation and the experimental trend. The dotted line represents the simulation result, while the solid line represents the experimental result.

Figure 7a indicates that the mallet and masonry of auditory ossicles are both TC4; Figure 7b indicates that the ankle is TC4, and the silicon muscle is 316L; Figure 7c indicates that the ankle is TC4, and the silicon muscle is HA/PCL. Based on this configuration, the displacement trend of the stapes floor is studied by replacing the stapes with three different materials. In Figure 7, the solid

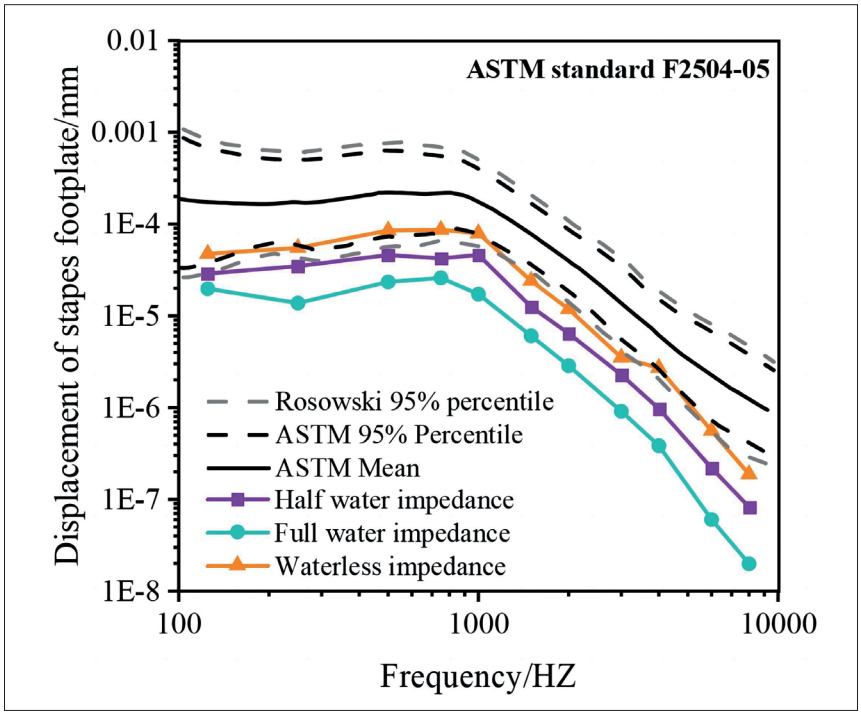


Figure 6. *In vitro* test validation.

line represents the result of finite element numerical simulation, while the dotted line represents the result of the experiment. The error band between them is also shown in the figure. The transmission characteristics of the healthy human middle ear can be simplified by considering two areas: the lower-frequency platform area and the higher-frequency roll-off area.

From Figure 7, it can be observed that the stapes floor vibration displacement measured via the laser vibration measurement system in the experiment is generally lower than the results of finite element analysis. The displacement values are 10% to 38% lower than the finite element values. While the overall curve trend is roughly consistent, some local curves of the ossicular material combination exhibit resonance, which is not clearly reflected in the actual measurement process. The main factors contributing to the discrepancies between the two are as follows:

(i) In the experiment, the 3D-printed ossicular chain omits the ligaments (malleus ligament, incus ligament, and stapes ligament). These ligaments play a crucial role in supporting and positioning the ossicles, allowing for sound amplification during the transmission process.

(ii) The 3D-printed ossicles are bonded with glue, and the contact position angle between the ossicles can also impact the measured values.

(iii) The experiment uses normal saline to replace the impedance brought by the inner ear lymph, and the tympanic membrane is replaced with a silicone rubber turnover mold.

Despite these experimental factors, the overall trend aligns well with the existing literature on the subject. The simulation and experimental results resonate in the frequency range of 750 Hz to 1000 Hz, with the frequency of 1000 Hz marking the transition from the plateau area to the roll-off area. The response displacement of the 3D-printed model can be measured in this frequency range.

When the malleus was fixed to TC4, and the incus material was the same, the stapes material being HA/PCL resulted in the highest stapes displacement value, followed by TC4, and finally 316L. The same trend was observed when the stapes material was kept constant, and the incus was replaced accordingly. In Figure 7d, the malleus is made of 316L and the incus is TC4; in Figure 7e, both the malleus and incus are 316L; in Figure 7f, the malleus is 316L, and the incus is HA/PCL; the trend of experimental results roughly aligns with that of simulation results. In Figure 7g, the malleus of the auditory ossicle is HA/PCL, and the incus is TC4; in Figure 7h, the malleus is HA/PCL, and the incus is 316L; in Figure 7i, both the malleus and incus are HA/PCL and exhibit similar trends in the experimental and simulation results when the stapes is replaced.

Based on the overall curve trend, the positions obtained through simulation are smoother compared with the experiment, where the data fluctuated in some positions. In the preferred material combinations, most intervals between 250 Hz to 750 Hz show an upward trend. At around 1000 Hz, there is a relatively stable stage. After 4000 Hz, there is a significant roll-off area. The human ear cannot perceive sounds below 20 Hz and above 20,000 Hz. The clinical hearing test frequency range is generally 125 Hz to 8000 Hz, and human speech frequencies fall between 500 Hz and 2000 Hz. The clinical calculation of decibels of hearing loss involves averaging the hearing thresholds of 500 Hz, 1000 Hz, and 2000 Hz. Comparing the above combinations of ossicular chain materials with the model itself, specific analysis selects the combination of materials resembling the normal human ear. The frequency displacement parameters of this combination are shown in Table 4. Although there is a discrepancy between the simulation and experimental values, the general trend is essentially consistent. In theory, the simulation results are also reliable.

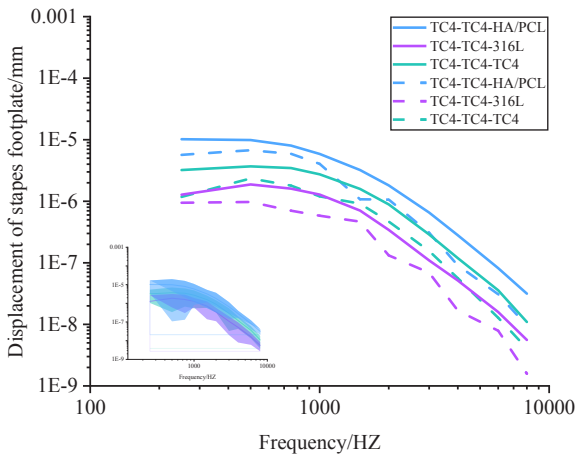
4. Discussion

4.1. Corrosion resistance analysis

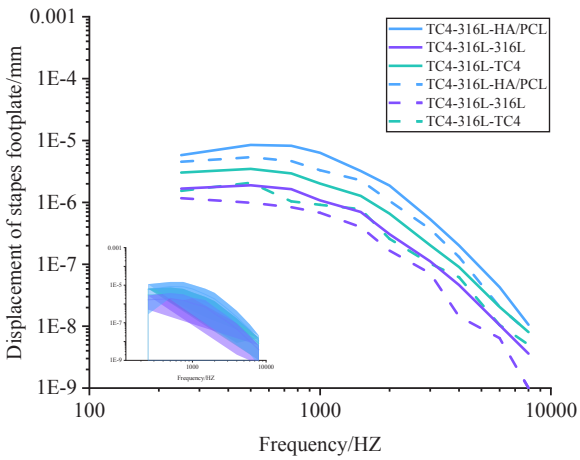
The 10 mm × 10 mm × 10 mm sample block's corroded contact surface was ground and polished until no scratches were present. Wires were drawn from other surfaces and insulated with glue to conduct the open circuit potential and moving point polarization curves. During the open circuit potential test, the metal sample block was immersed in a NaCl solution without any external current applied. This allows the sample to reach a stable potential value in a corrosive state. The results obtained indicate the material's stability in the corrosive solution. A more positive open circuit potential value in the material test reflects better stability, less corrosion tendency, and stronger corrosion resistance. Conversely, a poorer electrochemical stability was indicated by a less positive value.

Figure 8 illustrates the potentiodynamic polarization curve, which is obtained by adjusting the potential to observe changes in current density. This curve reflects the polarization and passivation process characteristics of the sample block, allowing the extraction of relevant parameters for analysis.

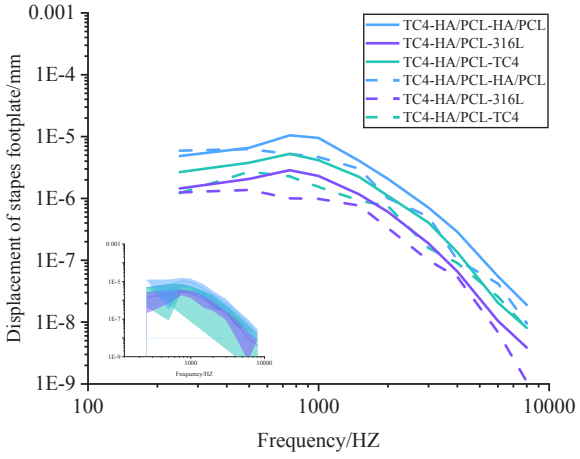
It can be observed that although the corrosion potential and current of TC4 and 316L are different, the overall trend of the potentiodynamic polarization



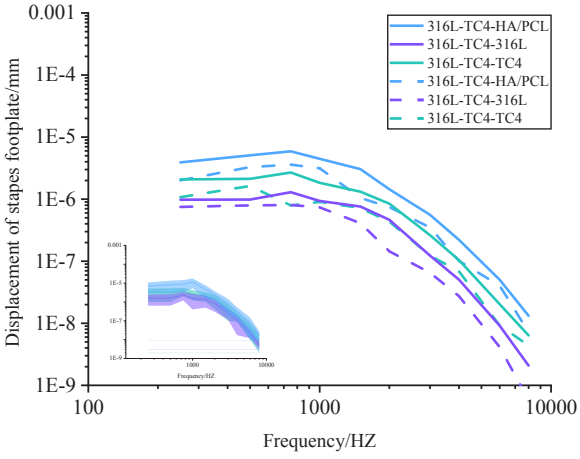
(a) Stapes floor displacement of TTx



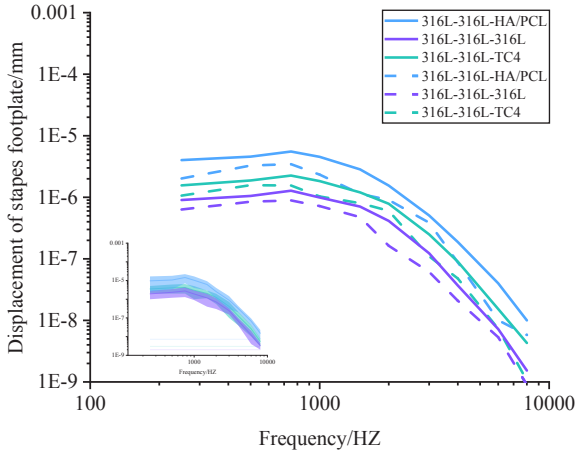
(b) Stapes floor displacement of T3x



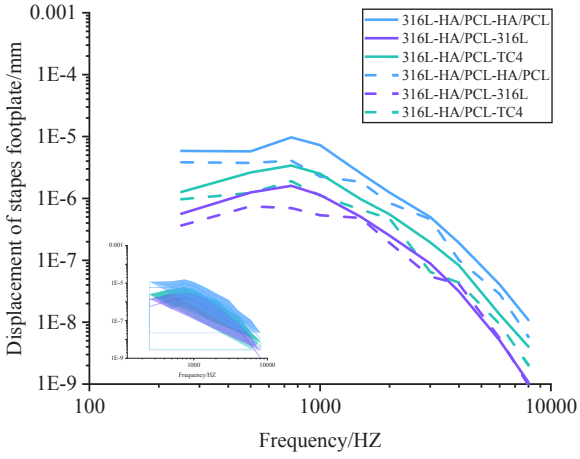
(c) Stapes floor displacement of THx



(d) Stapes floor displacement of 3Tx

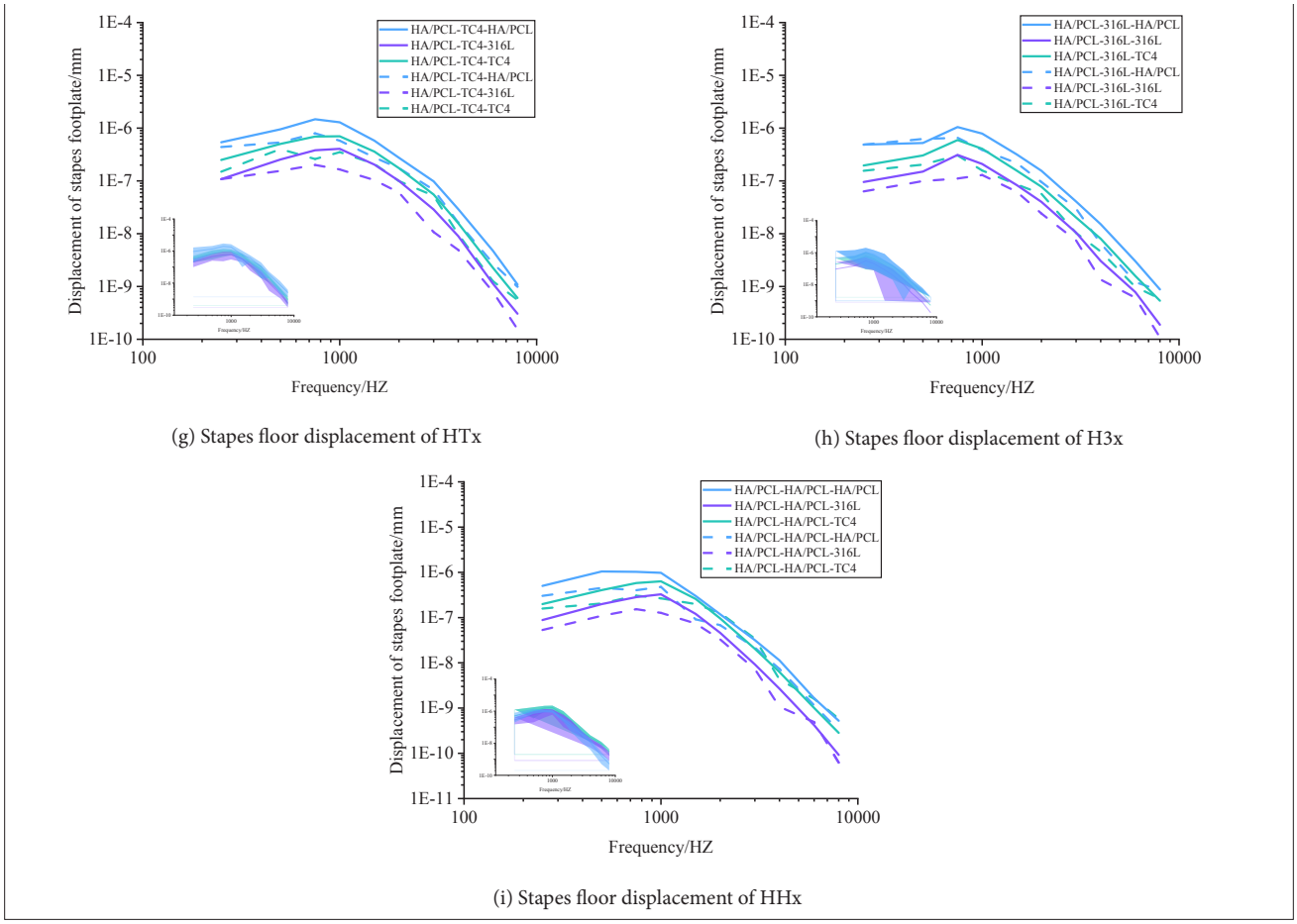


(e) Stapes floor displacement of 33x



(f) Stapes floor displacement of 3Hx

Continued...



(g) Stapes floor displacement of HTx

(h) Stapes floor displacement of H3x

(i) Stapes floor displacement of HHx

Figure 7. Comparison of stapes floor displacement between experimental results (dotted line) and simulation results (solid line).

curves is roughly similar. By performing Tafel linear extrapolation, the values of E_{corr} (self-corrosion potential) and I_{corr} (self-corrosion current density) can be obtained, as shown in Table 5. I_{corr} (self-corrosion current density) is an indicator of the corrosion rate, with a smaller value indicating slower corrosion, and vice versa. The corrosion rate of SLM TC4 was faster than that of 316L. E_{corr} (self-corrosion potential) reflects the corrosion trend of metal materials. A smaller value suggests higher susceptibility to corrosion, whereas a higher value indicates better corrosion resistance. The corrosion potential of SLM 316L (-0.355 V) is 37.5% higher than that of TC4 (-0.568 V). Both 316L and TC4 exhibit distinct passivation regions, with the corrosion resistance of 316L being superior to that of TC4.

Table 6 presents data obtained from tensile tests conducted on the three materials. The results indicate that the tensile properties of metal-molded parts are significantly better than those of plastic parts. Additionally, TC4 exhibits better tensile properties than 316L. In terms of molding, 316L outperforms both TC4 and HA/PCL. The average values from the table data are used to represent the material property parameters of the ossicular materials.

4.2. Frequency response analysis of TxH

Figure 9 shows the stapes floor displacement of three material combinations: TC4-TC4-HA/PCL (TTH), TC4-316L-HA/PCL (T3H), and TC4-HA/PCL-HA/PCL (THH). The densities of the malleus head, malleus neck, and malleus handle are 2.55 g/cm^3, 4.53 g/cm^3, and 3.7 g/cm^3, while the density of the malleus replaced with TC4 becomes 4.42 g/cm^3. The masses of the three parts became 1.73, 0.97, and 1.19 times the normal value, respectively, resulting in an overall mass improvement compared with the original parameter model. The elastic modulus of the malleus changed from 14.1 GPa to 110.4 GPa, and Poisson's ratio increased by 0.4. The stapes was replaced with HA/PCL, and its density changed from 2.2 g/cm^3 to

Table 4. Frequency displacement analysis

Category	Ossicular combination	Frequency (Hz)		
		500	1000	2000
Simulation	TC4+TC4+HA/PCL (TTH)	1.428E-5	9.564E-6	3.790E-6
	TC4+316L+HA/PCL (T3H)	1.599E-5	7.022E-6	2.667E-6
	TC4+HA/PCL+HA/PCL (THH)	1.058E-5	1.099E-5	2.572E-6
	316L+TC4+HA/PCL (3TH)	9.083E-6	7.066E-6	2.241E-6
	316L+316L+HA/PCL (33H)	4.575E-6	4.533E-6	1.548E-6
	316L+HA/PCL+HA/PCL (3HH)	4.751E-6	5.266E-6	9.463E-7
	HA/PCL-TC4-HA/PCL (HTH)	9.490E-6	1.2905E-5	2.741E-6
	HA/PCL-316L-HA/PCL (H3H)	5.232E-6	7.874E-6	1.553E-6
	HA/PCL-HA/PCL-HA/PCL (HHH)	1.046E-5	9.766E-6	1.180E-6
Experiment	TC4+TC4+HA/PCL (TTH)	6.775E-6	4.049E-6	1.064E-6
	TC4+316L+HA/PCL (T3H)	5.674E-6	3.613E-6	1.057E-6
	TC4+HA/PCL+HA/PCL (THH)	6.284E-6	2.264E-6	1.009E-6
	316L+TC4+HA/PCL (3TH)	3.283E-6	3.146E-6	7.415E-7
	316L+316L+HA/PCL (33H)	3.275E-6	2.336E-6	9.048E-7
	316L+HA/PCL+HA/PCL (3HH)	3.751E-6	2.266E-6	8.463E-7
	HA/PCL-TC4-HA/PCL (HTH)	5.349E-6	5.790E-6	1.741E-6
	HA/PCL-316L-HA/PCL (H3H)	6.232E-6	3.874E-6	9.531E-7
	HA/PCL-HA/PCL-HA/PCL (HHH)	4.546E-6	4.766E-6	6.802E-7

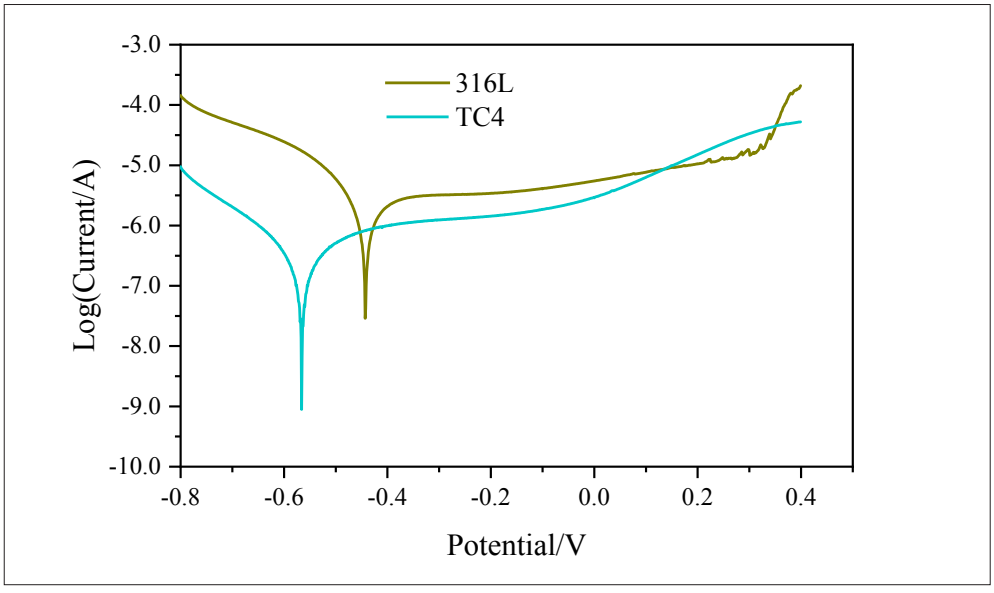


Figure 8. Polar potential curve of samples.

1.26 g/cm^3. The mass of the stapes was reduced to 0.57 times the normal value. Additionally, the elastic modulus of the stapes decreased from 14.1 GPa to 769.2 MPa, and the Poisson's ratio decreased by 0.3. The difference among the three combinations was the incus part (incus body, incus long leg, and incus short leg), with a density of 2.36 g/cm^3, 5.08 g/cm^3, and 2.26 g/cm^3, and the elastic modulus was 14.1 GPa. When the incus part was TC4, the masses of the three parts were 1.91, 0.87, and 1.99 times the normal value, respectively, and the elastic modulus increased from

Table 5. Electrochemical parameters

Sample	E_{corr} (V)	I_{corr} (A/cm²)
316L	-0.355	5.61E-04
TC4	-0.568	6.15E-04

14.1 GPa to 110.4 GPa. When the incus part was 316L, the masses of the three parts were 3.42, 1.57, and 3.53 times the normal value, respectively, and the elastic modulus increased from 14.1 GPa to 172.9 GPa. When the incus part was HA/PCL, the masses of the three parts were 0.53, 0.25, and 0.56 times the normal value, respectively, and the elastic modulus decreased from 14.1 GPa to 769.2 MPa.

Figure 10 shows the equivalent sound pressure (ESP) level changes in TTH, T3H, and THH. In the frequency range of 0.25–0.50 kHz, all three combinations exhibit a gradual upward trend in the ESP curves. The T3H has slightly higher ESP curve values compared with TTH and THH. However, all three combinations are in a state of hearing impairment. The maximum deterioration values occur at 0.25 kHz, with respective values of 2.36 dB, 3.1 dB, and 6.6 dB. As the frequency increases, the degree of hearing impairment decreases. In the frequency range of 0.5–1.0 kHz, the ESP curve of TTH shows a gradual upward trend, and the hearing progressively improves. Around 1 kHz, the hearing returns to normal levels. As for T3H, the ESP curve initially exhibits an upward trend followed by a decline, with a minimum worsening value of 0.64 dB at 0.75 kHz. On the other hand, THH shows significant fluctuations in the ESP curve, first demonstrating a sharp rise and then a slight decrease.

Table 6. Tensile test data

Number	Tensile strength (MPa)	Yield strength (MPa)	Elongation at break (%)	Elastic modulus (Ma)
TC4 1	997	946	15.7	107.4×10^6
TC4 2	987	937	14.6	108.2×10^6
TC4 3	981	928	14.3	106.9×10^6
316L 1	681	528	46.3	182.7×10^6
316L 2	677	534	47.2	176.5×10^6
316L 3	674	532	46.8	181.6×10^6
HA/PCL 1	18.96	17.67	13.12	58.06
HA/PCL 2	18.47	16.94	12.29	60.23
HA/PCL 3	18.16	17.52	11.96	59.68

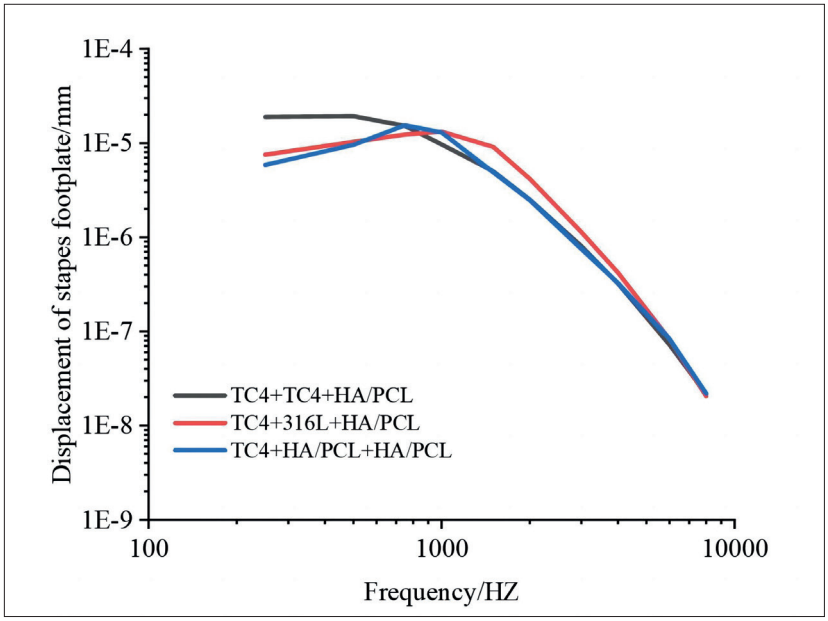


Figure 9. Stapes floor displacement of TTH, T3H, and THH.

The hearing changes range from -4.6 dB to 1.39 dB. In the frequency range of 1–4 kHz, the ESP curve of TTH shows a notched trend followed by a gradual slope. At 1.5 kHz, the hearing decreases by 1.38 dB. In the 2–4 kHz range, the average hearing gain is 0.52 dB. On the other hand, both T3H and THH exhibited a decline in their ESP curves initially, with reductions of 2.1 dB and 3.5 dB, respectively. Later, they stabilize into a mild slope, with average worsening values of 3 dB and 2.8 dB, respectively. In the frequency range of 4–8 kHz, both TTH and T3H show similar trends in their ESP curves, displaying an upward slope. TTH experiences a hearing gain, with the maximum compensatory value being 1.63 dB at 8 kHz. T3H also shows hearing improvement, with the worsening value reduced to 2.7 dB at 8 kHz. Conversely, the ESP curve of THH initially declines before rising, but compared with the mid-frequency range, there is a decline in hearing sensitivity, with a maximum worsening value of 5.8 dB.

4.3. Frequency response analysis of 3xH

Figure 11 shows the stapes floor displacement of three material combinations: 316L-TC4-HA/PCL (3TH), 316L-316L-HA/PCL (33H), and 316L-HA/PCL-HA/PCL (3HH). In these three combinations, the malleus is fixed as 316L, the stapes is fixed as HA/PCL, and the incus material is replaced. The density of the stapes bone is altered from the normal values of 2.55 g/cm^3, 4.53 g/cm^3, and 3.7 g/cm^3 to 7.82 g/cm^3, and the mass increases to 3.0, 4.4, and 2.1 times the normal values, respectively. Additionally, the elastic modulus changes from 14.1 GPa to 172.9 GPa, which is equivalent to 12.2 times that of a normal human ear. However, the Poisson's ratio remains unchanged.

Figure 12 shows the ESP level changes in 3TH, 33H, and 3HH. In the frequency range of 0.25–0.5 kHz, all three ESP curves are below the threshold line and exhibit varying degrees of hearing impact. For 3TH and 33H, the trend shows a slow upward slope, with average worsening values of 6.7 dB and 12.7 dB, respectively. On the other hand, 3HH demonstrates a relatively stable trend, with a consistent worsening value of around 11.6 dB. In the frequency range of 0.5–1.0 kHz, the ESP curves of 3TH and 3HH initially show an upward trend followed by a decline, resulting in improved hearing compared with the previous range, with reduced worsening values of 1.6 dB and 4.7 dB, respectively. On the other hand, the ESP curve for 33H continues to rise, although with varying magnitudes, leading to an improved worsening value of 6.6 dB. In the frequency range of 1–4 kHz, the three combinations exhibit significant fluctuations. The ESP curve of 3TH initially experiences a slow decline from 1 to 3 kHz, followed by a sharp drop with a total change of 5.6 dB. The average worsening value reaches 7.2 dB. The ESP curve of 33H shows a notched pattern, indicating unstable auditory behavior, with an average worsening

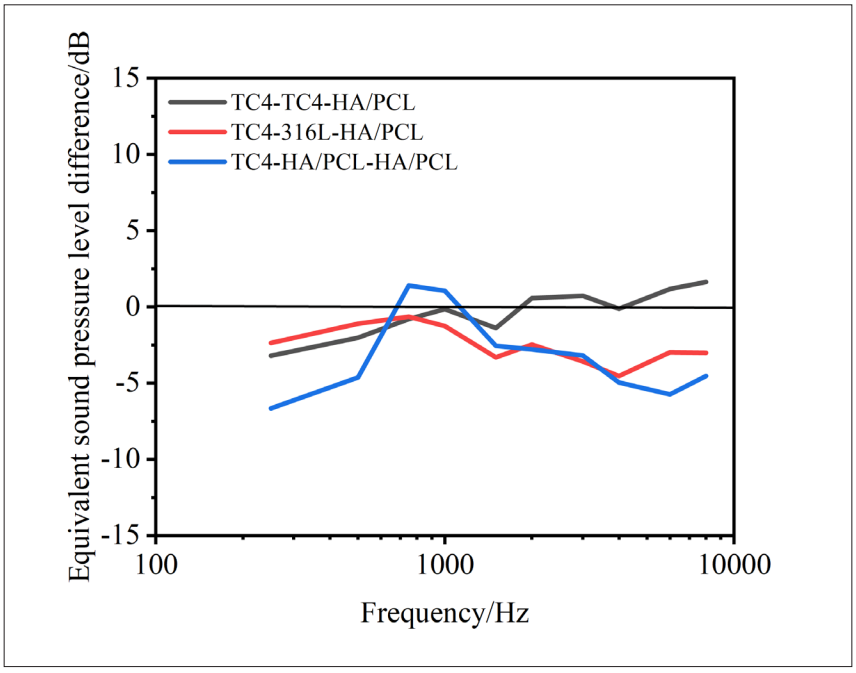


Figure 10. ESP curves of TTH, T3H, and THH.

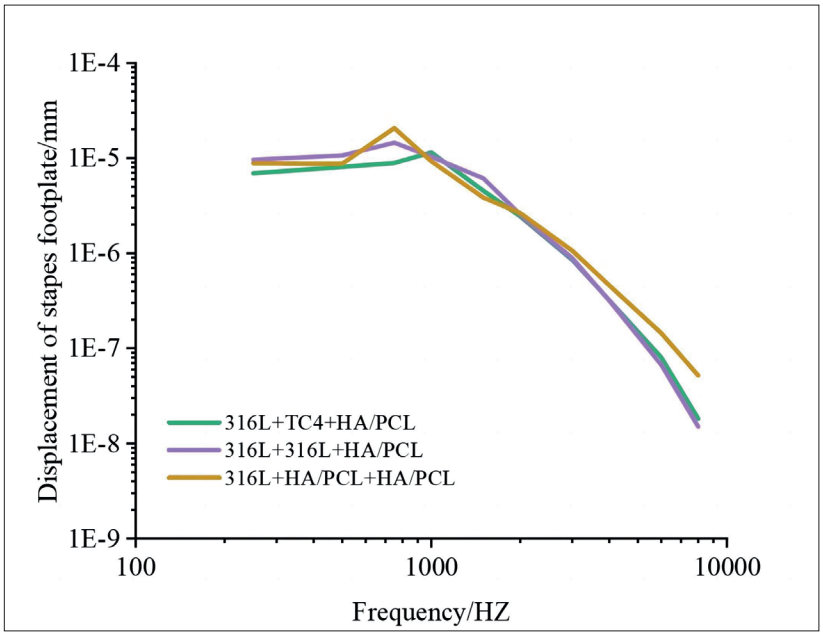


Figure 11. Stapes floor displacement of 3TH, 33H, and 3HH.

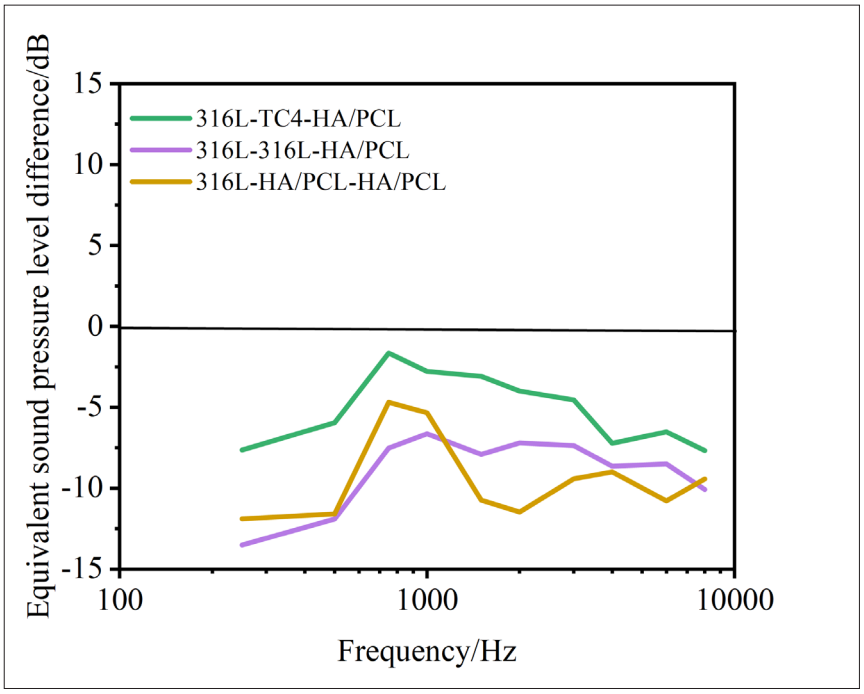


Figure 12. ESP curves of 3TH, 33H, and 3HH.

value of 7.4 dB. As for 3HH, the ESP curve first undergoes a significant decline in hearing by 11.4 dB, but later shows signs of improvement in auditory responses. In the frequency range of 4–8 kHz, both 3TH and 33H show an upward trend followed by a decline in their ESP curves. In the higher frequency range, the average hearing effect decreases by 7.3 dB and 8.9 dB, respectively, indicating a weakening of auditory behavior compared with the mid-frequency range. On the other hand, 3HH shows a trend of first declining and then rising, with minimal fluctuations between frequencies. The worsening value at 6 kHz reaches 10.7 dB.

4.4. Frequency response analysis of HxH

Figure 13 shows the stapes floor displacement of three material combinations: HA/PCL-TC4-HA/PCL (HTH), HA/PCL-316L-HA/PCL (H3H), and HA/PCL-HA/PCL-HA/PCL (HHH). In these three combinations, the malleus and stapes are fixed as HA/PCL, and the incus material is replaced. The density of the malleus bone is altered from the normal values of 2.55 g/cm^3, 4.53 g/cm^3, and 3.7 g/cm^3 to 1.58 g/cm^3, and the mass decreases to 0.61, 0.34, and 0.42 times the normal values, respectively. Additionally, the elastic modulus changes from 14.1 GPa to 787.2 MPa, which is reduced to 1/17.9 times that of a normal human ear.

Figure 14 shows the ESP level changes in HTH, H3H, and HHH. It can be clearly seen that when both the malleus and stapes are HA/PCL, the three curves mostly lie below the threshold line. In the frequency range of 0.25–0.5kHz, the hearing response values of HTH vary from -10.9 dB to 2.5 dB as the frequency increases. The HHH curve also shows an upward trend, precisely recovering to the normal hearing level at 1 kHz. The H3H curve exhibits an initial rise followed by a plateau, with no feedback in the low-frequency range, and the minimum worsening value is 1.84 dB.

Among the nine different combinations of ossicular chain materials mentioned above, TTH shows an improved hearing gain in the mid-high frequency range, with an overall hearing change of within 3 dB. T3H and 3TH exhibit an overall hearing change of ±5 dB. HTH, H3H, and HHH demonstrate hearing behavior within ±2.5 dB of the normal ear in the 0.75–2.00 kHz frequency range. The other combinations all have significantly reduced hearing levels.

5. Conclusion

Titanium alloy TC4, stainless steel 316L, and composite HA/PCL were chosen as materials for ossicular replacement. Using finite element analysis and an in vitro verification experiment, individual replacements of the ossicles and three bone material replacements were conducted for frequency response analysis. In the individual ossicle replacements, both TC4 and 316L effectively replaced the malleus and incus, with a significant increase in average displacement of the stapes, achieving a match in auditory behavior. However, when replacing the malleus and incus with HA/PCL, there was a slight decrease in hearing in the low-frequency range. On the other hand, when replacing the stapes with the three mentioned materials, varying degrees of worsening were observed. When all three ossicles were replaced simultaneously and the finite element simulation results were compared with laser vibrometer data, it was found that among the three ossicles, with the same incus and stapes materials, the malleus performed better with TC4, followed by 316L. With the same malleus and stapes materials, the incus made of TC4 still performed better than 316L and HA/PCL. With the same malleus and incus materials, the stapes made of HA/PCL performed better than TC4 and 316L. Furthermore, the combination of TTH was found to bear a higher resemblance to a real

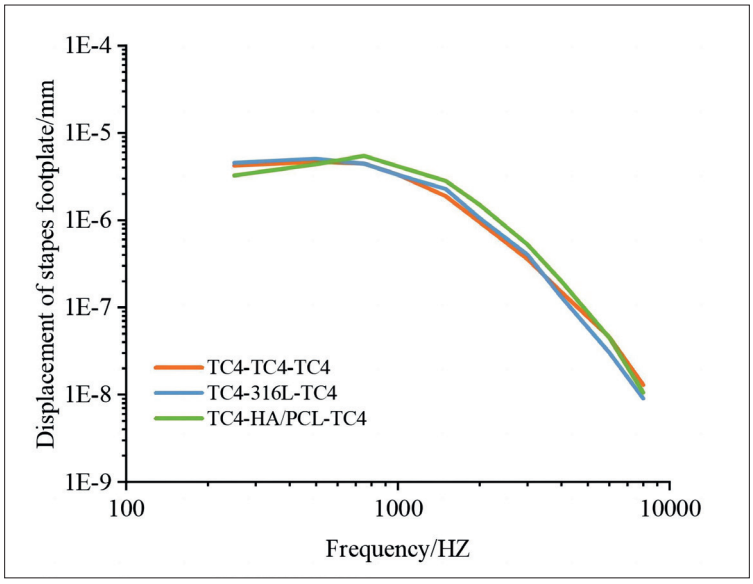


Figure 13. Stapes floor displacement of HTH, H3H, and HHH.

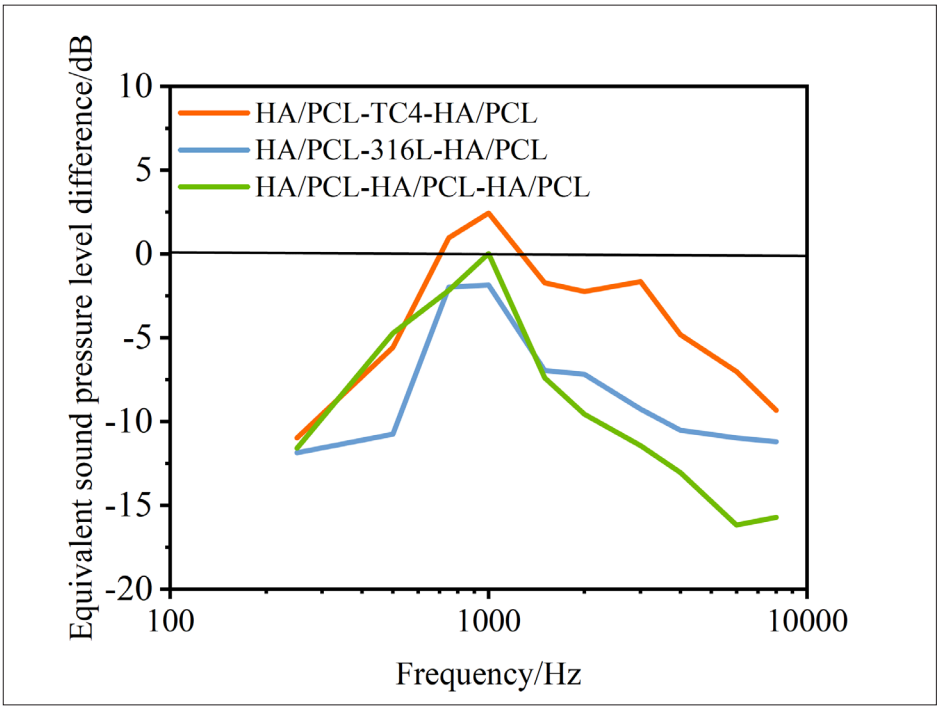


Figure 14. ESP curves of HTH, H3H, and HHH.

normal ear ossicular model, with the malleus made of TC4, the incus made of TC4, and the stapes made of HA/PCL.

Considering the different combinations of ossicular chain materials, only a few combinations meet the hearing requirements, while most of the combinations do not yield satisfactory results. However, from the perspective of finite element analysis, these combinations provide preoperative predictions for the reconstruction of the entire ossicular chain. In future research, considering the difficulty in obtaining temporal bone specimens, the focus can be shifted to developing external auxiliary detection devices for the middle ear ossicular chain. Resonance phenomena in numerical simulations can be addressed to improve the accuracy of measurement results. *In vitro* simulations of various middle ear pathological environments can be conducted to provide theoretical predictions for actual ossicular surgery. Finite element models of auditory ossicles can be used to predict the effects of different materials, allowing for the rational selection and matching of ideal materials for each ossicular position. Additionally, the material properties of each part of the ossicles and their various positions can be studied in detail to ensure closer alignment with autologous ossicles' biocompatibility requirements. Optimization of the entire ossicular chain's material combination, as well as the connection and structure of each part, should also be considered.

Acknowledgments

None.

Funding

This work was financially supported by the National Natural Science Foundation of China (52275224, 52275296), the Fundamental Research Funds for the Central Universities (2020ZDPYMS22), and the Priority Academic Program Development of Jiangsu Higher Education Institutions (PAPD).

Conflict of interest

The authors declare no conflicts of interest.

Author contributions

Conceptualization: Jingbin Hao, Yin Zhu
Funding acquisition: Jingbin Hao, Houguang Liu
Investigation: Yin Zhu
Methodology: Jingbin Hao
Supervision: Jingbin Hao, Houguang Liu
Writing – original draft: Jingbin Hao, Yin Zhu, Ding Shen
Writing – review & editing: Md Thowfiqure Rahman, Yinxin Kou

Ethics approval and consent to participate

Not applicable.

Consent for publication

Not applicable.

Availability of data

The data generated in this study are available from the corresponding author upon reasonable request.

References

1. Bornitz M, Hardtke HJ, Zahnert T. Evaluation of implantable actuators by means of a middle ear simulation model. *Hear Res*. 2010;263(1-2):145-151.
doi: 10.1016/j.heares.2010.02.007

2. Cheng JT, Ravicz M, Guignard J, Furlong C, Rosowski JJ. The effect of ear canal orientation on tympanic membrane motion and the sound field near the tympanic membrane. *J Assoc Res Otolaryngol.* 2015;16:413-432.
doi: 10.1007/s10162-015-0516-x

3. Eiber A. Mechanical modeling and dynamical behavior of the human middle ear. *Audiol Neurotol.* 1999;4(3-4): 170-177.
doi: 10.1159/000013837

4. Ferris P, Prendergast PJ. Middle-ear dynamics before and after ossicular replacement. *J Biomech.* 2000;33(5):581-590.
doi: 10.1016/s0021-9290(99)00213-4

5. Aernouts J, Aerts JR, Dirckx JJ. Mechanical properties of human tympanic membrane in the quasi-static regime from in situ point indentation measurements. *Hear Res.* 2012;290(1-2):45-54.
doi: 10.1016/j.heares.2012.05.001

6. De Greef D, Pires F, Dirckx JJ. Effects of model definitions and parameter values in finite element modeling of human middle ear mechanics. *Hear Res.* 2017;344:195-206.
doi: 10.1016/j.heares.2016.11.011

7. Kim N, Steele CR, Puria S. The importance of the hook region of the cochlea for bone-conduction hearing. *Biophys J.* 2014;107(1):233-241.
doi: 10.1016/j.bpj.2014.04.052

8. Aibara R, Welsh JT, Puria S, Goode RL. Human middle-ear sound transfer function and cochlear input impedance. *Hear Res.* 2001;152(1-2):100-109.
doi: 10.1016/S0378-5955(00)00240-9

9. Gan RZ, Sun Q, Dyer RK, Chang K-H, Dormer KJ. Three-dimensional modeling of middle ear biomechanics and its applications. *Otol Neurotol.* 2002;23(3):271-280.
doi: 10.1097/00129492-200205000-00008

10. Huber A, Linder T, Dillier N, et al. Intraoperative assessment of stapes movement. *Ann Otol Rhinol Laryngol.* 2001;110(1):31-35.
doi: 10.1177/000348940111000106

11. Rohani SA, Ghomashchi S, Agrawal SK, Ladak HM. Estimation of the Young's modulus of the human pars tensa using in-situ pressurization and inverse finite-element analysis. *Hear Res.* 2017;345:69-78.
doi: 10.1016/j.heares.2017.01.002

12. De Greef D, Aernouts J, Aerts J, et al. Viscoelastic properties of the human tympanic membrane studied with stroboscopic holography and finite element modeling. *Hear Res.* 2014;312:69-80.
doi: 10.1016/j.heares.2014.03.002

13. Salmi M. Additive manufacturing processes in medical applications. *Materials*. 2021;14(1):191.
doi: 10.3390/ma14010191

14. Iwasa J, Engebretsen L, Shima Y, Ochi M. Clinical application of scaffolds for cartilage tissue engineering. *Knee Surg Sports Traumatol Arthrosc*. 2009;17(6):561-577.
doi: 10.1007/s00167-008-0663-2

15. Liu H, Cheng J, Yang J, et al. Concept and evaluation of a new piezoelectric transducer for an implantable middle ear hearing device. *Sensors*. 2017;17(11):2515.
doi: 10.3390/s17112515

16. Xue L, Liu H, Yang J, Liu S, Zhao Y, Huang X. Research on coupling effects of actuator and round window membrane on reverse stimulation of human cochlea. *Proc Inst Mech Eng H*. 2021;235(4):447-458.
doi: 10.1177/0954411920987960

17. Kuru I, Maier H, Müller M, Lenarz T, Lueth TC. A 3D-printed functioning anatomical human middle ear model. *Hear Res.* 2016;340:204-213.
doi: 10.1016/j.heares.2015.12.025

ACCSCIENCE PUBLISHING

International Journal of Bioprinting

RESEARCH ARTICLE

A parallel multilayered neurovascular unit-on-a-chip for modeling neurovascular microenvironment and screening chemotherapeutic drugs

Yuanyuan Xu[1,2,3], Dongsheng Kong[4], Ting Zhang[1,2,3]*, Zhuo Xiong[1,2,3]*, and Wei Sun[1,2,3,5]*

[1]Biomanufacturing Center, Department of Mechanical Engineering, Tsinghua University, Beijing, China

[2]Biomanufacturing and Rapid Forming Technology Key Laboratory of Beijing, Beijing, China

[3]Biomanufacturing and Engineering Living Systems Innovation International Talents Base (111 Base), Beijing, China

[4]The First Medical Center of the PLA General Hospital, Beijing, China

[5]Department of Mechanical Engineering, Drexel University, Philadelphia, United States of America

(This article belongs to the *Special Issue: Bioprinting Process for Tumor Model Development*)

Abstract

Humans are grappling with increasing occurrence rate of brain tumors, which are associated with unfavorable prognosis and cognitive neurotoxicity caused by chemotherapy. Ideally, therapeutic drugs for brain tumors should efficiently suppress the tumors while minimizing neurotoxic effects. To facilitate drug development, *in vitro* pathological models of human brain tumors are essential. Here, we engineered a sophisticated human neurovascular unit (hNVU) chip that simulates the microenvironment of pediatric brain using three-dimensional bioprinting technology. The hNVU chip featured a multilayer parallel architecture composed of a biomimetic blood–blood barrier (BBB) and brain region. An automated perfusion system in the chip simulated the blood flow within the brain. The specialized liquid channels within the brain region enabled comprehensive analysis of drug metabolites. The blood–brain barrier (BBB) structure is composed of endothelial cells, pericytes, and astrocytes, and the brain region contains endothelial cells, pericytes, astrocytes, microglia, and neural progenitor cells, representing the cellular components found in pediatric brain. To replicate the basal membrane, we utilized GelMA (gelatin methacryloyl), gelatin, and laminin as primary bioinks, with the addition of fibrin to mimic the pathological characteristics of brain extracellular matrix (ECM). The BBB membrane exhibited a maximum electrical resistance of 360 Ω cm^2 and demonstrated impressive semipermeability by effectively blocking the permeability of large molecules with a molecular weight of 10 kDa. Gene expression analysis and immunofluorescence staining revealed a gradual increase in COL4A1 and fibrin, indicating remodeling of the ECM by the cells. Astrocytoma cells (SF188) were introduced in the model to construct a neurovascular unit containing pediatric brain tumor cells. We evaluated the therapeutic effects and toxicity profiles of chemotherapeutic drugs, including vorinostat and 5-fluorouracil. Encouragingly, our investigations revealed that vorinostat not only exhibited remarkable tumor-suppressing efficacy but also induced lower neurocognitive toxicity than

***Corresponding authors:**
Ting Zhang
(t-zhang@tsinghua.edu.cn)

Zhuo Xiong
(xiongzhuo@tsinghua.edu.cn)

Wei Sun
(weisun@mail.tsinghua.edu.cn)

Citation: Xu Y, Kong D, Zhang T, Xiong Z, Sun W. A parallel multilayered neurovascular unit-on-a-chip for modeling neurovascular microenvironment and screening chemotherapeutic drugs. *Int J Bioprint.* 2024;10(3):1684. doi: 10.36922/ijb.1684

Received: August 26, 2023
Accepted: November 8, 2023
Published Online: February 28, 2024

Copyright: © 2024 Author(s). This is an Open Access article distributed under the terms of the Creative Commons Attribution License, permitting distribution, and reproduction in any medium, provided the original work is properly cited.

Publisher's Note: AccScience Publishing remains neutral with regard to jurisdictional claims in published maps and institutional affiliations.

5-fluorouracil. In summary, the hNVU chip served as a reliable and versatile platform for conducting comprehensive studies on the therapeutic effects of chemotherapy drugs for brain tumors.

Keywords: Blood–brain barrier; Brain tumors; Organ-on-a-chip

1. Introduction

Pediatric brain tumors, including medulloblastoma, diffuse high-grade glioma, and teratomas, are the primary cause of mortality among children with cancers, with an incidence rate of 30 cases per million.[1] The characteristics of pathogenesis and oncogenic targets of pediatric brain tumors differ from adult brain tumors, such as cellular constituent, expression of tumor molecular targets, and even the structure of the blood–brain barrier (BBB). For example, the neurovascular unit (NVU) of pediatric brain tumors includes neural progenitor cells (NPCs) that possess the capacity for differentiation into neurons and glia.[2] NPCs are almost absent in the adult brain,[3] but play a major role in childhood gliomas,[4-6] such as high-grade childhood gliomas.[7-9] Additionally, the epigenetic and genetic alterations of pediatric glioblastomas are different from adult glioblastomas.[10-12] For example, compared to adult glioblastoma, the relative low level of O^6-methylguanine-DNA methyltransferase hypermethylation in pediatric brain tumors may explain the differences in response to therapeutics with temozolomide.[13,14] Fibrin is usually absent in the brains of healthy adults but linked to brain diseases such as multiple sclerosis.[15] Therefore, the pathological mechanisms and therapeutic strategies used in adult brain tumors cannot be simply extrapolated to pediatric patients.[16] Pediatric brain tumors treated with therapeutic strategies of adult brain tumor often have poor prognosis and neuronal cognitive impairment. Therefore, pediatric brain tumor models must be employed to identify therapeutic agents that have not only chemotherapeutic efficacy but also minimal neurocognitive toxicity.[17]

The BBB plays critical roles in preventing harmful substances in the blood from entering the brain tissue.[18] The physiological structure of the neonatal BBB shares common properties with the mature adult BBB, such as the cellular and matrix constituents including brain microvascular endothelial cells, pericytes, glial cells, neurons, and basement membrane. However, since newborn BBB is not yet fully developed, it exhibits specific features like loose connections between cerebrovascular endothelial cells, insufficient basement membrane, and relatively high permeability.[19] Additionally, the expression of brain efflux transporters associated with BBB function differs between neonates and adults. For example, the newborn BBB shows a relatively low expression of brain efflux transporters like P-glycoprotein (P-gp) and breast cancer resistance protein (BCRP) compared to the adult BBB.[15]

The development of brain tumor disrupts the structure of BBB, known as the blood–tumor barrier (BTB),[20] affecting drug permeability and bioavailability.[20] This change also occurs in the BBB of pediatric brain tumors. Furthermore, pediatric brain tumors are associated with metabolic dysregulation, such as elevated levels of glycolysis, making metabolic abnormalities a target for drug development in the realm of neuro-oncology.[21] Different cell types within the neurovascular unit have distinct metabolic functions. For example, endothelial cells and glial cells mainly rely on and participate in glycolysis, while neurons mainly rely on ketone bodies as metabolic substrates.[22] The diverse cellular constituent of pediatric brain tumor models is critical to accurately mimic their metabolic pathology. Therefore, it is crucial to develop a model that mimics the structure and cellular composition of the neonatal BBB, providing a platform for the development of therapeutic drugs for brain tumors in children.

The human neurovascular unit (hNVU) organ chip, composed of human cells, can mimic the structure and functions of the BBB and brain region, offering a powerful platform for investigating both the physiological and pathological mechanisms of hNVU, as well as for developing therapeutic strategies for brain tumors.[23-25] Using microfluidic chip technology, Kim et al. developed a polydimethyl-siloxane (PDMS)-based hNVU chip consisted of multibranched microchannels that allowed for unidirectional flow.[23] The vascular channels within the chip were injected with a blend of biomimetic materials, including collagen I, hyaluronic acid, fibrin, neural stem cells (NSCs), brain endothelial cells (ECs), and brain pericytes (PCs). Although the complex geometric configuration of these microchannels successfully mimics the heterogeneity of the BBB, it was impractical for conducting the analysis of BBB functionality, such as barrier integrity assessments and drug permeability analyses. Furthermore, Maoz et al. developed an organ-on-chip model of the hNVU consisting of three linked chambers.[22] Each chamber simulated a different stage of the BBB process: inflow, brain, and outflow. This model facilitated the analysis of the metabolic function of various types of cells within the BBB without disrupting the model. However, the lack of spatial interactions between cells in

different chambers failed to fully replicate the intricate cellular interactions in the brain.

Compared to the linked organ chip, the multilayer parallel hNVU chip can mimic the multilayer microstructure of hNVU but also stimulate the interaction between the BBB and brain regions. Additionally, the parallel hNVU chip facilitates the observation of drug effects on the integrity of the BBB and the morphology and behavior of brain region cells through imaging. Bioprinting technology, which allows for the three-dimensional (3D) spatial positioning of multiple cell types blended with biometric hydrogels, offers prominent advantages in constructing multilayered parallel NVU models.[26-28] Moreover, the incorporation of biomimetic hydrogels that resemble the native brain extracellular matrix (ECM) not only provides biochemical and mechanical support for brain cells but also simulates the barrier function of the basement membrane.[29,30]

In this study, we employed organ-on-a chip and extrusion bioprinting techniques to develop a multilayered parallel NVU model that features the structural and cellular composition of BBB in pediatric brain. The model architecture would resemble a sandwich structure, with the upper and lower layers simulating the BBB and the intermediate layer imitating the brain tissue structure (Figure 1). The architecture is incorporated with the necessary cell types of pediatric brain, such as brain microvascular endothelial cells, brain microvascular pericytes (HBVP), embryo-derived astrocytes and microglia (HMC3), and induced pluripotent stem cell (iPSC)-derived NPCs. We induced differentiation of NPC cells into early neurons within the hydrogel matrix. This not only mimics the presence of neural stem cells in brain but also incorporates neuronal components. Furthermore, nutrient perfusion through the upper and lower BBB structures of the chip ensured sufficient nutrient supply. Notably, the two perfusion channels in the brain region could serve the dual purpose of nourishing the brain tissue region and evaluating drug permeability across the BBB as well as facilitating analysis of the metabolism of drugs in the brain region. Astroglioma cell SF188 (derived from the left temporal lobe tumor of an 8-year-old male patient) was introduced in the model to construct an hNVU chip with tumor cells to mimic the pediatric brain tumors for the study of chemotherapeutic drugs.

2. Materials and methods

2.1. Cell culture

Human cerebral microvascular endothelial cells (hCMEC/D3; ZQ0961, Zhong Qiao Xin Zhou Biotechnology Co., Ltd., Shanghai, China) were cultured in endothelial growth medium (ZQ-1304, Zhong Qiao Xin Zhou Biotechnology Co., Ltd., Shanghai, China) containing 5% fetal bovine serum (FBS; Gibco), 1% penicillin–streptomycin (Gibco), and EC growth supplement (ScienCell). Cell culture flasks for hCMEC/D3 culture were coated with 150 μg/mL of a collagen solution (Meilunbio, Dalian, China).

Human brain microvascular pericytes (HBVPs; ZQY006, Zhong Qiao Xin Zhou Biotechnology Co., Ltd., Shanghai, China) were cultured in pericyte medium (ZQ-1321; Zhong Qiao Xin Zhou Biotechnology Co., Ltd., Shanghai, China) containing 2% FBS (Gibco), 1% penicillin–streptomycin (Gibco), and PC growth supplement (ScienCell). Cell culture flasks for HBVP culture were coated with 20 μg/mL PLL solution (Beyotime, Shanghai, China) prior to cell seeding.

Immortalized human astrocytes (AC; CTCC-001-0398, Meisen Co., Ltd., Zhejiang, China) were cultured in astrocyte medium (Meisen Co., Ltd., Zhejiang, China) containing 5% FBS (Gibco), 1% penicillin–streptomycin (Gibco), and AC growth supplement (Meisen Co., Ltd., Zhejiang, China). The immortalized human astrocytes were established through hTERT-dependent immortalization of a human fetal (18 weeks gestation) brain-derived primary astrocytes culture. Cell culture flasks for astrocyte culture were coated with 0.15 mg/mL rat tail type-I collagen solution (Meisen Co., Ltd., Zhejiang, China) prior to cell seeding.

HMC3 cells (CRL-3304, ATCC) were cultured in HMC3 medium (ZQ-320, Zhong Qiao Xin Zhou Biotechnology Co., Ltd., Shanghai, China) containing 10% FBS (Gibco) and 1% penicillin–streptomycin (Gibco). The HMC3 cell line was established through SV40-dependent immortalization of a human fetal (embryo) brain-derived primary microglia culture.

Neural precursor cells (NPCs; Nuwacell, Hefei, China) were cultured in NPC medium (Nuwacell, Hefei, China) containing 2.5 μM blebbistatin (Nuwacell, Hefei, China). Cell culture flasks for astrocyte culture were coated with 0.5 μg/cm^2 ncLaminin511 solution (Nuwacell, Hefei, China) prior to cell seeding.

Malignant astrocytoma cells (SF188; WM-23XM167, Shen Zhen Wei Sa Biotechnology Co., Ltd., Shenzhen, China) were cultured in SF188 medium containing 10% FBS (Gibco) and 1% penicillin–streptomycin (Gibco). The SF188 glioblastoma cell line was derived from the left temporal lobe tumor of an 8-year-old male patient.

hCMEC/D3 cells between passages 6 and 15, HBVP cells between passages 8 and 15, immortalized human astrocytes between passages 8 and 15, HMC3 cells between passages 6 and 15, and SF188 cells between passages 6 and

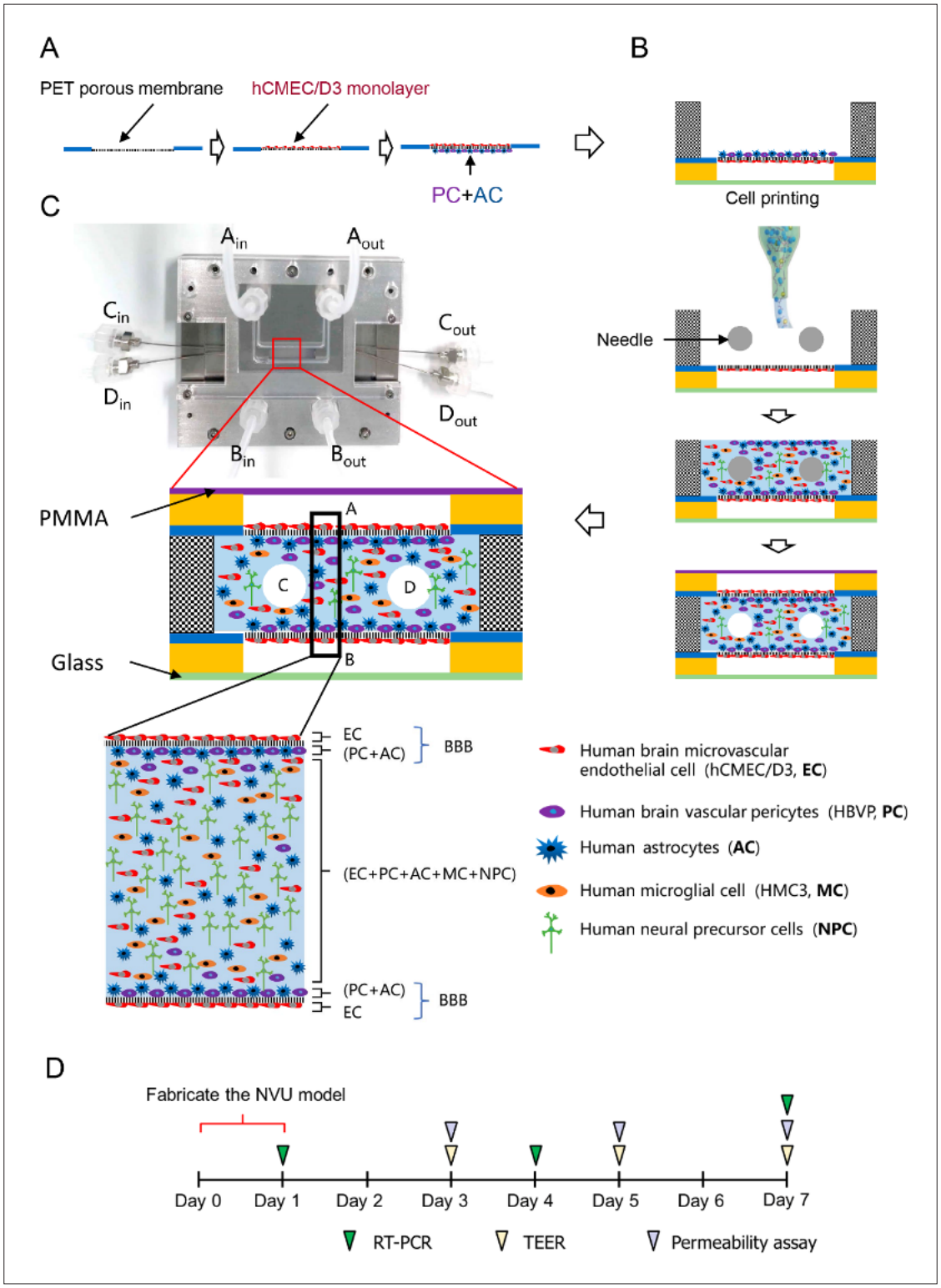


Figure 1. Schematic of the multilayered parallel hNVU chip. (A) Fabrication of upper and lower layers simulating the BBB. (B) Assembly process of the hNVU chip. (C) Macroscopic architecture of the hNVU chip and multilayered arrangement of five cell types within the chip. (D) Timeline of this study.

15 were used for all experiments. Cells were cultured in a humidified incubator with 5% CO_2 at 37°C.

2.2. Fabrication of the hNVU perfusion channel

The perfusion channel structure was made by printing SE1700. The SE1700 prepolymer (DOWSILTM SE1700 Clear Base) was mixed with a curing agent (DOWSILTM SE1700 Catalyst) at a 10:0.6 (w/w) ratio before printing. The mixed SE1700 silica gel was loaded into a 5 mL screw syringe (BD 302135), and then a 21G tapered needle was installed. The syringe was loaded onto the nozzle of the printer (SUNP Biotech, Biomaker2i), and the printing temperature was set to 26°C. The perfused channel B structure was obtained by printing SE1700 silica gel on a 160-μm-thick glass slide. Then, the samples were placed in an oven at 80°C for 1 h to fully cure the material. Ultraviolet (UV) irradiation and ozone sterilization treatment of the device was performed. A 160-μm glass was used for the convenience of confocal microscopy. Perfusion channel A was printed on 1-mm-thick PMMA (printing parameters are the same as printing SE1700 on 160-μm-thick glass slide). SE1700 prepolymer was used to bond the Luer female connector (1.6 mm (1/16 inch)) to the PMMA board, which was then sterilized with UV light and ozone. The pagoda end of the Luer female connector was connected to a 0.5 × 0.8 mm sterile silicone hose. M2 screws were used to fix the PMMA board to the hNVU device. The Luer male connector was connected to a stainless steel needle, and the pagoda end was connected to a 0.5 × 0.8 mm sterile silicone hose prior to assembly and perfusion (Figure S1 in Supplementary File).

2.3. Fabrication of the BBB structure for the hNVU chip

Cell printing technology and gravity-driven cell sedimentation technology were used for the fabrication of the BBB structure (Figure S2, Step 1, in Supplementary File). To prepare the cell suspension, we first digested cells from T75 cell culture flasks and prepared a cell suspension at a density of 4.67 × 10^6 cells/mL. Subsequently, we transferred 100 μL of cell suspension into 2 mL of cell culture medium using a pipette gun and mixed them by pipetting to prepare the cell suspension. Next, the cell suspension was transferred into a container with a Corning 3450 chamber PET membrane and mixed through shaking. Afterward, the cell suspension was left to rest for 6 h until the cells were fully attached to the PET membrane. On the other side of the PET film, we uniformly printed 7.5% gelatin ink material mixed with cells using extrusion technology (SUNP Biotech, Biomaker2i, Beijing, China) (Figure S3 in Supplementary File). During printing, the nozzle temperature was set to 21°C, the bottom plate temperature was set to 18°C, and a 25G needle was used. Subsequently, we placed the PET membrane containing the cells and gelatin in an incubator at 37°C. After 2 h, the gelatin turned into a sol state, and the cells began to settle and aggregate on the porous PET membrane. In the printing process, we used human brain microvascular pericytes (PCs) and human astrocytes (ACs), and their cell densities were 4 × 10^5 cells/mL and 4 × 10^5 cells/mL, respectively. Finally, adequate volume of medium was added for further cultivation.

2.4. Preparation of bioink for the brain regions in the hNVU chip

Phosphate-buffered saline (PBS; VivaCell, catalog number C3580-0500) was used to dissolve biomaterials including GelMA freeze-dried powder (stock solution concentration 12.5 wt. %), gelatin powder (stock solution concentration 12.5 wt. %), fibrinogen (25 mg/mL), thrombin powder (stock solution concentration 200 U/mL), and transglutaminase powder (stock solution concentration 30 U/mL). GelMA was purchased from SunP (Beijing) Biotech Co., Ltd (SUNP-Gel-G1); gelatin from MERCK (48722-100G-F); fibrinogen and thrombin from Solarbio (F8050 and T8021, respectively); and transglutaminase from Shanghai Yuanye Biotechnology Co., Ltd (S10156). $GelMA^+$ ink comprising 5% GelMA + 2.5 mg/mL fibrinogen + 5% gelatin + 20 μg/mL laminin + 3 U/mL transglutaminase was prepared by combining 0.4 mL GelMA (12.5 wt. %), 0.4 mL gelatin (12.5 wt. %), 0.1 mL fibrinogen (25 mg/mL), 0.1 mL transglutaminase (30 U/mL), and 10 μL laminin (2 mg/mL). Printing ink was prepared by mixing cells into the hydrogel; specifically, hCMEC/D3 cells (12 × 10^6 cells), HBVPs (4 × 10^6 cells), astrocytes (4 × 10^6 cells), HMC3 cells (4 × 10^6 cells), and NPC cells (1 × 10^6 cells) were mixed into 1 mL $GelMA^+$ ink.

2.5. Fabrication of the hNVU chip system

Sterile scalpels and scissors were used to cut out the constructed barrier structure (Figure S2, Step 1, in Supplementary File), which was installed on the NVU microenvironment device (Figure S2, Step 3, in Supplementary File). The outer frame structure of the hNVU device is installed (Figure S2, Step 4, in Supplementary File). The cell-containing $GelMA^+$ ink was loaded into a 3 mL screw-top syringe (BD 302113) installed with an autoclaved 25G stainless steel needle. The 3 mL screw-top syringe was installed on the printing nozzle of the cell printer (SUNP Biotech, Biomaker2i). A layer of cell ink material was printed at the temperature of the nozzle at 25°C (the temperature of the bottom plate of the printing platform was set at 18°C). The stainless steel needle (Figure S2, Step 5, in

Supplementary File) used to construct the perfusion channel into the chip device was inserted and centered axially (a 250 μm diameter silver needle was inserted into the inner tube of the stainless steel needle). The print cell ink material fills the area where the stainless steel needle was located at a nozzle temperature of 21°C. The cell ink material was printed at a nozzle temperature of 25°C to fill the entire "brain area" chamber. Then, UV crosslinking (wavelength = 405 nm) was performed with 50 mW irradiation for 30 s. Medium containing 100 U/mL thrombin and transglutaminase was sprayed on the ink material, and the constructed barrier structure was cut out with a sterile scalpel and scissors after 10 min and installed in the hNVU microenvironment device (Figure S2, Step 6, in Supplementary File). Perfusion channel A was installed on the hNVU device (Figure S2, Step 7, in Supplementary File), and then the hNVU device was placed in a 37°C incubator and incubated for 30 min (during this period, the hNVU device was placed on a homemade rotating device so that the cells in the model would not settle rapidly due to gravity). The needle was pulled out to form a hollow hydrogel channel in the chip device. It should be noted that no spatial control of cells was achieved within each layer of the printing process.

An exploded view of the hNVU chip is shown in **Figure S1** (Supplementary File). For the perfusion culture of the hNVU chip device, a 100 mL glass bottle (Shu cattle, high borosilicate material) was chosen as the storage chamber for the perfusion culture (**Figure S4B** in Supplementary File). A sterile silicone hose of 0.5 × 0.8 mm (inner diameter × wall thickness) connects the liquid storage chamber and the microenvironment device of the neurovascular unit (**Figure S4A** in Supplementary File). Using a rotation speed of 16 rpm, the BT100-2J driver (Rongbai Tech, Baoding, China) and the DG10 pump head could achieve a shear rate of approximately 0.02 dyne/cm^2. The connection method of the perfusion channel interface and the peristaltic pump tube is shown in **Figure S4C** (Supplementary File). Continuous perfusion culture was carried out for 10 days, and half of the medium (20 mL) was renewed on the 5th day.

2.6. Cell viability assay and cell tracking in the 3D hNVU chip

Cell viability was determined using the Calcein-AM/PI Cell Double Staining Kit (C542, Dojindo, Japan). Briefly, calcein-AM stock solution and propidium iodide (PI) stock solution were added to PBS to generate working solutions with concentrations of 2 μmol/L and 4.5 μmol/L, respectively. The working solution was added to the model and incubated at 37°C for 15 min prior to observing living cells at an excitation wavelength of 490 ± 10 nm and dead cells at an excitation wavelength of 545 nm. This method can be used in studies assessing cell viability and toxicity. GFP and RFP (Hanheng Technology Corporation, Shanghai, China) were transfected as tracer markers into cells to observe their positions.

2.7. Immunohistochemistry

The cells in the hNVU chips were fixed with 4% paraformaldehyde (Beyotime, Shanghai, China) for 30 min and permeabilized with 0.05% Triton X-100 (Beyotime, Shanghai, China) for 30 min. After washing and blocking with 5% bovine serum albumin (Leagene), the samples were incubated with primary antibodies at 4°C for 1 day, followed by washing with PBS (BIOIND) for more than 5 h. The samples were then incubated with Alexa Fluor 488 (Thermo Fisher Scientific) or Alexa Fluor 594 (Thermo Fisher Scientific)-tagged secondary antibodies at 4°C for 1 day, followed by washing with PBS (BIOIND) for more than 5 h. The nuclei were counterstained with 4′,6-diamidino-2-phenylindole (DAPI, Thermo Fisher Scientific #D1306). The primary and secondary antibodies used in this study were listed in the Table S1 (Supplementary File).

2.8. TEER measurement

The trans-epithelial electrical resistance (TEER) of the endothelial monolayer formed in the device was measured using a Millicell ERS-2. We cut and fixed the constructed BBB structure on a homemade jig (**Figure S5A** in Supplementary File) and inserted the jig with the barrier structure into the corresponding test slot to ensure good contact. After 1 min of stabilization, three multiple readings were averaged for each device. To calculate TEER, the measurements from the chips in the absence of the cells were subtracted from the resistance of each device. The transmembrane impedance of the barrier was measured using the Millicell ERS-2 instrument, the measured values of each sample were recorded, and the data were processed. The measured value multiplied by the area is the displayed TEER value.

2.9. Quantification of barrier permeability

To evaluate BBB permeability, the BBB structures of the hNVU chips were placed horizontally on a custom device (**Figure S5B** in Supplementary File), and FITC–dextran (10 kDa, 40 kDa, and 70 kDa) (Sigma-Aldrich) was administered into the device. A cell-free PET membrane was used as the control group. The detection reagent was extracted, and the fluorescence intensity was measured with a fluorescence spectrophotometer (excitation wavelength 485 nm, emission wavelength 535 nm). The permeability coefficient P = F/F0 was calculated, where F represents the fluorescence intensity value of the transmembrane liquid (reservoir B) and F0 is the fluorescence intensity of the initial FITC–dextran solution (reservoir A).

2.10. Detection of chemotherapeutic drug concentration

Samples (50 μL) were extracted and accurately added to 5-fluorouracil (5-FU). The solution (or vorinota) was placed in a clean 1.5 mL centrifuge tube, and acetonitrile/methanol (1:1, v/v) solution containing 0.1% formic acid, four times the volume of the samples, was added to the centrifuge tube and then vortexed for 5 min. The mixture was centrifuged for 10 min at 13,000 rpm at 4°C, and then the mixture in the centrifuge tube was transferred into a sample bottle for LC-MS/MS analysis. At the same time, the standard curve for the preparation of blank 5-FU (or vorinota) solution without drugs was used for calculation. Detailed instrument parameters are provided in the Supplementary File.

2.11. Rheological measurements

GelMA and hydrogels were prepared in accordance with the procedures described in section 2.4. To determine the thermal responsivity of the hydrogels, an oscillation temperature sweep was performed using a rheometer (MCR302, Anton Paar) employing a cylindrical geometry (NO. PP25/TG-SN32620, diameter 25 mm), which corresponded to a sample volume of 350 μL. The temperature was set for a ramp change from 37°C to 4°C and then back to 37°C at a rate of 5°C/min. To determine the UV illumination responsivity of the hydrogels, the temperature was set at 25°C. The hydrogels were maintained at 25°C for 5 min before the rheological experiment begins. Five minutes after the start of the experiment, the UV light (405 nm, 30 mW, 60 s) was turned on to crosslink the hydrogels. A consistent strain (1%) and frequency (1.5 Hz) were used throughout the temperature ramp.

2.12. Statistical analysis

All data are presented as the mean ± standard deviation (S.D.). Unpaired Student's *t*-test was applied to calculate statistical probability. Unless otherwise stated, at least three biological replicates were performed for each experiment. Statistical analysis was performed using GraphPad Prism 8 software (GraphPad Software, San Diego, CA, USA). The statistical significance of the data was determined as $^{*}p < 0.05$, $^{**}p < 0.01$, $^{***}p < 0.001$, and $^{****}p < 0.0001$.

Other experimental procedures and methods are given in the Supplementary File.

3. Results and discussion

3.1. The BBB in the hNVU chip mimics the characteristics of the BBB in brain

We selected a semipermeable PET porous membrane with a pore size of 0.4 μm to serve as the physical support for the BBB model. On the outside of the PET membrane, hCMEC/D3 (EC) cells and vascular extracellular matrix fibrinogen were added, facilitating rapid cell attachment to the PET membrane. On the inner side, human brain vascular pericytes (HBVPs; PC is also used in this article to denote HBVPs) and astrocytes (ACs) with hydrogel were uniformly deposited by extrusion bioprinting (Figure 2A). The BBB cells of hCMEC/D3 (EC), HBVPs (PC), and astrocytes (ACs) were recovered to high viability after 5 days of culture (Figure 2C and D), and the endothelial cells were observed to form a dense endothelial barrier after seven days of culture (Figure 2E), confirming the long-term structural stability of the co-cultured BBB.

3.1.1. The BBB structure closely resembles the in vivo BBB

A 3D reconstruction of the fluorescence image revealed a dense distribution of hCMEC/D3 cells on one side and HBVP cells/astrocytes on the other side of the structure. The thickness of the BBB model structure was approximately 34 μm (Figure 2F). Furthermore, green-labeled endothelial cells intersected with red-labeled PC+AC cells, suggesting potential interactions between astrocytes and endothelial cells through the voids of the PET membrane (Figure 2F). Immunofluorescence staining of tight junction protein ZO-1 and adherens junction protein CD144 on day 7 revealed the formation of a tight arrangement of the endothelial cells (Figure 3A and B). Furthermore, we comprehensively investigated the dynamic expression of genes related to BBB integrity, nutrient transporters, and cell–matrix interactions (Figure 3C; Figure S6 in Supplementary File). qRT-PCR analysis demonstrated an upregulation of genes associated with BBB integrity (occludin, claudins, ZOs, CD144) (Figure 3C) and cell-cell interactions in the BBB (CX30, CX43) (Figure S6 in Supplementary File), as well as genes controlling amino acid transport (LAT1) and excitatory neurotransmission termination in the central nervous system (EAAT1) (Figure 3D). These genes exhibited significant upregulation on day 7, indicating an enhancement in the tightness of the BBB and improved cellular communication between barrier cells.

Moreover, no significant changes were observed in the expression of P-gp (also known as ABCB1/MDR1), an important protein associated with multidrug resistance, suggesting that the model's drug resistance was unlikely to be altered during the culturing process (Figure 3D).

3.1.2. Barrier function of the reconstituted BBB in the hNVU chip

We subsequently assessed the integrity and barrier function of the BBB by evaluating permeability and transmembrane impedance. Permeability analysis demonstrated that after 3 days of BBB membrane formation, dextran macromolecules with molecular weights of 10 kDa, 40 kDa,

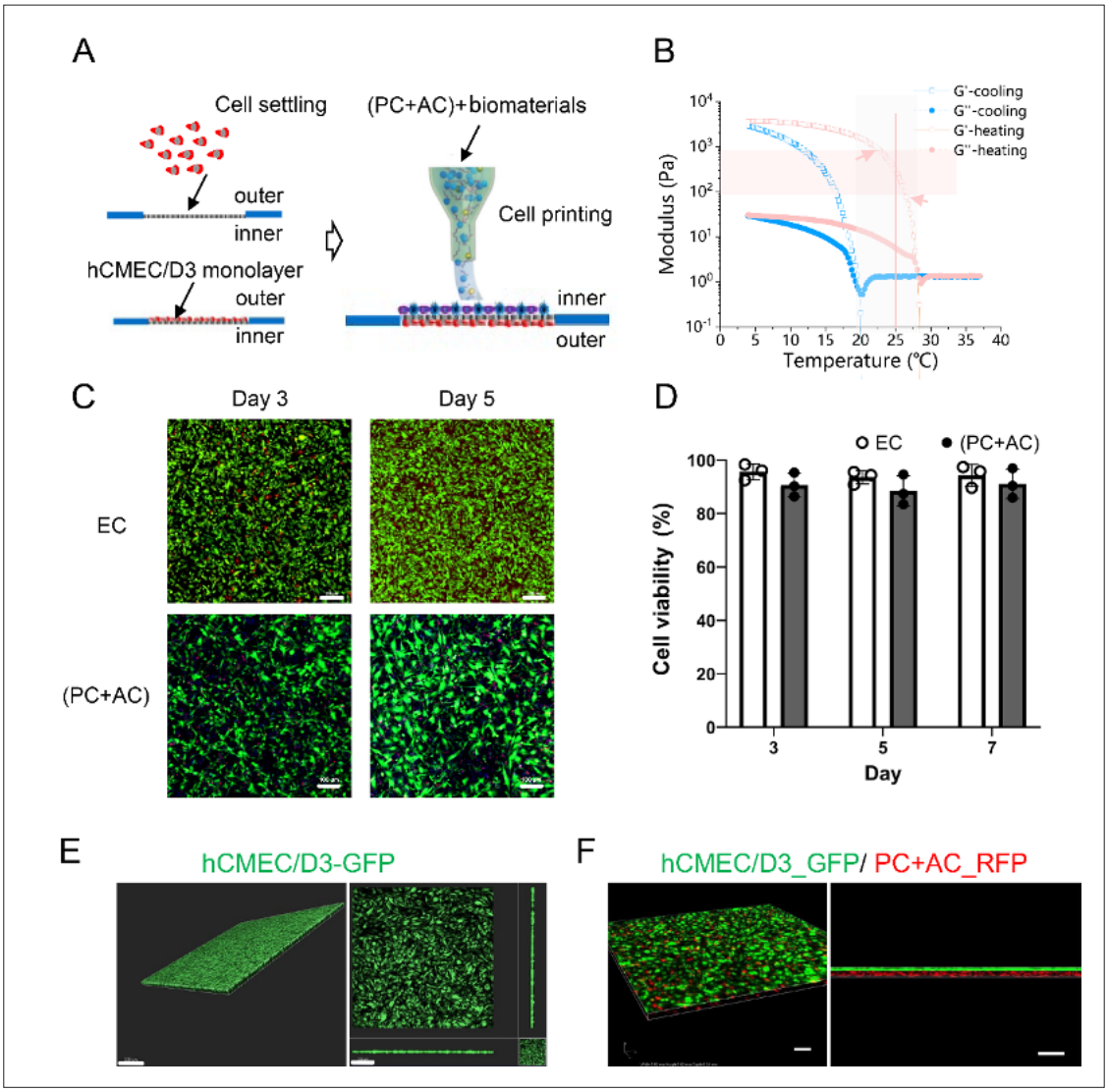


Figure 2. Fabrication and characteristics of BBB. (A) Schematic illustrating the fabrication process of the BBB. (B) Measurement of storage modulus (G') and loss modulus (G") of the bioink of BBB under cooling and heating conditions. (C) Fluorescence images showing live (green) and dead (red) endothelial cells (ECs) on the external side of the BBB and PC+AC on the internal side of the BBB. Scale bars: 200 μm (upper panel) and 100 μm (lower panel). (D) Column graph representing the cell viability of ECs and PC+AC after printing, $n = 3$. (E) Immunofluorescence staining images of green fluorescent protein-labeled hCMEC/D3 cells. Scale bar: 200 μm. (F) 3D fluorescence images of the BBB, with green indicating ECs and red indicating PC+AC. Scale bar: 100 μm ($n = 3$, independent experiments). Data are presented as the mean ± S.D. Significant differences between the groups were determined by *t*-test.

and 70 kDa were effectively intercepted compared to the 0.4 μm PET film (Figure 3E). Notably, the BBB structure exhibited a significantly stronger ability to intercept 10 kDa dextran macromolecules (Figure 3F) as compared to Transwell-based models described in a previous study that primarily exhibited a significant barrier capability to 40 kDa macromolecules.[31,32] As the culture time extended, the barrier capability gradually improved, indicating stability in the barrier function. However, it should be noted that some larger molecules can still pass through the model, indicating the increased permeability in the BBB.[20] Furthermore, on the third day of model culture, the transmembrane impedance of the model was approximately 240 Ω cm^2 (Figure 3G), and the transmembrane impedance gradually increased, reaching a maximum value of 360 Ω cm^2 (Figure 3G) with the extension of culture time.

Taken together, the aforementioned findings suggest that the BBB model exhibits long-term structural stability and emulates the resistance barrier function of the neonatal BBB. This provides a foundational model for constructing neurovascular unit models.

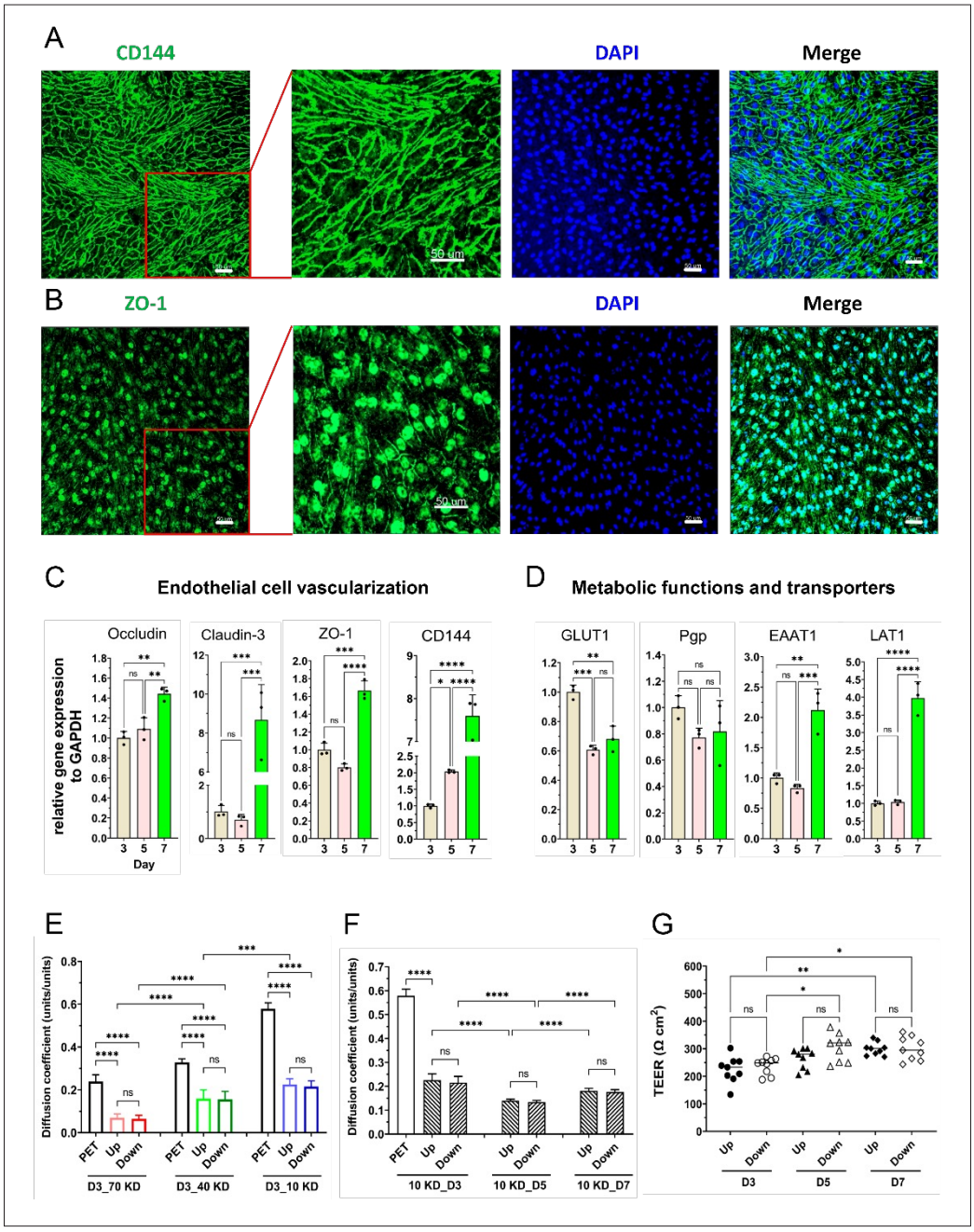


Figure 3. Characterization of EC intercellular junction proteins and evaluation of BBB function in the hNVU chip. (A, B) Representative immunocytochemistry analysis of CD144 (adherens junction) and ZO1 (tight junctions) deposition by hCMEC/D3 cells. Scale bar: 50 μm. (C, D) qRT-PCR analysis of genes associated with BBB integrity and BBB metabolic functions and transporters. (E) Permeability coefficients for three different dextrans. (F) Permeability coefficients of 10 kDa FTIC–dextrans at three different detection times (days 3, 5, and 7). (G) TEER measurement of the BBB. n = 3, independent experiments. Data are presented as the mean ± S.D. Significant differences between the groups were determined by t-test.

3.2. The brain region of the hNVU chip recapitulates the microenvironment of NVU cells in brain

Based on the BBB structure, we constructed a brain region structure in the middle of the sandwich structure. This structure included astrocytes, microglias, ECs, pericytes, and iPSC-NPCs capable of differentiating into neuronal cells. The simulated brain model consists of a diverse cellular composition, including neural stem cells, recapitulating the pathological cell microenvironment and pathological process of microangiogenesis in brain.

3.2.1. Bioink biometric ECM of NVU cells in brain by modulating 3D bioprinting parameters.

The bioprinting process faces a challenge arising from the contradiction between the high modulus required for 3D printing of hydrogels and the low modulus of brain tissue, which typically ranges from 100 to 3000 Pa.[33,34] Collagen-hydrolyzed gelatin and its derivative, GelMA, provide cell adhesion sites and have long been used for constructing tumor angiogenesis models.[30] In this study, we utilized temperature-responsive gelatin and low-concentration GelMA that can be dual-controlled by light and temperature to create a 3D printing-friendly and low-modulus ECM mechanical environment. Precise control of parameters such as light exposure and temperature during printing allowed us to achieve optimal results. Rheological analysis demonstrated that a mixture of 5% GelMA and 5% gelatin achieved a modulus ranging from 100 to 1000 Pa within the printing window of 20°C–29°C (Figure 4A). To recapitulate the pathological ECM microenvironment, we incorporated fibrinogen into the bioink cocktail, which is known to be increased in the glioma area and associated with perivascular growth and glioma infiltration.[35] To provide adhesion sites for NPCs,[36] we also added laminin to the ink. Finally, GelMA$^+$ (5% GelMA + 2.5 mg/mL fibrinogen + 5% gelatin + 20 μg/mL laminin + 3 U/mL transglutaminase) was used as the primary hydrogel material. After extrusion-based printing, photocrosslinking was employed to confer long-term stability to the printed structures.

3.2.2. Brain regions with the biomimetic cellular composition of neurovascular unit cells in brain

To better replicate microstructural assembly and the high cell density in the brain region, our study focused on investigating the different ratios and cell densities of five distinct cell types, namely ECs, pericytes, astrocytes, microglias, and iPSC-NPCs. The findings revealed that a cell ratio of 12:4:4:4:1 and a total cell density of 2.5×10^7/mL demonstrated optimal spreading of endothelial cells (Figure S7 in Supplementary File) as well as the highest cell survival rate (Figure 4B and C). A cell ratio of 12:4:4:4:1 and a total cell density of 2.5×10^7/mL were used in subsequent experiments. A schematic diagram of the constructed structure with a hierarchical cell distribution is shown in Figure S8A (Supplementary File), and the experimental picture is shown in Figure 4B (red: mixture of pericytes and astrocytes, layer 2 and layer 4 in Figure S8A in Supplementary File; green with tube: "brain region", layer 3 in Figure S8A in Supplementary File; green (up layer and down layer): endothelial cells, layer 1 and layer 5 in Figure S8A in Supplementary File).

After 7 days of culture, immunofluorescence (IF) staining of identity markers for ECs (CD31), pericytes (NG2), glioma cells (GFAP), microglias (IBA1), and neurons (β3-tubulin) depicted cell spreading and even distribution in the brain region (Figure 4D). These results indicated that the modulus of the hydrogel was appropriate for the five-cell co-culture and iPSC-NPCs differentiation. Meanwhile, the upregulation of the gene expression of the neuron marker β3-tubulin and nestin indicated that iPSC-NPCs not only differentiated into neurons (Figure S9 in Supplementary File) but also potentially proliferated (Figure 4E). These characteristics mimic the pathological features observed in the brain, which involve the presence of neural stem cells.

3.2.3. The cells in the brain regions of the hNVU chip remodel the ECM

The assembly of microstructures within the structure is achieved through the remodeling of the ECM and the cell–ECM interactions.[37-39] Immunofluorescence staining showed high protein expression of COL4A1 and laminin, which are the main constituent ECM proteins in the brain (Figure 4F). Furthermore, we conducted an investigation into the gene expression associated with ECM and cell–ECM interactions to gain a deeper understanding of brain region models (Figure 4G). Analysis of gene expression patterns revealed an upregulation of key ECM protein components, namely fibronectin (FN1), collagen IV, and laminin, indicating cellular remodeling and a tendency toward biomimicry in the models. Additionally, the genes *ND1* (mitochondrially encoded NADH dehydrogenase 1) and *SPARC* (secreted protein acidic and cysteine rich), known for their involvement in cell–ECM interactions, exhibited increased expression levels. ND1, widely distributed in basement membranes, tightly interacts with laminin, collagen IV, and perlecan.[40,41]

Taken together, these findings indicated that the brain region structure can replicate the cellular composition and ECM of brain tumors.

3.3. The hNVU chip exhibits pathological features of NVU cells in brain

To assess the pathological characteristics of glioma in the hNVU model, we evaluated the dynamic changes in the gene expression levels of typical markers and revealed the biological processes occurring within the cells in the brain region, which are related to angiogenesis and glioma mass transport.

The gene expression levels of the endothelial cell marker *CD31*, tight junction protein *ZO-1*, and pericyte markers *SM22A* and *aSMA* were upregulated (Figure 5A), indicating the trend of angiogenesis within the model. The genes expression patterns of the glial marker *GFAP* and *S100B* suggested a strong association between angiogenesis and glioma cells. Furthermore, the

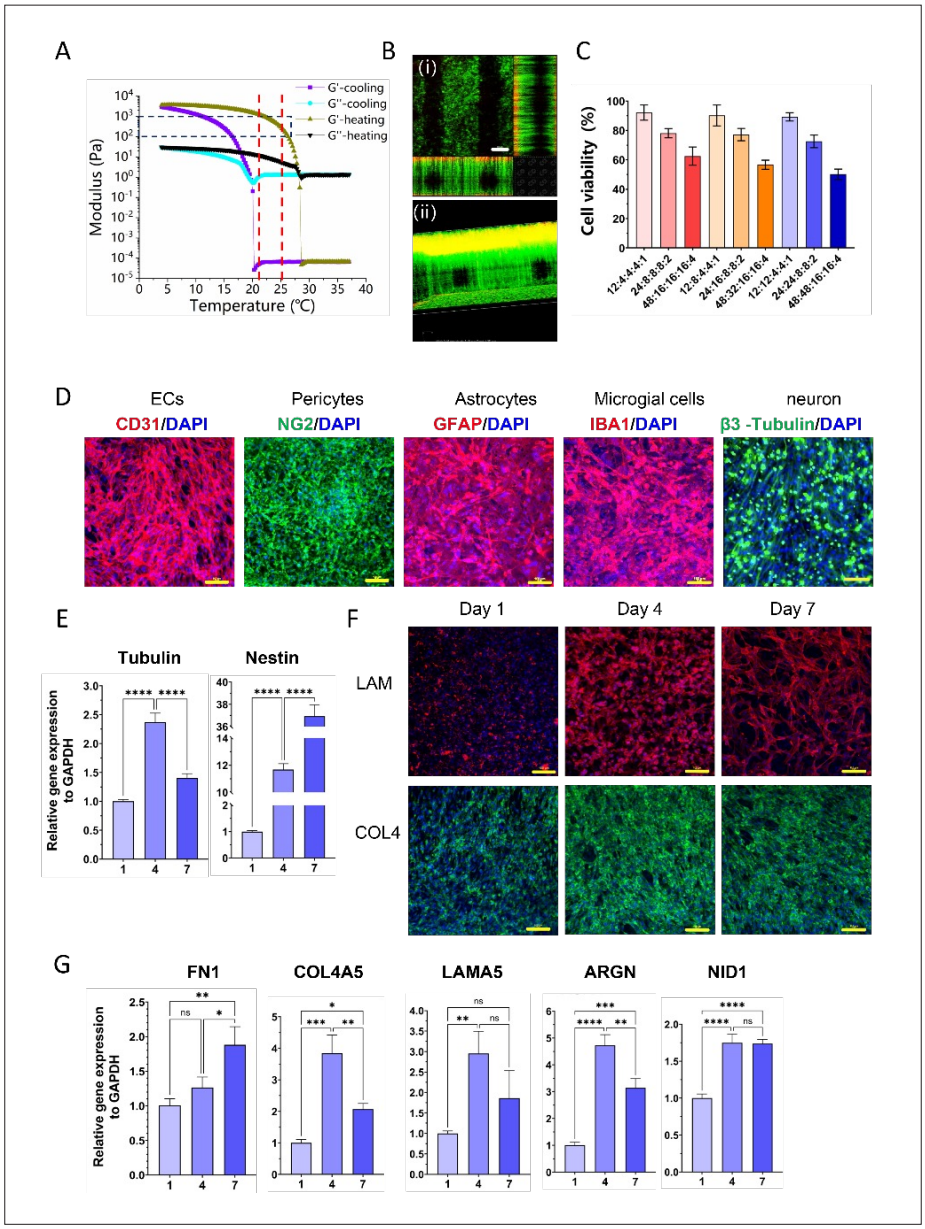


Figure 4. Fabrication and characteristics of the brain region. (A) Measurement of storage modulus (G') and loss modulus (G") of the bioink of the brain region under cooling and heating conditions. (B) Confocal images illustrating the organization of hNVU structures. Red: mixture of pericytes and astrocytes; green with tube: "brain region"; green (up layer and down layer): endothelial cells. (C) Cell viability of different cell densities within the brain region after printing (the base unit for proportional numbers is 10^6 cells). (D) Immunofluorescence staining images of cell identity markers for endothelial cells (CD31), pericytes (NG2), astrocytes (GFAP), microglia (IBA1), and neurons (β3-tubulin) on day 7. Blue represents nuclei. Scale bar: 200 μm. (E) Gene expression of the neuron markers β3-tubulin and nestin in iPSC-NPCs. (F) Representative immunofluorescence staining images of ECM proteins (COL4A1 and laminin) in the 7-day experiment. Scale bar: 100 μm. (G) Representative gene expression associated with ECM and cell–ECM interactions. $n = 3$, independent experiments. Data are presented as the mean ± S.D. Significant differences between the groups were determined by *t*-test.

expression of endothelial cell tight junction proteins (OCLN, CLDN1, CLDN5) and an adhesion link protein (CDH5) showed a significant downward trend, while the gap junction-related gene *GJB6* (gap junction protein beta 6) was upregulated (Figure 5B). GJB6 is an intercellular communication marker in glioma that plays a crucial role in the malignant proliferation of glioma.[42,43] These results suggest that cells in the brain region exhibit a tendency to undergo angiogenesis and display pathological features associated with malignant glioma metastasis. Moreover, we determined the upregulation of *SPARC* and fibrinogen (*FGB*) (Figure 5A). SPARC plays a role in brain tumor

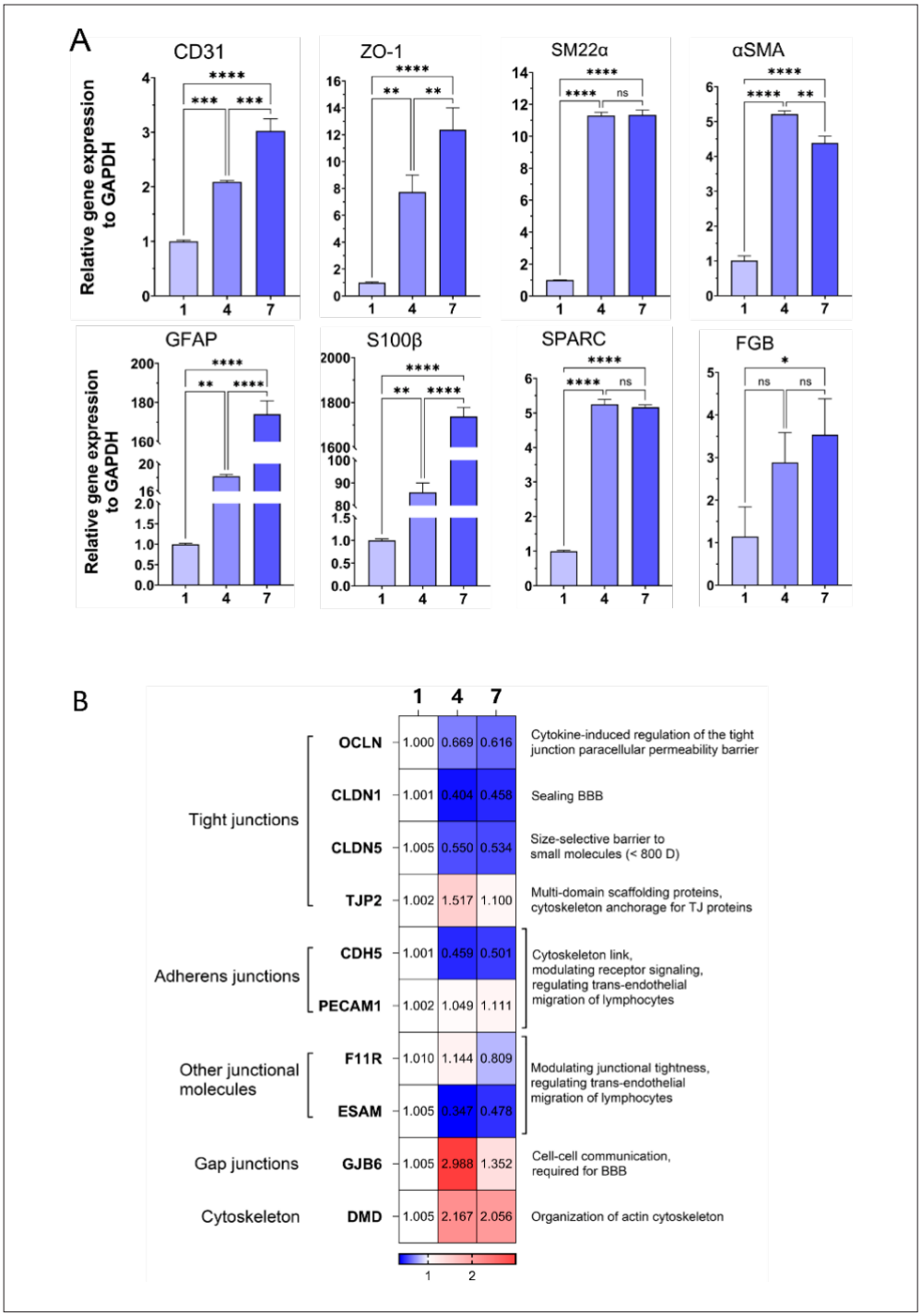


Figure 5. Representative expression of angiogenesis-related genes in brain tumors. (A) Expression analysis of genes related to angiogenesis and glioma development. (B) Heatmap of gene expression profiling of typical genes in cell–cell interactions and cell–matrix interactions in the brain region at different time points during co-culture. Data normalization was performed using the samples obtained on the first day of the model. Blue represents downregulated gene expression, while red represents upregulated gene expression. $n = 3$, independent experiments. Data are presented as the mean ± S.D. Significant differences between the groups were determined by *t*-test.

development, proliferation, invasion, and angiogenesis by regulating cell growth and cell–ECM interactions.[44,45] FGB is typically absent in a healthy adult brain but is associated with brain disorders such as multiple sclerosis, Alzheimer's disease, brain injury, and ischemia/hypoxia.[46,47] This suggests that the cellular remodeling of the ECM exhibits pathological features. Finally, *DMD* (dystrophin), another glioma marker closely associated with cytoskeletal proteins, was also upregulated (Figure 5B).

The heatmap (Figure S10 in Supplementary File) revealed the altered expression of transporters during the development of the hNVU chip. The downregulation of a glucose transport-related gene (SLC5A1) suggests a disturbance in glucose metabolism. On the other hand, fatty acid (SLC27A1)- and glutamine (SLC38A1, SLC38A3)-related genes showed significant upregulation, indicating a potential enhancement of aerobic respiration metabolism and increased neurotransmitter metabolism within the brain region. Notably, this gene expression profiling was consistent with the trend of expression of transporter-related genes in glioma lesions.[48-50]

Taken together, these gene expression results suggest that the brain region structure of the hNVU chip may possess pathological features such as tumor angiogenesis and altered transporters.

3.4. The evaluation of therapeutic effects demonstrates the reliability of the hNVU chip for drug screening in pediatric brain tumors

Therapy for pediatric brain tumors requires not only considering the effectiveness of killing tumor cells, antitumor angiogenesis, and alteration of tumor glucose metabolism but also evaluating the effects on neuronal cells to avoid cognitive impairments during treatment. 5-FU was applicable to colon cancer and breast cancer and possessed anti-angiogenic ability.[51] However, 5-FU could cause cognitive impairments in clinical trials of chemotherapy. Vorinostat has entered phase II clinical trials for pediatric brain tumors, but our understanding about the metabolism of vorinostat is still limited. We chose these two classic drugs, 5-FU and vorinostat, for research to further test the capabilities of our model in drug screening for pediatric brain tumor treatment. Astrocytoma cell SF188 was introduced in the model to construct an hNVU chip with tumor cells for the study of chemotherapeutic drugs (Figure S8B in Supplementary File). This study found that when astrocytoma cells were introduced into the model, the BTB compromises the BBB integrity (Figure S11 in Supplementary File). We administered these chemotherapeutic drugs through the A and B channels of the chip and investigated their cytotoxicity, their ability to penetrate the BBB, their impact on the expression of tumor-related genes, and their effects on metabolism (Figure 6A).

3.4.1. 5-FU and vorinostat showed tolerable cytotoxicity with the hNVU chip

To investigate the effects of the two drugs on angiogenesis, we first conducted cytotoxicity assessments on brain vascular constituent cells (ECs, pericytes, and SF188 cells) using planar cell culture conditions (Figure S12 in Supplementary File). At blood concentrations, 5-FU (50 μg/mL) reduced the viability of ECs and pericytes, while vorinostat (0.24 μg/mL, equal to 0.9 μM) significantly damaged the viability of glioma cells and ECs. Specifically, 5-FU exhibited stronger cytotoxic effects on ECs than vorinostat at blood concentrations, whereas vorinostat demonstrated stronger cytotoxicity toward glioma cells. This suggests that both drugs have the potential to disrupt angiogenesis, but they may target different cell types. Subsequently, we examined the cytotoxicity of the two drugs at blood concentrations on the overall 3D hNVU chip. Within 24 and 48 h, 5-FU and vorinostat reduced the viability to approximately 70%, showing that they were less cytotoxic than in two-dimensional cell culture conditions (Figure 6B; Figure S13 in Supplementary File). This indicates a certain level of tolerance to the cytotoxic effects to hNVU caused by 5-FU and vorinostat at blood concentrations.

3.4.2. 5-FU and vorinostat can permeate across the BBB

Furthermore, we evaluated the penetration of 5-FU (50 μg/mL) and vorinostat (0.24 μg/mL) at blood concentrations across the BBB (Figure 6C and D). One hour after perfusion administration through channels A and B, both drugs were detected in wells C and D in the brain region. The concentration of 5-FU in the brain region (channel C) reached its peak (17.5 μg/mL) after 8 h (Figure 6C), while vorinostat reached its peak (0.14 μg/mL) at 16 h (Figure 6D). The slower penetration rate of vorinostat compared to 5-FU may be attributed to its relatively poor permeability.[52,53] In view of the ability of 5-FU to cross the BBB, the cytotoxicity results offer a plausible explanation for cognitive impairment observed in human patients during chemotherapy.[54-56] It also confirms that vorinostat can penetrate the BBB and reach the brain region, justifying its application in clinical trials for the treatment of brain tumors.[16] After administration, 5-FU and vorinostat significantly reduced gene expression of model barrier tight junctions (Figure S14 in Supplementary File), adhesion junctions (Figure S15 in Supplementary File), gap junctions (Figure S16 in Supplementary File), cytoskeletons, and other molecules (Figure S17 in Supplementary File). The BBB was destroyed, and the drug increased the penetration rate of the BBB (Figure S18 in Supplementary File). This

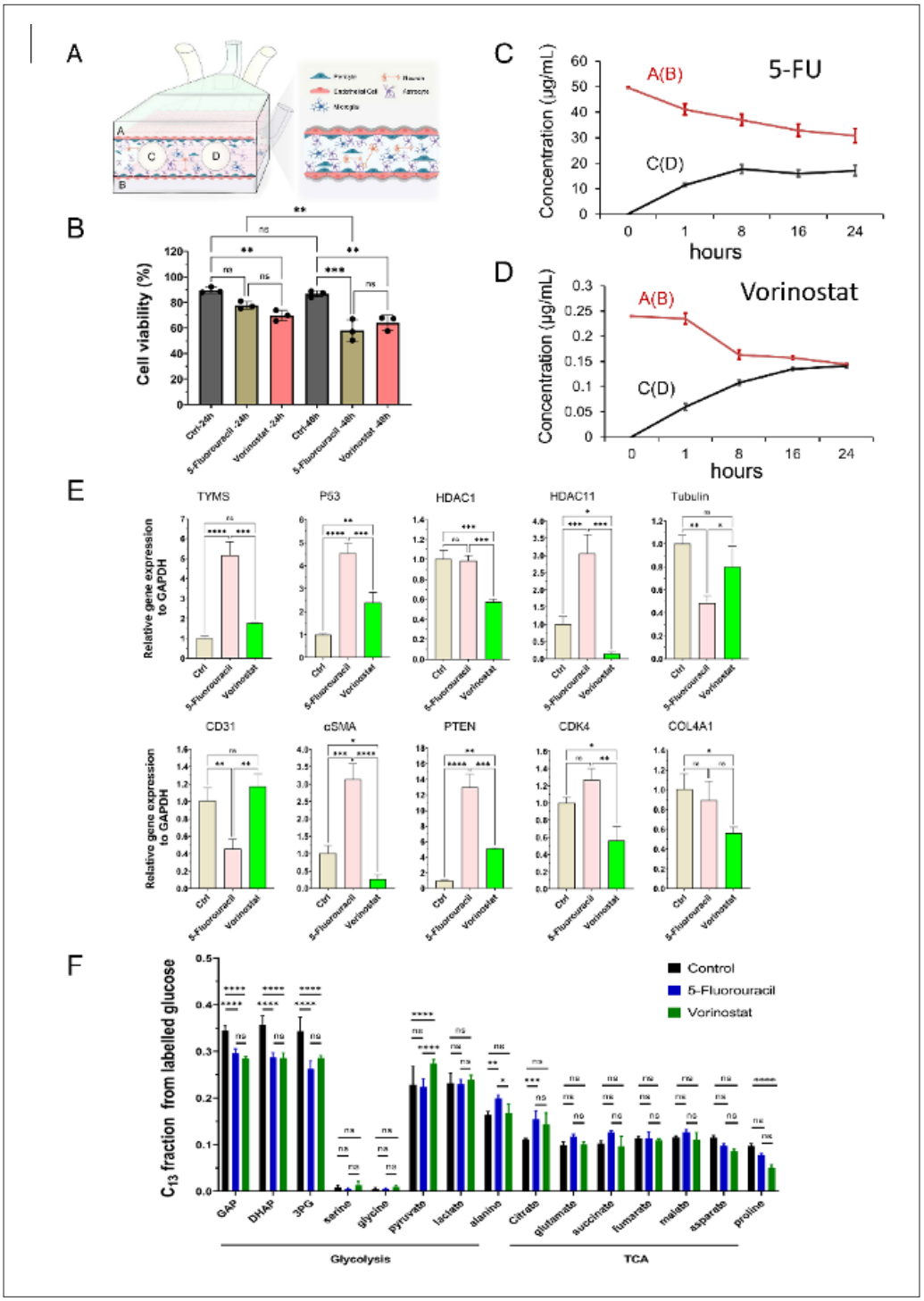


Figure 6. Evaluation of the therapeutic effects of the hNVU chip for screening drugs against pediatric brain tumors. (A) Schematic representation of the hNVU model. (B) Live and dead results of cells in the brain region under the action of chemotherapeutic drugs. (C, D) Evaluation of the penetration of 5-FU (50 μg/mL) and vorinostat (0.24 μg/mL) at blood concentrations across the BBB. (E) Drug genotoxicity and expression changes of therapeutic target genes. (F) Metabolic flux analysis of brain region cells reveals the therapeutic effects of 5-FU and vorinostat. C13-labeled glucose was provided as the glucose source in the system. $n = 3$, independent experiments. Data are presented as the mean ± S.D. Significant differences between the groups were determined by *t*-test.

suggests that the penetration of the drug may be caused by the destruction of BBB.

3.4.3. The drugs show genotoxicity in both the BBB and brain regions in the hNVU chip

Subsequently, we investigated the effects of 5-FU and vorinostat on gene expression in the brain region and BTB at their respective therapeutic concentrations. First, we analyzed the impact of these two drugs on the genes in the brain region to evaluate their therapeutic efficacy against tumors (Figure 6E). 5-FU significantly upregulated the gene expression of its target genes *TYMS* and *P53*, decreased the expression of the EC marker gene *CD31*, and upregulated the pericyte marker gene *αSMA*. Importantly, 5-FU disrupted the expression of tubulin, a neuronal marker, indicating its destructive effect on neurons and establishing its role in cognitive impairment. In terms of treatment prognosis-related genes, only the tumor suppressor gene (*PTEN*) and *P53* displayed significant upregulation, while the metastasis-associated gene *COL4A1* and cell cycle regulatory protein *CDK4* did not exhibit significant changes.[57,58]

Vorinostat specifically targets HDAC family genes, with *HDAC1* being significantly overexpressed in glioma, making it a crucial therapeutic target and prognostic marker for glioma.[59-61] Vorinostat effectively downregulated the gene expression of *HDAC1* and *HDAC11* (Figure 6E). In addition, vorinostat did not impact the expression of the EC identity gene *CD31* and reduced the pericyte marker gene *αSMA*, an indication of its potential to suppress angiogenesis in brain tumors. In contrast to 5-FU, vorinostat did not disrupt the expression of tubulin, a neuron marker gene, effecting minimal cytotoxicity toward neurons. These findings align with clinical research highlighting lower neurotoxicity and diminished neurocognitive effects associated with vorinostat-based chemotherapy.[16] Regarding treatment prognosis-related genes, the tumor suppressor genes *PTEN* and *P53* were upregulated, while the cell cycle regulatory protein *CDK4* and metastasis-associated gene *COL4A1* were downregulated. These observations are consistent with clinical investigations demonstrating that vorinostat treatment prolongs patient survival and improves overall prognosis.[62]

Then, we analyzed the effects of these two drugs on the genes associated with drug and nutrient transport channels in the BBB (Figure S19 in Supplementary File). The research results revealed that 5-FU upregulated the expression of the glucose transporter protein Glut1. Additionally, both drugs significantly downregulated the expression of genes related to barrier permeability function, such as *LAT1*, *EAAT1*, *CX30*, and *CX43*, indicating a significant disruptive effect on barrier function. Furthermore, the notable upregulation of the multidrug resistance gene *P-gp* by vorinostat provides additional evidence that its use as a monotherapy could lead to the development of multidrug resistance in the treatment of brain tumors.[63]

3.4.4. The drugs repress glycolysis

Disruption to glucose metabolism is a significant characteristic of brain tumors, accompanied by an increase in glycolytic metabolism.[22,64,65] In this study, we examined the effects of 5-FU and vorinostat on glucose metabolism in the hNVU model (Figure 6F). Within the hNVU, endothelial cells, astrocytes, and neural stem cells primarily relied on glycolysis, while neurons predominantly utilized aerobic respiration with acetate metabolism.[25] Upon administration of these two chemotherapeutic drugs, there was a significant decrease in glycolytic metabolism, as evidenced by the downregulation of key intermediates in glycolysis (Glyceraldehyde-3-phosphate [GAP], dihydroxyacetone phosphate [DHAP], 3-phosphoglycerate [3PG]). However, the changes in aerobic respiration with acetate metabolism were not substantial, except for the notable upregulation of an intermediate metabolite called citrate. These findings indicated that these chemotherapeutic drugs have major impact on glycolysis, suggesting potential effects on endothelial cells or astrocytes. Furthermore, 5-FU significantly disrupted the metabolism of the neurotransmitter intermediate glutamate, while vorinostat had a minimal effect. This suggested that 5-FU may influence neurotransmitter transmission and the development of the neurocognitive system, while vorinostat has limited impact on these processes.

The findings in this study were focused on cellular toxicity, BBB permeability, gene expression, and energy metabolism. Compared to 5-FU, vorinostat exhibits therapeutic effects on brain tumors while having relatively lower neurocognitive toxicity. Therefore, our hNVU chip provides a reliable model platform for the comprehensive study of the therapeutic effects of chemotherapeutic drugs at multiple levels, facilitating the screening of brain tumor medications.

4. Conclusion

We developed a sandwich parallel structure hNVU chip that incorporates a functional BBB, brain region, and perfusion system. Compared to previous NVU simulation techniques, our hNVU chip offers several advantages: (i) The 3D co-culture of five essential cell types (endothelial cells, pericytes, astrocytes [or astrocytoma], microglia, and NPCs) better replicates the cellular components of pediatric brain tumors and enables cell communication between the BBB and brain region. (ii) The multilayer parallel structure allows for easy quantitative and real-time observation within the chip. (iii) The design of four channels facilitates specialized nutrient supply and

nondestructive drug detection within the brain region of the chip. One of the two perfusion systems (channels A and B) provides a special medium for the endothelial cells of the BBB, while the other sets (channels C and D) supply a mixed medium to the co-culture environment of brain cells. The previously reported method mainly targets the drug penetration and efflux of BBB and the response to the drug, and has not been applied to study the mechanism of action of chemotherapeutic drugs, and the model only has BBB, lacking the 3D NVU environment *in vivo*.[22] The hNVU device we developed in this study can be used to study the behavior and mechanism of action of cells during drug administration. One of the characteristics of the NVU chip model based on PDMS is that vascular endothelial cells grow on the surface of the hydrogel, resulting in their TEER being unmeasurable.[23,24] The structure of the hNVU chip requires the mechanical properties of the brain region to support the structure while maintaining a high proportion of cell survival. This results in less stretching of cells in hydrocoagulation, with some cells present in the ECM as multicellular spheroids, unlike the intricate cell-to-cell contact in the body. The elastic modulus of ECM was reduced to about 3 kPa on the seventh day, which is close to the mechanical properties of brain tissue *in vivo*.[33] In view of the material system used in this study, it is currently impossible to simultaneously achieve the desired structural integrity and 3D cell growth. In terms of construction, it is unfortunate that the endothelial cell monolayer formed by hCMEC/D3 cells with a more complete phenotype has a lower electrical impedance and leakage, which cannot be solved at present. The cell density and proportion relationship in this study are not consistent with the actual proportion relationship *in vivo* (there were no *in vivo* data from the previous fundamental studies), but the use of cell printing technology enables the fabrication of models based on cell types and cell density gradient distributions in the future. Nevertheless, this study has broad application value. Using the hNVU chip, we investigated the therapeutic effects and toxicity of chemotherapeutic drugs such as vorinostat and 5-FU. Vorinostat not only exhibits excellent therapeutic efficacy but also has lower neurocognitive toxicity than 5-FU in the hNVU chip; this suggests that experimental results from 3D models can be used to guide new treatment strategies. In summary, the hNVU chip provides a reliable platform for comprehensive studies on the therapeutic effects of chemotherapeutic drugs for brain tumors at multiple levels.

Acknowledgments

The authors would like to acknowledge the assistance of Yanli Zhang, Imaging Core Facility, Technology Center for Protein Sciences, Tsinghua University, for assistance in using the spinning disk confocal microscopy (Dragonfly, Andor); Weihua Wang, Engineer Center of Pharmaceutical Technology, Tsinghua University, for assistance in using HPLC (Agilent, America); and Yongzhen Tao, Shanghai Institutes for Biological Sciences, Chinese Academy of Sciences, for assistance in using GCMS-QP2010 Ultra (SHIMADZU).

Funding

The work was financially supported by the National Key Research and Development Program of China (2018YFA0703004).

Conflict of interest

The authors declare no conflicts of interest.

Author contributions

Conceptualization: Yuanyuan Xu, Wei Sun, Zhuo Xiong, Ting Zhang
Formal analysis: Yuanyuan Xu
Investigation: Yuanyuan Xu
Methodology: Yuanyuan Xu, Zhuo Xiong, Ting Zhang
Writing – original draft: Yuanyuan Xu
Writing – review & editing: Wei Sun, Zhuo Xiong, Ting Zhang, Dongsheng Kong

Ethics approval and consent to participate

Not applicable.

Consent for publication

Not applicable.

Availability of data

All data that support the findings of this study are included within the article.

References

1. Louis DN, Ohgaki H, Wiestler OD, et al. The 2007 WHO classification of tumors of the central nervous system. *Acta Neuropathol*. 2007;114:97-109.
doi: 10.1007/s00401-007-0243-4

2. Biserova K, Jakovlevs A, Uljanovs R, Strumfa I. Cancer stem cells: significance in origin, pathogenesis and treatment of glioblastoma. *Cells*. 2021;10(3):621.
doi: 10.3390/cells10030621

3. Manoranjan B, Garg N, Bakhshinyan D, Singh SK. The role of stem cells in pediatric central nervous system malignancies. *Adv Exp Med Biol*. 2015;853:49-68.
doi: 10.1007/978-3-319-16537-0_4

4. Jessa S, Blanchet-Cohen A, Krug B, et al. Stalled developmental programs at the root of pediatric brain tumors. *Nat Genet*. 2019;51:1702-1713. doi: 10.1038/s41588-019-0531-7

5. Mackay A, Burford A, Carvalho D, et al. Integrated molecular meta-analysis of 1,000 pediatric high-grade and diffuse intrinsic pontine glioma. *Cancer Cell*. 2017;32(4): 520-537.e5. doi: 10.1016/j.ccell.2017.08.017

6. Ray S. Tumorsphere formation assay: a cancer stem-like cell characterization in pediatric brain cancer medulloblastoma. In: Bhakat KK, Hazra TK, eds. *Base Excision Repair Pathway. Methods in Molecular Biology*, vol. 2701. New York, NY: Humana; 2023. doi: 10.1007/978-1-0716-3373-1_17

7. Mo J, Anastasaki C, Chen Z. Humanized neurofibroma model from induced pluripotent stem cells delineates tumor pathogenesis and developmental origins. *J Clin Invest*. 2021;131(1):e139807. doi: 10.1172/JCI139807

8. Maurange C. Temporal patterning in neural progenitors: from Drosophila development to childhood cancers. *Dis Model Mech*. 2020;13(7):dmm044883. doi: 10.1242/dmm.044883

9. Lin S, Li K, Qi L. Cancer stem cells in brain tumors: from origin to clinical implications. *MedComm*. 2023;4:e341. doi: 10.1002/mco2.341

10. Mascelli S, Raso A, Biassoni R, et al. Analysis of NADP+-dependent isocitrate dehydrogenase-1/2 gene mutations in pediatric brain tumors: report of a secondary anaplastic astrocytoma carrying the IDH1 mutation. *J Neurooncol*. 2012;109(3):477-484. doi: 10.1007/s11060-012-0925-1

11. Dubuc AM, Northcott PA, Mack S, Witt H, Pfister S, Taylor MD. The genetics of pediatric brain tumors. *Curr Neurol Neurosci Rep*. 2010;10:215-223. doi: 10.1007/s11910-010-0103-9

12. Deng MY, Sturm D, Pfaff E, et al. Radiation-induced gliomas represent H3-/IDH-wild type pediatric gliomas with recurrent PDGFRA amplification and loss of CDKN2A/B. *Nat Commun*. 2021;12:5530. doi: 10.1038/s41467-021-25708-y

13. Kitange GJ, Carlson BL, Schroeder MA, et al. Induction of MGMT expression is associated with temozolomide resistance in glioblastoma xenografts. *Neuro-Oncol*. 2009,11(3):281-291. doi: 10.1215/15228517-2008-090

14. Alnahhas I, Alsawas M, Rayi A, et al. Characterizing benefit from temozolomide in MGMT promoter unmethylated and methylated glioblastoma: a systematic review and meta-analysis. *Neuro-Oncol Adv*. 2020;3(1):vdaa082. doi: 10.1093/noajnl/vdaa082

15. Verscheijden LFM, van Hattem AC, Pertijs JCLM, et al. Developmental patterns in human blood–brain barrier and blood–cerebrospinal fluid barrier ABC drug transporter expression. *Histochem Cell Biol*. 2020;154:265-273. doi: 10.1007/s00418-020-01884-8

16. Partap S, Monje M. Pediatric brain tumors. *Continuum (Minneap Minn)*. 2020;26:1553-1583. doi: 10.1212/CON.0000000000000955

17. Leary SES, Kilburn L, Geyer JR, et al. Vorinostat and isotretinoin with chemotherapy in young children with embryonal brain tumors: a report from the Pediatric Brain Tumor Consortium (PBTC-026). *Neuro Oncol*. 2022;24(7):1178-1190. doi: 10.1093/neuonc/noab293

18. Lam S, Lin Y, Warnke PC. Permeability imaging in pediatric brain tumors. *Transl Pediatr*. 2014;3(3):218-228. doi: 10.3978/j.issn.2224-4336.2014.07.01

19. Langen UH, Ayloo S, Gu C. Development and cell biology of the blood-brain barrier. *Annu Rev Cell Dev Biol*. 2019;35:591-613. doi: 10.1146/annurev-cellbio-100617-062608

20. Arvanitis CD, Ferraro GB, Jain RK. The blood–brain barrier and blood–tumor barrier in brain tumors and metastases. *Nat Rev Cancer*. 2020;20:26-41. doi: 10.1038/s41568-019-0205-x

21. Venneti S, Thompson CB. Metabolic reprogramming in brain tumors. *Annu Rev Pathol*. 2017;12:515-545. doi: 10.1146/annurev-pathol-012615-044329

22. Maoz B, Herland A, FitzGerald EA, et al. A linked organ-on-chip model of the human neurovascular unit reveals the metabolic coupling of endothelial and neuronal cells. *Nat Biotechnol*. 2018;36:865-874. doi: 10.1038/nbt.4226

23. Kim J, Lee KT, Lee JS, et al. Fungal brain infection modeled in a human-neurovascular-unit-on-a-chip with a functional blood–brain barrier. *Nat Biomed Eng*. 2021;5:830-846. doi: 10.1038/s41551-021-00743-8

24. Ahn SI, Sei YJ, Park HJ, et al. Microengineered human blood–brain barrier platform for understanding nanoparticle transport mechanisms. *Nat Commun*. 2020;11:175. doi: 10.1038/s41467-019-13896-7

25. Lyu Z, Park J, Kim KM, et al. A neurovascular-unit-on-a-chip for the evaluation of the restorative potential of stem cell therapies for ischemic stroke. *Nat Biomed Eng*. 2021;5:847-863. doi: 10.1038/s41551-021-00744-7

26. Ouyang L, Armstrong JPK, Chen Q, Lin Y, Stevens MM. Void-free 3D bioprinting for in situ endothelialization and microfluidic perfusion. *Adv Funct Mater*. 2020; 30:1908349. doi: 10.1002/adfm.201908349

27. Cho WW, Ahn M, Kim BS, Cho DW. Blood-lymphatic integrated system with heterogeneous melanoma spheroids via in-bath three-dimensional bioprinting for modeling of combinational targeted therapy. *Adv Sci*. 2022;9(29):e2202093.
doi: 10.1002/advs.202202093

28. Potjewyd G, Moxon S, Wang T, Domingos M, Hooper NM. Tissue engineering 3D neurovascular units: a biomaterials and bioprinting perspective. *Trends Biotechnol*. 2018;36(4):457-472.
doi: 10.1016/j.tibtech.2018.01.003

29. Neufeld L, Yeini E, Reisman N, et al. Microengineered perfusable 3D-bioprinted glioblastoma model for in vivo mimicry of tumor microenvironment. *Sci Adv*. 2021;7(34):eabi9119.
doi: 10.1126/sciadv.abi9119

30. Nothdurfter D, Ploner C, Coraça-Huber DC, et al. 3D bioprinted, vascularized neuroblastoma tumor environment in fluidic chip devices for precision medicine drug testing. *Biofabrication*. 2022;14(3):035002.
doi: 10.1088/1758-5090/ac5fb7

31. Appelt-Menzel A, Cubukova A, Günther K, et al. Establishment of a human blood-brain barrier coculture model mimicking the neurovascular unit using induced pluri- and multipotent stem cells. *Stem Cell Rep*. 2017;8(4):894-906.
doi: 10.1016/j.stemcr.2017.02.021

32. Cucullo L, Couraud PO, Weksler B, et al. Immortalized human brain endothelial cells and flow-based vascular modeling: a marriage of convenience for rational neurovascular studies. *J Cereb Blood Flow Metab*. 2008;28:312-328.
doi: 10.1038/sj.jcbfm.9600525

33. Tabet A, Mommer S, Vigil JA, Hallou C, Bulstrode H, Scherman OA. Mechanical characterization of human brain tissue and soft dynamic gels exhibiting electromechanical neuro-mimicry. *Adv Healthc Mater*. 2019;8(10):e1900068.
doi: 10.1002/adhm.201900068

34. Fallenstein GT, Hulce VD, Melvin JW. Dynamic mechanical properties of human brain tissue. *J Biomech*. 1969;2(3):217-226.
doi: 10.1016/0021-9290(69)90079-7

35. Dzikowski L, Mirzaei R, Sarkar S, et al. Fibrinogen in the glioblastoma microenvironment contributes to the invasiveness of brain tumor-initiating cells. *Brain Pathol*. 2021;31(5):e12947.
doi: 10.1111/bpa.12947

36. Luckenbill-Edds L. Laminin and the mechanism of neuronal outgrowth. *Brain Res Brain Res Rev*. 1997;23(1-2):1-27.
doi: 10.1016/S0165-0173(96)00013-6

37. Le LV, Mkrtschjan MA, Russell B, Desai TA. Hang on tight: reprogramming the cell with microstructural cues. *Biomed Microdevices*. 2019;21(2):43.
doi: 10.1007/s10544-019-0394-9

38. Pizzo AM, Kokini K, Vaughn LC, Waisner BZ, Voytik-Harbin SL. Extracellular matrix (ECM) microstructural composition regulates local cell-ECM biomechanics and fundamental fibroblast behavior: a multidimensional perspective. *J Appl Physiol*. 2005;98(5):1909-1921.
doi: 10.1152/japplphysiol.01137.2004

39. Roeder BA. *The Influence of Extracellular Matrix (ECM) Microstructure on the Macro and Microlevel Biomechanical Behavior of Tissue Constructs and Cell-ECM Interactions*. Dissertation. Purdue University; 2003.

40. Mokkapati S, Fleger-Weckmann A, Bechtel M, et al. Basement membrane deposition of nidogen 1 but not nidogen 2 requires the nidogen binding module of the laminin gamma1 chain. *J Biol Chem*. 2011;286(3):1911-1918.
doi: 10.1074/jbc.M110.149864

41. Yurchenco PD, Patton BL. Developmental and pathogenic mechanisms of basement membrane assembly. *Curr Pharm Des*. 2009;15(12):1277-1294.
doi: 10.2174/138161209787846766

42. Wang LB, Karpova A, Gritsenko MA, et al. Proteogenomic and metabolomic characterization of human glioblastoma. *Cancer Cell*. 2021;39(4):509-528.e20.
doi: 10.1016/j.ccell.2021.01.006

43. Wu JI, Wang LH. Emerging roles of gap junction proteins connexins in cancer metastasis, chemoresistance and clinical application. *J Biomed Sci*. 2019;26:8.
doi: 10.1186/s12929-019-0497-x

44. Yunker CK, Golembieski W, Lemke N, et al. SPARC-induced increase in glioma matrix and decrease in vascularity are associated with reduced VEGF expression and secretion. *Int J Cancer*. 2008;122(12):2735-2743.
doi: 10.1002/ijc.23450

45. Arnold SA, Brekken RA. SPARC: a matricellular regulator of tumorigenesis. *J Cell Commun Signal*. 2009;3(3-4):255-273.
doi: 10.1007/s12079-009-0072-4

46. Sun Y, Li Q, Liu W, Zhang B. Relationship between fibrinogen level and its regulatory gene with Alzheimer's disease and vascular dementia. *J Int Med Res*. 2020;48(2):211476875.
doi: 10.1177/0300060520902578

47. Golanov EV, Sharpe MA, Regnier-Golanov AS, Del Zoppo GJ, Baskin DS, Britz GW. Fibrinogen chains intrinsic to the brain. *Front Neurosci*. 2019;13:541.
doi: 10.3389/fnins.2019.00541

48. Xie Y, He L, Lugano R, et al. Key molecular alterations in endothelial cells in human glioblastoma uncovered through single-cell RNA sequencing. *JCI Insight*. 2021;6(15):e150861.
doi: 10.1172/jci.insight.150861

49. Tanase C, Enciu AM, Codrici E, et al. Fatty acids, CD36, thrombospondin-1, and CD47 in glioblastoma: together and/or separately? *Int J Mol Sci*. 2022;23(2):604.
doi: 10.3390/ijms23020604

50. Shergalis A, Bankhead A, Luesakul U, Muangsin N, Neamati N. Current challenges and opportunities in treating glioblastoma. *Pharmacol Rev*. 2018;70(3):412-445. doi: 10.1124/pr.117.014944

51. Abudumijiti A, Jianhua Rn, Yuwei Y, et al. Ganoderic acid improves 5-fluorouracil-induced cognitive dysfunction in mice. *Food Funct*. 2021;12:12325-12337. doi: 10.1039/D1FO03055H

52. Cai YY, Yap CW, Wang Z, et al. Solubilization of vorinostat by cyclodextrins. *J Clin Pharm Ther*. 2010;35(5):521-526. doi: 10.1111/j.1365-2710.2009.01095.x

53. Rompicharla SVK, Trivedi P, Kumari P, et al. Evaluation of anti-tumor efficacy of vorinostat encapsulated self-assembled polymeric micelles in solid tumors. *AAPS PharmSciTech*. 2018;19(7):3141-3151. doi: 10.1208/s12249-018-1149-2

54. Wefel JS, Saleeba AK, Buzdar AU, Meyers CA. Acute and late onset cognitive dysfunction associated with chemotherapy in women with breast cancer. *Cancer*. 2010;116(14):3348-3356. doi: 10.1002/cncr.25098

55. Schagen SB, Muller MJ, Boogerd W, Mellenbergh GJ, van Dam FSAM. Change in cognitive function after chemotherapy: a prospective longitudinal study in breast cancer patients. *J Natl Cancer Inst*. 2006;98(23):1742-1745. doi: 10.1093/jnci/djj470

56. Collins B, MacKenzie J, Tasca GA, Scherling C, Smith A. Cognitive effects of chemotherapy in breast cancer patients: a dose–response study. *Psychooncology*. 2013;22(7):1517-1527. doi: 10.1002/pon.3163

57. Wang H, Liu Z, Li A, et al. COL4A1 as a novel oncogene associated with the clinical characteristics of malignancy predicts poor prognosis in glioma. *Exp Ther Med*. 2021;22(5):1224. doi: 10.3892/etm.2021.10658

58. Baker SJ, Poulikakos PI, Irie HY, Parekh S, Reddy EP. CDK4: a master regulator of the cell cycle and its role in cancer. *Genes Cancer*. 2022;25(13):21-45. doi: 10.18632/genesandcancer.221

59. Fan Y, Peng X, Wang Y, Li B, Zhao G. Comprehensive analysis of HDAC family identifies HDAC1 as a prognostic and immune infiltration indicator and HDAC1-related signature for prognosis in glioma. *Front Mol Biosci*. 2021;8:720020. doi: 10.3389/fmolb.2021.720020

60. Hrzenjak A, Moinfar F, Kremser ML, et al. Histone deacetylase inhibitor vorinostat suppresses the growth of uterine sarcomas in vitro and in vivo. *Mol Cancer*. 2010;9:49. doi: 10.1186/1476-4598-9-49

61. Xu WS, Parmigiani R, Marks P. Histone deacetylase inhibitors: molecular mechanisms of action. *Oncogene*. 2007;26:5541-5552. doi: 10.1038/sj.onc.1210620

62. Yin D, Ong JM, Hu J, et al. Suberoylanilide hydroxamic acid, a histone deacetylase inhibitor: effects on gene expression and growth of glioma cells in vitro and in vivo. *Clin Cancer Res*. 2007;13(3):1045-1052. doi: 10.1158/1078-0432.CCR-06-1261

63. Kang DW, Hwang WC, Noh YN, et al. Phospholipase D1 is upregulated by vorinostat and confers resistance to vorinostat in glioblastoma. *J Cell Physiol*. 2021; 236(1):549-560. doi: 10.1002/jcp.29882

64. Huang CY, Huang CY, Pai YC, et al. Glucose metabolites exert opposing roles in tumor chemoresistance. *Front Oncol*. 2019;9:1282. doi: 10.3389/fonc.2019.01282

65. Miura K, Kinouchi M, Ishida K, et al. 5-FU metabolism in cancer and orally administrable 5-FU drugs. *Cancers*. 2010;2:1717-1730. doi: 10.3390/cancers2031717

ACCSCIENCE PUBLISHING

International Journal of Bioprinting

RESEARCH ARTICLE

Multi-physical field control piezoelectric inkjet bioprinting for 3D tissue-like structure manufacturing

Huixuan Zhu[1,2,3], Run Li[1,2], Song Li[1,2], Kai Guo[1,2], Chuang Ji[1,2], Feiyang Gao[1,2], Yuejing Zheng[1,2], Runyang Zhu[1,2], Heran Wang[1,2,3], Liming Zhang[1,2], Lianqing Liu[1,2]*, and Xiongfei Zheng[1,2]*

[1]State Key Laboratory of Robotics, Shenyang Institute of Automation, Chinese Academy of Sciences, Shenyang, Liaoning, China

[2]Institutes for Robotics and Intelligent Manufacturing, Chinese Academy of Sciences, Shenyang, Liaoning, China

[3]University of Chinese Academy of Sciences, Beijing, China

Abstract

With high precision, drop-on-demand, and noncontact material delivery advantages, inkjet bioprinting technology has been widely used in tissue manufacturing. However, the main challenge of inkjet bioprinting is that the bioink must be liquid-like in the printhead to avoid clogging the nozzle, then form microdroplets, and finally undergo crosslinking to quickly form a gel and make an object with strength and precision. The primary solution relies on the fast crosslinking of sodium alginate by calcium chloride. Nevertheless, it is difficult to guarantee the precision of inkjet bioprinting with this method, and cumulative errors lead to the inability to print high aspect ratio three-dimensional (3D) structures. Additionally, sodium alginate lacks cell adhesion sites, and calcium chloride at high concentrations is toxic to cells. To solve the above problems, we present a new printing method called multi-physical field control piezoelectric inkjet bioprinting (MFCPIB) for making 3D tissue-like structures using 5% gelatin methacryloyl (GelMA). For extrusion and photocuring 3D bioprinting tasks, 5% GelMA is widely used due to its favorable biocompatibility. In this study, we accomplished a 5% GelMA inkjet bioprinting for the first time by leveraging the MFCPIB method. Our experimental results demonstrated the feasibility of this approach for printing GelMA of different concentrations. The temperature-sensitive GelMA was utilized during the printing process in which GelMA is liquid-like in the high-temperature printhead, cools in the form of microdroplets in cold air after injection, and finally photocrosslinks to form a permanent gel. We analyzed the inverse piezoelectric effect and fluid dynamics to control the pressure field, which in turn controls the velocity and diameter of the microdroplets. After conducting a simulation analysis of the temperature field and performing calculations using the lumped parameter method, we implemented a dual closed-loop control strategy to ensure precise temperature control of the microdroplets. Furthermore, based on the analysis of energy conversion, we obtained the pressure and temperature field control laws corresponding to the ideal printable temperature of the microdroplet. Using the MFCPIB method, different 3D structures were successfully printed with GelMA. For example, a cell-laden vessel-like structure with an aspect ratio of 4.0

***Corresponding authors:**
Lianqing Liu
(lqliu@sia.cn)

Xiongfei Zheng
(zhengxiongfei@sia.cn)

Citation: Zhu H, Li R, Li S, et al. Multi-physical field control piezoelectric inkjet bioprinting for 3D tissue-like structure manufacturing. *Int J Bioprint*. 2024;10(3):2120. doi: 10.36922/ijb.2120

Received: October 26, 2023
Accepted: January 3, 2024
Published Online: February 29, 2024

Copyright: © 2024 Author(s). This is an Open Access article distributed under the terms of the Creative Commons Attribution License, permitting distribution, and reproduction in any medium, provided the original work is properly cited.

Publisher's Note: AccScience Publishing remains neutral with regard to jurisdictional claims in published maps and institutional affiliations.

was achieved. The proposed MFCPIB method did not influence the viability of smooth muscle cells after printing, demonstrating the potential for fabricating tissues with high bioactivity.

Keywords: Piezoelectric inkjet bioprinting; Multi-physical field; GelMA jetting; Temperature-sensitive material; 3D structure

1. Introduction

Three-dimensional (3D) bioprinting offers excellent potential for regenerative medicine.[1] Current 3D bioprinting methods mainly include material extrusion, material jetting, and vat photopolymerization bioprinting.[2] Extrusion bioprinting is the mainstream 3D bioprinting method that can print high-viscosity bioink.[3] However, cells in bioink are damaged during the extrusion process because bioink is subjected to enormous shear stress in the nozzle.[4] The shear stress of inkjet printing is lesser at the nozzle than in extrusion printing. It has been verified that appropriate shear force had a negligible effect on cell activity, and thus, inkjet printing ensures that cells have a very high survival rate.[5,6] Furthermore, the capability of 3D bioprinting to produce microdroplets at the micron scale is conducive for the development of high-precision printing, thereby expanding inkjet printing technology.[7,8] As a result, inkjet printing has attracted much attention in biofabrication applications.[9]

However, the disadvantages of inkjet printing cannot be neglected. Due to the small size of the nozzle, the inkjet printing nozzle can be easily clogged.[10] In addition, inkjet printers cannot print high-viscosity biomaterials, and the materials require suitable mechanical properties for molding after printing.[11] Therefore, the main problems restricting inkjet bioprinting are ensuring that materials have low viscosity in the printhead and that printed objects maintain their structure.[12] In order to address this issue, most inkjet bioprinting techniques rely on the use of crosslinkable materials. Typically, these materials remain in liquid state prior to the crosslinking process, but once they are crosslinked, they offer remarkable stability and support. The most commonly used method for crosslinking is ion crosslinking, which involves using substances like sodium alginate (NaAlg) and $CaCl_2$ or fibrinogen and thrombin reflection. NaAlg and $CaCl_2$ are the most commonly utilized materials in this process.[13,14] Table 1 illustrates three methods for crosslinking NaAlg and $CaCl_2$. The first method is immersion printing. NaAlg microdroplets are printed on a platform as it descends into a solution of $CaCl_2$.[15] However, crosslinking in the plating bath risks flushing the printing structure and reducing the printing resolution. The second method combines drop-on-demand (DOD) inkjet printing with a spray-coating method. Yoon et al. designed an inkjet-spray printing process to fabricate laminated hydrogel structures.[16] However, the spray microdroplets easily dehydrate during the deposition process, which changes the mechanical properties of the structure.[17] Due to the longitudinal accumulation error, it is difficult for this method to print the structure with high aspect ratio. The third method is to let the two inks collide in the air, but it is difficult to control where the microdroplets fall, resulting in reduced accuracy.[18,19] In summary, this method reduces resolution and printing scale, and cannot achieve high aspect ratio printing.

From the viewpoint of materials, sodium alginate has poor biocompatibility and no cell adhesion ligands that are needed to allow cell growth and proliferation.[20] Gelatin methacryloyl (GelMA) is a new biomaterial with excellent biocompatibility that is used in extrusion and photocuring 3D bioprinting.[21-23] It has been verified that GelMA is a

Table 1. Comparison of the studies between the experimental factors and the aspect ratio of printed structure

Author	Inkjet type	Method	Materials	Cells	Chemical modifications	Printed structure L ×W × H (mm)	Maximum aspect ratio
Christensen et al.[15]	Piezoelectric	Inkjet–bath	NaAlg, $CaCl_2$	NIH 3T3	N/A	19 × 12 × 12	2
Yoon et al.[16]	Piezoelectric	Inkjet–spray	NaAlg, $CaCl_2$ GelMA (≈6 %)	NIH 3T3	Characterization of Saponified GelMA	40 × 105 × 1	0.1
Sakurada et al.[18]	Piezoelectric	Inkjet–intersecting	NaAlg, $CaCl_2$,	NIH 3T3	N/A	5× 12 × 12.5	2.5
Present work	Piezoelectric	MFCPIB method	GelMA (3%, 5%, 10%)	SMCs	N/A	34 × 20 × 20	4

viable option for tissue regeneration and replacement in *in vivo* experiments.[24,25] Numerous studies have utilized GelMA to conduct printing on human tissues such as skin, blood vessels, lungs, and bones, verifying its safety *in vivo* and highlighting its significant potential for practical application.[21] Table 1 illustrates that Yoon et al. can improve the biocompatibility of biological ink by combining sodium alginate with GelMA, but GelMA still necessitates saponification treatment for printing.[16] Obviously, using GelMA as ink for inkjet printing is excellent. The 5% concentration of GelMA is beneficial for cell growth[26] and is commonly used in extrusion bioprinting.[27] However, GelMA is in a liquid state at high temperatures and a gelatinous state at low temperatures, implying that it is a thermosensitive material. Besides, a higher concentration results in a higher temperature sensitivity. Because inkjet printing differs from extrusion printing, it is not feasible for GelMA to have a pre-gel structure at low temperatures inside the printhead because it would clog the nozzle and prevent the formation of a jet.[28] Maintaining the right temperature can be challenging when using inkjet bioprinting to print with 5% GelMA. GelMA must be liquefied in the high-temperature inkjet printhead and then cooled in microdroplets in cold air after injection. Temperature control is crucial throughout printing, including the printing head, feeding system, printing substrate, and ambient air. While extrusion printing is often used to regulate the printing head temperature, inkjet printing lacks sufficient research on temperature control for both the printing head and feeding system due to the complex structure of the printhead. As a result, some two-dimensional images were only printed after modification of lower-concentration GelMA.[29] Unfortunately, a lower concentration is unsuitable for cell growth and does not offer enough strength to maintain the geometry or function of 3D tissue-like structures.[30] On the other hand, the process of curing GelMA heavily relies on precise temperature control. However, current bioprinting devices can only control the temperature of the substrate, but it cannot control the ambient air above it.[31] Because the cells will perish if the substrate temperature drops below 0°C,[32] the minimum temperature of the bottom plate cannot be lower than 4°C. Given that the air temperature above the bottom plate exceeds 4°C, the temperature of microdroplet passing through the air cannot be decreased to a printable temperature to prevent model collapse. Achieving high aspect ratios in printed structures can prove to be a challenging task in the absence of appropriate ambient air temperature regulation. Therefore, the temperature field must be strictly controlled during the GelMA inkjet printing process, rendering the implementation of inkjet printing with 5% GelMA impossible.

In this study, we proposed a more straightforward method to use 5% GelMA for inkjet bioprinting. The inkjet printing process can be classified as drop-on-demand (DOD) or continuous inkjet (CIJ),[33] and the DOD printing can be divided into three types: hot bubble, mechanical, and piezoelectric printing.[34] We chose a piezoelectric inkjet printhead, which allows the control of microdroplet diameter and velocity by tweaking the pressure field, and the control of proposed bioink's temperature. A new printing approach, multi-physical field control piezoelectric inkjet bioprinting (MFCPIB), was developed for making 3D tissue-like structures with 5% GelMA. This new printing method provided a high level of bioactivity and was used to make cell-laden hydrogel 3D tissue-like structures from GelMA. We developed an inkjet bioprinting system with MFCPIB and optimized the inkjet printing method. Finally, we used 5% GelMA to fabricate 3D structures with a high aspect ratio that can potentially mimic the functions of native tissues such as blood vessels and skin.

2. Materials and methods

2.1. Biomaterial inks

The preparation process of GelMA was as follows. Gelatin (type A from porcine, Sigma-Aldrich, St. Louis, MO, USA) was dissolved in phosphate-buffered saline (PBS; Adamas, Shanghai, China) and stirred at 60°C to dissolve fully and obtain a 10% w/v gelatin solution. Methacrylic anhydride (Sigma-Aldrich, St. Louis, MO, USA) was added at a 0.5 mL/min rate at 50°C and reacted for 1 h. The reaction was terminated by adding five times the volume of PBS, and then the mixture was dialyzed for 1 week at 40°C to remove salts and methacrylic acid. The reaction solution was aliquoted, lyophilized, and stored at -80°C. Lyophilized GelMA was dissolved in PBS at 50°C for 4 h. After adding 0.15% w/v lithium phenyl-(2, 4, 6-trimethyl benzoyl) phosphinate (LAP; Sigma-Aldrich, St. Louis, MO, USA), the solution was filtered using a 0.22 μm filter (Millipore, BOS, USA). The mixture was exposed to 5 mW/cm^2 ultraviolet light (365 nm) for 60 s to form stable GelMA hydrogels.

To prepare cell-laden bioink, we added 1 mL of the cell suspension to 4 mL of GelMA solution to form cell-laden hydrogels. The final concentration of cells was 5×10^5/mL, and the final concentration of GelMA was 5% w/v.

2.2. Cell culture

Smooth muscle cells (SMCs; ScienCell, San Diego, USA) were used to prepare the bioink for cell printing studies. SMCs were maintained in DMEM/F12-Dulbecco's Modified Eagle Medium (ThermoFisher Scientific, Waltham, USA) with 10% fetal bovine serum (FBS) in a 5% CO_2 atmosphere at 37°C. Culture medium was exchanged every 2 days.

2.3. Rheological test

To comprehend the physical properties of the GelMA hydrogel, we analyzed the rheological properties of GelMA before the printing test with a rheometer (MARS 60, HAAKE, Germany). The parameters for our experiment involve using an oscillation frequency of 1 Hz and a cooling rate of 2 Temp/min. We monitored the results closely to ensure accuracy and consistency of the findings. The rheological study mainly included energy storage and loss modulus measurements.

2.4. Cell viability

After printing the cell-laden vessel-like structures, in order to analyze the cell viability, LIVE/DEAD Viability/Cytotoxicity Kit for mammalian cells (Thermo Fisher Scientific, Waltham, USA) was used to examine the post-fabrication cell viability after 24 h. The vessel-like structure was sliced at the top and bottom and mid-height of 10 mm. The slices were washed with PBS twice. Subsequently, a diluted LIVE/DEAD staining solution was added to cover the hydrogel for 60 min. Finally, the gel was cleaned with PBS for 10 min. A fluorescent microscope (DMi8, LEICA, Germany) was used to image the stained hydrogels, and ImageJ (National Institutes of Health, USA) was used to quantify the live and dead cells. The test was repeated three times to obtain the survival rate of cells.

To examine cell proliferation in various layers, the upper, middle, and lower layers of the blood vessel model were separated into evenly weighted sheets. The cell counting kit-8 assay (CCK-8) was used to measure cell proliferation. Next, hydrogels were incubated in 200 μL of cell culture media mixed with 10% CCK-8 solution at 37°C for 30 min in a 48-well plate. Afterward, 100 μL of the resulting liquid was transferred to a 96-well plate, and absorbance for each group was read at the wavelength of 450 nm.

For actin staining, cell-laden hydrogels were fixed with 4% paraformaldehyde for 2 h at room temperature. Subsequently, hydrogels were washed twice with Dulbecco's PBS (D-PBS) for 10 min and permeabilized with 0.5% of Triton X-100 in D-PBS for 2 h followed by washing twice with D-PBS for 10 min. Hydrogels were incubated in 100 μL of TRITC phalloidin diluted by D-PBS containing 1% bovine serum albumin (BSA) overnight. Hydrogels were washed twice with D-PBS for 10 min, and cell nuclei were stained with DAPI for 10 min and washed twice with D-PBS. Hydrogels were imaged with a fluorescent microscope.

2.5. MFCPIB method

The MFCPIB method was realized by controlling the pressure field and temperature field. The pressure field controlled the formation of microdroplets, and the temperature field controlled the assembly of microdroplets. The core component of the printhead was a piezoelectric ceramic tube (C82, FUJI, Japan). According to the inverse piezoelectric effect of ceramic, when an external electric field was applied to the tube, it would deform along the radial direction, and Equation I describes the relationship between its displacement and the electric field:[35]

$$\Delta d = d_{33}U \quad \text{(I)}$$

where Δd, d_{33}, and U are shape changes of the piezoelectric ceramic, piezoelectric constant, and applied voltage, respectively. The d_{33} of our used ceramic is 600×10^{-12} m/V. The equation expresses that the shape change is proportional to the voltage. We controlled the deformation of a piezoelectric ceramic by controlling the driving voltage to adjust the pressure field in the printhead and regulate microdroplet formation.

The proposed printhead was actuated by a signal generator (FY3200S-20M, FeelTech, China) and high-voltage amplifiers (Model 2350, TEGAM, USA), and we optimized the actuating waveform online by adjusting various parameters. As shown in Figure 1A, we selected the square wave as the actuation waveform. The rectangular wave made the pressure field change rapidly and encouraged the formation of microdroplets. A square wave is defined by voltage amplitude, pulse width, and frequency. In the waveform optimization process, the voltage amplitude and pulse width affected the strength and action time of the pressure field. Therefore, we chose them as the critical parameters for optimization. This study set the voltage amplitude in the range from 0 to 300 V and pulse width in the range from 0 to 2 ms. To ensure that the second droplet was printed only after the first droplet had completely solidified and to avoid the high temperature of the second droplet from melting the first droplet, the printing frequency was set at a low rate. This provides enough time for the first droplet to cure, which is usually set at 1–5 Hz. To maintain cell activity, the temperature of the bottom plate of the temperature-controlled chamber had to be set at a minimum of 4°C. Although the gelling speed of GelMA is not very fast at this temperature, reducing the printing speed ensures that the microdroplet on the bottom plate can fully cool the gel, allowing the next microdroplet of GelMA with a higher temperature not to affect the formation of the previous microdroplet after it falls. By adopting a lower frequency, better control of the temperature field shaping was achieved. Printing the vascular structure took about 2 h, and the low-frequency printing ensured good structural shaping without affecting cell activity.

Figure 1B shows the process of printing a tubular piezoelectric ceramic. According to the inverse piezoelectric

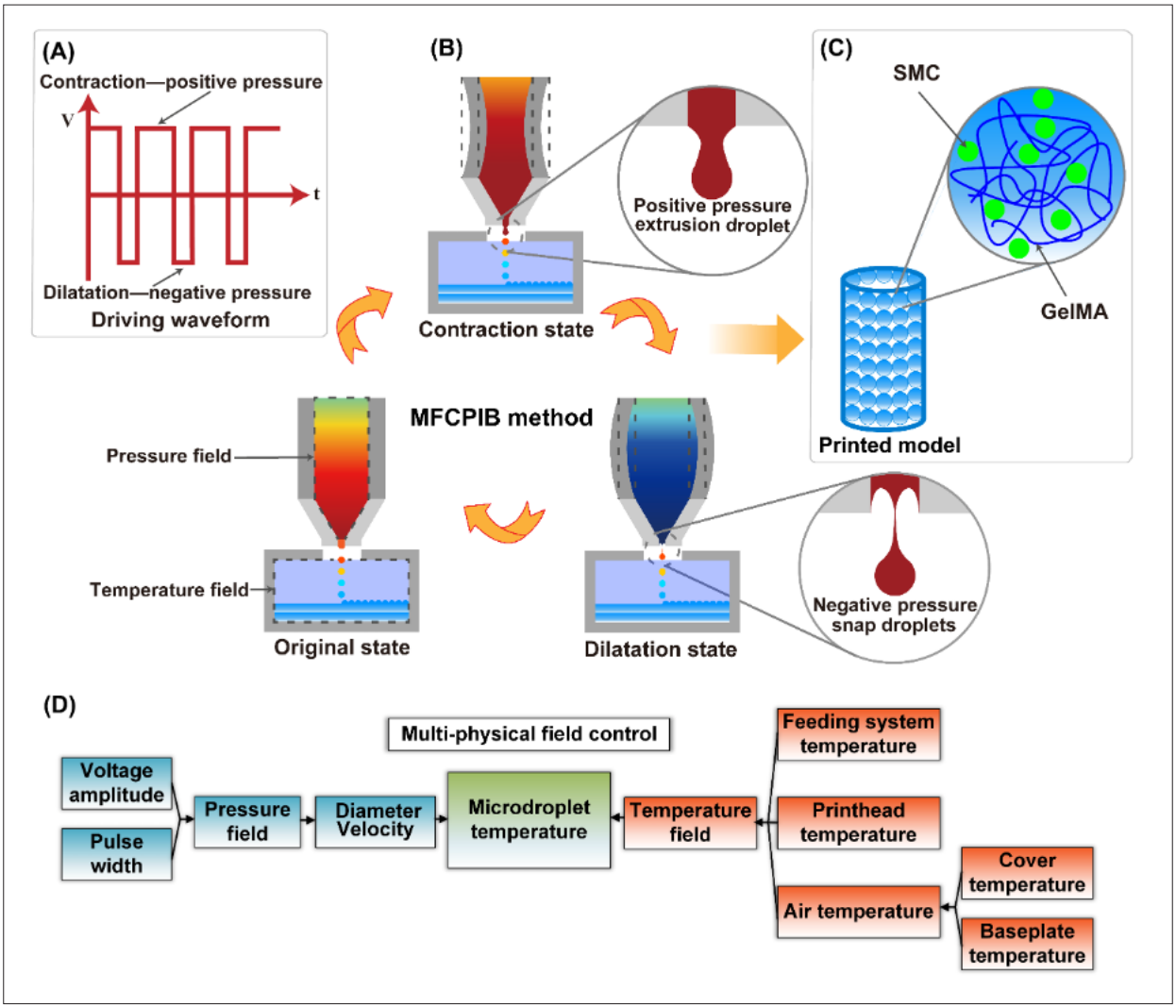


Figure 1. Principle of microdroplet formation based on multi-physical field control piezoelectric inkjet bioprinting (MFCPIB). **(A)** Actuation waveform. **(B)** Schematic representation of the MFCPIB method mechanism. **(C)** Schematic of the vascular model and gelatin methacryloyl (GelMA) microdroplets containing smooth muscle cells (SMCs). **(D)** Technical route of MFCPIB.

effect, the piezoceramic stretched along the direction of the tube radius when the strong electrical level caused the inner diameter of the tubular piezoelectric ceramic to shrink and the pressure field strength to increase. This process squeezed the bioink out of the nozzle. The inner diameter of the tubular piezoelectric ceramic expanded at a low electrical level, increasing the tube volume and decreasing the strength of the pressure field. The ink contracted at the nozzle orifice, and the liquid column was pulled by microdroplets formed by GelMA and SMCs. The piezoelectric effect and fluid-structure coupling module of COMSOL (version 5.6, COMSOL Inc., Sweden) were used for simulation and analysis, and the law of pressure field controlling microdroplet diameter and velocity was obtained. We controlled the formation, diameter, and velocity of microdroplets as required.

The assembly of microdroplets depended on the control of the temperature field, as shown in Figure 1B, and microdroplets formed with a certain velocity and diameter under the effect of the pressure field and entered the temperature field. According to the velocity and diameter of a microdroplet, its physical properties were controlled by adjusting the temperature of the thermosensitive materials. As a result, the high-temperature microdroplets passed through the temperature field, cooled, solidified, and assembled; then, layer by layer, the gel formed vessel-like structures, as shown in Figure 1C.

The technical route of MFCPIB is shown in Figure 1D. The voltage amplitude and pulse width were used to adjust the pressure field. The pressure field controlled the diameter and velocity of the microdroplets. The speed

of a microdroplet determined the time it took to pass through the temperature field, and the diameter of the droplet determined the heat required for curing. After the speed and diameter of the microdroplet were determined by adjusting the pressure field, the temperature field was adjusted to realize microdroplet formation. The temperature field included the feeding system, printhead, and air temperatures. The temperatures of the feeding system and printing head were adjusted using a water bath equipped with temperature control. The temperature of the cover and baseplate of the temperature controlled chamber were adjusted to control the air temperature. The temperature field was used to control the temperature of the microdroplets to complete the assembly process. Finally, the MFCPIB method was realized by controlling the pressure and temperature fields to print 3D tissue-like structures.

2.6. Printing system of MFCPIB

2.6.1. Pressure field control system

The printing system based on MFCPIB is illustrated in Figure 2. The system responsible for microdroplet formation and deposition consists of three parts. The first part is a pressure field control system for forming microdroplets. The self-made printhead relies on the vibration of the piezoelectric ceramic tube to form microdroplets, which can be used to replace the nozzle of 50 to 300 μm diameter. The printhead is attached to the *Z*-axis through a custom-made mount, and the nozzle is 10 cm away from the baseplate. In this study, we set printhead moving speed from 3 to 8 mm/s. When the system began to operate, the reservoir of the feeding system was filled with bioink. A pressure controller (E19KP, OBKZN, China) was used to provide negative pressure in the reservoir to prevent the bioink from leaking out of the printhead. This study maintained the back pressure in the range from 0.9 to 1.7 kPa. Next, the printhead controller sent a square driving wave that caused piezoelectric ceramics to control the pressure field in the printhead. Under the control of the pressure field, the microdroplets of appropriate diameter ultimately dropped with suitable velocity.

2.6.2. Temperature field control system

The second part of the printing system was the temperature field control system, which controls the temperature of the entire printing process. The system mainly consists of a temperature-controlled piezoelectric printhead system and temperature-controlled chamber. The system can be adjusted using cascade control. The temperature-controlled printhead system includes a piezoelectric printhead, temperature control feed bin, and delivery pipe. The printhead has a closed-loop water bath temperature control system, ensuring accuracy up to 0.1°C. The pump (Q2, Watertiger, Canada) circulates the hot water in the water bath (LKTC-L, Yuanlu, China) to the temperature-controlled printhead system. As the temperature increases, the viscosity of the GelMA solution decreases. The temperature inside the printhead should be kept within a specific temperature range to prevent clogging of the

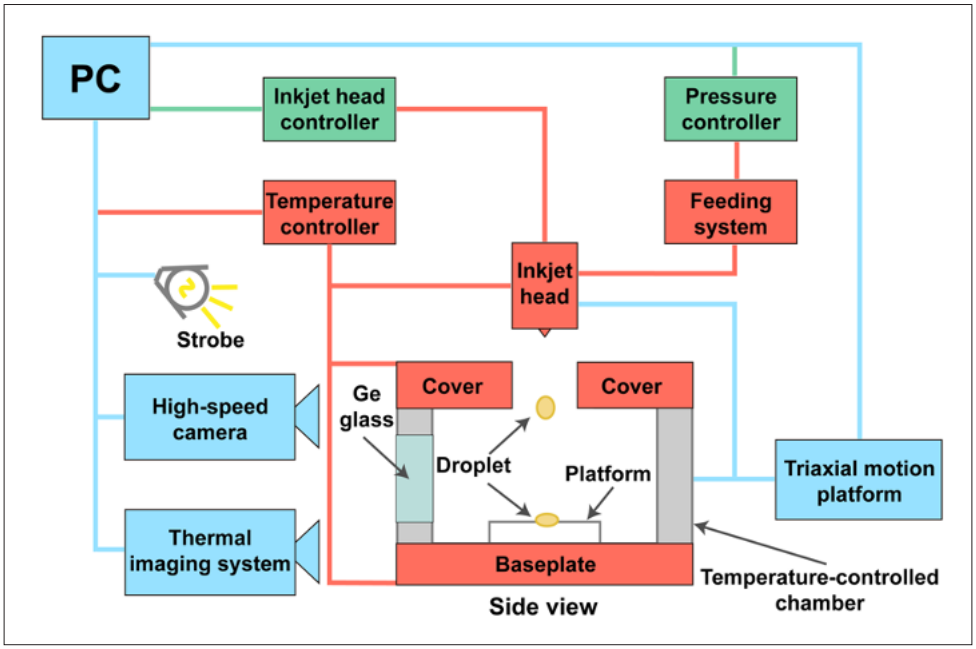


Figure 2. Printing system for multi-physical field control piezoelectric inkjet bioprinting (MFCPIB).

printhead. Therefore, considering the rheological properties of GelMA and the temperature range suitable for cell survival, the printhead system temperature was set at 37°C.

The temperature-controlled chamber is responsible for microdroplet shaping after injection. An observation window made it possible to monitor print status, and the thermal insulation cover of resin reduced heat exchange between the chamber and the outside environment. Usually, only the baseplate of the temperature-controlled chamber could be used for temperature control. Since microdroplets were deposited on the floor for a long time, it was difficult for cells to survive for a long time at 4°C or lower. Therefore, it was challenging for the temperature of only the cooling floor chamber to meet the requirements. We developed a temperature-controlled chamber with upper and lower covers to solve this problem. The upper cover and baseplate inside the chamber were refrigerated using the Peltier effect for cooling. The baseplate has six semiconductor chips (TEC2-19008, Yandong, China), and the top cover has four semiconductor chips. The air in the temperature-controlled chamber transferred heat between the top cover and the baseplate, keeping the internal gas temperature uniform and low enough to shape the GelMA microdroplets. After 15 min of system operation, a uniform temperature field can be formed in the temperature-controlled chamber.

2.6.3. Printing assist system

The third part of the printing system is the printing assist system, which includes motion control and monitoring equipment to ensure high-quality printing. A 3D printer with motion resolution and positioning accuracy of 10 μm in the *X*, *Y*, and *Z* directions made in this laboratory (SIA Inkjet Bioprinter) was utilized for driving the displacement of the printing platform. The monitoring equipment includes a high-speed camera (DimaxHS4, Pco, Germany), thermal imager (A615, FLIR, USA), and a strobe light emitting diode (LED). The monitoring equipment is separately fixed with tripods. The high-speed camera photographed falling microdroplets to measure their diameters and velocities. The diameter and velocity of the microdroplet were measured by adopting the Image-Pro Plus (version 6.0, MEDIA CYBERNETICS, USA). The image's resolution acquired in this work is 1920 × 1080 pixels, and one pixel corresponds to an area of 22.32 × 37.74 μm^2. In the image processing software, the microdroplet diameter and velocity were calculated according to the number of marked pixels and the time per frame. A thermal imager was used to measure the air temperature field in the temperature-controlled chamber and the temperature of the printed structure. We used the printing system to conduct printing experiments.

3. Results and discussion

3.1. Control of pressure field to adjust microdroplet diameter and velocity

The key to MFCPIB was the precise control of the temperature of the microdroplets, and the diameters and velocity of the microdroplets profoundly influenced printing. Because the amount of heat needed to cool a microdroplet depended on its diameter, the velocity of a microdroplet determined the time available for heat exchange with the temperature field. Therefore, it was necessary to use the pressure field to control the microdroplet diameter and velocity precisely. In this section, we studied the law and mechanism of the pressure field regulating droplet velocity and diameter.

3.1.1. Pressure field control and optimization

The deformation of the piezoelectric ceramic was controlled by adjusting the driving wave. The deformation of the piezoelectric ceramic changed the pressure field inside the printhead. The GelMA in the printhead is maintained at a temperature of 37°C. Rheological testing results displayed in Figure 6E indicate that GelMA has very low viscoelasticity at this temperature, with the storage modulus and loss modulus measuring approximately 0.01 Pa, which is almost negligible. It is worth noting that GelMA has been observed to exhibit a Newtonian fluid behavior under 37°C. This means that it can be described by the Navier–Stokes equation, which is commonly used to calculate the behavior of fluids that follow Newton's laws of viscosity. Specifically, Equation II can be used to predict the flow of the fluid under various conditions and to calculate various properties such as speed and pressure:[36]

$$\rho \frac{Dv}{Dt} = \rho f - \nabla p + \mu \nabla^2 v \quad \text{(II)}$$

where v, t, ρ, f, p, and are the fluid speed, time, density, body force, pressure, and dynamic viscosity, respectively. The left side of this equation represents the rate of change in momentum per unit volume of fluid. On the right side, the first term represents the volumetric force acting on the fluid, the second represents the pressure acting on the fluid, and the third represents the viscous force acting on the fluid.[37] When piezoelectric ceramics vibrate, the boundary conditions of the control equation change, and the pressure on the fluid microelements in contact with the piezoelectric ceramics changes. This change also simultaneously occurs at other microelements, forming a pressure wave that changes the pressure field inside the printhead. The pressure field ultimately determined the formation of the microdroplets. The two most essential parameters in the driving wave were the voltage amplitude and pulse width, which determined the size and duration of the deformation of the piezoelectric ceramic. Thus, these

two parameters determined the size and duration of the external force on the fluid, which affected the pressure field and ultimately determined the diameters and velocities of the microdroplets.

Based on the above-mentioned control theory, we conducted a simulation using piezoelectricity and fluid–structure interaction modules. To set the simulation boundary conditions, we applied a back pressure of 970 Pa at the entrance, and set the exit speed to 0. Additionally, we made the inner and outer walls of the piezoelectric ceramics bipolar, with the inner wall grounded and the outer wall applied with driving voltage. The driving waveform is presented in Figure 1A, with a voltage amplitude of 192 V. We conducted simulations to investigate the effects of the voltage amplitude and pulse width. By controlling the voltage amplitude and pulse width, the deformation of the piezoelectric ceramic and the change in pressure field at the corresponding time were studied (Figure 3A). The driving wave controlled the vibration of the piezoelectric ceramic, and the piezoelectric ceramic controlled the internal pressure field of the printhead through deformation.

Since the pressure at the nozzle was the most critical factor for the formation of microdroplets, we used the simulation to obtain the relationship between the pressure at the nozzle and the voltage amplitude (Figure 3B). When the pulse width was set to 1.5 ms, the pressure increased directly to the voltage amplitude. Therefore, it could be inferred that the diameter and velocity of the microdroplet were directly proportional to the voltage amplitude. We also simulated the relationship between pressure and pulse width (Figure 3C). By converting acoustic pressure wave oscillation problems into electrical oscillation problems, the difficulty of process analysis and modeling can be greatly simplified.[38] During the process of analogy, the similarity between the physical processes of pressure release and capacitor discharge is used to liken the process of pressure change to the process of capacitor charging and discharging.[39,40] The present work also used the mathematical form of capacitor charging and discharging to express the changes in pressure, as defined by Equation III, which can be applied for piezoelectric inkjet printing. Experimental observation can solve the formula coefficient when there is a change in the printing material or printhead structure (the formula derivation process is shown in the Supplementary File),

$$P = Ae^{(-t/T)} \quad \text{(III)}$$

where P, A, t, and T are pressure, coefficient, time, and time constant, respectively. The change in pressure followed the functional relationship of capacitance

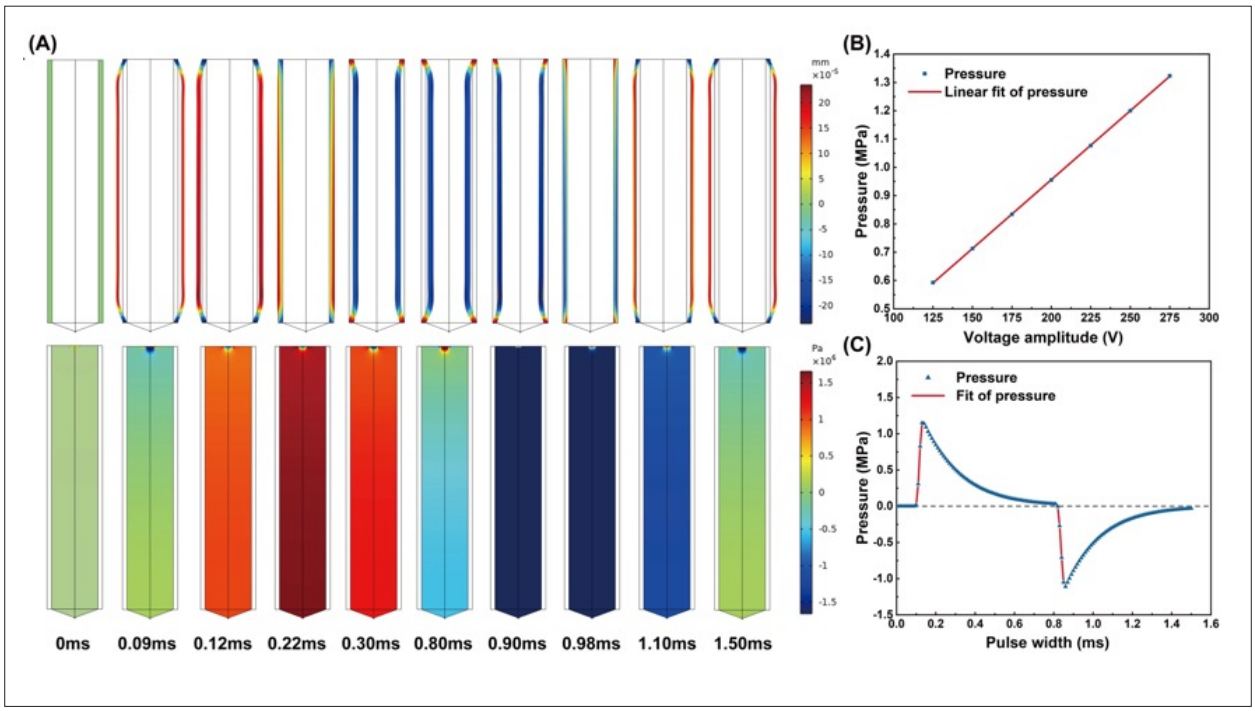


Figure 3. Pressure field control. **(A)** The upper half of the graph shows the control of piezoelectric ceramic deformation by the driving wave, and the lower half shows at the same time the internal pressure field in the printhead controlled by piezoelectric ceramic deformation. **(B)** Effect of the applied voltage amplitude on pressure at the nozzle. **(C)** Effect of the applied pulse width on pressure at the nozzle.

discharge. The function of microdroplet velocity was obtained by integrating this function, and the second integration obtained the expression for the diameter. The experimental data were fitted using the integral form.

3.1.2. Effect of voltage amplitude on microdroplet diameter and velocity

Since bipolar waves drove piezoelectric ceramic, the vibration of the piezoelectric ceramic depended on the voltage amplitude between the positive and negative levels. For microdroplet formation, the voltage amplitude determined the deformation of the piezoelectric ceramic, which affected the formation of the pressure field and then affected the diameter and velocity of the microdroplets. The relationships between voltage amplitude and piezoelectric ceramic shape variable, piezoelectric ceramic shape variable and printing head internal pressure, pressure and microdroplet acceleration, microdroplet acceleration and velocity, and diameter are all linear. Therefore, we employed a linear fitting method, based on experimental data, to control microdroplet velocity and diameter using voltage amplitude. A linear equation for controlling microdroplet velocity and diameter by voltage amplitude was derived by fitting the experimental data. According to the specifications, the piezoelectric ceramic has a maximum working voltage of 144 V. Therefore, in order to maintain its regular operation, we utilized a maximum voltage amplitude of 288 V. Moreover, we used a high-speed camera to observe the diameter and velocity of a microdroplet. The results are shown in Figure 4.

When the voltage amplitude was less than 132 V, the microdroplet could not be formed because the deformation of the piezoelectric ceramic was too slight. Microdroplet

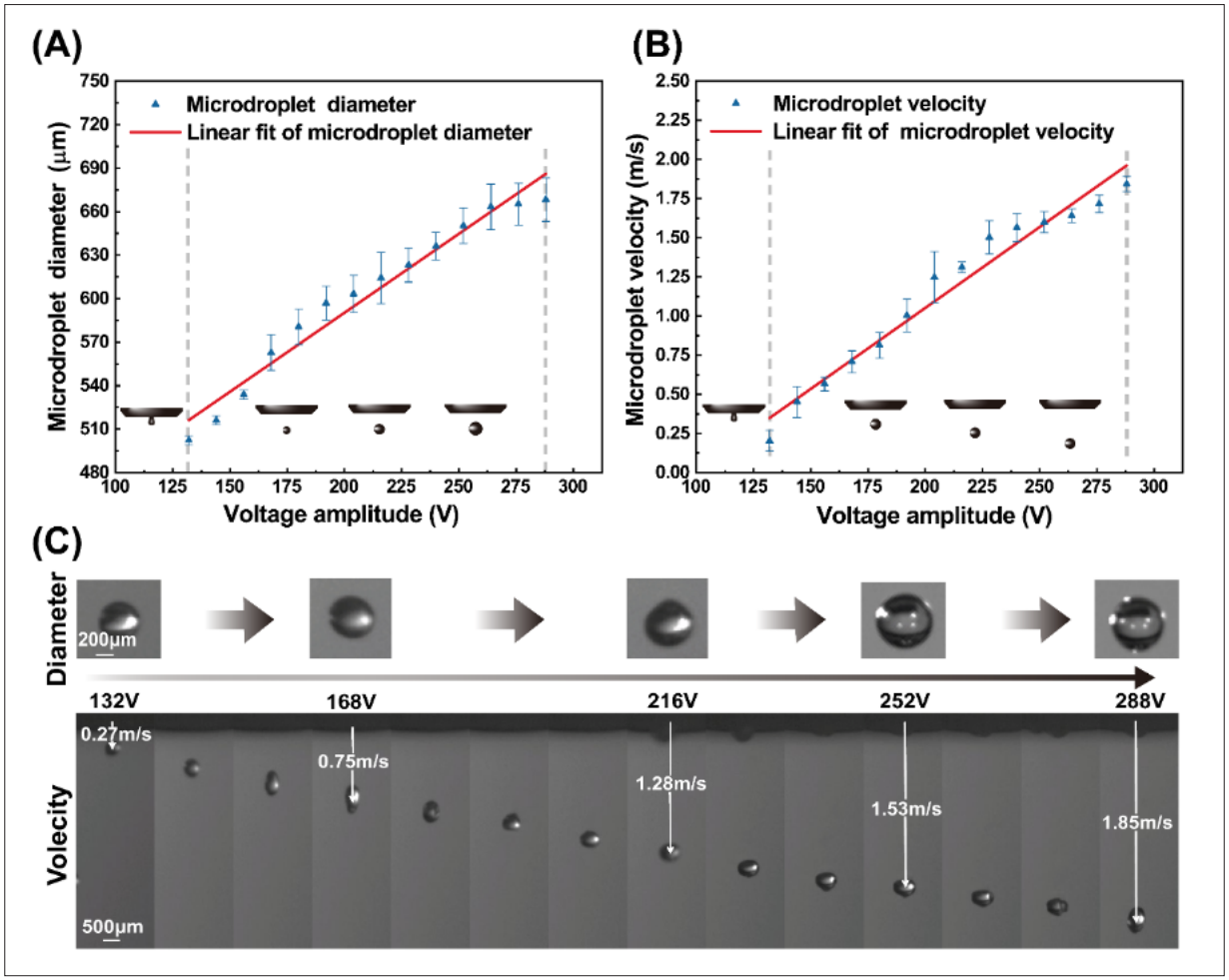


Figure 4. Effect of the applied voltage amplitude on the microdroplet diameter **(A)** and velocity **(B)**, $n = 3$. **(C)** A high-speed camera captured images of a microdroplet at different voltage amplitudes. As the voltage amplitude increased, the diameter and velocity of the microdroplet also increased. By measuring the distance the microdroplets traveled, it was observed that they moved faster as the voltage amplitude increased. Several voltage amplitudes were displayed to showcase the varying velocity and diameter of the microdroplets.

injection was stable when the voltage amplitude ranged from 132 V to 288 V. We conducted three sets of tests at the same voltage amplitude to determine the average diameter and velocity of microdroplets. Both the microdroplet diameter and velocity increased with increasing voltage amplitude, and the relationship was approximately proportional. The microdroplet diameter ranged from 502 μm to 668 μm when the applied voltage varied from 132 V to 288 V (Figure 4A).

The experimental results were consistent with the simulation results of the pressure field and voltage amplitude. We utilized linear equations to establish a correlation between pressure, microdroplet velocity, and diameter. This approach is based on the fact that as the driving voltage increases, the piezoelectric ceramic deforms more, resulting in a more substantial pressure field. As a consequence, the liquid column experiences a greater acceleration, leading to the formation of larger-diameter microdroplets with faster velocities. We used this linear relationship to control microdroplet formation, diameter, and velocity. Equations IV and V are suitable for piezoelectric inkjet printing. Experimental observation can solve the formula coefficient when there is a change in the printing material or printhead structure. The relationship between the microdroplet diameter and the voltage amplitude was linear, as defined by Equation IV:

$$D = a_1 U + b_1 \quad \text{(IV)}$$

where D and U are the diameter and voltage amplitude, and a_1 and b_1 are 1.09 and 372.44. Figure 4B shows that when the voltage amplitude was 132 V, the minimum speed was approximately 0.2 m/s. When the voltage amplitude was 288 V, the maximum speed reached approximately 1.84 m/s. The GelMA microdroplets took about 0.1 to 0.5 s to gel when exposed to cold air. The fitted equation of the microdroplet velocity and voltage amplitude is shown in Equation V:

$$V = a_2 U - b_2 \quad \text{(V)}$$

where V and U are velocity and voltage amplitude, and a_2 and b_2 are 0.01 and 1.02. The experiment utilized high-speed camera footage to illustrate changes in microdroplet diameter and velocity, as depicted in Figure 4C. The resulting graph confirms a linear relationship between voltage amplitude and the adjustments in microdroplet diameter and velocity. Multiple voltage amplitudes were tested, and their respective diameter and velocity were displayed. It is worth noting that altering the printed material will not affect the linear relationship between voltage amplitude and velocity diameter. Therefore, if the material is changed, only the equation coefficients need to be determined through experiments.

3.1.3. Effect of pulse width on diameter and velocity

Notably, the pulse width of the piezoelectric ceramic directly affected the ejection process because the pulse width determined the duration of the positive pressure field. We controlled the frequency and duty ratio in the actuation waveform to adjust the pulse width. When the pulse width applied to the piezoceramic tube changed, the time the pressure field stayed at its maximum positive value changed, and the time the microdroplets were pulled apart changed. As shown in Figure 1B, when the duration of the high pulse width level increased, the duration of the positive pressure field increased. In contrast, the piezoceramic expanded earlier when the pulse width decreased, which increased the negative pressure in the tube and caused the liquid column to be pulled apart sooner to form microdroplets. Therefore, the pulse width affected the moment when the liquid column snapped, which changed the diameters and velocities of the microdroplets.

Then, we experimentally studied how the pulse width affected the diameter and velocity of the microdroplet. In the experiment, we kept the voltage amplitude at 160 V and changed the duty ratio or frequency to change the pulse width. We used a high-speed camera to film a microdroplet falling in the above experiments.

As shown in Figure 5, the microdroplet diameter and velocity exponentially increased at first and remained constant as the pulse width increased. When the pulse width was too small, GelMA could not be ejected from the nozzle, and it only floated periodically at the nozzle orifice because the piezoelectric ceramic shrank too quickly to allow a microdroplet to form. When the pulse width increased to 0.25 ms, microdroplets were ejected from the nozzle orifice. According to the functional relationship between pressure and pulse width obtained by simulation, in the range from 0.25 ms to 0.8 ms, there were exponential relationships between pulse width and microdroplet diameter and velocity. The microdroplet diameter ranged from 480 μm to 658 μm while the pulse width varied from 0.25 ms to 0.8 ms (Figure 5A). Equation VI was calculated by double-integrating the pressure and pulse width function (Equation III) and fitting the test data (the formula derivation process shown in the Supplementary File). Equations VI and VII are suitable for piezoelectric inkjet printing. Experimental observation can solve the formula coefficient when there is a change in the printing material or printhead structure. The relationship between microdroplet diameter and the pulse width is defined by Equation VI:

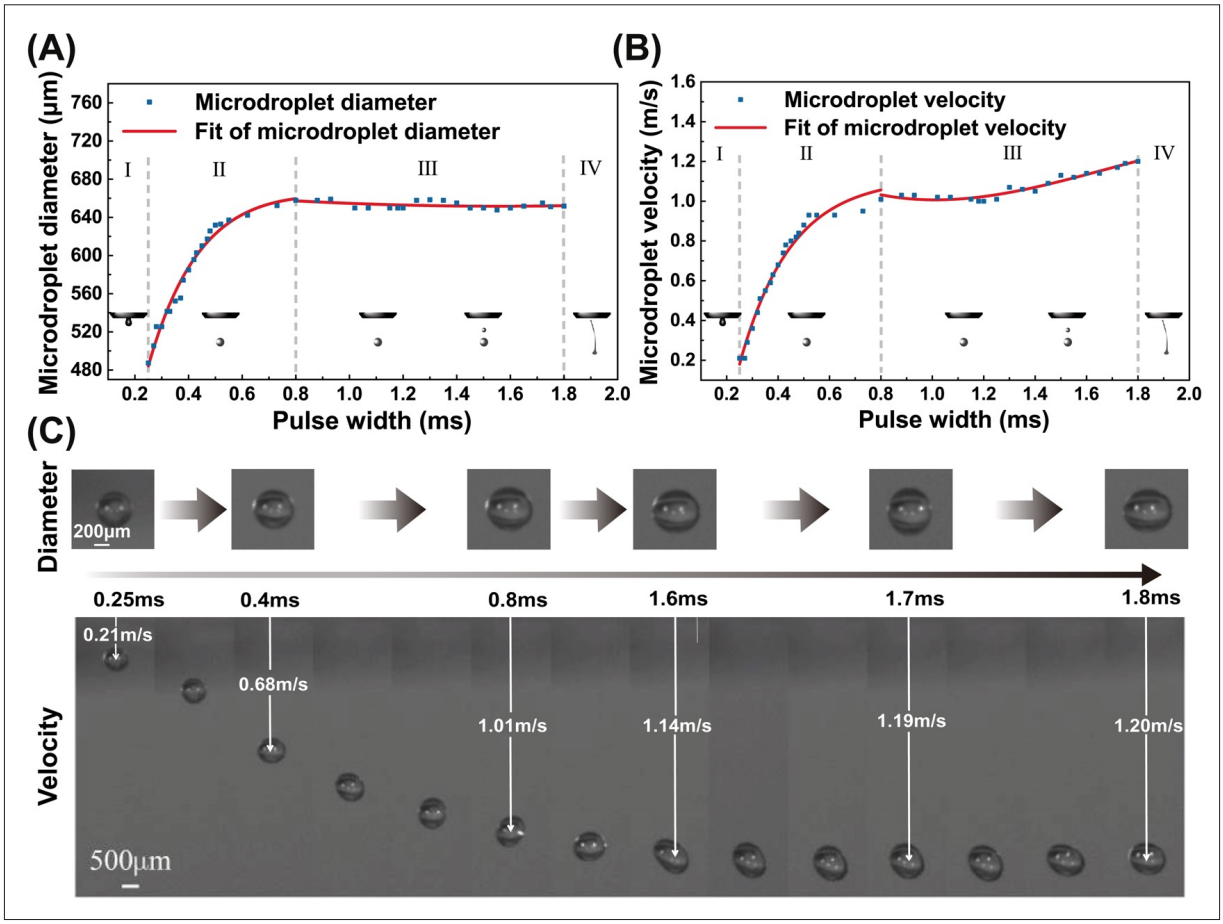


Figure 5. Effect of the applied pulse width on the microdroplet diameter **(A)** and velocity **(B)**. **(C)** Experiments show that the microdroplet diameter and velocity increased at first and remained constant as the pulse width increased.

$$D = a_3 t + b_3 e^{(-t/0.2)} + c_1 \quad \text{(VI)}$$

where D and t are the diameter and pulse width, respectively, and a_3, b_3, and c_1 are -28.1, -711.3, and 695.1, respectively. Analyzing the experimental results showed that when a microdroplet was extruded, the pressure remained positive for a short time, and the microdroplet was not dispensed entirely. The negative pressure caused the microdroplet to snap earlier, which reduced the microdroplet diameter. As shown in the chart, the positive pressure time increased with the increase in pulse width, increasing the microdroplet's diameter. When the pulse width increased to 0.8 ms, the positive pressure pushed the microdroplets entirely away from the nozzle, and thus the pulse width had little effect on the diameter of the microdroplet.

Figures 5B shows that when the pulse width was 0.25 ms, the minimum speed was approximately 0.2 m/s. When the pulse width reached 0.8 ms, the maximum velocity was approximately 1 m/s. Equation VI was calculated by integrating the pressure and pulse width function (Equation III) and fitting the test data (the formula derivation process shown in the Supplementary File). The relationship between microdroplet velocity and the pulse width, as defined by Equation VII, is:

$$V = -a_4 e^{(-t/0.2)} + b_4 \quad \text{(VII)}$$

where V and t are velocities and pulse width, respectively, and a_4 and b_4 are 3.27 and 1.12, respectively. In Figure 5C, several special pulse widths were selected to display the velocity and diameter of the microdroplets. The figure shows the variation of microdroplet velocity and diameter with pulse width. These formulas for pulse width remain valid even if the printing material is altered. Only the coefficients of the formulas need to be determined through experiments before using them. The reasons for the experimental results for microdroplet speed were analyzed. When the pulse width was small, a large part

of each microdroplet was connected to the nozzle. Then, the negative pressure forced the microdroplet to move off the nozzle, significantly reducing the microdroplet's velocity. When the pulse width increased gradually, the size of the part of the microdroplet connected to the nozzle decreased with time, and the effect of the negative pressure on the microdroplet velocity decreased. When the pulse was longer than 0.8 ms and the microdroplet was wholly separated from the nozzle, the negative pressure had little effect on the microdroplet velocity. Jet flow occurred at the nozzle when the pulse was over 1.8 ms.

According to the analysis of the test results, we effectively controlled the microdroplet diameter and velocity by adjusting the voltage amplitude and the pulse width. The diameter and velocity of the microdroplet were controlled through the adjustment of the pressure field, which is instrumental for MFCPIB.

3.2. Temperature field control and optimization

To precisely control the microdroplet temperature, we completed the microdroplet diameter and velocity control by adjusting the pressure field and also controlled and optimized the temperature field. The temperature field before injection prevented GelMA from clogging the nozzle and ensured cell survival. After injection, the amount of heat needed to cool a microdroplet depended on its diameter, and the speed of the microdroplet determined the time available for heat exchange. However, the amount of heat exchanged at a given time depended on the temperature field. Thus, precisely controlling the temperature field for the MFCPIB was necessary.

3.2.1. Temperature field simulation analysis

The temperature control system of MFCPIB is shown in Figure 6A. The printhead is mounted on the three-axis platform, which positions it to create a 3D structure. The temperature-controlled chamber was a high-delay system, and thus a double closed-loop control strategy was adopted to solve the high delay. As shown in the enlarged image, the printhead is primarily composed of piezoelectric ceramics, a temperature-controlled housing, nozzle, and other components. The temperature-controlled housing has inlet and outlet ports for the water bath, and a pump circulates hot water in the water bath to the printhead. The closed-loop water bath temperature control system ensures accuracy up to 0.1°C. To guide the temperature field control experiment, the "Solid and fluid heat transfer" interface of COMSOL (version 5.6, COMSOL Inc., Sweden) was used to simulate convection heat transfer between printhead, chamber, and air and obtain the control law of the temperature field. Considering the requirements for GelMA molding and the cell survival rate, the baseplate temperature was set to 4°C. The ambient temperature was set to 25°C and the printhead temperature to 37°C. The air temperature distribution could be obtained under the corresponding conditions by adjusting the temperature of the upper cover. Figure 6B shows a group of simulated images in which the bottom plate was 4°C, the bottom plate was -5°C, and the air was 2.1°C. We also performed a series of simulation experiments. The simulation results showed that when the temperature of the upper cover increased from -5°C to 10°C, the air temperature ranged from 2.1°C to 9.7°C. The air temperature increased faster when the top cover temperature exceeded 4°C. Subsequently, we used a thermal imager to observe the actual air temperature and verified the accuracy of the simulation results. Because the thermal imager could not be used to photograph the temperature field of the air inside, we placed a custom-designed copper sheet in the chamber. Figure 6C shows the temperature field of internal air that could be obtained by observing the temperature of the copper sheet. Through the comparison of the results of the simulation and the observations, we verified the accuracy of the simulation. Figure 6D depicts the simulated and observed air and cover temperatures, which are divided into two linear variations with a boundary at 4°C.

We obtained the relationship between the upper and lower cover temperatures and the air temperature through simulations. We used this relationship to control the air temperature by adjusting the upper and lower cover temperatures to control the microdroplet temperature and achieve MFCPIB.

3.2.2. Calculation of microdroplet temperature

We were able to control the air temperature accurately. Next, we needed to obtain the relationship between the air temperature and the microdroplet temperature to control the microdroplet temperature and achieve MFCPIB accurately.

In order to obtain the gel temperature of the microdroplet, we first conducted the rheological test of 5% GelMA. As shown in Figure 6E, the storage and loss moduli of the GelMA solution were measured with temperature reduction. We divided the image into three parts. In part I, the storage and loss modulus were stable, indicating that GelMA had not started to form a gel when the temperature was above 17°C. The viscosity of this part of GelMA approached zero. In part II, the storage modulus and loss modulus of GelMA increased simultaneously, and the increase in the storage modulus was much larger than the increase in the loss modulus when the temperature range was 15°C to 17°C—the intersection of storage modulus and loss modulus to describe the gel point.[41-43] When the temperature reached 16°C, the storage and loss modulus curves intersected at the gel point of GelMA,

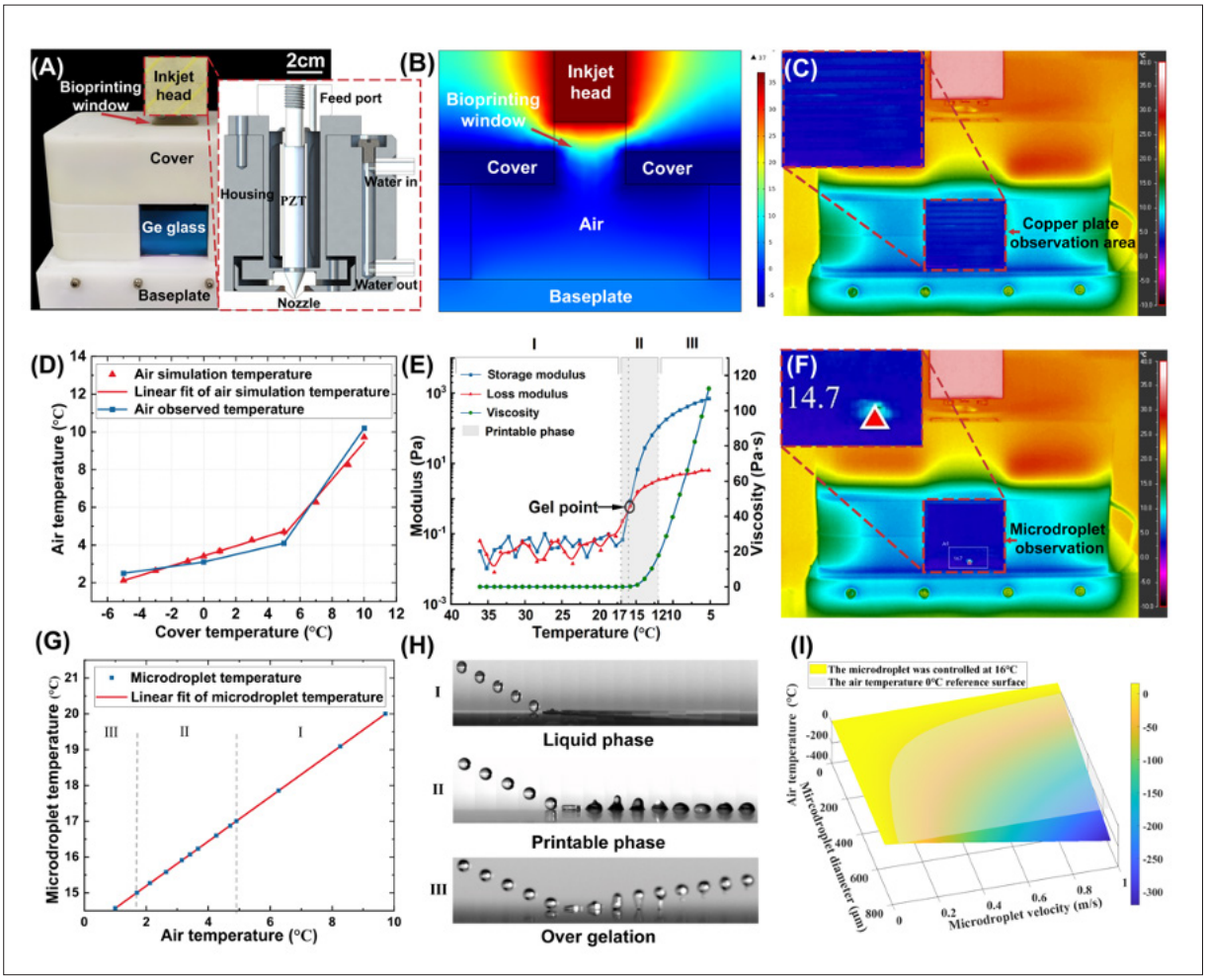


Figure 6. Controlling and optimization of the temperature field for the full process. **(A)** The temperature control system of MFCPIB. Enlarged image shows the internal structure of the temperature-controlled printhead. **(B)** Simulation of the temperature-controlled chamber. **(C)** Infrared thermography of the system. **(D)** Fitted curve of the top cover temperature and air temperature. The correctness of the simulation was verified by comparing two curves. The functional relationship between the temperatures of the upper cover and the air was obtained. **(E)** Rheological properties of GelMA. **(F)** Infrared thermography of microdroplet temperature. The red triangle represents the maximum temperature of 14.7°C in the chamber, representing the microdroplet temperature. The correctness of the microdroplet temperature calculation was verified. **(G)** Diagram of the relationship between air temperature and microdroplet temperature. The microdroplet temperature was proportional to the air temperature. **(H)** Observation of microdroplet formation. **(I)** Summary of the MFCPIB relationship. To accurately control the final microdroplet molding temperature at 16°C, the corresponding air temperature to achieve good microdroplet molding was found for different microdroplet diameters and velocities.

and at this point, GelMA began to form a gel and the viscosity began to increase slowly. The microdroplets in this range are at a critical point of a sudden change in viscosity, making GelMA printable. We used the MFCPIB method to control the assembled microdroplets within this temperature range. In part III, when the temperature was below 15°C, the storage modulus was much higher than the loss modulus and gradually leveled off. GelMA gradually completely gelled and the viscosity of GelMA rapidly increased in this part. The rheological properties shown in Figure 6E provided a theoretical basis for subsequent accurate temperature control of microdroplets. Using the MFCPIB method, the final assembly temperature of the microdroplet was controlled near the gel point of 16°C and in part II.

In order to calculate the temperature of microdroplets, we utilized the lumped parameter method. This method is a simplified analysis technique that disregards the thermal conductivity resistance of an object. It is applicable when the heat transfer resistance on the object's surface is much greater than the thermal conductivity inside the object. Under these conditions, the temperature will remain constant, assuming the object is at the same temperature at a given moment. To determine the suitability of the

lumped parameter method, we evaluated the Biot number using Equation VIII:[44]

$$B_i = \frac{h(V/A)}{\lambda} < 0.1M \quad \text{(VIII)}$$

where , h, V, A, λ, and M are the Biot number, convection transfer rate, superficial volume, superficial area, thermal conductivity, and geometric parameter, respectively. We used 192 V for the inkjet test and the relationship between microdroplet diameter and velocity distribution obtained in the previous section. In this test, a 150 μm diameter nozzle was used. The microdroplet diameter was 192 μm, and the falling velocity was 0.23 m/s. The Bi was 0.016, which is less than 0.033.

Newton's cooling law describes the behavior of objects that are hotter than their surroundings and gradually cool down by releasing heat. This law is also applicable to the process of cooling microdroplets in a temperature-controlled chamber. The heat balance of GelMA microdroplets can be explained by Equations IX and X, which follow Newton's cooling law:[45]

$$\rho c V \frac{d\theta}{d\tau} = -hA\theta \quad \text{(IX)}$$

$$\frac{\theta}{\theta_0} = \frac{T - T_a}{T_0 - T_a} = exp\left(-\frac{hA}{\rho c V}\tau\right) = exp\left(-\frac{hA}{\rho c V}\cdot\frac{l}{v}\right) \quad \text{(X)}$$

where T, T_0, T_a, ρ, c, τ, l, v, A, and V are the actual temperature of the microdroplet, the initial temperature of the GelMA microdroplet, the actual temperature of the air, the microdroplet density, the microdroplet-specific heat capacity, the falling time of the microdroplet, the distance between the nozzle and the baseplate, the GelMA microdroplet falling speed, superficial area, and volume, respectively.

We substituted the physical parameters of GelMA and the relevant temperature into the above equation. The calculation showed that when the air temperature increased from 2.1°C to 9.7°C, the microdroplet temperature ranged from 15.3°C to 20.0°C. To verify the correctness of the calculation, the thermal imager was used to observe the highest temperature of the microdroplet falling to the rectangular area of the baseplate, which was the instantaneous temperature of the microdroplet contacting the baseplate. As shown in Figure 6F, when the air temperature was 2.1°C, the calculated GelMA microdroplet temperature was 15.3°C, and the measured microdroplet temperature was 14.7°C. The margin of error was only 2.8%, which indicated that the system could accurately control the microdroplet temperature. The relationship between air temperature and microdroplet temperature is shown in Figure 6G.

3.2.3. GelMA microdroplet assembly process optimization

The assembly of microdroplets is a complex process that depends on several critical factors such as the forces of inertia, viscosity, and wettability. During this process, energy is transformed in various ways, including kinetic energy, surface tension potential energy, gravitational potential energy, elastic potential energy resulting from solidification, and dissipated work from viscosity. These complex interactions are accounted for in the comprehensive energy balance equation in Equation XI:[46]

$$\frac{d}{dt}\left[\Delta E_k(t) + \Delta E_{p1}(t) + \Delta E_{p2}(t) + \Delta E_{p3}(t)\right] + \frac{d\Delta L_f(t)}{dt} = 0 \quad \text{(XI)}$$

where ΔE_k is the kinetic energy of the microdroplet; ΔE_{p1}, ΔE_{p2}, and ΔE_{p3} are the gravitational potential energy, elastic potential energy, and surface tension potential energy of the microdroplet, respectively; and ΔL_f is the viscous dissipation. The integral form of the equation in Equation XII is:

$$\Delta E_k(t) + \Delta E_{p1}(t) + \Delta E_{p2}(t) + \Delta E_{p3}(t) + \Delta L_f(t) = 0 \quad \text{(XII)}$$

At different temperatures, GelMA microdroplets were in different states of gelation that corresponded to different physical characteristics, and thus, the energy transformation in the assembly process was also different. To achieve a good assembly effect, according to the GelMA gel point measured previously at 16°C, we expected to control the temperature of the microdroplet at approximately 16°C when the microdroplet assembled. The ideal microdroplet assembly temperature was obtained using the control relationships pressure field and temperature field obtained previously. To obtain a suitable microdroplet temperature for assembly, we performed a GelMA printing experiment. We adopted a nozzle with a diameter of 150 μm, an actuation waveform of 192 V, and a pulse width parameter of 1 ms for the inkjet test, and we set the printhead temperature to 37°C. Referring to the data in Figure 6G, we gradually reduced the air temperature inside the temperature-controlled chamber and observed the assembly phase of GelMA microdroplets with a high-speed camera.

As shown in Figure 6H, there were three phases in the process of microdroplet assembly. The first was the liquid phase, as shown in Figure 6H(I). When the air temperature was above 4.9°C, the GelMA microdroplet temperature was over 17°C. The microdroplet was in the liquid phase when it fell to the floor and could not assemble into

a shape. As shown in Figure 6E, at this stage , when the GelMA microdroplet began to assemble, its kinetic and gravitational potential energies were converted into surface tension potential energy and viscous dissipation, and there was no elastic potential energy in the equation. Because the GelMA microdroplet showed liquid properties, it was prone to collapse during assembly. This phase did not meet the requirements for printing.

The second phase was the printable phase, as shown in Figure 6H(II). When the internal air temperature was between 4.9°C and 1.7°C, the GelMA microdroplet temperature was between 17°C and 15°C. The microdroplet did not collapse on the baseplate and bonded to form a hemisphere. As shown in Figure 6E, and were similar at this stage. When the GelMA microdroplet touched the bottom plate, its kinetic and gravitational potential energies were converted into surface tension, elastic potential energy, and viscous dissipation. The properties of the microdroplets were between those of a liquid and a solid, and they characterized a glassy phase. During assembly, the microdroplet was glassy at the initial assembly stage and rapidly became solid after completion of assembly. Therefore, the GelMA microdroplet in this phase was suitable for printing.

The third phase was the excessive gelation phase, as shown in Figure 6H(III). When the internal air temperature dropped below 1.7°C, the gelation of the GelMA microdroplet was complete, and the microdroplet exhibited the properties of a solid. When the microdroplet reached the floor, it bounced. At this stage, , and elastic potential energy and viscous dissipation were generated during assembly. The kinetic and gravitational potential energies decreased, and there was no surface tension potential. When the elastic potential energy reached its maximum value, it was converted into gravitational potential and kinetic energies. Therefore, the GelMA microdroplet bounced, and the assembly could not be achieved.

Based on the above experimental results, we determined that the optimal printing temperature of the GelMA microdroplet was 16°C. As in a previous study, we adjusted the microdroplet diameter and velocity by adjusting the pressure field. After obtaining the desired microdroplet diameter and velocity, we controlled the temperature during assembly at 16°C by controlling the air temperature. According to the results of the temperature calculation, we obtained the relationship of MFCPIB, as shown in Figure 6I. The surface was fitted by the microdroplet diameter, velocity, and air temperature, which controlled the temperature at 16°C. The gray plane in Figure 6I is a 0°C isothermal surface. The appropriate point above the isothermal surface was selected for the test in the cell-laden structure printing experiment. In the printing test process, first, we adjusted the voltage amplitude and pulse width to achieve the suitable diameter and velocity of the microdroplet. Then, the corresponding air temperature was found on the fitted surface in Figure 6I. Moreover, according to the air temperature control relationship obtained above, the temperatures of the upper and lower floors of the temperature controlled chamber were adjusted. Finally, we controlled the final assembly temperature of the microdroplets at 16°C.

This study aims to expand the scope of the proposed method by conducting printability tests of GelMA at different concentrations. Specifically, printability tests were conducted on 3% and 10% GelMA, which are widely adopted concentrations in printing experiments (**Figure S1** in Supplementary File). Therefore, we accurately controlled the temperature of the GelMA microdroplets and realized the MFCPIB. Next, we performed a series of printing experiments using MFCPIB.

3.3. Printing 3D structures with MFCPIB

To verify the printing effect of the MFCPIB method, we performed a series of printing tests using 5% GelMA. First, we printed a pyramid (Figure 7A) to demonstrate the 3D printing capability of the MFCPIB method. The top of Figure 7A shows the computer-aided design (CAD) model of the design; the pyramid was 20 mm long, 16 mm wide, and 20 mm high. Using the MFCPIB method in printing for 1.5 h, the top of the pyramid structure had well-defined edges and did not collapse. It was not easy to achieve this level of performance with the previous inkjet molding method. The MFCPIB method could form structures from temperature-sensitive materials such as GelMA.

Next, we fabricated a stereoscopic letter structure (Figure 7B) to verify the ability to adapt the MFCPIB method to DOD printing using a printhead that started and stopped. In inkjet printing, many structures cannot be completed; for example, the pyramid model can be printed at one time, but it is necessary to pause several times during DOD printing. When printing is paused, this significantly challenges the use of thermosensitive materials because they easily gel and clog the nozzle. Additionally, after the printing is stopped, material that is in the temperature-controlled chamber for a long time undergoes excessive gelation, which affects the assembly of the microdroplets of the gel. The MFCPIB technique should solve this problem by applying temperature control to the printing process. Since the printhead is kept at 37°C, the material will not clog the nozzle when the printing process is suspended for a long time. Although the deposited microdroplets stay in the temperature-controlled chamber for 1 h, the

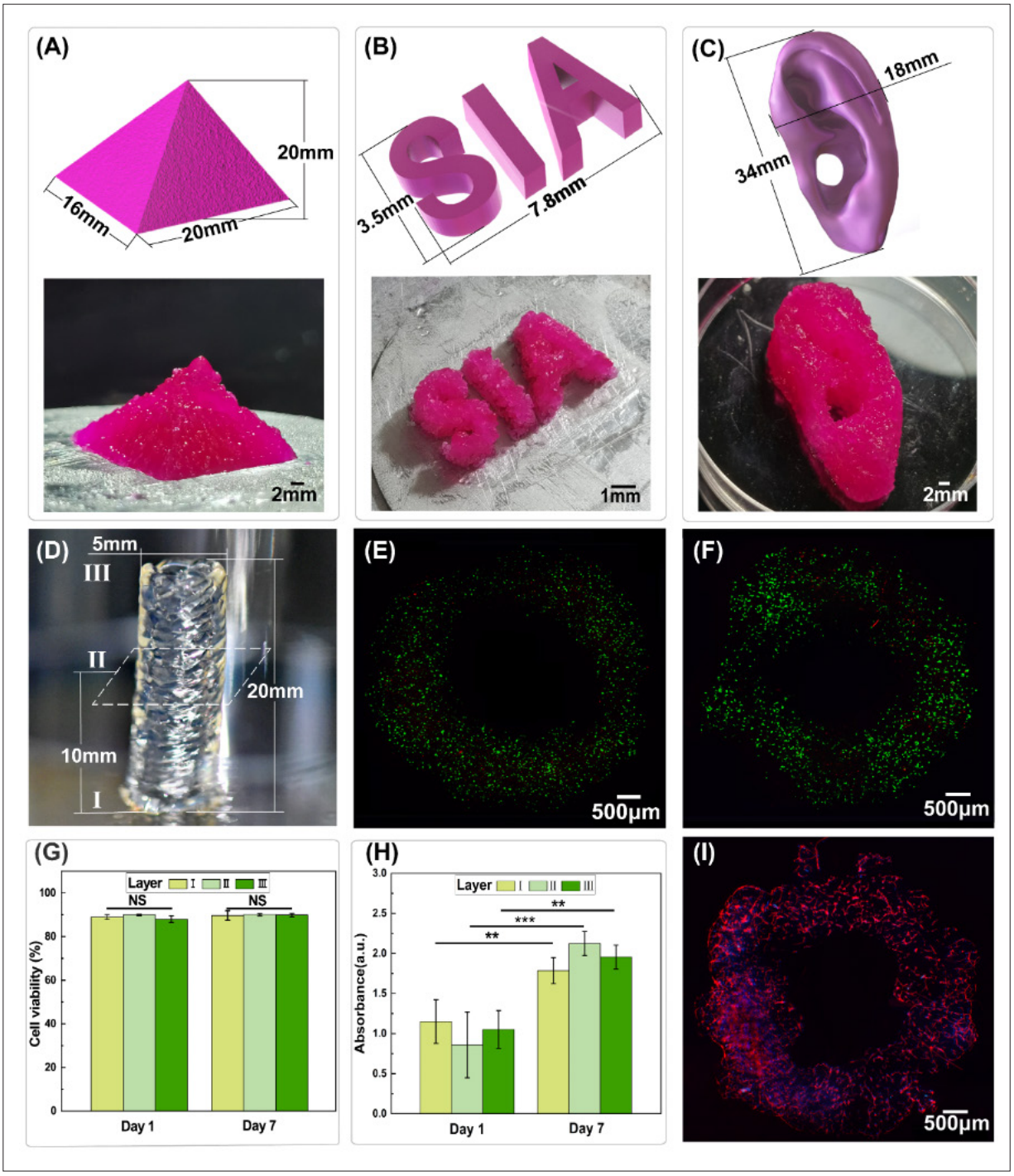


Figure 7. Printing test of MFCPIB method. **(A)** Schematic drawing and photograph of the polyhedral pyramid. **(B)** Schematic drawing and photograph of the stereoscopic text "SIA." **(C)** Schematic drawing and photograph of the ear-shaped 3D structure. **(D)** Cell-laden vessel-like structures. **(E, F)** LIVE-DEAD staining of vessel-like structure with SMCs on day 1 **(E)** and day 7**(F)**. **(G)** Cell viability of SMCs in different layers of the vessel on day 1 and day 7. **(H)** Quantification of cell proliferation on day 1 and day 7 using the CCK-8 assay; $^{**}p < 0.01$, $^{***}p < 0.001$. **(I)** Fluorescence micrographs showing SMCs spreading morphology within the GelMA hydrogels.

chamber temperature is uniform. The temperature does not decrease too much when the single bottom plate cools, and thus the printing material will remain uniform and not undergo gelation, a condition convenient for the subsequent assembly and molding of microdroplets. We used the MFCPIB method to print the text structure "SIA,"

to demonstrate the ability to DOD-print thermosensitive materials; the ability of microdroplets to bond into curves was also found to be good.

Inkjet printing has been widely used in industrial curved surface structure manufacturing due to its advantages of noncontact printing. We printed an ear-shaped object with sharp and well-defined edges in 2.5 h (Figure 7C). This demonstrated the promising fabrication capability of the MFCPIB method, which can be utilized for manufacturing tissue with curved surfaces. In the process of printing the complex curved surface, when a microdroplet combined with the microdroplet that had been printed previously, the contact surface was not smooth but irregular in shape, such as a slope; the microdroplet easily collapsed and rebounded due to the uneven contact surface, making it difficult to achieve ideal printing. However, this method accurately controls the microdroplet bonding temperature, which ensures good printing resolution and achieves a good printing effect, even for the formation of complex curved surfaces, and provides the possibility to manufacture clinically complex organs.

To demonstrate the suitability of the MFCPIB method for producing cell-laden constructs, large aspect ratio cell-laden vessel-like structures (Figure 7D) with a diameter of 5.0 mm were fabricated using the MFCPIB method. Printing tubular structures with a large aspect ratio is beneficial because such structures are needed for various biomedical applications, such as vascular applications. Considering the temperature control and printing effect, we used a 150 μm nozzle. The voltage amplitude of the driving waveform was 160 V, and the pulse width was 1 ms. The microdroplet diameter was 197 ± 15 μm, and the velocity was 0.17 ± 0.02 m/s. The MFCPIB method helped control the microdroplet temperature throughout the printing process. Following the relationships in Figure 6I, we set the top cover temperature to -5°C, the bottom plate temperature to 4°C, and the air temperature to 2.2°C. Finally, the microdroplet molding temperature was also approximately 16°C, which met printing requirements. While printing the first few layers that become the base of a structure, it was necessary to deposit the material not only on a surface that was homogeneous and smooth, but also on one that ensured that the cells did not die from prolonged hypothermia. The gradually rising vessel-like structure is also needed to ensure the same molding effect as the first few layers while printing successive layers. Otherwise, the printing of the structure with a large aspect ratio could not be realized because of the accumulation of errors. In this case, the MFCPIB method satisfied these requirements by using the uniform temperature field formed by the dual-machine temperature control and thus realized the printing of structures with large aspect ratios. The maximum height of a vascular structure obtained using the MFCPIB method was approximately 20 mm. The achievable aspect ratio with GelMA during inkjet printing with the MFCPIB method was 4.0. The maximum aspect ratio in previous studies was only 2.5.[18] This demonstrated the promising fabrication capability of the MFCPIB method, which could be utilized for the direct biofabrication of thermosensitive materials in structures needed for patients.

For the bioprinting of living cells, the viability of cells after printing is of great concern. SMCs were mixed in GelMA to print the vascular structures. After printing the cell-laden vessel-like structures, we sectioned and observed the bottom (I), middle (II), and top (III) of the vessel-like structure, as shown in Figure 7D. We applied live-dead staining after culturing on day 1 (Figure 7E), and we also added dead and live staining test on day 7 (Figure 7F). Most stained cells showed green fluorescence, indicating living cells, while only a few cells showed red fluorescence, indicating dead cells. The test was repeated three times. The analyzed results, shown in Figure 7G, revealed that the cell viability at all three heights was about 90%, regardless of whether the cells have been cultured for 1 day or 7 days. According to the data presented in Figure 7G, the viability of SMCs in layer I on day 1 was 89.0 ± 1.1%, in layer II was 89.9 ± 0.4%, and in layer III was 88.0 ± 1.5%. Similarly, on day 7, the viability of SMCs in layer I was 89.7 ± 2.1%, in layer II was 90.1 ± 0.5%, and in layer III was 89.8 ± 0.8%. We conducted significance calculations on cells of different heights on the same day, yielding p-values of 0.52 for significance tests of layer I and layer II, 0.13 for significance tests of layer II and layer III, and 0.52 for significance tests of layer I and layer III. All p-values were greater than 0.05, indicating that there was no significant difference in cell viability at each height layer. The same was true for the cell activity test on day 7, with p-values of 0.85 for significance tests of layer I and layer II, 0.98 for significance tests of layer II and layer III, and 0.94 for significance tests of layer I and layer III. Again, all p-values were greater than 0.05, indicating no significant difference in cell activity at each height layer on day 7. Our experimental results demonstrate that the MFCPIB method has low effect on cell viability. Furthermore, we conducted the CCK-8 assay to evaluate the proliferation of the SMCs. Based on the experimental findings, it was observed that the cells cultured in the three gel layers for a period of 7 days exhibited a remarkable improvement in absorbance as determined by the CCK-8 assay. This also correlated with an increase in cell area and fluorescence intensity as observed in our fluorescence staining. These results further validate that the MFCPIB method is safe for cells. Finally, hydrogels were fixed and stained for cell nuclei (DAPI, blue) and F-actin (phalloidin, red) on day 10. As shown in Figure 7I, most cells encapsulated in the gel showed excellent spreading, which is similar to mature SMCs *in vivo*. These results indicated

that the MFCPIB method caused slight damage to cells and maintained a high survival rate of cells after printing. Thus, the MFCPIB method exhibits promising potential for the utilization in printing cell-laden thermosensitive biomaterial and the *in vivo* experiments in future.

4. Conclusion

In conclusion, we successfully developed, tested, and implemented an innovative MFCPIB method for creating highly bioactive tissue-like structures using 5% GelMA. We also demonstrated the feasibility of using this approach with other concentrations of GelMA. Our method enables precise control of the formation and properties of microdroplets through temperature and pressure regulation. With this method, we have successfully printed various 3D structures, including a cell-laden vascular structure with an aspect ratio of 4.0, without compromising the viability of cells. The MFCPIB method provides a new approach for inkjet printing of thermosensitive materials such as GelMA. This printing method has potential applications in biological research and clinical medicine, particularly for creating tissues such as esophageal tissues and skin with high bioactivity. While the current method is unable to print hollow structures, we believe that future work involving multi-printheads and low-concentration GelMA as a sacrificial material will contribute to the creation of more complex tissues and organs for utilization in clinical medicine.

Acknowledgments

None.

Funding

This study was partially supported by the National Key Research and Development Program of China (SQ2020YFB130100), the Youth Innovation Promotion Association of the Chinese Academy of Sciences (2021200), the Research Equipment Development Program of the Chinese Academy of Sciences (YJKYYQ20190045), the National Natural Science Foundation of China (52205319), CAS Project for Young Scientists in Basic Research (YSBR-041), and the Foundation of State Key Laboratory of Robotics (2021-Z01, 2022-Z04, 2023-Z01).

Conflict of interest

The authors declare no conflicts of interest.

Author contributions

Conceptualization: Huixuan Zhu, Xiongfei Zheng
Data curation: Huixuan Zhu, Chuang Ji, Runyang Zhu
Formal analysis: Huixuan Zhu, Kai Guo
Funding acquisition: Run Li, Liming Zhang
Investigation: Huixuan Zhu, Run Li
Methodology: Huixuan Zhu, Yuejing Zheng, Heran Wang
Project administration: Kai Guo
Resources: Huixuan Zhu, Xiongfei Zheng
Software: Song Li, Feiyang Gao
Validation: Yuejing Zheng
Writing – original draft: Huixuan Zhu
Writing – review & editing: Lianqing Liu

Ethics approval and consent to participate

Not applicable.

Consent for publication

Not applicable.

Availability of data

Data are available from the corresponding author upon reasonable request.

References

1. Mota C, Camarero-Espinosa S, Baker MB, Wieringa P, Moroni L. Bioprinting: from tissue and organ development to in vitro models. *Chem Rev.* 2020;120:10547–10607. doi: 10.1021/acs.chemrev.9b00789
2. Zhou L, Fu J, He Y. A review of 3D printing technologies for soft polymer materials. *Adv Funct Mater.* 2020;30:2000187. doi: 10.1002/adfm.202000187
3. Wang H, Guo K, Zhang L, et al. Valve-based consecutive bioprinting method for multimaterial tissue-like constructs with controllable interfaces. *Biofabrication.* 2021;13:035001. doi: 10.1088/1758-5090/abdb86
4. Guo K, Wang H, Li S, et al. Bioprinting of light-crosslinkable neutral-dissolved collagen to build implantable connective tissue with programmable cellular orientation. *Biofabrication.* 2023;15:035007. doi: 10.1088/1758-5090/acc760
5. Blaeser A, Duarte Campos DF, Puster U, Richtering W, Stevens MM, Fischer H. Controlling shear stress in 3D bioprinting is a key factor to balance printing resolution and stem cell integrity. *Adv Healthc Mater.* 2016;5:326-333. doi: 10.1002/adhm.201500677
6. Masaeli E, Marquette C. Direct-write bioprinting approach to construct multilayer cellular tissues. *Front Bioeng Biotechnol.* 2020;7:478. doi: 10.3389/fbioe.2019.00478
7. Li X, Chen J, Liu B, Wang X, Ren D, Xu T. Inkjet printing for biofabrication. In: Ovsianikov A, Yoo J, Mironov V, eds. *3D Printing and Biofabrication*. Cham: Springer; 2018: 283-301. doi: 10.1007/978-3-319-45444-3_26

8. Zhao L, Chang Yan K, Yao R, Lin F, Sun W. Alternating force based drop-on-demand microdroplet formation and three-dimensional deposition. *J Manuf Sci Eng.* 2015;137:031009. doi: 10.1115/1.4029803

9. Takagi D, Lin W, Matsumoto T, et al. High-precision three-dimensional inkjet technology for live cell bioprinting. *Int J Bioprint.* 2019;5(2):208. doi: 10.18063/ijb.v5i2.208.

10. Li EQ, Xu Q, Sun J, Fuh JYH, Wong YS, Thoroddsen ST. Design and fabrication of a PET/PTFE-based piezoelectric squeeze mode drop-on-demand inkjet printhead with interchangeable nozzle. *Sens Actuators Phys.* 2010;163:315-322. doi: 10.1016/j.sna.2010.07.014

11. Foresti D, Kroll KT, Amissah R, et al. Acoustophoretic printing. *Sci Adv.* 2018;4:eaat1659. doi: 10.1126/sciadv.aat1659

12. Li X, Liu B, Pei B, et al. Inkjet bioprinting of biomaterials. *Chem Rev.* 2020;120:10793-10833. doi: 10.1021/acs.chemrev.0c00008

13. Ringeisen BR, Spargo BJ, Wu PK, eds. *Cell and Organ Printing*. New York, NY: Springer; 2010. doi: 10.1007/978-90-481-9145-1

14. Zimmermann R, Hentschel C, Schrön F, et al. High resolution bioprinting of multi-component hydrogels. *Biofabrication.* 2019;11:045008. doi: 10.1088/1758-5090/ab2aa1

15. Christensen K, Xu C, Chai W, Zhang Z, Fu J, Huang Y. Freeform inkjet printing of cellular structures with bifurcations. *Biotechnol Bioeng.* 2015;112:1047-1055. doi: 10.1002/bit.25501

16. Yoon S, Park JA, Lee H-R, Yoon WH, Hwang DS, Jung S. Inkjet-spray hybrid printing for 3D freeform fabrication of multilayered hydrogel structures. *Adv Healthc Mater.* 2018;7:1800050. doi: 10.1002/adhm.201800050

17. Cheng C, Moon YJ, Kim SH, et al. Water-matrix interaction at the drop-drop interface during drop-on-demand printing of hydrogels. *Int J Heat Mass Transf.* 2020;150:119327. doi: 10.1016/j.ijheatmasstransfer.2020.119327

18. Sakurada S, Sole-Gras M, Christensen K, Wallace DB, Huang Y. Liquid-absorbing system-assisted intersecting jets printing of soft structures from reactive biomaterials. *Addit Manuf.* 2020;31:100934. doi: 10.1016/j.addma.2019.100934

19. Teo MY, Kee S, RaviChandran N, Stuart L, Aw KC, Stringer J. Enabling free-standing 3D hydrogel microstructures with microreactive inkjet printing. *ACS Appl Mater Interfaces.* 2020;12:1832-1839. doi: 10.1021/acsami.9b17192

20. Guo K, Wang H, Li S, et al. Collagen-based thiol–norbornene photoclick bio-ink with excellent bioactivity and printability. *ACS Appl Mater Interfaces.* 2021;13:7037-7050. doi: 10.1021/acsami.0c16714

21. Yue K, Trujillo-de Santiago G, Alvarez MM, Tamayol A, Annabi N, Khademhosseini A. Synthesis, properties, and biomedical applications of gelatin methacryloyl (GelMA) hydrogels. *Biomaterials.* 2015;73:254-271. doi: 10.1016/j.biomaterials.2015.08.045

22. Zhang F, Zhang Z, Duan X, et al. Integrating zinc/silicon dual ions with 3D-printed GelMA hydrogel promotes in situ hair follicle regeneration. *Int J Bioprint.* 2023;9(3):703. doi: 10.18063/ijb.703

23. Klotz BJ, Gawlitta D, Rosenberg AJWP, Malda J, Melchels FPW. Gelatin-methacryloyl hydrogels: towards biofabrication-based tissue repair. *Trends Biotechnol.* 2016;34:394-407. doi: 10.1016/j.tibtech.2016.01.002

24. Sun M, You D, Zhan N, et al. 4D oriented dynamic scaffold for promoting peripheral nerve regeneration and functional recovery. *Adv Funct Mater.* 2023;2305827. doi: 10.1002/adfm.202305827

25. Zhang J, Chen Y, Huang Y, et al. A 3D-printed self-adhesive bandage with drug release for peripheral nerve repair. *Adv Sci.* 2020;7:2002601. doi: 10.1002/advs.202002601

26. Liu W, Heinrich MA, Zhou Y, et al. Extrusion bioprinting of shear-thinning gelatin methacryloyl bioinks. *Adv Healthc Mater.* 2017;6:1601451. doi: 10.1002/adhm.201601451

27. Ying G, Jiang N, Yu C, Zhang YS. Three-dimensional bioprinting of gelatin methacryloyl (GelMA). *Bio-Des Manuf.* 2018;1(4):215-224. doi: 10.1007/s42242-018-0028-8

28. Zhang L, Zhang H, Wang H, et al. Fabrication of multi-channel nerve guidance conduits containing schwann cells based on multi-material 3D bioprinting. *3D Print Addit Manuf.* 2022;10(5):1046-1054. doi: 10.1089/3dp.2021.0203

29. Suntornnond R, Ng WL, Huang X, Yeowa CHE, Yeong WY. Improving printability of hydrogel-based bio-inks for thermal inkjet bioprinting applications *via* saponification and heat treatment processes. *J Mater Chem B.* 2022;10:5989-6000. doi: 10.1039/D2TB00442A

30. Liu X, Wang X, Zhang L, et al. 3D liver tissue model with branched vascular networks by multimaterial bioprinting. *Adv Healthc Mater.* 2021;10:2101405. doi: 10.1002/adhm.202101405

31. Shao L, Gao Q, Xie C, et al. Sacrificial microgel-laden bioink-enabled 3D bioprinting of mesoscale pore networks. *Bio-Des Manuf.* 2020;3:30-39. doi: 10.1007/s42242-020-00062-y

32. Mazur P. Freezing of living cells: mechanisms and implications. *Am J Physiol.* 1984;247:C125-C142. doi: 10.1152/ajpcell.1984.247.3.C125

33. Zhou J, Pei Z. Experimental study of the piezoelectric drop-on-demand drop formation in a coaxial airflow. *Chem Eng Process.* 2020;147:107778.
doi: 10.1016/j.cep.2019.107778

34. Binder KW, Allen AJ, Yoo JJ, Atala A. Drop-on-demand inkjet bioprinting: a primer. *Gene Ther Regul.* 2011;06: 33-49.
doi: 10.1142/S1568558611000258

35. Jaffe H, Berlincourt DA. Piezoelectric transducer materials. *Proc IEEE.* 1965;53:1372-1386.
doi: 10.1109/PROC.1965.4253

36. McLean D. *Understanding Aerodynamics: Arguing from the Real Physics*. Chichester, West Sussex: McLean John Wiley and Sons 2012.
doi: 10.1002/9781118454190

37. Chang H-J, Tsai MH, Hwang W-S. The simulation of micro droplet behavior of molten lead-free solder in inkjet printing process and its experimental validation. *Appl Math Model.* 2012;36:3067–-3079.
doi: 10.1016/j.apm.2011.09.094

38. He M, Sun L, Hu K, Zhu Y, Ma L, Chen H. Drop-on-demand inkjet printhead performance enhancement by dynamic lumped element modeling for printable electronics fabrication. *Math Probl Eng.* 2014;2014:1-16.
doi: 10.1155/2014/270679

39. Gallas Q, Sheplak M, Kaysap A, et al. Lumped element modeling of piezoelectric-driven synthetic jet actuators. 40th AIAA Aerospace Sciences Meeting & Exhibit. 2002.
doi: 10.2514/6.2002-125

40. Shah MA, Lee D-G, Lee BY, Kim NW, An H, Hur S. Actuating voltage waveform optimization of piezoelectric inkjet printhead for suppression of residual vibrations. *Micromachines.* 2020;11:900.
doi: 2072-666X/11/10/900

41. Liu H, Liu J, Qi C, et al. Thermosensitive injectable in-situ forming carboxymethyl chitin hydrogel for three-dimensional cell culture. *Acta Biomater.* 2016; 35:228-237.
doi: 10.1016/j.actbio.2016.02.028

42. Shih H, Lin C-C. Visible-light-mediated thiol-ene hydrogelation using eosin-Y as the only photoinitiator. *Macromol Rapid Commun.* 2013;34:269-273.
doi: 10.1002/marc.201200605

43. Guvendiren M, Burdick JA. Stiffening hydrogels to probe short- and long-term cellular responses to dynamic mechanics. *Nat Commun*. 2012;3:792.
doi: 10.1038/ncomms1792

44. Csemány D. Thermal analysis of suspended single droplet evaporation measurements with a coupled lumped parameter model. *Heat Mass Transf.* 2023;59:2181-2195.
doi: 10.1007/s00231-023-03403-6

45. Sazhin SS, Gol'dshtein VA, Heikal MR. A transient formulation of newton's cooling law for spherical bodies. *J Heat Transf.* 2001;123:63-64.
doi: 10.1115/1.1337650

46. Gong Y, Bi Z, Bian X, et al. Study on linear bio-structure print process based on alginate bio-ink in 3D bio-fabrication. *Bio-Des Manuf.* 2020;3:109-121.
doi: 10.1007/s42242-020-00065-9

ACCSCIENCE PUBLISHING

International Journal of Bioprinting

RESEARCH ARTICLE

Optimizing additively manufactured mouthguards: An evaluation of multi-layer materials for improved shock absorption and durability compared to conventionally fabricated samples

Chenyuan Li[1], Takahiro Wada[2], Yumi Tsuchida[3], Kairi Hayashi[1], Gen Tanabe[1,4], Toshiaki Ueno[1,4], and Hiroshi Churei[1]*

[1]Department of Masticatory Function and Health Science, Graduate School of Medical and Dental Science, Tokyo Medical and Dental University, Tokyo, Japan

[2]Department of Advanced Biomaterials, Graduate School of Medical and Dental Science, Tokyo Medical and Dental University, Tokyo, Japan

[3]Department of Digital Dentistry, Graduate School of Medical and Dental Science, Tokyo Medical and Dental University, Tokyo, Japan

[4]Department of Sports Dentistry, School of Dentistry, Meikai University, Sakado, Japan

Abstract

Although sports mouthguards (MGs) are mandatory in some contact sports, the use of conventional fabricated materials for making MGs is time-consuming and lacks precision, limiting their widespread application. In this study, we compared mouthguards designed using digital software with conventional ones. The conventional mouthguards were categorized into two types: those constructed from a poly-(ethylene vinyl acetate)-base material, and those constructed from MG21, a polyolefin-base material. The shock absorption and durability were assessed through a free-falling steel ball test and a fatigue test. The durability of the MGs was evaluated by measuring the retention force in the inner layer and deviations at consistent points on the outer layer during various fatigue test stages. Additively manufactured samples showed superior shock absorption performance, except for the double-layer samples with an inner layer of Shore A hardness 95. All single-layer additively manufactured MGs were damaged during the mid-fatigue test stage, while both double-layer additively manufactured and conventional MGs remained undamaged. Throughout all fatigue test stages, the retention force of double-layer additively manufactured MGs was significantly lower than that of conventional MGs. However, the retention force of double-layer additively manufactured samples with an inner layer of Shore A hardness 70 (D-A70) was superior to the average of all MGs in the wet condition, which was 6.4 ± 2.5 N in the previous study. The results of this study demonstrated the benefits of a hybrid design of hard and soft materials, particularly the promising combination of D-A70, which exhibited comparable shock absorption and durability to conventional MGs.

Keywords: Sports mouthguards; Additively manufactured; Photoinitiator; Shock absorption; Durability; Retention force

***Corresponding author:**
Hiroshi Churei
(chu.spmd@tmd.ac.jp)

Citation: Li C, Wada T, Tsuchida Y, et al. Optimizing additively manufactured mouthguards: An evaluation of multi-layer materials for improved shock absorption and durability compared to conventionally fabricated samples. *Int J Bioprint*. 2024;10(3):2469. doi: 10.36922/ijb.2469

Received: December 18, 2023
Accepted: January 23, 2024
Published Online: March 18, 2024

Copyright: © 2024 Author(s). This is an Open Access article distributed under the terms of the Creative Commons Attribution License, permitting distribution, and reproduction in any medium, provided the original work is properly cited.

Publisher's Note: AccScience Publishing remains neutral with regard to jurisdictional claims in published maps and institutional affiliations.

1. Introduction

A sports mouthguard (MG) is essential for protecting the hard and soft tissues of the oral cavity, including teeth and gums, from impact during athletic activities. The World Dental Federation emphasizes the importance of custom-made sports MGs in preventing trauma.[1] In certain contact sports, such as boxing, MGs usage is mandatory because they reduce the risk of traumatic dental injuries and brain concussions, as demonstrated by extensive research.[2-8]

Despite their importance, creating a comfortable and durable MG is a complex challenge. The fabrication process, particularly the thermoforming phase, often results in diminished thickness around the anterior teeth, which can affect both comfort and protection.[9] Additionally, each MG must be tailored to fit comfortably, adding to the complexity of the design.

The emergence of three-dimensional (3D) digital design and additive manufacturing process, known for its customization, rapid production, and cost-efficiency, has attracted substantial interest. Prior studies have validated its safety and effectiveness,[10-13] suggesting a promising future for additively manufactured sports MGs.

In 2020, Li et al. published an extensive exposition of the digital design and manufacturing of sports MGs.[14] By implementing a semi-digital workflow, Hada et al. examined how temperature fluctuations affected the material properties of sports MGs.[15] After investigating various materials, Sousa et al.[16] found that three additively manufactured materials—recycled polylactic acid (rPLA), polymethyl methacrylate (PMMA), and high-impact polystyrene (HIPS)—outperformed a conventional material, poly-(ethylene vinyl acetate) (EVA) in the shock absorption experiment. A study by Pinho et al.[17] demonstrated increased elasticity and resistance in aged sandwich samples.

The processes are categorized into International Organization for Standardization/American Society for Testing and Materials (ISO/ASTM) process classes in medical applications of additively manufactured powder bed fusion, material extrusion, vat photopolymerization, material jetting, binder jetting, sheet lamination, and directed energy deposition.[18] The Polyjet process (Stratasys Ltd., Rehovot, Israel), a revolutionary multi-material jetting process, was widely applied for higher precision and printing speed, the ability to print multiple materials, and hands-free removal of support structure.[19]

Materials of acrylate-base photoinitiator composites (Agilus, Vero, digital poly-(acrylonitrile-butadiene-styrene) [D-ABS]) are preferred for additively manufactured MGs due to their excellent protection capability, which is the most critical ability of MG. These materials are competitive with those of conventional fabricated materials like EVA and polyolefin (PO).[20,21] It has been demonstrated that incorporating a hard insert within a conventional material can significantly enhance the protection capability.[22]

While the shock absorption and dispersion properties of additively manufactured MGs have been extensively studied, there is a need for more focused research on their durability, especially considering the intermittent occlusal forces during athletic activities.[21] Durability is another crucial factor for the long-term, effective, and safe use of MGs. The resistance to surface wear and deformation from continuous use has been evaluated for conventional MG materials,[23] but the durability of additively manufactured MGs requires further investigation. Hard occlusal surfaces in devices such as night guards, which prevent bruxism, have been shown to improve durability and reduce wear.[24]

This study aimed to assess the effectiveness of combining hard and soft materials in additively manufactured MGs to enhance shock absorption and dispersion properties in simulated oral environments. Additionally, it evaluated the durability, retention force, and morphological changes of these MGs, particularly in response to the effects of intermittent occlusal forces on their surfaces in simulated oral environments.

2. Materials and methods

2.1. Samples preparation and digital model design

Acrylate-base photoinitiator composites Agilus, Vero, and D-ABS (Stratasys Ltd., Rehovot, Israel) were utilized (Table 1). Seven types of Agilus and/or Vero composites with Shore A hardness values of 30, 40, 50, 60, 70, 85, and 95 were produced under controlled conditions of 20±5°C and 50% humidity, denoted as A30, A40, A50, A60, A70, A85, and A95, respectively (Table 2). The composites were blended in their liquid state before the printing process.[25] Single-layer samples were specified as having a diameter of 50 mm and a thickness of 3 mm. Double-layer samples consist of a 0.5 mm thick hard layer of D-ABS and a 2.5 mm thick, soft layer of Agilus or/and Vero composites (A30-95), designated as D-A30 through D-A95, respectively (Figure 1). Material samples were printed by a J850 Digital Anatomy 3D printer (Stratasys Ltd., Rehovot, Israel) with a dual-head liquid output. Conventional MG sheets made of PO-base material (MG21; CGK, Hiroshima, Japan) and EVA-base material (Erkoflex [ERK]; Erkodent Erich Kopp GmbH, Pfalzgrafenweiler, Germany) were molded for comparison. The shock absorption test was conducted on 16 samples.

Materials for additively manufactured MG samples were divided into two groups: single-layer soft samples

Table 1. Mechanical properties of photoinitiators and conventional material ERK

	Agilus 30	Vero	D-ABS	ERK
Tensile strength (MPa)	2.4–3.1	40.0–55.0	55.0–60.0	31.0
Elongation at break (%)	220.0–270.0	5.0–20.0	25.0–40.0	4.5
Modulus of elasticity (MPa)	N/A	2200–3000	2600–3000	N/A
Flexural strength (MPa)	N/A	70–85 MPa	65–75 MPa	N/A
Flexual modulus (MPa)	N/A	2000–2500	1700–2200	N/A
Izod notched impact (J/m)	N/A	20–30	90–115	N/A
Compressive set (%)	6–7	N/A	N/A	N/A
Tensile tear resistance (N/cm)	4.1–7.1	N/A	N/A	N/A
Shore hardness	A25–30	D83–86	D85–87	A92
Density (g/cm^3)	1.140–1.150	1.170–1.180	1.170–1.180	0.935

Abbreviations: D-ABS, digital poly-(acrylonitrile-butadiene-styrene); ERK, Erkoflex; N/A, no available data.

Table 2. Mechanical properties of Agilus or/and Vero composited materials (A) defined by various Shore A hardness in average conditions

	A30	A40	A50	A60	A70	A80	A90
Tensile strength (MPa)	2.4–3.1	3–4	3–4	3.5–4.5	4–6	6–10	10–14
Elongation at break (%)	220–270	190–210	170–210	150–170	120–140	70–90	50–70
Shore hardness (A)	25–30	40–50	50–55	55–60	60–70	80–85	85–90
Tensile tear resistance (kg/cm)	4.1–7.1	6.0–8.0	7.0–9.0	7.0–10.0	12.0–14.0	22.0–26.0	26.0–30.0

(A30, A50, A70) with an average thickness of 3 mm on the labial and buccal surfaces and 2 mm on the occlusal and palatal surfaces and double-layer samples, hard outer layers (D-ABS) covered 0.5 mm for the labial surfaces of the anterior region and 1 mm for the entire occlusal surface while soft inner layers covered the remainder, defined as D-A30, D-A50, and D-A70. Additively manufactured MG samples were deposited with single or multiple drops of photoinitiator on the build platform and immediately solidified with the ultraviolet light passed over the layer (Figure 2). By setting the 3D printing process, drops of different photoinitiators can be stacked in sequence. Two types of conventional custom-made MGs, ERK and MG21, were fabricated for comparison with the same specifications. Three samples of each type were fabricated to decrease the research error.

Materials samples were designed using Shapr3D, a solid modeling computer-aided design application (Shapr3D, Budapest, Hungary). MG samples were sculpted in Zbrush (Maxon Computer GmbH, Homburg, Germany) following the scanning of dental models (Dental standard stone models; D18FE-500A-QF Nissin Dental Products Inc., Kyoto, Japan) with an extraoral scanner (D2000, 3shape, Copenhagen, Denmark). This scanner has a high accuracy of 5 μm. MG thickness was measured using Materialise Magics software (Materialise, Leuven, Belgium) for precise splitting into two pieces.

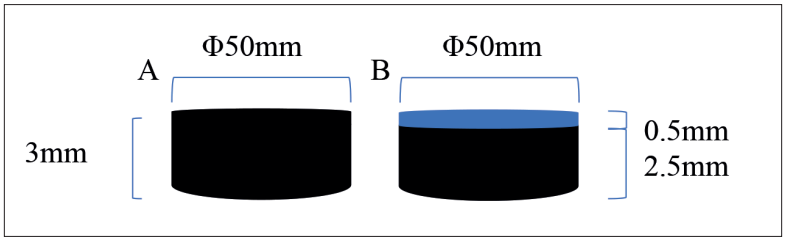


Figure 1. Schematic of the two types of materials. (A) Single-layer material sheet sample, 3 mm thickness; (B) double-layer additively manufactured material sheet sample, 0.5 mm thickness D-ABS and 2.5 mm thickness Agilus or/and Vero composites.

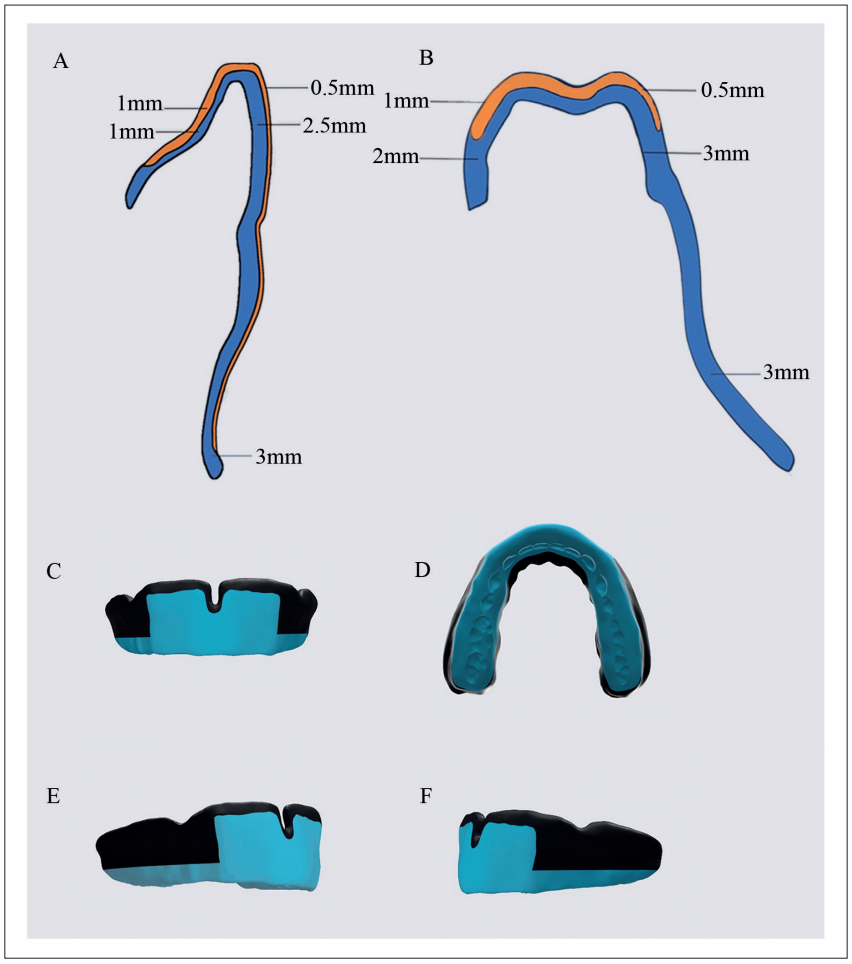


Figure 2. Cross-section schematics of double-layer additively manufactured MG samples in the anterior area (A) and posterior area (B); side views of double-layer additively manufactured MG samples (C, D, E, F). Double-layer additively manufactured MG samples were split from single-layer additively manufactured MG samples.

2.2. Shock absorption test

According to Fukusawa et al.'s research,[26] a shock absorption test was conducted using a 32.6 g metal ball with a 20 mm diameter, dropped from a height of about 615 mm onto a steel platform. A load cell sensor system was positioned at the bottom of the impact load machine. In this research, physical experiments were performed in a simulated oral environment to be consistent with future clinical evaluations.[27] Samples were placed in a thermostat set at 37°C and 100% relative humidity for 24 h before testing. A custom-made chamber maintained the sample temperature and humidity during the shock absorption test.

A previous study showed that the fracture load of human teeth falls within the range of 689–1093 N.[28] In the same mechanical situation, to verify the protective effect of MG, the impact force without a sample in this experiment was controlled within this range. Impact loads were measured using three dynamic compression load cells (LMA-A-1kN; Kyowa Electronic Instruments Co., Tokyo, Japan) with a capacity of 1 kilo Newton (kN), arranged in a triangle under a 10 mm thick stainless-steel platform. The sample was centered on this platform. During the test, loads were recorded at a 50 kHz sampling rate using data analysis software (EDX-100A and DCS-100A, Kyowa Electronic Instruments, Inc.). The total impact load was the sum of the three load cell readings, with the maximum load defined as the maximal impact force (MIF). The arrival time to MIF was denoted as MIF-t. Each sample was tested five times (Figure 3).[26]

2.3. Fatigue test

The fatigue test was designed on the basis of Sugimoto et al.'s research.[29] A concavity was ground at the center of gravity on the maxillary stone model plane. An iron ball was placed in this concavity on the maxillary stone model, which was worn with a MG and meshed with the mandibular stone model. Loading forces were examined

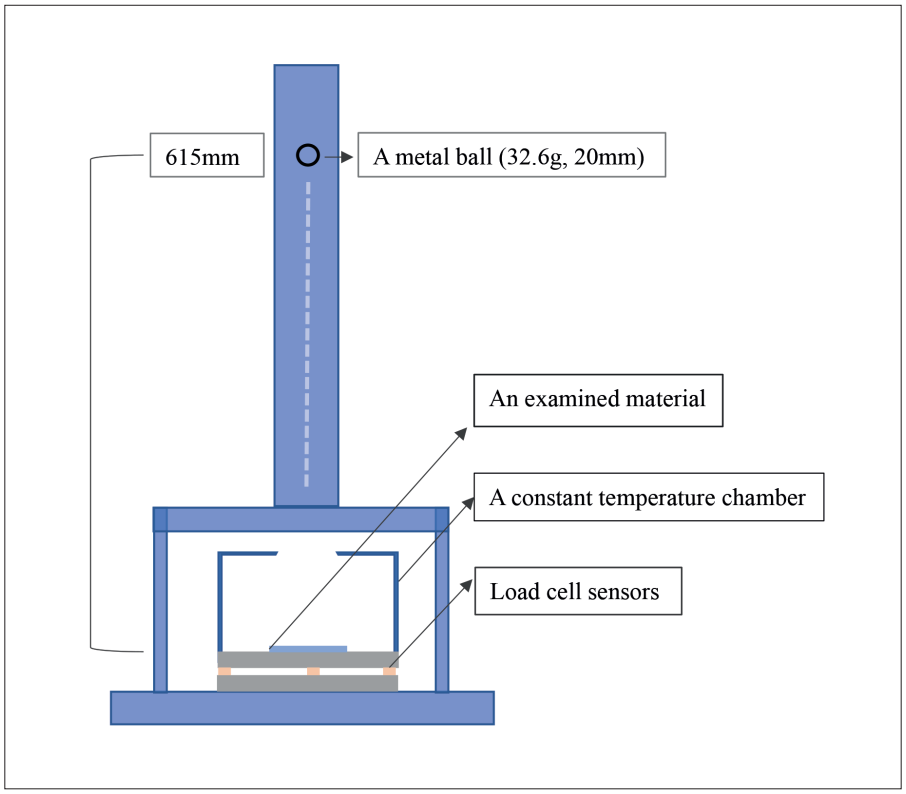


Figure 3. The setting of the free-falling steel ball test.

using an electromagnetic force testing machine (MICRO MMT-250NV-10; Shimadzu Corporation, Kyoto, Japan), with real-time data output in a cycle-loading wave-shape pattern to simulate oral occlusion movements. The load ranged from 70 N to 200 N at 1 Hz, within the normal bite-force range on the test controller (4830 controller; Shimadzu Corporation). Temperature and humidity conditions were consistent with the shock absorption test before and during the fatigue test (Figure 4). Each sample underwent 5000 bite cycles per experimental stage.[29] The cycle-loading fatigue test was conducted in two stages unless cracks appeared during the test.

2.3.1. Retention force evaluation of MG inlayer in fatigue test

According to Karaganeva et al.'s study,[30] a parallel plate and three hooks were molded from personal tray material (Ostron II, GC Corporation, Tokyo, Japan). A parallel plate was attached to the universal testing machine, and three hooks were utilized to pull the MG sample from the upper dental stone model.

A retention force test was executed on each MG by hooking the labial or buccal and palatal margins of three anatomical points including anterior and posterior (center of two central incisors, the left first molar, the right first molar). Three non-elastic wires connected the MG sample to the plate vertically. A retention force test was conducted on each MG by hooking the labial or buccal and palatal margins at three anatomical locations. Shock absorption and fatigue tests were conducted under the same setup conditions for temperature and humidity control (Figure 5).

Each MG was hauled from the maxillary model at a constant rate of 50 mm/min.[30] The test was executed five times on a universal machine (SCG-5KNA, Shimadzu Corporation), with data output from the software (Trapezium x, version 1.4.0, Shimadzu Corporation). The gauges were recalibrated after each measurement. The maximum force represented the retention force. The retention forces of conventionally fabricated and additively manufactured MGs were recorded in pre- (0th), mid- (5000th), and post- (10,000th) fatigue tests.

2.3.2. Evaluation of morphological changes of outer surfaces in fatigue test

Morphological changes were evaluated based on the procedure described by Tsuchida et al.[31] MG samples were scanned in pre-, mid-, and post-fatigue tests with the extraoral 3D scanner. The scanner was calibrated after each

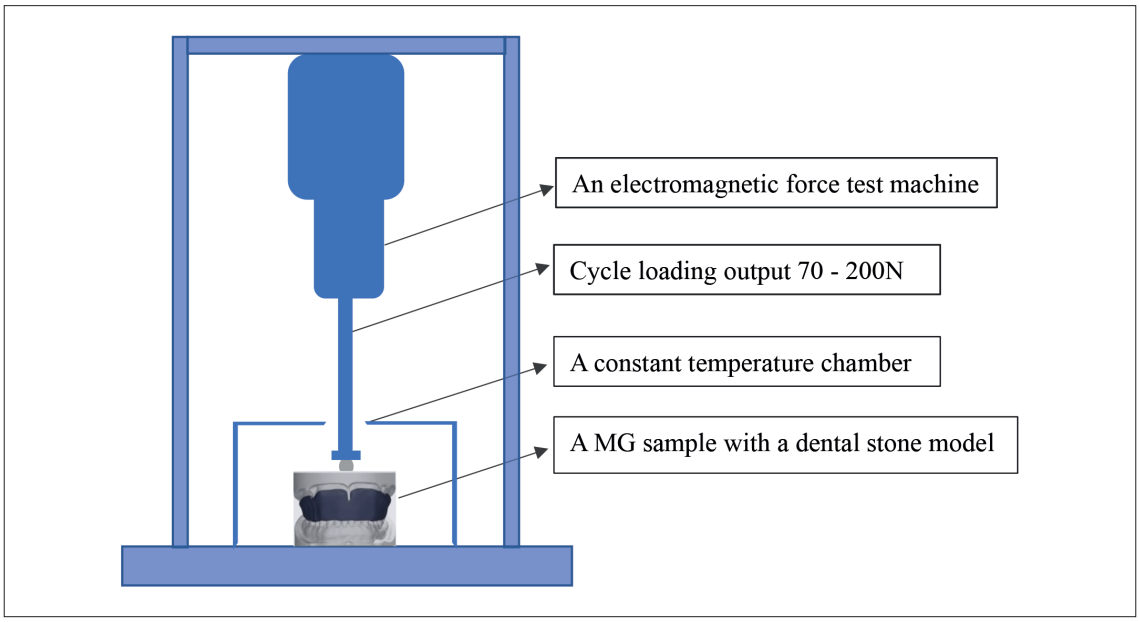


Figure 4. The setting of the cycle-loading fatigue test.

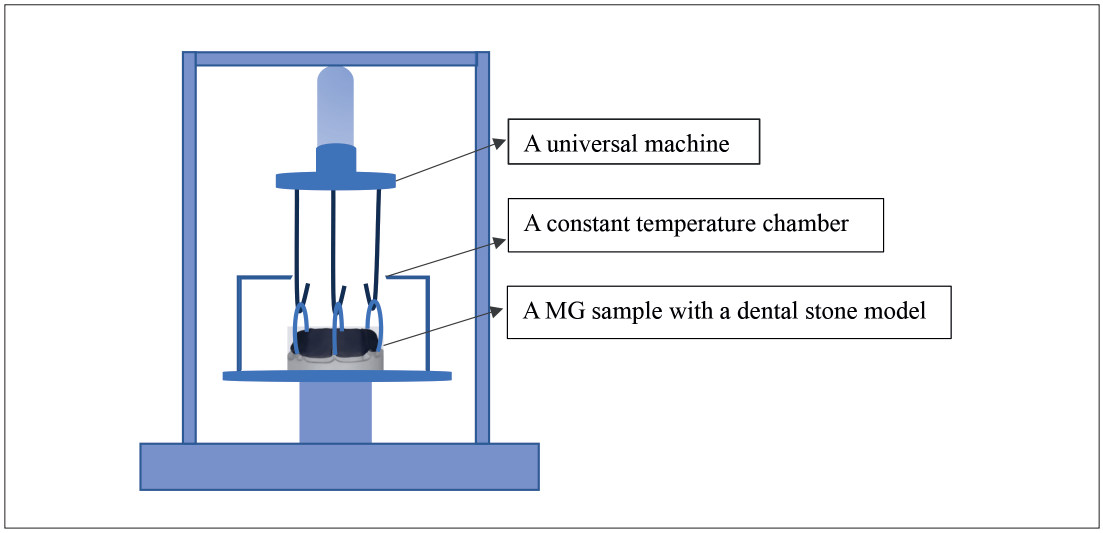


Figure 5. The setting of the retention force test.

measurement. Calculations were performed automatically to determine the most appropriate scanning position. The root-mean-square (RMS) differences of the model surfaces were calculated by 3D software (Artec STUDIO; 3DS Co., Kanagawa, Japan) based on the RMS formula, representing the average distances of the surface points at different stages where the straight lines crossed in two same position point, respectively.[32,33] The formula for calculating the RMS is as follows:

$$X_{rms} = sqrt\left((1/n)sum_{i=1}^{n} x_i^2\right) \quad \text{(I)}$$

2.4. Statistical analysis

The normality of data distribution was assessed using the Shapiro–Wilk test. Mean ± standard deviation was used to represent average values and dispersion. One-way analysis of variance (ANOVA) analyzed the shock absorption test data for MIF and MIF-t. The Fisher test with Bonferroni's

correction was used to analyze the number of MG samples destroyed during the mid-fatigue test. One-way ANOVA tested the retention force and RMS at each stage. Tukey test was performed if there was a statistical significance for each ANOVA test. The Friedman test and Dunn's pairwise test analyzed the retention force at various stages, while the paired *t*-test compared RMS differences at each fatigue test stage. The significance was set at $P < 0.05$. All statistical analyses were conducted using SPSS software (version 25.0, IBM Corp.).

3. Results

3.1. MIF and MIF-t during shock absorption test

The MIF of the free-falling steel ball without a sample was 709.0 ± 16.7 N. The MIF of conventional materials, ERK and MG21, were 386.5 ± 5.5 N and 393.9 ± 6.9 N, respectively. The MIF for single-layer additively manufactured samples increased progressively from 245.8 ± 3.2 N to 318.5 ± 10.8 N with increasing Shore A hardness of materials. The lowest MIF among the double-layer additively manufactured samples was observed for D-A70 at 328.2 ± 7.3 N, with values increasing sequentially on both sides of the Shore A hardness scale. All additively manufactured materials (except D-A95) absorbed more impact force than conventional materials ERK and MG21 (Figure 6).

Each single-layer additively manufactured sample was statistically significant compared to its corresponding double-layer additively manufactured sample of the same hardness of soft layer that was superior to the double-layer sample in shock absorption (all pairs; $P < 0.001$).

Figure 7 illustrated the approximation function of the material for additively manufactured D-A and A samples in a variety of layer designs. A linear approximation function was found in single-layer designed samples ($R^2 = 0.9749$), but a quartic approximation function was found in double-layer designed samples ($R^2 = 0.9928$), with

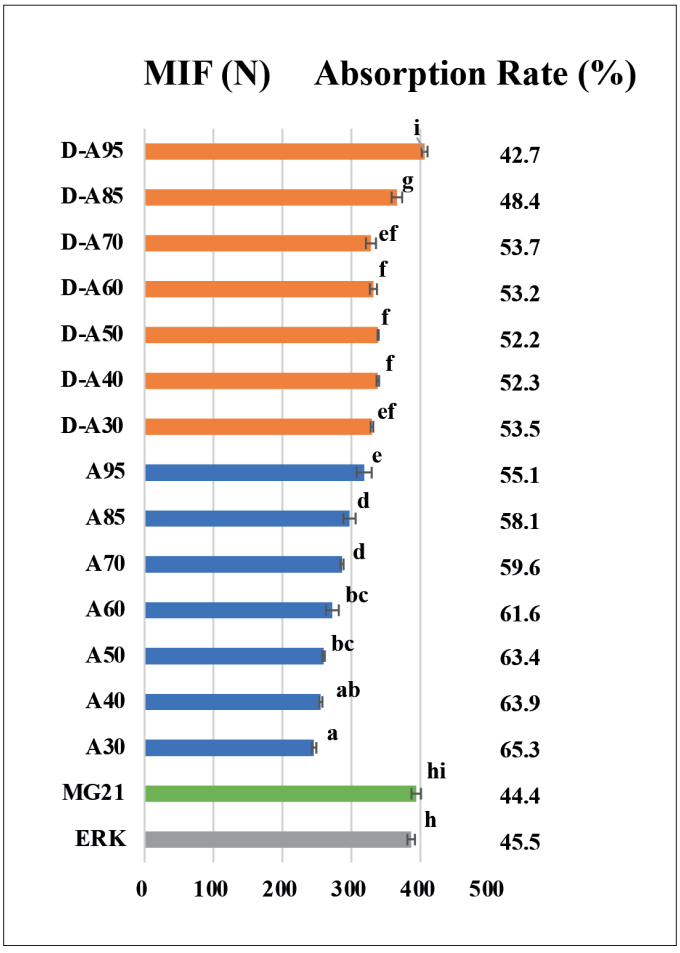


Figure 6. Maximal impact force (MIF) of various material samples in shock absorption test. Abbreviations: A, single-layer Agilus or/and Vero composites MG samples; D-A, double-layer MG samples without layer D-ABS, inlayer Agilus, or/and Vero composites; ERK, Erkoflex.

lower values for D-A30 and the range between D-A60 and D-A70 in MIF.

As described in methods, the arrival time to MIF was denoted as MIF-t. The MIF-t without samples as the control group was 0.21 ± 0.03 ms; this increased once the material sample was implemented. The average MIF-t for conventional materials, ERK and MG21, was 0.58 ± 0.04 ms and 0.55 ± 0.04 ms, respectively. There was a statistically significant difference in MIF-t between single-layer and double-layer additively manufactured samples ($P < 0.001$), except at Shore A hardness of 50 and 60 ($P = 0.179$ and $P = 0.975$). Single-layer designed samples showed a quintic approximation function, which indicated multiple wave crests ($R^2 = 0.9037$). Double-layer designed samples exhibited a quartic approximation function with lower values between D-A50 and D-A70 ($R^2 = 0.9586$) (Figures 8 and 9).

3.2. Durability under cycle-loading fatigue test

All single-layer additively manufactured MG samples had cracks on the molar occlusal surface by approximately the 1000th cycle. These cracks of the MG's occlusal surface were bitten through by the 5000th cycle; all single-layer additively manufactured MG samples were discontinued during the mid-fatigue test (Figure 10). Table 3 shows the statistical significance among the three types of MG samples (conventional, $n = 6$; single-layer additively manufactured, $n = 9$; double-layer additively manufactured, $n = 9$) ($P < 0.001$). Double-layer additively manufactured MG samples and conventionally fabricated MG samples were more durable than single-layer additively manufactured MG samples.

3.2.1. Assessment of retention force in MG inlayer

There was a statistical significance in retention force between each conventionally fabricated MG and each double-layer additively manufactured MG sample at any fatigue test stage ($P < 0.001$). In the comparison of retention forces, only MG21 had a statistical significance that increased retention force throughout the whole fatigue tests ($P = 0.028$); significant increases in retention force were also observed from the pre- to post-fatigue test ($P = 0.043$). In general, all MGs showed an inapparent increase in retention force from the pre-fatigue test to the mid-fatigue test (Table 4). During the fatigue test, the retention force in double-layer additively manufactured MG samples was found to be increased corresponding to the higher value in Shore A hardness of soft-layer materials (A) (Figure 11).

3.2.2. Assessment of morphological changes in MG outer layer

MG outer layer morphological changes were evaluated using RMS values. There was no statistical significance in RMS values in the pre-mid and mid-post fatigue test periods for MG samples (conventional, $n = 6$; double-layer additively manufactured, $n = 9$) ($P = 0.159$ and $P = 0.438$, respectively) (Table 5). Compared to pre-mid and pre-post fatigue tests, the RMS of ERK samples decreased after a period of cycle-loading fatigue tests. However, the high standard deviation among ERK samples made it difficult to achieve statistical significance. Only MG21 presented a statistically significant decrease in RMS at the pre-post-fatigue test stage, and the morphological changes reduced

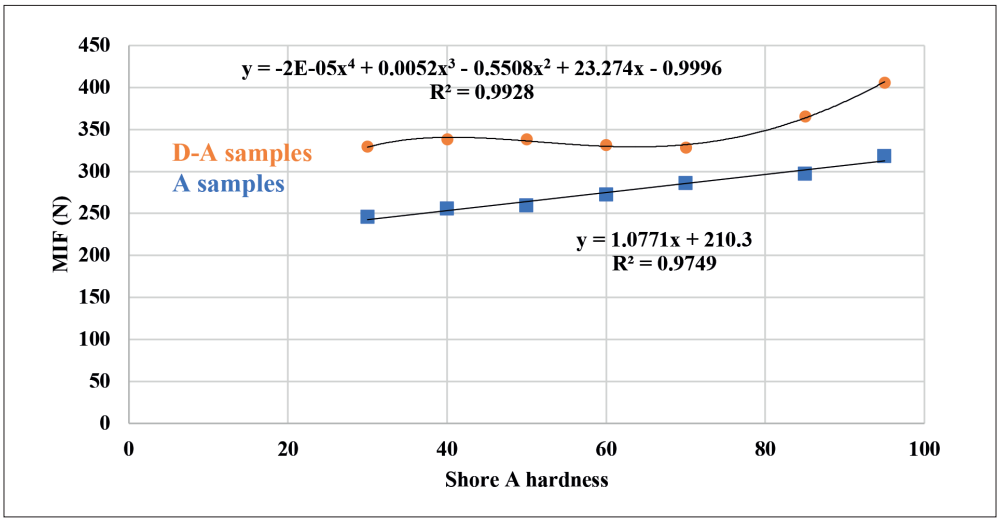


Figure 7. Maximal impact force (MIF) run chart for single-layer and double-layer additively manufactured samples according to different hardness of materials. Abbreviations: A, single-layer Agilus or/and Vero composites MG samples; D-A, double-layer MG samples without layer D-ABS, inlayer Agilus, or/and Vero composites.

Table 3. Fisher analysis of the broken result of three types of MG samples during mid-fatigue test

MG groups	Broken (%)	Unbroken (%)	χ^2 value	*P*-value
Conventional MGs (*n* = 6)	0 (0.0)	6 (100.0)	24.39	<0.001
Single-layer additively manufactured MGs (*n* = 9)	9 (100)	0 (0.0)		
Double-layer additively manufactured MGs (*n* = 9)	0 (0.0)	9 (100.0)		

Table 4. Retention force for each sample in each fatigue test stage

Fatigue test stages	Retention force (N)		
	Pre	Mid	Post
ERK MGs	29.0 ± 2.2	37.4 ± 4.2	34.9 ± 9.4
MG21 MGs	33.0 ± 4.7	42.7 ± 3.1	44.0 ± 4.4
D-A30 MGs	5.7 ± 0.6	5.4 ± 0.3	4.9 ± 0.1
D-A50 MGs	5.9 ± 0.4	5.9 ± 0.0	7.4 ± 0.3
D-A70 MGs	6.9 ± 0.2	9.5 ± 0.4	8.6 ± 1.5

MG21: P < 0.043 pre v. post.
Pre-fatigue: P < 0.001 ERK, MG21 v. D-A all MGs
Mid-fatigue: P < 0.001 ERK, MG21 v. D-A all MGs
Post-fatigue: P < 0.001 ERK, MG21 v. D-A all MGs

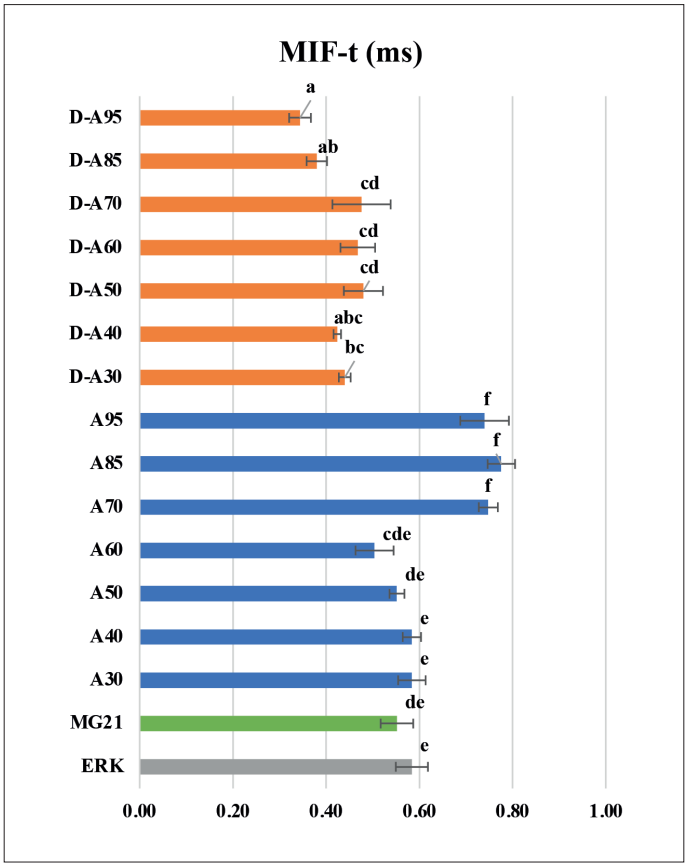


Figure 8. Arrival time of maximal impact force (MIF-t) of various material samples in shock absorption test. Abbreviations: A, single-layer Agilus or/and Vero composites MG samples; D-A, double-layer MG samples without layer D-ABS, inlayer Agilus, or/and Vero composites; ERK, Erkoflex.

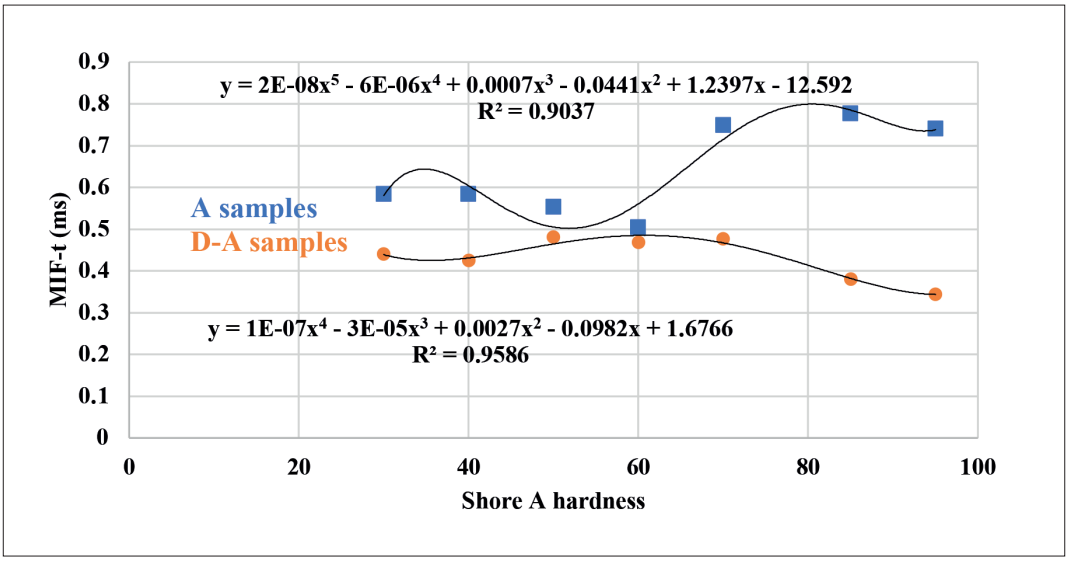


Figure 9. Arrival time of maximal impact force (MIF-t) run chart for single-layer and double-layer additively manufactured samples according to different hardness of materials. Abbreviations: A, single-layer Agilus or/and Vero composites MG samples; D-A, double-layer MG samples without layer D-ABS, inlayer Agilus, or/and Vero composites.

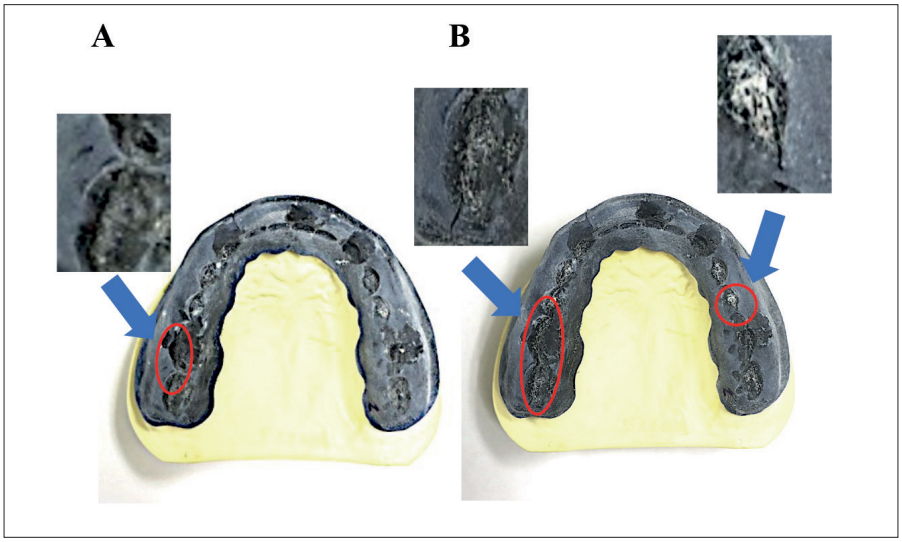


Figure 10. Occlusal surface cracks of MGs under fatigue tests. Occlusal view of single-layer additively manufactured MG samples in 1000th fatigue test (A); occlusal view of single-layer additively manufactured MG samples in 5000th fatigue test (B). Insets show three enlarged images.

after a period of cycle-loading fatigue testing (P = 0.011) (Table 6).

4. Discussion

Most existing articles mainly focus on the digital design and 3D printing processes of additively manufactured sports MGs or the physical performance testing of these materials. So far, sports MGs have mainly been examined for their shock absorption property; in additively manufactured MGs, durability is insufficient compared to conventionally manufactured MGs. Thus, this study examines the possibility of improving shock-absorbing ability and durability. Additionally, previous studies conducted fused deposition modeling (FDM), a process in which filaments are fed through a heated extruder head of a printer.[16,17] Despite its widespread use, FDM may not provide the precision and smoothness of surface required for applications such as dental devices.[34] This paper describes the first study that emphasizes the digital design for sports MGs, prioritizing patient comfort and utilizing the Polyjet process that covers

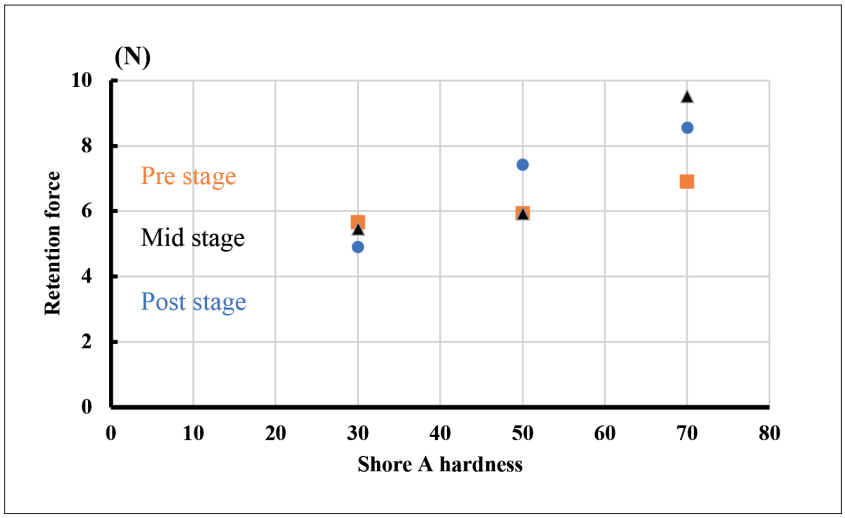


Figure 11. Relationships between Shore A hardness of soft materials and retention force in double-layer additively manufactured MG samples. As the Shore A hardness increased, the retention force of MG samples increased.

Table 5. Root-mean-square deviation of various MG samples in each fatigue test stage

Pre-mid	Retention force (N)	95% CI for mean	F-value	*P*-value
ERK MGs	200.7 ± 98.5 a	(-44.07,445.41)		
MG21 MGs	140.3 ± 14.2 a	(105.00,175.67)		
D-A30 MGs	117.3 ± 23.1 a	(59.91, 174.76)	2.078	0.159
D-A50 MGs	119.3 ± 12.7 a	(87.88, 150.79)		
D-A70 MGs	102.0 ± 13.9 a	(67.58, 136.42)		
Mid-post	**Retention force (N)**	**95% CI for mean**	**F-value**	***P*-value**
ERK MGs	179.3 ± 131.5 a	(-144.03, 502.69)		
MG21 MGs	124.7 ± 24.9 b	(62.80,186.54)		
D-A30 MGs	97.0 ± 18.2 a	(51.81, 142.19)	1.029	0.438
D-A50 MGs	120.0 ± 9.5 a	(96.30, 143.70)		
D-A70 MGs	89.0 ± 16.5 a	(48.11, 129.89)		

Abbreviation: A, single-layer Agilus or/and Vero composites MG samples; CI, confidence interval; D-A, double-layer MG samples without layer D-ABS, inlayer Agilus, or/and Vero composites; ERK, Erkoflex.

Table 6. Root-mean-square difference in each sample between the pre-mid and pre-post experimental stage

Samples	Mean and 95% CI	T-value	*P*-value
ERK MGs	75.00 (-153.53, 303.52)	1.412	0.293
MG21 MGs	50.33 (27.25, 73.42)	9.383	0.011
D-A30 MGs	-2.67 (-22.90,17.57)	-0.567	0.628
D-A50 MGs	-10.33 (-37.79,17.03)	-1.625	0.246
D-A70 MGs	17.67 (-23.18, 58.51)	1.861	0.204

Abbreviation: A, single-layer Agilus or/and Vero composites MG samples; CI, confidence interval; D-A, double-layer MG samples without layer D-ABS, inlayer Agilus, or/and Vero composites; ERK, Erkoflex.

the lack of FDM process.[35] In addition, it conducted a series of physical performance tests on the MG materials and samples in a simulated oral environment.

Recently, Unkovskiy et al. presented the workflow of a multi-layer customized sports MG design.[36] Despite the well-designed shape, its crucial physical property has not

been validated. Moreover, the clinical perspective was not considered. Schewe et al. explored the shock absorption of photoinitiators, but did not clarify the specific requirements for designing MGs with a thickness of 2–4 mm.[37] MGs thicker than 4 mm may cause joint discomfort due to the 2–4 mm freeway space in the mouth.[38] Previous studies have not extensively considered the effects of the oral environment, such as temperature and humidity.[21,37] Most experiments have been executed at room temperature and humidity because the conditions follow international standards, and are globally applicable.[39] In Tun et al.'s study,[21] the shock absorption rate of Agilus30 at room temperature was 26.9%, but it increased to 65.3% in this study. As with Compo50, Agilus50 (A50) showed an increased absorption rate from 44.8% at room temperature and humidity to 63.3% under simulated oral conditions. In contrast, conventional MG materials, ERK and MG21, demonstrated consistent absorption rates of around 43.5% and 41.8% at room temperature, and approximately 45.5% and 44.5% under simulated oral conditions. Our study demonstrated that additively manufactured material samples had an improvement in shock absorption in a simulated oral environment.

Both layer design and Shore A hardness affect shock absorption properties. The free-falling steel ball test indicated layered design was more influential than hardness of materials, as demonstrated by statistical significance between hardness-paired material samples (Figure 7). The MIF-t approximation function for single-layer samples suggested a more complex relationship, with an additional peak in growth after A70 samples, encouraging further investigation (Figure 9).

Our research confirmed that double-layer additively manufactured MG samples were preferred to single-layer MG samples, as the single-layer MG samples can be damaged at fatigue tests. Despite the superior shock absorption ability of single-layer additively manufactured samples, their propensity to crack during cycle-loading fatigue tests suggests that single-layer designs are not feasible for future use. Double-layer additively manufactured MG samples exhibited superior shock absorption than conventionally fabricated MG samples ERK and MG21, except for the type of D-A95 samples. In addition, double-layer additively manufactured materials (D-A50, D-A60, D-A70) had the same MIF-t values as conventional materials.

Our research also proved that fabricating inconsistencies affected the retention force of conventionally fabricated MG samples. However, additively manufactured MG samples have manufacturing consistencies, superior shock absorption, and acceptable durability, providing more consistent, standardized, and reliable safety protection. In addition to shock absorption, a MG must ensure a sufficient retention force to avoid dislocation during rapid movement. Previous research[30] indicated that the average retention force of conventionally fabricated MGs was 6.4 ± 2.5 N in wet conditions. This value was exceeded only by D-A70 type of MG samples when without any use. The MG sample is expected to have more specialized applications for individuals involved in fast-moving contact sports, such as football players and boxers.

According to the evaluation of retention force and RMS, only MG21 samples showed a statistical significance of a larger retention force with a smaller RMS deviation in fatigue tests (Tables 5 and 6). However, previous studies suggest that the MG retention force decreases with continued use.[40] MGs initially increase or stand the retention force before decreasing it. This may be conducive to the preparation of MG samples in future clinical applications. Further research is necessary to determine the most appropriate load preparation for MGs during fatigue tests.

There are some limitations in our study. We excluded certain values due to similar shock absorption results between the intermediate Shore A hardness number of additively manufactured material samples. Besides, the unsatisfactory results of the shock absorption tests conducted in MIF-t on D-A85 and D-A95 types of material samples removed the need for further durability tests, potentially resulting in a data exclusion. Biocompatibility is another consideration. Agilus series materials have already been applied in several medical devices, including stethoscopes[41] and eye gear with prescription glasses,[42] and the same type of materials are being employed in this study. However, little is known about the biocompatibility of these materials. Despite these limitations, the findings of this study may contribute to MG enhancement as a medical device in the future.

5. Conclusion

In this study, additively manufactured material samples (except for D-A95) made by Agilus, Vero, and D-ABS performed better in shock absorption than conventional material samples ERK and MG21 in simulated oral environments, with additively manufactured single-layer MG samples and specific types of double-layer MG samples (D-A50, D-A60, D-A70) demonstrating the same arrival time of maximum impact force (MIF-t) as conventionally fabricated MGs.

Moreover, this study provides insights into the durability and retention forces of additively manufactured MG samples, indicating that single-layer additively manufactured MG samples are less durable, but highlighting the benefits of utilizing hard materials on occlusal surfaces and effective shock absorption capabilities

of these samples. D-A70 type of MG samples had superior retention forces under wet conditions than the average of all MGs, previously reported as 6.4 ± 2.5 N.

MGs manufactured by digital design and additive manufacturing process are expected to replace conventionally custom-made MGs because of their improved standardization and convenience. Additively manufactured MG samples can be improved substantially by combining D-ABS and Agilus materials due to their effective shock absorption and durability. With these findings showcasing their benefits, a transition to fully adopting additively manufactured MGs for more enhanced athlete protection in contact sports is foreseeable in future.

Acknowledgments

We would like to thank Dr. Changyu Chen for unwavering support throughout the entire research and thank Dr. Thet Khaing Aung, Dr. Yun- Chia Lian and Dr. Siti Salwa Binti Idris for undertaking supportive work without managing data. We also extend our gratitude to the entire Sports Dentistry Group at Tokyo Medical and Dental University for active engagement in academic discussions and continuous assistance.

Funding

This work was supported by the Pioneering Research Initiated by the Next Generation (SPRING) under the Japan Science and Technology Agency (JST) (grant no. JPMJSP 2120). The funding organization did not play a role in the design or conduct of this study.

Conflict of interest

The authors declare no conflicts of interest.

Author contributions

Conceptualization: Chenyuan Li, Hiroshi Churei, Toshiaki Ueno
Data curation: Chenyuan Li
Formal analysis: Chenyuan Li
Funding acquisition: Chenyuan Li, Toshiaki Ueno
Investigation: Chenyuan Li
Methodology: Chenyuan Li, Hiroshi Churei, Toshiaki Ueno
Project administration: Hiroshi Churei
Resources: Hiroshi Churei, Yumi Tsuchida, Takahiro Wada
Software: Yumi Tsuchida, Takahiro Wada
Supervision: Hiroshi Churei
Validation: Chenyuan Li
Visualization: Chenyuan Li, Hiroshi Churei
Writing – original draft: Chenyuan Li
Writing – review & editing: Gen Tanabe, Kairi Hayashi, Takahiro Wada, Yumi Tsuchida

Ethics approval and consent to participate

Not applicable.

Consent for publication

Not applicable.

Availability of data

The datasets are not publicly available due to intellectual property considerations, but are available from the corresponding author upon reasonable request. Requests for access to these data should be directed to Dr. Hiroshi Churei (chu.spmd@tmd.ac.jp).

References

1. FDI World Dental Federation. FDI policy statement on Sports dentistry: Adopted by the FDI General Assembly, September 2016, Poznan, Poland. *Int Dent J*. 2017;67(1):18-19. doi: 10.1111/idj.12314
2. Elena-Lito E, Ioannis K, Nikolaos K. Use of mouthguards by amateur basketball athletes in Greece and the USA. *Trauma Cases Rev*. 2019;5(1). doi: 10.23937/2469-5777/1510071
3. Galic T, Kuncic D, Poklepovic Pericic T, et al. Knowledge and attitudes about sports-related dental injuries and mouthguard use in young athletes in four different contact sports-water polo, karate, taekwondo and handball. *Dent Traumatol*. 2018;34(3):175-181. doi: 10.1111/edt.12394
4. Gomez-Gimeno A, Zamora-Olave C, Cordobes-Navarro M, Willaert E, Martinez-Gomis J. Satisfaction with shortening the palatal extension of a mouthguard for water polo players: a randomized crossover study. *Dent Traumatol*. 2019;35(2):135-141. doi: 10.1111/edt.12455
5. Knapik JJ, Hoedebecke BL, Rogers GG, Sharp MA, Marshall SW. Effectiveness of mouthguards for the prevention of orofacial injuries and concussions in sports: systematic review and meta-analysis. *Sports Med*. 2019;49(8):1217-1232. doi: 10.1007/s40279-019-01121-w
6. Allison P, Tamimi F. Mouthguards should be worn in contact sports. *Br J Sports Med*. 2020;54(17):1016-1017. doi: 10.1136/bjsports-2020-102041
7. Chisholm DA, Black AM, Palacios-Derflingher L, et al. Mouthguard use in youth ice hockey and the risk of concussion: nested case–control study of 315 cases. *Br J Sports Med*. 2020;54(14):866-870. doi: 10.1136/bjsports-2019-101011

8. Green JI. The role of mouthguards in preventing and reducing sports-related trauma. *Prim Dent J*. 2017;6(2):27-34. doi: 10.1308/205016817821281738

9. Mizuhashi F, Koide K, Takahashi M. Variations in mouthguard thickness according to fabrication method. *Dent Traumatol*. 2015;31(2):130-135. doi: 10.1111/edt.12128

10. Rajkumari K, Chandra P, Balaji P. Three-dimensional printing- a revolutionary technology. *J Clin Diagn Res*. 2018;12(12):12-18. doi: 10.7860/jcdr/2018/37752.12410

11. Mancilla-De-la-Cruz J, Rodriguez-Salvador M, An J, Chua CK. Three-dimensional printing technologies for drug delivery applications: processes, materials, and effects. *Int J Bioprint*. 2022;8(4):622. doi: 10.18063/ijb.v8i4.622

12. Dawood A, Marti Marti B, Sauret-Jackson V, Darwood A. 3D printing in dentistry. *Br Dent J*. 2015;219(11):521-529. doi: 10.1038/sj.bdj.2015.914

13. Pillai S, Upadhyay A, Khayambashi P, et al. Dental 3D-printing: transferring art from the laboratories to the clinics. *Polymers (Basel)*. 2021;13(1). doi: 10.3390/polym13010157

14. Li Z, Wang S, Ye H, et al. Preliminary clinical application of complete workflow of digitally designed and manufactured sports mouthguards. *Int J Prosthodont*. 2020;33(1):99-104. doi: 10.11607/ijp.6348

15. Hada T, Komagamine Y, Kanazawa M, Minakuchi S. Fabrication of sports mouthguards using a semi-digital workflow with 4D-printing technology. *J Prosthodont Res*. 2024;68(1):181-185. doi: 10.2186/jpr.JPR_D_22_00274

16. Sousa AM, Pinho AC, Piedade AP. Mechanical properties of 3D printed mouthguards: influence of layer height and device thickness. *Mater Des*. 2021;203:109624. doi: org/10.1016/j.matdes.2021.109624

17. Pinho AC, Piedade AP. Sandwich multi-material 3D-printed polymers: influence of aging on the impact and flexure resistances. *Polymers (Basel)*. 2021;13(22). doi: 10.3390/polym13224030

18. ISO. *Additive Manufacturing — General Principles — Fundamentals and Vocabulary*. ASTM; 2021. https://www.iso.org/obp/ui/#iso:std:iso-astm:52900:ed-2:v1:en

19. Palanisamy C, Raman R, Dhanraj PK. Additive manufacturing: a review on mechanical properties of polyjet and FDM printed parts. *Polym Bull*. 2022;79(9):7065-7116. doi: 10.1007/s00289-021-03899-0

20. Aung TK, Churei H, Tanabe G, et al. Air permeability, shock absorption ability, and flexural strength of 3D-printed perforated ABS polymer sheets with 3D-knitted fabric cushioning for sports face guard applications. *Polymers (Basel)*. 2021;13(11). doi: 10.3390/polym13111879

21. Tun PS, Churei H, Hikita K, et al. Fabrication of shock absorbing photopolymer composite material for 3D printing sports mouthguard. *J Photopolym Sci Technol*. 2020;33(6):615-622. doi: 10.2494/photopolymer.33.615

22. Handa J, Takeda T, Kurokawa K, Ozawa T, Nakajima K, Ishigami K. Influence of pre-laminated material on shock absorption ability in specially designed mouthguard with hard insert and space. *Journal of Prosthodontic Research*. 2011;55(4):214-220. doi: 10.1016/j.jpor.2011.02.003

23. Kawamura S, Nakajima K, Handa J, Nara K, Miyajima S, Suda S, et al. The influence of repeated impact loads on the impact absorption ability of mouthguard materials. *J Prosthodont Res*. 2006/7;50:500-500. doi: mol.medicalonline.jp/library/journal/abstract?GoodsID=dv5hotet/2006/005003/024&name=0500-0500j&UserID=202.242.187.105

24. Longridge NN, Milosevic A. The bilaminar (dual-laminate) protective night guard. *Dent Update*. 2017;44(7):648-654. doi: 10.12968/denu.2017.44.7.648

25. ASTM. *Standard Test Methods for Vulcanized Rubber and Thermoplastic Elastomers–Tension*. ASTM; 2021. https://www.astm.org/d0412-16r21.html

26. Fukasawa S, Churei H, Chowdhury RU, et al. Difference among shock-absorbing capabilities of mouthguard materials. *Dent Traumatol*. 2016;32(6):474-479. doi: 10.1111/edt.12275

27. Ioannidis K, Beltes P, Lambrianidis T, Kapagiannidis D, Karagiannis V. Crown discoloration induced by endodontic sealers: spectrophotometric measurement of Commission International de I'Eclairage's L*, a*, b* chromatic parameters. *Oper Dent*. 2013;38(3):E1-12. doi: 10.2341/11-266-l

28. Sherfudhin H, Hobeich J, Carvalho CA, Aboushelib MN, Sadig W, Salameh Z. Effect of different ferrule designs on the fracture resistance and failure pattern of endodontically treated teeth restored with fiber posts and all-ceramic crowns. *J Appl Oral Sci*. 2011;19(1):28-33. doi: 10.1590/s1678-77572011000100007

29. Sugimoto A, Abe M, Gonda T, Yamaguchi S, Maeda M, Ikebe K. Fit of custom-made mouthguards after cyclic loading. In: *Proceedings of the 30th Annual Meeting of Japanese Academy of Sports Dentistry*. 2020. doi: mol.medicalonline.jp/library/journal/download?GoodsID=dv2sposi/2020/s02302/018&name=0062-0062j&UserID=202.242.187.110

30. Karaganeva R, Pinner S, Tomlinson D, et al. Effect of mouthguard design on retention and potential issues arising with usability in sport. *Dent Traumatol*. 2019;35(1):73-79. doi: 10.1111/edt.12446

31. Tsuchida Y, Shiozawa M, Handa K, Takahashi H, Nikawa H. Comparison of the accuracy of different handheld-type scanners in three-dimensional facial image recognition. *J Prosthodont Res*. 2023;67(2):222-230. doi: 10.2186/jpr.JPR_D_22_00001

32. Muta S, Ikeda M, Nikaido T, et al. Chairside fabrication of provisional crowns on FDM 3D-printed PVA model. *J Prosthodont Res*. 2020;64(4):401-407. doi: 10.1016/j.jpor.2019.11.004

33. Diken Turksayar AA, Donmez MB, Olcay EO, Demirel M, Demir E. Effect of printing orientation on the fracture strength of additively manufactured 3-unit interim fixed dental prostheses after aging. *J Dent*. 2022;124:104155. doi: 10.1016/j.jdent.2022.104155

34. Guerra Silva R, Torres MJ, Zahr Viñuela J. A comparison of miniature lattice structures produced by material extrusion and vat photopolymerization additive manufacturing. *Polymers*. 2021;13(13):2163. doi: 10.3390/polym13132163

35. Layani M, Wang X, Magdassi S. Novel materials for 3D printing by photopolymerization. *Adv Mater*. 2018;30(41):e1706344. doi: 10.1002/adma.201706344

36. Unkovskiy A, Huettig F, Kraemer-Fernandez P, Spintzyk S. Multi-material 3D printing of a customized sports mouth guard: proof-of-concept clinical case. *Int J Environ Res Public Health*. 2021;18(23):12762. doi: 10.3390/ijerph182312762

37. Schewe P, Roehler A, Spintzyk S, Huettig F. Shock absorption behavior of elastic polymers for sports mouthguards: an in vitro comparison of thermoplastic forming and additive manufacturing. *Materials*. 2022; 15(8):2928. doi: 10.3390/ma15082928

38. Johnson A, Wildgoose DG, Wood DJ. The determination of freeway space using two different methods. *J Oral Rehabil*. 2002;29(10):1010-1013. doi: 10.1046/j.1365-2842.2002.00950.x

39. ISO. *Standard Atmospheres for Conditioning and/or Testing*. ISO; 1976. https://www.iso.org/obp/ui/#iso:std:iso:554:ed-1:v1:en

40. Hayashi K, Chowdhury RU, Chowdhury NU, et al. Thickness change and deformation of custom-made mouthguards after two years of use by Bangladeshi field hockey players. *Dent Traumatol*. 2021;37(4):617-622. doi: 10.1111/edt.12666

41. Popkin R, Lobo F, Stubbs J. Multimaterial 3D printing for the fabrication of functional stethoscopes. In: *Proceedings of the 2019 Design of Medical Devices Conference*. ASME; 2019. doi: 10.1115/DMD2019-3297

42. Singh R, Singh R, Suri A. Personalized 3D printed eye gear for microscopic surgeons amidst and beyond COVID-19. *Bioengineering*. 2023;10(10):1129. doi: 10.3390/bioengineering10101129

ACCSCIENCE PUBLISHING

International Journal of Bioprinting

RESEARCH ARTICLE

A new solution for *in situ* monitoring of shape fidelity in extrusion-based bioprinting via thermal imaging

Simone Giovanni Gugliandolo[1,2], Egon Prioglio[1], Davide Moscatelli[2], and Bianca Maria Colosimo[1]*

[1]Department of Mechanical Engineering, Politecnico di Milano, Via La Masa, 1, 20156, Milano, Italy

[2]Department of Chemistry, Materials and Chemical Engineering "Giulio Natta", Politecnico di Milano, Piazza Leonardo da Vinci, 32, 20133, Milano, Italy

Abstract

Bioprinting is an interdisciplinary study field, where additive manufacturing is combined with tissue engineering and material sciences. The ever-increasing need for personalized medicine fueled interest in the possibility of using this technique to reproduce biological tissues, allowing bioprinting to establish itself as one of the most promising approach in biomedical research. Producing bioconstructs that resemble living tissues is a very complex and multi-step procedure. Given the complexity of the processes involved, the literature still lacks robust solutions for monitoring the bioprinted construct quality, especially *in situ* and in-line. Here, a novel non-destructive approach for monitoring the geometries of bioprinted constructs based on infrared (IR) imaging is proposed. Besides the intuitive use of IR information to gain insight on the temperature signature, we propose IR video imaging as a viable solution to overcome traditional problems of visible-range imaging for geometry reconstruction with transparent bioinks, especially when precise information on the last printed layer only is required. The results obtained show a significant new direction for in-line monitoring of bioprinting processes.

Keywords: Additive manufacturing; 3D bioprinting; Thermal imaging; Monitoring

***Corresponding author:**
Bianca Maria Colosimo
(biancamaria.colosimo@polimi.it)

Citation: Gugliandolo SG, Prioglio E, Moscatelli D, Colosimo BM. A new solution for *in situ* monitoring of shape fidelity in extrusion-based bioprinting via thermal imaging. *Int J Bioprint*. 2024;10(3):2021. doi: 10.36922/ijb.2021

Received: October 12, 2023
Accepted: December 28, 2023
Published Online: March 22, 2024

Copyright: © 2024 Author(s). This is an Open Access article distributed under the terms of the Creative Commons Attribution License, permitting distribution, and reproduction in any medium, provided the original work is properly cited.

Publisher's Note: AccScience Publishing remains neutral with regard to jurisdictional claims in published maps and institutional affiliations.

1. Introduction

Bioprinting is an additive manufacturing (AM) technology whose goal is to fabricate parts that mimic the functionality of real tissues and organs by combining cells and biomaterials with a specific three-dimensional (3D) spatial organization. As in traditional AM, the goal is achieved with the use of computer-aided design (CAD) to generate 3D models of the geometry of the tissue or organ of interest to produce bioconstructs that have many applications in regenerative medicine, tissue engineering, reconstructive surgery, drug discovery, pharmacokinetics, food sector, and basic medical and cell biology research.[1,2] Thus, one of the main challenges is to avoid the death of living cells during the printing process. In light of these numerous applications and due to the increasing interest especially in personalized medicine, bioprinting has attracted attention in recent years from both academia and industry.[3] During the last decade, many new techniques and

technologies related to bioprinting have emerged in the state of the art, from specific 3D printers, the bioprinters, to specific soft biomaterials in which living cells can be embedded, called bioinks.[4,5]

Although the bioprinting literature does not typically use the specific terminology defined in AM standards (ISO/ASTM 52900:2021), technologies similar to those used for polymers are often employed. We can identify two main classes of bioprinting technologies:[3] laser-assisted bioprinting and laser-free bioprinting, each of which includes several sub-categories. There are also hybrid technologies or those with particular processes like melt electrowriting (MEW),[6] magnetic 3D cell culture,[7] acoustic assembly,[8] microneedle array,[9] and single-cell printing[10] among the most known.

Laser-free bioprinting offers varying resolutions and speeds influenced by factors like bioprinting head precision, material extrusion mechanisms, nozzle types, and droplet formation methods. Extrusion-based bioprinting (EBB) is widely studied and known for its affordability and compatibility with various biomaterials.[11] In EBB, the impact of mechanical forces, particularly shear stress, on cells and bioink properties must be properly mitigated to preserve cell viability and structural integrity.[12] Inkjet bioprinting is suitable for smaller features but requires low-viscosity biomaterials.[13] Higher viscoelasticity stabilizes droplets, reducing displacement, while increased viscosity improves accuracy and enhances cell viability and proliferation. This highlights the crucial role of bioink properties in optimizing precision and creating tunable cell spheroids.[14] Laser-assisted bioprinting notably utilizes vat photopolymerization methods such as stereolithography (SLA) and digital light processing (DLP). In this sophisticated approach, light serves as the catalyst to either initiate photopolymerization reactions or generate controlled heat and pressure, enabling the precise and intricate fabrication of 3D structures.

Stereolithography and DLP contribute significantly to the refinement and efficacy of laser-assisted bioprinting. These vat photopolymerization techniques excel in providing a higher resolution during the bioprinting process, ensuring the creation of detailed and complex structures with higher precision. The ability to precisely control the initiation of photopolymerization reactions through light-based technologies enhances the accuracy of the deposited bioink materials. One notable advantage of vat photopolymerization methods, particularly SLA and DLP, is their broader compatibility with a diverse range of bioinks.[15] Two-photon polymerization (2PP) achieves nanoscale detail using laser-induced photopolymerization.[16-19] Volumetric bioprinting constructs free-form structures inspired by optical tomography but is limited to photo-curable bioinks and can potentially cause cell damage.[18]

The bioprinting literature is rich with articles studying the bioprinting process capabilities, the development and classification of novel biomaterials, and a specific focus on the tissue of interest.[5,20,21] However, few studies have been investigating solutions for *in situ* monitoring and inspection of bioprinted constructs, as the ones observed in the literature on more conventional AM processes.[22-27] In fact, a few papers mostly from the same research groups have been presented inspecting the quality of the printed construct, detecting defects as well as tools to control and correct deposition errors *in situ*.[28-42]

The lack of repeatability, process stability, and error detection and monitoring in bioprinting represent key technological barriers to the development of products of increasing complexity, especially when hard-to-print biomaterials are involved and the shape fidelity layer-wise can then affect the capability of printing multilayer constructs.[28] Indeed, the industrial repeatability and reproducibility of the printing process is still far from being reached, especially in EBB.[43]

On the other side, the growing advance of non-destructive sensors could bring a significant impact on the development of new solutions for in-line inspection, monitoring, and control in bioprinting.[34] Among non-destructive and non-invasive methods for quality inspection, the most used solutions are image-based methods, which are perceived as time- and cost-effective approaches. In the context of bioprinting, image-based methods could potentially streamline processes by offering precise visualization and automation. This might enhance planning accuracy, reduce the likelihood of errors, and theoretically minimize material wastage, potentially contributing to cost savings. Real-time monitoring might ensure quality control, allowing for quick adjustments and potentially minimizing trial-and-error iterations. It is important to note that the actual efficiency gains would depend on various factors, including tissue complexity and the sophistication of the imaging technologies and data mining approach. Usually, data analysis of the last layer can be done in masked time, while the process is printing the new layer. Once the data mining algorithm is also defined, different solutions to reduce the computational time can be considered by extracting just the relevant features and acting on them. *In situ* monitoring and control via image-based analysis can bring advantages, which are printer capability characterization, bioink printability assessment, and process optimization.[28-42] Image processing can also be used for the study of reproducibility since reliable production is important in the transition from research

to industrial application, and more precisely to clinical studies.[44]

In the case of *in situ* process monitoring, even fewer studies have used image analysis to obtain layer-wise information in grid-like printing considering non-industrial devices.[28,30,35-42] Most of the approaches used top-view imaging, while some others considered also the lateral perspective to oversee the height of the printed scaffold.[36,37] Additional work was done to emphasize the role of *in situ* monitoring to investigate the influence of the rheological properties and printing parameters on the shape of the 3D-printed lines.[30] A different approach was used by Wang et al.[35] and Yang et al.[38] with the use of optical coherence tomography (OCT) to acquire high-resolution images of hydrogel scaffolds with the aim of accurately quantifying relevant morphological parameters (pore size, pore shape, surface area, porosity, and interconnectivity) for non-destructive geometric assessment and characterization of printed scaffolds. Jin et al. obtained pictures of separate layers to observe rough surfaces, fractured lines, and irregular abnormalities.[39] Eventually, Armstrong et al.[40-42] contributed significantly to the literature showing how laser scanners can be used for monitoring the nozzle trajectory and the filament width in extrusion-based 3D printing, fostering some possible solutions for *in situ* in-line feedback control. Also in our previous work, we used a camera operating in the visible to acquire images from above a construct for the identification of drift processes affecting EBB.[28]

Many of those presented works, however, suffer from the typical limitations of approaches operating in the field of visible light, namely the difficulty in discerning between target and background when they present very similar features or when, as in the case of bioinks, they are completely transparent, a feature that is very common and also essential to enable biological readouts and microscopic inspections of bioprinted constructs.

As far as we know, Moncal et al.[45] are the only ones in the literature proposing to use a thermal camera in bioprinting. However, this study has a quite different perspective compared with the one proposed in our study. In fact, Moncal et al. propose the use of thermal imaging to thermally control the extrusion process and ensure the appropriate temperatures of the printbed and printhead for promoting crosslinking for thermoresponsive hydrogels. In other words, thermal imaging is used in this study to measure the local temperature during the extrusion process.

The aim of this paper is to propose a novel solution that can overcome the previously mentioned limits of *in situ* monitoring and in-line defect detection in bioprinting when visible-range imaging is assumed. In fact, we propose the use of infrared (IR) thermal imaging for *in situ* inspection and monitoring of multi-layered 3D-bioprinted constructs. This solution is specifically suitable for transparent bioinks, where images in the visible range make edge detection hard to be implemented to detect local defects and severe deviation from the nominal shape. In this case, thermal imaging allows a clear identification of the printed geometry, which is usually deposited at a different temperature with respect to the underneath layer. This thermal signature is exploited to identify and reconstruct the printed geometry.

As a second main advantage, the thermal-based *in situ* monitoring can be used to identify defects arising on the last printed layer only. In fact, by exploiting the thermal differences between layers, the last printed layer geometry can be easily distinguished from the shapes printed on the underlying layers. Again, this capability can be hardly obtained with top-view imaging in the visible range, which allows one to obtain at each location the cumulative effect of the materials printed on different layers.

Our novel solution opens new opportunities for detecting different possible defects, such as uneven depositions and shape deviations with respect to the nominal pattern, which may arise during the bioprinting process. The proposed monitoring system based on thermal imaging would fit in the context of advanced manufacturing solutions, improving the digitization of processes and systems, the management of "Big Data," and the fusion/integration of information from multiple sensors. It would also open the opportunity to develop a process control system, to modify control inputs to correct errors in subsequent layers. Such an approach could be used not only to study geometry as has been done in this work but also to study the thermal history of thermoresponsive materials[46-48] widely used in this field. This would be a key contribution to defining a new method to quantitatively evaluate the accuracy of printed constructs and improve their quality.

The paper is structured as follows: In section 2, the biomaterials and the monitoring system used are described. In section 3, the preliminary results of such an approach are herein presented. In section 4, critical issues and advantages of this innovative approach are discussed. Finally, the main conclusions are drawn in section 5.

2. Materials and methods

2.1. Biomaterials

Two different test campaigns were conducted. In the first one, the capability of inspecting the extrusion process with thermal imaging was firstly tested without cells and considering a commercial bioink, namely CELLINK Bioink

(CELLINK, Gothenburg, Sweden), that is composed of non-animal-derived polysaccharide components, alginate, and highly hydrated cellulose nanofibrils. It is a transparent bioink selected for its consistent and temperature-independent shear-thinning properties and its similarity to the extracellular matrix, both morphological and biological.

In the second experimental campaign, bioprinting was carried out by combining the neonatal human dermal fibroblasts (nHDF; PromoCell, Heidelberg, Germany) with a custom-made alginate-gelatin hydrogel (8% w/v for both components), to test the capability of the approach of expanding its usefulness on different biomaterial and process conditions. The alginate-gelatin hydrogel represents a water-rich network of hydrophilic polymers that absorb water while maintaining their physical structure. This bioink reaches a liquid state at a temperature of 30°C and due to the presence of gelatin shows a shear-thinning behavior and undergoes gelation below room temperature, forming a gel starting from a liquid state.

2.2. Cell culture

nHDFs were used for bioprinting experiments. For expansion, cells were plated in T75 flasks at a seeding density of 3×10^4 cells/cm^2 in 15 mL of PromoCell Fibroblasts Growth Medium and then incubated at 37°C (with 5% CO_2). For bioink preparation, the volume of cell suspension needed for the desired cell count was centrifuged at 220 rpm for 3 min at 37°C. The resulting pellet was resuspended and manually mixed in a 1:9 ratio with the tested hydrogel. The bioink was prepared with a cell concentration of 1×10^6 cells/mL.

Given the interest of our work in the technological innovation represented by the use of a thermal imaging camera for *in situ* monitoring, no viability tests or follow-up activities of the bioprinted constructs were carried out. The cellular component was introduced inside the hydrogels in order to monitor the extrusion process of a bioink whose printing properties were representative of the process under investigation, and thus with the rheological properties of the hydrogels considered modified by the presence of the cell suspension.

2.3. Bioprinting set-up

The process monitoring method was applied to a pneumatic extrusion-based bioprinter, the BIO X (CELLINK, Gothenburg, Sweden), that was used to fabricate biocompatible scaffolds suitable for cells.

For the current work, general-purpose sterile high-precision conical bioprinting nozzles with a nozzle internal diameter of 0.41 (22 G) mm and a 32 mm conical nozzle length were used. For the first campaign, according to the manufacturer's indications to obtain the best printability for the selected bioink, pressure and print speed were set at 11 kPa and 20 mm/s respectively. For the second campaign, due to the custom-made nature of the bioink, after several calibration sessions, for optimal printing, the pressure and speed parameters were set at 7 kPa and 14 mm/s, respectively.

The printbed and printhead temperatures were fixed at 20°C and 30°C, respectively, for all experimentations. For the second campaign, the printbed temperature acted also as a thermal crosslinker for gelatin in the alginate–gelatin hydrogels. Printed constructs were then ionically crosslinked at the end of the printing process by dropping on them a solution of calcium chloride ($CaCl_2$).

2.4. 3D models

Square lattice patterns (20% infill density), commonly used in the EBB, were chosen as printing samples. At first, models of $10 \times 10 \times 1.6$ mm were chosen (Figure 1). The 3D models in STL format were created on SolidWorks software (Dassault Systèmes SE, Vélizy-Villacoublay, France).

In the first campaign, the same square lattice pattern was repeated on each layer. In the second experimental campaign, i.e., combining bioink with the nHDF, we used a different test where a different geometry was used at each layer to produce a scaffold of $14 \times 14 \times 1.6$ mm (the "step" model), just to show the impact of a temperature-based reconstruction of the geometry, which allows in principle to observe/monitor the geometry of the last layer only.

In order to produce this second model of interest, the G-code was modified using NC Viewer, an online open-source G-code programming application to obtain a model where only a partial portion of the layer was printed at layers 2, 3, and 4, as shown in Figure 2.

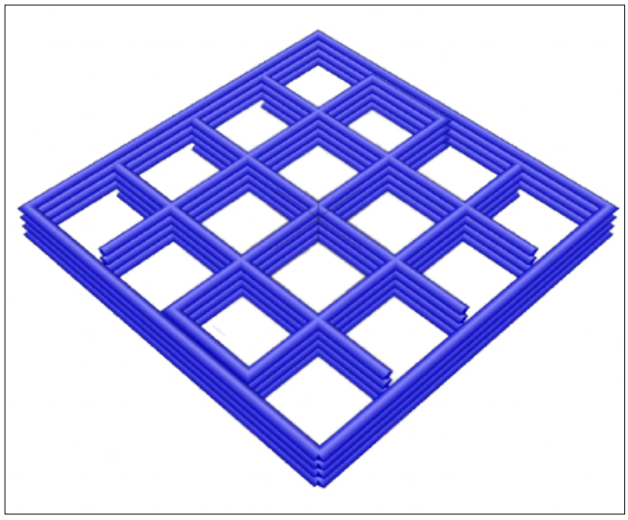


Figure 1. 3D representation of the standard model.

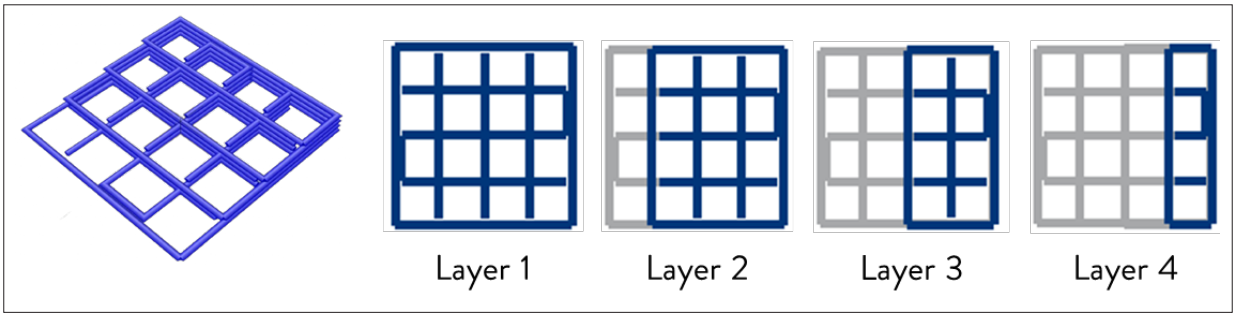


Figure 2. 3D and sliced layers representation of the "steps" model.

In all the experimental campaigns, Slic3r software (a free 3D slicing engine software for 3D printers) was used for slicing the STL models.

2.5. Process sensing

The apparatus for monitoring the bioprinted geometries consists of the following components:

(i) A visible-range (VR) camera. The first sensing equipment is an integrated camera (1600 × 1200 pixels), which is already mounted on the bioprinter on one of the three available heads and is thus able to acquire *in situ* co-axial HD images after each printed layer.

(ii) An infrared-range (IR) camera. This second sensing system is a high-frequency thermal camera, namely a mid-wave infrared indium antimonide thermocamera (temperature sensibility ±1°C, 640 × 512 pixels) for video detection, the FLIR X6900sc MWIR (FLIR® Systems Inc., Wilsonville, US), allowing acquisition of *in situ* off-axis IR images.

As the second camera can acquire images at high frequency, the whole printing process was recorded continuously using an optic with focal distances of 25 mm, which led to an image resolution of 200 µm/pixel (Figure 3). This resolution is quite low and was the effect of considering our existing camera, usually used for monitoring other AM processes (namely powder bed fusion processes). However, as this study was just designed to prove the feasibility of a new sensing architecture for geometrical reconstruction, we did not decide to acquire a new ad-hoc thermal sensing appropriately focusing on EBB. Significant improvements in the current results are currently observed using an IR camera and optics specifically selected for EBB processes.

The camera was previously calibrated in a temperature range between 0°C and 150°C, with an accuracy of 1°C. Videos were acquired with a frequency of 30 fps. The acquisition frequency has to be sufficiently high to notice the temperature change. Before the acquisition, during the calibration phase, fiducial points were also marked on a sample of graph paper placed on the printbed at the acquisition target area, for further registration operations.

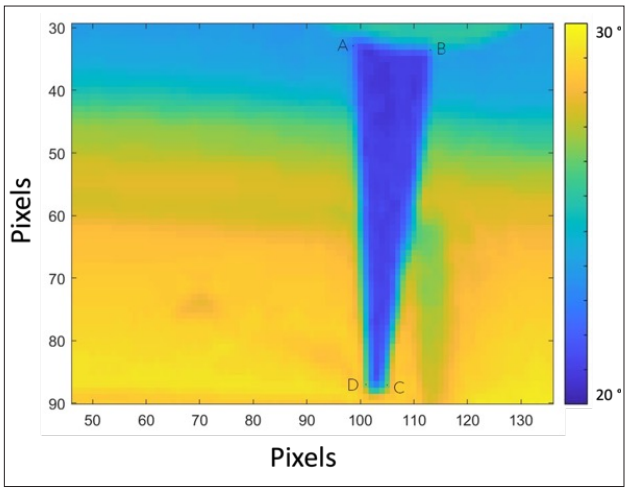


Figure 3. Image resolution sensibility for the 25 mm optic. The nozzle with a diameter of 0.41 mm (22 G) and a conical length of 32 mm was used as the calibration target.

The image acquisition environment conditions tested are shown in Figure 4.

Temperature data were exported using ExaminIR software (FLIR® Systems Inc., Wilsonville, USA), and then post-processed with different custom-made Matlab® R2020b (MathWorks, Natick, USA) algorithms. The main image processing steps are briefly reviewed in the next section.

2.6. Layer-wise image analysis: a novel solution for thermal image processing

In this work, a custom-made algorithm was developed, optimized, and tested on images gathered with the two different cameras (the VR and IR images). The algorithm was applied to images gained at each layer. The image processing was based on custom-made methods of image rectification (roto translation), segmentation, and binarization (Figure 5). Cropping was also used to focus on the region of interest. Only crop and rotation were applied

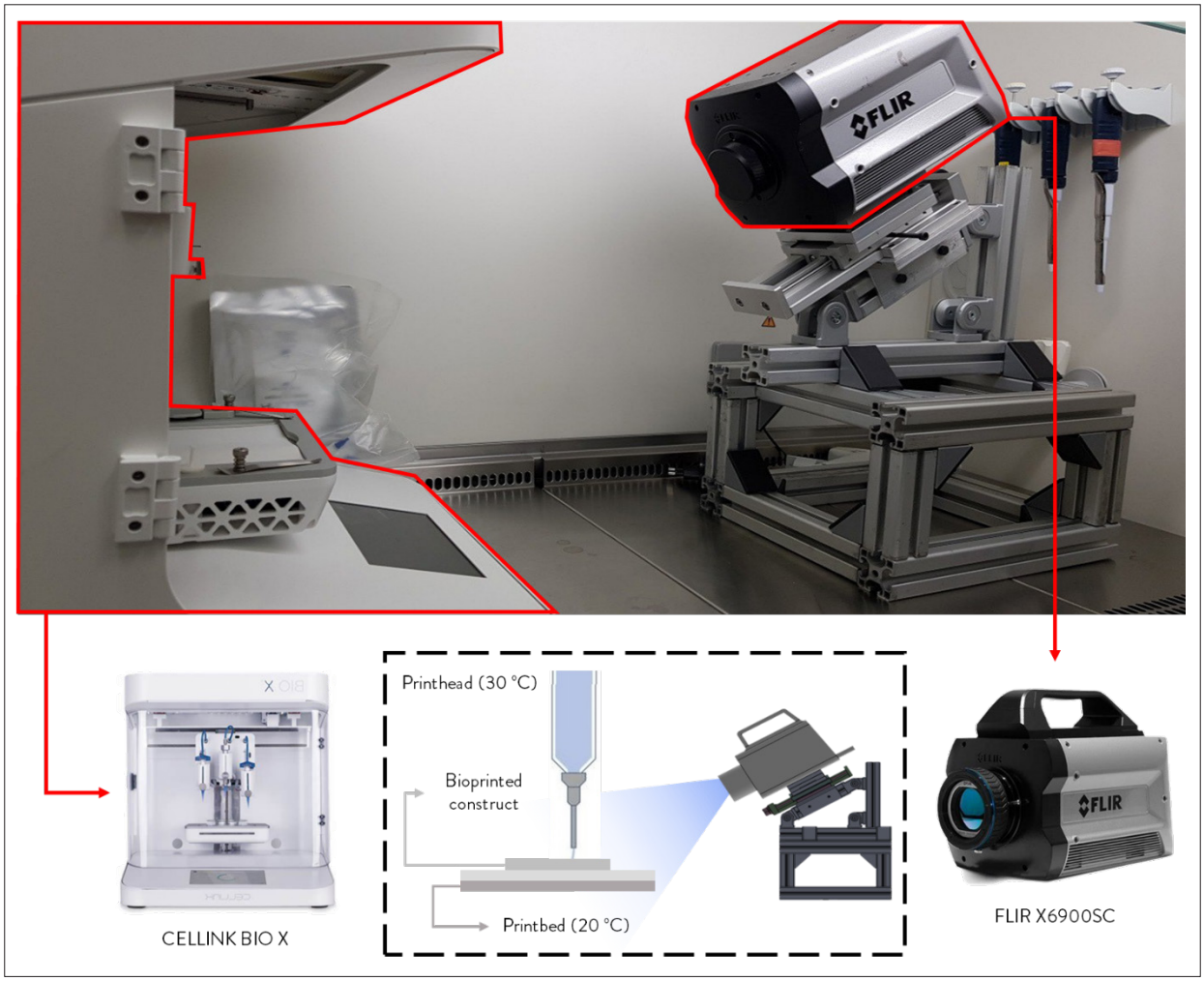


Figure 4. Monitoring system and printbed acquisition scheme. Under normal circumstances, the bioprinted construct is deposited on a sterilized substrate (glass petri dish in this case) positioned upon the printbed for better temperature control.

to VR images, as a top-view solution was available in this case. The function *mat2gray* was used for each frame of the series, to rescale the pixel intensity linearly between 0 and 1. This was done because even if HD images were characterized by an 8-bit integer value pixel-wise, the IR camera provided a radiance value on a continuous scale.

2.7. Bradley adaptive thresholding algorithm

Segmentation is a diverse and dynamic field within computer vision and image processing, characterized by a wide range of algorithms and approaches tailored to various applications and imaging modalities. In previous internal experimentations, we conducted extensive testing of both supervised and unsupervised algorithms, aiming to identify the most effective method for achieving reconstructions with less error in both thermal and visible image datasets. Despite the diverse algorithms employed, our analyses consistently demonstrated that image thresholding methods outperformed others in terms of quantitative metrics. Whether applied to visible or thermal images, this method consistently yielded superior results, showcasing its robustness in image reconstruction. Moreover, when considering the utility of image thresholding, particularly in the context of VR and IR images, its appeal lies in its simplicity and effectiveness. While more complex segmentation methods exist, such as region-growing, edge detection, or deep learning-based techniques, image thresholding offers a straightforward and computationally efficient solution. Thus, the choice to use image thresholding over more complex methods in this context was driven by the need for simplicity and speed.

In global thresholding, a single threshold value is applied uniformly to the entire image, which may lead to suboptimal results when dealing with images characterized by non-uniform lighting conditions or

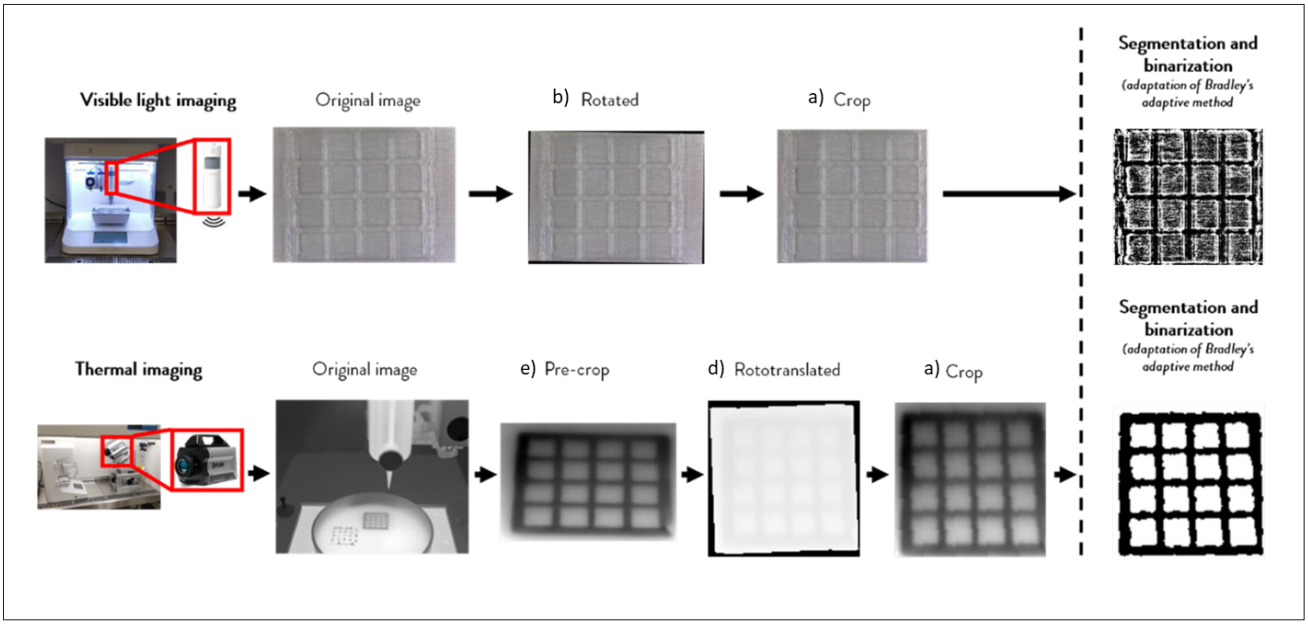


Figure 5. Steps of the procedure. Cropping (a) and rotation (b) and operations were applied to the VR images using MATLAB basic functions, to standardize the application of segmentation algorithms. In the case of IR images, due to the off-axis positioning of the thermal camera, the roto translation (c) operations were applied via MATLAB *fitgeotform2d* function only to the region of interest of the whole frame (d).

variations in object intensity. Adaptive thresholding, as opposed to global thresholding, offers a notable advantage in scenarios where image illumination and contrast vary across different regions such as in our VR images, or where there are variations in object intensity like in IR images, where these discrepancies are common. Adaptive thresholding addresses these challenges by determining a local threshold value for each pixel based on its immediate neighborhood. This adaptive approach allows the algorithm to account for local variations in intensity, resulting in improved segmentation accuracy and robustness. By tailoring the threshold to the specific characteristics of our images, adaptive thresholding effectively mitigates the shortcomings of global thresholding, making it a superior choice for applications where precise object delineation is paramount.

The developed algorithm consisted briefly of two steps:

(i) In the first step, the image underwent morphological opening processing for removing small noises while preserving the shape and size of larger objects with *imopen* and *imsubtract* Matlab® built-in functions. With this operation, the image was eroded and then dilated using a disk structuring element of radius r with the *strel* Matlab® built-in function for both operations.

(ii) In the second step, a binary image was obtained from the pre-processed thermal image by using Bradley's "adaptive" method[49] within the *imbinarize* Matlab® built-in function. This method binarizes the image using a locally adaptive threshold. The threshold was automatically computed by *adaptthresh* Matlab® built-in function based on the local mean intensity in the neighborhood of each pixel at a given sensitivity s, which indicates sensitivity toward thresholding more pixels as foreground.

(iii) The radius r and the sensitivity s within the algorithm were chosen following a visual inspection of the quality of the segmentation process through an empirical approach. This led to $r = 20$ and $s = 0.5$.

The proposed process monitoring approach relied on a comparison between both the binarized VR images and IR images obtained with the respective nominal shape of each layer. The image registration with the nominal shape was conducted with the utilization of the landmark points previously mentioned. To accomplish this registration, we employed the "*fitgeotrans*" function within the MATLAB® software platform. This function was configured to utilize the "*nonreflectivesimilarity*" property, a transformation type well-suited for preserving shape integrity while enabling translation, rotation, and scaling adjustments. Notably, this approach ensured that the relative shapes within the moving image remained unaltered, with the primary variations being attributed to transformations preserving parallelism and straightness, thereby upholding the integrity of our comparative analysis. The comparison evaluation was conducted by calculating the Dice

similarity coefficient (DSC),[50] a well-established measure commonly employed in image analysis and medical imaging applications, between the binarized target image (VR or IR) and the relative binarized nominal shape image:

$$DSC = 2 \cdot \frac{|X \text{ I } Y|}{|X| + |Y|} \quad \text{(I)}$$

where X is the set of foreground pixels in the target image and Y is the corresponding set of foreground pixels in the binarized nominal shape image, respectively. The DSC value ranges between 0 and 1, where a value closer to 0 indicates less spatial overlap between regions X and Y, while a value closer to 1 indicates a higher degree of spatial overlap. By employing this metric, we aimed to quantify the degree of similarity between the two image sets.

2.8. Proof-of-concept of on-line geometric reconstruction capability

Since different materials exhibit different thermal properties, during the second campaign, it was also decided to implement the developed segmentation algorithm along with a tracking algorithm, which relied on the Kanade–Lucas–Tomasi (KLT) algorithm, to perform segmentation of the deposited construct at the time of maximum thermal gradient between background and foreground (Figure 6), to enhance the monitoring capabilities of our system. For further details on algorithm implementation, we suggest the reader refer to a previous work of ours,[51] where the KLT algorithm, renowned within the field of computer vision for its effectiveness as a feature-based tracking method, showed excellent performance in the tracking of the extruder of a 3D printer across consecutive thermal video frames.

Since the extruder of our bioprinter operated under the fundamental assumptions of consistent object brightness, limited displacement, and full visibility in all video frames, it was possible to apply a similar approach to reconstruct the geometry of each layer of the "step" model, through an integration of the segmented pixel obtained frame-by-frame.

3. Results

3.1 Comparison of segmentation performance between VR and IR images

In the following, results obtained on a seven-layer construct printed in the before-mentioned conditions were used as a reference to show the promising advantage of IR images. In Figure 7, it is possible to see the images of each of the seven layers captured with the two types of cameras. Each image demonstrates the respective reconstructed geometry and the calculated DSC value. It is possible to notice that IR images led to a better geometry reconstruction, confirmed not only by visual inspection, albeit with all the relevant hardware resolution limitations, but also by the DSC values obtained, which were always higher than those obtained for VR images. Furthermore, it is possible to identify trends in the performance of the metrics in the two different sets of images.

3.2. Last layer detection

In the course of the experimental campaigns, several samples quite frequently suffered from printing problems, which resulted in defects on their appearance. Figure 8 shows the original VR image, the original IR image, and the IR segmented image of the third layer of a three-layer construct that, despite being printed with the same printing parameters as the other samples, ran into under-extrusion problems, presenting a "pillar" geometry in the last printed

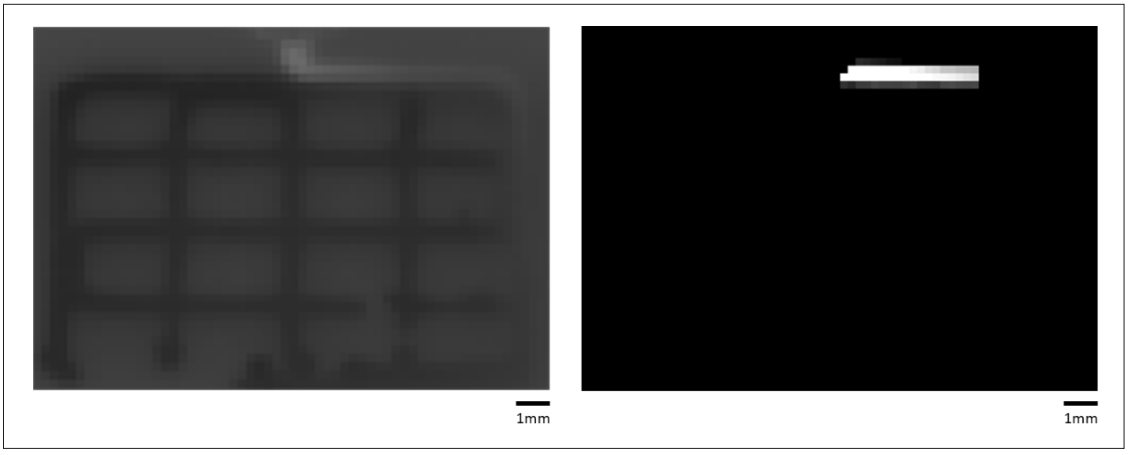


Figure 6. On the left, the original IR frame from a video of the second campaign. On the right frame-by-frame integration of the segmented pixel once extruded from the nozzle of the first instants of the process.

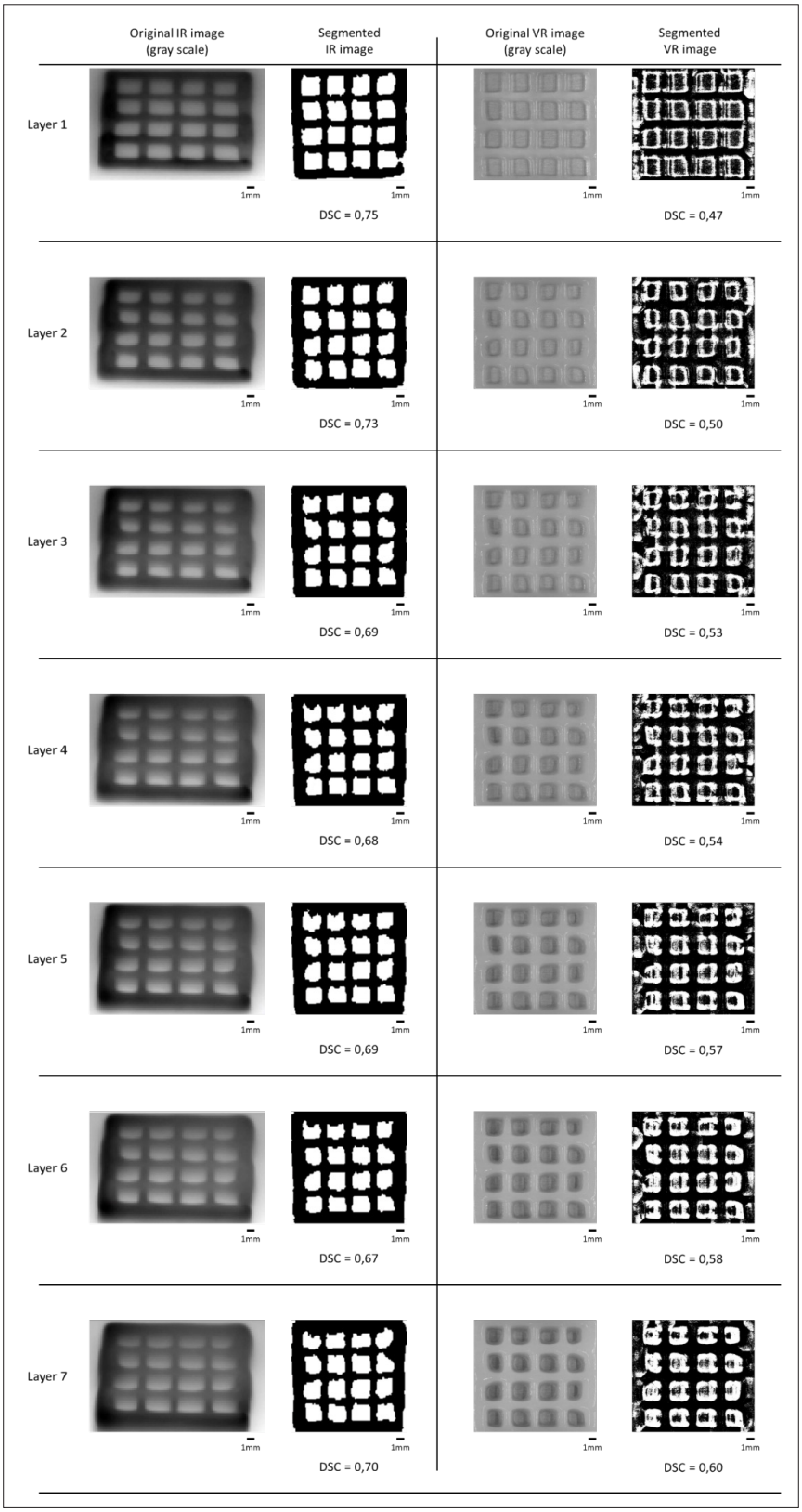


Figure 7. Images of each of the seven layers of the printed sample. On the left panel, there are original and segmented IR images; on the right panel, there are original and segmented VR images. For each reconstructed geometry, the DSC index is also reported.

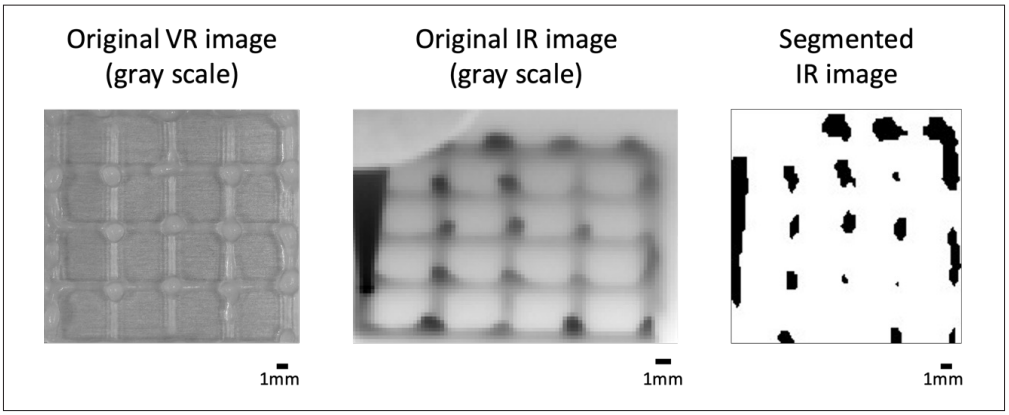


Figure 8. Defective layer reconstruction. From left to right: the original VR image, the original IR image, and the result of the segmentation of the IR image.

layer instead of the expected grid. It is possible to notice that the thermal imaging was able to clearly highlight the defective zones of the constructs, especially in the node where the excess of material translates in a higher temperature locally affecting the last "layer" deposited.

3.3. Proof-of-concept of in-line geometric reconstruction capability

Despite the limitations due to the resolution of the acquisition system in our possession, it is possible to see the outcomes of the extruder tracking process, as shown in Figure 9, where only the first three layers of a sample are shown as an example. It can be seen that the IR images allowed the reconstruction of the geometry of individual layers also with a transparent bioink with fast thermal kinetics. This would have been quite hard with VR cameras since due to the transparency of the bioink it would not have been possible to discern the background from the foreground as previously demonstrated.

4. Discussion

The work here presented describes a simple monitoring experiment in which the feasibility of using thermal imaging for geometry detection of printed constructs was demonstrated. The literature did not provide any previous examples of utilizing thermographic imaging for the geometric analysis of bioprinting constructs. However, the employed thermographic imaging device successfully captured thermal image sequences of bioprinting experiments, allowing for *in situ* analysis and evaluation of the geometric characteristics of the constructs. More specifically, we have demonstrated the effectiveness in being able to discriminate qualitatively between different layers because of the differences in temperature between them. Having set the temperature of the printhead at 30°C and of the printbed at 20°C has created a temperature gradient typical for this type of process, in which temperatures must be guaranteed at the same time to ensure good printability characteristics of the materials and also cell survival. The fine identification of this temperature difference was granted by the high sensitivity of the thermal imaging camera used.

Among the reviewed literature, only Wang et al.[34] presented their experimental design method utilizing a cell-loaded bioink. Despite the fact that most of the *in situ* methods were theoretically applicable to working with cells, Wang et al. were the only ones to demonstrate its practical implementation. One of the major challenges in utilizing a cell-loaded bioink was ensuring sterile conditions throughout the bioprinting experiments and process monitoring. Our proposed method exploits IR radiation to overcome the limitations of systems and devices operating in visible light (such as the VR camera used in this work) since they would not be affected by the ambient brightness and transparency conditions of the bioink.

The capability to identify and segment the deposited bioink filament in real time allowed for the measurement of filament width at every time instant during the printing process. Previous studies by Yang et al.[34] and Armstrong et al.[40-42] characterized the filament width in *in situ* bioprinting experiments, but they utilized more viscous and opaque bioinks compared to the transparent alginate-gelatin hydrogel used in this work. The viscosity of the bioink affects the distinguishability of different layers on the *Z*-axis. Additionally, the previous studies employed simplified layer designs without intersections or adjacent filaments, whereas this work demonstrated the technique with layered constructs featuring grid patterns. Consequently, filament quality characteristics were assessed even at intersections and when a filament was printed close to a previously deposited one, thanks to the distinguishability of hot bioink from cold bioink using thermal imaging.

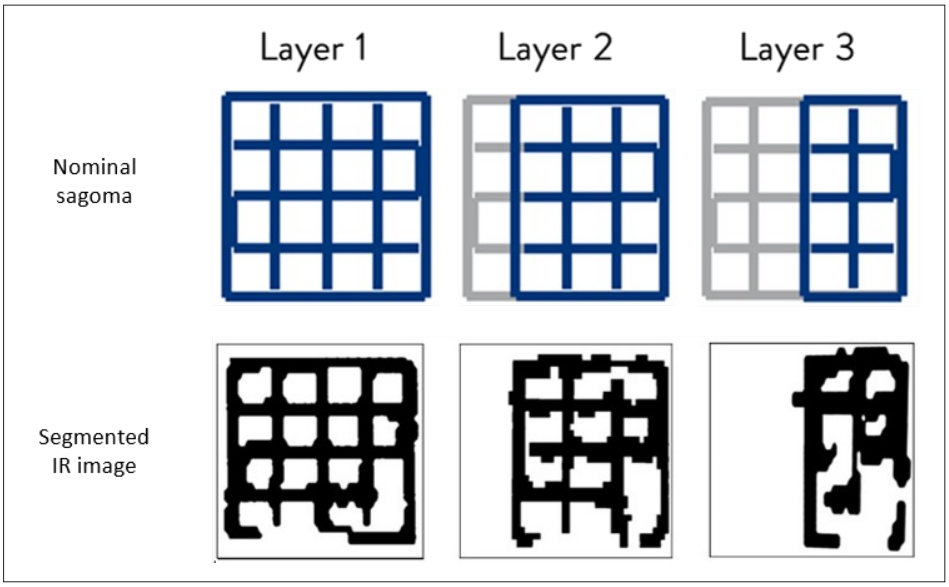


Figure 9. Geometric reconstruction from tracking approach outcomes. Top row shows the nominal sagoma images of the first three layers of a construct (highlighted in blue). Bottom row shows the respective reconstructed layers obtained from the application of our algorithm during the tracking process.

The capability to segment the bioink filament at each moment in the 3D printing process provides a unique advantage: the reconstruction of the distinct profile of each individual layer, isolated from the layers beneath or the substrate. This is especially crucial when dealing with transparent bioink. Traditional visible range images encounter challenges in distinguishing between multiple layers deposited on top of each other. This issue becomes particularly pronounced when transparent bioink is employed, as the cumulative effect of all printed layers results in an overall image that combines these layers. Consequently, the visual representation becomes a summation of all the printed layers, obscuring the details of individual layers and compromising the ability to discern their distinct characteristics.[30] In contrast, the developed method could isolate the bioink belonging to a layer printed on top of a previous one, effectively separating it from the rest of the printed construct. It is important to note that the proposed method considers the shape of the bioink at the moment of deposition and does not account for spreading or diffusion that may occur between material deposition and image acquisition. This distinction is evident in VR images where certain pores may appear occluded while being open in the thermal reconstruction of the equivalent layer.

Upon reconstructing the profile of a layer, the developed method enabled the evaluation of its geometric accuracy. The DSC was assessed by measuring the similarity between the reconstructed profile and the binarized image of the corresponding nominal layer. Of course, this method is not exempt from limitations. Monitoring devices in the IR field have a higher purchase price. They are advanced devices built with complicated components, and in the case of IR devices, their purchase prices are higher than those in visible light. Optics and detection systems in the IR are not as widely used as those in VR. These components are more expensive, thus increasing the initial cost. Moreover, thermal images cannot be captured if certain materials, such as water and glass, are used. Unlike VR, IR radiation cannot pass through water or glass, from which it is reflected as in a mirror, unless special arrangements are made, such as the use of special filters or windows made of materials that allow the radiation to be transmitted without interference. In addition, the monitoring system can only be used in printing processes where the geometry of the last printed layer (or the construct in general) can be captured by registration systems (not applicable in SLA bioprinting, for example, unless custom-made systems are foreseen at the machine design stage).

Despite these limitations, this approach would also open the opportunity to develop a process control system and to modify control inputs for correcting errors in subsequent layers. It is recommended that the approach be followed both by the end-users of extrusion bioprinters and the manufacturer of bioprinters, since the monitoring system like the one proposed can be implemented also in the machines already on the market without having to create new bioprinters integrated with this system.

For future development, a better image processing system capable of identifying more features and operating in real-time should be developed. *In situ* monitoring techniques incorporated with the feedback systems for process control should also be implemented.

5. Conclusion

In conclusion, this study has introduced a novel approach for monitoring bioprinted constructs using thermal imaging, demonstrating its feasibility and effectiveness. The absence of previous instances employing thermographic imaging for the geometric analysis of bioprinting constructs emphasizes the innovative nature of this work. The successful capture of thermal image sequences in real-time using the employed thermographic imaging device allowed for *in situ* assessment of construct's geometrical characteristics. Specifically, the method highlighted the ability to qualitatively distinguish between different layers based on their temperature disparities.

Our method effectively overcomes limitations posed by visible light systems in discerning bioink layers, particularly in transparent bioinks. The method's capacity to segment deposited bioink filaments in real time enables the measurement of filament width during the printing process. Additionally, the technique permitted the isolation and separate reconstruction of individual layer profiles, addressing the challenge of layer superposition.

In summary, the application of thermal imaging technology to construct bioprinting represents an innovative step toward enhancing process monitoring and quality control, laying the foundation for further advancements in bioprinting technology and its industrial implementation.

Acknowledgments

None.

Funding

This research was partially funded by the European Commission under the "HORIZON-CL4-2021-DIGITAL-EMERGING-01 project BioProS - Biointelligent Production Sensor to Measure Viral Activity" (grant agreement no. 101070120, 2022–2026).

Conflict of interest

The authors declare no conflicts of interest.

Author contributions

Conceptualization: Bianca Maria Colosimo, Davide Moscatelli, Simone Giovanni Gugliandolo
Data curation: Simone Giovanni Gugliandolo
Formal analysis: Simone Giovanni Gugliandolo, Egon Prioglio
Investigation: Simone Giovanni Gugliandolo, Egon Prioglio
Methodology: Bianca Maria Colosimo, Simone Giovanni Gugliandolo, Egon Prioglio
Supervision: Bianca Maria Colosimo, Davide Moscatelli
Writing – original draft: Simone Giovanni Gugliandolo, Bianca Maria Colosimo
Writing – review & editing: Bianca Maria Colosimo, Davide Moscatelli

Ethics approval and consent to participate

Not applicable.

Consent for publication

Not applicable.

Availability of data

Data are available from the corresponding author upon reasonable request.

References

1. Moroni L, Boland T, Burdick JA, et al. Biofabrication: a guide to technology and terminology. *Trends Biotechnol*. 2018;36(4):384-402. doi: 10.1016/j.tibtech.2017.10.015
2. Ng WL, Chua CK, Shen YF. Print me an organ! Why we are not there yet. *Prog Polym Sci*. 2019;97:101145. doi: 10.1016/j.progpolymsci.2019.101145
3. Santoni S, Gugliandolo SG, Sponchioni M, Moscatelli D, Colosimo BM. 3D bioprinting: current status and trends—a guide to the literature and industrial practice. *Bio-Des Manuf*. 2021;5(1):14-42. doi: 10.1007/S42242-021-00165-0
4. Pereira FDAS, Parfenov V, Khesuani YD, Ovsianikov A, Mironov V. Commercial 3D bioprinters. In: Ovsianikov A, Yoo J, Mironov V, eds. *3D Printing and Biofabrication*. Cham: Springer; 2018: 535-549. doi: 10.1007/978-3-319-45444-3_12
5. Jang J, Park JY, Gao G, Cho D-W. Biomaterials-based 3D cell printing for next-generation therapeutics and diagnostics. *Biomaterials*. 2018;156:88-106. doi: 10.1016/j.biomaterials.2017.11.030
6. Constante G, Apsite I, Alkhamis H, et al. 4D biofabrication using a combination of 3D printing and melt-electrowriting of shape-morphing polymers. *ACS Appl Mater Interfaces*. 2021;13(11):12767-12776. doi: 10.1021/acsami.0c18608
7. Caleffi JT, Aal MCE, Gallindo H de OM, et al. Magnetic 3D cell culture: state of the art and current advances. *Life Sci*. 2021;286:120028. doi: 10.1016/j.lfs.2021.120028
8. Hu X, Zheng J, Hu Q, et al. Smart acoustic 3D cell construct assembly with high-resolution. *Biofabrication*. 2022;14(4). doi: 10.1088/1758-5090/ac7c90

9. Moldovan NI, Hibino N, Nakayama K. Principles of the kenzan method for robotic cell spheroid-based three-dimensional bioprinting. *Tissue Eng Part B Rev*. 2017;23(3):237-244. doi: 10.1089/ten.teb.2016.0322
10. Zhou X, Wu H, Wen H, Zheng B. Advances in single-cell printing. *Micromachines*. 2022;13(1):80. doi: 10.3390/mi13010080
11. Ramesh S, Harrysson OLA, Rao PK, et al. Extrusion bioprinting: recent progress, challenges, and future opportunities. *Bioprinting*. 2021;21:e00116. doi: 10.1016/j.bprint.2020.e00116
12. Boularaoui S, Al Hussein G, Khan KA, Christoforou N, Stefanini C. An overview of extrusion-based bioprinting with a focus on induced shear stress and its effect on cell viability. *Bioprinting*. 2020;20:e00093. doi: 10.1016/J.BPRINT.2020.E00093
13. Saunders RE, Derby B. Inkjet printing biomaterials for tissue engineering: bioprinting. *Int Mater Rev.* 2014;59(8):430-448. doi: 10.1179/1743280414Y.0000000040
14. Ng WL, Huang X, Shkolnikov V, Suntornnond R, Yeong WY. Polyvinylpyrrolidone-based bioink: influence of bioink properties on printing performance and cell proliferation during inkjet-based bioprinting. *Bio-Des Manuf*. 2023;6(6):676-690. doi: 10.1007/S42242-023-00245-3/FIGURES/5
15. Levato R, Dudaryeva O, Garciamendez-Mijares CE, et al. Light-based vat-polymerization bioprinting. *Nat Rev Methods Primers*. 2023;3(1):1-19. doi: 10.1038/s43586-023-00231-0
16. Gao G, Kim BS, Jang J, Cho D-W. Recent strategies in extrusion-based three-dimensional cell printing toward organ biofabrication. *ACS Biomater Sci Eng*. 2019;5(3):1150-1169. doi: 10.1021/acsbiomaterials.8b00691
17. Antoshin AA, Churbanov SN, Minaev NV, et al. LIFT-bioprinting, is it worth it? *Bioprinting*. 2019;15(May):e00052. doi: 10.1016/j.bprint.2019.e00052
18. Nuñez Bernal P, Delrot P, Loterie D, et al. Volumetric bioprinting of complex living-tissue constructs within seconds. *Adv Mater.* 2019;31(42):1904209. doi: 10.1002/ADMA.201904209
19. Kumar H, Kim K. Stereolithography 3D bioprinting. *Methods Mol Biol*. 2020;2140:93-108. doi: 10.1007/978-1-0716-0520-2_6
20. Sheth R, Balesh ER, Zhang YS, Hirsch JA, Khademhosseini A, Oklu R. Three-dimensional printing: an enabling technology for IR. *J Vasc Interv Radiol*. 2016;27(6):859-865. doi: 10.1016/j.jvir.2016.02.029
21. Bouguéon G, Kauss T, Dessane B et al., 2019, Micro- and nano-formulations for bioprinting and additive manufacturing. Drug Discov Today 24 (1): 163–178. doi: 10.1016/j.drudis.2018.10.013
22. Caltanissetta F, Grasso M, Petrò S, Colosimo BM. Characterization of in-situ measurements based on layerwise imaging in laser powder bed fusion. *Addit Manuf*. 2018;24:183-199. doi: 10.1016/J.ADDMA.2018.09.017
23. Grasso M, Remani A, Dickins A, Colosimo BM, Leach RK. In-situ measurement and monitoring methods for metal powder bed fusion: an updated review. *Meas Sci Technol*. 2021;32(11):112001. doi: 10.1088/1361-6501/AC0B6B
24. Grasso M, Colosimo BM. Process defects and in situ monitoring methods in metal powder bed fusion: a review. *Meas Sci Technol*. 2017;28(4):044005. doi: 10.1088/1361-6501/AA5C4F
25. Colosimo BM, Huang Q, Dasgupta T, Tsung F. Opportunities and challenges of quality engineering for additive manufacturing. *J Qual Technol.* 2018;50(3):233-252. doi: 10.1080/00224065.2018.1487726
26. AbouelNour Y, Gupta N. Assisted defect detection by in-process monitoring of additive manufacturing using optical imaging and infrared thermography. *Addit Manuf*. 2023;67:103483. doi: 10.1016/J.ADDMA.2023.103483
27. Hossain REN, Lewis J, Moore AL. In situ infrared temperature sensing for real-time defect detection in additive manufacturing. *Addit Manuf*. 2021;47:102328. doi: 10.1016/J.ADDMA.2021.102328
28. Gugliandolo SG, Margarita A, Santoni S, Moscatelli D, Colosimo BM. In-situ monitoring of defects in extrusion-based bioprinting processes using visible light imaging. *Procedia CIRP*. 2022;110(C):219-224. doi: 10.1016/J.PROCIR.2022.06.040
29. Schmieg B, Gretzinger S, Schuhmann S, Guthausen G, Hubbuch J. Magnetic resonance imaging as a tool for quality control in extrusion-based bioprinting. *Biotechnol J*. 2022;17(5):2100336. doi: 10.1002/BIOT.202100336
30. Strauß S, Meutelet R, Radosevic L, Gretzinger S, Hubbuch J. Image analysis as PAT-tool for use in extrusion-based bioprinting. *Bioprinting*. 2021;21:e00112. doi: 10.1016/J.BPRINT.2020.E00112
31. Uzun-Per M, Gillispie GJ, Tavolara TE, et al. Automated image analysis methodologies to compute bioink printability. *Adv Eng Mater*. 2021;23(4):2000900. doi: 10.1002/ADEM.202000900
32. Bone JM, Childs CM, Menon A, et al. Hierarchical machine learning for high-fidelity 3D printed biopolymers. *ACS Biomater Sci Eng*. 2020;6(12):7021-7031. doi: 10.1021/acsbiomaterials.0c00755
33. Sedigh A, DiPiero D, Shine KM, Tomlinson RE. Enhancing precision in bioprinting utilizing fuzzy systems. *Bioprinting*. 2022;25:e00190. doi: 10.1016/J.BPRINT.2021.E00190

34. Wang L, Xu ME, Luo L, Zhou Y, Si P. Iterative feedback bio-printing-derived cell-laden hydrogel scaffolds with optimal geometrical fidelity and cellular controllability. *Sci Rep*. 2018;8(1):1-13.
doi: 10.1038/s41598-018-21274-4

35. Wang L, Xu M, Zhang L, Zhou Q, Luo L. Automated quantitative assessment of three-dimensional bioprinted hydrogel scaffolds using optical coherence tomography. *Biomed Opt Express*. 2016;7(3):894.
doi: 10.1364/boe.7.000894

36. Bonatti AF, Vozzi G, Chua CK, De Maria C. A deep learning approach for error detection and quantification in extrusion-based bioprinting. *Mater Today Proc*. 2022;70:131-135.
doi: 10.1016/J.MATPR.2022.09.006

37. Bonatti AF, Vozzi G, Chua CK, De Maria C. A deep learning quality control loop of the extrusion-based bioprinting process. *Int J Bioprint*. 2022;8(4):307-320.
doi: 10.18063/IJB.V8I4.620

38. Yang S, Chen Q, Wang L, Xu M. In situ defect detection and feedback control with three-dimensional extrusion-based bioprinter-associated optical coherence tomography. *Int J Bioprint*. 2022;9(1):47-62.
doi: 10.18063/IJB.V9I1.624

39. Jin Z, Zhang Z, Shao X, Gu GX. Monitoring anomalies in 3D bioprinting with deep neural networks. *ACS Biomater Sci Eng*. 2023;9(7):3945-3952.
doi: 10.1021/acsbiomaterials.0c01761

40. Armstrong AA, Alleyne AG, Wagoner Johnson AJ. 1D and 2D error assessment and correction for extrusion-based bioprinting using process sensing and control strategies. *Biofabrication*. 2020;12(4):045023.
doi: 10.1088/1758-5090/ABA8EE

41. Armstrong AA, Norato J, Alleyne AG, Johnson AJW. Direct process feedback in extrusion-based 3D bioprinting. *Biofabrication*. 2019;12(1):015017.
doi: 10.1088/1758-5090/AB4D97

42. Armstrong AA, Pfeil A, Alleyne AG, Johnson AJW. Process monitoring and control strategies in extrusion-based bioprinting to fabricate spatially graded structures. *Bioprinting*. 2021;21:e00126.
doi: 10.1016/J.BPRINT.2020.E00126

43. Gao T, Gillispie GJ, Copus JS, et al. Optimization of gelatin-alginate composite bioink printability using rheological parameters: a systematic approach. *Biofabrication*. 2018;10(3):034106.
doi: 10.1088/1758-5090/aacdc7

44. Yaneva A, Shopova D, Bakova D, et al. The progress in bioprinting and its potential impact on health-related quality of life. *Bioengineering*. 2023;10(8):910.
doi: 10.3390/BIOENGINEERING10080910

45. Moncal KK, Ozbolat V, Datta P, Heo DN, Ozbolat IT. Thermally-controlled extrusion-based bioprinting of collagen. *J Mater Sci Mater Med*. 2019;30:55.
doi: 10.1007/s10856-019-6258-2

46. Santoni S, Sponchioni M, Gugliandolo SG, Colosimo BM, Moscatelli D. Preliminary tests on PEG-based thermoresponsive polymers for the production of 3D bioprinted constructs. *Procedia CIRP*. 2022;110(C): 350-355.
doi: 10.1016/j.procir.2022.06.062

47. Suntornnond R, An J, Chua CK. Bioprinting of thermoresponsive hydrogels for next generation tissue engineering: a review. *Macromol Mater Eng*. 2017;302(1):1600266.
doi: 10.1002/mame.201600266

48. Hsieh FY, Lin HH, Hsu S-H. 3D bioprinting of neural stem cell-laden thermoresponsive biodegradable polyurethane hydrogel and potential in central nervous system repair. *Biomaterials*. 2015;71:48-57.
doi: 10.1016/j.biomaterials.2015.08.028

49. Bradley D, Roth G. Adaptive thresholding using the integral image. *J Graph Tools*. 2007;12(2):13-21.
doi: 10.1080/2151237X.2007.10129236

50. Dice LR. Measures of the amount of ecologic association between species. *Ecology*. 1945;26(3):297-302.
doi: 10.2307/1932409

51. Caltanissetta F, Dreifus G, Hart AJ, Colosimo BM. In-situ monitoring of material extrusion processes via thermal videoimaging with application to big area additive manufacturing (BAAM). *Addit Manuf*. 2022;58:102995.
doi: 10.1016/J.ADDMA.2022.102995

ACCSCIENCE PUBLISHING

International Journal of Bioprinting

RESEARCH ARTICLE

Enhancing cell proliferation in three-dimensional hydrogel scaffolds using digital light processing bioprinting technology

Yejin Choi[1†], Jeong Wook Seo[1,2†], Goo Jang[3], Woo Kyung Jung[2], Yong Ho Park[2,4], and Hojae Bae[1,5*]

[1]Department of Stem Cell and Regenerative Biotechnology, KU Convergence Science and Technology Institute, Konkuk University, Seoul, Republic of Korea

[2]NoAH Biotech Co., Ltd., Suwon-si, Gyeonggi-do, Republic of Korea

[3]Laboratory of Theriogenology and Biotechnology, Department of Veterinary Clinical Science, College of Veterinary Medicine and the Research Institute of Veterinary Science, Seoul National University, 1 Gwanak-ro, Gwanak-gu, Seoul, Korea

[4]Department of Microbiology, College of Veterinary Medicine, Seoul National University, 1 Gwanak-ro, Gwanak-gu, Seoul, Republic of Korea

[5]Institute of Advanced Regenerative Science, Konkuk University, 120 Neungdong-ro, Gwangjin-gu, Seoul, Republic of Korea

(This article belongs to the *Special Issue: Light-Based Bioprinted Scaffolds for Tissue Engineering*)

Abstract

Three-dimensional (3D) bioprinting is gradually emerging as a popular technique driving as a new paradigm in tissue engineering. Enhancing cell proliferation and engraftment within volumetric 3D-bioprinted scaffolds is a key challenge in its implementation. However, basic exploratory studies on cell proliferation enhancement in 3D-bioprinted scaffolds using digital light processing (DLP) technology are still lacking. Traditionally, microchannels in scaffolds have been regarded as non-functional, empty spaces. In this paper, however, we propose that microchannels implanted in DLP-bioprinted scaffolds can provide space for cell proliferation, giving a new definition to microchannel function. To this end, we used fish gelatin methacrylate (F-GelMA) as a bioink with photocurable properties, followed by functional evaluation and optimization through rheological analysis. The morphology of DLP-printed scaffolds using the bioink was analyzed, and their biocompatibility was demonstrated through cell viability analysis. Microchannels of three different sizes were implanted to facilitate oxygenation, nutrient delivery, and media flow by addressing structural barriers identified via morphological analysis. Cell viability and proliferation rates in outer and inner microchannels were then comparatively analyzed. During the long-term culture period (about 5 weeks), the differences in proliferation rates due to changes in the media flow environment were assessed. The results demonstrated that cell survival, growth, and proliferation were significantly enhanced within the DLP-printed scaffolds in which the cells were encapsulated. This approach lends itself useful for basic exploratory study utilizing 3D culture technology in the realms of regenerative medicine and tissue engineering, where effective cell proliferation relative to the same volume is required.

Keywords: Tissue engineering; Digital light processing; Three-dimensional printing; Hydrogel scaffold; Cell proliferation; Microchannel

†These authors contributed equally to this work.

***Corresponding author:**
Hojae Bae
(hojaebae@konkuk.ac.kr)

Citation: Choi Y, Seo JW, Jang G, Jung WK, Park YH, Bae H. Enhancing cell proliferation in three-dimensional hydrogel scaffolds using digital light processing bioprinting technology. *Int J Bioprint*. 2024;10(3):2219.
doi: 10.36922/ijb.2219

Received: November 9, 2023
Accepted: February 1, 2024
Published Online: March 28, 2024

Copyright: © 2024 Author(s). This is an Open Access article distributed under the terms of the Creative Commons Attribution License, permitting distribution, and reproduction in any medium, provided the original work is properly cited.

Publisher's Note: AccScience Publishing remains neutral with regard to jurisdictional claims in published maps and institutional affiliations.

1. Introduction

A new paradigm is emerging in tissue engineering. Recently, certain high-profile companies such as Steakholder, Aleph Farms, and BlueNalu have utilized three-dimensional (3D) bioprinting, a tissue engineering technology, to produce steak-like cultured meats and launch industrial-scale prototypes of cultured meats.[1-4] As such, 3D bioprinting is progressing rapidly, and numerous researchers have attempted creation of meat substitutes utilizing 3D scaffolds with various cells, as documented in several published reports.[5-8] Digital light processing (DLP) bioprinting has attracted attention due to its nozzle-free structure, fast printing speed, high resolution, and ease of automation for various tissue requirements.[9-12] Gelatin methacrylate (GelMA), a gelatin-derived, biocompatible, biodegradable, and photocurable material, has been utilized in 3D bioprinting technologies such as DLP for applications in producing functional tissue analogs.[6,13-15] Nonetheless, enhancing cell proliferation and increasing yield within 3D-printed scaffolds remain hurdles to overcome and important goals for future applications.

Controlling the scaffold microenvironment is crucial for manipulating cell attachment, viability, and proliferation, as well as regenerating tissue function.[10,16] However, poor transportation and slow diffusion of oxygen and nutrients pose notable challenges to the viability of encapsulated cells.[17] Furthermore, merely controlling scaffold porosity is unable to provide sufficient oxygen and nutrients, which leads to reduced diffusion capabilities and waste accumulation, ultimately causing cell death and apoptosis at the scaffold center.[18,19] However, introducing microchannels and media flow environments could enhance cell attachment and proliferation.[20,21] The microchannels effectively enhance cell viability by providing nutrients within the scaffold while promoting cell adhesion, growth, and migration, as well as providing space for mass transport.[22-25] Media flow environments transport oxygen and nutrients by exposing cells to mechanical stimulation, enhancing cell viability, ATP production, and mitochondrial activity compared to non-shaking culture environments.[20,26,27] However, no basic research reported on the implantation of microchannels within DLP-bioprinted scaffolds via cell encapsulation in GelMA hydrogel and its impact on cell proliferation differences and enhancements in a media flow environment. Traditionally, microchannels implanted within a scaffold have been considered empty spaces.[25,28-30] In this paper, we propose a new and expanded perspective that these microchannels offer space with the potential to increase cell proliferation more effectively. Therefore, this study aims to fabricate cell encapsulated DLP-bioprinted scaffolds using fish GelMA (F-GelMA), a photocurable bioink, and to conduct basic exploratory studies on cell proliferation enhancement by utilizing microchannels and media flow environments.

To this end, based on our previous work,[31] we fabricated high-resolution 3D DLP-printed scaffolds by evaluating the functionalization of F-GelMA and optimizing it through rheology analysis. Morphological analysis of the DLP-printed scaffolds revealed wall-like structures of 100 μm, which were limited in mass transport due to their porous structure. To solve this issue, we introduced microchannels into the scaffold and observed the difference in cell viability and proliferation inside the hydrogel and microchannels over time. We also introduced a media flow environment to observe and analyze the changes in cell attachment and proliferation inside and outside the microchannels during long-term cell culture for about 5 weeks. Finally, the analysis of DLP-printed hydrogel scaffolds demonstrated significant cell proliferation inside the microchannels, proving the new function of such structures.

Overall, our results demonstrate the feasibility of microchannels as a space for cell proliferation in DLP-printed cell-encapsulated F-GelMA scaffolds, offering a new strategy to enhance cell attachment and proliferation. Our results are expected to serve the basic exploratory research that utilizes 3D culture techniques for regenerative medicine and tissue engineering applications, where effective cell proliferation relative to the same volume is required, such as in the cases of artificial organs and disease models fabrication (Figure 1).[6,32-37]

2. Materials and methods

2.1. Materials

In this study, we used Dulbecco's modified Eagle's medium (DMEM, high glucose) and Dulbecco's phosphate-buffered saline (DPBS) purchased from WelGENE (Daegu, Gyeongbuk, South Korea) for cell culture. Fetal bovine serum (FBS), penicillin–streptomycin (P/S), L-glutamine, phosphate-buffered saline (PBS, pH 7.4), and 0.05% trypsin-EDTA solution were also obtained from WelGENE. Gelatin from cold-water fish skin, methacrylic anhydride (MA), and lithium phenyl-2,4,6-trimethylbenzoylphosphinate (LAP; ≥95%) were purchased from Sigma Aldrich (St. Louis, MO, USA). Tartrazine, the light absorber, was purchased from GreenTech (Daejeon, South Korea). A Live/Dead® cell viability kit containing calcein-AM, ethidium homodimer-1, and fluorescent Alexa Fluor® 488 was purchased from Invitrogen (Carlsbad, CA, USA). All other chemicals used in this study were of analytical grade.

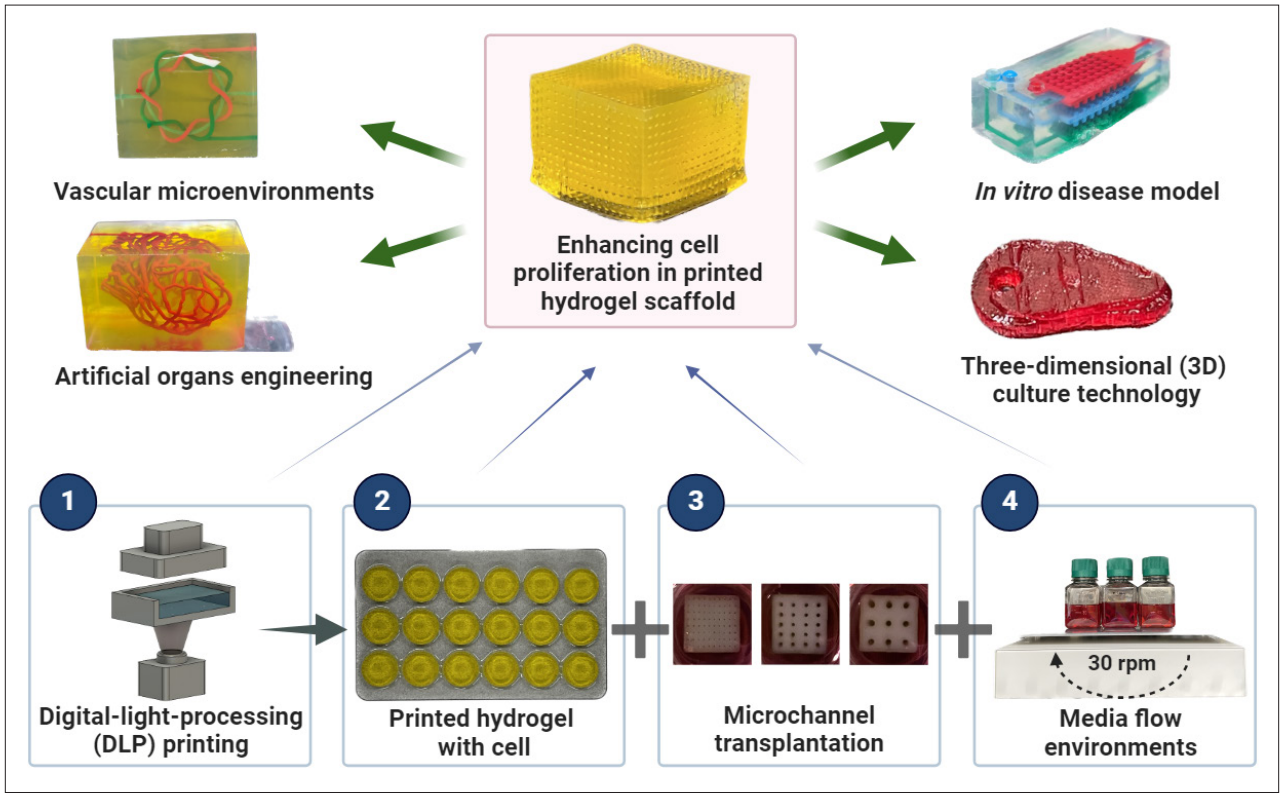


Figure 1. Schematic of research and applications for enhancing cell proliferation using digital light processing (DLP) printing. Specifically, this method utilizes a DLP printer to control microchannels and cell culture environments during three-dimensional (3D) culture, ultimately resulting in enhanced proliferation. This approach has broad applications in various tissue engineering fields.

2.2. Preparation of DLP 3D bioprinting

2.2.1. Synthesis of fish gelatin methacrylate

Fish GelMA (F-GelMA) was prepared by reacting the gelatin (from the skin of cold-water fish) with MA. Upon dissolution of 10% (w/v) gelatin in PBS (pH 7.5) at 50°C, MA was added at a rate of 0.5 mL/min until a concentration of 15% (v/v) was achieved. To stop the reaction after 4 h, 100% (v/v) PBS was added at 45°C and stirred until completely mixed. The stirred mixture was centrifuged at 3000 rpm for 5 min to obtain the solution supernatant. The gelatin supernatant was reacted with MA and dialyzed using Spectra/Por® (12–14 kDa cutoff) dialysis tubes (Spectra Laboratories, Texas, USA) for 7 days at 45°C with three daily changes of distilled water. The filtered solution was frozen at -80°C for 4 h and then lyophilized for 7 days to obtain F-GelMA.

2.2.2. ^{1}H nuclear magnetic resonance spectroscopy

To evaluate the degree of functionalization (DoF) of F-GelMA, ^{1}H nuclear magnetic resonance spectroscopy (^{1}H-NMR) was performed using a 500 MHz FT-NMR spectrometer (Varian, Palo Alto, CA, USA). The samples (gelatin and F-GelMA) were dissolved in D_2O at 37°C for these measurements. The data analysis was carried out using MestReNova (Mestrelab research, v14.2.1) software.

2.2.3. Preparation of bioink and DLP 3D printing process

To prepare the photocurable bioink for DLP printing, 10% (w/v) lyophilized F-GelMA, 0.5% (w/v) photoinitiator (LAP), and 1% (v/v) tartrazine were completely dissolved in 37°C DPBS with 1% P/S. Fibroblasts cultured on a plate were detached and mixed with the prepared solution at a concentration of 2×10^6 cells/mL.

All the printed hydrogel scaffolds used in the experiments were designed by using Autodesk® Fusion 360® software (San Rafael, CA, USA). Pre-designed STL models were uploaded to a DLP printer (IM2 model; Carima, Seoul, South Korea). All printing was performed at a light intensity setting of 1.97 mW/cm^2, and a single layer thickness of 100 μm was used. The bioink reservoir was preheated to 37°C before printing. The rheology test indicated a light exposure time of 31.13 s. However, to maintain the stability of the fabricated structure and prevent detachment from the polymerization plate during crosslinking, the first three layers were fabricated with

a total light exposure time of 36.13 s (31.13 s plus an additional 5 s).

After printing, the fabricated scaffold was removed from the plate and incubated in high-glucose DMEM supplemented with 10% FBS, 1% L-glutamine, and 1% P/S.

2.2.4. Photorheological analysis

To evaluate the rheological characteristics of the produced F-GelMA bioink during the crosslinking process, we performed a photorheological experiment using a HAKKE™ MARS™ 40 (Thermo Fisher Scientific, Waltham, MA, USA) equipped with a light module accessory. Measurements were taken with a 100 μm gap between the glass and the bottom to load the bioink. The light intensity is set to 2.45 mW/cm^2. We used the OmniCure® LX 505 (Lumen Dynamics; Mississauga, ON, Canada) as the light source, equipped with a 405 nm light-emitting diode channel that matched the wavelength of the DLP printer (IM2). We conducted an oscillation experiment at 37°C with an oscillatory shear strain of 0.008% and a frequency of 20 Hz.

2.3. Scanning electron microscopy

To confirm the morphological characterization of the printed F-GelMA via DLP printing, we measured the cross-section of vertically cut 3D-printed scaffolds using a field-emission scanning electron microscope (FE-SEM; SU8010, Hitachi, Tokyo, Japan). The scaffold had a rectangular shape, with dimensions of 6 mm × 6 mm × 6 mm (width, length, and height, respectively). It was printed using F-GelMA bioink and deionized water without cells. The printed F-GelMA hydrogels were first observed under a light microscope (Nikon ECLIPSE Ts2; Nikon, Tokyo, Japan) at 4× and 10× magnifications. Subsequently, the surface of the scaffold was quickly blotted and frozen in liquid nitrogen for 10 min. After lyophilization (3 days in a freeze-dryer at -80°C), the frozen hydrogel was vertically cut and fixed onto a stub using carbon tape. The sample was then coated with platinum for 2 min. We measured the pores size of the scaffolds using SEM images (300× magnification) and analyzed the data using ImageJ 1.52v software (National Institutes of Health, Bethesda, Maryland, USA).

2.4. Cell culture

Bovine ear fibroblast cells (BEFCs), generously provided by LARTbio, Seoul, South Korea, were cultured and maintained at 37°C and 5% CO_2 in high-glucose DMEM supplemented with 10% (v/v) FBS, 1% (v/v) L-glutamine, and 1% (v/v) P/S. The cells were passaged twice using 0.05% trypsin-EDTA for 7 days, and the media were changed every 2 days.

2.5. Live/Dead assay

To evaluate cell viability (on two-dimensional [2D] cell culture plate and the surface of printed hydrogel), staining was performed for each time course using a Live/Dead® cell viability kit containing calcein-AM and ethidium homodimer-1. The printed hydrogel was prepared in a cylindrical shape with dimensions of 8 mm × 1 mm (width and height, respectively). During the time course experiment (1, 3, 5, 7, 14, 21, 28, and 35 days), 500 μL of staining solution was added to the sample following the manufacturer's protocol, and the sample was incubated at 37°C for 15 min. The cells were seeded at a concentration of 2 × 10^6 cells/mL. Cell viability was calculated as the proportion of live cells relative to the total number of cells, as determined by image analysis using a Lionheart™ FX microscope (BioTek Instruments, Winooski, VT, USA).

2.6. Fabrication and accuracy analysis of three different sizes of microchannel in a DLP-printed 3D hydrogel scaffold

Three different sizes of cross-sectioned microchannel hydrogels were fabricated, with dimensions of 3 mm × 3 mm × 3 mm (width, length, and height, respectively) for immunocytochemical analysis. To prepare the samples for measurement, they were placed on a microscope slide (Paul Marienfeld, Lauda-Königshofen, Germany), and internal sections were cut using 22 mm × 22 mm cover glass (Fisherfinest® Premium cover glass, 12548B, Fisher Scientific, OH, USA). In this study, after a 3-day cell stabilization period post-printing, a media flow environment of 30 rpm orbital shaking was introduced to a non-shaking culture. Observation and analysis were conducted through α-tubulin/DAPI immunocytochemistry staining starting from 5 days at different time course (5, 7, 14, 21, 28, and 35 days). The cross-sectioned samples were fixed with 4% paraformaldehyde at 37°C for 10 min and permeabilized with 0.25% Triton X-100 in PBS for 10 min. After rinsing in PBS, the samples were blocked with 5% bovine serum albumin and 0.1% Triton X-100 in PBS at 37°C for 1 h. Primary antibody was administered for 1 h at 37°C, using mouse monoclonal anti-α-tubulin antibody 12G10 (dilution 1:300; Developmental Studies Hybridoma Bank, Iowa City, MA, USA). After rinsing five times in PBS, a secondary antibody was administered for a 1-h incubation at 37°C using goat anti-mouse IgG H&L (dilution 1:300; Invitrogen, Carlsbad, CA, USA). The nuclei were stained with 4',6-diamidino-2-phenylindole dihydrochloride (DAPI) (dilution 1:1000; 10236276001, Sigma Aldrich, St. Louis, MO, USA), and after a 15 min incubation at 37°C, the samples were washed in PBS. Fluorescent signals were observed using a Lionheart™ FX microscope (BioTek Instruments, Winooski, VT, USA). The analysis for α-tubulin confluency was measured as a percentage using ImageJ 1.25v software (U.S. National Institutes of Health, Bethesda, Maryland, USA). The confluency of α-tubulin (Equation I) was analyzed based on the difference between

the total area of each microchannel (A_t) and the proportion of each microchannel α-tubulin area (A_p).

$$\alpha - tubulin\ confluency\ (\%) = \frac{A_p}{A_t} \times 100\ (\%) \quad (I)$$

2.7. Immunocytochemistry

The Cell Titer®-Glo 3.0® reagent (Promega, Madison, WI, USA) was used to analyze cell proliferation for each time course (1, 7, 14, 21, 28, and 35 days), following the manufacturer's protocol. This study examined a control, small microchannel hydrogel (SMH), medium microchannel hydrogel (MMH), and large microchannel hydrogel (LMH). A total of four samples were analyzed comparatively over a time course, with the volume standardized to 128 mm^3 to ensure an equal number of cells in each sample. Each hydrogel was converted into a media flow environment after an incubation for 3 days in a non-shaking culture environment for cell stabilization. Samples were placed in a 24-well plate and washed with DPBS, and the reagent was added to each sample at a 1:1 ratio. The plates were placed on a shaker for 5 min, followed by incubation for 25 min at room temperature. Each mixed sample reagent was transferred to a light-blocked 96-well plate using 100 μL. Luminescence was measured using the GloMax® Explorer multimode microplate reader.

2.8. Cell Titer®-Glo 3.0® cell proliferation assay

The 3D DLP-printed hydrogel scaffolds with three different sizes of microchannels were fabricated, with dimensions of 3 mm × 3 mm × 3 mm (width, length, and height, respectively). To evaluate the accuracy of the fabricated scaffolds, samples were prepared in a lyophilized state at -80°C for 7 days. The prepared whole samples and transversely cut cross-sectional samples were observed using FE-SEM (SU8010, Hitachi, Tokyo, Japan). For measurements, the samples were fixed with carbon tape on a stub and platinum coated for 2 min. SEM measurements were taken at 30× and 100× magnifications for whole samples and at 100× magnification for transversely cut cross-sectional samples. Measurement of microchannel size for all samples was performed using ImageJ 1.25v software (U.S. National Institutes of Health, Bethesda, Maryland, USA). Five samples of each microchannel size were measured and analyzed using the GraphPad Prism 8.0.2 program (GraphPad Software, LA Jolla, CA, USA).

2.9. Analysis following geographic location of 3D multichannels within the hydrogel scaffolds

The 3D hydrogel scaffolds with different geographical locations of multichannel were designed and printed with the overall dimensions of 8 mm × 5 mm × 3.6 mm in width, length, and height, respectively. We performed immunocytochemical staining of α-tubulin and DAPI, followed by observation under a Lionheart™ FX microscope (BioTek Instruments, Winooski, VT, USA) during the time course (1, 7, 14, 21, 28, and 35 days). The analysis for α-tubulin, DAPI, and microchannel space was estimated as the percentage of α-tubulin confluency and units of DAPI. Microchannel space analysis was performed using ImageJ 1.25v software (U.S. National Institutes of Health, Bethesda, Maryland, USA) by measuring the area of the remaining space compared to the initial remaining space. We analyzed the microchannel space ratio (Equation II) by calculating the difference between the initial microchannel space area (M_i) and the remaining microchannel space area (M_r). A conceptual methodology was designed to analyze the remaining microchannel space compared to the initial microchannel space due to cell survival and proliferation by integrating and summing the corresponding values (Figure S1 in Supplementary File).

$$Microchannel\ space\ ratio\ (\%) = \frac{M_r}{M_i} \times 100\ (\%) \quad (II)$$

2.10. Statistical analysis

All statistical analyses were performed using the GraphPad Prism 8.0.2 program (GraphPad Software, LA Jolla, CA, USA). The results are expressed as mean ± standard deviation (SD). Unpaired *t*-tests were performed when two groups were compared, while analysis of variance (ANOVA) followed by Tukey's post-hoc test was performed when more than two groups were compared. Difference with $p \leq 0.05$ was considered statistically significant.

3. Results and discussion

3.1. Preparation and optimization of DLP 3D bioprinting

3.1.1. Preparation of bioink

The aim of our study is to develop and optimize photocurable bioinks suitable for DLP printing. In bioprinting, bioinks need to provide a biomimetic environment, such as the extracellular matrix, to facilitate high cell viability, non-inflammation, non-cytotoxicity, attachment and proliferation, and adequate mechanical strength and stiffness after printing.[38] GelMA is created by covalently bonding natural polymer gelatin with MA, containing essential arginine-glycine-aspartic acid sequences that target matrix metalloproteinases involved in cell remodeling.[39,40] GelMA is biodegradable and biocompatible, and can effectively interact with cells.[40] In this study, we used F-GelMA because of its different mechanical properties from mammalian gelatin-

derived GelMA, considerations of religious restrictions or limitations due to mammalian infectious diseases, and a lower melting point, which enables large-scale synthesis.[41] In addition to GelMA, a variety of other photocurable polymers (e.g., methacrylated collagen, methacrylated alginate, methacrylated hyaluronic acid, methacryloyl-modified silk, and methacrylated chitosan) have been utilized and studied for 3D printing using photopolymerization in recent years.[12,42]

Achieving high-resolution and biocompatible 3D bioprinting requires selecting appropriate photoinitiator concentration and wavelength. The photoinitiator LAP, with its fast speed and high-resolution printability, has been utilized in DLP printing as a chemical covalent crosslinker of polymers with biocompatible properties and absorption at ultraviolet (UV) and blue light wavelengths.[43] Recently, the range of wavelengths used in DLP printing has expanded to include long wavelengths, such as green light (500–580 nm) and near-infrared wavelengths (900–1000 nm), to improve tissue penetration, cell viability rates, and printing resolution.[44,45] Furthermore, the addition of a light-absorbing agent during DLP printing can help resolve any mismatches between the bioink polymer and the light wavelength, thereby improving printing accuracy. Previous studies in our laboratory compared eight colors of light-absorbing agents used in DLP printing and found that yellow (405 nm) had the most suitable peak at a UV-Vis wavelength of 380–450 nm.[31] Tartrazine, a yellow pigment, was added to the bioink to prevent excessive crosslinking and improve printability. The cells encapsulated in the bioink were bovine ear-derived fibroblasts. Fibroblasts, a type of cell that synthesizes ECM and collagen, are widely recognized as the primary cellular component of connective tissue in animals.[46,47] They also play pivotal roles in the formation of the structural skeleton and wound healing in animals.[48-50] Therefore, they offer the advantage of mimicking the dermis layer of the skin and have the potential for application as cell-cultivated meat and cultured leather.[6,37] In addition, our laboratory has been conducting basic research on cell-cultivated meat and the utilization of GelMA scaffolds; therefore, we utilized bovine ear-derived fibroblasts for the current research[6,51] (Figure 2A).

The DoF of the F-gelatin molecules was determined by analyzing the ^{1}H NMR spectra.[52,53] F-Gelatin and F-GelMA contain a wide range of amino acids, and their complex spectra can be used to determine the DoF of the molecules. F-GelMA showed the emergence of a distinct yellow (a) functional group, while the red (b) and blue (c) functional groups decreased compared to F-gelatin (Figure 2A). The chemical shift of the δ = 5.4/5.7 ppm portion of the yellow (a) functional group is attributed to the acryl protons (2H) of the methacrylate group and increases, while the chemical shift of the δ = 1.8 portion of the blue (c) functional group is due to the decrease in the methyl group (3H) (Figure 2B). Successful methacrylation of gelatin resulted in a decrease in the chemical shift of the red (b) functional group at δ = 2.9 ppm, which is assigned to the lysine methylene (2H) protons (Figure 2B). To calculate the DoF of F-gelatin, the decrease in the lysine spectrum resulting from the formation of a new functional group due to the reaction between gelatin and MA was targeted.[54] Based on these results, the DoF of F-GelMA was confirmed to be 95.6 ± 2.8% (Figure 2B).

3.1.2. Photorheological analysis of bioink

Rheological analysis of the bioink was performed to determine the optimal exposure time for successful DLP bioprinting. Gelation time, which is the minimum exposure time, can affect the cellular microenvironment and cell viability.[31] Therefore, determining the appropriate exposure time and applying it to printing enable sophisticated, high-resolution printing. The bioink was measured using a rheometer with a gap distance of 100 μm, and the phase transition was explored by examining the storage modulus (G') and loss modulus (G"). Before photopolymerization, G' was lower than G", indicating solution-state dominance, which lasted for up to 27 s. Once photopolymerization occurred under 405 nm visible light, a rapid increase was observed in both G' and G", which resulted in a crossover point indicating the gelation time. This point represents the occurrence of the solution-to-gel phase change, and the gelation time was determined to be 31.13 s. However, between 27 and 29 s, there was a sharp decrease in G', which may have been caused by the coexistence of solution and gel and the inaccurate measurement values by the rheometer due to uneven polymer formation.[31,55] After the completion of photopolymerization, G" was significantly higher than G', and there was a tendency for both to rapidly increase due to the continuous crosslinking reaction. The printable window highlighted in yellow shows the range of optimized printing times after gelation[56] (Figure 2C). The optimal exposure time required for bioink photocrosslinking using 3D DLP printing was determined to be 31.13 s.

3.2. Morphological analysis of printed F-GelMA hydrogel using DLP bioprinting

For analyzing the morphological characteristics of printed F-GelMA 3D hydrogel cross-sections, bioink was printed at 100 μm intervals (Figure 2D-(a)). The resulting samples were prepared by cutting the sections after freeze-drying (Figure 2D-(b)). The porous structure of the resulting hydrogel scaffold was observed and analyzed via SEM (Figure 2D-(c)). The resulting structure using the DLP stacking method had a layered structure with 100 μm spacing, and multiple pore structures were observed

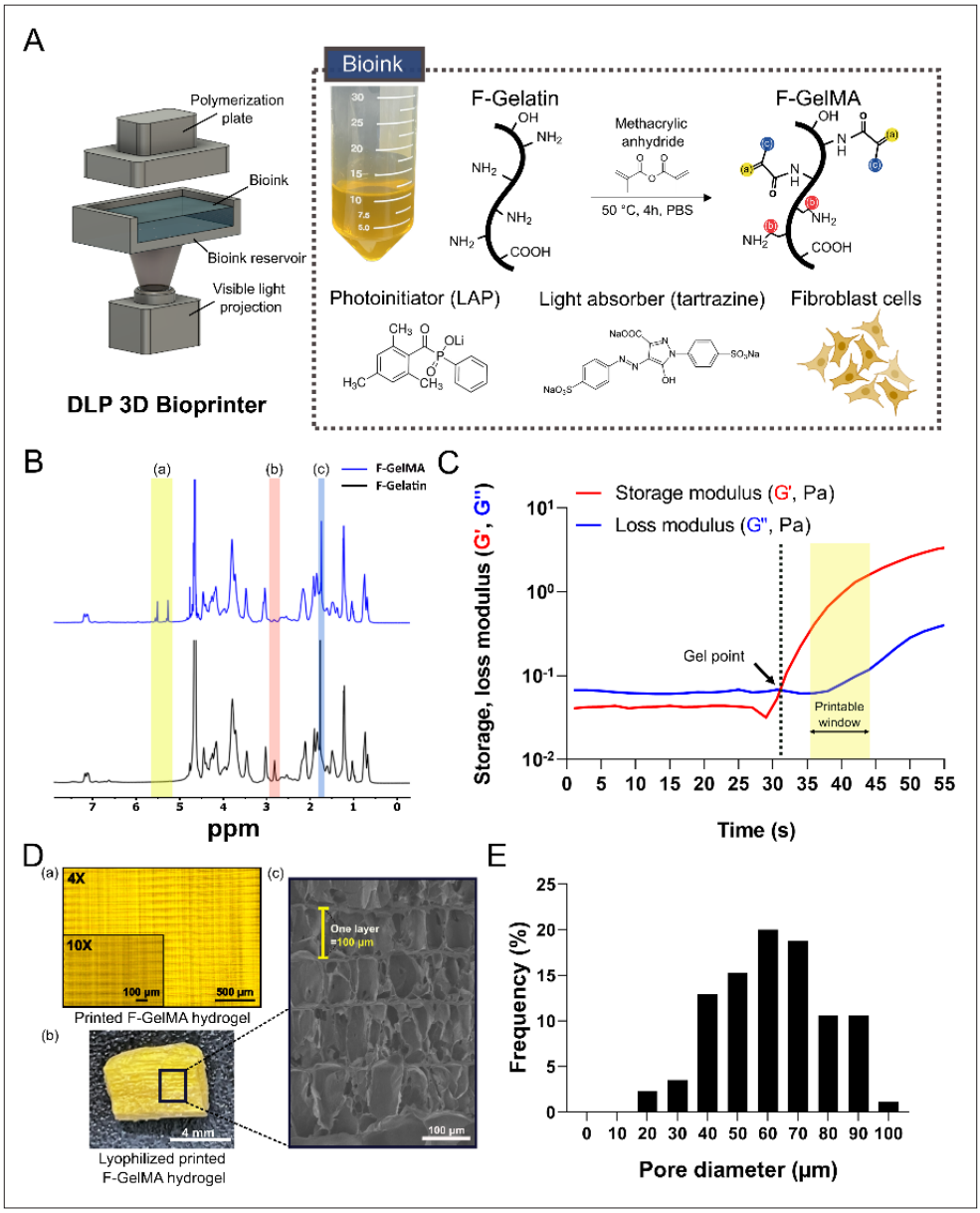


Figure 2. Preparation and optimization of digital light processing (DLP) bioprinting process and morphological features. (A) Composition of bioink and synthesis of F-GelMA by reacting fish gelatin with methacrylic anhydride. **(B)** ^{1}H NMR of F-gelatin and F-GelMA. Yellow (a) indicates the 2H proton of the methyl group, red (b) indicates the methylene group of lysine, and blue (c) indicates the 3H proton of the methyl group. Data are shown as means ± SD ($n = 3$). **(C)** Photorheological measurements of bioink. The intersection of G' and G" represents the gel point, and the yellow part is shown as a printable window. **(D)** (a) The light microscope images of printed F-GelMA hydrogel. Scale bars: 500 µm (4× magnification) and 100 µm (10× magnification). (b) Scanning electron microscopic (SEM) images of lyophilized printed F-GelMA hydrogel. Scale bar: 4 mm. (c) The SEM images are obtained at 300× magnifications. One layer shows 100 µm. Scale bar: 100 µm. **(E)** Pore distribution frequency is obtained from SEM images of F-GelMA hydrogel. Data are shown as means ± SD ($n = 3$).

in the space where one layer was formed. Therefore, the average pore size within the F-GelMA hydrogel scaffold was 64.44 ± 3.42 µm (Figure 2E), which is larger than the pore size of untreated F-GelMA, measuring 22.4 ± 2.2 µm.[41] The porous structure of the GelMA hydrogel scaffold is also critical for cell viability, proliferation, and movement. This is because it plays a crucial role in the transport of oxygen and nutrients.[57] F-gelatin derived from cold-water fishes typically exhibits lower hydroxyproline content in comparison to F-gelatin sourced from warm-water fishes and mammalian gelatin.[58] This results in fewer hydrogen bonds in the helix structure compared to mammalian gelatin. It forms a triple-helix structure with a low mechanical coefficient because of its high expansion

characteristics.[41,59] These characteristics allow the cells encapsulated in the F-GelMA hydrogel to exhibit better diffusion, movement, and proliferation. Therefore, the layered structure within the F-GelMA hydrogel printed by the DLP printing method was observed, and the pores within each layer were predicted to serve as pathways for the transport of oxygen and nutrients necessary for cell attachment and proliferation, providing a space for cell attachment and proliferation.

3.3. Cell viability analysis on F-GelMA hydrogel printed by DLP

In this study, cell viability on F-GelMA hydrogels printed by DLP was analyzed and evaluated. A Live/Dead assay was performed on the control group of cells cultured in 2D culture (Figure 3A). Cell viability was 75.49 ± 9.58% at day 1 following incubation. Cell viability continued to increase at days 3 and 5, reaching 94.56 ± 3.34% and 96.84 ± 4.33%, respectively, and 99.39 ± 0.66% at day 7, a statistically significant difference from the group at day 1 ($p < 0.01$) (Figure 3C). Since 2D cultures grow by adhering to cross-section, there is limited space for cell adhesion and proliferation during long-term culture compared to 3D cultures.[60] However, the printed GelMA hydrogels are predicted to promote cell adhesion by providing a microcellular environment for cell culture.[51]

Difficulties in distributing cells arise evenly using extrusion-based 3D printing methods due to the accumulation of cells at the bottom caused by gravity.[61] Therefore, in this study, we utilized the advantages of DLP printing to encapsulate cells in a hydrogel and achieve

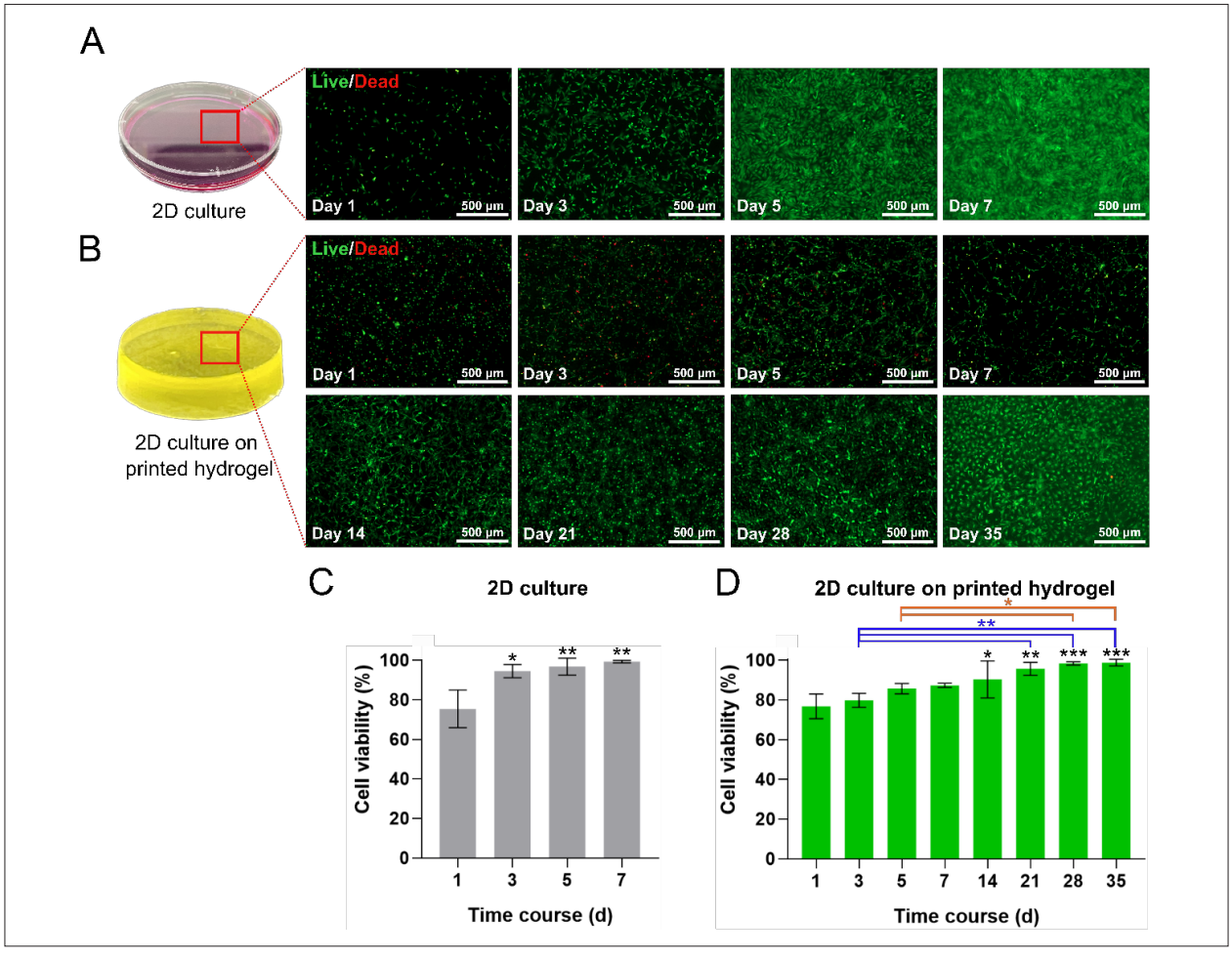


Figure 3. Cell viability on printed F-GelMA hydrogel by digital light processing (DLP). (A, B) Fluorescence images of a Live/Dead assay of fibroblasts on 2D culture for 1, 3, 5, and 7 days and the surface of printed hydrogel for 1, 3, 5, 7, 14, 21, 28, and 35 days. Live cells produce green fluorescence, and dead cells show red fluorescence. Scale bars: 500 μm. **(C)** Cell viability of 2D culture was determined using Live/Dead assay. Data are shown as means ± SD ($n = 3$). *$p < 0.05$, **$p < 0.01$ vs. time course 1 day, and data are analyzed by one-way ANOVA followed by Tukey's post-hoc test. **(D)** Using the Live/Dead assay, 2D cell viability is determined on printed hydrogels. Data are shown as means ± SD ($n = 3$). *$p < 0.05$, **$p < 0.01$, ***$p < 0.001$ vs. time course 1 day and between the indicated groups. Data are analyzed by a one-way ANOVA followed by Tukey's post-hoc test.

a uniform cell distribution. We observed the internal cell morphology within the hydrogel and analyzed cell viability (Figure 3B). The observation results over time showed that on day 1, a cell viability of 76.88 ± 6.22% was achieved. This could be attributed to the loss of initial viability caused by cell encapsulation stress, nutrient restriction, drying, or temporary swelling during printing.[40] The cell viability showed a gradual increase on days 3, 5, and 7, reaching 79.85 ± 3.51%, 85.72 ± 2.61%, and 87.38 ± 1.04%, respectively, but did not exceed 90%. However, the cell viability showed significant improvement on days 14, 21, and 28, reaching 90.41 ± 9.33%, 95.74 ± 3.26%, and 98.48 ± 0.81%, respectively, which surpassed 90%. A statistically significant increase in the cell viability was observed on day 35 compared to day 1, with cell viability of 98.89 ± 1.7% ($p < 0.001$; Figure 3D). Other reported studies have also shown that GelMA hydrogel scaffold encapsulating fibroblasts as well as various cells such as human hepatocellular carcinoma and human umbilical endothelial cells exhibit good cell viability, diffusion, and proliferation for 7 days, indicating high biocompatibility of the scaffolds.[62] Printed GelMA is known for being highly compatible with cells and did not exhibit cytotoxicity. Moreover, the cells encapsulated in the F-GelMA hydrogel showed high uniform distribution and biocompatibility. This indicates that DLP-printed F-GelMA has the potential to serve as a scaffold for cell adhesion and proliferation.

3.4. Fabrication and accuracy analysis of three different sizes of microchannel in a DLP-printed 3D hydrogel scaffold

Here, we investigated the viability of cells on a DLP-printed hydrogel scaffold. While we confirmed that the scaffolds exhibit high cell viability, challenges remain as DLP printing is unable to address the microscale barrier structures that impede cell adhesion and proliferation (Figure 2D). Three different sizes of microchannels suitable for increasing cell adhesion and proliferation within the same volume were introduced to facilitate bulk transport of scaffold cell contents, enhance cell viability, and improve cell proliferation.[23,24,63] The 3D hydrogel scaffolds were printed with small microchannel hydrogel (SMH; 250 μm), medium microchannel hydrogel (MMH; 500 μm), and large microchannel hydrogel (LMH; 750 μm).

To fabricate microchannel hydrogels of three different sizes using DLP printing technology and to measure their accuracy, lyophilized samples were prepared for SEM analysis (Figure 4A). For the measurement of three different sizes of microchannels, the top-view overall image and magnified image of the microchannel were acquired. In addition, transverse sections were prepared to capture images of each microchannel size (Figure 4B). The microchannel sizes of SMH, MMH, and LMH were then analyzed for each sample; the sizes of SMH, MMH, and LMH were 249.4 ± 6.86 μm, 487.4 ± 42.59 μm, and 748.0 ± 27.86 μm, respectively (Figure 4C). The three different sizes of microchannel hydrogels were close to the desired diameter. The observed slight differences could be attributed to shrinkage during freeze-drying.[15] The microchannels effectively enhance cell viability by providing nutrients within the scaffold while promoting cell adhesion, growth, and migration, as well as providing space for mass transport.[22-25] Based on the results of this study, we predicted that the carefully fabricated microchannels would provide not only a supply channel for oxygen and nutrients but also a space for cell proliferation.

3.5. Analysis of immunostaining in outer microchannel and inner microchannel upon introduction of microchannels of three different sizes in DLP-printed 3D hydrogel scaffold

The hydrogel scaffolds were DLP-printed with three different sizes of microchannel, and cells were encapsulated within the hydrogels. The purpose of this experiment was to observe the cell behavior in outer microchannel (O.M.C) and inner microchannel (I.M.C) in each scaffold group. Cell encapsulation was followed by 3 days stabilization period. Subsequently, we analyzed the α-tubulin/DAPI immunocytochemistry of the O.M.C and I.M.C of sample cross-sections from 5 to 35 days (Figure 5A-(a), (b), and (c)). All size groups successfully encapsulated cells during the O.M.C time course. However, single-cell morphology was observed, and no network formation or cell adhesion and proliferation were observed during long-term culture. No significant (ns) difference in α-tubulin confluency was observed over the time course of cell encapsulation within the O.M.C (ns; Figure 5B, D, and F). This lack of proliferation was likely due to the flow and supply restriction of the media, which facilitates nutrient supply to the interior of the encapsulated cells.[64,65]

The α-tubulin confluency in the I.M.C showed the following results during the entire time course (5, 7, 14, 21, 28, and 35 days): 7.11 ± 2.15%, 7.52 ± 1.77%, 8.58 ± 2.16%, 12.32 ± 2.98%, 13.21 ± 2.05%, and 9.22 ± 1.67% in SMH, respectively (Figure 5C). A significant difference was observed in SMH between 5 and 28 days ($p < 0.05$). In MMH, α-tubulin confluency increased to 4.53 ± 1.08%, 9.20 ± 3.53%, 12.09 ± 0.83%, 13.72 ± 4.37%, 15.24 ± 4.17%, and 17.78 ± 0.94% during the time course, and statistically significant differences were observed between 5 and 21 days and 28 and 35 days ($p < 0.05$, $p < 0.01$, and $p < 0.001$; Figure 5E). Similarly, in LMH during the same time course, α-tubulin confluency increased to 8.31 ± 1.16%, 8.17 ±

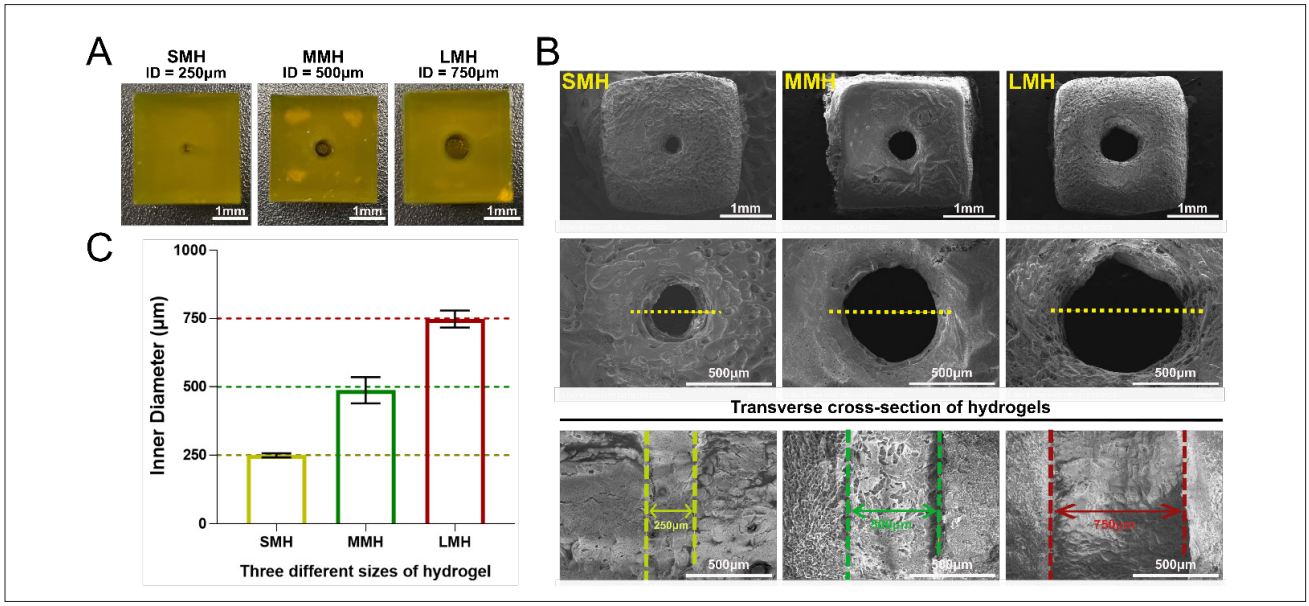


Figure 4. Fabrication and accuracy analysis of three different sizes of microchannels in a digital light processing (DLP)-printed 3D hydrogel scaffold. **(A)** Three different sizes of microchannel hydrogels made with DLP printing technology (small microchannel hydrogel [SMH], medium microchannel hydrogel [MMH], and large microchannel hydrogel [LMH]). Scale bars: 1 mm. **(B)** Scanning electron microscopic (SEM) images of three different sizes of microchannel hydrogels. The top images were acquired at 30× magnification; scale bars: 1 mm. The middle images were acquired at 100× magnification; scale bars: 500 μm. The bottom row shows transverse cross-section images of microchannel hydrogels with three different sizes at 100× magnification. Scale bars: 500 μm. **(C)** Inner diameter analysis of three different sizes of microchannel hydrogel. Data are shown as means ± SD (n = 5).

1.96%, 12.82 ± 3.96%, 14.04 ± 4.51%, 15.75 ± 1.42%, and 21.01 ± 3.18%, and a statistically significant difference was observed between 5 and 35 days ($p < 0.001$; Figure 5G).

In the I.M.C, we observed an increasing trend in α-tubulin confluency from SMH to MMH to LMH. As reported by others, the presence of microchannels can lead to higher cell viability, increased urea synthesis, and albumin secretion in adjacent regions of the hydrogel.[25] The presence of microchannels also reportedly offers biocompatibility benefits, such as improved cell penetration throughout the hydrogel scaffold, uniform cell distribution, and higher oxygen saturation.[64] Despite these benefits, we did not observe a significant increase in cell proliferation after the inclusion of microchannels. Even after a long-term culture period, the α-tubulin confluency did not exceed 30% for all sizes of O.M.C and I.M.C. Our results suggest that another effective method may be necessary to induce cell proliferation.

3.6. Analysis of immunostaining and cell proliferation in O.M.C and I.M.C from three different sizes of DLP-printed 3D hydrogel scaffolds with a change in media flow environment

To facilitate effective cell culture and improve the oxygen and nutrient supply to cells within the microchannels, we modified the media flow environment. It has been reported that media flow environment could enhance biological function of cells and facilitate the supply of oxygen and nutrients to the center of the scaffold, as compared to a non-shaking culture.[66-68] Encapsulation in the O.M.C resulted in cells maintaining a round morphology without proliferation, regardless of the media flow environment. However, in the I.M.C, the media flow environment allowed for the smooth transport of oxygen and nutrients inside the microchannel, leading to high cell proliferation and network formation (Figure 6A). Throughout the time course, α-tubulin confluency in O.M.C remained low at 5–10% among different sizes of hydrogels during the long-term culture lasting for 5 to 35 days (ns; Figure 6B, D, and F), consistent with previous experiments. Conversely, cells in the I.M.C formed a network and changed shape during the long-term culture period. The α-tubulin confluency increased from 11.77 ± 4.07% to 31.91 ± 6.19% from 5 to 35 days, with statistically significant differences observed between 5 and 35 days ($p < 0.05$; Figure 6C).

During the time course of MMH, α-tubulin confluency increased to 21.47 ± 4.65%, 23.36 ± 3.65%, 25.49 ± 1.70%, 32.88 ± 14.84%, 39.84 ± 2.51%, and 40.74 ± 2.87%, respectively, with a statistically significant difference between 5 and 35 days ($p < 0.05$; Figure 6E). Similarly, at LMH, α-tubulin confluency increased to 16.38 ± 2.28%, 27.13 ± 3.69%, 30.61 ± 0.73%, 36.61 ± 4.03%, 47.84 ± 8.22%, and 71.97 ± 3.32%, respectively, with a statistically significant difference between 5 and 35 days ($p < 0.001$; Figure 6G).

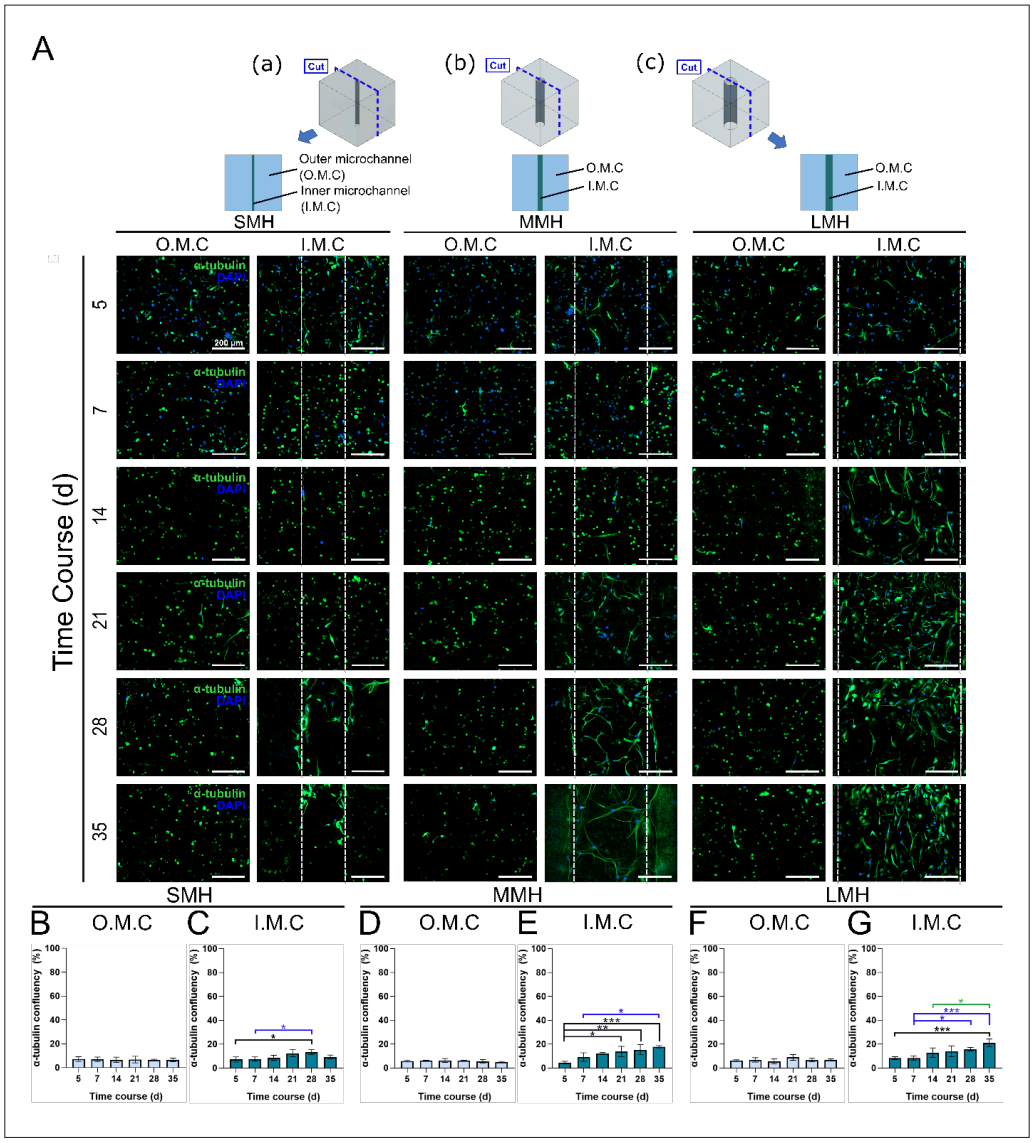
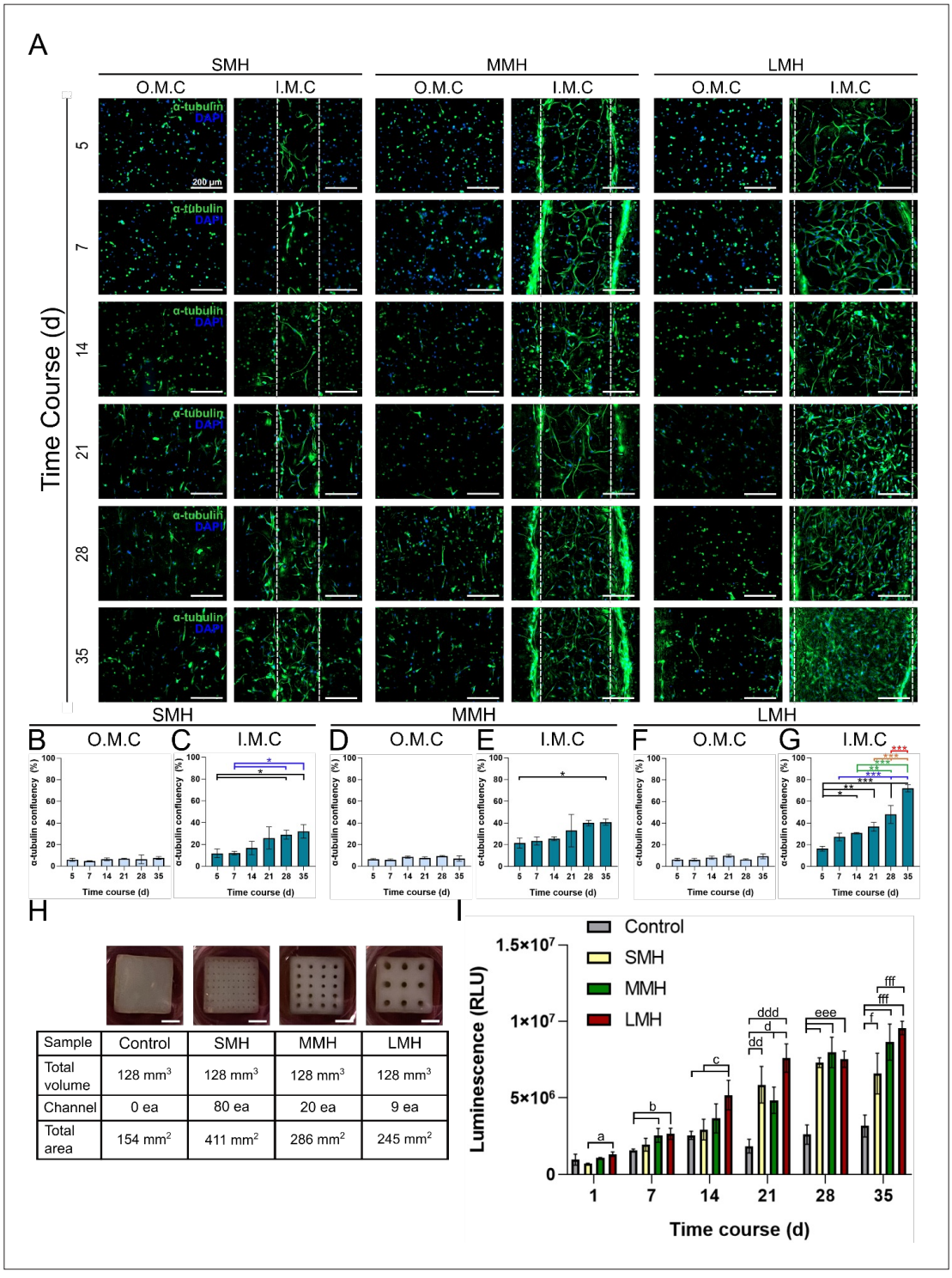


Figure 5. Immunostaining analysis of three different sizes of microchannel in a digital light processing (DLP)-printed 3D hydrogel scaffold. **(A)** Schematic diagram of three different microchannel hydrogels: (a) SMH, (b) MMH, and (c) LMH. Immunofluorescence images of three different microchannel hydrogels on non-shaking culture for 5, 7, 14, 21, 28, and 35 days. Cells are stained with an α-tubulin (green), and nuclei are stained with DAPI (blue). Scale bars: 200 μm. **(B–G)** α-tubulin confluency analysis of (a) SMH, (b) MMH, and (c) LMH in non-shaking culture. Data are shown as means ± SD ($n = 3$). $^{*}p < 0.05$, $^{**}p < 0.01$, $^{***}p < 0.001$ by one-way ANOVA followed by Tukey's post-hoc tests.

LMH at day 35 exhibited the highest α-tubulin confluency among the three sizes of microchannel hydrogels. The results of media flow within the microchannel indicated an increase in α-tubulin confluency in all I.M.C groups compared to that in the non-shaking culture.

As reported by other researchers, the introduction of microchannels during long-term culture resulted in higher oxygen saturation and cell density,[64] and increased mineralization during perfusion culture (7 mL/min) in 3D constructs aimed at cartilage structures.[26] This supports the effectiveness and potential of the microchannels and the media flow environment as demonstrated in the present study. In summary, introducing media flow into the microchannel did not affect cell proliferation in O.M.C, but effectively formed a cell network in the microchannel space of the I.M.C. This suggests that introducing media flow and microchannels can supplement the network of cells that do not reach the center of large tissue scaffolds. Additionally, the study was conducted at 30 rpm, the lowest rpm setting for a shaking incubator. However, when we examined the



Sample	Control	SMH	MMH	LMH
Total volume	128 mm^3	128 mm^3	128 mm^3	128 mm^3
Channel	0 ea	80 ea	20 ea	9 ea
Total area	154 mm^2	411 mm^2	286 mm^2	245 mm^2

Figure 6. Immunostaining analysis of three different sizes of microchannel in DLP-printed 3D hydrogel scaffold in media flow environments. (A) Immunofluorescence images of three different sizes of microchannel hydrogel scaffold in media flow environments for 5, 7, 14, 21, 28, and 35 days. Cells are stained with an α-tubulin (green), and nuclei are stained with DAPI (blue). Scale bars: 200 μm. **(B–G)** α-tubulin confluency analysis of SMH, MMH, and LMH in media flow environments. Data are shown as means ± SD ($n = 3$). $^*p < 0.05$, $^{**}p < 0.01$, $^{***}p < 0.001$ by one-way ANOVA followed by Tukey's post-hoc tests. **(H)** Different sizes of microchannel hydrogel (control, SMH, MMH, and LMH). Scale bar: 2 mm. **(I)** Cell proliferation assay of control, SMH, MMH, and LMH for 1, 7, 14, 21, 28, and 35 days are measured using the Cell Titer®-Glo 3.0® cell proliferation assay. Data are shown as means ± SD ($n = 3$). $^*p < 0.05$, $^{**}p < 0.01$, $^{***}p < 0.001$ by one-way ANOVA followed by Tukey's post-hoc tests.

behavior of the cells at 60 rpm and 90 rpm for 14 days, we observed a significant increase in cell proliferation with the rising rpm (Figure S2 in Supplementary File).

To observe the differences in cell proliferation over each time course of the three sizes of microchannel hydrogels and the effect of the microchannels, we performed cell luminescence-based quantification. The volume was fixed at 128 mm^3 to equalize the number of cells in each hydrogel (Figure 6H). Statistical analysis of the differences between each time course showed no significant difference in all groups compared to the control group on day 1 (ns). There was a statistically significant difference in the luminescence levels between the MMH and LMH groups compared to the control group on day 7 ($*b < 0.05$). A significant increase was observed in the LMH group compared to the control group on day 14 ($*c < 0.05$). All three groups showed a significant difference from the control group on day 21 ($*d < 0.05$, $**d < 0.01$, and $*ddd < 0.001$). Additionally, all three groups showed a significant increase on day 28 compared to the control group ($***e < 0.001$). Throughout the time course, LMH exhibited the highest luminescence levels. Despite having a small surface area, LMH showed the highest luminescence level, indicating high cell viability and proliferation due to the presence of media supply within the channel (Figure 6I). Our results suggest that microchannels not only increase surface area but also function as a conduit to supply oxygen and nutrients to encapsulated cells and facilitate media flow. Thus, the introduction of microchannels into DLP-printed 3D hydrogel scaffolds, along with the introduction of media flow, enhances cell proliferation compared to the same volume of scaffold cultured under non-shaking culture conditions during long-term culture.

3.7. Analysis of cell morphology and proliferation enhancement by geographic location of DLP-printed 3D hydrogel scaffolds with multichannel (LMH) during long-term culture

The purpose of this study was to introduce LMH, which has been proven to be effective in cell proliferation, and to observe and analyze cell morphology, viability, and proliferation following the geographic location (top and side views) of scaffolds (Figure 7A). We conducted immunocytochemistry staining using α-tubulin/DAPI and observed the top view of the cells to assess their morphology and proliferation. Over time, the cells elongated and proliferated, forming multiple layers, which led to an increase in α-tubulin/DAPI (Figure 7B). The percentage of cells exhibiting α-tubulin confluency consistently increased throughout the experiment, with values of 14.89 ± 2.45%, 22.28 ± 3.14%, 24.42 ± 2.83%, 32.35 ± 2.53%, 37.29 ± 2.54%, and 43.46 ± 10.46%. A statistically significant difference between day 35 and day 1 was observed ($p < 0.001$; Figure 7C).

Based on DAPI analysis, the number of cells increased during the entire time course to 286 ± 25.71, 290 ± 58.13, 366 ± 38.55, 376 ± 35.73, 401 ± 50.57, and 464 ± 60.10, with a statistically significant difference between day 1 and day 35 ($p < 0.01$; Figure 7D). The side view of the microchannel cross-section shows that the cells adhered to a circular shape and formed a network (Figure 7E). The analysis was performed based on the ratio of the remaining area to the initial microchannel space, showing 91.31 ± 0.06% of the inner space area of the channel on day 1 and 64.10 ± 0.06% on day 7, a sharp decrease with statistical significance ($p < 0.001$). Then, the remaining space area decreased by around 40%, showing 64.10 ± 0.06% and 60.21 ± 0.04% of the space area on day 14 and day 21, respectively, with no significant difference between them (ns). As time progressed to day 21 and day 28, cells filled the unoccupied space inside the channel, and the area of the remaining space decreased sharply again from 59.07 ± 0.03% to 33.76 ± 0.10% ($p < 0.01$). Finally, on day 35, 28.80 ± 0.05% of the inner space area of the channel was filled, leaving approximately 30% of the printed microchannel shape unoccupied due to cell proliferation from long-term culture (Figure 7F).

It is well known that a high-flow culture environment is more effective than a non-shaking culture in promoting cell proliferation and maturation *in vitro*.[27] In addition, it has been reported that aligned microchannels in printed 3D hydrogel scaffolds affect the spatial migration and survival of neural stem cell spheroids.[69]

Here, we observed that cell proliferation resulted in the formation of a single layer of cells in the microchannel space during the early-time cultivation (until day 7), whereas two or more layers of cells were formed during the mid- and late-time cultivation (until day 21 and day 35; **Videos S1–S3** in Supplementary File). However, contrary to our expectation that cells would completely fill the empty space inside the microchannel, we found that the flow of media provided a continuous supply of nutrients and oxygen to the cells without blocking the channel. This ensured the effectiveness of introducing vertical multichannel arrays into the DLP-printed 3D hydrogel scaffolds and changing the culture environment to enhance cell proliferation. Ultimately, this method provides a fast, simple, and efficient means of significantly improving cell seeding, distribution, and proliferation in various geographical aspects (top and side) during long-term culture.

4. Conclusion

In this study, we aimed to enhance the survival and proliferation of cells encapsulated within DLP-printed

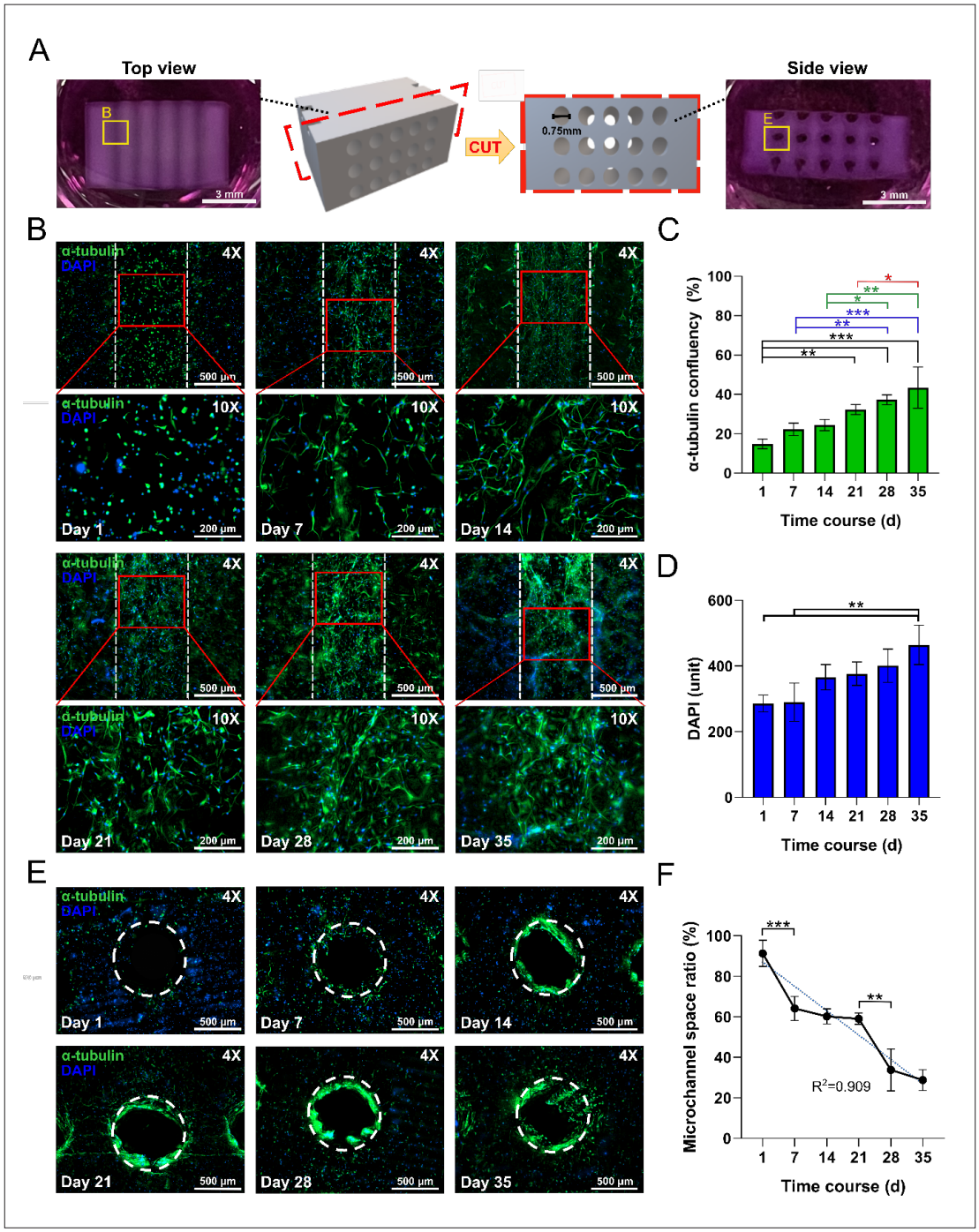


Figure 7. Immunostaining analysis following geographic location of multichannel (LMH) in digital light processing (DLP)-printed 3D hydrogel scaffold. (A) Schematic diagram of multichannel in DLP-printed 3D hydrogel scaffold of the top and side view in media flow environments. Scale bars: 3 mm. **(B)** Immunofluorescence images of top view for 1, 7, 14, 21, 28, and 35 days. The images acquired are magnifications of area B (top view) indicated in panel (A). Cells are stained with an α-tubulin (green), and nuclei are stained with DAPI (blue). Scale bars: 500 μm (upper) and 200 μm (lower). **(C)** α-tubulin confluency analysis. Data are shown as means ± SD ($n = 4$). $^{*}p < 0.05$, $^{**}p < 0.01$, $^{***}p < 0.001$ vs. time course 1 day and between the indicated groups. Data are analyzed by one-way ANOVA followed by Tukey's post-hoc test. **(D)** DAPI analysis. Data are shown as means ± SD ($n = 3$). $^{**}p < 0.01$ vs. time course 1 day and between the indicated groups. Data are analyzed by a one-way ANOVA followed by Tukey's post-hoc test. **(E)** Immunofluorescence images of side view for 1, 7, 14, 21, 28, and 35 days. These are the magnified images of area E (side view) indicated in panel (A). Cells are stained with an α-tubulin (green), and nuclei are stained with DAPI (blue). Scale bars: 500 μm. **(F)** Analysis of the microchannel space for immunostaining after 1, 7, 14, 21, 28, and 35 days. Data are shown as means ± SD ($n = 4$). $^{**}p < 0.01$, $^{***}p < 0.001$ by unpaired *t*-tests.

hydrogel scaffolds. We fabricated precise hydrogel scaffolds with an optimized photocurable bioink and characterized the morphological features of the microscale barrier structures generated by DLP printing. Next, we demonstrated cellular compatibility with cell viability exceeding 95% on the surface of the printed F-GelMA hydrogel. Three sizes of microchannel hydrogels (SMH, MMH, and LMH) were introduced to overcome the limitations caused by the barrier structure in DLP printing, and their O.M.C and I.M.C were analyzed. The results showed that α-tubulin confluency did not exceed 30% in any of the O.M.C and I.M.C samples, indicating that additional culture conditions were required. Finally, a significant improvement in cell proliferation was demonstrated in I.M.C through a shift from a non-shaking culture to a media flow environment ($p < 0.001$). Among them, the LMH vertical multichannel showed the highest cell proliferation, demonstrating remarkable improvements in cell adhesion, viability, and proliferation following the geographical location of the multichannel (top and side) during long-term culture.

We offer a novel functional definition for microchannels implanted into DLP-printed scaffolds, based on what we have shown that microchannels offer regions that promote cell survival and proliferation. The approach can also be applied as a basic research methodology for enhancing the proliferation of cells encapsulated within F-GelMA scaffolds. Future work will require microfluidic studies incorporating the use of fluidic bioreactors for larger tissue cultures,[70,71] as well as *in vivo* studies to demonstrate regeneration of scaffolds as cell grafts.[72-74] Nevertheless, taken together, this study provides valuable insights into advanced bioprinting techniques for achieving simple and effective cell proliferation, with the potential for future applications in tissue engineering (artificial organs),[34,35,73] regenerative medicine (vascular microenvironments),[32,33,74] *in vitro* disease models,[36] and 3D culture technologies[6,37] that require large-scale cell production on volumetric scaffolds using DLP bioprinting (Figure S3 in Supplementary File).

Acknowledgments

We are grateful to the LARTbio for generously providing the Bovine ear fibroblast cells (BEFCs). J.W.S. is now employed by the Division of Engineering in Medicine, Department of Medicine, Brigham and Women's Hospital, Harvard Medical School, Cambridge, MA 02139, USA.

Funding

This work was supported by the Creative and Challenging Convergence Model Development Program (RS-2023-00232550) from the Korea Institute of Planning and Evaluation for Technology in Food, Agriculture, Forestry, and Fisheries (iPET). The authors are grateful for the financial support from the National Research Foundation of Korea (NRF) grant funded by the Korean Government (NRF-2018R1D1A1B05047274) and NoAH Biotech Co., Ltd. Korea.

Conflict of interest

The authors declare no conflicts of interest.

Author contributions

Conceptualization: Yejin Choi, Jeong Wook Seo, Hojae Bae
Data curation: Yejin Choi, Jeong Wook Seo
Formal analysis: Yejin Choi, Jeong Wook Seo
Investigation: Yejin Choi
Methodology: Yejin Choi, Jeong Wook Seo
Project administration: Hojae Bae
Resources: Goo Jang, Woo Kyung Jung, Yong Ho Park
Supervision: Hojae Bae
Writing – original draft: Yejin Choi, Jeong Wook Seo
Writing – review & editing: Yejin Choi, Jeong Wook Seo, Hojae Bae

Availability of data

Data are available from the corresponding author upon reasonable request.

References

1. Cohan M. From petri dish to dinner plate: this is the world's first 3D-printed, cultivated fish fillet. *CNN*; 2023. https://edition.cnn.com/travel/article/steakholder-foods-3d-printed-cultivated-fish-fillet-spc-intl/index.html
2. Listek V. Aleph farms' new cultured steak to join the cultured meat race. *3D print.com*; 2023. https://3dprint.com/299484/aleph-farms-new-3d-printed-steak-to-join-the-cultured-meat-race/
3. Marr B. The future of food: amazing lab grown and 3D printed meat and fish. *Forbes*; 2019. https://www.forbes.com/sites/bernardmarr/2019/06/28/the-future-of-food-amazing-lab-grown-and-3d-printed-meat-and-fish/?sh=6fdf360446f6
4. Reiley L. Raising the steaks: first 3-D-printed rib-eye is unveiled. *The Washington Post*; 2021. https://www.washingtonpost.com/business/2021/02/09/3d-printed-ribeye-steak-usda-fda/
5. Ianovici I, Zagury Y, Redenski I, Lavon N, Levenberg S. 3D-printable plant protein-enriched scaffolds for cultivated meat development. *Biomaterials*. 2022;284:121487. doi: 10.1016/j.biomaterials.2022.121487
6. Jeong D, Seo JW, Lee H-G, Jung WK, Park YH, Bae H. Efficient myogenic/adipogenic transdifferentiation of bovine fibroblasts in a 3D bioprinting system for steak-

type cultured meat production. *Adv Sci*. 2022;9(31): 2202877.
doi: 10.1002/advs.202202877

7. Su L, Jing L, Zeng X, et al. 3D-printed prolamin scaffolds for cell-based meat culture. *Adv Mater.* 2023;35(2):2207397.
doi: 10.1002/adma.202207397

8. Nam HK, Kang TW, Kim I-W, Choi R-Y, Kim HW, Park HJ. Physicochemical properties of cricket (Gryllus bimaculatus) gel fraction with soy protein isolate for 3D printing-based meat analogue. *Food Biosci*. 2023;53:102772.
doi: 10.1016/j.fbio.2023.102772

9. Mani MP, Sadia M, Jaganathan SK, et al. A review on 3D printing in tissue engineering applications. *J Polym Eng*. 2022;42(3):243-265.
doi: 10.1515/polyeng-2021-0059

10. Samadi A, Moammeri A, Pourmadadi M, et al. Cell encapsulation and 3D bioprinting for therapeutic cell transplantation. *ACS Biomater Sci Eng*. 2023;9(4):1862-1890.
doi: 10.1021/acsbiomaterials.2c01183

11. Wu Y, Su H, Li M, Xing H. Digital light processing-based multi-material bioprinting: processes, applications, and perspectives. *J Biomed Mater Res A*. 2023;111(4):527-542.
doi: 10.1002/jbm.a.37473

12. Li W, Wang M, Ma H, Chapa-Villarreal FA, Lobo AO, Zhang YS. Stereolithography apparatus and digital light processing-based 3D bioprinting for tissue fabrication. *Iscience*. 2023;26(2):106039.
doi: 10.1016/j.isci.2023.106039

13. Xing F, Xu J, Yu P, et al. Recent advances in biofabrication strategies based on bioprinting for vascularized tissue repair and regeneration. *Mater Des*. 2023;111885.
doi: 10.1016/j.matdes.2023.111885

14. Song P, Li M, Zhang B, et al. DLP fabricating of precision GelMA/HAp porous composite scaffold for bone tissue engineering application. *Compos Part B: Eng*. 2022;244:110163.
doi: 10.1016/j.compositesb.2022.110163

15. Ye W, Li H, Yu K, et al. 3D printing of gelatin methacrylate-based nerve guidance conduits with multiple channels. *Mater Des*. 2020;192:108757.
doi: 10.1016/j.matdes.2020.108757

16. Peng M, Zhao Q, Wang M, Du X. Reconfigurable scaffolds for adaptive tissue regeneration. *Nanoscale*. 2023;15(13): 6105-6120.
doi: 10.1039/D3NR00281K

17. Pham CH, Zuo Y, Chen Y, Tran NM, Nguyen DT, Dang TT. Waffle-inspired hydrogel-based macrodevice for spatially controlled distribution of encapsulated therapeutic microtissues and pro-angiogenic endothelial cells. *Bioeng Transl Med*. 2023;8(3):e10495.
doi: 10.1002/btm2.10495

18. Malda J, Rouwkema J, Martens DE, et al. Oxygen gradients in tissue-engineered Pegt/Pbt cartilaginous constructs: measurement and modeling. *Biotechnol Bioeng.* 2004;86(1):9-18.
doi: 10.1002/bit.20038

19. Laschke MW, Harder Y, Amon M, et al. Angiogenesis in tissue engineering: breathing life into constructed tissue substitutes. *Tissue Eng*. 2006;12(8):2093-2104.
doi: 10.1089/ten.2006.12.2093

20. Grebenyuk S, Abdel Fattah AR, Kumar M, et al. Large-scale perfused tissues via synthetic 3D soft microfluidics. *Nat Commun*. 2023;14(1):193.
doi: 10.1038/s41467-022-35619-1

21. Zohar B, Debbi L, Machour M, et al. A micro-channel array in a tissue engineered vessel graft guides vascular morphogenesis for anastomosis with self-assembled vascular networks. *Acta Biomater*. 2022;163:182-193.
doi: 10.1016/j.actbio.2022.05.026

22. Luo Y, Zhang T, Lin X. 3D printed hydrogel scaffolds with macro pores and interconnected microchannel networks for tissue engineering vascularization. *Chem Eng J*. 2022;430:132926.
doi: 10.1016/j.cej.2021.132926

23. Tang F, Manz XD, Bongers A, et al. Microchannels are an architectural cue that promotes integration and vascularization of silk biomaterials in vivo. *ACS Biomater Sci Eng*. 2020;6(3):1476-1486.
doi: 10.1021/acsbiomaterials.9b01624

24. Lim KS, Baptista M, Moon S, Woodfield TBF, Rnjak-Kovacina J. Microchannels in development, survival, and vascularisation of tissue analogues for regenerative medicine. *Trends Biotechnol*. 2019;37(11):1189-1201.
doi: 10.1016/j.tibtech.2019.04.004

25. Miller JS, Stevens KR, Yang MT, et al. Rapid casting of patterned vascular networks for perfusable engineered three-dimensional tissues. *Nat Mater*. 2012;11(9):768-774.
doi: 10.1038/nmat3357

26. Mainardi VL, Rubert M, Sabato C, et al. Culture of 3D bioprinted bone constructs requires an increased fluid dynamic stimulation. *Acta Biomater*. 2022;153:374-385.
doi: 10.1016/j.actbio.2022.09.011

27. Homan KA, Gupta N, Kroll KT, et al. Flow-enhanced vascularization and maturation of kidney organoids in vitro. *Nat Methods*. 2019;16(3):255-262.
doi: 10.1038/s41592-019-0325-y

28. Tang MD, Golden AP, Tien J. Fabrication of collagen gels that contain patterned, micrometer-scale cavities. *Adv Mater*. 2004;16(15):1345-1348.
doi: 10.1002/adma.200400766

29. Rouwkema J, Rivron NC, van Blitterswijk CA. Vascularization in tissue engineering. *Trends Biotechnol*. 2008;26(8):434-441.
doi: 10.1016/j.tibtech.2008.04.009

30. Xia P, Luo Y. Vascularization in tissue engineering: the architecture cues of pores in scaffolds. *J Biomed Mater Res Part B App Biomater*. 2022;110(5):1206-1214. doi: 10.1002/jbm.b.34979

31. Seo JW, Kim GM, Choi Y, Cha JM, Bae H. Improving printability of digital-light-processing 3D bioprinting via photoabsorber pigment adjustment. *Int J Mol Sci*. 2022;23(10):5428. doi: 10.3390/ijms23105428

32. Chavez T, Gerecht S. Engineering of the microenvironment to accelerate vascular regeneration. *Trends Mol Med*. 2023;29(1):35-47. doi: 10.1016/j.molmed.2022.10.005

33. de Souza A, Martignago CCS, Santo GdE, et al. 3D printed wound constructs for skin tissue engineering: a systematic review in experimental animal models. *J Biomed Mater Res Part B Appl Biomater*. 2023;111(7):1419-1433. doi: 10.1002/jbm.b.35237

34. Jodat YA, Zhang T, Tanoury Z, et al. *hiPSC-Derived 3D Bioprinted Skeletal Muscle Tissue Implants Regenerate Skeletal Muscle Following Volumetric Muscle Loss*. Research Square Publications; 2021. doi: 10.21203/rs.3.rs-146091/v1

35. Ciolacu DE, Nicu R, Ciolacu F. Natural polymers in heart valve tissue engineering: strategies, advances and challenges. *Biomedicines*. 2022;10(5):1095. doi: 10.3390/biomedicines10051095

36. Yan J, Li Z, Guo J, Liu S, Guo J. Organ-on-a-chip: a new tool for in vitro research. *Biosens Bioelectron*. 2022;216:114626. doi: 10.1016/j.bios.2022.114626

37. Jakab K, Marga F, Kaesser R, et al. Non-medical applications of tissue engineering: biofabrication of a leather-like material. Mater Today Sustain. 2019;5:100018. doi: 10.1016/j.mtsust.2019.100018

38. Decante G, Costa JB, Silva-Correia J, Collins MN, Reis RL, Oliveira JM. Engineering bioinks for 3D bioprinting. *Biofabrication*. 2021;13(3):032001. doi: 10.1088/1758-5090/abec2c

39. Van den Steen PE, Dubois B, Nelissen I, Rudd PM, Dwek RA, Opdenakker G. Biochemistry and molecular biology of gelatinase B or matrix metalloproteinase-9 (MMP-9). *Crit Rev Biochem Mol Biol*. 2002;37(6):375-536. doi: 10.1080/10409230290771546

40. Nichol JW, Koshy ST, Bae H, Hwang CM, Yamanlar S, Khademhosseini A. Cell-laden microengineered gelatin methacrylate hydrogels. *Biomaterials*. 2010;31(21): 5536-5544. doi: 10.1016/j.biomaterials.2010.03.064

41. Yoon HJ, Shin SR, Cha JM, et al. Cold water fish gelatin methacryloyl hydrogel for tissue engineering application. *PLOS ONE*. 2016;11(10):e0163902. doi: 10.1371/journal.pone.0163902

42. Randhawa A, Dutta SD, Ganguly K, Patel DK, Patil TV, Lim K-T. Recent advances in 3D printing of photocurable polymers: types, mechanism, and tissue engineering application. *Macromol Biosci*. 2023;23(1):2200278. doi: 10.1002/mabi.202200278

43. Huh J, Moon Y-W, Park J, Atala A, Yoo JJ, Lee SJ. Combinations of photoinitiator and UV absorber for cell-based digital light processing (DLP) bioprinting. *Biofabrication*. 2021;13(3):034103. doi: 10.1088/1758-5090/abfd7a

44. Chen Y, Zhang J, Liu X, et al. Noninvasive in vivo 3D bioprinting. *Sci Adv*. 2020;6(23):eaba7406. doi: 10.1126/sciadv.aba7406

45. Goodarzi Hosseinabadi H, Dogan E, Miri AK, Ionov L. Digital light processing bioprinting advances for microtissue models. *ACS Biomater Sci Eng*. 2022;8(4):1381-1395. doi: 10.1021/acsbiomaterials.1c01509

46. Alberts B, Johnson A, Lewis J, et al. The extracellular matrix of animals. In: *Molecular Biology of the Cell*. 4th ed. New York: Garland Science; 2002.

47. Lee RC, Ping J. Calcium antagonists retard extracellular matrix production in connective tissue equivalent. *J Surg Res*. 1990;49(5):463-466. doi: 10.1016/0022-4804(90)90197-A

48. Schmid GJ, Kobayashi C, Sandell LJ, Ornitz DM. Fibroblast growth factor expression during skeletal fracture healing in mice. *Dev Dyn*. 2009;238(3):766-774. doi: 10.1002/dvdy.21882

49. Ross R. The fibroblast and wound repair. *Biol Rev*. 1968;43(1):51-91. doi: 10.1111/j.1469-185X.1968.tb01109.x

50. Darby IA, Hewitson TD. Fibroblast differentiation in wound healing and fibrosis. *Int Rev Cytol.* 2007;257:143-179. doi: 10.1016/S0074-7696(07)57004-X

51. Seo JW, Moon JH, Jang G, et al. Cell-laden gelatin methacryloyl bioink for the fabrication of Z-stacked hydrogel scaffolds for tissue engineering. *Polymers*. 2020;12(12):3027. doi: 10.3390/polym12123027

52. Leu Alexa R, Iovu H, Ghitman J, et al. 3D-printed gelatin methacryloyl-based scaffolds with potential application in tissue engineering. *Polymers*. 2021;13(5):727. doi: 10.3390/polym13050727

53. Zu G, Meijer M, Mergel O, Zhang H, van Rijn P. 3D-printable hierarchical nanogel-GelMA composite hydrogel system. *Polymers*. 2021;13(15):2508. doi: 10.3390/polym13152508

54. Ma C, Choi J-B, Jang Y-S, et al. Mammalian and fish gelatin methacryloyl–alginate interpenetrating polymer network hydrogels for tissue engineering. *ACS Omega*. 2021;6(27):17433-17441. doi: 10.1021/acsomega.1c01806

55. Garbern JC, Hoffman AS, Stayton PS. Injectable pH- and temperature-responsive poly(N-isopropylacrylamide-co-propylacrylic acid) copolymers for delivery of angiogenic growth factors. *Biomacromolecules*. 2010;11(7):1833-1839.
doi: 10.1021/bm100318z

56. Yu K, Zhang X, Sun Y, et al. Printability during projection-based 3D bioprinting. *Bioact Mater*. 2022;11:254-267.
doi: 10.1016/j.bioactmat.2021.09.021

57. Zeltinger J, Sherwood JK, Graham DA, Müeller R, Griffith LG. Effect of pore size and void fraction on cellular adhesion, proliferation, and matrix deposition. *Tissue Eng*. 2001;7(5):557-572.
doi: 10.1089/107632701753213183

58. Rather JA, Akhter N, Ashraf QS, et al. A comprehensive review on gelatin: Understanding impact of the sources, extraction methods, and modifications on potential packaging applications. *Food Pkg Shelf Life*. 2022;34:100945.
https://www.sciencedirect.com/science/article/pii/S2214289422001375

59. Andreazza R, Morales A, Pieniz S, Labidi J. Gelatin-based hydrogels: potential biomaterials for remediation. *Polymers*. 2023;15(4):1026.
doi: 10.3390/polym15041026

60. Jensen C, Teng Y. Is it time to start transitioning from 2D to 3D cell culture? *Front Mol Biosci*. 2020;7:33.
doi: 10.3389/fmolb.2020.00033

61. Wang Y, Huang X, Shen Y, et al. Direct writing alginate bioink inside pre-polymers of hydrogels to create patterned vascular networks. *J Mater Sci*. 2019;54(10):7883-7892.
doi: 10.1007/s10853-019-03447-2

62. Ying GL, Jiang N, Maharjan S, et al. Aqueous two-phase emulsion bioink-enabled 3D bioprinting of porous hydrogels. *Adv Mater*. 2018;30(50):e1805460.
doi: 10.1002/adma.201805460

63. Song YS, Lin RL, Montesano G, et al. Engineered 3D tissue models for cell-laden microfluidic channels. *Anal Bioanal Chem*. 2009;395(1):185-193.
doi: 10.1007/s00216-009-2935-1

64. Rnjak-Kovacina J, Wray LS, Golinski JM, Kaplan DL. Arrayed hollow channels in silk-based scaffolds provide functional outcomes for engineering critically sized tissue constructs. *Adv Funct Mater*. 2014;24(15):2188-2196.
doi: 10.1002/adfm.201302901

65. Wen N, Qian E, Kang Y. Effects of macro-/micro-channels on vascularization and immune response of tissue engineering scaffolds. *Cells*. 2021;10(6):1514.
doi: 10.3390/cells10061514

66. Xie Y, Hardouin P, Zhu Z, Tang T, Dai K, Lu J. Three-dimensional flow perfusion culture system for stem cell proliferation inside the critical-size β-tricalcium phosphate scaffold. *Tissue Eng*. 2006;12(12):3535-3543.
doi: 10.1089/ten.2006.12.3535

67. Nii T, Makino K, Tabata Y. Influence of shaking culture on the biological functions of cell aggregates incorporating gelatin hydrogel microspheres. *J Biosci Bioeng*. 2019;128(5):606-612.
doi: 10.1016/j.jbiosc.2019.04.013

68. Limraksasin P, Kosaka Y, Zhang M, et al. Shaking culture enhances chondrogenic differentiation of mouse induced pluripotent stem cell constructs. *Sci Rep*. 2020;10(1):14996.
doi: 10.1038/s41598-020-72038-y

69. Li C, Kuss M, Kong Y, et al. 3D printed hydrogels with aligned microchannels to guide neural stem cell migration. *ACS Biomater Sci Eng*. 2021;7(2):690-700.
doi: 10.1021/acsbiomaterials.0c01619

70. Han J, Park S, Kim JE, et al. Development of a scaffold-on-a-chip platform to evaluate cell infiltration and osteogenesis on the 3D-printed scaffold for bone regeneration. *ACS Biomater Sci Eng*. 2023;9(2):968-977.
doi: 10.1021/acsbiomaterials.2c01367

71. Dhwaj A, Roy N, Jaiswar A, Prabhakar A, Verma D. 3D-printed impedance micropump for continuous perfusion of the sample and nutrient medium integrated with a liver-on-chip prototype. *ACS Omega*. 2022;7(45):40900-40910.
doi: 10.1021/acsomega.2c03818

72. Gao J, Li M, Cheng J, et al. 3D-printed GelMA/PEGDA/F127DA scaffolds for bone regeneration. *J Funct Biomater*. 2023;14(2):96.
doi: 10.3390/jfb14020096

73. Ma H, Xing F, Yu P, et al. Integrated design and fabrication strategies based on bioprinting for skeletal muscle regeneration: current status and future perspectives. *Mater Des*. 2023;225:111591.
doi: 10.1016/j.matdes.2023.111591

74. Yu Q, Wang Q, Zhang L, et al. The applications of 3D printing in wound healing: the external delivery of stem cells and antibiosis. *Adv Drug Del Rev*. 2023;197:114823.
doi: 10.1016/j.addr.2023.114823

ACCSCIENCE PUBLISHING

International Journal of Bioprinting

RESEARCH ARTICLE

Effects of modeling strategies of triply periodic minimal surface on the mechanical properties and permeability of biomedical TC4 porous scaffolds

Binghao Wang[1,2†], Chengliang Yang[1,2†], Chuanchuan Zheng[1,2†], Miao Luo[1,2], Zheng Shi[3], Yuting Lv[3*], Wen Peng[4*], and Liqiang Wang[5,6*]

[1]Affiliated Hospital of Youjiang Medical University for Nationalities, Youjiang Medical University for Nationalities, Baise, Guangxi, China

[2]Guangxi Key Laboratory of Basic and Translational Research of Bone and Joint Degenerative Diseases, Guangxi Biomedical Materials Engineering Research Center for Bone and Joint Degenerative Diseases, Guangxi Health Commission Key Laboratory of Clinical Medicine Research on Bone and Joint Degenerative Diseases Cohort, Guangxi Health Commission Key Laboratory of Biomedical Materials Research, Baise, Guangxi, China

[3]College of Mechanical and Electronic Engineering, Shandong University of Science and Technology, Qingdao, Shandong, China

[4]Orthopedic Implant (Stable) Engineering Technology Research Center, Foshan, Guangdong, China

[5]State Key Laboratory of Metal Matrix Composites, Shanghai Jiao Tong University, Shanghai, China

[6]National Center for Translational Medicine, Shanghai Jiao Tong University, Shanghai, China

(This article belongs to the Special Issue: *Special Issue of International Journal of Bioprinting in the BDMC 2023 Conference*)

Abstract

Modeling strategies play a crucial role in determining the unit shapes of triply periodic minimal surface (TPMS), significantly affecting the mechanical and permeability properties of porous scaffolds. In this study, two distinct strategies including surface thickening and surface filling were used to construct scaffold models based on four basic TPMS structures (Primitive [P], Gyroid [G], Diamond [D], and I-graph-wrapped package [IW-P]). These models were successfully prepared using TC4 alloy and selective laser melting technology. Macro/micro morphology, mechanical properties, and permeability tests of porous implants were carried out. The results indicate that the scaffolds effectively replicated the designed models, exhibiting mechanical properties that match those of human tissue. The elastic modulus ranges from 3.03 to 4.57 GPa, and the tensile strength varies between 135.78 and 250.90 MPa. The surface thickening strategy alters the material distribution within the unit, enhancing load uniformity on the scaffolds, thereby increasing the strength of the scaffolds with G, D, and IW-P units, while reducing stress fluctuations during compression. In contrast, the surface filling structure exhibits excellent permeability, with permeability rates falling within the range of 0.88 to 1.91 $\times 10^{-9}$ m^2, aligning with the permeability performance of trabecular bone. This study offers new insights into the design of porous scaffold models tailored for various application scenarios.

Keywords: Porous scaffolds; Triply periodic minimal surface; Mechanical performance; Modeling strategies

†These authors contributed equally to this work.

***Corresponding authors:**
Yuting Lv
(lyt8608@126.com)

Wen Peng
(pw911210@hotmail.com)

Liqiang Wang
(Wang_liqiang@sjtu.edu.cn)

Citation: Wang B, Yang C, Zheng C, et al. Effects of modeling strategies of triply periodic minimal surface on the mechanical properties and permeability of biomedical TC4 porous scaffolds. *Int J Bioprint*. 2024;10(3):2565. doi: 10.36922/ijb.2565

Received: December 28, 2023
Accepted: February 16, 2024
Published Online: March 29, 2024

Copyright: © 2024 Author(s). This is an Open Access article distributed under the terms of the Creative Commons Attribution License, permitting distribution, and reproduction in any medium, provided the original work is properly cited.

Publisher's Note: AccScience Publishing remains neutral with regard to jurisdictional claims in published maps and institutional affiliations.

1. Introduction

Titanium and its alloys are known for their excellent strength, corrosion resistance, and biocompatibility, making them widely utilized in the treatment of various medical conditions, such as orthopedics, cardiovascular surgery, and dental procedures.[1-3] However, the commonly used Ti alloy such as TC4 alloy possesses an elastic modulus as high as 110 GPa, which significantly exceeds the 0.3–30 GPa range of the human bone's modulus. The prolonged presence of the alloy in the human body can lead to the "stress shielding" effect, causing atrophy in the surrounding tissues due to the lack of mechanical stimulation and resulting in the instability of hard tissue interfaces.[4] Therefore, reducing the modulus of titanium alloy implants and improving the adaptation of mechanical properties are the key problems waiting to be addressed.

The porous structure design can reduce the amount of material used, improve the deformation of the implant when loaded, and reduce the modulus of elasticity.[5] Additionally, interconnected porous structures promote cell adhesion, proliferation, and differentiation.[6] The preparation process of porous titanium structures has a bearing on the excellent properties in the structures produced. With the continuous upgrading of processing technology, the technologies employed in the preparation approaches of medical porous titanium alloys have underwent tremendous transition, encompassing powder sintering method,[7] porogen methods,[8] fiber weaving,[9] and gel injection molding.[10] The rise of additive manufacturing technology has facilitated the gradual development of structure and properties of porous titanium alloy implants in terms of complexity and precision control. Selective laser melting (SLM) is a widely used method in additive manufacturing of metallic materials. This process involves slicing the three-dimensional (3D) model to obtain the shape of each section, followed by path planning. The laser or nozzle scanning path is then passed to the control system, allowing for the "free manufacturing" of the part by sintering or extruding the material.[11] In the SLM process, parameters such as laser power and scan rate have an impact on the microstructure and mechanical properties of the sample. When dealing with complex porous structures, the spot diameter and powder properties directly influence the surface quality of the material.[12-14] This technology has led to the development of systematic modeling approaches, including computer-aided design (CAD)-assisted design, topology optimization, medical image-based reverse modeling, and digital design.[15] Among these digital modeling methods, minimal surface structures have gained extensive attention from researchers due to their continuous inter-unit transition, substantial surface area, and controllable characteristics.

The triply periodic minimal surface (TPMS) structure is a lattice arrangement characterized by a zero mean radius of curvature.[16] It exhibits notable features, including high specific strength and enhanced permeability,[17,18] and is widely used in energy absorption,[19] porous electrodes,[20] heat exchangers,[21] porous filters, and other fields.[22] In addition, the structural parameters (such as cell type, pore size, and porosity) of the minimal surface can be adjusted by digital modeling to achieve the regulation of the mechanical properties of the tissue engineering scaffold.[23] Lv et al.[24] investigated scaffolds with different pore sizes (500, 750, and 900 μm) using the G unit as the basic structure, and found that the scaffolds exhibited an elastic modulus ranging from 0.80 to 1.05 GPa with high ductility (15.3–19.1%). The strength of scaffolds was significantly influenced by pore size, with the 750 μm pore size exhibiting the highest strength. Ma et al.[25] explored the impact of varying porosities (75.1–88.8%) on the mechanical and permeability properties of scaffolds, and found that the modulus and strength of scaffold ranged from 0.31 to 1.12 GPa and 6.93 to 29.15 MPa, respectively, with mechanical performance decreasing as porosity increased. Permeability ranged from 0.29 to 3.91×10^{-9} m^2, increasing with greater pore size and porosity. In addition to adjusting the cell and porosity, the researchers took full advantage of the digital tuning of the minimal surface structure to obtain the bionic porous gradient porous structure. Ma et al.[26] discretized the original model using a conformal refinement of all-hexahedral meshes and mapped the TPMS cells onto the mesh elements with the help of shape functions. The finite element simulation results show that the mechanical properties of the improved scaffold model exhibit anisotropy, with improved elasticity, strength, and especially energy absorption. Yang et al.[27] utilized the sigmoid function (SF) method and the Gaussian radial basis function (GRBF) method to place the TPMS cells on a given 3D subspace and make a perfect transition with their neighboring substructures in the scaffold domain to achieve the fusion of different cells.

Besides pore size, porosity, and gradient distribution, differences between the modeling strategies can also have an impact on porous structural changes, such as on the human spine, which serves as a critical support structure. The interior of spinal joints features a filled porous structure (see Figure 1A), ensuring load-bearing capability in the vertical direction. Additionally, leg bones, as one of the largest and longest bones in the human body (see Figure 1B), have thicker cortical bone sections on the periphery to bear loads, while the interior evolves into a hollow structure to reduce modulus and provide cushioning and shock absorption. It is reasonable to infer that, based on minimal surface structures and employing different modeling methods, it is possible to enhance their

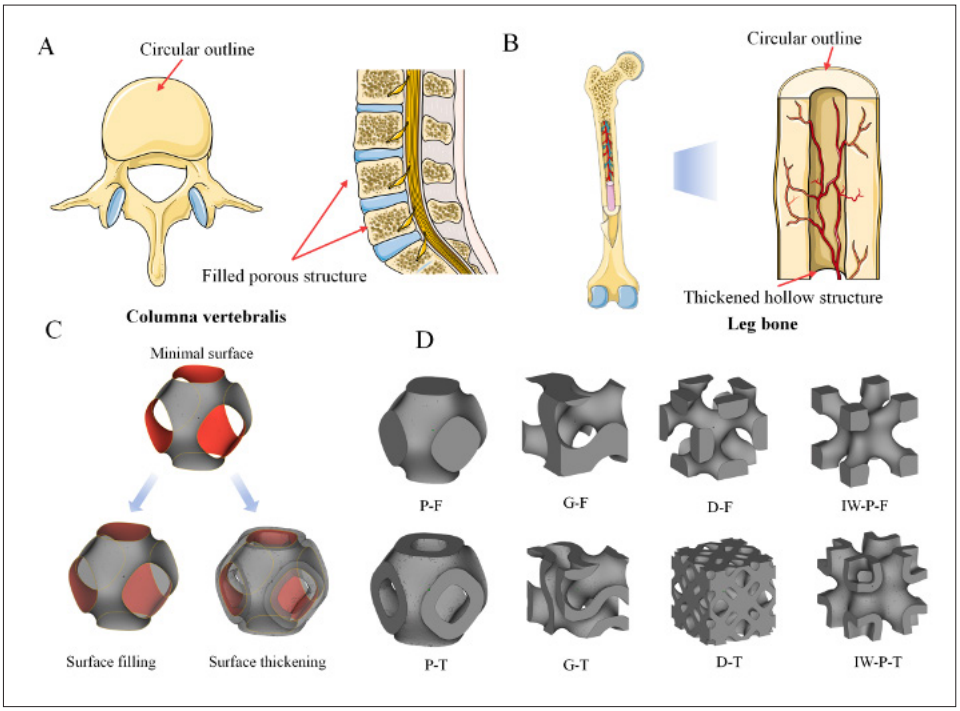


Figure 1. (A) Filling structure in the spine. (B) Thickening structure in the leg bone. (C) Minimal surface units with thickening and filling. (D) Resulting units under the two modeling strategies. Abbreviations: D, Diamond; F, Fill; G, Gyroid; IW-P, I-graph-wrapped package; P, Primitive; T, Thicken.

mechanical performance while retaining their continuous transition advantages.

Hence, four commonly used minimal surfaces—Primitive (P), Gyroid (G), Diamond (D), and I-graph-wrapped package (IW-P)—were selected as the basic units of minimal porous scaffolds in this study. Maintaining consistent unit size, surface offset, and porosity, two modeling strategies, filling and thickening, were employed on these surfaces (see Figure 1C) to create porous scaffold units (see Figure 1D). Scanning electron microscopy, micro-computed tomography (micro-CT), and other equipment were used to observe the macro/micro morphologies of the additive-manufactured porous TC4 alloy scaffolds. Compression tests were carried out to investigate the deformation mechanism and mechanical performance variations of the scaffolds. The effect of filling and thickening strategies on the permeability of the scaffold was investigated by using the descending head method and finite element analysis.

2. Scaffold fabrication and performance characterization

2.1. Scaffold design and fabrication

The mathematical functions from Table 1 were imported into Mathematica software to generate surfaces and fill porous scaffolds. For the filled structure, the ContourPlot3D command in Mathematica software was employed, where the formula was input, and the offset position of the surface was adjusted by controlling the parameter C to achieve a filled porous scaffold with a porosity of 60%. As for the thickened structure, the surface is imported into Wrap software for surface thickening to obtain the thickened porous scaffolds (as shown in Figure 2). The samples were fabricated using a selective laser melting device (Dimetal 280, Tridonic Additive Technology Co., Ltd., Canton, China) with a powder composition of Ti6Al4V (TC4) alloy. The printing parameters were as follows: laser power of 175 W, powder layer thickness of 30 μm, laser spot size of 180 μm, and scanning speed of 1000 mm/s. The scan direction was rotated by 67° between consecutive layers. After printing was completed, the scaffolds were cut from the substrate and cleaned in ultrasonic baths with ethanol for further use.

2.2. Macro- and microscopic characterization of scaffolds

The scaffold porosity was determined using the drainage method,[28] with the calculation formula presented in Equation I. In the equation, P represents the sample's porosity (%), m_w is the mass (g) of the sample immersed in pure water, m_d is the mass (g) of the scaffold, V_d is the

Table 1. Modeling formulas for triply minimal surface structures

Unit structure	Formulas
P	$\phi(x,y,z)=\cos\left(\frac{2\pi}{3L}x\right)+\cos\left(\frac{2\pi}{3L}y\right)+\cos\left(\frac{2\pi}{3L}z\right)=C$
G	$\phi(x,y,z)=\cos\left(\frac{2\pi}{3L}x\right)\sin\left(\frac{2\pi}{3L}y\right)+\cos\left(\frac{2\pi}{3L}y\right)\sin\left(\frac{2\pi}{3L}z\right)+\cos\left(\frac{2\pi}{3L}z\right)\sin\left(\frac{2\pi}{3L}x\right)=C$
D	$\phi(x,y,z)=\cos\left(\frac{2\pi}{3L}x\right)\cos\left(\frac{2\pi}{3L}y\right)\cos\left(\frac{2\pi}{3L}z\right)-\sin\left(\frac{2\pi}{3L}x\right)\sin\left(\frac{2\pi}{3L}y\right)\sin\left(\frac{2\pi}{3L}z\right)=C$
IW-P	$\phi(x,y,z)=2\left(\cos\left(\frac{2\pi}{3L}x\right)\cos\left(\frac{2\pi}{3L}y\right)+\cos\left(\frac{2\pi}{L}z\right)\cos\left(\frac{2\pi}{3L}x\right)\right.$ $\left.+\cos\left(\frac{2\pi}{3L}y\right)\cos\left(\frac{2\pi}{3L}z\right)\right)-\left(\cos\left(\frac{4\pi}{3L}x\right)+\cos\left(\frac{4\pi}{3L}y\right)+\cos\left(\frac{4\pi}{3L}z\right)\right)=C$

Abbreviations: D, Diamond; G, Gyroid; IW-P, I-graph-wrapped package; P, Primitive.

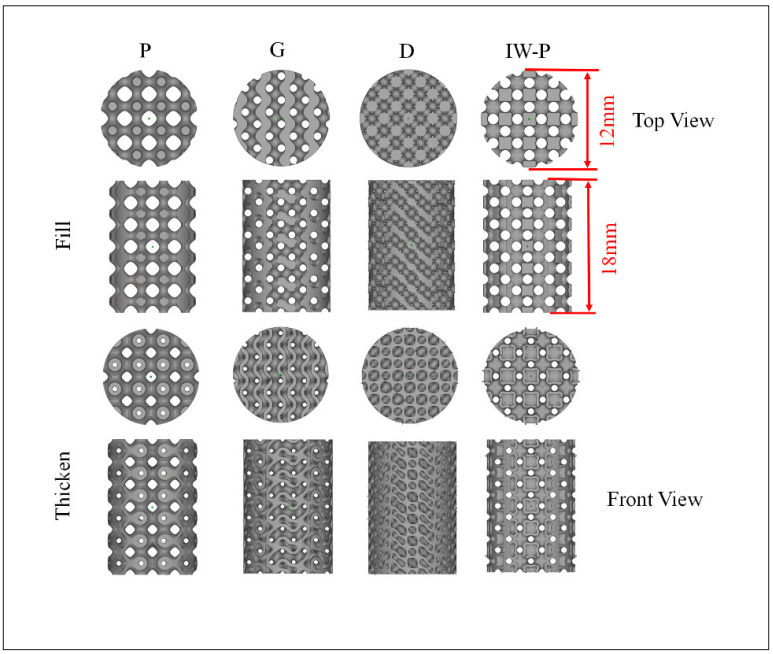


Figure 2. Porous scaffold models designed with two modeling strategies.

geometric volume of the porous scaffold (cm^3), and ρ_w is the density of pure water (g/cm^3). After cleaning and drying the scaffold, its weight was measured. The scaffold was then immersed in a beaker containing ultra-pure water and secured with a fine thread to ensure complete filling of the scaffold's pores. The weight of the scaffold in water was measured, and relevant parameters during the experiment were recorded.

$$P=\frac{m_w-m_d}{\rho_w V_d}\times 100\% \quad \text{(I)}$$

The geometric characteristics of the scaffolds were observed using an optical microscope (OM, VHX-500F, Keyence, Japan). The scaffolds were scanned, and their 3D images were reconstructed using micro-CT (PerkinElmer,

Quantum GX II), which allowed for the documentation of the external structure and the calculation of porosity. The CT scan parameters were set to 90 kV for voltage, 80 μA for current, and 14 min for scanning duration. The top of the porous scaffolds was imaged using a JEM-2100F scanning electron microscope, and DM software was used to analyze structural features, including pore size and strut dimensions.

2.3. Mechanical performance testing

According to the mechanical testing standard, ISO 13314, for porous and cellular metallic materials,[29-31] compression and tensile tests were conducted at room temperature using an electronic universal testing machine (Suns, Shenzhen, China). At least three samples were compressed for each structural sample. The compression strain rate was set at 0.5 mm/min until the samples became fully dense or fractured. The fracture morphology of the scaffolds was recorded using a camera. Stress–strain curves were plotted; yield strength, ultimate strength, elastic modulus, and other mechanical properties were calculated; and the data were expressed as mean ± standard deviation (SD).

2.4. Permeability performance testing and simulation of scaffolds

The permeability performance of the scaffolds was tested using the falling head method, as illustrated in Figure 3A. The scaffold permeability (k) was calculated using Darcy's law, given in Equation II.[32-34] To facilitate the calculation, the ratio of height H_1 to H_2 was set to be equal to *e*. The time difference *t* ($t = t_1 - t_0$) was recorded for the fall of the horizontal plane.

$$k = \frac{\mu h A}{\rho g t a} \times \frac{lgH_1 - lgH_2}{lg\, e} \quad \text{(II)}$$

The parameters used in the formula are selected and shown in Table 2.

Using the computational fluid dynamics software ANSYS 16.0 Workbench with the Fluent module, a fluid simulation analysis was conducted on individual scaffold units, as illustrated in Figure 3B. The entrance flow velocity was set to 0.01 m/s to investigate the structural factors affecting permeability, with an outlet pressure of 0 Pa. The wall was assumed to be non-slip, and the minimum unit size was set to 0.01 mm to analyze the effect of the modeling strategy on the permeability from a microscopic point of view.

3. Results and discussion

3.1. Macro- and microscopic characteristics of scaffolds

Figure 4A and B depicts the external morphology of the scaffolds under optical microscopy and the CT-reconstructed morphology for comparison. From the

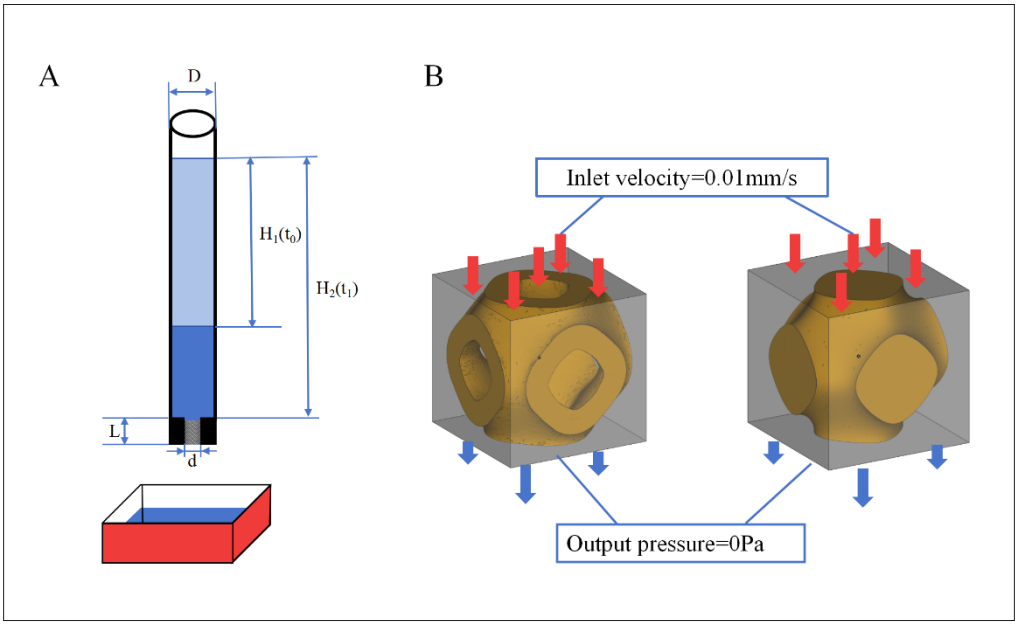


Figure 3. (A) Schematic of permeability experiment. (B) Finite element boundary conditions for permeability. Abbreviations: d, diameter of the sample; D, diameter of the water pipe; H1, height of the liquid level before the test; H2, height at which the test stops, where H2/H1 = e; L, length of the sample in the direction of the water flow.

Table 2. Parameters in the formula for calculating permeability

Symbol	Parameter	Value
M	Dynamic viscosity coefficient of water	10^{-3} Pa·s
H	Height of samples	18 mm
A	The cross-sectional area of the water column	490.625 mm^2
A	The cross-sectional area of the scaffold	113.04 mm^2
P	Density of water	10^3 kg/m^3
G	Gravity acceleration	9.8 m/s^2

images, it can be observed that the porous structures between different scaffolds are well-constructed, and there are no apparent blockages in the porous scaffolds. Interconnected porous networks have been shown to promote inward bone growth.[35] Table 3 shows the design parameters and measured porosities among different porous scaffolds. It is evident that there is a difference between the designed porosity and the porosity measured using the drainage method, with the printed scaffold's porosity being higher than the design value. However, the overall error in the scaffolds is approximately 2%, indicating a certain degree of repeatability in the additive manufacturing of porous scaffolds.

Table 3 presents the design parameters and actual porosity of the scaffold. A more in-depth analysis of the data reveals a discernible pattern in the impact of structural units and modeling strategies on scaffold porosity. It is evident that the porosity of the scaffolds consistently increased, indicating material reduction during processing. This reduction is primarily attributed to the step effect inherent in the printing process, particularly when there are substantial changes in the surface angles, resulting in material reduction at the scaffold edges. Notably, the porosity of the thickened minimum surface scaffold is significantly higher than that of the equivalent surface-filled scaffold across different modeling strategies.

Table 3. Parameters of the scaffolds

	Design porosity (%)	Design surface area (mm^2)	Actual porosity (%)
P-F	60	1831	61.95
P-T	60	3293	63.39
G-F	60	2416	60.09
G-T	60	4220	60.95
D-F	60	2860	61.84
D-T	60	5287	62.29
IW-P-F	60	2617	62.01
IW-P-T	60	4933	62.62

Abbreviations: D, Diamond; F, Fill; G, Gyroid; IW-P, I-graph-wrapped package; P, Primitive; T, Thicken.

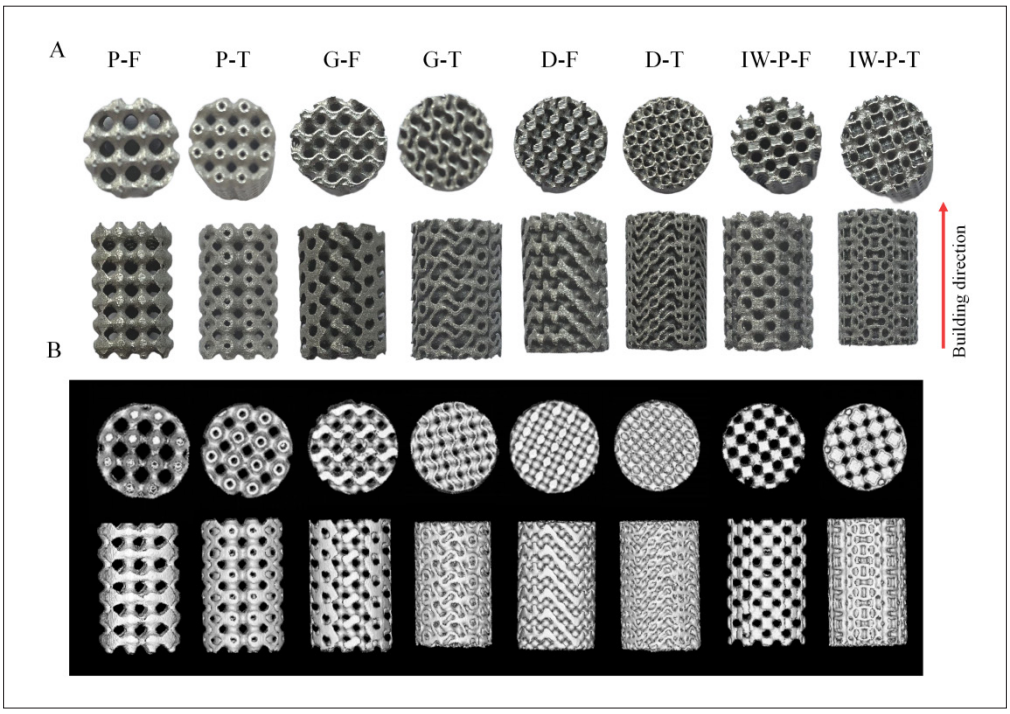


Figure 4. (A) Appearance of the scaffold under optical microscopy. (B) Scaffold's image captured with micro-CT. Abbreviations: D, Diamond; F, Fill; G, Gyroid; IW-P, I-graph-wrapped package; P, Primitive; T, Thicken.

This discrepancy arises from the larger surface area of the thickened scaffold compared to the filled scaffold, coupled with its more intricate surface structure. Consequently, the path of the laser scan is longer and errors accumulate, leading to greater differences in porosity.[36] Despite introducing some errors, the large specific surface area of the thickened surface structure is more advantageous for early osteoblast attachment than that of the filled structure.

To assess the dimensional accuracy of the samples, the top of the scaffolds was observed using a scanning electron microscope, and the morphological differences between different units and modeling methods were compared. The results are shown in Figure 5A–H. From the images, it is evident that there are manufacturing deviations on the top surface of different scaffolds. Some residual unmelted powder particles exist on the material surface, giving it a certain degree of roughness (as shown in Figure 5D). This roughness provides adhesion points for cell attachment, promoting cell adhesion, proliferation, differentiation, and the opening of membrane channels.[37] At the same time, there are potential defects in small or fragile structures (see Figure 5F and G). This is mainly because these areas have thinner dimensions, and the laser is more likely to cause damage due to high power, which is one of the significant reasons for the actual porosity of the scaffold being higher than the design porosity.[38]

From the images, it is also apparent that there are significant differences in the sizes of scaffolds with different units. The structure of porous units is intricate, and variations exist in the definitions of their pore diameters.[39,40] Taking into account the impact of the scaffold structure on permeability, this paper adopts the maximum projected diameter of the cross-sectional pore as the designated pore diameter. When viewed from the top, P unit-filled scaffolds have the largest pore size, measuring 2.08 mm. After the surface is thickened, the pore size decreases, and the pore distribution becomes more dispersed. Apart from the P unit scaffold, the order of pore sizes in the various unit scaffolds is IW-P > G > D. Biological materials require specific pore sizes to promote inward bone growth, and pore sizes within the range of 100–900 μm are considered suitable for bone ingrowth.[41] Therefore, the porous scaffolds prepared in this study possess favorable osteogenic properties in terms of size. In addition, different strut sizes and pore sizes also have a significant impact on subsequent mechanical and permeability performance.[42]

3.2. Deformation behavior and mechanical performance of the scaffolds

Figure 6A–D displays stress–strain curves after static compression tests. From the figures, it can be observed that the compression process of the scaffolds mainly goes through three stages, which are: (1) the linear increase in stress leading to the yielding stage, (2) fluctuations after the first stress peak, and (3) rapid stress increase in the densification stage (a typical case is shown in Figure 6D). Different modeling strategies have a significant impact on the stress–strain curves of the scaffolds. For G, D, and IW-P structures, surface thickening results in an increased ultimate strength of the porous scaffolds, reduces the fluctuation in the platform stage during the compression stage (2), and postpones the material's fracture strain.

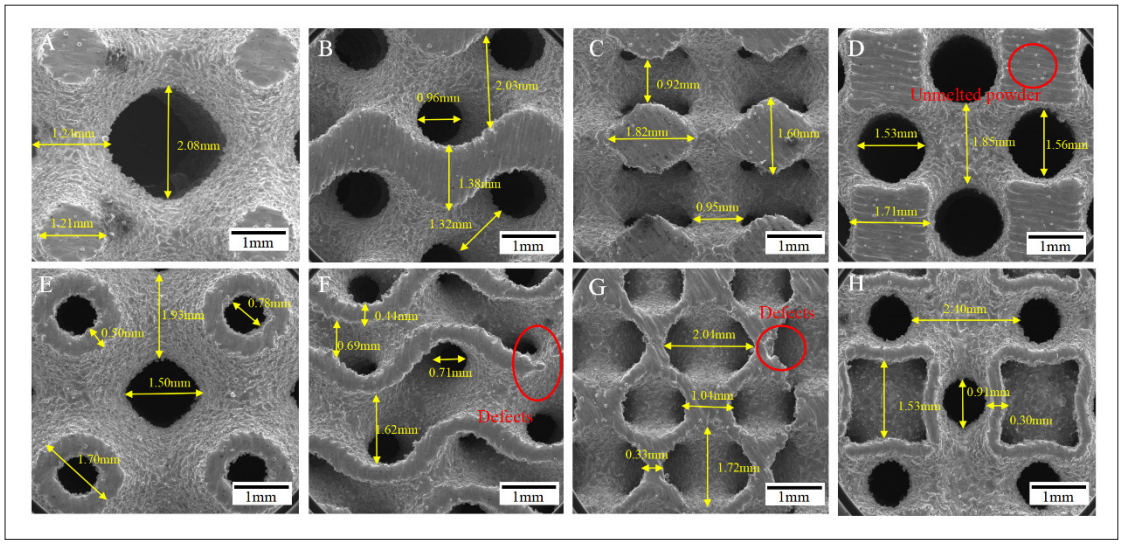


Figure 5. Scanning electron microscopy (SEM) images of the top surfaces of different units. (A) P-F structure. (B) G-F structure. (C) D-F structure. (D) IW-P-F structure. (E) P-T structure. (F) G-T structure. (G) D-T structure. (H) IW-P-T structure. The images were captured under 10 × magnification. Abbreviations: D, Diamond; F, Fill; G, Gyroid; IW-P, I-graph-wrapped package; P, Primitive; T, Thicken.

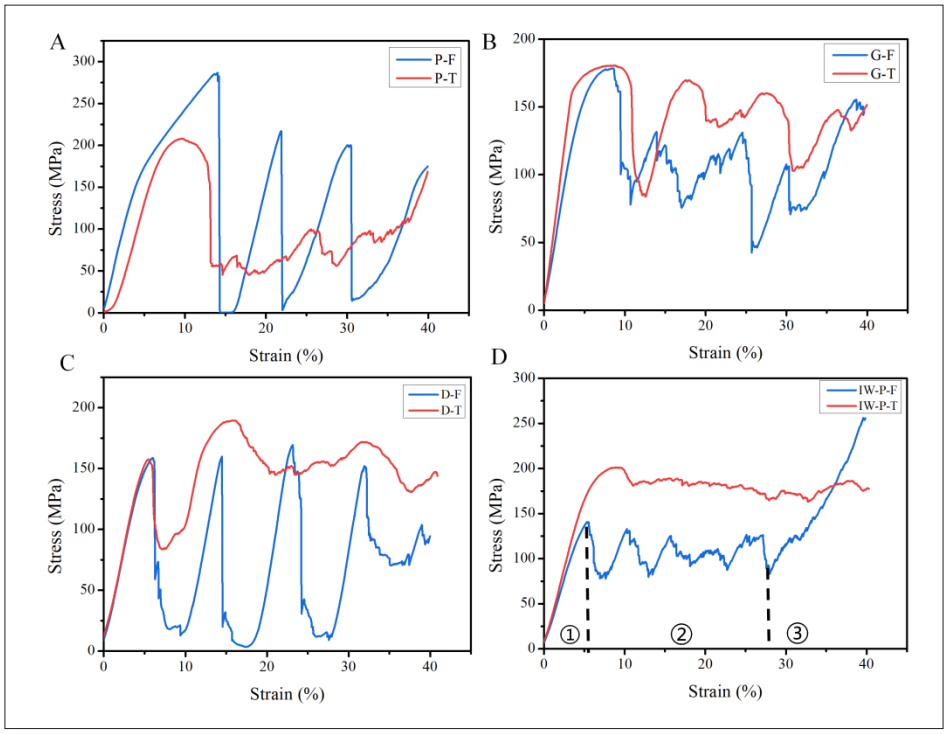


Figure 6. Stress–strain curves for different structures. (A) P-T and P-F scaffolds. (B) G-T and G-F scaffolds. (C) D-T and D-F scaffolds. (D) IW-P-T and IW-P-F scaffolds and three stages of the compression process. Abbreviations: D, Diamond; F, Fill; G, Gyroid; IW-P, I-graph-wrapped package; P, Primitive; T, Thicken.

However, the P structure exhibits different results from the other three structures, as it is a more concentrated material with larger pillar sizes, enabling it to bear stress more effectively in the vertical direction.[43]

Figure 7 shows the deformation behavior of the scaffolds at 5%, 10%, and 30% strain during the compression process. All scaffolds fracture through the formation of extrusion bands, but the position and angle of fracture faces vary for different units and modeling strategies. The results are consistent with the team's earlier research,[44,45] indicating that the fracture in scaffolds is most likely to occur at stress concentration points. In the P minimal surface-filled scaffold, the pillar sizes at the unit connections are the smallest and oriented horizontally. Thus, the maximum stress is in the horizontal direction, and the fracture face is also horizontal. When the pressure exceeds the load-bearing capacity, some pillar structures may fail, leading to collapse and fragmentation, and forming a serrated platform and pillar fracture.

The thickening strategy has an impact on the fracture faces of the scaffolds. The P minimal surface-thickened scaffold exhibits a different pattern, with shear band failure along the diagonal. The possible reason is that surface thickening disperses the material, reducing its resistance in the vertical direction, and internal defects can also lead to scaffold fracture along the diagonal.[46] The G, D, and IW-P-filled scaffolds correspond to previous research results, with failure occurring along the diagonal shear band.[47] It is worth noting that the fracture band of the D minimal surface-thickened scaffold is almost perpendicular to the loading direction of the scaffold. After compression, the scaffold shows a barrel-shaped contour, and this expansion increases the lateral resistance of the structure, enhancing its load-bearing capacity in the later stages of compression. Overall, the surface thickening method reduces the distance between units in the scaffold, improves the overall load uniformity, and enhances the deformability of the entire sample during the compression process. This is reflected in the significant reduction in stress fluctuations in the stress–strain curve for the thickened scaffold. Compared to the filled scaffold, the thickened scaffold can more effectively distribute the compression load, avoiding sudden and severe failure.

Table 4 shows the mechanical performance of the porous scaffolds. It can be observed that the ultimate strength of the scaffolds varies between 135.78 and 250.90 MPa, and the modulus ranges from 3.03 to 4.57 GPa. The compressive properties of human bone are influenced by age and location, with Young's modulus and yield strength in the range of 0.3–30 GPa and 33–193 MPa, respectively.[48]

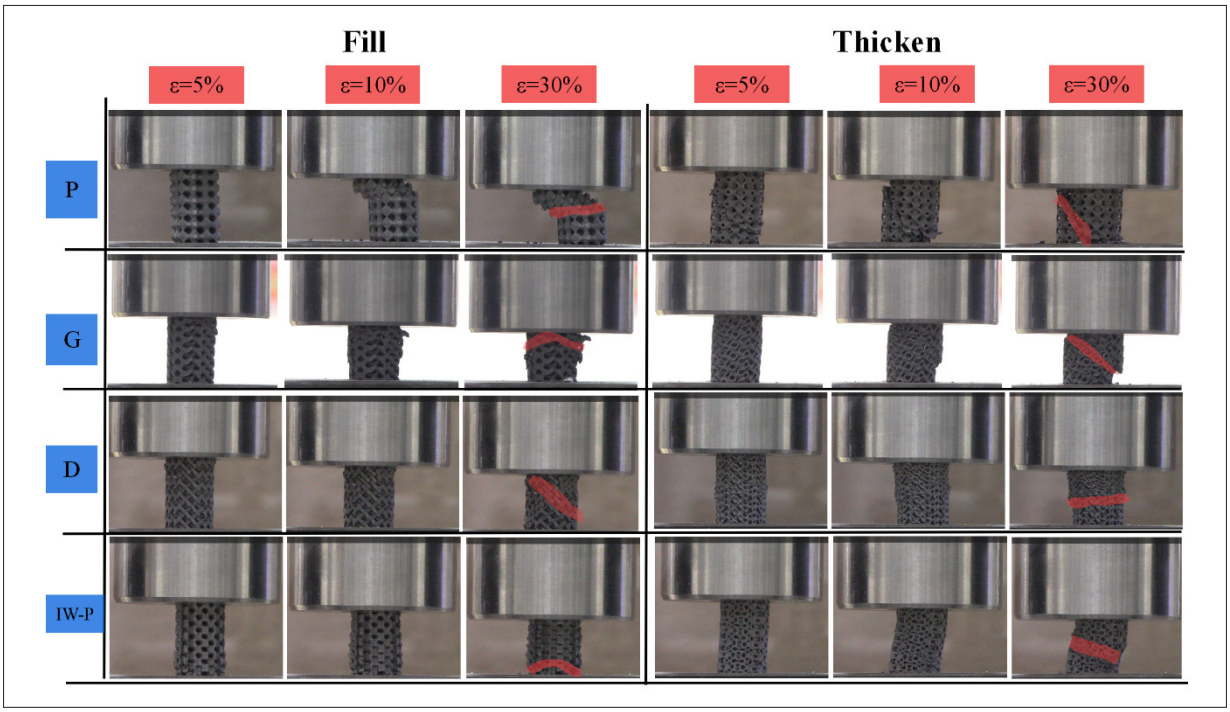


Figure 7. Compression deformation behavior of different scaffolds. Abbreviations: D, Diamond; F, Fill; G, Gyroid; IW-P, I-graph-wrapped package; P, Primitive; T, Thicken.

The results showed that the elastic modulus of the scaffolds was comparable to the modulus of human bone, confirming that the use of porous structures is an effective way to reduce the modulus and the "stress shielding" effect.[49]

Figure 8A–C shows the comparison of mechanical performance among different scaffolds. When looking at different minimal surface unit types, the order of scaffold ultimate strength is P > G > D > IW-P, and the order of elastic modulus is similar to the strength ranking. When considering the two modeling methods, surface thickening and filling, for G, D, and IW-P structures, surface thickening slightly increases or maintains the scaffold's ultimate strength, elastic modulus, and fracture strain. This is mainly because surface thickening increases the uniform distribution of material in the horizontal direction, enhancing the material's resistance to vertical loads. In the case of the P-filled structure, the material's own structural pillar size is larger, resulting in a more pronounced homogenization effect.[50] The stress it experiences is significantly greater in the vertical direction compared to the horizontal direction, with vertical pillars primarily bearing the load. Figure 8D demonstrates the performance of the scaffolds prepared in this work

Table 4. Mechanical performance of different scaffolds

	Yield strength (MPa)	Ultimate strength (MPa)	Elastic modulus (GPa)	Ductility (%)
P-F	155.14 ± 7.58	250.90 ± 35.57	3.91 ± 0.47	12.47 ± 1.86
P-T	170.87 ± 7.37	196.34 ± 10.41	3.29 ± 0.18	12.49 ± 1.14
G-F	136.66 ± 17.04	183.06 ± 7.81	3.55 ± 0.11	8.61 ± 0.97
G-T	162.00 ± 7.00	181.11 ± 7.51	4.57 ± 0.19	10.94 ± 0.36
D-F	119.35 ± 15.77	137.99 ± 19.88	3.45 ± 0.13	6.74 ± 0.45
D-T	152.39 ± 9.98	186.05 ± 12.44	3.24 ± 0.06	5.73 ± 0.82
IW-P-F	113.97 ± 8.14	135.78 ± 10.19	3.03 ± 0.11	6.02 ± 1.04
IW-P-T	170.71 ± 3.50	205.27 ± 4.90	3.51 ± 0.07	9.43 ± 2.44

Abbreviations: D, Diamond; F, Fill; G, Gyroid; IW-P, I-graph-wrapped package; P, Primitive; T, Thicken.

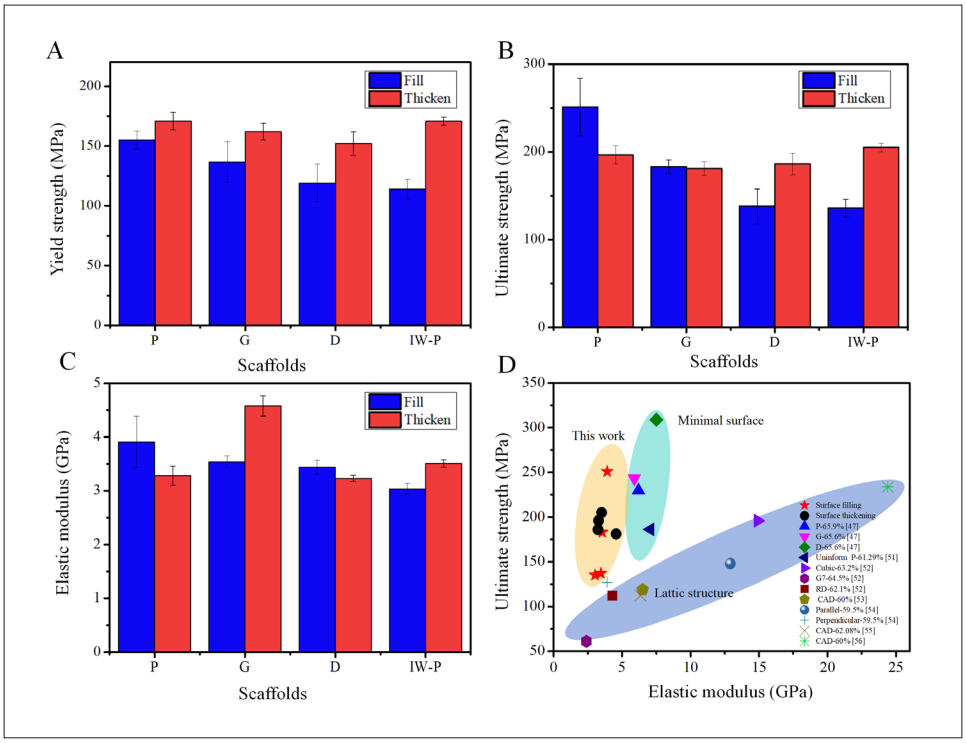


Figure 8. Comparison of mechanical performance of different scaffolds. (A) Yield strength of scaffolds. (B) Ultimate strength of scaffolds. (C) Elastic modulus of scaffolds. (D) Comparison of the mechanical properties of scaffolds prepared in this study with porous titanium scaffolds prepared in other published study.[47,51-56] Abbreviations: D, Diamond; G, Gyroid; IW-P, I-graph-wrapped package; P, Primitive.

compared to the existing scaffolds, from which it can be seen that, compared to scaffolds prepared in published works,[47,51-56] the modulus of the porous scaffolds prepared in this work is closer to that of cancellous bone under the condition of close porosity. The range of strength variation is also larger, showing the potential of the minimal surface unit and modeling strategy for performance tuning.

The elongation of the thickened scaffolds for G and IW-P structures is slightly higher than that of the filled scaffolds, with strains increasing from 8.60% and 6.01% to 10.94% and 9.43%, respectively. For P and D surface structures, the fracture strain of the filled structure is higher than that of the thickened structure due to its structural characteristics. The material's toughness determines its ability to absorb energy and undergo plastic deformation without breaking. High toughness can prevent catastrophic failures caused by unexpected overloads or localized strains, an attribute beneficial for the development of stable implants.[3]

3.3. Penetration properties of the scaffolds

Figure 9A shows the permeability of scaffolds obtained through the falling head method. It can be seen that the unit structure and modeling strategy have a significant impact on the permeability of the scaffolds.

Different scaffolds exhibit permeability values in the range of 0.88–1.93 × 10^{-9} m^2. In comparison, the average permeability of human trabecular bone falls within the range of 0.29–3.91 × 10^{-9} m^2.[57] Therefore, it is evident that the permeability of the porous scaffolds designed in this study meets the requirements of human skeletal structures. In terms of the filled structure, the permeability levels, from highest to lowest, are as follows: IW-P (1.91 × 10^{-9} m^2) > P (1.79 × 10^{-9} m^2) > G (1.66 × 10^{-9} m^2) > D (1.52 × 10^{-9} m^2). Here, the main reason for the greater permeability of the IW-P-filled scaffolds than the P-filled scaffold structures is the greater number and concentration of pores in the IW-P for the same inflow area (as shown in Figure 5A and D). For the thickened structure, the permeability levels between different units are as follows, from highest to lowest: G (1.01 × 10^{-9} m^2) > IW-P (0.97 × 10^{-9} m^2) > P (0.94 × 10^{-9} m^2) > D (0.88 × 10^{-9} m^2). In terms of modeling strategies, the porous scaffolds created using the filling method exhibit higher permeability compared to the thickened scaffolds. Compared with the existing work[47,58,59] (as shown in Figure 9B), the porous scaffolds prepared in this study maintained high permeability with lower porosity. It was demonstrated that the minimal surface porous scaffolds constructed by both filling and thickening modeling

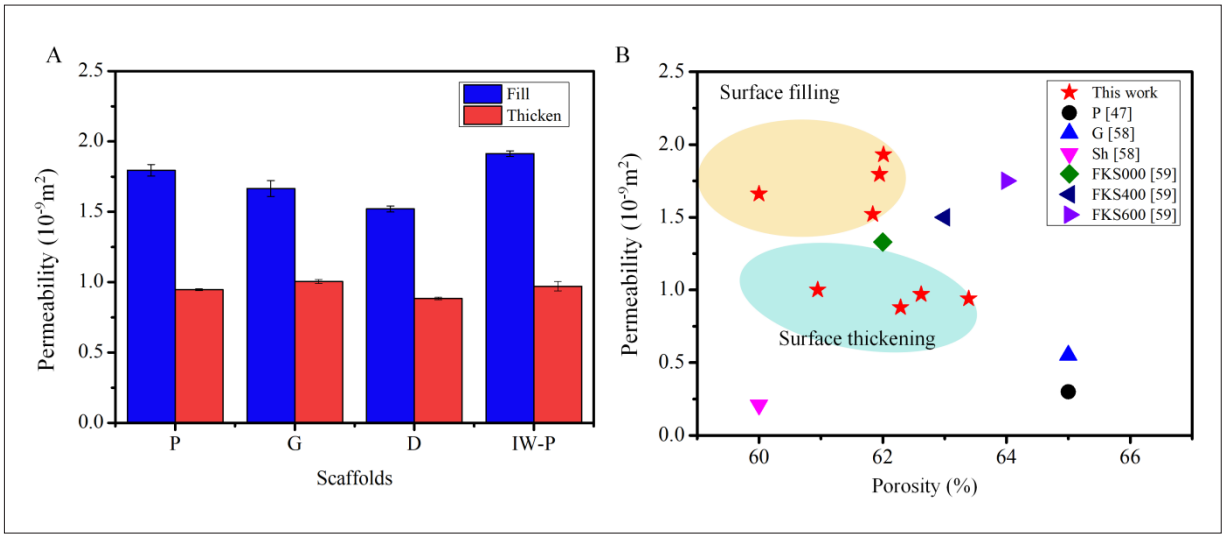


Figure 9. (A) Permeability of different scaffolds. (B) Permeability of scaffolds prepared in this work as compared to those in other published studies.[47,58,59] Abbreviations: D, Diamond; G, Gyroid; IW-P, I-graph-wrapped package; P, Primitive.

methods can provide sufficient support and surface area to safeguard the transport of waste nutrients and cell migration.

Figure 10 displays different flow velocity cloud maps in fluid simulations. It can be observed that P and IW-P structure scaffolds have larger pore sizes, and their pores are well-connected to fluid passages, posing minimal hindrance to fluid flow. As a result, they exhibit relatively higher permeability. In contrast, G and D structure scaffolds have complex internal structures with curved spiral designs that accelerate fluid flow, creating varying velocity gradients. These structures impede fluid flow to a greater extent, leading to lower permeability,[60] especially in the case of D

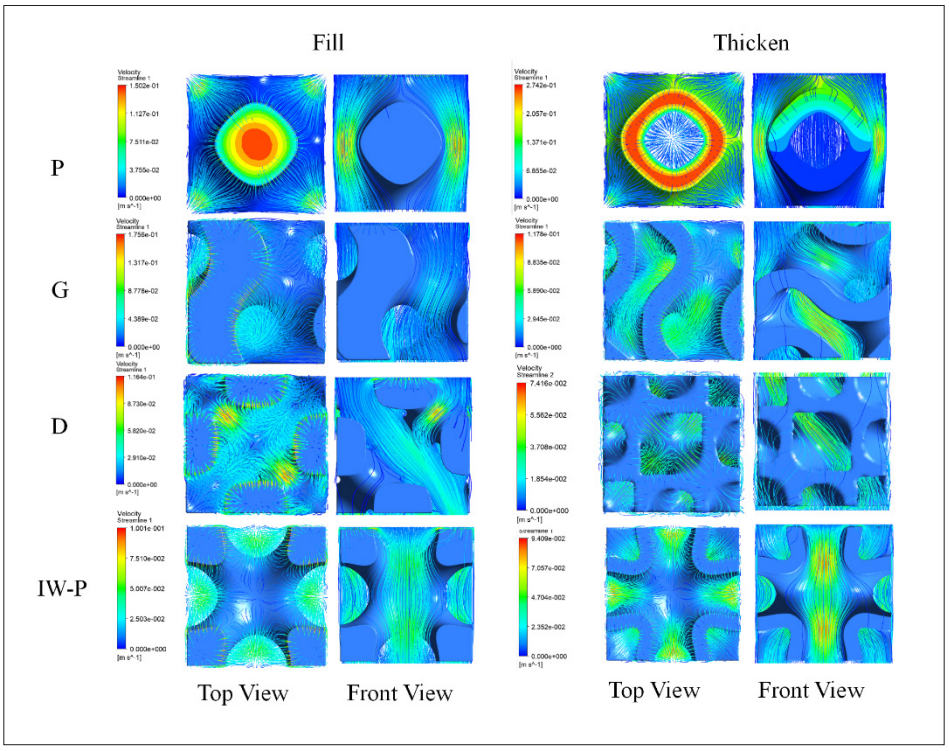


Figure 10. Flow velocity cloud maps for different scaffolds cells. Abbreviations: D, Diamond; G, Gyroid; IW-P, I-graph-wrapped package; P, Primitive.

structures. The D structure exhibits smaller projected pore areas in the direction of fluid flow, contributing to its lower permeability.[61] In practice, changes in scaffold structure and permeability have different effects on cell growth. Curved surface-thickened structures have a larger surface area and lower internal body fluid flow rate, which facilitates the deposition of cells and calcium-mineralized matrices and enhances cellular activity. Surface-filled structures have larger pore sizes and higher permeability, which facilitates the transport of substances and metabolic wastes, the migration of cells into the interior of the implant, and the reconstruction of blood vessels.[62] In addition, cells respond to the physical environment and are particularly sensitive to curved surfaces during tissue growth, and small changes in curvature may prompt cells to adjust themselves to be in a state of mechanical equilibrium.[63,64]

3.4. Mechanism analysis and further applications of modeling strategies

In this study, we compared the effects of two modeling strategies on scaffold performance. For load-bearing orthopedic implants, the most critical factors are high strength, low modulus, and good toughness to withstand rigorous loading conditions. Different from modeling methods that adjust parameters such as pore size and porosity by changing the size and offset position of minimal surface units, the surface thickening and surface filling strategies fundamentally alter the material distribution of the minimal surface units. In our previous works,[50,65-67] the main approach involved emulating the overall structure of bones to adjust parameters such as porosity, pore size, and unit combinations. This ensured that the limited material was concentrated in the primary load-bearing areas, enhancing the scaffold's overall moment of inertia to improve its strength (as shown in Figure 11).

Compared to TC4 porous scaffolds used in orthopedic applications in previous studies, the scaffolds developed in this work can offer lower modulus while maintaining high strength at similar porosity. The results of permeability experiments showed that the different cell-based porous scaffolds in this study could provide higher permeability with lower porosity, thus promoting osseointegration. The above analysis shows that two modeling approaches, thickening and filling, are suitable for the development of load-bearing orthopedic scaffolds. This study provides fundamental information for the rational design of additive manufacturing porous orthopedic implants, especially for patient-specific orthopedic implants.

4. Conclusion

In this study, four distinct porous scaffolds were designed employing different modeling strategies and fabricated using SLM technology. The objective of the study was to examine the impact of modeling strategies on the

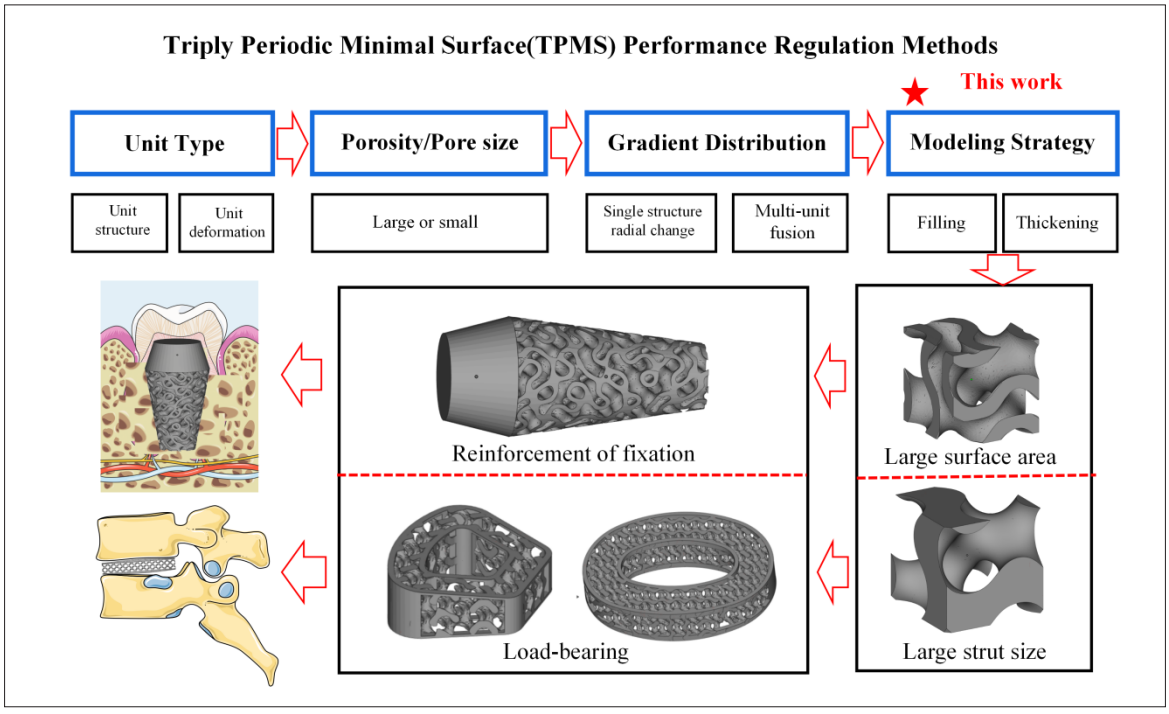


Figure 11. Application and outlook of two modeling strategies in the design of scaffolds with triple periodic minimum surface structures.

mechanical and permeability properties of the porous scaffolds. The summarized results are as follows:

(i) The mechanical properties of the scaffolds prepared through thickening and filling strategies were comparable to the mechanical properties of human bones. The elastic modulus (ranging from 3.03 to 4.57 GPa) for different scaffolds within the range of human bones and their ultimate strength (ranging from 135.78 to 250.90 MPa) met the biomechanical requirements of orthopedic applications.

(ii) Compared to the filling structure, the thickening strategy can improve the compressive strength and toughness of G, D, and IW-P scaffolds and reduce stress fluctuations during the collapse process.

(iii) The permeability of the scaffolds ranges from 0.88 to 1.91 × 10^{-9} m^2, which is close to the permeability of human bone. Filling structures exhibit higher permeability than thickening structures, mainly due to the significantly smaller specific surface area of the filling structure and larger pore size.

(iv) Thickening strategy fundamentally adjusts the material distribution of units and alters the load-bearing status of unit structures, thereby affecting the overall performance of the scaffolds. In the future, scaffold design can focus on the requirements for load, cell adhesion, modulus, and other factors, leveraging the advantages of thickened structures in terms of strength enhancement and specific surface area.

Acknowledgments

The authors extend their gratitude to Guangxi Key Laboratory of Basic and Translational Research of Bone and Joint Degenerative Diseases and Guangxi Biomedical Materials Engineering Research Center for Bone and Joint Degenerative Diseases for providing experimental equipment and technology. In addition, the authors thank Xiaoli Ma at the Instrumental Analysis in Shanghai Jiao Tong University for her guidance on experimental testing and analysis. We thank Guangxi Key Laboratory of Basic and Translational Research on Bone and Joint Degenerative Diseases (21-220-06) for the financial support.

Funding

The authors acknowledge the financial supports from National Natural Science Foundation of China (Grant Nos. 52274387 and 52311530772).

Conflict of interest

The authors declare no conflicts of interest.

Author contributions

Conceptualization: Binghao Wang, Chengliang Yang
Formal analysis: Zheng Shi
Investigation: Chuanchuan Zheng
Methodology: Wen Peng
Writing – original draft: Binghao Wang, Miao Luo
Writing – review & editing: Yuting Lv, Liqiang Wang

Ethics approval and consent to participate

Not applicable.

Consent for publication

Not applicable.

Availability of data

Data are available from the corresponding author upon reasonable request.

References

1. Gupta K, Meena K. Artificial bone scaffolds and bone joints by additive manufacturing: a review. *Bioprinting*. 2023;31:e00268.
doi: 10.1016/j.bprint.2023.e00268

2. Fang Y, Wang Q, Yang Z, et al. An efficient approach to endow TiNbTaZr implant with osteogenic differentiation and antibacterial activity in vitro. *Mater Des*. 2022;221:110987.
doi: 10.1016/j.matdes.2022.110987

3. Zhang Y, Attarilar S, Wang L, Lu W, Yang J, Fu Y. A review on design and mechanical properties of additively manufactured NiTi implants for orthopedic applications. *Int J Bioprint*. 2021;7(2):340.
doi: 10.18063/ijb.v7i2.340

4. Qu H. Additive manufacturing for bone tissue engineering scaffolds. *Mater Today Commun*. 2020;24:101024.
doi: 10.1016/j.mtcomm.2020.101024

5. Yuan L, Ding S, Wen C. Additive manufacturing technology for porous metal implant applications and triple minimal surface structures: a review. *Bioact Mater*. 2019;4:56-70.
doi: 10.1016/j.bioactmat.2018.12.003

6. Wang X, Xu S, Zhou S, et al. Topological design and additive manufacturing of porous metals for bone scaffolds and orthopaedic implants: a review. *Biomaterials*. 2016;83:127-141.
doi: 10.1016/j.biomaterials.2016.01.012

7. Oh I-H, Nomura N, Masahashi N, Hanada S. Mechanical properties of porous titanium compacts prepared by powder sintering. *Scr Mater*. 2003;49(12):1197-1202.
doi: 10.1016/j.scriptamat.2003.08.018

8. Yang G, Xu B, Lei X, et al. Preparation of porous titanium by direct in-situ reduction of titanium sesquioxide. *Vacuum*. 2018;157:453-457.
doi: 10.1016/j.vacuum.2018.09.021

9. Wang L, Xie L, Zhang L, et al. Microstructure evolution and superelasticity of layer-like NiTiNb porous metal prepared by eutectic reaction. *Acta Mater.* 2018;143:214-226.
doi: 10.1016/j.actamat.2017.10.021

10. Biasetto L, de Moraes EG, Colombo P, Bonollo F. Ovalbumin as foaming agent for Ti6Al4V foams produced by gelcasting. *J Alloys Compd.* 2016;687:839-844.
doi: 10.1016/j.jallcom.2016.06.218

11. Ma HY, Wang JC, Qin P, et al. Advances in additively manufactured titanium alloys by powder bed fusion and directed energy deposition: microstructure, defects, and mechanical behavior. *J Mech Behav Biomed Mater.* 2024;183:32-62.
doi: 10.1016/j.jmst.2023.11.003

12. Hafeez N, Liu J, Wang L, et al. Superelastic response of low-modulus porous beta-type Ti-35Nb-2Ta-3Zr alloy fabricated by laser powder bed fusion. *Addit Manuf.* 2020;34.
doi: 10.1016/j.addma.2020.101264

13. Hafeez N, Wei D, Xie L, et al. Evolution of microstructural complex transitions in low-modulus β-type Ti-35Nb-2Ta-3Zr alloy manufactured by laser powder bed fusion. *Addit Manuf.* 2021;48.
doi: 10.1016/j.addma.2021.102376

14. Zhang T, Wei D, Lu E, et al. Microstructure evolution and deformation mechanism of α+β dual-phase Ti-xNb-yTa-2Zr alloys with high performance. *J Mater Sci Technol.* 2022;131:68-81.
doi: 10.1016/j.jmst.2022.04.052

15. Lv Y, Wang B, Liu G, et al. Metal material, properties and design methods of porous biomedical scaffolds for additive manufacturing: a review. *Front Bioeng Biotechnol*. 2021;9:641130.
doi: 10.3389/fbioe.2021.641130

16. Guo W, Yang Y, Liu C, et al. 3D printed TPMS structural PLA/GO scaffold: process parameter optimization, porous structure, mechanical and biological properties. *J Mech Behav Biomed Mater.* 2023;142.
doi: 10.1016/j.jmbbm.2023.105848

17. Belda R, Megías R, Marco M, Vercher-Martínez A, Giner E. Numerical analysis of the influence of triply periodic minimal surface structures morphometry on the mechanical response. *Comput Methods Programs Biomed*. 2023;230:107342.
doi: 10.1016/j.cmpb.2023.107342

18. Yang L, Li Y, Wu S, et al. Tailorable and predictable mechanical responses of additive manufactured TPMS lattices with graded structures. *Mat Sci Eng A*. 2022;843.
doi: 10.1016/j.msea.2022.143109

19. Yang L, Han C, Wu H, et al. Insights into unit cell size effect on mechanical responses and energy absorption capability of titanium graded porous structures manufactured by laser powder bed fusion, *J Mech Behav Biomed Mater.* 2020;109:103843.
doi: 10.1016/j.jmbbm.2020.103843

20. Kaur I, Singh P. Flow and thermal transport characteristics of triply-periodic minimal surface (TPMS)-based gyroid and Schwarz-P cellular materials. *Numer Heat Transfer, Part A*. 2021;79(8):553-569.
doi: 10.1080/10407782.2021.1872260

21. Wu G, More KL, Johnston CM, Zelenay P. High-performance electrocatalysts for oxygen reduction derived from polyaniline, iron, and cobalt. *Science*. 2011;332(6028): 443-447.
doi: 10.1126/science.1200832

22. Yadroitsev I, Shishkovsky I, Bertrand P, Smurov I. Manufacturing of fine-structured 3D porous filter elements by selective laser melting. *Appl Surf Sci.* 2009;255(10): 5523-5527.
doi: 10.1016/j.apsusc.2008.07.154

23. Attarilar S, Ebrahimi M, Djavanroodi F, Fu Y, Wang L, Yang J. 3D printing technologies in metallic implants: a thematic review on the techniques and procedures. *Int J Bioprint.* 2021;7(1).
doi: 10.18063/ijb.v7i1.306

24. Yoo D. Computer-aided porous scaffold design for tissue engineering using triply periodic minimal surfaces. *Int J Precis Eng Manuf.* 2011;12(1):61-71.
doi: 10.1007/s12541-011-0008-9

25. Ma S, Tang Q, Han X, et al. Manufacturability, mechanical properties, mass-transport properties and biocompatibility of triply periodic minimal surface (TPMS) porous scaffolds fabricated by selective laser melting. *Mater Des.* 2020;195.
doi: 10.1016/j.matdes.2020.109034

26. Ma S, Tang Q, Feng Q, Song J, Han X, Guo F. Mechanical behaviours and mass transport properties of bone-mimicking scaffolds consisted of gyroid structures manufactured using selective laser melting. *J Mech Behav Biomed Mater.* 2019;93:158-169.
doi: 10.1016/j.jmbbm.2019.01.023

27. Yang N, Quan Z, Zhang D, Tian Y. Multi-morphology transition hybridization CAD design of minimal surface porous structures for use in tissue engineering. *Comput-Aided Des.* 2014;56:11-21.
doi: 10.1016/j.cad.2014.06.006

28. Aliyu A, Poungsiri K, Shinjo J, Panwisawas C, et al. Additive manufacturing of tantalum scaffolds:Processing, microstructure and process-induced defects, Int J Refract Met H. 2023;112:106132.
doi: 10.1016/j.ijrmhm.2023.106132

29. Naghavi SA, Tamaddon M, Marghoub A, et al. Mechanical characterisation and numerical modelling of TPMS-based gyroid and diamond Ti6Al4V scaffolds for bone implants: an integrated approach for translational consideration. *Bioengineering*. 2022;9(10). doi: 10.3390/bioengineering9100504

30. Lu Y, Cheng L, Yang Z, Li J, Zhu H. Relationship between the morphological, mechanical and permeability properties of porous bone scaffolds and the underlying microstructure. *Plos One*. 2020;15(9). doi: 10.1371/journal.pone.0238471

31. Guo X, Zheng X, Yang Y, Yang X, Yi Y. Mechanical behavior of TPMS-based scaffolds: a comparison between minimal surfaces and their lattice structures. *SN Appl Sci*. 2019;1(10). doi: 10.1007/s42452-019-1167-z

32. Zhang X, Fang G, Xing L, Liu W, Zhou J. Effect of porosity variation strategy on the performance of functionally graded Ti-6Al-4V scaffolds for bone tissue engineering. *Mater Des*. 2018;157:523-538. doi: 10.1016/j.matdes.2018.07.064

33. Pires T, Santos J, Ruben RB, Gouveia BP, Castro APG, Fernandes PR. Numerical-experimental analysis of the permeability-porosity relationship in triply periodic minimal surfaces scaffolds. *J Biomech*. 2021;117. doi: 10.1016/j.jbiomech.2021.110263

34. Santos J, Pires T, Gouveia BP, Castro APG, Fernandes PR. On the permeability of TPMS scaffolds. *J Mech Behav Biomed Mater*. 2020;110. doi: 10.1016/j.jmbbm.2020.103932

35. Zhao S, Hou W, Xu Q, Li SJ, Hao YL, Yang R. Ti-6Al-4V lattice structures fabricated by electron beam melting for biomedical applications. *Titanium Med Dent Appl*. 2018; 277-301. doi: 10.1016/B978-0-12-812456-7.00013-5

36. Yan C, Hao L, Hussein A, Young P, Raymont D. Advanced lightweight 316L stainless steel cellular lattice structures fabricated via selective laser melting. *Mater Des*. 2014;55: 533-541. doi: 10.1016/j.matdes.2013.10.027

37. Li X, Xiong Y-Z, Zhang H, Gao R-N. Development of functionally graded porous titanium/silk fibroin composite scaffold for bone repair. *Mater Lett*. 2021;282. doi: 10.1016/j.matlet.2020.128670

38. Huo P, Zhao Z, Bai P, et al. Deformation evolution and fracture mechanism of porous TC4 alloy scaffolds fabricated using selective laser melting under uniaxial compression. *J Alloys Compd*. 2021;861:158529. doi: 10.1016/j.jallcom.2020.158529

39. Wang S, Liu L, Li K, Zhu L, Chen J, Hao Y. Pore functionally graded Ti6Al4V scaffolds for bone tissue engineering application. *Mater Des*. 2019;168. doi: 10.1016/j.matdes.2019.107643

40. McGregor M, Patel S, McLachlin S, Vlasea M. Architectural bone parameters and the relationship to titanium lattice design for powder bed fusion additive manufacturing. *Addit Manuf*. 2021;47. doi: 10.1016/j.addma.2021.102273

41. Hara D, Nakashima Y, Sato T, et al. Bone bonding strength of diamond-structured porous titanium-alloy implants manufactured using the electron beam-melting technique. *Mater Sci Eng C Mater Biol Appl*. 2016;59:1047-1052. doi: 10.1016/j.msec.2015.11.025

42. Wang S, Shi Z, Liu L, Zhou X, Zhu L, Hao Y. The design of Ti6Al4V primitive surface structure with symmetrical gradient of pore size in biomimetic bone scaffold. *Mater Des*. 2020;193. doi: 10.1016/j.matdes.2020.108830

43. Carluccio D, Xu C, Venezuela J, et al. Additively manufactured iron-manganese for biodegradable porous load-bearing bone scaffold applications. *Acta Biomater*. 2020;103:346-360. doi: 10.1016/j.actbio.2019.12.018

44. Lv Y, Liu G, Wang B, et al. Pore strategy design of a novel NiTi-Nb biomedical porous scaffold based on a triply periodic minimal surface. *Front Bioeng Biotechnol*. 2022;10:910475. doi: 10.3389/fbioe.2022.910475

45. Lv Y, Guo J, Zhang Q, Wei G, Yu H. Design of low elastic modulus and high strength TC4 porous scaffolds via new variable gradient strategies. *Mater Lett*. 2022;325: 132616. doi: 10.1016/j.matlet.2022.132616

46. Tan C, Zou J, Li S, et al. Additive manufacturing of bio-inspired multi-scale hierarchically strengthened lattice structures. *Int J Mach Tools Manuf*. 2021;167. doi: 10.1016/j.ijmachtools.2021.103764

47. Yu G, Li Z, Li S, et al. The select of internal architecture for porous Ti alloy scaffold: a compromise between mechanical properties and permeability. *Mater Des*. 2020;192:108754. doi: 10.1016/j.matdes.2020.108754

48. Xiong Y, Gao R, Zhang H, Dong L-L, Li J-T, Li X. Rationally designed functionally graded porous Ti6Al4V scaffolds with high strength and toughness built via selective laser melting for load-bearing orthopedic applications. *J Mech Behav Biomed Mater*. 2020;104:103673. doi: 10.1016/j.jmbbm.2020.103673

49. Bobbert FSL, Lietaert K, Eftekhari AA, et al. Additively manufactured metallic porous biomaterials based on minimal surfaces: a unique combination of topological, mechanical, and mass transport properties. *Acta Biomater*. 2017;53:572-584. doi: 10.1016/j.actbio.2017.02.024

50. Lv Y, Wang B, Liu G, et al. Design of bone-like continuous gradient porous scaffold based on triply periodic minimal surfaces. *J Mater Res Technol*. 2022;21:3650-3665. doi: 10.1016/j.jmrt.2022.10.160

51. Xiong Y, Han Z, Qin J, et al. Effects of porosity gradient pattern on mechanical performance of additive manufactured Ti-6Al-4V functionally graded porous structure. *Mater Des.* 2021;208.
doi: 10.1016/j.matdes.2021.109911

52. Zhao S, Li S, Hou W, Hao YL, Yang R, Misra RDK. The influence of cell morphology on the compressive fatigue behavior of Ti-6Al-4V meshes fabricated by electron beam melting. *J Mech Behav Biomed Mater.* 2016;59: 251-264.
doi: 10.1016/j.jmbbm.2016.01.034

53. Heinl P, Muller L, Korner C, Singer RF, Müller FA. Cellular Ti-6Al-4V structures with interconnected macro porosity for bone implants fabricated by selective electron beam melting. *Acta Biomater.* 2008;4(5):1536-1544.
doi: 10.1016/j.actbio.2008.03.013

54. Heinl P, Körner C, Singer RF. Selective electron beam melting of cellular titanium: mechanical properties. *Adv Eng Mater.* 2008;10(9):882-888.
doi: 10.1002/adem.200800137

55. Cheng X, Li S, Murr L, et al. Compression deformation behavior of Ti-6Al-4V alloy with cellular structures fabricated by electron beam melting. *J Mech Behav Biomed Mater.* 2012;16:153-162.
doi: 10.1016/j.jmbbm.2012.10.005

56. Chen S, Huang J, Pan C, et al. Microstructure and mechanical properties of open-cell porous Ti-6Al-4V fabricated by selective laser melting. *J Alloys Compd.* 2017;713:248-254.
doi: 10.1016/j.jallcom.2017.04.190

57. Nauman EA, Fong KE, Keaveny TM. Dependence of intertrabecular permeability on flow direction and anatomic site. *Ann Biomed Eng.* 1999;27:517-524.
doi: 10.1114/1.195

58. Zhang X-Y, Yan X-C, Fang G, Liu M. Biomechanical influence of structural variation strategies on functionally graded scaffolds constructed with triply periodic minimal surface. *Addit Manuf.* 2020;32.
doi: 10.1016/j.addma.2019.101015

59. Zou S, Mu Y, Pan B, et al. Mechanical and biological properties of enhanced porous scaffolds based on triply periodic minimal surfaces. *Mater Des.* 2022;219.
doi: 10.1016/j.matdes.2022.110803

60. Wang S, Shi Z, Liu L, et al. Honeycomb structure is promising for the repair of human bone defects. *Mater Des.* 2021;207.
doi: 10.1016/j.matdes.2021.109832

61. Wang H, Su K, Su L, Liang P, Ji P, Wang C. Comparison of 3D-printed porous tantalum and titanium scaffolds on osteointegration and osteogenesis. *Mater Sci Eng C Mater Biol Appl.* 2019;104:109908.
doi: 10.1016/j.msec.2019.109908

62. Li Y, Zhou J, Pavanram P, et al. Additively manufactured biodegradable porous magnesium. *Acta Biomater.* 2018;67:378-392.
doi: 10.1016/j.actbio.2017.12.008

63. Wang Z, Wang C, Li C, et al. Analysis of factors influencing bone ingrowth into three-dimensional printed porous metal scaffolds: a review, *J Alloy Compd.* 2017;717: 271-285.
doi: 10.1016/j.jallcom.2017.05.079

64. Li Y, Shi Y, Lu Y, et al. Additive manufacturing of vascular stents. *Acta Biomater.* 2023;167:16-37.
doi: 10.1016/j.actbio.2023.06.014

65. Zhang Y, Liu J, Wang L, et al. Porous NiTiNb alloys with superior strength and ductility induced by modulating eutectic microregion. *Acta Mater.* 2022;239:118295.
doi: 10.1016/j.actamat.2022.118295

66. Lv Y, Shi Z, Wang B, et al. Design of biomedical gradient porous scaffold via a minimal surface dual-unit continuous transition connection strategy. *Int J Bioprint.* 2024;10(1).
doi: 10.36922/ijb.1263

67. Zhang Y, Wei D, Chen Y, et al. Non-negligible role of gradient porous structure in superelasticity deterioration and improvement of NiTi shape memory alloys. *J Mater Sci Technol.* 2024;186:48-63.
doi: 10.1016/j.jmst.2023.10.053

ACCSCIENCE PUBLISHING

International Journal of Bioprinting

RESEARCH ARTICLE

Hydrogel bioink formulation for 3D bioprinting: Sustained delivery of PDGF-BB and VEGF in biomimetic scaffolds for tendon partial rupture repair

Sandra Ruiz-Alonso[1,2,3], Jorge Ordoyo-Pascual[1,2,3], Markel Lafuente-Merchan[1,2,3], Fátima García-Villén[1,2,3], Myriam Sainz-Ramos[1,2,3], Idoia Gallego[1,2,3], Laura Saenz-Del-Burgo[1,2,3]*, and Jose L. Pedraz[1,2,3]*

[1]NanoBioCel Research Group, Laboratory of Pharmacy and Pharmaceutical Technology, Department of Pharmacy and Food Science, Faculty of Pharmacy, University of the Basque Country (UPV/EHU), Paseo de la Universidad 7, 01006 Vitoria-Gasteiz, Spain

[2]Bioaraba, NanoBioCel Research Group, 01009 Vitoria-Gasteiz, Spain

[3]Networking Research Centre of Bioengineering, Biomaterials and Nanomedicine (CIBER-BBN), Institute of Health Carlos III, 28029 Madrid, Spain

Abstract

In the evolving field of tissue engineering, the power of three-dimensional (3D) bioprinting technology can be harnessed by innovative methodologies to address the complex challenges of treating partial tendon injuries. In order to engineer a solution for this type of musculoskeletal injuries, a biomimetic bioink and a scaffold developed using 3D bioprinting technology and capable of delivering cells and growth factors were investigated. For the development of the bioink, a hydrogel type structure was selected based on a strategic combination of alginate, hyaluronic acid, gelatin, and fibrinogen. This tailored combination exhibited favorable rheological behavior and impeccable printability. The bioink, demonstrating promising characteristics, was then employed to fabricate both acellular scaffolds and tissue constructs. The structures possessed mechanical properties suitable and adequate for addressing partial tendon injuries and achieved a microenvironment that allowed good metabolic activity of tenocytes, maintenance of their phenotype, and overexpression of genes related to macromolecules of tendon extracellular matrix. Regarding growth factors delivery, vascular endothelial growth factor (VEGF165) and platelet-derived growth factor (PDGF-BB) were successfully incorporated into the bioink. Their release profile was thoroughly studied, and their activity once released was demonstrated. Together, these results suggest that the developed bioink and the resulting 3D structures can have an important impact on tendon partial injury therapies. The multifaceted capabilities of the bioink and the developed tissue constructs position them as crucial contributors to the advancement of tendon injury therapies, marking a significant stride toward enhanced patient outcomes and regenerative medicine practices.

Keywords: Regenerative medicine; Growth factors delivery; Biomimetic bioink; Rheological behavior; Hydrogel; Natural materials; Partial tendon injuries

***Corresponding authors:**
Laura Saenz-Del-Burgo (laura.saenzdelburgo@ehu.eus)

Jose L. Pedraz (joseluis.pedraz@ehu.eus)

Citation: Ruiz-Alonso S, Ordoyo-Pascual J, Lafuente-Merchan M, et al. Hydrogel bioink formulation for 3D bioprinting: Sustained delivery of PDGF-BB and VEGF in biomimetic scaffolds for tendon partial rupture repair. *Int J Bioprint*. 2024;10(3):2632. doi: 10.36922/ijb.2632

Received: January 4, 2024
Accepted: February 20, 2024
Published Online: April 1, 2024

Copyright: © 2024 Author(s). This is an Open Access article distributed under the terms of the Creative Commons Attribution License, permitting distribution, and reproduction in any medium, provided the original work is properly cited.

Publisher's Note: AccScience Publishing remains neutral with regard to jurisdictional claims in published maps and institutional affiliations.

1. Introduction

The global prevalence of musculoskeletal disorders is on the rise, representing a substantial burden for healthcare systems.[1,2] They compromise more than 150 diverse diseases that affect joints, bones, muscles, and connective tissues.[3,4] Included among them are tendon injuries, which can be affected by different pathologies. One of these pathologies is tendon rupture, which can be classified into partial tears (depending on the area of the tendon that is affected: minor 25%, moderate or severe 75%) and complete tears.[5] Although much emphasis is placed on complete injuries, it is of paramount importance to recall that partial injuries are very common and are equally limiting and painful for patients. The current principal treatment for tendon partial ruptures consists of surgery and rehabilitation for severe cases, and immobilization and repose for minor cases.[6] In a very significant number of cases, regeneration results in fibrotic tissue with poor mechanical properties, which hampers its function and limits patients' life quality.[7,8] With the advent of tissue engineering, an enormous field of possibilities has opened up to address this medical problem by utilizing different complex approaches.[9,10] Nevertheless, the strategies carried out to date in tissue engineering are still too technically simple and mainly based on the study of various elements independently.[11] In this sense, despite the significant progress, the successful fabrication of composite structures that combine different elements and allow the regeneration of partial damages in complex tissues, such as tendons, remains a considerable challenge.

To address this issue, extrusion three-dimensional (3D) bioprinting emerged as a promising and powerful technique for the development of highly complex scaffolds and tissue constructs suitable for the regeneration of partial tendon ruptures.[12] This technology makes it possible to combine semisolid, hydrogel-like materials, cells, and molecules with different designs, morphologies, and dimensions.[13,14] According to the ASTM standards and the physicochemical properties of the materials to be used (semisolid, hydrogel-like), the air-flow material extrusion 3D bioprinting is the most convenient for the purposes of this study.[15] Although this technique is being used to develop scaffolds and tissue constructs for total tendon ruptures (mainly using synthetic materials), it can also be adjusted for addressing partial ruptures.[16] In this study, the objective is not to provide complete mechanical support but to promote rapid regeneration of extracellular matrix (ECM) to recover the lost functionality of the tendon tissue. Potential strategies to achieve this purpose include the modification of the components that are used during 3D bioprinting, such as the type of materials and/or the use of growth factors.[13]

Regarding the materials used in extrusion-based 3D bioprinting, hydrogels are postulated as good candidates for the regeneration of partial tendon tears.[17] These 3D networks are formed by biopolymers capable of retaining a large amount of water in their structure.[18] Besides, they are highly biocompatible, reducing the risk of adverse responses once implanted in the body.[19] Nonetheless, until now, the hydrogels developed for 3D bioprinting applied to tissue regeneration suffer from several limitations. On the one hand, the mechanical properties of these hydrogels do not meet the minimum requirements for being used in 3D bioprinting. This can be attributed to the very low viscosities they exhibit in some cases, and the limitations in obtaining good shape fidelity or reproducibility in other cases.[20,21] On the other hand, under most circumstances, the composition of the hydrogel, although biocompatible, is sparingly biomimetic, as it is usually composed of only one or two molecules/macromolecules, with their concentrations being highly different from those in the ECM.[22] These factors lead to reduced effectiveness of the scaffolds. Consequently, the development of a 3D hydrogel-based structure, with controlled structural and mechanical properties, that allows improving tendon tissue regeneration through complex and biomimetic approaches, remains a hurdle to be overcome.

Growth factors are frequently used in the regeneration of damaged tissues.[23,24] They have generally been dosed directly through injections at the injured site,[25,26] generating excellent outcomes, despite some shortcomings such as the non-specific diffusion of molecules to other locations in the organism and the rapid degradation.[27,28] Multiple growth factors have been utilized in the case of tendon being the target tissue; for instance, transforming growth factor-beta (TGF-β), platelet-derived growth factor (PDGF), vascular endothelial growth factor (VEGF), basic fibroblast growth factor (bFGF or FGF-2), insulin-like growth factor-1 (IGF-1), and connective tissue growth factor (CTGF) are some of the previously tested growth factors.[29-33] Among them, VEGF and PDGF should be highlighted. First, VEGF favors the formation of new blood vessels, allowing a greater amount of nutrients and oxygen to reach the cells (necessary considering that collagen synthesis is an oxygen-dependent process).[34,35] Meanwhile, PDGF promotes cell proliferation and migration,[36] favoring the migration of stem cells to the damaged tendon and the proliferation of tenocytes and tenoblasts. Given their proven effectiveness, the incorporation of these molecules into 3D-bioprinted structures seems reasonable, giving rise to much more complex approaches that allow better regeneration of partial tendon injuries. Furthermore, this would reduce the diffusion limitation of the factors since they would be kept at the exact location where they are needed (where the

damaged tendinous tissue is located). Despite this, their incorporation into printed structures is challenging since the methodology to incorporate them, their stability, their release profile, and their bioactivity once released must be determined.[37] This is why, until now, their application in 3D bioprinting for tendon regeneration has been limited.

This study introduces a pioneering approach to developing hydrogel-based scaffolds and tissue constructs customized for tendon regeneration. Notably, we designed three distinct variants: one with embedded tenocytes, another loaded with VEGF, and the last one with PDGF-BB. An original combination of biological materials was selected: hyaluronic acid (HA), alginate (Alg), gelatin (Gel), and fibrinogen (Fg). After formulating the ink, the rheological properties and printability were determined. These properties are crucial for achieving accurate and reproducible 3D-printed structures. Furthermore, cells (tenocytes) and growth factors (VEGF165 and PDGF-BB) were incorporated into the hydrogel matrix. The viability, activity, proliferation, and gene expression of the tenocytes in the bioprinted hydrogel-based tissue construct were determined. The release rates and the half-life values of the growth factors were established. Finally, the potential of the factors released from the scaffold for promoting vascularization and cell proliferation was demonstrated. By elucidating the rheological behavior and the printability of ink formulations and evaluating the *in vitro* performance of the 3D-bioprinted scaffolds and tissue constructs, we aim to contribute to the advancement of tissue engineering strategies for partial tendon ruptures repair and regeneration.

2. Materials and methods

2.1. Materials

Normal primary human umbilical vein endothelial cells (HUVECs), vascular cell basal media, endothelial cell growth kit components, DMEM media, and immortalized mouse myoblast cells (C2C12) were acquired from ATCC® (Manassas, Virginia, USA). Immortalized mouse Achilles tendon (iMAT) cells, ABM's applied cell extracellular matrix, and Prigrow III culture medium were purchased from ABM (Richmond, Canada). Fetal bovine serum (FBS) and penicillin/streptomycin (P/S) were acquired from Gibco (San Diego, California, USA). Ultrapure low-viscosity high guluronic acid sodium alginate (UPLVG) was acquired from FMC Biopolymer (Sandvika, Norway). The following materials were obtained from Sigma-Aldrich (Merck KGaA, Munich, Germany): cell counting kit-8 assay, lactate dehydrogenase activity assay kit, hyaluronic acid sodium salt (from *Streptococcus equi*), gelatin tested according to Ph. Eur., fibrinogen from bovine plasma type I-S, thrombin from bovine plasma, 2-propanol (molecular biology grade), bovine serum albumin, TRI reagent, calcium chloride, alginate lyase, and triton™ X-100 molecular biology reagent. Chloroform was obtained from MP biomedicals (Santa Ana, California, USA). Fast gene scriptase II cDNA synthesis kit was acquired from Genetics Nippon (Düren, Germany). The primers for RT-qPCR were acquired from Applied Biosystems (Waltham, Massachusetts, USA). LIVE/DEAD™ viability/cytotoxicity kit was purchased from Life Technologies (Madrid, Spain). Phalloidin Alexa Fluor 488 was obtained from Molecular Probes (Eugene, Oregon, USA). Dulbecco's phosphate-buffered saline (DPBS) and phosphate-buffered saline (PBS) were obtained from Lonza (Porriño, Spain). Sodium chloride (NaCl) and formaldehyde 3.7–4.0% (w/v) were acquired from Panreac AppliChem (Monza, Italy). VEGF165 and PDGF-BB were acquired from Stemcell Technologies (Vancouver, Canada). Human VEGF165 standard TMB ELISA development kit and human PDGF-BB standard ABTS ELISA development kit were purchased from Peprotech (London, United Kingdom).

2.2. Cell culture conditions

iMAT cells were grown on T-flasks pretreated with ABM's applied cell extracellular matrix and Prigrow III culture medium. C2C12 cells were cultured using DMEM media. Both media were supplemented with 10% (v/v) FBS and 1% (v/v) P/S. HUVECs were cultivated using vascular cell basal media supplemented with endothelial cell growth kit components and 1% (v/v) P/S. All cell types were expanded at 37°C in a humid atmosphere with 5% CO_2. The culture medium was changed frequently, and when the culture had reached around 80% confluence, the cells were subcultured.

2.3. Ink and bioink preparation

The ink was progressively refined through a series of adjustments (set-up included in part (A) of the Supplementary File). The final ink consisted of the following combination of biomaterials: HA 0.36% (w/v), Alg 1% (w/v), Gel 4.2% (w/v), and Fg 3.6% (w/v). The HA and Alg were dissolved in DMEM. After both materials were dissolved, the Gel was added and was left overnight at 37°C. The Fg was dissolved in DMEM with 0.9% NaCl at 37°C for 4 h. The two parts of the ink were centrifuged to remove bubbles and then mixed.

Prior to the incorporation of cells (iMAT) or growth factors (VEGF165 or PDGF-BB), they were dissolved at the desired concentration (final concentration of 1×10^6 cell mL^{-1}, 2×10^6 cell mL^{-1}, and 5×10^6 cell mL^{-1} for the cells, 50 ng mL^{-1} for the VEGF165, and 10 ng mL^{-1}, 20 ng mL^{-1}, and 50 ng mL^{-1} for the PDGF-BB) in media inside a syringe. Finally, they were mixed with the rest of the ink before being transferred to a printer cartridge.

2.4 Rheological characterization

The rheological characterization of the final ink was carried out using an AR 1000 Rheometer (TA instrument, Waters Corporation, Milford, Massachusetts, USA) with a 20 mm flat steel plate. The tests were performed with a gap between the geometry and the Peltier plate of 600 μm and at a temperature of 25°C, unless otherwise stated. To ensure that the sample was at the test temperature and that the sample loading process did not affect the results, a sample-conditioning step was performed before each assay with an equilibrium time of 3 min (but for the gel formation assay). The software used to carry out the tests and the subsequent analysis was TRIOS 5.2 (TA instrument, Waters Corporation, Milford, Massachusetts, USA). Eight different rheological tests were performed.

In the shear rate sweep, the viscosity and shear stress values were calculated for shear rate values from 0.1 to 1000 s^{-1} (type of test: flow sweep). The sampling rate was set to 10 points per decade, with a 5 sec delay before measurement and a measurement duration of 30 sec. The zero-rate viscosity and the infinite-rate viscosity were determined from the representation of viscosity vs. shear rate by selecting the best mathematical fitting. The value of yield stress (σ_y) was determined from the representation of shear stress vs. shear rate; the value with the best mathematical fitting was selected.

In the recovery test, the viscosity values were recorded during five different steps (type of test: flow peak hold). In steps 1, 3, and 5, high shear rate of 200 s^{-1} was used, and in steps 2 and 4, low shear rate of 0.1 s^{-1} was used. Each of the steps lasted for 2 min. There was no recovery time between steps. The thixotropic character of the ink was established from representation of viscosity vs. time. The initial viscosity was calculated as the mean viscosity once the parameter had stabilized (variation less than 5%). The initial viscosity, determined as the mean stabilized viscosity with a variation of less than 5%, served as the baseline and was assigned a reference value of 100%. The viscosity values were measured at the conclusion of the 2-min, high-shear-rate periods. They were then compared to the corresponding 100% baseline (initial resting viscosity).

The strain sweep assay was used to determine the linear viscoelastic region (LVER) (type of test: oscillation amplitude). With a frequency of 1 Hz, the storage modulus (G') and the loss modulus (G") were determined at oscillation strains from 0.2% to 10000%. The points per decade were set to 6 and the ramp type to logarithmic. A deviation of ±5% in the value of the G' was used to determine the end of the LVER. The result of this assay served to determine the percentage of strain to use in the rest of the performed oscillatory tests.

To carry out the amplitude sweep assay, the values of G' and G" of the ink were measured in a range of oscillation stress between 0.1 and 2000 Pa (type of test: oscillation amplitude). The frequency used was 1 Hz, and the angular frequency was 6.28 rad s^{-1}. A deviation of ±5% was used to determine the end of the LVER. The values of G' and G" were taken into account during the LVER to characterize the ink. The yield point (τ_y), value of the shear stress at the limit of the LVER, and flow point (τ_f), value of the shear stress at the crossover of the moduli, were established.

In the gel-formation assay, the two parts of the ink, which were at 25°C, were mixed and loaded into the rheometer (type of test: oscillation time). No conditioning step was performed in this test. The G' and G" were measured from time 0 min to 60 min using a frequency of 0.1 Hz and a strain of 1%. The time-point where the beginning of a gel-formation process takes place is referred to as the gelation onset time (t_{CR}), and the time-point of the sol/gel transition point is known as the gel point time (t_{SG}). These values were determined from the modulus vs. time graph. The t_{CR} was calculated as the onset of the G' values (5% difference from the initially recorded values). The t_{SG} was determined as the time at which the G' and G" values intersect.

During the frequency sweep assay, the G', G", and complex viscosity (η*) were determined over the frequency range of 0.1 to 100 Hz (type of test: oscillation frequency). The oscillation amplitude was kept constant at a value of 8 rad and the strain at 1%. The points per decade were set to 10 and the ramp type to logarithmic. The properties of the ink were determined from the representation of the modulus vs. the frequency.

For the temperature sweep assay, three temperature ramps were performed (type of test: oscillation temperature sweep). In the first one, the values of G' and G" were calculated while decreasing the temperature from 37°C to 4°C (cooling curve). In the second one, the temperature was increased from 4°C to 37°C (heating curve). In the last one, the temperature decreased again from 37°C to 4°C (cooling curve). The temperature ramp was established at 1°C min^{-1}, the strain percentage at 0.1%, and the frequency at 1.0 Hz. The gelation point (T_g) determined from the cooling curve and the melting point (T_m) obtained from the heating curve were identified based on a change exceeding 5% in the G' value.

Temperature frequency sweep (type of test: oscillation frequency) was the last assay performed. The complex modulus (G*) was determined over the frequency range of 0.1 to 100 Hz at different temperatures. The oscillation amplitude was kept constant at a value of 8 rad and the strain at 1%. The points per decade were set to 10 and the

ramp type to logarithmic. The properties of the ink were determined from the graphical representation of modulus vs. frequency. All the obtained rheological parameters of the ink are summarized in part (B) of the Supplementary File.

2.5. Printability

For the study of printability, a CELLINK BIO X printer (Gothenburg, Sweden) was used. In order to control the printing temperature, the printing process was performed using a temperature-controlled printhead. The selected tip was a 22 G blue needle, and the speed was kept constant at 7 mm s^{-1}. The printability of the ink was studied at different pressures and temperatures. The extrudability of the ink at each temperature was tested. The photos of the obtained filaments were used to identify the level of gelation (relevant methodology is given in part (C) of the Supplementary File). To determine shape fidelity, also known as print accuracy, a computer-aided design (CAD) was made with horizontal and vertical lines at different distances in a single Z plane, as described in part (C) of the Supplementary File (panel 4 in Figure S4 in the Supplementary File).[38] For each temperature, the ink was printed at different pressures. A photo of the obtained structure was taken and, using ImageJ (National Institutes of Health, Bethesda, Maryland, USA), the area of the squares formed on the diagonal of the printed structure (actual area) was determined. Finally, the obtained actual area was compared with the theoretical area of the CAD design (Equation I).

$$Shape\ fidelity_{T_1,P_1,A_1}(\%) = \frac{Actual\,area_{T_1,P_1,A_1}}{Theoretical\,area_{T_1,P_1,A_1}} \times 100 \quad \text{(I)}$$

The diameter of the filaments was used as a parameter to determine the printability of the ink. In this case, the strand printability was defined, analogously to the shape fidelity, as follows (Equation II):

$$Strand\ printability_{T_1,P_1}(\%) = \frac{Experimental\ strand\ diameter_{T_1,P_1}}{Theoretical\ strand\ diameter_{T_1,P_1}} \times 100 \quad \text{(II)}$$

To calculate the strand printability, the average of eight filaments was calculated for each condition (relevant methodology is given in part (C) of the Supplementary File).

2.6. Three-dimensional printing and bioprinting

Scaffolds were obtained using the Cellink BIO X (Gothenburg, Sweden). To do this, the ink was transferred to a cartridge, which was subsequently introduced into a temperature-controlled printhead at 24°C. The selected tip was a 22 G blue needle. The speed was kept constant at 7 mm s^{-1} and the pressure at 120 kPa. The printbed temperature was established at 4°C. The designed scaffold was in a dimension of 1 cm (width) × 1 cm (length) × 1.44 cm (height), with 100% infill. This structure was used for all the assays described in this paper, unless otherwise stated. Once the structure was printed, it was crosslinked using 1 mL of a mixture of $CaCl_2$ (200 mM) and thrombin (40 IU mL^{-1}), mixed at a 1:1 ratio, for 30 min at room temperature.

For the 3D bioprinting process, the bioink containing tenocytes was utilized, using the same protocol and parameters as for the acellular scaffolds. After the crosslinking process, the tissue constructs were maintained in Prigrow III culture medium supplemented with 10% (v/v) FBS and 1% (v/v) P/S at 37°C in a humid atmosphere with 5% CO_2 until analysis.

2.7. Macroscopic imaging and cryo-SEM imaging

After printing, images of the scaffolds were captured to examine their dimensions and to compare them with those of the original design. These images were also used to verify the homogeneity of the obtained scaffolds. For analyzing the morphology of the surface, cryo-scanning electron microscopy (cryo-SEM) technology was employed using a TM4000Plus microscope (Hitachi, Japan).

2.8. Mechanical characterization

The mechanical properties of the acellular scaffolds and tissue constructs were determined using a TA.XTplusC texture analyzer and the exponent connect software version 7.0.6.0 (Stable Micro Systems, United Kingdom). The selected test was a static uniaxial compression test. A P/20 probe (20 mm diameter cylindrical aluminum probe) and a 5 kg loading cell were used. The initial position of the probe was 3 mm. The pre-test, test, and post-test speed were established at 1 mm s^{-1}. The target mode was the strain, which was set to 80%. The trigger force was 5 g. The mechanical properties of the two types of structures were analyzed at five different times. Four specimens were tested at each time point. The force and displacement values were measured by the machine. For the calculation of the stress and strain values, the following equations were employed (Equations III and IV).

$$Stress\left(\frac{N}{mm^2}\right) = \frac{F(N)}{A(mm^2)} \quad \text{(III)}$$

$$Strain\ (\%) = \frac{\Delta H\ (mm)}{H_0\ (mm)} \times 100 \quad \text{(IV)}$$

The parameters obtained from the two representations (force vs. displacement, and stress vs. strain) included: (i) the maximum force value, (ii) the stiffness, (iii) the maximum stress, (iv) the tangent elastic modulus, and (v) the work to break. The stiffness was determined as the slope of the tangent line to the force–displacement curve at 50% of the ultimate force. Similarly, the tangent elastic modulus was calculated

as the slope of the line tangent to the stress–strain curve at 50% of the ultimate stress.[39] Work to break was determined by calculating the area under the stress vs. strain curve until the breaking point was reached. Part (D) of the Supplementary File presents the results of the force vs. displacement graph along with the corresponding parameters derived from it.

2.9. Swelling study

In the swelling study, the acellular scaffolds were firstly printed, then crosslinked, and finally dried using a lyophilization process. Once lyophilized, their initial weight was measured (W_0). One milliliter of PBS was added to each scaffold. They were incubated under shaking conditions at 37°C for 24 h. At the established sampling time points, the scaffolds were removed from the PBS, slightly dried using a filter paper, and weighed (W_f). Ten specimens were tested during the different time points. The swelling ratio was established using the following equation (Equation V):

$$Swelling\ ratio = \frac{(W_f - W_0)}{W_0} \quad \text{(V)}$$

2.10. Degradation study

To establish the degradation rate, the acellular scaffolds were 3D-printed, crosslinked, dried with filter paper, and weighed (W_0). One milliliter of DMEM medium was added to each scaffold. Afterward, they were incubated under shaking conditions at 37°C for 85 days. At the established sampling time points, the scaffolds were removed from the media, slightly dried, and weighed (W_f). Twenty-five specimens were tested at each time point. The degradation percentage was established using the following equation (Equation VI):

$$Degradation\ (\%) = \frac{W_f}{W_0} \times 100 \quad \text{(VI)}$$

2.11. Assessment of cell viability

The viability of iMAT cells inside the tissue constructs was determined using the LIVE/DEAD™ Viability/Cytotoxicity Kit assay. Following the manufacturer's instructions, live cells were stained with calcein-AM (excitation/emission wavelength of 495/515 nm) and dead cells with ethidium homodimer-1 (excitation/emission wavelength of 495/635 nm). At the sampling time points, the tissue constructs were imaged using a Nikon TMS microscope (Virginia, USA).

2.12. Determination of metabolic activity

The metabolic activity of iMAT cells inside the tissue constructs was determined using the cell counting kit. Following the manufacturer's instructions, a 1:10 mixed solution of CCK-8 reagent (500 µL) was added to each tissue construct and was incubated for 4 h at 37°C. The fluorescence of the samples was determined in an Infinitive M200 microplate reader from TECAN Trading AG (Männedorf, Switzerland). The established parameters were a detection wavelength of 450 nm and a reference wavelength of 650 nm. Acellular scaffolds were used as blank. The results were represented as absorbance units vs. test condition (cell density and time). Five sampling times were established, and four replicates were performed in each condition.

2.13. Measurement of lactate dehydrogenase activity

The effect of the bioprinting process on the tenocytes was investigated using a lactate dehydrogenase activity assay kit. Following the manufacturer's instructions, 500 µL of master reaction mix was added to each tissue construct and incubated for 4 h at 37°C. Finally, the fluorescence of the samples was determined in an Infinitive M200 microplate reader. The established parameters were a detection wavelength of 490 nm and a reference wavelength of 680 nm. Acellular scaffolds were used as blank. The results were represented as absorbance signal vs. test condition (cell density and time) (part (E) of the Supplementary File). Three replicates were performed in each condition.

2.14. Gene expression study

The tissue constructs were cultured for 3 and 12 days under the previously mentioned conditions. At the mentioned time points, four of these tissue constructs were collected, enzymatically digested (using 1 mg mL^{-1} of alginate lyase, at 37°C, and for 15–25 min), and centrifuged to separate the cells from the rest of the scaffold. The TRIzol method was used to obtain the RNA of the samples. Finally, the total mRNA quantity and purity were measured with a SimpliNano Nanodrop from GE Healthcare Life Sciences (Madrid, Spain). The RNA was reverse-transcribed to cDNA using the Fast Gene Scriptase II, cDNA Synthesis Kit. Real-time PCR (RT-qPCR) was performed using StepOnePlus Real-Time PCR Systems. To determine the expression of the target genes (glyceraldehyde-3-phosphate dehydrogenase, *Gapdh*; Scleraxis BHLH transcription factor, *Scx*; Fos proto-oncogene, *c-Fos*; Tenascin C, *Tnc*; Collagen type I alpha 1 chain, *Col1a1*; Collagen type III alpha 1 chain, *Col3a1*; Fibronectin 1, *Fn1*), commercial

TaqMan primers were used. Gene expression was normalized to the housekeeping gene (*Gapdh*). The $2^{-\Delta\Delta CT}$ method was applied to determine the fold changes in gene expression between the samples at day 3 and day 12. The observed correlation between the expressions of tendon-related genes in the tissue constructs is shown in part (F) of the Supplementary File.

2.15. Growth factor release study

Once printed, the scaffolds were weighed in order to subsequently determine their exact amount of initial factor. Subsequently, they were crosslinked. After 30 min, the crosslinking medium was collected and stored at -20°C (for VEGF165) and at -80°C (for PDGF-BB) (first sample). One milliliter of DMEM medium was added to each of the acellular scaffolds. Sampling was performed in the span of 4 h. Before each interval, the medium was removed, and fresh medium was added. After this 4-h period, the supernatant was collected and stored at the aforementioned conditions. Once the assay was finished, the amount of factor released in each of the intervals was determined using the human VEGF165 standard TMB ELISA development kit and human PDGF-BB standard ABTS ELISA development kit. Three independent specimens for each time point were analyzed. The results were represented as the log of the release rate vs. the midpoint of each time interval. After performing the linear fits, the release constants, K, were calculated by multiplying the slopes of the lines by 2.303. The half-life values of the growth factors were calculated dividing 0.693 by the value of K.

2.16. *In vitro* analysis of biological activity of VEGF165

To analyze VEGF165's activity *in vitro*, an angiogenesis assay was performed via seeding HUVECs on top of the acellular scaffolds. The scaffolds were 3D printed with a specific rectangular design measuring 1 cm in width, 1 cm in length, and 1.44 cm in height (comprising two layers), with an additional two-layer perimeter printed on the top surface of the scaffold. Two types of scaffolds were printed for this assay: control scaffolds without growth factor, and scaffolds with 50 ng mL^{-1} VEGF165. Once printed, the scaffolds were crosslinked. After 30 min, the crosslinking media were removed and 100 µL of an HUVEC suspension (5×10^6 cells per mL) was seeded on top of the scaffold. The cells were left to adhere for 4 h before adding more media. At the established sampling times, the cells were fixed with 4% formaldehyde, permeabilized with 0.1% Triton™ X-100, and stained with phalloidin (concentration of 1.6 µM). Finally, the scaffolds were observed in a Nikon TMS microscope. An excitation/emission wavelength of 495/515 nm was used. ImageJ software was used for semi-quantitative measurements. The area covered by cells, the total number of loops, the area of all the loops, the mean area per loop, the length of all the tubes, and the mean length per tube were determined. Three independent scaffolds were evaluated for each condition and time.

2.17. *In vitro* analysis of biological activity of PDGF-BB

To analyze PDGF-BB's activity *in vitro*, a proliferation assay was performed using C2C12 cells. The cells were seeded in a 12-transwell plate (2.5×10^5 cells per well). After 24 h, acellular scaffolds with a specific 3D CAD design (circle of a diameter of 5.4 mm and a height of 1.23 mm) were placed in the upper part of the transwell. Four different groups were tested with different concentrations of PDGF-BB: 0 ng mL^{-1} (control), 10 ng mL^{-1}, 20 ng mL^{-1}, and 50 ng mL^{-1}. The number of cells after 24 h in each condition was determined using an automatic cell counter (Bio-Rad, Hercules, California, USA). Three independent scaffolds were evaluated for each condition.

2.18. Statistical analysis

Statistical differences were determined by non-parametric tests (Mann–Whitney *U* test for two-group comparison, and Kruskal–Wallis *H* test for comparison involving more than two groups). Non-parametric tests were selected to ensure robustness due to the low sample size ($n < 50$). Statistical analyses were conducted to compare all groups; however, in order to ensure result clarity, the figures only depict significant differences observed among the various groups on the same day of sampling. IBM SPSS statistics software was used to carry out the statistical analysis, and differences were considered significant at $p < 0.05$.

3. Results and discussion

3.1. Ink development for enhanced tendon regeneration

One of the primary objectives of this research was to develop an innovative ink tailored for 3D bioprinting. The ink was used to develop hydrogel-based scaffolds and tissue constructs that could improve the regeneration of partial tendon injuries. The initial design phase began by limiting the materials to those of biological origin. The function of these materials in the ink needed to be diverse. Additionally, properties inherent to the target tissue, namely tendons, were also considered.

Four natural polymers were selected: Gel, Alg, HA, and Fg. Gel, derived from the primary component of tendons—collagen (making up 60–85% of the tendon's dry weight),[40] was selected with a multifaceted approach. Its inclusion aimed not only to augment the ink's likeness to native tendons but also to deliver crucial functionalities. Gel was chosen for its ability to provide structural support, offer binding sites for cells, and enhance printability, attributable to its responsiveness to temperature.[41] HA was chosen for

its beneficial effects on lubrication, water retention, and viscoelasticity in the resulting ink.[42] Alg, recognized for providing sturdy structural support alongside excellent mechanical properties, played a pivotal role in the ink. It facilitates a crosslinking mechanism within the ink through cations and guarantees efficient water retention.[43] Lastly, Fg, bearing similarities to natural ECM components, was incorporated to enhance cellular viability within the ink and to introduce a second crosslinking mechanism (enzymatic, in this case).[44]

This meticulous selection process yielded an ink composed of polymeric natural materials, mirroring the composition of the ECM in the target tissue, tendons (Figure 1). The percentage of water is high in both the ECM (55–72%) and the scaffold (91.7%), but higher in the scaffold than in the ECM. The proportion of total proteins exhibited similarities in both cases, with collagen dominating the ECM (65–80%) and Gel being the major protein in the hydrogel (44.76%). Fg constituted the second major protein in the hydrogel at 39.30%. The percentage of total polysaccharides showed a distinct difference between tendon ECM (0.2–5%) and the hydrogel (14.85%), primarily due to Alg (10.92%). While not naturally occurring in tendons, Alg was introduced for its crosslinking potential and its role in conferring stiffness to the hydrogel. Conversely, the percentage of glycosaminoglycans (GAGs) remained similar for both (0.2–5% in tendons and 3.93% in the hydrogel). In summary, a high-degree resemblance of the hydrogel to the tendon ECM in terms of constituent compositions suggests that the hydrogel is an excellent candidate for tenocyte incorporation and for the regeneration of damaged tendons.

3.2. Ink characterization

3.2.1. Rheological characterization

The developed ink was rheologically characterized. These rheological characterization tests helped determine some of the most important mechanical properties of the ink (summarized in part (B) of the Supplementary File), allow comparison of the ink with other inks, and more importantly predict the ink's behavior during 3D printing.

First, the ability of the ink to be extruded during the 3D printing process is analyzed. By analyzing the results of the shear rate sweep test (Figure 2A), it can be established that the ink has a shear-thinning behavior, that is, the viscosity decreases as the shear rate increases. By performing a Carreau–Yasuda fit ($R^2 = 0.99$), we established that the zero-rate viscosity is 4039.11 Pa·s while the infinite-rate viscosity is 0.18 Pa·s.[45] The difference between the two is possibly attributed to the high concentration of polymers and their polydispersity (broad molecular weight distribution), among other reasons.[46] These properties confirmed that the ink was suitable for 3D printing since, after applying a certain pressure on the ink, it became less viscous and able to flow through the 3D printer needle. The same figure is also representative of the shear stress vs. the shear rate. A Herschel–Bulkley adjustment ($R^2 = 0.97$) established that the σ_y of this ink is 107.48 Pa. This parameter indicates that at stress values lower than 107.48 Pa, the ink will behave like a solid (it will support the suspended cells while it is in the cartridge) and that at higher stress values the ink will start to flow (it can be extruded in a controlled way). In any case, this value was regarded as a guide value since it was determined by carrying out a step-like ramp. In a real 3D printing situation, the stress is modified much faster, so σ_y value may be somewhat different.[47]

Once extruded, the ink must recover its mechanical properties to ensure that the 3D structure will form properly and will not collapse due to the force of gravity. To determine this property, a rotational thixotropic test was performed (viscosity was measured at different shear rates). This test, also known as the recovery test, showed that the ink is very thixotropic (Figure 2B), that is, it takes a certain time to reach equilibrium once a high mechanical force has been applied to it. In this case, each of the test steps lasted for 2 min, which were not enough for the ink to reach equilibrium (the rebuild time could not be determined from the procedure used in this test). Specifically, it recovered 36.12% of the initial viscosity the first time it was subjected to the stimulus (viscosity 455.925 Pa·s) and 24.38% of the initial viscosity from the second time (viscosity 307.767 Pa·s), with the initial viscosity being 1262.16 Pa·s. Regarding 3D printing, this result implies that once the ink has been deposited on the surface, it takes more than 2 min to recover the initial viscosity that it had in the cartridge. Even though the recovery of the solid-like behavior was not very fast under test conditions, the difference between the temperatures of the rheology test and the real 3D printing process (the cartridge temperature was lower than 25°C and the printing bed temperature was 4°C) suggests that the recovery after printing will become faster, allowing good shape fidelity.

The strain sweep allows determining the LVER, a region in which the G', which indicates the solid-like behavior, and the G", which indicates the liquid-like behavior, are independent of the applied stress (Figure 2C). The value of G' during the LVER is 323.18 Pa, and that of G" is 114.27 Pa; therefore, the values of tan d and G* are 0.35 Pa and 342.79 Pa, respectively. These values are typical of viscoelastic gels, usually between 100 Pa and 500 Pa.[48] The linearity limit (γ_L) is 67.18%. The crossover between G' and G", also known as critical strain, was found at 345.23% (G'=G"=107.21 Pa). This value indicates that from that percentage of strain, the ink will start to flow. In addition,

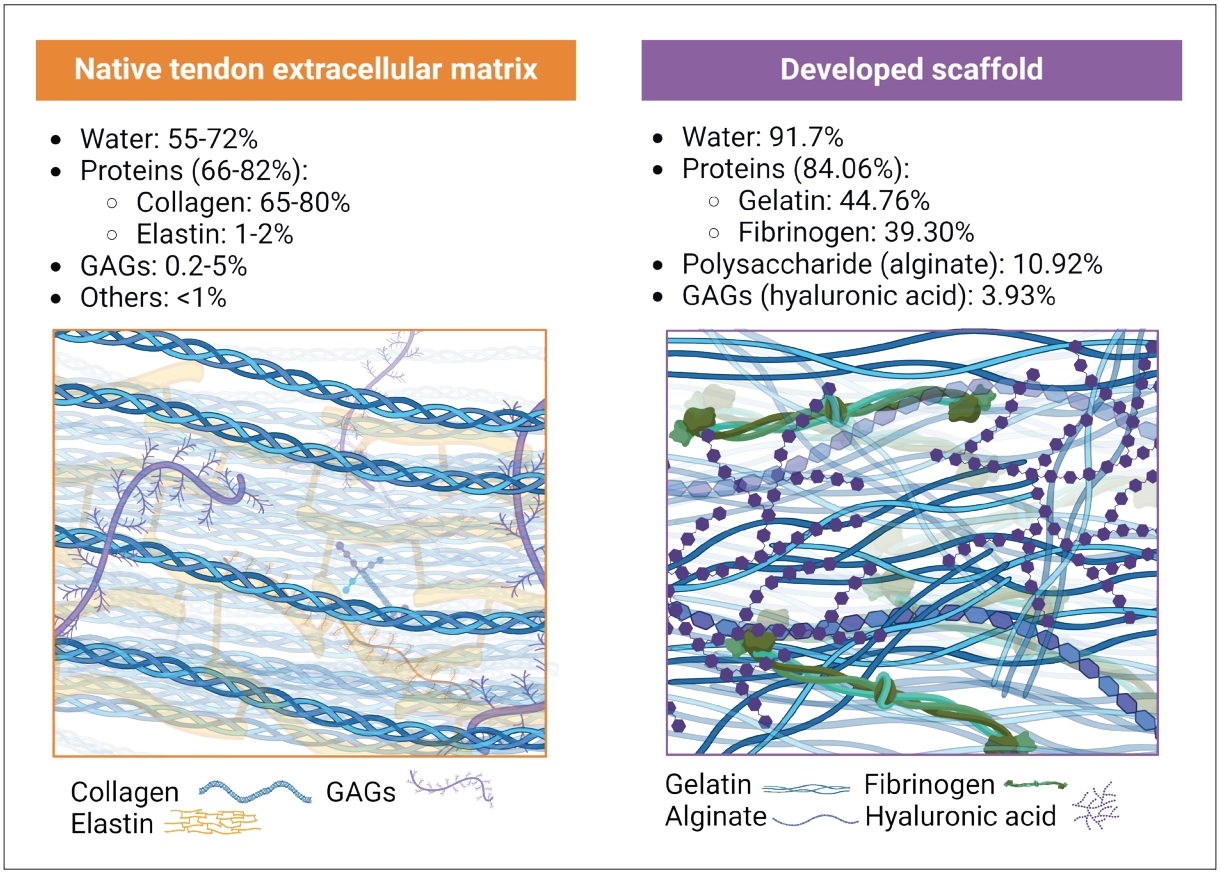


Figure 1. Comparison between the composition of the extracellular matrix (ECM) of tendons and the developed hydrogel. In the upper part, the percentages of each component are indicated. In the lower part, a schematic representation is shown. The ECM of tendons is mainly composed of oriented collagen fibers. Other important molecules include elastin and glycosaminoglycans (GAGs). Despite occurring at lower concentrations, these molecules are crucial for the normal development and function of tendons. The developed hydrogel-based scaffold is composed of different biomolecules, with the gelatin and the fibrinogen occurring at the highest concentrations. The polysaccharides alginate and hyaluronic acid are also present in the ink formulation. Note 1: cells are not included in the figure but are also present in both structures. Note 2: The percentages of the biomolecules represent their relative weight within the tendon and scaffold structures, with these percentages calculated based on the dry weight of the respective tissues created with biorender.com.

based on these results, a % strain, at which the rest of the tests were carried out within the LVER, was established. Specifically, the rest of the oscillatory tests were performed at 1% strain.

In addition, through representing the oscillation stress (oscillatory stress sweep) on the *X* axis, other important ink parameters can be determined: the τ_y and the τ_f (Figure 2D). The τ_y is the lowest shear-stress value, above which the material's structure breaks down and starts to flow (value of the stress at the end of the LVER region), whereas the τ_f is the stress necessary to maintain the strain rate constant during plastic deformation (value of the stress at the crossover point, G' = G").[48] The value of G' is 528.83 Pa and that of G" is 232.35 Pa. To determine the transition behavior of the ink, the flow transition index (τ_f/τ_y) was calculated, whose value is 2.28. This implies a moderately rapid transition between elastic and plastic behavior (the hydrogel will not suffer brittle fracturing).

To establish the gel formation process, a time sweep assay was performed (Figure 2E). Under the test conditions, the t_{CR} began at 3 min 30 s, while the point at which the crossover between the value of G' and that of G" occurs, known as t_{SG},[49] was 10 min 10 s. The values of G' and G" began to stabilize at 55 min. These results showed that, with a processing period of 30 min, the prepared ink could stabilize sufficiently and present a more-than-satisfactory elastic modulus for the subsequent printing process.

In the frequency sweep assay, it can be observed that the ink presents a sol/gel-like behavior. The value of G' is higher than the value G" for all the frequency range, a typical characteristic of sol-like gels (the

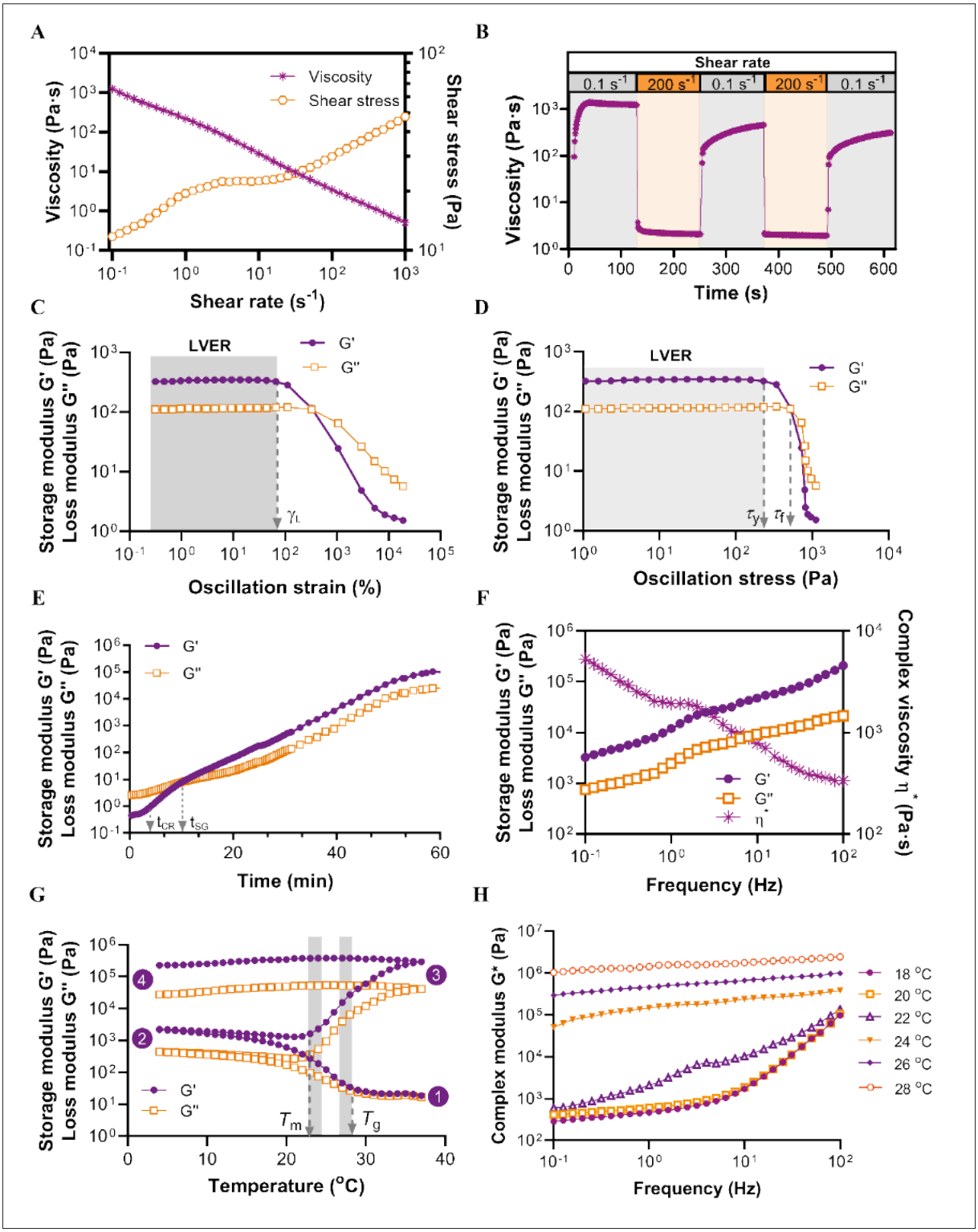


Figure 2. Rheological characterization of the developed ink. The performed tests were: (A) shear rate sweep, (B) recovery test, (C) strain sweep, (D) shear stress sweep, (E) time sweep, (F) frequency sweep, (G) temperature sweep, and (H) frequency sweep at different temperatures.

elastic behavior dominates). Both parameters have a very high frequency dependence (with increasing frequency, both moduli increase), which is typical in complex materials such as polymers and gels (Figure 2F).[50] The η* decreased at higher frequencies. The combination of these two results (increasing G' and G" and decreasing η* with frequency) indicates that the ink has a complex viscoelastic shear-thinning behavior (as previously indicated).

It is important to analyze the behavior of the ink with the change of temperatures since all the constituent materials of the ink are thermally sensitive. To analyze the ink's behavior and to define the best protocol for obtaining and printing the ink, a temperature sweep assay was performed (Figure 2G). The G' and G", when starting the test at 37°C, were almost similar, at 18.7 Pa and 16.9 Pa, respectively. When the temperature dropped to 4°C, both moduli increased to 2200 Pa and 441 Pa, respectively. During this cooling period, with a 5% change in the storage modulus value, the T_g was determined, which was established at 28.14°C. In the subsequent heating process, the moduli rose again to 2.94×10^5 Pa and 4.13×10^4 Pa, respectively, and with a 5% change in the value of the G', the T_m was determined, which was established at 23.56°C. This increase in the value of the moduli indicates that changes in temperature are irreversible (or at least requires more time than the one used in this assay). In the last step, the temperature was decreased again, producing a change in the values of the moduli, with a slight drop in this case. The information extracted from this test allows for the determination of a suitable temperature window for achieving good printing while maintaining shape fidelity and cell viability, i.e., 23.56–28.14°C.

Once the temperatures that are critical for ink development and 3D printing process had been estimated, the G* for each of those temperatures at different frequencies was determined (Figure 2H). The G* increased with temperature, with the results being very similar for 18°C and 20°C. A higher G* was observed when the temperature was raised to 22°C. The values kept increasing with temperature until reaching the maximum value at 28°C. This behavior is not uncommon in hydrogel-based inks. Specifically, this can be accounted for by different possible explanations surrounding the diverse materials used to compose the hydrogel. For instance, the increase in temperature can augment the mobility of the Alg chains and the diffusion rate of ions. This mobility improves the interactions and crosslinking between those chains, leading to a stiffer network.[50] Likewise, the gelation process can also be enhanced. The fibrin clot formation can, in addition, be thermally activated, resulting in an increase in gel stiffness.[51] The intermolecular interactions can be increased in the case of the HA and Gel, facilitating the associations between these molecules.[52]

3.2.2. Printability

The printability assay was performed to determine if the ink was printable under each test condition (assay explained in part (C) of the Supplementary File). Taking into account the results of the temperature sweep (T_g = 28.14°C and T_m = 23.56°C), the studies were carried out at six different temperatures: 18°C, 20°C, 22°C, 24°C, 26°C, and 28°C. The results in Figure 3A demonstrate that the ink can be extruded at any of the tested temperatures. Despite this, notable differences can be observed in the printed filaments due to the properties of the ink. At 18°C and 20°C, the ink was over-gelated, causing incomplete filling and structural disruption of the filaments. On the contrary, at 26°C and 28°C, the ink was under-gelated; therefore, continuous filaments could hardly be obtained. Optimal gelation was observed in the filaments extruded at 22°C and 24°C, with the situation at 24°C being slightly better than that at 22°C, where there was still some minimal degree of gelation.

The strand printability and shape fidelity analysis enabled the determination of the optimal 3D printing pressure and temperature at the selected speed (7 mm s^{-1}) and needle diameter (22 G) (Figure 3B). In the case of strand printability, the diameter of the obtained filaments was analyzed and represented as a percentage when compared to the theoretical diameter size (Figure 3B-i). For the shape fidelity, the area of the squares that were formed on the diagonal of the printed design (as described in Figure S4 in the Supplementary File) was analyzed and represented as a percentage when compared to the theoretical area size (Figure 3B-ii). For both parameters, the optimal pressure increased while the temperature decreased. Taking into account the results obtained during the extrudability and filament formation assay, the values obtained for strand printability and shape fidelity under optimal gelation conditions were analyzed in detail, that is, at 22°C and 24°C. In the case of 22°C, the best percentage of strand printability and shape fidelity was observed at 140 kPa, measuring 108.68% and 90.98%, respectively. In the case of 24°C, the best percentage of strand printability and shape fidelity was observed at 120 kPa, measuring 108.51% and 89.92%, respectively. These results indicate that the strand printability and the shape fidelity obtained at these two temperatures are very similar. In order to select the best printing parameters, two aspects were taken into account: the temperature *per se* and the used pressure. As previously described, high pressures during the printing process negatively affect cell viability.[53-55] In the same way, a decrease in temperature can also negatively affect cell viability.[56]

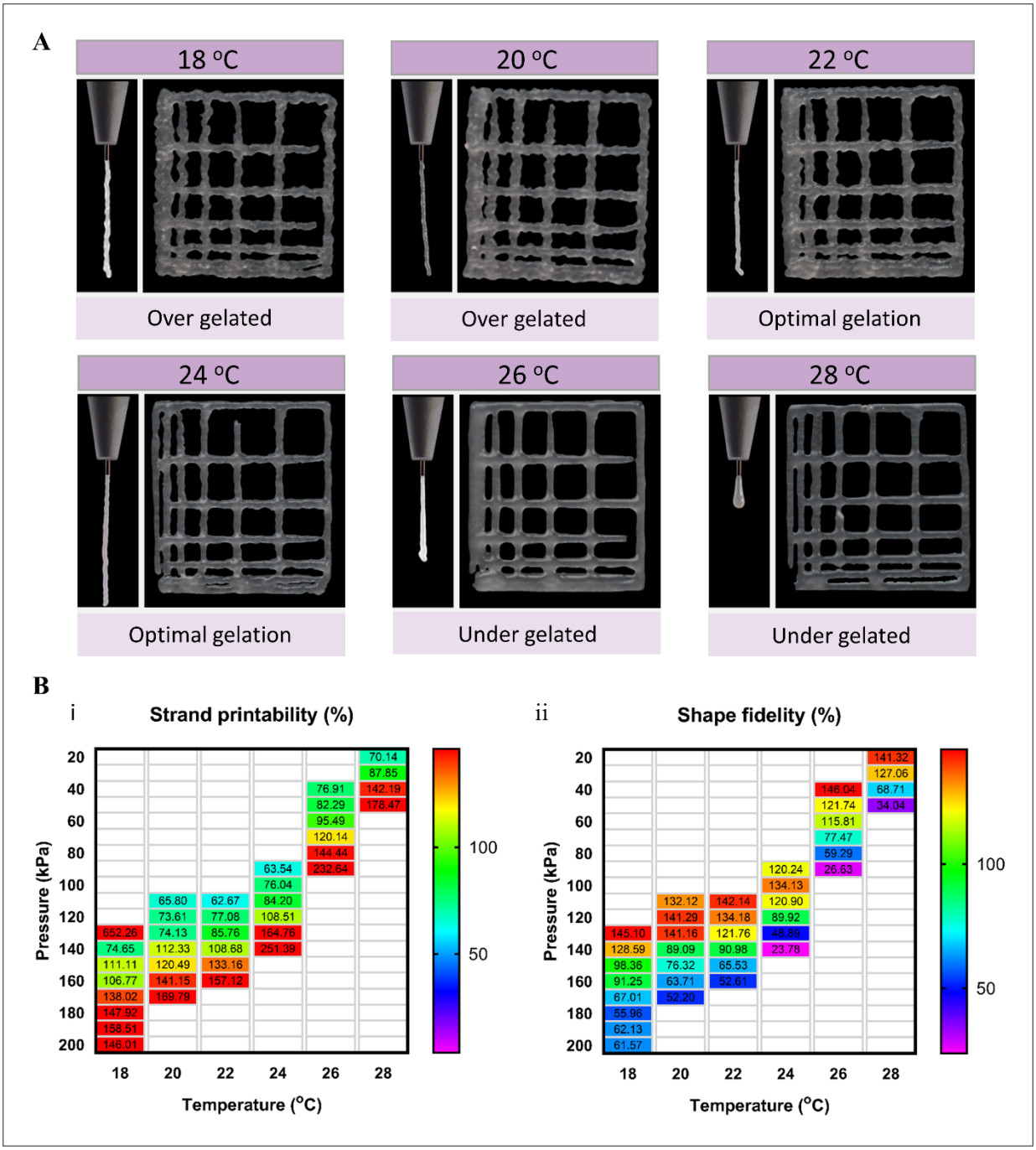


Figure 3. Study of the printability of the ink at different temperatures: 18°C, 20°C, 22°C, 24°C, 26°C, and 28°C. (A) Extrudability and filament formation assay. (B) Strand printability (%) (i) and shape fidelity (%) (ii) of the obtained ink at the different tested temperatures (*x*-axis) and pressures (*y*-axis). The conditions that allow obtaining better printability and fidelity parameters are indicated in green (values close to 100%).

This decrease of temperature increases the viscosity of the ink (increasing the stress suffered by the cells). It also can modify the metabolism of the cells (reduction of metabolic activity, disruption of the cell membrane, alteration of enzymatic activity, etc.). Although, in this case, there is not much difference, the temperature of 24°C was selected as the final parameter for bioprinting in order to use a lower pressure (120 kPa) and ensure better cell viability.

3.3. Scaffold development and characterization

The comparison between the CAD design and the printed scaffolds was analyzed using macroscopic images and

the ImageJ program (Figure 4A-i–iii and A-iv–vi). The intended dimensions of the CAD design are 1 cm × 1 cm, while the resulting 3D-printed structures measure 1.02 ± 0.03 cm × 0.99 ± 0.02 cm in length and width. The CAD design's height was set at two layers (resulting height of 1.44 mm). The actual height of the printed scaffolds is 1.49 ± 0.16 mm. This indicates that the ink enables the fabrication of scaffolds with a geometry very similar to that of the CAD design. Furthermore, the structure maintained its shape even before undergoing crosslinking. Once the parameters had been optimized, the scaffolds were automatically printed in culture dishes (Figure 4A-vii).

In the cryo-SEM images, the surface of the scaffolds exhibits a porous structure (Figure 4B). This rough surface may promote cell adhesion and proliferation, and the porosity may facilitate the diffusion of nutrients and other molecules within the microenvironment.[57,58]

The rate of degradation and the swelling ratio are two crucial parameters for characterizing scaffolds. The resulting values of degradation are represented as a percentage of the weight loss (degradation percentage) vs. time (Figure 5A-i). The scaffolds lose practically 30% of their weight in the first 7 days. From day 7 to day 42, the degradation was much more gradual and sustained, losing only 10% of the weight (in total, a 40% of the initial weight). These results indicate that the scaffolds maintained 60% of their weight after 85 days under the previously mentioned conditions. A period of 85 days, as previously described in literature, would be enough for the cells to produce ECM and for the tendon to begin to regenerate.[59,60] Meanwhile, the swelling ratio for each sampling time was calculated by correlating the weight of the wet scaffold to the weight of the dehydrated scaffold. The data presented in the graph (Figure 5A-ii) indicate that during the first hour, the scaffold absorbed a large amount of PBS, practically increasing its dehydrated weight by nine times. The maximum selling ratio was reached after 3 h, following which it remains constant for up to 24 h. This increase in water content could decrease the stiffness of the scaffold and favor the transport of nutrients and molecules of interest (important for the release of growth factors). Likewise, they may be related to the degradation process the scaffold underwent in the first several days of culture.

Other equally important parameters for the function of the scaffold are the mechanical properties. These properties can influence the proliferation, morphology, and activity of cells, as well as the release of factors or the transport of nutrients, among others.[61] In turn, the mechanical properties are influenced by other parameters such as the composition of the scaffold, the crosslinking process, or the aforementioned degradation and swelling parameters. To determine the mechanical performance, a compression test was performed. This test enabled the determination of the initial mechanical properties of the acellular scaffolds and

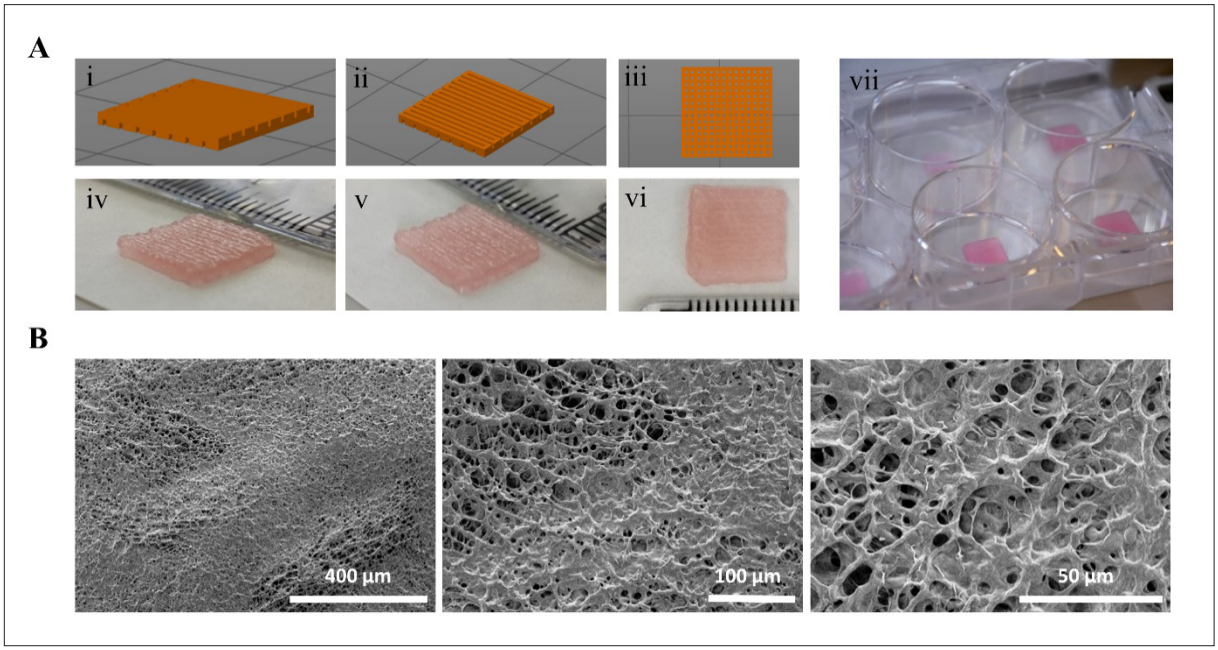


Figure 4. Characterization of the morphology of the 3D-printed scaffolds. (A) CAD designs (i–iii) and macroscopic images of the 3D-printed scaffolds (iv–vi). These scaffolds could also be printed in an automated way on culture plates (vii). (B) Cryo-SEM images of the surface of the scaffolds at different magnifications (from left to right: 120x, 300x, 1000x).

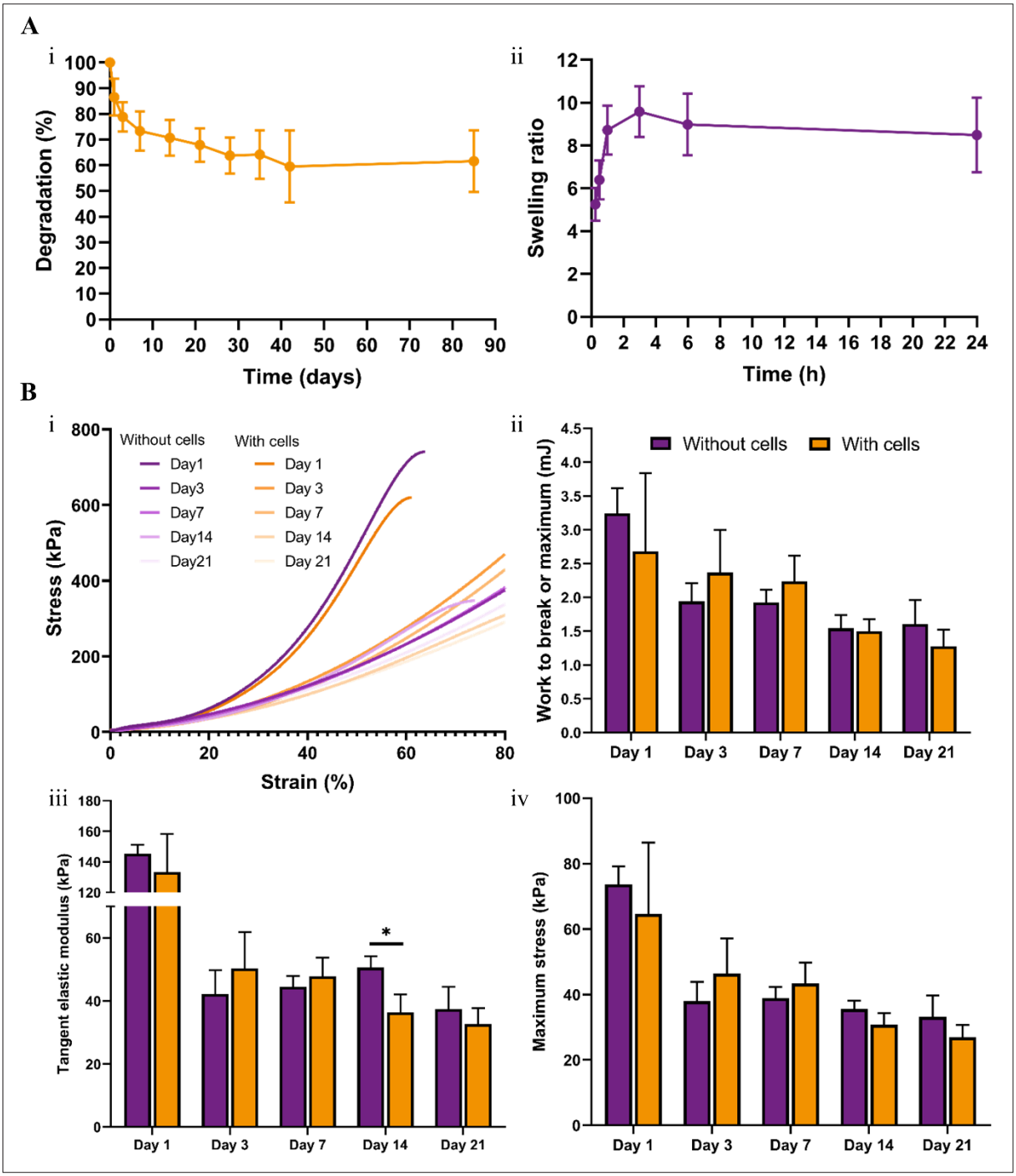


Figure 5. (A) Scaffold degradation over time (i) and swelling ratio (ii). Results are represented as mean ± SD (n = 25 in the degradation assay, and n = 10 in the swelling assay). (B) Mechanical characterization of the acellular scaffolds (purple) and tissue constructs (orange): (i) stress (kPa) vs. strain (%) curves, (ii) work to break or maximum (mJ), (iii) tangent elastic modulus (kPa), and (iv) maximum stress (kPa). This characterization was performed with a compression test at different time points. Results are represented as mean ± SD (n = 4). *p < 0.05.

tissue constructs as well as the variation of those properties over time. The force and displacement parameters were obtained from this test and further used to calculate the strain and stress values. In Figure 5B-i, the stress (kPa) is represented graphically against the strain (%). The main mechanical parameters of interest were obtained from this graph: work to break/maximum (mJ) (Figure 5B-ii), tangent compression elastic modulus (kPa) (Figure 5B-iii),

and maximum stress (kPa) (Figure 5B-iv). This assay was performed with and without cells. The results obtained from the force vs. displacement analysis are shown in part (D) of the Supplementary File.

An analysis of the initial values revealed that at day 1, the maximum stress was 76.6 ± 0.74 kPa in acellular scaffolds and 64.6 ± 2.17 kPa in tissue constructs. These values coincide with those described in the literature for the materials used in the ink (range between 1.5 kPa and 65 kPa for collagen, fibronectin, and Gel).[62] The other two parameters are the work to break/maximum, whose value is 3.24 ± 0.37 mJ in acellular scaffolds and 2.68 ± 1.15 mJ in tissue constructs, and the tangent compression elastic modulus, whose value is 145.37 ± 5.89 kPa in acellular scaffolds and 133.40 ± 24.88 kPa in tissue constructs. Considering the mechanical properties of the tissues, these values of elastic compression modulus are lower than the ones of native tendons.[63] However, as the objective is to regenerate partial tendon ruptures, these lower properties are more suitable. In particular, it could favor cell adhesion and proliferation, which in turn might enhance ECM deposition.[64,65] In addition to this, it offers other benefits that are not usually taken into account such as the reduction of the stress concentration (mechanical stress can be symmetrically distributed), the improvement of the biodegradability, the promotion of the vascularization, and the reduction of the inflammatory response (generally stiffer scaffolds activate the immune system more easily), among others.[66-68]

Since the first day, the mechanical parameters continued to decrease until day 21, and in most cases, the difference between days was statistically significant. This decrease was progressive but less pronounced compared to the change between day 1 and day 3. These profiles coincide with the degradation and swelling processes. With this, and based on the existing literature, it can be hypothesized that the degradation and swelling processes are responsible, at least in part, for the decrease in the mechanical properties of the scaffold over time.[69,70] No significant differences were observed between acellular scaffolds and tissue constructs (except for the tangent elastic modulus on day 14), although a greater variability was observed within the tissue constructs.

3.4. Cell incorporation

After characterizing the physical and mechanical properties of the structures, tenocytes were incorporated into the ink to obtain tissue constructs. Cell viability was analyzed qualitatively at different times and at three cell densities (1×10^6 cell mL^{-1}, 2×10^6 cell mL^{-1}, and 5×10^6 cell mL^{-1}) using the live-dead assay (Figure 6). The obtained micrographs showed high cell viability in all the tested conditions. The lower viability in the initial times could be related to the stress produced by the printing process.

To analyze the metabolic activity of the different cell densities over time, the CCK-8 reagent was used (Figure 7A). The metabolic activities of the three cell densities increased with time. Particularly, during the first 7 days, there was a more pronounced surge in cell metabolic activity. Subsequent to this initial period, the rate of increase in metabolic activity became more moderate, albeit remaining positive. Among the different cell densities, it can be seen that there are significant differences between the three densities in the first three sampling times, probably due to the difference in the number of cells. On both days 14 and 21, the signal became equal for the three cell densities. This finding suggests that an "equilibrium" was reached on day 14, where the limit of the number of cells in the scaffold could be observed.

To determine the effect of the printing conditions on the cells, the amount of lactate dehydrogenase enzyme in the culture medium (related to the amount of damaged or dead cells) was analyzed on days 1 and 3 after 3D bioprinting (Figure S7 in the Supplementary File). The results showed that the printing process affects the integrity and viability of the cells (high levels of lactate dehydrogenase in all cell densities on day 1). The level of lactate dehydrogenase in the highest cell density, i.e., 5×10^6 cell mL^{-1}, was significantly higher than those in other cell densities of 1×10^6 cell mL^{-1} and 2×10^6 cell mL^{-1}, which, however, did not show significant differences among themselves. Nevertheless, the difference between the values could be explained by the different number of cells in each scaffold. Lactate dehydrogenase enzyme levels underwent a substantial decrease on day 3 for cell densities at 1×10^6 cell mL^{-1} and 5×10^6 cell mL^{-1}. These results imply that the cells present a rapid recovery after the initial stress process. Likewise, they suggest that the scaffolds offer a suitable environment for cell growth and proliferation.

3.5. Gene expression

Gene expression analysis was used to determine the expression over time of characteristic markers of tenocytes (*Scx* and *Tnc*), markers of synthesis of macromolecules of the ECM (*Col1a1* and *Col3a1*), and markers of cellular activity (*c-Fos* and *Fn1*) (Figure 7B).

Scx has been identified as a very important marker of tendon neoformation and cellular differentiation to tenocytes.[71] It has also been reported that this gene plays an integral role in cellular differentiation and ECM organization.[72] In this case, no significant differences in the expression of this gene were observed over time. This same effect has previously been reported.[73] One possible

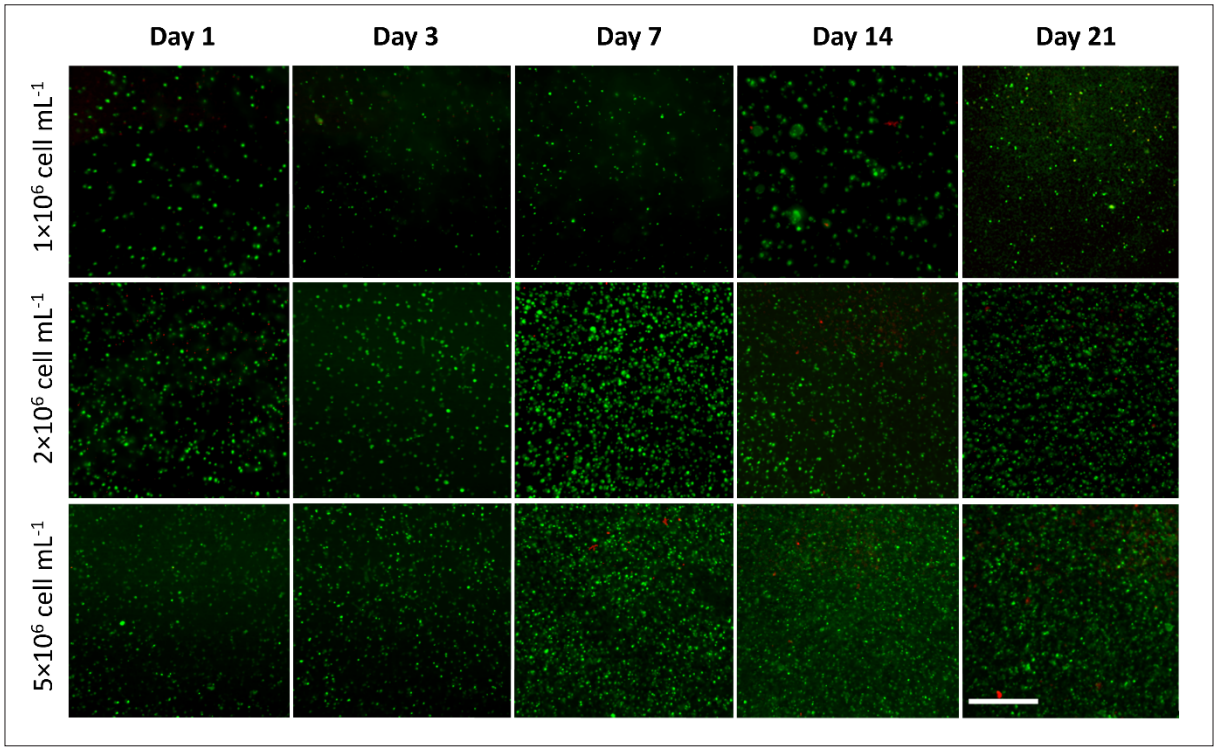


Figure 6. Results of cell viability assay. Fluorescence micrographs of live/dead-stained tissue constructs. The live (green) and dead (red) cells can be seen at the different time points and cells densities (4×). Scale bar: 500 μm.

reason is that when the tenocyte phenotype is established, the expression of this gene ceases to change. The *Tnc* gene encodes a glycoprotein that is essential during tendon regeneration because it is related to collagen fiber alignment and tissue homeostasis.[72,74] Although an increasing tendency was detected over time, it was not statistically significant. It has been previously reported that this gene is mechanosensitive, so its expression increases over time in response to the mechanical stimulation to which the cells are subjected when they are embedded in the hydrogel.[75] The maintenance of *Scx* expression and the slight increase in *Tnc* expression suggest that cell dedifferentiation is not occurring over time.[76]

c-Fos is a member of a family of intermediate early genes involved in a large number of biochemical processes. Its transcription is increased as a response to growth factors and during cell proliferation, differentiation, and transformation, among others.[71] In the tissue constructs, the expression of this gene increased significantly over time. This allows authors to hypothesize that the cells increase their proliferation rate over time within the scaffold, in agreement with the results observed in cell viability and metabolic activity assays. On the other hand, *Fn1* is a gene that encodes fibronectin. Its function is related to the processes of cell adhesion and migration.[77] The expression of *Fn1* in tenocytes embedded in the scaffold did not change with time.

Under normal conditions, the major component of tendons is collagen, specifically type I collagen.[13] When an injury occurs in this tissue, during the first phase of the regeneration process, collagen III is the one that is predominantly produced.[34] In later phases, this collagen is replaced by type I collagen, indicating greater maturity and mechanical resistance of the tissue.[78] This is why the expression of both collagens, as well as their proportion, is of great importance. In the developed tissue constructs, tenocytes presented a significant increase in the expression of *Col3a1* on day 12. In the case of *Col1a1*, its expression exhibited very slight and not significant changes. This result indicates that, during the first 12 days, the tenocytes embedded in the scaffold are still in an "initial" phase of production of the tendon's own ECM. It is necessary to mention that these genes, *Col1a1* and *Col3a1*, have also been used in many occasions as markers that indicate the differentiation or dedifferentiation of tenocytes.

In addition to the analysis of the variation of gene expression over time, it is also interesting to analyze the relationship between the expressions of the different genes.

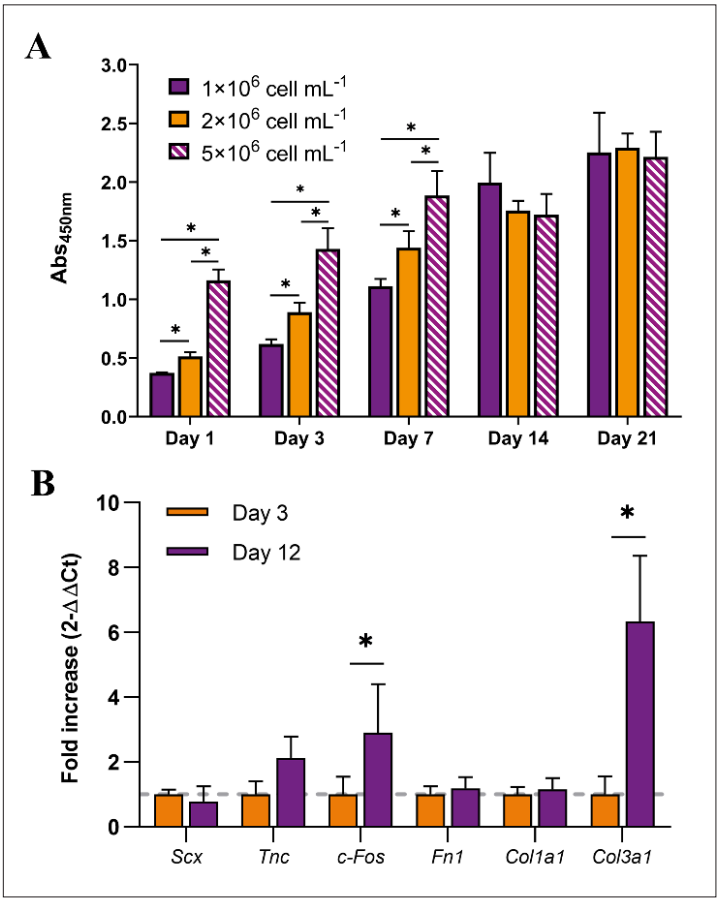


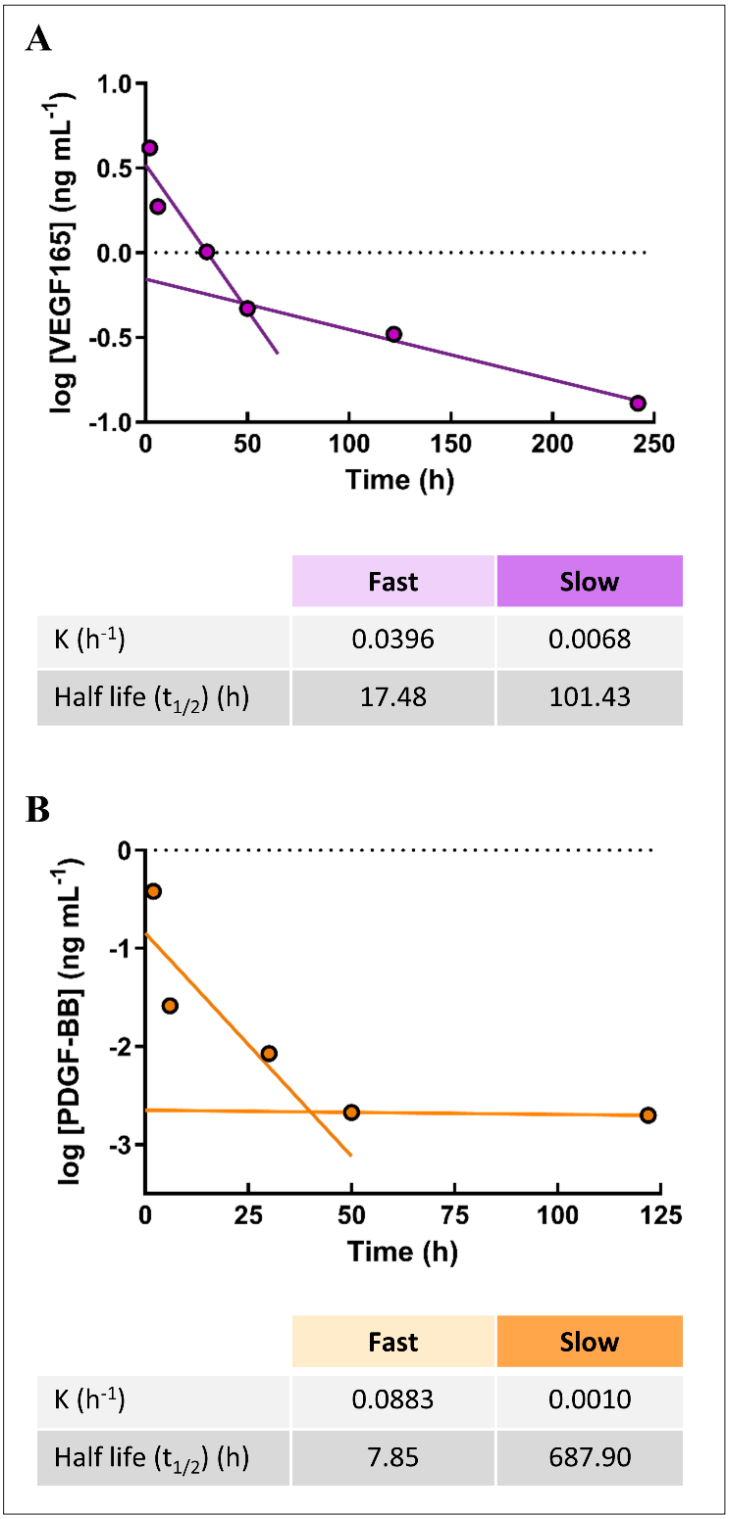
Figure 7. (A) Metabolic activity of iMATs. Five time points and three cell densities were analyzed. Results are represented as mean ± SD ($n = 4$). *$p < 0.05$. (B) Relative expression of tendon-related genes in iMATs incubated and embedded in the scaffolds for 3 and 12 days. Relative expression of tendon-related genes in iMATs embedded in the scaffolds after incubation for 3 and 12 days. The dashed line indicates equal expression of the analyzed gene on days 3 and 12. Results are represented as mean ± SD ($n = 4$). *$p < 0.05$.

As it is not the main objective of this study, the correlation is explained in part F of the Supplementary File.

3.6. Incorporation of growth factors

3.6.1. Release profiles from the scaffold

The use of growth factors inside the scaffolds requires prior characterization, which includes the determination of their release profiles. For this characterization, quantification by ELISA of the released factor into the culture media at different times was conducted, and the results are shown in Figure 8. Both factors, VEGF165 and PDGF-BB, showed a biphasic release. That is, during the initial phase, which lasts approximately for 50 h, the release happens at a faster rate (burst release). This rapid release is related to the swelling of the scaffold.[79] As it absorbs water, the space between the biomolecules is increased and the growth factors can more easily diffuse to the media. Afterward, the second phase begins, in which the release is much slower. Despite having a similar behavior, the parameters that characterize the release profile are different (probably due to the difference in the physicochemical composition of the two factors). On the one hand, the release rate, which is associated with the kinetic constant K, is different for the two factors. In the case of the initial phase or fast phase, the constant was greater for PDGF-BB ($K_{PDGF-BB}$ = 0.0883 h^{-1} and $K_{VEGF165}$ = 0.0396 h^{-1}), indicating that this factor was initially released more rapidly than VEGF165. However, during the slow phase, the VEGF165 constant was greater than that of PDGF-BB ($K_{PDGF-BB}$ = 0.0010 h^{-1} and $K_{VEGF165}$ = 0.0068 h^{-1}). Another parameter that can be determined from this test is the half-life value of the factor. This parameter indicates the time taken for the concentration of that drug to decrease by half of its initial value. It is inversely related to the constant K, so the value was lower for PDGF-BB than for VEGF165 (7.85 h and 17.48 h, respectively) in the fast phase and higher for PDGF-BB than for VEGF165 (687.90 h and 101.43 h, respectively) in the slow phase.



	Fast	Slow
K (h^{-1})	0.0396	0.0068
Half life ($t_{1/2}$) (h)	17.48	101.43

	Fast	Slow
K (h^{-1})	0.0883	0.0010
Half life ($t_{1/2}$) (h)	7.85	687.90

Figure 8. Release profile of VEGF165 (A) and PDGF-BB (B) from the scaffolds. The rates of the release can be observed in the graphical representations. Two of the main parameters that can be determined from this analysis, the release constant (K) and the half-life ($t_{1/2}$), are indicated in the tables (n = 3). The figure illustrates the most representative release profile obtained from independent experiments.

Concerning the regeneration of partial tendon injuries, some interesting results should be highlighted. VEGF165 and PDGF-BB had a rapid initial release, favoring the effect of these factors during the first 2 days. Afterward, the release of VEGF165 still remained fast. This is interesting since the aim of incorporating this factor is to increase the vascularization of the scaffold and the partially ruptured tendon mostly during the first days of regeneration (to increase the supply of oxygen and allow the synthesis of the different types of collagen). In the case of PDGF-BB, after the initial, fast release, the sustained release over time is beneficial for proliferation and migration of mesenchymal cells to the damaged tissue.

These values are widely applied in the pharmaceutical field but still not frequently used in tissue engineering field to characterize the release profiles from scaffolds in a more exact and comparable way between different structures. It is expected that this characterization based on modeling will become a truly relevant tool for the field.

3.6.2. In vitro bioactivity of the VEGF165 released from the scaffold

To analyze the activity of the released VEGF165, a vascularization assay was performed. This assay consisted of analyzing the reorganization of HUVECs on the surface of the scaffold to form tube or capillary-like structures. Two conditions (with and without factor) were tested during four sampling times. At each time point, cells were stained and the formation of structures was analyzed under the microscope (Figure 9).

In addition to the qualitative observation, a semiquantitative analysis of the area covered by cells, the total number of loops, the area of all the loops, the mean

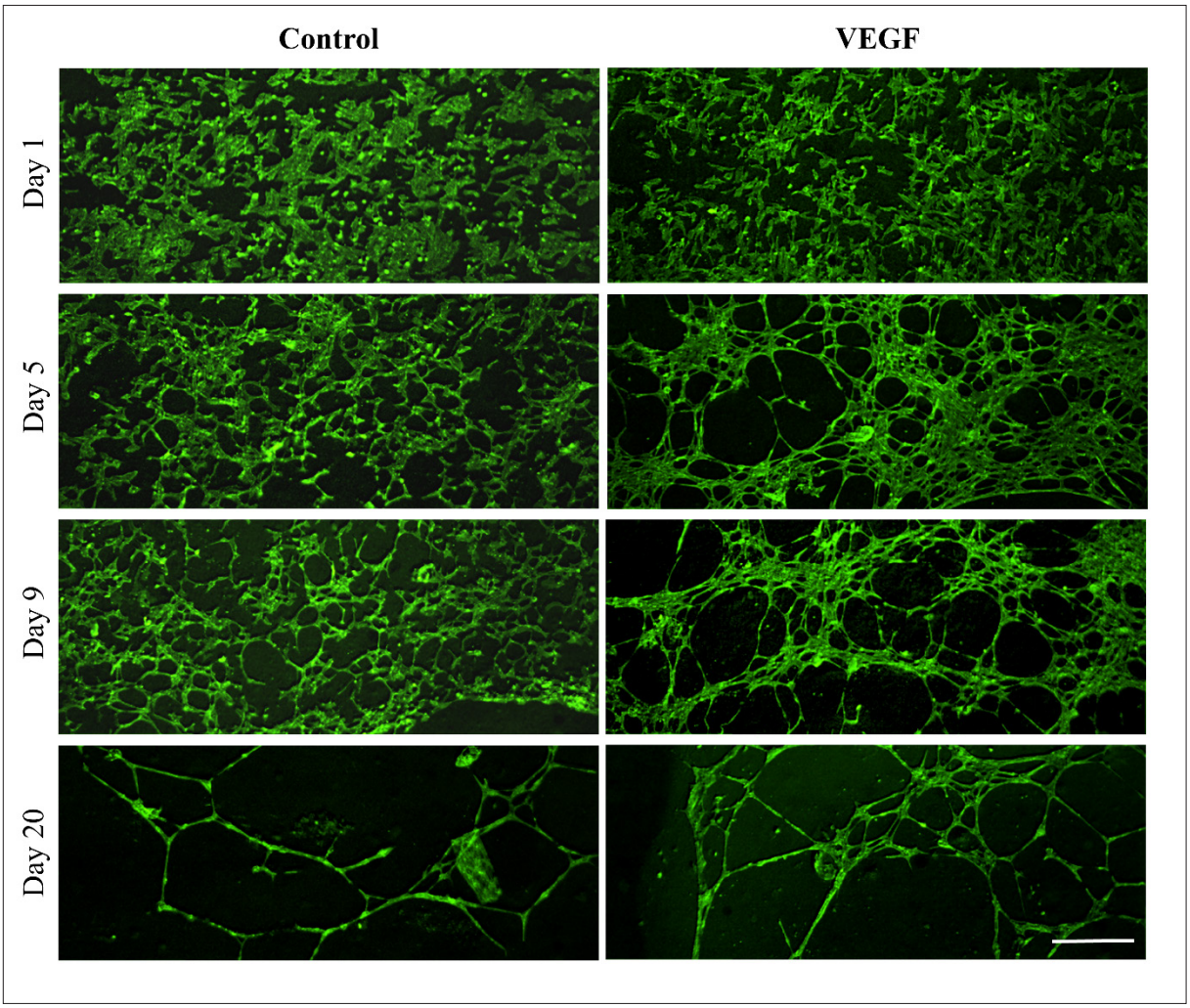


Figure 9. In vitro bioactivity of the VEGF165 and formation of pre-vascular structures. Micrographs of the HUVECs on the surface of the scaffolds (control and with VEGF165) were captured at the different time points at 4×. Scale bar: 500 μm.

area per loop, the length of all the tubes, and the mean length per tube was performed (Figure 10).

The area covered by the cells decreased significantly over time in all cases, except for D5–D9 with factor, whose difference is not significant (Figure 10A). There are no differences in the area covered by the cells between the two conditions (control and factor) until day 20. On this last day, the area covered by the cells was greater in the presence of factor compared to the control samples. This parameter indicated that the cells organize over time: They go from occupying the entire surface of the scaffold to reorganizing and grouping, ultimately forming structures akin to capillaries.

Regarding the formation of capillary-like structures, the samples with growth factor have a significantly higher number of loops and tubes and a larger area of loops than

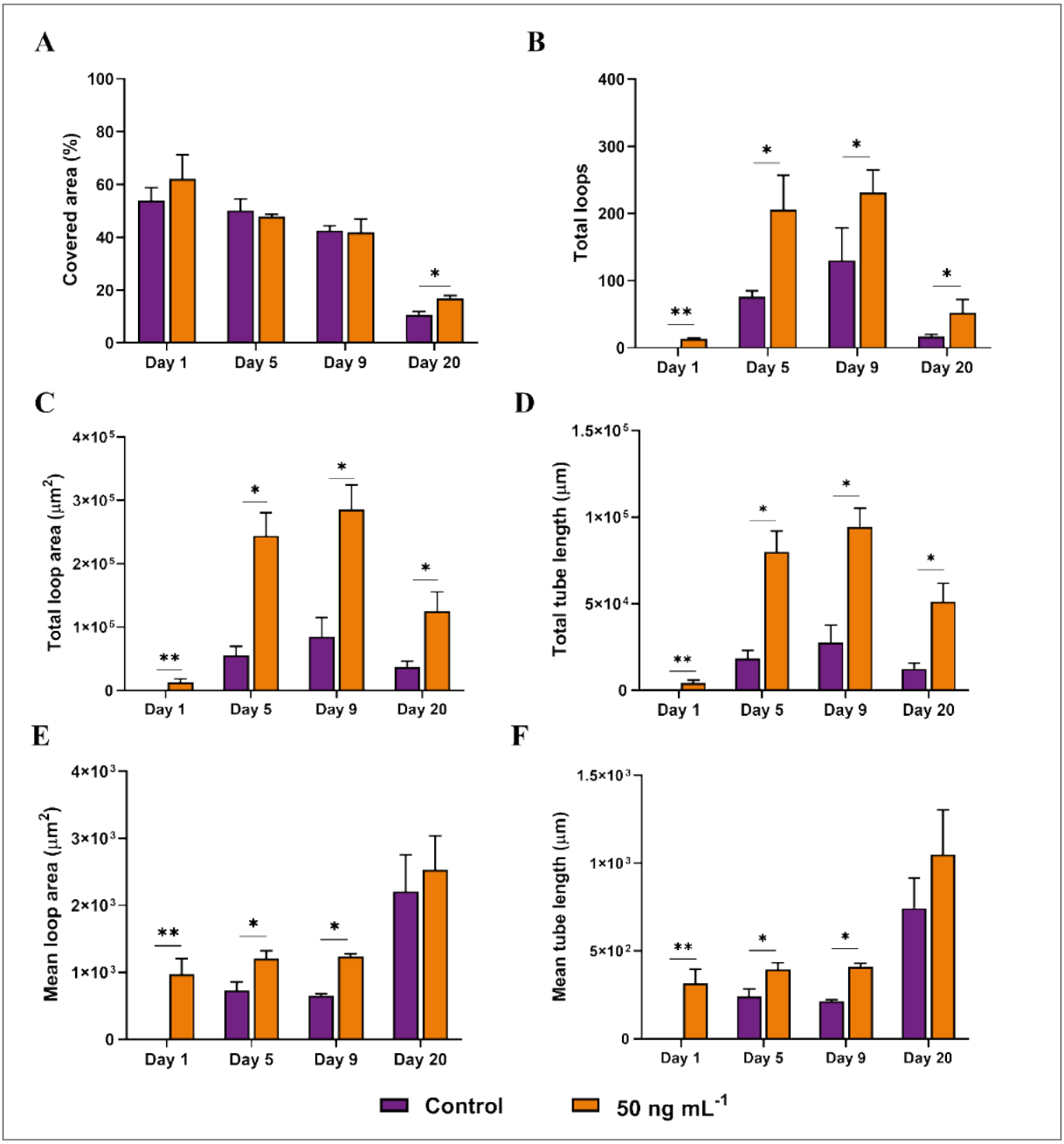


Figure 10. Semiquantitative analysis of parameters related to neovascularization. (A) Area covered by cells, (B) total number of loops, (C) total loop area, (D) mean loop area, (E) total tube length, and (F) mean tube length. Results are represented as mean ± SD ($n = 3$). *$p < 0.05$ and **$p < 0.01$.

the control samples for all time points (Figure 10B, C, and E). From the obtained results, it is noteworthy that for the samples with factor, the number of loops and tubes, as well as their total area and total length, was significantly greater on days 5 and 9 than other time points (but no significant differences were detected between day 5 and day 9). On day 20, however, loops and tubes with a greater area and length, respectively, were observed in the same samples (Figure 10D and F). These results demonstrate that the released factor influences HUVECs *in vitro* under the tested conditions.

3.6.3. In vitro bioactivity of the PDGF-BB released from the scaffold

The *in vitro* activity of PDGF-BB after being released from the scaffold was analyzed with a cell proliferation assay. In the cell proliferation assay, control scaffolds (without PDGF-BB) and scaffolds with three concentrations of PDGF-BB (10 ng mL^{-1}, 20 ng mL^{-1}, and 50 ng mL^{-1}) were placed on top of a transwell. In the wells of the plate, 2.5 × 10^5 C2C12 cells were cultured. After 24 h, the number of cells in each condition was determined (Figure 11). The results showed that the factor affects cell proliferation, in concordance with what has been previously reported in literature indicating that a concentration between 10 and 100 ng mL^{-1} of PDGF-BB increases cell proliferation and viability.[80] Concentrations at 20 ng mL^{-1} and 50 ng mL^{-1} were suitable for the regeneration of partial tendon injuries, the research focus of the current work. The concentration was selected based on different factors. Higher concentrations may be appropriate for treatments requiring longer periods of time.[81] However, the use of higher concentrations may be subject to greater restrictions imposed by health agencies. In this context, lower concentrations (such as 20 ng mL^{-1}) would be sufficient to provoke an initial increase of cell proliferation. These cells can then reduce their proliferation rate and increase their rate of ECM synthesis.

4. Conclusion

At present, rest and rehabilitation is the most common form of treatment for partial tendon injuries. Despite the clinical significance due to their prevalent incidence and the more severe consequences following inadequate treatment, there is yet no tissue engineering-based strategy developed to improve the regeneration process of partially injured tendons. Here, we showed that it is possible to combine multiple biological materials and 3D bioprinting to obtain a scaffold with a composition similar to that of the tendon ECM. The development of this bioink based on the combination of four biomolecules (Gel, Alg, HA, and Fg) represents a great advancement. This bioink possessed good rheological properties necessary for application in 3D bioprinting and good degradability and swelling properties. Likewise, it also showed good biocompatibility, allowing

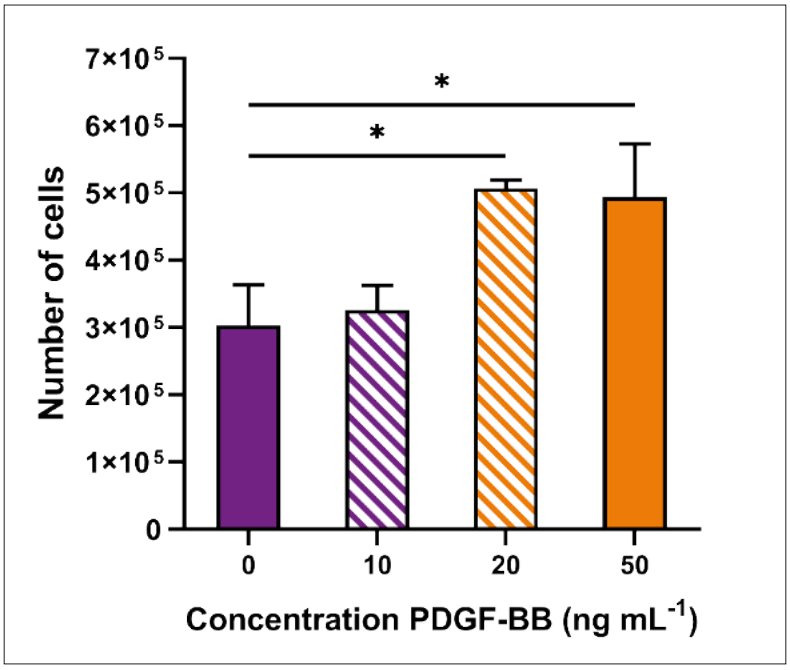


Figure 11. Proliferation of C2C12 cells when exposed to different concentrations of PDGF-BB. Results are represented as mean ± SD (n = 3). *p < 0.05.

cells to recover from the stress process of bioprinting and proliferate quickly over time. The cells embedded in the scaffold maintained their phenotype and responded to the stimuli provided by the developed structure; they also maintained the genetic expression of *Scx* and *Tnc*, while increasing the expression of *Fos*. The increased expression of *Col3a1* indicates the activity of embedded tenocytes and their ability to regenerate the extracellular matrix with characteristic biomolecules of the tendon. The developed scaffolds were also used for the release of growth factors that improve the regeneration of tendon injuries. On the one hand, the release of the factors from the scaffold occurs in two phases, namely the fast phase and the slow phase. PDGF-BB was released more rapidly at first, as shown by its constant, while VEGF165 was released somewhat more slowly at first. Furthermore, the two factors demonstrated biological activity once released; VEGF165 caused HUVECs to form a greater number of vascular loops with a larger area on days 5 and 9, and PDGF-BB increased the proliferation of C2C12 cells.

In view of these results, the use of the developed biomimetic tissue constructs and scaffolds could lead to an improved regeneration of partial tendon injuries through the four selected mechanisms: (i) a more complex and biomimetic combination of biomaterials, (ii) incorporation of tenocytes that produce elements of the ECM and manage to regenerate the tissue, (iii) incorporation of VEGF that enhances vascularization, thus increasing the supply of oxygen and nutrients to the damaged area, and (iv) incorporation of PDGF-BB that promotes cell proliferation and migration of cells to the damaged area.

Acknowledgments

S.R.-A. thanks the Basque Country Government for the granted fellowship (PRE_2022_2_0144). The authors wish to thank the intellectual and technical assistance from the ICTS "NANBIOSIS" more specifically by the Drug Formulation Unit (U10) of the CIBER in Bioengineering, Biomaterials, and Nanomedicine (CIBER-BBN) at the University of the Basque Country (UPV/EHU).

Funding

This project was supported by the Basque Country Government (Consolidated Groups, IT1448-22) and by the TriAnkle European project (Horizon 2020 TriAnkle 952981-2). This research was also supported by CIBER-Consorcio Centro de Investigación Biomédica en Red, Instituto de Salud Carlos III, Ministerio de Ciencia e Innovación.

Conflict of interest

The authors declare no conflicts of interest.

Author contributions

Conceptualization: Sandra Ruiz-Alonso, Fátima García-Villén, Idoia Gallego, Laura Saenz-Del-Burgo, Jose Luis Pedraz

Data curation: Sandra Ruiz-Alonso, Myriam Sainz-Ramos

Formal analysis: Sandra Ruiz-Alonso, Markel Lafuente-Merchan, Myriam Sainz-Ramos

Funding acquisition: Laura Saenz-Del-Burgo, Jose L. Pedraz

Investigation: Sandra Ruiz-Alonso, Jorge Ordoyo-Pascual, Markel Lafuente-Merchan, Myriam Sainz-Ramos

Methodology: Sandra Ruiz-Alonso, Markel Lafuente-Merchan, Fátima García-Villén, Idoia Gallego

Supervision: Idoia Gallego, Laura Saenz-Del-Burgo, Jose L. Pedraz

Validation: Jorge Ordoyo-Pascual, Laura Saenz-Del-Burgo

Writing – original draft: Sandra Ruiz-Alonso

Writing – review & editing: Fátima García-Villén, Idoia Gallego, Laura Saenz-Del-Burgo, Jose L. Pedraz

Ethics approval and consent to participate

This study had undergone ethical review by the Research Ethics Committee for Research with Biological Agents and/or Genetically Modified Organisms (CEIAB-UPV/EHU, BOPV 32, 17/2/2014). The research proposal with reference M30_2021_276 was evaluated in accordance with ethical considerations. The committee, in its meeting held on September 17, 2021 (record 137/2021), granted a favorable opinion for the execution of the research project.

Consent for publication

Not applicable.

Availability of data

The data supporting the findings of this study will be made available upon request from the corresponding authors.

Further disclosure

Part of the entire set of findings had been presented in national and international congresses:

(i) Ruiz-Alonso S, Lafuente-Merchan M, Gallego I, Saenz-Del-Burgo L, Luis Pedraz J. Development of scaffolds based on natural materials for tendon tissue regeneration. In: Caraballo I, Casas M, González-Rodríguez ML, Rabasco AM, eds. *XV Congreso de la Sociedad Española de Farmacia Industrial y Galénica*.

Sevilla: Sociedad Española de Farmacia Industrial y Galénica; 2021:258.

(ii) Ruiz-Alonso S, Ordoyo-Pascual J, Gallego I, et al. 3D printing technology in tendon tissue regeneration: scaffolds for tissue reinforcement and growth factor delivery. In: *TERMIS 2023 – European Chapter Manchester. Tissue Engineering Part A*. Manchester: Mary Ann Liebert, Inc., publishers; 2023:1022.

References

1. Cieza A, Causey K, Kamenov K, Hanson SW, Chatterji S, Vos T. Global estimates of the need for rehabilitation based on the Global Burden of Disease study 2019: a systematic analysis for the Global Burden of Disease Study 2019. *Lancet*. 2021;396(10267):2006-2017. doi: 10.1016/S0140-6736(20)32340-0
2. Liu S, Wang B, Fan S, Wang Y, Zhan Y, Ye D. Global burden of musculoskeletal disorders and attributable factors in 204 countries and territories: a secondary analysis of the Global Burden of Disease 2019 study. *BMJ Open*. 2022;12(6):e062183-062183. doi: 10.1136/bmjopen-2022-062183
3. National Academies of Sciences, Engineering, and Medicine; Health and Medicine Division; Board on Health Care Services; Committee on Identifying Disabling Medical Conditions Likely to Improve with Treatment. *Selected Health Conditions and Likelihood of Improvement with Treatment*. Washington, DC: National Academies Press; 2020.
4. Longo UG, Denaro V. *Textbook of Musculoskeletal Disorders*. 1st ed. Switzerland AG: Springer Cham; 2023. doi: 10.1007/978-3-031-20987-1
5. Mahler F, Fritschy D. Partial and complete ruptures of the Achilles tendon and local corticosteroid injections. *Br J Sports Med*. 1992;26(1):7-14. doi: 10.1136/bjsm.26.1.7
6. Gatz M, Spang C, Alfredson H. Partial Achilles tendon rupture-a neglected entity: a narrative literature review on diagnostics and treatment options. *J Clin Med*. 2020;9(10):3380. doi: 10.3390/jcm9103380
7. Riggin CN, Morris TR, Soslowsky LJ. Tendinopathy II: etiology, pathology, and healing of tendon injury and disease. In: Gomes ME, Reis RL, Rodrigues MT, eds. *Tendon Regeneration*. Academic Press; 2015:149-183. doi: 10.1016/B978-0-12-801590-2.00005-3
8. Andarawis-Puri N, Flatow EL, Soslowsky LJ. Tendon basic science: development, repair, regeneration, and healing. *J Orthop Res*. 2015;33(6):780-784. doi: 10.1002/jor.22869
9. Kwan TD, El Haj AJ. Multifactorial tendon tissue engineering strategies. In: Gomes ME, Reis RL, Rodrigues MT, eds. *Tendon Regeneration*. Cambridge, Massachusetts, US: Academic Press; 2015:281-320. doi: 10.1016/B978-0-12-801590-2.00011-9
10. Engebretson B, Mussett Z, Williams C, Simmons A, Sikavitsas V. Tendon tissue engineering: combined tissue engineering approach for the regeneration of tendons. In: Gomes ME, Reis RL, Rodrigues MT, eds. *Tendon Regeneration*. Cambridge, Massachusetts, US: Academic Press; 2015:281-320. doi: 10.1016/B978-0-12-801590-2.00011-9
11. Bianchi E, Ruggeri M, Rossi S, et al. Innovative strategies in tendon tissue engineering. *Pharmaceutics*. 2021;13(1):89. doi: 10.3390/pharmaceutics13010089
12. Matai I, Kaur G, Seyedsalehi A, McClinton A, Laurencin CT. Progress in 3D bioprinting technology for tissue/organ regenerative engineering. *Biomaterials*. 2020;226:119536. doi: 10.1016/j.biomaterials.2019.119536
13. Ruiz-Alonso S, Lafuente-Merchan M, Ciriza J, Saenz-Del-Burgo L, Pedraz JL. Tendon tissue engineering: cells, growth factors, scaffolds and production techniques. *J Control Release*. 2021;333:448-486. doi: 10.1016/j.jconrel.2021.03.040
14. Chen XB, Anvari-Yazdi AF, Duan X, et al. Biomaterials / bioinks and extrusion bioprinting. *Bioact Mater*. 2023;28:511-536. doi: 10.1016/j.bioactmat.2023.06.006
15. ASTM International. *ISO/ASTM 52900 2021(E). Additive Manufacturing—General Principles—Fundamentals and Vocabulary*. Geneva: ASTM International; 2021:1–5.
16. Hospodiuk M, Moncal KK, Dey M, Ozbolat IT. Extrusion-based biofabrication in tissue engineering and regenerative medicine. In Ovsianikov A, Yoo J, Mironov V, eds. *3D Printing and Biofabrication*. New York City, New York, US: Springer International Publishing; 2016:1-27. doi: 10.1007/978-3-319-40498-1_10-1
17. Kaliaraj GS, Shanmugam DK, Dasan A, Mosas KK. Hydrogels—a promising materials for 3D printing technology. *Gels*. 2023;9(3). doi: 10.3390/gels9030260
18. Li X, Sun Q, Li Q, Kawazoe N, Chen G. Functional hydrogels with tunable structures and properties for tissue engineering applications. *Front Chem*. 2018;6. doi: 10.3389/fchem.2018.00499
19. Thang NH, Chien TB, Cuong DX. Polymer-based hydrogels applied in drug delivery: an overview. *Gels*. 2023; 9(7):523. doi: 10.3390/gels9070523
20. Schwab A, Levato R, D'Este M, Piluso S, Eglin D, Malda J. Printability and shape fidelity of bioinks in 3D bioprinting. *Chem Rev.* 2020;120(19):11028-11055. doi: 10.1021/acs.chemrev.0c00084
21. Lin X, Zhao X, Xu C, Wang L, Xia Y. Progress in the mechanical enhancement of hydrogels: fabrication strategies and underlying mechanisms. *J Polym Sci*. 2022;60(17):2525-2542. doi: 10.1002/pol.20220154

22. Hu J, Liu S, Fan C. Applications of functionally-adapted hydrogels in tendon repair. *Front Bioeng Biotechnol*. 2023;11:1135090. doi: 10.3389/fbioe.2023.1135090

23. Tabata Y. Tissue regeneration based on growth factor release. *Tissue Eng*. 2003;9:5-15. doi: 10.1089/10763270360696941

24. Koria P. Delivery of growth factors for tissue regeneration and wound healing. *BioDrugs*. 2012;26(3):163-175. doi: 10.2165/11631850-000000000-00000

25. Creaney L, Hamilton B. Growth factor delivery methods in the management of sports injuries: the state of play. *Br J Sports Med*. 2008;42(5):314. doi: 10.1136/bjsm.2007.040071

26. Kuroda Y, Kawai T, Goto K, Matsuda S. Clinical application of injectable growth factor for bone regeneration: a systematic review. *Inflamm Regen*. 2019;39(1):20. doi: 10.1186/s41232-019-0109-x

27. Lee K, Silva EA, Mooney DJ. Growth factor delivery-based tissue engineering: general approaches and a review of recent developments. *J R Soc Interface*. 2011;8(55):153-170. doi: 10.1098/rsif.2010.0223

28. Wang Z, Wang Z, Lu WW, Zhen W, Yang D, Peng S. Novel biomaterial strategies for controlled growth factor delivery for biomedical applications. *NPG Asia Mater*. 2017;9(10):e435. doi: 10.1038/am.2017.171

29. Li H, Luo S, Wang H, et al. The mechanisms and functions of TGF-β1 in tendon healing. *Injury*. 2023;54(11):111052. doi: 10.1016/j.injury.2023.111052

30. Evrova O, Buschmann J. *In vitro* and *in vivo* effects of PDGF-BB delivery strategies on tendon healing: a review. *Eur Cell Mater*. 2017;34:15-39. doi: 10.22203/eCM.v034a02

31. Wang Y, Li J. Current progress in growth factors and extracellular vesicles in tendon healing. *Int Wound J*. 2023;20(9):3871-3883. doi: 10.1111/iwj.14261

32. Molloy T, Wang Y, Murrell G. The roles of growth factors in tendon and ligament healing. *Sports Med*. 2003;33(5): 381-394. doi: 10.2165/00007256-200333050-00004

33. Miescher I, Rieber J, Calcagni M, Buschmann J. *In vitro* and *in vivo* effects of IGF-1 delivery strategies on tendon healing: a review. *Int J Mol Sci*. 2023;24(3):2370. doi: 10.3390/ijms24032370

34. Leong NL, Kator JL, Clemens TL, James A, Enamoto-Iwamoto M, Jiang J. Tendon and ligament healing and current approaches to tendon and ligament regeneration. *J Orthop Res*. 2020;38(1):7-12. doi: 10.1002/jor.24475

35. Hope M, Saxby TS. Tendon healing. *Foot Ankle Clin*. 2007;12(4):553-567. doi: 10.1016/j.fcl.2007.07.003

36. Hee CK, Dines JS, Solchaga LA, Shah VR, Hollinger JO. Regenerative tendon and ligament healing: opportunities with recombinant human platelet-derived growth factor BB-homodimer. *Tissue Eng. Part B Rev*. 2012;18(3): 225-234. doi: 10.1089/ten.teb.2011.0603

37. Naderi H, Matin MM, Bahrami AR. Review paper: critical issues in tissue engineering: biomaterials, cell sources, angiogenesis, and drug delivery systems. *J Biomater Appl*. 2011;26(4):383-417. doi: 10.1177/0885328211408946

38. Naghieh S, Chen X. Printability–a key issue in extrusion-based bioprinting. *J Pharm Anal*. 2021;11(5):564-579. doi: 10.1016/j.jpha.2021.02.001

39. Małkowski P, Ostrowski L, Brodny J. Analysis of Young's modulus for carboniferous sedimentary rocks and its relationship with uniaxial compressive strength using different methods of modulus determination. *J Sustain Min*. 2018;17(3):145-157. doi: 10.1016/j.jsm.2018.07.002

40. Barreto IS, Pierantoni M, Hammerman M, et al. Nanoscale characterization of collagen structural responses to in situ loading in rat Achilles tendons. *Matrix Biol*. 2023;115:32-47. doi: 10.1016/j.matbio.2022.11.006

41. Lukin I, Erezuma I, Maeso L, et al. Progress in gelatin as biomaterial for tissue engineering. *Pharmaceutics*. 2022;14(6):1177. doi: 1110.3390/pharmaceutics14061177

42. Saravanakumar K, Park S, Santosh SS, et al. Application of hyaluronic acid in tissue engineering, regenerative medicine, and nanomedicine: a review. *Int J Biol Macromol*. 2022;222:2744-2760. doi: 10.1016/j.ijbiomac.2022.10.055

43 Farshidfar N, Iravani S, Varma RS. Alginate-based biomaterials in tissue engineering and regenerative medicine. *Mar Drugs*. 2023;21(3):189. doi: 10.3390/md21030189

44. Sanz-Horta R, Matesanz A, Gallardo A, et al. Technological advances in fibrin for tissue engineering. *J Tissue Eng*. 2023;14:20417314231190288. doi: 10.1177/20417314231190288

45. Bird B, Armstrong RC, Hassager O. *Dynamics of Polymeric Liquids. Volume 1 Fluid Mechanics*. Hoboken, New Jersey, US: John Wiley & Sons; 1987.

46. Cooke ME, Rosenzweig DH. The rheology of direct and suspended extrusion bioprinting. *APL Bioeng*. 2021;5(1):011502. doi: 10.1063/5.0031475

47. Thompson RL, Sica LUR, de Souza Mendes PR. The yield stress tensor. *J Non Newtonian Fluid Mech*. 2018;261:211-219. doi: 10.1016/j.jnnfm.2018.09.003

48. Mezger TG. *The Rheology Handbook*. 4th ed. Hanover, Germany: Vincentz Network; 2014.

49. Mortimer S, Ryan AJ, Stanford JL. Rheological behavior and gel-point determination for a model lewis acid-initiated chain growth epoxy resin. *Macromolecules*. 2001;34(9):2973-2980. doi: 10.1021/ma001835x

50. Augst AD, Kong HJ, Mooney DJ. Alginate hydrogels as biomaterials. *Macromol Biosci*. 2006;6(8):623-633. doi: 10.1002/mabi.200600069

51. Whelihan MF, Kiankhooy A, Brummel-Ziedins K. Thrombin generation and fibrin clot formation under hypothermic conditions: an *in vitro* evaluation of tissue factor initiated whole blood coagulation. *J Crit Care*. 2014;29(1):24-30. doi: 10.1016/j.jcrc.2013.10.010

52. Tang JD, Caliari SR, Lampe KJ. Temperature-dependent complex coacervation of engineered elastin-like polypeptide and hyaluronic acid polyelectrolytes. *Biomacromolecules*. 2018;19(10):3925-3935. doi: 10.1021/acs.biomac.8b00837

53. Boularaoui S, Al Hussein G, Khan KA, Christoforou N, Stefanini C. An overview of extrusion-based bioprinting with a focus on induced shear stress and its effect on cell viability. *Bioprinting*. 2020;20:e00093. doi: 10.1016/j.bprint.2020.e00093

54. Fakhruddin K, Hamzah MSA, Razak SIA. Effects of extrusion pressure and printing speed of 3D bioprinted construct on the fibroblast cells viability. *IOP Conf Ser: Mater Sci Eng*. 2018;440(1):012042. doi: 10.1088/1757-899X/440/1/012042

55. Xu H, Liu J, Zhang Z, Xu C. A review on cell damage, viability, and functionality during 3D bioprinting. *Mil Med Res*. 2022;9(1):70. doi: 10.1186/s40779-022-00429-5

56. Wang J, Wei Y, Zhao S, et al. The analysis of viability for mammalian cells treated at different temperatures and its application in cell shipment. *PLoS One*. 2017;12(4):e0176120. doi: 10.1371/journal.pone.0176120

57. Murphy CM, O'Brien FJ. Understanding the effect of mean pore size on cell activity in collagen-glycosaminoglycan scaffolds. *Cell Adh Migr*. 2010;4(3):377-381. doi: 10.4161/cam.4.3.11747

58. Loh QL, Choong C. Three-dimensional scaffolds for tissue engineering applications: role of porosity and pore size. *Tissue Eng Part B Rev*. 2013;19(6):485-502. doi: 10.1089/ten.TEB.2012.0437

59. Voleti PB, Buckley MR, Soslowsky LJ. Tendon healing: repair and regeneration. *Annu Rev Biomed Eng*. 2012;14(1):47-71. doi: 10.1146/annurev-bioeng-071811-150122

60. Rolnick KI, Choe JA, Leiferman EM, et al. Periostin modulates extracellular matrix behavior in tendons. *Matrix Biol Plus*. 2022;16:100124. doi: 10.1016/j.mbplus.2022.100124

61. Luo T, Tan B, Zhu L, Wang Y, Liao J. A review on the design of hydrogels with different stiffness and their effects on tissue repair. *Front Bioeng Biotechnol*. 2022;10:817391. doi: 10.3389/fbioe.2022.817391

62. Abalymov A, Parakhonskiy B, Skirtach AG. Polymer- and hybrid-based biomaterials for interstitial, connective, vascular, nerve, visceral and musculoskeletal tissue engineering. *Polymers*. 2020;12(3):620. doi: 10.3390/polym12030620

63. Cox TR, Erler JT. Remodeling and homeostasis of the extracellular matrix: implications for fibrotic diseases and cancer. *Dis Model Mech*. 2011;4(2):165-178. doi: 10.1242/dmm.004077

64. Saha K, Pollock JF, Schaffer DV, Healy KE. Designing synthetic materials to control stem cell phenotype. *Curr Opin Chem Biol*. 2007;11(4):381-387. doi: 10.1016/j.cbpa.2007.05.030

65. Hwang NS, Varghese S, Elisseeff J. Controlled differentiation of stem cells. *Adv Drug Deliv Rev*. 2008;60(2):199-214. doi: 10.1016/j.addr.2007.08.036

66. O'Brien FJ. Biomaterials & scaffolds for tissue engineering. *Mater Today*. 2011;14(3):88-95. doi: 10.1016/S1369-7021(11)70058-X

67. Zhang X, Kim T, Thauland TJ, et al. Unraveling the mechanobiology of immune cells. *Curr Opin Biotechnol*. 2020;66:236-245. doi: 10.1016/j.copbio.2020.09.004

68. Breuls RGM, Jiya TU, Smit TH. Scaffold stiffness influences cell behavior: opportunities for skeletal tissue engineering. *Open Orthop J*. 2008;2:103-109. doi: 10.2174/1874325000802010103

69. Schuurman W, Levett PA, Pot MW, et al. Gelatin-methacrylamide hydrogels as potential biomaterials for fabrication of tissue-engineered cartilage constructs. *Macromol Biosci*. 2013;13(5):551-561. doi: 10.1002/mabi.201200471

70. Zhao X, Lang Q, Yildirimer L, et al. Photocrosslinkable gelatin hydrogel for epidermal tissue engineering. *Adv Healthc Mater*. 2016;5(1):108-118. doi: 10.1002/adhm.201500005

71. Luo Q, Song G, Song Y, Xu B, Qin J, Shi Y. Indirect co-culture with tenocytes promotes proliferation and mRNA expression of tendon/ligament related genes in rat bone marrow mesenchymal stem cells. *Cytotechnology*. 2009;61(1-2):1-10. doi: 10.1007/s10616-009-9233-9

72. Güngörmüş C, Kolankaya D. Gene expression of tendon collagens and tenocyte markers in long-term monolayer and

high-density cultures of rat tenocytes. *Connect Tissue Res*. 2012;53(6):485-491.
doi: 10.3109/03008207.2012.694511

73. Taylor SE, Vaughan-Thomas A, Clements DN, et al. Gene expression markers of tendon fibroblasts in normal and diseased tissue compared to monolayer and three dimensional culture systems. *BMC Musculoskelet Disord*. 2009;10(1):27.
doi: 10.1186/1471-2474-10-27

74. Li Y, Wu T, Liu S. Identification and distinction of tenocytes and tendon-derived stem cells. *Front Cell Dev Biol*. 2021;9:629515.
doi: 10.3389/fcell.2021.629515

75. Wei Q, Wang S, Han F, et al. Cellular modulation by the mechanical cues from biomaterials for tissue engineering. *Biomater Transl*. 2021;2(4):323-342.
doi: 10.12336/biomatertransl.2021.04.001

76. Dede Eren A, Vasilevich A, Eren ED, et al. Tendon-derived biomimetic surface topographies induce phenotypic maintenance of tenocytes *in vitro*. *Tissue Eng Part A*. 2021;27(15-16):1023-1036.
doi: 10.1089/ten.tea.2020.0249

77. Kaur J, Reinhardt DP. Extracellular matrix (ECM) molecules. In: Vishwakarma A, Sharpe P, Shi S, Ramalingam M, eds. *Stem Cell Biology and Tissue Engineering in Dental Sciences*. Academic Press; 2015:25-45.

78. Buckley MR, Evans EB, Matuszewski PE, et al. Distributions of types I, II and III collagen by region in the human supraspinatus tendon. *Connect Tissue Res*. 2013;54(6):374-379.
doi: 10.3109/03008207.2013.847096

79. Laracuente M, Yu MH, McHugh KJ. Zero-order drug delivery: state of the art and future prospects. *J Control Release*. 2020;327:834-856.
doi: 10.1016/j.jconrel.2020.09.020

80. Paek S, Min SK, Park J. Effects of platelet-derived growth factor-BB on cellular morphology and cellular viability of stem cell spheroids composed of bone-marrow-derived stem cells. *Biomed Rep*. 2020;13(6):59.
doi: 10.3892/br.2020.1366

81. Mihaylova Z, Tsikandelova R, Sanimirov P, Gateva N, Mitev V, Ishkitiev N. Role of PDGF-BB in proliferation, differentiation and maintaining stem cell properties of PDL cells *in vitro*. *Arch Oral Biol*. 2018;85:1-9.
doi: 10.1016/j.archoralbio.2017.09.019

ACCSCIENCE PUBLISHING

International Journal of Bioprinting

RESEARCH ARTICLE

3D bioartificial stretchable scaffolds mimicking the mechanical hallmarks of human cardiac fibrotic tissue

Mattia Spedicati[1,2,3†], Francesca Tivano [1,2,3†], Alice Zoso[1,2,3], Janira Bei[1], Mario Lavella[4], Irene Carmagnola[1,2,3], and Valeria Chiono[1,2,3*]

[1]Department of Mechanical and Aerospace Engineering, Politecnico di Torino, Turin, Turin, Italy

[2]POLITO BioMedLab, Politecnico di Torino, Turin, Turin, Italy

[3]Interuniversity Centre for the Promotion of the 3Rs Principles in Teaching and Research (Centro 3R), Pisa, Italy

[4]Department of Management, Information and Production Engineering, University of Bergamo, Dalmine, Bergamo, Italy

Abstract

Human cardiac fibrotic tissues are characterized by a higher stiffness relative to healthy cardiac tissues. These tissues are unable to spontaneously contract and are subjected to passive mechanical stimulation during heart functionality. Moreover, scaffolds that can recapitulate the *in vivo* mechanical properties of the cardiac fibrotic tissues are lacking. Herein, this study aimed to design and fabricate mechanically stretchable bioartificial scaffolds with biomimetic composition and stiffness comparable to human cardiac fibrotic tissues. Poly(*ε*-caprolactone) (PCL) scaffolds with a stretchable mesh architecture were initially designed through structural and finite element method (FEM) analyses and subsequently fabricated by melt extrusion additive manufacturing (MEX). Scaffolds were surface functionalized by 3,4-dihydroxy-DL-phenylalanine (DOPA) polymerization (polyDOPA) to improve their interaction with natural polymers. Scaffold pores were then filled with different concentrations (5%, 7%, and 10% w/v) of gelatin methacryloyl (GelMA) hydrogels to support *in vitro* human cardiac fibroblasts (HCFs) 3D culture, thereby producing bioartificial PCL/GelMA scaffolds. Uniaxial tensile mechanical tests in static and dynamic conditions (1 Hz; 22% maximum strain) demonstrated that the bioartificial scaffolds had *in vivo*-like stretchability and similar stiffness to that of pathological cardiac tissue (tailored as a function of the number of PCL scaffold layers and GelMA hydrogel concentration). *In vitro* cell tests on bioartificial scaffolds using HCF-embedded GelMA hydrogels under static conditions displayed increasing cell viability, spreading, and cytoskeleton organization with decreasing GelMA hydrogel concentration. Moreover, *α*-smooth muscle actin (*α*-SMA)-positive cells were detected after 7 days of culture in static conditions followed by another 7 days of culture in dynamic conditions and not in HCF-loaded scaffolds cultured in static conditions for 14 days. These results suggested that *in vitro* culture under cyclic mechanical stimulations could induce an HCF phenotypic switch into myofibroblasts.

Keywords: Bioartificial scaffold; Cardiac fibrosis; Stretchable scaffold; GelMA hydrogel

†These authors contributed equally to this work.

***Corresponding author:**
Valeria Chiono
(valeria.chiono@polito.it)

Citation: Spedicati M, Tivano F, Zoso A, et al. 3D bioartificial stretchable scaffolds mimicking the mechanical hallmarks of human cardiac fibrotic tissue. *Int J Bioprint*. 2024;10(3):2247. doi: 10.36922/ijb.2247

Received: November 15, 2023
Accepted: March 21, 2024
Published Online: May 15, 2024

Copyright: © 2024 Author(s). This is an Open Access article distributed under the terms of the Creative Commons Attribution License, permitting distribution, and reproduction in any medium, provided the original work is properly cited.

Publisher's Note: AccScience Publishing remains neutral with regard to jurisdictional claims in published maps and institutional affiliations.

1. Introduction

Cardiovascular diseases (CVDs) are the leading cause of morbidity and mortality worldwide.[1] Among them, myocardial infarction (MI) causes the irreversible loss of billions of cardiomyocytes, followed by cardiac fibrosis and progressive heart failure.[1] From weeks to months post-MI, cardiac fibrotic scar forms in the infarcted area, consisting of a stiff extracellular matrix (ECM), populated with cardiac fibroblasts.[2] Predictive *in vitro* models of the human pathological cardiac tissue are highly demanded to support the *in vitro* preclinical validation of new therapeutic approaches, thereby minimizing *in vivo* trials on animal models and aligning with the 3Rs principle (i.e., replacement, reduction, and refinement).

Due to the high socioeconomic impact of ischemic heart disease, biomimetic scaffolds are highly demanded for the future *in vitro* engineering of human cardiac fibrotic tissue. An infarcted human heart is characterized by the presence of a stiff ECM that is rich in type I and III collagens.[2] Natural polymer hydrogels, including gelatin methacryloyl (GelMA), have been frequently used to support the *in vitro* culture of human cardiac fibroblasts (HCFs).[5–8] Sadeghi *et al.* employed GelMA hydrogels cultured with cardiac fibroblasts from neonatal rats to study pathological remodeling occurring during cardiac fibrosis. Different GelMA hydrogel concentrations (5%, 7%, and 10% w/v) and degrees of methacryloyl substitution (medium [53%] and high [81%]) were used in the study.[3,4] However, hydrogels lack structural biomimetic cues for cell guidance, cannot bear cardiac tissue-like cyclic mechanical deformations, and have short degradation times.[5] Synthetic polymer scaffolds could overcome the main limitations of natural polymer hydrogels, as they have superior stability in physiological media, may withstand cardiac tissue-like cyclic deformation, and provide topographical cues to cells. Among the synthetic polymers, thermoplastic polyesters, such as poly(ε-caprolactone) (PCL), have been widely used in tissue engineering. PCL is a biocompatible and bioresorbable polymer approved by the United States (US) Food and Drug Administration (FDA).[3] PCL is an optimal polymer for scaffold manufacturing by melt-processing techniques, owing to its low melting temperature (approximately 60 °C), which minimizes thermo-mechanical degradation during scaffold fabrication. As PCL is not elastomeric, PCL scaffold architecture can be designed to obtain stretchable substrates.[5–8] Indeed, Olvera *et al.*[6] fabricated PCL-based cardiac patches with high stretchability through a missing-rib unit network. Castilho *et al.*[12] fabricated PCL-based scaffolds for cardiac tissue engineering with rectangular-shaped mesh geometry, later improved through a hexagonal-shaped mesh geometry to best reproduce the native honeycomb microstructure of the myocardium.[6,7] Paxton *et al.*[9] employed bow-tie architecture for PCL stretchable tubular scaffolds, while Bas *et al.*[10] and Saidy *et al.*[11] investigated the mechanical tunability of PCL scaffolds provided with filaments with a wavy arrangement. PCL scaffolds have been previously used for the development of *in vitro* healthy cardiac tissue models[11] or as implantable cardiac patches.[6] Such platforms were fabricated by melt electrospinning writing (MEW), an additive-manufacturing (AM) technique that enables the production of polymeric scaffolds with complex geometries, based on filaments of a few microns in size. However, MEW scaffolds have an increased frequency of defects with increasing thickness due to charge interference between the nozzle and deposited layers.[12,13] Melt-extrusion additive manufacturing (MEX) is a simpler and more rapid prototyping approach that fabricates reproducible scaffolds by controlled deposition of molten polymer filaments.[14,15] Polymer filaments in MEX scaffolds generally have a larger size than the polymer filaments in MEW scaffolds (≥100–150 μm vs. ≤50–20μm,[3,14] respectively). To date, MEX has been mainly applied to prepare stiff PCL scaffolds with straight filaments and square-meshed geometry for subsequent *in vitro* cell cultures.[16] As human cardiac fibrotic tissues are incapable of spontaneous cyclic contraction, they are typically subjected to passive mechanical stimulation during heart-beating activity.

In this study, we fabricated and characterized 3D stretchable PCL scaffolds with wavy aligned filaments by MEX after an accurate structural and mechanical scaffold design by an analytical method and the finite element method (FEM).[18] Despite their superior processability and mechanical properties over natural polymers, synthetic polymers lack cell adhesive cues. In contrast, 3D hydrogels based on natural polymers support cell attachment but generally exhibit a limited ability to withstand cyclic mechanical stretching.[19–21] "Bioartificial" substrates, combining synthetic and natural polymers, may thus represent an optimal option, as they synergistically combine the promising properties of both polymer types.[17–21,25] Embedding the natural polymer hydrogel into a stretchable synthetic polymer scaffold improves its mechanical resistance and structural stability during cyclic mechanical stimulation of the whole construct.[19] Therefore, bioartificial scaffolds were prepared by filling PCL scaffold pores with 5%, 7%, and 10% w/v GelMA hydrogels, selected based on previous literature.[3] The elastic modulus of the bioartificial scaffolds could be modulated by hydrogel filler mechanical properties to mimic the mechanical properties of human cardiac fibrotic tissues. In detail, the reference values for Young's modulus of human cardiac fibrotic tissues (measured by tensile tests) range from 400 kPa to 9 MPa

as a function of patient sex, age, and pathophysiological conditions of the left ventricle.[22,23] In contrast, diastolic elastic deformation ranges at 10–22%.[21–23] The designed mechanically stretchable bioartificial scaffolds supported the *in vitro* 3D culture of HCFs. Dynamic *in vitro* cell culture studies using MechanoCulture T6 bioreactor displayed markers of cardiac fibrosis that could suggest HCFs activation into myofibroblasts. This work highlighted the potential of stretchable bioartificial scaffolds for human cardiac fibrotic tissue engineering by *in vitro* culture of HCFs under cyclic mechanical stimulation. In comparison to miniaturized cardiac fibrotic tissue models on a chip,[29] which are limited to the *in vitro* preclinical testing of drugs and nanotherapeutics, the present cardiac scar model could also be exploited for the testing of medical devices and advanced therapies based on scaffolds/hydrogels under dynamic mechanical stimulation. Future applications by our group will include the *in vitro* preclinical study of cardiac regenerative therapies under dynamic conditions, such as the direct reprogramming of HCFs into cardiomyocytes.[24,30,31]

2. Methods

2.1. Materials

PCL pellets with a molecular weight of 43,000 Da were purchased from Polysciences GmbH (Germany). GelMA (60% degree of methacryloyl substitution and a gel strength of 300 g Bloom), lithium phenyl-2,4,6-trimethylbenzoylphosphinate (LAP), and 3,4-dihydroxy-DL-phenylalanine (DOPA) were purchased from Sigma-Aldrich (USA). Phosphate buffered saline (PBS) was purchased from Thermo Fisher Scientific (USA), while HCFs and fibroblast growth medium-3 (FGM-3) were purchased from PromoCell GmbH (Germany).

2.2. Poly(ε-caprolactone) mesh geometry

A computer-aided design (CAD) model of the scaffold was designed based on eight superimposed layers (0.15 mm thickness per layer) (Figure 1). The geometry was based on the alternation of two superimposed layers: the first layer made of wavy equidistant filaments aligned along the *x*-direction and the other layer consisting of straight parallel filaments aligned along the *y*-direction (Figure 1). The wavy pattern was composed of a sequence of half

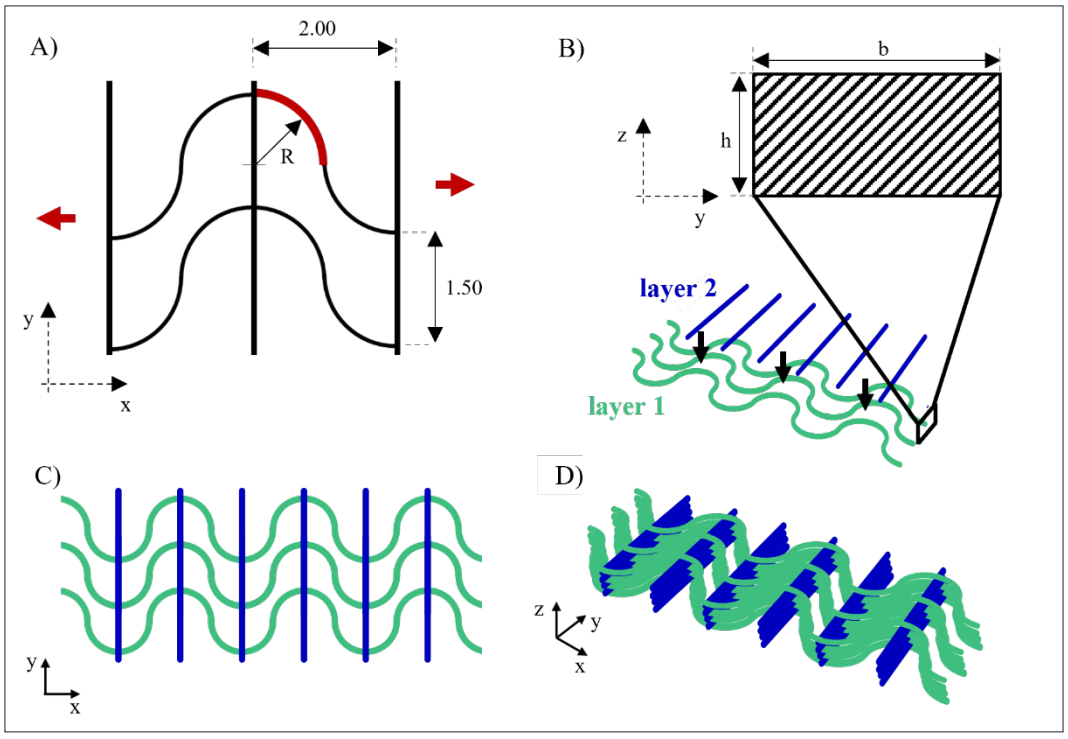


Figure 1. Poly(ε-caprolactone) (PCL) mesh geometry. (A) The geometry of a stretchable PCL mesh unit cell model. Red arrows in the *x*-direction indicate the direction of mechanical stretching applied to the mesh; the element portion considered for structural analysis is highlighted in red; spacing dimensions, expressed in mm, and radius (*R*) are reported. (B) Single filament cross-section and schematic representation of the superimposition of layers 1 and 2. (C) The 2D mesh geometry with layers 1 and 2. (D) The 3D mesh geometry is obtained by the superimposition of the eight layers (from layers 1 to 8), corresponding to four of the 2D mesh structures in (C).

semicircles with a radius (R) of 1 mm (Figure 1A). The inter-fiber distance between two close wavy and straight filaments in each layer was 1.5 and 2 mm, respectively (Figure 1A). This was considered as the unit cell for the stretchable PCL mesh. The cross-section of each filament was approximated to a rectangle with an area $b \times h$ derived from scanning electron microscopy (SEM) and optical microscopy analyses (Figure 1B). The 2D mesh model with two layers and the 3D mesh model with eight layers are displayed in Figure 1C and D, respectively.

2.3. Mechanical modeling

2.3.1. Structural analysis of scaffold stiffness

Structural analysis aimed to define the proper PCL mesh design in terms of thickness (number of layers) to ensure cardiac tissue-like stiffness and stretchability under physiological mechanical stimulation (i.e., Young's modulus between 400 kPa and 9 MPa, and bearing an elastic deformation ≤22%).[21–23] PCL mesh stiffness was calculated considering the repeating half-semicircle element of the wavy pattern (Figure 1A) approximated with a straight-line beam (S-L.B.) or a curved beam (C.B.) (Figure 2). The stiffness of a single element in the mesh was calculated:

$$K_{ij} = F / \delta \quad (1)$$

where F denotes the applied force and δ is the displacement, both of which are computed considering S-L.B. and C.B. approximations, respectively (**Equations SIII** and **SIV**). Calculated stiffnesses were considered a property along the x-axis according to the force (F) direction (Figure 2). In the case of S-L.B. approximation (Table 1), stiffness was calculated using displacement computed through the elastic line equation. On the other hand, in the case of the C.B. approximation (Table 1), stiffness was computed through Castigliano's theorem,[23] by determining the displacements due to tensile and bending contributions.

By considering a single beam element as a spring, each wavy filament is a spring series along the horizontal direction while their assembly along the vertical direction is a spring parallel (Figure 3A–C). Total scaffold stiffness was estimated by calculating the stiffness of a single wavy filament made of *j-beam* elements in series and multiplying this value by the i value of filaments along the vertical direction (Table 2).

2.3.2. Finite element method analysis of poly(ε-caprolactone) scaffolds

The mechanical behavior of the PCL scaffolds was investigated using 1D static structural FEM via the Ansys Workbench R22.1 software. In detail, FEM simulation was used for computing displacement behavior under tensile force and consequent stiffness evaluation. Moreover, Von Mises stress distribution was displaced to evaluate stress accumulation points. Since the construct was intended to be used within its elastic field limit, analysis was conducted assuming linear elastic material properties. Moreover, the model of the material was assumed to be linear and isotropic due to material homogeneity through the filament cross-section, while load distribution was distributed with stress applied along the wavy filaments' direction. For each analyzed stacking configuration with a different number of layers (alternating wavy and straight filaments in Figure 1B), a CAD model was prepared, consisting of beams discretized into 1D FEM mesh made of "BEAM188" elements (from the Ansys library). Specimen dimensions were set to 14 × 4.5 mm^2, resulting in a total of 3.5 unit cells along the x-axis and 1.5 unit cells along the y-axis (considering the dimensions in Figure 1A and configuration in Figure 1C). Poisson's ratio was derived from previous literature ($\nu = 0.3$).[32]

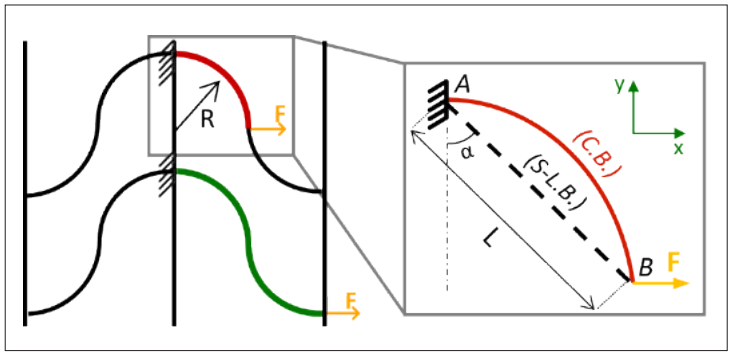


Figure 2. Straight-line beam (S-L.B.) and curved beam (C.B.) approximations. F is the applied force and M is the bending moment.

Table 1. Equations for stiffness computation for a single beam element, using the elastic line equation under S.-L.B. and C.B. approximations

Approximation type	Equation for stiffness calculation
S-L.B.	$K_{ij}^{SLB} = 3EAI/(L\cdot(3I\sin(\alpha)^2 + AL^2\cos(\alpha)^2))$
C.B.	$K_{ij}^{CB} = 12EAI/(R\cdot(3I\pi + AR^2\cdot(3\pi - 8)))$

Abbreviations: A: Cross-section area; alfa: Angle between the beam and vertical direction; **C.B.: Curved beam;** E: PCL Young's Modulus;I: Moment of inertia associated with the cross section; L: Straight beam length;R: Curvature radius of curved beam; **S-L.B.: Straight-line beam**.

A fixed support boundary condition of constrained displacement was imposed on a scaffold length corresponding to one unit cell length along the *x*-axis on one scaffold end, limiting both translational and rotational degrees of freedom (Figure 4). An external load, in the form of an imposed displacement, was applied to one unit cell length on the free side of the scaffold, simulating the action of a tensile force to stretch the scaffold along the *x*-direction. A central unconstrained scaffold portion with a total length of 1.5 unit cells was allowed to undergo deformation, representing the effective tested specimen. The imposed displacement along the *x*-direction (same as the F application) was 0.5 mm under the hypothesis of linear elastic deformation. Stiffness was calculated as the ratio between force and displacement (**Equation 1**).

To optimize the accuracy of FEM results and computational requirements for the simulations, a FEM mesh convergence study was performed by varying the refinement of the mesh during solution estimation. As the scaffolds were subjected to previously described boundary conditions, tensile force acting on a single beam was computed using an increasing number of nodes.

2.4. Fabrication of poly(ε-caprolactone) scaffolds

Based on the aforementioned mesh design, PCL scaffolds were produced through MEX using a commercially available 3D printer (ROKIT Invivo 3D Printer Premium, ROKIT Healthcare, Korea). Different sizes of PCL scaffolds were fabricated for structural and FEM analyses and mechanical tests: 6 × 4.5 mm² with thickness of 0.3 mm for cell tests; 14 × 4.5 mm² with thickness varying according to the number of layers (from two to eight layers). PCL pellets were loaded in a heated print head and melted at 100 °C. By applying compressed air with a pressure of 550 kPa, filaments were extruded through a nozzle with a diameter of 200 μm. The distance between the nozzle and the printing bed was customized through a G-code to achieve suitable print quality and resolution.

2.5. Preparation of photocurable gelatin methacryloyl hydrogels

GelMA prepolymer solution was prepared at three different concentrations (5, 7, and 10% w/v) in FGM-3 and stirred at 50 °C in dark conditions for 1 h. LAP was added (0.5% w/v) to the GelMA prepolymer solution and stirred for 15 min at 50 °C. Different volumes of GelMA solutions (30–300

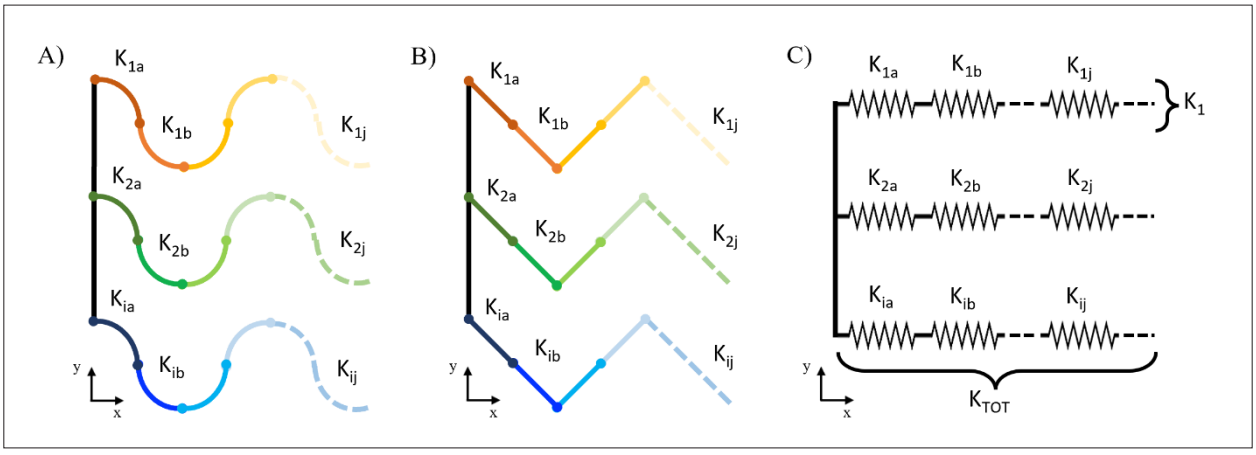


Figure 3. Single elements for total stiffness evaluation considering: (A) C.B. and (B) S-L.B. approximations, respectively. (C) 2D mesh model approximation to a spring with a defined stiffness. Abbreviations: C.B.: Curved beam; S-L.B.: Straight-line beam.

Table 2. Stiffness equations applied for calculating the total stiffness of stretchable PCL mesh

Stiffness for different samples	Equation for stiffness calculation
Series springs	$1/K_i = \sum_j 1/K_{ij}$
Parallel springs	$K_{TOT} = \sum_i K_i$
Total 2D mesh	$K_{mesh} = K_{TOT} = K \cdot (i/j)$

Note: K*ij* stiffness for a single element is constant and independent of *i*-*j* indexes. Abbreviations: K: stiffness; PCL: poly(ε-caprolactone); TOT: total.

μL) were prepared accordingly, and GelMA hydrogels were then formed by ultraviolet (UV) irradiation (wavelength: 365 nm; power density: 10 mW/cm^2) using a flexible light guide (Hamamatsu LC8 lamp, Hamamatsu Corporation, Japan). Light intensity was measured with a UV radiometer (UV Power Puck II, EIT, USA). GelMA hydrogels at the three different concentrations were coded as GelMA_5, GelMA_7, and GelMA_10, respectively.

2.6. Preparation of bioartificial scaffolds

PCL scaffolds were surface functionalized by a mussel-inspired approach, using DOPA to improve interfacial adhesion with GelMA hydrogels as previously reported.[33] GelMA solutions, with a volume ranging from 30 to 200 μL depending on the PCL scaffold size (i.e., 6 × 4.5 mm^2 with a thickness of 0.3 mm or 14 × 4.5 mm^2 with thickness varying according to the number of layers) were then poured into the pores of polyDOPA-functionalized PCL scaffolds. The scaffolds were then cured by UV irradiation (365 nm) at specific times based on the hydrogels' rheological properties (30 s for GelMA_5 and GelMA_7; 45 s for GelMA_10) (see section **2.9.**). The bioartificial scaffolds were coded as PCL/GelMA_5, PCL/GelMA_7, and PCL/GelMA_10, depending on the hydrogel concentration.

2.7. Mechanical characterization

2.7.1. Uniaxial tensile tests

The mechanical behavior of PCL and PCL/GelMA scaffolds was evaluated through uniaxial tensile tests in both dry and wet conditions using MTS QTest/10 MTS® System Corporation, Eden Prairie, MN, USA. Initially, tensile tests were carried out on straight PCL filaments fabricated by MEX (0.15 mm diameter and 25 mm length), using a load cell of 10 N and a velocity of 5 mm/min. These tests were performed to evaluate the Young's modulus (*E*)

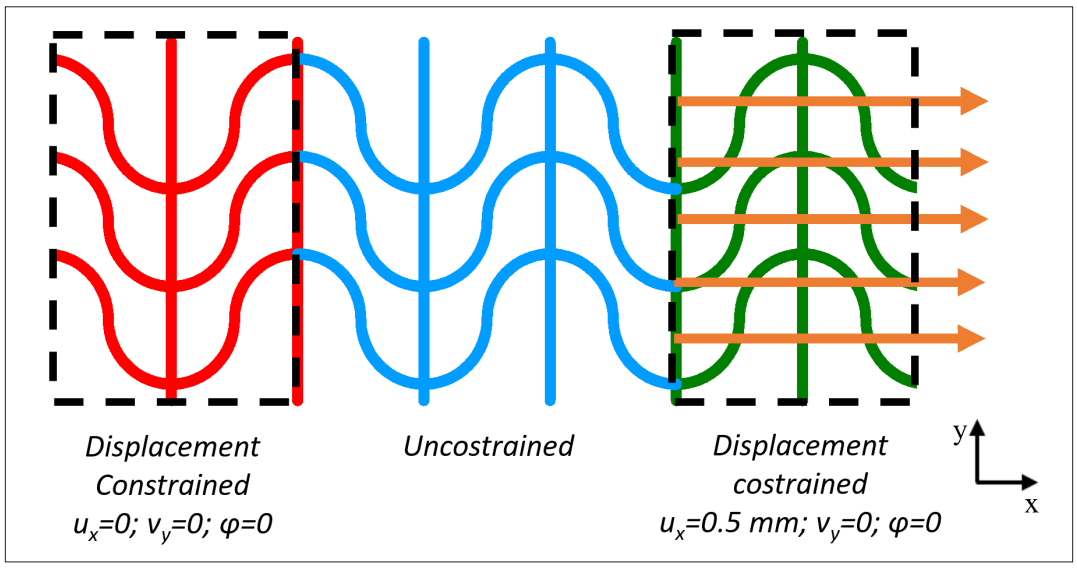


Figure 4. Boundary conditions of the FEM model were applied on stretchable PCL specimens for experimental analysis. Abbreviations: FEM: Finite element method; PCL: Poly(ε-caprolactone).

of a single PCL filament and subsequently used for analytic and FEM analyses. Tensile tests were also performed on dry PCL scaffolds with 3.5 × 1.5 unit cells in the *x*–*y* plane (corresponding to 14 × 4.5 mm^2), a gauge length of 1.5 unit cells along the *x*-axis (corresponding to 6 mm), and a thickness depending on the number of layers (0.3–0.9 mm). A load cell of 10 N and a velocity of 1 mm/min were used. Force–elongation and stress–strain curves were plotted to calculate the stiffness and Young's modulus of samples, respectively.

Based on the results of the PCL mesh tensile tests, bioartificial PCL/GelMA scaffolds (3.5 × 1.5 unit cells) with four and eight layers were characterized by uniaxial tensile tests in wet conditions using the same set-up previously described. Similar to that of PCL scaffolds, force–elongation and stress–strain curves were plotted and analyzed to calculate stiffness and Young's modulus of samples, respectively, in wet conditions.

In detail, stiffness (a parameter depending on scaffold mesh thickness and geometry) was measured by the 0.2% offset method from force–elongation curves by constructing a parallel line to the linear segment. Likewise, Young's modulus of the PCL/GelMA scaffold was determined from the stress–strain curve slope by applying the 0.2% offset method at the initial linear region and optimizing the PCL/GelMA scaffold cross-section as the bulk thickness. All samples were tested in triplicates.

2.7.2. Cyclic uniaxial tensile tests

The PCL/GelMA scaffolds were subjected to cyclic uniaxial tensile tests in wet conditions using MTS QTest/10 under 4% pre-deformation. The samples were then subjected to cyclic mechanical deformations with sinusoidal waveform up to 22% maximum deformation and at 1 Hz frequency for overall 100 cycles. Force–elongation and stress–strain curves were plotted to validate the elastic deformation behavior of PCL/GelMA scaffolds.

2.8. Morphological evaluations

PCL scaffold and freeze-dried GelMA hydrogel morphologies were observed by optical microscopy (Leica Z16 APO A Microscope, Leica Microsystems, Germany) and SEM (Tescan Vega Microscope, Tescan, USA) at different magnifications. Before SEM analysis, the samples were coated with a thin gold layer (Q150S, Quorum Technologies, United Kingdom [UK]). The ImageJ software was employed for image analysis of PCL scaffolds (top view and section) and freeze-dried GelMA hydrogels (section).

2.9. Physicochemical characterization of photocurable gelatin methacryloyl hydrogels

Photo-rheology was performed to investigate the kinetics and time of photocrosslinking the three different concentrations of GelMA hydrogels in response to UV and visible (Vis) light irradiation. A modular compact rheometer (MCR 302, Anton Paar, Austria) was equipped with parallel plates and a UV (bulb type: 365 nm; power density: 18 mW/cm^2; Hamamatsu LC8 lamp) or Vis (bulb type: 400–700 nm; power density: 18 mW/cm^2; Hamamatsu LC8 lamp) light source under the bottom quartz plate.[34] The gap between the two plates was set at 0.8 mm. The UV or Vis lamp was switched on 60 s after the start of the test to allow system stabilization before the beginning of the crosslinking process. After that, GelMA hydrogel solutions were exposed to irradiation for 3 min to evaluate their curing time. All the measurements were performed at a constant temperature (37 °C), with steady rotational oscillation at a frequency of 1 Hz and a constant strain amplitude of 1%.

The stability tests were evaluated in terms of dissolution behavior. GelMA_5, GelMA_7, and GelMA_10 hydrogels were dissolved in 200 µL water and subsequently in 400 µL sterile PBS) at 37 °C at different time steps (3, 7, and 14 days). PBS was refreshed every 3 days, keeping the solution sterile. At the end of each time point, the samples were washed with MilliQ water and then frozen at −20 °C. GelMA_5, GelMA_7, and GelMA_10 samples (in triplicate) were then freeze-dried and weighed. The dissolution degree (DD) was defined as:

$$DD\ (\%) = \left((w_0 - w_f) / w_0 \right) \times 100 \quad (2)$$

where w_f is the weight of incubated hydrogels after freeze-drying at each time point with respect to the initial weight (w_0).

2.10. Gelatin methacryloyl hydrogel cytocompatibility

Following the ISO 10993 regulation, a cytocompatibility assay was performed on eluates from GelMA_5, GelMA_7, and GelMA_10 hydrogels.[34]

HCFs from the human ventricle were extracted and cultured with FGM-3 in a humidified incubator at 37 °C and 5% CO_2. After trypsinization with 0.25% trypsin-ethylenediaminetetraacetic acid (EDTA) (Life Technologies, USA), HCFs were seeded in a 96-well plate with a cell density of 10^4 cells/well for 24 h to reach confluence and cultured in FGM-3 medium. Then, the culture medium was replaced with a conditioned medium, previously obtained by submerging 100 mg of GelMA_5, GelMA_7, and GelMA_10 hydrogels (prepared in FGM-3) in 1 mL of FGM-3 at 37 °C for 24 h. Before *in vitro* cell tests, the conditioned medium was sterilized by filtration through a sterile Biofil syringe filter with a 0.22 µm pore size. In the control samples, the culture medium was

also FGM-3. After 24 h of cell culture, the medium was replaced with 100 µL of non-fluorescent resazurin solution composed of CellTiter-Blue Cell Viability Assay reagent (Promega, USA), diluted to 1:10 in the new FGM-3. Cell viability was evaluated after a 4 h incubation in terms of fluorescence intensity measured by a microplate reader (BioTek Instruments, USA) at excitation (ex) and emission (em) wavelengths of 560 and 590 nm, respectively. Six measurements were performed for each hydrogel concentration to calculate the mean values and standard deviations compared to control samples.

2.11. Long-term cell viability and cytotoxicity tests on bioartificial stretchable scaffolds

PolyDOPA-PCL scaffolds with two layers (6 × 4.5 mm^2, considering the gauge length used in tensile tests) were sterilized by incubation in 70% ethanol solution for 30 min and subsequently dried in a biological hood before cell tests.

Sterile GelMA_5, GelMA_7, and GelMA_10 solutions were prepared as follows: (i) GelMA and LAP powders were UV-sterilized for 30 min in a biological hood (MSC-Advantage Class II Biological Safety Cabinet, Thermo Fisher Scientific); (ii) GelMA powders were mixed with sterile FGM-3 and incubated at 50 °C under stirring for 2 h until complete GelMA dissolution; (iii) LAP powder was added to each GelMA solution in the sterile hood and the system was stirred at 50 °C for 15 min in dark conditions.

HCFs were detached from the Petri dishes using trypsin-EDTA and centrifuged to obtain cell pellets with defined amounts of cells (1,000,000 cells/mL), which were then added to the GelMA_5, GelMA_7, and GelMA_10 solutions containing LAP at 37 °C. Cells were encapsulated by mixing GelMA solutions with cell pellets. Cellularized GelMA solutions (30 µL) were deposed into polyDOPA-PCL scaffold pores and on 48-well plates as the control and cured under UV irradiation at specific times based on the hydrogels' rheological properties (30 s for GelMA_5 and GelMA_7; 45 s for GelMA_10). After curing, viability and cytotoxicity tests were performed.

Live/Dead Cell Viability assay (Life Technologies, USA) was performed after 1, 7, and 14 days. Briefly, cellularized GelMA hydrogels cultured in 48-well plates were treated for 30 min with Live/Dead reagent (Life Technologies, USA), composed of 2 µM calcein acetoxymethyl (AM) and 4 µM ethidium homodimer-1 diluted in PBS. Samples were then imaged with a Nikon Ti2-E fluorescence microscope (Nikon Instruments, Japan).

Moreover, CellTiter-Blue Cell Viability Assay and CytoTox-ONE Homogeneous Membrane Integrity Assay (Promega, USA) were performed after 7 and 14 days of culture. CellTiter-Blue solution (300 µL) was incubated for 6 h with cellularized GelMA and PCL/GelMA samples, while CytoTox-ONE assay was performed on culture medium from both samples following manufacturer instructions (see section **2.10.**).

PCL/GelMA samples (with the three different GelMA concentrations) were cellularized with HCFs and cultured for 14 days in static conditions to assess the effect of GelMA concentration on cell viability, spreading, and cytoskeleton morphology. After selecting the optimum GelMA concentration for cell spreading and cytoskeleton conformation, *in vitro* cell tests were repeated under mechanical stimulation to assess its influence on HCF activation into myofibroblasts. PCL/GelMA samples were cultured for 7 days in static conditions (based on resultant cell morphologies within GelMA hydrogels in static conditions) and mechanical stimulation was subsequently applied to the scaffolds for 7 additional days. The MechanoCulture T6 bioreactor (CellScale, Canada) was employed to cyclically stretch the PCL/GelMA samples (4.5 × 1.5 unit cells) in the x–y plane (corresponding to 18 × 4.5 mm^2) with a gauge length of 1.5 unit cells along the x-axis (corresponding to 6 mm) and a four-layer thickness. The samples were subjected to cyclic mechanical deformations up to 10% maximum deformation (1 mm) at 1 Hz frequency and incubated in FGM-3 at 37 °C. The experimental setup is displayed in **Figure S6 and Video S1,** Supporting Information.

2.12. Immunofluorescence

Cellularized PCL/GelMA scaffolds were fixed in 4% w/v paraformaldehyde (Alfa Aesar, USA) in PBS for 15 min and subsequently washed with PBS. The cells were permeabilized with Triton X-100 (Sigma-Aldrich, USA) 0.5% in PBS for 10 min. The samples were then blocked with 2% bovine serum albumin (BSA, Sigma-Aldrich, USA) in PBS for 30 min, followed by either (i) staining with rhodamine-phalloidin (Life Technologies, USA) or (ii) incubation with primary antibodies (i.e., anti-actin smooth muscle [α-SMA; A7607, Sigma-Aldrich, US], anti-fibronectin [F3648, Sigma-Aldrich, USA], anti-collagen I [2456, Sigma-Aldrich, USA], and anti-collagen III [SAB4500367, Sigma-Aldrich, USA]), and secondary antibodies (i.e., anti-mouse Alexa Fluor 555 [Life Technologies, USA] or Alexa Fluor 488 [Life Technologies, USA]) diluted in 2% w/v BSA in PBS. Nuclei were counterstained with 4′,6-diamidino-2-phenylindole (DAPI; Sigma-Aldrich, USA). Samples were imaged using the Nikon Ti2-E fluorescence microscope (Nikon Instruments, Japan). Immunofluorescence experiments were performed in biological triplicates.

2.13. Statistical analysis

Statistical analysis of variance (ANOVA) was performed using GraphPad Prism version 9.0.0 (GraphPad Software Inc., USA).

3. Results and discussion

In this work, bioartificial PCL/GelMA scaffolds were designed and fabricated. These scaffolds were able to reproduce the stiffness of human cardiac fibrotic tissue to sustain *in vivo*-like cyclic mechanical deformations and support HCF culture. The ability of bioartificial scaffolds to sustain cyclic mechanical deformations was imparted by the PCL scaffold architecture, while stiffness could be adjusted by both the number of PCL scaffold layers and the concentration of GelMA hydrogels. Notably, the GelMA hydrogel concentration in bioartificial scaffolds was also optimized by static *in vitro* tests with HCFs to allow their long-term culture for at least 14 days. Finally, PCL/GelMA scaffolds cellularized with HCFs were cultured in dynamic conditions under cyclic mechanical stimulation to preliminarily assess the activation of HCFs into myofibroblasts.

3.1. Design and characterization of stretchable poly(ε-caprolactone) scaffolds

PCL scaffolds with cardiac tissue-like stretchability were designed to have a tailored mesh geometry with fixed filament size and a varying number of superimposed layers, to: (i) mimic the stiffness of human cardiac fibrotic tissues (Young's modulus of 0.4–9 MPa, as measured by uniaxial tensile tests using a 500 N load cell);[28] (ii) sustain *in vivo*-like maximum elastic deformation (≤22%);[5,21] (iii) display fatigue resistance under uniaxial cyclic tensile tests (with 22% maximum strain).

The scaffold mesh geometry was first defined (Figure 1), and PCL scaffolds with biomimetic stiffness were designed accordingly. Scaffolds with different numbers of layers (two, three, four, seven, and eight layers) were subjected to structural analysis under S-L.B. and C.B. hypotheses. Structure displacement computation was performed for stiffness analytic evaluation, considering both tensile force and bending moment (**Figure S1**). The analysis utilized Young's modulus (E) and yield stress (σ_{YS}) values of single PCL filaments fabricated by MEX that were measured by uniaxial tensile mechanical tests (E = 444 ± 46.32 *MPa* and σ_{YS} = 17.15 ± 2.36 *MPa*). Figures 5 and 9A displayed the stiffness of PCL scaffolds as a function of the number of scaffold layers, calculated according to the S-L.B. and C.B. approximations. Considering the PCL single filament section area ($b \times h$) of 0.2 × 0.15 mm^2, measured from SEM images (not shown), scaffold stiffness was found to increase as a function of the number of scaffold layers containing wavy filaments. Specifically, stiffness values increased twofold with the addition of any new layer containing wavy filaments, while layers containing straight filaments did not affect scaffold stiffness. This was a consequence of the dependence of the area moment on the scaffold cross-section. Indeed, the scaffold cross-section perpendicular to the x-direction (Figure 1) increased with the addition of any new layer containing wavy filaments. Hence, scaffolds with three, four, seven, and eight layers, that is, having the same number of layers with wavy filaments, displayed the same stiffness. As similar results were obtained using both S-L.B. and C.B. hypotheses (Figure 5), the S-L.B. approximation was then selected for further stiffness evaluations.

The mechanical behavior (e.g., stress distribution) of PCL scaffolds with up to eight stacked layers (Figure 1)

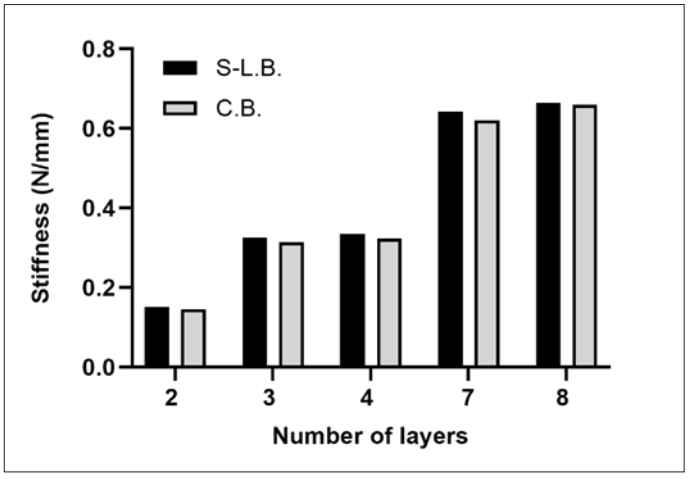


Figure 5. PCL: Poly(ε-caprolactone) (PCL) scaffold stiffness computed by structural analysis based on approximations of the single mesh element as a straight-line (S-L.B.) or a curved beam (C.B.). Abbreviations: C.B.: Curved beam; S-L.B.: Straight-line beam.

was investigated by FEM analysis. Initially, a mesh convergence study was performed: Figure 6A reports the axial force as a function of the number of nodes for scaffolds with a different number of layers, indicating an asymptotic behavior. On this basis, a mesh was selected, ensuring acceptable accuracy (i.e., <2% variation with respect to the previously computed value) and preventing computational power waste. Simulations were run by imposing the selected displacement with a ramped profile, setting 100 displacement–force data points, and obtaining the configuration as displayed in Figure 6B.

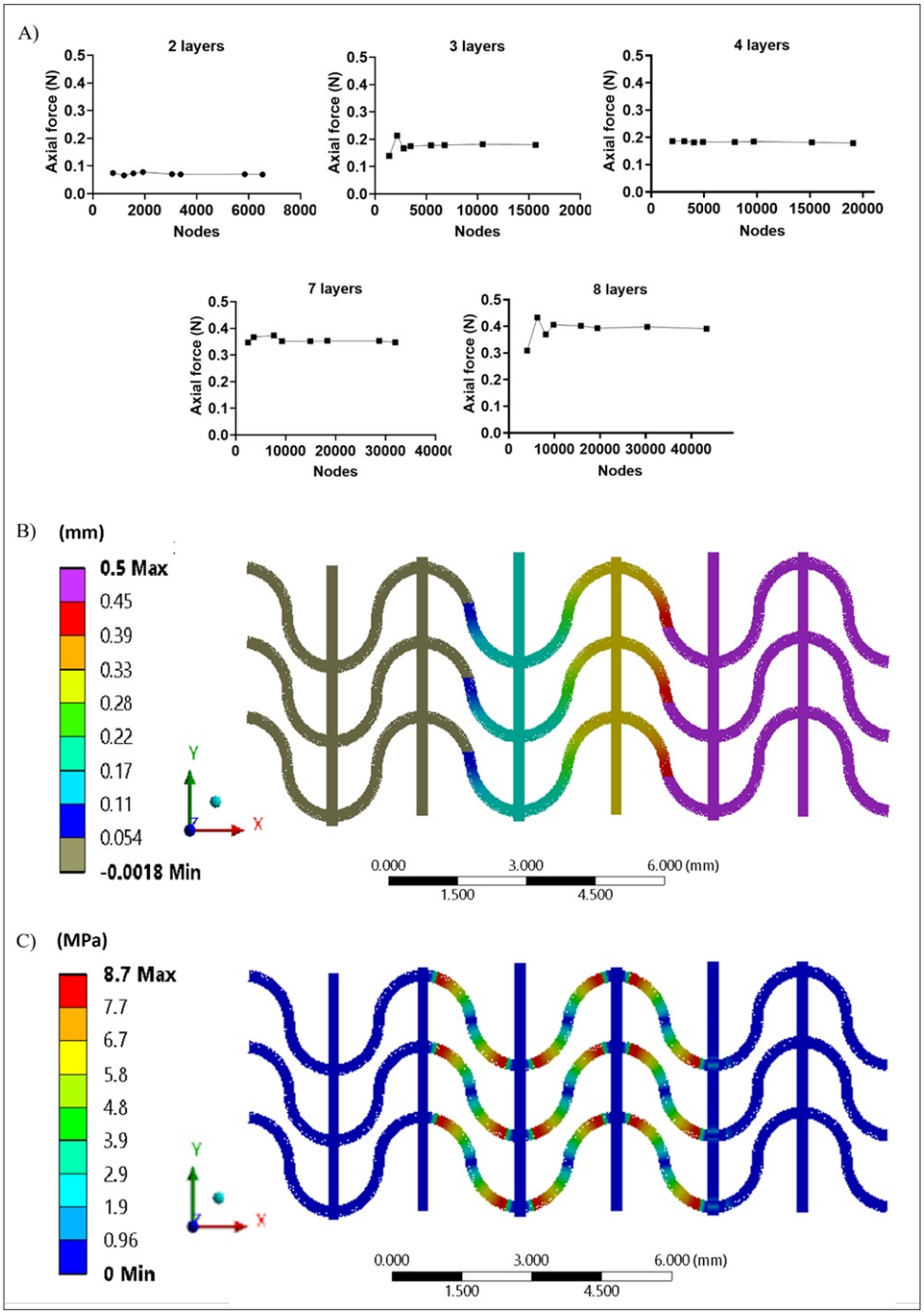


Figure 6. FEM analysis results: (A) FEM mesh convergence study; (B) applied displacement values retrieved from numerical simulations; (C) Von Mises stress distribution for PCL scaffolds with two layers. Abbreviations: FEM: Finite element method; PCL: Poly(ε-caprolactone).

Force values below yield stress conditions were obtained through a numerical algorithm for each of the imposed displacement points. Linear regression of the data was performed (Figure 6A), and the stiffness of PCL scaffolds with different thicknesses was computed as the angular coefficient of the curves displayed in **Figure S2A**. The evaluation of Von Mises stresses also enabled the validation of the elastic field hypothesis. Figure 6C illustrates an exemplary representation of Von Mises stress distributions for PCL scaffolds with two layers. Scaffolds with a different number of layers exhibited a similar distribution of Von Mises stresses. Qualitative considerations could be derived from the stress field of the 1D model: stress was distributed along the wavy filaments and the imposition of a bonded contact between straight and wavy filaments concentrated stress in proximity of such constraints regardless of the extinction zones present. The straight filaments were mostly unstressed and acted as load propagators in the direction of the deformation.

PCL scaffolds were then fabricated by MEX, and their morphology was analyzed by optical microscopy and SEM. Optical microscopy (Figure 7A and B) and SEM images (Figure 7C and D) of PCL scaffolds with eight layers demonstrated that the scaffold geometry accurately reproduced the designed CAD model. The images revealed an inter-fiber distance of close wavy and straight filaments of 1.15 ± 0.12 and 1.63 ± 0.07 mm, respectively, compared to the corresponding theoretical values of 1.5 and 2 mm, respectively, in the CAD model. ImageJ analysis of the cross-section optical images (Figure 7B) reported that the cross-section of joint wavy filaments had an average width (b) of 0.22 ± 0.02 mm and an average height (h) of 0.43 ± 0.02 mm.

3.2. Gelatin methacryloyl hydrogels: Physicochemical characterization and *in vitro* cell tests

GelMA hydrogel crosslinking kinetics was first analyzed by rheological characterization of GelMA solutions in the presence of LAP photoinitiators using two different light sources (UV and Vis). The sol-gel transition of the GelMA_5, GelMA_7, and GelMA_10 samples (occurring when G' exceeds G") was measured at 37°C during UV or Vis light irradiation. Strain sweep tests performed on

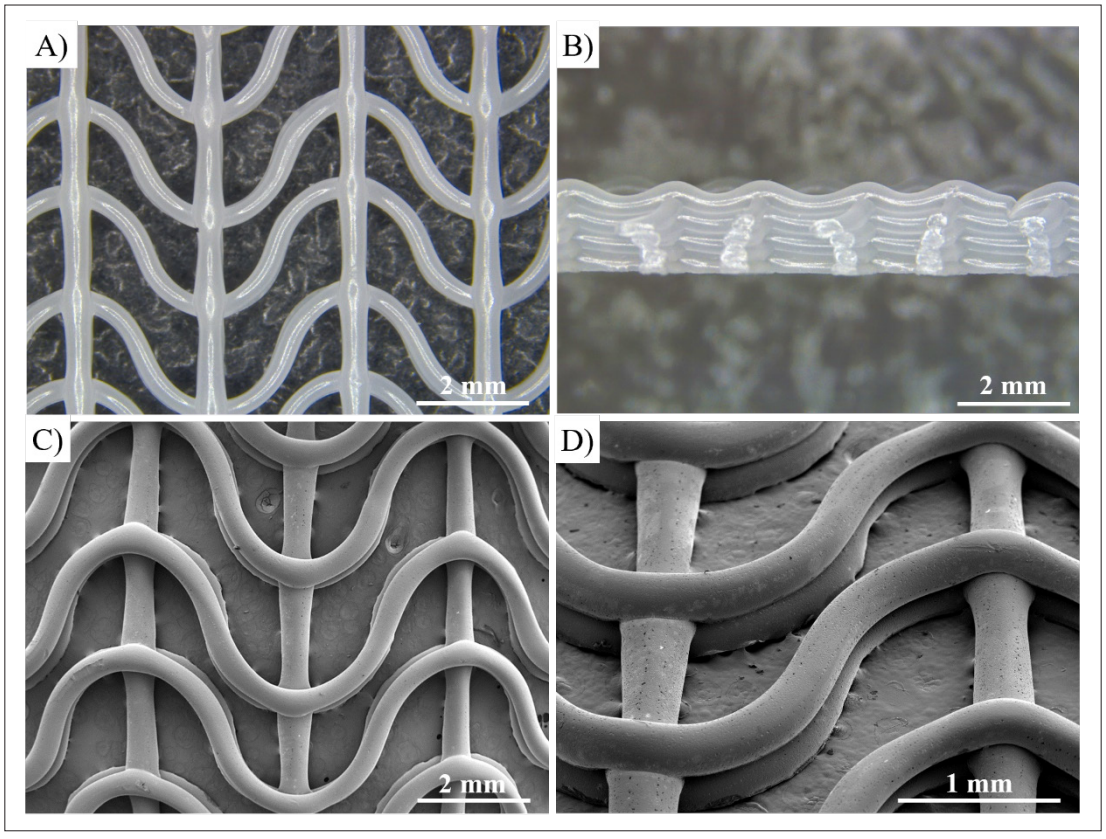


Figure 7. Optical images of the (A) top surface and (B) cross-section of an eight-layered PCL scaffold. SEM images of the (C) top surface and (D) tilted view of a three-layered PCL scaffold. Abbreviations: PCL: Poly(ε-caprolactone); SEM: Scanning electron microscopy.

GelMA_5, GelMA_7, and GelMA_10 hydrogels reported that the 1% strain amplitude used in time sweep tests was within the linear viscoelastic region (curves not shown). Upon irradiation, G' rapidly increased due to the photo-crosslinking process and reached a plateau at complete gelation.[28,29] The crosslinking time (defined as the time G' takes to reach the plateau value) for each GelMA hydrogel is reported in Figure 8A. At 37 °C and without irradiation, GelMA solutions retained a sol state as a function of time (data not shown). Under both UV and Vis irradiation, the crosslinking time increased as a function of GelMA solution concentration due to the presence of more reactive sites and increased viscosity.[35] UV-photopolymerization was complete within approximately 20 s for GelMA_5, 25 s for GelMA_7, and 40 s for GelMA_10, while the crosslinking time for Vis-photopolymerized hydrogels was approximately 70 s for GelMA_5, 85 s for GelMA_7, and 100 s for GelMA_10. As the UV–vis spectrum of LAP photoinitiators has a main absorption peak at 365 nm, GelMA_5, GelMA_7, and GelMA_10 solutions exposed to UV light reported faster photo-crosslinking than under Vis light irradiation. To prepare the hydrogels, curing times slightly higher than measured crosslinking times were selected: (i) UV irradiation: 30 s for GelMA_5 and GelMA_7 and 45 s for GelMA_10; (ii) Vis light irradiation: 100 s for GelMA_5 and GelMA_7 and 120 s for GelMA_10. Rapid UV-photocrosslinking is advantageous for embedding cells into hydrogels as it minimizes cell exposure to UV irradiation.[36] Biocompatibility was also demonstrated by Live/Dead analysis (Figure 8I) with no dead cells in GelMA hydrogels crosslinked under UV irradiation (30 s for GelMA_5 and GelMA_7 and 45 s for GelMA_10) and cultured for 24 h post-UV treatment.

G' plateau onset values reported in Figure 8B increased with increasing hydrogel concentration[37] from 1 to 8 kPa, and the values were higher for samples crosslinked under UV than Vis light irradiation. Interestingly, G' values of GelMA hydrogels prepared from sterile and non-sterile solutions were also similar (**Figure S3**). Hence, the sterilization process, based on UV irradiation of solutions before photo-crosslinking, did not affect the rheological properties of GelMA hydrogels. The selected degree of methacrylate substitution (60%) and hydrogel concentrations (5–10% w/v) limited hydrogel crosslinking and entanglement, leading to G' values in the range of stiffness of healthy cardiac tissue (1–40 kPa).[38] However, the stiffness of the final bioartificial scaffolds was higher than that of hydrogels alone due to the reinforcing effect of PCL scaffold structures, depending on the number of scaffold layers.

UV-photocrosslinking was selected for the preparation of cell-embedded GelMA hydrogels, as it provided hydrogels with superior G' upon brief exposure to UV irradiation, avoiding toxic effects on cells (Figure 8I).[36] SEM images of fractured sections of freeze-dried UV-photocrosslinked GelMA_5, GelMA_7, and GelMA_10 hydrogels (Figure 8C–E) revealed increased pore sizes with decreasing GelMA concentration[38] (Figure 8F). Figure 8G reports the weight loss of UV-photocrosslinked GelMA_5, GelMA_7, and GelMA_10 hydrogels incubated in sterile PBS at 37 °C for 14 days. Volumes of GelMA hydrogels and PBS were chosen at a 1:2 ratio (0.2 mL:0.4 mL). After 3 days, weight loss was less than 10% for all hydrogels, in agreement with previous reports.[39] All samples had a weight loss under 20% after 14 days of incubation with no significant differences between the samples of different concentrations.

When embedding cells into GelMA hydrogels, free radicals could cause cytotoxicity, both directly or indirectly through the generation of reactive oxygen species (ROS). Furthermore, LAP has been reported to induce dose-dependent cytotoxic effects.[37,41] To assess GelMA cytocompatibility, HCF viability was evaluated 24 h after culturing in hydrogel eluates (Figure 8H). Results indicated that the cell viability percentage was similar to control conditions (100%), that is, 98.9 ± 6.5%, 95.2 ± 5.3%, and 97.9 ± 5.4% for cells in contact with extracts from GelMA_5, GelMA_7, and GelMA_10 hydrogels, respectively. Hence, the hydrogels did not elicit cytotoxic effects.

3.3. Bioartificial poly(ε-caprolactone)-gelatin methacryloyl scaffolds: physicochemical characterization and *in vitro* cell tests

A polyDOPA coating was applied on the PCL scaffold surface, using a protocol previously reported by the authors,[24] to enhance the interaction between PCL filaments and GelMA hydrogels. Thereafter, GelMA hydrogels and PCL scaffolds were combined into bioartificial PCL/GelMA scaffolds and provided with ECM-like microenvironment (HCFs-adhesive GelMA hydrogel). The scaffold was able to sustain *in vivo*-like cyclic mechanical deformations (stretchable PCL scaffolds) and exhibit cardiac fibrotic tissue-like Young's modulus (400 kPa to 9 MPa).[22,20]

3.3.1. Tensile testing

PCL scaffolds, with 12 mm length, 4.5 mm width, and a thickness dependent on the number of layers, were subjected to tensile tests with and without GelMA_5, GelMA_7, and GelMA_10 hydrogel fillers to experimentally derive stiffness values (Figure 9 and Table 3). Stress–strain curves of PCL scaffolds displayed a J-shaped trend (Figure 9A).[6] Stiffness values of PCL scaffolds with two, three, four, seven, and eight layers (Figure 9B) were comparable with those obtained by S-L.B. approximation and FEM analysis (Figure 9C). Stiffness

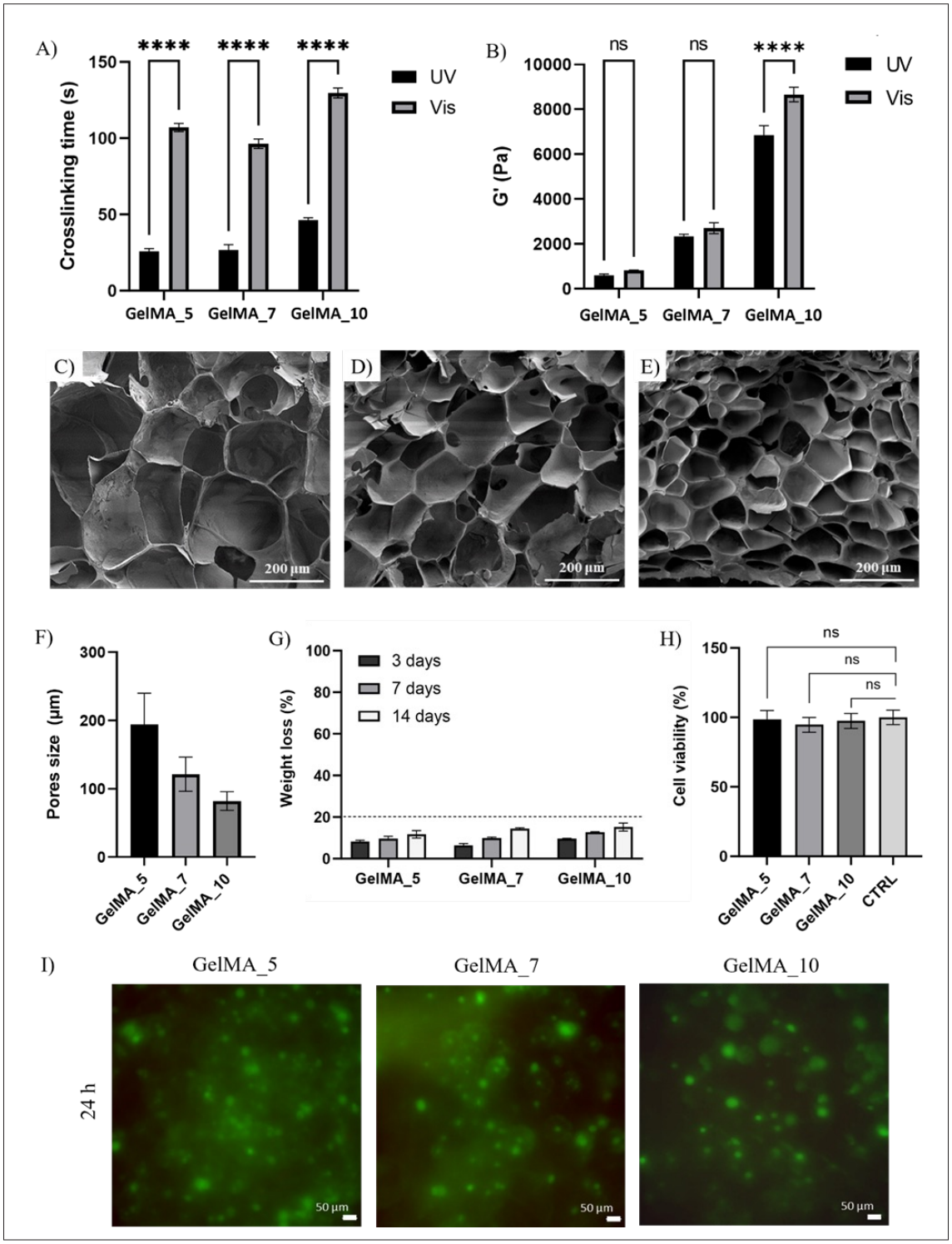


Figure 8. Gelatin methacryloyl (GelMA) hydrogel characterization: (A) crosslinking time and (B) plateau onset values of storage modulus (G') for GelMA_5, GelMA_7, and GelMA_10 hydrogels, exposed to ultraviolet (UV) and visible (Vis) light, measured from time-sweep curves (1% strain amplitude and 1 Hz frequency). ****$p < 0.0001$. (C–E) Scanning electron microscopy (SEM) images of freeze-dried samples: (C) GelMA_5, (D) GelMA_7, and (E) GelMA_10. (F) Pore size distribution of the freeze-dried samples and (G) weight loss percentage of GelMA_5, GelMA_7, and GelMA_10 hydrogels incubated in PBS at 37 °C. (H) Viability (CellTiter-Blue®) of cultured human cardiac fibroblasts (HCFs) in a culture medium containing eluates from GelMA_5, GelMA_7, and GelMA_10 hydrogels after 24 h incubation. (I) Live/Dead Cell Viability assay (green: live cells, red: dead cells) performed on HCF-cellularized GelMA hydrogels cultured for 24 h and cured accordingly (i.e., 30 s for GelMA_5 and 45 s for both GelMA_7 and GelMA_10 samples). Abbreviation: ns: Non-significant.

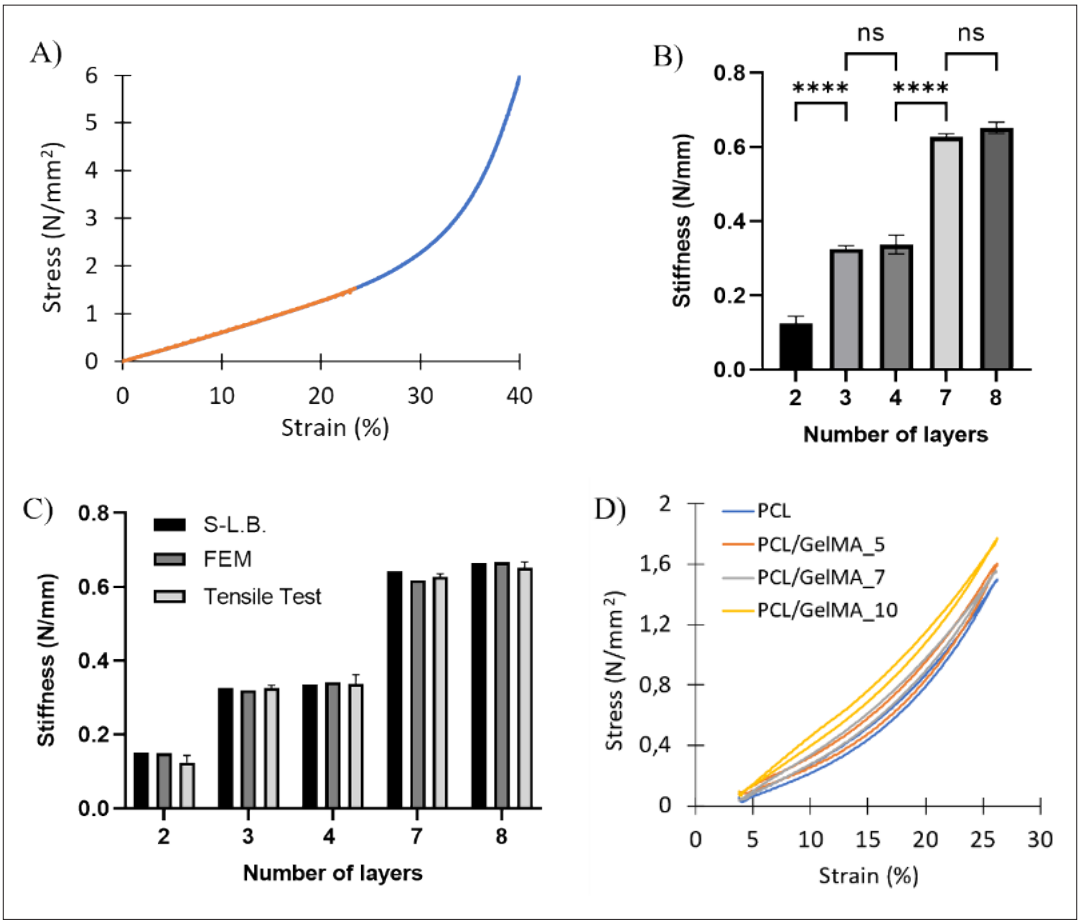


Figure 9. Stiffness and stress testing of the PCL scaffolds: (A) PCL scaffold stress-strain curve; (B) Young's modulus of PCL scaffolds with a different number of layers, calculated by tensile tests (****$p < 0.0001$); (C) stiffness of PCL scaffolds with a different number of layers, calculated by S-L.B. approximation, FEM analysis, and tensile tests; (D) cyclic stress-strain curves for PCL (blue), PCL/GelMA_5 (red), PCL/GelMA_7 (grey), and PCL/GelMA_10 (yellow) scaffolds (n = 3). Abbreviations: FEM: Finite element method; ns: Non-significant; PCL: Poly(ε-caprolactone); PCL/GelMA: Poly(ε-caprolactone)-gelatin methacryloyl; S-L.B: Straight-line beam.

Table 3. Stiffness and Young's modulus values of PCL/GelMA scaffolds derived from uniaxial tensile tests in wet condition

Number of layers	Bioartificial scaffold	Tensile test	
		Stiffness (N/mm)	Young's modulus (MPa)
4	PCL/GelMA_5	0.51 ± 0.01	6.76 ± 0.18
	PCL/GelMA_7	0.56 ± 0.01	7.66 ± 0.18
	PCL/GelMA_10	0.65 ± 0.10	9.47 ± 1.39
8	PCL/GelMA_5	0.85 ± 0.07	8.21 ± 0.68
	PCL/GelMA_7	0.96 ± 0.03	8.88 ± 0.26
	PCL/GelMA_10	1.18 ± 0.01	10.46 ± 0.03

Abbreviation: PCL/GelMA: poly(ε-caprolactone)-gelatin methacryloyl.

increased with increasing the number of layers containing wavy filaments. The stiffness values (Figure 9B) and FEM outputs (**Figure S2A**) were similar for PCL scaffolds with three and four layers or with seven and eight layers. Hence, as aforementioned, the addition of a supplementary layer with straight filaments, perpendicularly oriented with respect to the load direction, did not vary scaffold stiffness. Scaffold mechanical response to the applied load was primarily due to the layers containing wavy filaments, while layers with straight filaments only behaved as strain distributors. Furthermore, PCL scaffolds with two to eight layers displayed a maximum elastic deformation equal to or superior to that of heart tissues at late-stage diastole (18–22%).[5,20]

The PCL scaffolds were functionalized with polyDOPA before the addition of GelMA hydrogels, obtaining PCL/GelMA scaffolds. Notably, polyDOPA coating did not affect the mechanical properties of PCL scaffolds, as previously reported for square grid-shaped scaffolds.[24] PCL/GelMA scaffolds with four and eight layers were analyzed by tensile tests in wet conditions, and the stress–strain curves are reported in **Figure S2B**. The average stiffness and Young's modulus values of the PCL/GelMA scaffolds, as derived from the tensile tests, are reported in Table 3.

Data collected in Table 3 indicated that stiffness and Young's modulus of bioartificial PCL/GelMA scaffolds with a fixed number of layers slightly increased as a function of GelMA hydrogel concentration. At fixed GelMA hydrogel concentration, stiffness and Young's modulus increased as a function of the number of layers. Young's modulus of PCL/GelMA scaffolds was in the range of 6.8–10.5 MPa, which was in agreement with values reported in the literature for pathological cardiac tissues of men and women aged from 61 to 70.[19,20,38,43-45] The literature reference values (i.e., between 400 kPa and 9 MPa) were derived from tensile tests performed on biopsies of human hearts extracted during autopsy.[5] By increasing the concentration of GelMA hydrogel (and/or the number of scaffold layers), the mechanical properties of fibrotic human myocardium could be approached in terms of Young's modulus (400 kPa to 9 MPa compared to 1–40 kPa for healthy cardiac tissue).[27,31,38] For all bioartificial PCL/GelMA scaffolds, the maximum elastic deformation was equal to or slightly higher than the maximum elastic deformation of late-stage diastole (18–22%).[5,20,22]

Additionally, PCL/GelMA scaffolds were designed to exhibit dynamic stretchability for *in vitro* culture experiments under cardiac tissue-like cyclic mechanical stimulation (Figures 9D and **S6 and Video S1**). PCL scaffold geometry was mainly responsible for scaffold elastic stretchability. The maximum elastic deformation for PCL scaffolds was approximately 30% *versus* 3–4% for PCL dog-bone substrates and single filaments. Figure 9D reports one cycle of the cyclic mechanical test (100 cycles) displaying hysteretic behavior with structural damping. Hence, such preliminary tests suggested that PCL/GelMA scaffolds allowed cyclic mechanical deformation, while their stiffness could be adjusted by GelMA hydrogel concentration and the number of PCL scaffold layers.

3.3.2. Biological evaluation

In vitro cell tests were performed on HCF-embedded GelMA hydrogels within bioartificial PCL/GelMA scaffolds with two layers, minimizing the use of cells. Cell viability, cytotoxicity, and immunofluorescence imaging were analyzed 7 and 14 days after cell culture.

No dead cells were observed in the Live/Dead images of GelMA_5, GelMA_7, and GelMA_10 hydrogels (**Figure S4**). However, cell viability (determined from the CellTiter-Blue® Cell Viability Assay) at days 7 and 14 was significantly higher for cells cultured in PCL/GelMA_5 and PCL/GelMA_7 compared to PCL/GelMA_10 scaffolds (Figure 10A). The high concentration of GelMA_10 hydrogel caused a reduction in its intrinsic porosity and permeability to nutrients and catabolites, affecting cell viability. This hypothesis was supported by SEM analysis of the freeze-dried hydrogel samples (Figure 8C–E) and previous findings.[34,42,46-47] In contrast, the cytotoxicity assay did not reveal any cytotoxic effect on cells cultured on bioartificial scaffolds (Figure 10B). Cytotoxicity was evaluated by measuring lactate release in the medium from dead cells. Low cytotoxicity of cells cultured in PCL/GelMA_10 scaffolds suggested that HCFs populating the inner part of the hydrogel could be in a quiescent state. This hypothesis was supported by confocal microscopy analysis (Figures 11C and F and S5C and F) and by Live/Dead assay (**Figure S4C and F**), suggesting the presence of live cells with a rounded shape and less spread morphology within GelMA_10 hydrogels in PCL/GelMA_10 scaffolds even at 14 days after culture.

Cell F-actin and nuclei were stained to evaluate the 3D distribution of HCFs in the bioartificial scaffolds and their cytoskeleton morphology. Figures 11 and S5 report confocal microscopy images displaying a homogeneous distribution of cells inside the PCL/GelMA scaffolds and GelMA hydrogels, respectively, 7 and 14 days after culture. F-actin staining revealed a different cell cytoskeleton organization that depended on GelMA concentration, which is in agreement with previous literature,[4,37,48] such that the hydrogels of lower concentrations and stiffness supported optimal cell spreading. Conversely, cells in the GelMA_10 hydrogel were rounded and not completely spread. Moreover, in PCL/GelMA_5 and PCL/

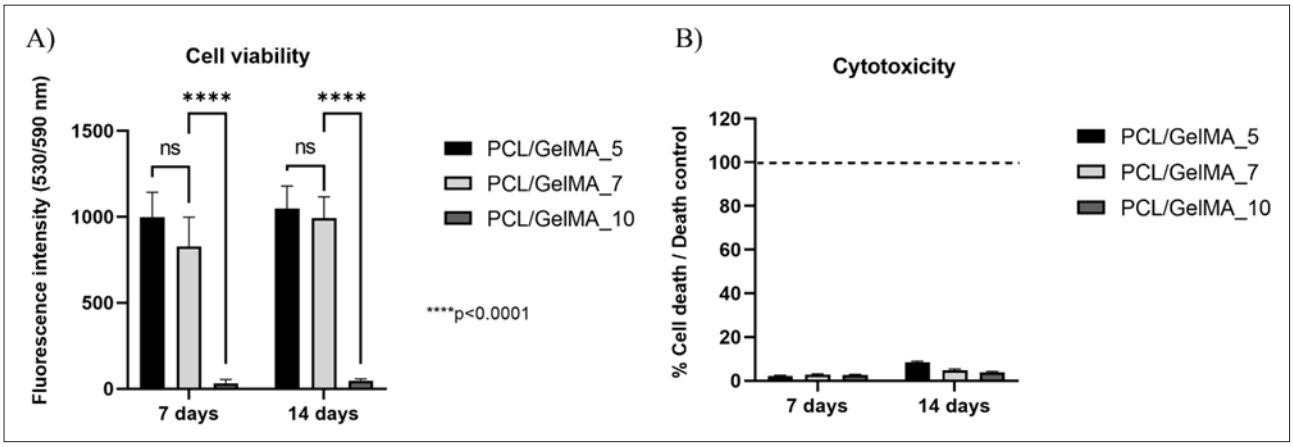


Figure 10. Biological evaluation of the PCL/GelMA scaffolds. (A) Cell viability percentage seven and 14 days after HCF culture in PCL/GelMA scaffolds with different GelMA concentrations (****$p < 0.0001$). (B) Cytotoxicity percentage seven and 14 days after HCF culture in PCL/GelMA scaffolds with different GelMA concentrations. The dashed line denotes the control cells; cultured HCFs displayed $p < 0.0001$ relative to the control cells. Abbreviations: GelMA: Gelatin methacryloyl; HCF: Human cardiac fibroblasts; PCL/GelMA: Poly(ε-caprolactone)-gelatin methacryloyl.

GelMA_7 scaffolds, cells also colonized the PCL filaments (Figure 11D and E). PCL/GelMA_5 scaffolds were found to be the most suitable for HCF colonization of both PCL structure and GelMA hydrogel. Bright-field images were taken as a reference to localize the scaffold position in the hydrogel and to better inspect its effect on cell organization through confocal microscopy images. Overall, under static culture conditions, the presence of PCL scaffolds did not significantly influence cell orientation and distribution at the tested cell density.

Previous literature reported that chemical (e.g., TGF-β) or mechanical (e.g., stretching) pro-fibrotic stimuli[29,37] can trigger α-SMA expression and modify the expression pattern of different ECM proteins, particularly the overexpression of fibronectin and collagen I and the downregulation of collagen III.[5,37,48] Cyclic mechanical stimulation was applied by culturing HCF within PCL/GelMA_5 scaffolds in a MechanoCulture T6 bioreactor (under the experimental setup illustrated in **Figure S6**). Mechanical stimulation was applied 7 days after the initial culture in static conditions to allow cell attachment and spreading within GelMA_5 hydrogels (Figure 11A). Results revealed that mechanical stimulation triggered α-SMA overexpression in HCFs (Figure 12A), suggesting a phenotypic switch into myofibroblasts, of which was conversely not obtained in static culture conditions. Moreover, ECM protein staining indicated a decrease in the production of collagen III (Figure 12B), while fibronectin and collagen I were slightly more expressed after mechanical triggering (Figure 12C and D). Taken together, these results suggest that mechanical stimulation could favor pathological ECM deposition. However, these qualitative observations should be validated by quantifying protein production using immunoblotting and analyzing gene expression via real-time polymerase chain reaction (qPCR).[5,29] Furthermore, longer stimulation periods could enhance tissue response to the mechanical stimulus, warranting future investigations to elucidate the role of mechanical stress in the onset of fibrosis.

Overall, the results suggested that bioartificial PCL/GelMA scaffolds cultured with HCFs can potentially recreate an *in vitro* cardiac fibrotic tissue model with *in vivo*-like cyclic stretching. Although miniaturized platforms (organ-on-chips) have been developed (e.g., to reproduce heartbeats),[29] the advantage of a tissue-engineered cardiac scar model is represented by its potential exploitation to test not only drugs and nanotherapeutics, but also medical devices, cell therapies, and tissue engineering solutions.

4. Conclusion

In this work, 3D bioartificial stretchable scaffolds were designed, combining GelMA hydrogels and PCL scaffolds fabricated by MEX. Stretchability was imparted by PCL scaffold architecture, consisting of alternating layers of parallel wavy and straight filaments with 90° inclination with respect to the wavy filaments. Stiffness values of PCL scaffolds, obtained by structural and FEM analyses, were in agreement with experimental data derived by tensile tests: stiffness increased from 0.15 to 0.66 N/mm as a function of the number of layers (from two to eight), and only additional layers containing wavy filaments contributed to stiffness increase.

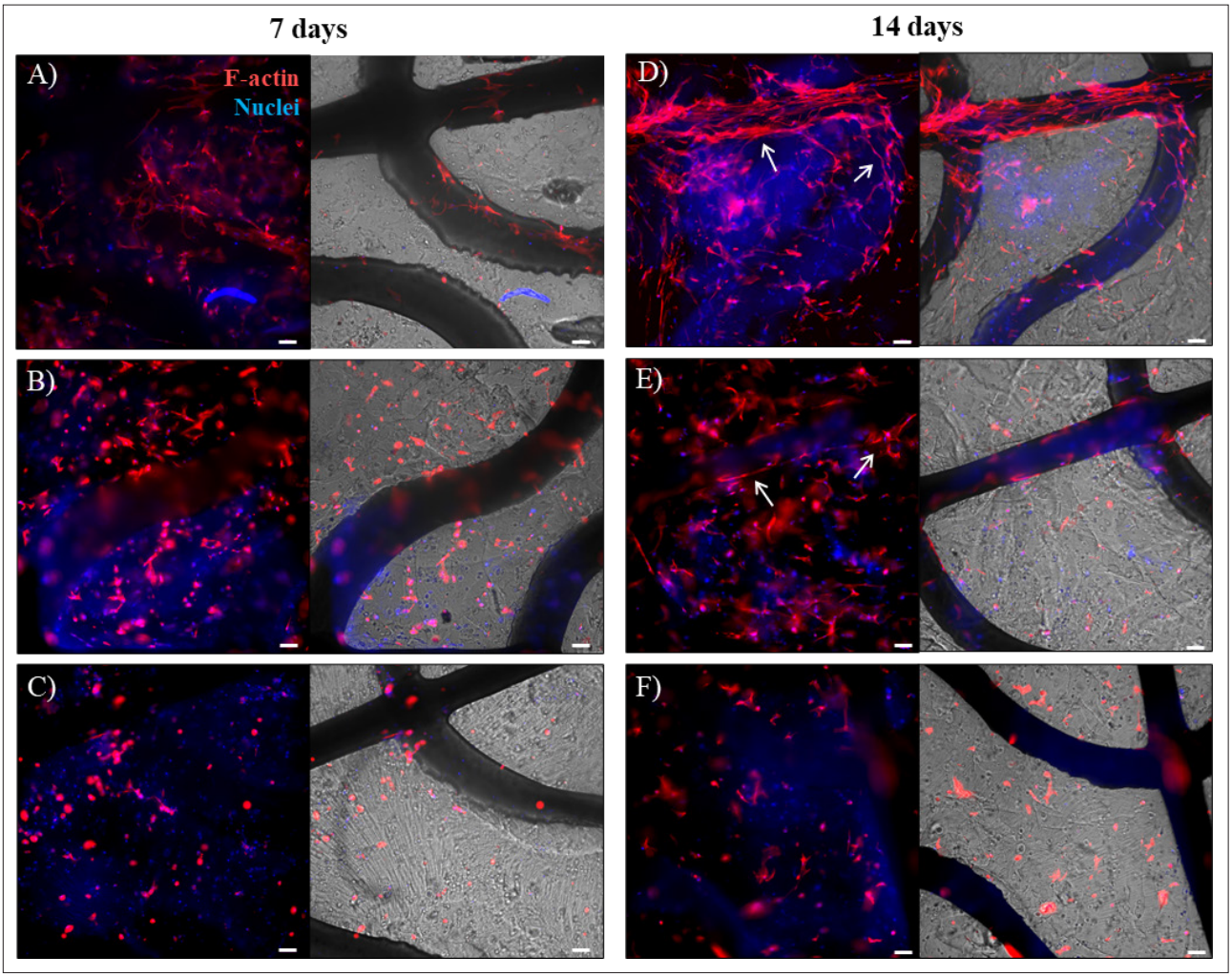


Figure 11. Immunofluorescence (red: F-actin; blue: nuclei) and bright-field images of cells and scaffolds after culture. HCFs on PCL/GelMA scaffolds with two layers seven days after HCF culture: (A) PCL/GelMA_5, (B) PCL/GelMA_7, and (C) PCL/GelMA_10. HCFs on PCL/GelMA scaffolds with two layers 14 days after HCF culture: (D) PCL/GelMA_5, (E) PCL/GelMA_7, and (F) PCL/GelMA_10. White arrows denote cell colonization in the PCL area. Scale bar: 100 μm. Abbreviations: HCF: Human cardiac fibroblasts; PCL/GelMA: Poly(ε-caprolactone)-gelatin methacryloyl.

Photocrosslinked GelMA hydrogels were prepared at three different concentrations via visible or UV light crosslinking to determine optimal biomimetic support for embedding cells into bioartificial scaffolds. UV photocrosslinking and exposure time were selected based on photo-rheological characterization and Live/Dead assay. GelMA_5, GelMA_7, and GelMA_10 hydrogels exhibited biomimetic stiffness (1–8 kPa) comparable to healthy cardiac tissues. Moreover, sterilized hydrogels were stable for up to 14 days of incubation in sterile PBS. Their biocompatibility was assessed by *in vitro* cell tests on hydrogel eluates.

Before the PCL and GelMA combination, polyDOPA coating was applied on the PCL scaffolds to improve GelMA adhesion onto the PCL scaffold surface. Bioartificial PCL/GelMA scaffolds reported stiffness and Young's modulus values of 0.51–1.18 N/mm and 6.8–10.5 MPa, respectively, and these parameters were dependent on the number of layers and GelMA hydrogel concentration. Nonetheless, Young's modulus values were in agreement with literature data on pathological cardiac tissue for men and women between the ages of 61 and 70.[27] Furthermore, bioartificial PCL/GelMA scaffolds displayed biomimetic elastic deformation of up to 22% strain.[25]

In vitro cell tests were performed by embedding HCFs into GelMA hydrogels, filling the pores of PCL/GelMA scaffolds with two layers. The cells were well-distributed throughout the hydrogel. Likewise, the cytoskeletal conformation was strongly influenced by GelMA hydrogel

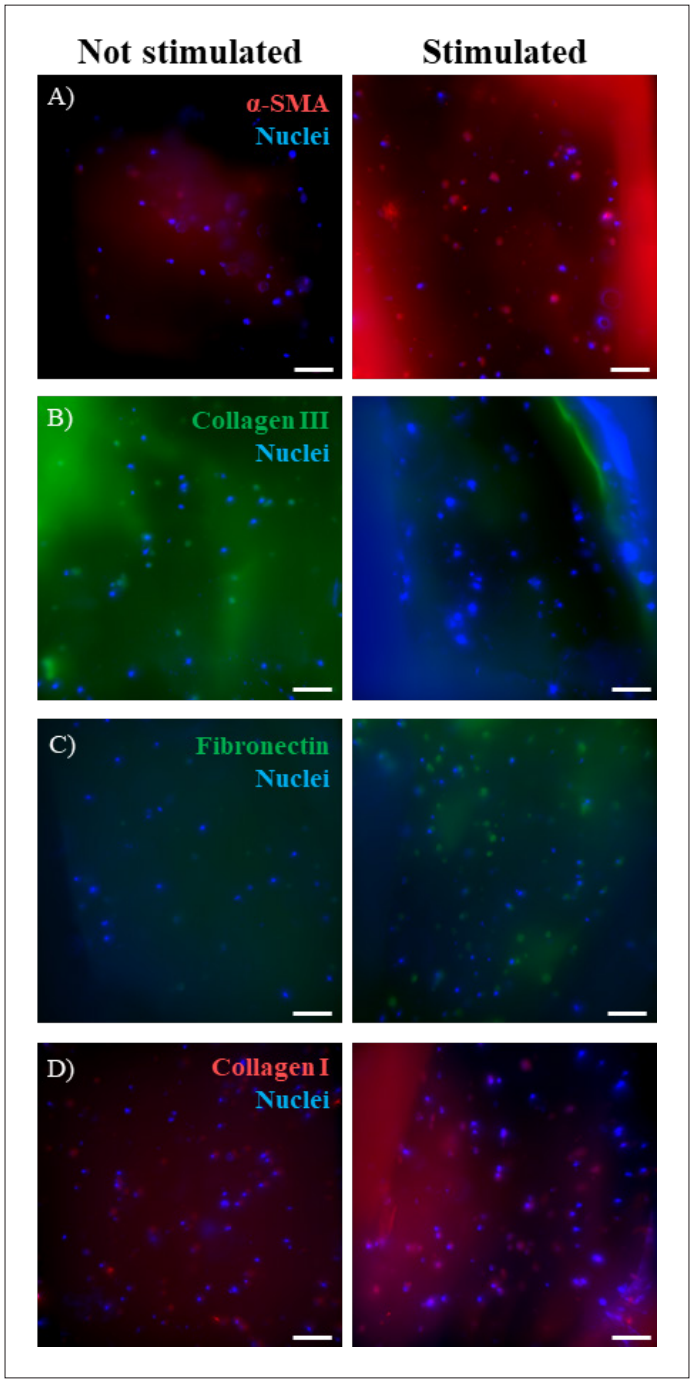


Figure 12. Immunostaining of HCFs on PCL/GelMA_5 scaffolds with and without mechanical cyclic stimulation (i.e., [left] not stimulated and [right] stimulated samples) for (A) *α*-SMA, (B) collagen III, (C) fibronectin, and (D) collagen I. Scale bar: 50 μm. Abbreviations: *α*-SMA: *α*-Smooth muscle actin; HCFs: Human cardiac fibroblasts; PCL/GelMA_5: Poly(*ε*-caprolactone)-gelatin methacryloyl.

concentration, inferring better cell spreading within the PCL/GelMA_5 scaffold. Although all hydrogels were not cytotoxic, only GelMA_5 and GelMA_7 hydrogels supported the viability of embedded cells, probably due to their superior permeability to nutrients and metabolites. Moreover, cell-loaded PCL/GelMA_5 scaffolds mechanically stimulated with MechanoCulture T6 bioreactor reported higher expressions of proteins involved

in fibrosis, compared to scaffolds under static conditions. In particular, stimulated cells had increased expressions of the α-SMA and fibronectin and decreased expression of collagen III.[48] These results supported the hypothesis that the application of cyclic mechanical stimulations to cellularized bioartificial scaffolds may trigger HCF activation into myofibroblasts. Deeper investigations through protein and gene expression quantifications (e.g., qPCR) are warranted to validate the effect of mechanical stimulation on HCF phenotype and culture time. This system would allow us to better understand and manage fibrosis onset by tuning stretch timing and rate.

In summation, the mechanical and biological properties of bioartificial PCL/GelMA scaffolds make them a promising platform with *in vivo*-like mechanical properties, tailored by PCL scaffold architecture and GelMA hydrogel concentration, for the development of dynamic *in vitro* models of human cardiac fibrotic tissues. Further validation will allow their use for the *in vitro* preclinical testing of medical devices and advanced therapies.

Acknowledgments

The authors would like to acknowledge CellScale (Canada) for kindly lending us the MechanoCulture T6 bioreactor and especially Johannes de Bondt (Business Unit Manager, Germany at World Precision Instruments - Europe) for his support.

Funding

This work was supported by the European Research Council (ERC) under the European Union's Horizon 2020 research and innovation funding program (BIORECAR; Grant Agreement No. 772168).

Conflict of interest

The authors declare no conflicts of interest.

Author contributions

Conceptualization: Irene Carmagnola, Valeria Chiono
Data curation: Mattia Spedicati, Francesca Tivano, Janira Bei, Mario Lavella, Alice Zoso
Formal analysis: Mattia Spedicati, Francesca Tivano, Janira Bei, Mario Lavella
Funding acquisition: Valeria Chiono
Investigation: Mattia Spedicati, Francesca Tivano, Janira Bei, Mario Lavella, Alice Zoso
Methodology: Mattia Spedicati, Francesca Tivano, Janira Bei, Mario Lavella, Alice Zoso
Project administration: Valeria Chiono
Resources: Valeria Chiono
Software: Mattia Spedicati, Francesca Tivano, Janira Bei, Mario Lavella
Supervision: Irene Carmagnola, Valeria Chiono
Validation: Mattia Spedicati, Francesca Tivano, Janira Bei, Mario Lavella, Alice Zoso
Writing – original draft: Mattia Spedicati, Francesca Tivano
Writing – review & editing: Mario Lavella, Alice Zoso, Irene Carmagnola, Valeria Chiono

Ethics approval and consent to participate

Not applicable.

Consent for publication

Not applicable.

Availability of data

Data are available from the corresponding author upon reasonable request.

References

1. World Health Organization (WHO). *Cardiovascular Diseases (CVDs)*. https://www.Who.Int/En/News-Room/Fact-Sheets/Detail/Cardiovascular-Diseases-(Cvds); 2019.
2. Talman V, Ruskoaho H. Cardiac fibrosis in myocardial infarction—from repair and remodeling to regeneration. *Cell Tissue Res*. 2016;365(3):563-581. doi: 10.1007/s00441-016-2431-9
3. Woodruff MA, Hutmacher DW. The return of a forgotten polymer – polycaprolactone in the 21st century. *Prog Polym Sci*. 2010;35(10):1217-1256. doi: 10.1021/acsami.3c04362
4. Nichol JW, Koshy ST, Bae H, Hwang CM, Yamanlar S, Khademhosseini A. Cell-laden microengineered gelatin methacrylate hydrogels. *Biomaterials*. 2010;31(21):5536-5544. doi: 10.1016/j.biomaterials.2010.03.064
5. Deddens JC, Sadeghi AH, Hjortnaes J, et al. Modeling the human scarred heart in vitro: toward new tissue engineered models. *Adv Healthc Mater*. 2017;6(3):1-21. doi: 10.1002/adhm.201600571
6. Olvera D, Sohrabi Molina M, Hendy G, Monaghan MG. Electroconductive melt electrowritten patches matching the mechanical anisotropy of human myocardium. *Adv Funct Mater*. 2020;30(44):1-10. doi: 10.1002/adfm.201909880
7. Castilho M, van Mil A, Maher M, et al. Melt electrowriting allows tailored microstructural and mechanical design of scaffolds to advance functional human myocardial tissue formation. *Adv Funct Mater*. 2018;28(40):1-10. doi: 10.1002/adfm.201803151.

8. Castilho M, Feyen D, Flandes-Iparraguirre M, et al. Melt electrospinning writing of poly-hydroxymethylglycolide-co-ε-Caprolactone-based scaffolds for cardiac tissue engineering. *Adv Healthc Mater*. 2017;6(18):1-9. doi: 10.1002/adhm.201700311

9. Paxton NC, Daley R, Forrestal DP, Allenby MC, Woodruff MA. Auxetic tubular scaffolds via melt electrowriting. *Mater Des*. 2020;193:108787. doi: 10.1016/j.matdes.2020.108787.

10. Bas O, D'Angella D, Baldwin JG, et al. An integrated design, material, and fabrication platform for engineering biomechanically and biologically functional soft tissues. *ACS Appl Mater Interfaces*. 2017;9(35):29430-29437. doi: 10.1021/acsami.7b08617

11. Saidy NT, Wolf F, Bas O, et al. Biologically inspired scaffolds for heart valve tissue engineering via melt electrowriting. *Small*. 2019;15(24):e1900873. doi: 10.1002/smll.201900873

12. Robinson TM, Hutmacher DW, Dalton PD. The next frontier in melt electrospinning: taming the jet. *Adv Funct Mater*. 2019;29(44):1904664. doi: 10.1002/adfm.201904664

13. Hochleitner G, Jüngst T, Brown TD, et al. Additive manufacturing of scaffolds with sub-micron filaments via melt electrospinning writing. *Biofabrication*. 2015;7(3):035002. doi: 10.1088/1758-5090/7/3/035002

14. Hutmacher DW, Schantz T, Zein I, Ng KW, Teoh SH, Tan KC. Mechanical properties and cell cultural response of polycaprolactone scaffolds designed and fabricated via fused deposition modeling. *J Biomed Mater Res*. 2001;55(2):203-216. doi: 10.1002/1097-4636(200105)55:2<203::aid-jbm1007>3.0.CO;2-7

15. Agarwala MK, Jamalabad VR, Langrana NA, Safari A, Whalen PJ, Danforth SC. Structural quality of parts processed by fused deposition. *Rapid Prototyp J*. 1996:2(4):4-19. doi: 10.1108/13552549610732034

16. Meng Z, He J, Li J, Su Y, Li D. Melt-based, solvent-free additive manufacturing of biodegradable polymeric scaffolds with designer microstructures for tailored mechanical/biological properties and clinical applications. *Virtual Phys Prototyp*. 2020;15(4):417-444. doi: 10.1080/17452759.2020.1808937

17. Emig R, Zgierski-Johnston CM, Timmermann V, et al. Passive myocardial mechanical properties: meaning, measurement, models. *Biophys Rev*. 2021;13(5):587-610. doi: 10.1007/s12551-021-00838-1

18. Zhang W, Huang G, Xu F. Engineering biomaterials and approaches for mechanical stretching of cells in three dimensions. *Front Bioeng Biotechnol*. 2020;8:589590. doi: 10.3389/fbioe.2020.589590

19. Huang G, Wang L, Wang S, et al. Engineering three-dimensional cell mechanical microenvironment with hydrogels. *Biofabrication*. 2012;4(4):042001. doi: 10.1088/1758-5082/4/4/042001

20. Park N, Kim J. Hydrogel-based artificial muscles: overview and recent progress. *Adv Intell Syst*. 2020;2(4):1900135. doi: 10.1002/aisy.201900135

21. Boffito M, Di Meglio F, Mozetic P, et al. Surface functionalization of polyurethane scaffolds mimicking the myocardial microenvironment to support cardiac primitive cells. *PLoS One*. 2018;13(7):e0199896. doi: 10.1371/journal.pone.0199896

22. Chiono V, Ciardelli G, Vozzi G, et al. Enzymatically-modified melt-extruded guides for peripheral nerve repair. *Eng Life Sci*. 2008; 8(3):226-237. doi: 10.1002/elsc.200700069

23. Chiono V, Vozzi G, Acunto MD, et al. Characterisation of blends between poly (ε-caprolactone) and polysaccharides for tissue engineering applications. *Mater Sci Eng C*. 2009;29(7):2174-2187. doi: 10.1016/j.msec.2009.04.020

24. Spedicati M, Ruocco G, Zoso A, et al. Biomimetic design of bioartificial scaffolds for the *in vitro* modelling of human cardiac fibrosis. *Front Bioeng Biotechnol*. 2022;10:983872. doi: 10.3389/fbioe.2022.983872.

25. Bari E, Scocozza F, Perteghella S, et al. 3D bioprinted scaffolds containing mesenchymal stem/stromal lyosecretome: next generation controlled release device for bone regenerative medicine. *Pharmaceutics*. 2021;13(4):515. doi: 10.3390/pharmaceutics13040515

26. Chen QZ, Harding SE, Ali NN, Lyon AR, Boccaccini AR. Biomaterials in cardiac tissue engineering: ten years of research survey. *Mater Sci Eng R Rep*. 2008;59(1–6): 1-37. doi: 10.1016/j.mser.2007.08.001

27. Guimarães CF, Gasperini L, Marques AP, Reis RL. The stiffness of living tissues and its implications for tissue engineering. *Nat Rev Mater*. 2020;5:351-370. doi: 10.1038/s41578-019-0169-1

28. Chelnokova NO, Golyadkina AA, Kirillova IV, Polienko AV, Ivanov DV. Morphology and biomechanics of human heart. *Proc SPIE*. 2016;9710:971013. doi: 10.1117/12.2208423

29. Visone R, Paoletti A, Cordiale L, et al. In vitro mechanical stimulation to reproduce the pathological Hallmarks of human cardiac fibrosis on a beating chip and predict the efficacy of drugs and advanced therapies. *Adv Healthc Mater*. 2024;13(4):e2301481. doi: 10.1002/adhm.202301481

30. Paoletti C, Divieto C, Tarricone G, Di Meglio F, Nurzynska D, Chiono V. MicroRNA-mediated direct reprogramming

of human adult fibroblasts toward cardiac Phenotype. *Front Bioeng Biotechnol*. 2020;8:529.
doi: 10.3389/fbioe.2020.00529

31. Nicoletti L, Paoletti C, Tarricone G, et al. Lipoplexes for effective in vitro delivery of microRNAs to adult human cardiac fibroblasts for perspective direct cardiac cell reprogramming. *Nanomedicine*. 2022;45:102589.
doi: 10.1016/j.nano.2022.102589

32. Schipani R, Nolan DR, Lally C, Kelly DJ. Integrating finite element modelling and 3D printing to engineer biomimetic polymeric scaffolds for tissue engineering. *Connect Tissue Res*. 2020;61(2):174-189.
doi: 10.1080/03008207.2019.1656720

33. Carmagnola I, Chiono V, Ruocco G, et al. Plga membranes functionalized with gelatin through biomimetic mussel-inspired strategy. *Nanomaterials*. 2020;10(11):1-17.
doi: 10.3390/nano10112184

34. Melilli G, Carmagnola I, Tonda-Turo C, et al. DLP 3D printing meets lignocellulosic biopolymers: carboxymethyl cellulose inks for 3D biocompatible hydrogels. *Polymers (Basel)*. 2020;12(8):1-11.
doi: 10.3390/POLYM12081655

35. Ding H, Illsley NP, Chang RC. 3D Bioprinted GelMA based models for the study of Trophoblast cell invasion. *Sci Rep*. 2019;9(1):18854.
doi: 10.1038/s41598-019-55052-7

36. Fedorovich NE, Oudshoorn MH, van Geemen D, Hennink WE, Alblas J, Dhert WJ. The effect of photopolymerization on stem cells embedded in hydrogels. *Biomaterials*. 2009;30(3):344-353.
doi: 10.1016/j.biomaterials.2008.09.037

37. Sadeghi AH, Shin SR, Deddens JC, et al. Engineered 3D cardiac fibrotic tissue to study fibrotic remodeling. *Adv Healthc Mater*. 2017;6(11):1-14.
doi: 10.1002/adhm.201601434

38. McCain ML, Lee H, Aratyn-Schaus Y, Kléber AG, Parker KK. Cooperative coupling of cell-matrix and cell-cell adhesions in cardiac muscle. *Proc Natl Acad Sci U S A*. 2012;109(25):9881-9886.
doi: 10.1073/pnas.1203007109

39. Rajabi N, Kharaziha M, Emadi R, Zarrabi A, Mokhtari H, Salehi S. An adhesive and injectable nanocomposite hydrogel of thiolated gelatin/gelatin methacrylate/Laponite® as a potential surgical sealant. *J Colloid Interface Sci*. 2020;564:155-169.
doi: 10.1016/j.jcis.2019.12.048

40. Chen YW, Wang K, Ho CC, Kao CT, Ng HY, Shie MY. Cyclic tensile stimulation enrichment of Schwann cell-laden auxetic hydrogel scaffolds towards peripheral nerve tissue engineering. *Mater Des*. 2020;195:108982.
doi: 10.1016/j.matdes.2020.108982

41. Donderwinkel I, Van Hest JCM, Cameron NR. Bio-inks for 3D bioprinting: recent advances and future prospects. *Polym Chem*. 2017;8:4451-71.
doi: 10.1039/c7py00826k

42. Ward M, Iskratsch T. Mix and (mis-)match – the mechanosensing machinery in the changing environment of the developing, healthy adult and diseased heart. *Biochim Biophys Acta Mol Cell Res*. 2020;1867(3):118436.
doi: 10.1016/j.bbamcr.2019.01.017

43. Sirry MS, Butler JR, Patnaik SS, et al. Characterisation of the mechanical properties of infarcted myocardium in the rat under biaxial tension and uniaxial compression. *J Mech Behav Biomed Mater*. 2016;63:252-264.
doi: 10.1016/j.jmbbm.2016.06.029

44. Arani A, Arunachalam SP, Chang ICY, et al. Cardiac MR elastography for quantitative assessment of elevated myocardial stiffness in cardiac amyloidosis. *J Magn Reson Imaging*. 2017;46(5):1361-1367.
doi: 10.1002/JMRI.25678

45. Vedadghavami A, Minooei F, Mohammadi MH, et al. Manufacturing of hydrogel biomaterials with controlled mechanical properties for tissue engineering applications. *Acta Biomater*. 2017;62:42-63.
doi: 10.1016/j.actbio.2017.07.028

46. Chaudhuri O, Cooper-White J, Janmey PA, Mooney DJ, Shenoy VB. Effects of extracellular matrix viscoelasticity on cellular behaviour. *Nature*. 2020;584(7822):535-546.
doi: 10.1038/s41586-020-2612-2O

47. Choi JR, Yong KW, Choi JY, Cowie AC. Recent advances in photo-crosslinkable hydrogels for biomedical applications. *Biotechniques*. 2019;66(1):40-53.
doi: 10.2144/btn-2018-0083

48. Ruocco G, Zoso A, Mortati L, Carmagnola I, Chiono V. Biomimetic electrospun scaffold-based in vitro model resembling the Hallmarks of human myocardial fibrotic tissue. *ACS Biomater Sci Eng*. 2023;9(7):4368-4380.
doi: 10.1021/acsbiomaterials.3c00483

ACCSCIENCE PUBLISHING

International Journal of Bioprinting

RESEARCH ARTICLE

Stereolithography 3D printing of microgroove master moulds for topography-induced nerve guidance conduits

Hexin Yue[1], Xuzhao Liu[1], Kejian Hou[1], Cian Vyas[1,2*], and Paulo Bartolo[1,2*]

[1]School of Mechanical, Aerospace and Civil Engineering, University of Manchester, Manchester, United Kingdom

[2]Singapore Centre for 3D Printing, School of Mechanical and Aerospace Engineering, Nanyang Technological University, Singapore

Abstract

Patients who have peripheral nerve damage from trauma or disease may suffer lifelong disability. Current interventions such as nerve allografts are inadequate due to limited availability of tissue and donor-site morbidity. Commercial nerve guidance conduits are used to bridge the damaged nerve gap and restore function. Typically, however, they lack cell-instructive guidance cues to promote directed regeneration. Tissue-engineered nerve guidance conduits that utilise micro- and nano-topographical architectures have been demonstrated to direct cell behaviour and contact guidance. This study uses projection micro-stereolithography-based three-dimensional (3D) printing to fabricate microgrooved (10–30 μm) master moulds to produce polydimethylsiloxane (PDMS) moulds and solvent cast polycaprolactone and polylactic acid films. The polymer microgrooves were successfully fabricated and were able to be formed into tubular nerve guidance conduits. The surface morphology, roughness, wettability, and thermal properties of the films were characterised. The microgroove topography improved proliferation and induced alignment of SH-SY5Y cells. This facile 3D printing approach is promising for the fabrication of nerve guidance conduits with topographical guidance cues as it obviates the need for using photolithographic techniques. Thus, this approach provides an alternative that is simpler, faster, cheaper, and offers greater design freedom.

Keywords: Bioprinting; Microgroove; Moulds; Nerve guidance conduit; Peripheral nerve repair; Stereolithography

***Corresponding authors:**
Cian Vyas
(cian.vyas@ntu.edu.sg)

Paulo Bartolo
(paulojorge.dasilvabartolo@manchester.ac.uk)

Citation: Yue H, Liu X, Hou K, Vyas C, Bartolo P. Stereolithography 3D printing of microgroove master moulds for topography-induced nerve guidance conduits. *Int J Bioprint.* 2024;10(3):2725. doi: 10.36922/ijb.2725

Received: January 12, 2024
Accepted: February 23, 2024
Published Online: May 31, 2024

Copyright: © 2024 Author(s). This is an Open Access article distributed under the terms of the Creative Commons Attribution License, permitting distribution, and reproduction in any medium, provided the original work is properly cited.

Publisher's Note: AccScience Publishing remains neutral with regard to jurisdictional claims in published maps and institutional affiliations.

1. Introduction

The peripheral nervous system (PNS) connects the central nervous system to the entire body, with its principal responsibilities encompassing the processing of incoming neural information, modulation of sensory perception, coordination of motor activities, and the preservation of homeostasis. Peripheral nerve injury (PNI) is a frequent occurrence, typically arising from trauma, and results in a complicated recovery process related to the specific gap size and the slow regeneration speed. Globally, there are over 5 million new cases of PNI annually.[1] Spontaneous regeneration of nerves is feasible for small gaps

measuring a few millimetres.[2] However, for larger nerve gaps, a regenerative rate of 1–3 mm per day is imperative for axons to reach the distal motor endplate, frequently leading to partial functional recovery.[3]

Current clinical interventions for PNI predominantly involve suturing and autologous transplantation.[4,5] The precision required in nerve suturing may result in excessive tension, and autologous transplantation encounters limitations due to donor tissue constraints and structural disparities between donor and recipient nerves. Clinically, up to 33% of PNI cases exhibit incomplete recovery and adverse outcomes, including chronic pain, compromised or partially restored motor and sensory function, and muscular atrophy and weakness.[6]

Peripheral nerves have a multi-fascicle structure with axons orientated in the same direction in each fascicle.[7] When peripheral nerves are injured, the nerve cells align longitudinally in the endoneurium, generating Büngner bands to direct the axons. Notably, when the PNI gap exceeds 10 mm, grafting interventions become imperative to bridge the proximal and distal nerve stumps, thereby fostering the requisite environment for regeneration.[8] The efficiency of nerve regeneration is enhanced when cell arrangement and axonal growth are directed.[9]

Commercially available nerve guidance conduits (NGCs) typically adopt a single-channel configuration.[10] They are usually restricted to short injury gaps (<20 mm) due to the absence of specific guidance cues.[11,12] Furthermore, single-channel nerve conduits are susceptible to collapse, impeding nerve growth, inadequately mimicking fascicle structures, and exhibiting suboptimal performance in guiding axonal growth.[13] Microchannel NGCs, whilst capable of directing cell alignment and promoting regenerating axons to aggregate in natural bundles, also present challenges such as potential insufficient nutrient supply to the regenerating tissue within the lumen.[5,14]

Tissue-engineered NGCs have been explored as potential alternatives to autografts.[5,14] NGCs are envisioned to serve as bridging devices capable of directing axonal growth and overcoming the impediments associated with traditional interventions. Various types of NGCs, including hydrogel fillers,[15] fibrous fillers,[16] and patterned scaffolds,[17] have been developed to create optimal intraluminal matrices for guiding neurite outgrowth. Specific guidance cues to direct regenerating axons to specific locations are essential.[18] Failure to provide guiding cues can result in dislocations, neuroma formation, and misconnections as regenerated axons lose their growth orientation.[19] Physical contact guidance cues, such as channels, aligned fibres, and grooves, significantly influence neural cell behaviour and axon pathfinding.[12] The design of topographical cues in NGCs to guide this directional growth has been shown to impact the morphology, adhesion, and proliferation of nerve cells. Topographical cues such as dots, pits, pillars, and grooves at the nano- and micro-scale can modulate cell behaviour, including cell morphology, alignment, proliferation, differentiation, and migration.[20,21]

Microgroove topographies have been explored as nerve guidance cues with the specific structure (e.g., shape, groove depth, groove width and spacing) influencing cell response.[22,23] Various synthetic NGCs based on biodegradable polyesters with microgroove architectures have shown promising potential including poly(ε-caprolactone) (PCL), poly-l-lactic acid (PLA), and poly(lactide-coglycolide).[24,25] Typically, the microgroove dimensions are between 5 μm and 60 μm as this range enables contact guidance for neuronal cell types.[9,26-36] For example, Béduer et al.[27] observed that microgroove-patterned polydimethylsiloxane (PDMS) substrates with small microgroove widths (5–10 μm) improved axonal alignment and reduced branching in human neural stem cells but delayed neurite development and differentiation compared to larger groove widths (20–60 μm). Hsu et al.[26] fabricated chitosan and PLA microgroove conduits (20/20/3 μm) that improved Schwann and glial cell orientation and neurotrophic factor expression *in vitro* and enhanced peripheral nerve regeneration *in vivo*. A conductive polydopamine-coated poly(L-lactide-caprolactone)/graphene (PLCL/GN) composite NGC with 20 μm microgrooves was shown to promote directional migration, cell adhesion, elongation, myelin sheath growth, more rapid neuron regeneration, and functional recovery *in vivo*.[28] Apart from microgroove dimensions, the morphology of the microgroove has been demonstrated to be important by Mobasseri et al.,[29,30] with V- and sloped-shaped grooves showing improved cell alignment, as compared with square grooves.

However, the studies that explored microgroove NGCs mostly utilised photolithography to fabricate the master mould. Photolithography and soft microlithography techniques allow the fabrication of highly detailed nano- and micro-scale-patterned moulds.[37] These are transferred to the biomaterial substrate through an intermediate (e.g., PDMS mould or stamp) followed by solvent casting or thermal pressing.[14,27,30,31,38] However, photolithography is expensive and time-consuming, as well as requires stringent clean room facilities and entails complex processing steps. Soft lithography can be performed generally outside a clean room with a wider range of materials but still relies on the generation of a master mould via photolithography. Thus, this limits research accessibility, design freedom, and inability to rapidly prototype different configurations.

The resolution and capability of three-dimensional (3D) printing technology is improving, offering the benefits of design flexibility, precise geometric control, and wide variety of applicable materials. Subsequently, 3D printing has extensively been explored in biomedical applications, although the resolution of extrusion and inkjet-based machines is limited for fabricating microgroove architectures. Light-based vat photopolymerisation, such as stereolithography (SL), offers high resolution and has been utilised to fabricate NGCs with single- and multi-channel architectures.[39-42] For example, Pateman et al.[42] developed a single-channel NGC that exhibited an axially aligned microtopography due to the pixelation effect in digital light processing (DLP). However, a photocurable biomaterial is required for direct NGC fabrication, thus restricting the materials applicable.

SL has been used as an alternative to photolithography in the fabrication of master moulds for microfluidics.[43] Moulds can be rapidly fabricated and iterated at a lower cost than conventional photolithography. This makes them suitable for soft lithography and casting of PDMS, a polymer used for intermediate templates and prototyping microfluidic devices due to the relatively chemical inertness, biocompatibility, low cost, and transparency in ultraviolet-visible spectrum.[44] However, this approach has not yet been explored for the specific design and fabrication of cell-instructive microgroove topographies in NGCs.

This study explores the replacement of photolithography with SL for the fabrication of master moulds for the development of microgroove NGCs using soft lithography. Considering dimensions commonly employed in the literature to support contact guidance for neuronal cells, four different microgroove master mould architectures were fabricated: 10/10/10 μm, 20/20/10 μm, 25/25/10 μm, and 30/30/10 μm (width/spacing/depth). The 3D-printed master mould was used to fabricate a PDMS mould to enable casting of PCL and PCL/PLA thin films. The morphology, roughness, mechanical, wettability, and thermal properties were characterised, and SH-SY5Y cells were seeded to evaluate morphology and proliferation. This approach highlights the capability of high-resolution 3D printing to compete with photolithography in specific applications. Furthermore, this study provides understanding of appropriate microgroove dimensions to promote cell alignment for NGC applications.

2. Material and methods

2.1. Materials

PCL (Mn 80,000 g/mol), PLA (Mn 30,000 g/mol), SYLGARD™ 184 poly(dimethylsiloxane) (PDMS), foetal bovine serum (FBS), trypsin-EDTA, penicillin–streptomycin, glutamine, all-trans-retinoic acid (ATRA), paraformaldehyde (PFA), and Triton X-100 were purchased from Sigma-Aldrich (UK). Dichloromethane (CH_2Cl_2), Ethanol, Dulbecco's phosphate-buffered saline (PBS), DMEM/F-12, AlamarBlue™ Cell Viability Reagent, LIVE/DEAD Viability/Cytotoxicity Assay Kit, Alexa Fluor® 488 Phalloidin, and DAPI (4',6-diamidino-2-phenylindole) were purchased from Thermo Fisher Scientific (UK). SH-SY5Y (human neuroblastoma cell line CRL-2266) was purchased from ATCC (USA).

2.2. Design and 3D printing of master moulds

The master moulds were designed by computer-aided design (CAD) software (Siemens NX, Germany) with dimensions of 12.5 × 12.5 × 1 mm (*xyz*). Four different surface topographies were considered with microgroove dimensions of 10/10/10 μm, 20/20/10 μm, 25/25/10 μm, and 30/30/10 μm (width, spacing, and depth) (Figure 1a). A projection micro-stereolithography (PμSL) 3D printer (MicroArch™ S130, Boston Micro Fabrication, USA) with *x*–*y* resolution of 2 μm, layer thickness of 5–20 μm, and build volume of 50 × 50 × 10 mm (*xyz*) was used to fabricate the master moulds using the HTL photopolymer resin (Boston Micro Fabrication, USA). The 3D-printed moulds were examined using an upright digital microscope (VHX-5000, Keyence, Japan).

2.3. Fabrication of PDMS moulds and microgroove films

The fabrication of microgroove topographies on polymer films involves multiple steps (Figure 1b). Residual photoinitiators and unreacted oligomers may be left behind in the 3D-printed master mould, inhibiting PDMS curing.[45] To minimise inhibition, the 3D-printed master moulds were immersed in 95% ethanol for 24 h in a sealed container and placed on a shaker. The ethanol was removed and refreshed, sealed, and shaken for another 24 h. The moulds were then rinsed with water and air-dried for 1 h at room temperature.

The PDMS was mixed at a 10:1 (wt./wt.) ratio of prepolymer to curing agent, degassed under vacuum to remove air bubbles, and poured onto the 3D-printed master moulds to achieve a thickness of ~10 mm. The moulds were placed at the bottom of the PDMS prepolymer to guarantee the same solution volume can be casted onto the PDMS moulds. The PDMS was cured overnight (12–16 h) in a dry oven at 65°C. The moulds were removed to release the cured PDMS mould. No releasing agents were required for the release of PDMS replicas.

A 1, 3, and 5% wt./vol PCL and blend of PCL/PLA (4:1) solution in dichloromethane (DCM) was prepared and casted onto the microgroove PDMS moulds

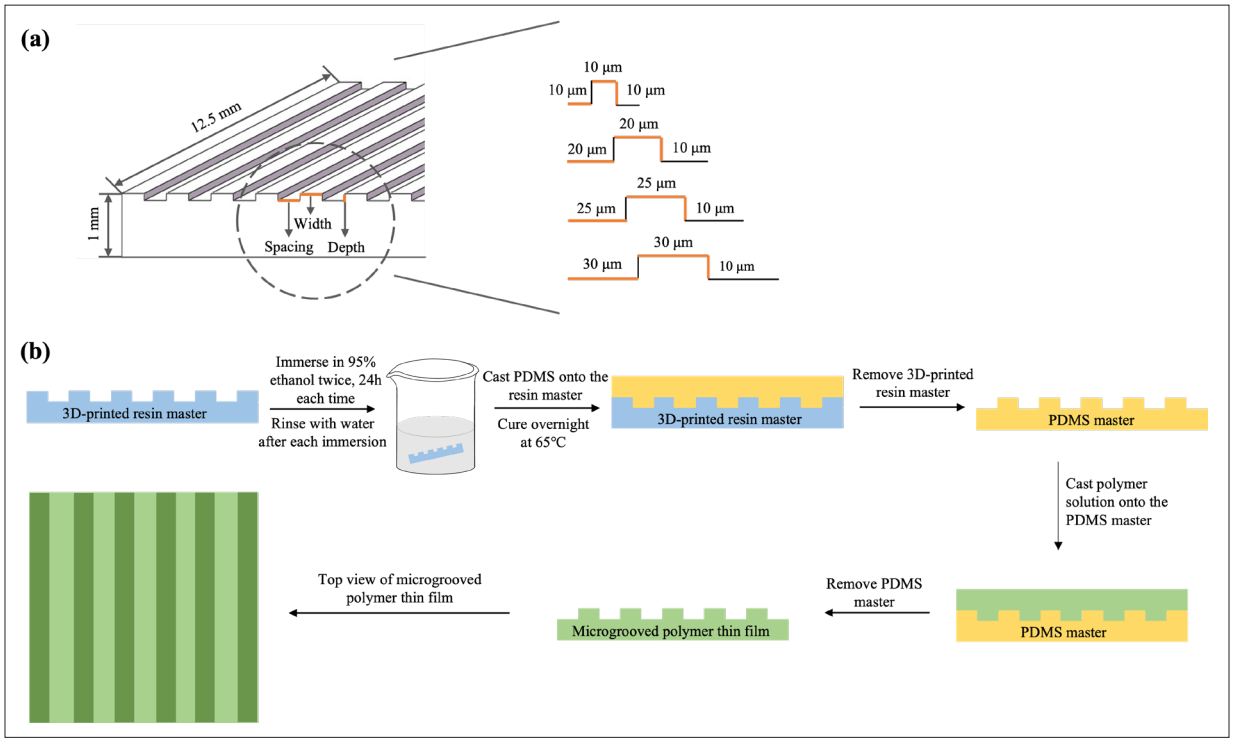


Figure 1. (a) Design specification of 3D-printed moulds with designs of 10/10/10 µm, 20/20/10 µm, 25/25/10 µm, and 30/30/10 µm; and (b) the procedures for preparation of the microgrooved PCL or PCL/PLA substrates.

(Figure 1b). The solutions were left to evaporate in a fume cabinet for 1 h, and the casted films were removed. Microgroove samples consisting of the designs, flat (no microgrooves), 10/10/10 µm, 20/20/10 µm, 25/25/10 µm, and 30/30/10 µm, are referred to as PCL-F, PCL-10, PCL-20, PCL-25, and PCL-30 or PCL/PLA-F, PCL/PLA-10, PCL/PLA-20, PCL/PLA-25, and PCL/PLA-30, respectively. Different layer thicknesses (~10, 20, or 30 µm) of thin films were produced by using different volumes of polymer solution, and the thickness of casted films was inspected with a digital calliper. Except for mechanical testing, 20 µm thick samples were utilised throughout the study.

2.4. Morphology and roughness of moulds and microgroove films

The 3D-printed moulds, PDMS moulds, and casted microgroove films were assessed using an upright digital light microscope (VHX-5000, Keyence, Japan), a laser scanning confocal microscope (LSCM; VK-X250, Keyence, Osaka, Japan), a scanning electron microscope (SEM; Zeiss Sigma VP, Carl Zeiss, USA), and an atomic force microscope (AFM; Multimode 8-HR, Bruker, Germany).

The LSCM with 120 nm lateral resolution using a 408 nm violet laser and a 16-bit photomultiplier to receive the laser light was utilised to analyse the surface topography (scan area: 95 × 71 µm and 50× magnification). The roughness of the upper groove surface (400×) was assessed with a scan area of 10 × 7 µm (20, 25, and 30 µm microgrooves) and 6 × 5 µm (10 µm microgroove). Images were post-processed using Gwyddion software.

The casted microgroove thin films for SEM were sputter-coated (Q150R S, Quorum Technologies, UK) with gold/palladium (80/20) to obtain ~6 nm thick coating. Images from the top surface of the microgroove thin film were captured and analysed using ImageJ software.[46]

The surface roughness of the thin films was analysed through AFM equipped with a ScanAsyst-Air probe (shape: pyramid; height: 10 µm; radius: <10 nm) in Peak Force tapping mode. The topographic profiles refer to scan areas of 0.5 × 0.5 µm with a resolution of 512 × 512 pixels. The image processing and roughness values measurement were performed by Gwyddion software.

2.5. Thermal evaluation

Thermogravimetric analysis (TGA) of the PCL, PLA, and PCL/PLA samples (mass ~10 mg) was performed using TA Instruments Q50 (TA Instruments, New Castle, USA). The test was carried out in an air atmosphere between 25 and 600°C with a heating rate of 10°C/min.

The differential scanning calorimetry (DSC) test, which analyses thermal behaviour and crystallisation of samples, was performed using TA Instruments Q-100 (TA Instruments, New Castle, USA) from 0 to 200°C at a heating rate of 10°C/min in a nitrogen atmosphere. The degree of crystallinity (X_c) and melting point (T_m) of PCL and PLA were determined. X_c was calculated using Equation I:

$$X_c\,(\%) = \Delta H_m/(f \times \Delta H_0) \times 100 \quad \text{(I)}$$

where ΔH_m is the specific melting enthalpy of the sample, f is the weight percentage of PCL or PLA, and ΔH_0 is the melting enthalpy of completely crystalline polymer (132 J/g for PCL, 93.7 J/g for PLA).[47]

2.6. Tensile mechanical assessment

Tensile tests were conducted with the Instron 3344 (Instron, USA) and integrated software (Bluehill Universal, Instron, USA). The samples (n = 5), each measuring 1.5 mm and 10 mm, for width and length, respectively, were prepared. A crosshead speed of 1 mm/min, 6 mm grip distance, and a 10 N load cell were used with the force applied in parallel to the direction of the grooves. The samples were prepared with different thickness (10, 20, or 30 μm), different solvent concentration (1, 3, or 5 wt%), and different groove morphologies. The maximum tensile strength, the strain at breaking, and the Young's modulus were analysed using Origin software (OriginLab, USA).

2.7. Surface wettability

The wettability of the microgroove films was assessed by water contact angle (WCA) measurement. The microgroove thin films with different groove sizes, different materials, and different solvent concentrations were prepared for the WCA to examine the hydrophilicity. The wetting behaviour of the films (n = 5) was evaluated using a DSA100B (KRÜSS, Germany) with an image taken at 0 s and 60 s after droplet formation on the sample surface (static sessile drop). The contact angle was automatically calculated by Attention Theta software (Biolin Scientific, Sweden) through the sessile drop and drop profile fitting method.

2.8. *In vitro* cell culture

The SH-SY5Y neuroblastoma cell line (ATCC® CRL-2266) is a well-established *in vitro* model for neuronal differentiation and neurotoxicity.[48] SH-SY5Y cells were cultured in T75 cell culture flasks (Sigma-Aldrich, UK) with DMEM/F-12 (1:1, v:v) medium supplemented with 10% foetal bovine serum (FBS), 1% penicillin/streptomycin, and 1% glutamine, in an incubator at 37°C and 5% CO_2. The growth medium was changed every 3 days. Cells were sub-cultured after reaching 80–90% confluence by rinsing with PBS, trypsinising (0.25% Trypsin-EDTA), and neutralising with fresh media.

The microgroove films (3 wt% concentration and 20 μm thickness) were fixed in CellCrown™ inserts (Sigma-Aldrich, UK) within 48-well plates to prevent them from floating, sterilised with ethanol for 4 h, and washed twice with PBS. Cells were counted (Cellometer Auto 1000, Nexcelom Bioscience, USA), and films were seeded with 1.9×10^4 cells in 0.1 mL of cell culture medium specifically on the surface. After incubating for 30 min to allow the cells to attach, 0.4 mL of cell culture medium was added. The media was refreshed every 3 days.

2.9. Cell viability, proliferation, and morphology

The Alamar Blue assay was used to monitor cell metabolic activity, which serves as an indicator of cell viability and proliferation. Following the manufacturer's instructions, briefly, 50 μL of Alamar Blue solution was added to each well and incubated for 4 h at 1, 3, 5, and 7 days after cell seeding, and 150 μL of the solution was transferred to 96-well plate (n = 5). The fluorescence (ex 530 nm/em 590 nm) was measured by a microplate reader (Synergy HT, BioTec, USA). The well plate was changed every time after Alamar Blue assay.

Cell viability was observed on day 7 using a live/dead kit and following the manufacturer's instructions. Calcein-AM (green) and ethidium homodimer-1 (EthD-1) (red) were used to fluorescently label live and dead cells, respectively. Samples (n = 3) were washed three times with PBS before staining in a calcein-AM (1/2000 dilution) and EthD-1 (1/500 dilution) PBS solution and incubated for 20 min prior to imaging with a confocal microscope (Lecia SP-8 Lightning, Lecia Microsystems, Germany). A minimum of three images per sample and a minimum of 180 cells in total were used to calculate the percentage viability.

Cell morphology was observed on day 7. The samples (n = 3) were rinsed twice with PBS (37°C), fixed with 4% PFA for 15 min, washed with PBS three times, permeabilised with 0.1% Triton X-100 for 15 min at room temperature, and washed with PBS three times. A 5% FBS solution was then added to block non-specific binding, and the samples were incubated for 1 h and washed once with PBS. Alexa Fluor® 488 Phalloidin (1:400) in 1% FBS solution was added to each sample and incubated for 45 min at room temperature and protected from light. The samples were rinsed in PBS, and DAPI (1:1000) was added and incubated for 10 min at room temperature in the dark. The samples were washed twice with PBS and stored at 4°C prior to imaging. Cell morphology was visualised with confocal microscope (Leica SP8 Lightning, Leica Microsystems, Germany), and cell orientation was quantitatively analysed by ImageJ software.[46]

2.10. Statistical analysis

Statistical analysis, specifically one-way analysis of variance (ANOVA) with Tukey test, was carried out using Origin software (OriginLab, USA). The data are expressed as the mean ± standard deviation. The significance levels were set at $*P < 0.05$, $**P < 0.01$, and $***P < 0.001$ when comparing PCL and PCL/PLA with the same groove parameters.

3. Results and discussion

3.1. Morphology of moulds and microgroove films

Light microscopy and SEM were used to evaluate the suitability of 3D printing to fabricate micropatterned master moulds for the casting of PDMS moulds and subsequent solvent casting of microgroove substrates (Figure 2). The microgroove dimensions (width, spacing, and depth) of the master moulds and corresponding PDMS moulds and microgroove films are depicted in Table 1 and Table S1 (Supplementary File), based on the use of light microscopy and LSCM, respectively. The depth measurement accuracy is limited due to the limitations of light microscopy on these types of samples. Qualitative and quantitative observation of the 3D-printed master mould shows a highly ordered, smooth, and well-defined microgroove architecture that closely matches the design parameters (Figure 2a). Flat 3D-printed master mould and flat PDMS mould were fabricated as a control (Figure S1 in Supplementary File). These dimensions are closely transferred to the PDMS mould, and the microgrooves are clear and uniform, although surface deviations and imperfections are visible due to the casting process (Figure 2b). This evidently demonstrates the suitability of (PμSL) 3D printing for the fabrication of microscale master moulds for microgroove patterning.

The microgroove thin films consisting of PCL and PCL/PLA at different concentrations (1, 3, and 5 wt%) and dimensions were successfully fabricated using solvent casting (Figure 2c; Figure S2 in Supplementary File). As observed, the films present microgroove dimensions similar to the original design and the PDMS and 3D-printed moulds. The microgroove surfaces are smooth; however, there is a slight irregularity to the groove shape, which is not perfectly straight but is similar to other comparable microgroove PCL and PCL/PLA films.[29,49] Micro- and nanoscale pores are observed on the lower groove surface due to the rapid evaporation of DCM causing bubbling (Figure 2c, inset). Whilst the upper grooves have the presence of nano-fissures, potentially due to the greater thickness of material at this area and a slower evaporation rate during casting. To attenuate the rapid evaporation, a multi-solvent system can be explored to optimise the solvent casting process. The addition of PLA generally reduced the appearance of pores and fissures. Similarly, lower polymer concentration solutions produced films with a smoother appearance (Figure S2 in Supplementary File).

To demonstrate the feasibility of this approach to fabricate NGCs, the film was rolled around a mandrel and sealed with an adhesive to form a tube with an inner diameter of 1.7 mm and length of 12.5 mm (Figure 2d-i and 2d-ii). SEM showed uniform microgroove structures on the inner wall of the NGC that act as topographical guidance pathways (Figure 2d-iii) and a clean seal (Figure 2d-iv). The tube was flexible and has dimensions suitable for NGC applications, warranting further study.

An alternative 3D printing system (M-50, CADworks3D, Canada) based on digital light processing (DLP) technology was similarly evaluated to determine the machine system specifications required to achieve dimensions suitable for NGCs (Figure S3 and Table S2 in Supplementary File). 3D-printed master moulds with microgroove dimensions of 100/100/50 μm, 150/150/50 μm, and 200/200/50 μm were achievable, but a smaller microgroove of 30/30/10 μm was not possible. Further study was discounted due to the inability of achieving a resolution suitable for NGCs.

The use of PμSL to fabricate microgroove topographies offers significant advantages and comparable results compared to conventional approaches such as photolithography, soft lithography, and electron beam lithography that have been utilised up till now. The lower production cost, shorter experimental time, ease of access, and greater design freedom can allow more complex 3D structures to be fabricated for use in casting rather than traditional planar substrates. However, the PDMS mould degrades with multiple exposures to the solvent. Thus, differences between batches are possible, and the PDMS mould should be replaced once noticeable deterioration in microgroove quality is observed.

3.2. Surface roughness

The surface roughness of the microgroove films with different concentrations was evaluated using AFM with a scan area of 0.5 μm^2 (Figure 3a). The mean roughness (Sa) values of the 3 wt% PCL, PLA, and PCL/PLA surface are 8.31 nm, 4.28 nm, and 4.20 nm, respectively. The addition of PLA reduces the surface roughness, agreeing with the SEM observations. The 1 wt% samples show consistently lower surface roughness than the 3 and 5 wt% films. There is a change in nanoscale features from a relatively homogenous and smooth appearance at 1 wt% to a more spherical and undulating surface at higher concentrations.

LSCM was used to map the 3D topographic surface of the 3D-printed master mould and microgroove films at

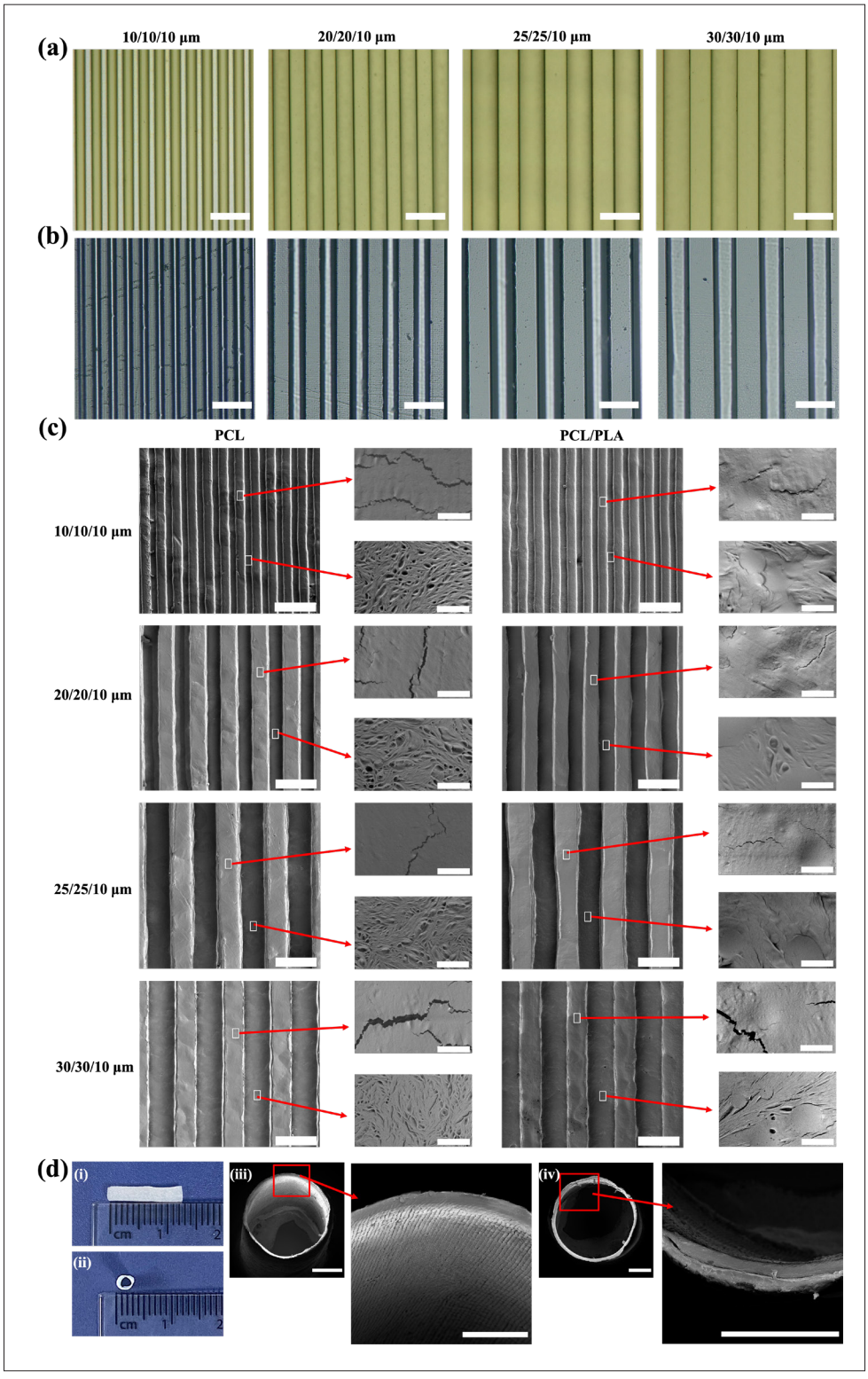


Figure 2. (a) Microscope images of 3D-printed moulds (scale bar: 50 µm) and (b) PDMS moulds (scale bar: 50 µm). (c) SEM images of the 3 wt% PCL and PCL/PLA thin films with different groove architectures: 10/10/10 µm, 20/20/10 µm, 25/25/10 µm, and 30/30/10 µm (scale bar: 50 µm; inset images scale bar: 1 µm). (d) Rolled and sealed PCL-10 NGC tube showing a photograph of (i) the side view, (ii) top view, and SEM image of (iii) inside the tube with microgroove topography and (iv) location of the film overlap and sealant (scale bar: 500 µm; low- and high-magnification images scale bar: 500 µm).

Table 1. Dimensions of the 3D-printed master moulds, PDMS moulds, and microgroove films, based on light microscopy

	Average width (μm)			Average spacing (μm)			Average depth (μm)		
	Master mould	PDMS mould	Casted film	Master mould	PDMS mould	Casted film	Master mould	PDMS mould	Casted film
PCL-10	10.44 ± 0.38	9.53 ± 0.56	11.74 ± 0.37	9.69 ± 0.75	10.35 ± 0.36	8.97 ± 0.56	10.38 ± 0.52	11.78 ± 0.67	12.47 ± 0.89
PCL-20	20.44 ± 0.73	19.28 ± 0.78	21.21 ± 1.03	19.4 ± 0.84	20.24 ± 0.56	18.56 ± 0.67	12.51 ± 0.87	12.96 ± 0.90	13.67 ± 0.66
PCL-25	25.52 ± 0.64	24.08 ± 0.81	26.39 ± 1.73	24.13 ± 0.85	25.47 ± 0.49	23.75 ± 0.86	14.15 ± 0.92	14.83 ± 0.75	15.91 ± 0.73
PCL-30	30.61 ± 0.67	28.68 ± 0.57	31.94 ± 1.21	28.85 ± 0.64	30.44 ± 0.66	27.28 ± 0.97	13.59 ± 0.63	13.87 ± 0.69	14.87 ± 0.79
PCL/PLA-10	/	/	11.41 ± 0.55	/	/	9.13 ± 0.63	/	/	12.38 ± 0.59
PCL/PLA-20	/	/	20.44 ± 0.23	/	/	18.87 ± 0.56	/	/	13.32 ± 0.61
PCL/PLA-25	/	/	26.30 ± 1.01	/	/	24.09 ± 0.78	/	/	15.34 ± 0.71
PCL/PLA-30	/	/	31.48 ± 1.27	/	/	27.85 ± 0.88	/	/	14.29 ± 0.76

The 3D-printed master moulds and PDMS moulds are the same for both PCL and PCL/PLA groups.

both large (95 × 71 μm) and small (10 × 7 μm) scan areas (Figure 3b). The PDMS moulds were not able to be assessed using LSCM due to the optical transparency. This revealed that the 3D-printed master moulds had significantly lower surface roughness (root mean square height area roughness, Sq: ~90.9 nm; arithmetical mean height area roughness, Sa: ~68.6 nm) than the microgrooved films (Sq: ~371.4 nm, Sa: ~248.1 nm) (Figure 3b-ii and 3b-iii). The PDMS moulds appear smooth, although further quantitative verification is required. The subsequent microgroove pattern transfers from the original 3D-printed master mould to the PDMS mould, and finally, the polymer film introduces a considerable amount of surface roughness.

The PCL films had an average mean surface roughness, Sa, of 331.83 nm, which was higher than PCL/PLA of 167.65 nm. The PCL microgroove films have a consistent surface roughness even with different microgroove sizes. However, the PCL/PLA-25 and 30 groove sizes (Sa: ~118.3 nm) showed a lower roughness than the PCL/PLA-10 and 20 (Sa: ~217 nm). A similar trend is observed for Sq. Surface measurements including skewness (Ssk), kurtosis (Sku), and maximum peak, pit depth, and height are shown in Table S3. All the moulds and microgroove films have an Ssk close to 0 and are generally positive, indicating a height distribution close to the mean surface plane with peaks. The Sku is predominately below 3, representing a lack of high peaks or deep valleys.

3.3. Thermal evaluation

DSC was used to assess the thermal and crystallisation properties of PCL, PLA, and the PCL/PLA blend with different concentrations (1, 3, and 5 wt%) (Figure 4 and Table 2). The T_m of PCL/PLA blend is consistently slightly lower than PCL and PLA at the same concentration, which can be seen clearly with the shift in the DSC curves (dotted lines). The ΔH_m for PCL and PLA are both decreased after they are blended. TGA and derivative thermogravimetric analysis were additionally assessed to understand the thermal degradation behaviour (Figure S4 in Supplementary File).

The crystallinity data indicate that PCL is highly crystalline (X_c ~55%), whilst PLA has a considerably lower crystallinity (X_c ~25%). Increasing the polymer concentration for both PCL and PLA resulted in a slight increase in crystallinity. The PCL/PLA blend showed a slight decrease in crystallinity of the PCL phase, but the PLA phase increases in crystallinity considerably. This observation is similar to a previous study by Carmona et al.[50] as the PLA limits the mobility of PCL chains, whereas PCL provides additional mobility to the PLA chains.

Crystallinity has a significant impact on the mechanical, degradation, and biological properties of thermoplastics. Increasing crystallinity tends to improve stiffness and tensile strength, whereas the amorphous phase absorbs more impact energy.[51] During degradation of polymers, the amorphous phase is preferentially degraded.[52,53] Subsequently, polymer crystallinity is essential in tuning material properties for specific tissue engineering applications.

3.4. Tensile properties of microgroove films

The mechanical properties of the microgroove film with different topographical designs, thickness (10, 20, and 30 μm), and concentrations (1, 3, and 5 wt%) were assessed using tensile testing (Figure 5). The PCL films had a significantly higher tensile strength (~18.1 MPa) and maximum strain (~4.3 mm/mm) in comparison to the PCL/PLA films (~12.4 MPa, ~0.15 mm/mm). The PCL/PLA films had a higher Young's modulus (~109.6 MPa) than the PCL films (~56.7 MPa), indicating the increased stiffness and deformation-resistant properties of PCL/PLA

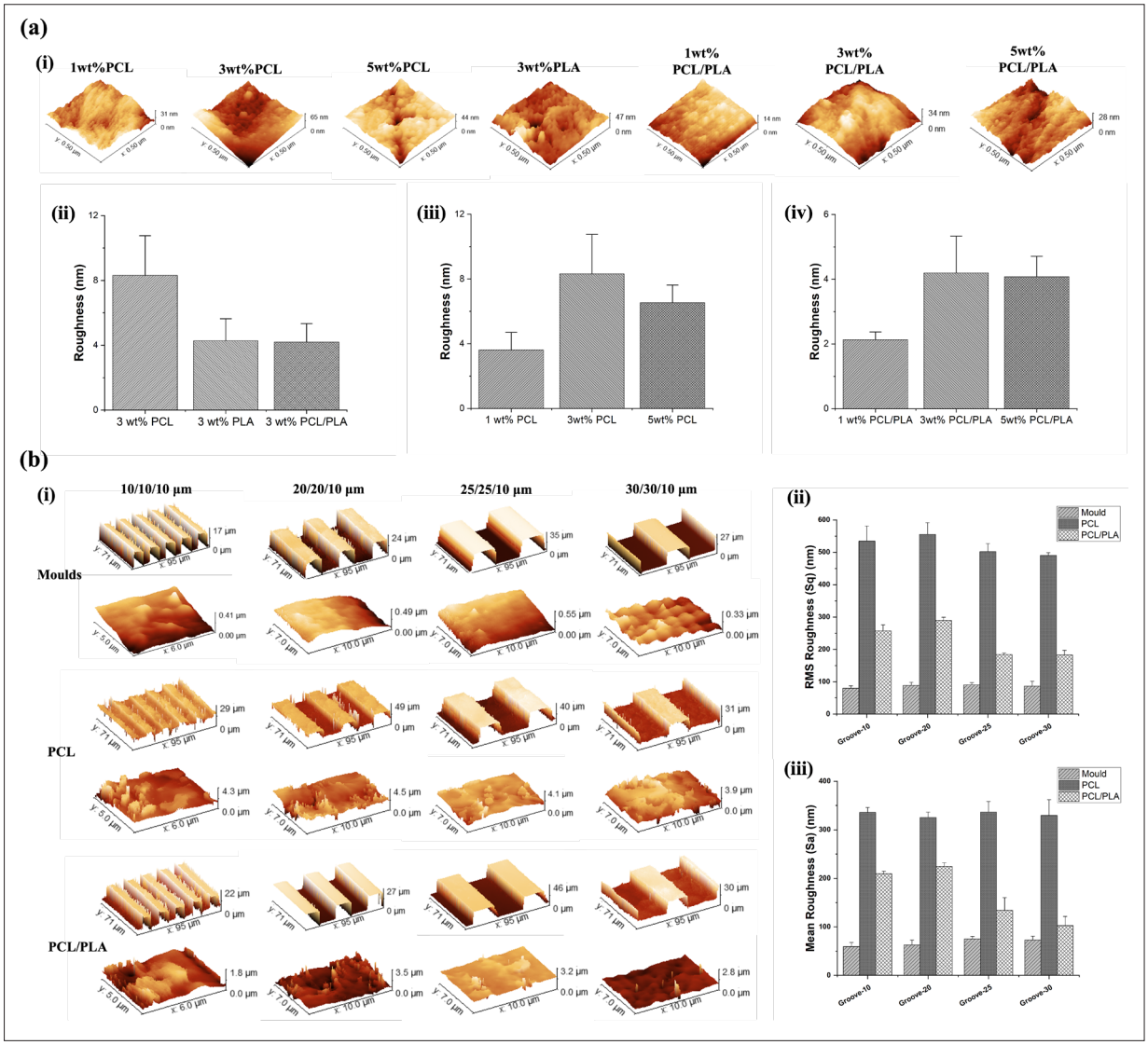


Figure 3. (a) AFM results of flat PCL, PLA, and PCL/PLA thin films with different concentration. (i) Images of the films and roughness comparison among (ii) the PCL, PLA, and PCL/PLA thin films (3 wt% concentration), (iii) different concentration PCL films, and (iv) different concentration PCL/PLA films. (b) 3D LSCM results of 3D-printed master mould and 3 wt% microgroove thin films. (i) Images of the 3D-printed moulds and thin films, (ii) the RMS roughness result, and (iii) the mean roughness result.

films, an observation consistent with previous studies.[30,54] Thus, the material compositions follow a trend of maximum tensile strength and strain at breaking of PCL>PCL/PLA and Young's modulus of PCL/PLA>PCL.

No significant difference in mechanical properties was observed as a function of microgroove size with the same film thickness. The total mass of the film is the same regardless of microgroove dimensions; therefore, any contribution by the microgroove topography to the mechanical properties is not observed or is negligible.

However, the thickness of the films had a significant influence on the mechanical properties. Among them, the 20 µm thickness PCL groups (~17.5 MPa) showed the highest tensile strength followed by the 30 µm PCL groups (~16.5 MPa). Whilst the 10 µm thickness PCL group yielded the highest strain value (~4.04 mm/mm), smaller thickness resulted in high elongation or stretching.

The effect of different polymer concentrations (1, 3, and 5 wt%) used during solvent casting on the mechanical properties was observed using the 10 µm thickness films (Figure 5b). The mechanical properties for material composition follow a similar trend.

PCL-10 samples have a higher tensile strength and maximum strain at breaking, and lower Young's modulus

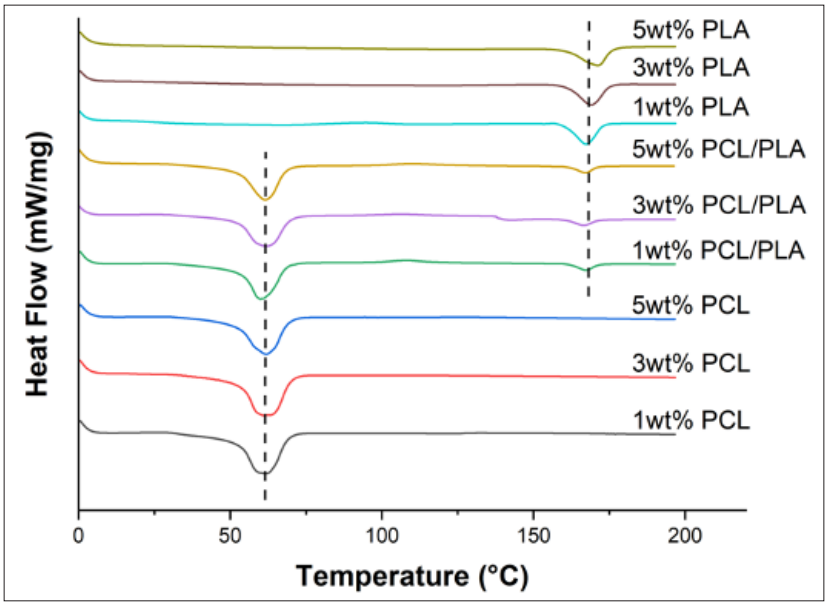


Figure 4. Thermal analysis showing DSC (1, 3, and 5 wt%) curves of PCL, PLA, and PCL/PLA blends (dotted lines represent the T_m).

Table 2. Thermal data for PCL, PLA, and PCL/PLA blend with 1, 3, and 5 wt% concentration.

	wt%	PCL			PLA		
		T_m (°C)	ΔH_m (J/g)	X_c (%)	T_m (°C)	ΔH_m (J/g)	X_c (%)
PCL	**1**	62.51	68.80	52.12	/	/	/
	3	62.34	77.40	58.63	/	/	/
	5	61.97	71.49	54.16	/	/	/
PLA	**1**	/	/	/	167.59	23.31	24.88
	3	/	/	/	168.88	24.33	25.97
	5	/	/	/	170.61	25.15	26.84
PCL/PLA	**1**	61.81	54.11	51.24	166.44	5.86	31.27
	3	61.72	60.52	57.31	166.79	6.12	32.65
	5	60.25	56.30	53.31	167.37	6.15	32.82

compared to PCL/PLA-10. The 3 wt% PCL-10 and PCL/PLA-10 films had higher tensile strength (12.60 MPa and 8.59 MPa, respectively) than 1 and 5 wt% PCL-10 and PCL/PLA-10. However, the 5 wt% samples had the highest Young's modulus and maximum strain. The 1 wt% samples showed the lowest maximum stress, Young's modulus, and maximum strain. The concentration of the polymer solution, the polymer molecular weight, and the nucleating agents all influence the crystal microstructure of the polymer.[52,55] The higher crystallinity of PCL films specifically and the 3 and 5 wt% PCL and PCL/PLA films can contribute to the improved mechanical properties observed.

Further investigation is required to understand the flexural rigidity and strength of the films with the mechanical testing extended to the rolled and sealed microgroove film tubes. The current microgroove films (except 3 wt% PCL films) are within the range of reported value for maximum tensile strength of the rat sciatic nerve (1.7–7.6 MPa) and the rabbit tibial nerve (11.7 ± 0.7 MPa).[56,57] However, the Young's modulus exceeds the range of values observed in humans, rats, and rabbits.[56-58] Subsequently, the composition and design require re-evaluation. For the current study, the 3 wt% PCL/PLA samples with 10, 20, and 30 μm thickness films have the most appropriate properties for an NGC and further testing.

3.5. Surface wettability

The wettability of the microgroove surfaces (hydrophilic < 90° and hydrophobic > 90°) was evaluated to understand the role of microgroove topography, material composition, and concentration (Figure 6). The wettability can influence

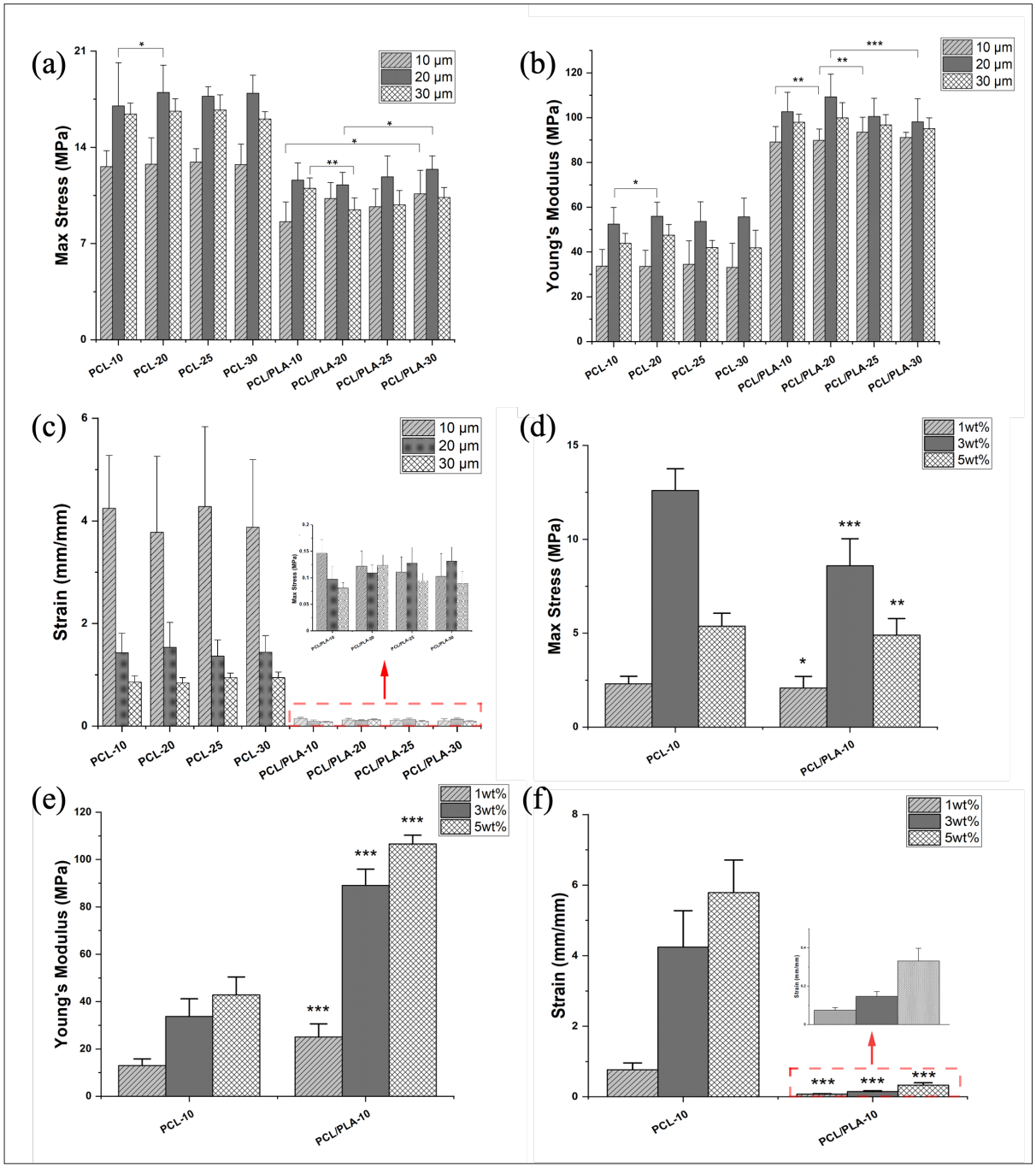


Figure 5. (a) Mechanical properties of 3 wt% PCL and PCL/PLA films with different thickness showing (i) maximum tensile stress, (ii) Young's modulus, and (iii) strain at breaking. (b) Mechanical properties of 20 μm thickness film with different polymer concentration of PCL-10 and PCL/PLA-10 showing (i) maximum tensile stress, (ii) Young's modulus, and (iii) strain at breaking.

cell attachment and proliferation and requires engineering for specific applications.[59]

The films showed a significant decrease in water contact angle (WCA) from 0 to 60 s in all groups. The addition of PLA slightly reduced the WCA; hence, PCL/PLA films became more hydrophilic than PCL films. This may be related to the higher surface roughness of PCL films, the decrease in surface roughness with the inclusion of PLA in the films (Figure 3a), and the inherently less hydrophobic nature of PLA.[60] Additionally, the WCA showed a decreasing trend with increasing microgroove size. The flat samples had the

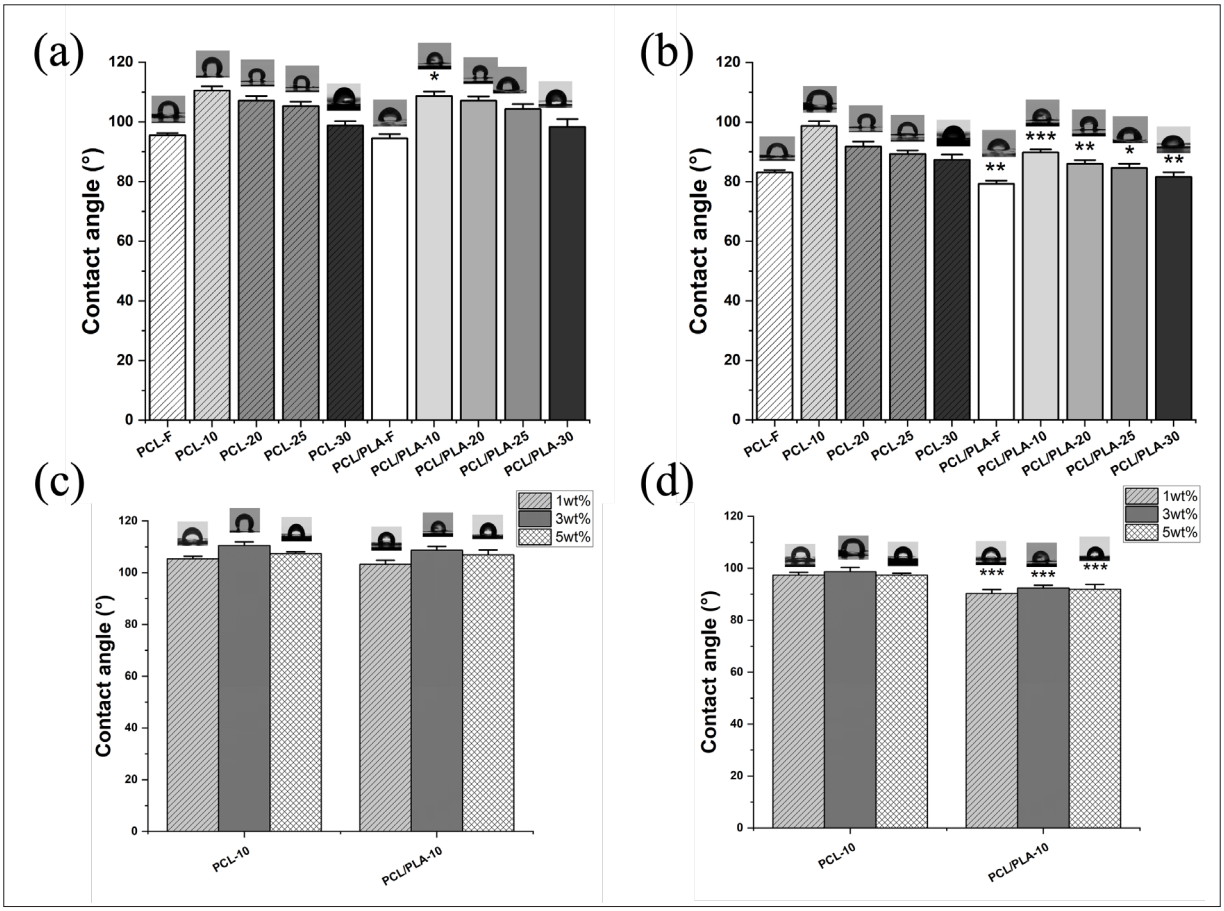


Figure 6. WCA results at (a) 0 s and (b) 60 s with different microgroove dimensions at 3 wt% concentration and for PCL-10 and PCL/PLA-10 with 1, 3, and 5 wt% concentration at (c) 0 s and (d) 60 s. *$P < 0.05$, **$P < 0.01$, and ***$P < 0.001$ between a PCL/PLA group and its corresponding PCL group.

lowest WCA. PCL-10 and PCL/PLA-10 were selected to evaluate the influence of polymer concentration (1, 3, and 5 wt%) on wettability. The 3 wt% PCL-10 and PCL/PLA-10 groups showed slightly higher WCA when compared to the 1 and 5 wt% groups, potentially due to the higher surface roughness.

3.6. Cell viability, proliferation, and alignment

The behaviour of the SH-SY5Y cells on the microgroove films was observed through cell viability, proliferation, and morphological assessment. These studies were used to determine the suitability of the PμSL 3D printing process to fabricate microgroove topographies with comparable biological properties (e.g., cell contact guidance) to conventionally fabricated microgroove films.

Cell viability was assessed on day 7 (Figure 7a and b). SH-SY5Y cells were evenly distributed on the thin film and showed high cell viability (~80%). There was no significant difference in cell viability between the material groups or different microgroove parameters, indicating that all thin films have good cytocompatibility.

The metabolic activity of the SH-SY5Y cells was assessed through the Alamar blue assay, and the value was normalised to day 1 (Figure 7c). All samples presented a significant increase in cell metabolic activity over 7 days. Cell proliferation on flat surfaces was significantly lower than microgroove films on day 7. PCL/PLA samples showed a trend of higher proliferation than PCL. On days 3, 5, and 7 after cell seeding, the PCL-30 and PCL/PLA-30 groups showed the lowest fluorescence compared to other microgrooved groups with the same material.

The results demonstrated that microgrooves could promote cell proliferation over time compared with the flat groups, with no significant differences between microgroove groups with the same material, and that the PCL/PLA films have slightly higher cell proliferation than PCL films.

Evaluation of cell morphology on day 7 revealed that the material composition and microgroove topography

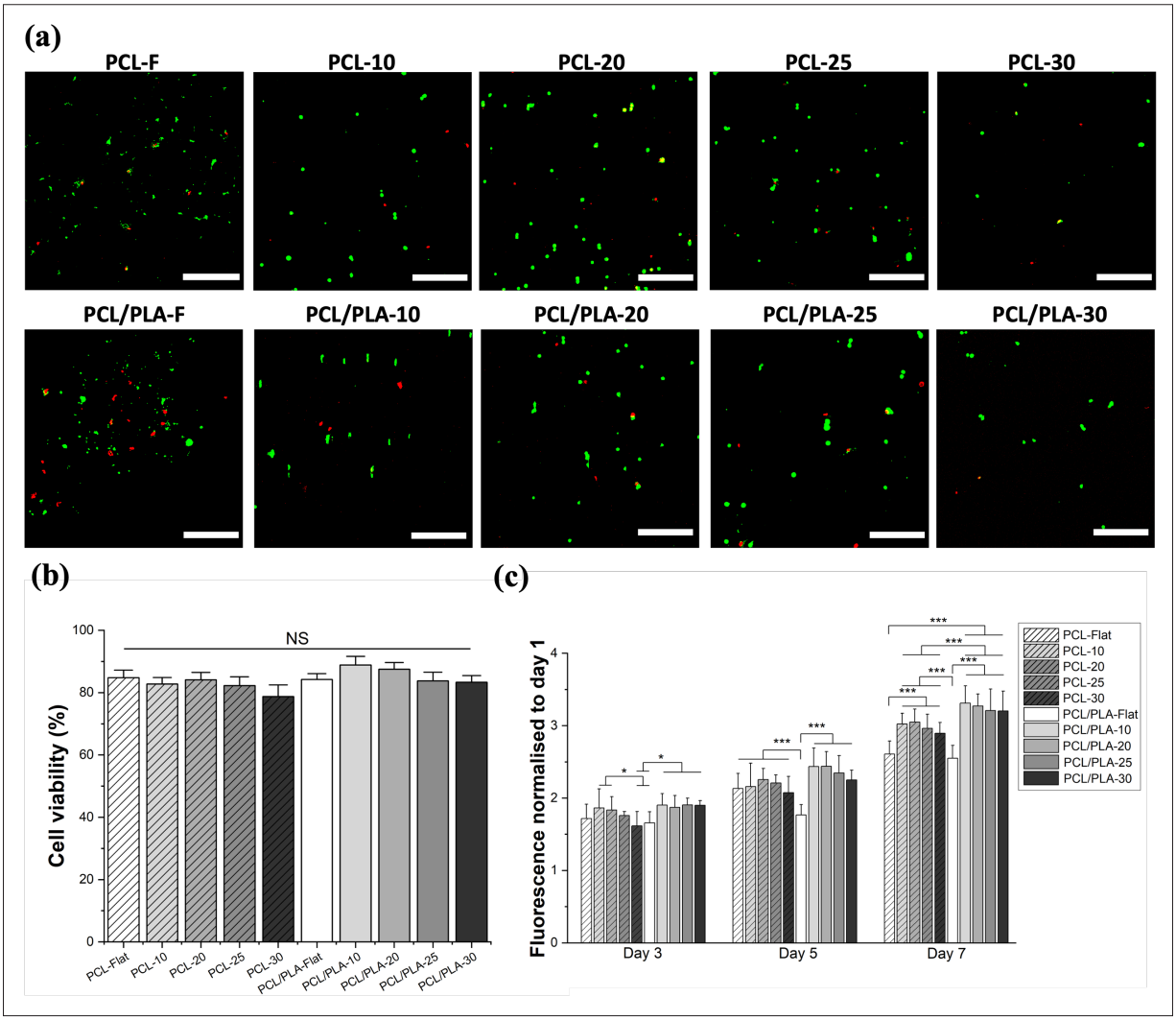


Figure 7. (a) Confocal microscopic images showing live (green) and dead (red) cells on day 7 (scale bar: 300 μm); (b) cell viability on day 7; (c) metabolic activity on PCL and PCL/PLA films for 7 days.

affected cell attachment, alignment, and neurite extension (Figure 8). Cells cultured on flat surfaces with no microgrooves had a spread morphology with protrusions and growth in multiple directions (Figure 8a and b). In contrast, the microgroove films induced cell alignment and confined growth in the direction of the grooves. Cells were observed typically attaching and growing within the depth of the microgroove rather than on top. Typically, only a single cell attached across the groove spacing in 10/10/10 μm and 20/20/10 μm microgrooves, but multiple cells or clusters were more regularly observed within the larger grooves.

Cell alignment was highest in the 10/10/10 μm, 20/20/10 μm, and 25/25/10 μm microgroove groups with an orientation angle close to 0° (Figure 9a and b). Cells cultured on PCL and PCL/PLA films possessed a length of ~200 μm and ~275 μm, respectively. The cell elongation percentage and length/width ratio were significantly higher on microgrooved and PCL/PLA films compared to flat and PCL films, respectively (Figure 9c and d). The largest microgroove size (30/30/10 μm) showed the lowest cell length and elongation.

Finally, a greater number of cells were attached on the PCL/PLA microgroove films compared to those on the PCL films, consistent with the trend shown in cell proliferation. The results showed that, in addition to the influence of the material itself, the groove dimension is an important factor affecting cell attachment and morphology.

Cells can align along the microgrooves due to the topographical pattern, providing guided cytoplasmic stress

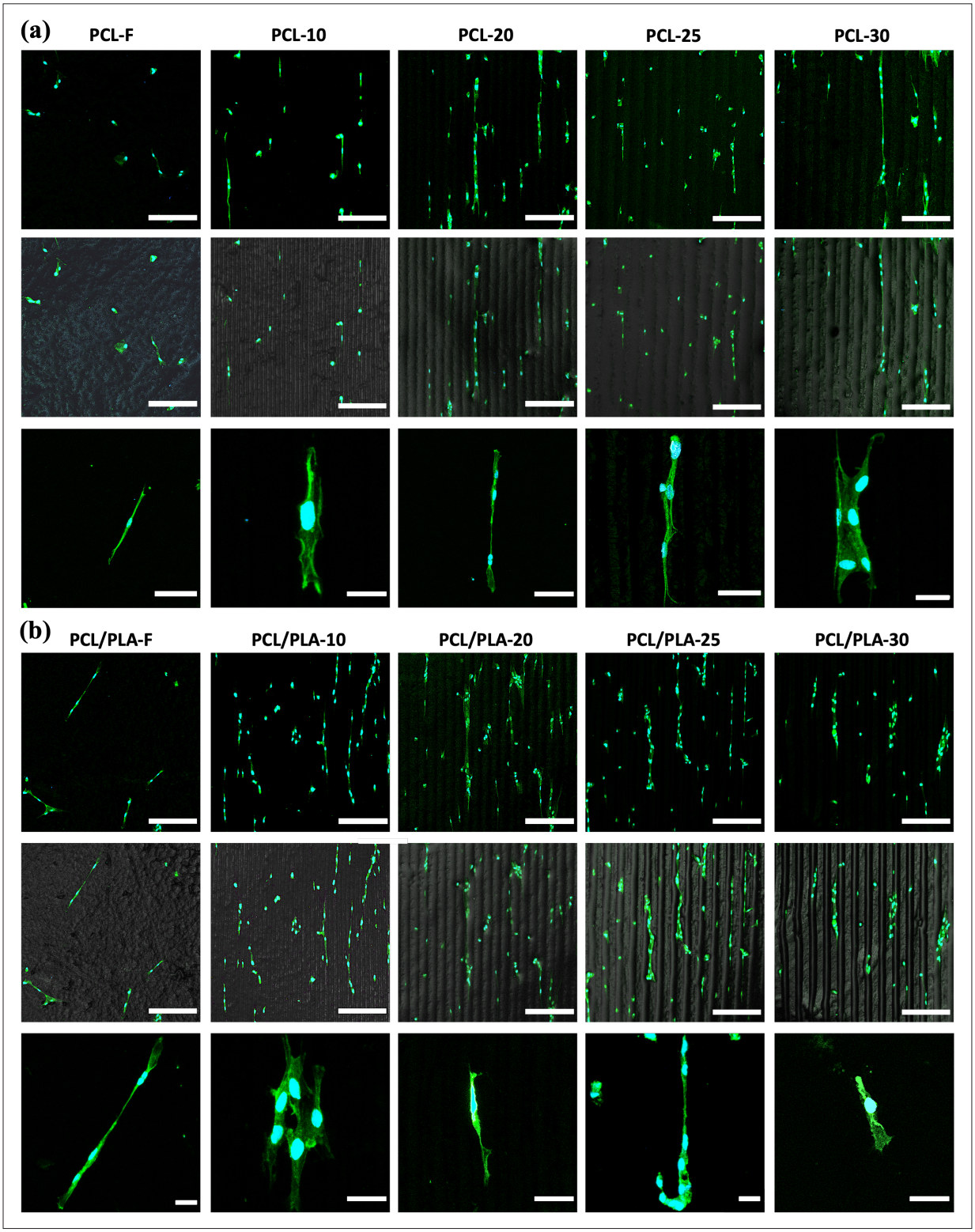


Figure 8. Confocal microscopy images of SH-SY5Y cells on (a) PCL and (b) PCL/PLA films on day 7. Cell nuclei and actin cytoskeletons, which were stained blue and green (top row), respectively, were merged with confocal reflectance (middle row) (scale bar: 200 μm), and higher-magnification images of elongated and clusters of SH-SY5Y cells (bottom row) (scale bar: 30 μm) are also shown.

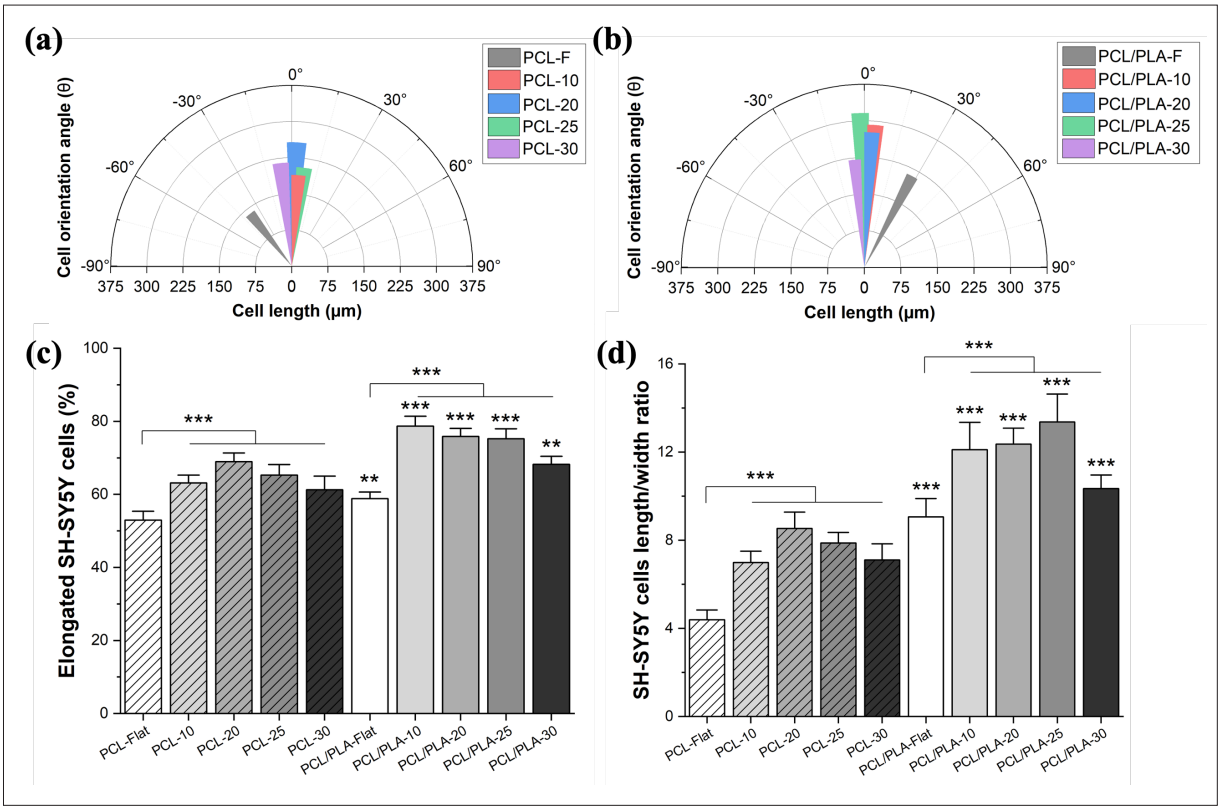


Figure 9. (a) Orientation angle of elongated SH-SY5Y cells on PCL thin films; (b) orientation angle of elongated SH-SY5Y cells on PCL/PLA thin films; (c) percentage of elongated SH-SY5Y cells; and (d) the length/width ratio of elongated SH-SY5Y cells on thin films.

to the cells, initiating multiple cellular events, and providing contact guidance.[20,21] The contact guidance can regulate cell adhesion, proliferation, differentiation, morphology, and migration. The proliferation and directional growth of cells on the PμSL-casted microgroove films observed in this study is consistent with other studies, and microgrooved NGCs were demonstrated to have higher performance compared to unpatterned NGCs.[9,27,31-33]

This study demonstrates that microgroove dimensions between 10 and 25 μm are preferable for promoting SH-SY5Y proliferation and alignment. Additionally, PCL/PLA films show higher cell proliferation potentially due to the more hydrophilic and smoother surface. The largest microgroove width, 30 μm, has a relatively lower proliferation and cell elongation, although not significant, and a large number of cell clusters. This is possibly due to the size of the smaller grooves being closer to the size of the SH-SY5Y cell body (~12 μm); therefore, cells tend to be restricted within the grooves, and axonal outgrowth is directed along the grooves, limiting axonal branching.

The observations made in this study agree with several studies.[24,29,34-36] For example, Sun et al.[24] demonstrated alignment of NG108-15 cells on microgroove films with higher attachment and proliferation on PCL/PLA films than PCL. Mobasseri et al.[29] showed that adipose-derived stem cells (ASCs), differentiated toward a Schwann cell phenotype, preferentially aligned along ~20 μm wide microgrooves in PCL/PLA films, and that proliferation declined in flat films. Pardo-Figuerez et al.[34] showed that, in chemical patterning of cell-repulsive polymers to fabricate varying gap sizes, smaller patterns (20 μm) promoted SH-SY5Y attachment and neurite extension, as compared to larger patterns (50, 75, and 100 μm). A similar phenomenon for neurite alignment and elongation was observed by Nam et al.[35] Klein et al.[36] investigated small microgrooves (5, 8, 10, and 20 μm) and found that single SH-SY5Y cells could elongate in 5, 8, and 10 μm microgrooves, but double lines of elongated cells appeared in 20 μm microgrooves. Additionally, studies by Miller et al.[23,38] have indicated that microgrooves with a width interval of 10–20 μm are the ideal size for Schwann cell attachment and alignment.

The films investigated in this study were not treated chemically or with bioadhesion molecules, and the only engineered guidance cues were the microgroove topography. Thus, further studies are warranted to develop

advanced composite materials that include natural polymers such as gelatin, collagen, fibrin, chitosan, and silk fibroin to promote cell attachment and proliferation.[61] Furthermore, incorporation of other guidance modalities (e.g., aligned fibres and channels) and patterning of neurotrophic factors including nerve growth factor (NGF), neurotrophin-3 (NT-3), glial-derived neurotrophic factor (GDNF), and vascular endothelial growth factor (VEGF) to promote axonal outgrowth and cell migration are desirable. Additionally, the role of microgroove size and shape in other relevant neuronal cell types should be explored. The versatility of the PμSL casting technique enables these further outlined studies to be achieved.

4. Conclusion

This study used PμSL 3D printing as an alternative to the expensive, time-consuming, and complex conventional photolithography techniques to fabricate master moulds for the casting of microgroove topographies for PNI applications. The 3D-printed master moulds and the casted PDMS moulds closely match the microgroove design and exhibit high-quality surface features. This enabled the casting of biodegradable PCL and PCL/PLA films with microgroove topographies (10/10/10, 20/20/10, 25/25/10, and 30/30/10 μm) that could be assembled into a cylindrical NGC.

The PCL/PLA films exhibited a more hydrophilic and smoother surface with lower mechanical properties, closer to native peripheral nerve tissue, in comparison to PCL. PCL and PCL/PLA showed high SH-SY5Y cell viability, but higher cell attachment and proliferation was observed on PCL/PLA films. All microgroove films induced cell alignment. The smaller microgrooves (10–25 μm) exhibited a more highly ordered cell arrangement and elongation with less cell clustering. Thus, the PCL/PLA smaller microgroove films show potential for inducing cell contact guidance for peripheral nerve applications.

The simplicity and low cost of the PμSL approach to fabricate the master mould offer the potential to directly cast samples and remove the intermediate PDMS mould. This can help accelerate the manufacturing process, and extra moulds can be printed rapidly in the case of master mould damage. Furthermore, 3D printing can allow the development of more complex moulds to fabricate the entire cylindrical conduit whilst incorporating microgroove topographies. This is especially relevant for non-photocrosslinkable biomaterials, as demonstrated in this study, that are not suitable for direct processing with PμSL. Subsequently, this study establishes the potential of using PμSL for fabricating microtemplated moulds for PNI applications.

Acknowledgements

We are grateful for the technical support from Boston Micro Fabrication.

Funding

This work was supported by the Engineering and Physical Sciences Research Council (UK) Doctoral Prize Fellowship (EP/R513131/1) and the Henry Royce Institute for Advanced Materials, funded through EPSRC grants EP/R00661X/1, EP/S019367/1, EP/P025021/1, and EP/P025498/1.

Conflict of interest

The authors declare no conflicts of interest.

Author contributions

Conceptualization: Hexin Yue, Cian Vyas, Paulo Bartolo
Formal analysis: Hexin Yue, Cian Vyas
Investigation: Hexin Yue, Xuzhao Liu, Kejian Hou, Cian Vyas
Methodology: Hexin Yue, Xuzhao Liu, Kejian Hou, Cian Vyas
Writing – original draft: Hexin Yue
Writing – review & editing: Cian Vyas, Paulo Bartolo

Ethics approval and consent to participate

Not applicable.

Consent for publication

Not applicable.

Availability of data

The data utilised in this study are available from the corresponding author upon reasonable request.

References

1. Lackington WA, Ryan AJ, O'Brien FJ. Advances in nerve guidance conduit-based therapeutics for peripheral nerve repair. *ACS Biomater Sci Eng*. 2017;3(7):1221-1235. doi: 10.1021/acsbiomaterials.6b00500

2. Bryan DJ, Tang JB, Doherty SA, et al. Enhanced peripheral nerve regeneration through a poled bioresorbable poly (lactic-co-glycolic acid) guidance channel. *J Neural Eng*. 2004;1(2):91. doi: 10.1088/1741-2560/1/2/004

3. Slavin BR, Sarhane KA, von Guionneau N, et al. Insulin-like growth factor-1: a promising therapeutic target for peripheral nerve injury. *Front Bioeng Biotechnol*. 2021;9:695850. doi: 10.3389/fbioe.2021.695850

4. Pabari A, Yang SY, Seifalian AM, Mosahebi A. Modern surgical management of peripheral nerve gap. *J Plast Reconstr Aesthet Surg*. 2010;63(12):1941-1948. doi: 10.1016/j.bjps.2009.12.010

5. Vijayavenkataraman S. Nerve guide conduits for peripheral nerve injury repair: a review on design, materials and fabrication methods. *Acta Biomater*. 2020;106:54-69. doi: 10.1016/j.actbio.2020.02.003

6. Wang ML, Rivlin M, Graham JG, Beredjiklian PK. Peripheral nerve injury, scarring, and recovery. *Connect Tissue Res*. 2019;60(1):3-9. doi: 10.1080/03008207.2018.1489381

7. Siemionow M, Brzezicki G. Chapter 8: Current techniques and concepts in peripheral nerve repair. *Int Rev Neurobiol*. 2009;87:141-172. doi: 10.1016/S0074-7742(09)87008-6

8. Deumens R, Bozkurt A, Meek MF, et al. Repairing injured peripheral nerves: bridging the gap. *Prog Neurobiol*. 2010;92(3):245-276. doi: 10.1016/j.pneurobio.2010.10.002

9. Suo H, Wang Z, Dai G, Fu J, Yin J, Chang L. Polyacrylonitrile nerve conduits with inner longitudinal grooved textures to enhance neuron directional outgrowth. *J Microelectromech Syst*. 2018;27(3):457-463. doi: 10.1109/JMEMS.2018.2810097

10. Taylor CS, Haycock JW. Biomaterials and scaffolds for repair of the peripheral nervous system. In: Phillips JB, Hercher D, Hausner T, eds. *Peripheral Nerve Tissue Engineering and Regeneration*. Cham: Springer; 2022: 245-279. doi: 10.1007/978-3-030-21052-6_3

11. Wangensteen KJ, Kalliainen LK. Collagen tube conduits in peripheral nerve repair: a retrospective analysis. *Hand*. 2010;5(3):273-277. doi: 10.1007/s11552-009-9245-0

12. Spivey EC, Khaing ZZ, Shear JB, Schmidt CE. The fundamental role of subcellular topography in peripheral nerve repair therapies. *Biomaterials*. 2012;33(17):4264-4276. doi: 10.1016/j.biomaterials.2012.02.043

13. Kehoe S, Zhang XF, Boyd D. FDA approved guidance conduits and wraps for peripheral nerve injury: a review of materials and efficacy. *Injury*. 2012;43(5):553-572. doi: 10.1016/j.injury.2010.12.030

14. Papadimitriou L, Manganas P, Ranella A, Stratakis E. Biofabrication for neural tissue engineering applications. *Mater Today Bio*. 2020;6:100043. doi: 10.1016/j.mtbio.2020.100043

15. Tonda-Turo C, Gnavi S, Ruini F, et al. Development and characterization of novel agar and gelatin injectable hydrogel as filler for peripheral nerve guidance channels. *J Tissue Eng Regen Med*. 2017;11(1):197-208. doi: 10.1002/term.1902

16. Du J, Liu J, Yao S, et al. Prompt peripheral nerve regeneration induced by a hierarchically aligned fibrin nanofiber hydrogel. *Acta Biomater*. 2017;55:296-309. doi: 10.1016/j.actbio.2017.04.010

17. Ma Y, Wang H, Wang Q, Cao X, Gao H. Piezoelectric conduit combined with multi-channel conductive scaffold for peripheral nerve regeneration. *Chem Eng J*. 2023;452:139424. doi: 10.1016/j.cej.2022.139424

18. Sharma AD, Zbarska S, Petersen EM, Marti ME, Mallapragada SK, Sakaguchi DS. Oriented growth and transdifferentiation of mesenchymal stem cells towards a Schwann cell fate on micropatterned substrates. *J Biosci Bioeng*. 2016;121(3):325-335. doi: 10.1016/j.jbiosc.2015.07.006

19. Long Y, Zhang N, Huang Y, Wen X. Formation of highly aligned grooves on inner surface of semipermeable hollow fiber membrane for directional axonal outgrowth. *J Manuf Sci Eng*. 2008;130(2):021011. doi: 10.1115/1.2896111

20. Yang CY, Huang WY, Chen LH, et al. Neural tissue engineering: the influence of scaffold surface topography and extracellular matrix microenvironment. *J Mater Chem B*. 2021;9(3):567-584. doi: 10.1039/d0tb01605e

21. Ma Y, Gao H, Wang H, Cao X. Engineering topography: effects on nerve cell behaviors and applications in peripheral nerve repair. *J Mater Chem B*. 2021;9(32):6310-6325. doi: 10.1039/d1tb00782c

22. Zhang D, Wu S, Feng J, Duan Y, Xing D, Gao C. Micropatterned biodegradable polyesters clicked with CQAASIKVAV promote cell alignment, directional migration, and neurite outgrowth. *Acta Biomater*. 2018;74:143-155. doi: 10.1016/j.actbio.2018.05.018

23. Miller C, Jeftinija S, Mallapragada S. Micropatterned Schwann cell-seeded biodegradable polymer substrates significantly enhance neurite alignment and outgrowth. *Tissue Eng*. 2001;7(6):705-715. doi: 10.1089/107632701753337663

24. Sun M, Kingham PJ, Reid AJ, Armstrong SJ, Terenghi G, Downes S. In vitro and in vivo testing of novel ultrathin PCL and PCL/PLA blend films as peripheral nerve conduit. *J Biomed Mater Res Part A*. 2010;93(4):1470-1481. doi: 10.1002/jbm.a.32681

25. Hwang CM, Park Y, Park JY, et al. Controlled cellular orientation on PLGA microfibers with defined diameters. *Biomed Microdevices*. 2009;11(4):739-746. doi: 10.1007/s10544-009-9287-7

26. Hsu SH, Lu PS, Ni HC, Su CH. Fabrication and evaluation of microgrooved polymers as peripheral nerve conduits. *Biomed Microdevices*. 2007;9:665-674. doi: 10.1007/s10544-007-9068-0

27. Béduer A, Vieu C, Arnauduc F, Sol JC, Loubinoux I, Vaysse L. Engineering of adult human neural stem cells differentiation through surface micropatterning. *Biomaterials*. 2012;33(2):504-514.
doi: 10.1016/j.biomaterials.2011.09.073

28. Lu S, Chen W, Wang J, et al. Polydopamine-decorated PLCL conduit to induce synergetic effect of electrical stimulation and topological morphology for peripheral nerve regeneration. *Small Methods*. 2023;7(2):e2200883.
doi: 10.1002/smtd.202200883

29. Mobasseri A, Faroni A, Minogue BM, Downes S, Terenghi G, Reid AJ. Polymer scaffolds with preferential parallel grooves enhance nerve regeneration. *Tissue Eng Part A*. 2015;21(5-6):1152-1162.
doi: 10.1089/ten.TEA.2014.0266

30. Mobasseri SA, Terenghi G, Downes S. Micro-structural geometry of thin films intended for the inner lumen of nerve conduits affects nerve repair. *J Mater Sci Mater Med*. 2013;24(7):1639-1647.
doi: 10.1007/s10856-013-4922-5

31. Hsu SH, Ni HC. Fabrication of the microgrooved/microporous polylactide substrates as peripheral nerve conduits and in vivo evaluation. *Tissue Eng Part A*. 2009;15(6):1381-1390.
doi: 10.1089/ten.tea.2008.0175

32. Litowczenko J, Maciejewska BM, Wychowaniec JK, Koscinski M, Jurga S, Warowicka A. Groove-patterned surfaces induce morphological changes in cells of neuronal origin. *J Biomed Mater Res A*. 2019;107(10):2244-2256.
doi: 10.1002/jbm.a.36733

33. Yu S, Liu D, Wang T, Lee YZ, Wong JCN, Song X. Micropatterning of polymer substrates for cell culture. *J Biomed Mater Res B Appl Biomater*. 2021;109(10):1525-1533.
doi: 10.1002/jbm.b.34811

34. Pardo-Figuerez M, Martin NRW, Player DJ, et al. Controlled arrangement of neuronal cells on surfaces functionalized with micropatterned polymer brushes. *ACS Omega*. 2018;3(10):12383-12391.
doi: 10.1021/acsomega.8b01698

35. Nam KH, Jamilpour N, Mfoumou E, Wang FY, Zhang DD, Wong PK. Probing mechanoregulation of neuronal differentiation by plasma lithography patterned elastomeric substrates. *Sci Rep*. 2014;4(1):6965.
doi: 10.1038/srep06965

36. Klein CL, Scholl M, Maelicke A. Neuronal networks in vitro: formation and organization on biofunctionalized surfaces. *J Mater Sci Mater Med*. 1999;10(12):721-727.
doi: 10.1023/a:1008975105243

37. Qin D, Xia Y, Whitesides GM. Soft lithography for micro- and nanoscale patterning. *Nat Protoc*. 2010;5(3):491-502.
doi: 10.1038/nprot.2009.234

38. Miller C, Shanks H, Witt A, Rutkowski G, Mallapragada S. Oriented Schwann cell growth on micropatterned biodegradable polymer substrates. *Biomaterials*. 2001;22(11):1263-1269.
doi: 10.1016/s0142-9612(00)00278-7

39. Ge Q, Li Z, Wang Z, et al. Projection micro stereolithography based 3D printing and its applications. *Int J Extreme Manuf*. 2020;2(2):022004.
doi: 10.1088/2631-7990/ab8d9a

40. Evangelista MS, Perez M, Salibian AA, et al. Single-lumen and multi-lumen poly(ethylene glycol) nerve conduits fabricated by stereolithography for peripheral nerve regeneration in vivo. *J Reconstr Microsurg*. 2015;31(5):327-335.
doi: 10.1055/s-0034-1395415

41. Singh A, Asikainen S, Teotia AK, et al. Biomimetic photocurable three-dimensional printed nerve guidance channels with aligned cryomatrix lumen for peripheral nerve regeneration. *ACS Appl Mater Interfaces*. 2018;10(50):43327-43342.
doi: 10.1021/acsami.8b11677

42. Pateman CJ, Harding AJ, Glen A, et al. Nerve guides manufactured from photocurable polymers to aid peripheral nerve repair. *Biomaterials*. 2015;49:77-89.
doi: 10.1016/j.biomaterials.2015.01.055

43. Moreno-Rivas O, Hernández-Velázquez D, Piazza V, Marquez S. Rapid prototyping of microfluidic devices by SL 3D printing and their biocompatibility study for cell culturing. *Mater Today Proc*. 2019;13:436-445.
doi: 10.1016/j.matpr.2019.03.189

44. Villegas M, Cetinic Z, Shakeri A, Didar TF. Fabricating smooth PDMS microfluidic channels from low-resolution 3D printed molds using an omniphobic lubricant-infused coating. *Anal Chim Acta*. 2018;1000:248-255.
doi: 10.1016/j.aca.2017.11.063

45. Jonathan Tjong AGT, John PF. Solvent extraction of 3D printed molds for soft lithography. *R Soc Chem*. 2020.

46. Schneider CA, Rasband WS, Eliceiri KW. NIH image to ImageJ: 25 years of image analysis. *Nat Methods*. 2012;9(7):671-675.
doi: 10.1038/nmeth.2089

47. Vertuccio L, Gorrasi G, Sorrentino A, Vittoria V. Nano clay reinforced PCL/starch blends obtained by high energy ball milling. *Carbohydr Polym*. 2009;75(1):172-179.
doi: 10.1016/j.carbpol.2008.07.020

48. Tonazzini I, Cecchini A, Elgersma Y, Cecchini M. Interaction of SH-SY5Y cells with nanogratings during neuronal differentiation: comparison with primary neurons. *Adv Healthc Mater*. 2014;3(4):581-587.
doi: 10.1002/adhm.201300216

49. Alvim Valente C, Cesar Chagastelles P, Fontana Nicoletti N, et al. Design and optimization of biocompatible

polycaprolactone/poly (l-lactic-co-glycolic acid) scaffolds with and without microgrooves for tissue engineering applications. *J Biomed Mater Res Part A*. 2018;106(6):1522-1534.
doi: 10.1002/jbm.a.36355

50. Carmona VB, Corrêa AC, Marconcini JM, Mattoso LHC. Properties of a biodegradable ternary blend of thermoplastic starch (TPS), poly (ε-caprolactone)(PCL) and poly (lactic acid)(PLA). *J Polym Environ*. 2015;23(1):83-89.
doi: 10.1007/s10924-014-0666-7

51. Vieille B, Albouy W, Chevalier L, Taleb L. About the influence of stamping on thermoplastic-based composites for aeronautical applications. *Compos Part B: Eng*. 2013;45(1):821-834.
doi: 10.1016/j.compositesb.2012.07.047

52. Kostakova E, Mészáros L, Maskova G, Blazkova L, Turcsan T, Lukas D. Crystallinity of electrospun and centrifugal spun polycaprolactone fibers: a comparative study. *J Nanomater*. 2017;1-9.
doi: 10.1155/2017/8952390

53. Huang B, Wang Y, Vyas C, Bartolo P. Crystal growth of 3D poly(ε-caprolactone) based bone scaffolds and its effects on the physical properties and cellular interactions. *Adv Sci*. 2023;10(1):2203183.
doi: 10.1002/advs.202203183

54. Sun M, Downes S. Physicochemical characterisation of novel ultra-thin biodegradable scaffolds for peripheral nerve repair. *J Mater Sci Mater Med*. 2009;20(5):1181-1192.
doi: 10.1007/s10856-008-3671-3

55. Dong J, Liu J, Li X, Liang Q, Xu X. Relationship between the Young's modulus and the crystallinity of cross-linked poly (ε-caprolactone) as an immobilization membrane for cancer radiotherapy. *Glob Chall*. 2020;4(8):2000008.
doi: 10.1002/gch2.202000008

56. Borschel GH, Kia KF, Kuzon WM, Jr., Dennis RG. Mechanical properties of acellular peripheral nerve. *J Surg Res*. 2003;114(2):133-139.
doi: 10.1016/s0022-4804(03)00255-5

57. Rydevik BL, Kwan MK, Myers RR, et al. An in vitro mechanical and histological study of acute stretching on rabbit tibial nerve. *J Orthop Res*. 1990;8(5):694-701.
doi: 10.1002/jor.1100080511

58. Kerns J, Piponov H, Helder C, Amirouche F, Solitro G, Gonzalez M. Mechanical properties of the human tibial and peroneal nerves following stretch with histological correlations. *Anat Rec*. 2019;302(11):2030-2039.
doi: 10.1002/ar.24250

59. Rahmati M, Silva EA, Reseland JE, Heyward CA, Haugen HJ. Biological responses to physicochemical properties of biomaterial surface. *Chem Soc Rev*. 2020;49(15):5178-5224.
doi: 10.1039/D0CS00103A

60. Patr T, Glória A. Mechanical and biological behaviour of PCL and PCL/PLA scaffolds for tissue engineering applications. *Chem Eng Trans*. 2013;32:1645-1650.
doi: 10.3303/CET1332275

61. Zhang H, Guo J, Wang Y, Shang L, Chai R, Zhao Y. Natural polymer-derived bioscaffolds for peripheral nerve regeneration. *Adv Funct Mater*. 2022;32(41):2203829.
doi: 10.1002/adfm.202203829

ACCSCIENCE PUBLISHING

International Journal of Bioprinting

RESEARCH ARTICLE

Drop-on-demand bioprinting: A redesigned laser-induced side transfer approach with continuous capillary perfusion

Mahyar Erfanian[1,2], Ahad Mohammadi[1,2], Hamid Ebrahimi Orimi[1,3], Jennyfer Zapata-Farfan[4], Joe Saade[1,5], Michel Meunier[4], Bruno Larrivée[1,6,7], and Christos Boutopoulos[1,2,6]*

[1]Centre de Recherche Hôpital Maisonneuve-Rosemont, Montreal, Quebec, Canada

[2]Institute of Biomedical Engineering, University of Montreal, Montreal, Quebec, Canada

[3]Department of Mechanical, Industrial and Aerospace Engineering, Concordia University, Montreal, Quebec, Canada

[4]Engineering Physics Department, Polytechnique Montreal, Montreal, Quebec, Canada

[5]Biomedical Engineering, Polytechnique Montreal, Montreal, Quebec, Canada

[6]Department of Ophthalmology, Faculty of Medicine, University of Montreal, Montreal, Quebec, Canada

[7]Department of Molecular Biology, Faculty of Medicine, University of Montreal, Montreal, Quebec, Canada

Abstract

We present a drop-on-demand (DOD) bioprinting method based on a novel implementation of laser-induced side transfer (LIST). Our approach involves continuous bioink perfusion through a glass capillary featuring a laser-machined hole in the capillary wall, serving as a nozzle. Focused low-energy nanosecond laser pulses are employed for precise droplet ejection. This innovative design separates the control of the bioink flow rate inside the capillary from the printing rate (drop ejection), leading to an enhanced printing workflow. We assessed the impact of key printing parameters, such as laser energy and flow conditions, on printing quality. Furthermore, we utilized the redesigned LIST to bioprint human umbilical vein endothelial cells (HUVECs). Our findings indicate that the printed HUVECs exhibit no viability loss and demonstrate the ability to recruit perivascular cells, including pericytes and fibroblasts. The redesigned LIST can be utilized in tissue engineering applications requiring DOD cell printing.

Keywords: Laser-assisted bioprinting; Laser-induced forward transfer; Ink-jet; Microvasculature; Biofabrication

***Corresponding author:**
Christos Boutopoulos
(christos.boutopoulos@umontreal.ca)

Citation: Erfanian M, Mohammadi A, Orimi HE, et al. Drop-on-demand bioprinting: A redesigned laser-induced side transfer approach with continuous capillary perfusion. *Int J Bioprint*. 2024;10(3):2832. doi: 10.36922/ijb.2832

Received: January 26, 2024
Accepted: April 26, 2024
Published Online: June 5, 2024

Copyright: © 2024 Author(s). This is an Open Access article distributed under the terms of the Creative Commons Attribution License, permitting distribution, and reproduction in any medium, provided the original work is properly cited.

Publisher's Note: AccScience Publishing remains neutral with regard to jurisdictional claims in published maps and institutional affiliations.

1. Introduction

Bioprinting technologies aim to construct functional artificial tissues that possess lasting mechanical and biological stability. These tissues can be used to address the shortage of donors and as physiologically relevant models for drug discovery.[1,2] Central to bioprinting is the layer-by-layer deposition of bioinks containing living cells and/

or other biomaterials. This is achieved via a variety of technologies, including drop-on-demand (DOD) techniques (such as inkjet printing[3] and laser-induced forward transfer [LIFT]),[4] light-assisted volumetric printing,[5] and microextrusion-based bioprinting (MBB).[2,6] These technologies have varying degrees of compatibility with bioink formulations.[2] Factors, such as bioink viscosity, often restrict their compatibility and range of applications.

To bioprint functional living constructs of clinically relevant size, it is essential to incorporate a microvasculature network. This network facilitates cell access to nutrients and oxygen while enabling the removal of metabolic wastes, which is vital for the long-term survival of the printed constructs and their connection to the host vasculature.[7-9] However, current technologies have not yet achieved the necessary versatility to replicate such complex architecture, comprising a network of small blood vessels, including capillaries (5–10 μm), arterioles, and venules (10–300 μm), collectively supporting various physiological functions. Most efforts have been focused on using MBB to create artificial mm-sized vascular networks.[10-16] DOD bioprinting methods (such as inkjet[17,18] and LIFT[19-22]) exhibit superior spatial resolution compared to MBB[2] and have primarily been used for printing including human umbilical vein endothelial cells (HUVECs) to replicate networks known as capillary beds, a subset of the physiological microvasculature. Despite these advancements, there is a consensus in the bioprinting field that no single technology can achieve the required multiscale capability for printing multiple cell types at the scales encountered in physiological microvascular systems.

Our laboratory has pioneered laser-induced side transfer (LIST), a DOD method for printing both cellular and acellular inks. LIST employs laser pulses to transfer cell-laden inks from the tip of a glass microcapillary to a receiving substrate with high precision.[23-26] We have demonstrated that LIST-printed primary cells (HUVECs and sensory neurons) maintain high viability post-printing.[23,24] We have also demonstrated that HUVECs printed using LIST retain their ability to migrate and form tubular-like networks,[23,25] and that LIST-printed sensory neurons exhibit no differentially expressed genes compared to control neurons and maintain responsiveness to external stimuli.[24]

Despite these advancements, a few challenges have been identified in the initial LIST implementation.[26] First, there is a need to actively perfuse the capillary to compensate for the liquid lost via drop ejection. This is a challenging step that requires a complex flow monitoring approach. Second, printing cell-laden inks for a long time faces the major challenge of cell accumulation at the capillary tip due to gravity. Both challenges hinder the printing workflow in applications requiring long printing time.

In this work, we present a redesigned implementation of LIST that uses continuous perfusion of a capillary, with a laser-machined hole acting as a nozzle. By separating capillary perfusion and drop ejection flow rates, the new design addresses the key challenges of the initial design and enables additional opportunities, such as controlling bioink shear rate. We have used a model ink to assess the influence of key printing parameters, such as laser energy, ink flow rate, and direction on the printing quality. Furthermore, we have used the redesigned LIST to print HUVECs and several assays to validate the viability of HUVECs, as well as their capacity to recruit perivascular cells.

2. Methods

2.1. Cell culture

HUVECs (pooled donors, C-12203; PromoCell, Germany) were cultured in endothelial cell growth medium-2 (EGM-2; CC-3162 Lonza, Switzerland). Passage 3 or 4 was used for bioinks preparation. Normal human lung fibroblast cells (IMR90) (CCL-186; ATCC, United States of America [USA]) were cultured in 1× Dulbecco's Modified Eagle medium (DMEM) (319-016-CL; Wisent Inc., Canada) supplemented with 10% fetal bovine serum (16000044; Thermo Fisher Scientific, USA) and utilized at passages 17 to 30 for cell seeding experiments. Human brain pericytes (HBPC) (ACBRI 498; Cell Systems, USA) were cultured in Pericyte Growth Medium 2 (C-28041; PromoCell, Germany) and utilized at passages 7 or 8 for cell seeding experiments. To minimize contamination, a 2% penicillin–streptomycin solution (30-002-CI; Corning, USA) was added to the culture medium for all cell types. The cells were grown in Petri dishes coated with 0.1% bovine gelatin (G9391; Sigma-Aldrich, USA) in sterile water and maintained at 5% CO_2 and 37°C. The culture media were replaced three times per week, and cells were split when they reached 90% confluency.

2.2. Model inks and bioink formulations

The model ink consisted of fibrinogen (13.2 μM) (F8630-5G; Sigma-Aldrich, USA) and Allura Red (10 mM) (458848; Sigma-Aldrich, USA) dissolved in phosphate-buffered saline (PBS, 311-010-CL; Wisent Inc., Canada). The bioink consisted of HUVECs (5×10^6 cells/mL) suspended in endothelial basal medium (EBM-2; CC-3156, Lonza, Switzerland) supplemented with fibrinogen (13.2 μM), Allura Red (10 mM), and aprotinin (7.7 μM) (10820–25MG; Sigma-Aldrich, USA). The role of Allura Red, a food dye, is to enhance bioink absorption at the laser-printing wavelength (532 nm). We used glycerol–water mixtures and Allura Red (10 mM) to prepare model inks of different viscosity (2.8, 17, 32, 75, 105, and 140 mPa·s).

2.3. Matrices

We used 18 × 18 mm microscope cover glasses (12-545-A; Fisher Scientific, USA) as the substrate for all gels. For cell recruitment experiments, HUVECs were bioprinted on Matrigel/thrombin gel. Matrigel (#35623; Corning, USA) (100 μL) was thawed at room temperature and mixed with 5 μL thrombin (100 U/mL) (T7513-100UN; Sigma-Aldrich, USA). The mixtures were drop-cast onto cover glasses and then placed in an incubator (5% CO_2 at 37°C) for 3 h before use in printing experiments. For cell viability experiments, HUVECs were bioprinted on a fibrin gel. Fibrinogen (10 mg/mL) was dissolved in PBS and sterilized using a syringe filter with a pore size of 0.45 μm. Aprotinin (7.68 μM) was added to the fibrinogen solution. Then, 285 μL of the fibrin solution was drop-cast onto a cover glass covered with 15 μL of a thrombin solution (100 U/mL). The hydrogels were allowed to sit at room temperature for 1 h before use in printing experiments.

2.4. Printing setup and protocol

The core of the printing setup, including the translation stage and optics, has been described in detail elsewhere.[26] Briefly, a pulsed 532-nm Nd:YAG laser (Nano S 60-30; Litron Lasers, United Kingdom [UK]) and beam delivery system, along with an objective lens (PLN4X; Olympus, Japan), are used to focus nanosecond (ns) laser pulses (20–150 μJ) in the middle of a square glass capillary (8250-050; Vitrocom, USA; inner dimensions: 500 × 500 μm; wall thickness: 150 μm) perfused with a model or cell-laden bioink (Figure 1A). The primary modification in the capillary used in this work comprises a 200 μm femtosecond (fs) laser-machined hole in its side wall, acting as a nozzle (Figure 1B). A three-dimensional-printed holder was used to align the capillary with the laser beam and imaging paths, as well as to support the perfusion tubing (89404-042; VWR, USA). Capillary perfusion at various flow rates (6, 30, 90, and 300 μL/min) was applied using a syringe pump (NE-1000; New Era Pump Systems Inc., USA) in either perfusion or withdrawal mode. Arrays of droplets of the model ink were printed at 20 Hz onto microscope glass slides (SKU BI0082B; Eisco Labs, India), with each droplet positioned 500 μm apart. For the printing of HUVECs lines, cell-laden droplets were deposited onto Matrigel/thrombin gel with a spacing of 200 μm using a laser energy of 60 μJ/pulse.

2.5. Laser micromachining of the capillary opening

A Ti:sapphire laser (λ = 800 nm; 1 kHz repetition rate) was used to fabricate 200 μm holes in the glass capillaries. A 5× (0.14 NA) apochromatic microscope objective (M Plan Apo; Mitutoyo, Japan) was used to focus the beam, achieving a Gaussian beam with a full width at half maximum of 10 μm at focus. The capillaries were mounted on a translational stage (ABL10150; Aerotech, USA) programmed to generate cutting paths. We utilized optimized cutting speed and mean power of 1 mm/s and 400 mW, respectively. An air jet was used during machining to cool the material and remove debris from the cutting area.

2.6. Cell viability assays

Bioprinted HUVECs were stained with Hoechst 33342 (14.2 μM) (14533–100 MG; Sigma-Aldrich, USA) and calcein AM (0.4 μM) (400146; Cayman Chemical, USA). Hoechst 33342 effectively stained all cells, whereas calcein AM specifically targeted live cells. Fluorescence images of the printed cells were captured at 0, 1, and 3 days post-printing using a motorized microscope (Zeiss AxioObserver Z1; Carl Zeiss AG, Germany). Control samples were prepared through bioink pipetting. Image processing involved utilizing a built-in MATLAB algorithm, which segmented individual cells based on Hoechst 33342 staining and assessed the intensity of the colocalized green channel (calcein AM). The green fluorescence signal threshold to identify live cells was set to $I_b + 5 \times \sigma_{Ib}$, where I_b and σ_{Ib} represent the background intensity and its standard deviation, respectively. For the MTT assay, ~1000 HUVECs were printed into vials at different laser energies, counted, and then seeded in a 96-well plate at a density of 800 cells/well. One day after printing, cell viability was assessed using an MTT assay kit (ab211091; Abcam, UK) according to the manufacturer's instruction, and absorbance (590 nm) was measured using a spark multimode microplate reader (Tecan, Switzerland).

2.7. Cell recruitment assay

Four days post-HUVECs printing, fibroblasts were seeded at 34,000 cells/mL or pericytes at 17,000 cells/mL. For imaging purposes, fibroblasts and pericytes were labeled with PKH26 red fluorescent dye (PKH26GL; Sigma-Aldrich, USA). Cell recruitment, assessed from 1 to 19 h post-seeding at 1 h intervals, was monitored using a Zeiss AxioObserver Z1 live-cell imaging system. Quantification of cell recruitment involved manual segmentation of the bioprinted HUVECs lines and calculation of the average fluorescence intensity for pericytes or fibroblasts within the segmented area. Control measurements were obtained using the same metric but outside the segmented area, distant (> 1 mm) from the printed HUVECs lines.

2.8. Comparative printing stability

For assessing the comparative printing stability, HUVECs bioink (5×10^6 cells/mL), suspended in EBM-2 supplemented with fibrinogen (13.2 μM), Allura Red (10 mM), and aprotinin (7.7 μM), was loaded into the capillary of both the redesigned (Figure 1B) and initial LIST implementations (Figure 1A). A total of 1800 drops were printed over 2 min (~ 3.6 μL) into collecting vials at time durations of 1, 15, 45, and 60 min. The cells were then counted, and the cell density was reported normalized to the 1-min time point.

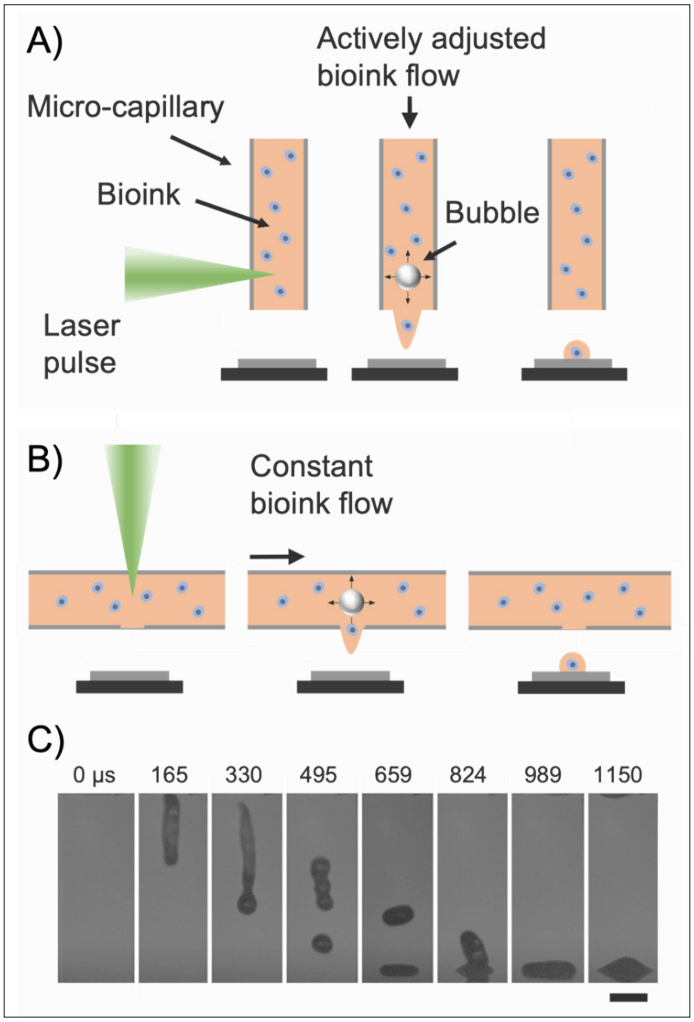


Figure 1. Side-view representations of (A) conventional laser-induced side transfer (LIST) bioprinting and (B) the redesigned LIST incorporating continuous capillary perfusion. (C) High-speed imaging captures the bioink ejection process. Scale bar: 200 µm.

2.9. Statistical analysis

All results are reported as the mean and standard deviation of three independent experiments. We conducted a statistical analysis using two-way Analysis of Variance (ANOVA) in GraphPad Prism 10 software (Figures 2, 3, 4B, and 5) and one-way ANOVA (Figure 4C). The graphs were prepared using the same software. We employed the Comparison of Coefficients of Variation Calculator in MedCalc Software to generate **Figure S1** (Supplementary File).

3. Results and discussion

3.1. Laser-induced side transfer using a continuously perfused capillary

In the initial implementation, LIST[23-26] utilizes low-energy ns laser pulses (532 nm) in the range of 50 to 150 µJ to create a microbubble near the tip of a bioink-filled glass microcapillary (Figure 1A). The expansion of the microbubble elevates the pressure within the microcapillary, leading to the ejection of micro-jets from its tip and the deposition of tiny droplets (Figure 1A).

The redesigned LIST approach presented in this work is outlined in Figure 2A. Similar to the original design, droplet ejection is accomplished using focused ns laser pulses. However, in this modified approach, ink is continually perfused through a glass capillary with a 200-µm laser-machined hole in its side wall, functioning as a nozzle. Surface tension prevents leakage in the absence of laser pulses. This design offers separate control of the bioink flow rate inside the capillary from the printing (i.e., drop ejection) rate, leading to four significant advancements compared to the initial design: (i) elimination of the need to actively compensate for liquid lost via droplet ejection;

(ii) flow-enabled removal of residual bubbles resulting from the collapse of the main bubble; (iii) flexibility in controlling bioink shear rate (scales with the volumetric flow rate); and (iv) prevention of cell agglomeration in cell-laden inks, a phenomenon observed in long-term printing due to gravity in the initial design.

These advancements led to notably enhanced printing stability, as indicated by the decrease in variation of cell density in printed drops compared to the initial setup. Specifically, when analyzing the normalized cell drop density for both approaches over 1 h of printing, a significant decrease in the coefficient of variation was observed within the redesigned setup in comparison to the initial configuration (41% vs. 151%, $p = 0.016$) (**Figure S1** in Supplementary File). Furthermore, using glycerol-based model inks, we found that the printability range is significantly increased in the redesigned LIST compared to the initial implementation in terms of maximum ink viscosity (140 mPa·s vs. 32 mPa·s) (**Figure S2** in Supplementary File).

3.2. Impact of laser pulse energy and ink flow rate on droplet size and shape

Prior to initiating cell printing, we examined the new LIST printing architecture using a model ink consisting of a water and Allura Red mixture. We investigated the effect of key printing settings, such as capillary flow rate, driving pressure (i.e., perfusion/withdrawal), and laser energy, on the printing process. We focused on determining drop size and circularity, which are determinants of printing resolution.

To accomplish this, we printed droplets on microscope slides at a 20 Hz printing speed, employing a range of laser pulse energies (20–120 μJ) and flow rates (6–90 μL/min) under perfusion or withdrawal pressure flow conditions (Figure 2). For flow initiation, pressure > 1 atm was applied in the perfusion pressure configuration (Figure 2A), whereas pressure < 1 atm was applied in the withdrawal pressure configuration (Figure 2E). We determined that the threshold for achieving stable printing conditions is 40 μJ, whereas printing at 100 μJ or higher energy resulted in splashing (Figure 2B and F). The droplet radius increased progressively with increasing laser pulse energy (Figure 2C and G) ($p < 0.001$), while droplet circularity exhibited an inverted relationship with laser energy (Figure 2D and H) ($p < 0.001$). These findings were consistent in both flow configurations. Notably, the printing workflow remained stable for a flow rate of up to 90 μL/min, representing 15 times the rate of ink loss via drop ejection at 20 Hz, considering an average drop volume of 5 nL.

Although increasing the laser pulse energy yielded results similar to the initial LIST configuration,[23-26] the laser pulse energy threshold for ejection is two times lower, and the droplet size is 1.5 times larger. This is likely because the bubble is generated much closer to the nozzle (~250 μm) compared to the edge of the capillary (~500 μm) in the initial configuration. One might expect that the conversion of bubble energy to jet kinetic energy is more efficient for a shorter bubble–nozzle distance. This effect has been previously observed in works exploiting laser-induced flow focusing for jet generation and drug ejection.[27]

3.3. Impact of ink flow rate on printing workflow and jet directionality

Using the same model ink, we aimed to establish the maximum flow rate for stable printing—a critical factor influencing ink viscosity in shear-thinning inks and a decisive factor in determining the potential maximum printing speed. In our initial experiments, we observed that the ink tended to leak through the nozzle under perfusion pressure when flow rates exceeded 300 μL/min. Conversely, during withdrawal pressure, occasional air suction through the nozzle introduced bubbles into the ink. Consequently, we identified 300 μL/min as the maximum flow rate for this specific capillary geometry and further examined if flow rates affected jetting directionality.

Jet angle measurements at 80 μJ laser energy and flow rates of 90 and 300 μL/min indicated that the mean change in the jet angle ranged between -1° and 1° (Figure 3). These findings suggest that flow rate variation within this range is unlikely to significantly affect bioprinting precision and accuracy. A jet angle divergence of 1° results in a 9-micron divergence in drop deposition, considering the typical capillary-to-sample distance of 0.5 mm. This divergence represents a negligible loss of accuracy given the typical drop size (300 μm). Importantly, a flow rate of 300 μL/min is 50-fold the liquid ejection volume for drops printed at 20 Hz, suggesting that higher printing speeds may be achievable with a laser operating at a higher repetition rate. Finally, the negligible effect of the flow rate on the jet directionality suggests that jetting dynamics are primarily influenced by the bubble dynamics for the examined setting.

3.4. Human umbilical vein endothelial cell viability is maintained in redesigned laser-induced side transfer

Despite the established viability of primary cell types in LIST,[23-26] it remained unclear whether the redesigned LIST approach would yield similar outcomes. LIST involves cell exposure to both laser irradiation and thermomechanical stress, including (i) long-term (few minutes) shear stress from bioink flow inside the capillary and loading tube,

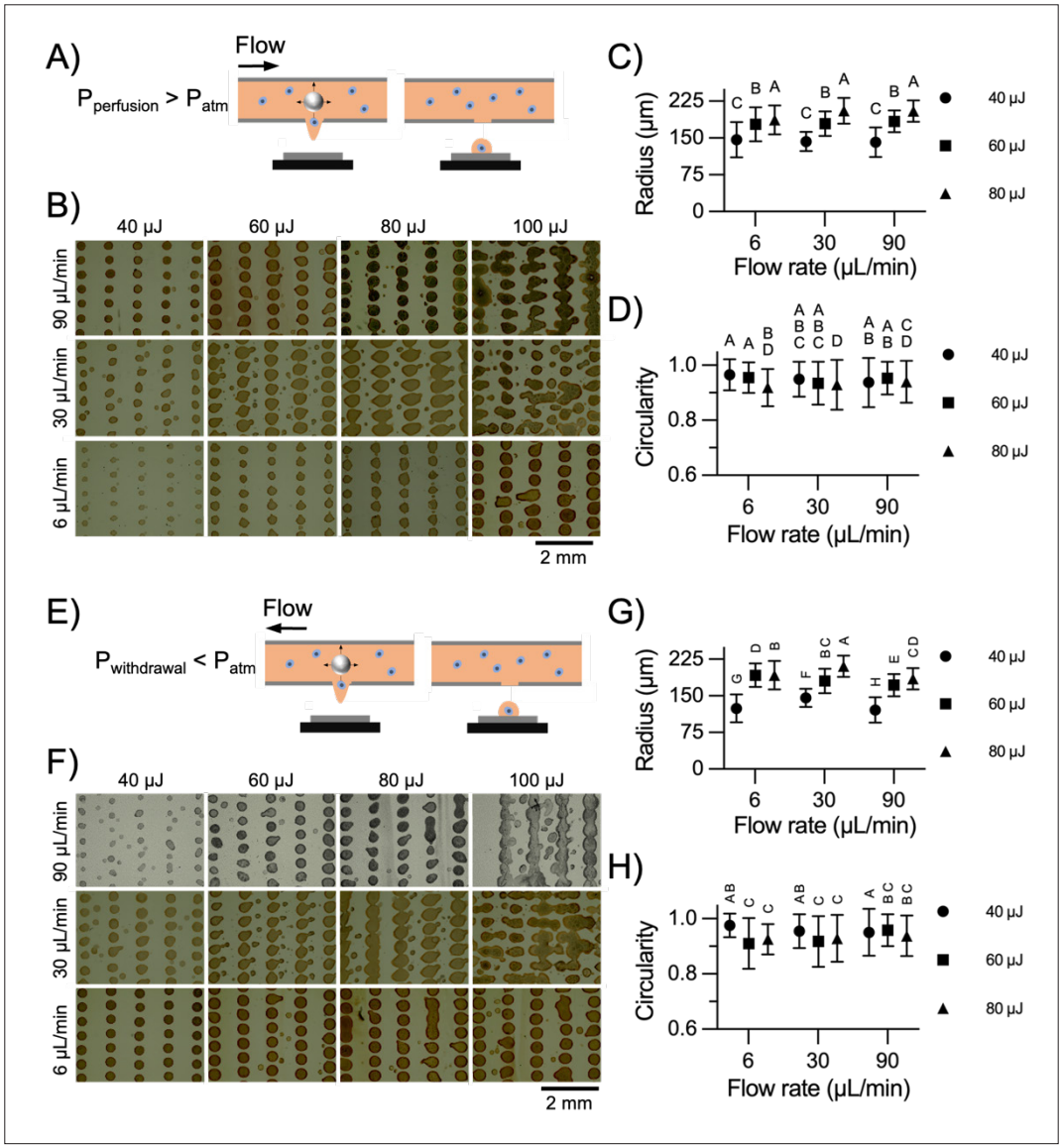


Figure 2. Validation of the printing setup using a model ink and (A) perfusion pressure flow ($P_{perfusion}$) or (E) withdrawal pressure flow ($P_{withdrawal}$). Optical microscopy images of droplets printed on microscope slides at a 20 Hz printing speed and different laser pulse energies and flow rates, for (B) perfusion pressure flow and (F) withdrawal pressure flow. Quantification of the droplet radius and circularity for different experimental conditions for (C and D) perfusion pressure flow and (G and H) withdrawal pressure flow. Data were analyzed using two-way Analysis of Variance (ANOVA). Groups are statistically indistinguishable if they share at least one letter. Error bars represent the standard deviation calculated from three independent experiments. The number of measured drops per condition ranged from 100 to 200 drops. Abbreviation: P_{atm}: Atmospheric pressure.

(ii) short-term (sub-millisecond) shear stress from bubble expansion, jetting, and substrate impact, and (iii) thermal stress. To assess potential cell damage, we sought to validate post-printing cell viability in the redesigned LIST using HUVECs.

HUVECs were printed on fibrin using various laser energies (60–120 µJ), and viability was measured and compared to a control (i.e., bioink pipetting) up to 3 days post-printing using calcein staining for live cells. The viability of printed HUVECs was 90–100% for the examined conditions, with no significant difference compared to the control (Figure 4B). Consistent with findings on the initial LIST design,[23-25] these results indicate that cells are subjected to tolerable thermomechanical stress during printing. Interestingly, prior evidence suggests that thermal stress may contribute to the survival and angiogenesis potential of endothelial cells via the expression of growth factors in response to heat shock.[28]

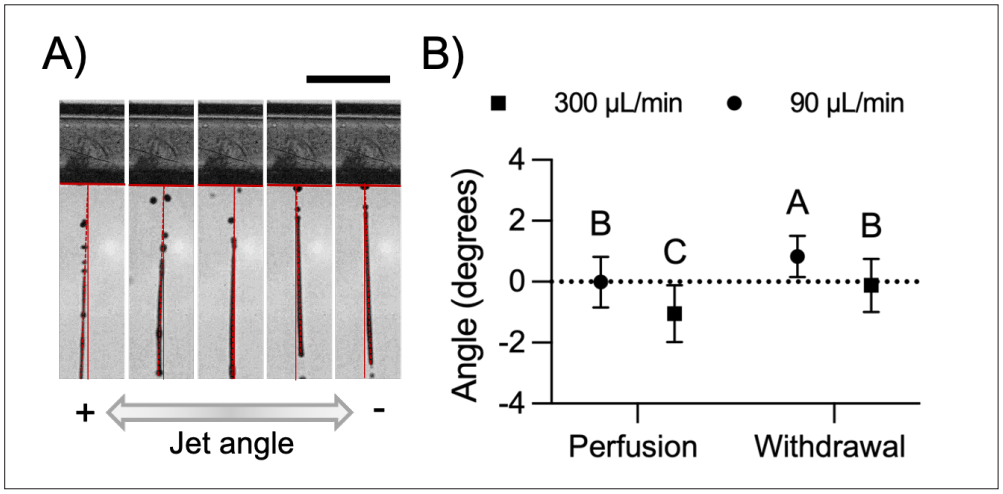


Figure 3. The effect of flow configuration and flow rate on the jet ejection angle. (A) Jet images indicate the assignment of signs to the jet angles. A positive sign indicates jet inclination toward the flow direction, whereas a negative sign indicates jet inclination against the flow direction. (B) The angle of the ejected jets for various flow conditions. Data were analyzed using two-way Analysis of Variance (ANOVA). Groups are statistically indistinguishable if they share at least one letter. Error bars represent the standard deviation calculated from three independent experiments. Scale bar: 500 µm.

We further validated post-printing viability using an MTT assay, employing a method that minimized potential variability in cell density through the collection and controlled seeding of printed cells. The MTT assay also demonstrates that printed cells exhibit viability levels indistinguishable from those of the control group (i.e., pipetted bioink) (Figure 4C).

However, cell exposure to stress is heterogeneous in LIST, with a small fraction of cells situated in the heat-affected zone around the bubble (a few microns) being exposed to significantly higher thermomechanical stress compared to those located outside this zone. It is essential to acknowledge that probing these individual cells in a large cell population is challenging and may approach the detection limit of the conventional viability assays used in this work.

3.5. Bioprinted human umbilical vein endothelial cell patterns recruit perivascular cells

Our prior findings demonstrated that HUVECs printed using the previous LIST implementation can generate tubular-like structures on Matrigel in response to angio-modulating compounds.[23] In this study, as an

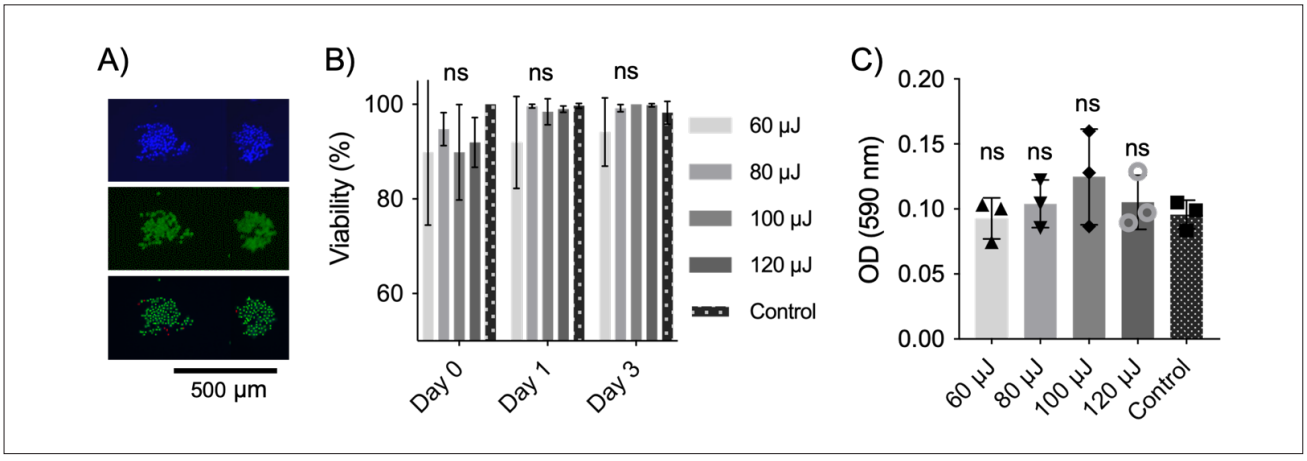


Figure 4. Assessment of HUVEC viability. (A) Indicative fluorescence microscopy images of printed drops on the printing date. All cells are stained with blue (Hoechst 33342) (top), while live cells are stained green (calcein AM) (middle). Cell tracing and artificial coloring based on our viability calculation and representation algorithm: live cells are represented as green dots; dead cells are represented as red dots (bottom). (B) HUVECs viability at different laser energies and time points using calcein imaging. (C) MTT assay absorbance readings 1 day post-printing of HUVECs at different energies compared to the control (i.e., pipetted bioink). Data in graphs (B) and (C) were analyzed using two-way Analysis of Variance (ANOVA) and one-way ANOVA, respectively. Error bars represent the standard deviation calculated from three independent experiments. Abbreviations: ns: Not significant; OD: Optical density.

initial exploration of the vascular modeling capability of printed HUVECs, we investigated their potential to attract perivascular cells, a critical component of vascular remodeling.

Printed HUVECs on Matrigel underwent self-organization to form line patterns over 4 days, followed by seeding with stained pericytes (HBPC) or fibroblasts (IMR90). Our observations revealed progressive recruitment of both pericytes and fibroblasts by the HUVEC line formations, commencing at 6 h post-seeding (Figure 5). Statistical significance was observed for recruited pericytes (Figure 5B) but not for fibroblasts (Figure 5D). Intriguingly, recruited cells exhibited movement along the printed lines, whereas those situated farther from the lines tended to cluster without a discernible directional preference.

Quantification, as detailed in the experimental section, involved monitoring the average cell density along the HUVEC lines or in areas distant from them (control area), relative to the seeding time. The slight increase in cell signal observed in the control area is attributed to cell precipitation. The latter reached a plateau within 1 h after cell seeding (Figure 5). These results suggest that printed HUVECs maintain the capability to secrete factors crucial for recruiting perivascular cells.

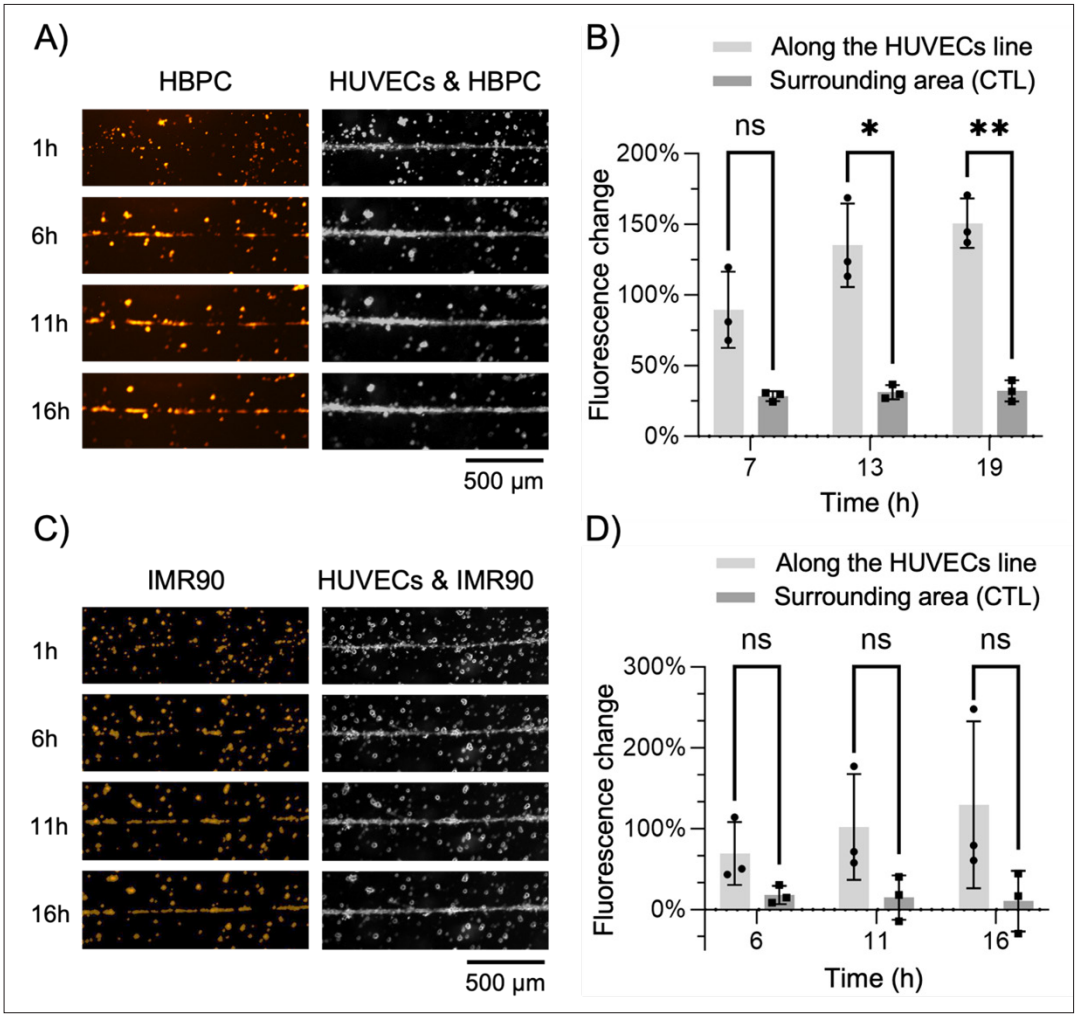


Figure 5. Recruitment of perivascular cells by the printed HUVECs line patterns. (A) Fluorescence images of human brain pericytes (HBPC) exhibiting progressive recruitment along the printed HUVECs line patterns (left). Phase-contrast images of both HUVECs and pericytes (right). (B) The relative fluorescence intensity along the HUVECs line patterns and at control (CTL) areas as a function of time post-pericyte seeding. (C) Fluorescence images of fibroblasts (IMR90) exhibiting progressive recruitment along the printed HUVECs line patterns (left). Phase-contrast images of both HUVECs and fibroblasts (right). (D) The relative fluorescence intensity along the HUVECs line patterns and at control areas as a function of time post-fibroblast seeding. The data were analyzed using two-way Analysis of Variance (ANOVA). Error bars represent the standard deviation calculated from three independent experiments. *$p \leq 0.05$; **$p \leq 0.01$. Abbreviation: ns: Not significant.

3.6. Limitations and future perspectives

The new LIST approach significantly enhances the printing workflow compared to the initial implementation, all while maintaining the viability of primary cells. Interestingly, the stable printing observed at high flow rates (300 μL/min) in both withdrawal and perfusion pressure modes suggests the potential for achieving higher printing speeds. However, our exploration of printing speeds above 30 Hz was limited by the maximum repetition rate of our available laser system. High repetition rate (kHz) and small footprint lasers are available at the required power levels in the market and can be used to explore the maximum printing speed.

A limitation in LIST using 532 nm is the necessity of adding a biocompatible light-absorbing dye to bioinks. This constraint restricts the applicability of LIST in bioprinting applications involving transparent constructs. An alternative approach to achieve dye-free printing can be the use of near-infrared irradiation at 1064 nm, as water-based inks are expected to absorb 30 times more light at 1064 nm than at 532 nm. Utilizing ns laser pulses at mid-infrared wavelengths can further reduce the required energy for dye-free printing, as water exhibits even higher absorption at these wavelengths. In fact, ns laser irradiation at 2.9 μm has already been considered as an attempt to avoid the use of sacrificial layers in nozzle-less LIFT.[29]

Another limitation in our approach is the requirement for micromachining commercially available capillaries, as fs-machining equipment can be expensive and not widely available. However, several companies commercially offer fs-machining services, providing a potential solution for those lacking access to the necessary infrastructure. We used the inner capillary size in the initial LIST demonstration as a guide for our selection of the hole size (200 μm) in the redesigned LIST. Yet, the effects of the hole size on printability and cell viability remain unknown. Our future work will focus on developing a computational model of the entire setup to optimize the architecture and study these effects. A potential opportunity in the new LIST implementation is to exploit continuous perfusion as a means to control the bioink temperature or to introduce bioink multiplexing using an external fluidic control system.

4. Conclusion

In conclusion, we have introduced and validated a new approach for performing DOD bioprinting using LIST. The primary advancement in this new implementation involves continuous capillary perfusion, eliminating the need for active compensation for liquid loss during drop ejection. The redesigned approach enables the control of bioink shear rate through flow rate adjustments, catering to various bioprinting applications. Stable printing conditions were successfully established with a model ink, and our results affirm that bioprinted HUVECs exhibit no viability loss, maintaining the ability to recruit perivascular cells. Overall, these findings underscore the method's potential for applications requiring DOD bioprinting of HUVECs.

Acknowledgments

The authors would like to thank Dr. Malcolm Latorre for technical support on the bioprinting setup, Dr. Mikhail Sergeev for technical support on microscopy, as well as Dr. Erika Hooker and Mr. Kevin Lanthier for assisting in establishing the cell culture and staining protocols.

Funding

Christos Boutopoulos acknowledges financial support from the Natural Sciences and Engineering Research Council of Canada (RGPIN-2018-06767) and the Fonds de la Recherche en Santé du Quebec (#312263). Hamid Ebrahimi Orimi acknowledges the financial support from the Fonds de Recherche du Quebec Nature et Technologies (#263066).

Conflict of interest

The authors declare no conflicts of interest.

Author contributions

Conceptualization: Mahyar Erfanian, Bruno Larrivée, Christos Boutopoulos

Formal analysis: Mahyar Erfanian, Christos Boutopoulos

Funding acquisition: Christos Boutopoulos

Investigation: Mahyar Erfanian, Ahad Mohammadi, Hamid Ebrahimi Orimi, Jennyfer Zapata-Farfan, Joe Saade, Bruno Larrivée, Christos Boutopoulos

Methodology: Mahyar Erfanian, Ahad Mohammadi, Hamid Ebrahimi Orimi, Jennyfer Zapata-Farfan, Joe Saade, Michel Meunier, Bruno Larrivée, Christos Boutopoulos

Resources: Michel Meunier, Bruno Larrivée, Christos Boutopoulos

Supervision: Michel Meunier, Bruno Larrivée, Christos Boutopoulos

Visualization: Mahyar Erfanian, Christos Boutopoulos

Writing – original draft: Mahyar Erfanian

Writing – review & editing: Mahyar Erfanian, Ahad Mohammadi, Hamid Ebrahimi Orimi, Jennyfer Zapata-Farfan, Joe Saade, Michel Meunier, Bruno Larrivée, Christos Boutopoulos

Ethics approval and consent to participate

Not applicable.

Consent for publication

Not applicable.

Availability of data

The data can be obtained from the corresponding author upon reasonable request.

References

1. Ozbolat I. *3D Bioprinting: Fundamentals, Principles and Applications*. Academic Press; 2016. doi: 10.1016/C2014-0-02349-0
2. Murphy SV, Atala A. 3D bioprinting of tissues and organs. *Nat Biotechnol*. 2014;32(8):773-785. doi: 10.1038/nbt.2958
3. Negro A, Cherbuin T, Lutolf MP. 3D inkjet printing of complex, cell-laden hydrogel structures. *Sci Rep*. 2018;8(1):1-9. doi: 10.1038/s41598-018-35504-2
4. Antoshin AA, Churbanov SN, Minaev NV, et al. LIFT-bioprinting, is it worth it? *Bioprinting*. 2019;15(May):e00052. doi: 10.1016/j.bprint.2019.e00052
5. Bernal PN, Delrot P, Loterie D, et al. Volumetric bioprinting of complex living-tissue constructs within seconds. *Adv Mater*. 2019;31(42). doi: 10.1002/adma.201904209
6. Panwar A, Tan LP. Current status of bioinks for micro-extrusion-based 3D bioprinting. *Molecules*. 2016;21(6). doi: 10.3390/molecules21060685
7. Tomasina C, Bodet T, Mota C, Moroni L, Camarero-Espinosa S. Bioprinting vasculature: materials, cells and emergent techniques. *Mater (Basel, Switzerland)*. 2019;12(17). doi: 10.3390/ma12172701
8. Rouwkema J, Khademhosseini A. Vascularization and angiogenesis in tissue engineering: beyond creating static networks. *Trends Biotechnol*. 2016;34(9):733-745. doi: 10.1016/j.tibtech.2016.03.002
9. Jain RK, Au P, Tam J, Duda DG, Fukumura D. Engineering vascularized tissue. *Nat Biotechnol*. 2005;23(7):821-823. doi: 10.1038/nbt0705-821
10. Lee JW, Choi YJ, Yong WJ, et al. Development of a 3D cell printed construct considering angiogenesis for liver tissue engineering. *Biofabrication*. 2016;8(1): 15007. doi: 10.1088/1758-5090/8/1/015007
11. Kolesky DB, Homan KA, Skylar-Scott MA, Lewis JA. Three-dimensional bioprinting of thick vascularized tissues. *Proc Natl Acad Sci U S A*. 2016;113(12):3179-3184. doi: 10.1073/pnas.1521342113
12. Hinton TJ, Jallerat Q, Palchesko RN, et al. Three-dimensional printing of complex biological structures by freeform reversible embedding of suspended hydrogels. *Sci Adv*. 2015;1(9). doi: 10.1126/sciadv.1500758
13. Maiullari F, Costantini M, Milan M, et al. A multi-cellular 3D bioprinting approach for vascularized heart tissue engineering based on HUVECs and iPSC-derived cardiomyocytes. *Sci Rep*. 2018;8(1):1-15. doi: 10.1038/s41598-018-31848-x
14. Xu L, Varkey M, Jorgensen A, et al. Bioprinting small diameter blood vessel constructs with an endothelial and smooth muscle cell bilayer in a single step. *Biofabrication*. 2020;12(4). doi: 10.1088/1758-5090/aba2b6
15. Skylar-Scott MA, Uzel SGM, Nam LL, et al. Biomanufacturing of organ-specific tissues with high cellular density and embedded vascular channels. *Sci Adv*. 2019;5(9). doi: 10.1126/sciadv.aaw2459
16. Jia W, Gungor-Ozkerim PS, Zhang YS, et al. Direct 3D bioprinting of perfusable vascular constructs using a blend bioink. *Biomaterials*. 2016;106:58-68. doi: 10.1016/j.biomaterials.2016.07.038
17. Takagi D, Lin W, Matsumoto T, et al. High-precision three-dimensional inkjet technology for live cell bioprinting. *Int J Bioprint*. 2019;5(2):27-38. doi: 10.18063/ijb.v5i2.208
18. Yanez M, Rincon J, Dones A, De Maria C, Gonzales R, Boland T. In vivo assessment of printed microvasculature in a bilayer skin graft to treat full-thickness wounds. *Tissue Eng - Part A*. 2015;21(1-2):224-233. doi: 10.1089/ten.tea.2013.0561
19. Kérourédan O, Hakobyan D, Rémy M, et al. In situ prevascularization designed by laser-assisted bioprinting: effect on bone regeneration. *Biofabrication*. 2019;11(4): 45002. doi: 10.1088/1758-5090/ab2620
20. Bourget JM, Kérourédan O, Medina M, et al. Patterning of endothelial cells and mesenchymal stem cells by laser-assisted bioprinting to study cell migration. *Biomed Res Int*. 2016;2016. doi: 10.1155/2016/3569843
21. Kérourédan O, Bourget JM, Rémy M, et al. Micropatterning of endothelial cells to create a capillary-like network with defined architecture by laser-assisted bioprinting. *J Mater Sci Mater Med*. 2019;30(2). doi: 10.1007/s10856-019-6230-1

22. Koch L, Deiwick A, Chichkov B. Capillary-like formations of endothelial cells in defined patterns generated by laser bioprinting. *Micromachines*. 2021;12(12):1-14. doi: 10.3390/mi12121538

23. Orimi HE, Hooker E, Narayanswamy S, Larrivée B, Boutopoulos C. Spatially guided endothelial tubulogenesis by laser-induced side transfer (LIST) bioprinting of HUVECs. *Bioprinting*. 2022;28(August): e00240. doi: 10.1016/j.bprint.2022.e00240

24. Roversi K, Orimi HE, Falchetti M, Lummertz da Rocha E, Talbot S, Boutopoulos C. Bioprinting of adult dorsal root ganglion (DRG) neurons using laser-induced side transfer (LIST). *Micromachines*. 2021;12(8):865. doi: 10.3390/mi12080865

25. Orimi HE, Kolkooh HSS, Hooker E, Narayanswamy S, Larrivée B, Boutopoulos C. Drop-on-demand cell bioprinting via laser induced side transfer (LIST). *Sci Rep*. 2020;10(1):9730. doi: 10.1038/s41598-020-66565-x

26. Roversi K, Orimi HE, Erfanian M, Talbot S, Boutopoulos C. LIST: a newly developed laser-assisted cell bioprinting technology. *Bio Protoc*. 2022;12(19):1-12. doi: 10.21769/BioProtoc.4527

27. Tagawa Y, Oudalov N, Visser CW, et al. Highly focused supersonic microjets. *Phys Rev X*. 2012;2(3):1-10. doi: 10.1103/PhysRevX.2.031002

28. Solis LH, Ayala Y, Portillo S, Varela-Ramirez A, Aguilera R, Boland T. Thermal inkjet bioprinting triggers the activation of the VEGF pathway in human microvascular endothelial cells in vitro. *Biofabrication*. 2019;11(4):045005. doi: 10.1088/1758-5090/ab25f9

29. Mohajan S, Delagnes J-C, Allisy B, Iazzolino A, Viellerobe B, Petit S. Plasma-free bubble cavitation in water by a 2.9 μ m laser for bioprinting applications. *Appl Phys Lett*. 2022;121(24). doi: 10.1063/5.0126355

ACCSCIENCE PUBLISHING

International Journal of Bioprinting

RESEARCH ARTICLE

Tuning the mechanical responses of 3D-printed ankle-foot orthoses: A numerical study

Chenxi Peng[1,2], Phuong Tran[3], Simon Lalor[4], Oren Tirosh[5], and Erich Rutz[1,2,6,7,8,9]*

[1]Department of Paediatrics, The University of Melbourne, Parkville, Victoria, Australia

[2]Murdoch Children's Research Institute, Parkville, Victoria, Australia

[3]RMIT Centre for Additive Manufacturing, School of Engineering, RMIT University, Melbourne, Victoria, Australia

[4]Orthotic and Prosthetic Department, The Royal Children's Hospital Melbourne, Parkville, Victoria, Australia

[5]School of Health and Biomedical Sciences, STEM College, RMIT University, Bundoora, Victoria, Australia

[6]Bob Dickens Chair Paediatric Orthopaedic Surgery, The University of Melbourne, Parkville, Victoria, Australia

[7]Orthopaedics Department, The Royal Children's Hospital Melbourne, Parkville, Victoria, Australia

[8]The Hugh Williamson Gait Analysis Laboratory, The Royal Children's Hospital Melbourne, Parkville, Victoria, Australia

[9]Medical Faculty, The University of Basel, Basel, Switzerland

***Corresponding author:**
Erich Rutz
(erich.rutz@unimelb.edu.au)

Citation: Peng C, Tran P, Lalor S, Tirosh O, Rutz E. Tuning the mechanical responses of 3D-printed ankle-foot orthoses: A numerical study. *Int J Bioprint*. 2024;10(3):3390.
doi: 10.36922/ijb.3390

Received: April 9, 2024
Accepted: May 8, 2024
Published Online: June 7, 2024

Copyright: © 2024 Author(s). This is an Open Access article distributed under the terms of the Creative Commons Attribution License, permitting distribution, and reproduction in any medium, provided the original work is properly cited.

Publisher's Note: AccScience Publishing remains neutral with regard to jurisdictional claims in published maps and institutional affiliations.

Abstract

Ankle-foot orthoses (AFOs) are frequently prescribed for children with cerebral palsy (CP) to correct specific features of abnormal gait. However, traditional AFO manufacturing and design involve labor-intensive processes and rely on subjective evaluations of clinicians. Recent advances in three-dimensional (3D) printing allow the rapid prototyping of AFOs, but the expanded design options complicate decision-making. This study aims to evaluate how AFO design affects the mechanical responses of 3D-printed AFOs. The lower limb geometry is established by a 3D-scanning system, and a prototypical AFO is designed, 3D printed, and tested under compression. A parametric study on the effect of base materials, thickness, and trimline location is conducted based on a validated numerical model. The results reveal that AFOs exhibit distinct behaviors under plantarflexion and dorsiflexion motions, with AFO stiffness correlating to thickness through a power function. AFO stiffness is more sensitive to posterior trim depth than inferior, while both trim depths significantly influence stress concentration around the ankle region. This investigation demonstrates the potential of combining 3D printing and computational modeling to improve the design and fabrication process of AFOs, providing insights into the development and customization of 3D-printed AFOs.

Keywords: Cerebral Palsy; Ankle-foot orthoses; 3D printing; Computational modeling; Stiffness; Dorsiflexion; Plantarflexion

1. Introduction

Gait deviations are a common problem in ambulant children with cerebral palsy (CP) due to a combination of impaired motor control, movement disorders such as spasticity, and secondary musculoskeletal deformities such as equinus contractures.[1] Besides single-event multilevel surgery,[2] nonoperative management options to improve gait impairments include physical therapy,[3] pharmacological interventions (e.g., injections of botulinum toxin A),[4,5] and the use of an ankle-foot orthosis (AFO).[6-8] AFOs are externally applied devices encompassing the foot, ankle, and leg from just below the knee. They are used to compensate for impairments in the structure and function of the neuromuscular and musculoskeletal systems.[7,9] Traditionally, patient-specific AFOs are handmade by experienced orthotists. The whole process includes six main steps and is labor-intensive, consuming about 6–8 h per device (Figure 1a).[10,11] The first step is taking a negative impression of the foot, ankle, and leg using a plaster bandage or fiberglass type. Then, a positive model is obtained by pouring plaster slurry into the negative model and adding additional plaster to adjust the geometry. Once the positive model is smoothed, a heated polypropylene (PP) sheet is wrapped around it, and vacuum is formed. Finally, the cooled plastic is cut to the AFO trimlines determined by the orthotist and fitted to the patient.

With rapid advances in three-dimensional (3D) printing techniques, complex geometry can be fabricated with exceptional quality using various metallic or polymeric materials for different applications.[12] Recent reviews indicate that it is feasible to produce AFOs using 3D printing techniques.[13,14] Researchers have considered different 3D printing techniques, such as fused deposition modeling (FDM),[15-19] multijet fusion (MJF),[20] selective laser sintering (SLS),[21,22] and stereolithography (SLA),[23] to manufacture AFOs. As presented in Figure 1b, the fabrication processes of 3D-printed AFOs start with the acquisition of the patient-specific geometry using 3D-scanning, microcomputed tomography (CT), or magnetic resonance imaging (MRI) data. Subsequently, a smooth foot-leg model can be reconstructed by repairing and fitting raw scanning data. AFOs can be designed based on the foot-leg model according to clinical requirements using computer-aided design (CAD) software, followed by converting the design to G-code compatible with the 3D printer for printing. Finally, the 3D-printed AFO can be inspected and delivered to the patient (Figure 1b). Compared to traditional plaster molding techniques, 3D printing has the potential to eliminate several steps and simplify the process, as well as provide repeatability and design options that are not available through traditional methods. Table 1 compares the traditional plaster-molding techniques and 3D printing techniques.

An important characteristic of AFOs that needs to be considered by clinicians is rotational stiffness, which is determined by the resistance of AFOs against the ankle joint plantarflexion (PF) and dorsiflexion (DF) motions in the sagittal plane.[24-26] While the stiffness of AFOs can be affected by the location of the trimline, base materials, and thickness,[27,28] evaluating this crucial property has received increasing attention from researchers.[29,30] Several testing systems, such as BRUCE,[31] EMPIRE,[32] and SMApp,[33] have been developed to measure the torque required to move AFOs to a certain PF or DF angle for stiffness calculation. In addition to experimental methods, attempts have also been made to develop finite element (FE) models to

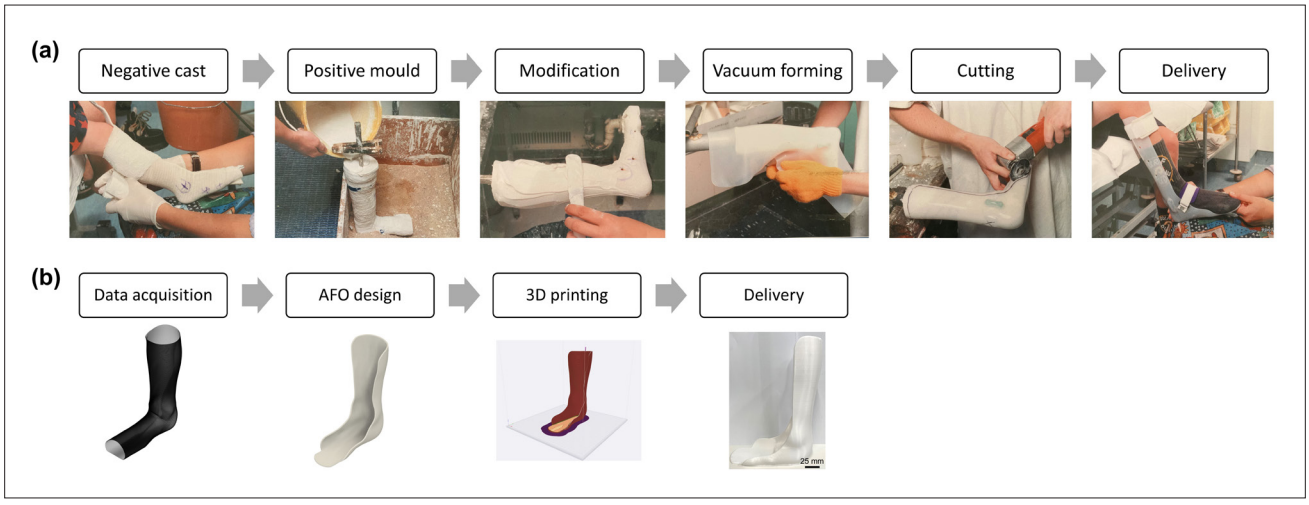


Figure 1. Comparison between ankle-foot orthosis (AFO) fabrication processes: (a) traditional method and (b) 3D printing method.

Table 1. Comparison between traditional methods and 3D printing for ankle-foot orthosis (AFO) production

Parameter	Traditional techniques	3D printing techniques
Material options	Limited	Most engineering thermoplastics
Labor requirement	Skilled	Technical
Material waste	High	Low
Design repeatability	Low	High
Design freedom	Moderate	High
Accuracy	Low	High

predict the stiffness of AFOs.[34-40] Still, the design of an AFO is dependent on subjective evaluation and the experience of the orthotist, and remains largely empirical. Clinicians typically rely on observational evaluations and their own professional experience to decide the material and trimline for the AFO design. Meanwhile, limited information on how AFO trimline, base materials, and thickness affect their stiffness is currently available.[41] With 3D printing techniques, the design space becomes even larger. As more options become available and design decision processes become more complex, a comprehensive analysis of the effects of AFO design variables on stiffness and deformation behavior is warranted.

This study aims to reveal the effect of base materials, thickness, and trimline on the stiffness and deformation of AFOs through a comprehensive parametric study based on numerical simulations. Firstly, the anatomical geometry of the foot-leg is established by a 3D-scanning system. Then, a baseline AFO design is created and 3D printed. An FE model is developed and validated using experimental data. A parametric study on the effect of base materials, thickness, and trimline location is conducted. The results provide insights into the development and customization of 3D-printed AFOs for individuals with specific ankle and foot conditions.

2. Methods

2.1. Surface modeling of the foot and leg

The 3D surface model of the foot and leg was acquired for the virtual design of the AFO. A progressive sequence of 3dMD images of the foot, ankle, and leg was generated using the 3dMDflex™ system (3dMD, United States of America [USA]). These image series were then rendered into high-precision 3D surface images with an accuracy of 0.2 mm and exported as a stereolithography file (STL) (Figure 2a). The scanned mesh of the leg was imported to Fusion 360 (Autodesk, USA) for repair, and a smooth surface was fitted. The location of the pseudo-foot-ankle center was approximated as the midpoint between the medial malleolus and the lateral malleolus, and a coordinate system with sagittal, axial, and coronal planes was defined. Figure 2b presents the 3D imaging process and reconstructed surface representation of the foot-leg geometry.

2.2. AFO design

A baseline design, similar to rigid AFOs used in clinical practice, was generated by cutting the anterior region of the foot-leg model according to the trimline, with consultation from an experienced orthotist, while a standard 3 mm thickness was used, as presented in Figure 2c. For the

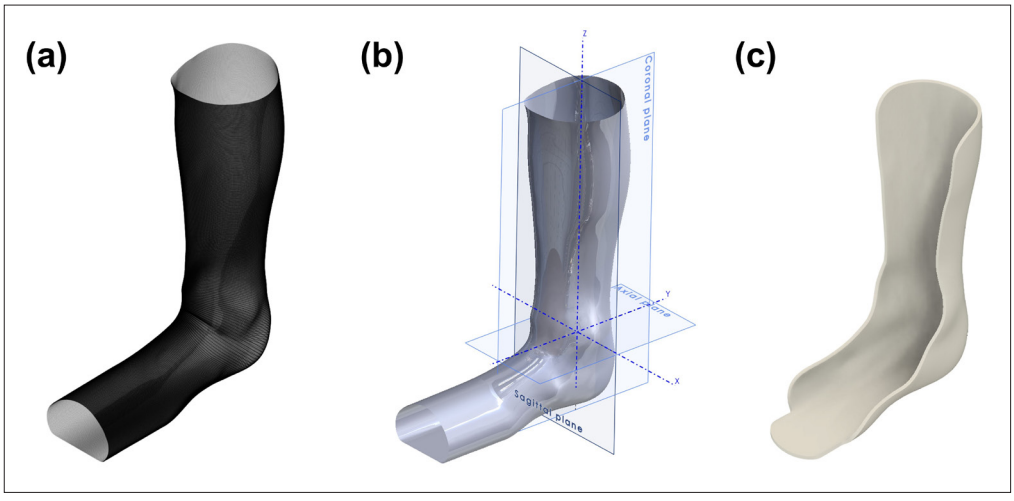


Figure 2. Surface modeling of the foot and leg. (a) Surface mesh of the foot and leg from scanning. (b) Reconstructed smooth surface of the foot and leg. (c) Baseline rigid ankle-foot orthosis (AFO).

parametric design, different AFO thicknesses, base materials, and trimline locations were considered in this study. The baseline AFO design was used to study the thickness and base materials. The thickness of the AFO was determined from the shell thickness, and trimline location was determined from the portion of the AFO trimmed from the pseudo-foot-ankle center to the posterior and inferior directions. The location of the trimline was adjusted accordingly to produce different AFO designs, while the calf height was kept at 45 mm for consistency. Table 2 summarizes the design variables considered in this work.

2.3. Sample fabrication

The samples were fabricated via FDM using a Creality K1 Max 3D printer. The CAD model of the samples was first converted to STL and sliced with a 0.1 mm layer height. Each slice of the model has two perimeter walls and an infill density of 100%. Then, the toolpath information was written into G-code and sent to the printer. A 0.4-mm hardened steel nozzle was utilized, and the standard 1.75-mm filament was used for all materials. All filaments were dried before printing to avoid moisture absorption from the air. During the printing process, the thermoplastic filament was heated to a semiliquid state and extruded through the nozzle onto the heated build platform to facilitate adhesion between the first layer and the build platform. A printing speed of 100 mm/s was used for all samples. The nozzle and build platform temperatures for different materials are summarized in Table 3.

2.4. Mechanical testing

Tensile tests were conducted to characterize the mechanical properties of base materials. Samples were designed according to ASTM standard D638.[42] Three Type IV samples with gauge length of 33 mm, width of 6 mm, and thickness of 4 mm were printed for each material according to the conditions described in the previous section. An Instron 5900R universal testing machine with a load capacity of 30 kN was utilized. The testing was performed at a loading rate of 1 mm/min. The reaction force from the load cell and displacement were measured by a long travel extensometer. Additionally, a uniaxial compression test was conducted on the baseline AFO printed with PA12 material. A digital camera was used to capture the deformation of the AFO during testing.

Table 2. Variables considered for parametric design of ankle-foot orthoses (AFOs)

Variable	Conditions
AFO thickness (mm)	2; 3; 4; 5; 6
Base material	Polycyclohexylene dimethylene terephthalate glycol-modified (PCTG); polyamide 12 (PA12); carbon fiber-reinforced polyamide 12 (PA12-CF); polylactic acid (PLA)
Trimline/trim depth (mm)	
Posterior	10; 15; 20; 25
Inferior	10; 15; 20; 25

Table 3. Printing temperature for different materials

Material	Temperature (°C)	
	Nozzle	Build platform
Polycyclohexylene dimethylene terephthalate glycol-modified (PCTG)	265	90
Polyamide 12 (PA12)	270	100
Carbon fiber-reinforced polyamide 12 (PA12-CF)	285	90
Polylactic acid (PLA)	220	45

2.5. Numerical model

FE modeling was employed to investigate the mechanical responses of AFOs under PF- and DF-loading conditions. The FE package ABAQUS/Implicit 2020 (Dassault Systèmes Simulia Corp, USA) was used to develop the computational model. The CAD model of AFOs was imported into HyperMesh (Altair, USA) to create the FE mesh and exported to ABAQUS. Figure 3a presents the boundary conditions of the computational model. A coupling constraint was assigned between the calf section of the AFO and a reference point, while a second coupling constraint was assigned between the foot section of the AFO and another reference point.

To simulate the PF and DF motions, the bottom part of the AFO was fixed, and a 10° rotation about the virtual ankle center was applied through the reference points. The contact behavior was modeled by general contact with a hard formulation for the normal direction and a penalty friction formulation with a friction coefficient of 0.3 for the tangential direction. The constitutive behavior of the base material was simplified to be elastic perfectly plastic[43] based on the tensile results in Figure 4. The rotational displacement and reaction moment of the calf section were extracted for further evaluation. The PF and DF stiffnesses of the AFO were calculated as the slope of the linear region in the AFO moment–ankle angle relationship.

A mesh convergence analysis was conducted to evaluate the mesh density required based on the optimization of computational cost and accuracy. Four-node linear tetrahedral solid element (C3D4) and four-node linear quadrilateral shell element (S4) were considered for

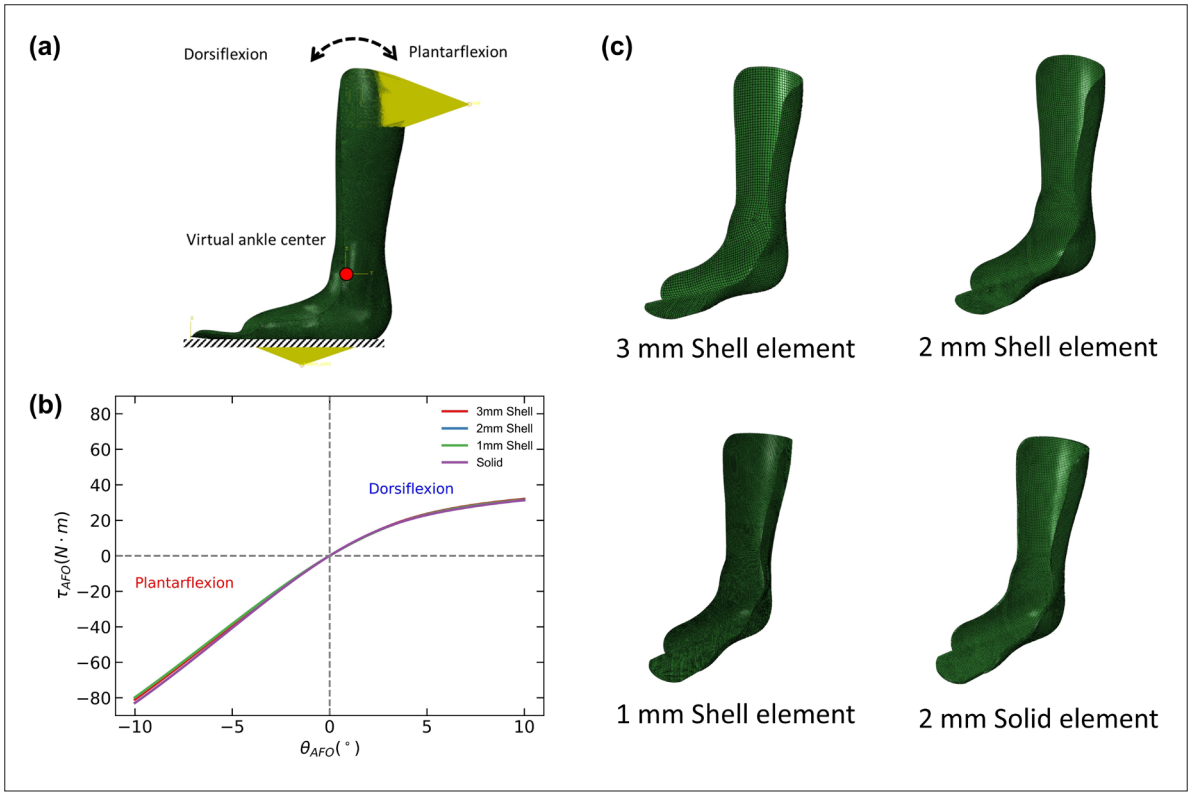


Figure 3. Numerical modeling of the ankle-foot orthosis (AFO). (a) Finite element (FE) model to simulate plantarflexion and dorsiflexion motions of AFO. (b) AFO moment–ankle angle relationships of different mesh configurations. (c) Comparisons of different mesh configurations.

modeling (Figure 3c). The resulting AFO moment–ankle angle relationships are displayed in Figure 3b. A good convergence was achieved with a 2-mm element size shell element (11,659 elements), and no significant difference between shell and solid elements was observed. To reduce the computational cost, a 2-mm shell element was selected for this study.

3. Results and discussion

3.1. Validation of numerical results

The numerical results were validated by experimental data through a uniaxial compression test on a baseline AFO printed with PA12. As there is no standard method for testing the stiffness of AFOs, uniaxial compression was

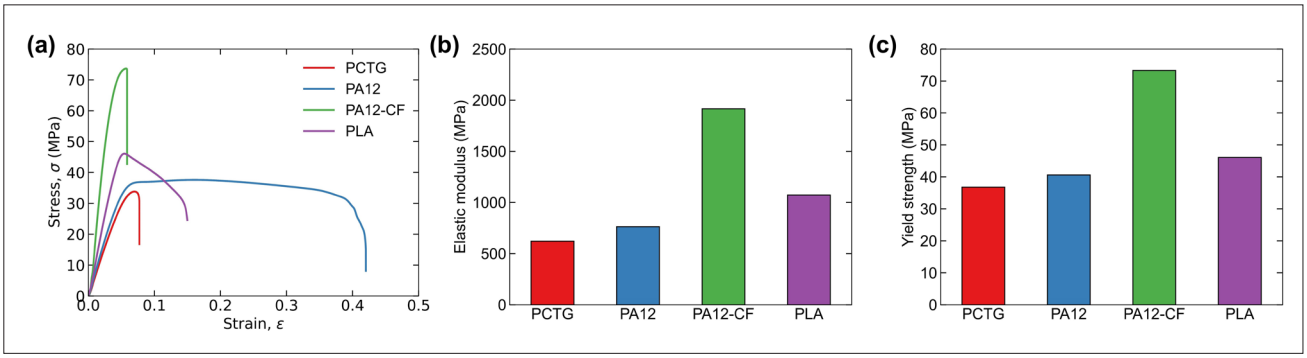


Figure 4. Tensile testing results of different base materials: (a) stress–strain curves, (b) elastic modulus, and (c) yield strength. Abbreviations: PCTG: Polycyclohexylene dimethylene terephthalate glycol-modified; PA12: Polyamide 12; PA12-CF: Carbon fiber-reinforced polyamide 12; PLA: Polylactic acid.

chosen to provide more controllable testing conditions. The displacement control method was utilized in the test with a loading rate of 1 mm/min to eliminate dynamic effects. Figure 5a presents the comparison between force–displacement curves obtained from experiments and numerical simulations. It can be observed from the experimental data that the reaction force initially exhibited a linear region followed by a significant drop after the peak load, which can be attributed to the buckling of the AFO wall. As displayed in Figure 5b, the AFO wall started to buckle inward after the compressive displacement reached 2 mm. The numerical simulations captured the force–displacement relationships of the AFO under compression well. It was noticeable that the numerical simulations predicted a slightly higher force compared to the experimental data at the same displacement, most likely due to anomalies in the sample introduced by the 3D printing process. The AFO used in computational modeling was assumed to be perfect, but a 3D-printed AFO may have defects and a level of porosity instead of being perfectly solid, leading to a compromised load-bearing capacity. Figure 5c displays the deformation and stress contour of the AFO from simulations. The computational modeling predicted localized buckling of the AFO, similar to experimental results. A good agreement was achieved between experiments and numerical results.

3.2. Effect of base materials

The effect of base materials on the mechanical responses of an AFO under PF and DF was investigated through computational simulation. Four base materials, polycyclohexylene dimethylene terephthalate glycol-modified (PCTG), polyamide 12 (PA12), carbon fiber-reinforced polyamide 12 (PA12-CF), and polylactic acid (PLA), were considered based on the tensile testing results. Figure 6a presents the resulting AFO moment–ankle angle relationships. The AFOs exhibited different behaviors under PF and DF loading. A linear moment–ankle angle relationship was found for all AFOs under PF loading. In comparison, the moment first increased linearly with an increase in ankle angle and was followed by a softening phase under DF loading. It was noticeable that the ankle angle required to reach the nonlinear region was significantly higher for PA12-CF compared to other materials, attributing to the higher stiffness and yield strength of PA12-CF. The slope of the moment–ankle angle curves in the linear region was calculated as the stiffness of the AFO. Figure 6b and c compares the stiffness of AFOs under DF and PF, respectively. The AFOs present different stiffness under DF and PF due to their asymmetrical geometry. The PA12-CF AFO exhibited the highest stiffness for both DF and PF, while PA12 and PLA AFOs exhibited similar properties.

Figure 6d and e displays the deformation and stress contours of different AFOs under 10° DF and PF loading, respectively. Stress was concentrated around the ankle region for AFOs. The PA12-CF AFO developed much higher stress compared to other materials due to the high stiffness of the carbon fiber-reinforced material. The results also revealed that higher stress was found on the AFOs under PF loading compared to that under DF loading. The maximum stress on AFOs during DF was still within the elastic limit of the base materials. Thus, the nonlinear moment–ankle angle relationship of DF was caused by the nonlinearity of the geometry, not the plastic deformation of the materials. This could be attributed to the fact that the ankle region of the AFO is under tension when subjected to DF, making localized buckling of the AFO wall less likely to occur compared to PF when the ankle region is under compression. It should be noted that the AFOs may be subjected to cyclic loading during usage, leading to fatigue failure. The damage is more likely to occur where higher stress is presented. Thus, it is important to reduce

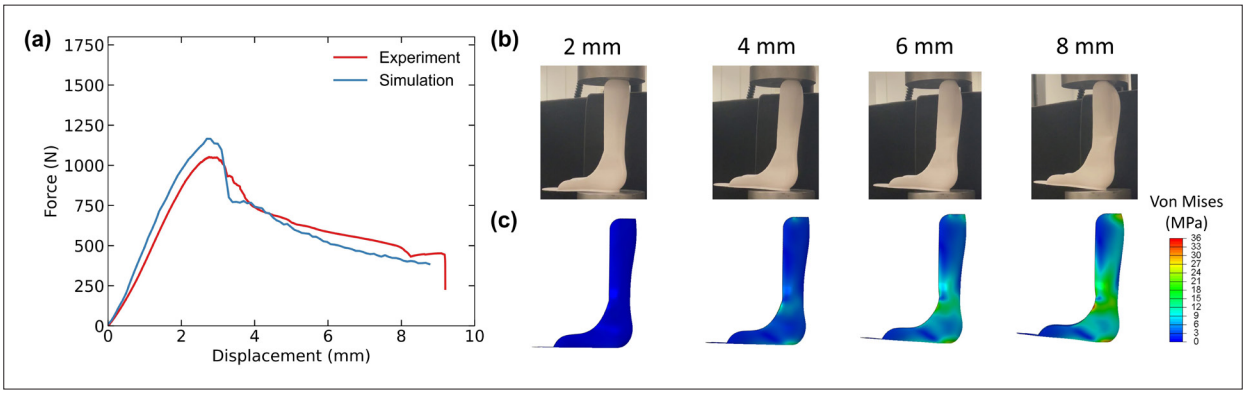


Figure 5. Comparison of numerical and experimental results. (a) Force–displacement curves obtained from experiments and numerical simulations. Deformations of the ankle-foot orthosis (AFO) under compression based on (b) experiments and (c) numerical simulations.

the stress concentration on the AFO. As the PA12 AFO can provide sufficient stiffness and PA12 has excellent ductility compared to other materials, it can be a favorable candidate for 3D-printed AFOs. The remainder of the parametric study was based on the PA12 material.

3.3. Effect of ankle-foot orthosis thickness

3D printing can provide more flexibility in terms of AFO thickness compared to the limited thickness options available for traditionally fabricated AFOs. The effect of AFO thickness on AFO mechanical responses was evaluated. Figure 7a compares moment–ankle angle relationships for AFOs with thicknesses of 2–6 mm. The increase in AFO thickness resulted in a higher moment at the same DF or PF angles but had a limited effect on mechanical responses. A linear moment–ankle angle relationship was found for all AFO thicknesses under PF, while DF displayed nonlinearity. A larger ankle angle was required to reach nonlinear deformation with increased AFO stiffness. The slope of the moment–ankle angle curves in the linear region was calculated as the stiffness of the AFO. Figure 7b presents the DF and PF stiffness by AFO thickness. A power function was used to fit the AFO stiffness–thickness relationships. It can be seen that both DF and PF stiffness increased with increased AFO thickness.

Although all AFOs exhibited higher stiffness under PF than DF, the DF stiffness increased at a higher rate. This can be attributed to the fact that stiffness is dominated by thickness, and the asymmetrical geometry has a more limited effect. With 3D-printed AFOs, a wide range of stiffness can be achieved by selecting the proper thickness according to clinical requirements. Figure 7c and d features the deformation and stress contour of AFOs with different thicknesses at 10° of DF and PF, respectively. Stress concentration was found for AFOs with various thicknesses at the ankle region. The AFO thickness had a limited effect on the deformation and stress distributions of the AFO.

3.4. Effect of trimline location

In practice, the trimline of AFOs is determined by observational evaluations and the professional experience of clinicians. This section provides a quantitative evaluation of how trimline location affects the DF and PF stiffness of AFOs. Two major trim directions, namely the inferior and posterior trim depths, were examined.

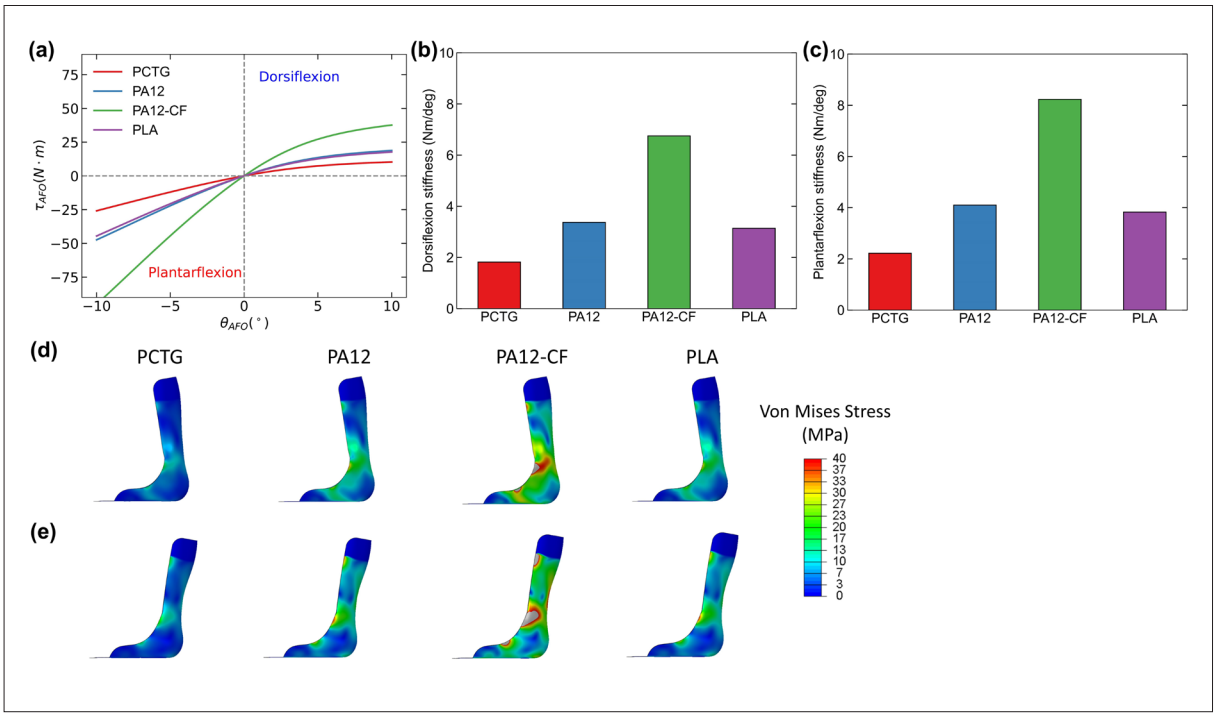


Figure 6. Effect of base materials. (a) Ankle-foot orthosis (AFO) moment–ankle angle relationships of baseline rigid AFO with different base materials under plantarflexion and dorsiflexion. The stiffness of baseline rigid AFO with different base materials: (b) dorsiflexion and (c) plantarflexion. Deformation and stress contour of baseline with different base materials at 10° rotation: (d) dorsiflexion and (e) plantarflexion. Abbreviations: PCTG: Polycyclohexylene dimethylene terephthalate glycol-modified; PA12: Polyamide 12; PA12-CF: Carbon fiber-reinforced polyamide 12; PLA: Polylactic acid.

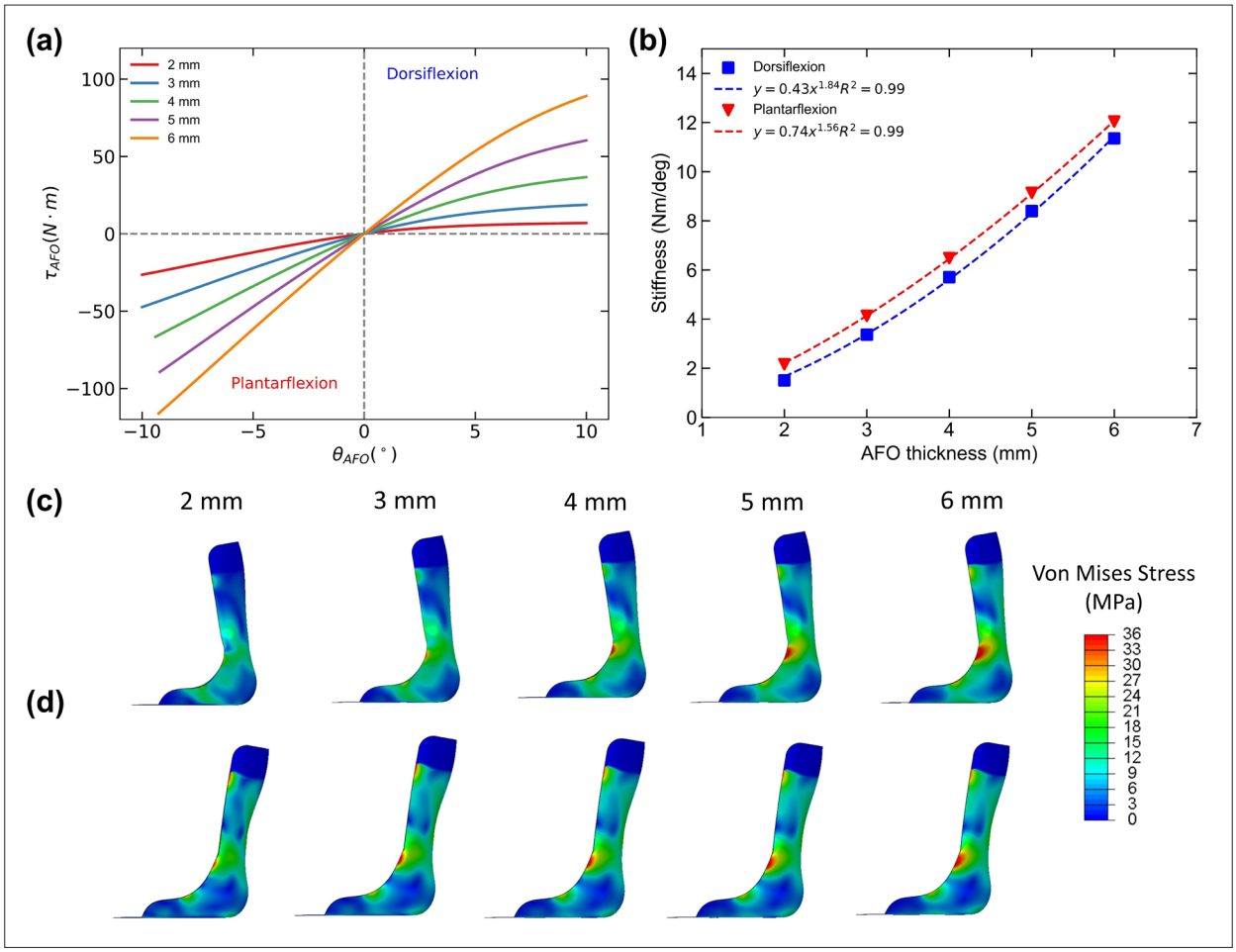


Figure 7. Effect of ankle-foot orthosis (AFO) thickness. (a) AFO moment–ankle angle relationships of baseline AFO with various thicknesses under plantarflexion and dorsiflexion. (b) The stiffness of baseline AFO with various thicknesses. Deformation and stress contours of the baseline with various thicknesses at 10° rotation: (c) dorsiflexion and (d) plantarflexion.

Figure 8a compares moment–ankle angle relationships for AFOs with inferior trim depths ranging from 10 to 25 mm. The changes in trimline depth in the inferior direction had limited effects on the DF and PF behaviors of AFOs. A linear moment–ankle angle relationship was found for all AFOs under plantarflexion. By comparison, the moment increased linearly with an increase in ankle angle and was followed by a diminishing phase under DF motions. Figure 8b displays the DF and PF stiffness of AFOs with different inferior trim depths. With a further trim of AFO along the inferior direction from 10 to 25 mm, the decreases in both DF and PF stiffness were less than 10%. The impact of varying inferior trim depth on the overall stiffness of AFOs was modest. Figure 8c and d presents the deformation and stress contour of AFOs. The overall stress distribution remained consistent for all AFOs, with a notable reduction in stress around the ankle region for AFOs with higher trim depth along the inferior direction. This suggests that increasing the trim depth in the inferior direction may contribute to a more even stress distribution across the AFO, potentially mitigating stress concentrations around the ankle region and preventing potential fatigue damage.

Figure 9a compares moment–ankle angle relationships for AFOs with posterior trim depths ranging from 10 to 25 mm. The increase in trim depth along the posterior direction reduced the moment required at the same DF or PF angles and also affected the mechanical responses. A linear moment–ankle angle relationship was found for AFOs with small posterior trim depth under PF, while DF response displayed nonlinearity. However, with further trimming of the AFO along the posterior direction, the DF of the AFO resulted in a linear response only. Meanwhile, a higher moment was required to deform the AFO to the same DF and PF angle with an increase in posterior trim depth. Figure 9b compares the stiffness of different AFOs

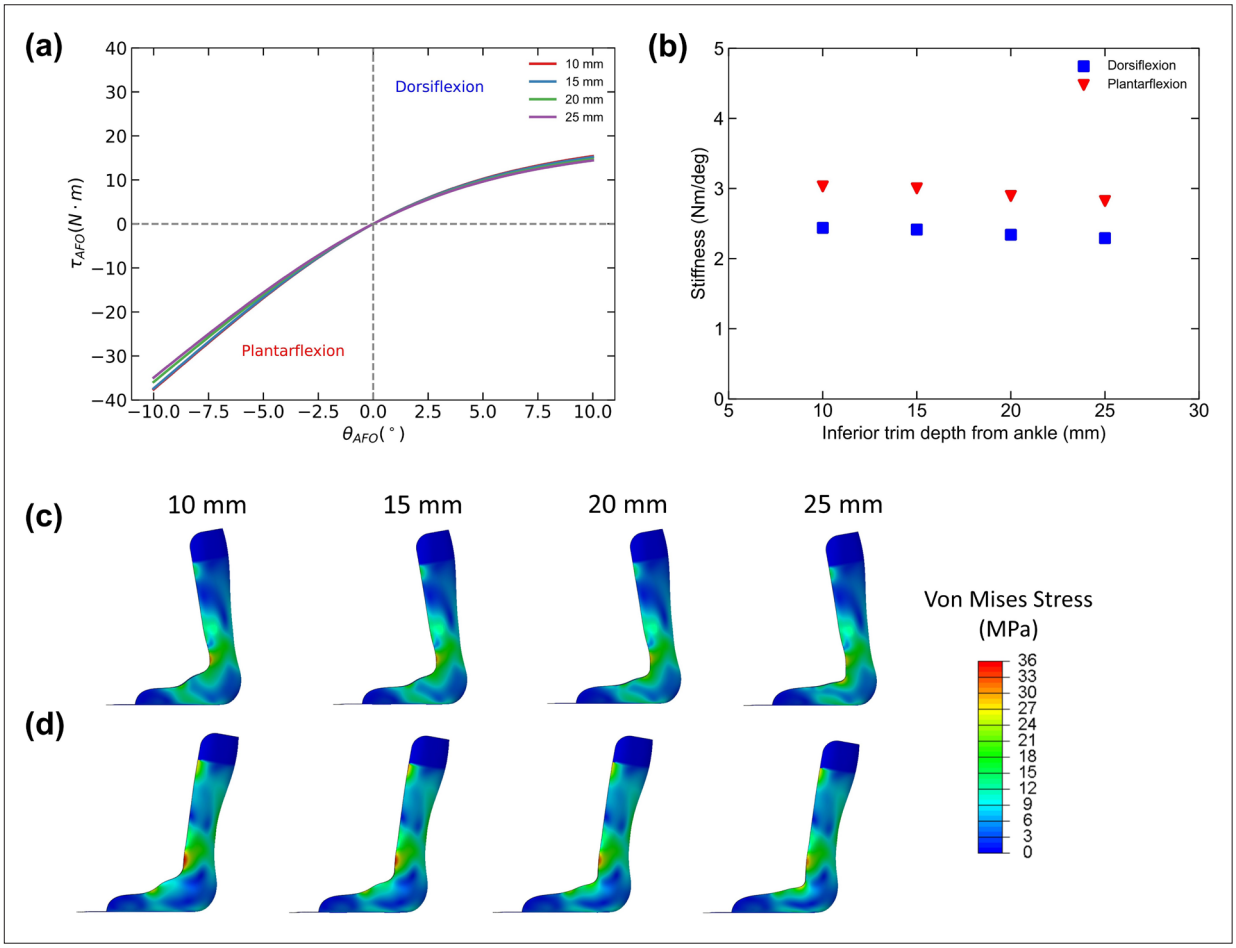


Figure 8. Effect of inferior trimline. (a) Ankle-foot orthosis (AFO) moment–ankle angle relationships of AFO with different inferior trim depths under plantarflexion and dorsiflexion. (b) The stiffness of AFO with different inferior trim depths. Deformation and stress contour of baseline with different inferior trim depths at 10° rotation: (c) dorsiflexion and (d) plantarflexion.

under DF and PF. The stiffness decreased linearly with the increase of posterior trim depth for both DF and PF. With a 5-mm trim depth, the stiffness was reduced by about 15% during DF and 25% during PF. The difference between the DF and PF stiffness was also reduced when AFOs were trimmed to the posterior side of the ankle. With a 25-mm posterior trim depth, the AFO exhibited the same resistance to DF and PF motions. Figure 9c and d presents the deformation and stress contour of AFOs. The stress concentration on the ankle region reduced significantly when the posterior trim depth was increased. This suggests that increasing the trim depth in the posterior direction may reduce the stress concentration on the AFO, which is also beneficial to prevent potential fatigue failure.

A Design of Experiment (DoE) was also conducted to investigate the combined effects of posterior and inferior trim depths on AFO properties. Trim depths from 0 to 25 mm were considered for both directions, and 25 designs were evaluated to produce the response surface. A Python script was developed to prepare the FE model, extract the results, and calculate the DF and PF stiffness automatically. Figure 10a and b presents the DF and PF stiffness responses, respectively. It can be seen that both stiffnesses were sensitive to changes in posterior trim depth, while the increase of inferior trim depth led to reduced DF stiffness but posed limited effects on PF stiffness. Besides, both symmetrical and asymmetrical resistance of AFO against ankle rotations can be achieved. With a posterior trim depth of less than 5 mm, the AFO exhibited higher PF stiffness than DF stiffness, especially with increased inferior trim depth. By comparison, AFO can present symmetrical resistance against PF and DF by increasing the trim depth along the posterior direction. This enables the possibility of fine-tuning the responses of AFO to meet individual needs.

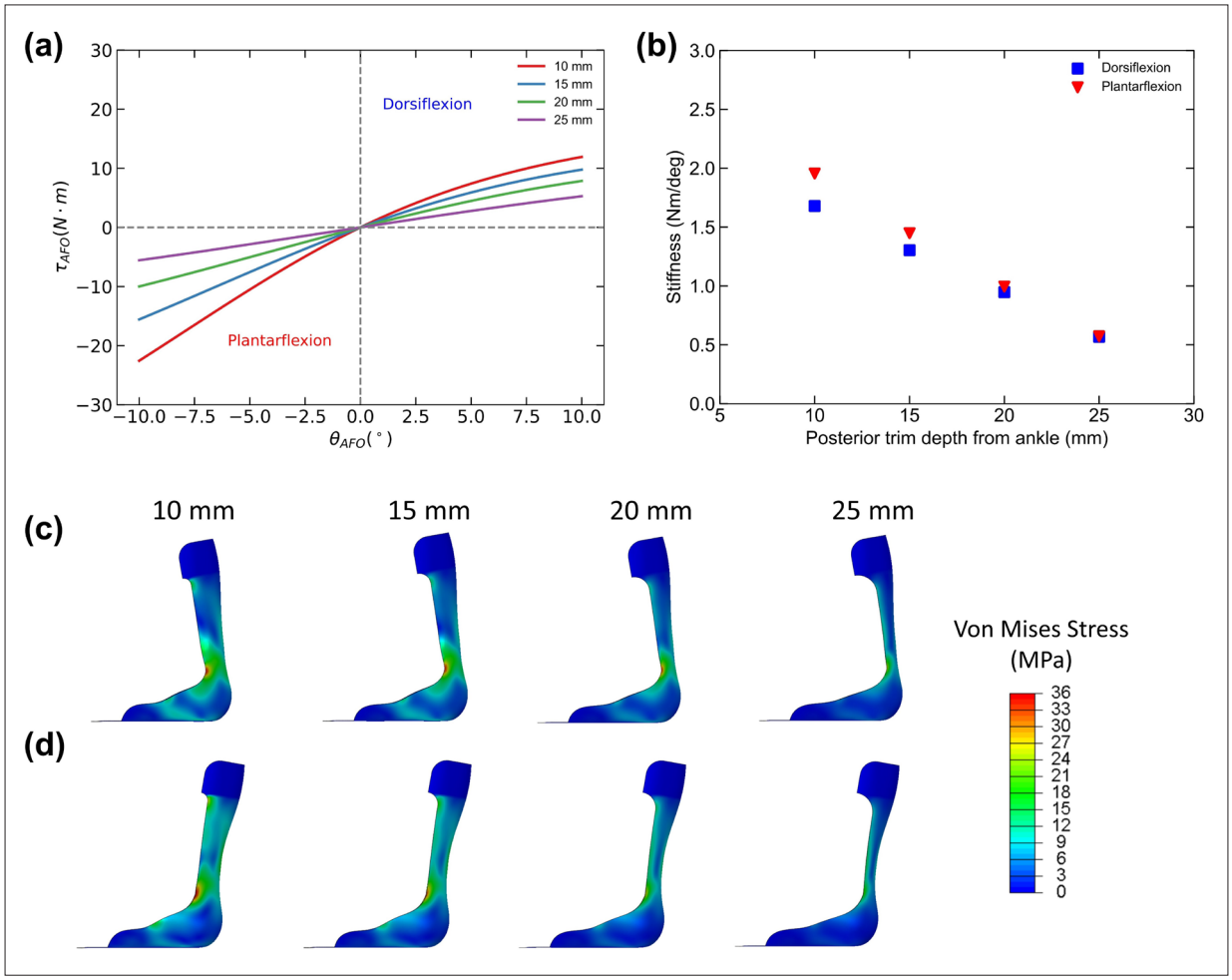


Figure 9. Effect of posterior trimline. (a) Ankle-foot orthosis (AFO) moment–ankle angle relationships of AFO with different posterior trim depths under plantarflexion and dorsiflexion; (b) The stiffness of AFO with different posterior trim depths. Deformation and stress contour of baseline with different posterior trim depths at 10° rotation: (c) dorsiflexion and (d) plantarflexion.

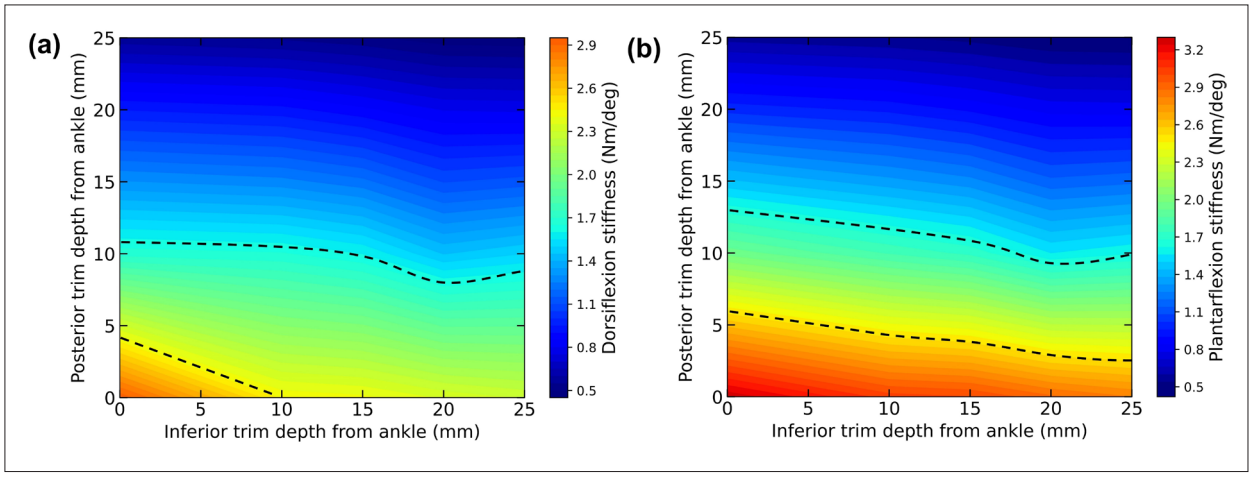


Figure 10. The effect of trimline location on (a) dorsiflexion and (b) plantarflexion stiffness.

Overall, the minimal impact of inferior trim depth on AFO stiffness suggested that alterations in the inferior direction may not be as critical in influencing the overall mechanical response of AFOs. Clinicians may find reassurance in maintaining flexibility in choosing inferior trim depths within a certain range without significantly compromising stiffness. On the other hand, the notable changes observed in DF and PF stiffness with variations in posterior trim depth highlight the importance of this parameter in determining the overall rigidity of AFOs. The substantial decrease in stress concentration around the ankle region with higher posterior trim depth suggested a potential enhancement in the overall comfort of AFOs. This reduction in stress concentration could be particularly beneficial in mitigating discomfort or pressure points around the ankle, enhancing its wearability, and minimizing the risk of adverse effects on the skin and soft tissues. Meanwhile, the reduction of stress concentrations may also be beneficial to prevent potential fatigue failure of AFOs.

4. Conclusion

The present study was designed to investigate the impact of base materials, thickness, and trimline variations on the stiffness and deformation of 3D-printed AFOs through a comprehensive parametric study based on numerical modeling. Firstly, the anatomical geometry of the foot and leg was established using a 3D-scanning system and reconstructed into a smooth surface representation. Subsequently, a baseline AFO design was created, 3D printed, and subjected to testing under uniaxial compression. An FE model was developed and validated using experimental data. The mechanical properties of PCTG, PA12, PA12-CF, and PLA were characterized through tensile tests. A parametric study on the effects of base materials, thickness, and trimline location was conducted.

The results indicated that AFOs responded differently to PF and DF stress, displaying a linear moment–ankle angle relationship in PF and a nonlinear response in DF with stress concentration around the ankle region. Increasing AFO thickness enhanced stiffness during both loading conditions with minimal impact on stress distribution, while the AFO stiffness–thickness relationship can be described by a power function. Trimline locations influenced AFO stiffness, with limited effect from inferior trim depth but linear reductions in stiffness with further posterior trimming. Larger trim depths reduced stress concentration around the ankle, potentially leading to better fatigue resistance.

Currently, AFO design relies heavily on observational assessments and clinical experience. 3D printing offers opportunities for standardization and expanded design possibilities, though decision-making becomes more complex. By bridging the gap between empirical design and technological advancements, the findings of this study can offer insights into the development and customization of 3D-printed AFOs for individuals with specific conditions.

Acknowledgments

This research was supported by The Lorenzo and Pamela Galli Medical Research Trust. The authors would like to thank Prof. Kerr Graham for reviewing and editing the manuscript.

Funding

None.

Conflict of interest

The authors declare no conflicts of interest.

Author contributions

Conceptualization: Chenxi Peng, Phuong Tran, Erich Rutz
Formal analysis: Chenxi Peng
Investigation: Chenxi Peng, Phuong Tran, Simon Lalor
Methodology: Chenxi Peng, Erich Rutz
Supervision: Erich Rutz
Writing – original draft: Chenxi Peng
Writing – review & editing: Phuong Tran, Simon Lalor, Oren Tirosh, Erich Rutz

Ethics approval and consent to participate

Not applicable.

Consent for publication

Not applicable.

Availability of data

The data that support the findings of this study are available from the corresponding author upon reasonable request.

References

1. Graham HK, Rosenbaum P, Paneth N, et al. Cerebral palsy. *Nat Rev Dis Primers*. 2016;2:15082. doi: 10.1038/nrdp.2015.82
2. Ma N, Gould D, Camathias C, Graham K, Rutz E. Single-event multi-level surgery in cerebral palsy: a bibliometric analysis. *Medicina*. 2023;59(11). doi: 10.3390/medicina59111922

3. Palmer FB, Shapiro BK, Wachtel RC, et al. The effects of physical therapy on cerebral palsy. A controlled trial in infants with spastic diplegia. *N Engl J Med*. 1988;318(13): 803-808.
doi: 10.1056/NEJM198803313181302

4. Rutz E, Hofmann E, Brunner R. Preoperative botulinum toxin test injections before muscle lengthening in cerebral palsy. *J Orthop Sci*. 2010;15(5):647-653.
doi: 10.1007/s00776-010-1509-6

5. De Pieri E, Romkes J, Wyss C, et al. Effect of botulinum toxin A on muscle function in patients with cerebral palsy and its relation to gait. *Gait Posture*. 2020;81:74-76.
doi: 10.1016/j.gaitpost.2020.07.062

6. Lintanf M, Bourseul JS, Houx L, Lempereur M, Brochard S, Pons C. Effect of ankle-foot orthoses on gait, balance and gross motor function in children with cerebral palsy: a systematic review and meta-analysis. *Clin Rehabil*. 2018;32(9):1175-1188.
doi: 10.1177/0269215518771824

7. Chisholm AE, Perry SD. Ankle-foot orthotic management in neuromuscular disorders: recommendations for future research. *Disabil Rehabil Assist Technol*. 2012;7(6):437-449.
doi: 10.3109/17483107.2012.680940

8. Schröder J-H, Barandun GA, Leimer P, Morand R, Göpfert B, Rutz E. Novel modular walking orthosis (MOWA) for powerful correction of gait deviations in subjects with a neurological disease. *Children*. 2024;11(1).
doi: 10.3390/children11010030

9. Ridgewell E, Dobson F, Bach T, Baker R. A systematic review to determine best practice reporting guidelines for AFO interventions in studies involving children with cerebral palsy. *Prosthet Orthot Int*. 2010;34(2):129-145.
doi: 10.3109/03093641003674288

10. Mason RDF, Vuletich W. Ankle-foot orthosis. Google Patents; 1981.

11. Zhou C, Yang Z, Li K, Ye X. Research and development of ankle-foot orthoses: a review. *Sensors*. 2022;22(17).
doi: 10.3390/s22176596

12. Wickramasinghe S, Do T, Tran P. FDM-based 3D printing of polymer and associated composite: a review on mechanical properties, defects and treatments. *Polymers*. 2020;12(7).
doi: 10.3390/polym12071529

13. Silva R, Veloso A, Alves N, Fernandes C, Morouco P. A review of additive manufacturing studies for producing customized ankle-foot orthoses. *Bioengineering (Basel)*. 2022;9(6).
doi: 10.3390/bioengineering9060249

14. Wojciechowski E, Chang AY, Balassone D, et al. Feasibility of designing, manufacturing and delivering 3D printed ankle-foot orthoses: a systematic review. *J Foot Ankle Res*. 2019;12(1):11.
doi: 10.1186/s13047-019-0321-6

15. Chen RK, Chen L, Tai BL, Wang Y, Shih AJ, Wensman J. Additive manufacturing of personalized ankle-foot orthosis. In: *Proceedings of Transactions of the North American Manufacturing Research Institution of SME (NAMRC42)*; 2014:42.

16. Cha YH, Lee KH, Ryu HJ, et al. Ankle-foot orthosis made by 3D printing technique and automated design software. *Appl Bionics Biomech*. 2017;2017:9610468.
doi: 10.1155/2017/9610468

17. Wojciechowski EA, Cheng TL, Hogan SM, et al. Replicating and redesigning ankle-foot orthoses with 3D printing for children with Charcot-Marie-Tooth disease. *Gait Posture*. 2022;96:73-80.
doi: 10.1016/j.gaitpost.2022.05.006

18. Kumar R, Kumar R, Kalra P, et al. Effectiveness of 3D printed carbon fiber composite strut in customized ankle foot orthosis. *Compos Struct*. 2023;324:117540.
doi: 10.1016/j.compstruct.2023.117540

19. Teng PSP, Leong KF, Kong PW, et al. A methodology to design and fabricate a smart brace using low-cost additive manufacturing. *Virtual Phys Prototyp*. 2022;17(4):932-947.
doi: 10.1080/17452759.2022.2090384

20. Liu Z, Zhang P, Yan M, Xie YM, Huang GZ. Additive manufacturing of specific ankle-foot orthoses for persons after stroke: a preliminary study based on gait analysis data. *Math Biosci Eng*. 2019;16(6):8134-8143.
doi: 10.3934/mbe.2019410

21. Ranz EC, Russell Esposito E, Wilken JM, Neptune RR. The influence of passive-dynamic ankle-foot orthosis bending axis location on gait performance in individuals with lower-limb impairments. *Clin Biomech (Bristol, Avon)*. 2016;37: 13-21.
doi: 10.1016/j.clinbiomech.2016.05.001

22. Vasiliauskaite E, Ielapi A, De Beule M, et al. A study on the efficacy of AFO stiffness prescriptions. *Disabil Rehabil Assist Technol*. 2021;16(1):27-39.
doi: 10.1080/17483107.2019.1629114

23. Mavroidis C, Ranky RG, Sivak ML, et al. Patient specific ankle-foot orthoses using rapid prototyping. *J Neuroeng Rehabil*. 2011;8(1):1.
doi: 10.1186/1743-0003-8-1

24. Totah D, Menon M, Jones-Hershinow C, Barton K, Gates DH. The impact of ankle-foot orthosis stiffness on gait: a systematic literature review. *Gait Posture*. 2019;69: 101-111.
doi: 10.1016/j.gaitpost.2019.01.020

25. Kerkum YL, Buizer AI, van den Noort JC, Becher JG, Harlaar J, Brehm MA. The effects of varying ankle foot orthosis stiffness on gait in children with spastic cerebral palsy who walk with excessive knee flexion. *PLoS One*. 2015;10(11):e0142878.
doi: 10.1371/journal.pone.0142878

26. Aboutorabi A, Arazpour M, Ahmadi Bani M, Saeedi H, Head JS. Efficacy of ankle foot orthoses types on walking in children with cerebral palsy: a systematic review. *Ann Phys Rehabil Med*. 2017;60(6):393-402. doi: 10.1016/j.rehab.2017.05.004

27. Sumiya T, Suzuki Y, Kasahara T. Stiffness control in posterior-type plastic ankle-foot orthoses: effect of ankle trimline. Part 2: orthosis characteristics and orthosis/patient matching. *Prosthet Orthot Int*. 1996;20(2):132-137. doi: 10.3109/03093649609164431

28. Bielby SA, Warrick TJ, Benson D, et al. Trimline severity significantly affects rotational stiffness of ankle-foot orthosis. *J Prosthet Orthot*. 2010;22(4):204-210. doi: 10.1097/JPO.0b013e3181f9082e

29. Shuman BR, Totah D, Gates DH, Gao F, Ries AJ, Russell Esposito E. Comparison of five different methodologies for evaluating ankle-foot orthosis stiffness. *J Neuroeng Rehabil*. 2023;20(1):11. doi: 10.1186/s12984-023-01126-7

30. Ielapi A, Forward M, De Beule M. Computational and experimental evaluation of the mechanical properties of ankle foot orthoses: a literature review. *Prosthet Orthot Int*. 2019;43(3):339-348. doi: 10.1177/0309364618824452

31. Bregman DJ, Rozumalski A, Koops D, de Groot V, Schwartz M, Harlaar J. A new method for evaluating ankle foot orthosis characteristics: BRUCE. *Gait Posture*. 2009;30(2):144-149. doi: 10.1016/j.gaitpost.2009.05.012

32. Shuman BR, Russell Esposito E. Multiplanar stiffness of commercial carbon composite ankle-foot orthoses. *J Biomech Eng*. 2022;144(1). doi: 10.1115/1.4051845

33. Totah D, Menon M, Gates DH, Barton K. Design and evaluation of the SMApp: a stiffness measurement apparatus for ankle–foot orthoses. *Mechatronics*. 2021;77. doi: 10.1016/j.mechatronics.2021.102572

34. Zou D, He T, Dailey M, et al. Experimental and computational analysis of composite ankle-foot orthosis. *J Rehabil Res Dev*. 2014;51(10):1525-1536. doi: 10.1682/JRRD.2014-02-0046

35. Stier B, Simon JW, Reese S. Numerical and experimental investigation of the structural behavior of a carbon fiber reinforced ankle-foot orthosis. *Med Eng Phys*. 2015;37(5):505-511. doi: 10.1016/j.medengphy.2015.02.002

36. Schrank ES, Hitch L, Wallace K, Moore R, Stanhope SJ. Assessment of a virtual functional prototyping process for the rapid manufacture of passive-dynamic ankle-foot orthoses. *J Biomech Eng*. 2013;135(10):101011-101017. doi: 10.1115/1.4024825

37. Syngellakis S, Arnold MA, Rassoulian H. Assessment of the non-linear behaviour of plastic ankle foot orthoses by the finite element method. *Proc Inst Mech Eng H*. 2000;214(5):527-539. doi: 10.1243/0954411001535561

38. Ielapi A, Lammens N, Van Paepegem W, et al. A validated computational framework to evaluate the stiffness of 3D printed ankle foot orthoses. *Comput Methods Biomech Biomed Engin*. 2019;22(8):880-887. doi: 10.1080/10255842.2019.1601712

39. Abdalsadah FH, Hasan F, Murtaza Q, Khan AA. Design and manufacture of a custom ankle–foot orthoses using traditional manufacturing and fused deposition modeling. *Prog Addit Manuf*. 2021;6(3):555-570. doi: 10.1007/s40964-021-00178-2

40. Sumihira W, Otani T, Kobayashi Y, Tanaka M. Computational modelling of ankle-foot orthosis to evaluate spatially asymmetric structural stiffness: importance of geometric nonlinearity. *Proc Inst Mech Eng H*. 2022;236(9):1357-1364. doi: 10.1177/09544119221114199

41. Eddison N, Mulholland M, Chockalingam N. Do research papers provide enough information on design and material used in ankle foot orthoses for children with cerebral palsy? A systematic review. *J Child Orthop*. 2017;11(4): 263-271. doi: 10.1302/1863-2548.11.160256

42. ASTM International. *Standard Test Method for Tensile Properties of Plastics*. West Conshohocken, PA: ASTM International; 2014. doi: 10.1520/D0638-14

43. Wickramasinghe S, Peng C, Ladani R, Tran P. Analysing fracture properties of bio-inspired 3D printed suture structures. *Thin Wall Struct*. 2022;176:109317. doi: 10.1016/j.tws.2022.109317

ACCSCIENCE PUBLISHING

International Journal of Bioprinting

RESEARCH ARTICLE

Engineered 3D-printed poly(vinyl alcohol) vascular grafts: Impact of thermal treatment and functionalization

Ionut-Cristian Radu[1], Derniza Cozorici[1], Madalina-Ioana Necolau[1], Roxana Cristina Popescu[2,3], Eugenia Tanasa[1], Laurentia Alexandrescu[4], Catalin Zaharia[1]*, and Rafael Luque[5]

[1]Advanced Polymer Materials Group, Department of Bioresources and Polymer Science, Faculty of Chemical Engineering and Biotechnology, National University of Science and Technology POLITEHNICA Bucharest, Bucharest, Romania

[2]Department of Bioengineering and Biotechnology, Faculty of Medical Engineering, National University of Science and Technology POLITEHNICA Bucharest, Bucharest, Romania

[3]Group of Biophysics and Radiobiology, Department of Life and Environmental Physics, National Institute for R&D in Physics and Nuclear Engineering "Horia Hulubei," Magurele, Romania

[4]Rubber Research Department, National Research and Development Institute for Textile and Leather, Division Leather and Footwear Research Institute (INCDTP Division ICPI), Bucharest, Romania

[5]Universidad ECOTEC, Km. 13.5 Samborondón, Samborondón, Ecuador

(This article belongs to the *Special Issue: Biomimetic and bioinspired printed structures*)

Abstract

Cardiovascular diseases, a leading cause of global mortality, are driving increased demand for artificial blood vessels for surgical repair. This study discloses the fabrication of three-dimensional (3D)-printed small blood vessels as tissue-engineered grafts. Large-diameter artery and vein grafts are readily available in the market, but small-diameter blood vessels face issues due to the lack of suitable materials. Lysine-biofunctionalized and unmodified poly(vinyl alcohol) grafts (PVA grafts) (2 mm inner diameter and 3 mm outer diameter) suitable for veins and venules were designed using Fusion 360 software, Autodesk Fusion. The PVA channels were fabricated from the 3D virtual model through fused deposition modeling using a PVA filament. These channels underwent thermal treatment to adjust their crystallinity, chemical crosslinking, and functionalization to optimize their mechanical properties and biocompatibility. Crosslinking and biofunctionalization were assessed using Fourier-transform infrared spectroscopy with attenuated total reflectance, while X-ray diffraction and differential scanning calorimetry were utilized for structural analysis. PVA grafts were biologically tested using three specific types of cell cultures: bEnd.3 brain endothelial cells, L929 fibroblast cells, and U937 monocyte-like cells. The hemocompatibility of the optimized vascular grafts was evaluated using horse blood, following the guidelines outlined in ASTM F756-13 Standard Practice for Assessment of Hemolytic Properties of Materials. The direct method for hemoglobin determination was specifically employed. Additionally, we developed an external polyethylene terephthalate glycol (PETG) 3D-printed platform to house the PVA grafts in parallel. The assembled platform (PETG and PVA graft) was connected to both an inlet and an outlet to facilitate the passage of an aqueous flow through the

***Corresponding author:**
Catalin Zaharia
(catalin.zaharia@upb.ro)

Citation: Radu IC, Cozorici D, Necolau MI, et al. Engineered 3D-printed poly(vinyl alcohol) vascular grafts: Impact of thermal treatment and functionalization. *Int J Bioprint*. 2024;10(3):2193. doi: 10.36922/ijb.2193

Received: November 6, 2023
Accepted: March 31, 2024
Published Online: June 10, 2024

Copyright: © 2024 Author(s). This is an Open Access article distributed under the terms of the Creative Commons Attribution License, permitting distribution, and reproduction in any medium, provided the original work is properly cited.

Publisher's Note: AccScience Publishing remains neutral with regard to jurisdictional claims in published maps and institutional affiliations.

internal section of the PVA grafts during a flow test conducted under simulated body conditions (vacuum and blood pressure: 40 mbar). The flow was induced by a vacuum pump connected to the outlet of the platform, while the inlet was connected to a feeding glass. In summation, we have established a suitable protocol for producing small vascular grafts and demonstrated that the optimization process could significantly affect graft properties.

Keywords: 3D printing; Poly(vinyl alcohol); Channel; Crosslinking; Vascular graft; Small vein

1. Introduction

Cardiovascular diseases have been one of the main causes of death around the world for decades. By 2030, the global annual mortality is predicted to increase to 23.3 million.[1,2] Demand for artificial blood vessels is increasing due to the growing incidence of vascular diseases, including occlusive vascular disease (coronary heart disease, peripheral arterial disease, critical atherosclerotic narrowing, rupture of the vascular walls, etc.)[3–6] or different types of cancer.[7,8] Despite the use of pharmacotherapy like vasodilators or anticoagulants, surgical repair remains an indispensable treatment option for patients with severe vascular diseases.[9] In this context, artificial blood vessels, serving as vascular grafts, are essential for surgical repair.

Their principle of artificial blood vessel development is conceptually simple and clinically attractive. In the current global vascular grafts market, artificial vascular grafts are widely employed, especially for larger diameter requirements. These advanced grafts play crucial roles in diverse medical scenarios, including facilitating hemodialysis blood access, addressing vascular trauma, managing aneurysms, and contributing to cardiovascular reconstruction.[10,11]

However, this approach has proven to be a significant challenge.[12,13] The history of vascular interventions began with early advancements in suturing and vessel replacement, with pioneers like Carrel and Goyanes demonstrating the feasibility of arteriovenous anastomoses and paving the way for modern vascular treatment.[14–16] The commonly used revascularization techniques include stent replacement, angioplasty, or bypass graft surgery. The autograft vessel approach is a preferred vascular technique for coronary artery bypass grafts but is inadequate and unsuitable for one-third of patients.[17,18] The commonly used and most efficient grafts are composed of non-biodegradable polymers, including poly(ethylene terephthalate) (PET), poly(tetrafluoroethylene) (PTFE), and expanded PTFE. These grafts are effective for large vessel replacement (>6 mm internal diameter), but lowly effective for small-diameter replacement (<5 mm internal diameter).[5,19,20] Polyurethanes, a non-biodegradable polymer class, are also used for small vessel replacement, owing to their compatibility (similar to PTFE-Dacron), thromboresistance (e.g., to thrombotic occlusion or anastomotic intimal hyperplasia),[21,22] and ability to promote tissue growth inside and around the grafts. However, their clinical use is limited by low biostability.[22] The low patency of most synthetic grafts in small-diameter vessel reconstruction is caused by reduced blood flow velocity, leading to thrombosis.[23] Hence, there is a need for alternative grafts to offer innovative solutions for small-diameter vessel replacement. Tissue engineering is an interdisciplinary alternative approach to designing grafts that meet clinical requirements. Tissue-engineered vascular grafts have been developed using acellular bovine and human tissue to construct a vessel-like structure.[24–26] However, collagen-based grafts exhibit inadequate mechanical properties, necessitating the use of an external mesh. The mechanical properties of grafts are extremely important, as biomaterial-based vascular grafts should support blood flow and maintain the featured structure in physiological conditions. The vascular graft should display both elasticity and fatigue resistance, among other properties.[27,28] For very small vessels, grafts must undergo permeability testing, with the fabrication process ensuring the formation of porous walls to sustain permeability.[29–32] These requirements often contribute to the failure of many biomaterial-based vascular grafts. Additionally, an ideal vascular graft should possess anti-thrombogenic features.

Poly(vinyl alcohol) (PVA) is a biodegradable synthetic polymer that features high biocompatibility, controlled water solubility, excellent charge storage ability, and nontoxicity, making it suitable for biomedical applications. In the pharmaceutical field, PVA is widely used for preparing solid dispersions aimed at enhancing drug solubility.[33,34] Other applications of PVA include the preparation of hydrogels,[35–39] sponges/meshes,[40,41] electrospun fibers,[42–44] films with high optical quality,[45] and membranes.[46] PVA hydrogels have been extensively researched over the years in various blends, owing to their excellent flexibility, biocompatibility, and versatility.[38] A synthetic small-diameter vascular graft was developed through the combination of PVA hydrogel with low-molecular-weight (low M_w) dextran, along with the incorporation of mesenchymal stem cells.[47–50] However, the mechanical

properties (crosslinking density, biofunctionalization, and elasticity) of PVA grafts require adjustments to be comparable to those of natural blood vessels as they are directly correlated to the crystalline and amorphous phases of PVA. The balance between crystalline and amorphous regions in polymers, including PVA can be optimized through thermal treatments.[51,52] Fabrication technique and parameters significantly influence compliance and mechanical integrity. A gold standard for these vascular grafts is rapid re-endothelialization of the luminal surface, as a healthy endothelium prevents thrombosis, stenosis, and intimal hyperplasia.[53,54] PVA vascular grafts have reported excellent bio-inertness, low thrombogenicity, high water content, and tunable properties, but challenges, such as immune response, rapid re-endothelialization, and complex viscoelastic behavior, remain to be addressed.

This study presents an innovative approach for the fabrication of PVA vascular grafts using fused deposition modeling. This approach is developed to enhance the production of small vascular grafts, vital in treating cardiovascular disorders. This study aimed to address two key challenges: optimizing mechanical properties and enhancing biocompatibility. Herein, we present the design of 3D-printed PVA channels subjected to thermal treatment, crosslinking, biofunctionalization, and comprehensive assessments. Taken together, we have established a suitable protocol for producing small vascular grafts and demonstrated that the optimization process could significantly affect graft properties.

2. Materials and methods

2.1. Materials

PVA (average M_w: 85,000–124,000 g/mol, 87–89% hydrolyzed; Sigma-Aldrich, United States of America [USA]), high M_w poly(lactic acid) (PLA) (PLA Crystal Clear, M_w: 182,000 g/mol; Fillamentum, Czech Republic), and polyethylene terephthalate glycol (PETG) (PolyLite PETG, M_w: 300,000 g/mol; Polymaker, China) filaments with a circular profile of 1.7 ± 0.1 mm in diameter and processing temperatures of 195–225, 200–210, and 210–240, respectively, were provided by 3D4ALL (Romania). Glutaraldehyde (GA) solution (25%) and acrylic resin (diurethane dimethacrylate, triethylene glycol dimethacrylate, DL-camphorquinone [CQ], and ethyl 4-dimethylaminobenzoate [EDMAB]) were purchased from Sigma-Aldrich (USA).

2.2. Cell culture

We cultured bEnd.3 brain endothelial cells (ATCC, USA) in Advanced Dulbecco's Modified Eagle Medium (ADMEM), supplemented with 10% fetal bovine serum, 1% L-glutamine, and 1% Penicillin-Streptomycin (Gibco, USA), in standard conditions (37°C; 5% CO_2; 90% humidity). L929 fibroblast cells (ATCC, USA) were cultured in Dulbecco's Modified Eagle Medium (DMEM), supplemented with 10% fetal bovine serum and 1% Penicillin-Streptomycin (Gibco, USA), in standard conditions (37°C; 5% CO_2; 90% humidity). U937 monocyte-like cells (ATCC, USA) were cultured in Roswell Park Memorial Institute Medium (RPMI) 1640, supplemented with 10% fetal bovine serum and 1% Penicillin-Streptomycin (Gibco, USA), in standard conditions (37°C; 5% CO_2; 90% humidity). Vascular graft samples were sterilized through gamma radiation exposure.

2.3. Design and 3D printing

The design of the channels and platform was created using Fusion 360 software. The channels had a diameter of 0.8 mm, a wall thickness of 0.4 mm, and a length of 50 mm (Figure 1A). The 3D printing model of the channels was configured using FlashPrint Software, version 5.5.1, Zhejiang Flashforge 3D technology Co., LTD before printing. In brief, the channels were secured on a support structure made from PLA (Figure 1B). The 3D printing parameters for the PVA channels were as follows: the hot end temperature was set to 220°C for PVA and 210°C for PLA, while the platform temperature was maintained at 60°C. The platform dimensions were 14 mm in height, 22 mm in width, and 50 mm in length (Figure 1C). Before printing, the platform 3D printing model was configured in FlashPrint software with the addition of supports (Figure 1D).

For the PETG platform, the 3D printing parameters included a hot end temperature of 240°C (due to the closed enclosure), with the platform temperature set to 70°C. Additionally, the 3D-printed platform was coated with acrylic resin on its surface to prevent fluid leakage. Acrylic resin is composed of a mixture of two monomers, diurethane dimethacrylate and triethylene glycol dimethacrylate, in a 1:1 weight ratio. The curing initiation system consists of a blend of DL-CQ and EDMAB in a 1:4 weight ratio. This curing mixture accounts for 1% (by weight) of the total amount of acrylic monomers. The curing process was carried out in an ultraviolet (UV) curing chamber (Figure 2).

2.4. Thermal treatment of poly (vinyl alcohol) channels

PVA is a synthetic water-soluble, whereby its solubility is closely associated with its crystallinity and degree of hydrolysis. PVA is obtained from the hydrolysis of poly(vinyl acetate) (PVAc). In basic conditions and with the use of a methanol/ethanol mixture, the acetate groups in PVAc are hydrolyzed into hydroxyl groups. A higher degree of hydrolysis (typically 98–99%) results in increased crystallinity, which makes dissolution more challenging (i.e., dissolution in >80°C water). Conversely, a hydrolysis

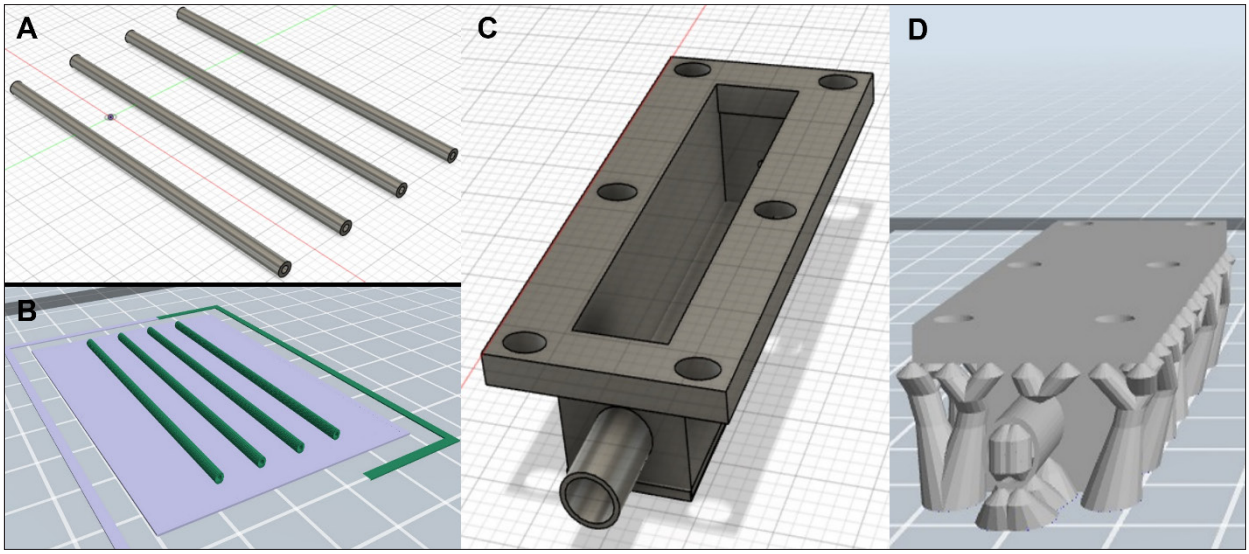


Figure 1. Computer-aided design of the polyvinyl alcohol (PVA) channels and platform: (A) 3D representation of the channels in Fusion 360 software; (B) 3D representation of the channels in the 3D printer software; (C) 3D representation of the polyethylene terephthalate glycol (PETG) platform in Fusion 360; (D) 3D representation of the PETG platform the 3D printer software.

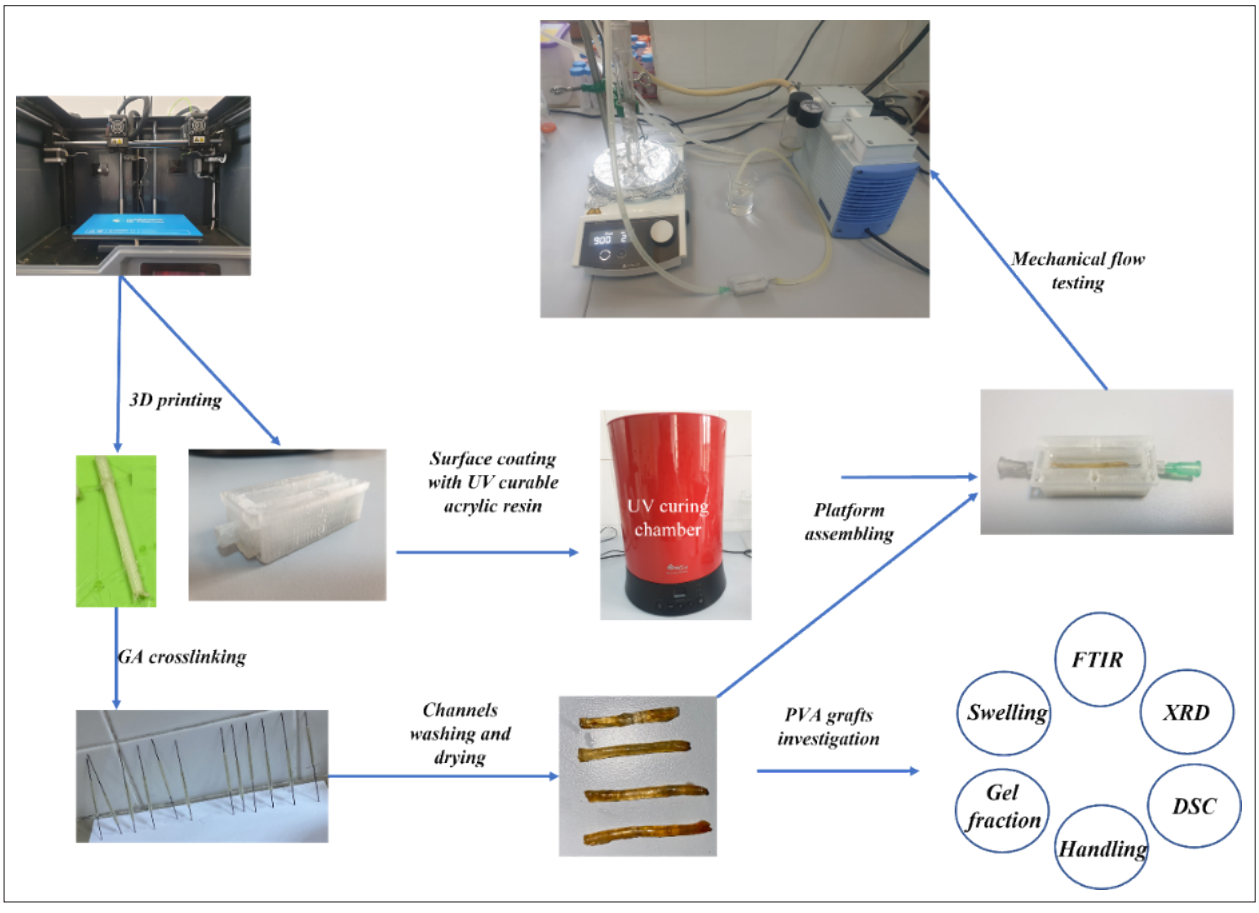


Figure 2. Schematic representation of the protocol for the fabrication and characterization of polyvinyl alcohol (PVA) grafts. Abbreviations: DSC: Differential scanning calorimetry; GA: Glutaraldehyde; FTIR: Fourier-transform infrared spectroscopy; UV: Ultraviolet; XRD: X-ray diffraction.

degree of approximately 88–92% facilitates dissolution (water temperature from room temperature to 40°C). Water solubility is also affected by the M_w of PVA, and the crystallinity is further affected by thermal treatment.

An increase in M_w or crystallinity negatively influences water solubility. The PVA filament used for channel development was water-soluble at room temperature (i.e., complete dissolution after 6–9 h at room temperature). The crosslinking process with GA was performed in aqueous media, which may be inconvenient from a dissolution perspective. To decrease PVA solubility at room temperature, thermal treatment was proposed to increase the degree of crystallinity. In this context, both the PVA filament and the PVA-printed channels underwent thermal treatment at 50°C (above the glass transition temperature [T_g]) for 1 and 3 days. The samples were labeled 0D (without any thermal treatment), 1D (1-day thermal treatment), and 3D (3-day thermal treatment), respectively, i.e., Filament 0D, Filament 1D, Filament 3D, Printed 0D, Printed 1D, and Printed 3D.

2.5. Crosslinking process

All channels subjected to crosslinking were derived from the untreated filaments. The crosslinking process was performed using GA aqueous solution. The printed channels (0D, 1D, and 3D) were subjected to crosslinking for 3 and 24 h (each sample was performed in triplicate) to study the effect of time. The samples are referred to as 0D-3H (no thermal treatment; 3 h crosslinking), 0D-24H (no thermal treatment; 24 h crosslinking), 1D-3H (1-day thermal treatment; 3 h crosslinking), 1D-24H (1-day thermal treatment; 24 h crosslinking), 3D-3H (3-day thermal treatment; 3 h crosslinking), and 3D-24H (3-day thermal treatment; 24 h crosslinking). After crosslinking, the channels were dried at room temperature for 1 week. The dried channels were immersed in a water bath for 1 day and dried again at room temperature for 1 week. After the crosslinking and drying-washing cycles were complete, the samples were considered PVA grafts (small veins).

2.6. Biofunctionalization of poly(vinyl alcohol) graft with lysine

Graft biofunctionalization plays a specific role in improving biocompatibility and cytotoxic responses. The 3D-3H graft was subjected to biofunctionalization with lysine. A lysine aqueous solution was prepared (2% w/v) at room temperature for 1 h (pH 8–8.5). Vascular grafts were added to the lysine solution: four grafts (~0.2 g each) in 20 mL solution. The biofunctionalization reaction was performed for 8 h at room temperature. After the reaction, the samples were washed with distilled water and placed in a glass bottle for purification for 1 week. The final sample was dried and stored. A schematic representation of the biofunctionalization reaction is displayed in Figure 3.

2.7. Characterization

2.7.1. Fourier-transform infrared spectroscopy

The Fourier-transform infrared spectroscopy (FTIR) spectra of PVA grafts were recorded on a Bruker Vertex 70 FTIR spectrophotometer with attenuated total reflectance (ATR) over 32 scans and 4 cm^{-1} resolution in the mid-InfraRed region.

2.7.2. X-ray diffraction

X-ray diffraction (XRD) spectra were recorded using the Panalytical X'PERT MPD X-ray Diffractometer in the 2θ range of 10–80°. A CuKα-radiation X-ray beam with a wavelength (λ) of 1.5418 Å was used. XRD analysis was conducted to investigate the effect of thermal treatment on the degree of crystallinity for both PVA channels (not crosslinked) and filaments.

2.7.3. Differential scanning calorimetry

The NETZECH differential scanning calorimeter (DSC) 204 was used to investigate the thermal and structural behavior of PVA channels (not crosslinked) and filaments. The analysis was performed in a nitrogen atmosphere (99.99% purity) with a 5°C/min heating rate and two complete heating–cooling cycles. Samples weighing 20 mg were placed into aluminum pans, covered, and secured onto the sample platform.

2.7.4. Swelling measurements

The swelling behavior (SD) of PVA grafts (both dried and crosslinked PVA channels) was assessed in phosphate-buffered saline (PBS) at 37°C. The mass change was recorded at regular time intervals during the swelling process. The swelling degree was determined according to the following equation:

$$SD = \frac{W_t - W_0}{W_0} \times 100\% \quad \text{(I)}$$

where W_t and W_0 represent the weight of the swollen samples at a predetermined time and the weight of the initial sample, respectively. The swelling measurement was conducted in triplicate for each sample. Swelling equilibrium was achieved when the weight of the swollen sample remained constant.

2.7.5. Morphological investigation by scanning electron microscopy

Morphological investigation of the functionalized vascular graft surface was performed using scanning electron microscopy (SEM). The analysis was performed using the

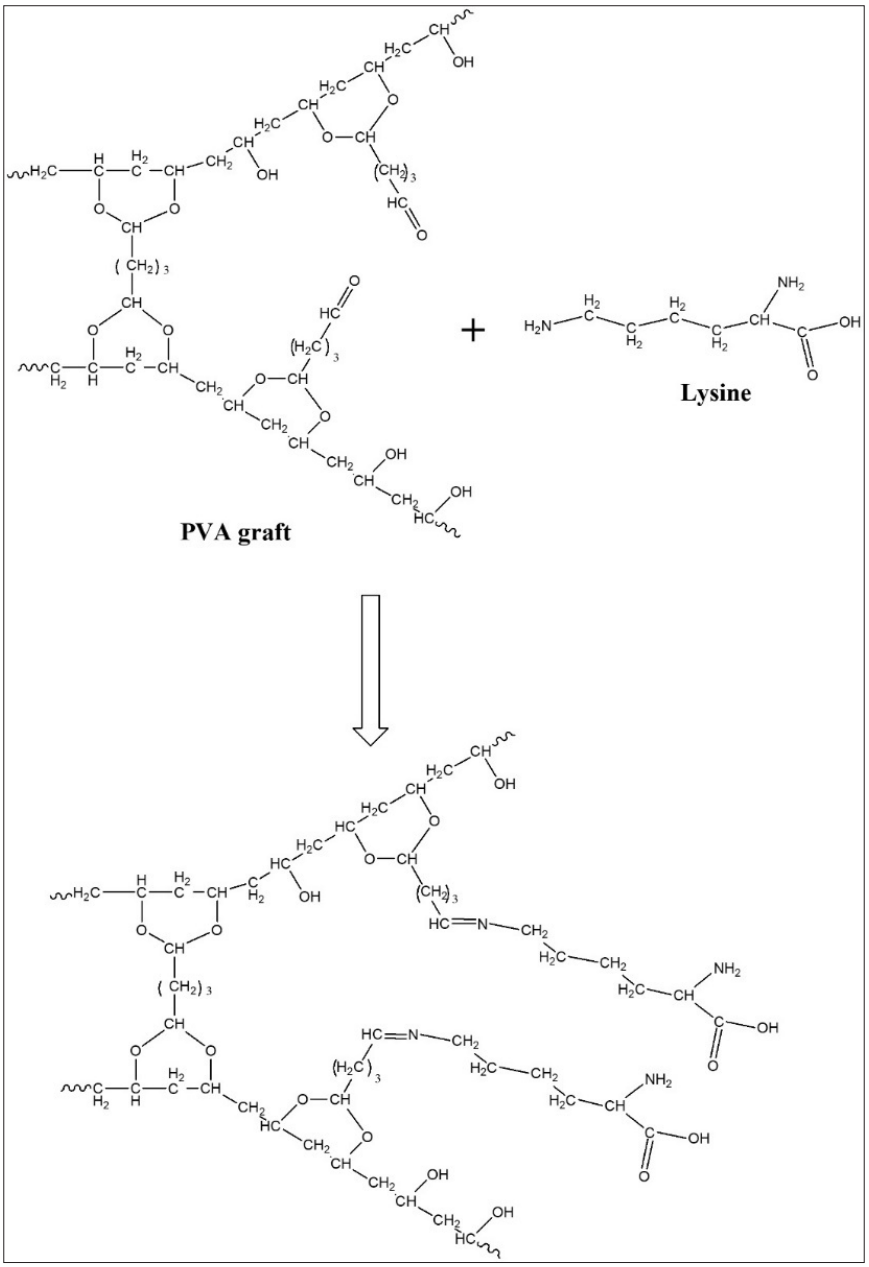


Figure 3. Schematic representation of the lysine-modified poly(vinyl alcohol) (PVA) graft.

QUANTA INSPECT F SEM device (FEI Company, USA) equipped with a field emission gun with a resolution of 1.2 nm and an X-ray energy dispersive spectrometer.

2.7.6. Tensile evaluation

Tensile testing of lysine-biofunctionalized and unmodified PVA grafts was performed using an Instron device equipped with a 5 kN load cell. Samples were swollen for 1 h before testing. Five specimens from each sample were securely fixed between the mechanical grips (model 2716-010) of the instrument by using a tightening mechanism for stability. Tests were conducted at room temperature, considering the average diameter of each type of specimen of 4 ± 0.05 mm and an elongation rate of 5 mm/min.

2.7.7. Mechanical flow testing

The mechanical flow testing involved assembling the PVA grafts into an external platform. This external platform featured two metallic channels: one with a diameter of 0.3 mm and another with a diameter of 0.8 mm. The smaller

metallic channel served as the platform input and was connected to the feeding glass via a flexible hose (Figure 8). The larger metallic channel represented the platform output and was linked to a collector and a vacuum pump using another flexible hose (Figure 8). Both ends of the PVA graft were secured onto the metallic channels using acrylic resin.

To initiate the water flow, the vacuum pump was activated, causing water to move from the feeding pump to the collector (feeding glass-hose-platform-hose-collector). The vacuum pump was set to 40 mbar to simulate normal vasculature conditions (resembling small veins). The water collected in the collector was then used to derive the velocity and fluid flow.

2.8. Biological assessment

2.8.1. Extract method

The extract was prepared according to ISO 10993-5:2009 (Biological evaluation of medical devices; Part 5: Tests for *in vitro* cytotoxicity) and ISO 10993-12:2012 (Biological evaluation of medical devices; Part 12: Sample preparation and reference materials). The previously sterilized samples were immersed in a complete culture medium at a ratio established according to ISO standards. The samples were incubated for 24 h at 37°C, under orbital shaking (50 rpm) inside a thermostatic bath. Following the incubation period, the extraction medium was separated from the samples and filtered using a 0.22-µm pore membrane. The prepared medium was used for cell treatment. The cellular substrate was prepared by seeding 5000 cells/well inside a 96-well plate. The cells were incubated for 24 h to facilitate their attachment. Following the incubation period, the culture medium (the supernatant) was removed from the wells and replaced with the extraction medium. The treated cells were incubated in standard conditions for another 24 h. Thereafter, optical microscopy images of the cells were captured, and cell viability, adenosine triphosphate (ATP) production, and lactate dehydrogenase (LDH) release were quantified as follows:

(i) MTT viability assay: Following the incubation period, the extraction medium was removed and replaced with MTT solution (Serva Electrophoresis Gmbh, Germany) in complete medium (10% 5 mg/mL MTT) and incubated for 2 h in standard conditions. This method measures cell metabolism following the transformation of the MTT tetrazolium salt into formazan crystals. Cell metabolism is directly proportional to its viability. Following the incubation period, the supernatant was removed, and the resultant formazan crystals were solubilized using dimethyl sulfoxide (DMSO). The absorbance of the samples was determined at 570 nm.

(ii) ATP production assay: ATP production is measured through luminescence produced via a reaction between luciferin and luciferase, catalyzed by ATP. The CellTiter-Glo 2.0 Viability Assay (Promega, USA) was used in this study. To measure luminescence, the cells were plated in solid white 96-well plates with a flat bottom (Corning, USA) and treated with graft extract according to the protocol described above. Following the incubation time, the cell samples were prepared according to the producer's specifications, and the luminescence was measured accordingly.

(iii) LDH release assay: Following the incubation period, 50 µL of the supernatant in each well was collected and added to a clean well in a new 96-well plate to measure LDH released by cells. LDH is a cytosolic enzyme that acts as a catalyst in the metabolism of lactate to pyruvate. LDH is released in the extracellular medium due to cell membrane breakages. Hence, extracellular LDH level is a measure of cell death following necrosis. To measure released LDH following the cells' exposure to the extract, the CyQUANT LDH Cytotoxicity Assay (Invitrogen, USA) was used. Samples were prepared according to the producer's specifications and the absorbance was measured at 490 nm.

2.8.2. Direct contact method

Vascular graft samples were immersed overnight in complete cell culture media to remove any possible cytotoxic residues resulting from the collection method. Following this, 100,000 cells/well were seeded in 24-well plates and incubated for 24 h to facilitate attachment. A graft sample was then directly added into each well and incubated for another 24 h in standard conditions. Thereafter, optical microscopy images of the cells were captured, and cell viability, ATP production, and LDH release were quantified as follows:

(i) MTT viability assay: Following the incubation period, the samples and medium were removed and replaced with MTT solution (Serva Electrophoresis Gmbh, Germany) in complete culture medium (10% 5 mg/mL MTT) and incubated for 2 h in standard conditions. Following incubation, the supernatant was removed, and the resultant formazan crystals were solubilized using DMSO. The absorbance of the samples was determined at 570 nm.

(ii) ATP production assay: Following the incubation period, the samples were removed from each well. ATP production was measured using CellTiter-Glo 2.0 Viability Assay (Promega, USA) according to the producer's specifications, and the luminescence was measured accordingly.

(iii) LDH release assay: Following the incubation period, 50 µL of the supernatant in each well was collected and added to a clean well in a new 96-well plate to measure LDH released by cells. To measure the released LDH following the cells' exposure to the vascular graft, the CyQUANT LDH Cytotoxicity Assay (Invitrogen, USA) was used. Samples were prepared according to the producer's specifications, and the absorbance was measured at 490 nm. For non-adherent U937 monocyte cells, the sample was removed from the well, and the cells and cell culture were collected in Eppendorf tubes to be centrifuged at 400 rpm for 5 min. The supernatant was collected, and LDH release was measured. For all quantitative measurements, blank samples were prepared (extract/medium without cells and dilutions). The blank absorbance was subtracted from the cell samples' absorbance to eliminate any possible interferences.

All experiments were performed in triplicate. Cell viability and LDH release were calculated relative to negative control samples (untreated cells). Data are reported as mean ± standard deviation (SD). Statistical analysis was performed using Student's *t*-test, with statistical significance at $^{*}p < 0.05$, $^{**}p < 0.01$, and $^{***}p < 0.001$.

2.9. Hemocompatibility evaluation

Hemocompatibility evaluation of the optimized vascular grafts was performed on horse blood acquired from the "Cantacuzino" National Medico-Military Institute Research and Development (Romania), which is accredited to produce and commercialize laboratory animals and serums. Whole blood from three healthy animal donors was collected on heparin. The testing was performed according to ASTM F756-13 (Standard practice for assessment of hemolytic properties of materials), i.e., the direct method for hemoglobin determination.

Drabkin's Reagent (Sigma-Aldrich, USA) was used to quantitatively determine hemoglobin release. The reagent was prepared according to the producer's specifications and reconstituted in deionized water with 30% Brij L23 solution (Sigma-Aldrich, USA).

A calibration curve was obtained using a cyanmethemoglobin standard solution of 180 mg/mL hemoglobin (hemoglobin equine; Sigma-Aldrich, USA) in Drabkin's regent. Serial dilutions of the standard were performed, and the absorbance was measured at 540 nm. The slope of the standard curve was determined using Microsoft Excel as 0.000134 mg/mL (absorbance).

Plasma-free hemoglobin and total blood hemoglobin (TBH) were determined according to ASTM F756-13, using Drabkin's reagent. To adjust the TBH concentration to 10 ± 1 mg/mL, whole pooled blood was diluted with Ca/Mg-free PBS. Following this step, the diluted TBH concentration was verified.

The samples were prepared according to the guidelines, and the corresponding quantities were suspended in 7 mL PBS. Negative control was prepared using 40% poly(ethylene glycol) (PEG) 8000 and positive control using 10% Tween-100 in PBS. Approximately 1 mL of diluted blood was added to each sample and then incubated at 37°C for 3 h with mixing every 30 min.

Following the incubation period, tubes containing the samples were centrifuged at 700 rpm for 15 min, and the supernatant was carefully collected. The supernatant of each sample was diluted to 1:1 with Drabkin's reagent and incubated for 15 min. Thereafter, the absorbance of the samples was measured at 540 nm. The percentage of hemolysis for each sample was determined as follows:

$$Hemolysis(\%) = \frac{Sample\ hemoglobin\ absorbance - blank\ absorbance}{TBH - blank\ absorbance} \times 100\% \quad \text{(II)}$$

by dividing the blank-corrected samples' supernatant hemoglobin absorbance by the blank-corrected TBH concentration of the diluted blood and subsequently multiplying with 100. The samples' acceptance criteria described in the ASTM F756-13 were followed.

3. Results and discussion

3.1. Development of lysine-functionalized and unmodified poly(vinyl alcohol) grafts

After crosslinking and drying, PVA channels are generally regarded as grafts. The starting material, PVA filament, was subjected to thermal treatment to investigate its potential impact on the PVC channels post-printing. The findings indicated a notable increase in the crystallinity of the PVA filament. However, there was no significant influence observed on the 3D-printed channels compared to the non-thermally treated filament. Henceforth, the study proceeded with thermal-treated 3D-printed channels, which demonstrate a significant impact on both crystallinity and crosslinking density. After crosslinking, only PVA grafts, 3D-1H and 3D-3H, exhibited sufficient stability for biofunctionalization with lysine and subsequent mechanical flow testing (Table 1). Specifically, PVA graft 3D-3H (biofunctionalized and unmodified) was successfully tested for mechanical flow and subsequently

Table 1. Essential insights into the polyvinyl alcohol (PVA) grafts

Sample	Stability		
	Microchannel development	Chemical modification and lyophilization	Flow testing
0D-3H	Not stable	Not stable	Not stable
1D-3H	Stable	Not stable	Not stable
3D-3H	Stable	Stable	Stable
0D-24H	Not stable	Not stable	Not stable
1D-24H	Not stable	Not stable	Not stable
3D-24H	Not stable	Not stable	Not stable

Abbreviations: D: Duration of thermal treatment (days); H: Duration of crosslinking (hours).

prepared for biological assessments (discussed in subsequent sections).

3.2. Fourier-transform infrared spectroscopy with attenuated total reflectance

Fourier-transform infrared spectroscopy with attenuated total reflectance (FTIR-ATR) was performed to assess the chemical interactions between the 3D-printed PVA channels and GA during the crosslinking process (Figure 4A). To illustrate the chemical interactions occurring within the PVA channels (0D-3H, 0D-24H, 1D-3H, 1D-24H, 3D-3H, and 3D-24H), the prominent peaks associated with acetate and hydroxyl groups from PVA were identified. Therefore, the main peaks are as follows: 3375 cm^{-1} attributed to the stretching vibration of the

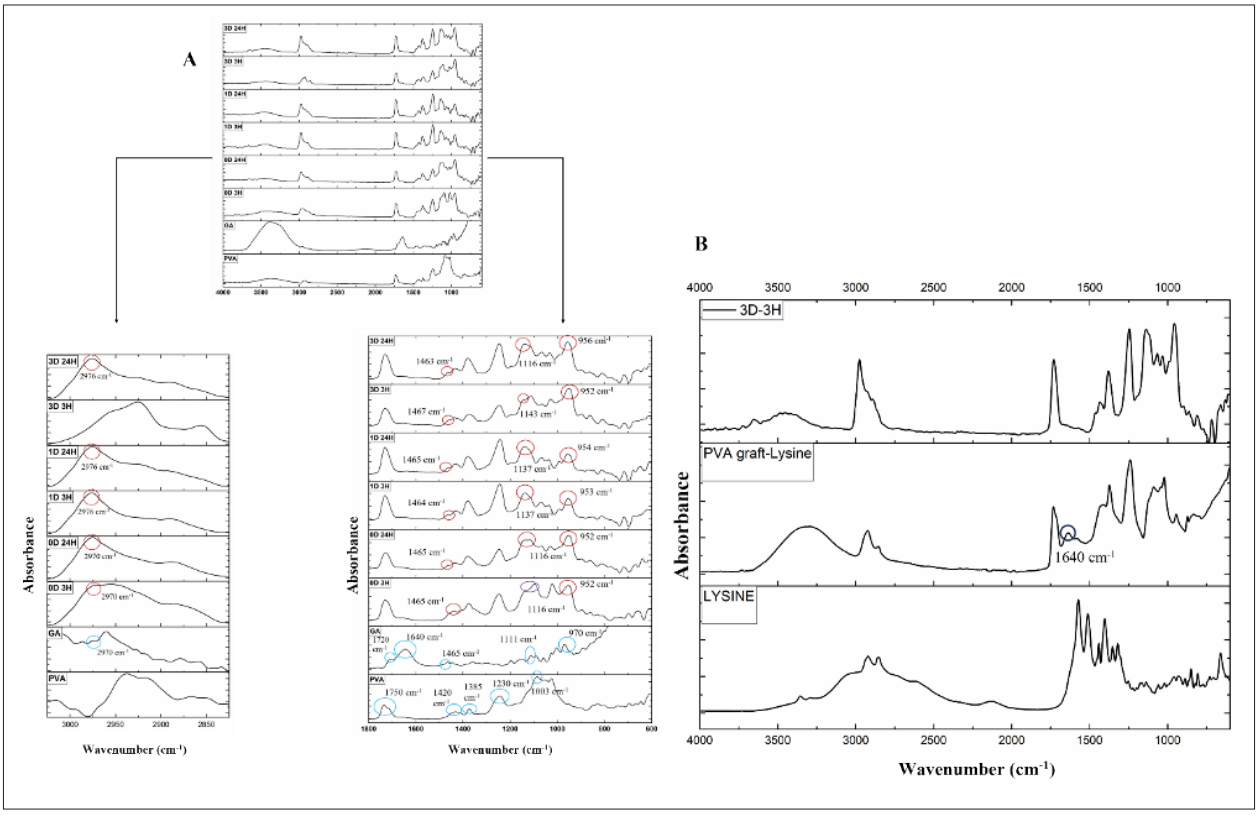


Figure 4. Fourier-transform infrared spectroscopy (FTIR) spectra: (A) poly(vinyl alcohol) (PVA), glutaraldehyde (GA), and crosslinked PVA channels; and (B) lysine-modified PVA graft (3D-3H-lysine) and unmodified PVA graft (3D-3H). Abbreviations: D: duration of thermal treatment (in days); H: duration of crosslinking (in hours).

hydroxyl group and intermolecular/intramolecular hydrogen bonding; 2940 and 2908 cm^{-1} attributed to the stretching vibration of C–H from alkyl groups (methyl and methylene); 1750 cm^{-1} assigned to the stretching vibration in the acetate group; 1420 and 1385 cm^{-1} attributed to the bending vibration of C–H from alkyl groups; 1230 cm^{-1} specific to the structural backbone; and 1090 cm^{-1} assigned to C–O–C and C–O stretching vibrations (crystallinity).[55] GA spectrum analysis suggests chemical interactions that occur during crosslinking: peak at 3381 cm^{-1} attributed to the intermolecular hydrogen bonding due to water presence (GA in aqueous solution); peaks at 2978, 2970, and 2760 cm^{-1} attributed to the stretching vibration of C–H from alkyl groups; peak at 1720 cm^{-1} assigned to the stretching vibration in carbonyl group; and the peak at 1640 cm^{-1} assigned to the hydrogen bonding of GA interaction with water molecules. Considering GA in aqueous solution, the hydrogen bonding contribution is high enough to appear in the hydroxyl region (3381 cm^{-1}) and carbonyl region;[56] however, the stretching vibration of C=C bond due to aldol condensation between two GA molecules is not excluded;[57] peaks in the region 1465–1380 cm^{-1} are attributed to the bending vibration of C–H from alkyl groups. The C–C bond and structural peaks in the region 1111–900 cm^{-1} are also present. The spectra of the crosslinked channels were directly related to the previously presented peaks. The main peaks that reveal chemical crosslinking are further described. The structural peak at 970 cm^{-1} from GA is present in all crosslinked samples (shifted toward lower values); a new peak in the region 1143–1111 cm^{-1} (specific for each crosslinked sample) may be attributed to acetal and semi-acetal bridges due to crosslinking; a peak at 1465 cm^{-1} is present in all crosslinked samples; the peak at 3375 cm^{-1} has a decreased intensity due to hydroxyl group consumption (specific for each crosslinked sample); a peak at 2970 cm^{-1} is present in almost all crosslinked samples (shifted toward higher values). Sample 3D-3H displayed only a shoulder of this peak without any shifting. Samples 0D-3H and 0D-24H revealed a peak decrease at 3375 cm^{-1} while samples 3D-3H and 3D-24H revealed a lower decrease. This result suggests that the hydroxyl group was consumed in a higher percentage of the samples without any thermal treatment.

The biofunctionalization of PVA grafts with lysine was examined using FTIR-ATR. The results are depicted in Figure 4B. The FTIR spectrum of the lysine-functionalized PVA graft revealed a new peak at 1640 cm^{-1}, which can be attributed to the stretching vibration in C=N bonds. This type of bonding is possible by the reaction of the carbonyl group of aldehydes with an amino group from lysine. Therefore, lysine was linked to PVA through GA. This reaction is possible because the acetal bridges provided by the aldehyde and hydroxyl groups of PVA do not always consume both sides of the aldehyde. Thus, the free sides of the aldehyde are available for new bonding of one of the amino groups from lysine. This approach is further supported by the reaction conditions, specifically the basic pH, which restricts esterification between the hydroxyl group from PVA and the carboxyl group from lysine (an alternative pathway).

3.3. X-ray diffraction analysis

XRD was conducted to reveal the direct relationship between the thermal treatment and crystallinity degree of PVA filament and 3D-printed channels. The correlation between thermal treatment and PVA crystallinity influenced the corresponding crosslinking behavior. Figure 5 (left side) displays the crystallinity of the PVA filament following thermal treatment. The filament without thermal treatment (Filament 0D) presented an important peak at 2θ 19.6° specific for the monoclinic crystal with an orthorhombic lattice (1 0 1 plane). In the case of PVA with a high crystallinity degree, the crystal was strong enough to exhibit two peaks for 1 0 1 and 2 0 0 planes. According to the literature, the second peak may appear before or after the main peak. The two peaks can merge into one if the crystal is not sufficiently strong, as in this case.[58–60] This main peak appears because of the intermolecular interactions between PVA chain segments in the main direction of the intermolecular hydrogen bonding. The peak intensity is correlated with the number of PVA chains packed together. The increased intensity indicates a larger crystallite size.[61] A secondary broad peak appeared at 2θ 46° due to the semi-crystalline arrangement of PVA chains. Filaments treated for 1 day (Filament 1D) and 3 days (Filament 3D) revealed a new peak at 2θ 12.6°, which corresponded to a strong PVA crystal. This result suggests a direct correlation between crystallinity and thermal treatment. Furthermore, the Debye–Scherrer equation was used to better observe the influence of thermal treatment on crystallinity by estimating the crystallite size.[62] Table 2 displays the estimated crystallite size, the relative number of layers in the crystallite, and the full width at half maximum (FWHM). The results reported an increase in crystallite size with thermal treatment time in the case of the filament. The relative number of the crystalline layers increased for the peak 2θ 46°, suggesting that less-ordered domains started to arrange due to hydrogen bonding. FWHM values revealed that the peaks tended to be sharper because of the more ordered crystalline state. For 3D-printed PVA channels (Figure 5, right side; Table 1), the investigation demonstrated the same correlation as in the case of the PVA filament. Thermal treatment favored chain-ordering behavior, resulting in higher crystallinity. PVA behavior is similar to that of other polymers that

Table 2. Values of crystallite size, number of crystalline layers, and full width at half maximum (FWHM) for thermally treated and untreated polyvinyl alcohol (PVA) channels (filament vs. 3D-printed)

PVA channel	Duration of thermal treatment (days [D])	Crystallite size (Å)			Number of crystalline layers			FWHM		
		12.6°	19.6°	46°	12.6°	19.6°	46°	12.6°	19.6°	46°
Filament	0	-	9.49	4.76	-	2.1	2.44	-	7.5	19
	1	13.93	9.6	5.17	2	2.13	2.55	6	6	17
	3	16.5	8.45	11.3	2.35	1.89	5.2	5	6.8	8
3D-printed	0	9	9.33	5.39	1.33	2.1	2.69	6	6.5	17
	1	13.58	9.37	4.7	1.88	2.13	2.21	6	6.2	13
	3	14.79	9.22	12.5	2.17	2.06	5.95	6	6.3	7

begin to undergo chain arrangements under thermal treatment.[63] The results suggest that crystallinity may be correlated with crosslinking ability, as indicated by the FTIR results. It appears that the hydroxyl groups, which are responsible for strong hydrogen bonding, are less involved in the crosslinking process.

3.4. Differential scanning calorimetry analysis

DSC analysis evaluated the impact of thermal treatment on T_g, the melting temperature (T_m), and the 3D printing process. In this context, the samples underwent two heating/cooling cycles within the range of −20–200 °C. Figure 6A illustrates the heating (left side) and cooling (right side) processes for the first run, while Figure 6B depicts the heating (left side) and cooling (right side) processes for the second run. The first heating run displayed an endothermic inflection with a hysteresis peak at approximately 40°C. This behavior is specific to glass transition events (T_g) with enthalpy relaxation. Another broad endothermic peak, specific to melting (T_m), was observed. However, the cold crystallization peak was absent. T_g and T_m values for the untreated filament (Filament 0D) and heat-treated filaments were similar, indicating the lack of significant effects. For 3D-printed channels, the T_g value increased by more than 20°C (30.6–52°C), owing to the thermal treatment process. Furthermore, the shape of the hysteresis peak changed upon thermal treatment until the treatment ended. These results suggest that significant changes occurred in the PVA amorphous phase in a more ordered state. The 3D-printed channel without any thermal treatment (Printed 0D) reported a particular endothermic peak at 108.6°C, which could be due

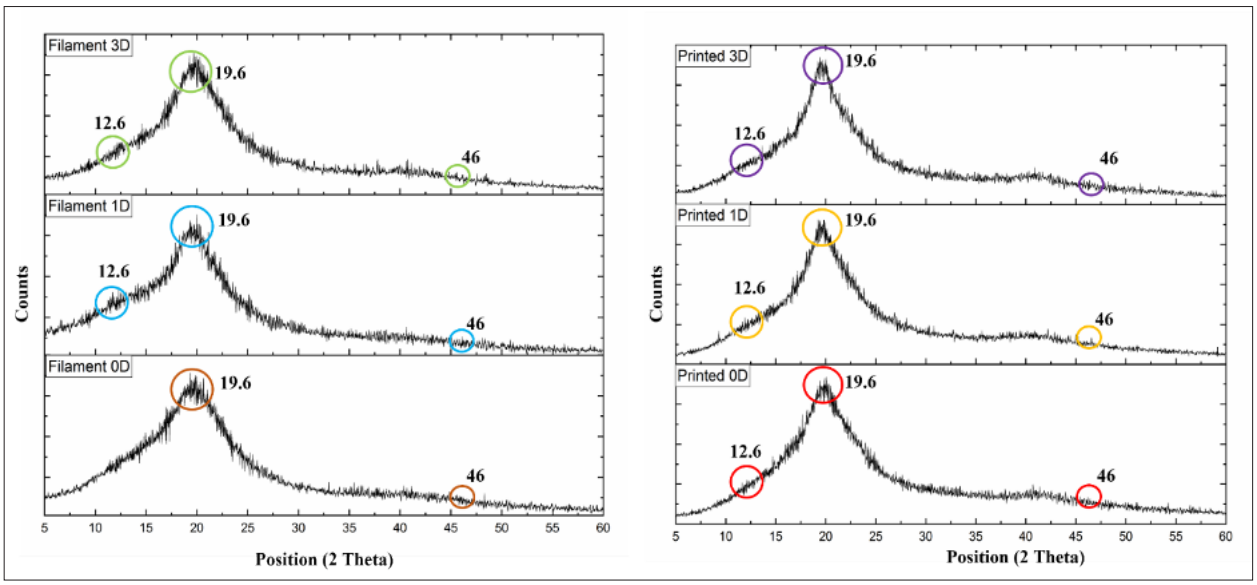


Figure 5. X-ray diffraction (XRD) diffractograms for thermally treated and untreated samples: filament (left side) and 3D-printed channels (right side). Abbreviation: D: duration of thermal treatment (in days).

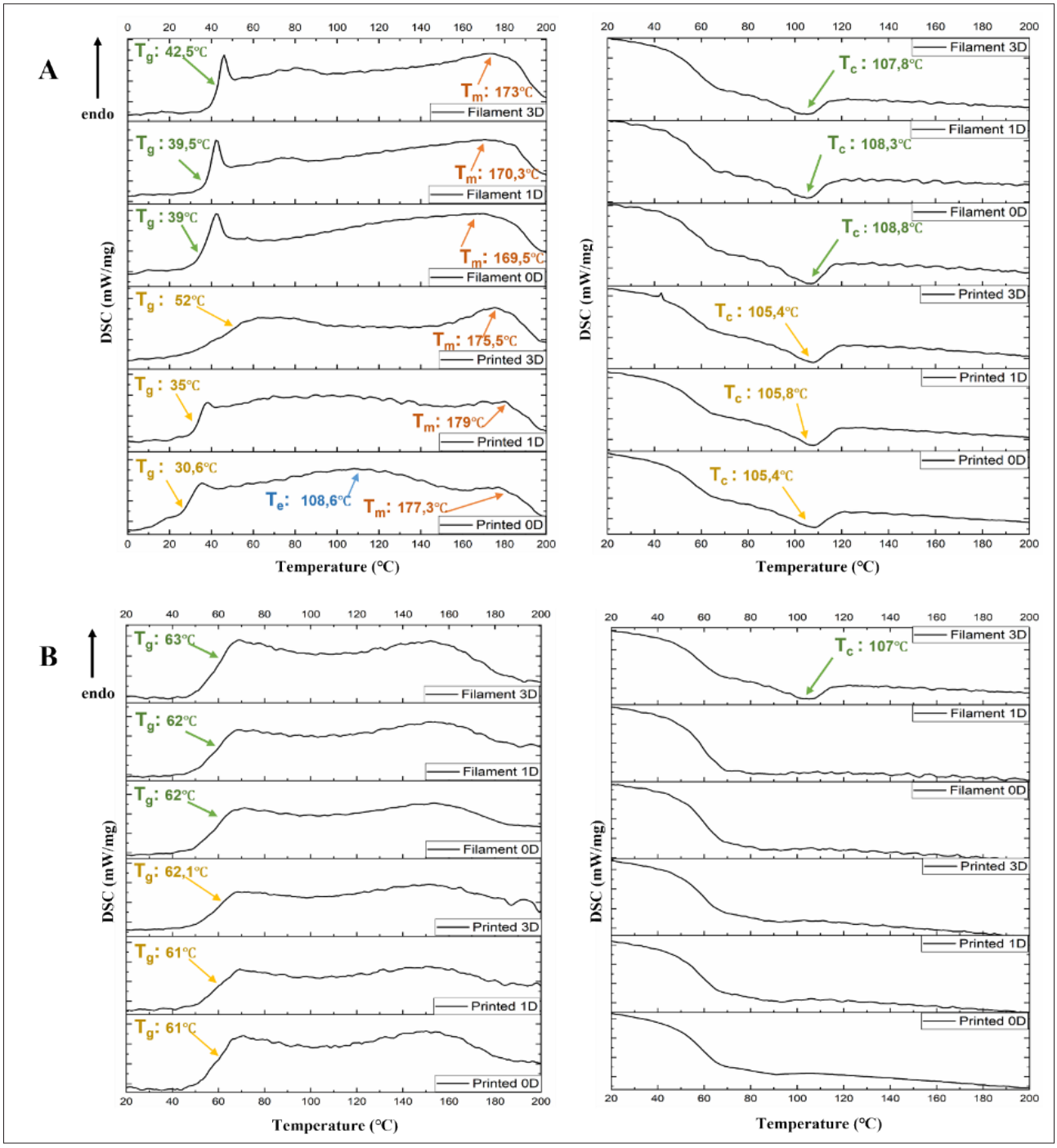


Figure 6. Differential scanning calorimetry (DSC) curves: (A) the first run of heating (left side) and cooling (right side); (B) the second run of heating (left side) and cooling (right side). Abbreviations: D: duration of thermal treatment (in days); T_c: crystallization temperature; T_e: water evaporation temperature; T_g: glass transition temperature; T_m: melting temperature.

to water molecule evaporation. As this peak was not present for samples Filament 1D and Filament 3D, two major conclusions may be drawn: (i) the 3D-printed PVA channels are more susceptible to water absorption than the original PVA filaments, and (ii) water molecules may play an important role in the crystallinity of PVA. Water molecules may act as plasticizers for PVA chains, hindering the crystallization process. During the thermal

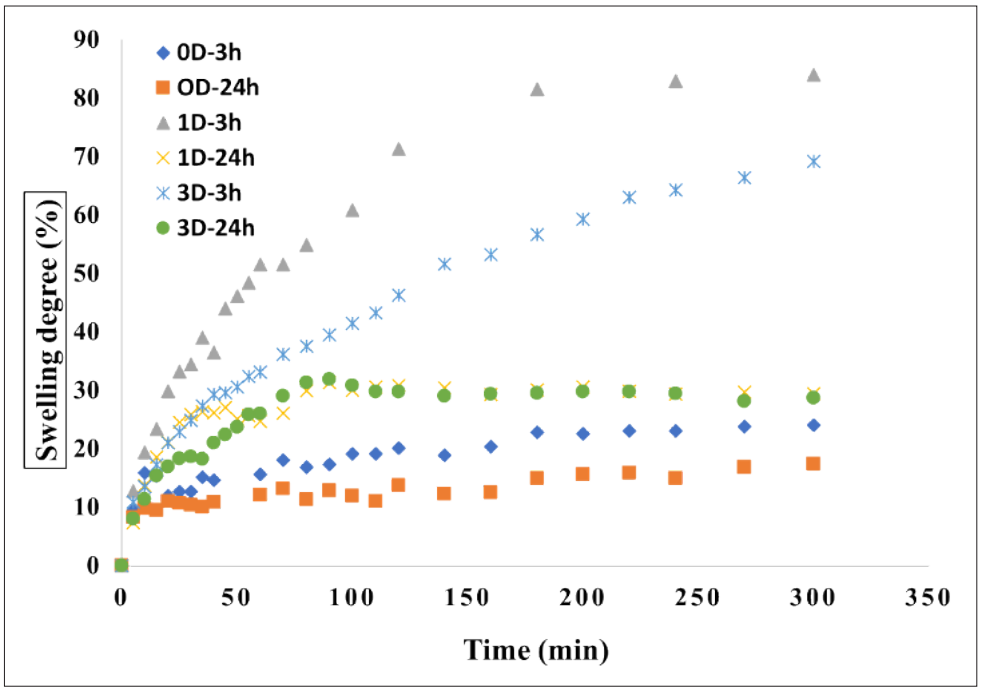


Figure 7. Swelling measurements. Abbreviations: D: duration of thermal treatment (in days); h: duration of crosslinking (in hours).

treatment lasting 1 or 3 days, the removal of water molecules occurred, thereby doubling the favorability of the crystallization process. Both the mobility of chain segments and the removal of water molecules influence this crystallization process.

The initial cooling run exhibited a broad exothermic peak characteristic of melt cooling within the range of 105–108°C, indicating the occurrence of crystallization. The second heating run was influenced by the first cooling event. The hysteresis peak disappeared, and the T_g values were approximately 60°C for all samples. The second cooling run revealed melt crystallization only for the sample Filament 3D, as there were remaining chains where ordering was favored.

The thermal treatment temperature is of utmost importance because a temperature similar to or above T_g promotes chain segment mobility. This rationale guided the decision to optimize the thermal treatment at 50°C. During 3D printing, PVA crystallites melted, and the highly ordered domains gained during the initial thermal treatment were lost. This indicates that the thermal treatment of the PVA filament would not have any additional influence on the 3D-printed channels. Consequently, the crystallinity of the 3D-printed channels can only be controlled through thermal treatment. This explains the absence of crosslinked channels from a heat-treated filament. The DSC results are consistent with the XRD data, indicating that thermal treatment favors chain crystallization.

3.5. Swelling degree

Swelling analysis is an important aspect of assessing the crosslinking process of the PVA channels. Crosslinked channels obtained under various conditions (0D-3h/0D-24h, 1D-3h/1D-24h, and 3D-3h/3D-24h) were used for the swelling investigation. Small pieces were cut and immersed in PBS at pH 7.4 and 37°C. Figure 7 displays the swelling behavior of various PVA grafts. The swelling equilibrium was reached after 300 min for all samples. Samples subjected to thermal treatment (1 and 3 days) and with 3 h of crosslinking had the highest swelling values, probably because of the decrease in network density (Figure 7, 1D-3h/3D-3h). The increase in crosslinking time to 24 h drastically reduced the swelling values, owing to the increase in network density (Figure 7, 1D-24h/3D-24h). For samples without any thermal treatment, the swelling degree was low for both 3 and 24 h of crosslinking because of the high network density. However, there was a small difference between 3 and 24 h of crosslinking (Figure 7, 0D-3h/0D-24h). Thermal treatment positively influenced the crystallinity degree. Higher PVA crystallinity resulted in decreased swelling and dissolution capacity during the crosslinking process. Specifically, higher crystallinity negatively affected the crosslinking process, leading to a lower network density. It was noted that samples 1D-3h and 3D-3h exhibited lower network densities. However, extending the crosslinking time to 24 h allowed sufficient time for the PVA channels to swell with GA, thereby

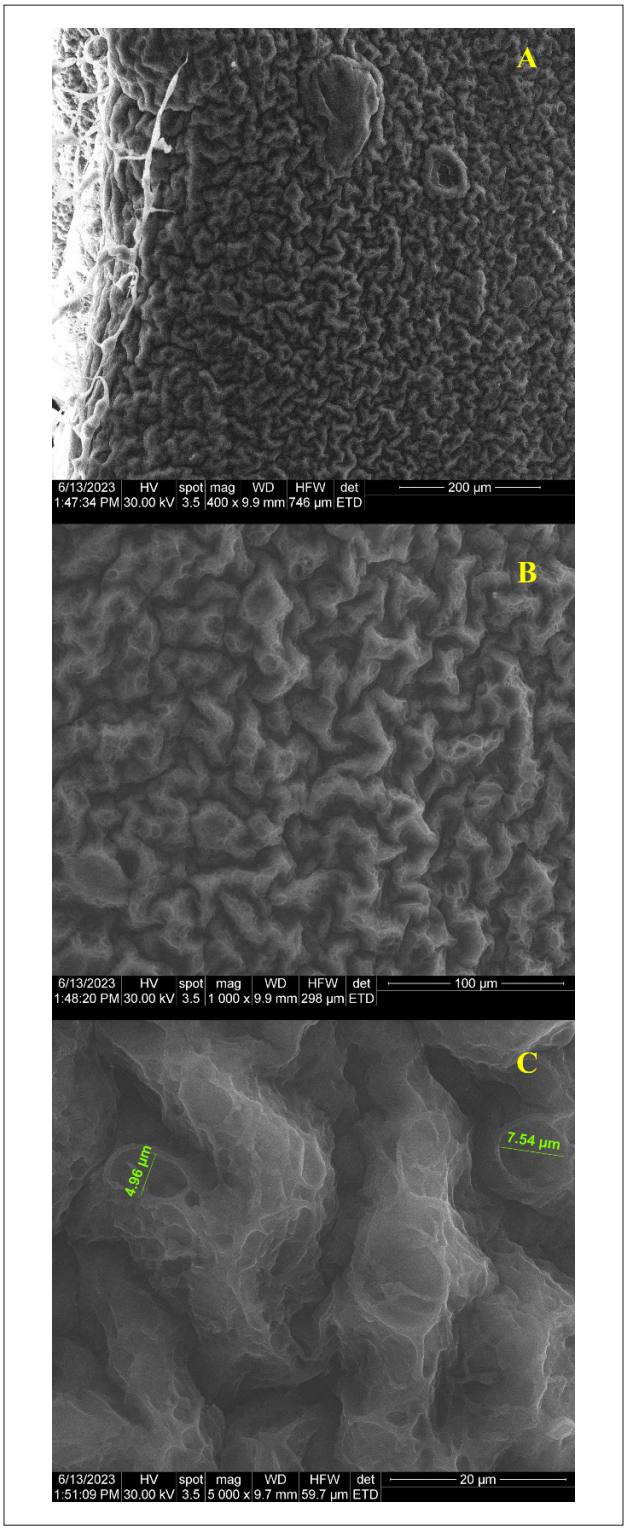


Figure 8. Scanning electron microscope (SEM) images of the lysine-functionalized poly(vinyl alcohol) (PVA) grafts. Magnification: (A) 400×; (B) 1000×; and (C) 5000×. Scale bars: (A) 200 µm; (B) 100 µm; and (C) 20µm.

increasing the degree of crosslinking or network density and decreasing the degree of swelling.

3.6. Poly(vinyl alcohol) graft morphology

The lysine-biofunctionalized PVA graft (3D-3H) was subjected to surface morphology investigation to unveil its support-like characteristics, crucial for biological assessment. The surface of the graft displayed a rough topography characterized by high irregularities and open pores measuring approximately 4–10 µm (Figure 8).

3.7. Tensile evaluation

A mechanical investigation was performed to determine the sample's response when subjected to tensile stress. The samples were pre-swollen in water for 1 h to induce the flexible behavior of a vascular graft. Figure 9 displays the response of both unmodified and lysine-biofunctionalized PVA grafts. The unmodified PVA graft displayed a broad yield region/plateau around 30–35% tensile strain, followed by gradual propagation of sample failure. Up to 30% strain, the unmodified PVA graft exhibited a gradual increase in response to the strain. The maximum stress in the yield region was 0.23 MPa. In contrast, the biofunctionalized PVA graft exhibited a distinct behavior compared to the unmodified PVA grafts. The sample displayed a linear stress/strain dependency, with increased resistance to stress propagation. The yield region was also broad, with a maximum tensile stress of about 0.58 MPa. The tensile stress at break was more than double that of the unmodified PVA graft, displaying a linear response. Biofunctionalization emerges as a key approach for both enhancing biocompatibility and improving mechanical properties. The biofunctionalized specimen demonstrated a more elastic behavior, likely due to the higher network density facilitated by new inter/intramolecular physical interactions and chemical bonding.

3.8. Mechanical flow testing

Among the PVA grafts, 1D-3H and 3D-3H exhibited sufficient stability for mechanical testing (for fatigue resistance). The grafts were secured onto the platform using acrylic resin, and the platform was then connected to both the feeding glass (containing water) and the vacuum pump (Figure 10). The vacuum pump was set to 40 mbar, and the test commenced. The vacuum induced the fluid (water) from the feeding glass to traverse the flexible hose and reach the PVA graft through the 0.3 mm metallic channel. The fluid passed through the PVA graft and exited via the 0.8 mm metallic channel. Subsequently, the fluid was collected in the glass collector. To detect any fluid leakage, the platform was filled with water to cover the PVA graft. During fluid drainage, the 1D-3H graft began to fracture due to the applied vacuum forces. However, the 3D-3H

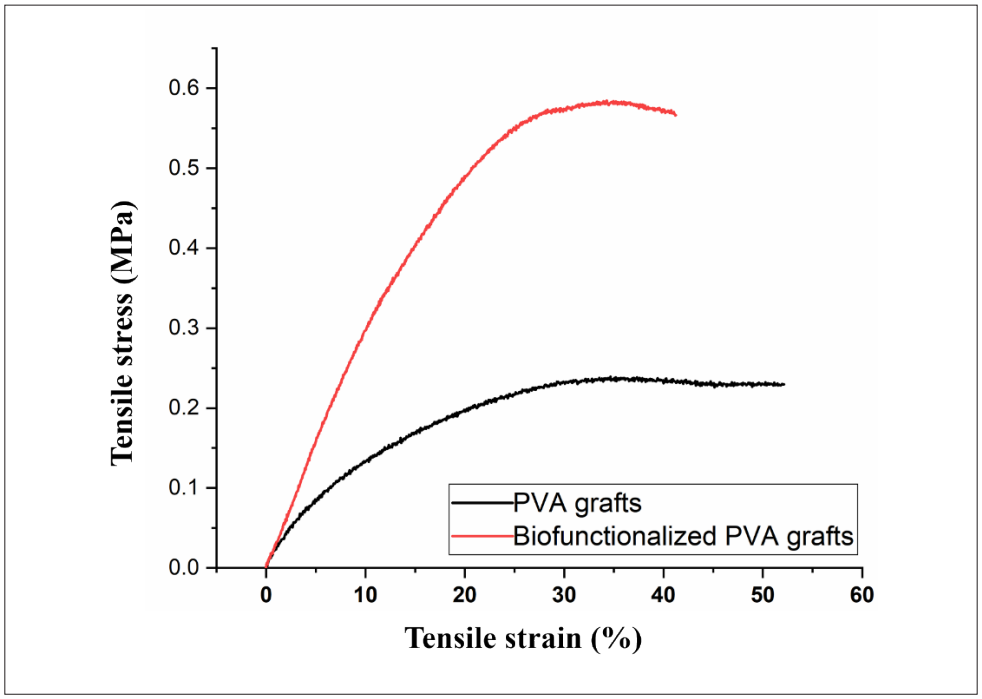


Figure 9. Stress–strain curves for unmodified poly(vinyl alcohol) (PVA) grafts and biofunctionalized PVA grafts.

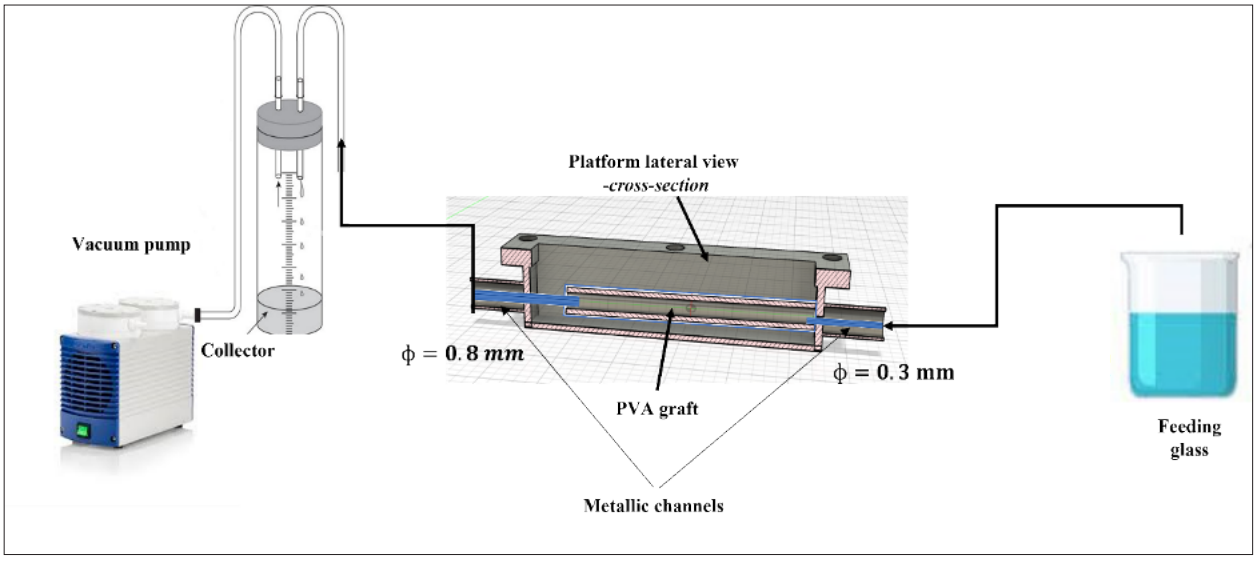


Figure 10. Schematic representation of biofunctionalized poly(vinyl alcohol) (PVA) graft flow testing.

graft successfully passed the test, owing to its greater mechanical stability. The input was facilitated by a metallic channel with a smaller diameter (0.3 mm) to maintain a continuous flow without fluctuations, while the metallic channel with a larger diameter (0.8 mm) served as the output. The fluid flow consisted of eight cycles, each lasting 60 min. Throughout the process, the water level covering the PVA graft remained constant, indicating that drainage occurred solely with water from the feeding glass. This observation suggests that any potential fluid leakage was effectively prevented. The collected water was measured to determine the flow velocity, which was calculated to be 11

cm/s. These results align well with the reported conditions of normal vasculature documented in the literature.[64]

3.9. Biological assessment

Vascular graft biocompatibility in the vascular tissue environment is an essential requirement for newly developed materials to be used for such applications.[65] The biological behavior of the vascular graft was investigated *in vitro* for cells present in the natural vascular tissue. For this, we employed (i) bEnd.3 endothelial cells to represent cells in the lumen; (ii) L929 to represent fibroblast cells normally present in the outer layer of the vascular wall; and (iii) U937 monocyte-like cells to represent immune cells.

3.9.1. Biocompatibility assessment of initial vascular grafts using the extract method

The biocompatibility of the initial vascular graft (unmodified and 3D-3H) for endothelial cells was tested using the extract method, according to ISO 10993-5:2009 and ISO 10993-12:2012. The extract medium was diluted to 1:1, 1:2, 1:5, and 1:10, respectively. The viability of the endothelial

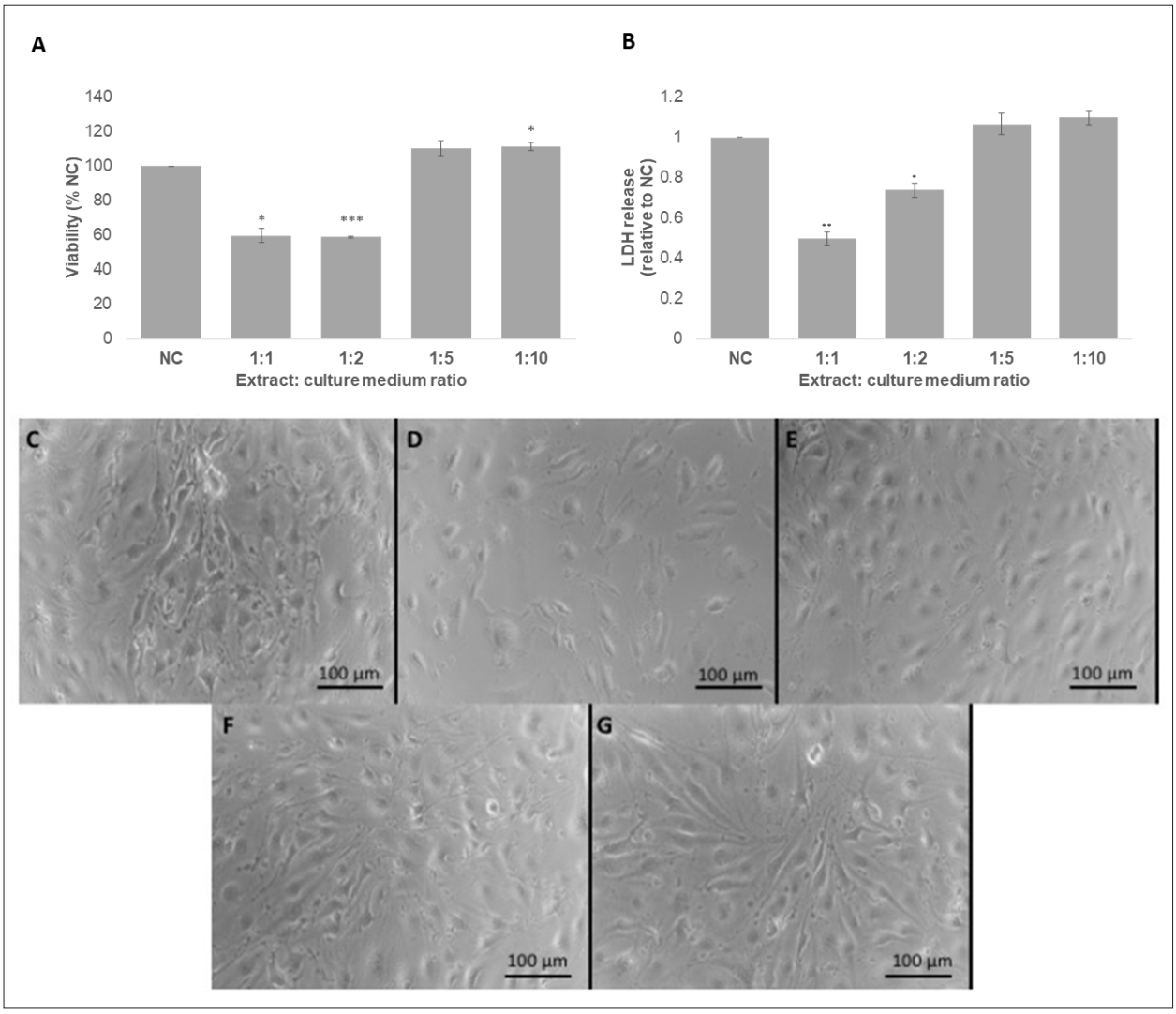


Figure 11. Biocompatibility assessment of initial vascular grafts using the extract method. (A) Viability of bEnd.3 endothelial cells following a 24-h incubation with vascular graft extract and dilutions of the extract in cell culture medium (via MTT assay). Data presented as mean ± standard deviation; $^{*}p < 0.05$; $^{***}p < 0.001$. (B) Levels of lactate dehydrogenase (LDH) released from bEnd.3 endothelial cells following a 24-h incubation with vascular graft extract and dilutions of the extract in cell culture medium (via LDH assay). Data presented as mean ± standard deviation; $^{*}p < 0.05$; $^{**}p < 0.01$. (C–G) Morphology of bEnd.3 endothelial cells following a 24-h incubation with vascular graft extract and dilutions of the extract in cell culture medium: (C) negative control (NC), (D) 1:1 graft extract, (E) 1:2 graft extract in cell culture medium, (F) 1:5 graft extract in cell culture medium, and (G) 1:10 graft extract in cell culture medium. Magnification: ×10.

cells, following a 24-h exposure to the biomaterial extract in cell culture medium and extract dilutions, was measured using the MTT assay. The metabolic activity of the cells is a direct measure of their viability and an indicator of vascular graft biocompatibility. Viability above 70% is considered a threshold for biocompatibility, according to ISO 10993-5:2009.

The viability of the endothelial cells exposed for 24 h to undiluted vascular graft extract decreased by 40.21 ± 4.25% compared to the control cells, resulting in a slightly cytotoxic behavior ($p < 0.05$) (Figure 11A). A similar effect was obtained for the 1:2 diluted extract in cell culture media, whereby the cells had a viability of 58.97 ± 0.58% compared to the control cells ($p < 0.001$) following a 24-h incubation period (Figure 11A). LDH release (Figure 11B) from cells exposed to undiluted extract and 1:2 diluted extract reported a reduced amount compared to the control cells ($p < 0.05$), indicating that necrosis is not the induced cell death pathway for bEnd.3 cells. Instead, this reduction suggests a decrease in cell number, evidenced by the slight reduction in cell density in the optical microscopy images (Figure 11D and E).

This slight cytotoxic effect can be attributed to the release of weakly attached GA molecules that were not incorporated into PVA via crosslinking. In contrast, 1:5 and 1:10 diluted extracts reported biocompatibility (cell viability was approximately 100%) with similar LDH release compared to the negative control (Figure 11A and B). Cellular morphology and density were also similar to the non-treated controls (Figure 11C, F, and G).

3.9.2. Biocompatibility assessment of initial vascular grafts using the direct contact method

To simulate the endothelial cells' direct contact with the initial vascular graft, an endothelial cell monolayer was seeded and grown for 24 h prior to the addition of the vascular graft sample. For this, samples of the graft were cut to have similar dimensions. Additionally, the samples were soaked and incubated overnight in a complete culture medium to eliminate any cytotoxic residues from the biomaterial extract. Thereafter, the graft samples were directly added on top of the cell monolayer and incubated for another 24 h in standard conditions.

Viability assay measurements displayed a slight reduction of the cells' metabolic activity with 13.47 ± 10.9% relative to the negative control (Figure 12A), indicating biocompatibility according to ISO 10993-5:2009. Additionally, LDH release reported no significant differences compared to the negative control (Figure 12B). These results were confirmed by morphological evaluations of the cell monolayer following incubation with the graft, displaying unchanged cell shape or density relative to the negative control (Figure 12C–F).

A cytotoxic effect is induced by the extract of the material in the cell culture of the initial vascular graft in the presence of bEnd.3 endothelial cells. A cell culture medium wash was subsequently applied to the graft to evaluate the direct contact effect on the endothelial cells. Following this washing step, the cytotoxic residues were removed from the graft, resulting in a biocompatible effect.

3.9.3. Biocompatibility assessment of the modified vascular graft using the extract method

Additionally, the material was functionalized using lysine to increase the biocompatibility of the graft for cells in the vascular environment. The resulting modified vascular graft biocompatibility was assessed for endothelial cells, fibroblasts, and monocytes to determine the metabolic behavior (MTT and ATP assays) and integrity (LDH assay) of the cells.

The modified graft 3D-3H-lysine displayed improved biocompatibility compared to the initial vascular graft for bEnd.3 endothelial cells, with a viability of 77.8 ± 2.56% compared to the negative control ($p < 0.01$) (Figure 13A). ATP production in the graft extract-treated endothelial cell culture was above 80% compared to the negative control ($p < 0.01$) (Figure 13B). LDH release is lower than the negative control, i.e., at 0.157 ± 0.051 compared to non-treated cells ($p < 0.05$). This could be due to a reduction in cell number and interference between the extract compounds and LDH (Figure 13C). However, optical microscopy observations did not reveal any obvious morphological and cell density changes in the treated bEnd.3 cells compared to negative control (Figure 13D and G).

The effect of the modified vascular graft extract on fibroblast cells also reported biocompatibility compared to the negative control, with cell viability of approximately 100% (Figure 13A). However, a reduction in fibroblasts' ability to produce ATP was noted, i.e., 29.71 ± 0.6% compared to non-treated cells ($p < 0.01$) (Figure 13B). Generally, the MTT assay evaluates the overall mitochondrial activity of the cells, while the ATP assay is a quantitative measure of the ATP molecules, which store the cell's energy. ATP measurements validated the biocompatibility of the vascular graft extract on L929 cells (ISO 10993-5). A small amount of extracellular LDH was quantified, albeit not significant compared to the negative control (Figure 13C). Cellular morphology was not affected by the treatment with undiluted graft extract. However, a slight reduction in cell density compared to negative control was noted (Figure 13E and H).

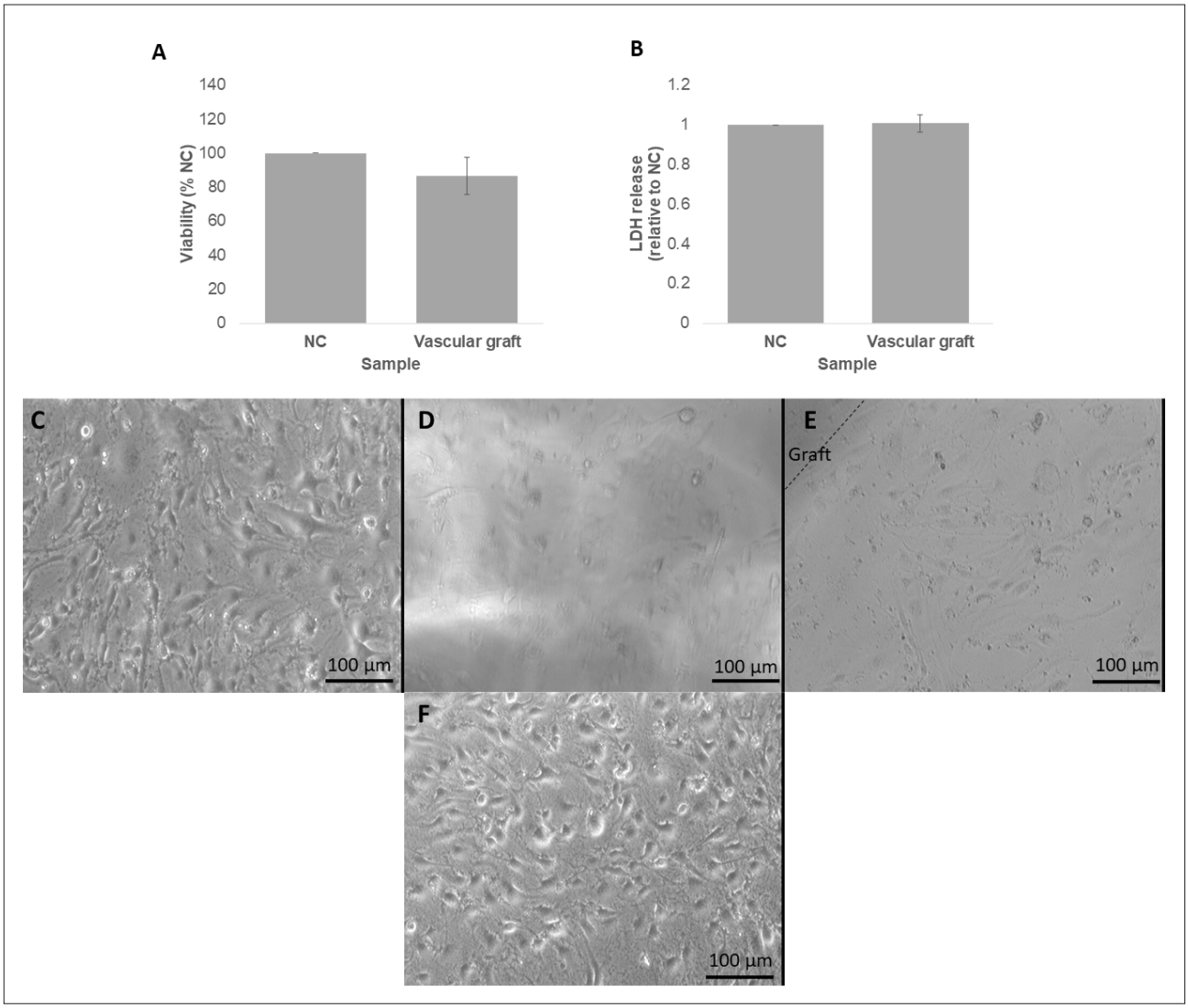


Figure 12. Biocompatibility assessment of initial vascular graft using the direct contact method. (A) Viability of bEnd.3 endothelial cells following a 24-h incubation in the presence of the vascular graft (via MTT assay). Data presented as mean ± standard deviation. (B) Levels of lactate dehydrogenase (LDH) released from bEnd.3 endothelial cells following a 24-h incubation in the presence of the vascular graft (via LDH assay). Data presented as mean ± standard deviation. (C–G) Morphology of bEend.3 endothelial cells following a 24-h incubation in the presence of the vascular graft: (C) negative control (NC), (D) cells under graft, (E) cells in the vicinity of the graft, and (F) cells situated far away from the graft. Magnification: ×10.

Evaluation of monocyte-like cell behavior determines the vascular graft's ability to induce an immune reaction in response to its integration into the body and exposure to blood flow. Treatment of U937 cells with vascular graft extract reduced cell metabolic activity compared to the negative control, i.e., 21.17 ± 1.5% ($p < 0.01$) (Figure 13A). This was validated by ATP measurements, which reported a reduction compared to the negative control, i.e., 17.6 ± 1.9% ($p < 0.01$) (Figure 13B). However, no extracellular LDH was detected (Figure 13C), suggesting that this effect is a temporary inhibition of monocyte activity. Morphological aspects of the cells were relatively normal compared to the control (Figure 13F and I).

3.9.4. Biocompatibility assessment of the modified vascular graft using the direct contact method

The direct contact effect of the modified vascular graft on bEnd.3 endothelial cells, L929 fibroblasts, and U937 monocyte-like cells were evaluated after incubation for 24 and 72 h. The effect of the vascular graft sample on

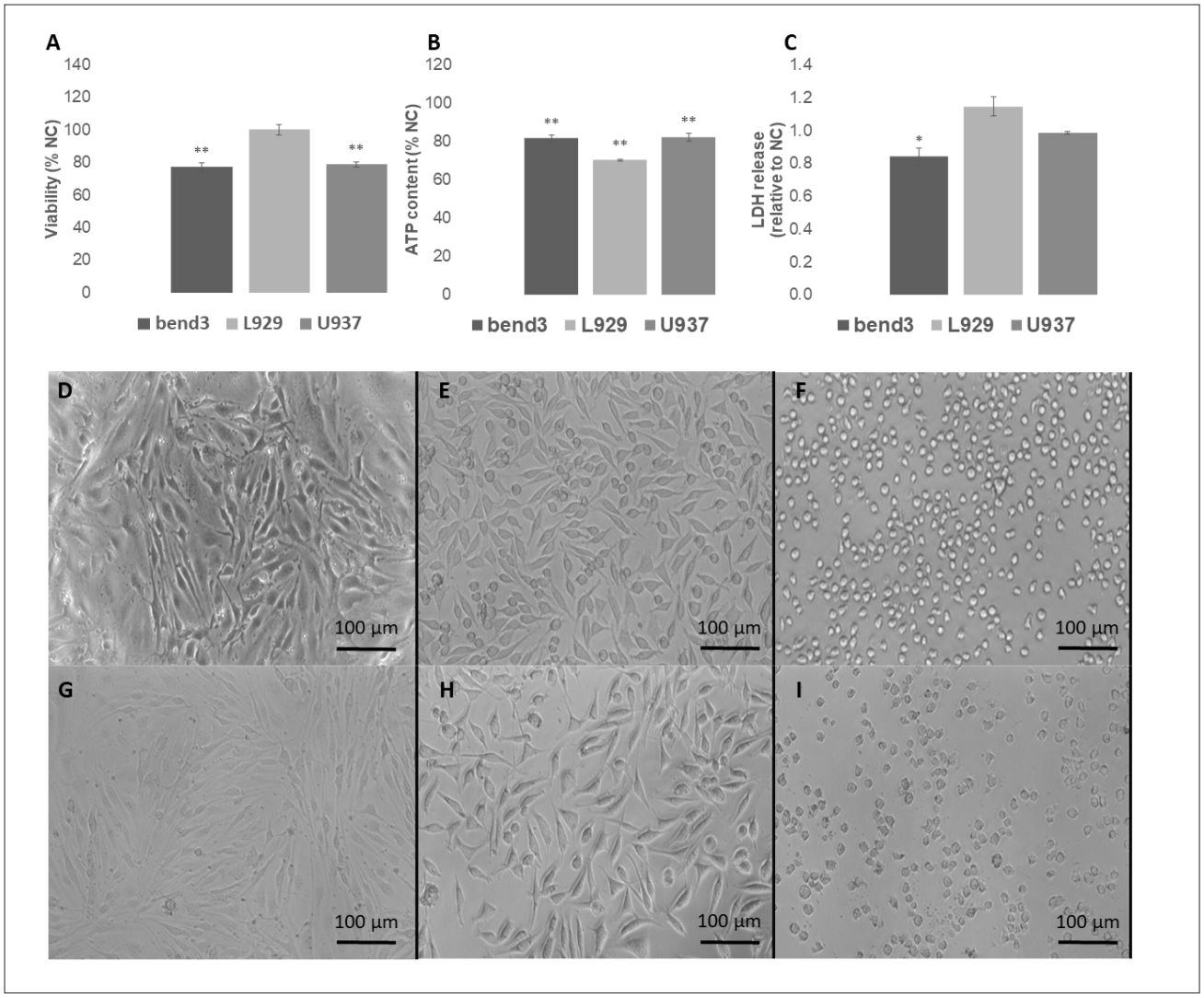


Figure 13. Biocompatibility assessment of the modified vascular graft using the extract method for bEnd.3 endothelial cells, L929 fibroblasts, and U937 monocyte-like cells. (A) Viability of cells following a 24-h incubation with the vascular graft extract (via MTT assay). Data presented as mean ± standard deviation; $^{**}p < 0.01$. (B) Adenosine triphosphate (ATP) content in cells following a 24-h incubation with the vascular graft extract (via ATP assay). Data presented as mean ± standard deviation; $^{**}p < 0.01$. (C) Levels of lactate dehydrogenase (LDH) released from cells following a 24-h incubation with the vascular graft extract (via LDH assay). Data presented as mean ± standard deviation; $^{*}p < 0.05$. (D–I) Cell morphology following a 24-h incubation with the vascular graft extract: (D–F) negative controls (NC) and (G–I) 1:1 graft extract; (D and G) bEnd.3 endothelial cells, (E and H) L929 fibroblasts, and (F and I) U937 monocyte cells. Magnification: ×10.

the endothelial cells' metabolism at 24 h was similar to the graft's extract, leading to a slight inhibition within the biocompatibility limits (ISO 10993-5) (Figure 14A, B, and D–G). However, a small amount of LDH was released from the cells due to contact with the modified vascular graft (0.27 ± 0.033% compared to the negative control; $p < 0.05$) (Figure 14C). At 72 h, the effect of the vascular graft on bEnd.3 metabolism was maintained under the same biocompatibility limits. However, no extracellular LDH was measured compared to the negative control (Figure 15A–C). These findings suggest that the modification of the vascular graft using lysine improved the material compatibility for endothelial cells *in vitro*, indicating biocompatibility according to ISO-10993-5 and maintenance of the cells' normal morphology.

At 24 h, the modified vascular graft had no significant effect on the L929 fibroblast cells' metabolism (compared to negative control) (Figure 14A and B). A small amount of LDH was measured in the extracellular environment of

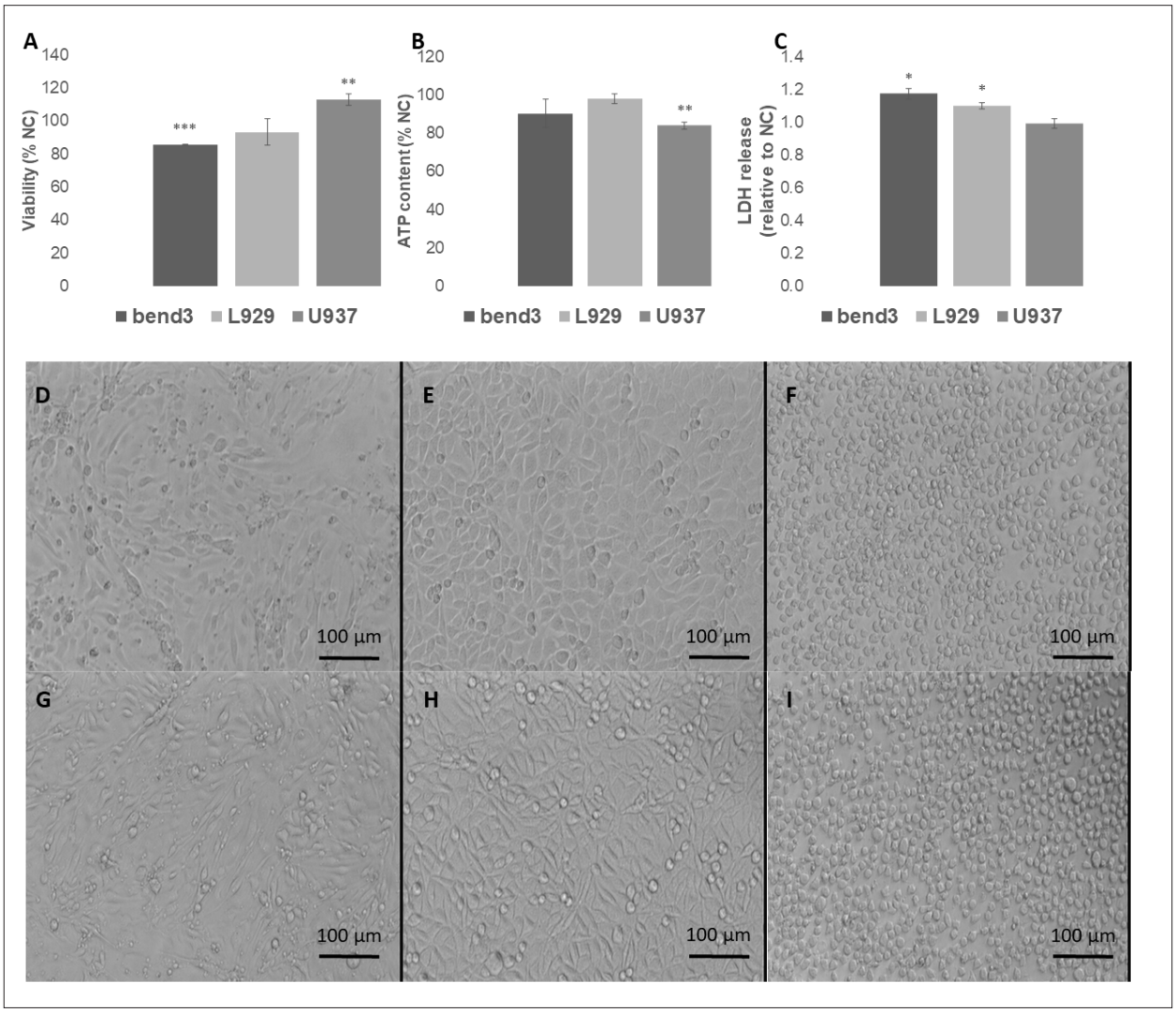


Figure 14. Biocompatibility assessment of the modified vascular graft using the direct contact method for bEnd.3 endothelial cells, L929 fibroblasts, and U937 monocyte-like cells. (A) Viability of cells following a 24-h incubation with the vascular graft (via MTT assay). Data presented as mean ± standard deviation; $^{**}p < 0.01$; $^{***}p < 0.001$. (B) Adenosine triphosphate (ATP) content in cells following a 24-h incubation with the vascular graft (via ATP assay). Data presented as mean ± standard deviation; $^{**}p < 0.01$. (C) Levels of lactate dehydrogenase (LDH) released from cells following a 24-h incubation with the vascular graft (via LDH assay). Data presented as mean ± standard deviation; $^{*}p < 0.05$. (D–I) Cell morphology following a 24-h incubation with the vascular graft: (D–F) negative controls (NC) and (G–I) graft samples; (D and G) bEnd.3 endothelial cells, (E and H) L929 fibroblasts, and (F and I) U937 monocyte cells. Magnification: ×10.

fibroblasts following incubation with the vascular graft for 24 h (0.101 ± 0.019% compared to negative control; $p < 0.05$) (Figure 14C). There were no obvious changes in the morphology of fibroblasts for this time interval (i.e., 24 h) (Figure 14E and H). A slight decrease in ATP concentration was noted following a 72-h incubation of fibroblasts in the presence of the vascular graft (15.87 ± 7.65% compared to the negative control; $p < 0.05$) (Figure 15B). No obvious changes in the morphology of the fibroblasts were noticed compared to the negative control at 72 h as well, following direct contact with the vascular graft (Figure 16E and H).

For monocytes, activation of the mitochondrial activity was noted following direct exposure to the modified vascular graft, i.e., an increase in MTT metabolism compared to the control at 12.99 ± 3.46%; $p < 0.01$ (Figure 14A). However, the production of ATP was slightly diminished compared to the negative control (84.03 ± 1.77% relative to the negative control; $p < 0.01$) (Figure 14B). It has been reported that mitochondrial metabolism affects immune cell activation.[66] Here, the increase in nicotinamide adenine dinucleotide phosphate ($NADP^+$), directly measured through MTT[67] and ATP assays, suggests

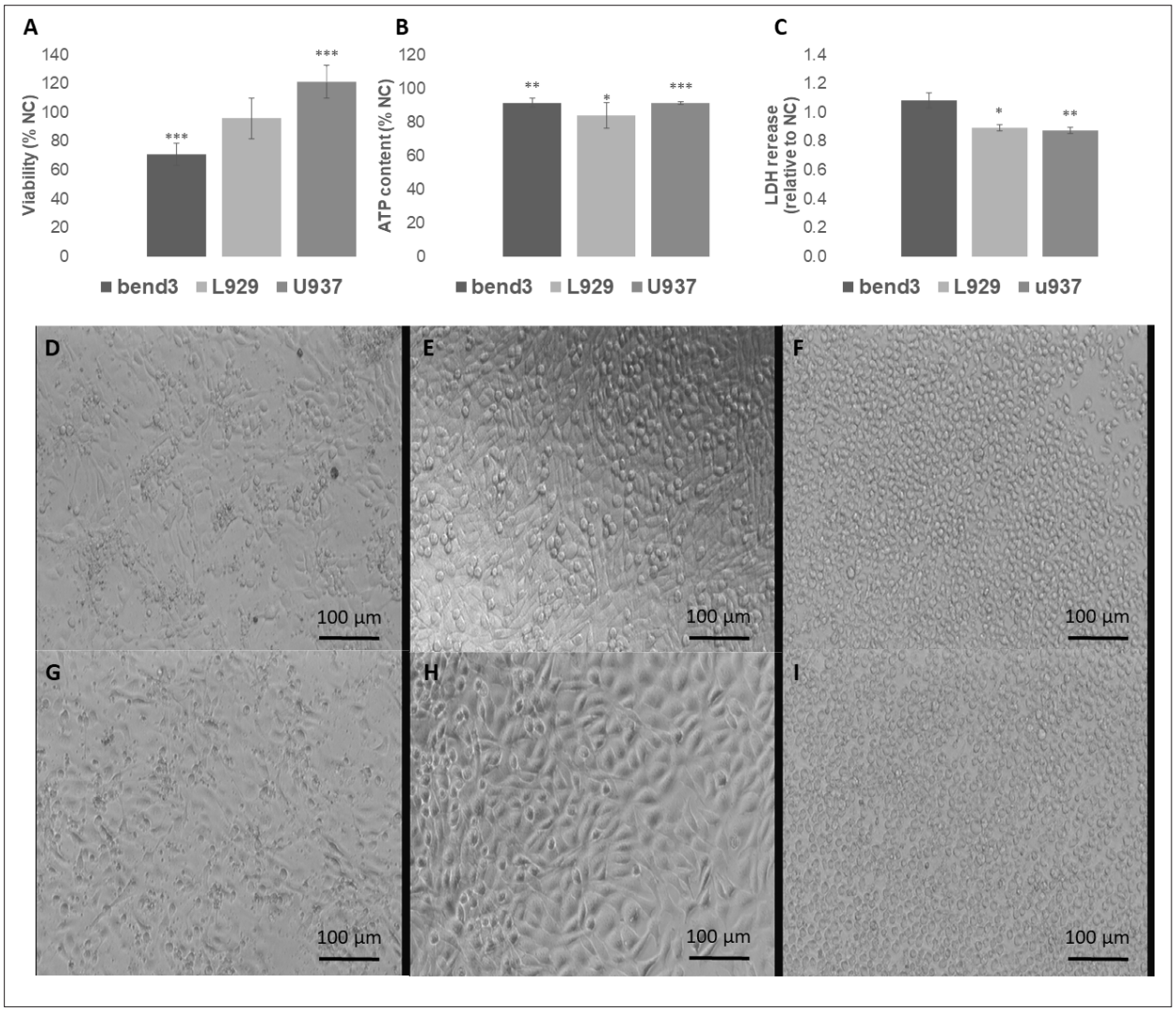


Figure 15. Biocompatibility assessment of the modified vascular graft using the direct contact method for bEnd.3 endothelial cells, L929 fibroblasts, and U937 monocyte-like cells. (A) Viability of cells following a 72-h incubation with the vascular graft (via MTT assay). Data presented as mean ± standard deviation; ***$p < 0.001$. (B) Adenosine triphosphate (ATP) content in cells following a 72-h incubation with the vascular graft (via ATP assay). Data presented as mean ± standard deviation; **$p < 0.01$; ***$p < 0.001$. (C) Levels of lactate dehydrogenase (LDH) released from cells following a 72-h incubation with the vascular graft (via LDH assay). Data presented as mean ± standard deviation; *$p < 0.05$; **$p < 0.01$. (D–I) Cell morphology following a 72-h incubation with the vascular graft: (D–F) negative controls (NC) and (G–I) graft samples; (D and G) bEnd.3 endothelial cells, (E and H) L929 fibroblasts, and (F and I) U937 monocyte cells. Magnification: ×10.

anabolic metabolism of the monocyte-like cells.[66] At 72 h, this effect is slightly increased: 21.27 ± 11.48% in MTT metabolism compared to the control ($p < 0.001$) and 91.19 ± 0.78% ATP content compared to the control ($p < 0.001$) (Figure 16A and B), validating the activation of monocyte-like cells following the modified vascular graft exposure.

In summation, MTT, ATP, and LDH assays demonstrated the biocompatibility of lysine-modified vascular grafts for endothelial cells, fibroblasts, and monocytes according to ISO 10993-5. However, slight monocyte activation was detected based on increased $NADP^+$ and reduced ATP levels following direct exposure to the graft. These findings warrant further validation in *in vivo* conditions. Nonetheless, the observed effects could be beneficial *in vivo*, such as facilitating tissue repair in acute inflammation.[68]

3.10. The evaluation of hemocompatibility

Hemocompatibility evaluation was performed according to the ASTM F756, i.e., the direct method for hemoglobin determination for the optimized vascular grafts. The

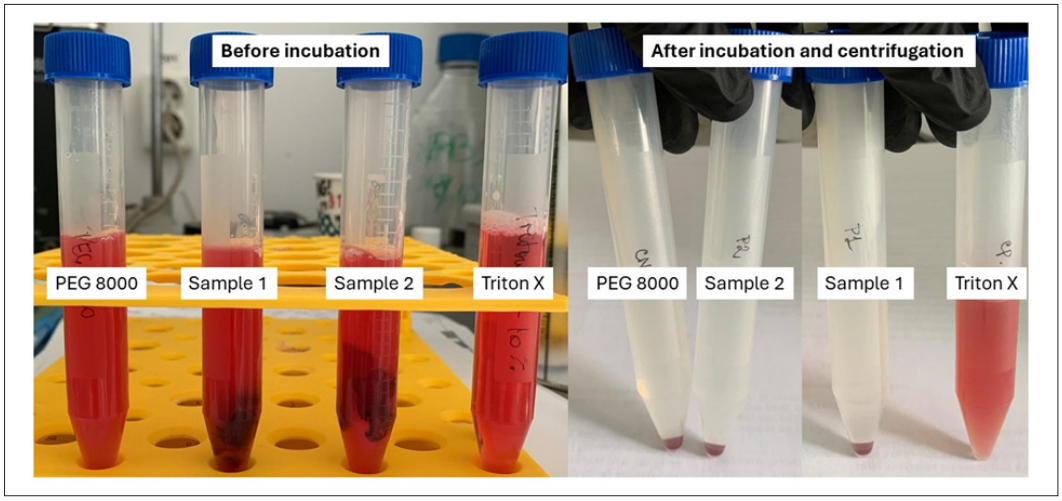


Figure 16. Aspects of blood in the presence of samples and controls before incubation (left). Aspects of the supernatant following a 3-h incubation of blood in the presence of the grafts and centrifugation (right). No obvious changes in the supernatant of the samples were observed com

test measures the ability of the material to provoke the destruction of the erythrocytes in whole blood through measurements of released hemoglobin in the plasma, following a 3-h incubation with the graft. The degree of hemolysis was calculated according to the guidelines, and the results were interpreted accordingly. The hemolysis level induced by the vascular graft was below 2%, as recommended by ASTM F756-13, highlighting the hemocompatibility of the material in whole blood (Figure 16; Table 3).

4. Conclusion

An innovative protocol for the fabrication of small vascular grafts by 3D printing was successfully developed in this work. The results demonstrate that PVA is a suitable synthetic polymer for vascular graft development under specific conditions. Thermal treatment notably influenced PVA channels by enhancing crystallinity and modifying crosslinking behavior, while biofunctionalization improved biocompatibility and immune response. Optimal combinations of parameters, such as thermal treatment duration, crosslinking time, and biofunctionalization processes, yielded suitable 3D-printed PVA channels for small vascular grafts. Biofunctionalized PVA grafts exhibited favorable fatigue resistance under continuous flow, mimicking normal vasculature conditions in small veins. 3D printing emerged as a crucial technique in PVA graft development, offering a rapid and efficient means to design and fabricate PVA channels.

3D printing can also be employed to produce vascular grafts with other dimensions, according to preclinical conditions. This work provides a novel approach for the design of small vascular grafts, as well as a candidate with the potential to revolutionize therapeutic applications, from coronary artery bypass to customized treatments for peripheral arterial diseases. One important aspect of 3D printing technology is its versatility, which opens possibilities for efficient and personalized vascular graft treatment in a range of clinical contexts.

Table 3. Evaluation of hemocompatibility of modified vascular grafts

Sample	Hemolysis level (%)
Control	
Positive	83.71 ± 4.9
Negative	0.87 ± 0.14
Graft	
1	1.49 ± 0.67
2	1.502 ± 0.52

Acknowledgments

None.

Funding

This work was supported by a grant from the Ministry of Research, Innovation, and Digitization (CNCS/CCCDI–UEFISCDI; project number: PN-III-P4-ID-PCE-2020-1448; within PNCDI III).

Conflict of interest

The authors declare no conflicts of interest.

Author contributions

Conceptualization: Ionut-Cristian Radu, Catalin Zaharia
Formal analysis: Ionut-Cristian Radu, Catalin Zaharia, Roxana Cristina Popescu
Investigation: Ionut-Cristian Radu, Madalina-Ioana Necolau, Eugenia Tanasa, Roxana Cristina Popescu
Methodology: Ionut-Cristian Radu, Madalina-Ioana Necolau, Eugenia Tanasa, Roxana Cristina Popescu
Validation: Laurentia Alexandrescu, Catalin Zaharia, Rafael Luque
Writing – original draft: Ionut-Cristian Radu, Roxana Cristina Popescu, Catalin Zaharia
Writing – review & editing: Catalin Zaharia, Rafael Luque

Ethics approval and consent to participate

Not applicable.

Consent for publication

Not applicable.

Availability of data

Data are available from the corresponding author upon reasonable request.

References

1. Criqui M, Aboyans V. Epidemiology of peripheral artery disease. *Circ Res*. 2015;116(9):1509-1526. doi: 10.1161/CIRCRESAHA.116.303849
2. Leal BBJ, Wakabayashi N, Oyama K, et al. Vascular tissue engineering: polymers and methodologies for small caliber vascular grafts. *Front Cardiovasc Med*. 2021;7:592361. doi: 10.3389/fcvm.2020.592361
3. Copes F, Pien N, Van Vlierberghe S, et al. Collagen-based tissue engineering strategies for vascular medicine. *Front Bioeng Biotechnol*. 2019;7:166. doi: 10.3389/fbioe.2019.00166
4. Herrington W, Lacey B, Sherliker P, et al. Epidemiology of atherosclerosis and the potential to reduce the global burden of atherothrombotic disease. *Circ Res*. 2016;118(4):535-546. doi: 10.1161/CIRCRESAHA.115.307611
5. Carrabba M, Madeddu P. Current strategies for the manufacture of small size tissue engineering vascular grafts. *Front Bioeng Biotechnol*. 2018;6:41. doi: 10.3389/fbioe.2018.00041
6. Ucuzian AA, Greisler HP. 6.628 - vascular grafts. In: Ducheyne P, ed. *Comprehensive Biomaterials*. Oxford: Elsevier; 2011: 449-467.
7. Shim TL, Wright JD, Rubin BG, et al. A vascular graft for endometrial cancer groin recurrence. *Gynecol Oncol*. 2007;104(3):753-756. doi: 10.1016/j.ygyno.2006.10.023
8. Song TK, Harris EJ, Jr, Raghavan S, et al. Major blood vessel reconstruction during sarcoma surgery. *Arch Surg*. 2009;144(9):817-822. doi: 10.1001/archsurg.2009.149
9. Radke D, Jia W, Sharma D, *et al*. Tissue engineering at the blood-contacting surface: a review of challenges and strategies in vascular graft development. *Adv Healthc Mater*. 2018;7(15):e1701461. doi: 10.1002/adhm.201701461
10. Li M-X, Wei Q-Q, Mo H-L, et al. Challenges and advances in materials and fabrication technologies of small-diameter vascular grafts. *Biomater Res*. 2023;27(1):91. doi: 10.1186/s40824-023-00424-4
11. Ratner B. Vascular grafts: technology success/technology failure. *BME Front*. 2023;4:0003. doi: 10.34133/bmef.0003
12. Seifu DG, Purnama A, Mequanint K, et al. Small-diameter vascular tissue engineering. *Nat Rev Cardiol*. 2013;10(7): 410-421. doi: 10.1038/nrcardio.2013.77
13. Hann SY, Cui H, Zalud NC, et al. An in vitro analysis of the effect of geometry-induced flows on endothelial cell behavior in 3D printed small-diameter blood vessels. *Biomater Adv*. 2022;137:212832. doi: 10.1016/j.bioadv.2022.212832
14. Vernon G. Alexis Carrel: 'father of transplant surgery' and supporter of eugenics. *Br J Gen Pract*. 2019;69(684):352. doi: 10.3399/bjgp19X704441
15. Dutkowski P, De Rougemont O, Clavien PA. Alexis Carrel: genius, innovator and ideologist. *Am J Transplant*. 2008;8(10):1998-2003. doi: 10.1111/j.1600-6143.2008.02364.x
16. Kunlin J. [Long vein transplantation in treatment of ischemia caused by arteritis]. *Rev Chir.* 1951;70(7-8):206-235.
17. Kannan RY, Salacinski HJ, Butler PE, et al. Current status of prosthetic bypass grafts: a review. *J Biomed Mater Res B Appl Biomater*. 2005;74(1):570-581. doi: 10.1002/jbm.b.30247
18. Rashid ST, Fuller B, Hamilton G, et al. Tissue engineering of a hybrid bypass graft for coronary and lower limb bypass surgery. *FASEB J*. 2008;22(6):2084-2089. doi: 10.1096/fj.07-096586
19. Abbott WM, Callow A, Moore W, et al. Evaluation and performance standards for arterial prostheses. *J Vasc Surg*. 1993;17(4):746-756. doi: 10.1067/mva.1993.45222
20. Jackson MR, Belott TP, Dickason T, et al. The consequences of a failed femoropopliteal bypass grafting: comparison of saphenous vein and PTFE grafts. *J Vasc Surg*. 2000;32(3):498-504; 504-505. doi: 10.1067/mva.2000.108634

21. Tiwari A, Salacinski H, Seifalian AM, et al. New prostheses for use in bypass grafts with special emphasis on polyurethanes. *Cardiovasc Surg*. 2002;10(3):191-197. doi: 10.1016/s0967-2109(02)00004-2

22. Brothers TE, Stanley JC, Burkel WE, et al. Small-caliber polyurethane and polytetrafluoroethylene grafts: a comparative study in a canine aortoiliac model. *J Biomed Mater Res*. 1990;24(6):761-771. doi: 10.1002/jbm.820240610

23. Desmet W, Vanhaecke J, Vrolix M, et al. Isolated single coronary artery: a review of 50,000 consecutive coronary angiographies. *Eur Heart J*. 1992;13(12):1637-1640. doi: 10.1093/oxfordjournals.eurheartj.a060117

24. Hutchin P, Jacobs JR, Devin JB, et al. Bovine graft arteriovenous fistulas for maintenance hemodialysis. *Surg Gynecol Obstet*. 1975;141(2): 255-258.

25. Hatzibaloglou A, Velissaris I, Kaitzis D, et al. ProCol vascular bioprosthesis for vascular access: midterm results. *J Vasc Access*. 2004;5(1):16-18. doi: 10.1177/112972980400500104

26. Madden RL, Lipkowitz GS, Browne BJ, et al. Experience with cryopreserved cadaveric femoral vein allografts used for hemodialysis access. *Ann Vasc Surg*. 2004;18(4):453-458. doi: 10.1007/s10016-004-0055-0

27. Braghirolli DI, Helfer VE, Chagastelles PC, et al. Electrospun scaffolds functionalized with heparin and vascular endothelial growth factor increase the proliferation of endothelial progenitor cells. *Biomed Mater*. 2017;12(2):025003. doi: 10.1088/1748-605X/aa5bbc

28. Benrashid E, McCoy CC, Youngwirth LM, et al. Tissue engineered vascular grafts: origins, development, and current strategies for clinical application. *Methods*. 2016;99:13-19. doi: 10.1016/j.ymeth.2015.07.014

29. Maurmann N, Sperling L-E, Pranke P. Electrospun and electrosprayed scaffolds for tissue engineering. In: Chun HJ, Park CH, Kwon IK, and Khang G, eds. *Cutting-Edge Enabling Technologies for Regenerative Medicine*. Singapore: Springer Singapore; 2018: 79-100.

30. Braghirolli DI, Steffens DPranke P. Electrospinning for regenerative medicine: a review of the main topics. *Drug Discov Today*. 2014;19(6):743-753. doi: 10.1016/j.drudis.2014.03.024

31. Li J, Cai Z, Cheng J, et al. Characterization of a heparinized decellularized scaffold and its effects on mechanical and structural properties. J *Biomater Sci Polym Ed*. 2020;31(8):999-1023. doi: 10.1080/09205063.2020.1736741

32. Eufrásio-da-Silva T, Ruiz-Hernandez E, O'Dwyer J, et al. Enhancing medial layer recellularization of tissue-engineered blood vessels using radial microchannels. *Regen Med*. 2019;14(11):1013-1028. doi: 10.2217/rme-2019-0011

33. Rivera-Hernández G, Antunes-Ricardo M, Martínez-Morales P, et al. Polyvinyl alcohol based-drug delivery systems for cancer treatment. *Int J Pharm*. 2021;600:120478. doi: 10.1016/j.ijpharm.2021.120478

34. Aslam M, Kalyar MA, Raza ZA. Polyvinyl alcohol: a review of research status and use of polyvinyl alcohol based nanocomposites. *Polymer Eng Sci*. 2018;58(12):2119-2132. doi: 10.1002/pen.24855

35. Dong R-s, Lu F, Liu P-d, et al. Preparation of nanocellulose-polyvinyl alcohol composite hydrogels from *Desmodium intortum* (Mill.) Urb.: chemical property characterization. *Ind Crops Prod*. 2022;176:114371. doi: 10.1016/j.indcrop.2021.114371

36. Ghafelebashi A, Khosravani S, Kazemi MH, et al. A novel fabricated polyvinyl alcohol/ bentonite nanocomposite hydrogel generated into colloidal gas aphron. *Colloids Surf A: Physicochem Eng Aspects*. 2022;650:129580. doi: 10.1016/j.colsurfa.2022.129580

37. Elamin D, Chami G. Description of a revision technique for failed polyvinyl alcohol hydrogel implant in patient with Freiberg's disease. *J Foot Ankle Surg*. 2022;61(1):181-184. doi: 10.1053/j.jfas.2021.07.013

38. Qin M, Huo Y, Han G, et al. Three-dimensional boron nitride network/polyvinyl alcohol composite hydrogel with solid-liquid interpenetrating heat conduction network for thermal management. *J Mater Sci Technol*. 2022;127:183-191. doi: 10.1016/j.jmst.2022.04.013

39. Zhang J, Wang Y, Wei Q, et al. A 3D printable, highly stretchable, self-healing hydrogel-based sensor based on polyvinyl alcohol/sodium tetraborate/sodium alginate for human motion monitoring. *Int J Biol Macromol*. 2022;219:1216-1226. doi: 10.1016/j.ijbiomac.2022.08.175

40. Verbraeken B, Lavrysen E, Aboukais R, et al. Polyvinyl alcohol sponges to facilitate cerebral bypass surgery: technical note. *World Neurosurg*. 2021;156:53-55. doi: 10.1016/j.wneu.2021.09.007

41. Li P, Cao L, Sang F, et al. Polyvinyl alcohol/sodium alginate composite sponge with 3D ordered/disordered porous structure for rapidly controlling noncompressible hemorrhage. *Biomater Adv*. 2022;134:112698. doi: 10.1016/j.msec.2022.112698

42. Darrell HRIksoo C. Nanometre diameter fibres of polymer, produced by electrospinning. *Nanotechnology*. 1996;7(3): 216. doi: 10.1088/0957-4484/7/3/009

43. García-Hernández AB, Morales-Sánchez E, Berdeja-Martínez BM, et al. PVA-based electrospun biomembranes with hydrolyzed collagen and ethanolic extract of hypericum perforatum for potential use as wound dressing: fabrication and characterization. *Polymers (Basel)*. 2022;14(10):1981. doi: 10.3390/polym14101981

44. Serio F, da Cruz AF, Chandra A, et al. Electrospun polyvinyl-alcohol/gum arabic nanofibers: biomimetic platform for in

vitro cell growth and cancer nanomedicine delivery. *Int J Biol Macromol*. 2021;188:764-773.
doi: 10.1016/j.ijbiomac.2021.08.069

45. Roy AS, Gupta S, Sindhu S, et al. Dielectric properties of novel PVA/ZnO hybrid nanocomposite films. *Composites Part B: Eng*. 2013;47:314-319.
doi: 10.1016/j.compositesb.2012.10.029

46. Itoh H, Li Y, Chan KHK, et al. Morphology and mechanical properties of PVA nanofibers spun by free surface electrospinning. *Polymer Bull*. 2016;73(10):2761-2777.
doi: 10.1007/s00289-016-1620-8

47. Alexandre N, Amorim I, Caseiro AR, et al. Long term performance evaluation of small-diameter vascular grafts based on polyvinyl alcohol hydrogel and dextran and MSCs-based therapies using the ovine pre-clinical animal model. *Int J Pharm*. 2016;513(1-2):332-346.
doi: 10.1016/j.ijpharm.2016.09.045

48. Zeng Y, Huang C, Duan D, et al. Injectable temperature-sensitive hydrogel system incorporating deferoxamine-loaded microspheres promotes H-type blood vessel-related bone repair of a critical size femoral defect. *Acta Biomater*. 2022;153:108-123.
doi: 10.1016/j.actbio.2022.09.018.

49. Jeong Y, Yao Y, Mekonnen TH, et al. Changing compliance of poly(vinyl alcohol) tubular scaffold for vascular graft applications through modifying interlayer adhesion and crosslinking density. Front Mater. 2021;7:595295.
doi: 10.3389/fmats.2020.595295

50. Chaouat M, Le Visage C, Baille WE, et al. A novel cross-linked poly(vinyl alcohol) (PVA) for vascular grafts. *Adv Funct Mater*. 2008;18(19):2855-2861.
doi: 10.1002/adfm.200701261

51. Tian Y, Zhou J, Feng J. The effect of thermal history on crystalline structure and mechanical properties of β-nucleated isotactic polypropylene. *Mater Res Express*. 2018;5(4):045304.
doi: 10.1088/2053-1591/aab9c7

52. Polaskova M, Peer P, Cermak R, et al. Effect of thermal treatment on crystallinity of poly(ethylene oxide) electrospun fibers. *Polymers*. 2019;11(9):1384.
doi: 10.3390/polym11091384

53. Zizhou R, Wang X, Houshyar S. Review of polymeric biomimetic small-diameter vascular grafts to tackle intimal hyperplasia. *ACS Omega*. 2022;7(26):22125-22148.
doi: 10.1021/acsomega.2c01740

54. Hao D, Fan Y, Xiao W, et al. Rapid endothelialization of small diameter vascular grafts by a bioactive integrin-binding ligand specifically targeting endothelial progenitor cells and endothelial cells. *Acta Biomater*. 2020;108:178-193.
doi: 10.1016/j.actbio.2020.03.005

55. Mansur HS, Sadahira CM, Souza AN, et al. FTIR spectroscopy characterization of poly (vinyl alcohol) hydrogel with different hydrolysis degree and chemically crosslinked with glutaraldehyde. *Mater Sci Eng. C*, 2008;28(4):539-548.
doi: 10.1016/j.msec.2007.10.088

56. Guo L, Sato H, Hashimoto T, et al. FTIR study on hydrogen-bonding interactions in biodegradable polymer blends of poly(3-hydroxybutyrate) and poly(4-vinylphenol). *Macromolecules* 2010;43(8):3897-3902.
doi: 10.1021/ma100307m

57. Farris S, Song J, Huang Q. Alternative reaction mechanism for the cross-linking of gelatin with glutaraldehyde. J Agric Food Chem. 2010;58(2):998-1003.
doi: 10.1021/jf9031603

58. Jessie Lue S, Chen JY, Ming Yang J. Crystallinity and stability of poly(vinyl alcohol)-fumed silica mixed matrix membranes. *J Macromol Sci, Part B* 2007;47(1):39-51.
doi: 10.1080/15568310701744133

59. Pingan H, Mengjun J, Yanyan Z, et al. A silica/PVA adhesive hybrid material with high transparency, thermostability and mechanical strength. *RSC Adv*. 2017;7(5):2450-2459.
doi: 10.1039/C6RA25579E

60. Aziz SB, Marf AS, Dannoun EMA, et al. The study of the degree of crystallinity, electrical equivalent circuit, and dielectric properties of polyvinyl alcohol (pva)-based biopolymer electrolytes. *Polymers*. 2020;12(10):2184.

61. Hong P-D, Chen J-H, Wu H-L. Solvent effect on structural change of poly(vinyl alcohol) physical gels. *J Appl Polymer Sci*. 1998;69(12):2477-2486.
doi: 10.1002/(SICI)1097-4628(19980919)69:12<2477::AID-APP19>3.0.CO;2-U

62. Vinila VS, Isac J. Chapter 14 - synthesis and structural studies of superconducting perovskite GdBa2Ca3Cu4O10.5+δ nanosystems. In: Thomas S, Kalarikkal N, Abraham AR, eds. *Design, Fabrication, and Characterization of Multifunctional Nanomaterials*. Amsterdam, Netherlands: Elsevier; 2022: 319-341.

63. Weidenfeller B, Rode H, Weidenfeller L, et al. Crystallinity, thermal diffusivity, and electrical conductivity of carbon black filled polyamide 46. *J Appl Polymer Sci*. 2020;137(29):48882.
doi: 10.1002/app.48882

64. Pellerito J, Polak J. *Introduction to Vascular Ultrasonography*. Elsevier; 2019: 882.

65. Shi X, He L, Zhang S-M, et al. Human iPS cell-derived tissue engineered vascular graft: recent advances and future directions. *Stem Cell Rev Rep*. 2021;17(3):862-877.
doi: 10.1007/s12015-020-10091-w

66. Angajala A, Lim S, Phillips JB, et al. Diverse roles of mitochondria in immune responses: novel insights into immuno-metabolism. *Front Immunol*. 2018;9:1605.
doi: 10.3389/fimmu.2018.01605

67. Ghasemi M, Turnbull T, Sebastian S, et al. The MTT assay: utility, limitations, pitfalls, and interpretation in bulk and single-cell analysis. *Int J Mol Sci*. 2021;22(23):12827.

68. Soliman AM, Barreda DR. Acute inflammation in tissue healing. *Int J Mol Sci*. 2023;24(1):641.

ACCSCIENCE PUBLISHING

International Journal of Bioprinting

RESEARCH ARTICLE

Bioprinting native-like 3D micro breast cancer tissues utilizing existing cancer cell lines

Brian E. Grottkau[1,2†*], Zhixin Hui[1†], and Yonggang Pang[1*]

[1]The Laboratory for Therapeutic 3D Bioprinting, Department of Orthopedic Surgery, Massachusetts General Hospital, Harvard Medical School, Boston, Massachusetts, USA

[2]Department of Orthopedics, University of Miami Medical Center and Jackson Memorial Hospital, Miami, FL 33136, USA

Abstract

3D cancer cell models provide a more accurate representation of *in vivo* conditions than traditional 2D cultures. Many cancer cell lines, while stable and extensively characterized in 2D environments, often underperform compared to primary cells in 3D models due to the inherent resource constraints and variability of the latter. To bridge this gap and harness the full potential of established cancer cell lines, we adopted the innovative direct volumetric drop-on-demand (DVDOD) bioprinting methodology that we have developed previously, leading to the inception of printed micro-cancer tissues (PMCaTs). Our method, notable for its bioink droplet scattering technique, enables the generation of intricate features within a droplet, allowing for the creation of typical architectures of breast cancer tissue. We created PMCaTs that captured the essence of micro breast cancer tissues, from native-like ductal structures and cancer nests to the intricate cancer microenvironment. This encompasses elements like cancer-associated fibroblasts, detailed microvasculature, and regions marked by both intensive proliferation and hypoxia. These bioprinted models demonstrate long-term viability and are instrumental for diverse research areas—from exploring cancer growth dynamics and hypoxia-induced behaviors to investigating the nuances of microvasculature, drug penetration capabilities, immune responses, metastatic trends, and clinical drug response predictions. Ultimately, our groundbreaking DVDOD bioprinting technique holds the promise of reshaping the landscape of cancer research, introducing advanced *in vitro* models poised to transform therapeutic exploration.

Keywords: Bioprinting; Direct volumetric drop-on-demand; 3D micro breast cancer tissues; Native-like; Cancer cell lines; 3D models

†These authors contributed equally to this work.

***Corresponding authors:**
Brian E. Grottkau
(bxg1729@med.miami.edu)

Yonggang Pang
(ypang11@outlook.com)

Citation: Grottkau BE, Hui Z, Pang Y. Bioprinting native-like 3D micro breast cancer tissues utilizing existing cancer cell lines. *Int J Bioprint*. 2024;10(3):2911. doi: 10.36922/ijb.2911

Received: February 9, 2024
Accepted: April 3, 2024
Published Online: June 13, 2024

Copyright: © 2024 Author(s). This is an Open Access article distributed under the terms of the Creative Commons Attribution License, permitting distribution, and reproduction in any medium, provided the original work is properly cited.

Publisher's Note: AccScience Publishing remains neutral with regard to jurisdictional claims in published maps and institutional affiliations.

1. Introduction

Despite significant advancements in cancer research,[1] recapitulating the complexities of human tumors for *in vitro* drug testing and disease modeling remains a challenge.[2] Numerous cancer cell lines have been established to deepen our comprehension of tumor biology and therapeutic responses. For example, the Cancer Cell Line Encyclopedia (CCLE) offers over 1000 cell lines, providing a comprehensive molecular characterization resource for cancer research.[3] Similarly, the cancer therapeutics response portal (CTRP) provides over 900 cell lines, helping researchers tailor therapeutic strategies based on

genetic backgrounds.[4] Notably, for breast cancer alone, more than 90 distinct cell lines have been identified.[5] These cell lines have proven invaluable in advancing basic cancer research, developing therapeutics, and facilitating their transition into clinical applications. However, this traditional 2D culture approach cannot capture the complex 3D nature of *in vivo* cancer, prompting researchers to explore more representative models.[6]

Recent research has shifted towards using primary cells to develop 3D structures, like organoids,[7] which offer a closer representation of native tissues. However, while these models demonstrate promise in emulating *in vivo* cancer tissues, they come with challenges. Predominantly relying on primary cells introduces limitations such as restricted availability, sourcing difficulties, patient consent issues, and technical challenges in isolation.[8,9] Moreover, the inherent genetic and phenotypic variability in primary cells from different patient tumors can result in inconsistent experimental outcomes.

3D bioprinting is a transformative technology in tissue engineering and regenerative medicine that enables the creation of complex, functional living tissues through various methods, each with distinct mechanisms and applications. Extrusion-based bioprinting methodically deposits bioink layerwise through a nozzle, offering the versatility to print a broad spectrum of materials with high cell densities.[10] Meanwhile, vat photopolymerization-based bioprinting harnesses light to cure liquid resin into solid 3D structures layerwise, achieving high resolution and smooth finishes. However, its utility is constrained by the requirement for bioinks that are compatible with the photopolymerization process.[11] The jetting-based or drop-on-demand (DOD) technique, known for its precision in ejecting bioink droplets onto a substrate,[12] is particularly adept at generating microtissues with the capability of controlling droplet sizes and deposition rate. To address these challenges, we have developed a novel direct-volumetric DOD (DVDOD) technology that distinguishes itself from other existing DOD technologies by directly controlling droplet volume via linear advancement and facilitating droplet release and deposition through pulsed air, enabling an almost seamless two-step process that allows for the precise dispensation of bioink droplets down to 10 nL with <5% variation.

To address these challenges, we utilized the previously developed DVDOD bioprinting method to generate printed micro-cancer tissues (PMCaTs).[13] To leverage bioink droplet scattering,[14] we were able to precisely construct cancer tissue structures that closely resemble native tissues. Furthermore, our approach leverages the stability, well-documented genetic profiles, and widespread availability of cancer cell lines, bypassing the need for primary cells and ensuring consistent and reproducible research outcomes.

Our bioprinting technologies bridge this divide, with 3D bioprinting presenting a physiologically relevant platform that encapsulates the intricacies of *in vivo* tumor environments. These 3D models, housing heterogeneous cell populations like cancer cells, fibroblasts, and endothelial cells, simulate the dynamic tumor interactions more effectively. They prove instrumental for drug testing, enabling the evaluation of drug penetration and tumor invasion, as well as immune and drug responses. Specifically, we focused on breast cancer tissues, given that breast cancer remains the most frequently diagnosed cancer worldwide.[15] Its incidence has surged in recent years. Despite significant advancements in therapeutic interventions, over 2.3 million individuals were diagnosed with breast cancer in 2020 alone, leading to 685,000 fatalities.[16] This underscores the pressing need for more effective treatment strategies.

Nonetheless, we aim to address this gap by leveraging PMCaTs. These models, comprising 3D configurations of multiple cell types, can mirror the actual physiological conditions, providing a platform that is both versatile and highly representative. By focusing on breast cancer, we not only address a significant public health concern but also offer an opportunity to study a variety of interactions that are pivotal for cancer progression and treatment responses. Given this critical context, exploring innovative methodologies to better understand and treat breast cancer becomes paramount. In our study, we harnessed 3D bioprinting, utilizing various breast cancer cell lines, fibroblasts, and endothelial cells, to delve into diverse cancer behaviors. This encompasses typical breast cancer morphology, cancer invasion, metastasis, drug penetration, immune therapy, and drug responsiveness. Taken together, our approach demonstrates promise in closely mimicking *in vivo* conditions.

2. Methods

The present study is proposed as a proof-of-concept study that utilizes the DVDOD method, following its successful applications in tissue regeneration. The assays are divided into two categories, each with corresponding goals:

(i) feasibility assays to evaluate morphology creation (an important aspect of cancer biology), where the goal is to analyze the morphology of PMCaTs in relation to the pathology studies of native cancer tissue.

(ii) A quantitative study aimed at assessing drug responses and comparing them with the data from a clinical trial.

2.1. Cell culture

In our study, we primarily selected the SUM149 cell line due to its aggressive nature and origin from ductal-type breast cancer, providing a more direct objective for mimicry. While SUM149 and MDA-MB-231 are both triple-negative cell lines, we limited the use of MDA-MB-231 and MCF-7 to the drug prediction segment of our study. This decision was informed by their relevance to corresponding clinical trials and previous studies, facilitating easier comparisons. Recognizing the challenges in harvesting breast-originated fibroblasts, we opted for normal human lung fibroblasts (NHLFs) to model cancer-associated fibroblasts (CAFs) for breast cancer, owing to the ectodermal origins and glandular structures shared by both the breast and lung. Lastly, we utilized human umbilical vein endothelial cells (HUVECs) to model microvasculature, given their wide availability and proven efficacy in such applications. Additionally, we incorporated the Jurkat cell line to represent T-cell interactions in the tumor microenvironment.

Three human breast cancer cell lines were utilized: SUM149 cells cultured in Ham's F-12 medium, and both MCF7 and MDA-MB-231 cells in Dulbecco's Modified Eagle Medium (DMEM), all supplemented with 10% fetal bovine serum (FBS) and 1% penicillin-streptomycin. NHLFs were grown in fibroblast basal medium with fibroblast growth kit components as per Lonza's specifications, and HUVECs were grown in endothelial basal medium-2 (EBM-2) enhanced with the EGM-2 SingleQuots kit, according to Lonza's guidelines. Jurkat cells, a T-cell line, were cultured in RPMI 1640 medium with the same supplements. All cells were maintained in a humidified atmosphere at 37°C and 5% CO_2, with media refreshed every 2–3 days. Adherent cells were passaged using a 0.05% trypsin-EDTA (ethylenediaminetetraacetic acid) solution at 70–80% confluency, while suspension-growing Jurkat cells were passaged by dilution. Rigorous standards were upheld throughout to prevent cross-contamination and ensure cell line purity.

2.2. Cell viability assessment using calcein AM staining

Cell viability within the bioprinted PMCaTs (n = 3) was assessed using calcein AM (Thermo Fisher Scientific, USA). Microtissues were first rinsed with phosphate-buffered saline (PBS) to remove any residual culture medium and then incubated with a 2 μM calcein AM solution at 37°C for 30 min. After washing with PBS, the tissues were immediately visualized under a fluorescent microscope. The observed green fluorescence, resulting from the conversion of calcein AM to fluorescent calcein in live cells, signifies viable cells.

To evaluate the impact of the bioprinting process on cell viability, we assessed the viability of cells before and after bioprinting in both the bioink and the bioprinted tissues. This assessment was conducted using the CellTiter-Glo® 3D Cell Viability Assay (Promega Corporation, USA), in accordance with the manufacturer's instructions. Briefly, the CellTiter-Glo® 3D reagent was added directly to each sample. To ensure complete cell lysis and optimal assay performance, the samples were gently mixed and then incubated, allowing the luminescent signal to stabilize. Luminescence was quantified using a luminescence counter, with the intensity of the luminescent signal serving as a readout for cell viability within the 3D structures. For comparative analysis, all data were normalized to the average luminosity observed prior to the bioprinting process.

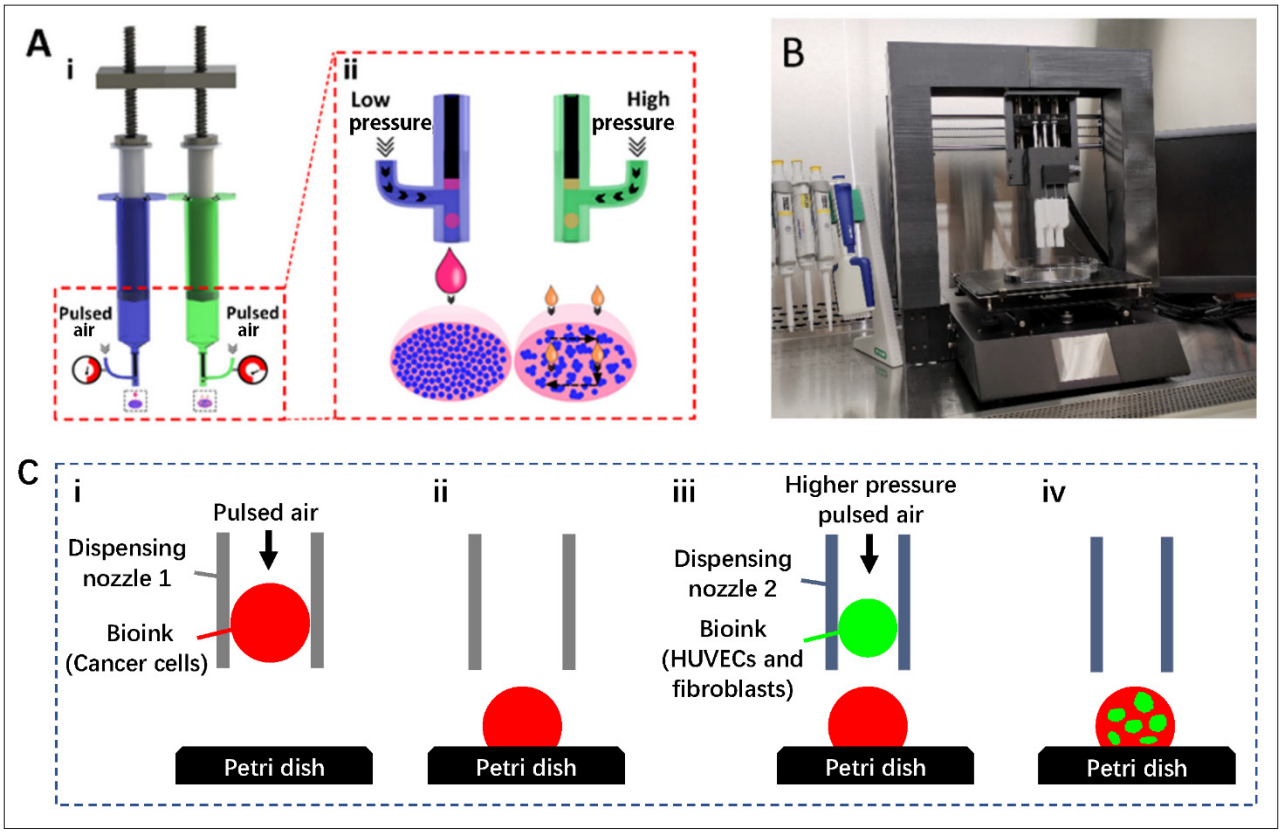
2.3. Cell labeling using CellBrite dyes

CellBrite Blue, Green, and Red Cytoplasmic Membrane Dyes (Biotium, USA) were utilized to label distinct cell types in bioprinted PMCaTs, as per the manufacturer's recommendations. Cells, upon reaching 70–80% confluence, were washed with PBS, treated with a serum-free medium, and subsequently incubated with a 5× dye solution at 37°C for 20 min. After washing off excess dye and a subsequent 30-min incubation in fresh medium, the cells were visualized under a fluorescence microscope to confirm successful labeling. Analysis of the labeled cells within the bioprinted tissues was conducted using image analysis software, with quantification based on the intensity and distribution of each fluorescent label. Experiments were carried out in triplicate.

2.4. Bioprinter design and mechanism

The DVDOD 3D bioprinting system has been detailed in prior publications,[13,14] and is also depicted in Scheme 1A and B. Our bioprinter distinctively utilizes a direct control mechanism whereby the bioink droplet volume is regulated by a linear actuator. This method contrasts existing systems, which commonly adjust fluid-valve durations or the bioink's applied pressure.

The bioprinter is constructed with a three-axis linear motion gantry equipped with multiple linear dispensing units, each designed to enhance the precision of the bioprinting process. Each of these units possesses a syringe driven by a linear actuator, enabling the volumetric manipulation of bioink dispensed. Upon the introduction of bioink into the air-driven dispensing nozzle, pulsed air is injected, facilitating the expulsion of the determined bioink volume. These dispensing units harmoniously control droplet locations and their volumes on the substrate. To ensure optimal bioprinting conditions, the printer is equipped with temperature and humidity control



Scheme 1. The direct volumetric drop-on-demand (DVDOD) bioprinting process for engineering micro-cancer tissues. (A) DVDOD mechanism, with red spheres indicating the placement of bioink droplets. Adapted from Grottkau et al.[14] (B) Representative photo of a bioprinter. Adapted from Grottkau et al.[13] (C-i and C-ii) The initial placement of a bioink droplet (symbolized in red) containing cancer cells onto the Petri dish. (C-iii and C-iv) Subsequent placement of a second bioink droplet (symbolized in green), which contains a mixture of human umbilical vein endothelial cells (HUVECs) and fibroblast cells, onto the Petri dish. The second droplet is dispensed under a higher pressure to merge it with the first. This collision-like action incurs both spatial separation and integration of the three cell types involved following the merging of the two droplets.

units. Significantly, varying outcomes can be achieved by dispensing the same droplet volume under different drive pressures, which can be used to generate droplet collisions to generate features within a droplet.[14]

The open-source GRBL control system, which incorporates GRBL firmware, Arduino boards, and motor controllers, governs the multi-linear actuator movements, covering the XYZ gantry and the syringe plunger motions. Activation of the pulsed air is streamlined via GRBL's in-built on-off control feature. Standard GRBL-backed G- and M-codes direct the bioprinter's motion and pulsed air toggling. These codes are relayed to the bioprinter through GRBL-compatible code senders. Moreover, a pressure regulator maintains consistent pulsed air pressure.

2.5. Bioprinting process

A specialized bioink was formulated by amalgamating specific cancer cells (either SUM149, MDA-MB-231, or MCF-7) with a matrix of collagen type I and fibrin hydrogels. Initially, using a designated dispenser, this bioink was deposited on a Petri dish surface, forming the primary droplet (Scheme 1C-i and C-ii). Subsequently, droplets holding the medium and a fibroblast–HUVEC mixture were released onto this primary droplet with increased pressure via a secondary dispenser (Scheme 1C-iii and C-iv).

To simulate cancer nests, the primary and relatively extensive homogeneous droplet containing cancer cells was fragmented into multiple smaller cellular clusters. As the high-pressure droplets collided with the initial droplet, they acted as disruptive forces. These forces compartmentalized the concentrated cancer cells into clusters, while enabling their merger into a larger droplet on the substrate. Notably, the fibroblasts and HUVECs surrounded and partially infiltrated these cancer cell clusters. Rapid solidification of the bioink was triggered by thrombin, stabilizing the created cellular structures, and preventing inter-cluster interfaces.

2.6. Detection of hypoxic regions in bioprinted micro-cancer tissues

Hypoxia in PMCaTs was evaluated using the Hypoxyprobe™-1 Omni Kit (Hypoxyprobe, Inc., USA). Pimonidazole in the kit binds to thiol groups in hypoxic cells (oxygen levels <10 mm Hg) for subsequent immunohistochemical detection. PMCaTs (n = 3) were treated with 200 μM pimonidazole hydrochloride for 3 h (omitted for the negative control), then fixed with 4% paraformaldehyde, permeabilized, and blocked with bovine serum albumin (BSA). Subsequent incubation with fluorescein isothiocyanate (FITC)-conjugated anti-pimonidazole antibody enabled visualization under a confocal microscope at excitation/emission wavelengths of 495/519 nm.

2.7. Hematoxylin and eosin staining of bioprinted tissues

PMCaTs were subjected to hematoxylin and eosin (H&E) staining for histological analysis. Following fixation in 10% neutral buffered formalin, the tissues underwent dehydration, xylene clearing, and paraffin embedding. Sections of 5 μm were prepared using a microtome and subsequently stained with hematoxylin for nuclei and eosin for cytoplasm and extracellular matrix.

2.8. Confocal analysis of microvascular development in bioprinted tissues

PMCaTs were composed of cancer cells labeled with CellBrite Red, NHLFs with CellBrite Blue, and HUVECs. These tissues were embedded in a collagen I hydrogel (Corning, USA) prepared at a concentration of 2 mg/mL, in line with the manufacturer's guidance. After a vascular development duration of 3 days, the tissues were fixed with 4% paraformaldehyde for 15 min at room temperature. Thereafter, they were permeabilized with 0.1% Triton X-100 for 10 min and blocked using 1% BSA in PBS for 1 h.

For the identification of endothelial cell markers, tissues were incubated overnight at 4°C with fluorescently conjugated antibodies targeting CD31 (at a 1:200 dilution in 1% BSA/PBS). Following three washes with PBS, these tissues were set up with a mounting medium optimized for fluorescence microscopy. Confocal imaging was executed using a Nikon confocal system, maintaining consistent image acquisition settings across samples. To visualize the intricate 3D structure of the newly formed microvascular networks inside the tissues, Z-stacks were captured and then 3D reconstructed, adhering to our previously documented protocol.[17]

2.9. Invasion assay

To examine the invasive properties of our PMCaTs, we utilized an invasion assay. The PMCaTs were embedded in a collagen I hydrogel at 2 mg/mL concentration, and subsequently cultured in a complete medium. For drug efficacy studies, we exposed the embedded PMCaTs to 0, 2, 20, 100, and 200 μM (n = 3 per concentration) of a 5-fluorouracil (5-FU) and then imaged them daily for 3 days using a phase contrast microscopy (Nikon, Japan). The invasion dynamics under drug treatments were benchmarked against untreated controls. Images of the invasion of cancer cells into the surrounding collagen matrix were binarized, and the ratios of the invaded area to the original microtissue area were computed as the primary metric. This analysis was conducted using ImageJ (https://imagej.nih.gov/ij/; National Institutes of Health, USA). For this assay, a 3-day endpoint was established based on preliminary empirical evidence that such a timeframe was adequate to observe the differential effects of the drug concentrations tested. The assay duration was limited to 3 days to prevent cell invasion from extending beyond the visual field of the microscope, which would impede accurate assessment and measurement.

2.10. Drug penetration modeling

The penetration of drug compounds into the PMCaTs (n = 3) was studied using a model drug, Alexa Fluor 488-labeled dextran (70,000 MW, Invitrogen, USA). The bioprinted PMCaTs were submerged in PBS containing Alexa Fluor 488-labeled dextran. The penetration and distribution of the Alexa Fluor 488-labeled dextran within the bioprinted PMCaTs were visualized using multiphoton microscopy (Olympus, Japan).

2.11. Modeling T cell-based immunotherapy

Before bioprinting, all cells designated for the micro-cancer tissue, including SUM149 cells, NHLF, and HUVECs, were labeled with PKH26 to ensure their traceability and visualization. These cells were subsequently 3D bioprinted to create PMCaTs. After a 5-day culture period, Jurkat cells, an immortalized line of human T lymphocyte cells, were labeled with CellBrite Green. These labeled Jurkat cells were then thoroughly mixed with collagen hydrogel, and the PMCaTs were delicately embedded within this mixture. Once embedded, the collagen was allowed to polymerize, securing the encapsulation of both the PMCaTs and Jurkat cells. After the collagen polymerization, the entire system, which comprised the PMCaTs surrounded by Jurkat T cells, was visualized and imaged using a fluorescent microscope to study the distribution and interaction of the labeled cells.

2.12. Modeling printed micro-cancer tissue metastasis

SUM149 cells, NHLFs, and HUVECs were labeled with PKH26 and bioprinted into PMCaTs (as detailed in section **2.5. Bioprinting process**). Given that the half-

life for elution of PKH26 from labeled cells exceeds 100 days, this enabled the tracking of all cells in PMCaTs throughout the metastasis simulation. Bioprinted PMCaTs were strategically positioned atop a nylon mesh and each microtissue was firmly attached to the mesh using a small droplet of fibrin glue, ensuring its stability during the observation period. Over a designated timeframe, two key metastatic behaviors were observed: (i) the release of small cellular aggregates from the original microtissue, emulating the initial step of *in vivo* cancer metastasis where tumor cells detach from the primary tumor, and (ii) the initiation of new tumor growth at a distance (>5 mm) from the original micro-cancer tissue. Remote tumor growth was identified as a metastatic event, especially given the lack of a fluorescent migration path linking it to the original tissue.

2.13. Cell proliferation upon alisertib treatment

2.13.1. Drug preparation

Alisertib was dissolved in dimethyl sulfoxide (DMSO) to create stock solutions. From this stock, it was diluted with culture medium to achieve the specified concentrations: 2, 20, 100, and 200 μM. For control experiments, an equivalent volume of DMSO, matching the highest alisertib concentration, was used to discern any potential effects of the solvent alone on cell viability.

2.13.2. 2D cell viability assay using CellTiter-Glo

MDA-MB-231 and MCF-7 cells were seeded into 96-well plates at a density of 5000 cells/well and incubated overnight to ensure complete attachment. Following attachment, the cells were treated with concentrations of 0, 2, 20, 100, and 200 μM of alisertib (n = 3 per condition) and incubated for an additional 48 h. Subsequently, 100 μL of CellTiter-Glo reagent was added to each well, ensuring thorough mixing for cell lysis. The plates were then set aside at room temperature for 10 min, allowing the luminescent signal to stabilize. Luminescence was quantified using a plate-reading luminometer.

2.13.3 Micro-cancer tissue bioprinting and cell viability assay using CellTiter-Glo 3D

PMCaTs were generated using the protocol detailed in section **2.5. Bioprinting process**. They were placed into the wells (n = 3 per concentration) of a 96-well plate, incubated, and treated with concentrations of 0, 2, 20, 100, and 200 μM of alisertib for 48 h. At the end of the assay, 100 μL of CellTiter-Glo 3D reagent was introduced to each well. The plates were subjected to agitation on an orbital shaker for 5 min. This was followed by a 25-min incubation at room temperature to stabilize the luminescent signal. Luminescence intensities were captured using a plate-reading luminometer. Luminescence readings were then normalized against the control group to determine relative cell viability.

2.14. Statistical analysis

Data are reported as mean ± standard deviation (SD). The independent t-test was employed to determine the differences between two distinct groups. For comparisons across multiple groups, analysis of variance (ANOVA) with the Tukey post-hoc test was used. A significance level was established at $p < 0.05$.

3. Results and discussion

3.1. Viability and structure of printed micro-cancer tissues under fluorescent microscopy

Our bioprinting technique proficiently produces PMCaTs with three distinct cell types (Figure 1A–D). Cancer cells, fluorescently labeled in red, mimic natural cancer nests with their sub-grouped arrangement. Fibroblasts, fluorescently labeled in blue, depict the role of CAFs in genuine tumor contexts. Additionally, the inclusion of endothelial cells, fluorescently labeled in green, simulate the microvascular system, underlining the intricacy of our bioprinting approach. Notably, the PMCaTs maintained consistent viability over 4 weeks (Figure 1E–G), illustrating the robustness of our technique. This sustained vitality not only attests to the method's efficiency but also suggests its suitability for prolonged research and therapeutic evaluations. Integrating pivotal elements of the cancer microenvironment like CAFs[18] and microvasculature,[19] alongside detailed tissue architecture and sustained viability, positions this approach as a valuable tool for comprehensive oncological studies.

In our current project, the data corroborate the efficacy of the DVDOD technique in maintaining cell viability, aligning with our prior observations. Notably, cell viability remained virtually unchanged during the bioprinting process (100.0 ± 6.03% before bioprinting vs. 94.6 ± 8.24% after bioprinting, with data normalized to pre-bioprinting values, $p > 0.05$) (Figure 1H). This outcome was attributed to the application of air pressures in a non-continuous mode, ensuring cells were exposed to pressure only during the fluid-driving phase. This approach contrasts with other DOD techniques where cells are subjected to continuous air pressure. We have tested various hydrogels, including collagen, alginate, and fibrin, in different concentrations and volumes. Unlike other DOD techniques, the DVDOD method maintains a more constant droplet velocity exiting the nozzle, as it does not rely on altering pressure to change the droplet size of bioink. This technique, which applies minimal pressures only during the fluid-driving phase, stands in stark contrast to the continuous pressure application seen in valve-based bioprinting. HUVECs

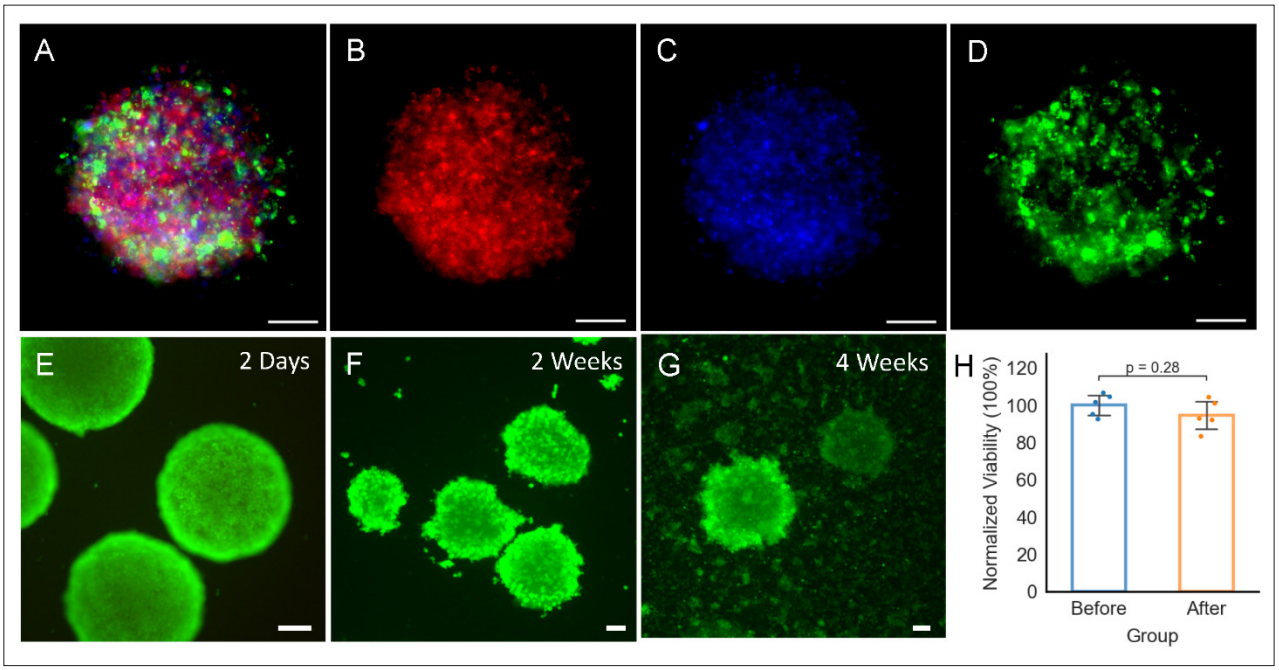


Figure 1. Viability and structure of printed micro-cancer tissues (PMCaTs). (A) The PMCaTs consist of three cell types. After bioprinting, (B) cancer cells (labeled in red) scatter into sub-groups to simulate cancer nests, while (B) fibroblasts (blue) represent cancer-associated fibroblasts, and (C) endothelial cells (green) replicate the microvascular system. (E–G) Viability of the PMCaTs across 4 weeks. (H) Cell viability before and after the printing process. Scale bars: 100 μm.

demonstrated no viability loss after DVDOD bioprinting ($p > 0.05$) (Figure 1H), a result that was consistent across other cell types utilized in our previous bioprinting projects, including chondrocytes, MC3T3-E1, 143B, and IPS cells.[13,14] These findings highlight the capability of DVDOD to maintain cellular integrity throughout the bioprinting process.

3.2. Morphology and proliferation pattern

Upon examining the architecture of the PMCaTs, a remarkable consistency emerged across the samples, underscoring the precision and reliability of the bioprinting process (Figure 2A). The presence of well-formed ductal structures and the conspicuous display of CAFs demonstrate the complex cellular interactions that these tissues can emulate, potentially providing valuable insights into tumor progression in more natural environments (Figure 2B).

Furthermore, the formation of cancer nests substantiates the capability of our bioprinted tissues to replicate intricate cellular arrangements *in vivo* (Figure 2C). The Ki-67 staining, a marker for cellular proliferation, revealed an intriguing gradient in proliferation patterns. Cells at the periphery exhibited pronounced proliferation due to higher oxygen availability (Figure 2D and E). This stands in contrast to the central cells that display reduced proliferation due to oxygen scarcity. Such a pattern mirrors the natural tumor microenvironment, where hypoxia at the tumor's core often inhibits cellular proliferation. The fidelity of this replication not only emphasized the significance of our bioprinted tissues but also suggested their potential utility in oncological studies. This notion was further solidified by the accompanying H&E staining (Figure 2F), which histologically validated the potential of these tissues as physiologically relevant platforms for therapeutic assessments and drug testing.

3.3. Hypoxia zone

In the PMCaTs, we observed a distinctive presence of hypoxic zones, reminiscent of the natural cancer microenvironment. As highlighted by the green fluorescent dye, cells in the hypoxic core of PMCaTs relatively dormant or quiescent. In contrast, cells in the non-hypoxic, oxygen-rich areas, as indicated by Ki-67 staining (Figures 2D and E), displayed signs of proliferation.

Hypoxia is a known feature of many solid tumors.[20] This cellular state, where cells in hypoxic regions remain largely inactive, while those in oxygenated regions continue to proliferate, has implications for therapeutic strategies.[21,22] Specifically, conventional treatments, such as chemotherapy and radiotherapy, often target cells that are actively dividing, potentially leaving those in the hypoxic zones unaffected. This difference in cell activity might contribute to some challenges faced in cancer treatments, such as therapy resistance.[23]

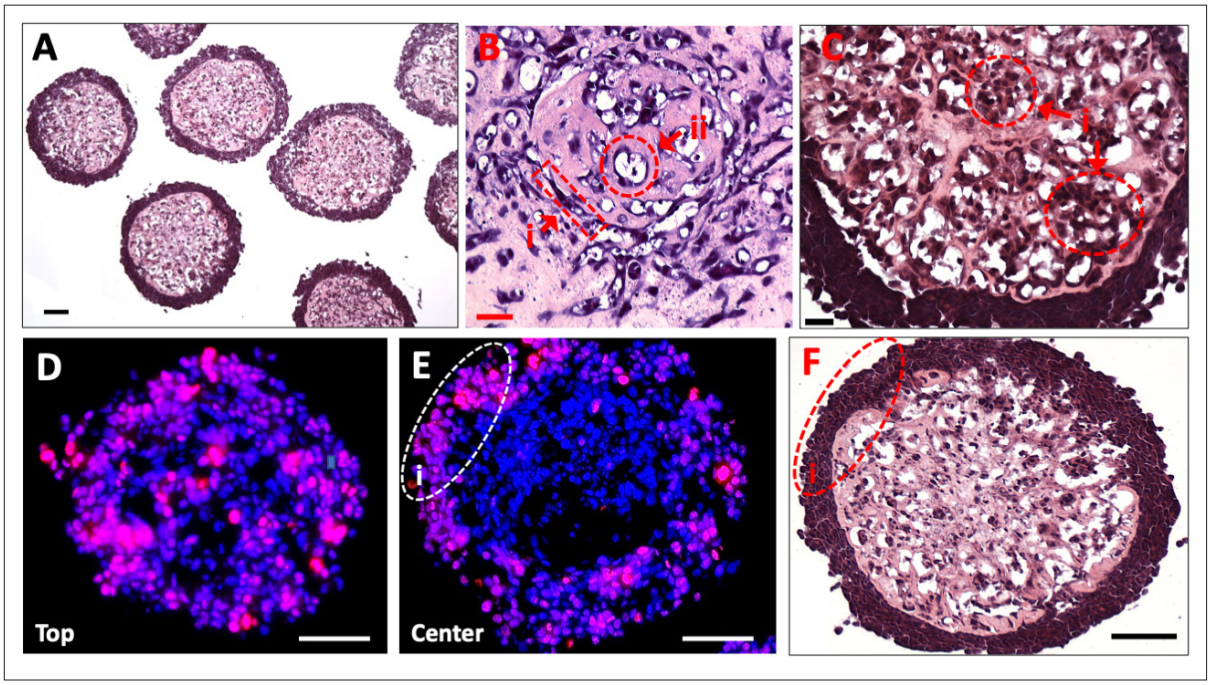


Figure 2. Morphology and proliferation patterns of printed micro-cancer tissues (PMCaTs). (A) Bioprinted tissues with uniformity and repeatability. (B-ii) Ductal structures; (B-i) presence of cancer-associated fibroblasts. (C-i) Formation of cancer nests. (D and E) The distinct tumor proliferation pattern, evident through intensified cell proliferation at the oxygen-abundant peripheries contrasted with the hypoxic center, is illuminated by Ki-67 staining in the (D) microtissue top sections and (E) central section. (F) Corresponding hematoxylin and eosin (H&E) staining. The oval dashed lines in (E) and (F) delineate the corresponding regions of two sections from the same PMCaT. Scale bars: (A) 100 μm; (B) 20 μm; (C) 40 μm; (D–F) 100 μm.

The presence of these hypoxic and non-hypoxic zones in our PMCaTs suggests that our bioprinted model may provide insights into tumor biology (Figure 3A–C). Notably, the outer region displays a higher cell density devoid of hypoxia, in contrast to the sparser cell density observes in the hypoxic center. Furthermore, understanding the behavior of cells in these regions might offer avenues for refining therapeutic approaches, though more studies would be required to ascertain the model's potential in this realm.

3.4. Printed micro-cancer tissues exhibit resistance to 5-fluorouracil during invasion

We closely monitored the invasion patterns of PMCaTs over 3 days in response to varied concentrations of 5-FU, a commonly used chemotherapy drug. As observed in Figure 4A, light microscopy consistently reveals the steady invasion of PMCaTs into the surrounding matrix across all 5-FU concentrations. The quantitative data presented in Figure 4B summarize the invasion outcomes. By Day 3, no significant differences were noted across any of the tested drug concentrations, even when compared to the control. This consistent pattern underscores the resistance of PMCaTs to 5-FU treatment. This drug resistance aligns with clinical observations that 5-FU is ineffective in preventing breast cancer invasion, particularly in the triple-negative subtype.

The significance of this observed resistance is amplified when considering the bioprinted composition of our PMCaTs, specifically the inclusion of CAFs. It has been identified that CAFs play a pivotal role in drug resistance, often modulating the tumor microenvironment in ways that reduce the efficacy of chemotherapy agents.[24] Given that our PMCaTs combine these fibroblasts with breast cancer cells, it stresses the importance of understanding the intricate interactions between cancer cells and their surrounding microenvironment when formulating therapeutic strategies. Investigating combination therapies or alternative drugs that target the protective mechanisms triggered by CAFs might hold the key to addressing this resistance challenge.

3.5. Establishment of printed micro-cancer tissues with microvasculature

The intricate interplay of microvasculature within PMCaTs (Figure 5) yields important insights into the behavior of breast cancer cells in conjunction with other cellular entities. Figure 5A projects a 3D visualization of the micro-cancer tissue, distinctly demarcating breast cancer cells, fibroblasts, and the intricate microvasculature. Figure 5B and C further

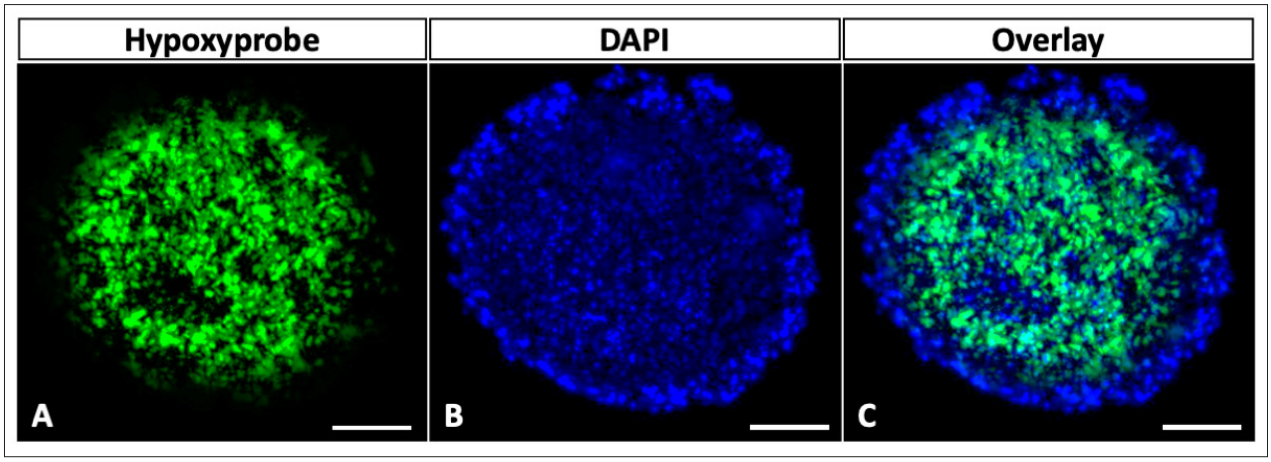


Figure 3. Visualization of hypoxia zones in the printed micro-cancer tissue (PMCaT). The green fluorescent dye illuminates the (A) inner core, marking regions of hypoxia, while DAPI staining outlines the (B) total cell population. (C) Combined green fluorescence-DAPI dye staining. Scale bars: 100 μm

illustrates the symbiotic relationship between the cancer cells and the microvasculature. Notably, the cancer cells are observed migrating into the lumens of the microvascular structures, all without causing external breaches.

An interesting observation from these panels was the directed migration of cancer cells into the lumen of the microvascular structures, underscoring the pivotal role of the microvascular system in cancer invasion and potential metastasis. The association between cancer cells and microvasculature suggests that these vascular conduits may be instrumental in facilitating the aggressive nature of malignant cells.[25]

The seamless migration of cancer cells into these channels, devoid of external ruptures, underscores the necessity of investigating the internal signaling pathways guiding this behavior. The inclination of cancer cells towards the lumen insinuates that certain molecular cues from the microvascular system may be drawing these cells, hinting at an influential role for the endothelial cells that constitute the microvascular linings.[19]

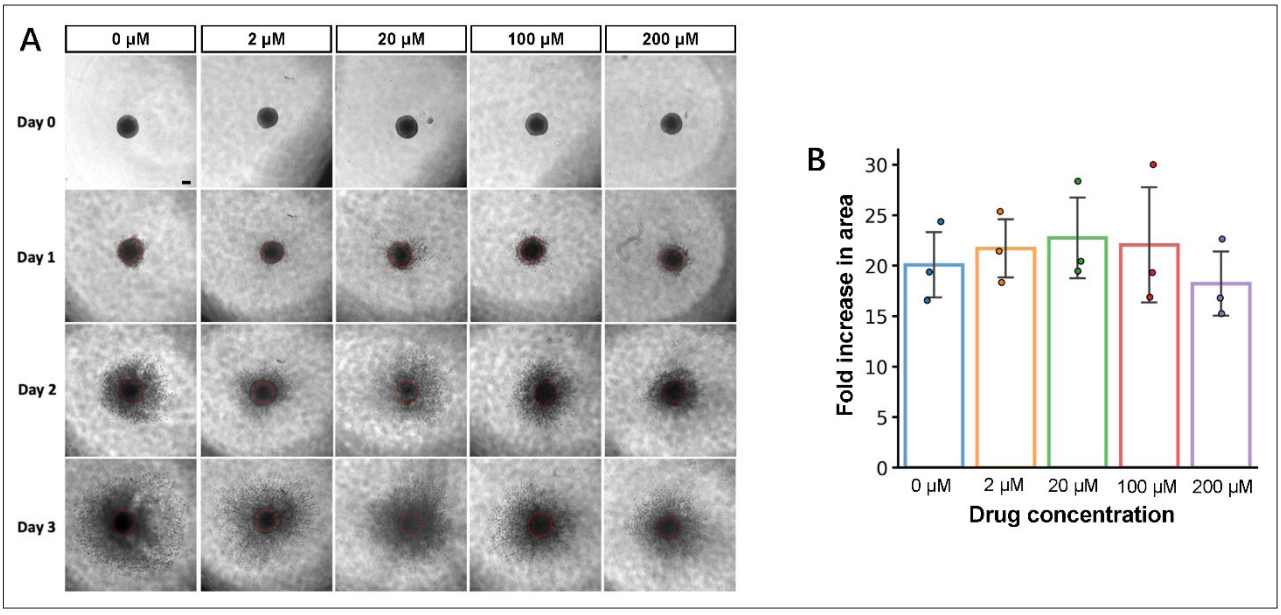


Figure 4. Printed micro-cancer tissue (PMCaT) invasion dynamics under different 5-Fluorouracil (5-FU) concentrations. (A) Daily progression from Day 0 to 3, illustrating the tissue invasion into the surrounding matrix across four different 5-FU concentrations. (B) Invasion outcomes on Day 3. Scale bar: 200 μm applies to all images in (A).

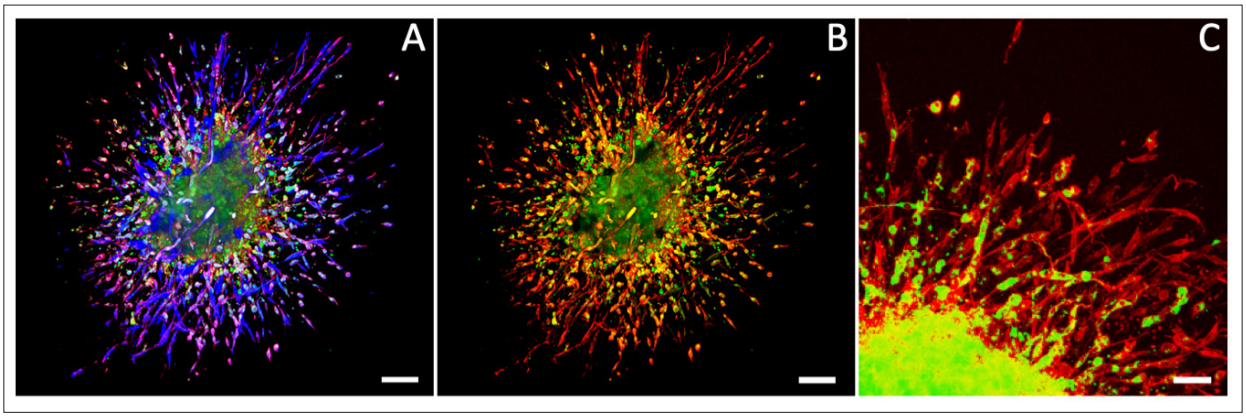


Figure 5. Microvasculature development within printed micro-cancer tissues (PMCaTs). (A) Architecture of the micro-cancer tissue, highlighting breast cancer cells (green), intricate microvasculature (red), and fibroblasts (blue). (B and C) Depiction of cancer cells (green) and microvasculature channels (red). Scale bars: 100 μm.

Such an observation not only deepens our understanding of tumor biology but also paves the way for novel therapeutic avenues. Given the central role of the microvascular system in tumor progression, targeting it could prove to be groundbreaking. Future therapies may not only aim to inhibit cancer cell growth but also target the cancer microvasculature, potentially arresting metastatic progression and offering a more comprehensive approach to cancer treatment.[26,27]

3.6. Dynamics of drug penetration

The penetration dynamics of therapeutics, especially those of high molecular weight, remain an area of intense research, particularly in the context of solid tumors. Many current therapies, such as monoclonal antibodies in immunotherapy or targeted therapy, have molecular weights around 150 kDa, while traditional chemotherapy agents are much smaller, typically ranging from 200 to 900 Da. Given the importance of understanding the penetration of larger molecules, we used AlexaFluo488-Dextran with a molecular weight of 70 kDa as a surrogate. This molecular weight is approximately half that of many therapeutic antibodies, suggesting its diffusion could be even slower than actual antibodies. Our experiments provide intriguing insights into its penetration within PMCaTs. As demonstrated in Figure 6A–C, the dye effectively penetrated the cell over time, suggesting time-dependent diffusion characteristics of the modeled drug.

Interestingly, the rate and pattern of dye diffusion in the PMCaTs provide cues to the matrix's inherent characteristics. One of the significant distinguishing features of PMCaTs, as compared to other models that embed cancer cells in hydrogel or rely solely on pure cell aggregates, is the presence of a considerable amount of relatively rigid matrix. Such a matrix can act as a barrier, potentially modulating the diffusion dynamics of drugs, slowing down their penetration, and influencing the overall therapeutic efficacy.

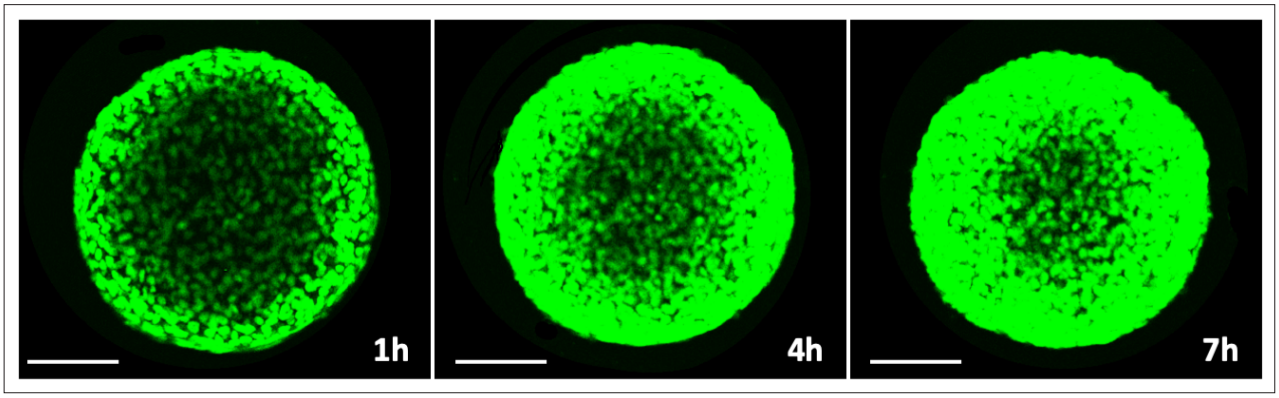


Figure 6. Modeling drug penetration using AlexaFluo488-Dextran (70 kDa). Evaluation of the depth of penetration of the fluorescent dye AlexaFluo488-Dextran, employed here as a representative model for large molecular weight compounds such as antibodies. Scale bars: 100 μm.

This unique matrix structure, while making PMCaTs more physiologically relevant by mimicking the natural tumor environment, also poses challenges for drug delivery. The intricate interplay between the rigidity of the matrix and the diffusion of large molecules may elucidate some of the obstacles encountered in clinical settings, especially when administering antibody-based therapies. Moreover, this has broader implications. The understanding that PMCaTs can accurately simulate drug penetration due to their matrix composition emphasizes the need for refined drug delivery techniques tailored for specific tumor microenvironments.

Going forward, these findings stress the importance of not only targeting cancer cells but also understanding and possibly manipulating the tumor microenvironment for better therapeutic outcomes. It might be worth exploring strategies to modulate matrix rigidity or enhance drug penetration by changing the tumor matrix architecture,[28] offering a two-pronged approach to tackle tumor resistance and ensure a more effective drug delivery.[29]

3.7. Modeling immunotherapy

Our experiments depicted the interaction between T cells and the PMCaTs (Figure 7). The close proximity of these cells highlighted their interactions and the potential of our model as a platform for examining T cell-mediated responses within the context of cancer immunotherapy.

In modern oncology, the potential of cell-based immunotherapy in treating solid tumors has been recognized,[30] but its efficacy is often limited due to the physical barriers presented by the tumor matrix and the immune-suppressive effects exerted by endothelial cells and CAFs.[31,32] Our PMCaT system, which integrates both these cellular components and the matrix, offers a more representative platform for studying these challenges. The interactions between T cells and cancerous tissues in our model provide insights into their engagement and potential neutralization mechanisms. However, while the model presents a valuable foundation, it is in its initial stages. Given the growing importance of immunotherapy, our findings highlight the need for rigorous validation, incorporation of varied immune cell dynamics, and evaluations in drug testing scenarios to ensure the model's relevance and applicability in therapeutic studies.

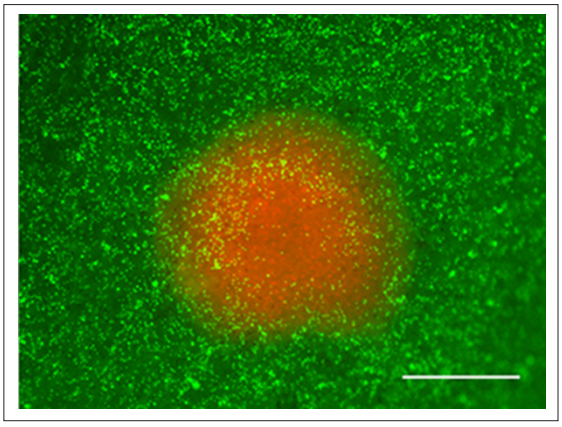


Figure 7. Visualization of T cell interaction with printed micro-cancer tissues (PMCaTs). The micro-cancer tissue is marked in red using PKH26, while a substantial surrounding population of T cells is highlighted in green with CellBrite Green. Scale bar: 300 μm.

3.8. Modeling cancer metastasis

Metastasis, the spread of cancer cells from the primary tumor to distant sites, is a key factor in cancer progression and the leading cause of cancer-related deaths.[33,34] By focusing on the dynamics of metastasis, our study aims to shed light on the mechanisms underlying cancer spread, offering potential avenues for therapeutic intervention.

Utilizing PMCaTs as our experimental model, we sought to visualize and understand the dynamics of metastasis in a controlled environment. All PMCaTs were stained with calcein AM for viability confirmation and visual enhancement. Non-mobilized PMCaTs exhibited the spontaneous release of small cell clusters, which then floated freely in the cell culture medium (Figure 8A).

More intriguingly, as illustrated in Figure 8B–D, once a PMCaT is secured to a mesh, the disengaged cell clusters travel in the medium, which serves as an analog to the bloodstream *in vivo*, and reattach themselves to more distant sites. This is evidenced by the absence of fluorescence between the original PMCaT and the distant reattachment sites, indicating a lack of cells. Essentially, the lack of cells between the original and the distant regrowth sites (indicated by an absence of fluorescence) verifies that the relocated cancer cells disperse from the PMCaTs into the medium before reattaching, negating the possibility of direct metastasis. Such insights are pivotal for understanding the intricate dynamics of metastatic behavior, particularly when tumor cells are found in locations far beyond their usual migratory range, as is the case during cancer invasion (Figure 4).

These findings not only offer a closer look into the complexities of metastasis but also emphasize the potential of our PMCaT model as a valuable tool in cancer research. By simulating *in vivo* metastatic processes, our model lays the groundwork for understanding the cellular dynamics involved. However, as with any model, it is imperative to recognize its limitations and the need for further validation. Future investigations should aim to delve deeper into the molecular cues guiding these behaviors and the potential variations with different cancer cell types or conditions,

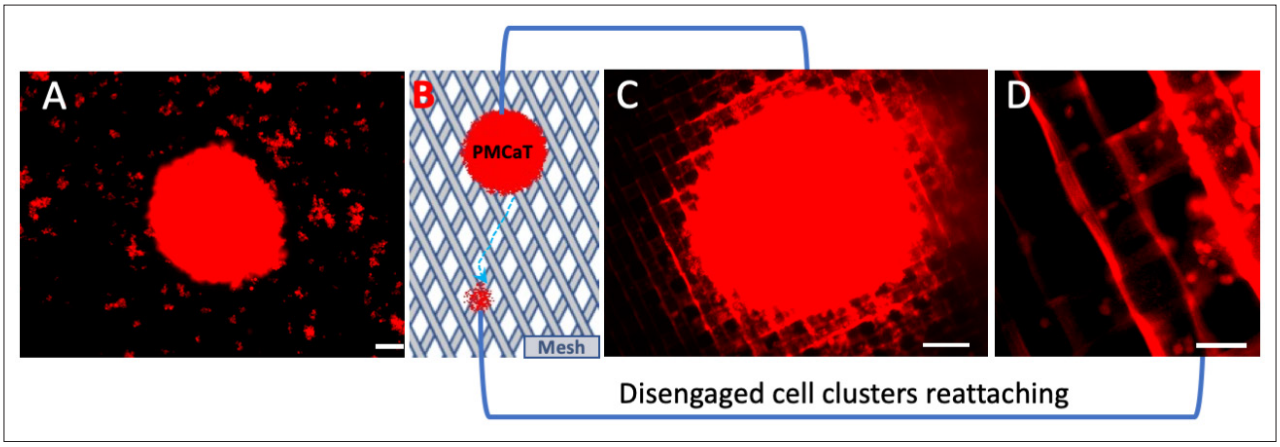


Figure 8. Visualization of metastasis in micro-cancer tissues. All cells in the printed micro-cancer tissues (PMCaTs) were labeled with PKH26. (A) A non-mobilized PMCaT from which small cell clusters are released, floating freely in the cell culture medium. (B–D) Sequence of PMCaT attachment to a mesh and reattachment of disengaged cell clusters to distant sites over time, emulating in vivo cancer metastasis. Scale bars: (A and C) 100 μm; (D) 50 μm.

ensuring our PMCaT system's continued relevance and utility in oncological studies.

3.9. Drug response prediction *in vivo*

We evaluated the response of MDA-MB-231 and MCF-7 cells to alisertib in both traditional 2D cultures and within our PMCaTs (**Figure 9**). No significant differences ($p > 0.05$) were observed between MDA-MB-231 and MCF-7 cells across all concentrations of alisertib. There was no significant difference between MDA-MB-231 and MCF-7 cells at lower concentrations of alisertib ($p > 0.05$), while PMCaTs with MDA-MB-231 cells exhibited significantly greater resistance (higher viability) at higher concentrations. Although Sum149, another typical negative breast cancer cell line, was predominantly used in our study due to its ductal breast cancer characteristics, we opted for MDA-MB-231 in this specific section. The extensive documentation of MDA-MB-231 in the existing literature potentially enhances the representativeness and comparability of our research.

Alisertib is an oral, selective inhibitor of aurora kinase A, which plays a crucial role in cell division and proliferation.[35] Currently under investigation for its therapeutic potential in various malignancies, alisertib has demonstrated promise in early-phase clinical trials due to its targeted mechanism of action.[36] Preliminary findings suggest that at lower concentrations of alisertib, no significant difference in response was observed between the two cell types. However, at higher concentrations, the MDA-MB-231 cells exhibited greater resistance to alisertib than MCF-7 cells. This increased sensitivity of the MCF-7 cells within the PMCaTs mirrors the results from phase 2 clinical trials where only the ER+/HER2- cells respond to alisertib.[37]

The outcomes from our PMCaT experiments align with the previous preclinical study that reported no difference

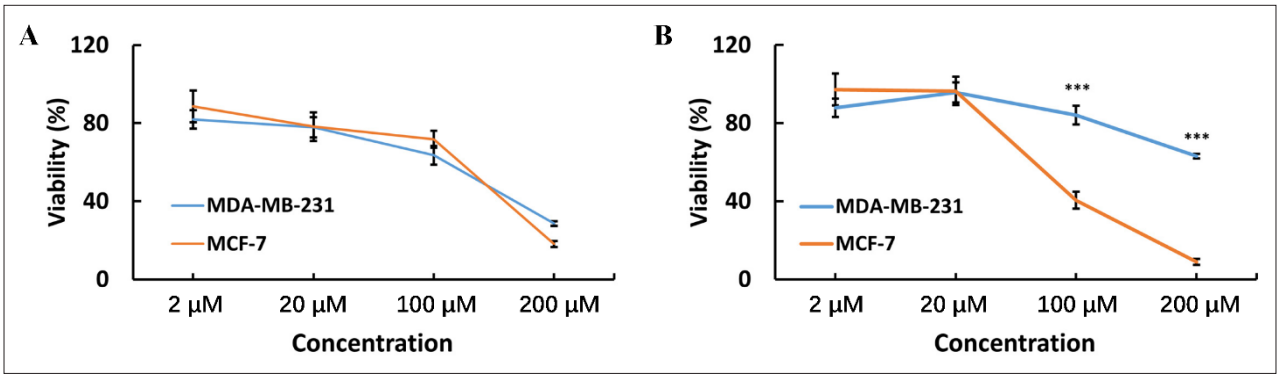


Figure 9. Comparative response of 2D cells and printed micro-cancer tissues (PMCaTs) to alisertib treatment. Assessment of viability in 2D MDA-MB-231 cells versus MCF-7 cells, and PMCaTs bioprinted using either MDA-MB-231 or MCF-7 cells, both co-printed with normal human lung fibroblasts (NHLF) and human umbilical vein endothelial cells (HUVECs). ***$p < 0.05$.

in alisertib's effect on the proliferation of ER+/HER2- cells (MCF-7) and triple-negative cells (MDA-MB-231).[38] The similar response at lower drug concentrations in our study suggests a drug-resistant characteristic in the bioprinted tissues, potentially masking differences between cell types. While the exact mechanism behind this drug resistance has not been systematically investigated, we predict that the native-like structure, combined with the microenvironment—encompassing CAFs and microvasculature—may contribute to it. However, it is worth noting that the results from the PMCaTs more closely matched the outcomes from the phase 2 clinical trials, which indicated the responsiveness of ER+/HER2- cells to alisertib. This suggests that our PMCaTs may have the potential to predict drug responses seen in clinical settings.

Our preliminary findings, which align with outcomes from human clinical trials, underscore the potential of our PMCaTs model as a significant advancement in cancer research. This comparative analysis is crucial, as it not only validates the model's fidelity to native-like tumor characteristics but also indicates its promising capacity for predicting human drug responses. The retrospective matches to clinical outcomes highlight the model's relevance and applicability, setting a foundation for its use in preclinical evaluations.

However, these observations are based on initial data and the forward-predictive power of our PMCaT model for drug responses warrants further exploration. To fully harness the potential of our model in aligning with clinical realities and enhancing patient treatment strategies, future work will concentrate on optimizing drug concentrations for more accurate predictions. Additionally, conducting more extensive quantitative studies is essential to verify the reliability of PMCaTs in drug response prediction, aiming to bridge the gap between experimental modeling and clinical application effectively.

Collectively, our study presents a comprehensive investigation into the capabilities of the DVDOD bioprinting technique in constructing PMCaTs with a focus on breast cancer. The results span both quantitative and non-quantitative aspects, contributing to a holistic understanding of the potential of 3D bioprinted models. Non-quantitative analyses, including viability and structure under fluorescent microscopy, morphology and proliferation patterns, establishment of PMCaTs with microvasculature, and the dynamics of drug penetration, underscored the technique's efficacy in replicating intricate *in vivo*-like tumor environments. These findings highlight the successful incorporation of heterogeneous cell populations and the formation of hypoxia zones, which are crucial for modeling cancer's complexity. Quantitative findings, particularly in the resistance of PMCaTs to 5-FU during invasion and the prediction of *in vivo* drug response, offered significant insights into the model's applicability for therapeutic evaluation. These findings provide statistical evidence supporting the utility of PMCaTs in assessing drug effectiveness and resistance patterns, enhancing the model's relevance for preclinical studies.

To further elucidate the model's predictive accuracy and therapeutic potential, more comprehensive future quantitative studies need to be designed. These studies are expected to not only validate the preliminary findings but also expand our understanding of the utility of PMCaTs across a wider range of cancer treatment scenarios.

4. Conclusion

The utilization of established cancer cell lines provides a robust foundation for advancing cancer research. A distinct advantage of our methodology is that it can rival models made with primary cells in predicting *in vivo* conditions. Crucially, this is achieved while mitigating the challenges of sample variability. Furthermore, our approach leverages the more abundant resource of established cancer cell lines compared to primary cells. The vast existing profile data associated with these cell lines complement our approach, enhancing the depth and reliability of our models. Although further optimization and rigorous validation of the PMCaT model remain essential, we believe that as we progress, our method has the potential to influence the methodologies of therapeutic research and drug testing in oncology.

Acknowledgments

Not applicable.

Funding

This project was funded by the Peabody Foundation, Inc., the Anthony and Constance Franchi Fund for Pediatric Orthopaedics, the Massachusetts General Hospital Department of Orthopaedic Surgery, and University of Miami Medical Center and Jackson Memorial Hospital Department of Orthopaedics.

Conflict of interest

Dr. Brian E. Grottkau is the founder of 3D Biotherapeutics, Inc. Dr. Yonggang Pang and Zhixin Hui declare no conflict of interest.

Author contributions

Conceptualization: Yonggang Pang, Brian E. Grottkau, Zhixin Hui

Formal analysis: Yonggang Pang, Brian E. Grottkau, Zhixin Hui
Investigation: Yonggang Pang, Brian E. Grottkau, Zhixin Hui
Methodology: Yonggang Pang
Supervision: Yonggang Pang
Validation: Zhixin Hui
Writing – original draft: Yonggang Pang, Brian E. Grottkau, Zhixin Hui
Writing – review & editing: Yonggang Pang, Brian E. Grottkau, Zhixin Hui

Ethics approval and consent to participate

Not applicable.

Consent for publication

Not applicable.

Availability of data

The data supporting the results of this study are available within the paper. Raw data generated for this study can be reasonably requested through the corresponding authors.

Further disclosure

Part of or the entire set of findings have been presented in TERMIS World Congress, Boston 2015. Brain Grottkau was affiliated with the Department of Orthopedic Surgery, Massachusetts General Hospital, at Harvard Medical School, Boston, Massachusetts, USA at the time of the research and is currently affiliated with University of Miami Medical Center and Jackson Memorial Hospital, Miami, USA.

References

1. Hidalgo M, Amant F, Biankin AV, et al. Patient-derived xenograft models: an emerging platform for translational cancer research. *Cancer Discov*. 2014;4(9):998–1013. doi: 10.1158/2159-8290.CD-14-0001
2. Langhans SA. Three-dimensional in vitro cell culture models in drug discovery and drug repositioning. *Front Pharmacol*. 2018;9:6. doi: 10.3389/fphar.2018.00006
3. Nusinow DP, Szpyt J, Ghandi M, et al. Quantitative proteomics of the cancer cell line encyclopedia. *Cell*. 2020;180(2):387–402.e16. doi: 10.1016/j.cell.2019.12.023
4. Cancer Therapeutics Response Portal. https://portals.broadinstitute.org/ctrp.v2.1/. Accessed August 13, 2023.
5. Dai X, Cheng H, Bai Z, Li J. Breast cancer cell line classification and its relevance with breast tumor subtyping. *J Cancer*. 2017;8(16):3131–3141. doi: 10.7150/jca.18457
6. Li Y, Kilian KA. Bridging the gap: from 2D cell culture to 3D microengineered extracellular matrices. *Adv Healthc Mater*. 2015;4(18):2780–2796.
7. Egeblad M, Nakasone ES, Werb Z. Tumors as organs: complex tissues that interface with the entire organism. *Dev Cell*. 2010;18(6):884–901. doi: 10.1016/j.devcel.2010.05.012
8. Sachs N, Clevers H. Organoid cultures for the analysis of cancer phenotypes. *Curr Opin Genet Dev*. 2014;24:68–73. doi: 10.1016/j.gde.2013.11.012
9. Clevers H. Modeling development and disease with organoids. *Cell*. 2016;165(7):1586–1597. doi: 10.1016/j.cell.2016.05.082
10. Ramesh S, Harrysson OLA, Rao PK, et al. Extrusion bioprinting: recent progress, challenges, and future opportunities. *Bioprinting*. 2021;21:e00116. doi: 10.1016/j.bprint.2020.e00116
11. Chartrain NA, Williams CB, Whittington AR. A review on fabricating tissue scaffolds using vat photopolymerization. *Acta Biomater*. 2018;74:90–111. doi: 10.1016/j.actbio.2018.05.010
12. Ng WL, Shkolnikov V. Optimizing cell deposition for inkjet-based bioprinting. *IJB*. 2024;0(0):2135. doi: 10.36922/ijb.2135
13. Grottkau BE, Hui Z, Pang Y. A novel 3D bioprinter using direct-volumetric drop-on-demand technology for fabricating micro-tissues and drug-delivery. *IJMS*. 2020;21(10):3482. doi: 10.3390/ijms21103482
14. Grottkau BE, Hui Z, Pang Y. Cellular patterning alone using bioprinting regenerates articular cartilage through native-like cartilagenesis. *Research Square*. 2023. doi: 10.21203/rs.3.rs-3380357/v1
15. Bashar MA, Begam N. Breast cancer surpasses lung cancer as the most commonly diagnosed cancer worldwide. *Indian J Cancer*. 2022;59(3):438–439. doi: 10.4103/ijc.IJC_83_21
16. Arnold M, Morgan E, Rumgay H, et al. Current and future burden of breast cancer: Global statistics for 2020 and 2040. *Breast*. 2022;66:15–23. doi: 10.1016/j.breast.2022.08.010
17. Pang Y, Ucuzian AA, Matsumura A, et al. The temporal and spatial dynamics of microscale collagen scaffold remodeling by smooth muscle cells. *Biomaterials*. 2009;30(11):2023–2031. doi: 10.1016/j.biomaterials.2008.12.064

18. Chen Y, McAndrews KM, Kalluri R. Clinical and therapeutic relevance of cancer-associated fibroblasts. *Nat Rev Clin Oncol*. 2021;18(12):792–804. doi: 10.1038/s41571-021-00546-5

19. Weiss L, Orr FW, Honn KV. Interactions of cancer cells with the microvasculature during metastasis. *FASEB J*. 1988;2(1):12–21. doi: 10.1096/fasebj.2.1.3275560

20. Strzyz P. Cancer biology: hypoxia as an off switch for gene expression. *Nat Rev Mol Cell Biol*. 2016;17(10):610. doi: 10.1038/nrm.2016.119

21. Koshiji M, Kageyama Y, Pete EA, Horikawa I, Barrett JC, Huang LE. HIF-1α induces cell cycle arrest by functionally counteracting Myc. *EMBO J*. 2004;23(9):1949–1956. doi: 10.1038/sj.emboj.7600196

22. Hubbi ME, Kshitiz, Gilkes DM, et al. A Nontranscriptional Role for HIF-1α as a Direct Inhibitor of DNA Replication. *Sci Signal*. 2013;6(262):ra10. doi: 10.1126/scisignal.2003417

23. Zhang Y, Zhang H, Wang M, et al. Hypoxia in breast cancer—scientific translation to therapeutic and diagnostic clinical applications. *Front Oncol*. 2021;11:652266. doi: 10.3389/fonc.2021.652266

24. Chen X, Song E. Turning foes to friends: targeting cancer-associated fibroblasts. *Nat Rev Drug Discov*. 2019;18(2): 99–115. doi: 10.1038/s41573-018-0004-1

25. Pepin F, Bertos N, Laferrière J, et al. Gene-expression profiling of microdissected breast cancer microvasculature identifies distinct tumor vascular subtypes. *Breast Cancer Res*. 2012;14(4):R120. doi: 10.1186/bcr3246

26. Frentzas S, Simoneau E, Bridgeman VL, et al. Vessel co-option mediates resistance to anti-angiogenic therapy in liver metastases. *Nat Med*. 2016;22(11):1294–1302. doi: 10.1038/nm.4197

27. Jain RK. Lessons from multidisciplinary translational trials on anti-angiogenic therapy of cancer. *Nat Rev Cancer*. 2008;8(4):309–316. doi: 10.1038/nrc2346

28. Yu M, Tannock IF. Targeting tumor architecture to favor drug penetration: a new weapon to combat chemoresistance in pancreatic cancer? *Cancer Cell*. 2012;21(3):327–329. doi: 10.1016/j.ccr.2012.03.002

29. Wang C, Chen S, Wang Y, et al. Lipase-triggered water-responsive "Pandora's Box" for cancer therapy: toward induced neighboring effect and enhanced drug penetration. *Adv Mater*. 2018;30(14):e1706407. doi: 10.1002/adma.201706407

30. Di Cosimo S. Advancing immunotherapy for early-stage triple-negative breast cancer. *Lancet*. 2020;396(10257):1046–1048. doi: 10.1016/S0140-6736(20)31962-0

31. Riley RS, June CH, Langer R, Mitchell MJ. Delivery technologies for cancer immunotherapy. *Nat Rev Drug Discov*. 2019;18(3):175–196. doi: 10.1038/s41573-018-0006-z

32. Becker JC, Andersen MH, Schrama D, Thor Straten P. Immune-suppressive properties of the tumor microenvironment. *Cancer Immunol Immunother*. 2013;62(7):1137–1148. doi: 10.1007/s00262-013-1434-6

33. Wirtz D, Konstantopoulos K, Searson PC. The physics of cancer: the role of physical interactions and mechanical forces in metastasis. *Nat Rev Cancer*. 2011;11(7):512–522. doi: 10.1038/nrc3080

34. Murphy PM. Chemokines and the molecular basis of cancer metastasis. *N Engl J Med*. 2001;345(11):833–835. doi: 10.1056/NEJM200109133451113

35. Zardavas D, Maetens M, Irrthum A, et al. The AURORA initiative for metastatic breast cancer. *Br J Cancer*. 2014;111(10):1881–1887. doi: 10.1038/bjc.2014.341

36. Haddad TC, Suman VJ, D'Assoro AB, et al. Evaluation of alisertib alone or combined with fulvestrant in patients with endocrine-resistant advanced breast cancer: the Phase 2 TBCRC041 randomized clinical trial. *JAMA Oncol*. 2023;9(6):815–824. doi: 10.1001/jamaoncol.2022.7949

37. Melichar B, Adenis A, Lockhart AC, et al. Safety and activity of alisertib, an investigational aurora kinase A inhibitor, in patients with breast cancer, small-cell lung cancer, non-small-cell lung cancer, head and neck squamous-cell carcinoma, and gastro-oesophageal adenocarcinoma: a five-arm phase 2 study. *Lancet Oncol*. 2015;16(4): 395–405. doi: 10.1016/S1470-2045(15)70051-3

38. Li JP, Yang YX, Liu QL, et al. The investigational Aurora kinase A inhibitor alisertib (MLN8237) induces cell cycle G2/M arrest, apoptosis, and autophagy via p38 MAPK and Akt/mTOR signaling pathways in human breast cancer cells. *Drug Des Devel Ther*. 2015;9:1627–1652. doi: 10.2147/DDDT.S75378

ACCSCIENCE PUBLISHING

International Journal of Bioprinting

RESEARCH ARTICLE

4D printing and simulation of body temperature-responsive shape-memory polymers for advanced biomedical applications

Dahong Kim[1,2], Kyung-Hyun Kim[3], Yong-Suk Yang[3], Keon-Soo Jang[4], Sohee Jeon[1], Jun-Ho Jeong[1], and Su A Park[1]*

[1]Nano Convergence & Manufacturing Systems, Korea Institute of Machinery and Materials (KIMM), Daejeon, South Korea

[2]Department of Applied Bioengineering, Graduate School of Convergence Science and Technology, Seoul National University, Seoul, South Korea

[3]Intelligent Components & Sensors Research Section, Electronics and Telecommunications Research Institute (ETRI), Daejeon, South Korea

[4]Department of Polymer Engineering, School of Chemical and Materials Engineering, University of Suwon, Suwon, South Korea

(This article belongs to the *Special Issue: 3D Printing of Bioinspired Materials*)

Abstract

Four-dimensional (4D) bioprinting holds significant promise in precision medicine, enabling the emulation of dynamic changes in the human body and tissues to provide personalized treatments. Smart materials for 4D printing (i.e., responsive to specific stimuli) should exhibit properties, such as biodegradability, biocompatibility, and ease of processing, while also enabling the prediction of time-dependent behavior in programmed geometry. This study focused on the development of a body temperature-responsive shape-memory polymer (SMP). The thermal properties of the SMP were analyzed, and its biodegradability and biocompatibility were assessed through structures fabricated by three-dimensional printing techniques. The simulation calculated with this finite element (FE) solution was in good agreement with those measured in experiments. The findings contribute to our understanding of the behavior of SMP under various conditions, validating the effectiveness of the developed material for potential applications in precision medicine and 4D bioprinting. It has the potential for use in medical devices, such as catheters, stents, and artificial scaffolds, prepared by 4D bioprinting.

Keywords: 4D printing; 4D printing simulation; 3D bioprinting; Biodegradable shape-memory polymer; Biocompatible shape-memory polymer

***Corresponding author:**
Su A Park (psa@kimm.re.kr)

Citation: Kim D, Kim KH, Yang YS, et al. 4D printing and simulation of body temperature-responsive shape-memory polymers for advanced biomedical applications. *Int J Bioprint*. 2024;10(3):3035. doi: 10.36922/ijb.3035

Received: February 27, 2024
Accepted: April 22, 2024
Published Online: June 13, 2024

Copyright: © 2024 Author(s). This is an Open Access article distributed under the terms of the Creative Commons Attribution License, permitting distribution, and reproduction in any medium, provided the original work is properly cited.

Publisher's Note: AccScience Publishing remains neutral with regard to jurisdictional claims in published maps and institutional affiliations.

1. Introduction

In the medical field, three-dimensional (3D) printing has encountered challenges due to its static characteristics and the absence of shape-morphing capabilities, hindering its ability to closely mimic the continuously changing dynamics of the human body and tissues. Four-dimensional (4D) bioprinting can be one of the alternatives that can overcome these hurdles in 3D printing. 4D printing has evolved by incorporating the time dimension as the fourth dimension into conventional 3D printing.[1-3] 3D structures

in 4D printing undergo changes in shape or function over time within a specific environment and in response to stimuli. Therefore, an ideal printed structure produced by 4D bioprinting should have the ability to respond to such dynamism for effective integration with the human body.[2,4-8] Furthermore, with minimal invasiveness and appropriate responses to human elements, there is considerable potential for applications in precision medicine, offering personalized treatments for individual patients.[9-13]

Smart materials, including shape-memory polymers (SMPs), shape-memory alloys (SMAs), and hydrogels, are utilized to enable programmed changes in shape over time in specific conditions.[14-17] Several characteristics of smart materials are particularly vital for their application in 4D bioprinting within the medical field. For suitability in 4D printing, the material should demonstrate flexible expansion and contraction in response to a specific stimulus, ensuring it is nonharmful to the human body. Additionally, the material must be easy to process, facilitating the manufacture of complex geometries tailored to the patient's characteristics. Furthermore, during the treatment period, metabolic interactions with surrounding human tissue are crucial, necessitating the use of materials that can be safely absorbed into the body at the appropriate time.[9,18-20]

To utilize 4D printing in precision medicine, it is crucial not only to design a well-formed programmable structure but also to accurately predict the time-dependent behavior resulting from specific stimuli. 4D printing is well-suited for applications within the human body, where it will be subjected to continuous change. Therefore, there is increasing interest in 4D bioprinting simulations, which are crucial for achieving 4D-printed biomaterials with the desired mechanical properties and structural integrity.[21-23] Simulation allows researchers and medical professionals to anticipate how printed structures will respond within the dynamic environment of the body, aiding in the optimization of designs and materials for enhanced biocompatibility and functionality. Thus, integrating 4D bioprinting simulations into the design and development process is essential for advancing the efficacy and reliability of precision medicine applications.

In this study, an SMP was developed to maintain shape-memory effects and self-deformation characteristics as a 4D printing material. This polymer demonstrated excellent processability with a 3D printer and exhibited biocompatibility and biodegradability through synthesis from polylactic acid (PLA) and polyethylene glycol (PEG) (Figure 1). Analysis of its thermomechanical properties revealed a glass transition temperature (T_g) within the body temperature range, and dynamic mechanical analysis (DMA) was performed. The processability of the material by 3D printing was confirmed through printability tests, and biodegradability characteristics were assessed using an accelerated decomposition method. Biocompatibility was established by investigating the interaction between the developed material and cells in a series of *in vitro* experiments. The experimental results verified that the developed material underwent shape deformation into the programmed shape in a specific stimulation environment. Furthermore, a simulation study was conducted to enable theoretical prediction of its shape. This study demonstrated that sophisticated shapes tailored to the individual characteristics of each patient can be fabricated with 4D printing and highlighted the ability to accurately predict shape recovery occurring in programmed shapes. This material will enhance the performance of medical devices, such as catheters, stents, and artificial scaffolds.

2. Materials and methods

2.1. Materials

Poly(lactic acid) (PLA) was sourced from PLA (Green Chemical Co., South Korea), while polyethylene glycol (PEG) was obtained from PEG (Samchun Co., South Korea).

2.2. Preparation of body temperature-responsive shape-memory polymers

Prior to extrusion, PLA and PEG were oven-dried at 45°C for 4 h. PLA and PEG were combined in plastic bags and mixed using a tumbler mixer. The blend was then fed at a rate of approximately 4 kg/h into the main hopper of a corotating intermeshing twin-screw extruder (STS25–44V–SF; Hankook EM Ltd., South Korea), set at a hopper temperature of 100°C. This extruder features a screw diameter of 25 mm and a length-to-diameter (L/D) ratio of 44. It is equipped with two die holes, each 4 mm in size, and operates at a screw speed of 180 rpm. The barrel temperature was maintained at 100–207°C to achieve a resin temperature of 225°C, slightly exceeding the barrel temperature due to internal friction and shearing effects. The pressure within the barrel was kept at 10 bar. The melted resins were cooled in a water bath at room temperature (22–24°C) and subsequently pelletized. The pellets were then oven-dried at 35°C for 24 h. For specimen preparation, the composite pellets were processed in an injection molding machine (LGH50N; LS Mtron Co., South Korea) with a screw diameter of 25 mm. The machine was operated at barrel temperatures of 220–230°C, with a maximum injection pressure of 2520 kgf/

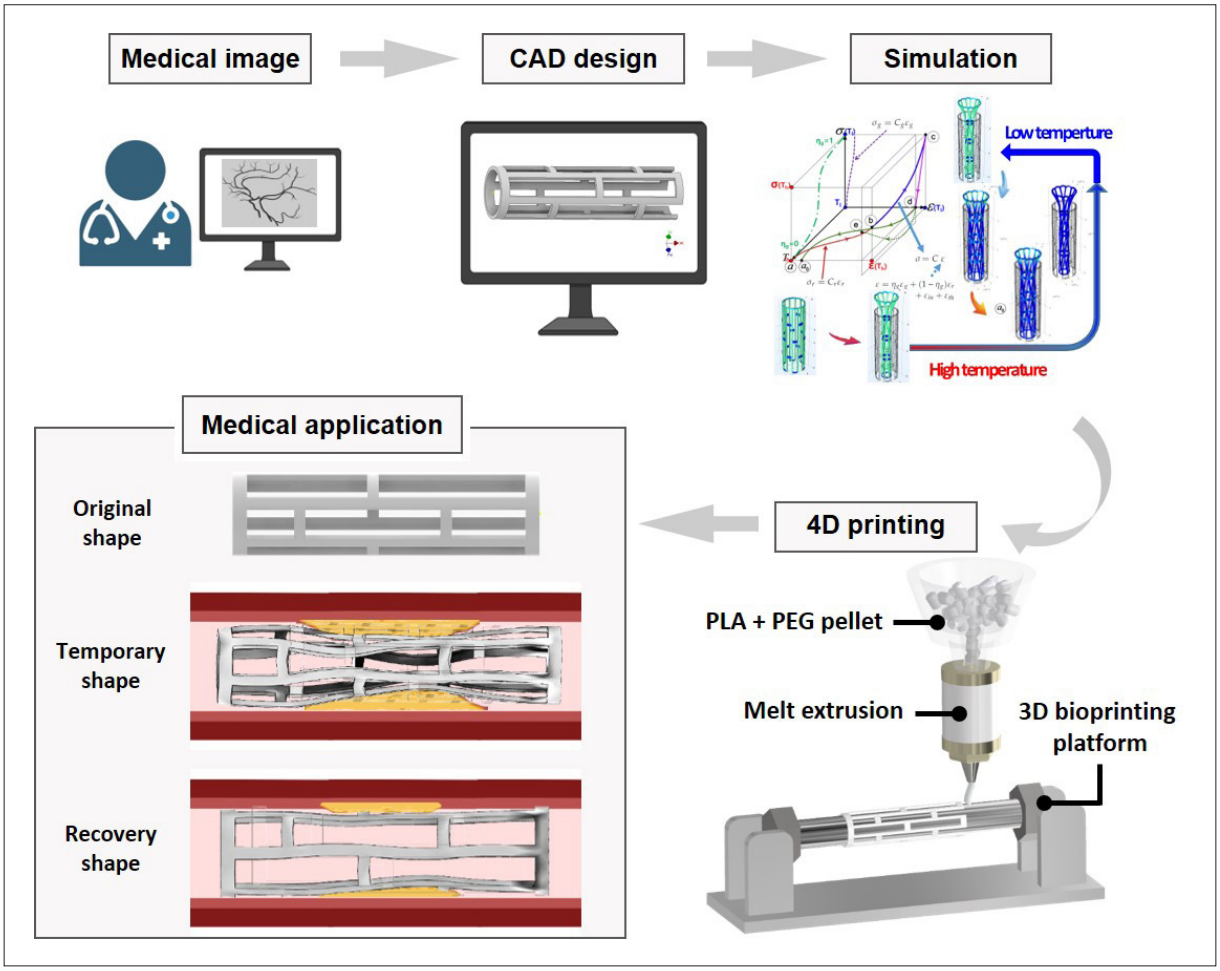


Figure 1. Schematic of the 4D bioprinting process for medical applications. The 4D bioprinting process involves the deformation and recovery of a 3D-printed structure utilizing a blend of biocompatible and biodegradable polylactic acid (PLA) and polyethylene glycol (PEG) polymers. The deformation and recovery processes are triggered by external stimuli, including heat and force. Abbreviation: CAD: Computer-aided design.

cm^2 and a maximum injection volume of 45 g/cycle. The injection pressures and times for tensile and Izod impact strength test specimens were set at 70 kgf/cm^2 for 8 s and 50 kgf/cm^2 for 4 s, respectively. The injected specimens were cooled in a mold at room temperature for 30 s.

2.3. Thermal and mechanical properties

The T_g was measured using a differential scanning calorimeter (DSC) (DSC25; TA Instruments, United States of America [USA]) with a temperature range of 10–80°C and a heating rate of 10°C/min. The thermal stability and degradation of the materials were determined by thermogravimetric analysis (TGA) (TGA4000; PerkinElmer, USA). The samples were heated from 30 to 700°C at a rate of 10°C/min. Viscoelastic properties were evaluated using a dynamic mechanical analyzer (DMA850; TA Instruments, USA) with a measurement temperature range of 10–80°C and a heating rate of 5°C/min. The single cantilever clamping method was utilized to measure the bar-type samples, 6 × 6 × 25 mm (oscillation frequency: 1 Hz; frequency stress: 0.1 N).

2.4. 3D printing and degradation of biodegradable shape-memory polymers

The SMP was 3D-bioprinted (PROTEK; Korea Institute of Machinery and Materials, South Korea) using the fused deposition modeling (FDM) method with controllable parameters, including temperature, printer head speed, and pneumatic printing pressure. To assess printability, the printing conditions were adjusted to closely match a nozzle size of 400 μm. The printing temperature was set to 200°C, the printer head speed was 420 mm/min, and the pneumatic pressure was maintained at 200 kPa.

A weight loss measurement method using a basic solution was used. The initial weight of the sample of the synthesized biodegradable polymer was measured. The sample size was 10 × 10 × 3 mm (width × diameter × height), and the initial weight was established as 0.2 g (± 10%) through 3D printer fabrication. Subsequently, a solution of 0.1 N NaOH, pH 12.5, was added to an inert plastic container, and the sample was placed in a decomposition environment at a temperature of 37°C with shaking at 120 rpm. After a specified decomposition period, the sample was taken out, washed with distilled water, and dried at 37°C, and the weight was measured. This process allowed the evaluation of the weight ratio of the decomposed sample in comparison to its initial weight. The weight loss was assessed using the following equation:

$$\text{Weight loss (\%)} = (W_0 - W)/W_0 \times 100 \quad \text{(I)}$$

where W_0 represents the initial weight, and W represents the weight measured after degradation.

2.5. Cell culture

NIH3T3 cells were cultured in Dulbecco's modified Eagle's medium-high glucose (DMEM) supplemented with 10% fetal bovine serum (FBS) and 1% penicillin in an incubator at 37°C with 5% CO_2.

2.6. Cell viability, proliferation, and cell morphology of biocompatible shape-memory polymers

Cell biocompatibility and viability were assessed using a live and dead assay. Aliquots of approximately 5×10^5 cells were seeded onto the samples and allowed to attach for 4 h in an incubator at 37°C with 5% CO_2. The samples were cultured for 1, 4, or 7 days, washed with phosphate-buffered saline (PBS) to remove the medium, and then stained for approximately 1 h with calcein-AM to identify live cells and homodimer-1 to identify dead cells. The stained cells were observed under a fluorescence microscope.

Cell proliferation was assessed by WST-1 assay. The WST-1 solution was prepared following the manufacturer's instructions. The polymer with cells was incubated with 500 µL of WST-1 solution in a 24-well plate for 1 h. After incubation, 100 µL of supernatant was transferred to a fresh 96-well plate, and the absorbance at 440 nm (A_{440}) was measured using a microplate reader.

The morphology of adherent cells on the SMP was investigated by scanning electron microscopy (SEM). After culture of the cells with polymer for 7 days, the samples were fixed overnight in 4% paraformaldehyde and subsequently dehydrated by passage through a series of ethanol solutions (10, 30, 50, 70, 90, and 100%) at 5-min intervals. Pt coating was performed using a sputter coater, and SEM images were captured at a voltage of 10 kV.

2.7. Fixation and recovery rate

The SMP was designed to enable two types of motions, bending and linear motion, through 3D printing. It was printed using PLA+PEG 10 phr and PLA+PEG 20 phr SMP compositions. The shape for bending motion was fabricated as follows: a hinge shape measuring 10 × 10 × 2 mm (width × depth × height). An external force was applied at a temperature higher than T_g to achieve an angle less than or greater than 90°. After maintaining room temperature for approximately 1 min while applying the external force, the cooling state was sustained. Subsequently, the external force was removed, and the free state was maintained for about 24 h. Following this period, a temperature higher than T_g was applied again to return to the recovery shape. The fixation and recovery rates of the bending motion were calculated as follows:

$$F_{rate}\,(\%) = (C_{angle}/F_{angle}) \times 100 \quad \text{(II)}$$

$$R_{rate}\,(\%) = (O_{angle}/R_{angle}) \times 100 \quad \text{(III)}$$

where F_{rate} refers to the fixation rate, C_{angle} refers to the angle during cooling, and F_{angle} refers to the angle when fixed in the free state; R_{rate} refers to the recovery rate, O_{angle} refers to the angle in the original shape, and R_{angle} refers to the angle value in the recovery state.

The shape for linear motion was manufactured in a sheet shape measuring 20 × 20 × 0.5 mm (width × diameter × height). Similar to the bending motion, for the linear motion, an external force was applied by stretching both sides at the extremes by about 3 mm when a temperature above the T_g was applied. The SMP underwent cooling, free, and recovery state-linked bending. The fixation and recovery rates of the linear motion were calculated as follows:

$$F_{rate}\,(\%) = (C_{length}/F_{length}) \times 100 \quad \text{(IV)}$$

$$R_{rate}\,(\%) = (O_{length}/R_{length}) \times 100 \quad \text{(V)}$$

where F_{rate} refers to the fixation rate, C_{length} refers to the length during cooling, and F_{length} refers to the length when fixed in the free state; R_{rate} refers to the recovery rate, O_{length} refers to the length in the original shape, and R_{length} refers to the length in the recovery state.

2.8. Shape-memory effect and experiment for simulation

The shape-memory characteristics of the 4D-printed polymer processed with a 3D printer were examined. The experiments were carried out over a temperature range of 40–55°C, which exceeded the material's T_g.

The experiments were conducted as follows. A cylindrical column was fabricated with an inner diameter of 8.45 mm, thickness of 0.80 mm, and height of 5.22 mm. The original shape, which represented the memorized shape, was exposed to a temperature exceeding the T_g (high temperature), and an external force was applied to induce a temporary shape change. The external force was sustained for 5 min while maintaining the high temperature. Subsequently, the temporary shape was allowed to remain in a free state without any external force applied for 24 h at room temperature (low temperature). With no external force applied, the temperature exceeding the T_g (high temperature) was applied, and the recovery process was maintained for 5 min. Throughout these stages, the inner diameter, thickness, and height of the structure in each state were examined.

A rigid-body hinge was fabricated by stereolithography (SLA) with a 3D printer (Objet30; Stratasys, USA). A hollow square shape was produced to match the 3-mm height of the hinge made of SMP. A hinge made of SMP was inserted into a rigid body to verify the shape-memory effect according to a method similar to that described above.

2.9. Statistical analysis

All of the quantitative data are presented as the mean ± standard deviation. The results were analyzed using a one-way analysis of variance, followed by Tukey's post hoc test. Statistical analysis was conducted using Origin (Origin 8.6 ver., OriginLab Corporation, USA).

3. Results and discussion

3.1. Thermal and mechanical properties of shape-memory polymers for 4D printing

SMPs generally retain their programmed shape and can recover their original shape in response to environmental stimuli. In medical applications, they offer the advantage of accommodating large deformation, making them well-suited for addressing the effects of minor invasions or changes in tissue.

Specifically, temperature-responsive SMPs, characterized by an amorphous network, typically exhibit shape-memory behavior in proximity to the T_g. In the shape-memory cycle, significant deformation can occur even under low stress due to rapid changes in material stiffness above T_g. Below T_g, the material transitions into a glassy state and can maintain its programmed shape.[24-26] Therefore, DSC was used to determine the T_g range of the SMP, which yielded T_g values of 59.1°C for PLA, 36.2°C for PLA+PEG 10 phr, and 34.0°C for PLA+PEG 20 phr (Figure 2a). It was confirmed that T_g was established within a range similar to the range of body temperature for both PEG 10 phr and PEG 20 phr compositions of PLA+PEG.

The range of thermal degradation, when heat was applied to the SMP, was assessed by TGA (Figure 2b). In FDM printing, which processes the polymer by melting, it is possible to identify the temperature range when thermal degradation does not occur during printing. The degradation temperature range was confirmed based on a weight reduction of 1.0%. The results indicated that degradation occurred at a temperature of 336.8°C for PLA, 306.9°C for PLA+PEG 10 phr, and 289.4°C for PLA+PEG 20 phr. With the addition of PEG, the degradation temperature decreased, indicating a tendency to become more vulnerable to thermal decomposition.

Next, using DMA, we confirmed the mechanical properties at each temperature relative to varying PEG concentrations. Analysis of temperature-dependent behavior displayed a typical amorphous thermoplastic polymer in all groups. The mechanical strength of the materials began to drop at higher temperatures, as indicated by the storage modulus (Figure 2c). Specifically, PLA exhibited high brittleness and susceptibility to breakage at temperatures < 10.00°C, necessitating measurements to be conducted at room temperature. The storage modulus tended to decrease with increasing PEG content. The peak loss modulus refers to the region where the molecular motion undergoes a significant change. Large segments of the polymer could move cooperatively, leading to increased energy dissipation. Simultaneously, the material began to deform more easily.[27,28] In each group, the loss modulus also tended to decrease with increasing PEG content, and the peak was confirmed to occur at low temperatures (Figure 2c). The peak of the tangent delta is the transition region where the material exhibits the most pronounced viscous response to deformation.[29] From these results, it was confirmed that all groups maintained the glassy state at temperatures < 23.42°C (Figure 2d). In particular, with PLA+PEG 10 phr and PLA+PEG 20 phr, the flow region was reached at a temperature > 67.60°C. The produced SMP could be expected to be printed smoothly at temperatures higher than the temperature range after reaching the flow region. Therefore, considering the characteristics of TGA and DMA, the temperature range for printing could be expected to be approximately 67.60–250°C.

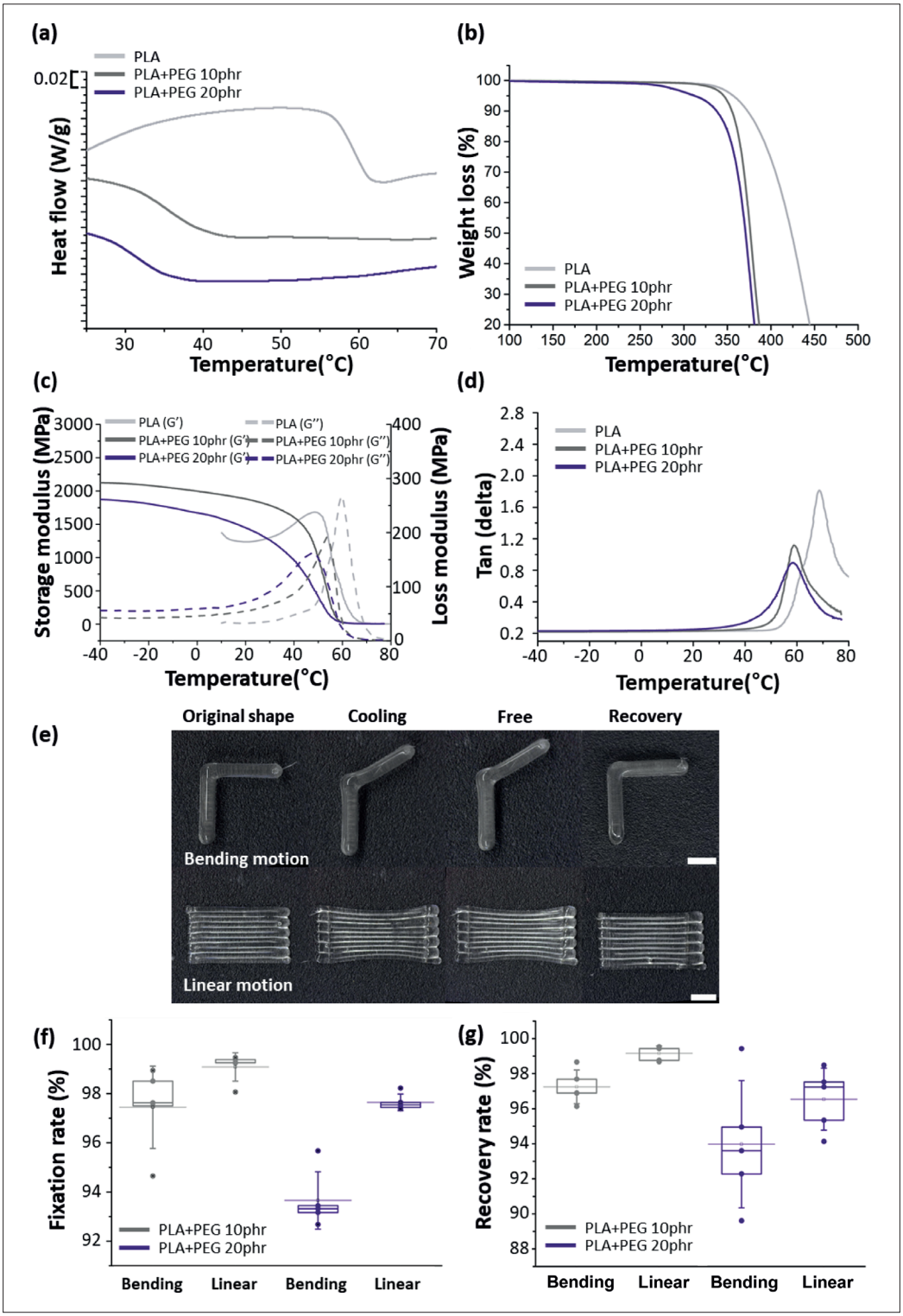


Figure 2. Thermal and thermomechanical properties of shape-memory polymers (SMPs) for 4D bioprinting. (a) Differential scanning calorimetry (DSC) of SMPs. (b) Thermogravimetric analysis of SMPs. (c) Dynamic mechanical analysis (DMA) of temperature-dependent dynamic shape-memory properties and (d) tangent delta. (e) The representative images of bending and linear motions of SMP. Scale bar = 5 mm. (f) Fixation rate of bending and linear motions according to polyethylene glycol (PEG) content in the SMP composite. (g) Recovery rate of bending and linear motions according to PEG content in the SMP composition. Abbreviation: PLA: Polylactic acid.

3.2. Fixation and recovery rate of shape-memory polymers

The fixation and recovery rates, which are key characteristics of SMPs, were examined. The fixation rate refers to the ability of SMP to maintain its shape after being subjected to an external force, retaining the deformed shape. The recovery rate refers to the ability of SMP to return to its initially programmed shape (original shape) after a specific stimulus is applied. For the application of SMP in medical devices, the fixation and recovery rates for two representative motions, bending and linear motion, were studied. The structures for the bending motion were designed in the form of a hinge, while the structures for the linear motion were designed as a thin sheet (Figure 2e). Furthermore, the fixation and recovery rates were investigated based on the content of PEG in the SMP composition.

Fixation and recovery rates exceeding 90% were observed across all motions and PEG contents. It was noted that bending motion exhibited slightly lower values compared to linear motion. Additionally, it was observed that the fixation and recovery rates tended to decrease with higher PEG content. Specifically, for PLA+PEG 10 phr, the fixation rates for the bending and linear motions were 97.44% (±1.67) and 99.08% (±0.57), respectively. For PLA+PEG 20 phr, the fixation rates for the bending and linear motions were 93.66% (±1.16) and 97.64% (±0.34), respectively (Figure 2f). For PLA+PEG 10 phr, the recovery rates for the bending and linear motions were 97.25% (±0.96) and 99.16% (±0.41), respectively. For PLA+PEG 20 phr, the recovery rates for the bending and linear motions were 93.97% (±3.63) and 99.16% (±1.76), respectively (Figure 2g).

Both the fixation and recovery rates for the two motions were close to 90–100%, indicating that the SMP effectively maintains the desired structure during cooling and returns to its original shape upon heating. This highlights its suitability for medical applications.

3.3. Printability and degradability of shape-memory polymers for 4D printing

Considering its thermal properties, a body temperature-responsive SMP was designed for 4D printing utilizing PLA+PEG 20 phr. FDM printing, a method involving melting and extrusion, was used to fabricate SMP at 200°C, which was below the thermal decomposition temperature of the material. Printability was confirmed by adjusting variables, such as the pressure pushing the molten SMP and feed rate, which is the speed of the printing head (Figure 3a). A printing nozzle with a diameter of 400 μm was used, and printing conditions ensuring strand thickness within a comparable size range (within ± 10%) were identified (Figure 3a). Validation experiments reported that increased pressure resulted in thicker strands, while higher feed rates yielded thinner strands. Notably, excessively fast feed rates led to strand movement before proper layer accumulation, resulting in a wavy shape. Based on these observations (**Table S1** in Supplementary File), subsequent printing was performed with the pressure set to 200 kPa and the feed rate set to 420 mm/min.

Biodegradable materials are substances whose molecular weight decreases through the disruption of chemical bonds within the human body. Specifically, for applications in the medical field, these materials must facilitate tissue regeneration during the period of use and assume structural functions within the human body once tissue regeneration has stabilized. The SMP developed in this study was a biodegradable composite polymer based on PLA and PEG. Biodegradability is widely assessed using hydrolytic degradation. Two techniques for evaluating biodegradability through hydrolytic degradation include a method using a neutral solution and another for accelerated decomposition.[30] In this study, the accelerated decomposition method, particularly the weight loss measurement method using alkaline solution, was employed.

The experiment was conducted with an initial weight of 0.2 g, and the extent of weight loss was assessed after decomposition for 0, 7, 14, 21, 35, and 49 days (Figure 3b). The degree of weight loss increased over time: 7.723% at 7 days, 20.837% at 14 days, 39.357% at 21 days, 59.676% at 35 days, and 79.174% at 49 days. Both the overall sample size and strand size decreased in proportion to weight loss as the polymer decomposed. In addition, SEM images revealed an increase in surface roughness with the progression of decomposition (Figure 3c).

Biodegradability through hydrolysis is known to occur by breaking the ester links of the polymer chain when reacting with water.[31] Decomposition typically begins in the amorphous region, which is the more flexible segment of the polymer and is more susceptible to the effects of water. Moreover, the decomposition mechanism of hydrolysis varies based on the solution used. In neutral or acidic solutions, hydrolysis destroys the ester linkages through protonation as water is added. Conversely, in alkaline solutions, decomposition occurs through a mechanism that breaks the ester linkages as a hydroxyl ion is added to the carbon of the carbonyl group.[31,32] This study confirmed the biodegradable properties of PLA- and PEG-based SMPs using a weight loss measurement method with an alkaline solution.

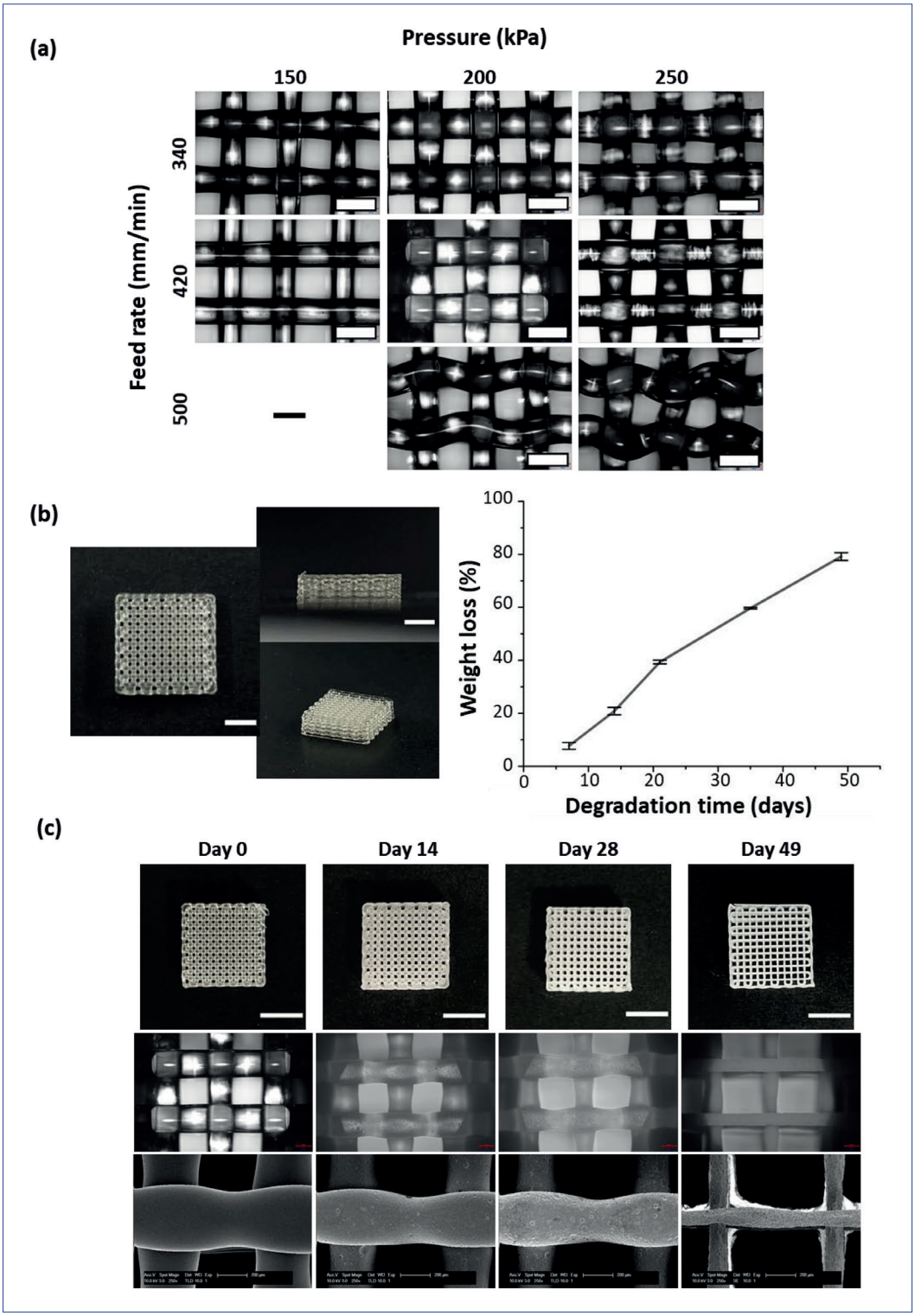


Figure 3. Printability and biodegradability of shape-memory polymers (SMPs). (a) Surface morphology of the SMP at different printing conditions (pressure and printing feed rate). Scale bar = 500 μm. (b) SMP weight loss throughout the degradation process, spanning 49 days. Scale bar = 3 mm. (c) Surface morphology of the degraded SMP. Scale bar = 1 mm.

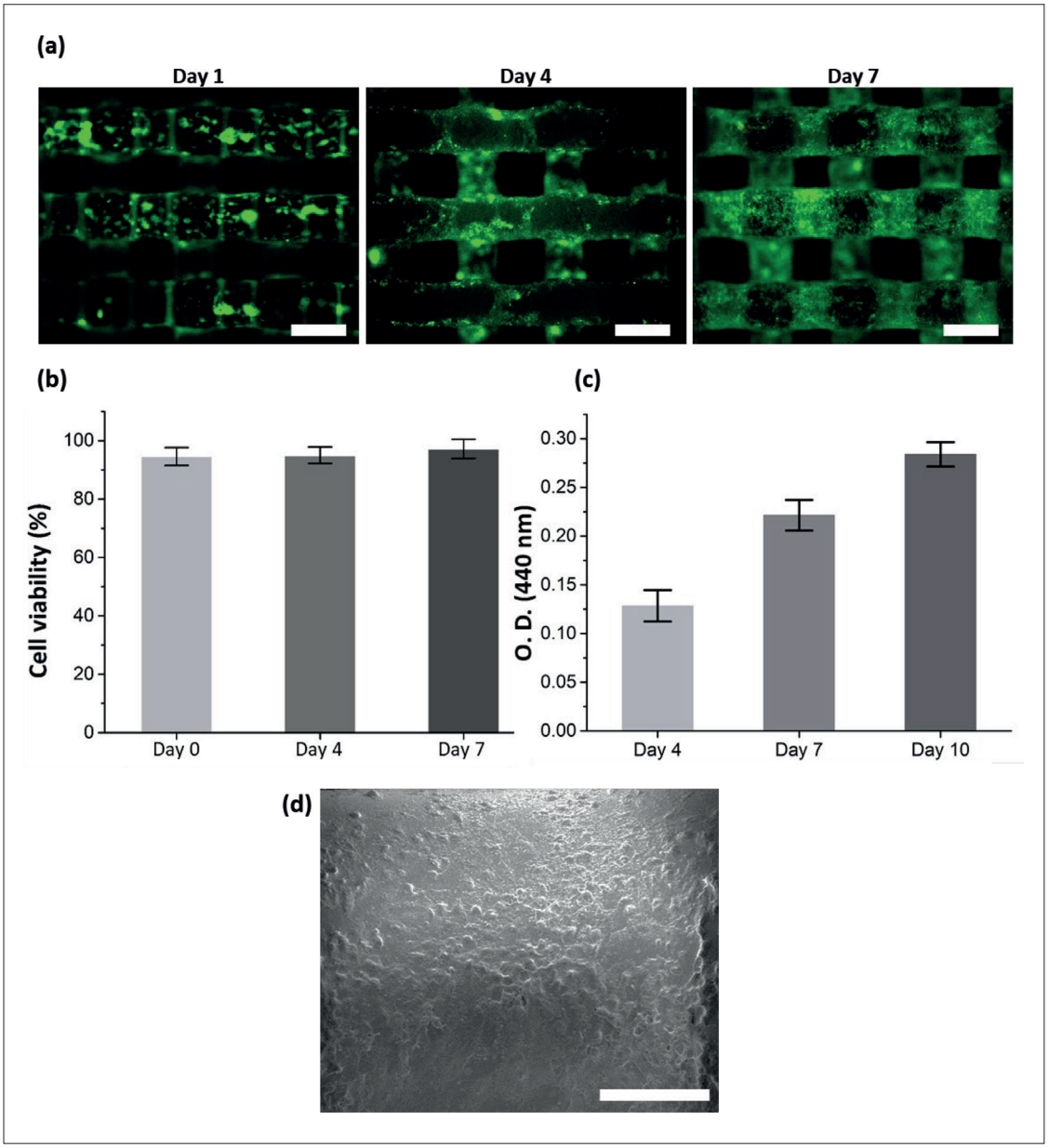


Figure 4. *In vitro* tests for cell viability and proliferation, and the cell morphology of biocompatible shape-memory polymers (SMPs). (a) Live and dead cell assay of biocompatible SMP. Scale bar = 500 μm. (b) Cell viability of biocompatible SMP. (c) WST-1 assay to determine cell proliferation. (d) The morphology of adherent cells on the surface of the SMP. Scale bar = 100 μm. Abbreviation: O.D.: Optical density.

3.4. Cell adhesion and biocompatibility of shape-memory polymers

Biocompatibility is a crucial characteristic required for biomaterials in the medical field. Biomaterials, which come into direct contact with living tissue to diagnose, treat, and prevent diseases, should not induce side effects, such as cellular toxicity, inflammation, or immune reactions. In this study, biocompatibility was assessed through a live and dead cell assay (Figure 4a). Considering the dominance of green fluorescence, which stains living cells, and the minimal emission of red fluorescence from damaged cells in the assay, the developed material displayed little cytotoxicity. Furthermore, the area occupied by living cells gradually increased over time due to cell proliferation. It was determined that viability remained above 90% throughout the experiment, with 94 ± 2.73% on day 0, 95.00 ± 2.82% on day 4, and 97.20 ± 3.28% on day 7 (Figure 4b). These results confirm that

the utilized SMP exhibits no cytotoxicity, indicating its potential suitability for use in biomedical devices. This trend was also evident in cell proliferation experiments using WST-1 (Figure 4c).

The biocompatibility of polymers is closely related to cell adhesion, as cells interact with the polymer surface to which they adhere. In the presence of a biocompatible polymer, protein adsorption occurs on the polymer surface, facilitating cell adhesion in the cytoskeleton. This interaction directly influences receptors, such as integrin, and plays a crucial role in cell survival and proliferation by impacting extracellular matrix (ECM) deposition, cell movement, and proliferation.[33-36] SEM was used to verify the morphology of adherent cells on the developed polymer (Figure 4d). The results confirmed that cells grew and formed a confluent layer that covered the surface of the polymer. In addition, microextensions were observed between adjacent cells, connecting them and forming a spindle shape.[37,38] These observations indicated that cell adhesion occurred smoothly on the surface of the developed polymer, thus confirming the biocompatibility of the developed SMP.

3.5. Shape-memory effect

To explain the thermodynamic behavior of the SMP mathematically, a two-phase model consisting of a rubber phase and a glass phase was used as a phenomenological constitutive model.[22,39,40] The two phases, the so-called glass phase and rubber phase, in the SMP were stable at temperatures above and below T_g, respectively. As the SMP is a mixture of the glass and rubber phases during the transition process, the volume fraction (η_g) of the rubber phase and the glass phase represents the state of the SMP. Considering the experimental results of the DMA test of PLA+PEG 20 phr, the η_g of the glass phase can be expressed approximately as a hyperbolic function, as described previously.[40] The values of a_1 and a_2 of the hyperbolic function, obtained by fitting the DMA curve, were 0.0956 and 0.0968, respectively. The changes in the glass and rubber phases of SMPs are generally only a function of temperature, and the total strain rate (ε) is expressed as follows:[40]

$$\varepsilon = \eta_g \varepsilon_g + (1-\eta_g)\varepsilon_r + \varepsilon_{in} + \varepsilon_{th} \quad \text{(VI)}$$

where ε_g and ε_r are the strains of the glass and rubber phases, respectively, and ε_{in} and ε_{th} represent the inelastic strain due to SMP phase transformation and thermal strain, respectively.[40]

The phase transformation mechanism between the glass and the rubber phases indicates that the rubber phase changes to the glass phase during the cooling process. In this process, the strain is stored in the SMP material, while the stored strain is returned during the heating process. The stress–strain relation of the SMP is expressed as follows:[40]

$$\sigma = (S_r + \eta_g (S_g - S_r))^{-1}(\varepsilon - \varepsilon_{in} - \varepsilon_{th}) \quad \text{(VII)}$$

where σ represents stress, and S_r and S_g represent the rubber phase and glass phase compliance matrix, respectively. S_i is expressed as follows:[22]

$$S_i = \begin{pmatrix} \frac{1}{E_i} & \frac{-\nu_i}{E_i} & \frac{-\nu_i}{E_i} & 0 & 0 & 0 \\ \frac{-\nu_i}{E_i} & \frac{1}{E_i} & \frac{-\nu_i}{E_i} & 0 & 0 & 0 \\ \frac{-\nu_i}{E_i} & \frac{-\nu_i}{E_i} & \frac{1}{E_i} & 0 & 0 & 0 \\ 0 & 0 & 0 & \frac{2(1+\nu_i)}{E_i} & & \\ 0 & 0 & 0 & 0 & \frac{2(1+\nu_i)}{E_i} & \\ 0 & 0 & 0 & 0 & 0 & \frac{2(1+\nu_i)}{E_i} \end{pmatrix} \quad \text{(VIII)}$$

where subscript $i = g$ represents the glass phase, and $i = r$ represents the rubber phase. Measurement of temperature-dependent Young's modulus revealed E_g and E_r values of 1880 and 5.63 MPa, respectively, and Poisson's ratios ν_g and ν_r were 0.35 and 0.4, respectively.

From a numerical perspective, nonlinear SMP behavior can be handled in an explicit time-discrete stress–strain temperature-based framework.[40] For the infinitesimal time domain $[t_n, t_{n+1}]$, the evolution equation of SMP in an n+1 step is expressed as follows:[40]

$$\varepsilon_{in}^{n+1} = \left(I + \Delta\eta_g^{n+1} S_r^{n+1} C_e^{n+1}\right)^{-1} \left(\varepsilon_{in}^{n} + \Delta\eta_g^{n+1} S_r^{n+1} C_e^{n+1}\left(\varepsilon^{n+1} - \varepsilon_{th}^{n+1}\right)\right) \quad \text{(IX)}$$

where the superscript n+1 represents the current step, the superscript n represents the previous step, $\Delta\eta_g^{n+1}$ is $\eta_g^{n+1} - \eta_g^n$, and C_e is the overall equivalent stiffness.[22,40]

Calculation of the inelastic strain (ε_{in}) due to the SMP phase transformation from the evolution equation of SMP was implemented using MATLAB software (MathWorks,

USA). For detailed information on finite element analysis (FEA), the solutions and numerical programming were reported previously.[22]

The shape-programming and recovery processes of the SMP were simulated using COMSOL Multiphysics (COMSOL Inc., Sweden). During the cooling step, the rubber phase changed to a glass phase, and the inelastic strain (ε_{in}) calculated using MATLAB was stored in the SMP material. This strain storage was proportional to η_g based on the rubber phase strain. In simulations of the heating step, the stored strain was gradually released proportional to η_g with respect to the previous glass phase and strain storage. Here, there were 600 temperature steps during cooling and heating.

3.6. Comparing the experimental and simulated behaviors of the shape-memory polymer

A cylindrical column was used to investigate for experimental behavior of the SMP (Figure 5a and b). It was initially fabricated with an inner diameter of 8.45 mm, a thickness of 0.80 mm, and a height of 5.22 mm, representing its original shape (the "a" point in the temperature-dependent stress–strain curves in Figure 5c). By subjecting it to temperatures above T_g, it transitioned to the "b" point state. Applying an external force and cooling resulted in the "c" point state, with a cooling shape having an inner diameter of 10.08 mm, thickness of 0.70 mm, and height of 4.90 mm. Upon removal of the external force to achieve the free state, it had a diameter of 10.00 mm, thickness of 0.73 mm, and height of 4.90 mm, representing the "d" point state. When T_o reverts to the memorized shape, raising the temperature led to the recovery shape ("a_0" point), experimentally confirmed to have a diameter of 8.94 mm, thickness of 0.79 mm, and height of 5.12 mm.

Figure 5c shows the FAE COMSOL Multiphysics simulation results of SMP. The original shape was 8.45 mm in diameter, 0.80 mm in thickness, and 5.25 mm in height, and was maintained at 10.08 mm in diameter, 0.73 mm in thickness, and 4.94 mm in height when cooling from a high to low temperature. In the free state with the applied external force removed, the shape had a diameter of 9.46 mm, thickness of 0.74 mm, and height of 5.00 mm, and after the temperature was raised again to a higher temperature, the recovery shape had a diameter of 8.5 mm, thickness of 0.8 mm, and height of 5.25 mm (Figure 5b and c). The results calculated with this FE solution were in good agreement with those measured in the experiments, indicating that they could be analyzed with COMSOL Multiphysics from a numerical perspective when verifying or predicting the memory phenomena observed in 4D printing samples. And the data in Supplementary 2 assumed of a conventional PLA polymer, rather than a shape-memory polymer. It illustrates the temperature-dependent stress–strain curve and the structure of thermoplastic polymers. In this instance, the memory effect is excluded, depicting the immediate return to the original state.

Shape-memory polymers that respond to body temperature can be used in a variety of applications. It has been confirmed that the shape-memory effect transitions through the stages of original shape, temporary shape, and recovery shape within the range of body temperature (Figure 6a). Using 3D printing, these polymers can be fabricated in appropriate sizes and diverse shapes (Figure 6b and c). It could demonstrate the polymer's ability to maintain complex geometries through the memory effect. Additionally, it has been demonstrated that shapes incorporating rigid bodies can function as hinges, further confirming the potential for these materials to act as actuators (Figure 6d).

4. Conclusion

3D printing is used to develop patient-specific biomedical applications, such as regenerative medicine tools, drug delivery devices, and implants, leveraging its ability to mimic physiological geometry. However, the dynamic nature of the human body presents a challenge, prompting the emergence of 4D printing, a concept in which the time domain is added to 3D printing, thus enabling shape or function changes over time in response to specific stimuli.

In this study, the SMP was newly developed for 4D bioprinting in the biomedical field. The thermal and physical properties of the manufactured SMPs were analyzed, and the results confirmed a suitable T_g range for PLA+PEG 10 phr and PLA+PEG 20 phr to react at human body temperature. Thermal stability was verified, confirming an appropriate processing temperature of 200°C for FDM printing. DMA analysis displayed that higher PEG content led to lower storage and loss modulus values and the transition from a glass to a viscous state at lower temperatures. PLA+PEG 20 phr was suggested to be suitable for printing based on thermal and mechanical analyses, and the results were used as data for SMP simulation. Printability conditions were determined with optimal results achieved at a temperature of 200°C, pneumatic pressure of 200 kPa, and feed rate of 420 mm/min. Hydrolytic degradation confirmed biodegradability, resulting in weight loss for 49 days. Biocompatibility was analyzed based on cell viability and proliferation. FE solution was used to predict the shape of the printed SMP. A two-phase model, consisting of rubber and glass

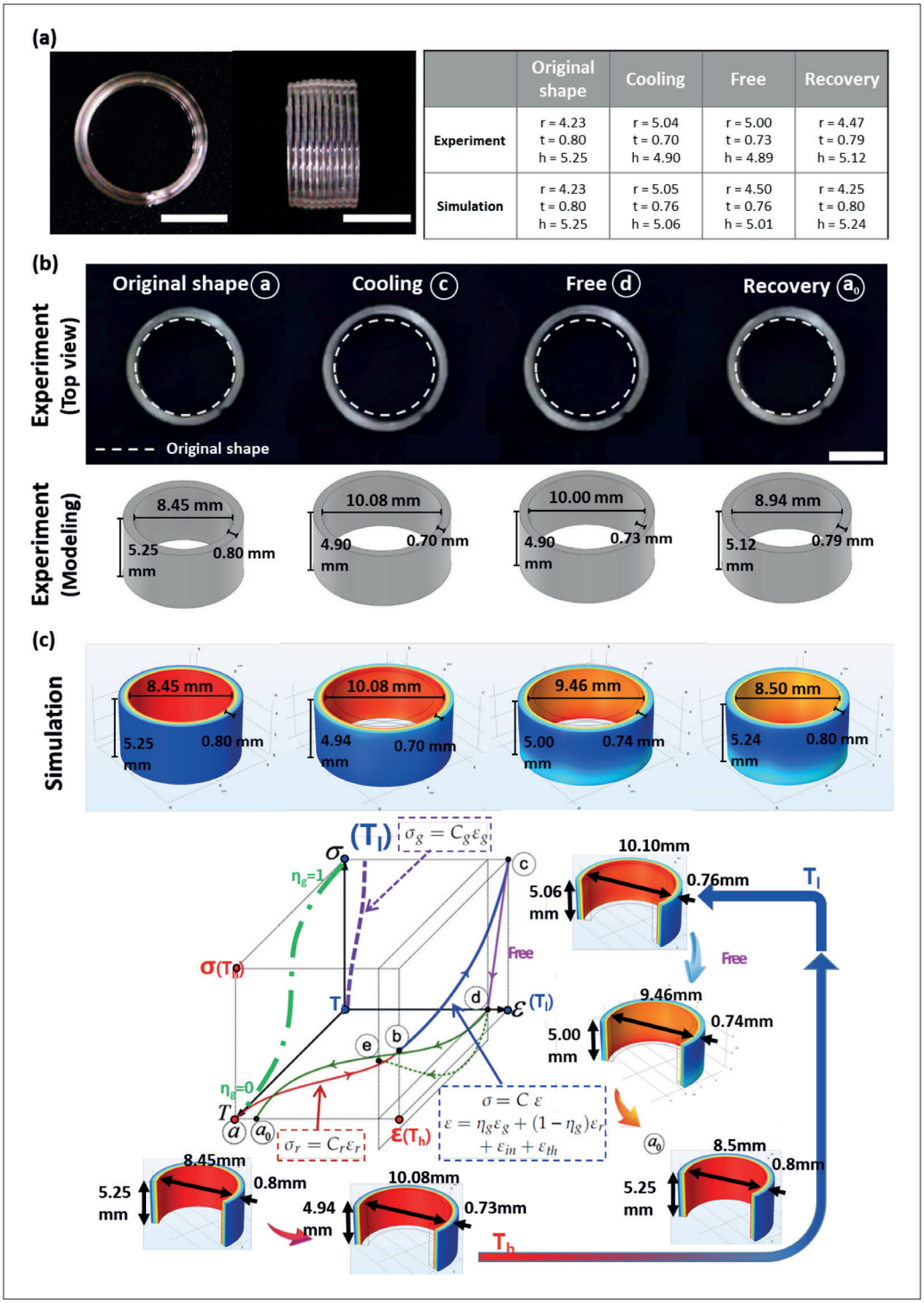


Figure 5. 4D bioprinting simulation of shape-memory effect. (a) The structure of 3D-printed shape-memory polymers (SMPs) for analyzing experimental and simulated behavior. Scale bar = 5 mm. (b) The experimental behavior of the shape-memory process. Scale bar = 5 mm. (c) The simulated behavior and the temperature-dependent stress–strain curve of the shape-memory process. In the absence of a memory effect, the material promptly returns to its original state upon the removal of external force.

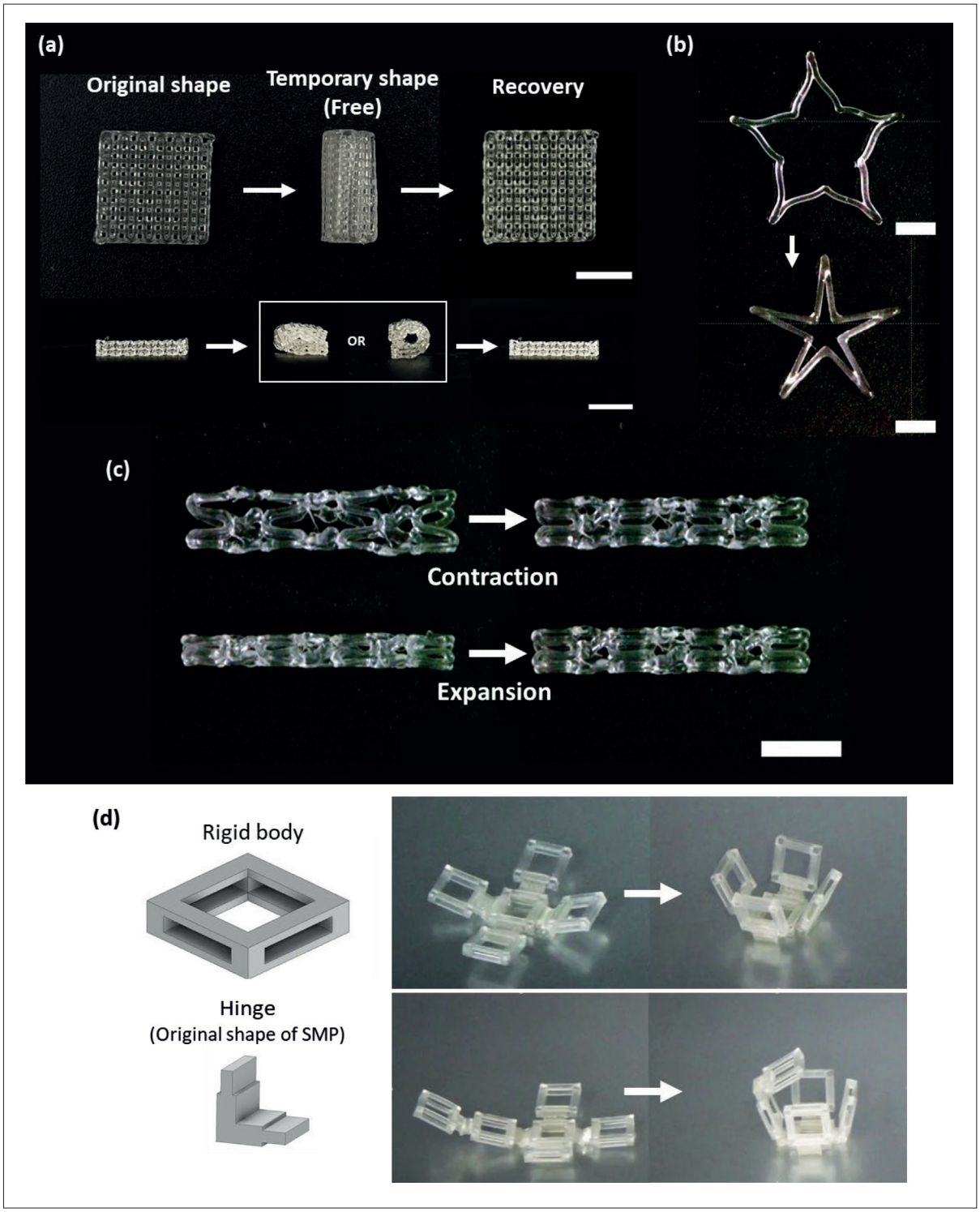


Figure 6. Various applications of 4D bioprinting. (a) The process of the shape-memory effect: original shape, temporary shape, and recovery shape. Scale bar = 5 mm. (b) Star shape transforming to recovery shape. Scale bar = 5 mm. (c) Contraction and expansion process of a 4D-bioprinted stent. Scale bar = 5 mm. (d) A folded box using rigid bodies and shape-memory polymers (SMP) as hinges.

phases, explained the thermodynamic behavior, while an explicit time-discrete stress–strain temperature-based framework addressed nonlinear SMP behavior. The FE solution results aligned well with experimental measurements, facilitating numerical analysis using COMSOL Multiphysics to verify or predict memory phenomena in 4D printing experiments.

While 4D bioprinting has potential for medical devices, further research is crucial as the materials are still in the exploratory stage. This research contributed to the development of materials supporting advanced tissue maturation and enhanced the simulation of tissues with complex structures. This study suggested applications in various biomedical and pharmaceutical industries, showcasing the potential for more accurate prediction of stimulus-induced shape changes, and addressing the limitations of the 4D system.

Acknowledgments

Not applicable.

Funding

This research was supported by the Development Program of Machinery and Equipment Industrial Technology (20018235, Development of inline nanoimprinter for nanophotonic device) funded by the Ministry of Trade, Industry & Energy (MI, Korea), the STEAM project (RS-2023-00302145) of the Ministry of Science and ICT, and Basic Research Program of KIMM (Korea Institute of Machinery and Materials, NK248B).

Conflict of interest

The authors declare no conflicts of interest.

Author contributions

Conceptualization: Dahong Kim
Formal analysis: Kyung-Hyun Kim, Yong-Suk Yang
Investigation: Keon-Soo Jang
Methodology: Sohee Jeon, Jun-Ho Jeong
Writing – original draft: Dahong Kim
Writing – review & editing: Su A Park
All authors have read and agreed to the published version of the manuscript.

Ethics approval and consent to participate

Not applicable.

Consent for publication

Not applicable.

Availability of data

Data are available from the corresponding author upon reasonable request.

References

1. Tibbits S. 4D printing: multi-material shape change. *Archit Des*. 2014;84(1):116-121.
doi: 10.1002/ad.1710

2. Gao B, Yang Q, Zhao X, Jin G, Ma Y, Xu F. 4D bioprinting for biomedical applications. *Trends Biotechnol*. 2016;34(9):746-756.
doi: 10.1016/j.tibtech.2016.03.004

3. Lui YS, Sow WT, Tan LP, Wu Y, Lai Y, Li H. 4D printing and stimuli-responsive materials in biomedical aspects. *Acta Biomater*. 2019;92:19-36.
doi: 10.1016/j.actbio.2019.05.005

4. Ghosh S, Chaudhuri S, Roy P, Lahiri D. 4D printing in biomedical engineering: a state-of-the-art review of technologies, biomaterials, and application. *Regen Eng Transl Med*. 2023;9(3):339-365.
doi: 10.1007/s40883-022-00288-5

5. Martinez-De-Anda AA, Rodriguez-Salvador M, Castillo-Valdez PF. The attractiveness of 4D printing in the medical field: revealing scientific and technological advances in design factors and applications. *Int J Bioprint*. 2023;9(6):187-199.
doi: 10.36922/IJB.1112

6. Han S, Wu J. Three-dimensional (3D) scaffolds as powerful weapons for tumor immunotherapy. *Bioact Mater*. 2022;17:300-319.
doi: 10.1016/j.bioactmat.2022.01.020

7. Chen X, Han S, Wu W, et al. Harnessing 4D printing bioscaffolds for advanced orthopedics. *Small*. 2022;18:2106824.
doi: 10.1002/smll.202106824

8. Chen A, Wang W, Mao Z, et al. Multimaterial 3D and 4D bioprinting of heterogenous constructs for tissue engineering. *Adv Mater*. 2023;2307686.
doi: 10.1002/adma.202307686

9. Yang Q, Gao B, Xu F. Recent advances in 4D bioprinting. *Biotechnol J*. 2020;15(1):1-10.
doi: 10.1002/biot.201900086

10. Zhang C, Cai D, Liao P, et al. 4D printing of shape-memory polymeric scaffolds for adaptive biomedical implantation. *Acta Biomater*. 2021;122:101-110.
doi: 10.1016/j.actbio.2020.12.042

11. Xu J, Song J. Polylactic acid (PLA)-based shape-memory materials for biomedical applications. *Shape Mem Polym Biomed Appl*. 2015:197-217.
doi: 10.1016/B978-0-85709-698-2.00010-6

12. Qu G, Huang J, Gu G, Li Z, Wu X, Ren J. Smart implants: 4D-printed shape-morphing scaffolds for medical implantation. *Int J Bioprint*. 2023;9(5). doi: 10.18063/ijb.764

13. Guo Y, Huang J, Fang Y, Huang H, Wu J. 1D, 2D, and 3D scaffolds promoting angiogenesis for enhanced wound healing. *Chem Eng J*. 2022;437:134690. doi: 10.1016/j.cej.2022.134690

14. Saska S, Pilatti L, Blay A, Shibli JA. Bioresorbable polymers: advanced materials and 4D printing for tissue engineering. *Polymers (Basel)*. 2021;13(4):1-24. doi: 10.3390/polym13040563

15. Khalid MY, Arif ZU, Noroozi R, Zolfagharian A, Bodaghi M. 4D printing of shape memory polymer composites: a review on fabrication techniques, applications, and future perspectives. *J Manuf Process*. 2022;81:759-797. doi: 10.1016/j.jmapro.2022.07.035

16. Sydney Gladman A, Matsumoto EA, Nuzzo RG, Mahadevan L, Lewis JA. Biomimetic 4D printing. *Nat Mater*. 2016;15(4):413-418. doi: 10.1038/nmat4544

17. Patil AN, Sarje SH. Additive manufacturing with shape changing/memory materials: a review on 4D printing technology. *Mater Today Proc*. 2021;44:1744-1749. doi: 10.1016/j.matpr.2020.11.907

18. Costa PDC, Costa DCS, Correia TR, Gaspar VM, Mano JF. Natural origin biomaterials for 4D bioprinting tissue-like constructs. *Adv Mater Technol*. 2021;6(10):1-21. doi: 10.1002/admt.202100168

19. Miao S, Castro N, Nowicki M, et al. 4D printing of polymeric materials for tissue and organ regeneration. *Mater Today*. 2017;20(10):577-591. doi: 10.1016/j.mattod.2017.06.005

20. Zhao W, Liu L, Zhang F, Leng J, Liu Y. Shape memory polymers and their composites in biomedical applications. *Mater Sci Eng C*. 2019;97:864-883. doi: 10.1016/j.msec.2018.12.054

21. Jin Z, Hu G, Zhang Z, Yu SY, Gu GX. Modeling and analysis of post-processing conditions on 4D-bioprinting of deformable hydrogel-based biomaterial inks. *Bioprinting*. 2023;33:e00286. doi: 10.1016/j.bprint.2023.e00286

22. Feng YC, Bodaghi M, Liao WH. Numerical/experimental assessment of 3D-printed shape-memory polymeric beams. *J Appl Polym Sci*. 2019;136(16):1-12. doi: 10.1002/app.47422

23. Yu K, Xie T, Leng J, Ding Y, Qi HJ. Mechanisms of multi-shape memory effects and associated energy release in shape memory polymers. *Soft Matter*. 2012;8(20):5687-5695. doi: 10.1039/c2sm25292a

24. Dogan SK, Boyacioglu S, Kodal M, Gokce O, Ozkoc G. Thermally induced shape memory behavior, enzymatic degradation and biocompatibility of PLA/TPU blends: "effects of compatibilization." *J Mech Behav Biomed Mater*. 2017;71:349-361. doi: 10.1016/j.jmbbm.2017.04.001

25. Yang B, Huang WM, Li C, Chor JH. Effects of moisture on the glass transition temperature of polyurethane shape memory polymer filled with nano-carbon powder. *Eur Polym J*. 2005;41(5):1123-1128. doi: 10.1016/j.eurpolymj.2004.11.029

26. Zhang H, Wang H, Zhong W, Du Q. A novel type of shape memory polymer blend and the shape memory mechanism. *Polymer (Guildf)*. 2009;50(6):1596-1601. doi: 10.1016/j.polymer.2009.01.011

27. Huskić M, Kusić D, Pulko I, Nardin B. Determination of residual stresses in amorphous thermoplastic polymers by DMA. *J Appl Polym Sci*. 2022;139(48):1-8. doi: 10.1002/app.53210

28. Ziegler W, Guttmann P, Kopeinig S, et al. Influence of different polyol segments on the crystallisation behavior of polyurethane elastomers measured with DSC and DMA experiments. *Polym Test*. 2018;71:18-26. doi: 10.1016/j.polymertesting.2018.08.021

29. De Nardo L, Farè S. Dynamico-mechanical characterization of polymer biomaterials. *Charact Polym Biomater*. 2017: 203-232. doi: 10.1016/B978-0-08-100737-2.00009-1

30. Göpferich A. Mechanisms of polymer degradation and erosion1. *Biomater Silver Jubil Compend*. 1996;17(2): 117-128. doi: 10.1016/B978-008045154-1.50016-2

31. Vasanthan N, Ly O. Effect of microstructure on hydrolytic degradation studies of poly (l-lactic acid) by FTIR spectroscopy and differential scanning calorimetry. *Polym Degrad Stab*. 2009;94(9):1364-1372. doi: 10.1016/j.polymdegradstab.2009.05.015

32. Araque-Monrós MC, Vidaurre A, Gil-Santos L, Gironés Bernabé S, Monleón-Pradas M, Más-Estellés J. Study of the degradation of a new PLA braided biomaterial in buffer phosphate saline, basic and acid media, intended for the regeneration of tendons and ligaments. *Polym Degrad Stab*. 2013;98(9):1563-1570. doi: 10.1016/j.polymdegradstab.2013.06.031

33. Kim D, Lee J, Min Seok J, et al. Three-dimensional bioprinting of bioactive scaffolds with thermally embedded abalone shell particles for bone tissue engineering. *Mater Des*. 2021;212. doi: 10.1016/j.matdes.2021.110228

34. Kohn DH, Sarmadi M, Helman JI, Krebsbach PH. Effects of pH on human bone marrow stromal cells in vitro: implications for tissue engineering of bone. *J Biomed Mater Res*. 2002;60(2):292-299. doi: 10.1002/jbm.10050

35. Mao H, Yang L, Zhu H, et al. Recent advances and challenges in materials for 3D bioprinting. *Prog Nat Sci Mater Int*. 2020;30(5):618-634.
doi: 10.1016/j.pnsc.2020.09.015

36. Kim D, Lee SJ, Lee D, et al. Biomimetic mineralization of 3D-printed polyhydroxyalkanoate-based microbial scaffolds for bone tissue engineering. *Int J Bioprint*. 2024;10(2):1806.
doi: 10.36922/ijb.1806

37. Yin GB, Zhang YZ, Wang SD, Shi DB, Dong ZH, Fu WG. Study of the electrospun PLA/silk fibroin-gelatin composite nanofibrous scaffold for tissue engineering. *J Biomed Mater Res - Part A*. 2010;93(1):158-163.
doi: 10.1002/jbm.a.32496

38. Wang S, Wang Y, Chen B, et al. Preparation and performance study of multichannel PLA artificial nerve conduits. *Biomed Mater*. 2023;18(6).
doi: 10.1088/1748-605X/acf0ae

39. Li Y, Liu Z. A novel constitutive model of shape memory polymers combining phase transition and viscoelasticity. *Polymer (Guildf)*. 2018;143:298-308.
doi: 10.1016/j.polymer.2018.04.026

40. Noroozi R, Bodaghi M, Jafari H, Zolfagharian A, Fotouhi M. Shape-adaptive metastructures with variable bandgap regions by 4D printing. *Polymers (Basel)*. 2020;12(3).
doi: 10.3390/polym12030519

ACCSCIENCE PUBLISHING

International Journal of Bioprinting

RESEARCH ARTICLE

Development of a five-axis printer for the fabrication of hybrid 3D scaffolds: From soft to hard phases and planar to curved surfaces

Michael Kainz[1]*, Isabel Caetano da Silva[1], Paula Schumann[1], Julia Kastner[1], Thomas Voglhuber[1], Lukas Hartung[2], Sandra Haas[1], Milan Rathod[1], Adrián Martínez Cendrero[3], Tilo Dehne[4], Daniel Seitz[5], Gunpreet Oberoi[6,7], Erik Kornfellner[6], Andrés Díaz Lantada[3], Francesco Moscato[6,8,9], and Elena Guillén[1]*

[1]Functional Surfaces and Nanostructures, Profactor GmbH, Steyr-Gleink, Upper Austria, Austria

[2]Machine Vision, Profactor GmbH, Steyr-Gleink, Upper Austria, Austria

[3]Department of Mechanical Engineering, Polytechnic University of Madrid, Madrid, Spain

[4]Laboratory for Tissue Engineering, Department of Rheumatology and Clinical Immunology, Charité - University Medicine Berlin, Berlin, Germany

[5]Laboratory of Additive Manufacture and Material Science, BioMed Center Innovation gGmbH, Bayreuth, Germany

[6]Center for Medical Physics and Biomedical Engineering, Medical University of Vienna, Vienna, Austria

[7]Austrian Center for Medical Innovation and Technology (ACMIT GmbH), Wiener Neustadt, Austria

[8]Ludwig Boltzmann Institute for Cardiovascular Research, Vienna, Austria

[9]Austrian Cluster for Tissue Regeneration, Vienna, Austria

***Corresponding authors:**
Michael Kainz
(michael.kainz@profactor.at)

Elena Guillén
(elena.guillen@profactor.at)

Citation: Kainz M, Caetano da Silva I, Schumann P, et al. Development of a five-axis printer for the fabrication of hybrid 3D scaffolds: From soft to hard phases and planar to curved surfaces. *Int J Bioprint*. 2024;10(3):3189. doi: 10.36922/ijb.3189

Received: March 17, 2024
Accepted: April 9, 2024
Published Online: June 14, 2024

Copyright: © 2024 Author(s). This is an Open Access article distributed under the terms of the Creative Commons Attribution License, permitting distribution, and reproduction in any medium, provided the original work is properly cited.

Publisher's Note: AccScience Publishing remains neutral with regard to jurisdictional claims in published maps and institutional affiliations.

Abstract

Three-dimensional (3D) printing of hybrid scaffolds with material gradients, combining soft and hard phases, is an appealing frontier in additive manufacturing. However, most 3D printers are limited to either three-axis or mono-material capabilities, rendering them unsuitable for fabricating hybrid scaffolds. Additionally, printing on curved surfaces requires advanced printing capabilities. Our work aims to advance additive manufacturing by developing a hybrid piezoelectric inkjet-extrusion printer equipped with five-axis functionalities. The printer could be used to fabricate customized hybrid scaffolds, surpassing conventional mono-material or linear three-axis printing strategies. The soft phase comprises a low-viscosity photocurable resin and a high-viscosity peptide hydrogel, while the hard phase comprises 3D-printed polylactic acid and hydroxyapatite parts. To validate the system, we fabricated three hybrid scaffolding use cases, characterized by multi-material porous structures fabricated on planar, single-curved, and free-form surfaces. The scaffolds were subsequently analyzed using digital microscopy to assess their accuracy, particularly the feature sizes of pores and struts (i.e., 0.8–3.6 mm). In the first part of the study, we demonstrated the versatility of inkjet and extrusion printing by hybrid printing an interconnected network in the soft phase on top of a planar ceramic hard phase. A pore width and height deviation of 6% was achieved compared to the intended design. In the second part of the study, we evaluated the 3D inkjet printing of a multi-material porous scaffold on a single-curved surface for

osteochondral defects. The circumferential pore width and radial pore height deviated by 0.8% and 2%, respectively. Finally, we inkjet-printed a mesh structure on a free-form surface, which acted as a membrane for palatal implants. In this case, the pore width deviations were -16% in the printing direction and 2% perpendicular to the printing direction.

Keywords: Hybrid 3D printing; Hybrid scaffolds; Non-planar inkjet printing

1. Introduction

Additive manufacturing technologies (AMTs) offer new opportunities for tissue engineering scaffold fabrication, enabling precise replication of natural tissue structural properties.[1] Biological structures are an ensemble of various materials, often with mechanical property gradients (between soft and hard phases), arranged in multiscale hierarchical structures with irregular topographies.[2] Although three-dimensional (3D)-printed scaffolds for hard[3] and soft tissue[4] regeneration have advanced significantly, the hybridization of printing technologies and printing on curved surfaces to fabricate patient-specific biomimetic hybrid scaffolds remains largely unexplored, particularly in the context of equipment and process development. To date, there are limited AMTs available that have demonstrated the capability to effectively print dissimilar materials, particularly for high-temperature sintered ceramics, hydrogels, and photopolymers. Hence, a sequential hybrid fabrication process between different AMTs holds significant promise. Osteochondral and maxillofacial defects can be treated using 3D-printed hard and soft hybrid scaffolds having different mechanical properties and could greatly benefit from a sequential hybrid fabrication process.[5,6]

The fabrication landscape of hybrid scaffolds, in terms of the materials and methods used, has undergone several stages of evolution over the past few decades. Taboas et al.[7] casted hard and soft polymeric-ceramic multi-material scaffolds for osteochondral repair. Similarly, Lantada et al.[8] reported a composite scaffold for osteochondral repair. The silicone soft cartilage phase was developed using sponge scaffold fabrication, whereas the titanium hard bone phase was developed using selective laser sintering. Besides casting, the hybridization of 3D printing technologies has also been presented in a sequential workflow for vat polymerization, combining lithographic ceramic manufacturing and two-photon polymerization using zirconia resins.[9] González-Pujana et al. utilized two different AMTs (i.e., filament extruding and electrospinning) to develop hybrid scaffolds for bone regeneration.[10] Similarly, Choi et al.[11] constructed hybrid skin substitutes by combining electrospinning and 3D printing. Additionally, several studies have leveraged the combination of thermoplastics and hydrogels for tissue engineering. Altunbek et al. reported the hybridization of thermoplastic polycaprolactone (hard phase) and polyethylene glycol hydrogels (soft phase) for critical-size bone defects,[12] while Milojevic et al. utilized hybrid hydrogel-thermoplastic polymer scaffolds for wound dressings.[13]

A few studies have reported the combination of biomaterial utilization and inkjet printing hybridized with other AMTs. Stögerer et al.[14] recently reported a hybrid 3D printing device, combining stereolithography and multinozzle inkjet printing, to manufacture composite laminates with specific material patterns to mimic the hierarchical structure of marine species. Moreover, Lee et al.[15] presented a hybrid process, combining micro-extrusion and single-nozzle inkjet printing, to fabricate skin equivalents.

Apart from hybrid printing, customized 3D printers for biomedical applications have emerged, particularly through adaptions of commercially available desktop fused filament fabrication (FFF) 3D printers. Jaksa et al.[16] demonstrated extrusion printing of multi-material anatomical structures by combining materials with different stiffness, namely silicone and polylactic acid (PLA). Tashman et al.[17] transformed a thermoplastic printer into a bioprinter, and Hinton et al.[18] upgraded a MakerBot Replicator with a custom-built syringe-based extruder for hydrogel printing.[19,20] Similarly, Khani et al.[21] presented a multi-material extrusion-based printer for the fabrication of bioinspired structures.

Notably, these models are restricted to a linear three-axis system. For example, rotational axes are required for printing on free-form surfaces. Hence, the development of five-axis printers using different AMTs has recently been reported. Hong et al.[22] successfully printed conductive traces on free-form surfaces using a five-axis printer upgraded from a mono-material three-axis FFF printer. Another approach to free-form 3D printing is to use robotic arms, which is especially interesting for large-area printing.[23] Several graphical applications have been reported for inkjet printing on non-planar surfaces. Arango et al.[24] presented a theoretical approach to print on single-curved surfaces, followed by printing tests to predict droplet position on non-planar substrates.[25] Fechtig[26]

incorporated one or two industrial inkjet printheads into robotic arms, while Thalheim et al.[27] developed a six-axis robot printer. Shen et al.[28] developed a five-axis platform using four single-nozzle printheads, while Gazeau et al.[29] presented a five-axis machine, augmented with a printing block including four industrial inkjet printheads, for large printing applications. Likewise, Urasinska-Wojciket et al. reported a novel approach to building a hybrid five-axis system using extrusion and single-nozzle inkjet printing[30] for fabricating components with embedded electrical circuitry.

With the design, assembly, and configuration of a prototype printer, the current work explores the hybrid fabrication of scaffolds on two fronts. Firstly, the printer allows multi-material fabrication of soft phases by combining two different AMTs: (i) 3D piezoelectric multi-material inkjet printing and (ii) extrusion printing. The former is capable of depositing drops of low-viscosity inks in the picoliter range in a spatially controlled manner in a non-contact approach and is ideal for future biofabrication.[31] Conversely, extrusion printing is a well-established AMT for tissue engineering scaffolds and is especially suited for printing highly viscous hydrogels, mimicking the extracellular matrix (ECM). Secondly, the printing module is integrated into a system with five-axis capabilities, which allows printing on curved surfaces to fabricate hybrid scaffolds of dissimilar materials. Our methodology follows a step-by-step progression through different levels of complexity by hybridizing soft and pre-fabricated hard phases in three different use cases for osteochondral and palatal scaffolds printed on planar, single-curved, and free-form surfaces. Our findings could potentially facilitate personalized scaffold fabrication and surpass conventional mono-material linear three-axis printing strategies, widening the potential of 3D printing for the fabrication of hybrid scaffolds.

2. Materials and methods

2.1. Hardware configuration

A commercially available three-axis computer numerical control (CNC) portal system (High-Z S720T, CNC Step, Germany) was augmented with a two-axis rotating gantry, and each axis was coupled to additional stepper motors to control the rotation angles. Designed originally for industrial tasks like engraving, milling, drilling, and cutting, the three-axis CNC portal serves as the base to bear the weight of the hardware components required for a fully equipped hybrid inkjet-extrusion printing system. Our setup incorporates three different families of inkjet printheads (Ricoh MH2820, Ricoh MH5421F, and Xaar 1003) controlled by driver electronics for the processing of different materials, including photocurable-, water-, solvent-, and particle-based inks with different viscosities. Ink supply systems, which can be used in gravity- or recirculation mode, were selected for all inkjet printheads. In addition, the system is equipped with a self-developed screw extrusion system for highly viscous materials and a curing module (FireEdge FE400 UV-LED, Phoseon Technology, United States of America [USA]). The ultraviolet light emitting diode (UV-LED), positioned on one side of the printing block, enables printing in one direction. Alignment and inspection cameras were integrated accordingly, and the printer was placed in a safety cabinet. The hardware configuration is depicted in Figure 1.

2.2. Software configuration

The operation of the system requires the use of different software packages. Mach3, a well-established software for stepper motor control, serves as the control hub for the machine's motion and reads G-codes stored in NC files. The communication with the inkjet printheads is achieved through a software development kit, providing control over the different printhead families. An in-house-developed graphical user interface enhances user interaction and enables the loading of pre-sliced STL files (in bitmap format) and the configuration of inkjet printing parameters (e.g., waveform, jetting frequency, and temperature of the printheads).

2.3. Materials

A low-viscosity photocurable resin[32] (for inkjet printing) and a high-viscosity amphiphilic peptide hydrogel (PuraStat RADA16, 3D-Matrix, France) capable of self-assembling into fibrils[33,34] (for extrusion printing) were used as soft-phase materials. WSS™150 (Stratasys Ltd., Israel) was used as support material for inkjet printing. Substrates that resembled hard phases were printed out of PLA fabricated by FFF (Bambu Lab Ltd.) and hydroxyapatite fabricated by lithographic ceramic manufacturing (Lithoz GmbH, Austria).

2.4. Methodology for hybrid printing and non-planar inkjet printing

Sequential hybrid printing is explored through three different strategies in matching use cases. Pre-fabricated 3D-printed parts, exhibiting topologies from planar to curved surfaces, served as hard phases. The first strategy is a hybrid approach that combines inkjet and extrusion printing on planar surfaces for soft and hard material interfaces; the second strategy employs multi-material inkjet printing on a single-curved surface, specifically addressing scaffolds for osteochondral defects; the third strategy involves mono-material inkjet printing on a free-form surface for palatal defect scaffolds. Each case was

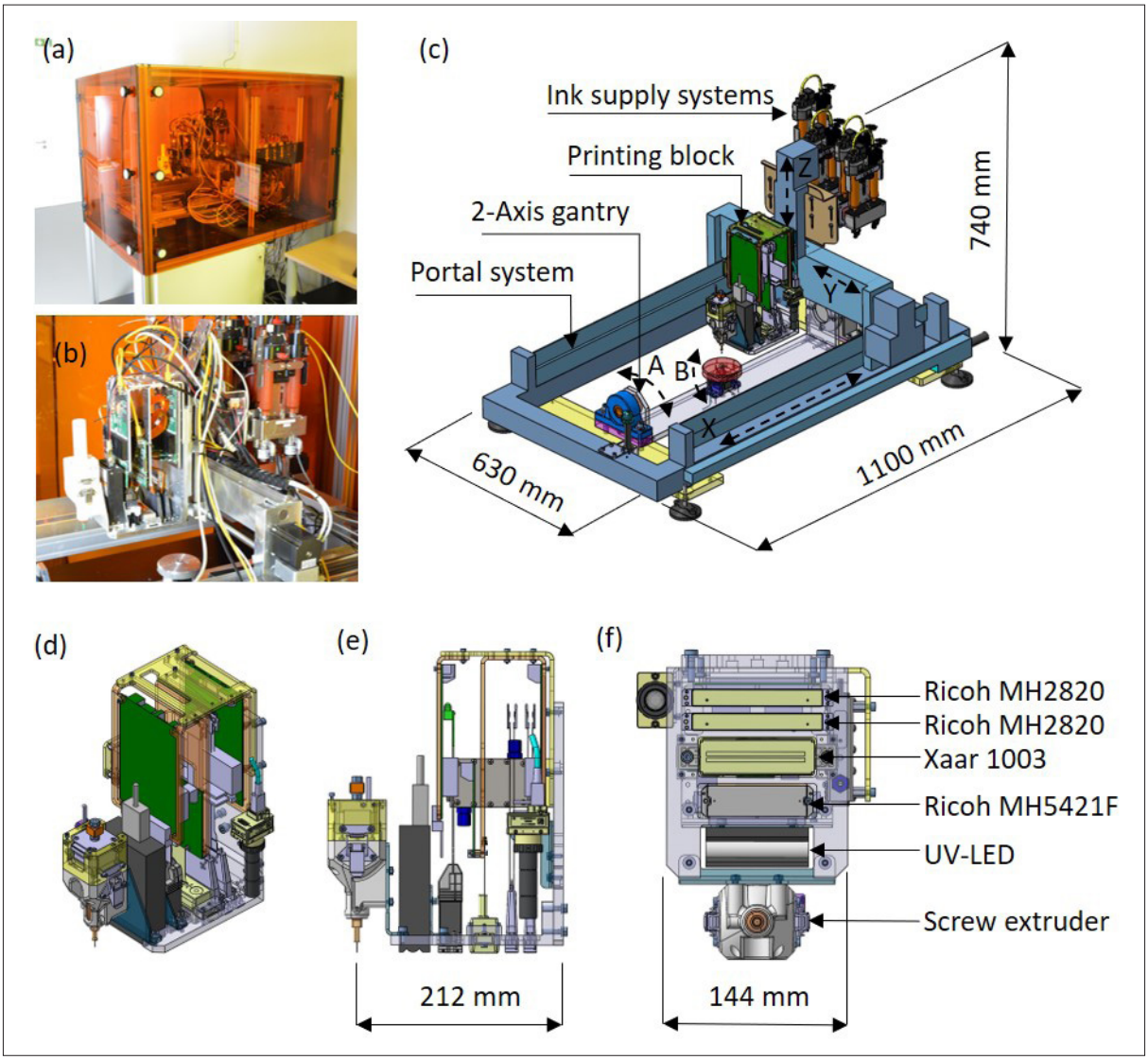


Figure 1. Configuration of the five-axis printer. (a) Photograph of the five-axis printer housed in the safety cabinet. (b) Close-up image of the printing block. (c) Computer-aided design (CAD) model of the five-axis printer with dimensions labeled with double-headed arrows. (d–f) Detailed CAD view of the printing block: (d) isometric view; (e) side view; and (f) bottom view. Abbreviation: UV-LED: Ultraviolet light-emitting diode.

systematically structured into three primary steps: (i) definition of the use case, (ii) preparation of printing files, and (iii) printing strategy.

2.4.1. Input parameters for inkjet and extrusion printing

Inkjet printing employs two-dimensional (2D) bitmaps that digitally apply materials in a non-contact approach. The printhead path and image processing are decoupled, and no image data is integrated into the G-code. However, the two processes are connected through the G-code. The printing process is initiated through on/off commands for the printheads, implemented as M-codes within the G-code. These M-codes facilitate communication between the two workflows, enabling the transmission of signals to the printing software and subsequently initiating the printing process by calling the images. Notably, the on/off command for the inkjet printhead cannot be transmitted without interrupting the movement of the axis system, and a trigger is activated before the movement starts.

In this study, Ricoh MH2820 inkjet printheads (native resolution: 150 dpi) and a screw extruder (with 0.41 mm nozzle tip) were used. The inkjet printing workflow is governed by the following input parameters: inkjet printing speed (v_{IJP}), resolution in printing direction (ϕ),

jetting frequency (f), and printhead movement strategies. The extrusion printing process is influenced by the extrusion printing speed (v_{EXT}) and the extrusion rate (C). The G-code for inkjet and extrusion printing on planar surfaces was generated through a Python script.

2.4.2. Non-planar inkjet printing process

For non-planar inkjet printing, we applied the Ricoh MH2820 printheads to single-curved and free-form surfaces. Due to the lack of available software for combining linear and rotational movements in inkjet printing, our methodology is heavily inspired by subtractive manufacturing, where multiaxis manufacturing is already state-of-the-art. We translated these concepts to additive manufacturing using hyperMILL® (OPEN MIND Technologies AG, Germany) as an established industrial software capable of programming combinations of linear and rotational toolpaths. The hyperMILL® software enables digital model development for computer-aided manufacturing (CAM) programming, visualization of toolpaths, and consequent G-code generation. The computer-aided design (CAD) environment offers the possibility of curve and surface creations, providing a powerful tool for path planning for inkjet printing. Our approach presents the printhead as a ball mill tool to move conformally on the trajectories over free-form surfaces. 5x Contouring is used as a program. The movement is referenced to the center of rotation of the two-axis gantry.

2.4.3. Image processing for non-planar inkjet printing

Implants tailored to the unique anatomy of individual patients, known as patient-specific implants (PSIs), have irregular shapes.[35,36] Unlike printing on planar surfaces, printing on curved geometries involves complexity in extracting surface topology and curvature information. Referring to mathematical terminology, we use the Gaussian curvature (K), given by the formula:

$$K = \kappa_1 \kappa_2 \quad (I)$$

where κ_1 and κ_2 represent the principal curvatures at a point, to distinguish between developable and non-developable surfaces (Figure 2). A developable surface exhibits zero Gaussian curvature,[37] allowing it to be unfolded onto a plane without distortion. An example of a developable surface is the lateral part of a cylinder, which is considered a relevant surface for a scaffolding structure for an osteochondral PSI. However, most topographies for PSIs, such as a palatal defect implant, often feature multiscale free-form surfaces, rendering them non-developable.

From a geometric perspective, printing on curved surfaces involves presenting a 3D curved surface with an equivalent 2D image, which can be used for inkjet printing. Hence, mapping images on 3D surfaces and correlating them with the printing path are essential for non-planar inkjet printing. For single-curved developable surfaces ($\kappa_1 = 0$ and $\kappa_2 > 0$), CAD-based resources are used to unfold the design from a curved to a planar surface. For free-form non-developable surfaces, there are no direct methods to derive 2D images from 3D surfaces. Thus, any attempt to project a free-form surface onto a 2D plane unavoidably introduces a degree of surface distortion. Based on the curvature, certain distortions may be tolerable, while some details of the free-form surface may be lost.[38] We used an approximation procedure, wherein the boundary of the surface is approximated using a point cloud and projected onto a 2D surface. Slicing of the 3D models was performed using open-source 3D slicer software in combination with a Python script. The sliced layers were then mapped onto curved surfaces. However, we did not slice the 3D non-planar models in their warped state, which would require dynamic z-position slicing to achieve continuous surface pattern layers. For this study, which primarily involves printing models with low z-height for cartilage layers and similar structures, mapping the sliced layers from planar 3D models onto curved surfaces was sufficient.

2.4.4. Printing accuracy

The printed structures were analyzed with a digital microscope (VHX-5000, Keyence, Japan). The assessment of printing performance involved the use of three test structures, featuring a mesh-like configuration, related to anatomical defect-filling implants from planar to free-

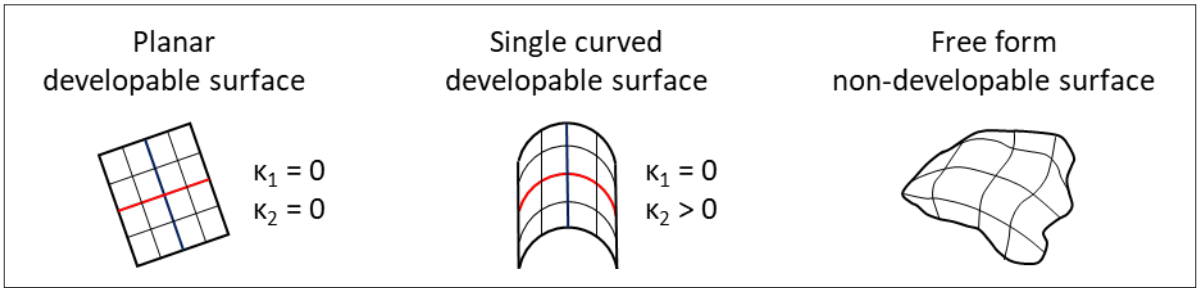


Figure 2. Illustration of the surface topologies and principal curvatures considered for hard phases.

form surfaces. The evaluation criteria included geometric accuracy of strut and pore sizes. Measurements involved assessing dimensions at half the width horizontally and half the height vertically. Printing accuracy is quantified as normalized deviation from the intended design.

3. Results and discussion

3.1. Hybrid printing on planar surfaces for hard and soft material interfaces

We first applied hybrid printing on planar surfaces by embedding a soft peptide hydrogel, capable of self-assembling into a fibrous network, into channels printed with a photocurable resin to fabricate a multiscale and multi-material structure (Figure 3). Herein, we have noted three key points of hybrid printing:

(i) Hydrogels have reduced mechanical strength and structural support for thicker structures (a few mm). Incorporating them within a photopolymer network can improve the mechanical strength and structural support.

(ii) Synthetic photopolymers often lack bioactivity, and integrating hydrogels could potentially augment the

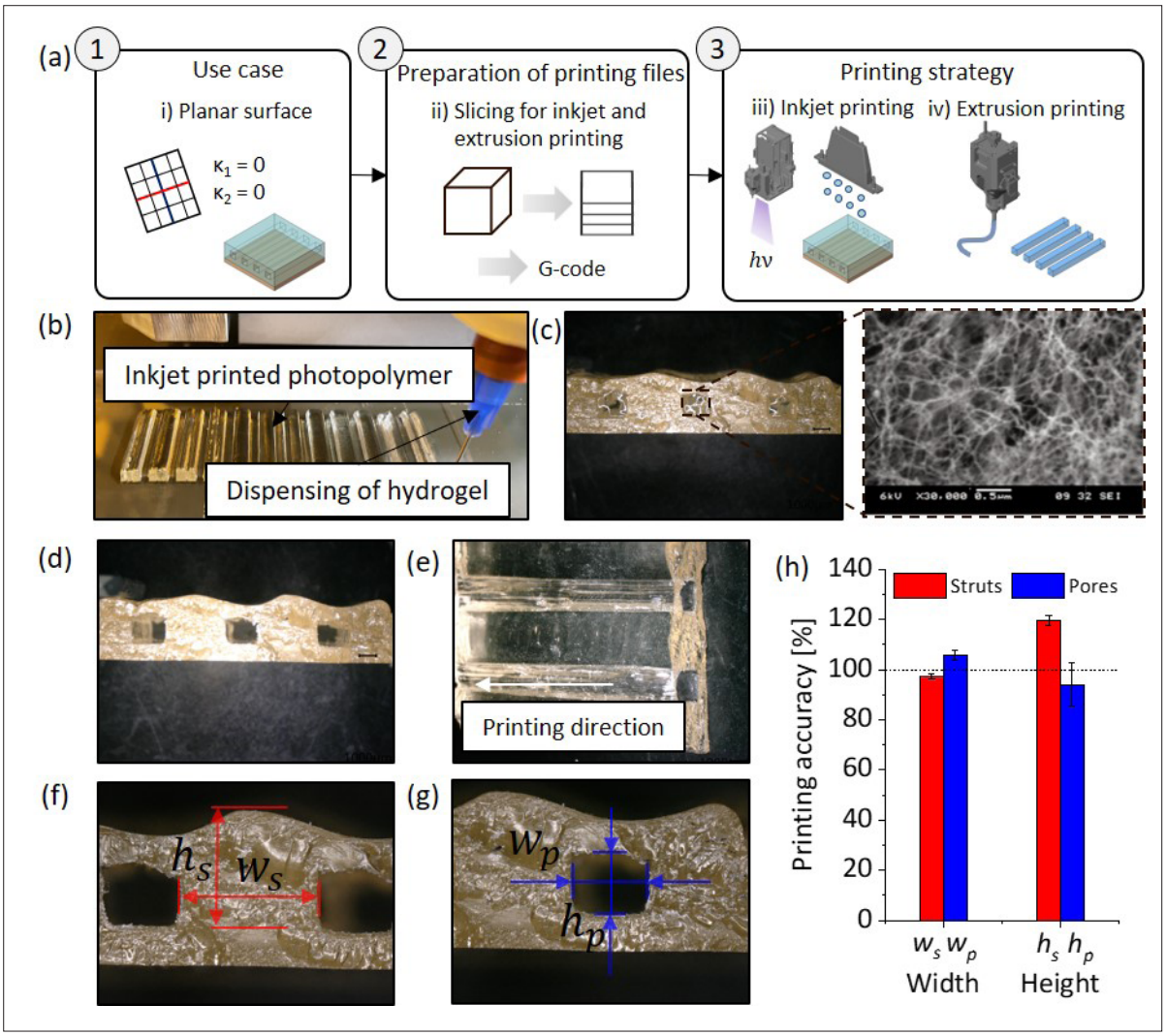


Figure 3. Workflow and accuracy visualization for a bi-phasic soft phase scaffold on a planar surface. (a) Schematic illustration of the hybrid fabrication of a bi-material soft phase using 3D inkjet and extrusion printing: (a, 1i) scaffold to be fabricated; (a, 2ii) slicing and G-code generation; and (a, 3iii and iv) printing strategy for 3D inkjet printing and extrusion printing. (b) 3D inkjet-printed channels using a photopolymer. (c) Overhanging structure printed with a peptide hydrogel as support material. Scanning electron microscopic (SEM) magnified image displaying the nanofiber network of the RADA-16 raw material state prior to printing (provided by 3D-Matrix). Magnification: ×20. Scale bar: 1 mm. (d–e) Inner structure of the channels before and after removing the hydrogel. (f–g) Measurement positions to determine printing accuracy. (h) Printing accuracy of the struts and pores.

bioactivity of co-printed synthetic photopolymers by promoting colonization (e.g., hydrogels resembling ECM in this study).

(iii) The support structure of hydrogels can be removed after printing to fabricate overhanging structures with interconnected porosity, avoiding the use of cytotoxic support materials for inkjet printing as there are no biocompatible support materials available.

The use case is first defined based on extrusion printing of a hydrogel and inkjet printing of a photocurable resin on a planar surface ($\kappa_1 = 0$; $\kappa_2 = 0$) (Figure 3a-1i). This is followed by the preparation of printing files, including G-code generation and bitmap preparation for both inkjet and extrusion printing (Figure 3a-2ii). The printing process starts with inkjet printing of the synthetic photopolymer, followed by a curing step (Figure 3a-3iii) and the deposition of the peptide hydrogel using extrusion printing (Figure 3a-3iv). This sequence is repeated to fabricate multilayer scaffolds.

In Figure 3b, the multilayer channel structure of the inkjet-printed photopolymer on a glass slide substrate is presented before the deposition of the hydrogel. A total of 240 layers of photopolymer struts were printed, followed by the extrusion of the hydrogel. The process is then complemented by 60 additional photopolymer layers for the topmost layer, effectively closing the channels filled with the hydrogel. The multiscale and multi-material bi-phasic structure is illustrated in Figure 3c, highlighting a nanofiber network in the millimeter-sized peptide hydrogel-filled pores of the photopolymer. Figure 3d and e presents a hybrid-printed sample after mechanically removing the hydrogel from the channels.

The printed model was characterized with respect to the pore width (w_p), pore height (h_p), strut width (w_s), and strut height (h_s) (Figure 3f and g). The analysis (n = 3 pores) revealed an accuracy mismatch for the intended $h_p = w_p = 1.8$ mm, revealing a deviation of 5.79 ± 2.1% in pore width and -6.06 ± 8.64% in pore height. Regarding the intended square strut size of $h_s = w_s = 3.6$ mm, the mismatch was 19.64 ± 2.09% for strut height and -2.5 ± 0.94% for strut width of the printed model (Figure 3h). The more pronounced mismatch in height may be attributed to two primary factors: (i) the use of soft materials leads to noticeable irregularities in the form of a wavy top layer pattern, and (ii) a mismatch in layer thickness between inkjet-printed and extrusion-printed structures was observed. The printing parameters are presented in Table 1.

Thereafter, we printed an interconnected network in the soft phase on top of a ceramic hard phase. The hard phase was composed of hydroxyapatite, fabricated through lithographic ceramic manufacturing. This process resulted in a multi-material and multiscale tri-phasic hybrid structure (Figure 4a–c). Notably, the microporosity of the 3D-printed ceramic facilitated adequate bonding between the photopolymer and the ceramic hard phase. The design featured square struts with w_s of 2 mm and w_p of 2 mm.

Table 1. Printing parameters for hybrid printing combining inkjet and extrusion printing on a planar surface

Printing parameter	Value
Inkjet printing speed, v_{IJP} (mm/s)	41.67
Jetting frequency, f (kHz)	13
Resolution, ϕ (dpi)	8100
Extrusion printing speed, v_{EXT} (mm/s)	1.17
Extrusion rate, C (mm/s)	0.2

The accuracy of the printed model perpendicular to the printing direction was characterized with respect to the pore width (w_p) and strut width (w_s) (Figure 4d and f). Struts exhibited a discrepancy of 7.73 ± 6.74%, whereas pores displayed a mismatch of 6.73 ± 8.04% (n = 3 struts and pores).

In the channels perpendicular to the printing direction, a notable printing artifact was evident, i.e., the presence of angled struts (approximately 22°) (Figure 4e). This observation implies a directional influence on the structural characteristics of the printed object. This artifact may be linked to the optimal printing speed of 41.67 mm/s, which was determined through an iterative process to be the most suitable. However, the optimized speed was still relatively slow, further increasing the time for the UV lamp to cure the deposited ink and resulting in ink spreading and the occurrence of angled struts. Hence, accurate measurements of the strut and pore sizes were challenging due to an angled wall, resulting in a gradient in pore size (Figure 4e).

3.2. Multi-material 3D inkjet printing on single-curved surfaces for osteochondral defects

Subsequently, we utilized 3D inkjet printing on a single-curved surface to fabricate implants for osteochondral defects. Osteochondral defect refers to damage of both articular cartilage and subchondral bone in a joint and is one of the most common orthopedic lesions, leading to pain, inflammation, and potential functional impairment. The articular cartilage tissue has a thickness of 2–4 mm and lacks blood vessels, and its ECM exhibits a network of fibers with diverse orientations. Additionally, the adaptation of implants to the curvature of the femoral condyle can be beneficial due to the anatomical irregular

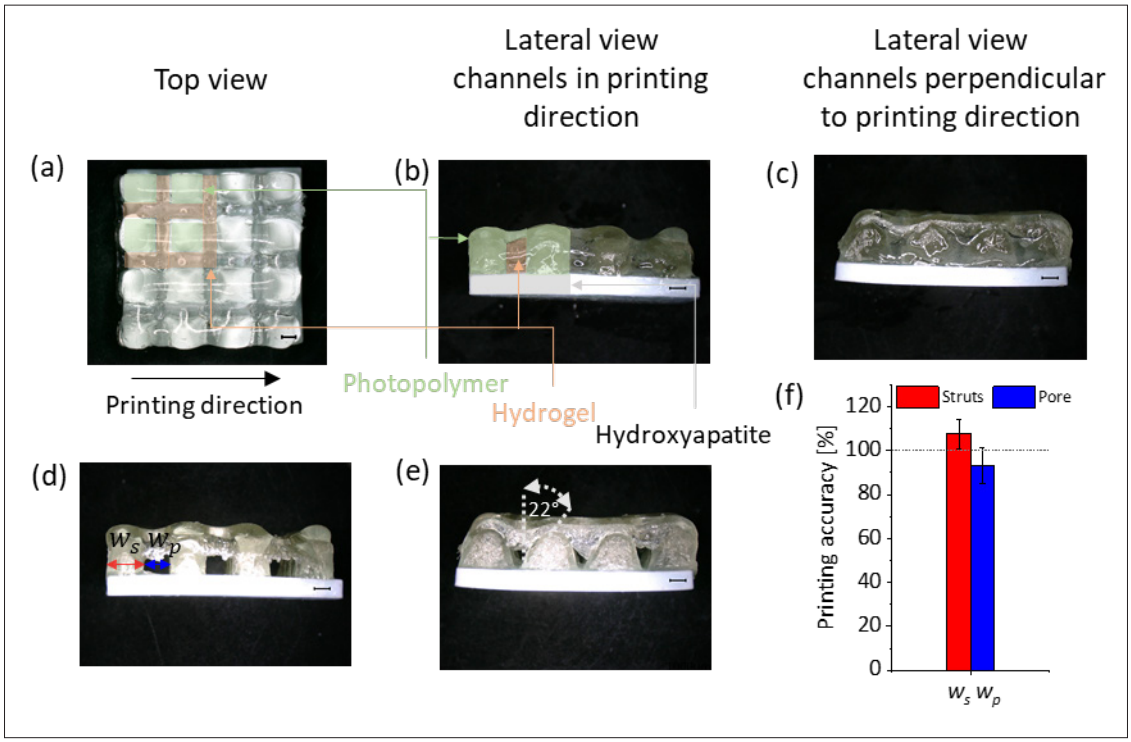


Figure 4. Tri-phasic scaffold consisting of a ceramic hard phase and a bi-material soft phase. (a) Top view displaying the interconnected polymer channels filled with hydrogel. (b) Lateral view in the printing direction displaying the channels filled with the hydrogel. (c) Lateral view perpendicular to the printing direction displaying the channels filled with the hydrogel. (d) Lateral view in the printing direction after hydrogel removal. (e) Lateral view perpendicular to the printing direction after hydrogel removal. Scale bar: 1 mm. (f) Printing accuracy between struts and pore.

topographies often encountered in orthopedic cases.[39-41] Implants that precisely conform to the subchondral bone could offer benefits, such as a better fit and alignment, minimizing the risk of loosening, and improved joint biomechanics resulting in reduced wear over time. Due to variations in size and depth, cartilage damage ranges from small, localized lesions to larger defects, while each cartilage has its unique curvature. Non-planar 3D printing is a promising approach to fabricating hybrid scaffolds, mimicking the gradient structure from bone to cartilage with hard and soft phases. We fabricated PSIs with a multi-material, hierarchical, and porous network for osteochondral defects using an articular cartilage scaffold on the subchondral bone with curvatures relevant to the anatomical structures of the femoral condyles.[42]

The workflow for multi-material 3D inkjet printing on single-curved surfaces ($\kappa_1 = 0; \kappa_2 > 0$) is presented in Figure 5a. We first define the use case, wherein the structure to be fabricated is a porous polymer network (resembling articular cartilage) on a pre-fabricated cylindrical hard phase (representing the subchondral bone) (Figure 5a-1i), and subsequently, the printing files were prepared accordingly (Figure 5a-2ii). The developable lateral surface of the cylinder is discretized into N points with constant arc lengths (Δs), hence described as a composition of undistorted partial surfaces. This method prevents ink spreading after the deposition onto the substrate and includes a curing step after each rotation of φ. With respect to image processing, printing on non-planar surfaces involves mapping an image onto a curved surface (Figure 5a-2iii). CAD and image-based resources are used for this purpose, and a Python script generated the G-code (Figure 5a-2iv). For the printing process, the cylinder is first mounted on a holder on the two-axis gantry, and the printhead is positioned over the apex of the convex surface, keeping a constant distance of 1 mm from the printhead nozzle plate to the surface during printing (Figure 5a-3v). During the printing process, the cylinder rotates steadily at a constant angular velocity (ω) beneath the stationary printhead (Figure 5a-3vi).

Following this, we successfully fabricated a porous scaffold on a cylinder, designed to mimic the patellar surface of the femur (length = 20 mm; radius = 10 mm; $\kappa_1 = 0$ mm^{-1}; $\kappa_2 = 0.1$ mm^{-1}). The process utilized multi-material inkjet printing using a photopolymer as the model material and WSS^{TM}150 as a support material.

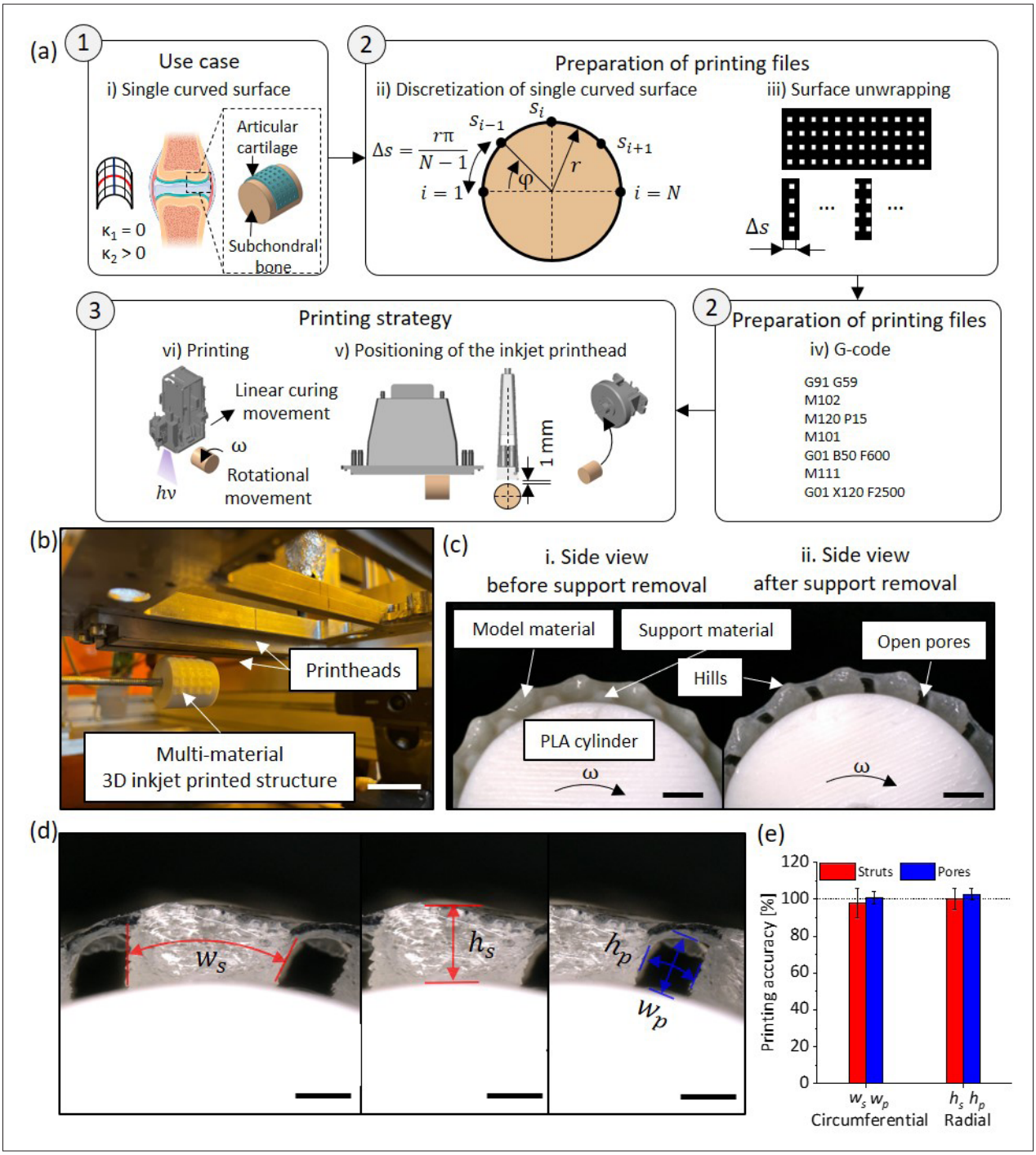


Figure 5. Workflow and accuracy visualization for a scaffold on a single-curved surface. (a) Fabrication of a hybrid-printed osteochondral implant using multi-material inkjet printing on a single-curved surface: (a, 1i) schematic representation of a knee joint (biorender.com) and scaffold to be fabricated and a cylinder resembling the subchondral bone and articular cartilage (inset); (a, 2ii–iv) preparation of printing files; and (a, 3v–iv) printing strategy. (b) Mounted cylinder on the printer with two Ricoh MH2820 printheads above. Scale bar: 20 mm. (c) Porous scaffold printed on a white polylactic acid (PLA) single-curved surface resembling the hard phase using 3D inkjet printing: (c, i) before and (c, ii) after support material removal. Angular velocity (ω) indicates rotation. Scale bar: 3 mm. (d) Measurement positions to determine printing accuracy. Scale bar: 1 mm. (e) Printing accuracy between struts and pores in the circumferential and radial direction.

Figure 5b displays the cylinder positioned on the printer. The printing parameters are summarized in Table 2.

The design features nine open channels, covering half the circumference of the cylinder. Pore width (w_p) and pore height (h_p) were set to 1 mm, while strut width (w_s) and strut height (h_s) were measured at 3 and 1.5 mm, respectively. A total of 120 and 60 layers of model and support materials were printed for the porous structure, due to different layer heights. Moreover, an additional 20 layers of the model material were printed to seal the pores from the top. The sample, both before and after support removal, is presented in Figure 5c.

Notably, a periodic wavy pattern appeared on the top layer, attributed to the rotation of the cylinder during printing. The rotation caused material flow in the direction of rotation, leading to the accumulation and formation of a small hill (Figure 5c-ii). This behavior aligns with the findings described by Thalheim et al.[27] After the curing process, this hill remained intact, leading to the wavy surface. Additionally, decreasing φ and increasing N points could potentially diminish the observed effect, with the disadvantage of prolonged printing time.

We conducted accuracy measurements of struts and pores in both the radial and circumferential directions (Figure 5d). A minor mismatch of -2.21 ± 3.53% for circumferential struts, 0.37 ± 3.21% for radial struts, 0.8 ± 8.07% for circumferential pores, and 2.06 ± 5.63% for radial pores (n = 9 measured pores and struts) from the intended design was observed (Figure 5e). The printing parameters employed are detailed in Table 2.

The accuracy of the printed model seems to improve significantly when using only the rotational axis and not involving the linear movement of the linear axis for printing. This improvement may be due to the rotational axis rotating only the part to be printed on, while the linear axis carries the mass of hardware components. The rotational axis allows for higher acceleration since it has to move a smaller mass, resulting in increased accuracy when printing on single-curved surfaces.

Table 2. Printing parameters for 3D inkjet printing on a single-curved surface

Printing parameter	Value
Angular velocity, ω (deg/s)	10
Jetting frequency, f (Hz)	555
Resolution, ϕ (dpi)	8100
Number of discretization points, N (-)	9
Arc length between discretization points, Δs (mm)	3.49
Angle between discretization points, φ (deg)	20
Radius of the cylinder, r (mm)	10

3.3. Inkjet printing on free-form surfaces for palatal defects

Finally, we printed a thin membrane on a free-form surface resembling a palatal implant. A palatal defect is an abnormal opening in the roof of the mouth that can significantly affect speech, eating, hearing, and breathing functions. The defect can vary in size and severity, affecting either the soft palate (posterior cleft palate) or both the soft and hard palate (complete cleft palate). The state-of-the-art treatment to close the defect is palatoplasty, which also often results in scarring and subsequently widens the gap and restricts maxillary growth as the patient grows into an adult.[43,44] These complications could be addressed by placing a resorbable palatal bone implant adapted to the patient's defect. A potential innovative development in the production of such PSIs may involve the integration of a soft membrane, printed conformally onto a patient-specific hard phase. In the context of palatal bone implants, the incorporation of a guided tissue regeneration (GTR) membrane can enhance post-surgical tissue regeneration. GTR membranes serve as barriers, selectively allowing the growth of desired bone cells while preventing the migration of undesirable epithelial cells into the healing site,[45-47] and are commonly employed in periodontal surgeries to facilitate bone regeneration. A GTR membrane should ideally cover both the nasal and oral surfaces of the hard phase and maintain a thickness of approximately 150 µm.[46] This can be achieved using inkjet printing, a non-contact AMT, to print a GTR membrane-inspired structure with a photopolymer on a free-from palatal implant.

The workflow for inkjet printing on a free-form surface, focusing on the bony part of a PSI for a palatal defect, is presented in Figure 6a. We first define the use case to fabricate a GTR-like structure on a palatal hard phase (Figure 6a-1i). Due to the anatomical situation of the palate, a PSI exhibits non-zero Gaussian curvature. Hence, prior to path planning, anatomical landmarks of the topology are identified using primitives, including points and curves, to set the boundary conditions of the movement. The landmarks include global maxima, inflection points, and principal curvatures (Figure 6a-1ii). Considering the dimensions of the printing block from Figure 2, our approach is viable for convex and low-curvature concave surfaces and involves approximating free-form surfaces as double-curved surfaces, where at least one of the principal curvatures is dominant ($\kappa_2 >> \kappa_1$), effectively treating free-form surfaces as single-curved surfaces.

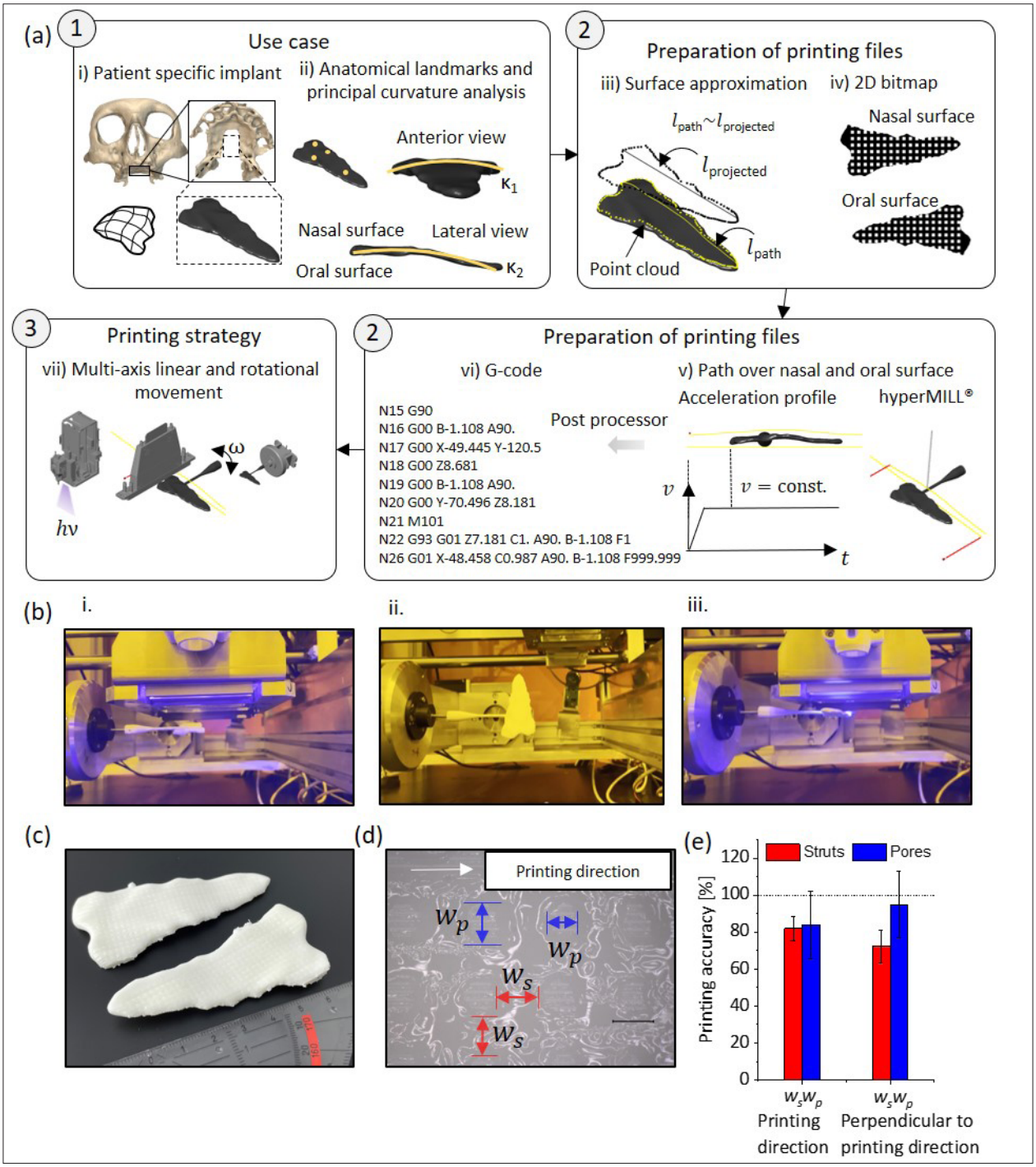


Figure 6. Workflow and accuracy visualization for a scaffold on a free-form surface. (a) Fabrication of a hybrid-printed palatal implant using inkjet printing on a free-form surface: (a,1i) Patient-specific hard phase; (a, 1ii) manual marking of anatomical landmarks (e.g., global maxima) and principal curvatures; (a, 2iii) manual approximation of a 3D surface and projection onto a 2D plane; (a, 2iv) sliced models of the nasal and oral surfaces (mirrored images); (a, 2v) computer-aided manufacturing (CAM) programming of the printhead path, where printhead paths are highlighted in yellow and the printhead is represented by a subtractive endmill tool type; (a, 2vi) automatic computation of the G-code; and (a, 3vii) the printing strategy. Size comparison of a Ricoh MH2820 to the hard phase (b) Mounting the palatal implant on the printer by: (b, i) moving with the printhead along the nasal surface; (b, ii) rotating the part by 180°; and (b, iii) moving over the oral surface. (c) Inkjet-printed mesh, resembling a guided-tissue regeneration (GTR) membrane soft phase, on the nasal and oral surfaces of a polylactic acid (PLA)-printed part resembling the hard phase of a patient-specific palatal implant. (d) Microscopic image with the measurement positions to determine printing accuracy. Magnification: ×50. Scale bar: 1 mm. (e) Printing accuracy of struts and pores along the printing direction and the perpendicular to it.

Additionally, inkjet printing offers greater flexibility for conformal movements over irregular free-form surfaces compared to conventional 3D printing technologies. With inkjet technology being a non-contact method, operating at a distance of 1 mm and a typical droplet speed ranging from 4 to 8 m/s, the inkjet printhead can navigate irregular surfaces with more freedom, unlike FFF, and the need for strict conformal movement can be partly eliminated.

This is followed by the preparation of the printing files (Figure 6a-2iii and 2iv). Working with free-form surfaces presents unique challenges in generating printable files compared to single-curved surfaces. Taking into account the aforementioned physical limitations of the printing block, creating an equivalent image for mapping 2D images on 3D surfaces requires surface approximation. To address this challenge, we introduced a set of requirements for the hard phase. Specifically, the surface under investigation should exhibit low curvature and minimal deviation from a straight line ($l_{path} \sim l_{projected}$) (Figure 6a-2iii). Meeting these requirements minimizes the impact of surface distortions. In a further step, we manually generated a point cloud representation of the surface. The point cloud undergoes a flattening process by projecting it onto a planar surface and creating a 2D bitmap (Figure 6a-2iv). The flattened surface serves as a canvas on which an image can be mapped. The image is mirrored to provide a printable file for the nasal and oral surfaces.

Thereafter, we programmed the printhead movement using hyperMILL® software to create the path over the nasal and oral surfaces. The design incorporates a handling element positioned on the lateral part of the hard phase, allowing for mounting on the machine (Figure 6a-2v). The five-axis capability of our machine allows for automatized printing on the nasal and oral surfaces of the palatal obturator in one printing process. In Figure 6a-2v, two trajectories are extracted—one over the nasal area and another over the oral region. Users have complete freedom in selecting the movement strategy, with the option to program either conformal or approximate surfaces. Path planning also incorporates considerations for the acceleration and deacceleration movements of the CNC portal. One significant advantage of our approach is the ability to program printhead paths independently from the hardware and control system. Once movement planning is complete, it is translated into G-code (Figure 6a-2vi). This transformation is completed using a post-processor that converts the programmed movement into machine-specific coordinates, incorporating commands for the printhead and UV-LED on/off controls. To ensure smooth synchronization of simultaneous linear movements of the printhead and rotary movements of the hard phase, rotary movements are commanded as angles and linear motions as lengths. The inverse time mode in the G-code, widely used in four and five-axis applications, was found to prevent jerky movements when synchronizing linear and rotation. In the subsequent step, the generated G-code can be imported into Mach3.

Finally, the printing strategy is initiated by mounting the implant on the two-axis gantry using the handling element (Figure 6a-3vii). The printing process starts with material deposition on the nasal surface, followed by a curing process. The printhead and the UV-LED move at a defined z height of approximately 5 mm, while the palatal implant rotates beneath the printing block during the printing process.

Following this workflow, a GTR membrane-inspired structure was printed on a free-form surface with variable topography (Figure 6). To validate our approach, we used a patient-specific geometry derived from a fetus for the hard phase. We scaled up the original model by a factor of seven to enhance the visual clarity. Figure 6b illustrates the printing strategy including various key stages: deposition of the photopolymer on the nasal palatal surface, displaying the distance between the printhead and surface (Figure 6b-i); the palatal implant being flipped 180° (Figure 6b-ii); and printing on the oral surface of the palatal implant (Figure 6b-iii). A total of 10 layers were printed.

During the process, partial nozzle clogging resulted in the local connection of certain sections within the mesh structures. The initially designed square pore width (w_p) of 800 µm and strut width (w_s) of 1500 µm exhibited transformations to circular shapes (Figure 6c and d). This could be attributed to two reasons: (i) the irregular surface of the hard phase may cause ink spreading before curing, and (ii) the slow printing speed might also facilitate ink spreading, contributing to the observed outcomes. The printed structures exhibited dimensions smaller than intended, with a deviation of -16.15 ± 18.18% for pore width in the printing direction and 1.8 ± 23.37% for pore width perpendicular to the printing direction. Likewise, the strut width deviated by -18.05 ± 6.61% in the printing direction and -27.79 ± 8.79% perpendicular to the printing direction (n = 10 struts and pores) (Figure 6e). Table 3 illustrates the printing parameters utilized.

These deviations could be attributed to several error sources. When printing on free-form surfaces, aligning the part and synchronizing it with multi-nozzle printheads present significant challenges. Achieving precise alignment is crucial for optimal results. Coordinating the triggering of printheads and setting acceleration parameters adds complexity to the process. Additionally, maintaining a constant speed while moving across the free-form surface

Table 3. Printing parameters for 3D inkjet printing on a free-form surface

Printing parameter	Value
Printing speed, ν (mm/s)	8.33
Jetting frequency, f (Hz)	2656
Resolution, ϕ (dpi)	8100

introduces further intricacies. Moreover, due to the irregularities of the surface, there is a risk of uncontrollable ink spreading before curing. Overcoming these challenges is essential to minimize deviations and ensure accurate and reliable printing on non-planar geometries.

While we provide a unique approach for the hardware/software and movement strategies for inkjet printing over curved surfaces and image processing, the surface approximation to print on surfaces with Gaussian curvature lacks precision. It is important to note that the approximations we utilized to map 2D images onto 3D surfaces were not the focus of our study, but rather means to demonstrate the validity of our approach. While this approximation lacks an underlying algorithm and the model building is not automated and strongly dependent on the user, it was deemed sufficient for the purpose of this study. Indeed, a numerical model to solve this problem would be ideal, but the complex mathematical calculations required are beyond the scope of this research.

4. Conclusion

The central topic of this paper was to provide insight into the development of a five-axis printer for the fabrication of hybrid scaffolding structures on two fronts: (i) multi-material fabrication of soft phases by combining two different AMTs, and (ii) printing on free-form surfaces to fabricate hybrid scaffolds of dissimilar materials. We divide the development into three main topics, namely, hardware/software setup, the establishment of workflows and printing strategies, and the demonstration of the potential of the printing system to fabricate different scaffolding structures. The workflows highlight the incorporation of inkjet printing within existing virtual path planning software and the combination of two different AMTs in one fabrication process.

Moving forward, future studies may explore the utilization of novel materials to augment scaffolds with nanotopography[48] and integrate materials to induce mechanical stimulation and enhance tissue regeneration.[49] When combined with hybrid printing processes, these innovative approaches hold promise for improving tissue remodeling. By leveraging the synergy between materials and additive manufacturing methodologies, researchers can further enhance the functionality and effectiveness of scaffolds in tissue engineering applications.

The developed printer can be used for fabricating hybrid scaffolding structures, integrating both hard and soft materials by combining 3D inkjet and extrusion printing on planar surfaces, as well as 3D inkjet printing of porous structures on single-curved and free-form surfaces. This integration streamlines the fabrication of multi-material osteochondral and palatal implants. We believe that our approach provides a solution for the aforementioned examples, thereby overcoming the limitations of traditional AMTs and demonstrating the fabrication of simple hybrid designs.

Acknowledgments

The authors would like to thank Lithoz GmbH (Austria) for providing ceramic platelets and Stratasys Ltd. (Israel) for providing the water-soluble support material. Additionally, the authors would like to thank Mr. Eduard Winter from the Natural History Museum Vienna and the pathological-anatomical collection in the Narrenturm for providing access to the resources.

Funding

This work was supported by the European Union's Horizon 2020 Research and Innovation Program (Grant number: 953134; INKplant: Ink-based hybrid multi-material fabrication of next-generation implants).

Conflict of interest

The authors declare no conflicts of interest.

Author contributions

Conceptualization: Michael Kainz, Elena Guillén
Formal Analysis: Michael Kainz
Funding Acquisition: Elena Guillén
Investigation: Michael Kainz, Isabel Caetano da Silva, Paula Schumann, Adrián Martínez Cendrero, Thomas Voglhuber
Methodology: Michael Kainz, Elena Guillén, Tilo Dehne, Gunpreet Oberoi, Julia Kastner, Erik Kornfellner, Daniel Seitz
Project Administration: Elena Guillén, Sandra Haas
Software: Milan Rathod, Lukas Hartung
Supervision: Elena Guillén, Francesco Moscato, Andrés Díaz Lantada
Visualization: Michael Kainz
Writing – original draft: Michael Kainz
Writing – review & editing: Michael Kainz, Elena Guillén, Francesco Moscato

Ethics approval and consent to participate

Not applicable.

Consent for publication

Not applicable.

Availability of data

Data is available from the corresponding author upon reasonable request.

References

1. Gleadall A, Visscher D, Yang J, Thomas D, Segal J. Review of additive manufactured tissue engineering scaffolds: relationship between geometry and performance. *Burns Trauma*. 2018;6:19. doi: 10.1186/s41038-018-0121-4
2. Seidi A, Ramalingam M, Elloumi-Hannachi I, Ostrovidov S, Khademhosseini A. Gradient biomaterials for soft-to-hard interface tissue engineering. *Acta Biomater*. 2011;7(4): 1441-1451. doi: 10.1016/j.actbio.2011.01.011
3. Wang C, Huang W, Zhou Y, et al. 3D printing of bone tissue engineering scaffolds. *Bioact Mater*. 2020;5(1):82-91. doi: 10.1016/j.bioactmat.2020.01.004
4. Truby RL, Lewis JA. Printing soft matter in three dimensions. *Nature*. 2016;540(7633):371-378. doi: 10.1038/nature21003
5. Haglin JM, Eltorai AEM, Gil JA, Marcaccio SE, Botero-Hincapie J, Daniels AH. Patient-specific orthopaedic implants. *Orthop Surg*. 2016;8(4):417-424. doi: 10.1111/os.12282
6. Bittner SM, Guo JL, Melchiorri A, Mikos AG. Three-dimensional printing of multilayered tissue engineering scaffolds. *Mater Today*. 2018;21(8):861-874. doi: 10.1016/J.MATTOD.2018.02.006
7. Taboas JM, Maddox RD, Krebsbach PH, Hollister SJ. Indirect solid free form fabrication of local and global porous, biomimetic and composite 3D polymer-ceramic scaffolds. *Biomaterials*. 2003;24(1):181-194. doi: 10.1016/S0142-9612(02)00276-4
8. Lantada AD, Iniesta HA, Garcia-Ruiz JP. Composite scaffolds for osteochondral repair obtained by combination of additive manufacturing, leaching processes and hMSC-CM functionalization. *Mater Sci Eng C*. 2016;59:218-227. doi: 10.1016/j.msec.2015.10.015
9. Sänger JC, Schwentenwein M, Bermejo R, Günster J. Hybridizing lithography-based ceramic additive manufacturing with two-photon-polymerization. *Appl Sci (Basel)*. 2023;13(6). doi: 10.3390/app13063974
10. Gonzalez-Pujana A, Carranza T, Santos-Vizcaino E, et al. Hybrid 3D printed and electrospun multi-scale hierarchical polycaprolactone scaffolds to induce bone differentiation. *Pharmaceutics*. 2022;14(12). doi: 10.3390/pharmaceutics14122843
11. Choi WS, Kim JH, Ahn CB, et al. Development of a multi-layer skin substitute using human hair keratinic extract-based hybrid 3D printing. *Polymers (Basel)*. 2021;13(16):2584. doi: 10.3390/polym13162584
12. Altunbek M, Afghah SF, Fallah A, Acar AA, Koc B. Design and 3D printing of personalized hybrid and gradient structures for critical size bone defects. *ACS Appl Bio Mater*. 2023;6(5):1873-1885. doi: 10.1021/acsabm.3c00107
13. Milojević M, Harih G, Vihar B, et al. Hybrid 3D printing of advanced hydrogel-based wound dressings with tailorable properties. *Pharmaceutics*. 2021;13(4):564. doi: 10.3390/pharmaceutics13040564
14. Stögerer J, Baumgartner S, Hochwallner A, Stampfl J. Bio-inspired toughening of composites in 3D-printing. *Materials (Basel)*. 2020;13(21). doi: 10.3390/ma13214714
15. Lee HR, Park JA, Kim S, Jo Y, Kang D, Jung S. 3D microextrusion-inkjet hybrid printing of structured human skin equivalents. *Bioprinting*. 2021;22:e00143. doi: 10.1016/j.bprint.2021.e00143
16. Jaksa L, Pahr D, Kronreif G, Lorenz A. Development of a multi-material 3D printer for functional anatomic models. *Int J Bioprint*. 2021;7(4):420. doi: 10.18063/ijb.v7i4.420
17. Tashman JW, Shiwarski DJ, Feinberg AW. Development of a high-performance open-source 3D bioprinter. *Sci Rep*. 2022;12(1):22652. doi: 10.1038/s41598-022-26809-4
18. Hinton TJ, Jallerat Q, Palchesko RN, et al. Three-dimensional printing of complex biological structures by freeform reversible embedding of suspended hydrogels. *Sci Adv*. 2015;1(9):e1500758. doi: 10.1126/sciadv.1500758
19. Pusch K, Hinton TJ, Feinberg AW. Large volume syringe pump extruder for desktop 3D printers. *HardwareX*. 2018;3:49-61. doi: 10.1016/j.ohx.2018.02.001
20. Mirdamadi E, Tashman JW, Shiwarski DJ, Palchesko RN, Feinberg AW. FRESH 3D bioprinting a full-size model of the human heart. *ACS Biomater Sci Eng*. 2020;6(11): 6453-6459. doi: 10.1021/acsbiomaterials.0c01133
21. Khani N, Nadernezhad A, Bartolo P, Koc B. Hierarchical and spatial modeling and bio-additive manufacturing of multi-material constructs. *CIRP Annals*. 2017;66(1):229-232. doi: 10.1016/j.cirp.2017.04.132

22. Hong F, Hodges S, Myant C, Boyle DE. Open5x: accessible 5-axis 3D printing and conformal slicing. *Ext Abstr Hum Factors Computing Syst*. 2022. doi: 10.1145/3491101.3519782

23. Sheng YT, Liong S, Wang SY, Gan YS. 3D printing on freeform surface: real-time and accurate 3D dynamic dense surface reconstruction with HoloLens and displacement measurement sensors. *Adv Mech Eng*. 2023;15(1):168781322211484. doi: 10.1177/16878132221148404

24. Arango I, Cifuentes C. Design to achieve accuracy in ink-jet cylindrical printing machines. *Machines*. 2019;7(1):6. doi: 10.3390/machines7010006

25. Arango I, Bonil L, Posada D, Arcila J. Prediction of a flying droplet landing over a non-flat substrates for ink-jet applications. *Int J Interact Des Manuf*. 2019;13:967-980 doi: 10.1007/s12008-019-00547-w

26. Fechtig D. Robot-based direct digital printing on freeform surfaces. In: Zapka W, ed. *Inkjet Printing in Industry*. Weinheim: Wiley-VCH; 2022:1269-1297. doi: 10.1002/9783527828074.CH55

27. Thalheim R, Willert A, Mitra D, Zichner R. Novel and efficient methodology for drop placement accuracy testing of robot-guided inkjet printing onto 3D objects. *Machines*. 2023;11(5):568. doi: 10.3390/machines11050568

28. Shen H, Liu B, Liu S, Fu J. Five-axis freeform surface color printing technology based on offset curve path planning method. *Appl Sci (Basel)*. 2020;10(5):1716. doi: 10.3390/app10051716

29. Gazeau JP, Said Z, Ramírez-Torres J. A novel 5-axis robot for printing high resolution pictures from media on 3D wide surfaces. *Proceedings of the IEEE International Conference on Industrial Technology*. 2009:1-6. doi: 10.1109/ICIT.2009.4939735

30. Urasinska-Wojcik B, Chilton N, Todd P, et al. Integrated manufacture of polymer and conductive tracks for real-world applications. *Addit Manuf*. 2019;29:100777. doi: 10.1016/j.addma.2019.06.028

31. Moroni L, Boland T, Burdick JA, et al. Biofabrication: a guide to technology and terminology. *Trends Biotechnol*. 2018;36(4):384-402. doi: 10.1016/j.tibtech.2017.10.015

32. Kainz M, Perak S, Stubauer G, et al. Additive and lithographic manufacturing of biomedical scaffold structures using a versatile thiol-ene photocurable resin. *Polymers (Basel)*. 2024;16(5):655. doi: 10.3390/polym16050655

33. Arosio P, Owczarz M, Wu H, Butté A, Morbidelli M. End-to-end self-assembly of RADA 16-I nanofibrils in aqueous solutions. *Biophys J*. 2012;102(7): 1617-1626. doi: 10.1016/j.bpj.2012.03.012

34. Sankar S, O'Neill K, Bagot D'Arc M, et al. Clinical use of the self-assembling peptide RADA16: a review of current and future trends in biomedicine. *Front Bioeng Biotechnol*. 2021;9. doi: 10.3389/fbioe.2021.679525

35. Wong KC. 3D-printed patient-specific applications in orthopedics. *Orthop Res Rev*. 2016;8:57-66. doi: 10.2147/ORR.S99614

36. Mobbs RJ, Coughlan M, Thompson R, Sutterlin CE, Phan K. The utility of 3D printing for surgical planning and patient-specific implant design for complex spinal pathologies: case report. *J Neurosurg*. 2017;26(4):513-518. doi: 10.13140/RG.2.2.18087.75686

37. Lawrence S. Developable surfaces: their history and application. *Nexus Netw J*. 2011;13(3):701-714. doi: 10.1007/s00004-011-0087-z

38. Baselga S, Olsen M. Approximations, errors, and misconceptions in the use of map projections. *Math Probl Eng*. 2021;2021:1-12. doi: 10.1155/2021/1094602

39. Roach BL, Hung CT, Cook JL, Ateshian GA, Tan AR. Fabrication of tissue engineered osteochondral grafts for restoring the articular surface of diarthrodial joints. *Methods*. 2015;84:103-108. doi: 10.1016/j.ymeth.2015.03.008

40. Woodfield TBF, Guggenheim M, von Rechenberg B, Riesle J, van Blitterswijk CA, Wedler V. Rapid prototyping of anatomically shaped, tissue-engineered implants for restoring congruent articulating surfaces in small joints. *Cell Prolif*. 2009;42(4):485-497. doi: 10.1111/j.1365-2184.2009.00608.x

41. Guilak F, Estes BT, Moutos FT. Functional tissue engineering of articular cartilage for biological joint resurfacing-The 2021 Elizabeth Winston Lanier Kappa Delta Award. *J Orthop Res*. 2022;40(8):1721-1734. doi: 10.1002/jor.25223

42. Kilian D, Ahlfeld T, Akkineni AR, Bernhardt A, Gelinsky M, Lode A. 3D bioprinting of osteochondral tissue substitutes – in vitro-chondrogenesis in multi-layered mineralized constructs. *Sci Rep*. 2020;10(1):8277. doi: 10.1038/s41598-020-65050-9

43. Fudalej P, Katsaros C, Dudkiewicz Z, et al. Dental arch relationships following palatoplasty for cleft lip and palate repair. *J Dent Res*. 2012;91(1):47-51. doi: 10.1177/0022034511425674

44. Figueroa AA, Murphy J, Tragos C. Intra-lesional injection of triamcinolone to palatoplasty scar to aid reversal of transverse maxillary relapse after orthognathic surgery. *J Craniofac Surg*. 2022;33(4):e416-e418. doi: 10.1097/SCS.0000000000008347

45. Ren Y, Fan L, Alkildani S, et al. Barrier membranes for guided bone regeneration (GBR): a focus on recent advances in collagen membranes. *Int J Mol Sci*. 2022;23(23):14987. doi: 10.3390/ijms232314987

46. Tayebi L, Rasoulianboroujeni M, Moharamzadeh K, Almela TKD, Cui Z, Ye H. 3D-printed membrane for guided tissue regeneration. *Mater Sci Eng C*. 2018;84:148-158.
doi: 10.1016/j.msec.2017.11.027

47. Vahdatinia F, Hooshyarfard A, Jamshidi S, et al. 3D-printed soft membrane for periodontal guided tissue regeneration. *Materials (Basel)*. 2023;16(4).
doi: 10.3390/ma16041364

48. Jang TS, Park SJ, Lee JE, et al. Topography-supported nanoarchitectonics of hybrid scaffold for systematically modulated bone regeneration and remodeling. *Adv Funct Mater*. 2022;32:2206863.
doi: 10.1002/adfm.202206863

49. Liang J, Zeng H, Qiao L, et al. 3D printed piezoelectric wound dressing with dual piezoelectric response models for scar-prevention wound healing. *ACS Appl Mater Interfaces*. 2022;14(27):30507-30522.
doi: 10.1021/acsami.2c04168

ACCSCIENCE PUBLISHING

International Journal of Bioprinting

RESEARCH ARTICLE

Early monitoring for 3D-printed patient-specific mandible reconstructive implant biomechanical behavior under different occlusal conditions using a wireless module system

Cheng-Hsien Wu[1,2], Hsiao-Kuan Wu[3], Pei-Jung Tsai[4], and Chun-Li Lin[5]*

[1]Oral & Maxillofacial Surgery, Department of Dentistry, Taipei Veterans General Hospital, Taipei, Taiwan

[2]Department of Dentistry, School of Dentistry, National Yang Ming Chiao Tung University, Taipei, Taiwan

[3]Department of Exercise and Health Science, National Taipei University Nursing and Health Sciences, Taipei, Taiwan

[4]Department of Biomedical Engineering, National Yang Ming Chiao Tung University, Taipei, Taiwan

[5]Department of Biomedical Engineering, Medical Device Innovation & Translation Center, National Yang Ming Chiao Tung University, Hsinchu, Taiwan

Abstract

Three-dimensional (3D) printing technology used to manufacture patient-specific, large-scale medical implants has become increasingly prevalent. Nevertheless, early biomechanics monitoring can enhance the implantation success rate. This study developed a wireless module system (WMS) for strain gauge measurement that can be placed within the implant to achieve early biomechanical behavior detection for an experimental 3D-printed metal model of a patient-specific segmental implant (MMPSI) after surgery. This WMS includes a chip, a circuit board, and a battery, all with dimensions smaller than 20 mm × 12 mm × 8 mm. This system can connect to strain gauges and interface with a mobile application for measuring and transmitting strain data. The WMS functionality was confirmed through cantilever beam experiments. Premature failure was detected using this WMS installed in an experimental 3D-printed MMPSI and through *in vitro* fatigue biomechanical testing under different occlusal forces applied on the plastic-simulated mandibular model. The WMS validation results indicated that the strain gauge measurement error compared to theoretical values was within 17%. Biomechanical fatigue results addressed the higher strain received and greater cyclic loads were recorded when occlusal force was applied onto the premolar under identical force application conditions because the premolar was closer to the strain gauge attachment location, resulting in a longer lever arm compared to the molar. This study concluded that the developed WMS for strain measurement can be installed in a patient-specific 3D-printed implant with enough internal space to detect early biomechanical behavior after surgery. Current results of *in vitro* fatigue test for segmental defect indicated that occlusal situation can be adjusted to reduce implantation failure risk.

Keywords: 3D-printed implant; Wireless; Biomechanics; Patient-specific; Mandibular defect

***Corresponding author:**
Chun-Li Lin (cllin2@nycu.edu.tw)

Citation: Wu CH, Wu HK, Tsai PJ, Lin CL. Early monitoring for 3D-printed patient-specific mandible reconstructive implant biomechanical behavior under different occlusal conditions using a wireless module system. *Int J Bioprint*. 2024;10(3):2553. doi: 10.36922/ijb.2553

Received: December 27, 2023
Accepted: February 19, 2024
Published Online: March 25, 2024

Copyright: © 2024 Author(s). This is an Open Access article distributed under the terms of the Creative Commons Attribution License, permitting distribution, and reproduction in any medium, provided the original work is properly cited.

Publisher's Note: AccScience Publishing remains neutral with regard to jurisdictional claims in published maps and institutional affiliations.

1. Introduction

Mandibular continuity defects refer to obvious bone or tissue loss in the mandibular region, primarily caused by malignant tumors, external traumas, or congenital genetic disorders.[1-3] These defects can have a detrimental impact on a patient's facial aesthetics and may lead to speech and chewing difficulties, affecting their quality of life.[4] Currently, fibula free flap (FFF) surgery used with traditional bone plates to secure the bone graft is the gold standard for such treatments. Several advantages of this approach include the exit of the fibular flap from the long vascular pedicle, segmented blood supply, availability as a composite tissue, and enough bone volume for host dental implants.[5-7] However, reconstruction procedures remain challenging for surgeons because bone plate fatigue fractures may occur due to pre-bent implants to conform to the mandibular curvature.[8-10] Furthermore, these implants may not precisely match the patient's mandibular curvature, resulting in the inability to fully restore patient appearance and bite functionality.

Recently, metal three-dimensional (3D) printing, medical image processing, and computer-aided design (CAD) technologies were integrated to develop a patient-specific reconstruction implant for mandibular continuity defect. This approach was accepted to restore the patient appearance and mandible structural strength.[11] However, metal 3D-printed implants introduce certain challenges, particularly in terms of implant weight and the potential stress-shielding effect.[12] To address these issues, topology optimization was proposed to preserve the implant mechanical strength while reducing its excessive weight.[13] Nonetheless, the instability of large 3D-printed implant is usually associated with their unfavorable biomechanical aspects, including experiencing high stress/strain and significant displacement. Abnormal biomechanical responses to the 3D-printed implant can result in implant loosening/extensive damage, and the implant might also become dislodged, penetrating through the adjacent soft tissue.[14,15] Therefore, ensuring the early detection of biomechanical anomalies in large implants is a critical consideration for mandibular reconstruction treatment.

Strain gauge used to measure deformation resulting from bending forces is a well-established technique in both the mechanical and medical fields.[16] Strain gauges work by utilizing piezoelectric materials to deform and then amplify the voltage, pass it through a Wheatstone bridge, and convert it into the strain measurement for the tested object. In recent years, placing strain gauges within a bone plate has been proposed to detect and track post-operative bone healing conditions.[17,18] However, the strain signals measurements typically require specific settings and the use of external wearable devices (such as wires) and peripheral measurement systems for data collection. As a result, current strain sensing devices do not facilitate real-time measurements performed by patients themselves or within a home setting. Therefore, the prime objective of this study is to integrate the strain gauge signal processor into a microchip that can be installed into mandibular implants to monitor the implant's biomechanical status at the initial period after surgery.

In this study, we developed a miniaturized WMS for strain gauge measurement to achieve early biomechanical behavior detection in an experimental 3D-printed metal model of a patient-specific segmental implant (MMPSI) after surgery. This system was installed into a 3D-printed mandibular implant for *in vitro* fatigue mechanical testing under different occlusal conditions applied on the simulated plastic mandibular model after validating the feasibility through cantilever beam modeling and mechanical tests. The goal was to prevent premature failure through understanding the relationship between the received strain signals from the *in vitro* simulated mandibular patient-specific 3D-printed implant and various occlusal forces.

2. Materials and methods

2.1. WMS design

The CYBLE-214015-01 (Infineon Technologies, Neubiberg, Germany) programmable microchip with a built-in low-power Bluetooth module was employed in this study. The internal amplifier and 12-bit analog-to-digital microchip converter were utilized for strain gauge signals acquisition at a sampling rate of 1500 Hz. The signals, following median filtering, were transmitted to a mobile application (APP) via low-power Bluetooth connection at a rate of 20 data points per second. To achieve power efficiency, the microchip system automatically entered a sleep state in case of transmission interruption. The chip awakened to resume data capture and transmission upon re-establishing the Bluetooth connection. The program design is illustrated in Figure 1a. The microchip underwent fabrication processes such as exposure, development, and etching, as depicted in Figure 1b. This chip measured 17.5 mm in length and 12 mm in width. The primary mobile APP functions can record data with data saved in text format and allow the APP interface to adjust the adaptation of both the Bluetooth connection time and the sleep interval time with the microchip to reduce chip power consumption. In subsequent steps, the strain gauge and power wires were sequentially soldered to the wireless module chip, forming a WMS to communicate with the mobile APP (Figure 1c).

2.2. WMS validation

Cantilever beam model structural mechanics were used to validate the WMS feasibility. Finite element (FE) analysis

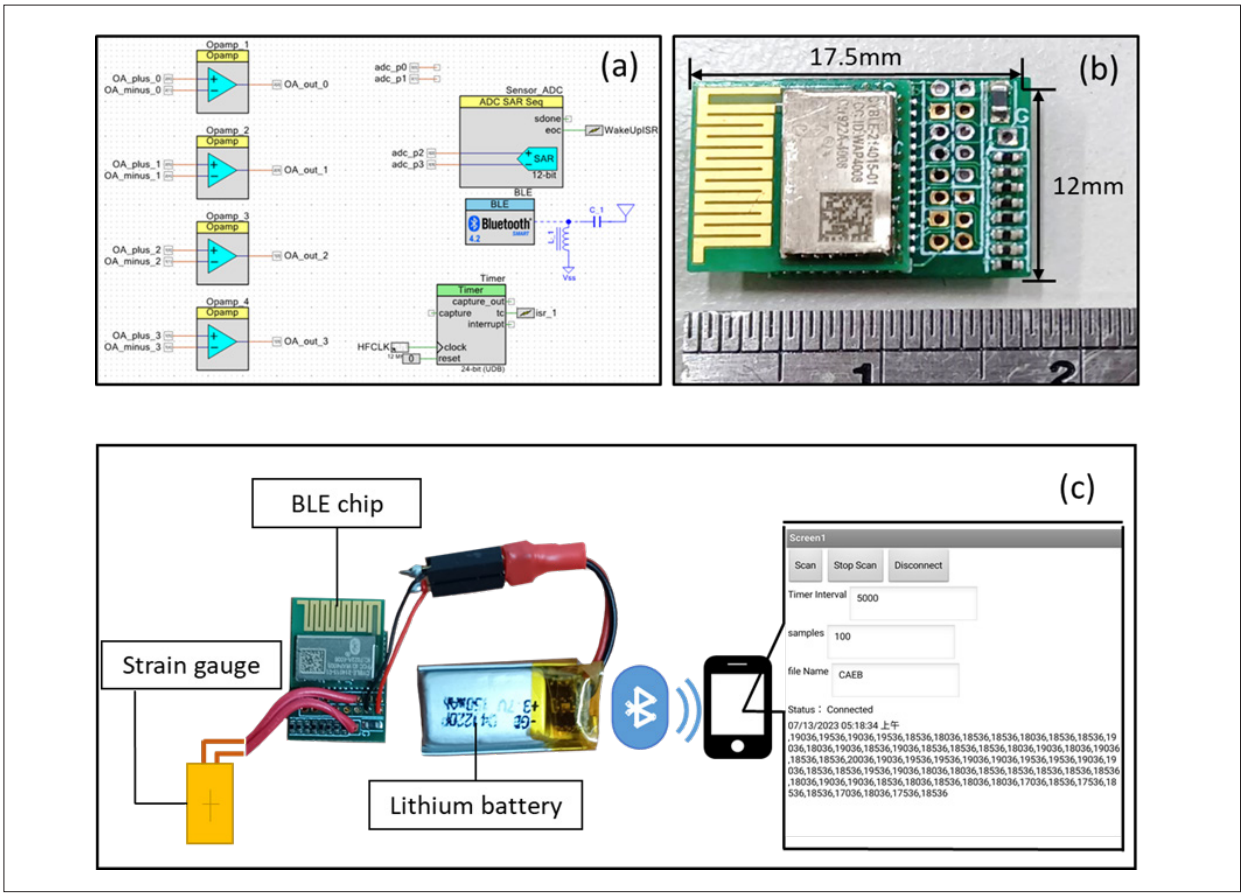


Figure 1. (a) The wireless modulus program design; (b) the wireless modulus system chip and circuit board; (c) illustration of function for wireless modulus system, which includes chip, circuit board, battery, strain gauges, and mobile APP. Abbreviation: BLE, Bluetooth low energy.

and *in vitro* experiments utilized traditional data log and wireless module signal acquisition systems after the forces applied on the cantilever beam were employed to obtain strain value validation of the corresponding strain gauge attachment positions.

A cantilever beam model 150 mm in length, 60 mm in width, and 5 mm in thickness was generated using CAD software (SpaceClaim, SpaceClaim Corporation, Concord, Massachusetts, USA) and imported into the FE software ANSYS (ANSYS, v21.1, ANSYS Inc., Canonsburg, PA, USA) for simulation (Figure 2a–c). The model was meshed using the free mesh approach with 2 mm element size, resulting in a total of 20,626 elements and 59,040 nodes. The elastic modulus and Poisson's ratio (70 GPa and 0.33) for aluminum were set as material properties. Nodes at the end of the cantilever beam were fixed in all directions as the boundary condition. The FE analysis was conducted to determine the strain values under forces of 50 N, 100 N, and 200 N applied in the *y*-direction at the middle width position 30 mm from the cantilever beam front end. The strain detection positions were located on the backside of the cantilever beam at distances of 15 mm (point B in Figure 2d) and 30 mm (point A in Figure 2d) from the loading position. Corresponding values were compared with the *in vitro* experiment results using traditional data log signal acquisition system.

The *in vitro* experiment entails using (1) the signal data log system for strain value validation with the results of FE analysis and (2) the WMS for voltage value conversion to those testing with using data log cases. First, strain gauges (N11-FA-1-120-11-P4-VSE1, Showa Measuring Instruments Co., Ltd., Japan) were glued to the backside of the cantilever beam that were at the same positions defined in the FE analysis. The cantilever beam specimen ends were securely clamped to the testing machine (Figure 2e).

For testing (1), the signal acquisition system was bridged to the strain gauges on a data log device (NI 9235, National Instruments Co., Austin, Texas). A vertical force (50 N/100 N/200 N) was applied at the position away from the front end of the aluminum plate, maintained for 10 s,

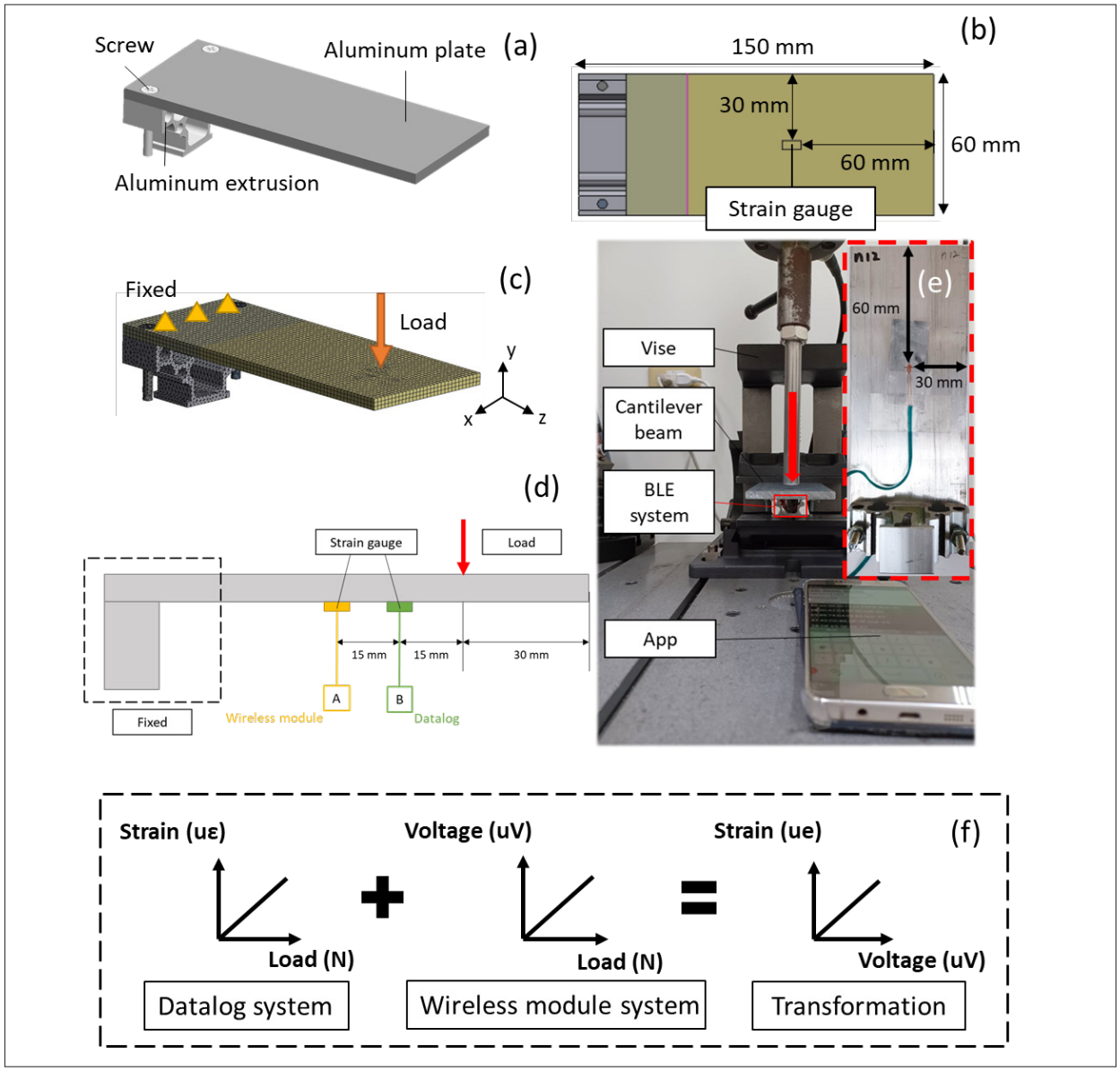


Figure 2. (a) The aluminum alloy cantilever beam solid model; (b) the cantilever beam size and corresponding strain gauge attachment position; (c) Cantilever FE mesh model; (d) strain gauges attachment positions for wireless system at point A and data log systems at point B; (e) illustration of validated experiment; (f) diagram depicting the correlation between FE analysis, wireless module, and data log acquisition experiments. Abbreviation: BLE, Bluetooth low energy.

and then removed. The signal acquisition system utilized data processing software (FleXense, Chief Technology Co., Ltd., Taiwan) to calculate the strain values. Strain values can be used to plot force–strain curves corresponding to the applied forces and validate the FE analysis results.

For testing (2), the WMS was soldered with strain gauge wires to the corresponding microchip pins. The WMS used previously developed mobile APP to receive voltage values and process for plotting force–voltage curves. The strain integration from the data log signal acquisition system and the WMS yield the conversion equations for both strain and voltage (Figure 2f).

To validate the strain–voltage conversion formula, strain gauges were placed at positions A and B at the backside of the cantilever beam (Figure 2d) at distances of 30 mm and 15 mm from the point of applied force, respectively. A force of 200 N was applied repeatedly five times under the same experimental conditions as before to record strain values at point A by WMS with strain–voltage conversion formula and at point B by data log

Table 1. Material properties input to FE analysis for aluminum alloy cantilever beam

Material	Young's modulus (GPa)	Poisson's ratio
Aluminum plate	70	0.33
Aluminum extrusion	70	0.33
Screw	200	0.3

device. The strain values ratio between points A and B was calculated, and the percentage error between this ratio and the theoretical value (theoretical strain at point A being twice that of point B) was determined (Table 1).

2.3. An experimental 3D-printed MMPSI design and manufacture

A digital mandible model with standardized segmental defect and corresponding reconstructed implant was selected as the testing sample. The segmental defect located between the bilateral premolars, including the incisors and canines, was constructed from a normal male patient computed tomography (CT) scan data. All DICOM CT cross-section image data were processed to identify the contours of different hard tissues (cortical and cancellous bone). Those contours were extracted and converted to reconstruct a 3D solid model of the mandible bone with segmental defect.

The segmental reconstructed implant was designed according to the previous work, i.e., (1) the implant body is equipped with shell structure of 0.5 mm thickness to reduce the implant weight, (2) the height of the implant is half of the height of the bone segment, and (3) the bone graft space for postoperative prosthesis is reserved at the top for subsequent follow-up. The implant thickness was two-third of the bone segment thickness to make space for the flap, vascular pedicle, and soft tissue to pass through. To maintain enough implant mechanical strength, two support beams located at the interaction of the side incisor axis on the left/right side and one-sixth of the bone segment height and extended from the buccal side to the lingual side within implant were designed based on the weighted topology optimization results from previous work.[12] Two extended side wings with a thickness of 2.8 mm and five 2.4 mm holes were reserved for bone screw fixation (Figure 3).

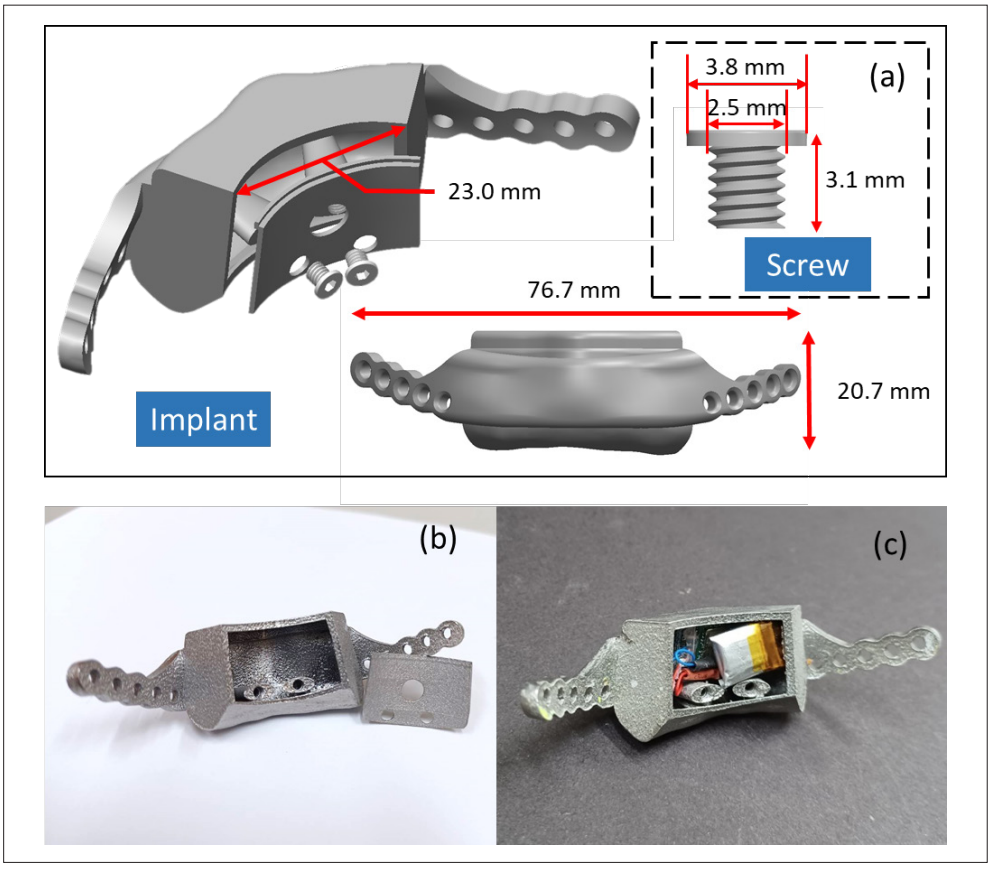


Figure 3. (a) Dimensions of an experimental 3D-printed MMPSI design; (b) back cover design and internal beam; (c) wireless modulus system, which includes chip, circuit board, and battery placed within the implant.

To place the developed WMS within the 3D-printed implant, an openable back cover was designed on the implant lingual side. Two screws with a diameter of 2.5 mm and length of 3.1 mm were used to secure the back cover to the supporting beams inside the implant. Additionally, a 6 mm hole was also made in the center of the back cover to allow Bluetooth signals to transmit to a mobile phone application (Figure 3).

A metal 3D printer (AM400, Renishaw, Gloucestershire, UK) with titanium alloy powder (Ti6Al4V powder with average grain size of 30 μm) was used to manufacture the implant. The 3D printing machine was operated with a laser power of 400 W, a scanning rate of 0.6 m/s, exposure time of 125 s with a spot diameter of 70 μm, and an accuracy of ±25 μm in the laser beam movement and positioning. The implants were then acid-etched to remove residual sandblast particles and cleaned using ultrasonic oscillations.[11,15]

2.4. *In vitro* biomechanical fatigue tests

The uniaxial strain gauge was glued to the inner right buccal wall of the 3D-printed implant at halfway up its height. The strain gauge axis was oriented perpendicular to the occlusal surface. Simultaneously, the strain gauge wires were soldered to the corresponding Bluetooth chip pins. The WMS (comprised of the chip and battery) was placed within the implant and the back cover secured in place with screws (Figure 4a).

The corresponding remaining mandibular plastic bone models were duplicated in acrylonitrile butadiene styrene (ABS-P430; Stratasys, Ltd., Minnesota, USA) using a 3D printer (Dimension 1200es SST, Stratasys, Ltd., Minnesota, USA). The 3D-printed metal implant included WMS was fixed onto the remaining mandibular ABS bone model with bone screws (Tandry Locking Bone Plate System ψ2.4 mm L18 mm, All Micro Precision Co., Ltd., Taiwan) as the test sample. The samples were clamped upside down onto a test machine (Instron E3000, Instron, Canton, MA, USA) and the condyle head fixed in an embedded resin block to apply a force to the mandible angle according to the Wiebke Schupp test method and the work of other scholars (Figure 4a).[19] The testing sample received cyclic loads ranging from 20 N to 200 N, 30 N to 300 N, and 40 N to 400 N, applied separately to the right mandibular molar/premolar area of the mandibular bone model at a frequency of 3 Hz until the sample exhibited noticeable failure or reached 250,000 cycles (Figure 4b). This was performed to simulate the mandibular occlusal conditions 6 months after surgery.[20] Three test samples were processed for each load value and position. Gauge strain values captured by the WMS were analyzed, and the sample failure locations were recorded.

3. Result

Under 50 N/100 N/200 N load conditions, the strain values derived from the FE analysis and the signal data log system were recorded as -82.95 ue/-165.90 ue/-331.81 ue and -78.17 ue/-161.49 ue/-319.67 ue, respectively. Based on the FE analysis results as reference, the percentage errors for the strain values measured by the signal data log system were 5.76%/2.66%/3.66% across the corresponding load conditions. Furthermore, a linear regression plot was created correlating the strain values from the signal data log system with the applied loads (Figure 5a), resulting in an R^2 value of 0.9991.

The voltage values obtained from the WMS under 50 N/100 N/200 N loads were recorded as -912.87 uV/-1828.75 uV/-3386.46 uV, respectively. After plotting the power-voltage results through linear regression (Figure 5b), an R^2 value of 0.9927 was obtained. Further analysis involved performing a linear trend analysis between the voltage values measured by the WMS and the strain values obtained from the signal acquisition system. The outcome is depicted in Figure 5c, presenting the derived equation for converting strain values to voltage values as $y = 10.166x - 147.39$ (where x = strain and y = voltage variation).

Based on the derived voltage conversion equation, the voltage values obtained from point A in the validation experiment can be converted into strain values using the formula provided in material mechanics. Simultaneously, a comparison can be made with the strain results obtained from the signal data log system at point B. The theoretical strain value at point A was expected to be twice that of point B. From Table 2, it was observed that the maximum error percentage was 17%.

Biomechanical fatigue test results indicated that average strain values obtained by the WMS were 146.96 ue ± 66.14 ue/230.49 ue ± 134.92 ue /336.80 ue ± 117.04 ue when 200 N/300 N/400 N were applied on the molar, while the corresponding strain values on the premolar were 248.19 ue ± 86.21 ue /316.30 ue ± 41.23 ue /402.82 ue ± 93.73 ue. From the stress–strain relationship plot in Figure 6a, it can be observed that the strain decreased as the applied load diminished. However, strain was lower when the same load was applied on the molar compared to that on the premolar.

Moreover, the corresponding average fatigue loading cycles for 200 N/300 N/400 N obtained applied on the premolars were 182,591 ± 63,633/38,354 ± 10174/13,416 ± 5072, and on the molars were 250,000 ± 0/210,324 ± 56,111/82,681 ± 11,887, respectively. As depicted in the stress–fatigue cycles relationship plot in Figure 6b, it was noted that fatigue loading cycles increased as the applied

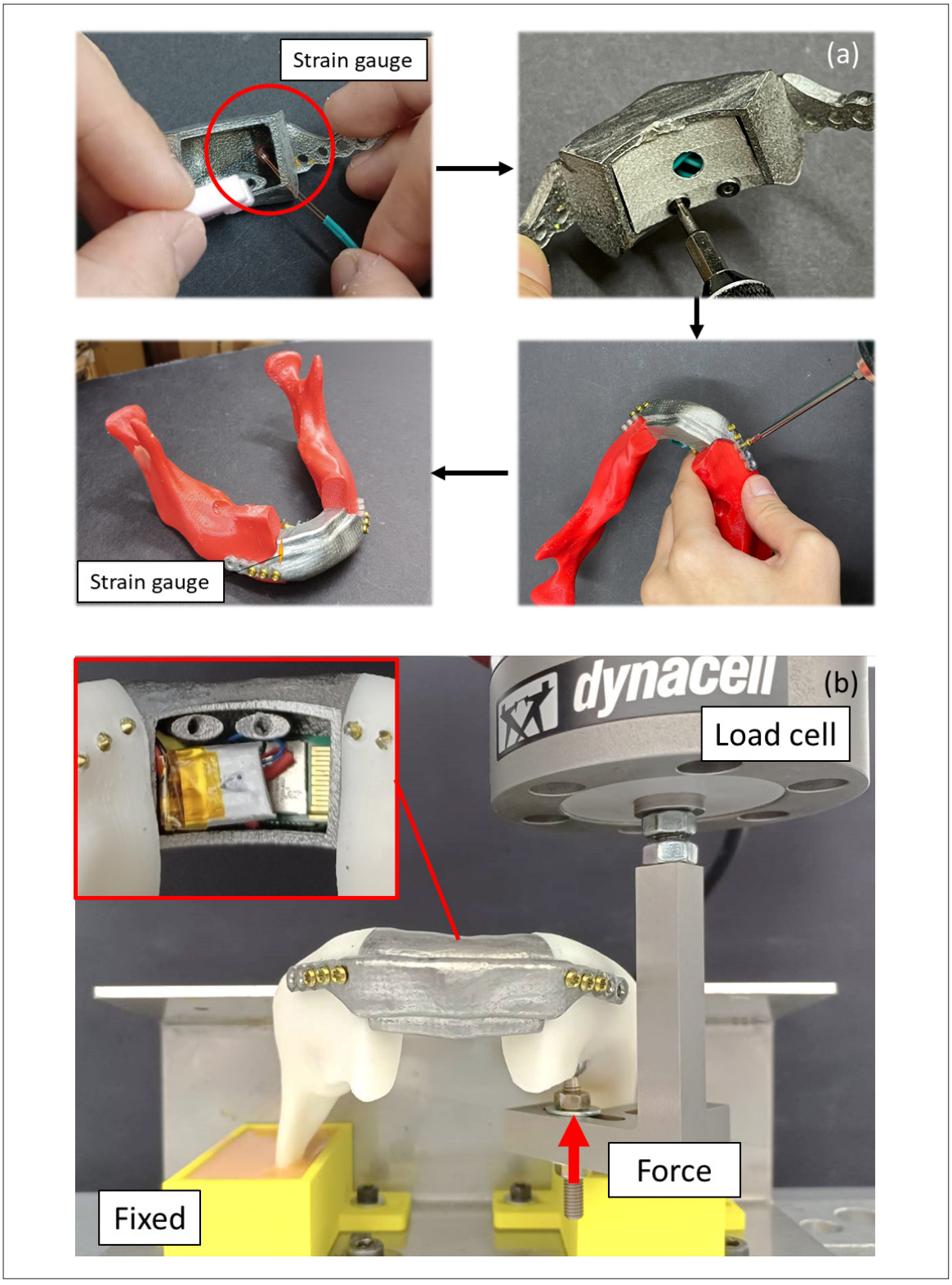


Figure 4. (a) Strain gauge glued to the inner right buccal wall of the reconstructed implant halfway up its height. The back cover was secured in place with screws. The reconstructed implant was fixed onto the remaining mandibular ABS bone model with bone screws as the test sample. (b) The samples were clamped upside down onto a test machine, the condyle head was fixed in an embedded resin block, and the testing sample received cyclic loads to the right mandibular molar/premolar area of the mandibular bone model.

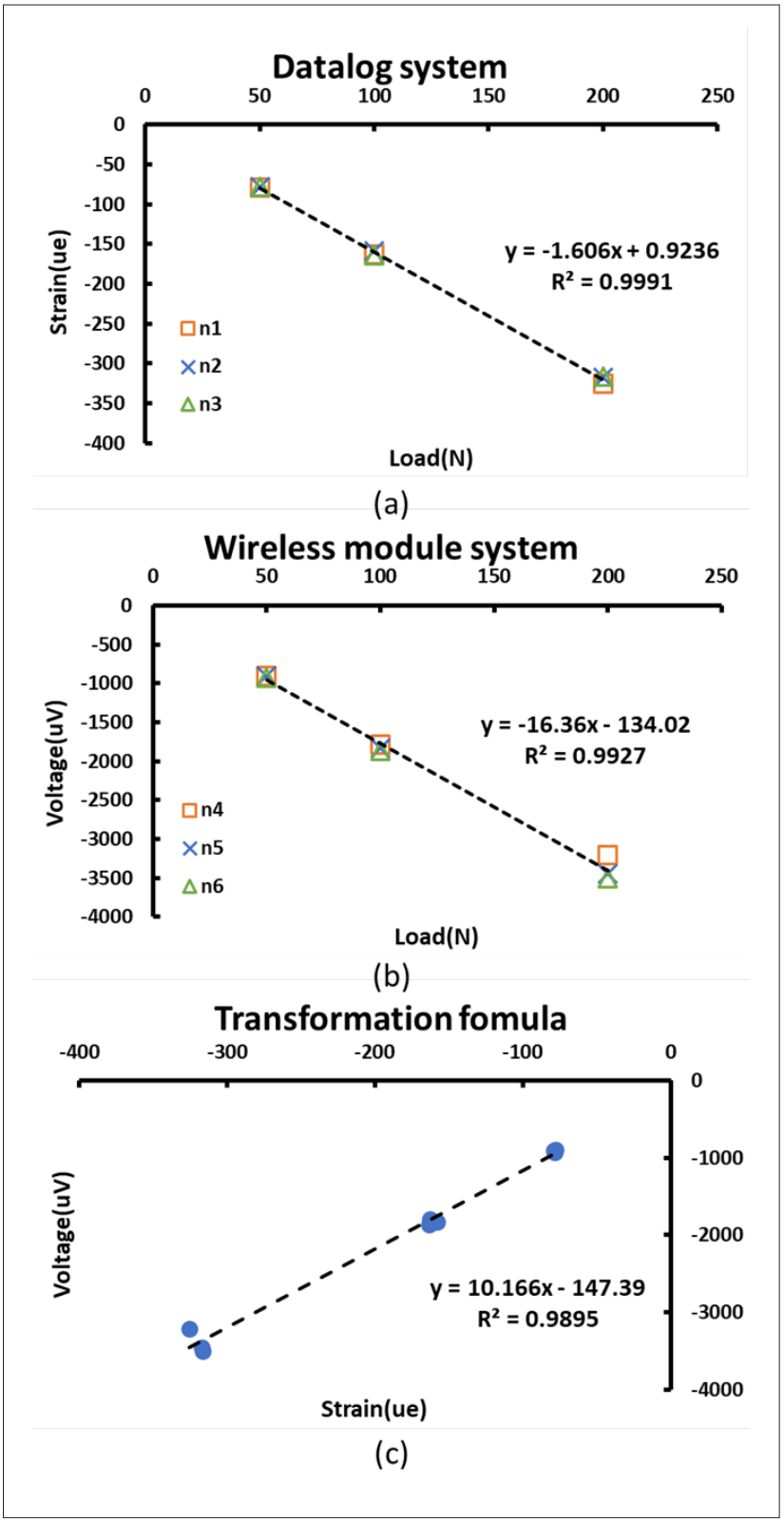


Figure 5. Linear regression plots for (a) the strain values vs. the applied load and recorded by signal data log system; (b) the voltage values vs. applied load and recorded using the wireless module system; (c) the voltage values measured using the wireless module system vs. the strain values obtained from the signal acquisition system.

Table 2. Strains obtained from wireless system at point A of cantilever and at point B derived from data log, and validated percentage error

	Strain (ue)			
	A	B	A/B	Error (%)
Test 1	-327.6	-151.5	2.16	16
Test 2	-327.0	-152.6	2.14	14
Test 3	-330.1	-154.9	2.13	13
Test 4	-322.7	-148.5	2.17	17
Test 5	-324.2	-150.3	2.16	16
Average	-326.3	-151.6	2.15	15.2
Std.	2.9	2.4	0.015	

load decreased. However, the fatigue loading cycles for the same load applied on the molars were higher compared to those on the premolars. Figure 7 shows that the failure patterns were the ramus fracture for the reconstructive plastic mandible under high applied loads even applied on the premolar or molar after fatigue tests.

4. Discussion

In recent years, the combination of sensors with implants and wearable devices to detect various physiological signals has emerged as an important research topic.[16,21] Commonly used sensors include accelerometers, gyroscopes, and strain gauges. However, accelerometers and gyroscopes are mostly utilized in wearable devices due to their larger size.[16,21] While wearable devices equipped with these sensors can

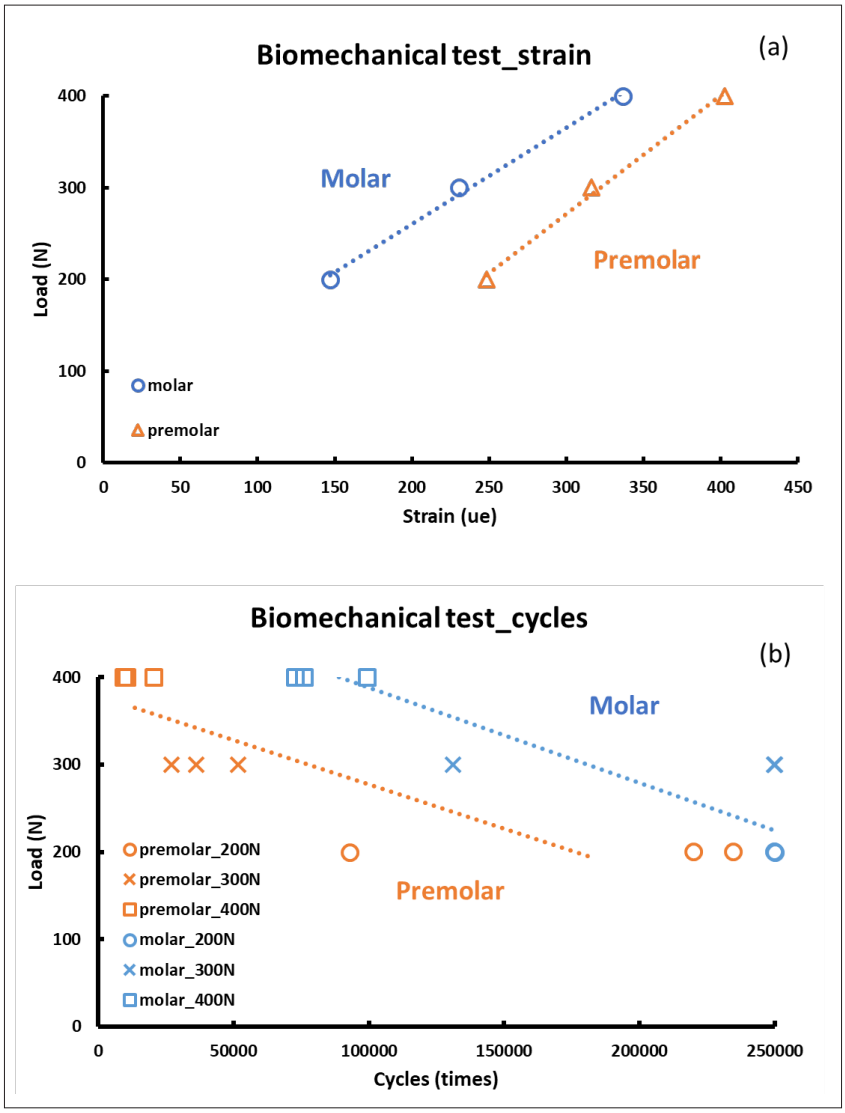


Figure 6. Biomechanical fatigue tests results for (a) average strain values vs. applied loads on the premolar/molar; (b) fatigue loading cycles vs. applied loads on the premolar/molar.

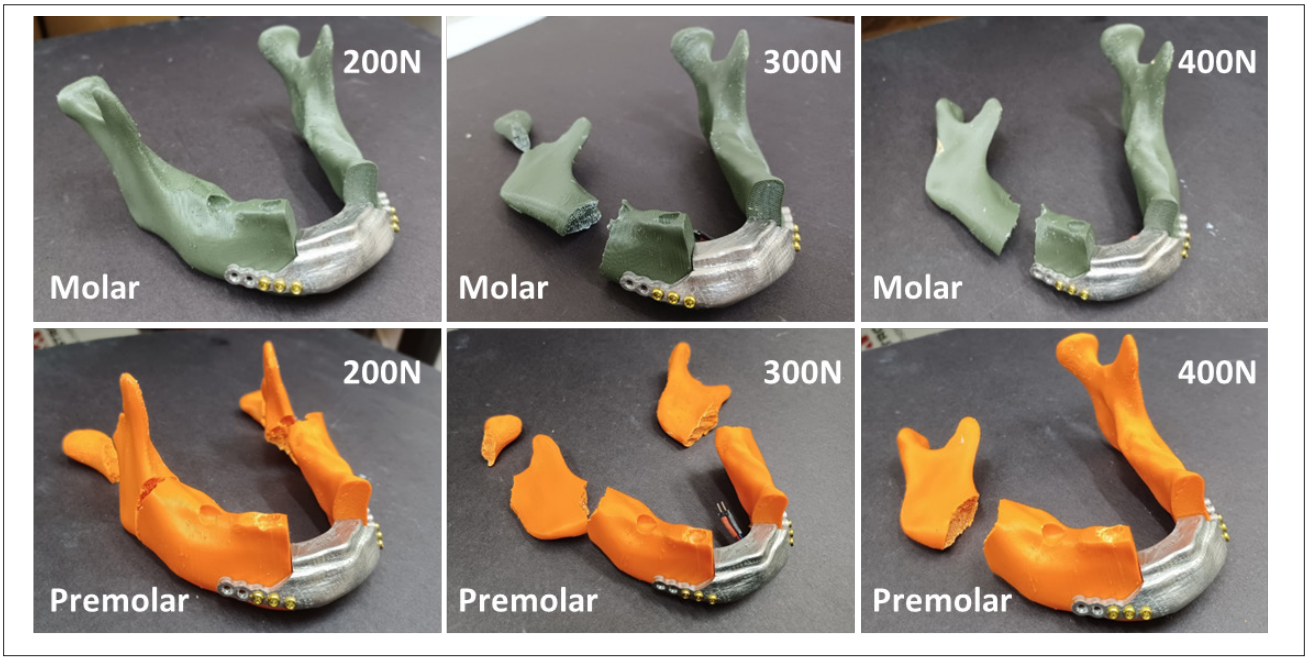


Figure 7. Failure patterns were found at the ramus fracture for the reconstructive mandible under different load magnitude applied on the premolar/molar after fatigue tests.

monitor and enhance musculoskeletal rehabilitation after surgery, the inherent larger size prevents their integration into 3D-printed mandibular reconstructive implants.

On the other hand, strain gauge-based measurement technology has been widely adopted in the medical field due to its advantages of small size and low cost. To achieve early biomechanical behavior detection after surgery, there is a need to develop miniaturized WMS for strain gauge measurements within the implant. This study focused only on modular development of single/uniaxial strain gauge systems, which was then installed in a 3D-printed MMPSI. This system enabled real-time monitoring of strain variations in the inner right buccal wall adjacent to the fixation wing under fatigue cyclic loads. Future developments may involve expanding this approach to multiple locations for further measurement and analysis.

The current WMS, including chips/circuit board/battery, measured approximately 20 mm × 12 mm × 8 mm in size. This indicated that the internal space design for a patient-specific 3D-printed reconstructive mandibular implant must be larger than this specific size when utilizing the WMS. Stability in the overall structure is a key factor guaranteeing internal space within mandibular implants. This can be accomplished through adherence to the design guidelines for patient-specific implants in various mandibular defects.

Our previous study proposed the design criterion for patient-specific 3D-printed reconstructed implants with appearance consideration and structural optimization of various mandibular continuity defects.[12] The different mandible continuity defects consist of five continuity mandibular defects, i.e., single B/C/A+B and combination of B+C and B+C+B segments, where defect C was the segmental defect and defined from left to right canines, defect B was defined from first premolar to third molar, and defect A was defined from third molar to ramus.[12] All five continuity mandibular defects had internal spaces larger than the volume of the WMS and possess adequate structural strength.

This study only focused initially on an experimental MMPSI and installed wireless modulus system as the testing sample in the available internal space. At the current stage, we aim to develop WMS for strain measurement and apply this system to understand its potential for early biomechanics monitoring verification of a patient-specific 3D-printed implant. However, smaller-sized chips are not feasible due to the higher production costs and the low demands. More applications can be realized in future through chip miniaturization if cost of making these chips through mass production can be reduced.

Furthermore, the current weight of the WMS was 4 g, and the total weight, including the 3D-printed metal implant, amounts to 17 g. However, the initial weight of

the removed bone segmental defect was approximately 6 g, implying the potential for further reduction in the volume of the WMS and the lightweight design of the 3D-printed implant.

In the biomechanical fatigue test, attaching strain gauges to the inner right buccal wall near the fixation wing was based on our previous FE study that highlighted this area as the most susceptible location for concentrated stress leading to implant fracture when occlusal force was applied on the 3D-printed implant.[12] Results from biomechanical *in vitro* fatigue tests revealed that strain values increased with higher applied force levels at the same load positions. Moreover, the strain received was higher when occlusal force was applied on the premolar under identical force application conditions, indicating that the premolar was closer to the strain gauge attachment location within the implant (as shown in Figure 8a). The applied load can be

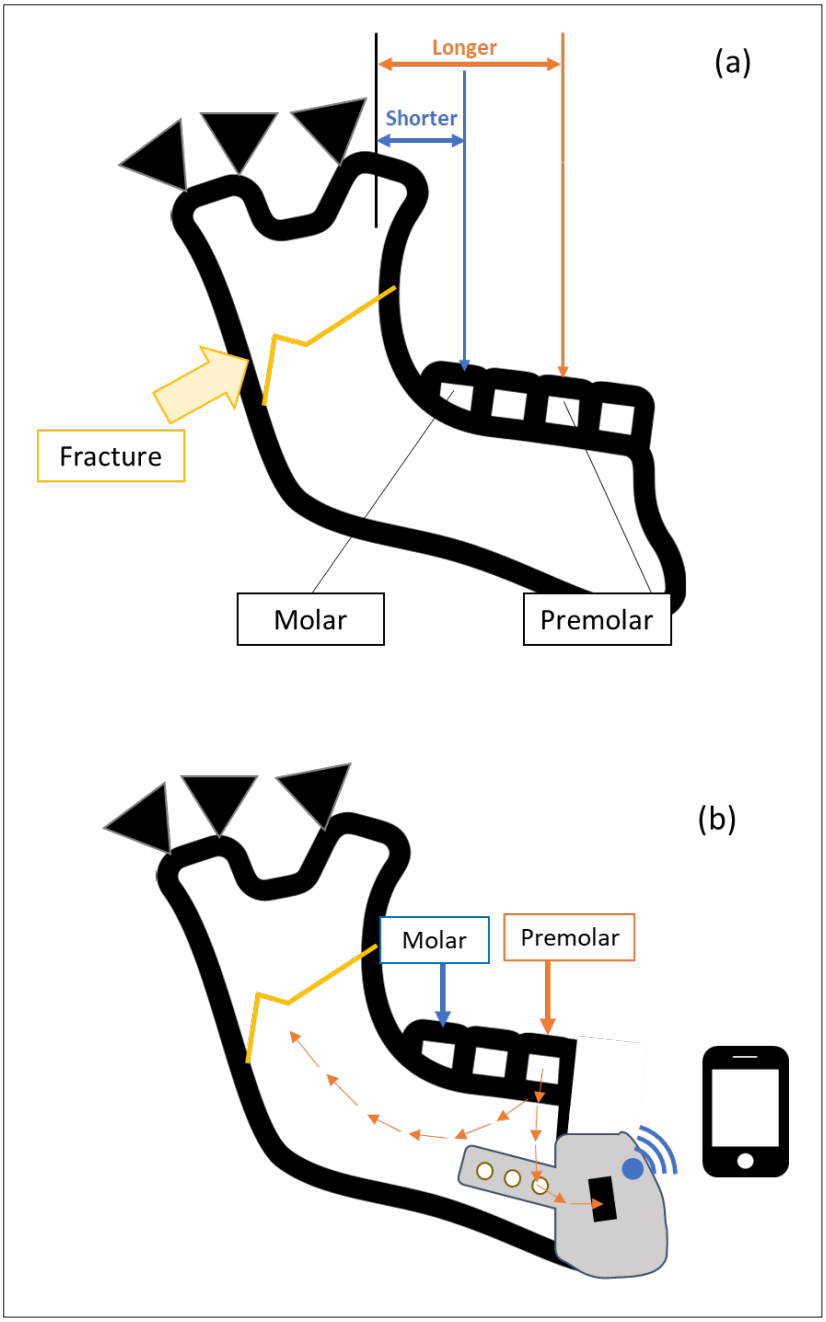


Figure 8. (a) Illustration of moment arms from condyle to premolar/molar; (b) applied load mechanism transmitted from premolar to implant and mandible.

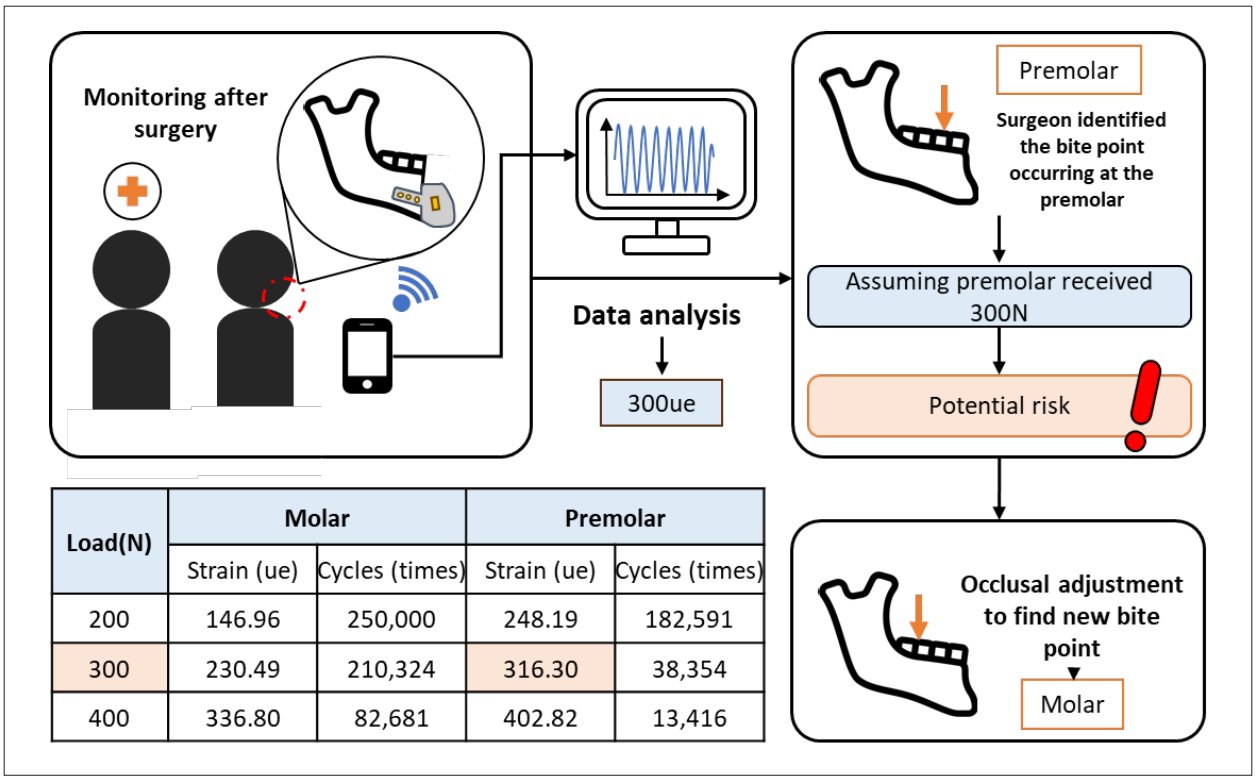
transmitted from the premolar separately to the mandible and the 3D-printed implant to receive higher strain values.

Comparing the fatigue cycles in the biomechanical fatigue tests revealed a decrease in fatigue cycles with an increase in applied force levels. Moreover, the mandible could endure more cyclic loads while the occlusal force is being applied on molar that is under the same load, due to the embedded location at the mandibular condyle, resulting in a longer lever arm for the premolar compared to the molar (as depicted in Figure 8b). This elongated lever arm at the premolar location generated a higher bending moment, making the mandibular model at the premolar position more susceptible to fracture.

The correlations derived from the biomechanical fatigue test between different occlusal forces, load positions, strains as well as fatigue cycles can offer valuable insights for monitoring the early mandibular stress conditions in patients after surgery (Figure 9). This information can assist surgeons in providing advice on bite adjustment and recommendations to patients, thereby reducing the probability of 3D-printed implant failure. Typically, the surgeon can identify the mandibular occlusion contact point (i.e., identifying the maximum occlusal force position) after surgery. The surgeon receives strain data through a mobile APP that enables stress condition assessment from our WMS employed for early monitoring after the surgery.

A schematic depicting the clinical application of our WMS is shown in Figure 9, under the premise that a surgeon has successfully identified the patient's bite point occurring at the premolar after surgery, and assuming that the accompanying APP received strain data of around 300 ue. Referring to the strain value/force location correlation, it is possible to estimate the current occlusal force at the bite point to be about 300 N, implying a potentially higher risk for mandibular implant failure in its current position. Therefore, the surgeon can consider adjusting the patient's bite location, shifting it toward the molar area, to mitigate the associated risk with the mandibular implant.

Several limitations of this study should be acknowledged. Presently, the internal space of the 3D-printed implant allowed for the insertion of only a 60 mAh lithium battery, which can only power the implants for approximately 10 h. Thus, this falls short of meeting the requirements for extended clinical usage. Future improvements should consider alternative power sources capable of providing longer-term power supply. In addition, the current developed WMS for strain measurement still needs to be improved in terms of size miniaturization,



Load(N)	Molar		Premolar	
	Strain (ue)	Cycles (times)	Strain (ue)	Cycles (times)
200	146.96	250,000	248.19	182,591
300	230.49	210,324	316.30	38,354
400	336.80	82,681	402.82	13,416

Figure 9. The correlations derived from the biomechanical fatigue test between different occlusal forces, loading positions, strains and fatigue cycles, and a schematic depicting the clinical application of WMS.

battery volume/overall weight reduction, and battery capability enhancement to allow for battery installation on the patient-specific implant for biomechanics detection. Besides, the WMS should also be compliant with U.S. Food and Drug Administration (FDA) pre-clinical testing requirements, such as meeting IEC60601 electrical safety standards to mitigate risks. Furthermore, the patient-specific implant may need to be designed with enough internal space to accommodate the WMS and should align with the surgical procedures of clinical physicians. It should be highlighted that conducting biomechanical *in vitro* fatigue tests with sole emphasis on single-point axial load forces is a limitation of this study for not able to explore the effects of other axial load forces. Following the successful application of the wireless module, future tests should expand their design to simulate more complex clinical occlusal scenarios. Moreover, it is essential to conduct tests on implants in other mandibular areas to provide a comprehensive assessment.

5. Conclusion

This study developed a miniature wireless module for strain measurement, capable of transmitting strain signals through a Bluetooth-enabled APP system. The relationships between strain, voltage, and force were determined, and the accuracy of our WMS was verified using cantilever beam model for the WMS. Biomechanical *in vitro* fatigue tests suggest that the developed wireless module's strain measurement system could potentially be utilized in a mandibular 3D-printed patient-specific implant to predict its biomechanical behavior in the future. Current fatigue experimental results revealed that applying single-point axial load force on the premolar led to fewer fatigue cycles and an increased susceptibility of the implant to failure due to the higher bending moment.

Acknowledgments

None.

Funding

This study was supported in part by NSTC project 112-2221-E-A49-009-MY3and111-2327-B-A49-006,Taiwan.

Conflict of interest

The authors declare no conflicts of interest.

Author contributions

Conceptualization: Cheng-Hsien Wu, Chun-Li Lin
Formal analysis: Hsiao-Kuan Wu, Pei-Jung Tsai
Investigation: Cheng-Hsien Wu, Hsiao-Kuan Wu, Pei-Jung Tsai, Chun-Li Lin
Methodology: Hsiao-Kuan Wu, Pei-Jung Tsai
Writing – original draft: Cheng-Hsien Wu, Chun-Li Lin
Writing – review & editing: Cheng-Hsien Wu, Chun-Li Lin

Ethics approval and consent to participate

Not applicable.

Consent for publication

Not applicable.

Availability of data

Data are available from the corresponding author upon reasonable request.

References

1. Lim HK, Choi YJ, Choi WC, Song IS, Lee UL. Reconstruction of maxillofacial bone defects using patient-specific long-lasting titanium implants. *Sci Rep*. 2022;12:7538. doi: 10.1038/s41598-022-11200-0
2. Cheng KJ, Liu YF, Wang R, et al. Topological optimization of 3D printed bone analog with PEKK for surgical mandibular reconstruction. *J Mech Behav Biomed Mater.* 2020;107:103758. doi: 10.1016/j.jmbbm.2020.103758
3. Jung HW, Lee BS, Kwon YD, et al. Retrospective clinical study of mandible fractures. *J Korean Assoc Oral Maxillofac Surg.* 2014;40(1):21-26. doi: 10.5125/jkaoms.2014.40.1.21
4. Maurer P, Eckert AW, Kriwalsky MS, Schubert J. Scope and limitations of methods of mandibular reconstruction: a long-term follow-up. *Br J Oral Maxillofac Surg.* 2010;48(2):100-104. doi: 10.1016/j.bjoms.2009.07.005
5. Lee SW, Kim HG, Ham MJ, Hong DGK, Kim SG, Rotaru H. Custom implant for reconstruction of mandibular continuity defect. *J Oral Maxillofac Surg.* 2018;76:1370-1376. doi: 10.1016/j.joms.2017.12.003
6. Patel A, Harrison P, Cheng A, Bray B, Bell RB. Fibular reconstruction of the maxilla and mandible with immediate implant-supported prosthetic rehabilitation: jaw in a day. *Oral Maxillofac Surg Clin North Am.* 2019;31:369-986. doi: 10.1016/j.coms.2019.03.002
7. Toure G, Gouet E. Use of a 3-dimensional custom-made porous titanium prosthesis for mandibular body reconstruction with prosthetic dental rehabilitation and lipofilling. *J Oral Maxillofac Surg.* 2019;77:1305-1313. doi: 10.1016/j.joms.2018.12.026
8. Zhang L, Liu Z, Li B, et al. Evaluation of computer-assisted mandibular reconstruction with vascularized fibular flap compared to conventional surgery. *Oral Surg Oral Med Oral Pathol Oral Radiol.* 2016;121(2):139-148.

doi: 10.1016/j.oooo.2015.10.005

9. Wilkman T, Apajalahti S, Wilkman E, Törnwall J, Lassus P. A comparison of bone resorption over time: an analysis of the free scapular, iliac crest, and fibular microvascular flaps in mandibular reconstruction. *J Oral Maxillofac Surg.* 2017;75(3):616-621.
doi: 10.1016/j.joms.2016.09.009

10. Kawasaki G, Imayama N, Yoshitomi I, Furukawa K, Umeda M. Clinical study of reconstruction plates used in the surgery for mandibular discontinuity defect. *In Vivo*. 2019;33(1):191-194.
doi: 10.21873/invivo.11458

11. van Kootwijk A, Moosabeiki V, Saldivar MC, et al. Semi-automated digital workflow to design and evaluate patient-specific mandibular reconstruction implants. *J Mech Behav Biomed Mater.* 2022;132:105291.
doi: 10.1016/j.jmbbm.2022.105291

12. Lin CL, Wang YT, Chang CM, Wu CH, Tsai WH. Design criteria for patient-specific mandibular continuity defect reconstructed implant with lightweight structure using weighted topology optimization and validated with biomechanical fatigue testing. *Int J Bioprint.* 2022;8(1):437.
doi: 10.18063/ijb.v8i1.437

13. Li CH, Wu CH, Lin CL. Design of a patient-specific mandible reconstruction implant with dental prosthesis for metal 3D printing using integrated weighted topology optimization and finite element analysis. *J Mech Behav Biomed Mater.* 2020;105:103700.
doi: 10.1016/j.jmbbm.2020.103700

14. Subash P, Nerurkar SA, Krishnadas A, Vinay V, Iyer S, Manju V. Patient specific alloplastic implant reconstruction of mandibular defects-safe practice recommendations and guidelines. *J Maxillofac Oral Surg.* 2023;22(Suppl 1):28-36.
doi: 10.1007/s12663-023-01881-z

15. Bedogni A, Bettini G, Bedogni G, et al. Safety of boneless reconstruction of the mandible with a CAD/CAM designed titanium device: the replica cohort study. *Oral Oncol.* 2021;112:105073.
doi: 10.1016/j.oraloncology.2020.105073

16. Cozzolino F, Apicella D, Wang G, Apicella A, Sorrentino R. Implant-to-bone force transmission: a pilot study for in vivo strain gauge measurement technique. *J Mech Behav Biomed Mater.* 2019;90:173-181.
doi: 10.1016/j.jmbbm.2018.10.014

17. Arami A, Delaloye JR, Rouhani H, Jolles BM, Aminian K. Knee implant loosening detection: a vibration analysis investigation. *Ann Biomed Eng.* 2018;46(1):97-107.
doi: 10.1007/s10439-017-1941-2

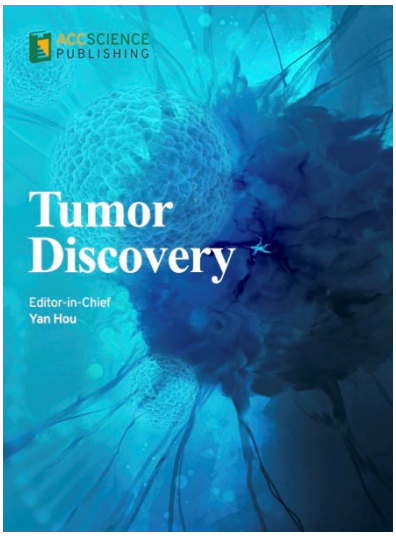
18. Seide K, Aljudaibi M, Weinrich N, et al. Telemetric assessment of bone healing with an instrumented internal fixator: a preliminary study. *J Bone Joint Surg Br.* 2012;94(3):398-404.
doi: 10.1302/0301-620X.94B3.27550

19. Schupp W, Arzdorf M, Linke B, Gutwald R. Biomechanical testing of different osteosynthesis systems for segmental resection of the mandible. *J Oral Maxillofac Surg.* 2007;65:924-930.
doi: 10.1016/j.joms.2006.06.306

20. Lin CL, Wang JC, Chang WJ. Biomechanical interactions in tooth-implant-supported fixed partial dentures with variations in the number of splinted teeth and connector type: a finite element analysis. *Clin Oral Implants Res.* 2008;19:107–117.
doi: 10.1111/j.1600-0501.2007.01363.x

21. Ren R, Spaan J, Jordan A, Shafiro A, Su EP. Novel use of an accelerometer to assess load asymmetry over time after hip resurfacing arthroplasty. *J Arthroplasty.* 2023;38(7S):S58-S64.
doi: 10.1016/j.arth.2023.04.015

Our Journals

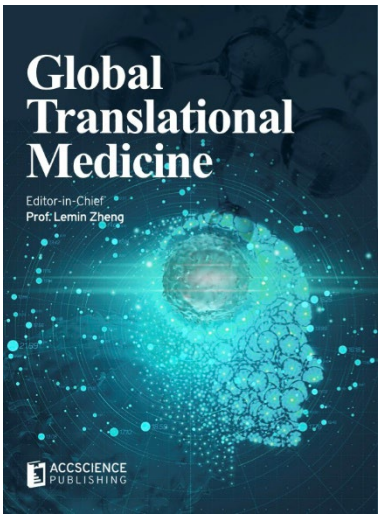


Tumor Discovery is a peer-reviewed and open-access journal that aims to present new cancer research with strong emphasis on fundamental and translational studies. *Tumor Discovery* covers topics, including but not limited to the following:

- Etiology and pathogenesis of cancer
- Mechanisms and molecular pathways underlying cancer initiation and progression
- Tumor metastasis
- Tumor evolution and heterogeneity
- Tumor microenvironment and tumor-host interactions
- Cancer genetics and genomics
- Cancer characterization using omics approaches
- Discovery and validation of cancer biomarker
- Discovery of new therapeutic targets
- New approaches of diagnostic and treatment modalities
- Statistical methods in cancer research

Global Translational Medicine is a quarterly journal that focuses on medicine, biological sciences, and biomaterials engineering. The goal of *Global Translational Medicine* is to provide a platform to researchers for showcasing their latest research works in translational medicine so as to advance the field towards the betterment of human health. Despite the advancement of omics and new technologies, the process of transforming these technologies and scientific research results into effective therapies and putting them into clinical use still has a long way to go. *Global Translational Medicine* provides a platform to fill the gaps in preclinical and inter-disciplinary research, to promote clinical translation of scientific research results, and to contribute to the conception of new and improved preventive measures as well as diagnostic and therapeutic techniques of diseases.

Global Translational Medicine covers the following themes: cardiovascular disease, metabolism/diabetes/obesity, neuroscience/neurology, cancer, biomaterials and their applications in medicine, proteomics/metabolomics, pharmacogenomics, biomarkers, bioinformatics and data mining, animal and clinical research, and medical methods arising from interdisciplinary crossover.



Start a new journal

Write to us via email if you are interested to start a new journal with AccScience Publishing. Please attach your CV, professional profile page and a brief pitch proposal in your email. We shall inform you of our decision whether we are interested to collaborate in starting a new journal.

Contact: info@accscience.com

ACCSCIENCE PUBLISHING

ACCSCIENCE PUBLISHING

Publishing Office:
8 Burn Road, #15-03 Trivex, Singapore 369977.
Editorial Office:
30-2, Jalan BS 1/2, Olive Hill Business Park, 43300 Seri Kembangan, Selangor. Malaysia.

Editorial Office: editor.ijb@accscience.com
General Inquires: info@accscience.com

https://accscience.com/journal/IJB